

# THIS WEEK



## EDITORIALS

**CLIMATE** Dishonesty is a weapon not suited to scientists **p.440**

**WORLD VIEW** How Alan Turing managed to go from zero to hero **p.441**

**GOING DOWN** Madagascan jungle harbours smallest lizard **p.442**

## Flu papers warrant full publication

*Although more debate is needed, the benefits of publishing sensitive data outweigh the risks that have so far been made public.*

**N**o one should presume to know all the ways in which influenza virus could be misused, and the motivations for doing so, but the consequences could be catastrophic. There are many scenarios to consider, ranging from mad lone scientists, desperate despots and members of millennial doomsday cults to nation states wanting mutually assured destruction options, bioterrorists or a single person's random acts of craziness. These are low-probability events, but they could introduce a new evolutionary H5N1 seed into the environment that seems not to exist in nature. This might not cause a pandemic instantly, but it could start the virus on a new path for pandemic evolution."

That is the rationale provided by Paul Keim, acting chair of the US National Science Advisory Board for Biosecurity (NSABB), in response to questions posed by *Nature* (P. S. Keim *Nature* **482**, 156–157; 2012) about the NSABB's recommendation that recent work on the transmissibility in mammals of artificial strains of avian H5N1 influenza virus should not be published in full. The work was conducted in ferrets — generally considered the best animal models for human transmission — and shows that avian H5N1 viruses have a greater potential to evolve into transmissible forms in mammals, including humans, than had been thought. The work is reported in two papers accepted but not yet published in *Nature* and *Science*.

Last week, a group of flu and public-health experts gathered at the World Health Organization (WHO) headquarters in Geneva, Switzerland, to discuss the matter (see [go.nature.com/uyr1uu](http://go.nature.com/uyr1uu)). And it was clear at the meeting that the above opening quote expresses the only rationale that attendees had received.

To its credit and that of the US government, the NSABB is the only body in the world set up to review these issues in a systematic fashion. It includes ex-officio representatives of all relevant government departments (including intelligence and security agencies), as well as independent researchers. The NSABB's guidance was an important first step in public consideration of the impacts and potential regulation of such research. The second step was last week's meeting at the WHO — again, like the NSABB, a body empowered to make recommendations.

Some context is important in considering the issues surrounding publication. In 2003, *Nature* and many other journals met to establish editorial procedures for considering papers that have public-health and scientific benefits but that might also have biosecurity risks (see *Nature* **421**, 771; 2003). The statement that emerged from that meeting envisaged the possibility that a journal would reject a paper if it was clear that the risks of publication outweighed the benefits. *Nature* accordingly used independent advisers in considering the submission of the latest paper, and most of the advisers recommended publication in full. This is also the first paper submitted to any *Nature* journal for which recommendations have been made against publication on biosecurity grounds.

Rather than simply reject the papers, given also the NSABB's opinion,

both *Nature* and *Science* decided to investigate another option: to publish a redacted version omitting key methods and data. But a condition of such an approach was that a method should exist for distributing a full version to those in need of the results for public-health reasons and those capable of pursuing the science. Both journals accordingly prepared full and redacted versions.

Those at the WHO meeting, under conditions of strict security, examined both versions of the two papers. It had already been said in blogs and news coverage that, because the methods used are not novel, and because one of the papers had been presented at an open meeting, redaction would be pointless. As one WHO participant said: "It was only when I'd seen both versions that I realized how ineffective redaction would be." What was also concluded was that a system for distributing the full paper only to selected individuals would be impossible to set up on any relevant timescale.

But what also became clear, partly from unpublished data, was that not only does the mammalian transmissibility threat seem greater than previously thought, but also that current avian viruses have some of the mutations identified in the new work. In other words, there is already a substantial immediate risk to humans. The meeting also concluded that the new data are of value for surveillance, and that the results should be built on to explore the mechanisms underlying transmissibility and the high fatality rate observed in humans infected by H5N1.

Given the inadequacy of redaction, and the immediate risks to global public health, the biosecurity objections expressed above seem too general and hypothetical to justify obstructing publication and further research. Moreover, with regard to the NSABB's recommendations and the recommendations of the WHO meeting (see [go.nature.com/ky2skc](http://go.nature.com/ky2skc)), neither of the discussions that preceded them were sufficiently inclusive of the security, societal and research interests at stake.

Therefore, further discussion is essential. That must include a review of the safety regimes (lab equipment, buildings and practices) in which future work should be conducted. The two laboratories in which the latest research originated are categorized as 'BSL-3 enhanced' (see *Nature* **480**, 421–422; 2011), a classification that, although rigorous in these cases, is not well defined in general. The Public Health Agency of Canada has deemed the highest level of BSL-4 to be required (see page 447). Safety-standards committees in the United States and Europe are currently assessing required safety levels, and may report within a few weeks.

As was agreed by the journals and the lead authors at the meeting, publication of the papers must wait at least for the outcome of those discussions. There may yet be regulatory or legal obstacles to publication, or biosecurity or biosafety risks sufficient to outweigh the health risks. Otherwise, it is *Nature's* view that the papers should ultimately be published in full. ■

**"There is already a substantial immediate risk to humans."**

# Turing at 100

*This year marks the centenary of the birth of Alan Turing. He deserves your attention.*

Come the summer, many minds will turn to sport as the London Olympics kicks off. So it seems apt that, in a special issue this week, *Nature* invites its readers to embrace and celebrate a superb marathon runner — who also happened to be one of the brightest minds of all time.

Alan Turing, computer pioneer, wartime code-breaker and polymath, was born in London on 23 June 1912. But for injury, he would probably have joined the British Olympic team for the London games of 1948. (His personal best marathon time of 2 hours and 46 minutes was barely 11 minutes behind the gold medallist that year.) Yet, 100 years and one month after his birth, when the Olympics will return to the city, no official celebration of the connection is planned. An opportunity to bring an intellectual giant — and science itself — to the attention of the international public will be missed.

Turing's marathon time gives us an objective quantification of his physical excellence. His scientific genius and legacy, however, are much more difficult to measure — as his biographer, Andrew Hodges, a mathematician at the University of Oxford, UK, points out on page 441. Still, setting aside quarrels over his role in the development of the computer, the scientific world should stand together and relish the wonderful diversity of a universal mind. (See the special section starting on page 455 and [www.nature.com/turing](http://www.nature.com/turing) for more.)

The scope of Turing's achievements is extraordinary. Mathematicians will honour the man who cracked David Hilbert's *Entscheidungsproblem* or 'decision problem', and cryptographers and historians will remember him as the man who broke Nazi Germany's Enigma code and helped to shorten the Second World War. Engineers will hail the founder of the digital age and artificial intelligence. Biologists will pay homage to the theoretician of morphogenesis, and physicists will raise a glass to

the pioneer of nonlinear dynamics. Philosophers, meanwhile, are likely to continue to frown over his one-liners on the limits of reason and intuition: "If a machine is expected to be infallible, it cannot also be intelligent," he said in a 1947 talk to the London Mathematical Society.

Turing demonstrated a terrific ability to combine first-hand experimentation, keen observation, rigorous theory and practical application. His multidisciplinary approach alone makes him of interest to this journal,

**"Turing's mind was truly his own, and this contributed to the tragedy of his life."**

yet questions still arise on whether the best papers in pure mathematics, computer science and artificial intelligence should be published in *Nature*. We certainly think so.

So, too, do the researchers invited to decode Turing's legacy in a series of Comment articles, starting on page 459. They are thought-provoking pieces in their own right, but, more importantly, we hope that they will entice readers to seek out Turing's original work (see, for example, B. J. Copeland (ed.) *The Essential Turing*; Clarendon, 2004). His papers are models of accessibility and clarity, despite their extreme conceptual depth and intellectual rigour. Even his throwaway comments — about symmetry in physics versus biology, randomness in intelligence, learning in unorganized machines, or emotions in extrasensory perception, for example — are gems.

Turing's mind was truly his own, and this contributed to the tragedy of his life. Turing was persecuted by the British authorities for his homosexuality, and used cyanide to take his own life, aged 41.

That 2012 will see numerous events commemorating Turing worldwide (see, for example, [www.turingcentenary.eu](http://www.turingcentenary.eu)) is almost entirely down to volunteers, who have received little or no official help. This is in stark contrast to the World Year of Physics in 2005, when the German state helped to promote the centenary of Albert Einstein's 'miracle year', in which he published his four groundbreaking papers.

What could 2012, the Alan Turing year, be named? *Nature* suggests 'The Year of Intelligence'. Of the finest types of intelligence — human, artificial and military — Turing is perhaps the only person to have made a world-changing contribution to all three. Use this special issue, and the rest of 2012, to discover and make up your own mind about this extraordinary man. ■

## Over the line

*Dishonesty, however tempting, is the wrong way to tackle climate sceptics.*

In a much-quoted Editorial in March 2010 (*Nature* **464**, 141; 2010), this publication urged researchers to acknowledge that they are involved in a street fight over the communication of climate science. So would it now be hypocritical to condemn Peter Gleick for fighting dirty? Gleick, a hydroclimatologist and president of the Pacific Institute for Studies in Development, Environment and Security in Oakland, California, admitted in a statement on news website *The Huffington Post* on 20 February that he had duped the Heartland Institute, a right-wing think tank based in Chicago, Illinois, into handing over documents that detailed its financial support for climate sceptics. Gleick had passed these documents on to the website DeSmogBlog.com, which made them public on 14 February.

Gleick's deception — using an e-mail address set up in someone else's name to request the documents from Heartland — is certainly in line with some of the tactics used to undermine climate science. When in November 2009 a hacker distributed thousands of e-mails stolen from climate researchers at the University of East Anglia in Norwich, UK, Heartland was prominent among those who criticized not the hacker, but the scientists who wrote the messages. However,

Gleick, as he has admitted, crossed an important line when he acted in such a duplicitous way. It was a foolish action for a scientist, especially one who regularly engages with the public and critics. Society rightly looks to scientists for fairness and impartiality. Dishonesty, whatever its form and motivation, is a stain on the individual and the profession. Gleick does deserve credit for coming clean — but, it must be said, he did so only after he was publicly accused on the Internet of being involved.

The original accusation, incidentally, was more serious: that Gleick had deliberately forged a Heartland Institute memo that brought together, with suspicious convenience, the most incriminating sections of the other climate documents, which seem to have been presented to the Heartland board meeting in January. He denies doing so, and says that he received the memo, in which he is named and which Heartland says has been faked, separately from an anonymous source. The e-mail chicanery, he says, was an attempt to check whether it was genuine.

In his statement on Monday, Gleick said: "My judgment was blinded by my frustration with the ongoing efforts — often anonymous, well-funded, and coordinated — to attack climate science and scientists and prevent this debate, and by the lack of transparency of the organizations involved. Nevertheless I deeply regret my own actions in this case."

On 24 January, Gleick had published another article in *The Huffington Post*, entitled 'Climate Change: Sifting Truth From Lies in a Complex World'. As he now knows, the best way for scientists to help people find this truth is through open and honest debate. ■

**➤ NATURE.COM**  
To comment online,  
click on Editorials at:  
[go.nature.com/xhunqv](http://go.nature.com/xhunqv)



## The man behind the machine

Alan Turing is famous for many reasons. Andrew Hodges delves into why Turing's achievements took so long to be recognized.

Alan Turing is always in the news — for his place in science, but also for his 1952 conviction for having gay sex (illegal in Britain until 1967) and his suicide two years later. Former Prime Minister Gordon Brown issued an apology to Turing in 2009, and a campaign for a 'pardon' was rebuffed earlier this month.

Must you be a great figure to merit a 'pardon' for being gay? If so, how great? Is it enough to break the Enigma ciphers used by Nazi Germany in the Second World War? Or do you need to invent the computer as well, with artificial intelligence as a bonus? Is that great enough?

Turing's reputation has gone from zero to hero, but defining what he achieved is not simple. Is it correct to credit Turing with the computer? To historians who focus on the engineering of early machines, Turing is an also-ran. Today's scientists know the maxim 'publish or perish', and Turing just did not publish enough about computers. He quickly became perishable goods. His major published papers on computability (in 1936) and artificial intelligence (in 1950) are some of the most cited in the scientific literature, but they leave a yawning gap. His extensive computer plans of 1946, 1947 and 1948 were left as unpublished reports. He never put into scientific journals the simple claim that he had worked out how to turn his 1936 "universal machine" into the practical electronic computer of 1945. Turing missed those first opportunities to explain the theory and strategy of programming, and instead got trapped in the technicalities of primitive storage mechanisms.

He could have caught up after 1949, had he used his time at the University of Manchester, UK, to write a definitive account of the theory and practice of computing. Instead, he founded a new field in mathematical biology and left other people to record the landscape of computers. They painted him out of it. The first book on computers to be published in Britain, *Faster than Thought* (Pitman, 1953), offered this derisive definition of Turing's theoretical contribution:

"Turing machine. In 1936 Dr. Turing wrote a paper on the design and limitations of computing machines. For this reason they are sometimes known by his name. The umlaut is an unearned and undesirable addition, due, presumably, to an impression that anything so incomprehensible must be Teutonic."

That a book on computers should describe the theory of computing as incomprehensible neatly illustrates the climate Turing had to endure. He did make a brief contribution to the book, buried in chapter 26, in which he summarized computability and the universal machine. However, his low-key account never conveyed that these central concepts were his own, or that he had planned the computer revolution.

The 1955 Royal Society's obituary of Turing, written by mathematician Max Newman, did him few favours when it claimed that computer designers were unaware of Turing's 1936 work. The Turing machines soon made a comeback, but Turing's image had become that of a pure mathematical logician, unrelated to practicality. It did not help that anyone looking into his story after his death would see dark hints that he had been *persona non grata* in an unmentionable manner — possibly excusable for a remote theorist from Cambridge University, but totally inappropriate for the founder of a mega-industry.

Yet the mid-1970s revealed Turing to have been highly practical: the chief scientific figure at code-breaking headquarters Bletchley Park, and in charge of methods and state-of-the-art machines for beating the German navy. Now it was clear why he had emerged as a computer builder in 1945 — he had gained experience he could never reveal. By the 1970s, there was also more room for his vision of computation. Software for "every known process", as he foresaw in 1946, was on the way. Turing's vision of mind and machine, which drew from his personal consciousness and experience, also became more acceptable. When in 1977 I started to investigate Turing's life, I found that his code-breaking was the hidden bridge between the 1936 theory and the "universal practical computing machine" he described in his unpublished 1948 work.

On the question of individual reputation, in that 1948 report he wrote: "The isolated man does not develop any intellectual power. It is necessary for him to be immersed in an environment ... He may then perhaps do a little research of his own and make a very few discoveries ... the search for new techniques must be regarded as carried out by the human community as a whole, rather than by individuals." Science is like that, and he effaced himself in that spirit. But he was a star nonetheless.

What would Turing have thought of the campaign for his 'pardon'? When arrested, he was unrepentant and told police he expected a "Royal Commission to legalize it". Sixty years later, British law has caught up, not for him as a special case, but as a matter of principle. That practical action speaks louder than symbolic words, and is truer to his vision. I see the question not as whether the government should have pardoned Turing, but how on Earth Turing could ever have pardoned the government. ■

ANYONE LOOKING  
INTO HIS  
**STORY**  
AFTER HIS DEATH  
WOULD SEE  
**DARK HINTS**  
THAT HE HAD BEEN  
**PERSONA NON GRATA.**



### TURING AT 100

A legacy that spans science:  
[nature.com/turing](http://nature.com/turing)

Andrew Hodges is a mathematician at the University of Oxford, UK, and author of *Alan Turing: the Enigma*.  
e-mail: [andrew.hodges@wadh.ox.ac.uk](mailto:andrew.hodges@wadh.ox.ac.uk)



# RESEARCH HIGHLIGHTS

Selections from the scientific literature

## BIOPHYSICS

### Claustrophobic DNA in tug of war

When a long thin polymer such as DNA is forced into a confined space — say a small membrane channel — it loses some of its freedom, and hence its entropy. Regaining that entropy is a powerful driving force for escape.

Chia-Fu Chou at the Academia Sinica in Taipei and his colleagues used an electric pulse to force a single DNA molecule to extend from one microchannel to another through a restrictive gap just nanometres high. When the electric field was turned off, a tug-of-war lasting from seconds to minutes occurred as both ends of the DNA tried to pull out of the nanometre-sized space. Eventually, one side won and the DNA retracted.

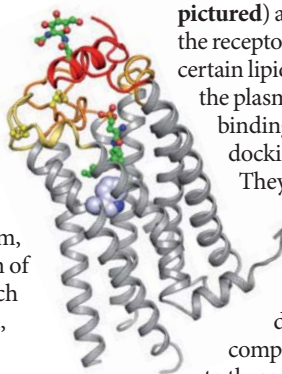
The forces acting on the DNA depended only on the height of the confined passage between channels, and not on its length or the length of DNA passing through it. This understanding could aid applications from molecular filters to nanopore transporters, the authors say. **Nano Lett.** <http://dx.doi.org/10.1021/nl2045292> (2012)

## CELL SIGNALLING

### Sideways activation

Elucidation of a cell receptor's crystal structure has revealed a unique lateral docking mechanism, report Hugh Rosen of the Scripps Research Institute in La Jolla, California, and his colleagues.

G-protein-coupled receptors (GPCRs) are



signalling molecules that span the plasma membranes of cells and are generally activated by external molecules that pass through a channel-like opening into a binding site. However, the researchers determined the crystal structure of the sphingosine 1-phosphate receptor 1 (S1P<sub>1</sub>, pictured) and showed that the receptor is triggered by certain lipids passing through the plasma membrane and binding through the lateral docking mechanism.

They also found that S1P<sub>1</sub> has atypical binding sites in less conserved regions of the docking site and that compounds that adhere to these activate S1P<sub>1</sub> more specifically than do lipids.

**Science** 335, 851–855 (2012)



## EVOLUTION

### Lilliputian lizards come to light

The forests of northern Madagascar harbour a dwarf chameleon that is the smallest lizard in the world in terms of total length. Adult males of the diminutive *Brookesia micra* reach a length of less than 24 millimetres.

*B. micra* and three other tiny lizard species were discovered in the region's rainforests and dry forests. Miguel Vences at the Technical

University of Braunschweig in Germany and his group analysed tail length and head width, male genital morphology and gene sequences to place each species within the chameleon taxonomy. All occupy a small, discrete geographical range, and probably evolved some 10 million to 20 million years ago, the authors suggest.

**PLoS ONE** 7, e31314 (2012)

## BIOLOGY

### Immunity's circadian link

Daily patterns in the body's biochemical and physiological processes called circadian rhythms may influence immune-system function. Erol Fikrig and his colleagues at Yale University in New Haven, Connecticut, have found that the expression of an immune protein called TLR9 rises and falls with the circadian cycle.

They induced sepsis in mice to examine whether pathogen recognition — a key part of the immune response — varies with circadian cycles. Higher TLR9 expression at the time of sepsis induction was linked to a worse outcome for mice. This suggests that daily fluctuations in biological processes may

influence vulnerability to infections, as well as the efficacy of immune therapies such as TLR9 agonists, which are currently in development. **Immunity** <http://dx.doi.org/10.1016/j.immuni.2011.12.017> (2012)

## STEM-CELL BIOLOGY

### Restore my beating heart

Infusions of a patient's own cardiac stem cells may reduce scar tissue and promote heart-muscle growth after a heart attack, according to a small safety study. Eduardo Marbán of the Cedars-Sinai Heart Institute in Los Angeles, California, and his colleagues harvested heart cells from 17 heart-attack patients. The cells were used to grow cardiac stem

J. KOEHLER



cells that were then reinfused.

Six months later, patients had 28% less scar tissue mass than control patients who did not receive the infusion. Viable heart tissue mass also increased following the treatment, suggesting partial restoration of tissue lost during the heart attack. However, patients showed no improvement in several measurements of heart function, such as the volume pumped out of the left ventricle with each heartbeat.

**Lancet** [http://dx.doi.org/10.1016/S0140-6736\(12\)60195-0](http://dx.doi.org/10.1016/S0140-6736(12)60195-0) (2012)

## GENOMICS

## Loss-of-function found in droves

Genome-sequencing work has suggested that even healthy humans carry hundreds of 'loss of function' (LoF) mutations that seriously disrupt protein-coding genes. Daniel MacArthur at the Wellcome Trust Sanger Institute in Hinxton, UK, and his colleagues performed extensive analysis on 185 genomes and determined that a typical individual carries around 100 LoF variants, of which about 20 inactivate both copies of a gene.

Most of the common mutations occurred in non-essential genes and didn't seem to affect health. The team also identified many rare LoF variants found in less than 1% of the population, including 47 serious disease mutations in one copy of a gene. By studying differences between the harmful and neutral variants, the scientists developed an algorithm to prioritize mutations found in medical genome sequencing for further investigation.

**Science** 335, 823–828 (2012)

## ASTROPHYSICS

## Zombie star rising

When a star suddenly brightened in 1961, many assumed it had died in a supernova — but it seems

that the light has not yet gone out. Schuyler Van Dyk at the California Institute of Technology in Pasadena and Thomas Matheson at the National Optical Astronomy Observatory in Tucson, Arizona, examined ground- and space-based observations, and say that it still lives.

The duo reports that the star, designated 'Object 7', can be seen on the Hubble Space Telescope as a luminous blue variable (LBV) star. The authors suggest that the decades-old outburst could represent a 'supernova imposter', a type of explosion for which LBVs are known that doesn't destroy the parent star. Nevertheless, Object 7 may be on course to explode, and astronomers should look out for its stellar death rattle.

**Astrophys. J.** 746, 179 (2012)

## IMMUNOLOGY

## Immune system master switch

The fetal immune system develops from stem cells in the liver, whereas the immune cells that protect adults form in the bone marrow. Moreover, early in life the immune system contains cells that quickly respond to only a limited number of foreign molecules; adult immune cells can recognize almost anything that might harm a host.

A 'master-switch' gene called *Lin28b* accounts for these differences, report Stefan Muljo and his team at the National Institute of Allergy and Infectious Diseases in Bethesda, Maryland. *Lin28b* — which blocks a class of gene-regulating RNA fragments called microRNAs — is active in the stem cells that form a mouse's immune system early in life, yet is absent from adult bone marrow. Marrow cells engineered to express a closely related gene, *Lin28*, and transplanted into adult mice form fetal-like immune cells.

Because the fetal-like immune cells are known to be effective against some pathogens, cancers and other

COMMUNITY  
CHOICE

The most viewed  
papers in science

CHEMISTRY

### Simple solution for tricky chemistry

HIGHLY READ  
on [pubs.acs.org](http://pubs.acs.org)  
in January

Chemists have invented a reagent to ease the addition of a desirable chemical group to many useful compounds. Pharmaceutical, medicinal and agricultural chemists add fluorine groups to molecules to improve certain properties — to lower toxicity, for example. However, adding a difluoromethyl group has proved complicated. The process developed by Phil Baran at the Scripps Research Institute in La Jolla, California, and his colleagues does the job in a simple one-pot reaction. The authors used zinc difluoromethylsulphinate salt, a white powder that is soluble in water and stable in air, making it easy to handle. In water, this produces a reactive difluoromethyl radical that targets specific sites on other molecules. In particular, Baran's reagent can add a difluoromethyl group to nitrogen-containing aromatic ring systems and onto some organic molecules containing sulphur. **J. Am. Chem. Soc.** 134, 1494–1497 (2012)

diseases, coaxing transplanted bone marrow cells to take on fetal properties could be used to improve immune responses.

**Science** <http://dx.doi.org/10.1126/science.1216557> (2012)

## ZOOLOGY

## Antifreeze's role in fish spread

Antifreeze proteins in the bodily fluids of Antarctic fishes are a crucial adaptation to life in the freezing waters — but their appearance alone is insufficient to explain the huge diversity of the region's fish species. Thomas Near of Yale University in New Haven, Connecticut, and his colleagues constructed a phylogeny of these notothenioid fishes (a sample pictured) and correlated it to both the appearance of the proteins and changes in global climate.

Contrary to the perception that the appearance of antifreeze proteins was the crucial factor driving evolution, they found that the most species-rich lineages diversified at least 10 million years after the proteins' appearance. This bout of evolution happened



during a second cooling event in the Late Miocene (11.6 million to 5.3 million years ago), when ice activity in the Southern Ocean is thought to have increased. The authors suggest that the appearance of this new polar habitat, combined with the pre-existing antifreeze proteins, spurred the evolution of notothenioids.

**Proc. Natl Acad. Sci. USA** <http://dx.doi.org/10.1073/pnas.1115169109> (2012)

### NATURE.COM

For the latest research published by Nature visit:  
[www.nature.com/latestresearch](http://www.nature.com/latestresearch)

T. J. NEAR

# SEVEN DAYS

The news in brief

## POLICY

### Flu work freed

Two studies that created ferret-transmissible strains of the highly pathogenic avian H5N1 influenza A virus should be published in full, a meeting of 22 experts convened by the World Health Organization in Geneva, Switzerland, concluded on 17 February. Last December, the US government and the US National Science Advisory Board for Biosecurity had asked that the research be censored. See pages 439 and 447 for more.

### Climate politics

A high-profile water and climate scientist acknowledged on 20 February that he had dishonestly acquired internal budget documents from the Heartland Institute, a libertarian think tank in Chicago, Illinois, that aims to combat climate science. Peter Gleick, president of the Pacific Institute in Oakland, California, released the documents to environmental website DeSmogBlog. Heartland has not disputed the authenticity of most of the papers, but says that a strategy memo — which Gleick says he received anonymously — is fake. See [go.nature.com/v1zrbu](http://go.nature.com/v1zrbu) and page 440 for more.

### Animal testing

Tens of millions of animals have been saved from use in chemical safety tests, after Europe's chemical regulator gave the go-ahead to a streamlined method for checking substances' effects on animals' reproductive systems. Toxicologists have been concerned that up to 54 million animals could be required for extra tests mandated by the European Union's sweeping 2007 chemicals legislation — with most of the

increase down to reproductive-toxicity tests that have to be done in two generations of animals. But on 15 February, the European Chemical Agency, based in Helsinki, approved a test that uses only one generation. See [go.nature.com/optzux](http://go.nature.com/optzux) for more.

### AIDS budget cut

Health advocates said last week that they were dismayed by planned cuts to the US administration's global AIDS programme. According to the Kaiser Family Foundation, health-policy analysts headquartered in Menlo Park, California, President Barack Obama's 2013 budget request would cut 13% (US\$543 million) from the US

state department's support for HIV work, although it would add 27% (\$350 million) to the Global Fund to Fight AIDS, Tuberculosis and Malaria. See [go.nature.com/rcdhhv](http://go.nature.com/rcdhhv) for more.

### Iran concern

Iran has responded to tightened trade sanctions by claiming that it has made technical advances in its nuclear programme, including building a new generation of centrifuges to enable faster enrichment of uranium. Diplomats from the United States and Europe dismissed the pronouncements on 15 February as political bluster. As *Nature* went to press, inspectors from the

International Atomic Energy Agency in Vienna were visiting Tehran to discuss Iran's nuclear programme for the second time in three weeks.

### Drug trials rap

On 14 February, three senior Democrats in the US House of Representatives questioned the National Institutes of Health and the Food and Drug Administration over their apparent failure to enforce the public reporting of clinical-trial results. Under a 2007 act, sponsors must report the results of trials of already-approved drugs and devices on [clinicaltrials.gov](http://clinicaltrials.gov) within a year of completion — or be fined. A study (A. P. Prayle *et al.* *Br. Med. J.* **344**, d7373; 2012)



S. MARAI/AFP/GETTY

## The struggle against soot

An international coalition has launched a modest fund to curb emissions of methane, black carbon (soot) and other short-lived climate-affecting pollutants (see *Nature* **481**, 245–246; 2012). The United States, Canada, Sweden, Mexico, Bangladesh and Ghana founded the programme, which was unveiled in Washington DC on 16

February. With initial funding of US\$15 million, it will aim to support projects such as cleaning up inefficient biomass stoves, brick kilns (pictured, in Kabul), diesel vehicles and coke ovens; and reducing gas leakage from rice paddies, landfills, wastewater systems and oil and gas extraction. See [go.nature.com/nu3ak5](http://go.nature.com/nu3ak5) for more.

published in January found that results of only 22% of 738 trials completed in 2009 were reported in time.

## RESEARCH

## Fracking risks

There is little or no evidence that fracking — pumping high-pressure fluids into shale to force out natural gas — has contaminated groundwater, according to a university-funded report (see [go.nature.com/sopiwm](http://go.nature.com/sopiwm)) from researchers assembled by the Energy Institute at the University of Texas at Austin. The report, released on 16 February at the meeting of the American Association for the Advancement of Science in Vancouver, Canada, found that harm ascribed to the controversial technique could usually be traced to above-ground chemical spills or problems common to all oil and gas drilling operations, such as casing failures.

## Dioxin health risk

The US Environmental Protection Agency has released a long-delayed assessment of the health risks of dioxins — work that has taken more than two decades to produce. In line with its 2010 draft report, the agency recommends a safe consumption limit for the chemicals that is well below that proposed by the World Health Organization. But it

also says that current exposure to dioxins “does not pose a significant health risk”. See [go.nature.com/dh3ary](http://go.nature.com/dh3ary) for more.

## EVENTS

## Greek robbery

Greece's economic suffering has been compounded by desecration of its archaeological heritage, with the robbery of 77 artefacts from the Museum of the History of the Olympic Games in Olympia on 17 February. Culture minister Pavlos Geroulanos offered to resign after the theft, which ministry officials said included a 3,300-year-old gold ring and a 2,400-year-old oil jar.

## BUSINESS

## Nanopore sequencer

Oxford Nanopore Technologies, a UK firm that promises its technology could theoretically sequence a human genome in 15 minutes, impressed scientists with the first public presentation of its data on 17 February, at the Advances in Genome Biology and Technology meeting in Marco Island, Florida. The technology identifies bases in real time by measuring electrical conductivity as a DNA strand is fed through a biological nanopore. The company expects to start selling its machine in the second half



of this year, and plans to sell a miniaturized, disposable sequencer (pictured) for less than US\$900. See [go.nature.com/evpc1e](http://go.nature.com/evpc1e) for more.

## PEOPLE

## Nobel laureate dies

Virologist Renato Dulbecco, who shared the 1975 Nobel Prize in Physiology or Medicine, died on 19 February, aged 97. Dulbecco won the Nobel for work in the 1950s and '60s showing that some viruses insert their genes into the genomes of the cells they infect, and that these changes can trigger cancer. Born in Italy, Dulbecco also worked in the United States and Britain. From 1988 to 1992 he was president of the Salk Institute for Biological Studies in San Diego, California.

## MIT head resigns

The first female president of the Massachusetts Institute of Technology (MIT) in Cambridge has announced that she will resign the post, after seven years in charge. Susan Hockfield, a

## COMING UP

### 26–29 FEBRUARY

In Washington DC, scientists and policy-makers discuss research and political efforts on biodefence and bioterrorism, including work that created mutant influenza. [go.nature.com/xnstjz](http://go.nature.com/xnstjz)

### 27 FEB–2 MARCH

Graphene, solar-energy technology and nanoscience remain hot topics at this year's American Physical Society meeting in Boston, Massachusetts. [go.nature.com/6m7ekb](http://go.nature.com/6m7ekb)

neuroscientist, has headed MIT since 2004; she previously spent two decades at Yale University in New Haven, Connecticut, including time as provost. On 16 February she said that she would step down when a successor was appointed, to pave the way for a new fund-raising effort.

## Italy research head

Italy's multidisciplinary National Research Council (CNR), which runs more than 100 institutes and research centres, finally has a new president. It should now be able to implement a 2009 law intended to make the country's research system more transparent and meritocratic (see *Nature* **476**, 386; 2011). The reform has dragged on because outgoing CNR president Francesco Profumo, appointed last August, declined to resign the post after becoming national research minister last November. On 18 February, after Profumo was finally pressed into resignation, Luigi Nicolais, a chemical engineer who is also a member of parliament, was appointed as president of the CNR.

► **NATURE.COM**

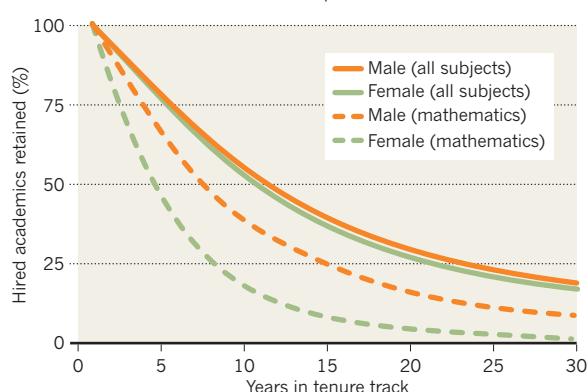
For daily news updates see: [www.nature.com/news](http://www.nature.com/news)

## TREND WATCH

A study of the careers of nearly 3,000 tenure-track science and engineering assistant professors in 14 US universities suggests that men and women are retained and promoted at about the same rate, spending a median time of 10.9 years at their first university. But in mathematics, women leave significantly sooner than men (see chart). A problem lies in hiring: only 27% of incoming academics are women, the authors point out. See [go.nature.com/nn23z1](http://go.nature.com/nn23z1) for more.

### RETAINING SCIENCE TALENT

Men and women hired by US science and engineering faculties are retained at about the same rate — except in mathematics.





# Flu meeting opts for openness

**Controversial virus studies should be published and oversight of such work strengthened, conference concludes.**

- **Declan Butler**

21 February 2012



After weeks of debate, two controversial papers describing forms of the H5N1 avian influenza virus capable of transmitting between mammals should be published in full. That was the unexpected outcome of a meeting convened last week in Geneva, Switzerland, by the World Health Organization (WHO), which also promised to create a more rigorous oversight system for such research.

The decision goes against a recommendation from the US National Science Advisory Board for Biosecurity (NSABB), which the US government has adopted as its official position. In December 2011, the board said that experimental details of the two studies should be redacted from any publications, because of concerns that the information could be used in a

bioterror attack. The board also feared that publishing the details would prompt more laboratories to work on the viruses, making an accidental release more likely.

The studies, which created forms of H5N1 that can spread between ferrets through airborne transmission, are likely to be published in a few months. The 22 experts at the meeting, mainly flu researchers, believe that the delay is needed to explain the benefits of the work to the public, and allay concerns about its safety. Meanwhile, a 60-day moratorium on similar research will be extended until a system is put in place to review levels of biosafety and biosecurity. To that end, the WHO intends to convene international discussions among regulators and other bodies in the next few months.

The two researchers at the centre of the controversy say that they are pleased with the outcome. “I was pleasantly surprised by the fact that there were unanimous decisions about most issues, and strong consensus on the others,” says Ron Fouchier, a flu virologist at Erasmus Medical Center in Rotterdam, the Netherlands, whose study has been accepted by the journal *Science*. Yoshihiro Kawaoka of the University of Wisconsin-Madison, lead researcher on the other study, adds that the meeting allowed him and Fouchier to explain their work, including the potential benefits for surveillance of emerging flu strains (*Nature* **481**, 417–418; 2012) and for vaccine preparation (*Nature* **482**, 142–143; 2012). “We presented why we did these experiments, what we did, what data we obtained, what these data contribute to public health and to the scientific field, and why we think the results should be shared,” says Kawaoka, whose paper has been accepted by *Nature*. He adds that data he and Fouchier presented on the evolution of H5N1 in the wild clarified the threat from the virus, although he would not be drawn on the details, citing confidentiality.

Microbiologist Paul Keim, who chairs the NSABB and attended the meeting, did not respond to *Nature*’s request for an interview, but is reportedly “disappointed” by the recommendation to publish the papers.

*Nature* and *Science* last year agreed in principle to redact the papers, on the condition that the US government would develop a mechanism to disseminate the full papers to researchers and health officials on a need-to-know basis. But meeting participants concluded that this was impractical, and that the potential public-health benefits of the work outweighed any risk of publishing the papers in full.

### **Biosafety first**

Many flu researchers have already seen the papers, so there was little to be gained by restricting their dissemination, says Richard Ebright, a molecular biologist and biodefence expert at Rutgers University in Piscataway, New Jersey. It is much more urgent, he says, to put in place strict biosafety, biosecurity and oversight provisions for such research.

David Fidler, an expert in international and national security law at Indiana University in Bloomington, points out that the meeting hasn't actually broken the publication deadlock, because Keim and representatives of the US government still do not agree with publishing the studies in full. "Most of the meeting's participants appear to have rejected the US position," says Fidler, "but [have] agreed to the extended moratorium and publication delay in the hope that the US government will change its mind."

Participants agreed that the mutant viruses should remain in their two containment facilities — rated at 'BSL-3 enhanced', the second-highest level of biosafety — and that both should be reviewed before any work restarts. Didier Houssin, president of the French Evaluation Agency for Research and Higher Education, says that the biosafety review of the work must consider whether studies of this kind should be conducted only in labs with the highest biosafety rating of BSL-4, a restriction imposed this month by Canada. Houssin, who attended the meeting, notes that imposing such a restriction globally would curtail similar work because there are just a few dozen BSL-4 labs worldwide. The safety level of BSL-3 labs is very variable, he says, and so any facilities working on such viruses would need to be rigorously assessed.

Fidler and other experts note that the meeting did not address the overall risks and benefits of the work, or how similar research might be overseen in future. Keiji Fukuda, WHO Assistant Director-General for Health Security and Environment, explains that later meetings will deal with these topics and will have wider participation.

Meanwhile, the meeting agreed that it was "critical" for the WHO to form a communications plan over the next few months to increase public awareness and understanding of the importance of the flu work, and to alleviate public anxieties. But Peter Sandman, a risk-communications consultant in Princeton, New Jersey, advises against any attempt by the WHO to "educate" the public out of its concerns. As a strategy, he says, it "is thoroughly discredited, because it doesn't work".

*Nature*

**482,**

447–448



(23 February 2012)  
doi:10.1038/482447a

US government would develop a mechanism to disseminate the full papers to researchers and health officials on a need-to-know basis. But meeting participants concluded that this was impractical, and that the potential public-health benefits of the work outweighed any risk of publishing the papers in full.

### BIO SAFETY FIRST

Many flu researchers have already seen the papers, so there was little to be gained by restricting their dissemination, says Richard Ebright, a molecular biologist and biodefence expert at Rutgers University in Piscataway, New Jersey. It is much more urgent, he says, to put in place strict biosafety, biosecurity and oversight provisions for such research.

David Fidler, an expert in international and national security law at Indiana University in Bloomington, points out that the meeting hasn't actually broken the publication deadlock, because Keim and representatives of the US government still do not agree with publishing the studies in full. "Most of the meeting's participants appear to have rejected the US position," says Fidler, "but [have] agreed to the extended moratorium and publication delay in the hope that the US government will change its mind."

Participants agreed that the mutant viruses should remain in their two containment facilities — rated at 'BSL-3 enhanced', the second-highest level of biosafety — and that both should be reviewed before any work restarts. Didier Houssin, president of the French Evaluation Agency for Research and Higher Education, says that the biosafety review of the work must consider whether studies of this kind should be conducted only in labs with the highest biosafety rating of BSL-4, a restriction imposed this month by Canada. Houssin, who attended the meeting, notes that imposing such a restriction globally would curtail similar work because there are just a few dozen BSL-4 labs worldwide. The safety level of BSL-3 labs is very variable, he says, and so any facilities working on such viruses would need to be rigorously assessed.

Fidler and other experts note that the meeting did not address the overall risks and benefits of the work, or how similar research might be overseen in future. Keiji Fukuda, WHO Assistant Director-General for Health Security and Environment, explains that later meetings will deal with these topics and will have wider participation.

Meanwhile, the meeting agreed that it was "critical" for the WHO to form a communications plan over the next few months to increase public awareness and understanding of the importance of the flu work, and to alleviate public anxieties. But Peter Sandman, a risk-communications consultant in Princeton, New Jersey, advises against any attempt by the WHO to "educate" the public out of its concerns. As a strategy, he says, it "is thoroughly discredited, because it doesn't work". ■ **SEE EDITORIAL P.439**

### EPIDEMIOLOGY

# Growing pains for children's study

*Door-to-door recruitment abandoned for US project.*

BY MEREDITH WADMAN

A proposed 15% budget cut is making for a troubled adolescence at the National Children's Study (NCS), an ambitious US government project that aims to chart biological, environmental and social influences on the health of 100,000 American children from before birth to age 21 years.

The study's managers at the National Institute of Child Health and Human Development (NICHD) in Bethesda, Maryland, say that they can cope with the White House's budget proposal, released on 13 February. This would cut funding for the programme by US\$28 million, to \$165 million in 2013 (see 'Belt tightening'). But their plan to save money, by recruiting study participants through health-care providers rather than by door-to-door recruitment, is worrying some of the study's scientists, who already feel shut out from its planning.

In 2010, a year after it started, the NCS's pilot phase had to expand from seven sites to 37 after recruitment rates fell well short of expectations. As the pilot winds down recruitment this year, it has enrolled only 4,000 subjects. The study, which could be used to probe the roots of conditions such as asthma, autism and diabetes, must therefore accelerate recruitment sharply after its main arm launches in 2013.

NICHD director Alan Guttmacher says that there was "understandable angst" among study-site directors the day the budget was made public. But NCS managers see room

for savings, estimating that \$30 million was spent on recruitment in 2011 alone. Although door-to-door recruitment is considered a gold standard in epidemiology, study managers believe that subjects can be recruited much more cheaply through health-care-providers' offices, where pilot-study data show that recruiters are much more likely to find eligible women who are pregnant or trying to become pregnant. The household recruitment has another downside, says Guttmacher: "It would take so long it would compromise the study." A "scientifically compelling" study with a budget of \$165 million is still possible, he says.

According to one of the study's principal investigators (PIs), however, money is already too tight. "The idea that there are cost savings to be made here is absolutely absurd," says the researcher, who contends that many PIs have yet to receive funding for their data-management systems that was promised by NICHD managers last October. Some are coping by diverting funds from other parts of the study; others have simply stopped entering data for study subjects. The study's managers say that the PIs have been adequately funded.

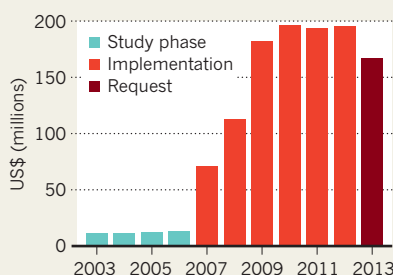
Some PIs are also worried that recruitment at health-care-providers' offices would bias the study and render its findings inapplicable to the wider population. They point to a 2008 Institute of Medicine report that called the household-based sampling approach one of the study's main strengths.

And some scientists complain that they had no input into the decision to change the recruiting strategy, which many failed to hear about even after the budget was announced. "We don't have any full, thorough discussion of this," says Nigel Paneth, a paediatrician at Michigan State University in East Lansing who is PI at the NCS site in Wayne County. "What this study needs is full scientific input, not Bureaucratic Planning Central." Guttmacher notes that government officials cannot talk about White House budget proposals before they are released.

But with many congressional districts hosting study centres, the programme has proved resilient. The administration of former president George W. Bush repeatedly tried to cancel it, but Congress always restored full funding. ■

### BELT TIGHTENING

Facing a proposed 15% cut, the US National Children's Study is seeking cheaper ways to recruit its cohort of more than 100,000 children.



SOURCE: NIH



Bioethicist Glenn McGee's new job raised questions of conflict of interest at the journal he founded.

## ETHICS

# Editor's move sparks backlash

*Bioethicists are forced to consider their purpose as leading practitioner joins controversial stem-cell company.*

BY DAVID CYRANOSKI

**T**he field of bioethics is embroiled in a period of soul-searching, sparked by a startling career move by one of its biggest names.

Glenn McGee is the editor-in-chief of the *American Journal of Bioethics* (AJOB), the most cited bioethics journal, which he founded in 1999. Since December 2011, he has also been president for ethics and strategic initiatives at CellTex Therapeutics in Houston, Texas, a controversial company involved in providing customers with unproven stem-cell therapies. A CellTex press release says that "Dr McGee's responsibilities will include ensuring that all of the firm's work, centered on adult stem cells, will meet the highest ethical standards of the medical and scientific communities."

Although McGee has said he will leave the journal on 1 March, many bioethicists have criticized him, the journal's editorial board and its publisher, London-based Taylor and Francis. They argue that in holding both posts, McGee has a conflict of interest between his responsibilities to the journal and his new employer's desire to promote the

clinical application of stem-cell treatments that are not approved by the US Food and Drug Administration.

"Imagine if the Editor of the *New England Journal of Medicine* took a job as Vice President at Merck, and the Mass Medical Society asked him to stay on as Editor, opining that the conflicts of interest would be manageable. One might rightly wonder, 'What are these people smoking?'" says John Lantos, director of the Children's Mercy Bioethics Center in Kansas City, Missouri, and a past president of the American Society for Bioethics and Humanities.

More broadly, bioethicists are questioning whether it can ever be acceptable to work for companies, which, they argue, may be using the appointment to present a veneer of ethical probity. The episode brings to a head concerns that have emerged among bioethicists over the past decade, says Insoo Hyun, a stem-cell bioethicist at Case Western Reserve University in Cleveland, Ohio. "It's a perfect storm," he says.

McGee is a leading voice on one side of the debate, arguing that bioethics must have practical relevance. For the past three years he has been chair of bioethics at the non-profit Center

for Practical Bioethics in Kansas City, where he ran a course for those who might go on to chair hospital ethics committees or serve as ethical advisers to corporations.

But during McGee's tenure as editor-in-chief of the AJOB, four editors are known to have resigned from the editorial board because of differences in opinion over how the journal handles conflicts of interest. Two left this month, including Lantos, who wrote on his blog that he will no longer work with the journal because of McGee's simultaneous employment at the AJOB and CellTex, and frustration over the lack of a clear conflict-of-interest policy at the AJOB. In response to *Nature's* questions about the situation, Taylor and Francis responded that it "is grateful for Dr McGee's editorship of AJOB" and "supportive of Glenn's decision to step down".

On 17 February, McGee announced that he is merely acting in an advisory capacity at the journal until 1 March, when its new editors-in-chief take over. They are David Magnus, director of the Center for Biomedical Ethics at Stanford University, California, and Summer Johnson McGee, director of graduate studies at the Center for Practical Bioethics and the journal's current executive editor. She is also Glenn McGee's wife.

Responding to questions from *Nature*, Summer Johnson McGee says that the journal has a conflict-of-interest policy that requires editors to withdraw from reviewing a manuscript if they perceive a conflict. She calls allegations that her appointment results from her relationship with her husband "baseless and sexist". "David Magnus and I were hired by our publisher, not by my husband," Magnus says that at least a dozen editorial board members have supported his and Summer Johnson McGee's appointments. Two even indicated that Glenn McGee should have been able to retain an advisory or editorial role.

Other bioethicists' blogs and Twitter feeds about the episode have expressed concerns,

however. Leigh Turner of the University of Minnesota, Minneapolis, called on the entire editorial board of the AJOB to resign for allowing

the situation to persist. And many say that McGee's move illustrates a broader problem. "Mainstream bioethics is no longer speaking truth to power," complains Jan Helge Solbakk at the University of Oslo. "Instead it has become the handmaiden of the medico-industrial complex, and of bioscience and technology."

So how should companies get their advice on bioethics? Magnus never takes cash from industry for advising or speaking — "I'm a hardass about that" — but he believes that bioethicists can work for industry as long as they give up their academic positions, including posts on journal editorial boards. ▶

**"Mainstream bioethics is no longer speaking truth to power."**



► Working for a respected company may be acceptable to some bioethicists, but McGee's new employer comes with a great deal of baggage. CellTex, which was founded last year and as yet has no website, licenses stem-cell technology from Seoul-based RNL Bio. The South Korean company has made a business out of taking fat cells from people, processing them in a way that they say increases the number of mesenchymal stem cells, and then reinjecting them in an effort to treat conditions such as spinal cord injury.

McGee already had a connection with RNL Bio. In 2010, two patients died following injections of RNL's cells. McGee, working for stem-cell lobby group the International Cellular Medicine Society, based in Salem, Oregon, helped to conduct an investigation into the company. This concluded that only one of the two cases was likely to be related to the injections, and because the patient understood the risk the company was not culpable.

Jin Han Hong, the then president of RNL's US subsidiary, admitted in 2010 that there was no clinical-trial evidence proving that these treatments are effective (*Nature* **468**, 485; 2010). As treatment with RNL's stem cells is not approved in the United States or South Korea, for the procedures the company sends patients to China or Japan, where regulations are less strictly enforced. Using RNL's methods, CellTex is banking stem cells that have gone on to be used in a number of patients, including Rick Perry, governor of Texas (*Nature* **477**, 377–378; 2011). CellTex says that it does not conduct medical procedures itself.

When *Nature* contacted McGee to put the criticisms to him, he directed us to previous statements indicating that he wants to put CellTex on firmer ethical ground by having it conduct clinical trials that meet standards set by the International Society for Stem Cell Research, based in Deerfield, Illinois, which represents most mainstream stem-cell researchers around the world.

Hyun warns that working directly for business can be fraught with danger, however good a bioethicist's intentions. In 2005, he helped to craft the informed consent procedure for egg donations used in a cloning procedure by disgraced Korean stem-cell scientist Woo Suk Hwang. Following Hwang's claim, later proved fraudulent, that he had cloned human embryos and harvested stem cells from them, it emerged that he had ignored the consent procedure for egg donations (*Nature* **438**, 536–537; 2005), leading to embarrassment for Hyun.

"I know first hand how difficult it is to separate conflict of interest — to maintain the role of bioethicist," says Hyun. "I know you need to not be too chummy with enterprises trying to speed ahead in stem cells." ■



S. RYAN/NORTHWESTERN UNIV.

Researchers who, like Vadim Backman, top \$1.5 million in NIH grants will face an extra layer of review.

## FUNDING

## Extra scrutiny for 'grandee grantees'

*An analysis by Nature reveals who holds the most grants from the US National Institutes of Health.*

BY ERIC HAND

Vadim Backman no longer relies on coffee to get him through the 100-hour weeks he puts in at his biomedical engineering laboratory at Northwestern University in Evanston, Illinois. Since giving up caffeine, he drops to the floor and does press-ups whenever he needs to clear his head. It certainly takes an alert mind to supervise 20 students, collaborate on clinical trials at 8 hospitals worldwide, and manage 7 grants worth a total of more than US\$3 million from the US National Institutes of Health (NIH) in Bethesda, Maryland.

At 38, Backman is already a biomedical superstar. He is developing an imaging technology that could detect abnormal structures in cells during the earliest stages of cancer. And a *Nature* analysis has identified him as one of seven scientists whom the NIH supports with the most grants (see 'Seven lucky seven'). That puts him near the top of a larger group of NIH-supported researchers who will

soon be targeted for extra scrutiny beyond the peer-review process.

As it released its 2013 budget proposal last week, the agency said that researchers who control more than \$1.5 million in grants will undergo an extra layer of review from external advisers before further grants are approved. The decision comes as the agency tries to scrape money together for new grants in order to raise its current grant success rate of 18%, a historic low. But the countermeasure — potentially penalizing applicants on the basis of their previous success — is also historic.

The basic rule for giving out grants at the NIH has always been simple: to fund the best science. A retreat from pure meritocracy is "shocking", says Howard Garrison, director of public affairs at the Federation of American Societies for Experimental Biology in Bethesda, Maryland. "It's a huge sea change."

Nevertheless, Garrison supports the new rule because he is concerned about the vast number of researchers who are struggling to win, or hold, just one grant.

Nearly 1,500 principal investigators (PIs) — about 5% of those who held grants in 2011 — come in above the \$1.5-million threshold and would be subject to the review. A \$750,000 threshold for a similar layer of extra review has been in place since the 1990s at one NIH institute, the National Institute of General Medical Sciences, and has worked well, says the institute's former director Jeremy Berg, now at the University of Pittsburgh in Pennsylvania.

## SHOPPING AROUND

Sally Rockey, the NIH deputy director for extramural research, says the agency isn't considering a hard cap based on the number of grants per scientist, nor extra review for those with many grants. She points out that a cap based on numbers of grants would have to be draconian to spread grants to a significantly greater number of researchers. An analysis she presented on her blog in October 2011 found that setting a maximum of two grants per PI would increase the grant success rate by just 2%.

In 2008, two NIH advisory panels tasked with reforming the peer-review process for grants recommended that PIs spend at least 20% of their time on any given grant — a de facto cap of five grants per researcher. Although most of the recommendations were ultimately adopted, the 20% rule was not. Berg, who was on one of the advisory panels, says he would still support a review threshold — although not a hard cap — for a certain number of grants. “You look at people with more than a certain number of grants and ask, ‘Is this a good investment for the NIH?’” he says. There are concerns, he adds, that PIs could gain multiple grants by presenting similar experiments to different NIH institutes.

Berg has tried to measure the output of laboratories of different sizes, and found that the richest are not necessarily the most productive (see *Nature* **468**, 356–357; 2010). “There are some people who are definitely capable of running bigger operations while maintaining tremendous productivity per dollar,” he says. “There are other people who are very well funded and aren't so productive.”

Those questions are especially important for the very top grant winners, whom *Nature* identified on the basis of ‘research project grants’, an NIH-defined category composed mostly of the R-01 grants that provide bread-and-butter support to most PIs.

John Tainer, a structural biologist at the Scripps Research Institute in La Jolla, California, feels that the new rule will only further entrench a bias against those with multiple grants, and worries that it could restrict innovation by the elite. With 7 grants worth a combined sum of more than \$5 million, it is hard to feel sorry for Tainer. But earlier this month, he lost a competitive renewal for a grant that he has held since 1985, to study the hair-like pili on the surface of bacteria that make them sticky and contribute to their pathogenicity. Because he relies on grants to pay the salaries of 18 lab members, as well as his own, this rejection could mean lay-offs.

Tainer suspects that the decision “reflects the fact that I have other projects”. But, he continues,

**“You look at people with more than a certain number of grants and ask, ‘Is this a good investment?’”**

“The science hasn't changed. What we're doing now is better than what we've ever done.”

The loss of the grant will extend beyond his own lab, he adds. “For the next decade, people will be publishing parts of things that I had done better. The cost to the NIH will be higher. If you're a leader and you have momentum and technology, the impact of taking that away and having other people do it at a different level is destructive.”

Backman also dislikes the idea of capping the number of grants that an individual can win, but is more relaxed about the proposed \$1.5-million threshold review. He is sympathetic to the plight of young researchers casting about for their first grant — he was in the same position just a few years ago — but says that the competition for established researchers must be based purely on the strength of their ideas. “I like the idea of meritocracy,” he says. ■

## SEVEN LUCKY SEVEN

Seven NIH-supported researchers are principal investigators on seven research project grants each.

Name	Grant total	Institution	Research
Ronald Davis	\$6,986,908	Stanford University	Genomics
John Tainer	\$5,069,800	Scripps Research Institute	Structural biology
Anjana Rao	\$3,512,571	La Jolla Institute for Allergy & Immunology	Signalling and gene expression
George Koob	\$3,365,229	Scripps Research Institute	Neurobiology of addiction
Vadim Backman	\$3,054,165	Northwestern University	Biophotonics
Pier Pandolfi	\$2,929,857	Beth Israel Deaconess Medical Center	Tumorigenesis
Pietro Sanna	\$2,114,278	Scripps Research Institute	Neurobiology of addiction

Fiscal 2011 grant data were used. Grant totals reflect fractional shares of multi-PI grants. Analysis excludes grants made to large research centres. Grant supplements are included as part of original grant, rather than as a separate award.

## HIGH-ENERGY PHYSICS

# Physicists raid Tevatron for parts

*Fermilab icon plundered amid tight budgets and shifting scientific aims.*

BY EUGENIE SAMUEL REICH

It is a 4,000-tonne edifice that stands three stories high, chock full of particle detectors, power supplies, electronics and photomultiplier tubes, all layered like a giant onion around a cylindrical magnet. During 26 years of operation at the Fermi National Accelerator Laboratory in Batavia, Illinois, this behemoth, the Collider Detector at Fermilab (CDF), helped to find the top quark and chased the Higgs boson. But since the lab's flagship particle collider, the Tevatron, was switched off in September 2011, the detector has been surplus stock — and it is now slowly being cannibalized for parts.

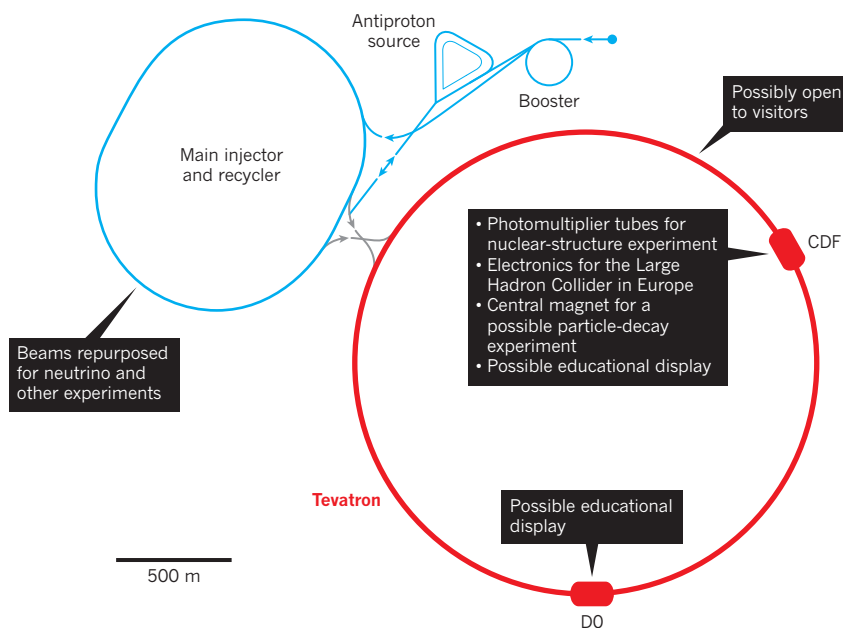
When the Tevatron closed, Fermilab announced that the CDF would become an educational display. Along with its companion experiment, D0, the detector was supposed to form the centrepiece of a tour through simulated control rooms and decommissioned accelerator tunnels. But tight budgets for experimental particle physicists — combined with their tendency to tinker and recycle — are pushing the outcome in a different direction, at least for the CDF.

"Some parts are worth pennies, but in this budgetary climate, even pennies are worth saving," says Rob Roser, who until recently was co-spokesman for the CDF and has now himself been recycled into a new position as head of scientific computing at Fermilab.

"Recycling equipment is as old as science itself," says Jonathan Lewis, the Fermilab scientist in charge of decommissioning the

## CANNIBALIZING THE TEVATRON

Parts at the Tevatron and its two main experiments, the CDF and D0, are being considered for recycling in the wake of the collider's closure in September 2011.



CDF. And thrift is in fashion. With most of the action in particle physics taking place at the Large Hadron Collider near Geneva in Switzerland, US researchers were preparing for hard times even before US President Barack Obama released his 2013 budget request on 13 February (see *Nature* **482**, 283–285; 2012). Although the Office of Science at the Department of Energy (DOE) got a 2.4% funding boost, the budget cut Fermilab's allotment by 5% and DOE funding for high-energy physics by 1.8%.

Looking for savings, Bogdan Wojtsekhowski, who leads three experiments to probe nuclear structure with an electron beam at the DOE's Jefferson Lab in Newport News, Virginia, convinced Fermilab to send him 600 photomultiplier tubes, which capture the light emitted as particles streak through detector materials. Buying them new would have cost \$600,000.

The recycling reflects not only parsimony, but also a programmatic shift in US particle physics. With the shutdown of the Tevatron, researchers moved from the energy frontier, where physics is tested with particle collisions at the highest energies, to the intensity frontier, where the highest numbers of particles are collided. The fate of the CDF's parts mirrors this switch.

Some power supplies are going to Mu2e, an intensity-frontier experiment at Fermilab to

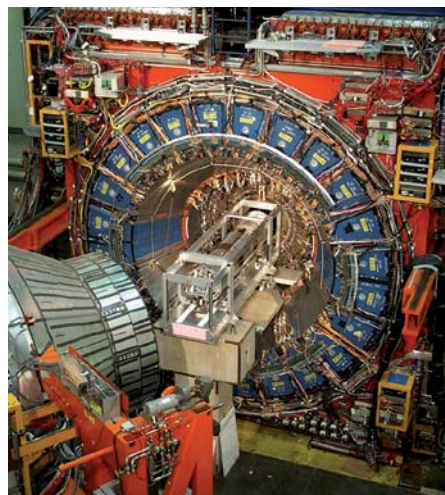
look for the rare conversion of muons to electrons. Amplifier chips are going to g-2, another intensity-frontier experiment at Fermilab to measure a key magnetic parameter of the muon. Some scintillation materials, which emit light along the path of charged particles passing through them, are destined for the Long-Baseline Neutrino Experiment, which plans to send neutrinos 1,300 kilometres from Fermilab to the Homestake Mine in Lead, South Dakota.

Although most of the donations involve small items that would not stop the CDF from going on display, the most ambitious recycling request so far would see it gutted. A proposed experiment called ORKA, which would search for a predicted, but as yet unobserved, rare decay of kaon particles, needs a massive solenoid magnet like the one at the CDF's heart. ORKA has yet to be funded by the DOE, but the Physics Advisory Committee at Fermilab approved its scientific goals in December 2011.

Robert Tschirhart, co-spokesman for ORKA, says that adapting the magnet from the CDF by replacing some of its present detectors with a kaon detector may cost several million dollars. That would still be about half the cost of buying a new magnet.

Lab management will make a decision about whether ORKA can eviscerate the CDF in about 6 months' time. ■

FERMILAB



The CDF, one of the Tevatron's two detectors, is slowly surrendering its parts to other experiments.



## PALAEOBOTANY

# Wild flower blooms again after 30,000 years on ice

*Fruits hoarded by ancient ground squirrels give new life to prehistoric plants.*

BY SHARON LEVY

During the Ice Age, Earth's northern reaches were covered by chilly, arid grasslands roamed by mammoths, woolly rhinoceros and long-horned bison. That ecosystem, known by palaeontologists as the mammoth steppe, vanished about 13,000 years ago. It has no modern counterpart.

Yet one of its plants has reportedly been resurrected by a team of scientists who tapped a treasure trove of fruits and seeds, buried some 30,000 years ago by ground squirrels and preserved in the permafrost (S. Yashina *et al. Proc. Natl Acad. Sci. USA* <http://dx.doi.org/10.1073/pnas.1118386109>; 2012). The plant would be by far the most ancient ever revived; the previous record holder was a date palm grown from seeds roughly 2,000 years old.

The squirrels' burrows, 70 in all, were found on the banks of the lower Kolyma River in northeastern Siberia, 20–40 metres below the current surface of the tundra and surrounded by the bones of mammoths and other creatures. Some burrows contained hundreds of thousands of fruits and seeds, wonderfully preserved by the cold, dry environment.

Researchers had previously attempted to grow plants from seeds found in these ancient burrows, including sedge, Arctic dock, alpine bearberry and the herbaceous plant *Silene stenophylla*. Those seeds did begin to germinate, but then faltered and died back.

Tantalized, David Gilichinsky of the Russian Academy of Sciences' Institute of Physicochemical and Biological Problems in Soil Science in Pushchino decided to try a different approach (sadly, Gilichinsky passed away last week). He and his colleagues took samples of placental tissue from *S. stenophylla* fruits. The plant placenta — an example of which is the white matter



A prehistoric plant resurrected from frozen tissue.

inside a bell pepper — gives rise to and holds the seeds. The tissue produced shoots when it was cultivated *in vitro*, and the scientists used these to propagate more plants. They are the oldest living multicellular organisms on Earth, the team says.

The plants have already blossomed to produce fertile seeds, which were grown into a

second generation of fertile plants. During propagation, the ancient form of the wild flower produced more buds but was slower to put out roots than modern *S. stenophylla*, which is found along the banks of the Kolyma. This suggests that the original has a distinct phenotype, adapted to the extreme environment of the Ice Age.

"I'm excited that someone has finally succeeded in doing this," says Grant Zazula of the Yukon Palaeontology Program in Whitehorse, Canada, who has investigated previous claims of ancient seed germination. "There is a good chance that extinct plant species could now be brought back to life from permafrost-preserved seeds."

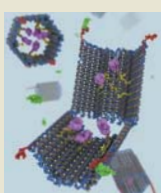
Although some members of the mammoth steppe ecosystem survive, no place on Earth currently holds the same combination of grasses, sedge and wild flowers that have been found in the mummified guts of Ice Age mammoths or in the frozen hoards of squirrels (B. V. Gaglioti *et al. Quatern. Res.* **76**, 373–382; 2011). Zazula speculates that living plant tissue from much earlier — hundreds of thousands of years ago — might also be revived, revealing evolutionary change over a longer timescale, and helping scientists to understand the lost ecology of periods such as the Ice Age. ■

## CLARIFICATION

The table in the News story 'Obama shoots for science increase' (*Nature* **482**, 283–285; 2012) was unclear about the make-up of the Food and Drug Administration's budget. Obama's request leaves the government's input nearly flat, but a rise in user fees from industry would lift the agency's overall 2013 budget to \$4,486 million.



## TOP STORY



● DNA robot could kill cancer cells by seeking them out and delivering a deadly payload. [go.nature.com/bzh4ya](http://go.nature.com/bzh4ya)

## MORE NEWS

● Tourette's-like disorder in New York school confounds experts. [go.nature.com/h6dmq1](http://go.nature.com/h6dmq1)  
 ● Citizen science goes extreme. [go.nature.com/7ghzol](http://go.nature.com/7ghzol)  
 ● Kilogram conundrum on the road to resolution [go.nature.com/u1dg1w](http://go.nature.com/u1dg1w)

## PODCAST



Alan Turing's birthday; the Y chromosome sticks around; and how cells sense pain. [go.nature.com/qnk7uv](http://go.nature.com/qnk7uv)



# LEGACY OF A UNIVERSAL MIND

**F**rom the day he was born — 23 June 1912 — Alan Mathison Turing seemed destined to solitude, misunderstanding and persecution (see page 441). As his centenary year opens, *Nature* hails him as one of the top scientific minds of all time (see page 440). This special issue sweeps through Turing's innumerable achievements, taking us from his most famous roles — wartime code-breaker and founder of computer science (see page 459) — to his lesser known interests of botany, neural nets, unorganized machines, quantum physics and, well, ghosts (see page 562).

Everyone sees a different Turing. A molecular biologist might surprise you by saying that Turing's most important paper is his 1936 work on the 'Turing machine' because of its relevance to DNA-based cellular operations (see page 461). A biophysicist could instead point to his 1952 work on the formation of biological patterns — the first simulation of nonlinear dynamics ever to be published (see page 464).

➔ **NATURE.COM**  
For more on  
Turing, see:  
[nature.com/turing](http://nature.com/turing)

Beneath it all, Turing was driven by the dream of reviving — possibly in the

form of a computer program — the soul of Christopher Morcom, perhaps his only true friend, who died abruptly when they were both teenagers. I want to "build a brain", he said. So does electrophysiologist Henry Markram (see page 456). But it is still a matter of debate whether machine intelligence should faithfully simulate neuronal circuitry, or just emulate brain function using whatever expedient (see page 462).

Even when Turing was kept busy by wartime code-breaking and the practical implementation of his universal computer, he never forgot that he had, in 1936, discovered something even bigger: the 'incomputable' world. Contemporary physics hasn't even started to work out the implications of that discovery (see page 465).

It is typical of Turing's brilliance and playfulness that even as he gave so many fields the tools that allowed them to blossom, he planted a concept that pushes science as we know it — physical reality and Newtonian causality — towards the abyss. ■

**Tanguy Chouard**, a biology editor at Nature, was the consulting editor for this special issue.

ANDY POTTS; TURING FAMILY



# BRAIN IN A BOX

*Henry Markram wants €1 billion  
to model the entire human brain.  
Sceptics don't think he should get it.*

BY M. MITCHELL WALDROP



**TURING AT 100**

A legacy that spans science:  
[nature.com/turing](http://nature.com/turing)

I

t wasn't quite the lynching that Henry Markram had expected. But the barrage of sceptical comments from his fellow neuroscientists — "It's crap," said one — definitely made the day feel like a tribunal.

Officially, the Swiss Academy of Sciences meeting in Bern on 20 January was an overview of large-scale computer modelling in neuroscience. Unofficially, it was neuroscientists' first

real chance to get answers about Markram's controversial proposal for the Human Brain Project (HBP) — an effort to build a supercomputer simulation that integrates everything known about the human brain, from the structures of ion channels in neural cell membranes up to mechanisms behind conscious decision-making.

Markram, a South-African-born brain electrophysiologist who joined the Swiss Federal Institute of Technology in Lausanne (EPFL) a decade ago, may soon see his ambition fulfilled. The project is one of six finalists vying to win €1 billion (US\$1.3 billion) as one of the European Union's two new decade-long Flagship initiatives.

"Brain researchers are generating 60,000 papers per year," said Markram as he explained the concept in Bern. "They're all beautiful, fantastic studies — but all focused on their one little corner: this molecule, this brain region, this function, this map." The HBP would integrate these discoveries, he said, and create models to explore how neural circuits are organized, and how they give rise to behaviour and cognition — among the deepest mysteries in neuroscience. Ultimately, said Markram, the HBP would even help researchers to grapple with disorders such as Alzheimer's disease. "If we don't have an integrated view, we won't understand these diseases," he declared.

As the response at the meeting made clear, however, there is deep unease about Markram's vision. Many neuroscientists think it is ill-conceived, not least because Markram's idiosyncratic approach to brain

D. BALBOUSE/REUTERS



simulation strikes them as grotesquely cumbersome and over-detailed. They see the HBP as overhyped, thanks to breathless media reports about what it will accomplish. And they're not at all sure that they can trust Markram to run a project that is truly open to other ideas.

"We need variance in neuroscience," declared Rodney Douglas, co-director of the Institute for Neuroinformatics (INI), a joint initiative of the University of Zurich and the Swiss Federal Institute of Technology in Zurich (ETH Zurich). Given how little is known about the brain, he said, "we need as many different people expressing as many different ideas as possible" — a diversity that would be threatened if so much scarce neuroscience research money were to be diverted into a single endeavour.

Markram was undeterred. Right now, he argued, neuroscientists have no plan for achieving a comprehensive understanding of the brain. "So this is the plan," he said. "Build unifying models."

### MARKRAM'S BIG IDEA

Markram has been on a quest for unity since at least 1980, when he began undergraduate studies at the University of Cape Town in South Africa. He abandoned his first field of study, psychiatry, when he decided that it was mainly about putting people into diagnostic pigeonholes and medicating them accordingly. "This was never going to tell us how the brain worked," he recalled in Bern.

His search for a new direction led Markram to the laboratory of Douglas, then a young neuroscientist at Cape Town. Markram was enthralled. "I said, 'That's it! For the rest of my life, I'm going to dig into the brain and understand how it works, down to the smallest detail we can possibly find.'"

That enthusiasm carried Markram to a PhD at the Weizmann Institute of Science in Rehovot, Israel; to postdoctoral stints at the US National Institutes of Health in Bethesda, Maryland, and at the Max Planck Institute for Medical Research in Heidelberg, Germany; and, in 1995, to a faculty position at Weizmann. He earned a formidable reputation as an experimenter, notably demonstrating spike-timing-dependent plasticity — in which the strength of neural connections changes according to when impulses arrive and leave (H. Markram *et al.* *Science* 275, 213–215; 1997).

By the mid-1990s, individual discoveries were leaving him dissatisfied. "I realized I could be doing this for the next 25, 30 years of my career, and it was still not going to help me understand how the brain works," he said.

To do better, he reasoned, neuroscientists would have to pool their discoveries systematically. Every experiment at least tacitly involves a model, whether it is the molecular structure of an ion channel or the dynamics of a cortical circuit. With computers, Markram realized, you could encode all of those models explicitly and get them to work together. That would help researchers to find the gaps and contradictions in their knowledge and identify the experiments needed to resolve them.

Markram's insight wasn't original: scientists have been devising mathematical models of neural activity since the early twentieth century, and using computers for the task since the 1950s (see page 462). But his ambition was vast. Instead of modelling each neuron as, say, a point-like node in a larger neural network, he proposed to model them in all their multi-branching detail — down to their myriad ion channels (see 'Building a brain'). And instead of modelling just the neural circuits involved in, say, the sense of smell, he wanted to model everything, "from the genetic level, the molecular level, the neurons and synapses, how microcircuits are formed, macrocircuits, mesocircuits, brain areas — until we get to understand how to link these levels, all the way up to behaviour and cognition".

The computer power required to run such a grand unified theory of the brain would be roughly an exaflop, or  $10^{18}$  operations per second — hopeless in the 1990s. But Markram was undaunted: available computer power doubles roughly every 18 months, which meant that exascale computers could be available by the 2020s (see 'Far to go').

And in the meantime, he argued, neuroscientists ought to be getting ready for them.

Markram's ambitions fit perfectly with those of Patrick Aebischer, a neuroscientist who became president of the EPFL in 2000 and wanted to make the university a powerhouse in both computation and biomedical research. Markram was one of his first recruits, in 2002. "Henry gave us an excuse to buy a Blue Gene," says Aebischer, referring to a then-new IBM supercomputer optimized for large-scale simulations. One was installed at the EPFL in 2005, allowing Markram to launch the Blue Brain Project: his first experiment in integrative neuroscience and, in retrospect, a prototype for the HBP.

Part of the project has been a demonstration of what a unifying model might mean, says Markram, who started with a data set on the rat cortex that he and his students had been accumulating since the 1990s. It included results from some 20,000 experiments in many labs, he says — "data on about every cell type that we had come across, the morphology, the reconstruction in three dimensions, the electrical properties, the synaptic communication, where the synapses are located, the way the synapses behave, even genetic data about what genes are expressed".

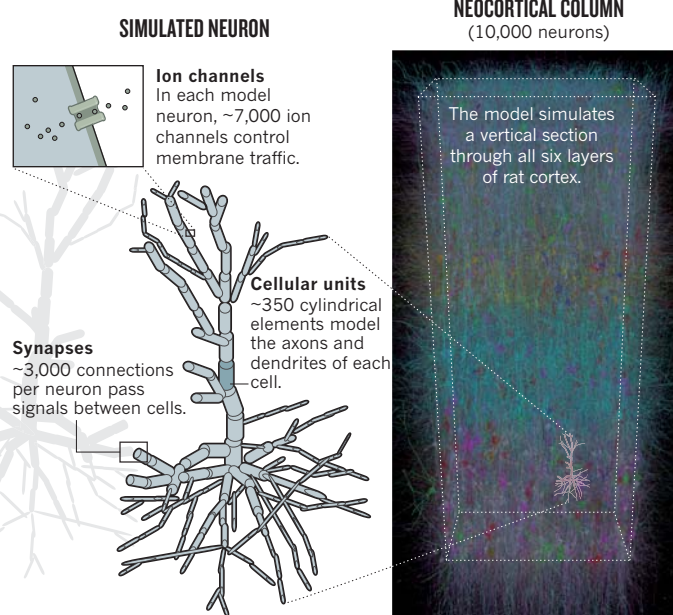
By the end of 2005, his team had integrated all the relevant portions of this data set into a single-neuron model. By 2008, the researchers had linked about 10,000 such models into a simulation of a tube-shaped piece of cortex known as a cortical column. Now, using a more advanced version of Blue Gene, they have simulated 100 interconnected columns.

The effort has yielded some discoveries, says Markram, such as the as-yet unpublished statistical distribution of synapses in a column. But its real achievement has been to prove that unifying models can, as promised, serve as repositories for data on cortical structure and function. Indeed, most of the team's efforts have gone into creating "the huge ecosystem of infrastructure and software" required to make Blue Brain useful to every neuroscientist, says Markram. This includes automatic tools for turning data into simulations, and informatics tools such as <http://channelpedia.net> — a user-editable website that automatically collates structural data

## "IT WILL BE LOTS OF EINSTEINS COMING TOGETHER TO BUILD A BRAIN."

### BUILDING A BRAIN

The Blue Brain simulation — a prototype for the Human Brain Project — constructs simulated sections of cortex from the bottom up, starting from detailed models of individual neurons.



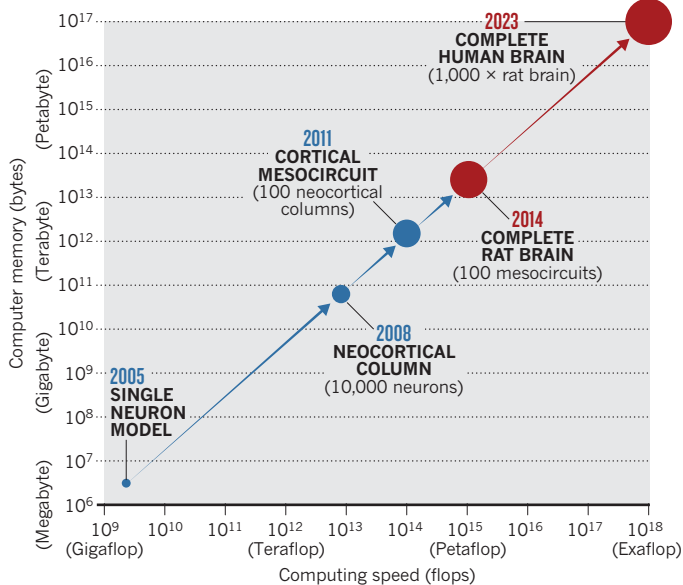
SOURCE: BBP/EPFL



SOURCE: BBP/EPFL

## FAR TO GO

The Blue Brain Project has steadily increased the scale of its cortical simulations through the use of cutting-edge supercomputers and ever-increasing memory resources. But the full-scale simulation called for in the proposed Human Brain Project (red) would require resources roughly 100,000 times larger still.



on ion channels from publications in the PubMed database, and currently incorporates some 180,000 abstracts.

The ultimate goal was always to integrate data across the entire brain, says Markram. The opportunity to approach that scale finally arose in December 2009, when the European Union announced that it was prepared to pour some €1 billion into each of two high-risk, but potentially transformational, Flagship projects. Markram, who had been part of the 27-member advisory group that endorsed the initiative, lost no time in organizing his own entry. And in May 2011, the HBP was named as one of six candidates that would receive seed money and prepare a full-scale proposal, due in May 2012.

If the HBP is selected, one of the key goals will be to make it highly collaborative and Internet-accessible, open to researchers from around the world, says Markram, adding that the project consortium already comprises some 150 principal investigators and 70 institutions in 22 countries. “It will be lots of Einsteins coming together to build a brain,” he says, each bringing his or her own ideas and expertise.

### BOTTOM TO TOP

The description of the HBP as an open user facility sparked interest and enthusiasm at the Bern meeting. But much more vocal were Markram's critics, many of whom focused on the perceived inadequacies of the Blue Brain model — and of Markram's approach to data integration.

At the heart of that approach is Markram's conviction that a good unifying model has to assimilate data from the bottom up. In his view, modellers should start at the most basic level — he focuses on ion channels because they determine when a neuron fires — and get everything working at one level before proceeding to the next. This requires a lot of educated guesses, but Markram argues that the admittedly huge gaps in knowledge about the brain can be filled with data as experiments are published — the Blue Brain model is updated once a week. The alternative approach, approximating and abstracting away the biological detail, leaves no way to be sure that the model's behaviour has anything to do with how the brain works, said Markram.

This is where other computational neuroscientists gnash their teeth. Most of them are already using simple models of individual neurons to explore high-level functions such as pattern recognition. Markram's bottom-up approach risks missing the wood for the trees, many of them argued in Bern: the model could be so detailed that it is no easier to

understand than the real brain. And that is if Markram can build it at all. Judging by what Blue Brain has accomplished in the past six years, critics said, that seems unlikely. The tiny swathe of simulated rat cortex has no inputs from sensory organs or outputs to other parts of the brain, and produces almost no interesting behaviour, pointed out Kevan Martin, co-director of the INI, in an e-mail. It is “certainly not the case” that Markram has simulated the column as it works in a whole animal, he said.

Markram's response to such criticisms in Bern was that more capabilities are always being added to the Blue Brain simulation. But Martin remained unimpressed. “I cannot imagine how this level of detail, which is still very incomplete even after Henry's considerable labours, is ever going to be obtained from more than a few regions of the rodent brain in the next decade, let alone brains of *Drosophila*, zebrafish, songbird, mouse or monkey,” his e-mail continued.

“Of course,” Martin added, “all this would be but a storm in the professors' teacups” if the HBP hadn't come along and raised the stakes enormously. It is all too easy to imagine other areas of neuroscience research being starved for resources by the HBP — especially in Switzerland, which as host country will have to provide a substantial, but still-undetermined, fraction of the funding. Douglas asks: should Europe be spending €1 billion to support the passionate quest of one man? He concedes that visionaries are sometimes necessary to drive progress. “But what if they're passionately wrong?”

Also fuelling anxiety — and irritation — is the widespread sense that Markram has been making his case through the news media, not through publishing, conferences and the other conventional channels of science. Reporters see much to like: Markram is tall, striking and explains his ideas with the clarity, quotability and urgency of a South African version of the late Carl Sagan. He has “a hypnotic effect,” says Richard Hahnloser, a computational neuroscientist at the INI. But critics say that this results in too many news accounts that leave the impression that the HBP will, say, eliminate the need for experimental animals.

“The whole neuroscience community will be in trouble ten years from now” when the implied predictions don't come true, says another INI researcher, who worries that the politicians will be right there saying, “But you promised!”

### MARCH OF PROGRESS

In Bern, Markram bristled at accusations that he has deliberately cultivated hype. “I have never said that the HBP would replace animal experiments,” he shot back at one questioner. “I said that simulation helps you choose the experiments that will best add value.”

Markram was also at pains to insist that the HBP will be open to other modelling approaches. “This concern is unfounded because they simply have not bothered to find out what is being proposed,” he told *Nature* after the meeting. The final facility “will allow anyone to build models at a range of levels of biological detail with as much data as possible from anywhere”.

Markram seems to be building support. Last year, the board that oversees both the ETH and the EPFL enthusiastically endorsed the Blue Brain Project after a rigorous review by a four-member panel that included two outspoken sceptics of Markram's approach. The board asked the Swiss parliament to commit 75 million Swiss francs (US\$81 million) to the project for 2013–16 — more than ten times Blue Brain's current budget. Parliament's decision is expected next month.

Markram is optimistic that the European Union will come to much the same conclusion about the HBP. However, if the project isn't endorsed, says Markram, “we'll just continue with Blue Brain” — although it may take a lot longer to reach a full brain simulation.

Markram clearly feels that history is on his side. “Simulation-based research is an inevitability,” he declared in Bern. “If I get stopped from doing this, it's going to happen. It has happened already in many areas of science. And it is going to happen in life science.” ■

**M. Mitchell Waldrop** is a features editor for *Nature* based in Washington DC.

# COMMENT

**INTELLIGENCE** Four experts compare brains with machines **p.462**

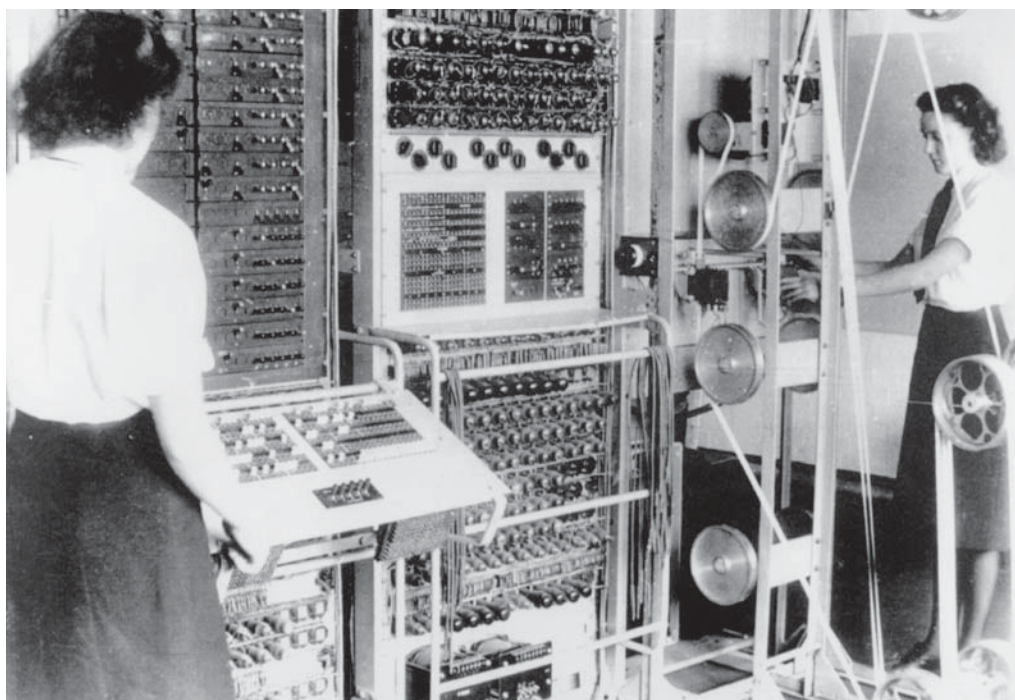
**MATHEMATICS** What lies beyond the limits of computability? **p.465**

**THEATRE** How actors use empathy to seduce an audience **p.466**

**VIROLOGY** Three books explore 30 years of developments in HIV / AIDS research **p.468**



BLECHLEY PARK TRUST/S&SP/L/GETTY



Using techniques developed by Alan Turing, the Colossus was able to decode German wartime communications.

## The dawn of computing

Alan Turing's bridging of logic and machines laid the foundation for digital computers, says **George Dyson**.

**T**he history of digital computing can be divided into an old testament and a new testament. The prophets of the old testament, led by Gottfried Wilhelm Leibniz in the 1670s, supplied the logic; those of the new testament, led by John von Neumann in the 1940s, built the machines. Alan Turing, born on 23 June 1912, falls in between. His paper 'On computable numbers, with an application to the *Entscheidungsproblem*', written in 1936 while he was a fellow at the University of Cambridge's King's College, UK, and published shortly after his arrival as a graduate student at Princeton University, New Jersey, in October 1936, led the way to the implementation of mathematical logic in machines<sup>1</sup>.

Turing was aiming to solve German mathematician David Hilbert's 1928

*Entscheidungsproblem* — the 'decision problem' of whether a mechanical procedure could determine the validity of any logical statement in a finite number of steps. Turing took the 1930s concept of a computer — a person equipped with pencil, paper and instructions — and deconstructed it by removing all traces of intelligence except for the ability to follow instructions and read and write a finite alphabet of symbols on an unbounded paper tape.

The result was the Turing machine: a mathematical black box that obeys preset instructions, represented by symbols encoded

on the tape or stored in the machine's internal 'state of mind'. At any moment, the machine can read, write or erase a symbol from a square; move a square to the right or left; or change its state of mind. Complex symbols can be represented by strings of simpler ones, the limit being the binary distinction between two symbols (or the presence or absence of a hole in the tape). These 'bits' of information can take two forms: patterns in space that are transmitted across time, termed memory; or patterns in time that are transmitted across space, called code. For a Turing machine, time exists not as a continuum, but as a sequence of changes of state.

Turing then demonstrated the existence of a single machine that could "compute any computable" sequence<sup>1</sup>. Such a 'universal computing machine' could mimic any ▶



### TURING AT 100

A legacy that spans science:  
[nature.com/turing](http://nature.com/turing)



► other machine by executing an encoded description of it. Thus, he foresaw the concept of software.

Finally, Turing answered Hilbert's conundrum. He identified a question that could not be answered by any machine in a finite number of steps: will a given encoded description come to a halt or run forever when executed by the universal computing machine? The answer to the *Entscheidungsproblem* was, therefore, no.

"You can build an organ which can do anything that can be done," explained von Neumann, paraphrasing Turing, in a lecture in 1949, "but you cannot build an organ which tells you whether it can be done"<sup>2</sup>. Sensing the limits of deterministic machines, Turing began to explore non-deterministic computation by 'oracle' machines. These proceed step-by-step, but occasionally make unpredictable leaps by consulting "a kind of oracle as it were"<sup>3</sup>.

### CODE BREAKING

Having completed his PhD, Turing returned to England in July 1938. The outbreak of the Second World War soon sparked demand for his ideas, and he was sequestered at the Government Code & Cypher School at Bletchley Park. There, Turing and his colleagues, including his mentor, topologist Maxwell 'Max' Newman, deciphered enemy communications, including messages encrypted by the German Enigma machine — a Turing machine with an internal mechanism that shifted through  $10^{20}$  possible configurations to scramble the input text.

Starting with a set of electromechanical devices called bombs, each of which could emulate 36 suspected Enigma configurations at a time, the researchers at Bletchley Park, assisted by engineer Thomas Flowers at the General Post Office Research Station in Dollis Hill, London, developed a machine called Colossus — a sophisticated electronic digital computer. A 1,500-vacuum-tube internal memory provided Colossus with a programmable state of mind that searched for clues in coded sequences scanned from punched paper tape.

Colossus was swiftly improved and duplicated, producing a second generation of 2,400-tube machines that influenced the outcome of the war and the development of modern computers, although Britain's Official Secrets Act kept the details embargoed for more than 30 years. When the war ended, the push for more powerful computers shifted from cryptanalysis to the design of nuclear weapons, and the United States, which had declassified its wartime computer, the ENIAC (Electronic Numerical Integrator and Computer), in February 1946, assumed the lead.

At the Institute for Advanced Study in Princeton, and with funding from the US Army, the Office of Naval Research and

the US Atomic Energy Commission, von Neumann set out to build an electronic version of Turing's universal computing machine. He wanted a Turing machine with a memory that was accessible at the speed of light, and he decided to build it himself. The US government wanted to know whether a hydrogen bomb was feasible, so von Neumann promised it a machine, with 5 kilobytes of storage, that could run the required hydrodynamic codes. The computer's design was made public so that copies could be freely duplicated — and commercialized by IBM. "Words coding the orders are handled in the memory just like numbers," von Neumann announced at the first project meeting, on 12 November 1945 (ref. 4). This mingling of data and instructions was central to Turing's model. Most computers today are the direct offspring, in terms of their logical architecture, of a Turing machine built from war-surplus components in an outbuilding on a former New Jersey farm.

Turing and von Neumann first met in Cambridge in 1935, and subsequently spent two years together in Princeton, where Newman joined them for 6 months. How

**"Most computers today are the direct offspring of a Turing machine built from war-surplus components."**

much Turing and von Neumann collaborated during the war remains unknown, but we do know that Turing was in the United States between November 1942 and March 1943, and that von Neumann was in England between February and July 1943. During the war, British physicists, in consultation with von Neumann, made important contributions to the atomic bomb project at Los Alamos in New Mexico; and US cryptanalysts, in consultation with Turing, contributed to the effort at Bletchley Park. Although they could not communicate them openly in writing, Turing, von Neumann and Newman probably shared their ideas verbally, both during and after the war.

Turing's model was one-dimensional: a string of symbols encoded on a tape. von Neumann's implementation was two-dimensional: the random-access address matrix that underlies most computers today. The Internet — many Turing machines with concurrent access to a shared tape — has made the landscape three-dimensional. Yet the way in which computers work has remained fundamentally unchanged since 1946.

### LEARNING FROM MISTAKES

Both Turing and von Neumann were conscious of processing errors in their machines. Early codes could be fully debugged, but the hardware was more unreliable, giving inconsistent results — a problem that has since

been reversed. Both men knew that biology relied on statistical, fault-tolerant methods for processing information (such as pulse-frequency coding in the brain) and assumed that technology would follow nature's lead. If "every error has to be caught, explained and corrected, a system of the complexity of the living organism would not run for a millisecond", von Neumann commented<sup>5</sup>.

"If a machine is expected to be infallible, it cannot also be intelligent," Turing noted in 1947 (ref. 6). When Turing joined Newman's group at the University of Manchester, UK, the following year and began designing the Manchester Mark 1 (a prototype for the Ferranti Mark 1, the first commercial stored-program electronic digital computer), he included a random-number generator, which allowed the computer to make guesses and learn from its mistakes.

Turing's deterministic universal machine receives the most attention, but his non-deterministic oracle machines are closer to the way in which intelligence really works: intuition bridging the gaps between logical sequences. Turing's oracle machines are no longer theoretical abstractions — an Internet search engine, for instance, operates deterministically until a person clicks on a link, adding non-deterministically to the search engine's map of where the meaningful information is.

Turing wanted to know how molecules were able to collectively self-organize, and whether machines could think. Von Neumann wanted to know how the brain worked and whether machines could reproduce. Turing, who died at the age of 41, left behind an unfinished theory of morphogenesis, and von Neumann, who died aged 53, left an unfinished theory of self-reproduction — a model inspired by the Turing machine's ability to generate copies of itself.

Had Turing and von Neumann lived longer, we can only imagine how their ideas might have merged. Their lives were both cut short just as the mechanism underlying the translation between sequence and structure in biology was revealed. ■

**George Dyson** is a writer based in Bellingham, Washington, and author of *Turing's Cathedral*.  
e-mail: Gdyson@ias.edu

1. Turing, A. M. *Proc. Lond. Math. Soc.* **s2-42**, 230–265 (1936–37).
2. von Neumann, J. In: *Theory of Self-Reproducing Automata* (ed. Burks, A. W.) 42–56 (Univ. Illinois Press, 1966).
3. Turing, A. M. *Proc. Lond. Math. Soc.* **s2-45**, 161–228 (1939).
4. Minutes of the Institute for Advanced Study Electronic Computer Project, Meeting 1, 12 November 1945.
5. von Neumann, J. In: *Theory of Self-reproducing Automata* (ed. Burks, A. W.) 74–87 (Univ. Illinois Press, 1966).
6. Turing, A. M. Lecture to London Mathematical Society 20 February 1947. Turing archive held at King's College, Cambridge.

# Life's code script

Turing machines and cells have much in common, argues **Sydney Brenner**.

Biological research is in crisis, and in Alan Turing's work there is much to guide us. Technology gives us the tools to analyse organisms at all scales, but we are drowning in a sea of data and thirsting for some theoretical framework with which to understand it. Although many believe that 'more is better', history tells us that 'least is best'. We need theory and a firm grasp on the nature of the objects we study to predict the rest.

Three of Turing's papers are relevant to biology. In 1952, 'The chemical basis of morphogenesis'<sup>1</sup> explored the hypothesis that patterns are generated in plants and animals by "chemical substances called morphogens, reacting together and diffusing through a tissue". Using differential equations, Turing set out how instabilities in a homogeneous medium could produce wave patterns that might account for processes such as the segregation of tissue types in the developing embryo.

Yet biological support for Turing's idea has been marginal. The pre-ordered patterns found in *Drosophila* development do not fit the instability theory, which, until recently, could describe only chemical systems. Skin patterning has, however, been shown to follow a broader interpretation of Turing's terms<sup>2</sup>, where cell-to-cell signalling pathways, rather than individual molecules, are considered. The ion channels postulated by Alan Lloyd Hodgkin and Andrew Huxley<sup>3</sup>, also in 1952, were discovered more immediately by molecular biology.

Turing published another biology-related paper, in 1950. 'Computing machinery and intelligence'<sup>4</sup> introduced the Turing test as an imitation game in which an outside interrogator tries to distinguish between a computing machine and a human foil through their responses to questions. But the Turing test does not say whether machines that match humans have intelligence, nor does it simulate the brain. For that, we need a theory for how the brain works.

The most interesting connection with biology, in my view, is in Turing's most important paper: 'On computable numbers with an application to the *Entscheidungsproblem*'<sup>5</sup>, published in 1936, when Turing was just 24.

Computable numbers are defined as those whose decimals are calculable by finite means. Turing introduced what became known as the Turing machine to formalize

the computation. The abstract machine is provided with a tape, which it scans one square at a time, and it can write, erase or omit symbols. The scanner may alter its mechanical state, and it can 'remember' previously read symbols. Essentially, the system is a set of instructions written on the tape, which describes the machine. Turing also defined a universal Turing machine, which can carry out any computation for which an instruction set can be written — this is the

von Neumann's machines are to be found in biology. Nowhere else are there such complicated systems, in which every organism contains an internal description of itself. The concept of the gene as a symbolic representation of the organism — a code script — is a fundamental feature of the living world and must form the kernel of biological theory.

Turing died in 1954, one year after the discovery of the double-helical structure of DNA by James Watson and Francis Crick, but before biology's subsequent revolution. Neither he nor von Neumann had any direct effect on molecular biology, but their work allows us to discipline our thoughts about machines, both natural and artificial.

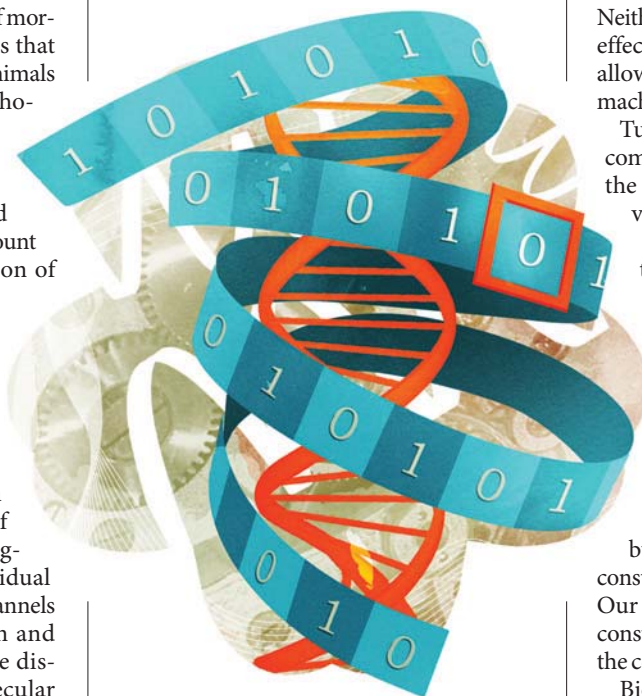
Turing invented the stored-program computer, and von Neumann showed that the description is separate from the universal constructor. This is not trivial. Physicist Erwin Schrödinger confused the program and the constructor in his 1944 book *What is Life?*, in which he saw chromosomes as "architect's plan and builder's craft in one". This is wrong. The code script contains only a description of the executive function, not the function itself.

Thus, Hodgkin and Huxley's equations represent properties of the nerve impulse as an electrical circuit, but the required channels and pumps are constructed from specifications in the genes. Our problems reside in understanding the constructor part of the machinery, and here the cell is the right level of abstraction<sup>6</sup>.

Biologists ask only three questions of a living organism: how does it work? How is it built? And how did it get that way? They are problems embodied in the classical fields of physiology, embryology and evolution. And at the core of everything are the tapes containing the descriptions to build these special Turing machines. ■

**Sydney Brenner** is a senior fellow at the Janelia Farm Research Campus, Howard Hughes Medical Institute, Ashburn, Virginia, 20147, USA.

1. Turing, A. M. *Phil. Trans. R. Soc. Lond. B* **237**, 37–72 (1952).
2. Kondo, S. & Miura, T. *Science* **329**, 1616–1620 (2010).
3. Hodgkin, A. L. & Huxley, A. F. *J. Physiol.* **117**, 500–544 (1952).
4. Turing, A. M. *Mind* **49**, 433–460 (1950).
5. Turing, A. M. *Proc. Lond. Math. Soc.* **s2-42**, 230–265 (1936–37).
6. Brenner, S. *Phil. Trans. R. Soc. B* **365**, 207–212 (2010).



origin of the digital computer.

Turing's ideas were carried further in the 1940s by mathematician and engineer John von Neumann, who conceived of a 'constructor' machine capable of assembling another according to a description. A universal constructor with its own description would build a machine like itself. To complete the task, the universal constructor needs to copy its description and insert the copy into the offspring machine. Von Neumann noted that if the copying machine made errors, these 'mutations' would provide inheritable changes in the progeny.

Arguably the best examples of Turing's and



## TURING AT 100

A legacy that spans science:  
[nature.com/turing](http://nature.com/turing)





# Is the brain a good model for machine intelligence?

To celebrate the centenary of the year of Alan Turing's birth, four scientists and entrepreneurs assess the divide between neuroscience and computing.

**RODNEY BROOKS**

## Avoid the cerebral blind alley

*Emeritus professor of robotics, Massachusetts Institute of Technology*

I believe that we are in an intellectual cul-de-sac, in which we model brains and computers on each other, and so prevent ourselves from having deep insights that would come with new models.

The first step in this back and forth was made by Alan Turing. In his 1936 paper<sup>1</sup> laying the foundations of computation, Turing used a person as the basis for his

model. He abstracted the actions of a human 'computer' using paper and pencil to perform a calculation (as the word meant then) into a formalized machine, manipulating symbols on an infinite paper tape.

But there is a worry that his version of computation, based on functions of integers, is limited. Biological systems clearly differ. They must respond to varied stimuli over long periods of time; those responses in turn alter their environment and subsequent stimuli. The individual behaviours of social insects, for example, are affected by the structure of the home they build and the behaviour of their siblings within it.

Nevertheless, for 70 years, those people working in what is now called computational neuroscience have assumed that the brain is a computer — a machine that is

equivalent to Turing's finite-state machine with an infinite tape and a finite symbol set, and that does computation.

In 1943, Warren McCulloch and Walter Pitts<sup>2</sup> noted the "all-or-none" nature of the firing of neurons in a nervous system, and suggested that networks of neurons could be modelled as logical propositions. They modelled a network of neurons as circuits of logic gates, noting that these may "compute only such numbers as can a Turing machine". But more, they proposed that everything at a psychological level happens in these networks. Over the decades, such ideas begat more studies in neural networks, which in turn begat computational neuroscience. Now those metaphors and models pervade explanations of how the brain 'computes'. But these binary abstractions do not capture all the complexities inherent in the brain.

So now I see circles before my eyes. The brain has become a digital computer; yet we are still trying to make our machines intelligent. Should those machines be modelled on the brain, given that our models of the brain are performed on such machines? That will probably not be enough.

When you are stuck, you are stuck. We will get out of this cul-de-sac, but it will take some brave and bright souls to break out of our circular confusions of models.

**DEMIS HASSABIS**

## Model the brain's algorithms

*Neuroscientist, computer-game producer and chess master, University College London*

Alan Turing looked to the human brain as the prototype for intelligence. If he were alive today, he would surely be working at the intersection of natural and artificial intelligence.

Yet to date, artificial intelligence (AI) researchers have mostly ignored the brain as a source of algorithmic ideas. Although in Turing's time we lacked the means to look inside this biological 'black box', we now have a host of tools, from functional magnetic resonance imaging to optogenetics, with which to do so.

Neuroscience has two key contributions to make towards progress in AI. First, the many structures being discovered in the brain — such as grid cells used for navigation, or hierarchical cell layers for vision processing — may inspire new computer



**TURING AT 100**

A legacy that spans science:  
[nature.com/turing](http://nature.com/turing)

algorithms and architectures. Second, neuroscience findings may validate the plausibility of existing algorithms being integral parts of a general AI system.

To advance AI, we need to better understand the brain's workings at the algorithmic level — the representations and processes that the brain uses to portray the world around us. For example, if we knew how conceptual knowledge was formed from perceptual inputs, it would crucially allow for the meaning of symbols in an artificial language system to be grounded in sensory 'reality'.

AI researchers should not only immerse themselves in the latest brain research, but also conduct neuroscience experiments to address key questions such as: "How is conceptual knowledge acquired?" Conversely, from a neuroscience perspective, attempting to distil intelligence into an algorithmic construct may prove to be the best path to understanding some of the enduring mysteries of our minds, such as consciousness and dreams.

**DENNIS BRAY**

## Brain emulation requires cells

*Department of Physiology,  
Development and Neuroscience,  
University of Cambridge*

Machines can match us in many tasks, but they work differently from networks of nerve cells. If our aim is to build machines that are ever more intelligent and dexterous, then we should use circuits of copper and silicon. But if our aim is to reproduce the human brain, with its quirky brilliance, capacity for multi-tasking and sense of self, we have to look for other materials and different designs.

Computers outperform us in complex mathematical calculations and are better at storing and retrieving data. We accept that they can beat us at chess — once regarded as the apogee of human intellect. But the success of a computer called Watson in US television quiz show *Jeopardy!* in 2011 was a nail in the coffin of human superiority. The machine beat two human contestants by answering questions posed in colloquial English, making sense of cultural allusions, metaphors, puns and jokes. If Alan Turing had been given a transcript of the show, would he have spotted the odd one out?

Watson may be the latest vindication of Turing's view of intellectual processes as a series of logical states. But its internal workings are not based on the human brain. Broad similarities in organization might be imposed by the nature of the task, but most software engineers neither know nor care about

anatomy or physiology. Even biologically inspired approaches such as cellular automata, genetic algorithms and neural networks have only a tenuous link to living tissue.

In 1944, Turing confessed his dream of building a brain, and many people continue in that endeavour to this day. Yet any neurobiologist will view such attempts as naive. How can you represent a neuronal synapse — a complex structure containing hundreds of different proteins, each a chemical prodigy in its own right and arranged in a mare's nest of interactions — with a single line of code? We still do not know the detailed circuitry of any region of the brain well enough to reproduce its structure. Brains are special. They steer us through the world, tell us what to do or say, and perform myriad vital functions. Brains are the source of our emotions, motivation, creativity and consciousness. Because no one knows how to reproduce any of these features in an artificial machine, we must consider that something important is missing from the canonical microchip.

Brains differ from computers in a number of key respects. They operate in cycles rather than in linear chains of causality, sending and receiving signals back and forth. Unlike the hardware and software of a machine, the mind and brain are not distinct entities. And then there is the question of chemistry.

Living cells process incoming sensory information and generate not just electrical signals but subtle biochemical changes. Cells are soft, malleable and built from an essentially infinite variety of macromolecular species quite unlike silicon chips. Organisms encode past experiences in distinct cellular states — in humans these are the substrate of goal-oriented movements and the sense of self. Perhaps machines built from cell-like components would be more like us.

**AMNON SHASHUA**

## Speed will trump brain's advantages

*Sachs Professor of Computer Science,  
Hebrew University of Jerusalem, and  
co-founder and chairman of Mobileye*

The saying that "people who are really serious about software should make their own hardware", attributed to computer scientist Alan Kay in the 1980s, still rings true today. The idea that the function and form of computing architecture should serve each other is at the root of algorithms in signal processing, image rendering, gaming, video compression and streaming. I believe that it is also true for the human brain — meaning that the brain does not implement 'intelligence' in the same way as a computer.

Two of the many fundamental differences between the brain and the computer are memory and processing speed. The analogue of long-term memory in a computer is the hard disk, which can store practically unlimited amounts of data. Short-term information is held in its random access memory (RAM), the capacity of which is astronomical compared with the human brain. Such quantitative differences become qualitative when

considering strategies for intelligence.

**"Signals in the brain are transmitted at a snail's pace."**

Intelligence is manifested by the ability to learn. Machine-learning practitioners use 'statistical learning' which

requires a very large collection of examples on which to generalize. This 'frequentist' approach to probabilistic reasoning needs vast memory capacity and algorithms that are at odds with available data on how the brain works. For example, IBM computer Watson needed to consume terabytes of reference material to beat human contestants on *Jeopardy!*. Volvo's pedestrian-detection system (developed by Mobileye) learned to identify people by using millions of pictures. In both cases, the human brain is considerably more parsimonious in the reliance on data — something that does not constrain the computer.

In terms of processing power, the brain can reach about 10–50 petaflops — equivalent to hundreds of thousands of the most advanced Intel Core i7 CPUs. Yet signals in the brain are transmitted at a snail's pace — five or six orders of magnitude slower than modern CPUs. This huge difference in communication speed drives vastly different architectures.

The brain compensates for the slow signal speed by adopting a hierarchical parallel structure, involving successive layers with increasing receptive field and complexity. By comparison, a computer architecture is usually flat and, because of its much faster clock rate, can employ brute-force techniques. Computer chess systems such as Deep Blue use pattern-recognition strategies, such as libraries of opening moves and completely solved end-games, complemented by their ability to evaluate the outcomes of some 200 million moves per second. This is way beyond the best grandmaster.

An intimate understanding of how cognitive tasks are performed at an algorithmic level would allow artificial intelligence to grow in leaps and bounds. But we must bear in mind that the vastly different architecture of the computer favours strategies that make optimal use of its practically unlimited memory capacity and brute-force search. ■

1. Turing, A. M. *Proc. Lond. Math. Soc.* **s2-42**, 230–265 (1936–37).
2. McCulloch, W. S. & Pitts, W. H. *Bull. Math. Biophys.* **5**, 115–133 (1943).





# Pattern formation

We are only beginning to see the impact of Turing's influential work on morphogenesis, says **John Reinitz**.

**A**lan Turing's 1952 paper on the origin of biological patterning<sup>1</sup> solved an intellectual problem that had seemed so hopeless that it caused a great developmental biologist, Hans Driesch, to give up science and turn to the philosophy of vitalism.

In the late nineteenth century, Driesch, and later Hans Spemann, demonstrated that animal bodies develop from a patternless single cell, rather than growing from a microscopic, preformed version of the adult body — in humans, the 'homunculus'. But such self-organization, Driesch realized, could not be understood with the ideas of that century. Before the invention of computers, applied mathematics dealt only with linear differential equations, which can amplify a pattern but not generate it.

In 'The chemical basis of morphogenesis', Turing showed that a pattern can indeed form *de novo*. In considering how an embryo's development unfolds instant by instant from its molecular and mechanical state, Turing was using a modern approach. Developmental biologists today similarly investigate how molecular determinants and forces exerted by cells control embryonic patterning.

Turing's focus was on chemical patterns: he coined the term 'morphogen' as an abstraction for a molecule capable of inducing tissue differentiation later on. This concept will be familiar to any molecular biologist: the protein products of the *HOX* gene cluster, for example, which are essential for body patterning throughout the animal kingdom, are

morphogens in Turing's sense. (Confusingly, the term has been more narrowly defined since.)

At the heart of pattern-making is symmetry-breaking. Turing considered an idealized embryo beginning with a uniform concentration of morphogens, which have translational symmetry that is lost as specific tissues emerge. He raised deep questions that are still unsolved, noting for instance that all physical laws known at the time had mirror-image symmetry, but biological systems did not. Turing speculated that the asymmetry of organisms originated from that of biological molecules. His point is still relevant to life's origins.

Turing's argument involved a mathematical trick: he created a nonlinear system by turning on diffusion discontinuously in an otherwise linear system at a specific instant. Without diffusion, the system is stable and homogeneous, but with diffusion, it becomes unstable and forms spatial pattern. The brilliance of the trick is that the nonlinearity is confined to a single point in time, so that at all other times, only the theory of linear equations is needed. Turing cleverly arranged to have diffusion generate pattern, rather than blur it, as it usually does.

The influence of Turing's paper is difficult



## TURING AT 100

A legacy that spans science:  
[nature.com/turing](http://nature.com/turing)

to overstate. It was a transition point from the era of analytical mathematics to that of computational mathematics. Although his proof was constructed analytically, Turing's paper contains the first computer simulations of pattern formation in the presence of stochastic fluctuations, and is possibly the first openly published case of computational experimentation.

Turing used analytical arguments of the nineteenth century to point the way towards the computational science of the twenty-first century. He was well aware, however, that nonlinear science and developmental biology would require more advanced computational methods. "Most of the organism, most of the time, is developing from one pattern into another, rather than from homogeneity into a pattern," he stated<sup>1</sup>. He realized that even though an embracing theory for such processes might not be possible, individual cases could be modelled with a digital computer.

Yet Turing's work is frequently misinterpreted, perhaps because he died tragically in 1954, before he could correct the record. His analytical arguments are often mistaken for biological predictions, although Turing did not intend them as such. His hypothetical system, based on two substances, was a simplification. For the pattern-forming trick to work, one substance should catalyse synthesis of both substances while diffusing slowly; the other should catalyse destruction of both substances while diffusing rapidly. For patterns that shift over time, three substances would be required. A field of investigation of these models has sprung up<sup>2</sup>, but credit or blame for the results rests with those authors, not Turing.

What Turing should receive credit for is opening the door to a new view of developmental biology, in which we deal directly with the chemical reactions and mechanical forces embryos use to self-organize their bodies from a single cell. He was well ahead of his time. It was three decades before the work on *Drosophila* embryos by Lewis<sup>3</sup>, Wieschaus and Nüsslein-Volhard<sup>4</sup> led to the discovery of real morphogens. It is the young researchers of today who will benefit most from reading Turing's work — seeing his ideas about morphogenesis not as speculation but as the conceptual framework for concrete problems. ■

**John Reinitz** is in the departments of statistics, ecology and evolution, and molecular genetics and cell biology at the University of Chicago, Chicago, Illinois 60637, USA.  
[reinitz@galton.uchicago.edu](mailto:reinitz@galton.uchicago.edu)

1. Turing, A. M. *Phil. Trans. R. Soc. Lond. B* **237**, 37–72 (1952).
2. Kondo, S. & Miura, T. *Science* **329**, 1616–1620 (2010).
3. Lewis, E. B. *Nature* **276**, 565–570 (1978).
4. Nüsslein-Volhard, C. & Wieschaus, E. *Nature* **287**, 795–801 (1980).



# The incomputable reality

The natural world's interconnectivity should inspire better models of the Universe, says **Barry Cooper**.

**A**lan Turing put bounds on what is computable in a famous 1936 paper<sup>1</sup>. The Turing machines he presented implement finite algorithms, handling data coded as real numbers. They are deterministic, but give some bizarre results. You can build a universal machine that can simulate any other Turing machine. But not every question you can ask of it has a computable answer: you cannot predict, for example, whether it ever spits out a given number or series of numbers.

By coincidence, our Newtonian view of physics faltered at about the same time as our computable view of mathematics. Linger problems in classical physics, such as the unpredictable trajectories of three bodies following a collision, may involve incomputability. Albert Einstein's theory of general relativity opens up a new world of computation with exotic objects such as spinning black holes. Quantum mechanics tells us that measurements are inherently uncertain.

The concept of computability is basic to modern science, from quantum gravity to artificial intelligence. It is also relevant in the everyday world, where it is useful to distinguish problems that are merely difficult to compute in practice from those that are intrinsically impossible with any machine. Incomputability should trouble economists, because breakdowns of control in chaotic markets can wreak havoc.

But disciplinary boundaries are preventing us from getting a full view of its role. Cosmetic differences may hide revealing parallels.

## EMERGENT PHENOMENA

Turing was interested in the mathematics of computing and also in its embodiment — the material environment that houses it. This theme links all of his work, from machines to the brain and morphogenesis. Although many mathematicians and software engineers today see it as irrelevant, embodiment is key to explaining the physical world.

Take turbulence: a river swollen by recent rain occasionally erupts into surprising formations that we would not expect from the basic dynamics of the water flow. The reason is coherence — non-local connectivity affects the water's motion. Turbulence, and



## TURING AT 100

A legacy that spans science:  
[nature.com/turing](http://nature.com/turing)

other 'emergent' nonlinear phenomena, may not be computable with a Turing machine. Zebra stripes and tropical-fish patterns, which Turing described in 1952–54 with his differential equations for morphogenesis, arise similarly.

Even in nonlinear systems, such high-order behaviour is causal — one phenomenon triggers another. Levels of explanation, from the quantum to the macroscopic, can be applied. But modelling the evolution of the higher-order effects is difficult in anything other than a broad-brush way. Such problems infiltrate all our models of the natural world.



The Universe is like that turbulent stream — its behaviour as a whole guided by myriad connections at various scales. It has many emergent levels of causality, bridged by phase transitions. The mechanistic structure that science deals with so well, and its invariant laws, are hard to explain in terms of the quantum level. Biology emerges from the quantum world, but is not computable from it. We are part of an organic whole — fragmented but coherent.

Across these boundaries, higher-level relations can feed back into lower ones. But looking up from a lower level, the causality will not be computable. For example, the uncertainty principle prevents the quantum world from fully describing the state

of a particle at any instant. A measurement produces a full description, but we cannot compute how it does it. In Turing's world, a description of reality is not always enough for a computable prediction.

Nature presents us with new ways of computing, from the Universe to the brain. Turing went on to build logical hierarchies to better understand real-world computation, which includes intuitive or unpredictable leaps<sup>2</sup>. Researchers experimenting with intelligent machines today see the possibilities in such an approach. But problems of control of higher-order behaviours still present formidable challenges to implementing it.

## BRIDGE BUILDING

It took nature millions of years to build a human brain. Meanwhile, we have to live with the stupidity of purely algorithmic processes. We need to embrace more experimental approaches to computation, and a renewed respect for embodied computing — as anticipated in Turing's late work in the 1950s on artificial intelligence and morphogenesis.

Bridges between mathematicians and physicists are important if we are to do this. It is a long time since Kurt Gödel and Albert Einstein chatted in the halls of Princeton University in New Jersey. Mathematicians can bring to the table Turing's model of basic causal structure. This would help physicists to discover more complete descriptions of the Universe — making redundant Hugh Everett's many-worlds interpretation and related multiverse hypotheses — and fix the arbitrariness of parts of the standard model of particle physics.

Samson Abramsky, a computer scientist at the University of Oxford, UK, recently asked: "Why do we compute?" Turing computation does not create anything that is not there already in the initial data. Can information increase in computation?

If we look at the world with new eyes, allowing computation full expression, we may come to startling conclusions. ■

**Barry Cooper** is in the School of Mathematics, University of Leeds, Leeds LS2 9JT, UK.  
e-mail: [pmt6sbc@leeds.ac.uk](mailto:pmt6sbc@leeds.ac.uk)

1. Turing, A. M. *Proc. Lond. Math. Soc.* **s2-42**, 230–265 (1936–37).
2. Turing, A. M. *Proc. Lond. Math. Soc.* **s2-45**, 161–228 (1939).



Our brains recreate the emotions of actors such as Geraldine James when we watch them perform.

## NEUROSCIENCE

# Powerful acts

**Giovanni Frazzetto** explores how theatre exerts its psychological effects on the emotions.

From rage and grief to exquisite tendresse, emotion is laid bare in theatre. Few art forms electrify or illuminate as powerfully as stage acting. But how have theatrical greats such as John Gielgud or Vanessa Redgrave cast their spell? Acting may be one of the most ancient arts, but science is only just beginning to get to grips with it.

Science started to seep into theatre in the late nineteenth and early twentieth centuries, with the Russian actor and theatre director Constantin Stanislavski. Founder of the influential Moscow Art Theatre, Stanislavski turned to physiologist Ivan Pavlov's research on conditioned reflexes to improve his acting method. The aim was to create performance

➔ **NATURE.COM**

A review of Danny Boyle's staging of *Frankenstein*:  
[go.nature.com/wqxshst](http://go.nature.com/wqxshst)

that united psychological experience and physical action.

Stanislavski sought a way to consciously trigger an actor's emotional expression. Science had begun to discover that neural pathways underlie complex behaviour and emotions, which can be conditioned in response to a changing environment. By practising key physical actions pertinent to the character and the play, Stanislavski realized, the actor could learn, by reflex, how to express the psychological experience of the emotion — with help from the imagination. A particular posture or movement would trigger a particular emotion. So by working hard on small actions such as clenching the fists and tensing the neck muscles, the actor could trigger anger, or they could awaken feelings of despair by shuffling, drooping and bowing the shoulders.

But, as we now know, the psychology of performance is more complex than this. To deliver a believable performance, actors need to remember not just emotions, body postures and expressions, but also their cues and lines. And, more importantly, they must seek ways of engaging with their audience to evoke empathy — the recognition or sharing of emotional states.

German philosopher Theodor Lipps was the first to use the term empathy (*Einfühlung*, literally 'feeling into') in the early twentieth century as a way of describing the relationship between artwork and observer in the psychology of aesthetic experience. In the 1990s, Italian neurophysiologists Giacomo Rizzolatti, Vittorio Gallese and their colleagues at the University of Parma in Italy offered a neurological framework for studying empathy through their discovery of mirror neurons — cells that fire both when we perform an action, and when we observe someone else performing it. They showed that our visual-motor system is activated as if we were executing an action that we are simply watching: the brain simulates that action.

These discoveries have resonated widely among theatrical professionals. They extend to intentionality (thinking of a way of doing some action), imitation (the replication of an action) and action understanding (grasping the import of an action) — all central to acting technique.

The actor must also demand something else of the audience: a suspension of disbelief. The phrase was coined in 1817 by English poet and philosopher Samuel Taylor Coleridge to describe how weaving enough facts into a fantastical narrative will help readers to accept the story, rather than judge it as implausible. Film-makers suspend disbelief by exploiting the power of moving images

in a darkened room, which lures an audience into their simulacrum of reality. In theatre, suspension of disbelief hinges on the switch

between two realities — the set and the cast of actors, and the places and characters they represent. In the prologue to *Henry V*, Shakespeare asks the audience to transform the bare stage by seeing it as the world of the king at war with France: "Piece out our imperfections with your thoughts ... and make imaginary puissance."

Twentieth-century German playwright Bertolt Brecht deliberately turned this tactic on its head in his 'epic theatre' system. By using techniques such as having the actors suddenly sing out of character, he ensured that his audiences became

**"Acting is predicated on technique and craft, but remains visceral and intuitive."**



emotionally detached from the characters. The audience members then became aware that they were witnessing fiction and were able to critically question the social realities represented in the play.

The cognitive processes underlying the suspension of disbelief have been the subject of several scientific studies. In 2010, Marie-Noëlle Metz-Lutz of the University of Strasbourg, France, and her colleagues used functional magnetic resonance imaging (fMRI) to scan the brains of people watching a play to pinpoint when they were transported into another reality. This was defined as when the subject's brain response tallied with a passage in the script intended to elicit such a response. The brain regions that fired at those moments included two areas involved in processing language and, specifically, in understanding metaphor, denoting the power of language to capture a spectator's attention. Both regions are also involved in processes of social and aesthetic judgements, probably governing appreciation of the writing style, plot or characterization.

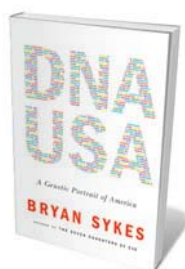
The French team also found that the subjects' heart rates slowed during transportation, and that brain activity fell in areas involved in building consciousness about the self and the external world. Without activity in these regions, an observer will take the fictionalized reality of the play at face value, despite the sensory perception of the stage, set and actors. Such results point to complete absorption in a play as a sort of hypnotic state involving the temporary loss of self-reference, and a disconnection from immediate sensory information — a distinct feeling of being 'carried away'.

In theory, such scanning experiments might help playwrights to identify specific language and theatrical devices that trigger audiences to become as absorbed as possible, and so enrich acting as an art and theatre as a vehicle of meaning and 'enchantment'. With a nod to Stanislavski, playwrights could focus on what movements or expressions are the most poignant, and which are most effective at conveying grief, compassion or joy. Such studies could also reveal which metaphors express an action or thought with the most brevity and wit, and what elements of plot device or vocal emphasis can make a difference in the brain.

Yet fMRI images and statistics will never replace the unpredictability and revelatory power of what is born in the rehearsal room. Acting is predicated on technique and craft, but remains visceral and intuitive. ■

**Giovanni Frazzetto** is a visiting research fellow in the School of Science and Social Policy at King's College London, Strand, London WC2R 2LS, UK.  
e-mail: gio@giovannifrazzetto.com

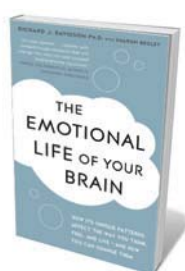
## Books in brief



### DNA USA: A Genetic Portrait of America

Bryan Sykes W. W. NORTON 320 pp. £19.99 (2012)

The US human population is a bouillabaisse of DNA. Geneticist Bryan Sykes took on the challenge of identifying its ingredients on an epic cross-country trip. He recounts the detective work — including interviews with genealogists and fellow geneticists — and methodology behind the findings. How did European genes appear in the DNA of Native Americans some 10,000 years ago, for instance? And why does the southwestern Hispanic population contain genes typically found in Jewish people? Ultimately, Sykes suggests, the country is an even richer human mix than we thought.



### The Emotional Life of Your Brain: How Its Unique Patterns Affect the Way You Think, Feel, and Live — And How You Can Change Them

Richard J. Davidson and Sharon Begley HUDSON STREET PRESS 279 pp. \$25.95 (2012)

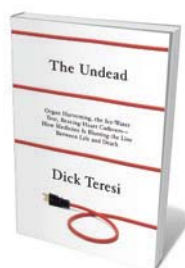
Why do some people plod stoically through crises while others collapse? Science writer Sharon Begley and neuropsychologist Richard Davidson argue that each of us has an 'emotional style': a pattern of responses to life's events that is allied to underlying brain systems. Looking at dimensions from social intuition to context sensitivity, the authors suggest that we can achieve better equilibrium by rewiring our emotional style through research-inspired exercises.



### Game Changer: Animal Rights and the Fate of Africa's Wildlife

Glen Martin UNIVERSITY OF CALIFORNIA PRESS 243 pp. £20.95 (2012)

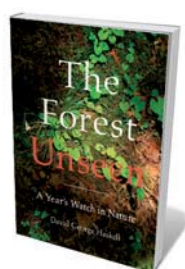
Africa's wild megafauna are caught in the crossfire between animal-welfare campaigners and conservationists, argues environmental reporter Glen Martin. In this pacy, unsentimental account, Martin interviews seasoned conservation biologists, zoologists and game wardens, focusing on practice in Kenya, Namibia and Tanzania. He concludes that holistic strategies incorporating habitat conservation, controlled hunting and respect for local people's needs are workable — and points out that measures such as ecotourism and protection for iconic species have backfired dramatically.



### The Undead: Organ Harvesting, the Ice-Water Test, Beating Heart Cadavers — How Medicine Is Blurring the Line Between Life and Death

Dick Teresi PANTHEON 368 pp. \$26.95 (2012)

The moment of death, suggests science writer Dick Teresi, is harder to pin down than ever. He introduces us to those who work at this borderline: cell biologists, specialist doctors, undertakers and people who have recovered from comas. Charting historical definitions of death, the thinking of research greats and debates over near-death experiences, Teresi notes that the ethical challenges are immense, asking, for instance, whether all organ donors are unrevivable.



### The Forest Unseen: A Year's Watch in Nature

David George Haskell VIKING 288 pp. \$25.95 (2012)

Training a biologist's eye on ecology, geology and climate, David Haskell visited a square metre of old-growth forest in southeastern Tennessee nearly every day for a year. His observations — of lichens, snowflakes, salamanders and more — are deftly interwoven with the science. His account is fascinating, whether he's stripping off in January to experience the physiological effects of severe cold, describing the symphonic sounds of trees in a high wind, or wondering at the bacteriocidal properties of a vulture's digestive tract.



## INFECTIOUS DISEASE

# Chronicles of a killer virus

Just over 30 years after HIV/AIDS was first recognized, three accounts of its ravages intrigue **Robin Weiss**.

As a frightening pandemic associated with sex, blood and death, AIDS was bound to evoke a rich mythology. Nicoli Nattrass's *The AIDS Conspiracy* deals with those myths and how scientific arguments counteract them. Jacques Pépin's *The Origins of AIDS* looks back at the emergence of HIV in the era before the syndrome was recognized, and Victoria Harden's *AIDS at 30* covers the period after its identification in 1981.

*The AIDS Conspiracy* is essential reading for anyone who is curious about why some people will not accept scientific facts about the nature, origin and lethality of HIV. As an HIV researcher, I used to divide people's strange beliefs about AIDS into myths of denial, and of blame and conspiracy. But Nattrass, who directs the AIDS and Society Research Unit at the University of Cape Town in South Africa, explains how HIV denialism has also become a conspiratorial attack on science and medicine — one that aims to convince people that antiretroviral therapy is more harmful than the 'blameless' virus.

Even when HIV is accepted as the cause of AIDS, Africa is blamed for its origin. Yet new diseases can arise anywhere: BSE or 'mad cow disease' in the United Kingdom, SARS in China and the 2009 H1N1 influenza pandemic in Mexico. Some AIDS creation myths continue to have an allure — for example, that HIV came out of oral polio vaccines, or that the virus is a man-made germ-warfare agent that was deliberately released in Africa by the United States.

Nattrass identifies four types of HIV denialist: the dissident scientist who lends credibility; the 'cultpreneur' who peddles quack therapies; the living icon or

## The AIDS Conspiracy: Science Fights Back

NICOLI NATTRASS

Columbia University Press: 2012. 240 pp.  
\$34.50, £24

## The Origins of AIDS

JACQUES PÉPIN

Cambridge University Press: 2011. 310 pp.  
£45, \$28.99

## AIDS at 30: A History

VICTORIA A. HARDEN

Potomac Books: 2012. 304 pp. \$29.95

long-term survivor; and the praise-singer or journalist who sows doubt about HIV causing AIDS. The dissidents are a tiny group, yet their campaign against antiretroviral therapy in South Africa has been estimated as leading to more than 300,000 preventable AIDS-related deaths. Science can respond through mechanisms such as the Durban Declaration on the link between HIV and AIDS, which was signed by more than 5,000 scientists and physicians (*Nature* **406**, 15–16, 2000). Nattrass also points out that social-media activists have often been more effective at tackling HIV denialism than official bodies.

In the superb *The Origins of AIDS*, Pépin — a Canadian epidemiologist who has worked across Africa — delves into the early phases of HIV emergence.

After the ancestor of the pandemic HIV-1 group M passed from a chimpanzee to a human in southeast Cameroon about 100 years ago, a few infected people travelled down the River Congo. AIDS became a community disease in Léopoldville (now Kinshasa), the capital of the Belgian Congo depicted in Joseph Conrad's 1903 novella *Heart of Darkness*. HIV began to thrive in its new host, Pépin shows, for several reasons.

There was a surge in medical injections using non-sterile syringes in mid-twentieth-century Africa, giving the transmission of HIV (and hepatitis viruses) a

crucial helping hand — a theory previously postulated by US epidemiologist Ernest Drucker. No Congolese physicians were trained under colonial rule, and when Belgium abandoned the Congo in 1960, few colonial or missionary doctors remained. Pépin describes a society in turbulent transition, with 'free women' and migrants swelling the capital. HIV became a mainly sexually transmitted infection. After the unsuccessful war of secession in Katanga in southeast Congo, Haitians among the United Nations troops brought HIV to the West. Homosexual men went to Haiti for sex, and Luckner Cambronne, leader of the country's Tonton Macoutes paramilitary force, sold more than 6,000 litres of blood plasma a month to the United States.

One question that Pépin skirts is why HIV prevalence in Kinshasa since 1980 remained relatively stable and low while it exploded elsewhere in Africa, spreading widely in southern Africa only in the 1990s. That mystery drives home the point that where a virus first enters the human population isn't necessarily where

it blooms; roots are not shoots. Another puzzle is why HIV-1 group M has been so successful compared with the other cross-species infections of HIV-1 groups N, O and P from apes, and of HIV-2 from monkeys. Pépin rightly argues that, apart from social factors promoting HIV spread, inherent properties of the virus must determine its fitness to become pandemic. He also provides the best analysis I have read of the declining HIV-2 epidemic in West Africa.

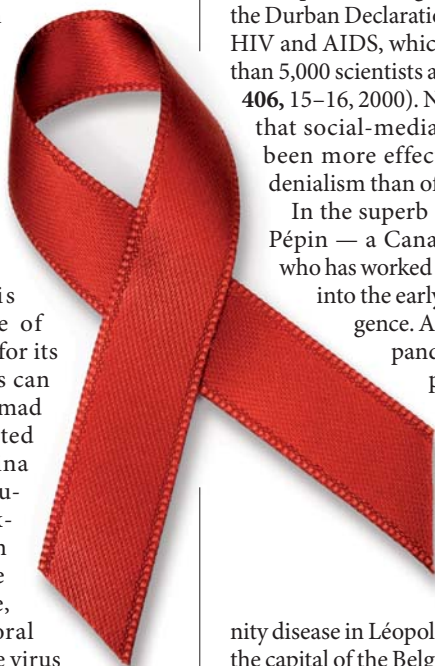
*AIDS at 30* begins where Pépin leaves off, with the appearance of AIDS in the United States. Harden, the retired doyenne of medical history at the US National Institutes of Health, draws extensively on that agency's archives for her narrative of the scientific advances in understanding HIV/AIDS, its treatment and prevention. She is particularly strong on the challenges of formulating US public-health policies for AIDS.

With 34 million people living with HIV, besides the 30 million it has already killed, seeking to understand the myths and the history of AIDS is surely important — although not as pressing as developing a safe and efficacious HIV vaccine. ■

With 34 million people living with HIV, besides the 30 million it has already killed, seeking to understand the myths and the history of AIDS is surely important — although not as pressing as developing a safe and efficacious HIV vaccine. ■

**Robin A. Weiss** is professor of viral oncology in the Division of Infection & Immunity, University College London, UK. e-mail: r.weiss@ucl.ac.uk

**"Where a virus first enters the human population isn't necessarily where it blooms; roots are not shoots."**





## Q&A Peter Diamandis

# The eternal optimist

*Peter Diamandis is the founder of the non-profit X Prize Foundation, which aims to kick-start research and development to solve humanity's biggest challenges. On the publication this week of his book *Abundance*, co-authored with journalist Steven Kotler, he explains how technological and social progress will enable us to provide enough food, water and energy for all.*

**Your book is optimistic about humanity's future. But aren't we already exceeding our planet's carrying capacity?**

The carrying capacity for Earth is a relative number. If I have an orange grove and I can reach only the lowest oranges on my trees, I need five trees to feed my family. If I can build a ladder, then I need only one tree. If humanity were to run out of food, our 'ladder' might be genetic engineering, or growing food hydroponically inside skyscrapers. It's not as if water is leaving the planet, or energy is not shining down, or we're not recycling food. These are all replenishable resources once we are able to use them more efficiently.

**How can we use resources better?**

We're living on a water planet; the challenge is that 98% is salt water. But there are technologies that can purify it — such as the Slingshot, a device the size of a mini refrigerator that can run on cow dung, which the Coca-Cola Company is helping to trial in

***Abundance: The Future Is Better Than You Think***

PETER H. DIAMANDIS  
AND STEVEN KOTLER  
Free Press: 2012.  
400 pp. \$26.99

Africa. With food, we now have the ability to go from evolution by natural selection to evolution by intelligent direction using genetic engineering. We will make cleaner energy through solar and nuclear approaches, which are the only ones that can scale to meet our needs. Mobile-phone use is growing exponentially, and soon more than 70% of the world will have one; the Qualcomm Tricorder X Prize is asking teams to build a mobile app that allows users to diagnose themselves as well as a physician can.

**How quickly can such technologies develop?**

The world is full of exponential technologies. When the Human Genome Project started in 1990, people said that it would take 50 years and would consume every scientist on the planet. These things can happen much more quickly. And now

there are new forces making them happen. Through the X Prize Foundation, I've witnessed individuals and small teams do things that, in the past, only governments could do. There is the DIY innovator: the person or team empowered by extraordinary technology, such as parents of sick children who create biolabs in their own kitchens. There are the techno-philanthropists: 'centimillionaires' who are being created younger and younger and tackling global challenges — just as Bill Gates has tackled malaria. In 2010 there were some 2 billion people online; by 2020 that is going to rise to 5 billion. These people are going to join the global economy, and innovate on a zero-cost basis.

**Are things better now than in the past?**

Over the twentieth century, lifespan has doubled. We're living in the most peaceful time ever. Every generation thinks that their problems are the biggest, but eventually we get around them. That was an important insight for me. People idealize the past but they forget how horrible it really was. Seeing problems is an evolutionary survival trait. The easiest way to survive is to be hyper-vigilant for problems.

**What about the growing gap between rich and poor?**

That's immaterial at some point. In the United States, happiness correlates with income only up to about US\$75,000. It's about providing for your needs. If someone in Africa can have first-tier [basic] health and education and access to abundant energy, food and water, they might still have little income, but those changes represent a huge step forward.

**You write of fulfilling basic needs for free and automating menial tasks. How would that affect the future economy?**

I don't know. 'Work' as a defined activity in society didn't exist for the first 100,000 years of our species. It was invented. If I own a nanobot that can create my food, a shelter, a car and anything else, I have everything I need. But what do you do with all your spare time? Does everyone become an artist? A thinker? An explorer? It is going to be interesting.

**Do you plan to live long enough to find out?**

When I was a first-year medical student I saw a television show about some turtles that might live as long as 700 years. So I asked, if they can, why can't I? We are on the edge of a revolution in health. We're designing an organogenesis X Prize for spare body parts. I'm staying in touch with the smartest researchers and physicians I know. ■

INTERVIEW BY NICOLA JONES

# Correspondence

## Mutant flu: preparing for a pandemic

We at the global humanitarian organization Save the Children agree that controversy over lab-created H5N1 avian influenza virus should not detract from the larger concern of global preparedness for a flu pandemic (*Nature* **482**, 131; 2012).

In a pandemic flu situation, when all countries and responding organizations are stricken, we think it is unrealistic to hope that the most resource-poor communities around the world will receive adequate supplies of vaccine, antivirals or antibiotics. We believe in preparing now so that community leaders, and the organizations working with them, can mitigate the effects of a severe wave of flu in the absence of substantial outside resources.

As the World Health Organization has noted, non-pharmaceutical interventions such as quarantine are crucial for an effective response, and may sometimes be the only means of delaying the spread of flu. Yet most national plans lack practical operational considerations (see [go.nature.com/mi9sr3](http://go.nature.com/mi9sr3)).

Detailed authoritative guidance on reducing flu transmission at household and community levels, and on the home-based care of flu patients, in low-resource settings is the most important, and needs to be published. Support should also be provided to governments in developing countries to adapt this guidance for their settings.

We believe that such efforts should be an urgent priority, and are concerned about this apparent gap in the most basic level of pandemic preparedness.  
**Eric S. Starbuck** *Save the Children, Westport, Connecticut, USA.*  
[estarbuck@savechildren.org](mailto:estarbuck@savechildren.org)

## Mutant flu: assessing biosecurity risks

In the ongoing controversy over the mutant H5N1 avian

influenza research (*Nature* **481**, 9–10, 2012), we should be wary of reducing biosecurity measures merely to assigning access rights to sensitive information and materials. A national security body made up of military and law-enforcement officials that puts confidentiality stamps on dual-use research is not in the long-term interest of scientific progress.

Biosecurity in research needs to be integrated into a more comprehensive strategy if it is to be effective and avoid harming public-health interests.

As a member and chair of several ethics-review panels of dual-use research for the European Union, I believe that these research projects, and their clearly foreseeable implications, should have undergone a proper risk–benefit assessment before funding. They could then have been modified to accommodate additional risk-management procedures.

For example, threats to biosecurity could have been minimized by developing diagnostic kits for early detection and surveillance of the new genetic variants, and by testing possible treatment strategies. It seems that none of this was done.

**Johannes Rath** *University of Vienna, Austria.*  
[johannes.rath@univie.ac.at](mailto:johannes.rath@univie.ac.at)

## Questionable use of chimpanzees

By conducting their experiments at US chimpanzee centres, foreign scientists have been circumventing their own nations' bans on chimpanzee research since 2005 (*Nature* **482**, 132; 2012). It is important to point out that those scientists are almost all employed by foreign-based drug companies — as reported by a US National Institutes of Health representative at the Institute of Medicine (IOM) public hearing in May 2011.

The US Food and Drug Administration's Office of New Drugs reported to the IOM committee in June 2011 that chimps are never required for preclinical drug testing in the United States, and that the agency discourages the use of chimps for this purpose. The IOM's report *Chimpanzees in Biomedical and Behavioral Research*, released in December 2011, also concludes that chimps are unnecessary for preclinical drug testing.

The use of chimps for preclinical drug trials in US centres by foreign drug companies is therefore contrary to US practice and should be banned.

**John J. Pippin** *Physicians Committee for Responsible Medicine, Washington DC, USA.*  
[jpippin@pcrm.org](mailto:jpippin@pcrm.org)

## Sugar: there's more to the obesity crisis

To describe sugar as “toxic” is extreme, as is its ludicrous comparison with alcohol (*Nature* **482**, 27–29; 2012). Such sensationalism could damage the livelihoods of thousands of people working in the sugar industry worldwide, and will be felt in countries such as Australia, the United States, Fiji, Mauritius, Indonesia and India.

As the senator for Queensland, Australia, where sugar is the most significant agricultural crop, I wish to voice the industry's concerns. Consumers should be assured that sugar is a safe ingredient and suitable for consumption as part of a balanced diet.

Nutritionist Jennie Brand-Miller of the University of Sydney is not alone in her disgust that you published this opinion piece (*The Australian*, 4 February 2012). The Dietitians Association of Australia believes that it is simplistic and unhelpful to blame sugar alone for the obesity crisis.

Alan Barclay of the Australian

Diabetes Council notes in the same article in *The Australian* that sugar consumption in Australia has dropped by 23% since 1980. But he adds that during that time, the number of overweight or obese people has doubled, while diabetes has tripled.

A literature review by Australia's National Health Medical Research Council, together with its draft dietary guidelines of December 2011, found that the evidence to support advice on added sugar and obesity was “limited, inconclusive or contradictory”.

Robert Lustig *et al.* have stimulated debate, yet have unnecessarily tarnished the image of sugar. There is no evidence to suggest that reducing sugar consumption will halt the rise in obesity. The contributing factors are far more complex.

**Ron Boswell** *Brisbane, Queensland, Australia.*  
[senator.boswell@aph.gov.au](mailto:senator.boswell@aph.gov.au)

## Sugar: fruit fructose is still healthy

Robert Lustig and colleagues argue that sugar is “toxic” (*Nature* **482**, 27–29; 2012), focusing on the “deadly effect” of the fructose moiety of sucrose. But they are directing attention away from the problem of general overconsumption.

Guidelines on healthy eating encourage fruit consumption, and fruit and fruit products are the third-largest source of fructose in the US diet.

Our meta-analyses of controlled feeding trials indicate a net metabolic benefit, with no harmful effects, from fructose at a level of intake obtainable from fruit (J. L. Sievenpiper *et al.* *Br. J. Nutr.*, in the press).

**John L. Sievenpiper, Russell J. de Souza, David J. A. Jenkins** *St Michael's Hospital, Toronto, Ontario, Canada.*  
[john.sievenpiper@utoronto.ca](mailto:john.sievenpiper@utoronto.ca)





## Sugar: a problem of developed countries

The contribution of sugar towards chronic disease is more relevant to developed countries than to the developing world (*Nature* **482**, 27–29; 2012). In Asia, for example, up to 10% of the population is obese and/or diabetic (see [go.nature.com/qmmoha](http://go.nature.com/qmmoha)), even though the daily energy contribution from sugar is less than 837 kilojoules per person. It is more likely that a high consumption of starch-based foods is to blame for this statistic (see [go.nature.com/2hoimi](http://go.nature.com/2hoimi)).

Overconsumption of foods that have a high glycaemic index (that trigger a rapid and sharp increase in blood glucose), such as wheat, potatoes and certain types of rice, also contributes to obesity and diabetes. Emphasis on sugar alone is therefore too narrow a basis for devising policies to curb these problems.

**Christiani Jeyakumar Henry, Viren Ranawana** *Clinical Nutrition Research Centre, Singapore Institute for Clinical Sciences, Singapore.*  
[jeya\\_henry@sics.a-star.edu.sg](mailto:jeya_henry@sics.a-star.edu.sg)

## Sugar: other 'toxic' factors play a part

Regulating products based on a scientific risk analysis is a worthy goal, but I contend that Robert Lustig and colleagues

oversimplify the "toxic" truth about refined carbohydrates (*Nature* **482**, 27–29; 2012). Rather than demonizing sugar, the authors would have better served public health with recommendations to manage a balanced diet with exercise.

The authors also downplay other complex factors that could contribute to non-communicable disease burdens. These include relatively recent changes in exercise patterns, and pollutants and additives that affect metabolic activity.

Putting sugars in a regulatory league with alcohol and tobacco is misleading. Sugars do not cause behavioural intoxication, nor do they have the second-hand proximity impact of tobacco smoking — key factors in their regulation.

**Saleem H. Ali** *University of Vermont, Burlington, USA.*  
[saleem.ali@uvm.edu](mailto:saleem.ali@uvm.edu)

## Australia: small steps to control invasives

We believe that there are more obvious and less destructive options for controlling gamba grass and other invasive weeds in Australia than introducing mega-herbivores such as elephants (*Nature* **482**, 30; 2012).

Biological control using carefully screened host-specific arthropods or pathogens, combined with quarantine and spread-prevention measures, is

a more balanced approach, and one with which Australia has considerable experience.

The world is littered with examples of generalist vertebrate species (cane toads, foxes, mynas, mosquito fish and so on) that were introduced in the misguided hope of controlling a pest species, only to have a substantial undesired impact on native biodiversity.

Credible solutions to these problems are more likely to come from small things done well, rather than through elephantine, rhinocerine, or even asinine fixes.

**Bruce L. Webber, John K. Scott, Raphael K. Didham** *CSIRO Ecosystem Sciences, Floreat, Australia; and University of Western Australia, Crawley, Australia.*

[bruce.webber@csiro.au](mailto:bruce.webber@csiro.au)

## Australia: better solutions to wildfires

Among David Bowman's more outlandish suggestions for dealing with Australia's massive problems of wildfires, feral animals and weeds, there are some workable ideas (*Nature* **482**, 30; 2012).

Some of these are already being implemented, such as the reinstatement of Aboriginal fire management in the north of the country. The Australian Wildlife Conservancy's prescribed-burn programme in the Kimberley region is having great success.

These innovations are radical,

but they are based on a sound ecological understanding.

**Richard J. Hobbs** *University of Western Australia, Crawley, Australia.*  
[richard.hobbs@uwa.edu.au](mailto:richard.hobbs@uwa.edu.au)

## Australia: a case for Aboriginal rangers

David Bowman makes a strong case for employing Aboriginal people to manage their own land and to reinstate traditional fire practices in Australia (*Nature* **482**, 30; 2012). This strategy could form the basis of a coordinated, long-term conservation service.

It would also provide desperately needed employment for landowners, as well as supplying them with a reliable source of protein from hunting feral animals (N. Collier *et al.* *Hum. Ecol.* **39**, 155–164; 2011).

In addition, the Aboriginal people, who have a deep spiritual connection to land, would be able to remain on their traditional territories and so maintain close functional relationships with their ancestors.

**Clive R. McMahon** *Charles Darwin University, Darwin, Northern Territory, Australia.*  
[clive.mcmahon@cdu.edu.au](mailto:clive.mcmahon@cdu.edu.au)

## Australia: no price on cutting fire risk

David Bowman proposes that elephants should be introduced into Australia as a cost-effective way to control invasive gamba grass, a major source of wildfire fuel (*Nature* **482**, 30; 2012). But managing the elephants could be more expensive than, say, launching a fleet of harvesters every year to reduce fire risk. We should start by asking what is likely to work best, regardless of the cost.

To combat the problems caused by invasive aliens, we should implement ecologically sound control mechanisms that have a reasonable probability of success. We can worry about the bill later.

**P. J. Nico de Bruyn, Andrew B. Davies** *University of Pretoria, Hatfield, South Africa.*  
[pjndebruyn@zoology.up.ac.za](mailto:pjnidebruyn@zoology.up.ac.za)

## Collagen secretion explained

Cells package proteins into vesicles for secretion to the extracellular milieu. A study has now identified an enzyme that modifies the packaging machinery to encapsulate unusually large proteins, such as collagen. [SEE ARTICLE P.495](#)

DAVID J. STEPHENS

Together with other extracellular proteins, collagen provides the structural framework on which tissues develop and function. It is synthesized in the endoplasmic reticulum, an intracellular organelle, as a rigid, rod-like precursor (procollagen) about 300 nanometres in length. Procollagen — like nearly all secreted proteins — is then packaged into transport vesicles for delivery to another organelle, the Golgi apparatus, before its secretion to the cell's surroundings. Transport vesicles, however, are typically smaller than 100 nm, as they are generated from the endoplasmic reticulum by a group of proteins (the COPII coat) that co-assemble as a structurally defined polyhedral cage<sup>1</sup>. On page 495 of this issue, Jin *et al.*<sup>2</sup> reveal that modification of one of the COPII proteins allows the formation of vesicles that are large enough to hold procollagen.

The outer layer of the COPII coat is assembled using structural elements comprised of the proteins SEC13 and SEC31 (Fig. 1a). Although it was thought that the hinges between these elements are flexible enough to allow vesicles of various sizes to form<sup>3,4</sup>, little was known about how vesicle size is controlled. Jin and colleagues<sup>2</sup> show that SEC31 can be modified by ubiquitination — the attachment of one or more copies of a small protein called ubiquitin. Although ubiquitination can 'mark' a protein for degradation, it is becoming increasingly clear that it can also affect protein function<sup>5</sup>.

Specifically, the authors<sup>2</sup> report that, in mouse cells, the enzyme CUL3–KLHL12 adds a single ubiquitin to a small pool of SEC31 molecules, and that this modification is required to drive the secretion of collagen. Using high-resolution electron microscopy, they found that overexpression of CUL3–KLHL12 leads to the production of large COPII structures, up to 500 nm in diameter — sufficient to accommodate procollagen. The simplest explanation for these observations is that ubiquitin attachment to SEC31 results in a structural change in the COPII cage that alters coat flexibility, and allows procollagen to be encapsulated in a nascent vesicle (Fig. 1b).

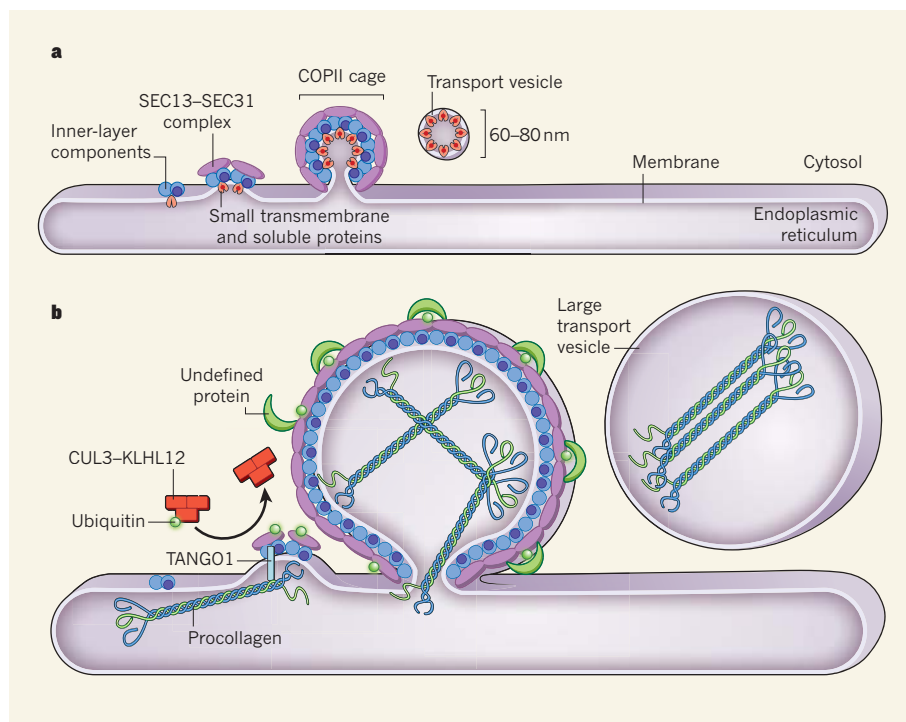


**Figure 1 | Big vesicles for collagen secretion.** **a**, Soluble proteins targeted for secretion, together with small transmembrane proteins, are packaged at the endoplasmic reticulum into vesicles that are coated by the COPII protein cage. Proteins that will form the inner layer of the COPII coat associate in an ordered fashion and then recruit the proteins SEC13 and SEC31, which form the outer layer. This leads to membrane deformation and ultimately to scission of 60–80-nm transport vesicles. **b**, Large proteins such as procollagen (the collagen precursor) do not fit into these typical vesicles. Jin *et al.*<sup>2</sup> report that, to encapsulate such large cargoes, the enzyme CUL3–KLHL12 attaches one copy of the small protein ubiquitin to SEC31 within the SEC13–SEC31 complex, and that this process facilitates collagen export. An additional, unknown protein might further stabilize lateral SEC13–SEC31 interactions. Although it is not known whether collagen synthesis directly triggers CUL3–KLHL12 activity, the transmembrane protein TANGO1 — which couples collagen in the endoplasmic reticulum to the assembling coat on the cytosolic face — might have a role in the process.

Jin and colleagues' observation that only some SEC31 molecules are modified indicates strongly that the addition of ubiquitin does not directly modulate the mechanics of COPII coat assembly. Instead, SEC31 ubiquitination might lead to recruitment of an additional, unknown protein to perform this role — for example, by further stabilizing lateral SEC13–SEC31 interactions. Identification of the additional factor and a more detailed molecular explanation of the modified geometry of the vesicle coat are challenges for the future.

Ubiquitination of some SEC31 molecules

could be an ongoing process that facilitates the formation of large COPII vesicles as a routine cell function; alternatively, large vesicles might be formed only on demand. In the latter case, however, it is not immediately obvious how CUL3–KLHL12, located in the cytoplasm, would sense the presence of newly synthesized procollagen in the endoplasmic reticulum. A potential candidate for relaying this information across the endoplasmic reticulum membrane is the transmembrane protein TANGO1, which forms part of a packaging receptor that is essential for



procollagen secretion<sup>6,7</sup>. TANGO1, however, does not make contact with SEC31 directly, nor is it found in fully formed vesicles, and so its possible connection to CUL3–KLHL12 is unclear.

Other questions remain. Does collagen become entirely encapsulated in a large COPII cage during vesicle formation (Fig. 1b), or does COPII somehow aid collagen export indirectly, without the need for a complete cage? And how does the addition of ubiquitin change the geometry of the COPII coat? Jin and colleagues' findings<sup>2</sup> might aid the development of a cell-free system for studying COPII-dependent packaging of collagen that would help to address these issues.

Moreover, is SEC31 ubiquitination relevant to the packaging of other large secreted macromolecules, such as lipoproteins?

These questions are relevant to our understanding not only of the fundamental mechanisms of cellular secretion, but also of diseases in which secretion (particularly of collagen) is defective because of gene mutation<sup>8</sup>. Furthermore, manipulation of the CUL3–KLHL12 ubiquitination pathway might be used to increase collagen secretion from cells for applications in stem-cell culture, for growth of tissue components in regenerative medicine, or perhaps for ameliorating age-related degeneration of connective tissue. ■

**David J. Stephens** is in the Cell Biology Laboratories, School of Biochemistry, University of Bristol, Bristol BS8 1TD, UK. e-mail: david.stephens@bristol.ac.uk

1. Zanetti, G., Pahuja, K. B., Studer, S., Shim, S. & Schekman, R. *Nature Cell Biol.* **14**, 20–28 (2011).
2. Jin, L. *et al. Nature* **482**, 495–500 (2012).
3. Stagg, S. M. *et al. Cell* **134**, 474–484 (2008).
4. Fath, S., Mancias, J. D., Bi, X. & Goldberg, J. *Cell* **129**, 1325–1336 (2007).
5. Komander, D. *Biochem. Soc. Trans.* **37**, 937–953 (2009).
6. Saito, K. *et al. Cell* **136**, 891–902 (2009).
7. Wilson, D. G. *et al. J. Cell Biol.* **193**, 935–951 (2011).
8. De Matteis, M. A. & Luini, A. *N. Engl. J. Med.* **365**, 927–938 (2011).

## ASTROPHYSICS

# First results from Planck observatory

**Early data from the Planck space satellite provide information about dust in distant galaxies, as well as in the Milky Way, and on the properties of gas in some of the largest clusters of galaxies in the Universe.**

UROŠ SELJAK

Astronomers have long known<sup>1</sup> that most of the stars in the Universe are born in messy environments containing dusty clouds. Young stars in such dust-enveloped regions are not visible to optical telescopes; thus, multi-wavelength studies, from the radio to the X-ray regime, are used to better understand how stars form in our Galaxy. But for more distant galaxies, including

some of the first galaxies in the Universe, such dusty expanses are essentially invisible across most wavelengths. One exception is the wavelengths in the far-infrared and microwave regimes, which are roughly 1,000 times longer than those of visible light. Stars heat up the dust surrounding them to temperatures of roughly 20 kelvin — much lower than that of the stars themselves, but nevertheless high enough for the dust to radiate microwave and far-infrared light. This warm-dust signature,

called the cosmic infrared background, has now been observed<sup>2</sup> by a large team of astronomers working with data from the Planck space observatory. The results are part of a series of studies that form a collection of 26 papers, published by the Planck team in *Astronomy & Astrophysics* (see [go.nature.com/au8vap](http://go.nature.com/au8vap)).

The Planck satellite's measurement of the cosmic infrared background<sup>2</sup> improves on previous measurements, including data<sup>3</sup> obtained by Herschel, a twin observatory to Planck launched by the European Space Agency aboard the same rocket in 2009. The rocket carried them to the Earth–Sun Lagrangian point L2 (1.5 million kilometres from Earth in the opposite direction from the Sun), where the satellites can be stationary relative to both the Sun and Earth, allowing for shielding from the Sun's radiation.

Planck detects microwave light in several wavelength bands in which the warm-dust emission can be observed (Fig. 1). Because the Universe is expanding and the wavelength of light stretches with the expansion, the light that we observe has a longer wavelength than it

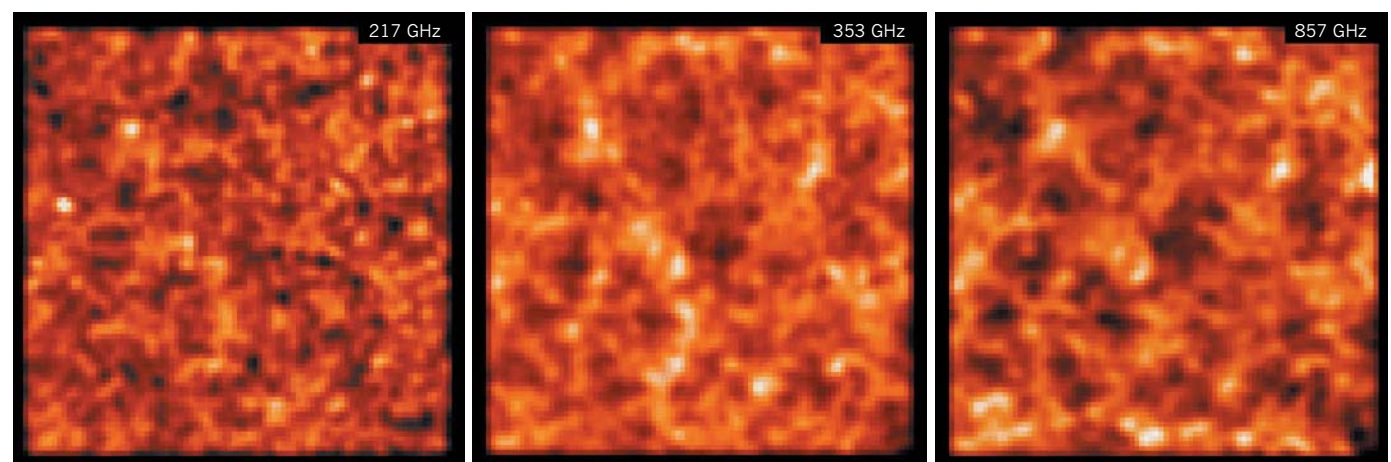


**Figure 1 | The cosmic infrared background.** The images show the anisotropies, or irregularities, of the cosmic infrared background in three of the frequency channels (217 gigahertz, 353 GHz and 857 GHz) probed by the Planck observatory<sup>2</sup> over a  $26^\circ \times 26^\circ$  patch of the sky. The anisotropies are visible as globular structures and correspond

to dusty galaxies clumped together on large scales. As we move across frequency channels, different epochs of cosmic time become visible: observations at 217 GHz offer a glimpse of some of the oldest galaxies in the Universe, which formed when the Universe was less than 2 billion years old.



procollagen secretion<sup>6,7</sup>. TANGO1, however, does not make contact with SEC31 directly, nor is it found in fully formed vesicles, and so its possible connection to CUL3–KLHL12 is unclear.

Other questions remain. Does collagen become entirely encapsulated in a large COPII cage during vesicle formation (Fig. 1b), or does COPII somehow aid collagen export indirectly, without the need for a complete cage? And how does the addition of ubiquitin change the geometry of the COPII coat? Jin and colleagues' findings<sup>2</sup> might aid the development of a cell-free system for studying COPII-dependent packaging of collagen that would help to address these issues.

Moreover, is SEC31 ubiquitination relevant to the packaging of other large secreted macromolecules, such as lipoproteins?

These questions are relevant to our understanding not only of the fundamental mechanisms of cellular secretion, but also of diseases in which secretion (particularly of collagen) is defective because of gene mutation<sup>8</sup>. Furthermore, manipulation of the CUL3–KLHL12 ubiquitination pathway might be used to increase collagen secretion from cells for applications in stem-cell culture, for growth of tissue components in regenerative medicine, or perhaps for ameliorating age-related degeneration of connective tissue. ■

**David J. Stephens** is in the Cell Biology Laboratories, School of Biochemistry, University of Bristol, Bristol BS8 1TD, UK. e-mail: david.stephens@bristol.ac.uk

1. Zanetti, G., Pahuja, K. B., Studer, S., Shim, S. & Schekman, R. *Nature Cell Biol.* **14**, 20–28 (2011).
2. Jin, L. *et al. Nature* **482**, 495–500 (2012).
3. Stagg, S. M. *et al. Cell* **134**, 474–484 (2008).
4. Fath, S., Mancias, J. D., Bi, X. & Goldberg, J. *Cell* **129**, 1325–1336 (2007).
5. Komander, D. *Biochem. Soc. Trans.* **37**, 937–953 (2009).
6. Saito, K. *et al. Cell* **136**, 891–902 (2009).
7. Wilson, D. G. *et al. J. Cell Biol.* **193**, 935–951 (2011).
8. De Matteis, M. A. & Luini, A. *N. Engl. J. Med.* **365**, 927–938 (2011).

## ASTROPHYSICS

# First results from Planck observatory

**Early data from the Planck space satellite provide information about dust in distant galaxies, as well as in the Milky Way, and on the properties of gas in some of the largest clusters of galaxies in the Universe.**

UROŠ SELJAK

Astronomers have long known<sup>1</sup> that most of the stars in the Universe are born in messy environments containing dusty clouds. Young stars in such dust-enveloped regions are not visible to optical telescopes; thus, multi-wavelength studies, from the radio to the X-ray regime, are used to better understand how stars form in our Galaxy. But for more distant galaxies, including

some of the first galaxies in the Universe, such dusty expanses are essentially invisible across most wavelengths. One exception is the wavelengths in the far-infrared and microwave regimes, which are roughly 1,000 times longer than those of visible light. Stars heat up the dust surrounding them to temperatures of roughly 20 kelvin — much lower than that of the stars themselves, but nevertheless high enough for the dust to radiate microwave and far-infrared light. This warm-dust signature,

called the cosmic infrared background, has now been observed<sup>2</sup> by a large team of astronomers working with data from the Planck space observatory. The results are part of a series of studies that form a collection of 26 papers, published by the Planck team in *Astronomy & Astrophysics* (see [go.nature.com/au8vap](http://go.nature.com/au8vap)).

The Planck satellite's measurement of the cosmic infrared background<sup>2</sup> improves on previous measurements, including data<sup>3</sup> obtained by Herschel, a twin observatory to Planck launched by the European Space Agency aboard the same rocket in 2009. The rocket carried them to the Earth–Sun Lagrangian point L2 (1.5 million kilometres from Earth in the opposite direction from the Sun), where the satellites can be stationary relative to both the Sun and Earth, allowing for shielding from the Sun's radiation.

Planck detects microwave light in several wavelength bands in which the warm-dust emission can be observed (Fig. 1). Because the Universe is expanding and the wavelength of light stretches with the expansion, the light that we observe has a longer wavelength than it

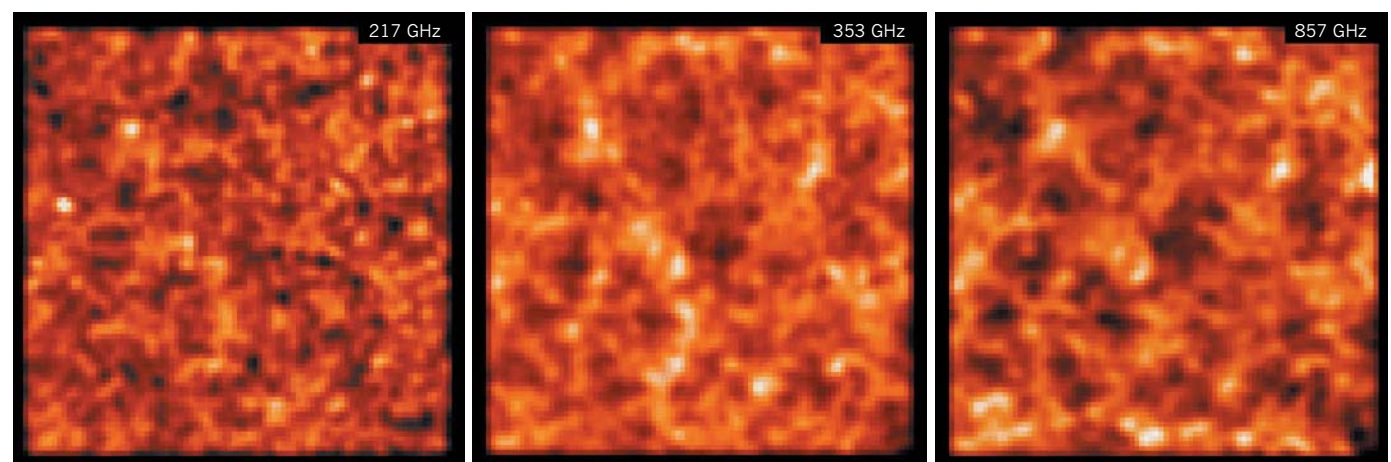


**Figure 1 | The cosmic infrared background.** The images show the anisotropies, or irregularities, of the cosmic infrared background in three of the frequency channels (217 gigahertz, 353 GHz and 857 GHz) probed by the Planck observatory<sup>2</sup> over a  $26^\circ \times 26^\circ$  patch of the sky. The anisotropies are visible as globular structures and correspond

to dusty galaxies clumped together on large scales. As we move across frequency channels, different epochs of cosmic time become visible: observations at 217 GHz offer a glimpse of some of the oldest galaxies in the Universe, which formed when the Universe was less than 2 billion years old.

ESA/PLANCK COLLABORATION

## FLUID MECHANICS

# Mist opportunities

From the fixative properties of hairsprays to the stickiness of filaments on beetles' feet, the wetting of flexible fibres with droplets of liquid is a universal phenomenon — but one we know surprisingly little about. On page 510 of this issue, Duprat *et al.* formulate rules to describe how mists of droplets interact with flexible fibre arrays (C. Duprat, S. Protière, A. Y. Beebe & H. A. Stone *Nature* **482**, 510–513; 2012).

The researchers began with the simplest possible model: the interactions of water droplets with a pair of closely aligned, flexible glass fibres that were clamped at one end but free to bend at the other. They observed that a droplet deposited close to the clamped ends adopts one of three forms: it could remain as a tight, spherical bridge between the filaments, or, depending on the conditions, it could either partially or completely spread along the fibres, in the latter case causing them to coalesce.

On further investigation, Duprat *et al.* found

that six physical parameters control droplet shape and spreading; they include fibre geometry, the distance between the fibres, and the fibres' mechanical properties. The authors also identified a critical droplet volume above which fibres do not coalesce, and a second critical volume at which droplet capture by fibres is maximized.

The team went on to explore the wetting of a natural fibre array by spraying a goose feather with oil droplets and observing the effects on the barbules (filaments projecting from each barb of a feather). They found that their theoretical model held up — small droplets spread along the barbules and caused barbule clumping, whereas larger droplets did not spread and could be easily dislodged — despite the roughness of the feather's barbules and the chemical affinity between the droplet



C. DUPRAT &amp; S. PROTIÈRE

and the barbules' surfaces.

Duprat and colleagues' discoveries suggest that the mechanical properties and spatial organization of biological fibre arrays may have evolved to optimize interactions with liquid droplets, and so enhance functions such as adhesion, dew collection and self-cleaning. The work also offers opportunities for improving the performance of technological wetting systems — for example, droplet volumes in sprays could be engineered to fine-tune their wetting interactions with relevant fibres. [Rosamund Daw](#)

had at its source. This means that, for the same dust temperature, observing the dust emission at the longer wavelengths corresponds to observing an epoch when the Universe was smaller, and hence younger. By measuring the dust at different wavelengths, Planck can track the emission from star-forming galaxies as a function of cosmic time. Planck's observations<sup>2</sup> suggest that most of the emission in the longer-wavelength bands comes from galaxies that formed at a time when the Universe was less than 2 billion years old (the age of the Universe today is approximately 14 billion years).

To achieve this measurement, the Planck team performed<sup>2</sup> a sophisticated software analysis called component separation. This was required because these wavelength bands contain radiation from many other sources, mostly the Milky Way, but also the cosmic microwave background (CMB, relic radiation from the early Universe glowing at 2.7 K). The strengths of these sources vary differently as a function of wavelength. By combining Planck's nine wavelength bands with additional external measurements, the team was able to separate the cosmic-infrared-background component from the other sources of radiation. The authors found<sup>2</sup> a broad agreement in results between different areas in the sky, which had been specially chosen for having low radiation from our Galaxy, suggesting that the component separation was successful.

The emission from the Milky Way is not just

a contaminant of the cosmic infrared background; it also contains some surprises of its own. One of these relates to the 'anomalous microwave emission' at centimetre wavelengths. This has been known about for a few years, but its origin has been controversial. In particular, although this radiation has been observed<sup>4</sup> to correlate with the emission from small dust grains in the Galaxy, simple models of thermal emission from dust could not explain its wavelength dependence. However, if the dust particles are spinning at high rates, they can radiate at a wavelength that relates to their spinning frequency and size. In this spinning-dust model, the emission occurs over a relatively narrow range of wavelengths that happens to coincide with the longest-wavelength band of the Planck observatory. Planck's observations of emission from the Milky Way provide<sup>5</sup> strong support for the spinning-dust model.

Not all of the results from Planck are related to dust radiation. Light propagating through hot gas can be scattered off electrons zooming around these high-temperature regions. The result of this process, named the Sunyaev–Zeldovich (SZ) effect after the two Russian scientists who first proposed<sup>6</sup> it, is that longer-wavelength light is shifted to shorter wavelengths. When viewed against the background provided by the CMB radiation, this effect leads to a dark hole at longer wavelengths at the position of a gas clump on the sky. Similarly, it causes a bright peak of light at shorter wavelengths at the same position.

With Planck's many wavelength bands, both of these features can be observed, leading to a convincing detection of the SZ effect. The sources most likely to provide a detectable SZ signal are the most massive galaxy clusters, which contain huge amounts of some of the hottest gas in the Universe. The Planck team found<sup>7</sup> nearly 200 cluster candidates with this technique, of which about 20 were previously unknown. Most of these have subsequently been confirmed as real clusters by follow-up studies, including X-ray observations<sup>8</sup> with the XMM-Newton satellite. Combined analysis of these data provides detailed information about the gas density and temperature distribution in the clusters, resulting in a better understanding of the processes that led to their formation.

These new results<sup>7</sup> demonstrate that it is possible to find clusters of galaxies with the SZ technique even for surveys looking at the entire sky, in contrast to previous SZ detections — by the South Pole Telescope<sup>9</sup> and Atacama Cosmology Telescope<sup>10</sup> — that searched smaller patches of the sky. Ultimately, the SZ method will allow clusters to be observed at a much larger distance from Earth than is possible with other methods, such as X-ray emission. One exciting application of the SZ approach would be to probe the growth of the largest (and thus rarest) structures at early times. Such observations would provide a measurement of the different components that make up the Universe and of the size of the initial density fluctuations that eventually



grew to become galaxies and galaxy clusters.

The early results from Planck demonstrate that the observatory is working flawlessly, and provide a first glimpse of its scientific potential. However, the best is yet to come. The main mission of Planck is to map the CMB radiation and its polarization with unprecedented precision. This measurement will provide a window onto the early Universe and offer clues as to what created the first seeds of structure. Planck may also detect the relic gravity waves from the Big Bang through the observations of CMB polarization. The task is complicated by the relative faintness of the CMB compared with other sources of radiation, such as dust emission, in most of the wavelength

bands. Careful separation of components is thus needed to isolate the CMB signal, a task that has proved challenging and is the main reason that these early results do not include any primary CMB data. These CMB results are expected to be announced in early 2013. Given the spectacular instrument performance of Planck shown by its early findings<sup>2,5,7</sup>, the cosmology community is eagerly awaiting more results. ■

**Uroš Seljak** is in the Physics and Astronomy Department and Lawrence Berkeley National Laboratory, University of California, Berkeley, California 94720, USA, and at the Institute for Theoretical Physics,

University of Zurich, Switzerland.  
e-mail: [useljak@berkeley.edu](mailto:useljak@berkeley.edu)

1. Shu, F. H., Adams, F. C. & Lizano, S. *Annu. Rev. Astron. Astrophys.* **25**, 23–81 (1987).
2. Planck Collaboration *Astron. Astrophys.* **536**, A18 (2011).
3. Amblard, A. *et al. Nature* **470**, 510–512 (2011).
4. Finkbeiner, D. P., Schlegel, D. J., Frank, C. & Heiles, C. *Astrophys. J.* **566**, 898–904 (2002).
5. Planck Collaboration *Astron. Astrophys.* **536**, A20 (2011).
6. Sunyaev, R. A. & Zeldovich, Y. B. *Comments Astrophys. Space Phys.* **4**, 173–178 (1972).
7. Planck Collaboration *Astron. Astrophys.* **536**, A8 (2011).
8. Planck Collaboration *Astron. Astrophys.* **536**, A9 (2011).
9. Carlstrom, J. E. *et al. Publ. Astron. Soc. Pacif.* **123**, 568–581 (2011).
10. Marriage, T. A. *et al. Astrophys. J.* **737**, 61 (2011).

## MATERIALS SCIENCE

# Cell environments programmed with light

**A combination of two light-induced reactions has been used to attach peptides to a polymeric gel, and then to detach them from it. This feat opens up opportunities for studying the effects of signalling molecules on cell behaviour *in vitro*.**

MATTHIAS P. LUTOLF

The ability to use light to precisely control the activity of cells has transformed the way many experiments in biology are performed. In particular, optogenetic techniques — in which light is used to manipulate cells that have been genetically engineered to be light responsive — have revolutionized neuroscience by providing a completely new way to modulate cell signalling, even in live animals<sup>1</sup>. Writing in *Angewandte Chemie*, DeForest and Anseth<sup>2</sup> report that light can be used to dynamically manipulate not only the intrinsic cellular regulatory machinery, but also the external microenvironment of a cell. Specifically, they showcase a class of ‘optobiomaterial’ whose biochemical properties can be changed to influence cellular activity simply by having different sources of light shone on it.

Far from being intrinsically determined, cell behaviour such as proliferation, differentiation and migration are tightly regulated by spatio-temporally complex signals originating from the surrounding milieu (the extracellular matrix, ECM). For instance, the microenvironments (known as niches) surrounding rare adult stem cells in human tissues regulate stem-cell behaviour using a combination of local cell–cell interactions, ECM-derived signals and soluble signalling molecules. Together, these niche signals are crucial for ensuring life-long maintenance of stem-cell function<sup>3</sup>. An

understanding of how stem cells respond to signals from their extracellular environment is therefore essential, especially for realizing the therapeutic potential of stem cells.

Biologists have a variety of *in vitro* model systems at hand to study such complex cell–ECM interactions, and this enables them to uncover cell-signalling mechanisms in near-physiological, three-dimensional contexts.

These models have been generated from crosslinked networks of protein components of the ECM such as collagen, or from ECM glycoproteins (polypeptides that have sugars attached) such as laminin. They have provided vital insight into extrinsic cell regulation, and in some cases have even made possible the formation of entire tissues from single stem cells *in vitro*<sup>4</sup>. Unfortunately, these biomaterials tend to suffer from uncontrollable batch-to-batch variability and are unable to modulate the availability of extrinsic signalling molecules — and thus cell function — controllably in space and time.

To recreate the dynamics of cellular microenvironments in three dimensions, researchers have sought strategies in materials chemistry that permit the biophysical and biochemical properties of matrices to be selectively modulated in a tailor-made fashion. Most approaches rely on well-characterized, cross-linked, synthetic polymers known as hydrogels that have ECM-like biophysical properties.

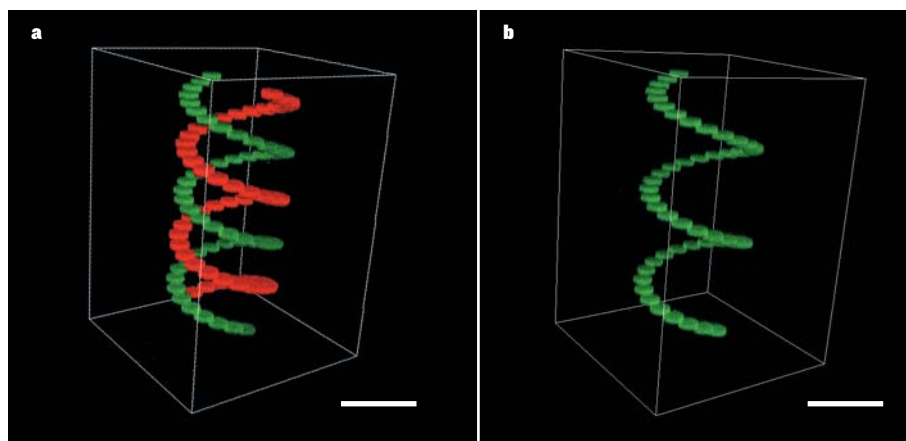


**Figure 1 | Reversible gel patterning.** DeForest and Anseth<sup>2</sup> have prepared hydrogels — water-absorbent polymeric networks — to which biologically active molecules can be attached and then removed using two light-induced reactions. By focusing light on specific regions of the gel, the authors precisely controlled the points of attachment. **a**, In this three-dimensional section of a hydrogel, fluorescently labelled peptides are bound in a double-helix pattern that was traced out using focused, visible laser light. False colour has been used to aid visualization. **b**, Subsequent irradiation of the red part of the helix with ultraviolet light has caused the peptides in that region to detach. Scale bars, 200 micrometres. (Images reproduced from ref. 2.)



## FLUID MECHANICS

# Mist opportunities

From the fixative properties of hairsprays to the stickiness of filaments on beetles' feet, the wetting of flexible fibres with droplets of liquid is a universal phenomenon — but one we know surprisingly little about. On page 510 of this issue, Duprat *et al.* formulate rules to describe how mists of droplets interact with flexible fibre arrays (C. Duprat, S. Protière, A. Y. Beebe & H. A. Stone *Nature* **482**, 510–513; 2012).

The researchers began with the simplest possible model: the interactions of water droplets with a pair of closely aligned, flexible glass fibres that were clamped at one end but free to bend at the other. They observed that a droplet deposited close to the clamped ends adopts one of three forms: it could remain as a tight, spherical bridge between the filaments, or, depending on the conditions, it could either partially or completely spread along the fibres, in the latter case causing them to coalesce.

On further investigation, Duprat *et al.* found

that six physical parameters control droplet shape and spreading; they include fibre geometry, the distance between the fibres, and the fibres' mechanical properties. The authors also identified a critical droplet volume above which fibres do not coalesce, and a second critical volume at which droplet capture by fibres is maximized.

The team went on to explore the wetting of a natural fibre array by spraying a goose feather with oil droplets and observing the effects on the barbules (filaments projecting from each barb of a feather). They found that their theoretical model held up — small droplets spread along the barbules and caused barbule clumping, whereas larger droplets did not spread and could be easily dislodged — despite the roughness of the feather's barbules and the chemical affinity between the droplet



C. DUPRAT &amp; S. PROTIÈRE

and the barbules' surfaces.

Duprat and colleagues' discoveries suggest that the mechanical properties and spatial organization of biological fibre arrays may have evolved to optimize interactions with liquid droplets, and so enhance functions such as adhesion, dew collection and self-cleaning. The work also offers opportunities for improving the performance of technological wetting systems — for example, droplet volumes in sprays could be engineered to fine-tune their wetting interactions with relevant fibres. [Rosamund Daw](#)

had at its source. This means that, for the same dust temperature, observing the dust emission at the longer wavelengths corresponds to observing an epoch when the Universe was smaller, and hence younger. By measuring the dust at different wavelengths, Planck can track the emission from star-forming galaxies as a function of cosmic time. Planck's observations<sup>2</sup> suggest that most of the emission in the longer-wavelength bands comes from galaxies that formed at a time when the Universe was less than 2 billion years old (the age of the Universe today is approximately 14 billion years).

To achieve this measurement, the Planck team performed<sup>2</sup> a sophisticated software analysis called component separation. This was required because these wavelength bands contain radiation from many other sources, mostly the Milky Way, but also the cosmic microwave background (CMB, relic radiation from the early Universe glowing at 2.7 K). The strengths of these sources vary differently as a function of wavelength. By combining Planck's nine wavelength bands with additional external measurements, the team was able to separate the cosmic-infrared-background component from the other sources of radiation. The authors found<sup>2</sup> a broad agreement in results between different areas in the sky, which had been specially chosen for having low radiation from our Galaxy, suggesting that the component separation was successful.

The emission from the Milky Way is not just

a contaminant of the cosmic infrared background; it also contains some surprises of its own. One of these relates to the 'anomalous microwave emission' at centimetre wavelengths. This has been known about for a few years, but its origin has been controversial. In particular, although this radiation has been observed<sup>4</sup> to correlate with the emission from small dust grains in the Galaxy, simple models of thermal emission from dust could not explain its wavelength dependence. However, if the dust particles are spinning at high rates, they can radiate at a wavelength that relates to their spinning frequency and size. In this spinning-dust model, the emission occurs over a relatively narrow range of wavelengths that happens to coincide with the longest-wavelength band of the Planck observatory. Planck's observations of emission from the Milky Way provide<sup>5</sup> strong support for the spinning-dust model.

Not all of the results from Planck are related to dust radiation. Light propagating through hot gas can be scattered off electrons zooming around these high-temperature regions. The result of this process, named the Sunyaev–Zeldovich (SZ) effect after the two Russian scientists who first proposed<sup>6</sup> it, is that longer-wavelength light is shifted to shorter wavelengths. When viewed against the background provided by the CMB radiation, this effect leads to a dark hole at longer wavelengths at the position of a gas clump on the sky. Similarly, it causes a bright peak of light at shorter wavelengths at the same position.

With Planck's many wavelength bands, both of these features can be observed, leading to a convincing detection of the SZ effect. The sources most likely to provide a detectable SZ signal are the most massive galaxy clusters, which contain huge amounts of some of the hottest gas in the Universe. The Planck team found<sup>7</sup> nearly 200 cluster candidates with this technique, of which about 20 were previously unknown. Most of these have subsequently been confirmed as real clusters by follow-up studies, including X-ray observations<sup>8</sup> with the XMM-Newton satellite. Combined analysis of these data provides detailed information about the gas density and temperature distribution in the clusters, resulting in a better understanding of the processes that led to their formation.

These new results<sup>7</sup> demonstrate that it is possible to find clusters of galaxies with the SZ technique even for surveys looking at the entire sky, in contrast to previous SZ detections — by the South Pole Telescope<sup>9</sup> and Atacama Cosmology Telescope<sup>10</sup> — that searched smaller patches of the sky. Ultimately, the SZ method will allow clusters to be observed at a much larger distance from Earth than is possible with other methods, such as X-ray emission. One exciting application of the SZ approach would be to probe the growth of the largest (and thus rarest) structures at early times. Such observations would provide a measurement of the different components that make up the Universe and of the size of the initial density fluctuations that eventually

grew to become galaxies and galaxy clusters.

The early results from Planck demonstrate that the observatory is working flawlessly, and provide a first glimpse of its scientific potential. However, the best is yet to come. The main mission of Planck is to map the CMB radiation and its polarization with unprecedented precision. This measurement will provide a window onto the early Universe and offer clues as to what created the first seeds of structure. Planck may also detect the relic gravity waves from the Big Bang through the observations of CMB polarization. The task is complicated by the relative faintness of the CMB compared with other sources of radiation, such as dust emission, in most of the wavelength

bands. Careful separation of components is thus needed to isolate the CMB signal, a task that has proved challenging and is the main reason that these early results do not include any primary CMB data. These CMB results are expected to be announced in early 2013. Given the spectacular instrument performance of Planck shown by its early findings<sup>2,5,7</sup>, the cosmology community is eagerly awaiting more results. ■

**Uroš Seljak** is in the Physics and Astronomy Department and Lawrence Berkeley National Laboratory, University of California, Berkeley, California 94720, USA, and at the Institute for Theoretical Physics,

University of Zurich, Switzerland.  
e-mail: [useljak@berkeley.edu](mailto:useljak@berkeley.edu)

1. Shu, F. H., Adams, F. C. & Lizano, S. *Annu. Rev. Astron. Astrophys.* **25**, 23–81 (1987).
2. Planck Collaboration *Astron. Astrophys.* **536**, A18 (2011).
3. Amblard, A. *et al. Nature* **470**, 510–512 (2011).
4. Finkbeiner, D. P., Schlegel, D. J., Frank, C. & Heiles, C. *Astrophys. J.* **566**, 898–904 (2002).
5. Planck Collaboration *Astron. Astrophys.* **536**, A20 (2011).
6. Sunyaev, R. A. & Zeldovich, Y. B. *Comments Astrophys. Space Phys.* **4**, 173–178 (1972).
7. Planck Collaboration *Astron. Astrophys.* **536**, A8 (2011).
8. Planck Collaboration *Astron. Astrophys.* **536**, A9 (2011).
9. Carlstrom, J. E. *et al. Publ. Astron. Soc. Pacif.* **123**, 568–581 (2011).
10. Marriage, T. A. *et al. Astrophys. J.* **737**, 61 (2011).

## MATERIALS SCIENCE

# Cell environments programmed with light

**A combination of two light-induced reactions has been used to attach peptides to a polymeric gel, and then to detach them from it. This feat opens up opportunities for studying the effects of signalling molecules on cell behaviour *in vitro*.**

MATTHIAS P. LUTOLF

The ability to use light to precisely control the activity of cells has transformed the way many experiments in biology are performed. In particular, optogenetic techniques — in which light is used to manipulate cells that have been genetically engineered to be light responsive — have revolutionized neuroscience by providing a completely new way to modulate cell signalling, even in live animals<sup>1</sup>. Writing in *Angewandte Chemie*, DeForest and Anseth<sup>2</sup> report that light can be used to dynamically manipulate not only the intrinsic cellular regulatory machinery, but also the external microenvironment of a cell. Specifically, they showcase a class of ‘optobiomaterial’ whose biochemical properties can be changed to influence cellular activity simply by having different sources of light shone on it.

Far from being intrinsically determined, cell behaviour such as proliferation, differentiation and migration are tightly regulated by spatio-temporally complex signals originating from the surrounding milieu (the extracellular matrix, ECM). For instance, the microenvironments (known as niches) surrounding rare adult stem cells in human tissues regulate stem-cell behaviour using a combination of local cell–cell interactions, ECM-derived signals and soluble signalling molecules. Together, these niche signals are crucial for ensuring life-long maintenance of stem-cell function<sup>3</sup>. An

understanding of how stem cells respond to signals from their extracellular environment is therefore essential, especially for realizing the therapeutic potential of stem cells.

Biologists have a variety of *in vitro* model systems at hand to study such complex cell–ECM interactions, and this enables them to uncover cell-signalling mechanisms in near-physiological, three-dimensional contexts.

These models have been generated from crosslinked networks of protein components of the ECM such as collagen, or from ECM glycoproteins (polypeptides that have sugars attached) such as laminin. They have provided vital insight into extrinsic cell regulation, and in some cases have even made possible the formation of entire tissues from single stem cells *in vitro*<sup>4</sup>. Unfortunately, these biomaterials tend to suffer from uncontrollable batch-to-batch variability and are unable to modulate the availability of extrinsic signalling molecules — and thus cell function — controllably in space and time.

To recreate the dynamics of cellular microenvironments in three dimensions, researchers have sought strategies in materials chemistry that permit the biophysical and biochemical properties of matrices to be selectively modulated in a tailor-made fashion. Most approaches rely on well-characterized, cross-linked, synthetic polymers known as hydrogels that have ECM-like biophysical properties.

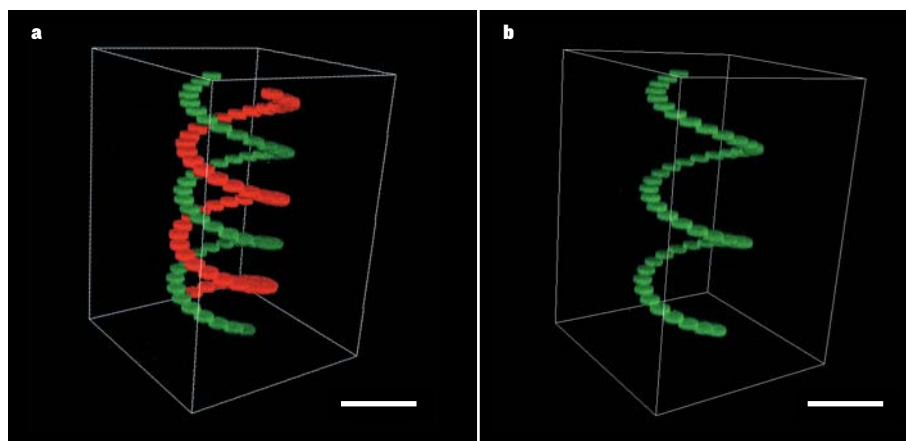


**Figure 1 | Reversible gel patterning.** DeForest and Anseth<sup>2</sup> have prepared hydrogels — water-absorbent polymeric networks — to which biologically active molecules can be attached and then removed using two light-induced reactions. By focusing light on specific regions of the gel, the authors precisely controlled the points of attachment. **a**, In this three-dimensional section of a hydrogel, fluorescently labelled peptides are bound in a double-helix pattern that was traced out using focused, visible laser light. False colour has been used to aid visualization. **b**, Subsequent irradiation of the red part of the helix with ultraviolet light has caused the peptides in that region to detach. Scale bars, 200 micrometres. (Images reproduced from ref. 2.)

But, in contrast to ECMs, most synthetic hydrogels are biologically inert because their polymer 'backbones' contain no biologically active components. This allows researchers to design very 'clean' experimental systems: biologically active molecules can be attached to hydrogels to perturb cell activity in a well-controlled fashion, without interference from the hydrogel itself.

Several research groups have carried out work in which light-sensitive molecular building blocks were attached to hydrogel networks to generate artificial ECMs in which the properties of microenvironments could be specifically modulated by light exposure<sup>3</sup>. For example, the introduction of chemical groups that can be cleaved by ultraviolet light has led to hydrogels that soften on light exposure<sup>6</sup>. Conversely, the incorporation of groups that form crosslinks between polymer chains when irradiated with ultraviolet light has resulted in materials that stiffen upon such irradiation<sup>7</sup>.

Systems in which light triggers the coupling<sup>8,9</sup> or removal<sup>6</sup> of biologically active molecules to or from hydrogel polymer networks have also been devised. These light-mediated approaches to modifying hydrogels have been used to control some aspects of the basic three-dimensional behaviour of cells embedded in the materials, such as adhesion to the artificial ECM or migration. But because the modifications involved are irreversible, they allow only one-way manipulation of cell activity.

DeForest and Anseth's work<sup>2</sup> now demonstrates fully reversible modulation of biologically active building blocks within light-sensitive hydrogels. They synthesized small peptides that can act as signals for cell adhesion, to which a short linker section was attached. The free end of the linker was a chemical group that can react with alkene groups in a hydrogel when irradiated with visible light, thereby attaching the peptide to the gel (Fig. 1). Another part of the linker was a group that breaks apart when irradiated with ultraviolet light; by shining this light on a hydrogel that had been decorated with the peptides, the authors could detach the peptides from the gel.

Crucially, both light-activated reactions are cell-compatible, which allowed DeForest and Anseth to attach (or detach) the peptides to (or from) their hydrogel in the presence of mouse embryonic fibroblast cells. By controlling precisely when and where the cell-adhesive peptides bound in the gel, the authors could control the duration and locations in which the cells attached and spread.

In a first gel-patterning step, DeForest and Anseth used visible light to create small 'islands' of peptides to which fibroblasts grown in culture with the gel adhered. In a second step, conducted after one day of culture, the authors removed peptides from areas of the islands using ultraviolet light. This caused

rapid, selective detachment of cells from those areas. The authors showed that the removed cells could then be grown again in culture, or analysed in other assays. As DeForest and Anseth suggest<sup>2</sup>, this kind of protocol could be widely used to manipulate and study subsets of cells (or even individual cells) of larger cell populations.

One long-term goal of work such as this is the development of materials to act as scaffolds for tissue regeneration. Can we expect this and/or similar techniques to transform tissue engineering in the same way that optogenetics is transforming neuroscience? This is, of course, difficult to predict. For DeForest and Anseth's hydrogel to be fully physiologically relevant, the ability to attach and release full-length proteins<sup>9</sup> — rather than short peptides — to the material needs to be developed. And it remains to be seen whether their approach is directly translatable to tissue regeneration *in vivo*. Furthermore, it could be argued that these methods will be valuable for tissue regeneration in only a relatively few cases, such as those in which much simpler scaffolds fail, because the spatial arrangement of ECM signals is necessary for driving regeneration.

Nevertheless, the reversible, dynamic control of chemical and physical gel properties should allow previously impossible experiments to be performed in cell culture. For example, it

might be used to investigate how individual stem cells differentiate or renew themselves in response to changes in signals from an artificial microenvironment that spatially resembles natural stem-cell niches. Alternatively, three-dimensional environments for stem cells could be made in which the display or release of molecular signals is graded, to mimic processes that occur during the embryonic development of an organism. DeForest and Anseth's optobiomaterials therefore represent a major contribution to a nascent field in stem-cell bioengineering. ■

**Matthias P. Lutolf** is at the School of Life Sciences and the Institute of Bioengineering, École Polytechnique Fédérale de Lausanne, Lausanne 1015, Switzerland.  
e-mail: matthias.lutolf@epfl.ch

1. Fenno, L., Yizhar, O. & Deisseroth, K. *Annu. Rev. Neurosci.* **34**, 389–412 (2011).
2. DeForest, C. A. & Anseth, K. S. *Angew. Chem. Int. Edn* **51**, 1816–1819 (2012).
3. Morrison, S. J. & Spradling, A. C. *Cell* **132**, 598–611 (2008).
4. Sato, T. *et al. Nature* **459**, 262–265 (2009).
5. Khetan, S. & Burdick, J. A. *Soft Matter* **7**, 830–838 (2011).
6. Kloxin, A. M., Kasko, A. M., Salinas, C. N. & Anseth, K. S. *Science* **324**, 59–63 (2009).
7. Khetan, S. & Burdick, J. A. *Biomaterials* **31**, 8228–8234 (2010).
8. Hahn, M. S., Miller, J. S. & West, J. L. *Adv. Mater.* **18**, 2679–2684 (2006).
9. Wylie, R. G. *et al. Nature Mater.* **10**, 799–806 (2011).

#### QUANTUM COMPUTING

## A topological route to error correction

**Quantum computing is plagued by noise and small errors. An approach based on topological techniques reduces the sensitivity to errors and boosts the prospects for building practical quantum computers. SEE ARTICLE P.489**

**JAMES D. FRANSON**

Quantum computers have the potential to solve numerical problems that would be impossible on a classical computer. Roughly speaking, the superposition principle of quantum mechanics allows a quantum computer to perform many calculations simultaneously on a single processor, and entanglement (non-classical correlations) provides an exponential increase in its memory capacity. Unfortunately, the same properties that enhance the computational power of a quantum computer also make it sensitive to errors produced by interactions with the environment or by imperfect logic operations. In this issue, Yao *et al.*<sup>1</sup> (page 489) describe the first experimental demonstration

of a technique that uses topological effects to reduce the sensitivity of a quantum computer to errors.

The bits in a quantum computer, commonly referred to as qubits, can be represented by a two-state quantum system, such as the two quantized energy levels of an atom (Fig. 1a). One state represents a logical value of '0' and the other state represents a '1' — meaning that, like a classical computer, a quantum computer is a digital device. But unlike classical physics, quantum mechanics allows situations in which both possibilities (0 or 1) exist simultaneously. The probability of finding the system in the 0 or 1 state is equal to the square of a complex number known as the probability amplitude. As a result, the information stored in a qubit corresponds to a continuous range of



But, in contrast to ECMs, most synthetic hydrogels are biologically inert because their polymer 'backbones' contain no biologically active components. This allows researchers to design very 'clean' experimental systems: biologically active molecules can be attached to hydrogels to perturb cell activity in a well-controlled fashion, without interference from the hydrogel itself.

Several research groups have carried out work in which light-sensitive molecular building blocks were attached to hydrogel networks to generate artificial ECMs in which the properties of microenvironments could be specifically modulated by light exposure<sup>3</sup>. For example, the introduction of chemical groups that can be cleaved by ultraviolet light has led to hydrogels that soften on light exposure<sup>6</sup>. Conversely, the incorporation of groups that form crosslinks between polymer chains when irradiated with ultraviolet light has resulted in materials that stiffen upon such irradiation<sup>7</sup>.

Systems in which light triggers the coupling<sup>8,9</sup> or removal<sup>6</sup> of biologically active molecules to or from hydrogel polymer networks have also been devised. These light-mediated approaches to modifying hydrogels have been used to control some aspects of the basic three-dimensional behaviour of cells embedded in the materials, such as adhesion to the artificial ECM or migration. But because the modifications involved are irreversible, they allow only one-way manipulation of cell activity.

DeForest and Anseth's work<sup>2</sup> now demonstrates fully reversible modulation of biologically active building blocks within light-sensitive hydrogels. They synthesized small peptides that can act as signals for cell adhesion, to which a short linker section was attached. The free end of the linker was a chemical group that can react with alkene groups in a hydrogel when irradiated with visible light, thereby attaching the peptide to the gel (Fig. 1). Another part of the linker was a group that breaks apart when irradiated with ultraviolet light; by shining this light on a hydrogel that had been decorated with the peptides, the authors could detach the peptides from the gel.

Crucially, both light-activated reactions are cell-compatible, which allowed DeForest and Anseth to attach (or detach) the peptides to (or from) their hydrogel in the presence of mouse embryonic fibroblast cells. By controlling precisely when and where the cell-adhesive peptides bound in the gel, the authors could control the duration and locations in which the cells attached and spread.

In a first gel-patterning step, DeForest and Anseth used visible light to create small 'islands' of peptides to which fibroblasts grown in culture with the gel adhered. In a second step, conducted after one day of culture, the authors removed peptides from areas of the islands using ultraviolet light. This caused

rapid, selective detachment of cells from those areas. The authors showed that the removed cells could then be grown again in culture, or analysed in other assays. As DeForest and Anseth suggest<sup>2</sup>, this kind of protocol could be widely used to manipulate and study subsets of cells (or even individual cells) of larger cell populations.

One long-term goal of work such as this is the development of materials to act as scaffolds for tissue regeneration. Can we expect this and/or similar techniques to transform tissue engineering in the same way that optogenetics is transforming neuroscience? This is, of course, difficult to predict. For DeForest and Anseth's hydrogel to be fully physiologically relevant, the ability to attach and release full-length proteins<sup>9</sup> — rather than short peptides — to the material needs to be developed. And it remains to be seen whether their approach is directly translatable to tissue regeneration *in vivo*. Furthermore, it could be argued that these methods will be valuable for tissue regeneration in only a relatively few cases, such as those in which much simpler scaffolds fail, because the spatial arrangement of ECM signals is necessary for driving regeneration.

Nevertheless, the reversible, dynamic control of chemical and physical gel properties should allow previously impossible experiments to be performed in cell culture. For example, it

might be used to investigate how individual stem cells differentiate or renew themselves in response to changes in signals from an artificial microenvironment that spatially resembles natural stem-cell niches. Alternatively, three-dimensional environments for stem cells could be made in which the display or release of molecular signals is graded, to mimic processes that occur during the embryonic development of an organism. DeForest and Anseth's optobiomaterials therefore represent a major contribution to a nascent field in stem-cell bioengineering. ■

**Matthias P. Lutolf** is at the School of Life Sciences and the Institute of Bioengineering, École Polytechnique Fédérale de Lausanne, Lausanne 1015, Switzerland.  
e-mail: matthias.lutolf@epfl.ch

1. Fenno, L., Yizhar, O. & Deisseroth, K. *Annu. Rev. Neurosci.* **34**, 389–412 (2011).
2. DeForest, C. A. & Anseth, K. S. *Angew. Chem. Int. Edn* **51**, 1816–1819 (2012).
3. Morrison, S. J. & Spradling, A. C. *Cell* **132**, 598–611 (2008).
4. Sato, T. *et al. Nature* **459**, 262–265 (2009).
5. Khetan, S. & Burdick, J. A. *Soft Matter* **7**, 830–838 (2011).
6. Kloxin, A. M., Kasko, A. M., Salinas, C. N. & Anseth, K. S. *Science* **324**, 59–63 (2009).
7. Khetan, S. & Burdick, J. A. *Biomaterials* **31**, 8228–8234 (2010).
8. Hahn, M. S., Miller, J. S. & West, J. L. *Adv. Mater.* **18**, 2679–2684 (2006).
9. Wylie, R. G. *et al. Nature Mater.* **10**, 799–806 (2011).

#### QUANTUM COMPUTING

## A topological route to error correction

**Quantum computing is plagued by noise and small errors. An approach based on topological techniques reduces the sensitivity to errors and boosts the prospects for building practical quantum computers. SEE ARTICLE P.489**

**JAMES D. FRANSON**

Quantum computers have the potential to solve numerical problems that would be impossible on a classical computer. Roughly speaking, the superposition principle of quantum mechanics allows a quantum computer to perform many calculations simultaneously on a single processor, and entanglement (non-classical correlations) provides an exponential increase in its memory capacity. Unfortunately, the same properties that enhance the computational power of a quantum computer also make it sensitive to errors produced by interactions with the environment or by imperfect logic operations. In this issue, Yao *et al.*<sup>1</sup> (page 489) describe the first experimental demonstration

of a technique that uses topological effects to reduce the sensitivity of a quantum computer to errors.

The bits in a quantum computer, commonly referred to as qubits, can be represented by a two-state quantum system, such as the two quantized energy levels of an atom (Fig. 1a). One state represents a logical value of '0' and the other state represents a '1' — meaning that, like a classical computer, a quantum computer is a digital device. But unlike classical physics, quantum mechanics allows situations in which both possibilities (0 or 1) exist simultaneously. The probability of finding the system in the 0 or 1 state is equal to the square of a complex number known as the probability amplitude. As a result, the information stored in a qubit corresponds to a continuous range of

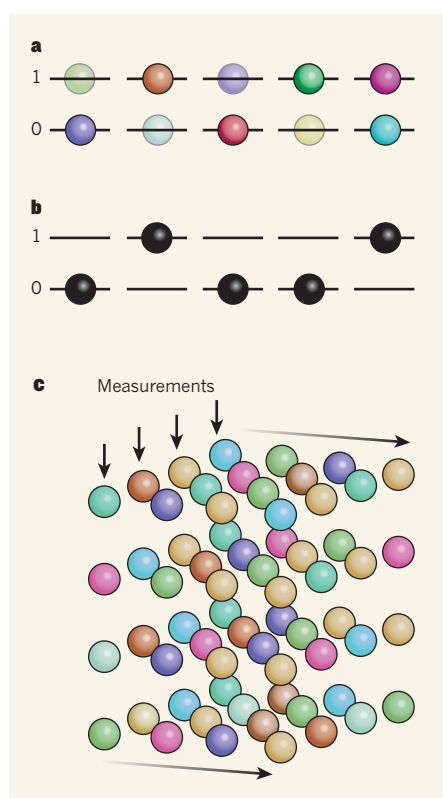


**Figure 1 | Measuring quantum bits.** **a**, Five qubits represented by the energy levels of five atoms (spheres). The ground state encodes the logical value '0', whereas the excited state encodes the value '1'. Because of their quantum nature, the atoms can be in both states simultaneously. The intensity of the spheres' colour denotes the probability that an energy level is occupied, and the colours indicate the phase of the oscillating probability amplitude associated with the energy level. **b**, After a measurement, the qubits collapse to classical states with a specific value of 0 or 1, and the phase information is destroyed, as illustrated by the black colour. **c**, A three-dimensional array of qubits can be used to implement topological error correction, which reduces the sensitivity of quantum computing to errors. The calculation consists of a series of measurements that proceeds from all of the qubits in the plane that forms the left side of the array through the adjacent planes to the right. Yao *et al.*<sup>1</sup> demonstrated topological error correction using an ensemble of eight qubits.

probability amplitudes. According to quantum mechanics, the probability amplitudes of both the 0 and 1 states have wave-like properties, and their relative position in an oscillatory cycle corresponds to an additional degree of freedom known as their phase. In addition, the qubits can be entangled with one another in many different ways. Thus a qubit can contain much more information than a classical bit, which can have only a specific value of 0 or 1.

Measuring the value of a qubit causes it to collapse to a specific value of 0 or 1, reducing it to a classical bit (Fig. 1b). Because measuring a qubit destroys its quantum-mechanical

properties, it was not initially apparent whether there was any way to correct for errors in qubits without destroying them. It was subsequently shown<sup>2</sup> that error correction was possible if a 'logical' qubit was constructed from a combination of multiple physical qubits (Fig. 1a). For example, the value of the logical qubit can be taken to be the parity of the ensemble of physical qubits, where parity is defined to be 0 if the sum of the qubit values is even and 1 if the sum is odd. But there are more efficient ways of encoding the logical information. Quantum logic operations on the qubit ensemble can be used to correct the errors in the individual qubits without measuring the value of the logical qubit, and thus without destroying the information it encodes. This allows the errors in a quantum computer to be made arbitrarily small — although additional errors will be introduced during the error-correction process itself, so the average error rate must be below a threshold on the order of  $10^{-4}$  for conventional error-correction techniques.

In the type of topological error correction<sup>3,4</sup> used by Yao *et al.*<sup>1</sup>, the logical qubits are distributed over a lattice of physical qubits in such a way that the information is automatically protected against most forms of error. This type of error correction is theoretically expected to increase the tolerance for errors to above 1%. The authors<sup>1</sup> demonstrated topological error correction by combining topological techniques with cluster-state quantum computing<sup>5</sup>, in which a three-dimensional array, or cluster, of qubits is prepared with a carefully chosen form of entanglement between nearest neighbours in the array.

Their approach begins with measurement of all the qubits in the plane that forms the left side of the array (Fig. 1c). The results of those measurements are then used to decide what kind of measurements to perform on the next layer of adjacent qubits. No active logic operations are performed — instead, the calculation depends on choosing the measurements in such a way that the collapse of the quantum state produces the desired logical operations<sup>6,7</sup>. The calculation proceeds until the final layer of qubits on the far right side of the array — the values of which give the desired output of the calculation — is reached. The authors reduced the sensitivity of the calculations to environmental noise and small errors in the logical operations by optimizing the spatial arrangement, or topology, of the qubits and the measurements.

Yao and colleagues<sup>1</sup> performed their experiment using an eight-qubit cluster, in which the value of each qubit (0 or 1) was represented by the polarization of a single photon (the direction of the photon's electric field). An optical route to quantum computing has the advantage that optical fibres can be readily used to transfer qubits from one location to another. The greatest challenge of an optical approach



## 50 Years Ago

Although the annual figures for carriage-rates of all pathogenic staphylococci follow no particular course, evidence from many sources in industrialized countries shows that this is not the case with regard to the proportions of penicillin-resistant organisms ... These findings raise many questions about the origin and spread of resistant strains. They are certainly consistent with the general impression of a relationship between the increased use of penicillin and the growth of resistant strains ... It has to be borne in mind that penicillin, with other antibiotics, is being used on a large scale for preserving food and controlling animal diseases in many countries. It is increasingly present in milk and cheese, and quite large numbers of hospital, veterinary and farm workers are intermittently or continuously exposed to small concentrations of the antibiotic. These are all factors likely to promote the emergence of resistant strains in man.

From *Nature* 24 February 1962

## 100 Years Ago

By the death of Lord Lister, the world has lost one of its greatest men ... it was his work which gave the main impulse to the development of the great science of bacteriology, a science which bids fair to occupy the most prominent place in medical work ... Until Pasteur's time the existence of bacteria and their life-history had been looked on as only an interesting but not very important study ... As soon as Lister showed that the exclusion of these organisms from wounds meant the disappearance of a variety of diseases to which man had been previously subject, the study of these organisms naturally advanced with great rapidity.

From *Nature* 22 February 1912

is developing an efficient mechanism for generating large numbers of entangled photons on demand. The authors were able to enhance the efficiency of their entangled-photon source using quantum-interference techniques, but further improvements in photon sources will be necessary.

Topological error correction could also be performed using qubits based on other physical systems, such as superconducting devices or trapped ions, which, like optical approaches, have allowed strong progress to be made in quantum computing. Other forms of topological error correction<sup>8</sup> may be able to further reduce the sensitivity to experimental errors beyond that achieved by the authors.

For example, it is possible to produce a change in the phase of a probability amplitude that depends only on the number of times that the trajectory of a quantum system circles a specific point in a complex mathematical space known as Hilbert space, regardless of the exact shape of the trajectory. Topological error correction can increase the tolerance for experimental errors to the point that it is consistent with experimental capabilities, and greatly increases the prospects for building large-scale quantum computers. The experiment by Yao *et al.* represents an essential first step in that direction. ■

**James D. Franson** is in the Physics Department, University of Maryland,

Baltimore County, Baltimore, Maryland 21250, USA.

e-mail: jfranson@umbc.edu

1. Yao, X.-C. *et al.* *Nature* **482**, 489–494 (2012).
2. Shor, P. W. *Phys. Rev. A* **52**, R2493–R2496 (1995).
3. Dennis, E., Kitaev, A., Landahl, A. & Preskill, J. *J. Math. Phys.* **43**, 4452–4505 (2002).
4. Barrett, S. D. & Stace, T. M. *Phys. Rev. Lett.* **105**, 200502 (2010).
5. Raussendorf, R. & Briegel, H. J. *Phys. Rev. Lett.* **86**, 5188–5191 (2001).
6. Knill, E., Laflamme, R. & Milburn, G. J. *Nature* **409**, 46–52 (2001).
7. Pittman, T. B., Jacobs, B. C. & Franson, J. D. *Phys. Rev. Lett.* **88**, 257902 (2002).
8. Nayak, C., Simon, S. H., Stern, A., Freedman, M. & Das Sarma, S. *Rev. Mod. Phys.* **80**, 1083–1159 (2008).

## STRUCTURAL BIOLOGY

# Muscarinic receptors become crystal clear

Muscarinic acetylcholine receptors mediate many physiological responses of the nervous system. Structures of two of these receptors yield insight into how they bind drugs and their mechanism of action. **SEE LETTERS P.547 & P.552**

REBECCA L. KOW & NEIL M. NATHANSON

G-protein-coupled receptors (GPCRs) are the darling drug targets of many pharmaceutical and biotech companies. This largest superfamily of cell-membrane receptors affects many aspects of life, including mood and behaviour, the immune system and the senses. In this issue, Haga *et al.*<sup>1</sup> and Kruse and colleagues<sup>2</sup> describe the crystal structures of two GPCRs — the M2 and M3 muscarinic acetylcholine receptors, which belong to the same GPCR family but couple to different effector proteins. The results not only advance our understanding of the structure and molecular pharmacology of this receptor family, but also contribute to our knowledge of GPCRs and membrane proteins in general.

Muscarinic acetylcholine receptors (mAChRs) are expressed on most target organs of the autonomic branch of the peripheral nervous system, which controls unconscious physiological responses such as heart rate, digestion, respiration and urination. They are also expressed in the central nervous system, where they modulate circuits that control movement and contribute to processes such as learning and memory. Drugs that target these receptors are being used and/or tested for conditions that include abnormal heart rate, asthma, overactive bladder, Alzheimer's disease, Parkinson's disease and schizophrenia.

Mammals have five subtypes of mAChR (M1–M5), which are divided into two

functional groups: M2 and M4 preferentially couple to the G<sub>i</sub> family of G proteins, whereas M1, M3 and M5 couple to the G<sub>q</sub> family. The receptors affect different aspects of body function. For instance, M2 decreases heart rate by controlling certain potassium-ion membrane channels, and M3 stimulates hormone secretion and relaxes airway smooth muscle. Understanding the intricate structural details of these receptors should help in the design of drugs that target specific mAChRs without producing undesirable side effects.

Solving crystal structures of GPCRs is notoriously difficult because of the proteins' natural flexibility. A trademark of these receptors is their seven transmembrane domains (TM1–TM7), which give rise to intracellular and extracellular loops. Of these, the third intracellular loop is particularly large and mobile. To solve the structures of M2 and M3, respectively, Haga *et al.* (page 547) and Kruse *et al.* (page 552) replaced this loop with phage T4 lysozyme, a protein that promotes crystal formation. As with other GPCRs previously crystallized by this approach, the modification did not alter the receptors' ability to bind agonist ligands (molecules that activate the receptors, such as the neurotransmitter acetylcholine) or antagonist ligands (molecules that block receptor activation).

Haga *et al.*<sup>1</sup> describe the structure of M2 bound to the muscarinic blocker 3-quinuclidinyl benzilate. They report that the structure of inactive M2 is similar to that of other inactive

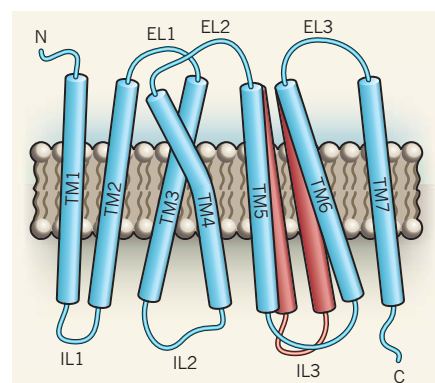


**Figure 1 | Differences between receptor subtypes.** G-protein-coupled receptors have seven transmembrane (TM) domains that span the cell membrane, giving rise to three intracellular loops (IL1–IL3) and three extracellular loops (EL1–EL3). Haga *et al.*<sup>1</sup> and Kruse and colleagues<sup>2</sup> report the crystal structures of two such receptors, M2 and M3, which are muscarinic acetylcholine receptors. The intracellular ends of TM5 and TM6 are farther apart in M2 (blue) and other G<sub>i</sub>-coupled receptors than in M3 (red) and other G<sub>q</sub>-coupled receptors. This and other structural differences between M2 and M3 may contribute to variations in the association and dissociation rates of drugs targeted to the two receptors.

GPCRs, particularly in the transmembrane domains. But M2 differs most from other GPCRs at its extracellular surface and in having a 33-ångström channel that contains the ligand binding pocket and extends beyond it. The ligand is oriented in the binding pocket by an aspartate amino-acid residue in TM3 and an asparagine residue in TM6. It also interacts with a lid formed by an 'aromatic cage' consisting of multiple tyrosine and tryptophan residues (located in TM3, TM6 and TM7). The authors found similar aromatic cages in three non-GPCR proteins that bind acetylcholine, which suggests that the aromatic cage is a common motif for binding this ligand.

Kruse *et al.*<sup>2</sup> determine the structure of M3 bound to tiotropium — a bronchodilator and mAChR blocker. Overall, the structures of inactive M3 and M2 are similar. For instance,



is developing an efficient mechanism for generating large numbers of entangled photons on demand. The authors were able to enhance the efficiency of their entangled-photon source using quantum-interference techniques, but further improvements in photon sources will be necessary.

Topological error correction could also be performed using qubits based on other physical systems, such as superconducting devices or trapped ions, which, like optical approaches, have allowed strong progress to be made in quantum computing. Other forms of topological error correction<sup>8</sup> may be able to further reduce the sensitivity to experimental errors beyond that achieved by the authors.

For example, it is possible to produce a change in the phase of a probability amplitude that depends only on the number of times that the trajectory of a quantum system circles a specific point in a complex mathematical space known as Hilbert space, regardless of the exact shape of the trajectory. Topological error correction can increase the tolerance for experimental errors to the point that it is consistent with experimental capabilities, and greatly increases the prospects for building large-scale quantum computers. The experiment by Yao *et al.* represents an essential first step in that direction. ■

**James D. Franson** is in the Physics Department, University of Maryland,

Baltimore County, Baltimore, Maryland 21250, USA.

e-mail: jfranson@umbc.edu

1. Yao, X.-C. *et al.* *Nature* **482**, 489–494 (2012).
2. Shor, P. W. *Phys. Rev. A* **52**, R2493–R2496 (1995).
3. Dennis, E., Kitaev, A., Landahl, A. & Preskill, J. *J. Math. Phys.* **43**, 4452–4505 (2002).
4. Barrett, S. D. & Stace, T. M. *Phys. Rev. Lett.* **105**, 200502 (2010).
5. Raussendorf, R. & Briegel, H. J. *Phys. Rev. Lett.* **86**, 5188–5191 (2001).
6. Knill, E., Laflamme, R. & Milburn, G. J. *Nature* **409**, 46–52 (2001).
7. Pittman, T. B., Jacobs, B. C. & Franson, J. D. *Phys. Rev. Lett.* **88**, 257902 (2002).
8. Nayak, C., Simon, S. H., Stern, A., Freedman, M. & Das Sarma, S. *Rev. Mod. Phys.* **80**, 1083–1159 (2008).

## STRUCTURAL BIOLOGY

# Muscarinic receptors become crystal clear

Muscarinic acetylcholine receptors mediate many physiological responses of the nervous system. Structures of two of these receptors yield insight into how they bind drugs and their mechanism of action. **SEE LETTERS P.547 & P.552**

REBECCA L. KOW & NEIL M. NATHANSON

G-protein-coupled receptors (GPCRs) are the darling drug targets of many pharmaceutical and biotech companies. This largest superfamily of cell-membrane receptors affects many aspects of life, including mood and behaviour, the immune system and the senses. In this issue, Haga *et al.*<sup>1</sup> and Kruse and colleagues<sup>2</sup> describe the crystal structures of two GPCRs — the M2 and M3 muscarinic acetylcholine receptors, which belong to the same GPCR family but couple to different effector proteins. The results not only advance our understanding of the structure and molecular pharmacology of this receptor family, but also contribute to our knowledge of GPCRs and membrane proteins in general.

Muscarinic acetylcholine receptors (mAChRs) are expressed on most target organs of the autonomic branch of the peripheral nervous system, which controls unconscious physiological responses such as heart rate, digestion, respiration and urination. They are also expressed in the central nervous system, where they modulate circuits that control movement and contribute to processes such as learning and memory. Drugs that target these receptors are being used and/or tested for conditions that include abnormal heart rate, asthma, overactive bladder, Alzheimer's disease, Parkinson's disease and schizophrenia.

Mammals have five subtypes of mAChR (M1–M5), which are divided into two

functional groups: M2 and M4 preferentially couple to the G<sub>i</sub> family of G proteins, whereas M1, M3 and M5 couple to the G<sub>q</sub> family. The receptors affect different aspects of body function. For instance, M2 decreases heart rate by controlling certain potassium-ion membrane channels, and M3 stimulates hormone secretion and relaxes airway smooth muscle. Understanding the intricate structural details of these receptors should help in the design of drugs that target specific mAChRs without producing undesirable side effects.

Solving crystal structures of GPCRs is notoriously difficult because of the proteins' natural flexibility. A trademark of these receptors is their seven transmembrane domains (TM1–TM7), which give rise to intracellular and extracellular loops. Of these, the third intracellular loop is particularly large and mobile. To solve the structures of M2 and M3, respectively, Haga *et al.* (page 547) and Kruse *et al.* (page 552) replaced this loop with phage T4 lysozyme, a protein that promotes crystal formation. As with other GPCRs previously crystallized by this approach, the modification did not alter the receptors' ability to bind agonist ligands (molecules that activate the receptors, such as the neurotransmitter acetylcholine) or antagonist ligands (molecules that block receptor activation).

Haga *et al.*<sup>1</sup> describe the structure of M2 bound to the muscarinic blocker 3-quinuclidinyl benzilate. They report that the structure of inactive M2 is similar to that of other inactive

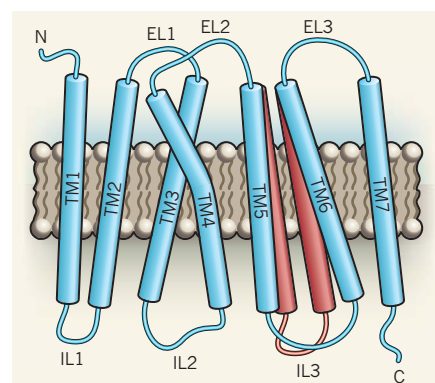


**Figure 1 | Differences between receptor subtypes.** G-protein-coupled receptors have seven transmembrane (TM) domains that span the cell membrane, giving rise to three intracellular loops (IL1–IL3) and three extracellular loops (EL1–EL3). Haga *et al.*<sup>1</sup> and Kruse and colleagues<sup>2</sup> report the crystal structures of two such receptors, M2 and M3, which are muscarinic acetylcholine receptors. The intracellular ends of TM5 and TM6 are farther apart in M2 (blue) and other G<sub>i</sub>-coupled receptors than in M3 (red) and other G<sub>q</sub>-coupled receptors. This and other structural differences between M2 and M3 may contribute to variations in the association and dissociation rates of drugs targeted to the two receptors.

GPCRs, particularly in the transmembrane domains. But M2 differs most from other GPCRs at its extracellular surface and in having a 33-ångström channel that contains the ligand binding pocket and extends beyond it. The ligand is oriented in the binding pocket by an aspartate amino-acid residue in TM3 and an asparagine residue in TM6. It also interacts with a lid formed by an 'aromatic cage' consisting of multiple tyrosine and tryptophan residues (located in TM3, TM6 and TM7). The authors found similar aromatic cages in three non-GPCR proteins that bind acetylcholine, which suggests that the aromatic cage is a common motif for binding this ligand.

Kruse *et al.*<sup>2</sup> determine the structure of M3 bound to tiotropium — a bronchodilator and mAChR blocker. Overall, the structures of inactive M3 and M2 are similar. For instance,

a characteristic of mAChRs seems to be an outward bend in TM4, which is not seen in other GPCRs. But the authors also identify a few notable differences in the structures of inactive M2 and M3. One is the presence of a phenylalanine residue (rather than, as in M2, a leucine) in the second extracellular loop of M3, which creates a space in the receptor's binding pocket. This small difference in the structure of the binding pocket may facilitate the development of drugs that have increased selectivity for a specific mAChR subtype. The relative position of TM7 in the two receptors also varies, possibly due to a difference in the TM2 amino acids with which TM7 interacts.

Another difference between M2 and M3 is in the position of TM5, especially at the cytoplasmic end of this domain. Specific TM6 residues that interact with TM5 at the cytoplasmic end determine the receptor's coupling selectivity for various G proteins. This difference may be a factor in the coupling selectivity of other GPCRs, as the TM5–TM6 distance in the M2 receptor is longer than that in M3 and similar to that in other G<sub>i</sub>-coupled GPCRs,

whereas in M3 this distance is similar to that in other G<sub>q</sub>-coupled GPCRs (Fig. 1).

Kruse *et al.* used molecular-dynamics simulations to investigate the binding of tiotropium to mAChRs. Although this blocker binds to the acetylcholine binding site, the simulations indicate that it pauses at a separate (allosteric) site during both association and dissociation from the mAChR. Tiotropium dissociation from M3 is slower than from M2, perhaps because the second extracellular loop in M3 is less mobile. Exploiting such differences in the extracellular surfaces of mAChRs may again contribute to the development of subtype-specific drugs, an endeavour that has previously been impeded by the close structural similarity of the ligand binding regions in the transmembrane core of mAChRs.

These latest advances inevitably raise further questions. For example, what are the differences in the receptors' structure on binding to antagonists, full agonists and 'biased' agonists (which elicit only a subset of physiological responses<sup>3</sup>)? Also, for the G-protein-interacting regions of GPCRs to be sufficiently ordered

for crystallization, the receptor must be bound to its G protein<sup>4</sup>. Yet replacement of the third intracellular loop with the phage T4 lysozyme eliminates receptor coupling to G proteins. The conformational changes involved on binding to the G protein are therefore unclear. Crystallization of more intact mAChRs in complex with their cognate G proteins is thus required for detailed information about the pathways of receptor–G-protein coupling. These are some of the challenges we face in our attempts to better understand mAChRs. ■

**Rebecca L. Kow and Neil M. Nathanson**  
are in the Department of Pharmacology,  
University of Washington, Seattle, Washington  
98195-7750, USA.  
e-mail: nathanso@u.washington.edu

1. Haga, K. *et al.* *Nature* **482**, 547–551 (2012).
2. Kruse, A. C. *et al.* *Nature* **482**, 552–556 (2012).
3. Reiter, E., Ahn, S., Shukla, A. K. & Lefkowitz, R. J. *Annu. Rev. Pharmacol. Toxicol.* **52**, 179–197 (2012).
4. Rasmussen, S. G. F. *et al.* *Nature* **477**, 549–555 (2011).

## CANCER GENETICS

# Evolution after tumour spread

**A genetic study of brain cancers in mice and humans reveals distinct mutations in primary tumours and their metastases, suggesting that the two disease 'compartments' may require different treatments. SEE LETTER P.529**

STEVEN C. CLIFFORD

**T**he spread of a primary tumour to secondary sites in the body is a key step in the development of many cancers, and treatment of these secondary metastatic tumours represents one of the foremost challenges in oncology. On page 529 of this issue, Wu *et al.*<sup>1</sup> describe two new mouse strains that serve as models of metastasis in the childhood brain cancer medulloblastoma\*. In the mice, primary and metastatic tumours seem to occupy two genetically distinct 'compartments', which arise from divergent DNA-sequence mutations that occur after metastasis. The authors also detect similar differences in human medulloblastoma tumours — a finding that may influence the development of anticancer therapies.

Wu *et al.* used an experimental system called Sleeping Beauty mutagenesis<sup>2,3</sup> to introduce random genetic mutations into cerebellar progenitor cells in the developing brains of

two strains of mice. These two new strains were derived by breeding the existing *Tp53*<sup>mut</sup> and *Ptch*<sup>+/-</sup> strains, which are predisposed to brain tumours<sup>1,4</sup>, with a strain that expresses the Sleeping Beauty mutagen in cerebellar progenitors. This system leaves a unique genetic 'footprint' at each mutation site, which allows mutated genes to be identified by DNA sequencing. Such mutagenesis experiments are used to identify genes in which mutations frequently arise, because the likelihood of these being involved in tumour development is reasoned to be above average<sup>2,3</sup>.

As in mouse models of other cancer types<sup>2,3</sup>, Wu and colleagues' Sleeping Beauty mutagenesis accelerated the development of medulloblastoma in both mouse strains. The authors identified a range of new and established cancer-related genes that had mutations, including some that have previously been implicated in medulloblastoma. They also observed that, following mutagenesis, mice of both strains developed metastases around a type of brain tissue called the leptomeninges, in patterns that are reminiscent of metastatic human

medulloblastoma<sup>5</sup>. The two mouse models thus provided an opportunity to track mutations present in the primary and metastatic disease, and to investigate their genetic provenance.

Wu *et al.* found that there were, in general, only a few mutations common to primary and metastatic tumours from the same mouse, but that the mutations in different metastases from the same mouse tended to be more similar to each other. Moreover, certain mutations observed in metastases were detected at only low levels within the primary tumour, and some mutations were unique to one or the other tumour type. The authors conclude that their findings are consistent with a model in which metastases originate from rare cells in the primary tumour, and that, following metastasis, additional mutations accumulate independently — both in the primary tumour (post-dispersion events) and in metastases (post-metastasis events) (Fig. 1).

Turning our attention away from mice, an obvious question is whether primary and metastatic tumours in the human disease also show 'bi-compartmental' genetics. Approximately 30% of patients with medulloblastoma already have metastases when they are first diagnosed, and this is associated with a poor prognosis<sup>5</sup>. However, few previous studies have compared the biology of human primary tumours with their associated metastases, mainly because metastases are not routinely biopsied. Despite the limited sample availability, Wu *et al.*<sup>1</sup> show initial evidence of differing genetics in primary and metastatic tumours from seven human patients.

Further investigation is required to establish whether the authors' findings are broadly relevant to human medulloblastoma. The

\*This article and the paper<sup>1</sup> under discussion were published online on 15 February 2012.

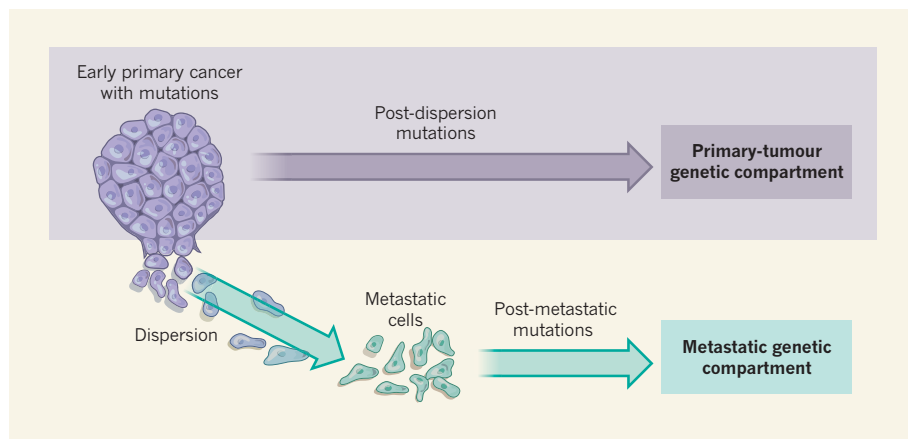


**Figure 1 | A bi-compartmental genetic model of cancer metastasis.** By analysing the tumours from two strains of mice that model the brain cancer medulloblastoma, Wu *et al.*<sup>1</sup> found differences in the DNA-sequence mutations present in primary and metastatic tumours. They propose that rare cells in the primary tumour that are capable of metastasizing disperse to other sites in the brain, where they form metastases. The cells of the primary tumour and the metastases then continue to accumulate mutations, generating two distinct genetic compartments.

human disease exhibits<sup>5</sup> more complex patterns of metastases than are observed in mice, and is classified into four molecular subgroups (WNT, SHH, Group 3 and Group 4), which each display distinct biological and clinical characteristics<sup>6</sup>. The *Ptch*<sup>+/-</sup> mice used by Wu *et al.*<sup>1</sup> develop SHH-associated medulloblastomas<sup>4</sup>; similar mutagenesis-driven approaches using existing mouse models of other medulloblastoma disease groups, such as WNT<sup>7</sup>, might prove informative.

Perhaps the most urgent question arising from this study<sup>1</sup> is whether the genetic differences between the two disease compartments lead to distinct biological features that make them respond differently to treatment. In mice, these compartments remain genomically characterized entities, the biological and therapeutic importance of which is untested. In humans, clinical-trial data show<sup>5</sup> that primary and metastatic sites respond similarly to current therapies (with cure achieved at both sites) in around 60% of children with metastatic disease, but a more objective assessment of treatment response is confounded by the fact that primary tumours are mostly removed by surgery prior to treatment. Wu *et al.* provide initial evidence that the tumour compartments may respond differently to current therapies in certain patients, but they rightly caution that these effects could also relate to clinical factors such as radiotherapy being delivered at different intensities to different tumour sites.

Some of the mutations identified by Wu and colleagues' experiments may also reveal biological processes or pathways that could offer drug targets for the improved treatment of primary tumours, metastases, or both. The new mouse strains provide excellent models in which to test this possibility. The multitude and variety of mutations described by Wu *et al.*<sup>1</sup> are noteworthy, but the next challenge is to determine which of

them can drive tumour development, which are therapeutically relevant, and which occur at sufficient frequency in the human disease to warrant their pursuit as potential targets. The authors justifiably reason that targets that are common to primary tumours and metastases, in both humans and mice, are those most attractive for further development. However, only one cellular pathway, insulin-dependent signalling, meets these

#### CLIMATE CHANGE

## Shrinking glaciers under scrutiny

**Melting glaciers contribute to sea-level rise, but measuring their mass loss over time is difficult. An analysis of satellite data on Earth's changing gravity field does just that, and delivers some unexpected results. SEE LETTER P.514**

JONATHAN BAMBER

Glaciers and ice caps are pivotal features of both water resources and tourism. They are also a significant contributor to sea-level rise. About 1.4 billion people are dependent on the rivers that flow from the Tibetan plateau and Himalayas<sup>1</sup>. Yet significant controversy<sup>2</sup> and uncertainty surround the recent past and future behaviour of glaciers in this region. This is not so surprising when one considers the problem in hand. There are more than 160,000 glaciers and ice caps worldwide. Fewer than 120 (0.075%) have had their mass balance (the sum of the annual mass gains and losses of the glacier or ice cap) directly measured, and for only 37 of these are there records

criteria on the basis of their current data.

Providing answers to all these questions will require further biological investigation across species, as well as clinical studies. An additional challenge is posed by the fact that there are fewer than 700 cases of medulloblastoma per year in Europe. More routine biopsy and characterization of human metastases will be essential, and the impetus and ethical justification for such a fundamental change to clinical practice will, at least in part, come from experimental studies such as those presented here. Time will tell whether this tale of Sleeping Beauty and mice develops into a clinically relevant human paradigm. ■

**Steven C. Clifford** is at the Northern Institute for Cancer Research, Newcastle University, Newcastle upon Tyne NE1 4LP, UK.  
e-mail: steve.clifford@ncl.ac.uk

1. Wu, X. *et al.* *Nature* **482**, 529–533 (2012).
2. Collier, L. S., Carlson, C. M., Ravimohan, S., Dupuy, A. J. & Largaespada, D. A. *Nature* **436**, 272–276 (2005).
3. Copeland, N. G. & Jenkins, N. A. *Nature Rev. Cancer* **10**, 696–706 (2010).
4. Goodrich, L. V., Milenković, L., Higgins, K. M. & Scott, M. P. *Science* **277**, 1109–1113 (1997).
5. Pizer, B. L. & Clifford, S. C. *Br. J. Neurosurg.* **23**, 364–375 (2009).
6. Taylor, M. D. *et al.* *Acta Neuropathol.* <http://dx.doi.org/10.1007/s00401-011-0922-z> (2011).
7. Gibson, P. *et al.* *Nature* **468**, 1095–1099 (2010).

extending beyond 30 years. Extrapolating this tiny sample of observations to all glaciers and ice caps is a challenging task that inevitably leads to large uncertainties.

On page 514 of this issue, Jacob and colleagues<sup>3</sup> describe a study based on satellite data for Earth's changing gravity field that tackles this problem\*. Their results have surprising implications for both the global contribution of glaciers to sea level and the changes occurring in the mountain regions of Asia.

Melting glaciers are an iconic symbol of climate change. On the basis of the limited data mentioned above, they seem to have been receding, largely uninterrupted, almost

\*This article and the paper<sup>3</sup> under discussion were published online on 8 February 2012.



everywhere around the world for several decades<sup>4</sup>. Scaling up the small sample of ground-based observations to produce global estimates is, however, fraught with difficulty. Size, local topography, altitude range, aspect and micro-climate all affect the response of individual glaciers in complex ways. Even the seasonality of changes in temperature and precipitation strongly influence the glaciers' response, and those that terminate in a lake or ocean behave differently again.

Nonetheless, until recently there was little alternative to some form of extrapolation of the terrestrial observations to large regions and numbers of glaciers. One such high-profile assessment<sup>5</sup> concluded that, during the period 1996–2006, the mass loss from glaciers and ice caps (GICs) increased steadily, contributing a sea-level rise of  $1.1 \pm 0.24$  millimetres per year by 2006. In this study<sup>5</sup>, the authors concluded that GICs had been the dominant mass contributor to sea-level rise over the study period, and they extrapolated their results forward to argue that this would also be the case in the future.

Then along came the Gravity Recovery and Climate Experiment (GRACE), which consists of a pair of satellites that have been making global observations of changes in Earth's gravity field since their launch in 2002. They have been used in various studies to examine the changing mass of the great ice sheets of Antarctica and Greenland<sup>6</sup> and several other large glaciated regions<sup>7</sup>. But, so far, the data have not been analysed simultaneously and consistently for all areas.

The difficulty with doing this is that GRACE measures the gravity field of the complete Earth system. This includes mass exchange and/or mass redistribution in the oceans, atmosphere, solid Earth and land hydrology, in addition to any changes in GIC volume. To determine the latter, it is clearly essential to be able to separate it from the other sources of mass movement that affect the gravity field. A second, related issue is the effective resolution of the observations. The GRACE satellites are sensitive to changes in the gravity field over distances of a few hundred kilometres. They cannot 'see' the difference between the signal from one glacier or small ice cap and another.

To isolate the GIC signal from others at the surface, Jacob and colleagues defined units of mass change — called mass concentrations, or mascons — within each of their 18 GIC regions (including the European Alps; Fig. 1). Each region might have many tens of mascons defining the geographic extent of significant ice volume within the sector<sup>3</sup>. Combined with global models of land hydrology and atmospheric-moisture content, the authors were able to isolate the GIC mass trends over the eight-year (2003–10) period of the observations. What they found was unexpected.

First, the contribution of GICs (excluding the Antarctica and Greenland peripheral



J. BALOG/EXTREME ICE SURVEY

**Figure 1 | The Leschaux and Talèfre glaciers in the French Alps.** The photograph highlights the complex and intricate topographic setting of these mountain glaciers and the difficulty in extrapolating observations from one glacier to others. Jacob and colleagues<sup>3</sup> avoided these difficulties by using the area-integrated signal from satellite gravity data.

GICs) to sea-level rise was less than half the value of the most recent, comprehensive estimate<sup>8</sup> obtained from extrapolation of *in situ* measurements for 2001–05 ( $0.41 \pm 0.08$  compared with  $1.1 \text{ mm yr}^{-1}$ ). Second, losses for the High Mountain Asia region — comprising the Himalayas, Karakoram, Tianshan, Pamirs and Tibet — were insignificant. Here, the mass-loss rate was just  $4 \pm 20$  gigatonnes per year (corresponding to  $0.01 \text{ mm yr}^{-1}$  of sea-level rise), compared with previous estimates that were well over ten times larger. By a careful analysis, the authors discounted a possible tectonic origin for the huge discrepancy, and it seems that this region is more stable than previously believed.

What is the significance of these results<sup>3</sup>? Understanding, and closing, the sea-level budget (the relative contributions of mass and thermal expansion to ocean-volume change) is crucial for testing predictions of future sea-level rise. Estimates of the future response of GICs to climate change are, in general, based on what we know about how they have responded in the past. A better estimate of past behaviour, such as that obtained by Jacob and colleagues, will therefore result in better estimates of future behaviour. Discussion of the demise of the Himalayan glaciers has been mired in controversy, partly because of basic errors<sup>2</sup>, but also because of the dearth of reliable data on past trends. Given their role as a water supply for so many people<sup>1</sup>, this has been a cause for concern and an outstanding issue.

Of course, eight years is a relatively short

observation period. Some of the regions, such as the Gulf of Alaska, experience large inter-annual variations in mass balance that are mainly due to variability in precipitation<sup>7</sup>. This is also true for the High Mountain Asia region<sup>3</sup>, and, as a consequence, a different measurement period could significantly alter the estimated trend for this sector. Furthermore, some areas, such as the European Alps and Scandinavia, have been relatively well monitored, and thus constrained, using other approaches. Nonetheless, Jacob and colleagues have dramatically altered our understanding of recent global GIC volume changes and their contribution to sea-level rise. Now we need to work out what this means for estimating their future response. ■

**Jonathan Bamber** is at the Bristol Glaciology Centre, School of Geographical Sciences, University of Bristol, Bristol BS8 1SS, UK. e-mail: j.bamber@bristol.ac.uk

1. Immerzeel, W. W., van Beek, L. P. H. & Bierkens, M. F. P. *Science* **328**, 1382–1385 (2010).
2. Cogley, J. G., Kargel, J. S., Kaser, G. & van der Veen, C. J. *Science* **327**, 522 (2010).
3. Jacob, T., Wahr, J., Pfeffer, W. T. & Swenson, S. *Nature* **482**, 514–518 (2012).
4. Kaser, G., Cogley, J. G., Dyurgerov, M. B., Meier, M. F. & Ohmura, A. *Geophys. Res. Lett.* **33**, L19501 (2006).
5. Meier, M. F. *et al. Science* **317**, 1064–1067 (2007).
6. Velicogna, I. *Geophys. Res. Lett.* **36**, L19503 (2009).
7. Luthcke, S. B., Arendt, A. A., Rowlands, D. D., McCarthy, J. J. & Larsen, C. F. *J. Glaciol.* **54**, 767–777 (2008).
8. Cogley, J. G. *Ann. Glaciol.* **50**, 96–100 (2009).

# The case for open computer programs

Darrel C. Ince<sup>1</sup>, Leslie Hatton<sup>2</sup> & John Graham-Cumming<sup>3</sup>

Scientific communication relies on evidence that cannot be entirely included in publications, but the rise of computational science has added a new layer of inaccessibility. Although it is now accepted that data should be made available on request, the current regulations regarding the availability of software are inconsistent. We argue that, with some exceptions, anything less than the release of source programs is intolerable for results that depend on computation. The vagaries of hardware, software and natural language will always ensure that exact reproducibility remains uncertain, but withholding code increases the chances that efforts to reproduce results will fail.

The rise of computational science has led to unprecedented opportunities for scientific advance. Ever more powerful computers enable theories to be investigated that were thought almost intractable a decade ago, robust hardware technologies allow data collection in the most inhospitable environments, more data are collected, and an increasingly rich set of software tools are now available with which to analyse computer-generated data.

However, there is the difficulty of reproducibility, by which we mean the reproduction of a scientific paper's central finding, rather than exact replication of each specific numerical result down to several decimal places. We examine the problem of reproducibility (for an early attempt at solving it, see ref. 1) in the context of openly available computer programs, or code. Our view is that we have reached the point that, with some exceptions, anything less than release of actual source code is an indefensible approach for any scientific results that depend on computation, because not releasing such code raises needless, and needlessly confusing, roadblocks to reproducibility.

At present, debate rages on the need to release computer programs associated with scientific experiments<sup>2–4</sup>, with policies still ranging from mandatory total release to the release only of natural language descriptions, that is, written descriptions of computer program algorithms. Some journals have already changed their policies on computer program openness; *Science*, for example, now includes code in the list of items that should be supplied by an author<sup>5</sup>. Other journals promoting code availability include *Geoscientific Model Development*, which is devoted, at least in part, to model description and code publication, and *Biostatistics*, which has appointed an editor to assess the reproducibility of the software and data associated with an article<sup>6</sup>.

In contrast, less stringent policies are exemplified by statements such as<sup>7</sup> “*Nature* does not require authors to make code available, but we do expect a description detailed enough to allow others to write their own code to do similar analysis.” Although *Nature*'s broader policy states that “...authors are required to make materials, data and associated protocols promptly available to readers...”, and editors and referees are fully empowered to demand and evaluate any specific code, we believe that its stated policy on code availability actively hinders reproducibility.

Much of the debate about code transparency involves the philosophy of science, error validation and research ethics<sup>8,9</sup>, but our contention is more practical: that the cause of reproducibility is best furthered by focusing on the dissection and understanding of code, a sentiment already appreciated by the growing open-source movement<sup>10</sup>. Dissection and understanding of open code would improve the chances of both direct and indirect reproducibility. Direct reproducibility refers to the recompilation and

rerunning of the code on, say, a different combination of hardware and systems software, to detect the sort of numerical computation<sup>11,12</sup> and interpretation<sup>13</sup> problems found in programming languages, which we discuss later. Without code, direct reproducibility is impossible. Indirect reproducibility refers to independent efforts to validate something other than the entire code package, for example a subset of equations or a particular code module. Here, before time-consuming reprogramming of an entire model, researchers may simply want to check that incorrect coding of previously published equations has not invalidated a paper's result, to extract and check detailed assumptions, or to run their own code against the original to check for statistical validity and explain any discrepancies.

Any debate over the difficulties of reproducibility (which, as we will show, are non-trivial) must of course be tempered by recognizing the undeniable benefits afforded by the explosion of internet facilities and the rapid increase in raw computational speed and data-handling capability that has occurred as a result of major advances in computer technology<sup>14</sup>. Such advances have presented science with a great opportunity to address problems that would have been intractable in even the recent past. It is our view, however, that the debate over code release should be resolved as soon as possible to benefit fully from our novel technical capabilities. On their own, finer computational grids, longer and more complex computations and larger data sets—although highly attractive to scientific researchers—do not resolve underlying computational uncertainties of proven intransigence and may even exacerbate them.

Although our arguments are focused on the implications of *Nature*'s code statement, it is symptomatic of a wider problem: the scientific community places more faith in computation than is justified. As we outline below and in two case studies (Boxes 1 and 2), ambiguity in its many forms and numerical errors render natural language descriptions insufficient and, in many cases, unintentionally misleading.

## The failure of code descriptions

### The curse of ambiguity

Ambiguity in program descriptions leads to the possibility, if not the certainty, that a given natural language description can be converted into computer code in various ways, each of which may lead to different numerical outcomes. Innumerable potential issues exist, but might include mistaken order of operations, reference to different model versions, or unclear calculations of uncertainties. The problem of ambiguity has haunted software development from its earliest days.

Ambiguity can occur at the lexical, syntactic or semantic level<sup>15</sup> and is not necessarily the result of incompetence or bad practice. It is a natural consequence of using natural language<sup>16</sup> and is unavoidable. The

<sup>1</sup>Department of Computing Open University, Walton Hall, Milton Keynes MK7 6AA, UK. <sup>2</sup>School of Computing and Information Systems, Kingston University, Kingston KT1 2EE, UK. <sup>3</sup>83 Victoria Street, London SW1H 0HW, UK.

## BOX 1

The United Kingdom Meteorological Office produces (in conjunction with the University of East Anglia's Climatic Research Unit) the downloadable and widely used gridded temperature anomaly data sets known as HadCRUT and CRUTEM3. Yet even such a high-profile data set, developed by an organization with a good standard of software development<sup>34</sup>, contained errors that would have been more quickly identified and rectified had the underlying code been readily available.

In 2009, on examining the available data sets and the description of the algorithm<sup>35</sup>, J.G.-C. identified a number of errors (the software he used to check the meteorological database is available upon request). One set of errors was procedural, and involved incorrect computation of historical average temperatures in a number of records in New Zealand and Australia. The Meteorological Office confirmed the errors, showed that they had resulted in errors up to 0.2 °C (either warmer or cooler) in the average temperature for Australia and New Zealand in some years before 1900, and issued an update to CRUTEM3. Two other errors occurred in the coding of the calculation of station errors (an estimate of the error in any average temperature reading). When corrected, a minor reduction in station errors resulted, improving the accuracy of the data. So, although these implementation problems did not lead to serious errors in the temperature data sets, they highlight the difficulty of translating a natural-language description (even with some formulae expressed mathematically) into code.

These errors do not in any way reflect badly on the original authors. The code rewriting simply plays the part of peer review and it is normal to find such errors. Indeed, the discovery of such errors in 'working' software is exceedingly common in all computing, even when the software has been in use for a considerable time. This was emphatically demonstrated in a seminal IBM study<sup>36</sup>, demonstrating that fully a third of all the software failures in the study took longer than 5,000 execution years (execution time indicates the total time taken executing a program) to fail for the first time.

problem is regarded as so axiomatic that its avoidance or minimization is routinely taught at the undergraduate level in computing degrees. Nor is the study of ambiguity confined to the classroom. Active research continues on the use of tools for the detection of ambiguity<sup>17</sup>, the avoidance of ambiguity in major projects<sup>18</sup>, and the clarification of the intended functions of computer programs<sup>15</sup>.

One proposed solution to the problem of ambiguity is to devote a large amount of attention to the description of a computer program, perhaps expressing it mathematically or in natural language augmented by mathematics. But this expectation would require researchers to acquire skills that are only peripheral to their work (set theory, predicate calculus and proof methods). Perhaps worse, investment of effort or resources alone cannot guarantee the absence of defect<sup>19</sup>. A recent study<sup>20</sup> of a tightly specified, short, simply expressed algorithm whose semi-mathematical specification was supplemented by example outputs showed that major problems still arose with large numbers of programs individually implemented to this specification. In short, natural language descriptions cannot hope to avoid ambiguous program implementations, with unpredictable effects on results.

### Errors exist within 'perfect' descriptions

Let us assume for a moment that a researcher, perhaps trained—as are computer scientists—to think of computer algorithms as mathematical objects, and fully versed in the formal semantics of software description, has managed to describe a computer program perfectly in some notation. Unfortunately, even such a description would not ensure direct or indirect reproducibility, because other forms of error or ambiguity (unrelated to natural language) are likely to creep in, leading to potentially serious uncertainties (Box 2).

## BOX 2

As discussed, unambiguous descriptions are no guarantee of reproducibility. One example from the geological literature makes the point<sup>37</sup>. This study compared nine different commercial implementations of the same seismic data-processing algorithms, developed independently. Several sources of ambiguity were successfully excluded, the same data set was used, the signal-processing algorithms used were unambiguously specified in mathematics, and the same programming language was used (Fortran 77). The individual companies followed industry standards in code implementation.

Approximately 200,000 lines of code were exercised in each of the packages in a 14-stage pipeline for which the output of each stage was the input to the next. The signal-processing algorithms used would be familiar to many scientists—such as Wiener deconvolution, acoustic wave equation solutions, fast Fourier transforms and numerous common statistical procedures.

The initial stage involved reading 32-bit pressure data from tapes recorded in a marine environment. During the processing pipeline, the agreement between the results of each package declined from the six significant figures present in the input data to only between one and two in the final output. These data, however, were used by geologists to site extremely expensive marine drilling rigs and could “fundamentally affect the conclusions reached as to the nature of potential hydrocarbon accumulations”<sup>37</sup>. Furthermore “it seems reasonable to infer that the primary source of disagreement is indeed software error”<sup>37</sup>. Even porting other seismic software between different architectures using the same input data lost two out of six significant places<sup>12</sup>. On the positive side, correction of the programming errors found during developer feedback led to considerably improved agreement.

Although conducted some years ago, the study is just as relevant today. Fortran 77 is still in use in one dialect or another in scientific research, the same software assurance procedures are still widely used, and scientific programmers are still people, subject to human fallibility.

First, there are programming errors. Over the years, researchers have quantified the occurrence rate of such defects to be approximately one to ten errors per thousand lines of source code<sup>21</sup>.

Second, there are errors associated with the numerical properties of scientific software. The execution of a program that manipulates the floating point numbers used by scientists is dependent on many factors outside the consideration of a program as a mathematical object<sup>22</sup>. Rounding errors can occur when numerous computations are repeatedly executed, as in weather forecasting<sup>23</sup>. Although there is considerable research in this area, for example in arithmetic and floating point calculations<sup>24–27</sup>, algorithms<sup>28</sup>, verification<sup>29</sup> and fundamental practice<sup>30</sup>, much of it is published in outlets not routinely accessed by scientists in generic journals, such as *Computers & Mathematics with Applications*, *Mathematics in Computer Science* and the *SIAM Journal on Scientific Computing*.

Third, there are well-known ambiguities in some of the internationally standardized versions of commonly used programming languages in scientific computation<sup>13</sup>. Monniaux<sup>22</sup> describes an alarming example relating to implementation of software features:

“More subtly, on some platforms, the exact same expression, with the same values in the same variables, and the same compiler, can be evaluated to different results, depending on seemingly irrelevant statements (printing debugging information or other constructs that do not openly change the values of variables).”

This is known as an order-of-evaluation problem and many programming languages are subject to its wilful ways. Ironically, such execution



ambiguity is quite deliberate and is present to allow a programming language compiler more flexibility in its optimization strategy. And even when programs are simple, or developed by the largest software companies, such errors remain surprisingly common: numerical ambiguity led Microsoft to declare in 2010 and reaffirm in September 2011, that the treatment of floating point numbers in its popular Excel spreadsheet “...may affect the results of some numbers or formulas due to rounding and/or data truncation.” (<http://support.microsoft.com/kb/78113>).

### Perfection is no guarantee of reproducibility

Finally, even if a computer program could be unambiguously described and implemented without error, other problems can arise in machine deployment whereby the results from identical code often diverge when hardware and software configurations are changed<sup>22</sup>. So even perfection in one's own software environment does not guarantee reproducibility. As a result, to maximize the chances of reproducibility and consistency, not only would we urge code release, but also a description of the hardware and software environment in which the program was executed and developed.

### Challenges are no excuse for closed code

*Nature's* policy on code release implies that algorithmic descriptions using mathematical specifications, equations, formal algorithmic descriptions or pseudocode (simplified version of complete code) may be required. But there is no guarantee that such tools can avoid ambiguity<sup>20</sup>, and even if they could, we have shown above that implementation and numerical errors—possibly compounded by differences in machine architecture—will still arise. So, even if complete code is made available, exact replication or even reproduction of central results may fail. A reasonable observer might therefore ask why code should be made available at all. Our response is that the alternative is far worse. Keeping code closed ensures that potential uncertainties or errors in a paper's conclusions cannot be traced to ambiguity, numerical implementation, or machine architecture issues and prevents testing of indirect reproducibility. Although it is true that independent efforts to reproduce computational results without recourse to the original source code constitute an important approach, the all-too-common treatment of code as a black box unnecessarily slows and impedes valid efforts to evaluate model results. We therefore regard the non-availability of code as a serious impediment to reproducibility.

### Potential barriers and proposed solutions

There are a number of barriers to the release of code. These include a shortage of tools that package up code and data in research articles; a shortage of central scientific repositories or indexes for program code; an understandable lack of perception of the computational problems with scientific code leading to the faulty assumption that program descriptions are adequate (something we address in this article); and finally that the development of program code is a subsidiary activity in the scientific effort.

### A modest proposal

An effective step forward would be for journals to adopt a standard for declaring the degree of source code accessibility associated with a scientific paper. A number of simple categories illustrate the idea:

- Full source code: full release of all source code used to produce the published results along with self-tests to build confidence in the quality of the delivered code, as is the case with Perl modules in the CPAN archive, for example (<http://cpan.org>).
- Partial source code: full release of source code written by the researcher accompanied by associated documentation of ancillary packages used, for example commercial scientific subroutine libraries.
- Marginal source code: release of executable code and an application programming interface to allow other researchers to write test cases.
- No source code: no code at all provided.

This hierarchy of disclosure would alert both the readers and authors of a journal article to the fact that the issue is important and would highlight the degree to which results might be reproduced independently. There remain, however, some potential stumbling blocks, a number of which can easily be resolved using existing facilities.

### Intellectual property rights

Clearly, if there is evidence of commercial potential or use, such as a patent or some copyright, then there is a problem. It is difficult to see how a journal might deal with this without substantial financial commitment to independent testing under a non-disclosure agreement or possibly even the purchase of commercial rights. Perhaps the simplest solution is for a journal to flag the software as ‘No source code’ (ideally giving the reasons) until such time as the source code can be included, either because the code goes into the public domain or is released under some free licence. Such a designation simply says that, for the moment, the results are not reproducible with the authors' own source code, and that testing of the main results must proceed with independent approaches.

### Limited access

Researchers may not have access to at least some of the software packages that are used for development. We suggest that this would not be a problem for most researchers: their institutions would normally provide such software. If it were to be a problem, then a journal could mark a publication as ‘Partial source code’. The release of the code, even without the software environment required for compilation and execution, would still be valuable in that it would address issues such as dissection and indirect reproducibility (see above) and would enable rewriting using other programming languages.

### Procedure

Adopting the simple disclosure of the availability of source code will help make it clear to the readership of a journal that this is an important issue, while also giving them an idea of the degree of code release. However, we would further suggest that journals adopt a standard that specifies that supplementary material supporting a research article must describe each of the released modular components of any software used. *Nature* editors and referees are already empowered to include an appraisal of code in their judgement about the publication potential of the article, and this practice should be more widely advertised and supported. A good example of this approach is the way that the journal *Geoscientific Model Development* asks authors to describe their program code.

### Logistics

Over the past two decades, the open-source community has solved the logistics of releasing and storing code while maintaining a cooperative development environment. SourceForge (<http://www.sourceforge.net/>) is an excellent example. Founded in 1999, it is a web-based source-code repository which acts as a free centralized location for developers working on open-source projects. It currently hosts around 300,000 projects and has over two million registered users. Not only does it store source code but also it provides access to version control information, project wikis (websites that are easily modifiable by its users) and database access. We urge funding agencies to investigate and adopt similar solutions.

### Packaging

There are a number of tools that enable code, data and the text of the article that depends on them to be packaged up. Two examples here are *Sweave* associated with the programming language R and the text-processing systems LaTeX and LyX, and *GenePattern-Word RRS*, a system specific to genomic research<sup>31</sup>. *Sweave* allows text documents, figures, experimental data and computer programs to be combined in such a way that, for example, a change in a data file will result in the regeneration of all the

research outputs. *GenePattern-Word RRS* is similar in that it enables an author to link text, tables and figures to the analysis and data that yielded the results, reported in a word-processed document; it also allows further experimentation (for example, additional analyses can be carried out). It is still early days, however, and localized solutions are emerging at the grassroots level. Donoho and co-workers, for example, have developed software packages that allow anyone with access to the *Matlab* programming language and development environment to reproduce figures from their harmonic analysis articles, inspect source code, change parameters and access data sets<sup>32</sup>.

## Steps to implementation

Our thesis is that journal and funding body strictures relating to code implementations of scientific ideas are now largely obsolete. We have suggested one modest path to code availability in this article. There are a number of further steps that journals, academics and educational organizations might consider taking:

- Research funding bodies should commission research and development on tools that enable code to be integrated with other elements of scientific research such as data, graphical displays and the text of an article.
- Research funding bodies should provide metadata repositories that describe both programs and data produced by researchers. The Australian National Data Service (<http://www.ands.org.au/>) which acts as an index to data held by Australian research organizations, is one example of this approach.
- Journals should expect researchers to provide some modular description of the components of the software that support a research result; referees should take advantage of their right to appraise software as part of their reviewing task. An example of a modular description can be seen in a recent article published in *Geoscientific Model Development*<sup>33</sup>.
- Science departments should expand their educational activities into reproducibility. Clearly such teaching should be relevant to the science at hand; however, courses on statistics, programming and experimental method could be easily expanded and combined to include the concept of reproducibility.

Received 9 May 2011; accepted 5 January 2012.

- Schwab, M., Karrenbach, M. & Claerbout, J. Making scientific computations reproducible. *Comput. Sci. Eng.* **2**, 61–67 (2000).
  - Barnes, N. Publish your computer code: it is good enough. *Nature* **467**, 753 (2010).
  - McCafferty, D. Should code be released? *Commun. ACM* **53**, 16–17 (2010).
  - Merali, Z. ...Error. *Nature* **467**, 775–777 (2010).
  - Hanson, B., Sugden, A. & Alberts, B. Making data maximally available. *Science* **331**, 649 (2011).
  - Peng, R. D. Reproducible research and biostatistics. *Biostatistics* **10**, 405–408 (2009).
- This work provides a succinct and convincing argument for reproducibility—*Biostatistics* is at the forefront of ensuring that code and data are provided for other researchers.**
- Devil in the details. *Nature* **470**, 305–306 (2011).
  - Pedersen, T. Empiricism is not a matter of faith. *Comput. Linguist.* **34**, 465–470 (2008).
  - Donoho, D. L. An invitation to reproducible computational research. *Biostatistics* **11**, 385–388 (2010).
  - Raymond, E. S. *The Cathedral and the Bazaar* (O'Reilly, 2001).
  - He, Y. & Ding, C. H. Q. Using accurate arithmetics to improve numerical reproducibility and stability in parallel applications. *J. Supercomput.* **18**, 259–277 (2011).

- Hatton, L. *et al.* The seismic kernel system—a large scale exercise in Fortran 77 portability. *Softw. Pract. Exper.* **18**, 301–329 (1988).
  - Hatton, L. The T experiments: errors in scientific software. *IEEE Comput. Sci. Eng.* **4**, 27–38 (1997).
  - Hey, T., Tansley, S. & Tolle, K. (eds) *The Fourth Paradigm: Data-Intensive Scientific Discovery* (Microsoft Press, 2009).
  - Gervasi, V. & Zowghi, D. On the role of ambiguity in RE. In *Requirements Engineering: Foundation for Software Quality* (eds Wieringa, R. & Persson, A) 248–254 (Springer, 2010).
  - van Deemter, K. *Not Exactly: In Praise of Vagueness* (Oxford University Press, 2010).
  - Yang, H., Willis, A., De Roeck, A. & Nuseibeh, B. Automatic detection of nocuous coordination ambiguities in natural language requirements. In *Proc. IEEE/ACM Intl Conf. on Automated Software Engineering* 53–62 (ACM, 2010).
  - de Bruijn, F. & Dekkers, H. L. Ambiguity in natural language software requirements: a case study. In *Requirements Engineering: Foundation for Software Quality* (eds Wieringa, R. & Persson, A.) 233–247 (Springer, 2010).
  - Pfleeger, S. L. & Hatton, L. Investigating the influence of formal methods. *IEEE Computer* **30**, 33–43 (1997).
  - van der Meulen, M. J. P. & Revilla, M. A. The effectiveness of software diversity in a large population of programs. *IEEE Trans. Softw. Eng.* **34**, 753–764 (2008).
  - Boehm, B., Rombach, H. D. & Zelkowitz, M. V. (eds) *Foundations of Empirical Software Engineering: the Legacy of Victor R. Basili* (Springer, 2005).
  - Monniaux, D. The pitfalls of verifying floating-point computations. *ACM Trans. Programming Languages Systems* **30** (3), 1–41 (2008).
  - Thomas, S. J., Hacker, J. P., Desagne, M. & Stull, R. B. An ensemble analysis of forecast errors related to floating point performance. *Weather Forecast.* **17**, 898–906 (2002).
  - Revol, N. Standardized interval arithmetic and interval arithmetic used in libraries. *Proc. 3rd Intl Congr. Mathematical Software* 337–341 (2010).
  - Rump, S. M., Ogita, T. & Oishi, S. Accurate floating point summation. Part 1: Faithful rounding. *SIAM J. Sci. Comput.* **31**, 189–224 (2009).
  - Rump, S. M. Accurate and reliable computing in floating-point arithmetic. *Proc. 3rd Intl Congr. Mathematical Software* 105–108 (2010).
  - Badin, M., Bic, L., Dillencourt, M., & Nicolau, A. Improving accuracy for matrix multiplications on GPUs. *Sci. Prog.* **19**, 3–11 (2011).
  - Pan, V. Y., Murphy, B., Qian, G. & Rosholt, R. E. A new error-free floating-point summation algorithm. *Comput. Math. Appl.* **57**, 560–564 (2009).
  - Boldo, S. & Muller, J.-M. Exact and approximated error of the FMA. *IEEE Trans. Comput.* **60**, 157–164 (2011).
  - Kahan, W. Desperately needed remedies for the undebuggability of large floating-point computations in science and engineering. *IFIP/SIAM/NIST Working Conf. Uncertainty Quantification in Scientific Computing* (Springer, in the press).
  - Mesirov, J. P. Accessible reproducible research. *Science* **327**, 415–416 (2010).
  - Donoho, D. L., Maleki, A., Rahman, I. U., Shahram, M. & Stodden, V. Reproducible research in computational harmonic analysis. *Comput. Sci. Eng.* **11**, 8–18 (2009).
- Donoho and fellow researchers have been at the forefront of reproducibility for many years; this article reviews their work, including facilities for code presentation.**
- Yool, A., Popova, E. E. & Anderson, T. R. Medusa-1.0: a new intermediate complexity plankton ecosystem model for the global domain. *Geosci. Model Develop.* **4**, 381–417 (2011).
- An example of an article from a journal that asks for code release for model description papers and encourages code release for other categories of paper.**
- Easterbrook, S. M. & Johns, T. C. Engineering the software for understanding climate change. *Comput. Sci. Eng.* **11**, 65–74 (2009).
  - Brohan, P., Kennedy, J. J., Harris, I., Tett, S. F. B. & Jones, P. D. Uncertainty estimates in regional and global observed temperature changes: a new dataset from 1850. *J. Geophys. Res.* **111**, D12106 (2006).
  - Adams, E. N. Optimizing preventive service of software products. *IBM J. Res. Develop.* **28**, 2–14 (1984).
  - Hatton, L. & Roberts, A. How accurate is scientific software? *IEEE Trans. Softw. Eng.* **20**, 785–797 (1994).

**Acknowledgements** We thank D. Hales of the Department of Design at the Open University and P. Piwak of the Department of Computing for pointing out some reproducibility work outside computing. J.G.-C. is grateful to I. Goz for pointing out the calculation errors in the CRUTEM data from the Meteorological Office.

**Author Contributions** D.C.I., L.H. and J.G.-C. contributed to all aspects of this article.

**Author Information** Reprints and permissions information is available at [www.nature.com/reprints](http://www.nature.com/reprints). The authors declare no competing financial interests. Readers are welcome to comment on the online version of this article at [www.nature.com/nature](http://www.nature.com/nature). Correspondence and requests for materials should be addressed to D.C.I. ([d.c.ince@open.ac.uk](mailto:d.c.ince@open.ac.uk)).

# Experimental demonstration of topological error correction

Xing-Can Yao<sup>1</sup>, Tian-Xiong Wang<sup>1</sup>, Hao-Ze Chen<sup>1</sup>, Wei-Bo Gao<sup>1</sup>, Austin G. Fowler<sup>2</sup>, Robert Raussendorf<sup>3</sup>, Zeng-Bing Chen<sup>1</sup>, Nai-Le Liu<sup>1</sup>, Chao-Yang Lu<sup>1</sup>, You-Jin Deng<sup>1</sup>, Yu-Ao Chen<sup>1</sup> & Jian-Wei Pan<sup>1</sup>

Scalable quantum computing can be achieved only if quantum bits are manipulated in a fault-tolerant fashion. Topological error correction—a method that combines topological quantum computation with quantum error correction—has the highest known tolerable error rate for a local architecture. The technique makes use of cluster states with topological properties and requires only nearest-neighbour interactions. Here we report the experimental demonstration of topological error correction with an eight-photon cluster state. We show that a correlation can be protected against a single error on any quantum bit. Also, when all quantum bits are simultaneously subjected to errors with equal probability, the effective error rate can be significantly reduced. Our work demonstrates the viability of topological error correction for fault-tolerant quantum information processing.

Quantum computers exploit the laws of quantum mechanics and can solve many problems exponentially more efficiently than their classical counterparts<sup>1–3</sup>. However, in the laboratory the ubiquitous decoherence of quantum states makes it notoriously hard to achieve the required high degree of quantum control. To overcome this problem, quantum error correction has been invented<sup>4–6</sup>. The principal result in quantum error correction, the threshold theorem<sup>7,8</sup>, states that as long as the error rate,  $p$ , per gate in a quantum computer is smaller than a threshold value,  $p_c$ , arbitrarily long and accurate quantum computation is efficiently possible. However, most methods of fault-tolerant quantum computing with a high threshold error rate ( $10^{-4}$ – $10^{-2}$ ) require strong and long-range interactions<sup>7–9</sup>, and are thus difficult to implement. Local architectures are normally associated with much lower thresholds. For traditional concatenated codes on a two-dimensional lattice of quantum bits (qubits) with nearest-neighbour gates, the highest threshold known at present<sup>10</sup> is  $2.02 \times 10^{-5}$ .

In such lattices, it is advantageous to use topological error correction<sup>11–15</sup> (TEC) in the framework of topological cluster-state quantum computing. This scheme makes use of the topological properties in three-dimensional (3D) cluster states, which form an inherently error-robust ‘fabric’ for computation. Local measurements drive the computation and, at the same time, implement the error correction. Active error correction and topological methods are combined, yielding a high error threshold<sup>12,13</sup> of 0.7–1.1% and tolerating loss rates<sup>15</sup> up to 24.9%. This allows for the unavoidable imperfections of physical devices, and makes our implementation of TEC close to the experimental state of the art. For practical quantum computation with TEC, a larger cluster state of more qubits would be needed. The 3D architecture can be further mapped onto a local setting in two spatial dimensions plus time<sup>14</sup>, also with nearest-neighbour interactions only. Two detailed architectures have already been proposed<sup>16,17</sup>. We note that a different topological scheme has been proposed in which quantum computation is driven by non-Abelian anyons<sup>18,19</sup> and fault tolerance is achieved through passive stabilization afforded by a ground-state energy gap.

Some simple quantum error correction codes have been experimentally demonstrated in nuclear magnetic resonance<sup>20,21</sup>, ion

traps<sup>22,23</sup> and optical systems<sup>24,25</sup>. However, the experimental realization of topological quantum error correction methods remains challenging. At present, multipartite cluster states can be generated with up to six photons and work is under way to create non-Abelian anyons for topological quantum computing<sup>18,19</sup>. Here we develop an ultrabright entangled-photon source by using an interferometric Bell-type synthesizer. With this and a noise-reduction interferometer, we generate a polarization-encoded eight-photon cluster state, which is shown to possess the required topological properties for TEC. In accordance with the TEC scheme, we measure each photon (qubit) locally. Error syndromes are constructed from the measurement outcomes, and one topological quantum correlation is protected. We demonstrate that if only one physical qubit suffers an error, the faulty qubit can be located and corrected, and that if all qubits are simultaneously subjected to errors with equal probability, the effective error rate is significantly reduced by error correction. This constitutes a proof-of-principle experiment that demonstrates the viability of TEC, a central ingredient in topological cluster-state computing.

## Cluster states and quantum computing

In cluster-state quantum computing<sup>26</sup>, projective one-qubit measurements replace unitary evolution as the elementary process driving a quantum computation. The computation begins with a highly entangled multi-qubit state, the ‘cluster state’  $|G\rangle$  (ref. 27), which is specified by an interaction graph,  $G$ , and can be created from a product state through the pairwise Ising interaction over the edges in  $G$ . For each vertex  $i \in G$ , we define a stabilizer as  $K_i \equiv X_i \otimes_{e_{ij}} Z_j$  where the product is over all the interaction edges,  $e_{ij}$ , connecting vertex  $i$  to its nearest-neighbouring vertices,  $j$ . The symbols  $X_i$  and  $Z_j$  denote the bit- and phase-flip Pauli operators, respectively, acting on qubits  $i$  and  $j$ . State  $|G\rangle$  is the unique joint eigenstate of a complete set of stabilizers  $K_i$  such that  $K_i|G\rangle = |G\rangle$  for all  $i \in G$ .

Cluster states in  $d \geq 3$  dimensions are resources for universal fault-tolerant quantum computing<sup>12</sup>, in which the TEC capability—shared with Kitaev’s toric code<sup>11,28</sup> and the colour code<sup>29</sup>—is combined with the capability to process quantum information.

<sup>1</sup>Shanghai Branch, National Laboratory for Physical Sciences at Microscale and Department of Modern Physics, University of Science and Technology of China, Shanghai 201315, China. <sup>2</sup>QC2T, School of Physics, University of Melbourne, Victoria 3010, Australia. <sup>3</sup>Department of Physics and Astronomy, University of British Columbia, Vancouver, British Columbia V6T 1Z1, Canada.



## Topological error correction

Quantum error correction and fault-tolerant quantum computing are possible with cluster states whenever the underlying interaction graph can be embedded in a 3D cell structure known as a cell complex<sup>30</sup>, which consists of volumes, faces, edges and vertices. Qubits are encoded on the edges and faces of a cell complex. The associated interaction graph connects the qubit on each face to the qubits on its surrounding edges through the interaction edges. Consider the elementary cell complex in Fig. 1a, shown by the dashed lines: it has one cubic volume, six square faces, twelve edges and eight vertices. The interaction edges, represented by the solid lines, form an 18-qubit cluster state,  $|G_{18}\rangle$ . There are six face stabilizers,  $K_f$  ( $f = 1, 2, \dots, 6$ ). It follows that multiplication of these stabilizers cancels out all  $Z$  operators in  $K_f$  and thus yields a unit expectation value:  $\langle X_1 X_2 \cdots X_6 \rangle = 1$ . This leads to the straightforward but important observation that despite the  $X$  measurement on each individual face qubit having the random outcome  $\pm 1$ , the product of all the outcomes on any closed surface,  $F$ , is  $+1$ . That is, any closed surface has the topological quantum correlation  $C_F \equiv \langle \otimes_{f \in F} X_f \rangle = 1$ , where  $f$  is a face of  $F$ .

A larger cell complex is displayed in Fig. 1b, which encodes and propagates a logical qubit. It consists of  $5 \times 5 \times T$  cells, where  $T$  specifies a span of simulated time ( $t$ ). A 'defect' along the  $t$  direction (Fig. 1b, line of green dots) is first produced by performing local  $Z$  measurements. Then the topological quantum correlation,  $C_{F_D} = 1$ , on a defect-enclosing closed surface ( $F_D$ ), combined with the boundary, is used to encode a logical qubit. The evolution of the logical state from  $t_1$  to  $t_2$  is achieved by local  $X$  measurements on all other physical qubits between  $t_1$  and  $t_2$  (see ref. 31 for details). Quantum computing requires a much larger cell complex and more defects, where quantum algorithms are realized by appropriate braiding-like manipulation of defects (a sketch of the logical controlled-NOT gate is shown in Supplementary Information).

The quantum computation is possible because the topological quantum correlation  $C_{F_D} = 1$  holds on defect-enclosing closed surfaces. The TEC capability arises from the  $\mathbb{Z}_2$  homology, a topological feature, of a sufficiently large 3D cell complex (Supplementary Information). For a given  $F_D$ , there exist many homologically equivalent closed surfaces with the same topological correlation ( $C_{F_D} = 1$ ). This redundancy leads to the topological protection of the correlation<sup>12</sup>.

Remarkably, in TEC it is sufficient to deal with  $Z$  errors, because an  $X$  error either has no effect, if it occurs immediately before an  $X$  measurement, or is equivalent to multiple  $Z$  errors. Finally, as TEC is implemented in topological cluster-state quantum computing—a

measurement-based process—corrections suggested by TEC are not applied to the remaining cluster state but rather to the classical outcomes of  $X$  measurements.

## Simpler topological cluster state

The cell complex in Fig. 1b encodes a propagating logical qubit in terms of one topological correlation,  $C_{F_D} = 1$ , and is robust against a local  $Z$  error. However, it contains 25 elementary cells and 180 physical qubits for each layer of complex over a unit time span, which is beyond the capacity of available experimental techniques. We design a simpler graph state,  $|G_8\rangle$  (Fig. 2a), to mimic the cell complex of Fig. 1b.

The topological feature of  $|G_8\rangle$  can be seen from its association with the 3D cell complex in Fig. 2b, which consists of four elementary volumes,  $\{v, w, y, z\}$ ; six faces,  $\{f_1, f_2, f_3, f_4, f_5, f_6\}$ ; two edges,  $\{e_7, e_8\}$ ; and two vertices,  $\{s, t\}$ . All six faces have the same boundary,  $e_7 \cup e_8$ , and any two of them form a closed surface,  $F$ . The centre volume is removed to resemble the defect in Fig. 1b, and the topological correlation to be protected,  $C_{F_D}$ , reads

$$C_{F_D} \equiv \langle X_5 X_6 \rangle = 1 \quad (1)$$

In this simple cell complex, the topological correlation  $C_{F_D} = 1$  is already multiply encoded: it is represented by any expectation  $\langle X_i X_j \rangle$  with  $i \in \{1, 2, 5\}$  and  $j \in \{3, 4, 6\}$ . Moreover, there exist four other closed surfaces, corresponding to the respective boundaries of the volumes  $\{v, w, y, z\}$ , that do not enclose the defect. The 'redundant' topological correlations are

$$\langle X_1 X_2 \rangle = \langle X_2 X_5 \rangle = \langle X_3 X_6 \rangle = \langle X_3 X_4 \rangle = 1 \quad (2)$$

These can be used as error syndromes in TEC, which makes one or more of them equal to  $-1$ . As shown in Table 1, a single  $Z$  error on any physical qubit can be located and corrected.

Therefore, from the aspect of TEC capability, the cluster state  $|G_8\rangle$  is analogous to the cell complex in Fig. 1b. Each protects one topological correlation and is robust against a single  $Z$  error, despite the cell complex in Fig. 2b being too small to propagate a logical qubit (see Supplementary Information for details).

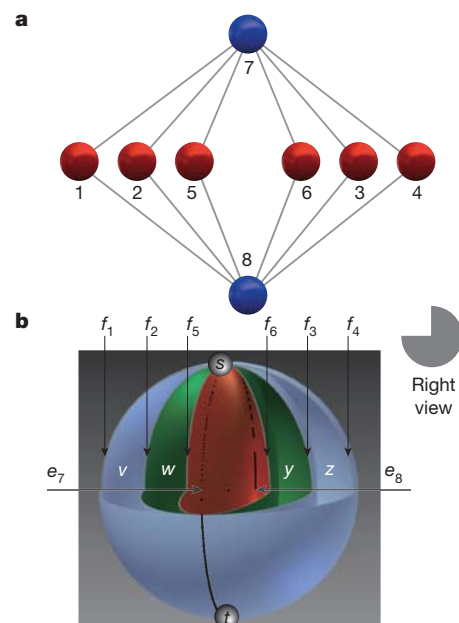


**Figure 2 | Cluster state  $|G_8\rangle$  and its cell complex.** **a**,  $G_8$ , the interaction graph of  $|G_8\rangle$ . **b**, The corresponding 3D cell complex, with volumes  $\{v, w, y, z\}$ , faces  $\{f_1, f_2, f_3, f_4, f_5, f_6\}$ , edges  $\{e_7, e_8\}$  and vertices  $\{s, t\}$ . The exterior and the centre volume are not in the complex. For better illustration, the cell complex is cut open and the foreground quarter is removed (silhouette view from right is shown for clarity).

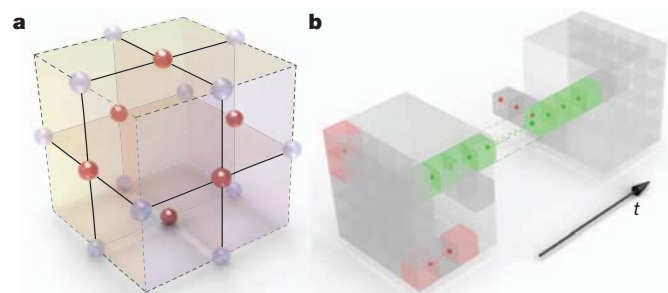


**Figure 1 | Topological cluster states.** **a**, Elementary lattice cell. Dashed lines represent the edges of the associated cell complex and solid lines represent the edges of the interaction graph. Qubits (spheres) are encoded on the faces and edges of the elementary cell. **b**, Larger topological cluster state of  $5 \times 5 \times T$  cells. Green dots represent local  $Z$  measurements, which effectively remove the measured qubits from the cluster state and thereby create a non-trivial topology capable of supporting a single correlation. Red dots represent  $Z$  errors. Red cells indicate the ends of error chains where  $C_F = -1$ . One axis of the cluster can be regarded as simulating the 'circuit time',  $t$ . The evolution of logical states from  $t_1$  to  $t_2$  is achieved by performing local  $X$  measurements on all physical qubits between  $t_1$  and  $t_2$ .

**Table 1** |  $G_8$  and the syndromes  $\langle X_i X_j \rangle$

Qubit with Z error	$\langle X_1 X_2 \rangle$	$\langle X_2 X_5 \rangle$	$\langle X_3 X_6 \rangle$	$\langle X_3 X_4 \rangle$
1	-1	1	1	1
2	-1	-1	1	1
3	1	1	-1	-1
4	1	1	1	-1
5	1	-1	1	1
6	1	1	-1	1

### Preparation of the eight-photon cluster state

In our experiment, we create the desired eight-photon cluster state using spontaneous parametric down-conversion and linear optics. The first step is to develop an ultrabright, high-fidelity entangled-photon source. As shown in Fig. 3a, an ultraviolet mode-locked laser pulse (power, 915 mW) passes through a  $\beta$ -barium borate crystal, generating a pair of polarization-entangled photons in the state  $|\phi\rangle = (|HH\rangle + |VV\rangle)/\sqrt{2}$ . Using an interferometric Bell-state synthesizer<sup>32</sup>, we guide photons of different bandwidths (Fig. 3a, red and blue dots, respectively) along separate paths. This disentangles the temporal information from the polarization information. By contrast with the conventional narrowband filtering technique, this process does not result in photon loss and we thus achieve ultrahigh brightness. Four pairs of such entangled photons are prepared and labelled as 1–2, 3–4, 5–6 and 7–8 (Fig. 3b). Then we generate two graph states, each of four photons. The first is a Greenberger–Horne–Zeilinger state,  $(|H^{\otimes 4}\rangle_{1-4} + |V^{\otimes 4}\rangle_{1-4})/\sqrt{2}$ , obtained by superposing photons 2 and 4 on a polarizing beam splitter (PBS<sub>1</sub>), which transmits horizontal polarization (H) and reflects vertical polarization (V). At the same time, photons 6 and 8 are interfered on a polarization-dependent beam splitter (PDBS) and then separately pass

through two other PDBSs. The first PDBS has transmitting probabilities  $T_H = 1$  and  $T_V = 1/3$ , and the second and third have  $T_H = 1/3$  and  $T_V = 1$ . The combination of these three PDBSs acts as a controlled-phase gate<sup>33,34</sup>. With a success probability of one-ninth, there is twofold coincidence in paths 6' and 8', yielding a four-photon cluster state<sup>34</sup>  $[|HH\rangle_{56}(|HH\rangle_{78} + |VV\rangle_{78}) + |VV\rangle_{56}(|HH\rangle_{78} - |VV\rangle_{78})]/2$ . Finally, photons 4' and 6' are superposed on PBS<sub>2</sub>. When eight photons come out of the output ports simultaneously, we obtain an entangled eight-photon cluster state:

$$|\psi\rangle = \frac{1}{2} \left[ |H^{\otimes 6}\rangle_{1-6} (|HH\rangle_{78} + |VV\rangle_{78}) + |V^{\otimes 6}\rangle_{1-6} (|HH\rangle_{78} - |VV\rangle_{78}) \right] \quad (3)$$

This is exactly the cluster state  $|G_8\rangle$  shown in Fig. 2a under Hadamard operations  $H^{\otimes 8}$  on all qubits. We note that the photons, which are interfered on the PBSs or the PDBSs, have the same bandwidth, and that a star topology of the eight-photon interferometer<sup>32</sup> leads to an effective noise reduction.

To ensure good spatial and temporal overlap, the photons are also spectrally filtered, with full-widths at half-maximum of  $\Delta\lambda_{\text{FWHM}} = 8$  nm for photons 1, 3, 5 and 7 and  $\Delta\lambda_{\text{FWHM}} = 2.8$  nm for photons 2, 4, 6 and 8, and are coupled by single-mode fibres. We obtain an average twofold coincidence count of  $\sim 3.4 \times 10^5 \text{ s}^{-1}$  and a visibility of  $\sim 94\%$  in the  $\{|H\rangle, |V\rangle\}$  basis as well as in the  $\{|+\rangle, |-\rangle\}$  basis, where  $|\pm\rangle = (|H\rangle \pm |V\rangle)/\sqrt{2}$ . Fine adjustments of the delays between the different paths are tuned to ensure that all the interfering photons arrive at the PBSs and the PDBSs simultaneously.

Measurement of each photon is made using a polarization analyser, which contains a combination of a QWP, a HWP and a PBS together

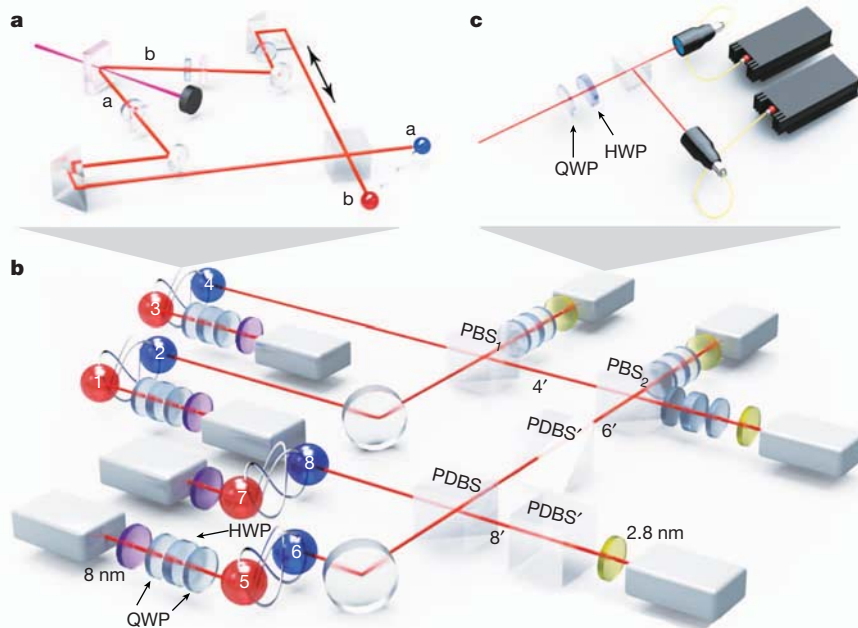


**Figure 3** | Experimental set-up for the generation of the eight-photon cluster state and the demonstration of topological error correction.

**a**, Creation of ultrabright entangled-photon pairs. An ultraviolet laser pulse passes through a 2-mm, nonlinear  $\beta$ -barium borate crystal, creating an entangled photon pair  $\{a, b\}$  with density matrix  $\rho = (|H_a^o\rangle\langle V_b^o| + |V_a^o\rangle\langle H_b^o| + |H_a^e\rangle\langle H_b^e| + |V_a^e\rangle\langle V_b^e|)/2$  by parametric down-conversion, where  $o$  and  $e$  indicate ordinary and extraordinary polarizations, respectively perpendicular and parallel relative to the  $V$ -polarized pump. After both photons pass through compensators, which include a  $45^\circ$  half-wave plate (HWP) and a 1-mm  $\beta$ -barium borate crystal, one of the photons' polarizations is rotated by another  $45^\circ$  HWP. Then we re-overlap the two photons on a PBS, creating an entangled photon pair in a state

$|\phi_{ab}\rangle = (|H\rangle|H\rangle + e^{i\varphi}|V\rangle|V\rangle) \otimes |e_a\rangle|o_b\rangle/\sqrt{2}$ , where  $|e_a\rangle$  is a state in which all photons in path  $a$  have extraordinary polarization and  $|o_b\rangle$  is a state in which all photons in path  $b$  have ordinary polarization. **b**, To create the desired cluster state, we combine photons from paths 6 and 8 at the first PDBS and let each photon pass through another PDBS (PDBS'), resulting a controlled-phase operation between the two photons. At the same time, photons 2 and 4 are interfered on PBS<sub>1</sub>. Then photons 4' and 6' are overlapped on PBS<sub>2</sub>. On coincidence detection, we create the eight-photon cluster state (equation (3)) for topological error correction. **c**, Polarization analyser for each individual photon, containing a quarter-wave plate (QWP), a HWP, a PBS and two single-mode, fibre-coupled single-photon detectors.

with a single-mode, fibre-coupled single-photon detectors in each output of the PBS (Fig. 3c). The complete set of all 256 possible combinations of eight-photon coincidence events is registered by a home-made programmable coincidence logic unit based on a field-programmable gate array. We obtain an eightfold coincidence rate of 3.2 per hour. On the basis of the measurements for the 256 possible polarization combinations in the  $\{|H\rangle, |V\rangle\}$  basis (Fig. 4a), we obtain a signal-to-noise ratio, defined as the ratio of the average number of desired components to that of non-desired components, of about 200:1. This indicates that we have been successful in preparing the desired eight-photon cluster state.

To characterize the cluster state more precisely, we use the entanglement witness method to determine its fidelity. For this purpose, we construct a witness that allows for the lower bound on the state fidelity and requires only eight measurement settings (Supplementary Information):

$$\begin{aligned} \mathcal{W}_8 &= \frac{1}{2} - (|\psi\rangle\langle\psi| - |\psi'\rangle\langle\psi'|) \\ &= \frac{1}{2} - \left[ \frac{1}{4} (|H\rangle\langle H|^{\otimes 6} - |V\rangle\langle V|^{\otimes 6})_{1-6} \otimes (X_7 X_8 - Y_7 Y_8) \right. \\ &\quad \left. + \frac{1}{12} \left( \sum_{k=0}^5 (-1)^k M_k^{\otimes 6} \right)_{1-6} \otimes (|H\rangle\langle H|^{\otimes 2} - |V\rangle\langle V|^{\otimes 2})_{78} \right] \end{aligned}$$

Here  $\langle\psi'|\psi\rangle = 0$  and  $M_k = \cos(k\pi/6)X + \sin(k\pi/6)Y$ . The measured expectation value of each measurement setting in  $\mathcal{W}_8$  is shown in Fig. 4b. These yield the witness  $\langle\mathcal{W}_8\rangle = -0.105 \pm 0.023$ , which is negative by 4.5 s.d. The state fidelity is  $F > 0.5 - \langle\mathcal{W}_8\rangle = 0.605 \pm 0.023$ . This confirmed the presence of genuine eight-photon entanglement.

### Experimental topological error correction

Given such a cluster state, topological error correction is implemented using a series of single-qubit measurements and classical correction operations. In the laboratory, operations are performed on state  $|\psi\rangle$  (equation (3)), which differs from  $|G_8\rangle$  in Fig. 2a by the Hadamard operation  $H^{\otimes 8}$ . Therefore, the correlation to be protected in equation (1),  $\langle X_5 X_6 \rangle$ , corresponds to  $\langle Z_5 Z_6 \rangle$  in the experiment; similarly, each  $\langle X_i X_j \rangle$  in equation (2) corresponds to  $\langle Z_i Z_j \rangle$ . Furthermore,  $X$  errors are simulated instead of  $Z$  errors.

In the experiment, the noisy quantum channels on polarization qubits are simulated by one HWP positioned between two QWPs, which are set at  $90^\circ$  relative to the horizontal. By randomly setting the HWP axis to be oriented at  $\pm\theta$  with respect to the horizontal direction, the noisy quantum channel can be simulated with a bit-flip error probability of  $p = \sin^2(2\theta)$ .

We first study the case in which only a single  $X$  error occurs on one of the six photons  $\{1, \dots, 6\}$ . The syndrome correlations are measured (Fig. 5). For comparison, in Fig. 4c we plot the correlations without any simulated error. This comparison, together with Table 1, makes it possible to locate precisely the physical qubit undergoing an  $X$  error.

We then consider the case in which all six photons are simultaneously subject to a random  $X$  error with equal probability  $0 < p < 1$  and study the rate of errors,  $\langle Z_5 Z_6 \rangle = -1$ , for the topological quantum correlation  $\langle Z_5 Z_6 \rangle$ . Without error correction, the error rate of correlation  $\langle Z_5 Z_6 \rangle$  is  $P = 1 - (1 - p)^2 - p^2$ . With error correction, the residual error becomes

$$\begin{aligned} P &= 1 - [(1-p)^6 + p^6] - [6p(1-p)^5 + 6(1-p)p^5] \\ &\quad - [9p^2(1-p)^4 + 9(1-p)^2 p^4] \end{aligned}$$

For small  $p$ , the residual error rate after error correction is significantly reduced relative to the unprotected case. As shown in Fig. 6, the experimental results are in good agreement with these theoretical predictions. Considerable improvement of the robustness of the correlation  $\langle Z_5 Z_6 \rangle$  can be seen both in theory and in practice.

In the experiment, the whole measurement takes about 80 days. This requires our set-up to be extremely stable. The imperfections in the experiment are mainly due to the undesired components in the  $\{|H\rangle, |V\rangle\}$  basis, which arise from higher-order emissions of entangled photons, and the imperfect photon overlapping at the PBSs and the PDBS. In spite of these issues, the viability of TEC is successfully demonstrated in the experiment.

### Discussion

In this work, we have experimentally demonstrated TEC with an eight-photon cluster state. This state represents the current state of the art for preparation of cluster states in qubit systems and is of particular interest in studying multipartite entanglement and quantum information processing. The scalable construction of cluster

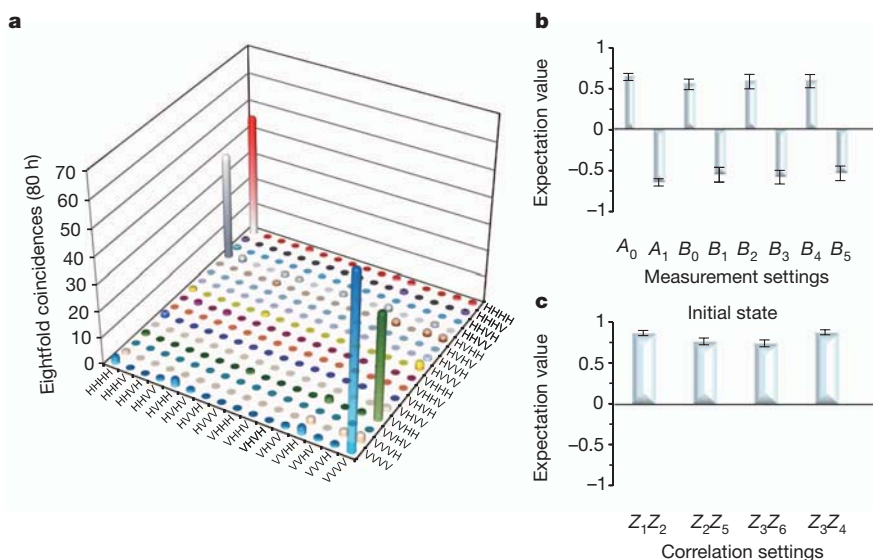


**Figure 4 | Experimental results for the created eight-photon cluster state.** **a**, Measured eightfold coincidence in the  $\{|H\rangle, |V\rangle\}$  basis. **b**, The expectation values for different witness measurement settings. The measurement settings are  $A_0 = (|H\rangle\langle H|^{\otimes 6} - |V\rangle\langle V|^{\otimes 6})_{1-6} X_7 X_8$ ,  $A_1 = (|H\rangle\langle H|^{\otimes 6} - |V\rangle\langle V|^{\otimes 6})_{1-6} Y_7 Y_8$  and  $B_i = M_i^{\otimes 6} (|H\rangle\langle H|^{\otimes 2} - |V\rangle\langle V|^{\otimes 2})_{78}$  with  $i = 0, \dots, 5$ . The

measurement of each setting takes 50 h for the first two settings and 30 h for the remaining settings. **c**, Correlations for the initial state without any simulated error. Error bars, 1 s.d., deduced from propagated Poissonian counting statistics of the raw detection events.



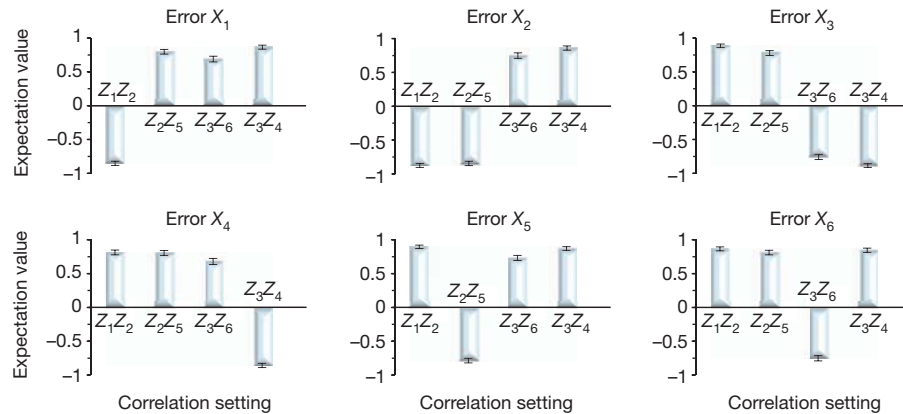


**Figure 5 | Experimental results of syndrome correlations for topological error correction.** Only one qubit is subjected to an  $X$  error in each plot. The measurement for each error setting takes about 80 h. Error bars, 1 s.d., deduced from propagated Poissonian counting statistics of the raw detection events.

states in future will require further development of high-efficiency entanglement sources and single-photon detectors<sup>35</sup>. Recent results have shown that if the product of the number-resolving detector efficiency and the source efficiency is greater than two-thirds, efficient linear optical quantum computation is possible<sup>36</sup>. There has been technical progress towards this goal, such as deterministic, storable, single-photon sources<sup>37</sup> and photon-number-resolving detectors<sup>38</sup>. Our demonstration of TEC is a further step towards fault-tolerant quantum computation. In the scheme, given sufficient qubits and physical error rates below 0.7–1.1%, arbitrary quantum computations can be performed arbitrarily reliably. The high threshold error rate is especially remarkable given that only nearest-neighbour interactions are required. Owing to these advantages, TEC is especially well suited for physical systems geometrically constrained to nearest-neighbour interactions, such as quantum dots<sup>39</sup>, Josephson junction qubits<sup>40</sup>, ion traps<sup>41</sup>, cold atoms in optical lattices<sup>42</sup> and photonic modules<sup>17</sup>. A quantum gate with an error rate below the threshold required in TEC is within reach of present technology<sup>43</sup>. It would be interesting in future work to exploit cluster states of the maximum achievable size, to implement topologically error-protected quantum algorithms using local measurements.

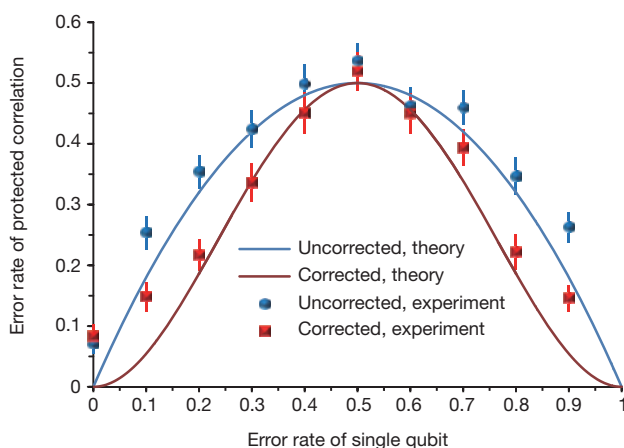


**Figure 6 | Experimental results of topological error correction.** All physical qubits are simultaneously subject to an  $X$  error with equal probability ranging from 0 to 1. The blue circles and blue lines represent the experimental and, respectively, theoretical values of the error rate for the protected correlation without TEC, and the red squares and red lines similarly represent the error rate with TEC. The agreement between the experimental and the theoretical results demonstrates the viability of TEC. The measurement of each data point takes 80 h. Error bars, 1 s.d., deduced from propagated Poissonian counting statistics of the raw detection events.

Received 26 October; accepted 7 December 2011.

- Shor, P. W. in *Proc. 35th Annu. Symp. Foundations Computer Sci.* 124–134 (IEEE, 1994).
- Grover, L. K. Quantum mechanics helps in searching for a needle in a haystack. *Phys. Rev. Lett.* **79**, 325–328 (1997).
- Feynman, R. P. Simulating physics with computers. *Int. J. Theor. Phys.* **21**, 467–488 (1982).
- Calderbank, A. R. & Shor, P. W. Good quantum error-correcting codes exist. *Phys. Rev. A* **54**, 1098–1105 (1996).
- Steane, A. M. Error correcting codes in quantum theory. *Phys. Rev. Lett.* **77**, 793–797 (1996).
- Gottesman, D. Theory of fault-tolerant quantum computation. *Phys. Rev. A* **57**, 127–137 (1998).
- Knill, E. Quantum computing with realistically noisy devices. *Nature* **434**, 39–44 (2005).
- Aliferis, P., Gottesman, D. & Preskill, J. Quantum accuracy threshold for concatenated distance-3 code. *Quantum Inf. Comput.* **6**, 97–165 (2006).
- Kitaev, A. Y. Quantum computations: algorithms and error correction. *Russ. Math. Surv.* **52**, 1191–1249 (1997).
- Spedalieri, F. & Roychowdhury, V. P. Latency in local, two-dimensional, fault-tolerant quantum computing. *Quantum Inf. Comput.* **9**, 666–682 (2009).
- Dennis, E., Landahl, A., Kitaev, A. & Preskill, J. Topological quantum memory. *J. Math. Phys.* **43**, 4452–4505 (2002).
- Raussendorf, R., Harrington, J. & Goyal, K. A fault-tolerant one-way quantum computer. *Ann. Phys.* **321**, 2242–2270 (2006).
- Wang, D. S., Austin, A. G. & Hollenberg, L. C. L. Quantum computing with nearest neighbor interactions and error rates over 1%. *Phys. Rev. A* **83**, 020302(R) (2011).
- Raussendorf, R. & Harrington, J. Fault-tolerant quantum computation with high threshold in two dimensions. *Phys. Rev. Lett.* **98**, 190504 (2007).
- Barrett, S. D. & Stace, T. M. Fault tolerant quantum computation with very high threshold for loss errors. *Phys. Rev. Lett.* **105**, 200502 (2010).
- Stock, R. & James, D. F. V. A scalable, high-speed measurement-based quantum computer using trapped ions. *Phys. Rev. Lett.* **102**, 170501 (2009).
- Devitt, S. J. *et al.* Topological cluster state computation with photons. *N. J. Phys.* **11**, 083032 (2009).
- Nayak, C., Simon, S. H., Stern, A., Freedman, M. & Sarma, S. D. Non-abelian anyons and topological quantum computation. *Rev. Mod. Phys.* **80**, 1083–1159 (2008).
- Wilczek, F. *Fractional Statistics and Anyon Superconductivity* (World Scientific, 1990).
- Cory, D. G. *et al.* Experimental quantum error correction. *Phys. Rev. Lett.* **81**, 2152–2155 (1998).
- Knill, E., Laflamme, R., Martinez, R. & Negrevergne, C. Benchmarking quantum computers: the five-qubit error correcting code. *Phys. Rev. Lett.* **86**, 5811–5814 (2001).
- Chiaverini, J. *et al.* Realization of quantum error correction. *Nature* **432**, 602–605 (2004).
- Schindler, P. *et al.* Experimental repetitive quantum error correction. *Science* **332**, 1059–1061 (2011).
- Lu, C.-Y. *et al.* Experimental quantum coding against qubit loss error. *Proc. Natl Acad. Sci. USA* **105**, 11050–11054 (2008).
- Aoki, T. *et al.* Quantum error correction beyond qubits. *Nature Phys.* **5**, 541–546 (2009).
- Raussendorf, R. & Briegel, H. J. A one-way quantum computer. *Phys. Rev. Lett.* **86**, 5188–5191 (2001).
- Schlingemann, D. & Werner, R. F. Quantum error-correcting codes associated with graphs. *Phys. Rev. A* **65**, 012308 (2001).
- Kitaev, A. Y. Fault-tolerant quantum computation by anyons. *Ann. Phys.* **303**, 2–30 (2003).
- Bombin, H. & Martin-Delgado, M. A. Topological quantum distillation. *Phys. Rev. Lett.* **97**, 180501 (2006).
- Hatcher, A. *Algebraic Topology* (Cambridge Univ. Press, 2002).

31. Fowler, A. G. & Goyal, K. Topological cluster state quantum computing. *Quantum Inf. Comput.* **9**, 727–738 (2009).
32. Yao, X.-C. *et al.* Observation of eight-photon entanglement. *Nature Photon.* (in the press); preprint at (<http://arxiv.org/abs/1105.6318>) (2011).
33. Hofmann, H. F. & Takeuchi, S. Quantum phase gate for photonic qubits using only beam splitters and postselection. *Phys. Rev. A* **66**, 024308 (2002).
34. Kiesel, N. *et al.* Experimental analysis of a four-qubit photon cluster state. *Phys. Rev. Lett.* **95**, 210502 (2005).
35. O'Brien, J. L. Optical quantum computing. *Science* **318**, 1567–1570 (2007).
36. Varnava, M., Browne, D. E. & Rudolph, T. How good must single photon sources and detectors be for efficient linear optical quantum computation? *Phys. Rev. Lett.* **100**, 060502 (2008).
37. Chen, S. *et al.* Deterministic and storable single-photon source based on quantum memory. *Phys. Rev. Lett.* **97**, 173004 (2006).
38. Kardynal, B. E., Yuan, Z. L. & Shields, A. J. An avalanche-photodiode-based photon-number-resolving detector. *Nature Phys.* **2**, 425–428 (2008).
39. Press, D. *et al.* Complete quantum control of a single quantum dot spin using ultrafast optical pulses. *Nature* **456**, 218–221 (2008).
40. Hime, T. *et al.* Solid-state qubits with current-controlled coupling. *Science* **314**, 1427–1429 (2006).
41. Hensinger, W. K. *et al.* T-junction ion trap array for two-dimensional ion shuttling, storage, and manipulation. *Appl. Phys. Lett.* **88**, 034101 (2006).
42. Jaksch, D. *et al.* Entanglement of atoms via cold controlled collisions. *Phys. Rev. Lett.* **82**, 1975–1978 (1999).
43. Benhelm, J., Kirchmair, G., Roos, C. F., & Blatt, R. Towards fault-tolerant quantum computing with trapped ions. *Nature Phys.* **4**, 463–466 (2008).

**Supplementary Information** is linked to the online version of the paper at [www.nature.com/nature](http://www.nature.com/nature).

**Acknowledgements** We acknowledge discussions with M. A. Martin-Delgado and O. Gühne. We are grateful to X.-H. Bao for his original idea of the ultrabright entanglement and to C.-Z. Peng for his idea of reducing high-order emission. We would also like to thank C. Liu and S. Fölling for their help in designing the figures. This work has been supported by the NNSF of China, the CAS, the National Fundamental Research Program (under grant no. 2011CB921300) and NSERC.

**Author Contributions** W.-B.G., A.G.F., R.R., Z.-B.C., Y.-J.D. and J.-W.P. had the idea for and initiated the experiment. A.G.F., R.R. and Y.-J.D. contributed to the general theoretical work. X.-C.Y., C.-Y.L., Y.-A.C. and J.-W.P. designed the experiment. X.-C.Y., T.-X.W. and H.-Z.C. carried out the experiment. X.-C.Y. and Y.-A.C. analysed the data. X.-C.Y., A.G.F., R.R., N.-L.L., C.-Y.L., Y.-J.D., Y.-A.C. and J.-W.P. wrote the manuscript. N.-L.L., Y.-A.C. and J.-W.P. supervised the whole project.

**Author Information** Reprints and permissions information is available at [www.nature.com/reprints](http://www.nature.com/reprints). The authors declare no competing financial interests. Readers are welcome to comment on the online version of this article at [www.nature.com/nature](http://www.nature.com/nature). Correspondence and requests for materials should be addressed to Y.-A.C. ([yuaochen@ustc.edu.cn](mailto:yuaochen@ustc.edu.cn)) or J.-W.P. ([pan@ustc.edu.cn](mailto:pan@ustc.edu.cn)).

# Ubiquitin-dependent regulation of COPII coat size and function

Lingyan Jin<sup>1\*</sup>, Kanika Bajaj Pahuja<sup>1,2\*</sup>, Katherine E. Wickliffe<sup>1</sup>, Amita Gorur<sup>1,2</sup>, Christine Baumgärtel<sup>1</sup>, Randy Schekman<sup>1,2</sup> & Michael Rape<sup>1</sup>

**Packaging of proteins from the endoplasmic reticulum into COPII vesicles is essential for secretion. In cells, most COPII vesicles are approximately 60–80 nm in diameter, yet some must increase their size to accommodate 300–400 nm procollagen fibres or chylomicrons. Impaired COPII function results in collagen deposition defects, cranio-lenticulo-sutural dysplasia, or chylomicron retention disease, but mechanisms to enlarge COPII coats have remained elusive. Here, we identified the ubiquitin ligase CUL3–KLHL12 as a regulator of COPII coat formation. CUL3–KLHL12 catalyses the monoubiquitylation of the COPII-component SEC31 and drives the assembly of large COPII coats. As a result, ubiquitylation by CUL3–KLHL12 is essential for collagen export, yet less important for the transport of small cargo. We conclude that monoubiquitylation controls the size and function of a vesicle coat.**

The extracellular matrix provides a scaffold for cell attachment and binding sites for membrane receptors, such as integrins, making it essential for the development of all metazoans<sup>1,2</sup>. When engaged with the extracellular matrix, integrins trigger signalling cascades that regulate cell morphology and division, yet in the absence of a functional extracellular matrix, integrins are removed from the plasma membrane by endocytosis<sup>3</sup>. The proper interplay between integrins and the extracellular matrix is particularly important during early development<sup>4</sup>, as stem cells depend on integrin-dependent signalling for division and survival<sup>5</sup>.

The establishment of the extracellular matrix requires secretion of several proteins, including its major constituent collagen. Following its synthesis in the endoplasmic reticulum, the export of collagen from cells depends on COPII vesicles<sup>6–9</sup>, and mutations in genes encoding COPII proteins lead to collagen deposition defects, skeletal aberrations and developmental diseases, such as cranio-lenticulo-sutural dysplasia<sup>10,11</sup>.

COPII vesicles are surrounded by a coat consisting of the SAR1 GTPase, SEC23–SEC24 adaptors, and an outer layer of SEC13–SEC31 heterotetramers<sup>12</sup>. These coat proteins self-assemble into cuboctahedral structures with a diameter of approximately 60–80 nm, which are too small to accommodate a procollagen fibre with a length of 300–400 nm<sup>13–15</sup>. Thus, collagen transport in cells must involve factors that are absent from *in vitro* self-assembly reactions. Indeed, TANGO1 (also known as MIA3) and its partner cTAGE5 interact with collagen and SEC23–SEC24, thereby recruiting collagen to nascent COPII coats<sup>16,17</sup>. The deletion of *Tango1* in mice resulted in collagen deposition defects similar to those caused by loss of COPII<sup>18</sup>, and mutations in human TANGO1 are associated with premature myocardial infarction<sup>19</sup>. However, TANGO1 is not known to regulate the size of COPII coats and mechanisms that permit the COPII coat to accommodate a large cargo remain poorly understood.

By analysing mouse embryonic stem (ES) cell division, we have identified CUL3–KLHL12 as a regulator of COPII coat formation. CUL3–KLHL12 monoubiquitylates SEC31 and drives assembly of large COPII coats. As a result, ubiquitylation by CUL3–KLHL12 is essential for collagen export, a step that is required for integrin-dependent mouse

ES cell division. We conclude that monoubiquitylation determines the size and function of a vesicle coat.

## CUL3 regulates mouse ES cell morphology

To provide insight into stem cell-specific division networks, we depleted ubiquitylation enzymes from mouse ES cells and scored for effects on proliferation and morphology. We found that loss of the ubiquitin ligase CUL3 caused mouse ES cells to form tightly packed cell clusters with prominent actin cables and aberrant adhesions, as seen by confocal microscopy analysis of actin and vinculin localization (Fig. 1a). A similar phenotype was observed upon depletion of UBA3, a component of the NEDD8 pathway that activates CUL3 (Supplementary Fig. 1a). CUL3-depleted mouse ES cells were delayed in proliferation (Supplementary Fig. 1b, d), yet retained their pluripotency, as seen by OCT4- and alkaline phosphatase-staining and the absence of differentiation markers in expression analyses (Supplementary Figs 1c, e, f and 2b). In contrast to mouse ES cells, depletion of CUL3 had weaker consequences in fibroblasts (Fig. 1a), although a previously reported increase in multinucleation was observed (Supplementary Fig. 1g; ref. 20).

Several observations show that the mouse ES cell phenotypes were caused by specific depletion of CUL3. First, several short interfering RNAs targeting distinct regions of the *Cul3* messenger RNA had the same effects on mouse ES cells, with a close correlation between knockdown efficiency and strength of phenotype (Supplementary Fig. 2a). Second, microarray analysis showed a strong reduction in *Cul3* mRNA upon siRNA treatment, whereas no other gene was significantly and reproducibly affected (Supplementary Fig. 2b). Third, siRNAs that target closely related proteins, such as other cullins, did not disturb the morphology of mouse ES cells (Supplementary Fig. 2c).

The aberrant morphology of CUL3-depleted mouse ES cells was reminiscent of increased RhoA GTPase activity, which triggers actin filament bundling<sup>21</sup>. Accordingly, a reduction in RhoA levels or inhibition of the RhoA effector kinase ROCK1 rescued CUL3-depleted mouse ES cells from compaction (Supplementary Fig. 3a). Among several possibilities, higher RhoA activity in the absence of CUL3 could result from RhoA stabilization or defective integrin signalling. Stabilization

<sup>1</sup>Department of Molecular and Cell Biology, University of California at Berkeley, California 94720, USA. <sup>2</sup>Howard Hughes Medical Institute, University of California at Berkeley, California 94720, USA.

\*These authors contributed equally to this work.



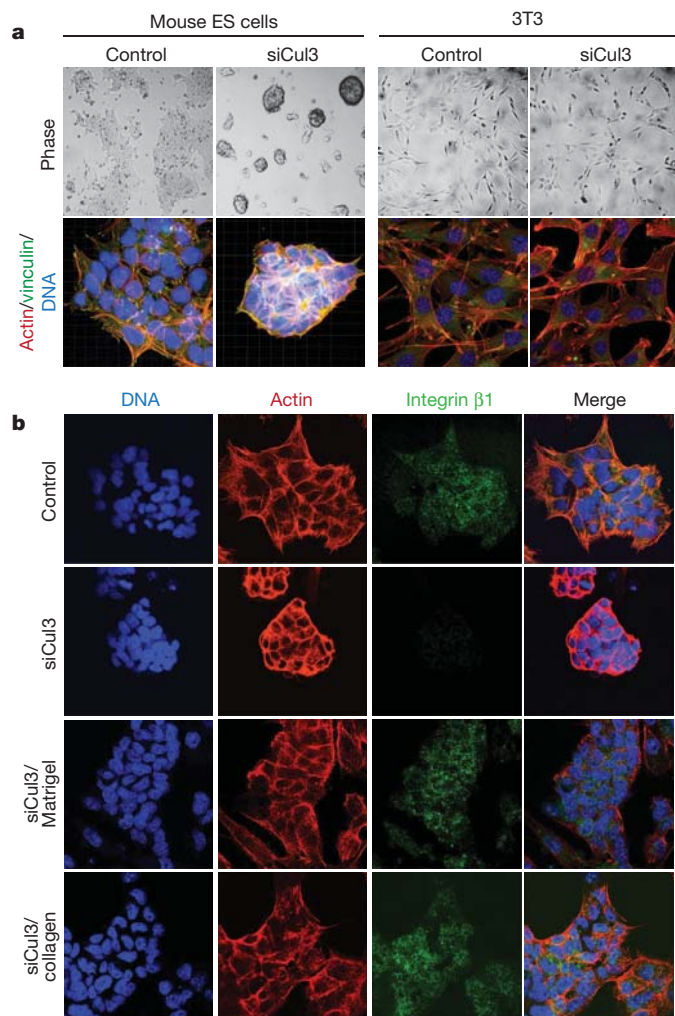


**Figure 1 | CUL3 regulates mouse ES cell morphology.** **a**, Left, D3 mouse ES cells were plated on gelatin and transfected with siRNAs targeting *Cul3* (siCul3), which resulted in cell clustering (phase microscopy; upper panel) and compaction (confocal microscopy: vinculin, green; actin, red; DNA, blue). Right, Depletion of CUL3 from mouse 3T3 fibroblasts did not cause cell compaction. Phase images original magnification was  $\times 10$ , fluorescence images  $\times 40$ . **b**, CUL3 is required for integrin localization to the mouse ES cell plasma membrane. D3 mouse ES cells were plated on gelatin (top two rows), growth-factor-depleted Matrigel or collagen IV. Following CUL3 depletion, cell compaction and integrin-targeting to the plasma membrane were analysed by confocal microscopy (actin, red; integrin  $\beta 1$ , green; DNA, blue). Original magnification  $\times 40$ .

of RhoA by co-depletion of all RhoA-specific CUL3 adaptors, the BACURDs<sup>22</sup>, did not affect mouse ES cell morphology (data not shown). By contrast, depletion of components of integrin signalling pathways phenocopied the loss of CUL3 in mouse ES cells (Supplementary Fig. 3b); partial reduction in CUL3 levels showed synthetic lethality with dasatinib, an inhibitor of the SRC kinase that acts downstream of integrin activation (Supplementary Fig. 3c); and integrin  $\beta 1$  was absent from the plasma membrane of CUL3-depleted mouse ES cells (Fig. 1b).

CUL3 could regulate integrin synthesis and trafficking, or it could allow for efficient deposition of extracellular matrix proteins to prevent integrin internalization<sup>3</sup>. To distinguish between these possibilities, we grew mouse ES cells on growth-factor-depleted Matrigel to provide an exogenous extracellular matrix. Strikingly, under these conditions, integrin  $\beta 1$  was found at the plasma membrane of CUL3-depleted mouse ES cells and no cell clustering was observed (Fig. 1b). Thus, CUL3 controls integrin signalling in mouse ES cells, most likely by supporting the establishment of a functional extracellular matrix.

## KLHL12 is a key CUL3 adaptor in mouse ES cells

CUL3 recruits substrates through adaptors with BTB domains<sup>23–26</sup>, yet siRNA approaches did not yield roles for BTB proteins in ES cells. As an alternative strategy to isolate CUL3 adaptors, we made use of the observation that stem cell regulators are highly expressed in ES cells, but downregulated upon differentiation<sup>27</sup>. Using affinity purification and mass spectrometry, we identified 31 BTB proteins that interact with CUL3 in mouse ES cells (Supplementary Fig. 4a; Supplementary Table 1). When analysed by quantitative polymerase chain reaction with reverse transcription (qRT-PCR) and immunoblot, we found that three adaptors, KLHL12, KBTBD8 and IBTK, were highly expressed in mouse ES cells, but downregulated upon differentiation (Fig. 2a, b and Supplementary Fig. 3d). Next, we depleted these adaptors from mouse ES cells that were sensitized for changes in integrin signalling by treatment with dasatinib. Importantly, depletion of KLHL12, but no other BTB protein, resulted in mouse ES cell compaction, as seen with loss of CUL3 (Fig. 2c). Accordingly, endogenous KLHL12 effectively binds CUL3 in mouse ES cells (Supplementary Fig. 4b). These experiments, therefore, identify KLHL12 as a key substrate-adaptor for CUL3 in mouse ES cells and the CUL3–KLHL12 ubiquitin ligase as an important regulator of mouse ES cell morphology.

## CUL3 monoubiquitylates SEC31

To isolate the substrates of CUL3–KLHL12, we constructed 293T cell lines that allowed for the inducible expression of Flag–KLHL12. By affinity chromatography and mass spectrometry, we identified the

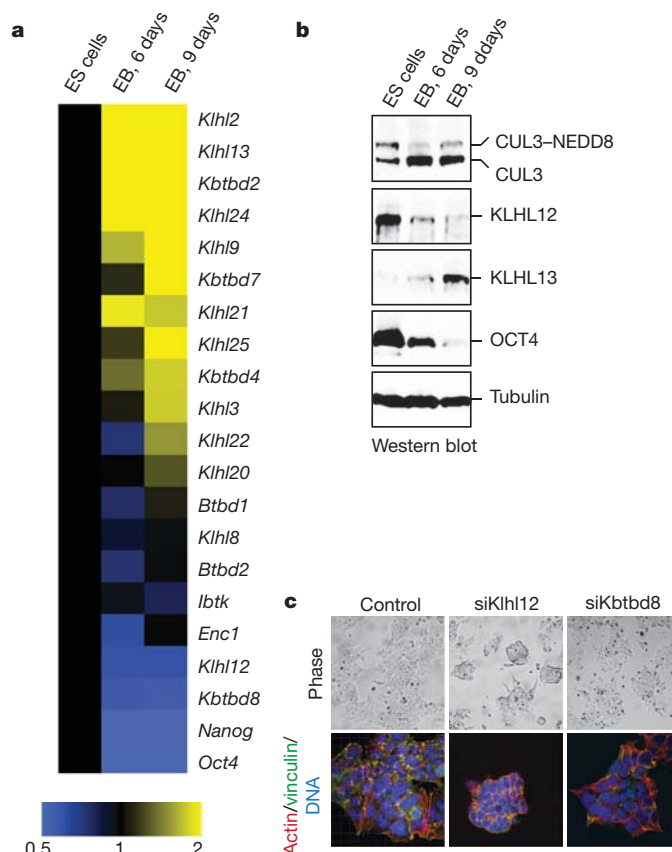


**Figure 2 | KLHL12 is a substrate adaptor for CUL3 in mouse ES cells.** **a**, D3 mouse ES cells were subjected to differentiation, and mRNA levels of indicated proteins were measured by qRT-PCR. EB, embryoid bodies. **b**, KLHL12 protein is downregulated upon differentiation, as observed by immunoblot of above samples. **c**, KLHL12 is a critical CUL3-adaptor in mouse ES cells. D3 mouse ES cells were sensitized towards altered integrin-signalling with dasatinib and monitored for compaction by phase (upper panel) or confocal microscopy (actin, red; vinculin, green; DNA, blue). Original magnification  $\times 40$ .

COPII proteins SEC13 and SEC31 as specific binding partners of KLHL12 (Fig. 3a and Supplementary Table 2). Immunoblotting confirmed retention of endogenous SEC13 and SEC31 in KLHL12 purifications, but not in precipitates of other BTB proteins (Supplementary Fig. 5a). As seen in pull-down assays, KLHL12 directly bound SEC31, but not SEC13 (Supplementary Fig. 5c, d), and this interaction was mediated by the amino terminus of SEC31 (Supplementary Fig. 6a) and the Kelch domain of KLHL12 (Supplementary Fig. 6b). In cells, approximately 30% of endogenous KLHL12 was associated with SEC13–SEC31 (Fig. 3b and Supplementary Fig. 5b). Consistent with such a prominent interaction, SEC13–SEC31 and KLHL12 colocalized in punctae, which are likely to represent endoplasmic reticulum exit sites of COPII vesicles (Fig. 3c;<sup>28</sup>). Importantly, siRNAs that compromise COPII resulted in mouse ES cell compaction (Fig. 3d), indicating that CUL3–KLHL12 and the COPII coat act in the same pathway.

*In vitro*, CUL3–KLHL12 catalysed the monoubiquitylation of SEC31 (Fig. 3e), which was not observed if a KLHL12 mutant with a defective SEC31-binding interface was used (Fig. 3f). SEC31 was also monoubiquitylated in cells, which was strongly increased upon expression of KLHL12 (Fig. 3g). KLHL12 mutants unable to bind SEC31 abolished its monoubiquitylation (Fig. 3h), which is likely to be due to dimerization with and inactivation of endogenous KLHL12 (Fig. 3a and Supplementary Fig. 6c). SEC31 monoubiquitylation was also strongly diminished upon expression of dominant-negative CUL3 (Fig. 3g) or depletion of CUL3–KLHL12 by siRNA (Fig. 3i). As seen upon expression of lysine-free ubiquitin, SEC31 was monoubiquitylated at one preferred and an alternative, less prominently used lysine (Fig. 3g), consistent with proteomic analyses that identified Lys 647 and Lys 1217 in SEC31A as ubiquitylation sites<sup>29,30</sup>. However, neither mutation of these residues nor any other of the 65

lysine residues of SEC31 blocked ubiquitylation by CUL3–KLHL12 (data not shown), revealing flexibility in the actual modification site.

Co-expression of KLHL12 and CUL3 triggered SEC31 multiubiquitylation and degradation (Figs 3g, 4e and Supplementary Fig. 6d), which was not observed with lysine-free ubiquitin (Fig. 3g). However, whereas SEC31 was monoubiquitylated by endogenous CUL3–KLHL12, its multiubiquitylation was only seen when CUL3 and KLHL12 were overexpressed. Depletion of CUL3–KLHL12 or proteasome inhibition did not change SEC31 levels in untransfected cells (Fig. 3i and Supplementary Fig. 6e), and blockade of ubiquitin chain formation or proteasome inhibition did not impair CUL3–KLHL12 function (see Fig. 5). Thus, multiubiquitylation of SEC31 is unlikely a key outcome of CUL3–KLHL12 activity in mouse ES cells. Instead, it seems that CUL3–KLHL12 acts by catalysing monoubiquitylation, with the COPII protein SEC31 as a major substrate.

### CUL3 regulates the size of COPII coats

To identify a role for monoubiquitylation by CUL3–KLHL12, we induced KLHL12 expression in cells and followed the fate of SEC31 by microscopy. Shortly after KLHL12 induction, the majority of KLHL12 and SEC31 colocalized in small punctae (Fig. 4a). Over time, these punctae grew into much larger structures that contained most of SEC31, as well as other COPII components, such as SEC13 or SEC24C (Fig. 4a, b). As seen by high-resolution confocal imaging, the large structures were hollow and spherical with a diameter of 200–500 nm, and they were decorated with the proteins of the COPII coat and with KLHL12 (Fig. 4c). Accordingly, thin-section electron microscopy revealed large, crescent-shaped tubules, possibly of endoplasmic reticulum origin, in cells transfected with KLHL12 (Fig. 4d). Immunogold-labelling electron microscopy showed comparable structures of

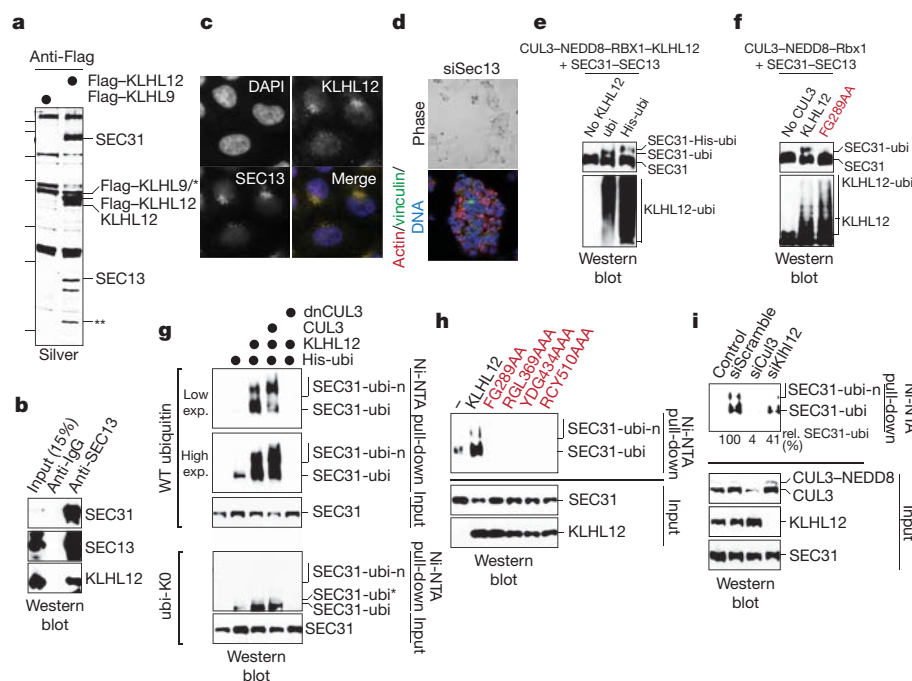


**Figure 3 | CUL3–KLHL12 monoubiquitylates SEC31.**

**a**, Immunoprecipitates of Flag–KLHL12 or Flag–KLHL9 were analysed by silver staining and mass spectrometry. Asterisk, non-specific band; double asterisk, breakdown product of KLHL12. **b**, SEC13 was immunoprecipitated from HeLa cell lysates, and SEC31 and KLHL12 were detected by immunoblot. **c**, KLHL12 colocalizes with COPII, as seen by confocal microscopy (KLHL12, green; SEC13, red; DNA, blue). Original magnification  $\times 60$ . **d**, D3 mouse ES cells grown on gelatin and depleted of SEC13 were analysed for compaction by phase (top) or confocal microscopy (actin, red; vinculin, green; DNA, blue). Original magnification  $\times 40$ . **e**, CUL3–KLHL12 monoubiquitylates SEC31. CUL3–NEDD8–RBX1 was incubated with KLHL12, SEC31/31 and ubiquitin (ubi) or His-ubiquitin (His-ubi). **f**, *In vitro* ubiquitylation of SEC31 by CUL3–KLHL12

or CUL3–KLHL12(FG289AA) (FG289AA) was performed as above. **g**, SEC31 is monoubiquitylated *in vivo*. Upper panels, ubiquitin conjugates were purified under denaturing conditions from MG132-treated 293T cells expressing His-ubiquitin, haemagglutinin–SEC31, KLHL12, CUL3 or dominant-negative CUL3 (dnCUL3), and analysed by anti-SEC31 Western blot. Lower panels, the same experiment was performed with lysine-free His-ubiquitin, which only allowed SEC31-monoubiquitylation on at least two sites (SEC31-ubi and SEC31-ubi\*). SEC31-ubi-n denotes multiubiquitylated SEC31. **h**, Ubiquitin conjugates were purified from 293T cells expressing KLHL12 or SEC31-ubiquitylation *in vivo*. 293T cells were transfected with His-ubiquitin and siRNAs, and ubiquitin conjugates were analysed for SEC31 by Western blot.



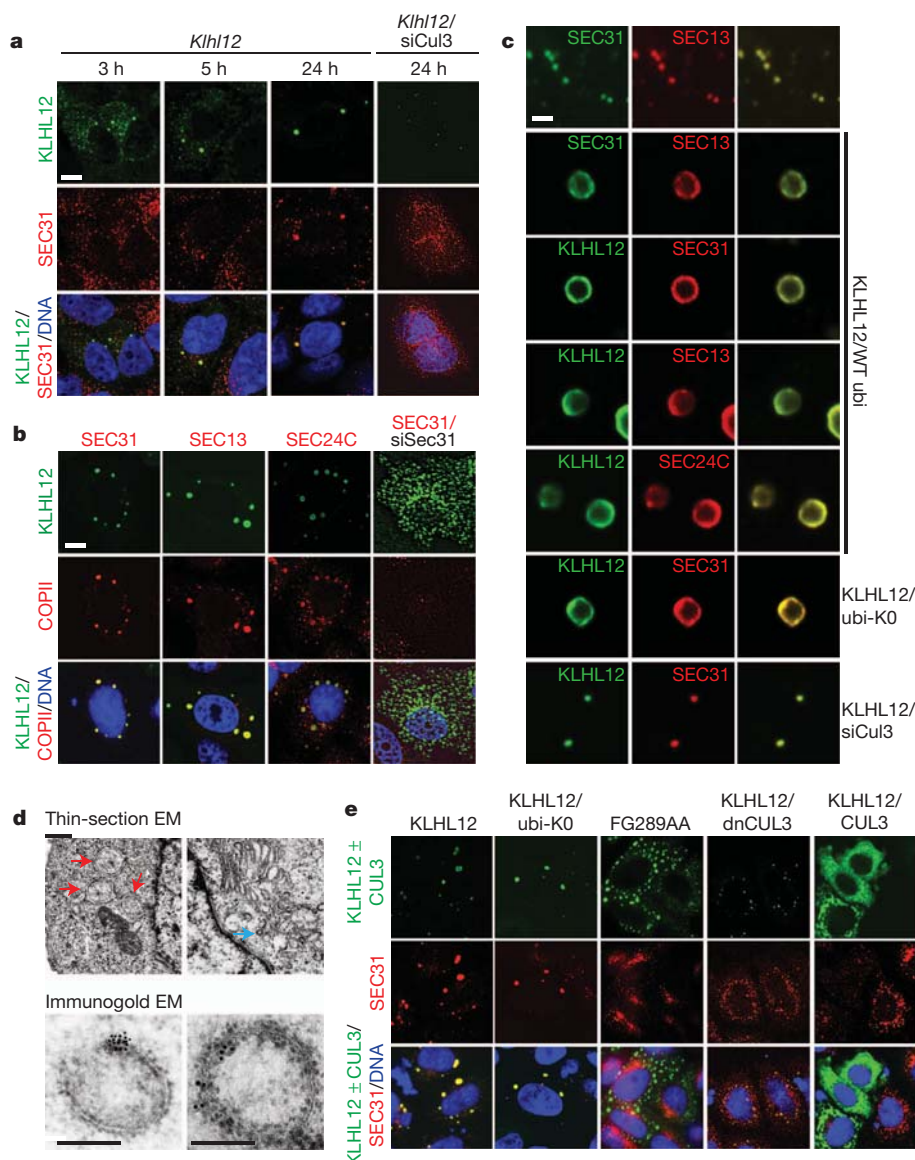


**Figure 4 | CUL3–KLHL12-dependent monoubiquitylation enlarges COPII-structures.** **a**, Localization of doxycycline (dox)-induced Flag–KLHL12 (dox::KLHL12, green) and SEC31 (red) in 293T cells, monitored by confocal microscopy. Scale bar, 3  $\mu$ m. **b**, KLHL12-expressing HeLa cells were analysed for KLHL12 (green) and SEC31, SEC13 or SEC24C (red) by confocal microscopy. Scale bar, 3  $\mu$ m. **c**, COPII-structures in HeLa cells transfected with Flag–KLHL12, lysine-free ubiquitin (ubi-K0) or Cul3-siRNA, analysed by confocal microscopy. Scale bar, 500 nm. **d**, Upper panel, thin-section electron microscopy (EM) of KLHL12-expressing or control HeLa cells (red arrow, KLHL12-dependent structures; blue arrow, small control vesicles). Scale bar, 500 nm. Lower panel, immunogold-EM of KLHL12 in transiently transfected HeLa (left) or stable 293T cells (right). Scale bar, 200 nm. **e**, HeLa cells transfected with Flag–KLHL12, lysine-free ubiquitin, Flag–KLHL12(FG289AA), Flag–CUL3(1–250) or Flag–CUL3 were analysed for localization of KLHL12/CUL3 (green) and SEC31 (red) by confocal microscopy. Original magnification  $\times 40$ .

200–500 nm that were decorated with KLHL12 (Fig. 4d). The KLHL12-dependent structures neither contained a *cis*-Golgi protein; ERGIC-53, which is absent from procollagen transport vesicles<sup>31</sup>; endoplasmic reticulum membrane markers that do not accumulate at endoplasmic reticulum exit sites<sup>32</sup>; nor endosomal or autophagosomal markers (Supplementary Fig. 7a–c). Importantly, SEC31-binding deficient mutants, including KLHL12(FG289AA), neither colocalized with SEC31 nor induced formation of large structures (Fig. 4e and Supplementary Fig. 7d), and depletion of SEC31 blocked formation of large structures by KLHL12 (Fig. 4b). Thus, binding of KLHL12 to SEC31 triggers formation of large COPII-containing structures.

When KLHL12 was expressed with a CUL3 mutant that blocks SEC31 ubiquitylation (CUL3(1–250)), COPII structures were not enlarged (Fig. 4e). In addition, depletion of CUL3 by siRNAs, which also abolishes SEC31 monoubiquitylation, prevented formation of large COPII structures by KLHL12 (Fig. 4a, c). By contrast, if KLHL12 was expressed with lysine-free ubiquitin to allow mono-, but not multiubiquitylation, large COPII structures were readily detected (Fig. 4c, e), and these structures were enriched for ubiquitin, consistent with monoubiquitylation being non-proteolytic (Supplementary Fig. 7e). Thus, monoubiquitylation by CUL3–KLHL12 promotes formation of large COPII structures, which probably represent a mixture of nascent coats at endoplasmic reticulum exit sites and budded coats on large COPII vesicles or tubules.

### CUL3 is required for collagen export

Our screen linked CUL3–KLHL12 to the establishment of the stem cell extracellular matrix, which requires collagen secretion. Thus, the CUL3–KLHL12-dependent increase in COPII size might function to promote collagen export from the endoplasmic reticulum. To test this hypothesis, we expressed KLHL12 in IMR90 cells, which at steady state accumulate collagen in the endoplasmic reticulum due to inefficient export. Strikingly, KLHL12, but not KLHL12(FG289AA) or unrelated BTB proteins, triggered depletion of procollagen I from intracellular endoplasmic reticulum pools (Fig. 5a). As a result, increased collagen levels were detected in the supernatant of cells expressing KLHL12, but not KLHL12(FG289AA) (Fig. 5b). When secretion was inhibited with brefeldin A, or if collagen folding in the endoplasmic reticulum was impaired by removal of ascorbate from the medium, procollagen remained within KLHL12-expressing cells (Fig. 5a). Time-resolved experiments showed that KLHL12 strongly accelerated collagen export from IMR90 cells (Fig. 5c). Shortly after inducing secretion, KLHL12 and collagen were detected at overlapping locations (Supplementary Fig. 7f), all of which indicates that CUL3–KLHL12 facilitates collagen traffic from the endoplasmic reticulum.

Blockade of SEC31 ubiquitylation by dominant-negative CUL3 interfered with the KLHL12-dependent export of collagen from IMR90 cells (Supplementary Fig. 8a). Similarly, depletion of CUL3–KLHL12 from engineered HT1080 fibrosarcoma cells severely



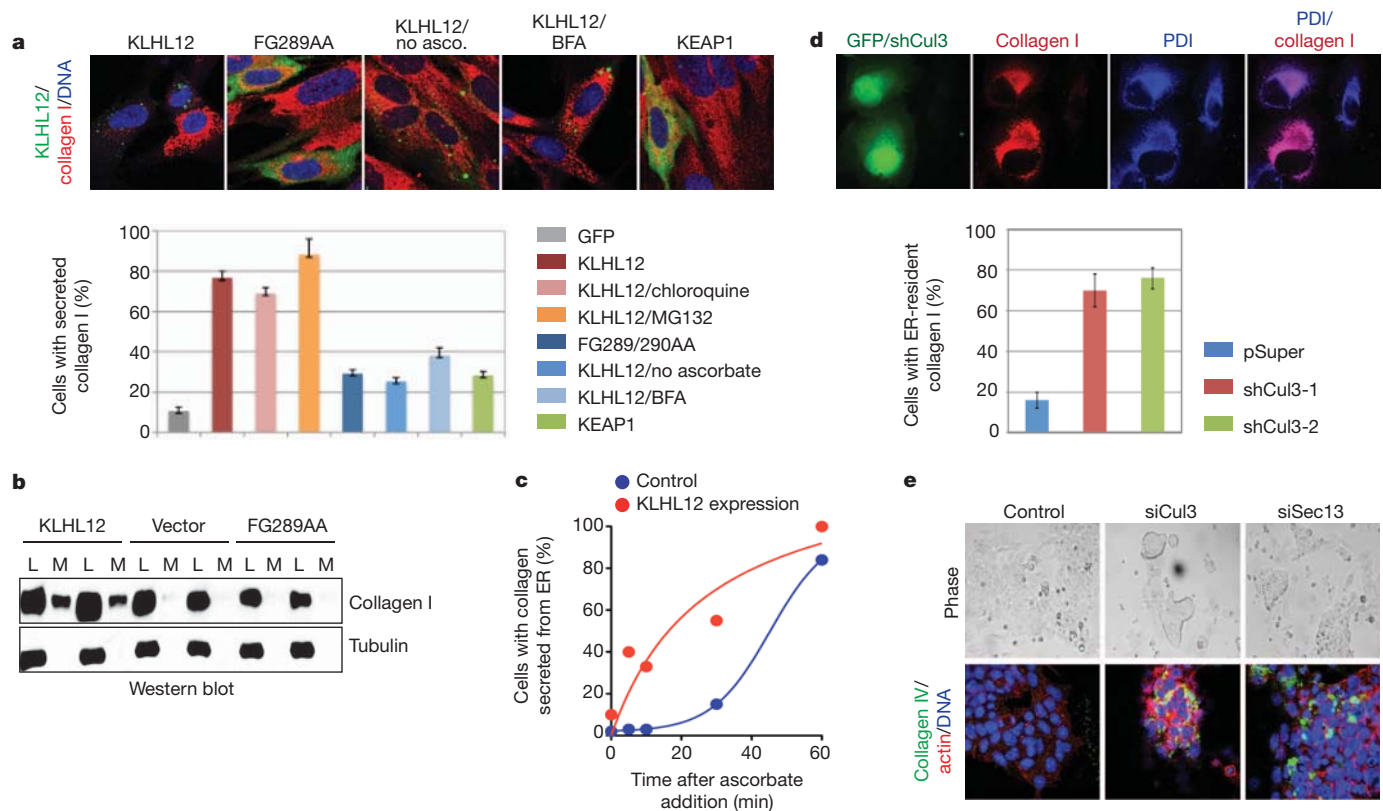


**Figure 5 | CUL3-KLHL12 promotes collagen export.** **a**, IMR90 cells transfected with Flag-KLHL12, Flag-KLHL12(FG289AA) or Flag-KEAP1 were analysed by confocal microscopy (BTB, green; collagen-I, red; DNA, blue). When noted, cells were treated with chloroquine, MG132, brefeldin A (BFA) or dialysed medium lacking ascorbate. Errors bars, standard deviation  $n = 3$ . Original magnification  $\times 60$ . **b**, Cell lysate (L) or culture medium (M) of IMR90 cells transfected with Flag-KLHL12 or Flag-KLHL12(FG289AA) was analysed by immunoblotting. **c**, Collagen I localization was analysed in IMR90

cells expressing KLHL12, after re-addition of ascorbate. Original magnification  $\times 40$ . **d**, HT1080 cells stably expressing collagen I were transfected with shRNAs against *Cul3* and analysed by confocal microscopy (transfection control green fluorescent protein (GFP), green; protein disulphide isomerase (PDI), blue; collagen I, red). Error bars, standard deviation  $n = 3$ . Original magnification  $\times 60$ . **e**, D3 mouse ES cells were treated with control siRNAs or siRNAs targeting *Cul3* or *Sec13* and analysed by confocal microscopy (collagen IV, green; actin, red; DNA, blue). Original magnification  $\times 40$ .

impaired collagen export, and most cells retained high levels of collagen in their endoplasmic reticulum (Fig. 5d and Supplementary Fig. 8b). In contrast, smaller COPII cargoes, such as fibronectin or EGF receptor, were properly localized in the absence of CUL3 (Supplementary Fig. 8c, d). Similar observations were made in mouse ES cells, where depletion of CUL3 led to a strong intracellular accumulation of collagen IV, comparable to the effects observed upon loss of SEC13 (Fig. 5e and Supplementary Fig. 8e). Thus, CUL3-KLHL12 is required for collagen export, whereas it is less important for the trafficking of smaller COPII cargo.

If promoting collagen export were the key role of CUL3 in mouse ES cells, the phenotypes of CUL3 depletion might be mitigated by addition of collagen *in trans*. Indeed, this was the case: when mouse ES cells were plated on purified collagen IV, depletion of CUL3 did not cause cell clustering, and integrin  $\beta 1$  was detected at the plasma membrane (Fig. 1b). We conclude that promoting collagen secretion is a key a function of CUL3, in agreement with its role in driving the assembly of large COPII coats.

## Discussion

In this study, we have identified CUL3-KLHL12 as an essential regulator of collagen export, which is required for mouse ES cell division. Deletion of *Cul3* in mice results in early embryonic lethality with completely disorganized extraembryonic tissues<sup>33</sup>, a phenotype that can in part be attributed to its role in collagen secretion. Moreover, KLHL12 has been identified as an autoantigen in the connective tissue disorder Sjogren's syndrome<sup>34</sup>, raising the possibility that aberrant function of CUL3-KLHL12 might be related to disease.

CUL3-KLHL12 monoubiquitylates SEC31 and promotes formation of large COPII coats that can accommodate unusually shaped cargo. As a result, CUL3 is essential for the secretion of procollagen fibres, whereas it is not required for the transport of smaller or more flexible molecules, such as fibronectin, EGF receptor or integrin  $\beta 1$ . Thus, CUL3-KLHL12 seems to be specifically required for the COPII-dependent transport of large cargo.

How ubiquitylation affects COPII coat size or structure is not known. None of the 65 lysine residues of SEC31 was essential for ubiquitylation by CUL3-KLHL12, showing that CUL3 can target alternative lysine residues if the primary site is blocked. Despite this flexibility, CUL3-KLHL12 does not stoichiometrically ubiquitylate SEC31. Thus, if SEC31 ubiquitylation performs a structural role, then few ubiquitylated molecules must suffice to produce large COPII coats, and these vesicles must tolerate considerable variation in the modification site. Alternatively, as often seen with monoubiquitylated proteins, modified SEC31 might recruit an effector that delays COPII budding or promotes coat polymerization. As CUL3-KLHL12 ubiquitylates other proteins<sup>35</sup>, SEC31 may not be its only substrate in the secretory pathway. Identification of the complete set of CUL3-KLHL12 substrates and potential effector molecules should reveal the mechanism underlying the ubiquitin-dependent regulation of vesicle size.

Our findings have the potential to be translated into therapeutic strategies. We envision that agonists of CUL3-KLHL12 function mitigate consequences of *Sec23A* mutations in cranio-lenticulo-sutural dysplasia or *Sar1* mutations in chylomicron retention disease<sup>10,11</sup>. By contrast, interfering with CUL3 activity may counteract increased collagen

deposition during fibrosis or keloid formation<sup>36</sup>. Given the strong clustering phenotypes observed in CUL3-depleted mouse ES cells, inhibition of CUL3–KLHL12 might impair the proliferation of metastatic cells, which display features of undifferentiated cells<sup>37,38</sup>. Thus, our identification of CUL3–KLHL12 as a regulator of COPII size and function provides an exciting starting point to understand and therapeutically exploit key events in protein trafficking.

## METHODS SUMMARY

For stem cell culture, mouse D3 ES cells were maintained in GIBCO Dulbecco's Modified Eagle ES cell medium containing 15% FBS, 1× sodium pyruvate, 1× non-essential amino acids, 1 mM β-mercaptoethanol and 1,000 U ml<sup>-1</sup> leukaemia inhibitory factor (Millipore), and grown on gelatin-coated culture plates. Doxycycline-inducible 293T Trex Flag–BTB stable cell lines were made with the Flp-In T-REx 293 Cell Line system (Invitrogen) and maintained with blasticidin and hygromycin B.

For screening, two siRNA oligonucleotides were designed against 40 mouse ubiquitin ligases (Qiagen). siRNA oligonucleotides (10 pmol) and Lipofectamine 2000 were pre-incubated in a gelatin-coated 96-well plate. D3 mouse ES cells were seeded at 15,000 cells per well on top of the siRNA mixture, and the morphology of ES cell colonies was examined by bright-field microscopy 48 h after transfection.

To identify CUL3–KLHL12 substrates, doxycycline-inducible 293T cell lines expressing Flag–KLHL12 or Flag–KLHL9 were induced for 48 h. Cleared lysate was subjected to anti-Flag M2 affinity gel (Sigma), and precipitations were eluted with 3×Flag peptide (Sigma). Concentrated eluates were analysed by SDS–PAGE, and specific bands were identified by mass spectrometry analysis by the Vincent J. Coates Proteomics/Mass Spectrometry Laboratory.

For *in vitro* ubiquitylation reactions, CUL3/RBX1 purified from Sf9 cells was conjugated to NEDD8 using recombinant APPBP1–UBA3, UBC12 (also known as UBE2M) and NEDD8. KLHL12 purified from *Escherichia coli* and SEC31A–SEC13 complexes from Sf9 cells were added together with energy mix, E1, UBCH5C (also known as UBE2D3) and ubiquitin and incubated at 30 °C for 1 h.

For confocal microscopy, cells fixed in paraformaldehyde and permeabilized with Triton X-100 were incubated with primary antibodies for 2 h and Alexa-labelled secondary antibodies (Invitrogen) for 1 h. Pictures were taken on Zeiss LSM 510 and 710 confocal microscopes and analysed with LSM image browser and Imaris 3D imaging processing software. Images were processed for contrast enhancement to remove noise.

**Full Methods** and any associated references are available in the online version of the paper at [www.nature.com/nature](http://www.nature.com/nature).

Received 3 August 2011; accepted 3 January 2012.

- Leitinger, B. Transmembrane collagen receptors. *Annu. Rev. Cell Dev. Biol.* **27**, 265–290 (2011).
- Wickström, S. A., Radovanac, K. & Fassler, R. Genetic analyses of integrin signaling. *Cold Spring Harb. Perspect. Biol.* doi:10.1101/cshperspect.a005116 (30 December 2010).
- Caswell, P. T., Vadrevu, S. & Norman, J. C. Integrins: masters and slaves of endocytic transport. *Nature Rev. Mol. Cell Biol.* **10**, 843–853 (2009).
- Stephens, L. E. *et al.* Deletion of beta 1 integrins in mice results in inner cell mass failure and peri-implantation lethality. *Genes Dev.* **9**, 1883–1895 (1995).
- Chen, S. S., Fitzgerald, W., Zimmerberg, J., Kleinman, H. K. & Margolis, L. Cell-cell and cell-extracellular matrix interactions regulate embryonic stem cell differentiation. *Stem Cells* **25**, 553–561 (2007).
- Lang, M. R., Lapierre, L. A., Frotscher, M., Goldenring, J. R. & Knapik, E. W. Secretory COPII coat component Sec23a is essential for craniofacial chondrocyte maturation. *Nature Genet.* **38**, 1198–1203 (2006).
- Townley, A. K. *et al.* Efficient coupling of Sec23–Sec24 to Sec13–Sec31 drives COPII-dependent collagen secretion and is essential for normal craniofacial development. *J. Cell Sci.* **121**, 3025–3034 (2008).
- Sarmah, S. *et al.* Sec24D-dependent transport of extracellular matrix proteins is required for zebrafish skeletal morphogenesis. *PLoS ONE* **5**, e10367 (2010).
- Ohisa, S., Inohaya, K., Takano, Y. & Kudo, A. sec24d encoding a component of COPII is essential for vertebral formation, revealed by the analysis of the medaka mutant, *vbi*. *Dev. Biol.* **342**, 85–95 (2010).
- Boyadiev, S. A. *et al.* Cranio-lenticulo-sutural dysplasia is caused by a SEC23A mutation leading to abnormal endoplasmic-reticulum-to-Golgi trafficking. *Nature Genet.* **38**, 1192–1197 (2006).
- Fromme, J. C. *et al.* The genetic basis of a craniofacial disease provides insight into COPII coat assembly. *Dev. Cell* **13**, 623–634 (2007).
- Jensen, D. & Schekman, R. COPII-mediated vesicle formation at a glance. *J. Cell Sci.* **124**, 1–4 (2011).

- Stagg, S. M. *et al.* Structural basis for cargo regulation of COPII coat assembly. *Cell* **134**, 474–484 (2008).
- Fath, S., Mancias, J. D., Bi, X. & Goldberg, J. Structure and organization of coat proteins in the COPII cage. *Cell* **129**, 1325–1336 (2007).
- Fromme, J. C. & Schekman, R. COPII-coated vesicles: flexible enough for large cargo? *Curr. Opin. Cell Biol.* **17**, 345–352 (2005).
- Saito, K. *et al.* TANGO1 facilitates cargo loading at endoplasmic reticulum exit sites. *Cell* **136**, 891–902 (2009).
- Saito, K. *et al.* cTAGE5 mediates collagen secretion through interaction with TANGO1 at endoplasmic reticulum exit sites. *Mol. Biol. Cell* **22**, 2301–2308 (2011).
- Wilson, D. G. *et al.* Global defects in collagen secretion in a *Mia3/TANGO1* knockout mouse. *J. Cell Biol.* **193**, 935–951 (2011).
- Kathiresan, S. *et al.* Genome-wide association of early-onset myocardial infarction with single nucleotide polymorphisms and copy number variants. *Nature Genet.* **41**, 334–341 (2009); corrigendum **41**, 762 (2009).
- Sumara, I. *et al.* A Cul3-based E3 ligase removes Aurora B from mitotic chromosomes, regulating mitotic progression and completion of cytokinesis in human cells. *Dev. Cell* **12**, 887–900 (2007).
- Shaw, L. M., Rabinovitz, I., Wang, H. H., Tokar, A. & Mercurio, A. M. Activation of phosphoinositide 3-OH kinase by the αβ4 integrin promotes carcinoma invasion. *Cell* **91**, 949–960 (1997).
- Chen, Y. *et al.* Cullin mediates degradation of RhoA through evolutionarily conserved BTB adaptors to control actin cytoskeleton structure and cell movement. *Mol. Cell* **35**, 841–855 (2009).
- Furukawa, M. & Xiong, Y. BTB protein Keap1 targets antioxidant transcription factor Nrf2 for ubiquitination by the Cullin 3-Roc1 ligase. *Mol. Cell Biol.* **25**, 162–171 (2005).
- Geyer, R., Wee, S., Anderson, S., Yates, J. & Wolf, D. A. BTB/POZ domain proteins are putative substrate adaptors for cullin 3 ubiquitin ligases. *Mol. Cell* **12**, 783–790 (2003).
- Pintard, L. *et al.* The BTB protein MEL-26 is a substrate-specific adaptor of the CUL-3 ubiquitin-ligase. *Nature* **425**, 311–316 (2003).
- Xu, L. *et al.* BTB proteins are substrate-specific adaptors in an SCF-like modular ubiquitin ligase containing CUL-3. *Nature* **425**, 316–321 (2003).
- Young, R. A. Control of the embryonic stem cell state. *Cell* **144**, 940–954 (2011).
- Hughes, H. *et al.* Organisation of human ER-exit sites: requirements for the localisation of Sec16 to transitional ER. *J. Cell Sci.* **122**, 2924–2934 (2009).
- Kim, W. *et al.* Systematic and quantitative assessment of the ubiquitin-modified proteome. *Mol. Cell* **44**, 325–340 (2011).
- Emanuele, M. J. *et al.* Global identification of modular cullin-RING ligase substrates. *Cell* **147**, 459–474 (2011).
- Stephens, D. J. & Pepperkok, R. Imaging of procollagen transport reveals COPII-dependent cargo sorting during ER-to-Golgi transport in mammalian cells. *J. Cell Sci.* **115**, 1149–1160 (2002).
- Zhu, W. *et al.* Bcl-2 mutants with restricted subcellular location reveal spatially distinct pathways for apoptosis in different cell types. *EMBO J.* **15**, 4130–4141 (1996).
- Singer, J. D., Gurian-West, M., Clurman, B. & Roberts, J. M. Cullin-3 targets cyclin E for ubiquitination and controls S phase in mammalian cells. *Genes Dev.* **13**, 2375–2387 (1999).
- Uchida, K. *et al.* Identification of specific autoantigens in Sjogren's syndrome by SEREX. *Immunology* **116**, 53–63 (2005).
- Angers, S. *et al.* The KLHL12–Cullin-3 ubiquitin ligase negatively regulates the Wnt–β-catenin pathway by targeting Dishevelled for degradation. *Nature Cell Biol.* **8**, 348–357 (2006).
- Schäfer, M. & Werner, S. Cancer as an overheating wound: an old hypothesis revisited. *Nature Rev. Mol. Cell Biol.* **9**, 628–638 (2008).
- Nguyen, D. X., Bos, P. D. & Massague, J. Metastasis: from dissemination to organ-specific colonization. *Nature Rev. Cancer* **9**, 274–284 (2009).
- Zhang, X. H. *et al.* Latent bone metastasis in breast cancer tied to Src-dependent survival signals. *Cancer Cell* **16**, 67–78 (2009).

**Acknowledgements** We thank B. Schulman for advice and gifts of cDNAs and proteins. We are grateful to J. Schaeletsky for critically reading the manuscript and many discussions. We thank the members of the Rape and Schekman labs for advice and suggestions, L. Lim for providing *Cul3*-shRNAs, C. Glazier for contributions on BTB protein cloning, and A. Fischer and M. Richner for tissue culture support. This work was funded by grants from the Pew Foundation (M.R.), the NIH (NIGMS-RO1, M.R.; NIH Director's New Innovator Award, M.R.), and the Howard Hughes Medical Institute (R.S.). L.J. was funded by a CIRM predoctoral fellowship; she is a Tang fellow. K.B.P. is an HFSP long term post-doctoral fellow.

**Author Contributions** Experiments were designed by L.J., K.B.P., R.S. and M.R.; L.J. performed the mouse ES cell screen, identified KLHL12 and SEC31, and analysed the role of CUL3 in COPII formation in cells and in collagen export in mouse ES cells; K.B.P. analysed collagen export in fibroblasts; K.E.W. analysed COPII formation in cells; C.B. identified inactive KLHL12; A.G. performed electron microscopy; L.J., K.B.P. and M.R. prepared the manuscript.

**Author Information** Reprints and permissions information is available at [www.nature.com/reprints](http://www.nature.com/reprints). The authors declare no competing financial interests. Readers are welcome to comment on the online version of this article at [www.nature.com/nature](http://www.nature.com/nature). Correspondence and requests for material should be addressed to M.R. ([mraper@berkeley.edu](mailto:mraper@berkeley.edu)).



## METHODS

**Plasmids, protein, antibodies.** Human *Cul3* and *Klhl12* were cloned into pcDNA4 and pcDNA5 vectors for expression in mammalian cells. *Cul3*, *Sec31A* and *Sec13* were also cloned into pCS2 vector for IVT/T and expression in mammalian cells. pcDNA4-Cul3<sup>N250</sup> contains the first cullin repeat of the N-terminal CUL3 (amino acids 1–250) which is sufficient for binding BTB proteins, but not RBX1 and serves as a dominant negative for CUL3/BTB-mediated ubiquitylation. The KLHL12 mutants FG289AA, RL342AA, RGL369AAA, RE416AA, YDG434AAA and RCY510AAA were made by site-directed mutagenesis.

CUL3 and RBX1 were cloned into pFastBac, co-expressed in Sf9 ES insect cells using the Bac-to-Bac baculovirus expression system (Invitrogen) and purified as a complex by Ni-NTA agarose (Qiagen). Similarly, the SEC31A–SEC13 heterodimer and UBA1 were purified from Sf9 ES insect cells. *UbcH5c* and *Ubc12* were cloned into pQE vector and purified from BL21(DE3) bacterial cells. Ubiquitin was cloned into pET and pCS2 vector with a N-terminal 6×His tag. The pET-His-ubiquitin was used for bacterial purification whereas pCS2-His-ubiquitin was expressed in mammalian cells. Wild-type ubiquitin, APPBP1–UBA3 and NEDD8 were purchased from Boston Biochem.

To purify recombinant KLHL12 for ubiquitylation assays, we expressed pMAL-TEV-KLHL12-his and pMAL-TEV-KLHL12<sup>FG289AA</sup>-his in BL21(DE3) cells, purified the proteins on amylose resin, cleaved them by TEV protease, and re-purified them on Ni-NTA agarose. Wild-type *Klhl12* and mutants were also cloned into pMAL vector and purified as maltose-binding protein (MBP)-tagged proteins for in-vitro protein binding assays.

All shRNAs were cloned in pSuper-GFP neo vector (from Oligoengine) into BglII and XhoI sites. The GFP–BCL2–CYB5 construct, a fusion between Bcl2 and cytochrome b5, was purchased from Clontech.

We raised mouse monoclonal antibodies against human KLHL12 and human KLHL13. Both antibodies are available at Promab Biotechnologies (catalogue nos 30058 and 30067). We also raised antibodies against SEC13, SEC24C and SEC24D. Other antibodies used in this study are: CUL3 (Bethyl Laboratories, catalogue no. A301-109A), SEC31A (BD Biosciences, catalogue no. 612350), collagen IV (Abcam, catalogue no. ab19808), anti-Flag (Sigma, catalogue nos F3165, F7425), Ubiquitin (Santa Cruz, catalogue no. sc-8017, P4D1), rhodamine phalloidin (Invitrogen, catalogue no. R415), PDI (ID3) (Assay Designs, catalogue no. SPA-891), anti LC-3 (Sigma, catalogue no. L-7543), anti-alpha tubulin (DM1A, Abcam, catalogue no. ab7291), anti-fibronectin (Abcam, ab2413), anti-GM130 (BD Biosciences, catalogue no. 610822), and anti-EGFR (Ab12, Neomarkers, MS-400P1). LF-67 (anti-sera for Type I procollagen) was obtained as a gift from L. Fisher.

**Cell culture.** The D3 mouse embryonic stem cells (mouse ES cell) were maintained in ES cell medium containing 15% FBS, 1× sodium pyruvate, 1× non-essential amino acids, 1 mM β-mercaptoethanol and 1,000 U ml<sup>−1</sup> leukaemia inhibitory factor (Millipore, catalogue no. ESG1107) in GIBCO Dulbecco's Modified Eagle Medium, and grown on 0.1% gelatin-coated tissue culture plates. HeLa cells, 293T cells, 3T3 cells and IMR90 cells were maintained in DMEM plus 10% FBS. Dialysed FBS was bought from HyClone. The doxycycline-inducible 293T Trex KLHL12-3×Flag stable cell line was made with Flp-In T-REx 293 Cell Line system from Invitrogen. Stable cell lines expressing other BTB-proteins were generated accordingly. These cell lines were maintained with 10% TET(−) FBS, blasticidin and hygromycin B as instructed and expression was induced by 1 μg ml<sup>−1</sup> doxycycline.

Human lung fibroblasts IMR-90 cells were obtained from the Coriell Institute: NIA (National Institute on Ageing) Ageing Cell Repository. For generating pro-collagen stable HT-1080 cell lines, we cloned proα1(1) into a pRMC/CMV-vector and selected for neomycin resistance<sup>39</sup>. This vector was provided as a gift by N. Balleid. Cells were kept in a 37 °C incubator with 5% CO<sub>2</sub>.

**siRNA screen in mouse ES cells.** siRNA oligonucleotides against 40 mouse ubiquitin E3 enzymes were pre-designed by Qiagen and handled as instructed. Two different siRNA oligonucleotides against each gene were included in the initial screen. 10 pmol of siRNA oligonucleotides and 0.25 μl of Lipofectamine2000 were pre-incubated in a 0.1% gelatin-coated 96-well plate in 20 μl of OPTIMEM for 15 min at room temperature. The D3 mouse ES cells were trypsinized and seeded at 15,000 cells per well in 80 μl of ES cell medium on top of the siRNA mixture. Fresh medium was added to the cells the next day and the morphology of ES cell colonies were examined using bright-field microscopy at 48 h post transfection. Hit validation was performed with additional siRNAs that were purchased from two distinct vendors (Qiagen, Dharmacon) and that target different sites of the *Cul3* mRNA. Knockdown efficiency was tested by qRT-PCR and immunoblot.

**Rescue of *Cul3*-siRNA phenotype in mouse ES cells by Matrigel and collagen IV.** D3 mouse ES cells were grown on tissue culture dishes coated with gelatin (negative control), growth-factor-depleted Matrigel (BD Biosciences, catalogue no. 356231), or purified collagen IV (BD Biosciences, catalogue no. 354233). Matrigel and collagen IV were applied at 10 μg cm<sup>−2</sup>. CUL3 was depleted 24 h

later using our standard siRNA transfection protocol, and mouse ES cell morphology was analysed by confocal microscopy against integrin β1, actin and DNA.

**Drug treatments of CUL3-depleted cells.** To study the synthetic lethal effect of SRC-inhibition with CUL3 knockdown, we treated wild-type and CUL3-depleted D3 mouse ES cells with 0, 25, 50 or 100 nM of dasatinib for 18 h before the phenotypes were analysed by light microscopy.

To study the effect of RHO-inhibition on CUL3 knockdown, CUL3-depleted D3 mouse ES cells were treated with ROCK inhibitor Y27632 at 10 μM for 24 h before phenotype analysis. Alternatively, RHOA was co-depleted using specific siRNAs.

**Cell cycle analysis.** To assess the division rate of CUL3-depleted mouse ES cells, we treated cells with control, *Cul3*-, or *Ube2C/Ube2S*-siRNA and seeded at 3 × 10<sup>5</sup> cells per well in gelatin-coated six-well plates. The specificity of *Ube2S*- and *Ube2C*-siRNAs was tested before<sup>40</sup>. The cells were trypsinized at 2, 3 and 4 days post transfection and counted by haemocytometer.

**ES cell differentiation analysis.** To differentiate mouse ES cells into embryoid bodies (EB), we trypsinized undifferentiated D3 mouse ES cells, washed once with leukaemia inhibitory factor-free ES cell media, and seeded the cells at 2 × 10<sup>6</sup> cells per dish onto 10-cm Corning Ultra-Low-Attachment Dishes (Corning catalogue no. 3262) containing 10 ml of ES cell medium without leukaemia inhibitory factor. After 24 h, the cells were dissociated from the plate by gentle pipetting of the medium and collected in a 15-ml Falcon tube by centrifugation. The supernatant was aspirated off and the cells were re-seeded onto 10-cm Corning Ultra-Low-Attachment Dishes containing fresh ES cell medium without leukaemia inhibitory factor. Medium was changed every other day for a total of 6 or 9 days. Total RNA of ES cells and EB samples was extracted using TRIzol (Invitrogen, catalogue no. 15596-026) and chloroform. The expression of pluripotent markers and BTB genes at various time points during differentiation was analysed using quantitative real-time PCR.

As a complementary experiment, D3 mouse ES cells were treated with control or *Oct4* siRNA. 48 h after transfection, cells were collected and total RNA was extracted using TRIzol as above. The expression of pluripotent markers, tissue specific genes and BTB genes in control and OCT4-depleted cells were analysed using qRT-PCR.

**Quantitative real-time PCR analysis.** We used TRIzol (Invitrogen, catalogue no. 15596-026) and chloroform to extract total RNA from cells. The first-strand cDNAs were synthesized by using RevertAid first strand cDNA synthesis kit (Fermentas, catalogue no. K1621). Gene-specific primers for qRT-PCR were designed by using NCBI Primer-Blast. The quantitative RT-PCR reaction was done with the Maxima SYBR Green/Rox qPCR system (Fermentas, catalogue no. K0221).

**Identification of CUL3–KLHL12 substrates.** To identify CUL3–KLHL12 substrates, we generated a doxycycline-inducible human KLHL12-3×Flag stable cell line using the Flp-In T-REx 293 Cell Line system (Invitrogen). As controls, we generated stable cell lines expressing other BTB proteins including KLHL9, KLHL12-3×Flag and KLHL9-3×Flag expression was induced in 30 × 15 cm plates by 1 μg ml<sup>−1</sup> of doxycycline for 48 h, and cells were collected by centrifugation and lysed by douncing 40 times in PBS+0.1%NP40. The cell lysate was cleared by centrifugation and then subjected to anti-Flag M2 affinity gel (Sigma, catalogue no. A2220-5mL) at 4 °C for 4 h on a rotator. Immunoprecipitations were eluted by 300 μl of 200 μg ml<sup>−1</sup> 3×Flag peptide (Sigma, catalogue no. F4799-4MG) in PBS. The elution was repeated three times for 1 h at room temperature. Eluates were pooled, concentrated to 100 μl using Amicon Ultra-0.5, Ultracel-10 Membrane (Millipore, catalogue no. UFC501008) and run on a SDS–PAGE gel. The gel was stained by SimplyBlue SafeStain (Invitrogen, catalogue no. LC6060), and specific gel bands were cut out and sent for mass spectrometry analysis by the Vincent J. Coates Proteomics/Mass Spectrometry Laboratory at UC Berkeley.

**Immunoprecipitation of endogenous protein complexes.** To confirm the interaction of endogenous proteins, we lysed HeLa cells or D3 mouse ES cells by freeze-thaw twice in 20 mM HEPES buffer pH 7.5, 5 mM KCl, 1.5 mM MgCl<sub>2</sub>, 1× protease inhibitor cocktail (Roche). Specific antibodies against CUL3, SEC13 or SEC31 conjugated to protein G agarose beads were added to the cleared cell lysate and incubated at 4 °C for 4 h. Protein complexes were eluted with gel-loading buffer at 95 °C. Endogenous proteins in complexes were detected by immunoblot using specific antibodies against CUL3, SEC13, SEC31 or KLHL12.

To detect ubiquitylation of endogenous COPII components, we incubated HeLa cell extract with pre-immune serum or antibody against SEC13 conjugated to protein G agarose beads at 4 °C for 4 h. Protein complexes were eluted with SDS gel-loading buffer at 95 °C. Ubiquitylated proteins in the complex were detected by immunoblot against ubiquitin.

**In vitro protein interaction assays.** To dissect the KLHL12 and SEC31A interaction, we coupled 20 μg recombinant MBP–KLHL12, various mutants or MBP as a control to 15 μl amylose resin by incubating at 4 °C for 1 h. CUL3, SEC31A and mutants were expressed from pCS2 and labelled with [<sup>35</sup>S]-Met using TnT Sp6 Quick Coupled Trnsc/trans Syst (Promega, catalogue no. L2080). The labelled CUL3 or SEC31A were incubated with MBP–KLHL12 or mutants at



4 °C for 3 h. Beads were washed four times with TBST and twice with TBS, and incubated in SDS loading buffer at 95 °C. Samples were run on SDS-PAGE and results were visualized by autoradiography.

**In vitro ubiquitylation assays with CUL3-KLHL12.** CUL3/RBX1 was conjugated to NEDD8 at 30 °C for 1 h with the following conditions: 2.5 mM Tris/HCl pH 7.5, 5 mM NaCl, 1 mM MgCl<sub>2</sub>, 1 mM DTT, 1× energy mix<sup>40</sup>, 1 μM APPBP1-UBA3, 1.2 μM UBC12, 4 μM CUL3/RBX1, and 60 μM NEDD8. For *in vitro* ubiquitylation of SEC31A, we set up a 10 μl reaction as follows: 2.5 mM Tris/HCl pH 7.5, 5 mM NaCl, 1 mM MgCl<sub>2</sub>, 1 mM DTT, 1× energy mix, 100 nM UBA1, 1 μM UBCH5C, 1 μM CUL3~NEDD8/RBX1, 1 μM KLHL12, 150 μM ubiquitin, 0.05 μg SEC13/31A. The reaction was carried out at 30 °C for 1 h and stopped by adding SDS gel loading buffer.

**In vivo ubiquitylation assays with CUL3-KLHL12.** 293T cells grown in 10-cm dishes were transfected with pCS2-HA-Sec13/31A, pCS2-His-ubiquitin, pcDNA5-Klhl12-FLAG, pcDNA4-Cul3-FLAG, or pcDNA4-Cul3<sup>N250</sup>-FLAG, as indicated, using calcium phosphate. 24 h later, 1 μM MG132 was added and cells were incubated overnight. Cells were harvested with gentle scraping and resuspended in 1 ml buffer A (6 M guanidine chloride, 0.1 M Na<sub>2</sub>HPO<sub>4</sub>/NaH<sub>2</sub>PO<sub>4</sub> and 10 mM imidazole, pH 8.0). Cells were lysed by sonication for 10 s and incubated with 25 μl Ni-NTA agarose at room temperature for 3 h. The beads were washed twice with buffer A, twice with buffer A/TI (1 volume buffer A and 3 volumes buffer TI), once with buffer TI (25 mM Tris-Cl, 20 mM imidazole, pH 6.8), and incubated in 60 μl SDS gel-loading buffer containing 300 mM imidazole and 50 mM β-mercaptoethanol at 95 °C. Samples were separated by SDS-PAGE and ubiquitylated SEC31A was detected by immunoblot using antibody against SEC31A.

To detect SEC31A ubiquitylation upon CUL3/KLHL12 depletion, we co-transfected 100 nM siRNAs against CUL3 or KLHL12 with pCS2-HA-Sec13/31A and pCS2-His-ubiquitin using calcium phosphate. The Ni-NTA purification was performed 48 h post transfection and SEC31A ubiquitylation was detected as described above.

**Confocal microscopy.** Cells were fixed in 4% paraformaldehyde and permeabilized with 0.5% Triton X-100 in 1× TBS, 2% BSA. Cells were incubated with primary antibodies against SEC31A, SEC13, SEC24C, ERGIC53, CD63, BiP (also known as HSPA5) or ubiquitin for 2 h and secondary antibodies (Invitrogen, Alexa Fluor 546 goat anti-rabbit IgG (H+L); Alexa Fluor 488 goat anti-mouse IgG (H+L); HOECHST 33342,) for 1 h at room temperature followed by extensive washing. Pictures were taken on Zeiss LSM 510 and 710 Confocal Microscope systems and analysed with LSM image browser and Imaris 3D imaging processing software.

**Transmission electron microscopy.** Mock- and KLHL12-transfected HeLa cells were grown to 70% confluence as a monolayer on an Aclar sheet (Electron Microscopy Sciences). The cells were fixed for 30 min in 0.1 M cacodylate buffer, pH 7.2, containing 2% glutaraldehyde, and subsequently washed with buffer before post-fixation with 1% osmium tetroxide on ice. This was followed by staining with 1% aqueous uranyl acetate for 30 min at room temperature. For dehydration with progressive lowering of temperature, each incubation period was 10 min, with exposure to 35% ethanol at 4 °C, to 50% ethanol and 70% ethanol at -20 °C, and 95%, and 100% ethanol at -35 °C. Cells were restored to room temperature in 100% ethanol before flat embedding in an Epon resin. Thin (70–100 nm) sections were collected on Formvar-coated 200-mesh copper grids and post-stained with 2% aqueous uranyl acetate and 2% tannic acid. The sections were imaged at 120 kV using a Tecnai 12 Transmission Electron Microscope (FEI).

For the purpose of immunolabelling, HeLa cells expressing Flag-KLHL12 or doxycycline-inducible 293T Trex Flag-KLHL12 stable cell lines were fixed in 2% paraformaldehyde and 0.5% glutaraldehyde and embedded in LR white resin. Fixation and infiltration were performed in a microwave oven (Pelco model 3450, Ted Pella). 70-nm thick sections were picked on 100-mesh nickel grids coated with Formvar film and carbon, incubated in blocking buffer (5% BSA, 0.1% fish gelatin, 0.05% Tween 20 in PBS) for 30 min, and followed by incubation with anti-Flag antibody at a dilution of 1:40 for 1 h. Goat anti-mouse IgG conjugated with 10-nm gold (BD Biosciences) was used as the secondary antibody at a dilution of 1:40 for 1 h. Sections were post stained in 2% uranyl acetate for 5 min.

**Gene expression analysis by microarray.** To compare gene expression profiles of wild-type mouse ES cells versus CUL3-depleted mouse ES cells, we transfected D3 mouse ES cells with control or CUL3-siRNA, followed by growth on gelatin-coated six-well plates. 48 h later, total RNA was extracted by TRIzol and chloroform, and further purified using RNeasy Mini Kit (Qiagen, catalogue no. 74104). Microarray analysis was performed by the Functional Genomics Laboratory (UC Berkeley) using Affymetrix Mouse 430A 2.0 chip.

**Analysis of collagen export from cells.** IMR-90 human lung fibroblasts grown on 100-mm dishes in DMEM/10% FBS were transfected with Flag-KLHL12, Flag-KLHL12(FG289AA), Flag-KEAP1 and pcDNA5-flag using nucleofection kit R (bought from Lonza) as described in the manufacturer's protocol and plated on six-well plate with 25-mm coverslips. When indicated, co-transfections with

2 μg each of Flag-KLHL12 and dominant-negative CUL3 were performed. Dialysed 10% FBS media was used for ascorbate free transfections. Brefeldin A (Sigma) was used at a concentration of 2.5 mg ml<sup>-1</sup> and cells were incubated for 30 min. MG132 was used at 20 μM for 2 h, chloroquine was used at 200 μM for 1 h. Media was collected the next day and cells on coverslips were fixed with 3% paraformaldehyde for 30 min and remaining cells on a plate were used to prepare lysates. Cells on coverslips were permeabilized with 0.1% Triton for 15 min at room temperature followed by blocking with 1%BSA for 30 min. Primary antibodies used were polyclonal anti-procollagen (LF-67,diluted 1:1,000) and anti-Flag (diluted 1:200). Secondary antibodies were Alexa Fluor 546 donkey anti-rabbit IgG and Alexa Fluor 488 goat anti-rabbit IgG (diluted 1:200). After staining cells with appropriate primary and secondary antibodies, we fixed coverslips on slides using mounting reagent containing DAPI. Images were analysed with a Zeiss LSM710 confocal microscope and captured with Zen10 software. Merges of images were performed with ImageJ and LSM image Browser. Media collected from six-well plates was normalized with respect to lysate protein concentration estimated using BCA method. Media and lysates of each reaction were checked by immunoblot analysis. Tubulin was used as loading control for lysates. Ascorbate chase experiments were done by adding ascorbate (0.25 mM ascorbic acid and 1 mM asc-2-phosphate) to KLHL12-transfected cells, followed by incubation for 5, 10, 30 and 60 min.

A human fibrosarcoma cell line (HT1080) stably transfected with proα1(1) was used for CUL3 knockdowns. CUL3- and Klhl12-shRNAs targeting two different regions in both genes were cloned into pSuperGFP and transfected using Lipofectamine 2000. pSuper GFP was used as negative control. Cells were grown on 25-mm coverslips in six-well plates and fixed 2 days post transfection. Collagen staining was done using LF-67 (1:1,000) and endoplasmic reticulum was stained with anti-PDI (1:1,000) antibody. Fibronectin and EGFR were stained in parallel experiments. Fibronectin expression was induced in HT1080 using 1 μM dexamethasone before CUL3 knockdowns. Endoplasmic reticulum retention or secretion was scored in cells expressing GFP shRNAs. Cells without GFP shRNAs and transfected with pSUPER GFP were quantified as well. Images were taken on a Zeiss LSM 710 confocal microscope and visualized with LSM image browser. Lysates were prepared from remaining cells on six-well plates and checked for knockdown efficiency.

**siRNA oligonucleotides used in this study.** RNA interference oligonucleotides: mCul3 #1, GAAGGAATGTTTAGGGGATA; mCul3 #2, GGAAGAAGATGCAG CACAA; mCul3 #3, GGTGATGATTAGAGACATA; mCul3 #4, CAACCTTCT TCAAACACTA; mCul3 #5, CATTATTTATTGATGATAA; mUBA3, CGTTTG AAGCAGAGAGAGAAA; mKlhl12, CCTTGAGAGTGGAGCAGAA; hKlhl12, CCAAAGACATAATGACAAA; mKBTBD8, GAACATGAGCAGAGTGAAA; mOct4, AGGCAAGGGAGGTAGACAA; hSec31, CCTGAAGTATTCTGAT AAA; mSec13 (pool of 4 oligonucleotides), CCATGTGTTTAGTAATTTA, GGCAATATGTGGTCACTTA, GCTGAAAGTATTCATGTAA and GGAAC AAATGACTATTATT; mCdc42 (pool of 4 oligonucleotides), GATCTAATT TGAAATATTA, GGATTGAGTTCCTAATTA, AGAGGATTATGACAGAC TA and AAATCAAACCTAAAGATTAA; mBcar1/CAS (pool of 4 oligonucleotides), GACTAATAGTCTACATTTA, GGAGGTGTCTCGTCCAATA, CTATGACA ATGTTGCTGTA and GGGCGTCCATGCTCCGGTA; mSrc (pool of 4 oligonucleotides), CCCTTGTTGCCATATTTAA, CCACGAGGGTTGCCATCAA, CA GACTTGTTGTACATATT and GCAACAAGAGCAAGCCCAA; mRhoG (pool of 4 oligonucleotides), GGTTTACCTAAGAGGCCAA, GCTGTGCCTTAAG GACTAA, GCACAATGCAGAGCATCAA and GCGCAGCCGTGAACCTA AA; mRhoA (pool of 4 oligonucleotides), GGATTCCTAATAGTATA, GAAAGTGTATTGGAAATA, AGCCCTATATATCATTCTA, CGTCTGCCA TGATTGGTTA; mRac1 (pool of 4 oligonucleotides), GGTTAATTTCTGTCA AACA, GCGTTGAGTCCATATTTAA, GCTTGATCTTAGGGATGAT and GGAGTAATTCAACTGAATA; mCdh1/E-cadherin (pool of 4 oligonucleotides), GGAGGAGAACGGTGGTCAA, CGCGGATAACCAGAACAAA, CCATGTTT GCTGTATTCTA and GGGACAATGTGTATTACTA; mIqgap1 (pool of 4 oligonucleotides), ACATGATGATGATAAACA, GGTTGATTTACAGAAAGAA, GTATAAATTTATTTCTTAA and GGTGGATCAGATTCAAGAA; mCul1 (pool of 2 oligonucleotides), GCATGATCTCCAAGTTAAA and CGTGTAAATC TGCTATGAAA; mCul2 (pool of 2 oligonucleotides), GCGCTGATTGAAC AATAA and CCAGAGTATTTATATCTAA; mCul4a (pool of 2 oligonucleotides), GTGTGATTACCATAAATAA and CCAGGAAGCTGGTCACTAA; mCul5 (pool of 2 oligonucleotides), CCCTCATATTTACAGCAA and ACATGAAGTT TATAATGAA; mCul7 (pool of 2 oligonucleotides), GCATCAAGTCCGTAA TAA and GGATGTGATTGATATTGAA.

39. Geddis, A. E. & Prockop, D. J. Expression of human COL1A1 gene in stably transfected HT1080 cells: the production of a thermostable homotrimer of type I collagen in a recombinant system. *Matrix* **13**, 399–405 (1993).
40. Williamson, A. *et al.* Identification of a physiological E2 module for the human anaphase-promoting complex. *Proc. Natl Acad. Sci. USA* **106**, 18213–18218 (2009).

# Structural basis of highly conserved ribosome recycling in eukaryotes and archaea

Thomas Becker<sup>1\*</sup>, Sibylle Franckenberg<sup>1\*</sup>, Stephan Wickles<sup>1</sup>, Christopher J. Shoemaker<sup>2</sup>, Andreas M. Anger<sup>1</sup>, Jean-Paul Armache<sup>1</sup>, Heidemarie Sieber<sup>1</sup>, Charlotte Ungewickell<sup>1</sup>, Otto Berninghausen<sup>1</sup>, Ingo Daberkow<sup>3</sup>, Annette Karcher<sup>1,4</sup>, Michael Thomm<sup>5</sup>, Karl-Peter Hopfner<sup>1</sup>, Rachel Green<sup>2</sup> & Roland Beckmann<sup>1</sup>

**Ribosome-driven protein biosynthesis is comprised of four phases: initiation, elongation, termination and recycling. In bacteria, ribosome recycling requires ribosome recycling factor and elongation factor G, and several structures of bacterial recycling complexes have been determined. In the eukaryotic and archaeal kingdoms, however, recycling involves the ABC-type ATPase ABCE1 and little is known about its structural basis. Here we present cryo-electron microscopy reconstructions of eukaryotic and archaeal ribosome recycling complexes containing ABCE1 and the termination factor paralogue Pelota. These structures reveal the overall binding mode of ABCE1 to be similar to canonical translation factors. Moreover, the iron-sulphur cluster domain of ABCE1 interacts with and stabilizes Pelota in a conformation that reaches towards the peptidyl transferase centre, thus explaining how ABCE1 may stimulate peptide-release activity of canonical termination factors. Using the mechanochemical properties of ABCE1, a conserved mechanism in archaea and eukaryotes is suggested that couples translation termination to recycling, and eventually to re-initiation.**

Recycling of ribosomes for a new round of translation initiation is an essential part of protein synthesis. In archaea and eukaryotes recycling has been shown to require the highly conserved and essential ABC-type ATPase ABCE1 (Rli1p in *Saccharomyces cerevisiae* with 46.7% identity to archaeal (a)ABCE1 in *Pyrococcus furiosus*)<sup>1–4</sup>. ABCE1 can dissociate ribosomes into subunits either after canonical termination by release factors<sup>4</sup> or after recognition of stalled ribosomes by messenger RNA surveillance factors such as Pelota (Dom34p in *S. cerevisiae*, aPelota in *P. furiosus*)<sup>5</sup>. Crystal structures of aABCE1 revealed two nucleotide-binding domains (NBDs) in a typical head-to-tail orientation as observed for most of the other members of the ABC protein family<sup>6–8</sup>. Additional unique structural features of ABCE1 proteins are a helix-loop-helix (HLH) motif, a highly conserved hinge domain and an iron-sulphur cluster domain (FeS) containing two [4Fe-4S]<sup>2+</sup> clusters<sup>6,9</sup>.

In eukaryotes ABCE1 can be found associated with ribosomes and small ribosomal subunits, but also with release factors and initiation factors (eRF1, eIF2, eIF3 and eIF5)<sup>10,11</sup>. Notably, ABCE1 physically interacts with eRF1 and directly influences its function in stop-codon recognition and peptidyl-transfer RNA (tRNA) hydrolysis<sup>12,13</sup>. During recycling ABCE1 can split post-termination complexes obtained with eRF1 and eRF3 into free 60S subunits and tRNA- and mRNA-bound 40S subunits<sup>4</sup>. A similar role for ABCE1 was found in an archaeal translation system in which aABCE1 together with aRF1 was shown to dissociate ribosomes into subunits upon ATP binding<sup>8</sup>.

ABCE1 also acts together with the eRF1 paralogue Pelota<sup>5</sup>. In *S. cerevisiae*, Dom34 and the eRF3 paralogue Hbs1 were described as mRNA surveillance factors recognizing stalled elongating ribosomes<sup>14</sup>.

Such stalls can occur on mRNAs with stable secondary structures, truncations or lacking a stop codon, so that further elongation or canonical termination is prevented. In the so called no-go mRNA decay (NGD) or non-stop mRNA decay (NSD) pathways, such stalled ribosomes are recognized by Dom34 and Hbs1 (NGD and NSD, respectively)<sup>14</sup> or by another eRF3 paralogue Ski7 (NSD), eventually triggering mRNA degradation<sup>14–18</sup>. A cryo-electron microscopy (cryo-EM) structure of a stalled ribosome bound to Dom34–Hbs1 shows that Dom34 occupies the ribosomal A site, whereas Hbs1 binds the ribosome similar to other translational GTPases, such as elongation factor Tu (EF-Tu)<sup>19</sup>. Dom34–Hbs1 alone shows ribosome dissociation activity and splits stalled reconstituted ribosomes that contain P-site peptidyl-tRNA<sup>20</sup>. In a mammalian system, however, ABCE1 is strictly required for ribosome disassembly of both programmed and vacant ribosomes by Pelota and Hbs15 (ref. 5). Taken together, ABCE1 is probably the general ribosome recycling factor in archaea and eukaryotes. In contrast to the analogous bacterial system, however, ABCE1 acts not only after canonical release-factor-dependent termination but also after Pelota-dependent recognition of stalled ribosomes.

It is not known how ABCE1 functions on the ribosome in concert with Pelota or release factors, and how the mechanochemical properties of ABCE1 are used for ribosome recycling. To address these questions, we determined cryo-EM structures of eukaryotic and archaeal recycling complexes containing Pelota and ABCE1.

## Model of Pelota–ABCE1–ribosome complexes

Recycling complexes were obtained by *in vitro* reconstitution of the 70S and 80S ribosomes with purified Pelota and ABCE1 orthologues.

<sup>1</sup>Gene Center and Center for Integrated Protein Science Munich (CiPSM), Department of Biochemistry, University of Munich, Feodor-Lynen-Straße 25, 81377 Munich, Germany. <sup>2</sup>Howard Hughes Medical Institute, Department of Molecular Biology and Genetics, Johns Hopkins University School of Medicine, Baltimore, Maryland 21205, USA. <sup>3</sup>Tietz Video and Image Processing Systems GmbH, Eremitenweg 1, 82131 Gauting, Germany. <sup>4</sup>Rainer-Maria-Rilke-Gymnasium Icking, Ulrichstraße 1–7, 82057 Icking, Germany. <sup>5</sup>NWFF III/Biology and Preclinical Medicine, Department of Microbiology, University of Regensburg, Universitätsstraße 31, 93053 Regensburg, Germany.

\*These authors contributed equally to this work.

For the generation of a *S. cerevisiae* 80S ribosome–Dom34–Rli1 complex we used ribosome nascent chain complexes (RNCs) stalled by an mRNA with a synthetic stem loop (SL)<sup>14,21</sup>, a complex used previously for an 80S–Dom34–Hbs1 cryo-EM reconstruction<sup>19</sup>. For archaeal (*P. furiosus*) 70S–aPelota–aABCE1 complexes, 70S ribosomes were purified from a translation extract<sup>22</sup>. Simultaneous ribosome binding of Pelota and ABCE1 in the presence of non-hydrolysable ADPNP was shown by pelleting assays in the yeast and archaeal systems (Supplementary Fig. 1a, b). Notably, aABCE1-dependent splitting of archaeal ribosomes was not detectable with ADPNP, but strictly required ATP (Supplementary Fig. 1c, d).

Using cryo-EM in combination with single-particle analysis, we determined the structures of the SL–RNC–Dom34–Rli1 complex from yeast and the 70S–aPelota–aABCE1 complex from *P. furiosus*. Computational sorting was performed to generate homogeneous populations of ribosomal complexes containing Pelota, ABCE1 and P-site tRNA. The resolution of the final maps was determined to be 7.2 Å for the yeast complex and 6.6 Å for the archaeal complex (Supplementary Fig. 2). In both reconstructions we observed density for Pelota in the ribosomal A site, for ABCE1 in the GTPase translation factor binding site, and for tRNA in the P site (Fig. 1a, b). Additional E-site tRNA density is present in the archaeal ribosome. Both reconstructions are remarkably similar with respect to conformation and the ribosomal interaction patterns of the ABCE1 and Pelota orthologues. Using available crystal structures we could unambiguously assign and position the individual domains of Pelota—divided into amino-terminal domain (NTD), central domain and carboxy-terminal domain (CTD)—and ABCE1—divided into the N-terminal FeS, NBD1 containing a HLH motif, NBD2 and the hinge domain (Fig. 1c and Supplementary Fig. 3).

Notably, the two electron dense [4Fe–4S]<sup>2+</sup> clusters of ABCE1 can be clearly resolved as distinct spheres at high contour levels in both the yeast and archaeal maps reconstructions, validating the positioning of crystal structures in the EM maps (Fig. 1d). For molecular analysis we

used the crystal structure of the yeast 40S subunit<sup>23</sup>, the model of the yeast 80S ribosome<sup>24,25</sup> and, in addition, we built a homology-based molecular model of the archaeal 70S ribosome.

### Ribosome–ABCE1 interaction

ABCE1 binds to ribosomes in the intersubunit space, where canonical translational GTPases such as EF-Tu, EF-G/eEF2 or Hbs1 also interact with the ribosome (Fig. 2a)<sup>19,26–29</sup>. ABCE1 excludes these factors from binding at the same time, and we thus conclude that dissociation of Hbs1 or aEF1 $\alpha$  or, in the case of termination, eRF3 or aEF1 $\alpha$ , has to precede ABCE1 binding. Similar to these GTPases, the ATPase ABCE1 contacts the small ribosomal subunit, specifically ribosomal RNA helices h5, h8, h14 and h15 (Supplementary Tables 1 and 2). The h5–h15 region interacts with domain II of the translational GTPases, whereas the h8–h14 junction is the most proximal region to the GTPase switch regions<sup>30,31</sup> (Supplementary Fig. 4). Interestingly, the same regions are contacted by ABCE1 via two specific, up to now unexplained, structural features of ABCE1-type ABC-ATPases. The HLH motif of ABCE1 contacts the h5–h15 junction, whereas the hinge region establishes extensive contacts with the h8–h14 junction. In contrast to translational GTPases that engage in close interaction with the sarcin–ricin loop (SRL) of the rRNA helix, H95, contacts of ABCE1 with the large subunit are essentially limited to L9 in both species. Despite the overall marked similarity between Rli1 and aABCE1 in their ribosome interaction mode, additional minor contacts are present in the yeast complex: Rli1 contacts rpS6e and rpS24e on the small subunit, and, on the large subunit, rpP0 and a small region of the SRL (H95), which is different from the binding region of translational GTPases (Fig. 2b, c). Unexpectedly, the FeS cluster domain of ABCE1 does not directly bind the ribosome but instead interacts with Pelota only. These interactions are conserved between yeast and archaea.

In summary, ABCE1 establishes multiple contacts with both small and large ribosomal subunits as well as with the release factors (and

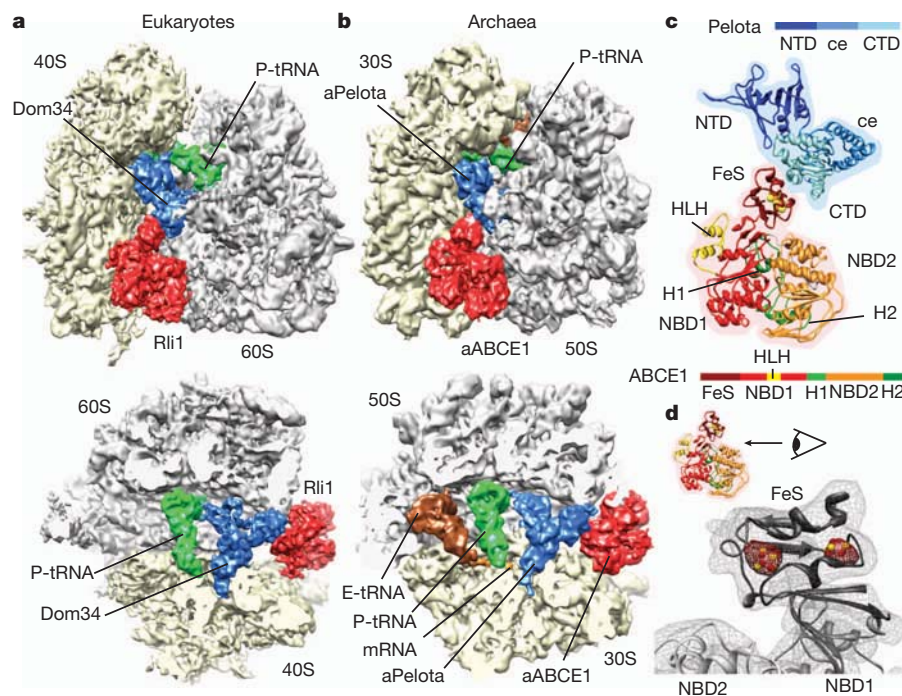


**Figure 1 | The ribosome-bound Pelota–ABCE1 complex.** **a, b**, Cryo-EM reconstructions of the eukaryotic SL–RNC–Dom34–Rli1 and the archaeal 70S–aPelota–aABCE1 complexes at 7.2 Å and 6.6 Å resolution, respectively. Extra densities were observed for Dom34/aPelota and Rli1/aABCE1 in the canonical factor binding site as well as for P-site tRNA, E-site tRNA and mRNA. The top section represents side views, the bottom section top views, where large and

small subunits were cut. **c**, Homology model for ribosome-bound Pelota and ABCE1 in transparent density. The individual domains are colour-coded as in the schematic representation of domain organization. The NTD, central domain (ce) and CTD are indicated. H1 and H2 indicate hinge 1 and hinge 2 domains. **d**, Zoom on the FeS domain of aABCE1. The density for the two [4Fe–4S]<sup>2+</sup> clusters is displayed in red mesh at high contour level.





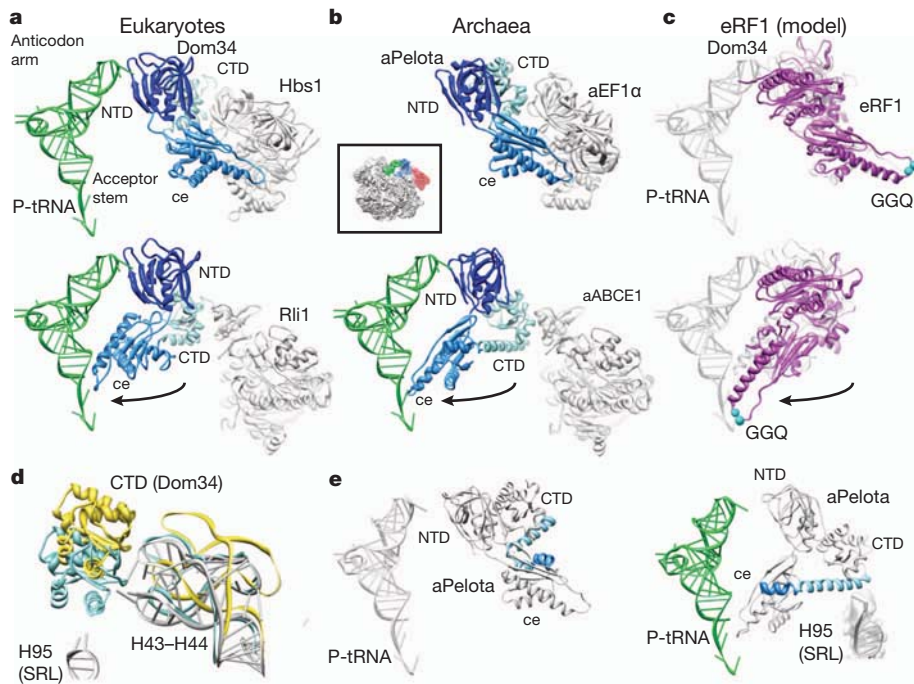


**Figure 3 | Domain movements in Pelota and eRF1.** **a**, Comparison of the ribosome-bound Dom34 conformation in complex with Hbs1 (top) and Rli1 (bottom). **b**, Comparison of the aPelota–aEF1 $\alpha$  crystal structure<sup>32</sup> with the ribosome-bound aPelota in complex with aABCE1. The central domain (ce) of Pelota swings out towards the P-site tRNA. The inset shows a thumbnail indicating the view. **c**, Models for eRF1 before and after the suggested

movement of the central domain. The arrows indicate the movement of the central domains. **d**, Conformation of the Dom34 CTD and the stalk base rRNA (H43–H44) when bound to Hbs1 (yellow) and to Rli1 (blue). rRNA conformation without factors bound is shown in grey. **e**, In aPelota three separate small helices refold into a long  $\alpha$ -helix during movement of the central domain bridging the CTD and the central domain.

neither the open nor the closed model can be easily modelled into the electron density in the reconstructions. In both reconstructions, we observe an intermediate, half-open state of the two NBDs: NBD2 rotates by approximately  $17^\circ$  towards NBD1 and the FeS cluster domain. However, an additional upward movement by  $8 \text{ \AA}$  of NBD2 would be required to obtain the fully closed conformation, in which the

signature motif of one NBD domain contacts the nucleotide-binding pocket of the other NBD domain (Supplementary Movie 3). Notably, in the observed half-open state of ABCE1 we find a contact between the NBD2 domain and the FeS cluster domain that is not seen in the crystal structures of the open state. Adoption of the fully closed ATP-bound conformation would therefore require a substantial shift of the FeS cluster domain, also of about  $8 \text{ \AA}$  (Fig. 4a), to avoid a steric clash. Although the limited resolution of the reconstruction does not allow for any conclusions regarding the nature of the bound nucleotide, the conformations of the individual lobes within the NBD1 and NBD2 domains more closely resemble those of the ADP-bound crystal structures. The similarity of the ‘intermediate’ conformation in both reconstructions suggests that binding to the ribosome induces an allosteric change in ABCE1, perhaps related to allosteric control of the ABC transporter by substrate binding<sup>37</sup>.

The finding that ATP hydrolysis<sup>4,5</sup> is required for full splitting activity strongly suggests that ABCE1 indeed has to undergo a conversion from the observed half-open pre-splitting conformation to the fully closed ATP state to efficiently dissociate ribosomes. Therefore, we analysed the effect of ATP-dependent NBD domain closure by superimposing the half-open ribosome-bound state of ABCE1 with the model for the closed state. ABCE1 in the closed conformation would not sterically clash with the ribosomal subunits

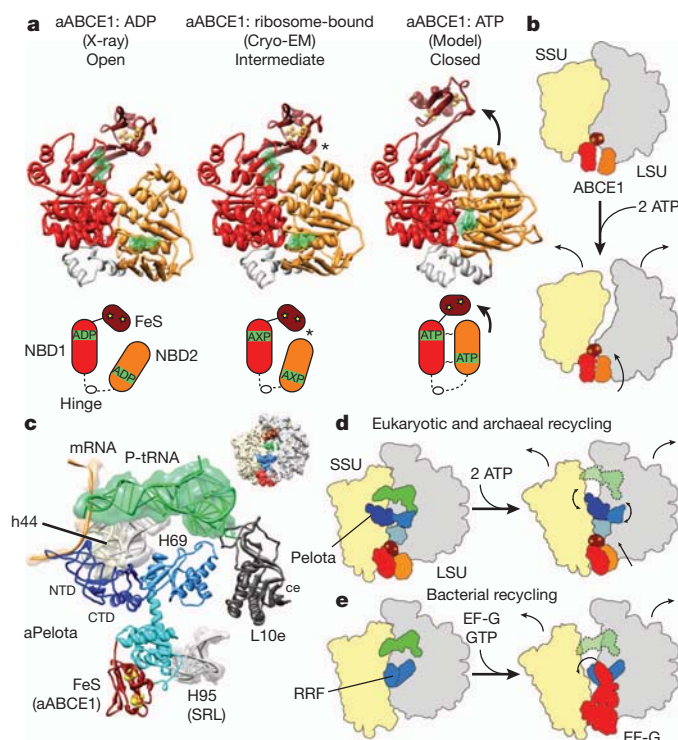


**Figure 4 | Mechanochemical activity of ABCE1 on the ribosome.** **a**, Crystal structure of the open (ADP-bound) aABCE1, the cryo-EM structure of the ribosome-bound aABCE1 and homology model of the closed (ATP-bound) aABCE1 including schematic drawings. An asterisk indicates a contact between NBD2 and the FeS domain of aABCE1. **b**, Ribosomal subunits may be dissociated by following the trajectory of aABCE1 domain closure upon ATP binding. **c**, Interactions of the aPelota NTD and central domain within the ribosome. **d**, ABCE1 domain closure could lead to an allosteric cascade with the FeS domain acting as a bolt on the CTD of Pelota to rearrange the NTD and central domain of Pelota. This mechanism would be analogous to the splitting reaction in bacteria by RRF and EF-G as depicted in **e**.



to induce splitting. One possibility is that the small and large ribosomal subunits follow the trajectory of NBD1 and NBD2 of ABCE1, respectively. In this case the ribosomal subunits would sufficiently rotate away from each other so as to affect the intersubunit bridges and, thus, the overall ribosome stability (Fig. 4b).

It is more likely, however, that the transition of ABCE1 through the closed conformation triggers an allosteric cascade affecting Pelota: the FeS cluster domain of ABCE1 contacts the NBD2 domain already in the half-open state and has to follow the movement of the NBD2 during closure. This conformational change of the FeS cluster domain towards the intersubunit space is likely to be transmitted to Pelota via the close interaction with its CTD. A shift of the CTD would in turn be transmitted to both the NTD and the central domain of Pelota. These Pelota domains establish a network of contacts with the small and the large ribosomal subunit as well as with the P-site tRNA (Fig. 4c). Indeed, numerous mutations underline the functional importance of these domains for the activity of Pelota (Supplementary Tables 1 and 2). A conformational shift can be easily envisaged to cause dissociation of the ribosome by destabilizing intersubunit bridges and the P-site tRNA. A function of the FeS cluster domain of ABCE1 as a structural bolt to remodel Pelota by transmitting ATP-induced changes from the NBDs is in good agreement with the finding that deletion of this domain abolishes splitting activity<sup>8</sup>. The enhanced stability of the domain provided by the FeS cluster may be required in the transmission of the mechanochemical power of ABCE1 for ribosome splitting.

Although using an entirely different cast of characters, this scenario is structurally reminiscent of bacterial ribosome recycling by ribosome recycling factor (RRF) and elongation factor G (EF-G). In this case, an EF-G-based GTP-dependent conformational switch positions RRF to clash with the small ribosomal subunit, inevitably promoting subunit dissociation<sup>8</sup> (Fig. 4d, e).

## Conclusion

We provide a structural basis and a universal mechanistic model for eukaryotic and archaeal ribosome recycling in which ABCE1 actively coordinates rescue (or translation termination) with recycling and re-initiation (Fig. 5):

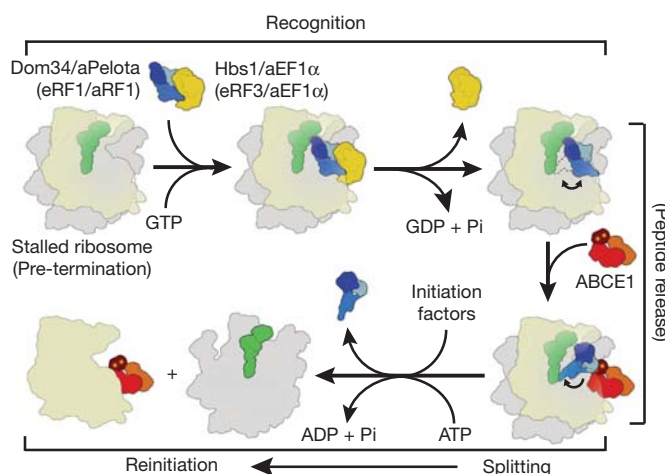


**Figure 5 | Scheme of archaeal and eukaryotic ribosome recycling bridging termination with initiation.** A translational GTPase (Hbs1/aEF1α/eRF3) delivers the factor, which recognizes stalled ribosomes (Pelota) or pre-termination complexes (eRF1/aRF1). After GTP hydrolysis, the GTPase dissociates and ABCE1 can bind. ABCE1 induces or stabilizes the swung-out conformation of Pelota (or RF1), which would lead to peptide release in case of termination. Ribosome splitting is induced after ATP binding to ABCE1 and hydrolysis. In eukaryotes, initiation factors can bind during the splitting reaction, coupling ribosome recycling with re-initiation. After splitting ABCE1 stays associated with the small ribosomal subunit.

In the first stage, the recognition stage, the sensing factors Pelota (for rescue) or RF1 (for termination) are delivered to stalled ribosomes or pre-termination complexes by EF-Tu-like GTPases. In the next step, the GTPase dissociates to allow ABCE1 binding to the ribosome. ABCE1 interacts with the CTD of Pelota (or of RF1 in termination) to stabilize the extended conformation of the central domain. In the case of translation termination, the GGQ motif of RF1 will be positioned proximal to the CCA-end of the P-site tRNA to catalyse peptide release; in the case of ribosome rescue, the central domain will be tightly accommodated proximal to the peptidyl transferase centre. Subsequently, in both cases, ABCE1 triggers ribosome disassembly into subunits by a power stroke upon NBD domain closure and ATP hydrolysis<sup>5</sup>. Our biochemical and structural data suggest a universal role of ATP hydrolysis in the mechanism of ABCE1-driven recycling. The conformational switch of ABCE1 could cause either a direct disruption of the ribosomal intersubunit bridges or, more likely, further conformational changes via an allosteric cascade from the FeS cluster domain of ABCE1 to the central domain and NTD of Pelota. In the archaeal system ABCE1 remains bound to the small ribosomal subunit after splitting<sup>8</sup> and it has been also found on the small subunit in eukaryotes<sup>10,11</sup>. Notably, ribosome recycling is coupled in eukaryotes with re-initiation when initiation factors such as eIF3, eIF1 and eIF1A bind the small ribosomal subunit as recycling is completed<sup>38</sup>. An initial recruitment of eIF3 to the 80S ribosome may even occur directly via ABCE1 interaction with the eIF3 subunit eIF3j (Hcr1p in yeast), even before recycling is completed<sup>13,39,40</sup>. In contrast, the analogous bacterial recycling system consisting of RRF and EF-G acts only after termination is completed and the participation of initiation factors is less clear<sup>41</sup>.

In conclusion, the archaeal and eukaryotic kingdoms have maintained an extremely conserved general ribosome recycling system with an ABC-type ATPase at the core: the mechanochemical properties of ABCE1 are used through a still somewhat enigmatic FeS cluster domain. This domain triggers an allosteric cascade that actively coordinates translation termination or rescue with recycling<sup>12</sup>, and eventually with re-initiation. It remains a puzzle as to why a complex FeS cluster domain is apparently used for a structural role only and has not been replaced by a simpler structure over billions of years of evolution. Thus, it is highly desirable to seek deeper insight into additional functions of ABCE1 in processes such as translation initiation and ribosome assembly.

## METHODS SUMMARY

Programmed yeast SL-RNCs were prepared from cell-free extracts as described<sup>19,42</sup>. Archaeal ribosomes were purified from cell-free extracts<sup>22</sup> by sucrose density centrifugation. Ribosome binding partners (Dom34, aPelota, ABCE1, aRF1 and aIF6) were expressed in *E. coli* or *S. cerevisiae* (Rli1) and purified using affinity chromatography. Ligands were reconstituted *in vitro* with SL-RNCs or 70S ribosomes, and binding was analysed by SDS-PAGE after pelleting of ribosome-bound fractions. Splitting activity was monitored in sucrose gradients using ultraviolet profiles. For cryo-EM, yeast and archaeal recycling complexes were vitrified and data were collected on a Titan Krios electron microscope (FEI Company). Single-particle analysis and three-dimensional reconstruction was done using the SPIDER software package<sup>43</sup>. Homology models were generated using HHPRED<sup>44</sup> and MODELLER<sup>45</sup>.

**Full Methods** and any associated references are available in the online version of the paper at [www.nature.com/nature](http://www.nature.com/nature).

Received 18 August 2011; accepted 5 January 2012.

1. Winzler, E. A. *et al.* Functional characterization of the *S. cerevisiae* genome by gene deletion and parallel analysis. *Science* **285**, 901–906 (1999).
2. Coelho, C. M. *et al.* Growth and cell survival are unevenly impaired in pixie mutant wing discs. *Development* **132**, 5411–5424 (2005).
3. Estevez, A. M., Haile, S., Steinbuechel, M., Quijada, L. & Clayton, C. Effects of depletion and overexpression of the *Trypanosoma brucei* ribonuclease L inhibitor homologue. *Mol. Biochem. Parasitol.* **133**, 137–141 (2004).
4. Pisarev, A. V. *et al.* The role of ABCE1 in eukaryotic posttermination ribosomal recycling. *Mol. Cell* **37**, 196–210 (2010).



5. Pisareva, V. P., Skabkin, M. A., Hellen, C. U., Pestova, T. V. & Pisarev, A. V. Dissociation by Pelota, Hbs1 and ABCE1 of mammalian vacant 80S ribosomes and stalled elongation complexes. *EMBO J.* **30**, 1804–1817 (2011).
6. Karcher, A., Schele, A. & Hopfner, K.-P. X-ray structure of the complete ABC enzyme ABCE1 from *Pyrococcus abyssi*. *J. Biol. Chem.* **283**, 7962–7971 (2008).
7. Karcher, A., Buttner, K., Martens, B., Jansen, R. P. & Hopfner, K. P. X-ray structure of Rli1, an essential twin cassette ABC ATPase involved in ribosome biogenesis and HIV capsid assembly. *Structure* **13**, 649–659 (2005).
8. Barthelme, D. *et al.* Ribosome recycling depends on a mechanistic link between the FeS cluster domain and a conformational switch of the twin-ATPase ABCE1. *Proc. Natl. Acad. Sci. USA* **108**, 3228–3233 (2011).
9. Barthelme, D. *et al.* Structural organization of essential iron-sulfur clusters in the evolutionarily highly conserved ATP-binding cassette protein ABCE1. *J. Biol. Chem.* **282**, 14598–14607 (2007).
10. Dong, J. *et al.* The essential ATP-binding cassette protein Rli1 functions in translation by promoting preinitiation complex assembly. *J. Biol. Chem.* **279**, 42157–42168 (2004).
11. Andersen, D. & Leever, S. The essential *Drosophila* ATP-binding cassette domain protein, Pixie, binds the 40S ribosome in an ATP-dependent manner and is required for translation initiation. *J. Biol. Chem.* **282**, 14752–14760 (2007).
12. Shoemaker, C. J. & Green, R. Kinetic analysis reveals the ordered coupling of translation termination and ribosome recycling in yeast. *Proc. Natl. Acad. Sci. USA* **108**, E1392–E1398 (2011).
13. Khoshnevis, S. *et al.* The iron-sulphur protein RNase L inhibitor functions in translation termination. *EMBO Rep.* **11**, 214–219 (2010).
14. Doma, M. & Parker, R. Endonucleolytic cleavage of eukaryotic mRNAs with stalls in translation elongation. *Nature* **440**, 561–564 (2006).
15. Atkinson, G., Baldauf, S. & Hauryliuk, V. Evolution of nonstop, no-go and nonsense-mediated mRNA decay and their termination factor-derived components. *BMC Evol. Biol.* **8**, 290 (2008).
16. Lee, H. H. *et al.* Structural and functional insights into Dom34, a key component of no-go mRNA decay. *Mol. Cell* **27**, 938–950 (2007).
17. Frischmeyer, P. *et al.* An mRNA surveillance mechanism that eliminates transcripts lacking termination codons. *Science* **295**, 2258–2261 (2002).
18. van Hoof, A., Frischmeyer, P. A., Dietz, H. C. & Parker, R. Exosome-mediated recognition and degradation of mRNAs lacking a termination codon. *Science* **295**, 2262–2264 (2002).
19. Becker, T. *et al.* Structure of the no-go mRNA decay complex Dom34–Hbs1 bound to a stalled 80S ribosome. *Nature Struct. Mol. Biol.* **18**, 715–720 (2011).
20. Shoemaker, C. J., Eyler, D. E. & Green, R. Dom34:Hbs1 promotes subunit dissociation and peptidyl-tRNA drop-off to initiate no-go decay. *Science* **330**, 369–372 (2010).
21. Hosoda, N. *et al.* Translation termination factor eRF3 mediates mRNA decay through the regulation of deadenylation. *J. Biol. Chem.* **278**, 38287–38291 (2003).
22. Endoh, T., Kanai, T. & Imanaka, T. A highly productive system for cell-free protein synthesis using a lysate of the hyperthermophilic archaeon, *Thermococcus kodakaraensis*. *Appl. Microbiol. Biotechnol.* **74**, 1153–1161 (2007).
23. Rabl, J., Leibundgut, M., Ataide, S. F., Haag, A. & Ban, N. Crystal structure of the eukaryotic 40S ribosomal subunit in complex with initiation factor 1. *Science* **331**, 730–736 (2011).
24. Armache, J. P. *et al.* Localization of eukaryote-specific ribosomal proteins in a 5.5-Å cryo-EM map of the 80S eukaryotic ribosome. *Proc. Natl. Acad. Sci. USA* **107**, 19754–19759 (2010).
25. Armache, J. P. *et al.* Cryo-EM structure and rRNA model of a translating eukaryotic 80S ribosome at 5.5-Å resolution. *Proc. Natl. Acad. Sci. USA* **107**, 19748–19753 (2010).
26. Schmeing, T. M. *et al.* The crystal structure of the ribosome bound to EF-Tu and aminoacyl-tRNA. *Science* **326**, 688–694 (2009).
27. Gao, Y. G. *et al.* The structure of the ribosome with elongation factor G trapped in the posttranslocational state. *Science* **326**, 694–699 (2009).
28. Taylor, D. J. *et al.* Structures of modified eEF2 80S ribosome complexes reveal the role of GTP hydrolysis in translocation. *EMBO J.* **26**, 2421–2431 (2007).
29. Spahn, C. M. *et al.* Domain movements of elongation factor eEF2 and the eukaryotic 80S ribosome facilitate tRNA translocation. *EMBO J.* **23**, 1008–1019 (2004).
30. Villa, E. *et al.* Ribosome-induced changes in elongation factor Tu conformation control GTP hydrolysis. *Proc. Natl. Acad. Sci. USA* **106**, 1063–1068 (2009).
31. Connell, S. R. *et al.* Structural basis for interaction of the ribosome with the switch regions of GTP-bound elongation factors. *Mol. Cell* **25**, 751–764 (2007).
32. Kobayashi, K. *et al.* Structural basis for mRNA surveillance by archaeal Pelota and GTP-bound EF1 $\alpha$  complex. *Proc. Natl. Acad. Sci. USA* **107**, 17575–17579 (2010).
33. Frolova, L. *et al.* Mutations in the highly conserved GGQ motif of class 1 polypeptide release factors abolish ability of human eRF1 to trigger peptidyl-tRNA hydrolysis. *RNA* **5**, 1014–1020 (1999).
34. Song, H. *et al.* The crystal structure of human eukaryotic release factor eRF1—mechanism of stop codon recognition and peptidyl-tRNA hydrolysis. *Cell* **100**, 311–321 (2000).
35. Hopfner, K. P. & Tainer, J. A. Rad50/SMC proteins and ABC transporters: unifying concepts from high-resolution structures. *Curr. Opin. Struct. Biol.* **13**, 249–255 (2003).
36. Smith, P. C. *et al.* ATP binding to the motor domain from an ABC transporter drives formation of a nucleotide sandwich dimer. *Mol. Cell* **10**, 139–149 (2002).
37. Locher, K. P. Structure and mechanism of ATP-binding cassette transporters. *Phil. Trans. R. Soc. Lond. B* **364**, 239–245 (2009).
38. Pisarev, A. V., Hellen, C. U. & Pestova, T. V. Recycling of eukaryotic posttermination ribosomal complexes. *Cell* **131**, 286–299 (2007).
39. Kispaal, G. *et al.* Biogenesis of cytosolic ribosomes requires the essential iron-sulphur protein Rli1p and mitochondria. *EMBO J.* **24**, 589–598 (2005).
40. Yarunin, A. *et al.* Functional link between ribosome formation and biogenesis of iron-sulfur proteins. *EMBO J.* **24**, 580–588 (2005).
41. Pavlov, M. Y., Antoun, A., Lovmar, M. & Ehrenberg, M. Complementary roles of initiation factor 1 and ribosome recycling factor in 70S ribosome splitting. *EMBO J.* **27**, 1706–1717 (2008).
42. Beckmann, R. *et al.* Architecture of the protein-conducting channel associated with the translating 80S ribosome. *Cell* **107**, 361–372 (2001).
43. Frank, J. *et al.* SPIDER and WEB: processing and visualization of images in 3D electron microscopy and related fields. *J. Struct. Biol.* **116**, 190–199 (1996).
44. Soding, J., Biegert, A. & Lupas, A. N. The HHpred interactive server for protein homology detection and structure prediction. *Nucleic Acids Res.* **33**, W244–W248 (2005).
45. Eswar, N., Eramian, D., Webb, B., Shen, M. Y. & Salí, A. Protein structure modeling with MODELLER. *Methods Mol. Biol.* **426**, 145–159 (2008).

**Supplementary Information** is linked to the online version of the paper at [www.nature.com/nature](http://www.nature.com/nature).

**Acknowledgements** We thank A. Schele and A. Gilmozzi for technical assistance, and D. Wilson for critical discussions. This work was supported by grants from the Deutsche Forschungsgemeinschaft, SFB594 (to R.B.), SFB646 (to T.B., R.B. and K.-P.H.), National Institutes of Health U19 AI083025 (to K.-P.H.) and by the Fonds der chemischen Industrie (to S.F.).

**Author Contributions** T.B. and R.B. designed the study, T.B. processed the yeast SL-RNC-Dom34-Rli1 complex and interpreted the cryo-EM structures, S.F. purified archaeal proteins and reconstituted the archaeal 70S-aPelota-aABCE1 sample, processed all archaeal data sets and interpreted the cryo-EM structures, S.W. developed an automated workflow for data processing from the Titan Krios microscope, C.J.S. purified yeast Rli1p, A.M.A. built the archaeal 70S ribosome rRNA model, J.-P.A. built the archaeal 70S ribosome protein models, H.S. reconstituted the SL-RNC-Dom34-Rli1 sample, C.U. prepared cryo-EM grids and assisted in data collection, O.B. optimized and performed cryo-EM data collection, I.D. implemented software for automated data collection on the Titan Krios microscope, A.K. purified archaeal ABCE1, M.T. provided *P. furiosus* and *Thermococcus kodakaraensis* cells, T.B., S.F., K.-P.H., R.G. and R.B. interpreted results.

**Author Information** EM density maps are deposited in the 3D-EM database (EMD-2008 and EMD-2010 for yeast maps, EMD-2009 for the archaeal map) and the coordinates for EM-based models are deposited in the Protein Data Bank (3J15 and 3J16). Reprints and permissions information is available at [www.nature.com/reprints](http://www.nature.com/reprints). The authors declare no competing financial interests. Readers are welcome to comment on the online version of this article at [www.nature.com/nature](http://www.nature.com/nature). Correspondence and requests for materials should be addressed to R.B. ([beckmann@lmb.uni-muenchen.de](mailto:beckmann@lmb.uni-muenchen.de)) or T.B. ([becker@lmb.uni-muenchen.de](mailto:becker@lmb.uni-muenchen.de)).

## METHODS

**Purification of SL-stalled RNCs.** Yeast (*S. cerevisiae*) ribosomes were stalled using a synthetic SL 3' of the coding region (sequence: 5'-GATATCCCGTG GAGGGGCGCGTGGTGGCGGCTGCAGCCGCCACACGCGCCCTCCAC GGGATATC-3') as described before<sup>14,19,21</sup>. The mRNA coded for the 120 N-terminal residues of DBAP-B with additional N-terminal haemagglutinin (HA) and His<sub>6</sub> tags. RNC complexes were purified after *in vitro* translation in a yeast cell-free translation extract as described previously<sup>42</sup>.

**Purification of ribosomes from *P. furiosus* or *T. kodakarensis*.** Ribosomes were purified from frozen *P. furiosus* or *T. kodakarensis* cell pellets. Cell pellets were suspended in 1.3× S30 buffer (10 mM Tris pH 7.4, 60 mM potassium acetate (KOAc), 14 mM MgCl<sub>2</sub>) overnight at 4 °C. The homogenous lysate was disrupted with a microfluidizer (Microfluidics). Cell debris was removed by centrifugation at 20,000g at 4 °C. The supernatant was decanted and ribosomes were pelleted through a high-salt sucrose cushion (1 M sucrose, 500 mM NH<sub>4</sub>OAc, S30 buffer) at 312,000g (RP80AT, Sorvall) for 60 min. The ribosomal pellet was suspended in buffer TrB25 (56 mM Tris pH 8.2, 250 mM KOAc, 80 mM NH<sub>4</sub>OAc, 25 mM MgCl<sub>2</sub>, 1 mM dithiothreitol (DTT)). The ribosomes were then gradient purified (10–40% sucrose, 10 mM Tris pH 7.4, 60 mM KOAc, 14 mM MgCl<sub>2</sub>) at 45,600g (SW40, Beckman Coulter) for 16 h at 4 °C. The fractions were collected using a Gradient Station (Biocomp) with an Econo UV Monitor (Biorad) and a FC203B Fraction Collector (Gilson). The fractions containing 70S ribosomes were washed with S30 buffer and concentrated using a 100 kDa Amicon Ultra Centrifugal Filter Unit (Millipore). S30 and TrB25 buffer are based on published protocols<sup>46,47</sup>. TrB25 is derived from the translation buffer and was modified for our purpose.

**Purification of aABCE1/Rli1p, aPelota/Dom34p, aRF1 and aIF6.** For, Rli1p, *Rli1* was cloned from yeast (*S. cerevisiae*) genomic DNA into pYES2 and induced in INVSc1 cells (Invitrogen) at 30 °C for 16 h. Cells were harvested and suspended in Ni-NTA lysis buffer (75 mM HEPES pH 8.0, 300 mM NaCl, 5 mM β-mercaptoethanol, 1% Tween, 20 mM imidazole, 10% glycerol), frozen in pellets and lysed in a liquid nitrogen Freezer/Mill (SPEX SamplePrep, LLC). Lysate was clarified and purified over a HisTrap FF column (GE Healthcare) on an ÄTKA FPLC (GE Healthcare). Additional purification was conducted over an S100 size exclusion column (GE Healthcare) pre-equilibrated in Buffer SE (20 mM Tris-Cl pH 7.5, 200 mM NaCl, 5 mM β-mercaptoethanol, 5% glycerol). Purified protein was observed to have a brown/yellow colour.

For Dom34p, N-terminally tagged *S. cerevisiae* protein Dom34p was over-expressed in *E. coli* in a pET21a(+) vector and purified via a Ni-NTA affinity chromatography as described before<sup>48,49</sup>.

For aABCE1, C-terminally strep-tagged aABCE1 from *P. furiosus* was expressed and reconstituted as described previously<sup>6</sup>. Aliquots were kept under anaerobic conditions and stored at –80 °C.

For aPelota, aPelota from *T. kodakarensis* genomic DNA was cloned into pET28 (Novagen) generating a C-terminally His-tagged construct. The *E. coli* strain Rosetta(DE3) (Novagen) was used for expression at 37 °C for 2–3 h. Cells were harvested and suspended in buffer A (10 mM Tris pH 8.0, 500 mM NaCl, 1 mM DTT) with 1× Complete EDTA-free Protease Inhibitor cocktail (Roche), 2 mM PMSE and 6 μg ml<sup>–1</sup> DNaseI. Lysis was achieved using a microfluidizer (Microfluidics) at 120.66 MPa. After centrifugation the supernatant was purified over a HisTrap HP column (GE Healthcare) on an ÄTKA FPLC Purifier (GE Healthcare).

For aRF1, aRF1 from *T. kodakarensis* was prepared as described above for aPelota. After elution from the HisTrap HP column, the protein was dialysed over night against a 1,000× excess of buffer A. After a heat denaturation step at 55 °C for 10 min, 1% glycerol was added before concentration. Precipitate was removed by centrifugation.

For aIF6, aIF6 from *T. kodakarensis* was prepared as described above for aPelota.

**Reconstitution of yeast RNC–Dom34–Rli1 complexes.** For *in vitro* binding assays and cryo-EM, 2 pmol of yeast SL–RNCs were reconstituted with a 10-fold molar excess of Dom34p and Rli1p in a volume of 25 μl under final conditions of 20 mM Tris/HCl pH 7.0, 150 mM KOAc, 10 mM Mg(OAc)<sub>2</sub>, 1.5 mM DTT, 0.005% Nikkol, 10 μg mg<sup>–1</sup> cycloheximide, 0.3% (w/v) digitonin, 500 μM ADPNP and incubated for 15 min at 25 °C and 10 min on ice. To assess ligand binding to ribosomes, reactions were applied to a 750 mM sucrose cushion and spun for 2.5 h at 152,000g. at 4 °C in a SW55 rotor (Beckman Coulter). Supernatant and pellet fractions were analysed by SDS–PAGE followed by SYPRO Orange (Bio-Rad) staining. Stained proteins were visualized on a phosphorimaging screen (Typhoon 9400, GE Healthcare).

**Reconstitution of archaeal 70S–aPelota–aABCE1 complexes.** Archaeal complexes for cryo-EM were reconstituted under anaerobic conditions (glove box, Coy Laboratories) in degassed buffer TrB50 (56 mM Tris pH 8.2, 250 mM KOAc, 80 mM NH<sub>4</sub>OAc, 50 mM MgCl<sub>2</sub>, 1 mM DTT) with 2 mM ADPNP. 8.5 pmol of

ribosomes (*P. furiosus*), 40 pmol of aPelota and 40 pmol of aABCE1 were incubated for 25 min at 30 °C. The complexes were then diluted to 4.0 OD<sub>260 nm</sub> for cryo-EM and kept at room temperature (23 °C) until vitrification.

Ligand binding assays were performed as described earlier for the archaeal cryo-EM complexes. After incubation the reactions were applied to a 1 M sucrose cushion and spun for 45 min at 189,000g in a TLA100 rotor (Beckman Coulter). Supernatant and pellet fractions were analysed as described above.

**Splitting of archaeal 70S ribosomes.** 15 pmol of ribosomes (*T. kodakarensis*) were incubated with a 2.5-fold molar excess of ligands under anaerobic conditions in buffer TrB25. ATP was added to a final concentration of 2 mM. The reaction was incubated for 25 min at 25 °C. Splitting of the ribosomes was evaluated by separation on a 15–40% sucrose gradient (56 mM Tris pH 8.2, 250 mM KOAc, 80 mM NH<sub>4</sub>OAc, 50 mM MgCl<sub>2</sub>, 1 mM DTT), at 164,000g (SW-60, Beckman Coulter) for 3 h at 4 °C. The gradients were analysed using a Gradient Station (Biocomp) with an Econo UV Monitor (Biorad) and a FC203B Fraction Collector (Gilson).

**Electron microscopy and image processing.** Freshly prepared sample was applied to 2 nm pre-coated Quantifoil R3/3 holey carbon supported grids and vitrified using a Vitrobot Mark IV (FEI Company) and visualized on a Titan Krios TEM (FEI Company) under low-dose conditions (about 20 e<sup>–</sup> per Å<sup>2</sup>) at a nominal magnification of ×75,000 with a nominal defocus between –1 μm and –3.5 μm.

The yeast SL–RNC–Dom34–Rli1 data set was collected at 300 keV at a magnification of ×128,200 at the plane of CCD using an Eagle 4k × 4k CCD camera (FEI Company, 4,096 × 4,096 pixel, 15 μm pixel, 5 s/full frame) resulting in an image pixel size of 1.17 Å (object scale). The archaeal aPelota–aABCE1 data set was collected at 200 keV at a magnification of ×148,721 at the plane of CCD using a faster TemCam-F416 CMOS camera (TVIPS GmbH, 4,096 × 4,096 pixel, 15.6 μm pixel, 1 s/full frame), resulting in an image pixel size of 1.049 Å (object scale).

Data collection was facilitated by the semi-automated software EM-TOOLS (TVIPS GmbH), allowing manual selection of appropriate grid meshes and holes in the holey carbon film. The acquisition automatically performed a re-centering, drift and focus correction before the final spot scan series were taken. Long-term TEM instabilities in beam shift, astigmatism and coma were corrected by EM-TOOLS regularly (for example, every 45 min). Selected on the basis of power spectra quality, typically 70% of the recorded images were used for the subsequent reconstruction.

Data processing was done using the SPIDER software package<sup>43</sup>. For data processing from the TITAN KRIOS microscope we developed a new automated workflow including import of the original .tif files, automated conversion into SPIDER and MRC format, CTF determination using the SPIDER TF ED command and automated particle selection based on the program Signature<sup>50</sup>. After initial particle selection a second selection of the data set was done using a newly developed machine-learning algorithm (MAPPOS; <http://arxiv.org/abs/1112.3173v2>) that detects wrongly selected particles ('non-particles') such as contaminations, noise, carbon edges etc. An ensemble classifier was trained to categorise the data set based on a smaller training set containing good and non-particles, respectively. This was achieved by discriminatory features that were extracted from each image. Identified non-particles were then omitted from the data set.

The 80S–SL–RNC–Dom34–Rli1 data set was refined to a final resolution of 7.2 Å (Fourier shell correlation (FSC) cut-off 0.5). Refinement and sorting of 144,500 particles was performed as described before<sup>19,51</sup>. The data set was first split into two subsets representing particles with and without Dom34 and Rli1 (101,700). This subset was further sorted according to presence of P-site tRNA (45,700 particles with tRNA, 56,000 particles without tRNA).

The entire 70S–aPelota–aABCE1 data set contained 365,000 particles. The data set was sorted according to the presence of aABCE1 and P-site tRNA<sup>19,51</sup>. The data subset with aABCE1 still displayed heterogeneity regarding occupation with tRNA or aPelota in the A site, and it was further sorted accordingly. The final data set contained 51,000 particles and the final resolution was 6.6 Å (FSC 0.5).

**Model building for aPelota/Dom34 and aABCE1/Rli1.** For the generation of protein homology models, the programs HHPRED<sup>44</sup> and MODELLER<sup>45</sup> were used. For generating the Dom34 model in the Rli1-bound state, the existing crystal structure in complex with Hbs1 (PDB accession 3MCA)<sup>52</sup> and the model for ribosome-bound Dom34 (PDB accession 3IZQ)<sup>19</sup> was used. The model for the *T. kodakarensis* aPelota was built using the X-ray structure (PDB accession 3AGJ)<sup>53</sup>. Models for *S. cerevisiae* Rli1 and *P. furiosus* aABCE1 were generated based on existing crystal structures (PDB accession 3BK7)<sup>6</sup>. Because in all electron densities the secondary structure of proteins was visible, a highly reliable initial rigid body fit for aPelota/Dom34 aABCE1/Rli1 could be performed using Coot and UCSF Chimera<sup>53,54</sup>. On the basis of this initial fit, we used the programs DireX<sup>55</sup> and the molecular dynamics flexible fitting (MDFF) method<sup>56,57</sup> to interactively refine the models. A model for the *S. cerevisiae* ribosome<sup>24,25</sup> was

used for molecular interpretation of Dom34/Hbs1–ribosome interactions. For analysing the archaeal complex a model for the *P. furiosus* 70S ribosome was built as described before<sup>24,25</sup>.

46. Endoh, T. *et al.* Cell-free protein synthesis at high temperatures using the lysate of a hyperthermophile. *J. Biotechnol.* **126**, 186–195 (2006).
47. Endoh, T., Kanai, T. & Imanaka, T. Effective approaches for the production of heterologous proteins using the *Thermococcus kodakaraensis*-based translation system. *J. Biotechnol.* **133**, 177–182 (2008).
48. Graille, M., Chaillet, M. & van Tilbeurgh, H. Structure of yeast Dom34: a protein related to translation termination factor eRF1 and involved in no-go decay. *J. Biol. Chem.* **283**, 7145–7154 (2008).
49. Lee, H. H. *et al.* Structural and functional insights into Dom34, a key component of no-go mRNA decay. *Mol. Cell* **27**, 938–950 (2007).
50. Chen, J. Z. & Grigorieff, N. SIGNATURE: a single-particle selection system for molecular electron microscopy. *J. Struct. Biol.* **157**, 168–173 (2007).
51. Becker, T. *et al.* Structure of monomeric yeast and mammalian Sec61 complexes interacting with the translating ribosome. *Science* **326**, 1369–1373 (2009).
52. Chen, L. *et al.* Structure of the Dom34–Hbs1 complex and implications for no-go decay. *Nature Struct. Mol. Biol.* **17**, 1233–1240 (2010).
53. Emsley, P. & Cowtan, K. Coot: model-building tools for molecular graphics. *Acta Crystallogr. D* **60**, 2126–2132 (2004).
54. Pettersen, E. F. *et al.* UCSF Chimera: a visualization system for exploratory research and analysis. *J. Comput. Chem.* **25**, 1605–1612 (2004).
55. Schröder, G. F., Brunger, A. T. & Levitt, M. Combining efficient conformational sampling with a deformable elastic network model facilitates structure refinement at low resolution. *Structure* **15**, 1630–1641 (2007).
56. Trabuco, L. G., Villa, E., Mitra, K., Frank, J. & Schulten, K. Flexible fitting of atomic structures into electron microscopy maps using molecular dynamics. *Structure* **16**, 673–683 (2008).
57. Phillips, J. C. *et al.* Scalable molecular dynamics with NAMD. *J. Comput. Chem.* **26**, 1781–1802 (2005).



# Abrupt acceleration of a ‘cold’ ultrarelativistic wind from the Crab pulsar

F. A. Aharonian<sup>1,2</sup>, S. V. Bogovalov<sup>3</sup> & D. Khangulyan<sup>4</sup>

Pulsars are thought to eject electron–positron winds that energize the surrounding environment, with the formation of a pulsar wind nebula<sup>1</sup>. The pulsar wind originates close to the light cylinder, the surface at which the pulsar co-rotation velocity equals the speed of light, and carries away much of the rotational energy lost by the pulsar. Initially the wind is dominated by electromagnetic energy (Poynting flux) but later this is converted to the kinetic energy of bulk motion<sup>2</sup>. It is unclear exactly where this takes place and to what speed the wind is accelerated. Although some preferred models imply a gradual acceleration over the entire distance from the magnetosphere to the point at which the wind terminates<sup>3,4</sup>, a rapid acceleration close to the light cylinder cannot be excluded<sup>5,6</sup>. Here we report that the recent observations of pulsed, very high-energy  $\gamma$ -ray emission from the Crab pulsar<sup>7–9</sup> are explained by the presence of a cold (in the sense of the low energy of the electrons in the frame of the moving plasma) ultrarelativistic wind dominated by kinetic energy. The conversion of the Poynting flux to kinetic energy should take place abruptly in the narrow cylindrical zone of radius between 20 and 50 light-cylinder radii centred on the axis of rotation of the pulsar, and should accelerate the wind to a Lorentz factor of  $(0.5\text{--}1.0) \times 10^6$ . Although the ultrarelativistic nature of the wind does support the general model of pulsars, the requirement of the very high acceleration of the wind in a narrow zone not far from the light cylinder challenges current models.

The Crab pulsar is one of the brightest  $\gamma$ -ray sources in the sky. Both the light curve and the energy spectrum have been studied<sup>10</sup> in great detail by the Large Area Telescope on board NASA’s Fermi Gamma-ray Space Telescope (Fermi). The phase-averaged spectrum is best fitted by a power law with a photon index of  $\alpha = 1.97$  and an exponential cut-off at  $E_c = 5.8$  GeV (Fig. 1). Although modified ‘outer gap’ models<sup>11</sup> do allow an extension of the spectrum up to 10 GeV, the detection of pulsed, very high-energy (VHE)  $\gamma$ -ray emission demands a different radiation component. The extrapolation of the fluxes reported by Fermi to the VHE domain as a power law with photon index  $\alpha \approx 3.8$ , and the claim that such a formal fit is evidence that  $\gamma$ -rays of gigaelectronvolt (GeV) energies have the same magnetospheric origin as those of teraelectronvolt (TeV) energies<sup>8,9,12</sup>, in fact requires a drastic revision of basic concepts used at present in magnetospheric models. Moreover, the assumption of a magnetospheric origin for radiation over the entire  $\gamma$ -ray domain contradicts the essentially different light curves reported at GeV (ref. 10) and TeV (refs 7, 9) energies (unless the production sites of these two components are well separated), as well as the apparent tendency of spectral flattening above 100 GeV (Fig. 1).

A natural and more plausible site of production of pulsed VHE  $\gamma$ -rays is the ultrarelativistic wind illuminated by photons originating in the pulsar’s magnetosphere and/or the surface of the neutron star<sup>13</sup>. In the case of the Crab pulsar, the phase-averaged flux of the pulsed (magnetospheric) component exceeds the flux of the thermal emission of the neutron star by two orders of magnitude. The combination of the hard spectral energy distribution of the pulsed emission and the

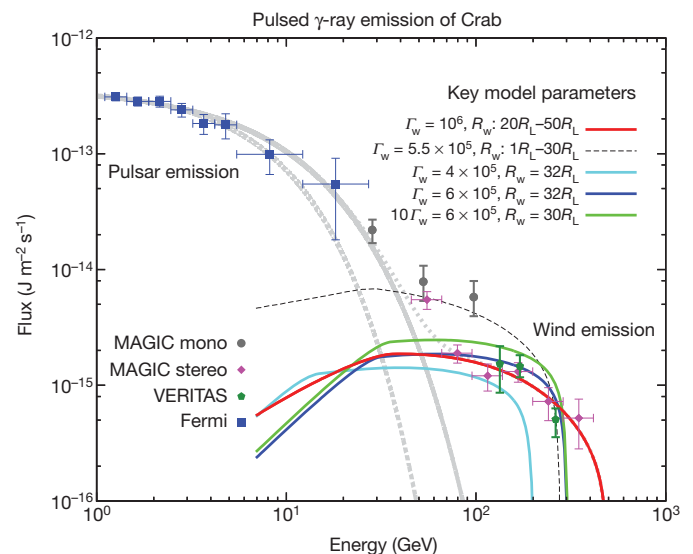


**Figure 1 | Spectral energy distribution of  $\gamma$ -ray radiation produced by the pulsar magnetosphere and by the pulsar wind.** Symbols show the reported  $\gamma$ -ray fluxes with 1-s.d. error bars<sup>7–10</sup>. Curves show theoretical predictions (this work). The Fermi Large Area Telescope points<sup>10</sup> are best fitted by the function  $F_E = 3.8 \times 10^{-13} E^{0.03} \exp[-E/5.8 \text{ GeV}] \text{ J m}^{-2} \text{ s}^{-1}$  (dashed grey line). Assuming a slightly harder spectrum in the cut-off region, with  $F_E = 3.8 \times 10^{-13} E^{0.03} \exp[-(E/7 \text{ GeV})^{0.85}] \text{ J m}^{-2} \text{ s}^{-1}$  (solid grey line), the MAGIC ‘mono’ data points<sup>8</sup> can be explained as well (because of large systematic uncertainties, the mono 100-GeV point, which differs by a factor of three from the flux measured by two MAGIC telescopes in the more reliable stereoscopic regime<sup>9</sup>, perhaps ought to be discarded). This spectrum is somewhat harder than that predicted by standard magnetospheric models, but does not challenge them<sup>16–18</sup>. The inverse-Compton  $\gamma$ -ray emission of the cold ultrarelativistic wind<sup>13</sup> can naturally explain the pulsed  $\gamma$ -ray fluxes reported<sup>7,9</sup> above 100 GeV. The solid light-blue, blue and green curves are calculated under the assumption of ‘instant’ acceleration of the wind at the fixed radius  $R_w$ . In principle, the acceleration can start earlier, but closer to the light cylinder the acceleration rate should be modest; otherwise it would lead to overproduction of inverse-Compton  $\gamma$ -rays. Earlier acceleration is demonstrated by the dashed black curve, which is calculated under the assumption that acceleration starts at the light cylinder with a rate that increases in proportion with  $R^3$  up to  $R_w = 30R_L$ , where the Lorentz factor equals  $5.5 \times 10^5$  (Supplementary Information). The solid red curve corresponds to the case in which the Poynting flux transformation takes place within the  $20R_L\text{--}50R_L$  zone, assuming the wind’s acceleration rate to be independent of distance; the maximum Lorentz factor, achieved at  $50R_L$ , is set to  $10^6$ . (The dotted grey line corresponds to the superposition of the red and solid grey lines and shows the transition between the two radiation components.) Because of the decrease in the density of target photons with distance, the main fraction of VHE radiation is produced at around  $30R_L$  with a Lorentz factor close to  $5 \times 10^5$ . This explains the general similarity of the red curve to the instant-acceleration curves, apart from in the highest-energy region, where the sharp cut-off of the red curve is shifted to  $\sim 500$  GeV.

<sup>1</sup>Dublin Institute for Advanced Studies, School of Cosmic Physics, 31 Fitzwilliam Place, Dublin 2, Ireland. <sup>2</sup>Max Planck Institute for Nuclear Physics, Saupfercheckweg 1, 69117 Heidelberg, Germany.

<sup>3</sup>National Research Nuclear University (MEPhI), Kashirskoe shosse 31, Moscow, 115409, Russia. <sup>4</sup>Institute of Space and Astronautical Science/JAXA, 3-1-1 Yoshinodai, Chuo-ku, Sagami-hara, Kanagawa 252-5210, Japan.

reduction of the Compton cross-section due to the Klein–Nishina effect means that the X-ray band is the main contributor to the Comptonization of the wind. The X-ray flux is well measured up to 100 keV (ref. 14) and therefore the calculations of the inverse-Compton radiation depend basically on the site and the dynamics (speed) of transformation of the Poynting flux to kinetic energy of bulk motion.

We assume that at a distance  $R_w$  from the pulsar, the wind is accelerated to the Lorentz factor  $\Gamma_w$  (Fig. 2). Particles of the accelerated wind cannot move purely radially, because the wind should carry both the energy and the angular momentum lost by the pulsar. From the relation between the rotation energy ( $E_{\text{rot}}$ ) and angular momentum ( $M_{\text{rot}}$ ) losses,  $\dot{E}_{\text{rot}} = \Omega \dot{M}_{\text{rot}}$ , where  $\Omega$  is the angular velocity of the rotating sphere and a dot denotes a time derivative, we can define the trajectory of the wind particles. Indeed, each particle of the wind carries energy  $\Gamma_w mc^2$  and angular momentum  $\Gamma_w m r_{\perp} v$ , where  $m$ ,  $r_{\perp}$  and  $v$  are the particle's mass, lever arm and speed, respectively, and  $c$  is the speed of light. Because  $\Gamma_w m r_{\perp} v \Omega = \Gamma_w mc^2$ , particles in the accelerated wind move along straight lines, tangent to the light cylinder. Therefore, all photons emitted by the magnetosphere will collide with electrons of the wind at a non-zero angle,  $\theta$ , resulting in inverse-Compton  $\gamma$ -rays. The  $\gamma$ -ray production efficiency depends on the electron Lorentz factor, the density of the target photons and the interaction angle. Because the cold wind carries almost the entire spin-down luminosity, even a tiny efficiency of about  $\kappa \approx 10^{-6}$  should be sufficient to produce detectable  $\gamma$ -rays at an energy flux level of  $F_E = \kappa \dot{E}_{\text{rot}} / 4\pi d^2 \approx 10^{-15} \text{ J m}^{-2} \text{ s}^{-1}$ , where  $d \approx 6 \times 10^{19} \text{ m}$  is the distance to the Crab.

Generally, the light curve of the target photons should be reflected in the time structure of the inverse-Compton  $\gamma$ -ray signal; however, they cannot be identical, owing, for example, to the effects related to the specifics of the anisotropic inverse-Compton scattering. More importantly, the geometrical effects may lead to non-negligible differences between the arrival times of the target photon and the secondary  $\gamma$ -ray pulses (Fig. 3). For wind located close to the light cylinder, the  $\gamma$ -ray signal seems shifted in time relative to the reported  $\gamma$ -ray data, by  $\Delta t \approx 0.1 T$ . By contrast, for wind acceleration at  $R_w = 30R_L$ , the widths and the positions of the predicted and observed  $\gamma$ -ray peaks (P1 and P2, respectively) are in very good agreement. However, whereas in the case of the isotropic wind the predicted P1/P2 flux ratio of the  $\gamma$ -ray signal mimics the X-ray light curve<sup>15</sup> (Fig. 3, black crosses), the reported  $\gamma$ -ray data<sup>7,9</sup> seem to correspond to a smaller ratio,  $P1/P2 < 1$ . This can be explained by there being a non-negligible wind

anisotropy, which would introduce noticeable corrections to the shape of the  $\gamma$ -ray light curve in general and to the P1/P2 ratio in particular (Fig. 3). The large uncertainties in the present  $\gamma$ -ray data prevent us from reaching a strong conclusion in this regard, but the improvement of the quality of VHE  $\gamma$ -ray light curves should in future allow the strength and the character of the wind anisotropy to be decisively probed.

GeV  $\gamma$ -rays have a light curve<sup>10</sup> that is essentially different from the reported VHE light curves<sup>7,9</sup>. This can be interpreted as a result of the production of GeV and TeV  $\gamma$ -rays in regions well separated from each other. This conclusion is supported by the spectral energy distribution of the time-averaged GeV and TeV signals. As demonstrated in Fig. 1, the entire  $\gamma$ -ray region can be considered a superposition of two separate components. Indeed, by introducing a new, flat-spectrum VHE component of the Comptonized wind, in addition to the nominal (magnetospheric) GeV component, the reported data in the GeV-to-TeV energy intervals can be smoothly matched.

Although inverse-Compton  $\gamma$ -rays are produced by mono-energetic electrons, the spectral energy distribution of  $\gamma$ -rays in the range of tens to hundreds of GeV is quite flat. This is caused by the combination of effects related to the broad power-law distribution of seed photons and the transition of the Compton cross-section from the Thomson regime to the Klein–Nishina regime. On the other hand, the spectrum is expected to have a very sharp cut-off at  $E = \Gamma_w mc^2$ . This not only can serve as a distinct feature for the identification of the wind origin of  $\gamma$ -rays, but also should allow us to determine the Lorentz factor of the wind. In fact, the measurements available at present do not allow strong deviation of the Lorentz factor from  $5 \times 10^5$ . We note that the calculations do not depend on the ‘magnetization parameter’  $\sigma$  (the ratio of the electromagnetic energy flux to the kinetic energy flux) as long as  $R_w \gg R_L$ . However, formally we can explain the pulsed VHE emission even for  $\sigma \geq 1$ . In this case, the acceleration should occur closer to the pulsar ( $R_w \propto 1/\sigma^{1/2}$ ) to compensate for the reduction in the wind's kinetic energy. But in this case, the inverse-Compton  $\gamma$ -ray radiation is expected to have quite different spectral and temporal features.

The above estimates of the location of wind's acceleration site and its Lorentz factor are quite robust, but they are obtained under the assumption that the transformation of the Poynting flux proceeds very quickly, at a specific radius between  $R_w$  and  $R_w \pm \delta R_w$  with  $\delta R_w/R_w \leq 1$ . This is not an obvious assumption, but is instead a working hypothesis that the wind acceleration takes place in a narrow zone at the radius  $R_w \approx 30R_L$ . We cannot a priori exclude the possibility

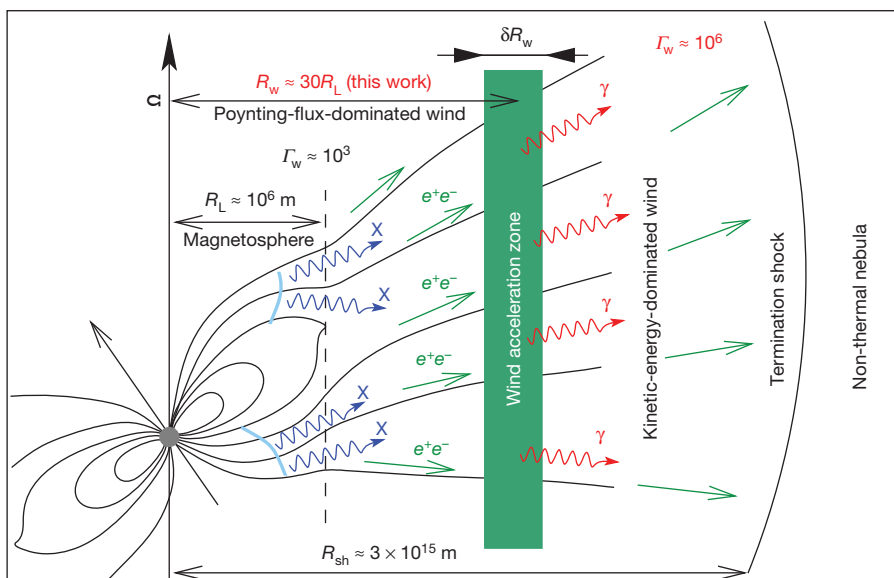


**Figure 2 | Complex comprising the pulsar magnetosphere, the ultrarelativistic wind and the pulsar wind nebula.** Dense electron ( $e^-$ )–positron ( $e^+$ ) plasma produced in the pulsar magnetosphere by pair creation processes<sup>19</sup> initiates an electron–positron wind at the light cylinder, which has radius  $R_L \approx 10^6 \text{ m}$ . Initially, the rotational energy lost by the pulsar,  $\dot{E}_{\text{rot}} = 5 \times 10^{31} \text{ J s}^{-1}$ , is released mainly in the form of electromagnetic energy (Poynting flux) and the wind's Lorentz factor therefore cannot be very large. At a distance  $R_w$ , the Poynting flux is converted to the kinetic energy of bulk motion (green zone), leading to an increase in the bulk-motion Lorentz factor to at least<sup>20</sup>  $\Gamma_w \approx 10^4$ . The termination of the wind by a standing reverse shock at  $R_{\text{sh}} \approx 3 \times 10^{15} \text{ m}$  boosts the energy of the electrons to  $10^{15} \text{ eV}$  and randomizes their pitch angles<sup>2</sup>. The radiative cooling of these electrons through the synchrotron and inverse-Compton processes results in an extended non-thermal source<sup>21–23</sup>, the Crab nebula.

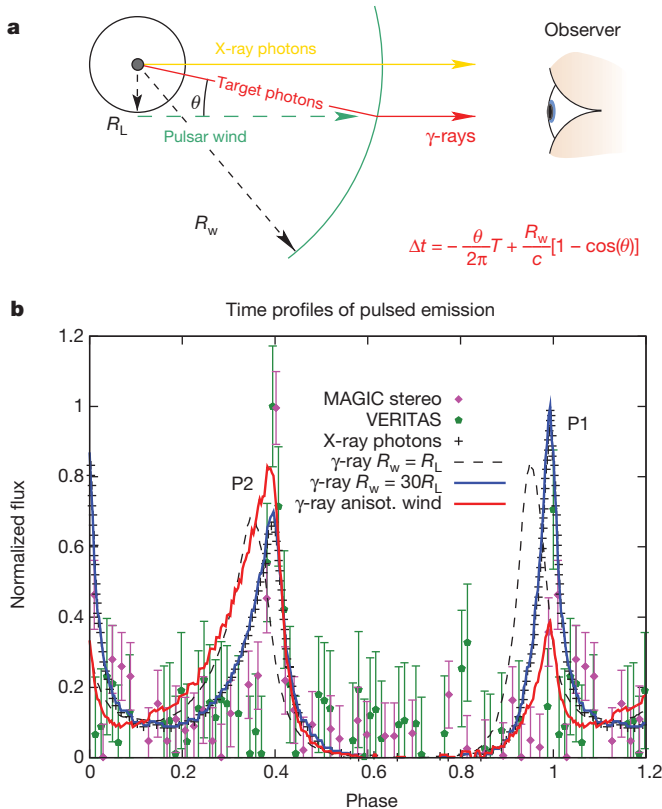


**Figure 3 | Formation of the pulsed VHE inverse-Compton  $\gamma$ -ray signal in the wind of the Crab pulsar.** **a**, Geometry of the inverse Compton scattering of magnetospheric X-rays by the electron-positron wind. **b**, Theoretical  $\gamma$ -ray light curves of the wind presented together with the reported VHE data<sup>7,9</sup>. The velocity of the accelerated wind is tangential to the light cylinder (the direction of motion of electrons towards the observer is shown by the dashed green arrow). The interaction of electrons with the magnetospheric X-rays occurs predominantly at a distance  $R \approx R_w$ , where the wind is accelerated. Owing to the decrease in the target photon density with distance, the production of inverse-Compton  $\gamma$ -rays is suppressed at larger distances. The target X-ray photon converted to a VHE  $\gamma$ -ray photon reaches the observer earlier than an 'identical' photon emitted directly towards the observer. Two factors contribute to the time shift,  $\Delta t$ : the up-scattered X-ray photon is emitted by the pulsar earlier, by a time  $\theta T/2\pi$ , where  $T$  is the pulsar period; and it travels an additional path length of  $R_w[1 - \cos(\theta)]$ . For  $R_w \gg R_L$ , the time shift is negligibly small:  $\Delta t \approx -(T/4\pi)R_L/R_w$ . For acceleration of the isotropic pulsar wind at  $R_w = 30R_L$ , the  $\gamma$ -ray light curve (solid blue line) closely resembles the shape of the measured X-ray light curve<sup>15</sup> (black crosses). For wind accelerated close to the light cylinder, the  $\gamma$ -ray light curve is shifted and somewhat broadened by comparison with wind accelerated at  $R_w \gg R_L$ . The anisotropy of the wind can also strongly deform the  $\gamma$ -ray light curve; in particular, it can change the ratio of the fluxes corresponding to peaks P1 and P2. The solid red line is calculated for an anisotropy factor proportional to the square of the sine of the angle between the line of sight and the direction of the magnetic momentum. This light curve seems to be in better agreement with the VERITAS<sup>7</sup> and MAGIC<sup>9</sup> points than the light curve corresponding to the fully isotropic wind, although the statistical and systematic uncertainties of observations (only Poisson error bars corresponding to the total count rates are shown on the plot) do not allow a definite conclusion in this regard.

that the wind is gradually accelerated starting from the edge of the magnetosphere, but our numerical calculations show that this cannot be the case (Fig. 1 and Supplementary Information). This is because the gradual acceleration would lead to a large number of high-energy electrons being accelerated close to the light cylinder and, consequently, to the prolific production of inverse-Compton  $\gamma$ -rays, in contradiction with the reported fluxes. Thus, the effective acceleration of the wind should start not much before the radius of  $30R_L$  and not much beyond it. Such a case, assuming a linear acceleration rate of  $I(R) = I_0 + a(R/R_L - 1)$  within the  $20R_L$ – $50R_L$  radial interval and a

maximum Lorentz factor of  $10^6$  achieved at  $50R_L$ , is shown in Fig. 1. The corresponding  $\gamma$ -ray spectrum is smoother than the energy spectra predicted in the case of an instant acceleration, and better fits the VHE spectral points (Fig. 1) with the position of the sharp cut-off in the  $\gamma$ -ray spectrum shifted to 500 GeV. Although the wind acceleration within the  $20R_L$ – $50R_L$  interval seems to be a physically more realistic scenario than an instant acceleration, this is still quite a narrow zone and the acceleration of the wind up to the Lorentz factor of  $10^6$  is therefore quite abrupt. This conclusion does not agree with those of alternative models, for example the so-called reconnection models of pulsar wind nebulae<sup>3,4</sup> based on the assumption that the transformation of the Poynting flux to kinetic energy of bulk motion is a slow process that takes place over the entire region of the unshocked wind.

Received 5 September; accepted 15 December 2011.

Published online 15 February 2012.

- Rees, M. J. & Gunn, J. E. The origin of the magnetic field and relativistic particles in the Crab Nebula. *Mon. Not. R. Astron. Soc.* **167**, 1–12 (1974).
- Kennel, C. F. & Coroniti, F. V. Magnetohydrodynamic model of Crab nebula radiation. *Astrophys. J.* **283**, 710–730 (1984).
- Coroniti, F. V. Magnetically striped relativistic magnetohydrodynamic winds: the Crab Nebula revisited. *Astrophys. J.* **349**, 538–545 (1990).
- Lyubarsky, Y. & Kirk, J. G. Reconnection in the striped pulsar wind. *Astrophys. J.* **547**, 437–448 (2001).
- Vlahakis, N. Ideal magnetohydrodynamic solution to the  $\sigma$  problem in Crab-like pulsar winds and general asymptotic analysis of magnetized outflows. *Astrophys. J.* **600**, 324–337 (2004).
- Beskin, V. S. & Nokhrina, E. E. The effective acceleration of plasma outflow in the paraboloidal magnetic field. *Mon. Not. R. Astron. Soc.* **367**, 375–386 (2006).
- Aliu, E. *et al.* Detection of pulsed gamma rays above 100 GeV from the Crab pulsar. *Science* **334**, 69–72 (2011).
- Aleksić, J. *et al.* Observations of the Crab pulsar between 25 and 100 GeV with the MAGIC I telescope. *Astrophys. J.* **742**, 43 (2011).
- Aleksić, J. *et al.* Phase-resolved energy spectra of the Crab Pulsar in the range of 50–400 GeV measured with the MAGIC Telescopes. *Astron. Astrophys.* (submitted); preprint at (<http://arxiv.org/abs/1109.6124>) (2011).
- Abdo, A. A. *et al.* Fermi Large Area Telescope observations of the Crab pulsar and nebula. *Astrophys. J.* **708**, 1254–1267 (2010).
- Tang, A. P. S., Takata, J., Jia, J. J. & Cheng, K. S. A revisit of the phase-resolved X-ray and  $\gamma$ -ray spectra of the Crab pulsar. *Astrophys. J.* **676**, 562–572 (2008).
- Lyutikov, M., Otte, N. & McCann, A. The very-high energy emission from pulsars: a case for inverse Compton scattering. *Astrophys. J.* (submitted); preprint at (<http://arxiv.org/abs/1108.3824>) (2011).
- Bogovalov, S. V. & Aharonian, F. A. Very-high-energy  $\gamma$  radiation associated with the unshocked wind of the Crab pulsar. *Mon. Not. R. Astron. Soc.* **313**, 504–514 (2000).
- Kuiper, L. *et al.* The Crab pulsar in the 0.75–30 MeV range as seen by the CGRO COMPTEL. A coherent high-energy picture from soft X-rays to high-energy  $\gamma$ -rays. *Astron. Astrophys.* **378**, 918–935 (2001).
- Rots, A. H. *et al.* Absolute timing of the Crab pulsar with the Rossi X-Ray Timing Explorer. *Astrophys. J.* **605**, L129–L132 (2004).
- Hirofani, K. Outer-gap versus slot-gap models for pulsar high-energy emissions: the case of the Crab pulsar. *Astrophys. J.* **688**, 1254–1267 (2010).
- Osmanov, Z. & Rieger, F. M. On particle acceleration and very high energy  $\gamma$ -ray emission in Crab-like pulsars. *Astron. Astrophys.* **502**, L25–L28 (2008).
- Chkheidze, N., Machabeli, G. & Osmanov, Z. On the very high energy spectrum of the Crab pulsar. *Astrophys. J.* **730**, 62 (2011).
- Sturrock, P. A. A model of pulsars. *Astrophys. J.* **164**, 529–556 (1971).
- Wilson, D. B. & Rees, M. J. Induced Compton scattering in pulsar winds. *Mon. Not. R. Astron. Soc.* **185**, 297–304 (1978).
- Gould, R. J. High-energy photons from the Compton-synchrotron process in the Crab nebula. *Phys. Rev. Lett.* **15**, 577–579 (1965).
- de Jager, O. C. & Harding, A. K. The expected high-energy to ultra-high-energy  $\gamma$ -ray spectrum of the Crab nebula. *Astrophys. J.* **283**, 710–730 (1992).
- Atayan, A. M. & Aharonian, F. A. On the mechanisms of  $\gamma$  radiation in the Crab nebula. *Mon. Not. R. Astron. Soc.* **278**, 161–172 (1992).

**Supplementary Information** is linked to the online version of the paper at [www.nature.com/nature](http://www.nature.com/nature).

**Acknowledgements** We would like to thank J. Cortina, E. de Ona Wilhemi, S. Klepser and N. Otte for information about high-energy  $\gamma$ -ray observations. We also appreciate discussions with F. Rieger, D. Jones and P. Gandhi.

**Author Contributions** F.A.A., S.V.B. and D.K. jointly contributed in comparable proportions to all aspects of the work, including the calculations and preparation of the manuscript.

**Author Information** Reprints and permissions information is available at [www.nature.com/reprints](http://www.nature.com/reprints). The authors declare no competing financial interests. Readers are welcome to comment on the online version of this article at [www.nature.com/nature](http://www.nature.com/nature). Correspondence and requests for materials should be addressed to F.A.A. ([felix.aharonian@dias.ie](mailto:felix.aharonian@dias.ie)).



# Wetting of flexible fibre arrays

C. Duprat<sup>1</sup>, S. Protière<sup>2,3</sup>, A. Y. Beebe<sup>1</sup> & H. A. Stone<sup>1</sup>

Fibrous media are functional and versatile materials, as demonstrated by their ubiquity both in natural systems such as feathers<sup>1–4</sup> and adhesive pads<sup>5</sup> and in engineered systems from nanotextured surfaces<sup>6</sup> to textile products<sup>7</sup>, where they offer benefits in filtration, insulation, wetting and colouring. The elasticity and high aspect ratios of the fibres allow deformation under capillary forces, which cause mechanical damage<sup>8</sup>, matting<sup>5,9</sup> self-assembly<sup>10,11</sup> or colour changes<sup>12</sup>, with many industrial and ecological consequences. Attempts to understand these systems have mostly focused on the wetting of rigid fibres<sup>13–17</sup> or on elastocapillary effects in planar geometries<sup>18</sup> and on a fibre brush withdrawn from an infinite bath<sup>19</sup>. Here we consider the frequently encountered case of a liquid drop deposited on a flexible fibre array and show that flexibility, fibre geometry and drop volume are the crucial parameters that are necessary to understand the various observations referred to above. We identify the conditions required for a drop to remain compact with minimal spreading or to cause a pair of elastic fibres to coalesce. We find that there is a critical volume of liquid, and, hence, a critical drop size, above which this coalescence does not occur. We also identify a drop size that maximizes liquid capture. For both wetting and deformation of the substrates, we present rules that are deduced from the geometric and material properties of the fibres and the volume of the drop. These ideas are applicable to a wide range of fibrous materials, as we illustrate with examples for feathers, beetle tarsi, sprays and microfabricated systems.

Owing to the numerous environmental and industrial applications of fibrous media, their wetting has been studied extensively. Most research focuses on drops or flow on individual rigid fibres, often in an array. However, in most applications, the elasticity of the fibres is important, as evidenced from the matting of feather barbules<sup>9</sup>, the shrinkage of porous fibre membranes<sup>8</sup>, strengthening of paper after drying<sup>20</sup>, the clumping of the setae of beetle tarsi after release of tarsal oil<sup>5</sup>, or the collapse of micro- or nanopillar arrays<sup>10–12</sup>. Therefore, we are motivated by the interaction of a mist of drops with a deformable, or flexible, array of fibres. The basic elastocapillary response is observed in the behaviour of a liquid drop on a pair of fibres, which is where we begin.

For a perfectly wetting drop (that is, a drop that connects with the fibre with a zero contact angle) deposited on two parallel, rigid fibres, the minimization of surface energy yields three distinct drop shapes depending on the ratio of the distance between the fibres,  $2d_0$  (measured from their outer surfaces), and their diameter,  $2r$  (Fig. 1b). As  $d_0/r$  is decreased, the drop evolves from a bridge to a barrel shape and then spreads out into a liquid column<sup>13–17</sup>: a drop forms for  $d_0/r > \sqrt{2}$ , a column forms for  $d_0/r < 0.57$  and there is non-uniqueness of the shape for  $0.57 < d_0/r < \sqrt{2}$ .

In this Letter, we investigate the behaviour of a perfectly wetting drop deposited onto two horizontal, flexible fibres that at one end are clamped, parallel to each other, a distance  $2d_0 > 2\sqrt{2}r$  apart and at the other end are free to move (Methods and Fig. 1a). Our results can be extended to the case of partial wetting by adding as an additional parameter the effective contact angle,  $\theta < \pi/2$  (Supplementary Fig. 4). We neglect gravitational effects because the fibres do not bend under

their own weight and the drop sizes are smaller than the capillary length,  $l_c$ , above which gravitational effects become important. By  $2d$  we denote the distance between the fibres at the drop location. When the drop is placed on the fibres close to the clamped ends, the fibres deflect inwards and the drop moves spontaneously towards the free ends, which are closer together (Fig. 1c and Supplementary Movie 2), as observed for a drop in a wedge<sup>21</sup>. As the drop advances, the deflection increases, that is,  $d/r$  continuously decreases. The drop accelerates, elongates and then spreads spontaneously between the fibres, drawing them together finally to form a liquid column between coalesced fibres.

We performed a large set of experiments to characterize the final state as a function of the drop volume,  $V$ ; the fibre length,  $L$ ; and the ratio  $d_0/r$  (Methods). For every value of  $d_0/r$ , we find three different final states as  $L$  and  $V$  are varied (Fig. 2a–c). Whereas the final state (drop or column) of a finite volume of liquid deposited on two rigid fibres depends on only one parameter, that is,  $d_0/r$ , and is hence independent of the drop volume and fibre length, we find that the final equilibrium state for a drop on two flexible fibres depends on six

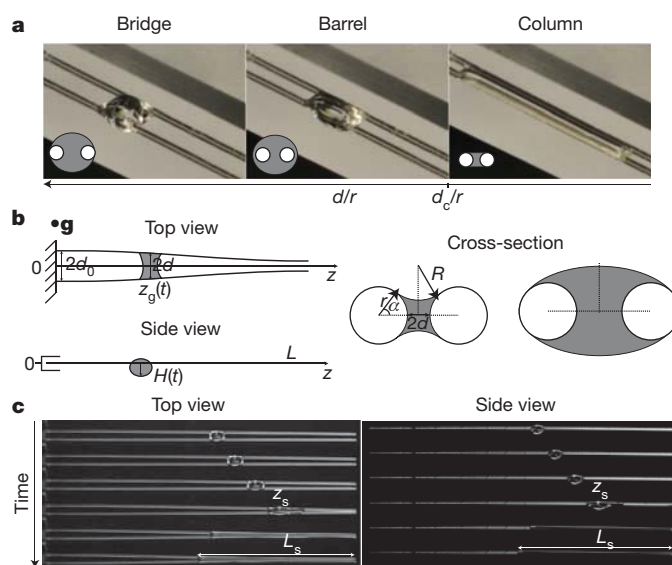


**Figure 1 | Shape transitions of a drop sitting on two parallel fibres.** **a**, A drop of perfectly wetting liquid (silicone oil) of volume  $2\ \mu\text{l}$  deposited on two parallel, rigid glass fibres (radius,  $r = 0.145\ \text{mm}$ ) adopts three different shapes depending on the distance between the fibres: a ‘bridge’ ( $d_0/r = 2.5$ ), a ‘barrel’ ( $d_0/r = 1.5$ ) and a column ( $d_0/r = 1$ ).  $d_c$ , critical distance at which the drop-to-column transition occurs. **b**, Experimental set-up used to investigate the behaviour of a drop deposited on two flexible fibres, which are clamped at one end and free to move at the other. Left: top and side views, recorded simultaneously using a mirror. Right: expected cross-sections for a concave liquid column and a convex drop. The direction of gravity is indicated by **g**. **c**, Typical experiment with  $d_0/r = 2.7$ ,  $V = 1.5\ \mu\text{l}$  and  $L = 4\ \text{cm}$ . The time between successive images is  $25\ \text{s}$ . When the drop is deposited on flexible fibres, the fibres deflect inward. The drop spontaneously moves towards the free ends of the fibres. At a given location,  $z_s$ , the drop starts spreading and the fibres are drawn together. The final wet length is denoted  $L_s$ .

<sup>1</sup>Department of Mechanical and Aerospace Engineering, Princeton University, Princeton, New Jersey 08544, USA. <sup>2</sup>CNRS, UMR 7190, Institut Jean le Rond d’Alembert, F-75005 Paris, France.

<sup>3</sup>UPMC Université Paris 06, UMR 7190, Institut Jean le Rond d’Alembert, F-75005 Paris, France.

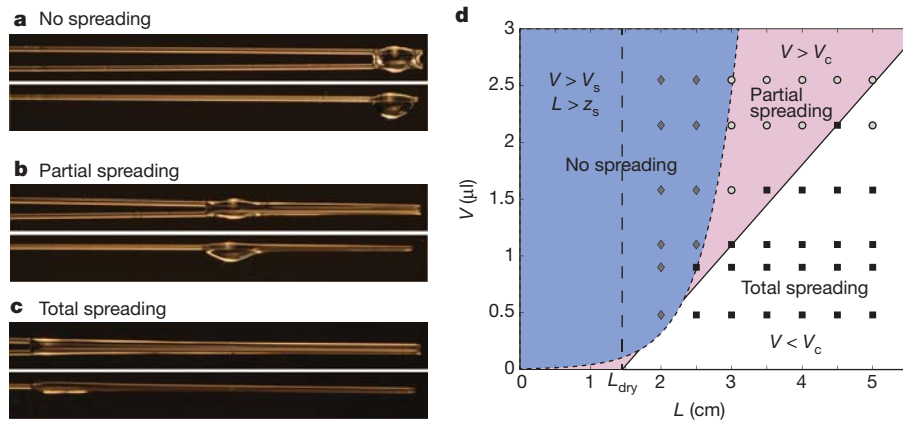


**Figure 2 | The three different final states of a drop between two flexible fibres.** **a–c**, Top and side views of the final state obtained for  $d_0/r = 2.6$ ; a fixed volume,  $V = 2 \mu\text{l}$ ; and increasing length,  $L = 3, 3.5$  and  $4$  cm. The final state changes from one of no spreading to one of partial spreading to one of total spreading as  $L$  increases. **d**, Phase diagram of the different regimes for

parameters:  $r$ ;  $d_0$ ;  $L$ ; the bending stiffness,  $B$ , of the fibre; the surface tension,  $\gamma$ ; and  $V$ . For short fibres ( $L \ll 2$  cm in the system presented in Fig. 2) and almost all drop volumes, the fibres deflect slightly inwards and the drop moves towards the free ends, but there is no spreading (Fig. 2a and Supplementary Movie 1). For longer fibres, there is a range of drop volumes such that when we increase  $L$ , the deflection increases and the whole drop spreads into a column ('total spreading'; Fig. 2c and Supplementary Movie 2). Alternatively, for sufficiently large volumes, we observe a state of 'partial spreading', where there is a liquid column with a smaller drop remaining at the edge (Fig. 2b and Supplementary Movie 3). We summarize in Fig. 2d our results in a phase diagram of  $V$  versus  $L$ , which suggests that a critical size of drops in a spray can trigger coalescence of a fibrous material.

To understand the transitions between the different regimes in Fig. 2d, we first consider the case of long fibres, for which either partial or total spreading occurs for all volumes investigated. We fix the fibre length and measure the length,  $L_s$ , along which the liquid spreads for various drop volumes (Fig. 3a). For small  $V$ , the whole drop spreads into a liquid column. As  $V$  increases, the column length increases until, above a critical volume,  $V_c$ , a drop remains at the wider end of the column and the length  $L_s$  actually decreases (Fig. 3a). The existence of a maximum spreading length here is a consequence of elasticity.

We can understand the maximum spreading length,  $L_{s,\text{max}}$ , reached at  $V_c$  as a balance between elasticity and capillarity. There is a minimal distance,  $L_{\text{dry}}$ , along which the dry portions of the fibres can be bent by

capillary forces. This is determined by minimizing the total energy of the system<sup>22</sup>, yielding

$$L_{\text{dry}} = \left( \frac{9Bd_0^2}{2\gamma r S(\alpha)} \right)^{1/4} \quad (1)$$

where  $S(\alpha)$  is a geometric factor evaluated approximately for a flat liquid column as  $S(\alpha = \pi/2) = \pi - 2$ . This length is the minimum length of the fibres beyond which collapse, or significant deformation, can occur. For a given  $d_0/r$  ratio,  $L_{\text{dry}}$  is constant and the maximum wet length,  $L_{s,\text{max}}$ , increases linearly with  $L$ , that is,  $L_{s,\text{max}} = L - L_{\text{dry}}$ , in agreement with our experiments (Supplementary Fig. 1). This elastocapillary balance results in an optimal, or critical, drop volume for which the spreading length is maximal:  $V_c = A(\alpha)L_{s,\text{max}}$ , where  $A(\alpha)$  is the column cross-section ( $A(\pi/2) \approx \pi r^2$  for a flat column). The boundary between total and partial spreading is then predicted to be

$$V = V_c = \pi r^2 (L - L_{\text{dry}}) \quad (2)$$

which is also in agreement with the experimental transition (Fig. 2d). When liquid is added to this maximum column (Supplementary Fig. 2), the configuration is unstable: the liquid forms a drop at the wider end of the column. Minimization of the surface energy causes the liquid to retract to form this spherical drop, decreasing the length of the column.

To understand the critical drop size beyond which no spreading (Fig. 2a) and, hence, no fibre coalescence occurs, we measured the spacing,  $d_s$ , at which the drop starts spreading. We find that the ratio

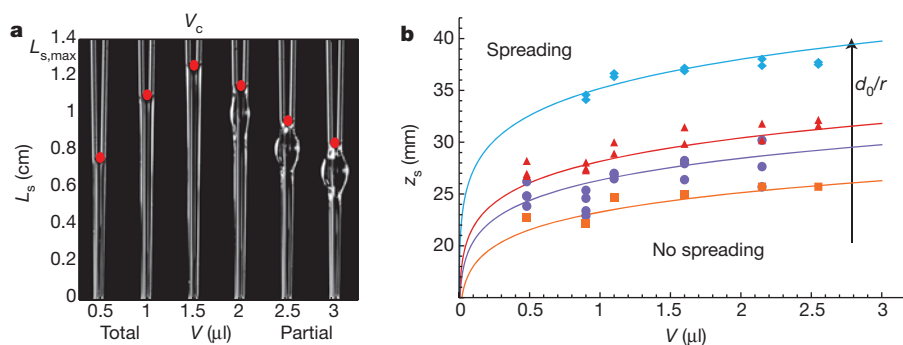


**Figure 3 | Influence of the initial drop volume on the final state.** **a**, Transition between total and partial spreading: evolution of the spreading length,  $L_s$ , with the volume,  $V$ , of the drop for  $d_0/r = 2.6$  and  $L = 3.5$  cm. We observe an optimum (maximum  $L_s$ ) at a critical volume of  $V_c = 1.5 \mu\text{l}$ . **b**, Transition between spreading and no spreading: evolution of the position of

the drop at spreading,  $z_s$ , with  $V$  for  $d_0/r = 1.9$  (orange),  $2.4$  (purple),  $2.7$  (red) and  $4.2$  (blue). The position of the drop at spreading is independent of the fibre length and increases with increasing volume, spacing and fibre rigidity (that is, the bending modulus, which is proportional to  $r^4$ ). The solid lines correspond to the theoretical prediction (Supplementary Information, equation (2)).

$d_s/r = 1.11 \pm 0.07$  is constant, independent of  $V$ ,  $L$  and  $d_0/r$ . We conclude that spreading occurs when locally the spacing between the fibres is such that a liquid column is energetically favourable relative to a drop. This criterion for spreading is similar to that obtained theoretically for rigid fibres<sup>13</sup> and similar to that found in our experiments on rigid glass fibres:  $d_s/r = 1.04 \pm 0.07$ .

Next we estimated the critical drop volume responsible for this spreading, where liquid is captured in a column. The drop is in a barrel shape (Fig. 1a) and thus is pierced by the two fibres. The capillary force applied by the drop,  $F \approx 2\gamma l^*$ , where  $l^*$  is the typical length of the contact line, brings the fibres together. Coalescence of fibres will therefore occur if  $F$  is great enough to achieve a deflection of  $d_0 - d_s$  along the fibres, that is, if the capillary torque,  $Fz_s$ , where  $z_s$  is the position of the drop, equals the elastic resisting torque,  $B(d_0 - d_s)/z_s^2$ . For a given value of  $V$  and, hence,  $F$ , this estimate leads to a critical drop position,  $z_s^3 \propto B(d_0 - d_s)/F$ , below which no spreading will occur, which is also verified experimentally (Fig. 3b). For a fixed value of  $d_0$ ,  $z_s$  increases with increasing volume and, hence, the capillary force decreases. Therefore, for a given fibre length, there is a minimal force, that is, a maximal drop volume, for spreading to occur, set by  $z_s = L$ . The force  $F \approx 2\gamma l^*$  depends on the complex shape of the contact line, which has a typical length  $l^* \propto 2\pi r d_s V^{-1/3}$  (Supplementary Information). Combining these results yields the critical volume for spreading

$$V_s \approx \left( \beta \frac{\gamma d_s r L^3}{B(d_0 - d_s)} \right)^3 \quad (3)$$

where the constant  $\beta$  depends only on the complex shape of the drop (Supplementary Fig. 3); this result involves all of the geometric and material properties. The boundary between the regimes of spreading and no spreading,  $V = V_s$ , is in agreement with the experiments (Fig. 2d).

Because the final state of the drop placed on the fibre array depends on the six parameters  $r$ ,  $d_0$ ,  $L$ ,  $B$ ,  $\gamma$  and  $V$ , we conclude by dimensional analysis that the system is characterized by three parameters,  $L/L_{s,\max}$ ,  $V/V_c$  and  $d_0/r$  where  $L_{s,\max} = L - L_{\text{dry}}$  (from equation (1)) and  $V_c = \pi r^2 L_{s,\max}$  (from equation (2)). We define a phase diagram of the three possible final states in the space of the two parameters  $L/L_{s,\max}$  and  $V/V_c$  (Fig. 4a). First we identify a threshold,  $V/V_c = 1$ , below which a drop will always totally spread, which maximizes the wetted length and the amount of trapped liquid. Second, for  $V/V_c > 1$ , the spreading is partial: the remaining edge drop can be shed by any perturbation such as shaking, which results in a smaller amount of liquid being captured by the fibre array. The transition from spreading to no spreading ( $V > V_s$ ) is identified by equation (3) and depends on the parameter  $d_0/r$  as reflected by the successive hyperbolic curves in Fig. 4a. For partial wetting,  $\theta$ , the effective contact angle, should be included in equations (1), (2) and (3) (Supplementary Information and Supplementary Figs 4–7). All of the experimental data (symbols in Fig. 4a) obtained by varying all of the parameters are well within each regime defined by the model.

This map allows us to predict the interaction of natural or engineered fibrous materials with a mist of drops. An example of a natural fibre array is a bird feather, which consists of well-ordered hair-like structures (barbs and barbules) that produce hydrophobicity and thermal insulation<sup>1,3</sup>. Small amounts of oil disrupt this arrangement by clumping adjacent barbules, affecting their water repellency and insulating properties and thus reducing the survival rate of oiled birds<sup>9,23</sup>. We sprayed a polydisperse aerosol of oil on goose feathers and observed all three possible final states (Fig. 4b). Using our model system, we find that a volume of oil less than  $V_c$  (here a drop radius less than 20  $\mu\text{m}$ ) spreads, thus clumping adjacent barbules and making the cleaning process difficult. Drops larger than  $V_s$  (drop radius, 140  $\mu\text{m}$ ) do not spread and may be dislodged from the bird's plumage. These results are in agreement with our map (Fig. 4a). Despite complex initial conditions (multiple fibres and/or drops, different wettabilities or surface

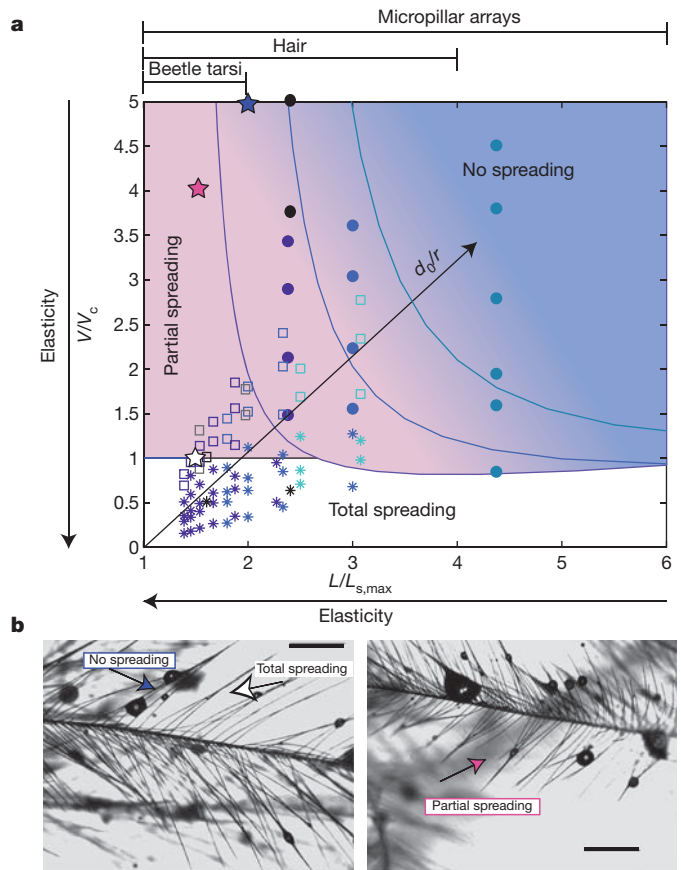


**Figure 4 | Aerosol size and fibre matrix properties needed to collect, trap or displace a known volume of liquid.** **a**, Map of the three spreading regimes as a function of the two dimensionless parameters  $L/L_{s,\max}$  and  $V/V_c$ . The solid curves show three limits for  $d_0/r = 2.4$ , 2.7 and 4.2 and the points show data for total spreading (asterisks), partial spreading (squares) and no spreading (circles) of silicone oil (total wetting,  $d_0/r = 2.1$ ; blue and purple points) and water (partial wetting,  $d_0/r = 3$ ; black and grey points). Stars correspond to the three situations observed in **b**. **b**, Microscope pictures of goose feathers sprayed with oil (smaller drops have volumes of order  $10^{-14}$ – $10^{-13}$   $\text{m}^3$ ), showing no spreading ( $d_0/r = 4.8$ ,  $L/L_{s,\max} = 2$ ,  $V/V_c \approx 5$ ; blue star in **a**), total spreading ( $d_0/r = 3.4$ ,  $L/L_{s,\max} = 1.5$  and  $L_s = L_{s,\max} = 0.8$  mm; white star in **a**) and partial spreading ( $d_0/r = 3.5$ ,  $L/L_{s,\max} = 1.5$ ,  $V/V_c \approx 4$ ; pink star in **a**) in agreement with our predictions. Scale bars, 500  $\mu\text{m}$ .

roughnesses) the final states can thus be captured by our model and we can predict the main effects arising when a mist of drops interacts with a dilute fibre array.

In addition, aerosol-removal filters, hairsprays, adhesive pads for insects and some applications in microstructure design require total spreading, that is, optimal coating of the fibres or maximal liquid capture. Conversely, fibres in living systems may have evolved a certain length or material properties to adapt to their environmental conditions. For example, we can now use our model to make quantitative estimates for various fibrous media and liquids (Supplementary Table 1) as reported in the universal map (Fig. 4a). For beetles, we predict that drops of optimal diameter 5  $\mu\text{m}$  released from ventral pores travel along the setae and spread totally (that is, without liquid loss) where the tarsi contact a substrate; we predict that the collapse of pillars in microfabrication, observed during solvent evaporation<sup>10–12</sup>, could be controlled by depositing an optimum volume of liquid (drops of diameter 0.9–5.4  $\mu\text{m}$ ); and we predict that microstructures could be designed to respond (by changing colour) to aerosols of different drop sizes because light scattering is influenced by clustering of the microelements. These examples illustrate the wide range of flexible systems that could be controlled using elastocapillarity and an optimally chosen drop volume.



## METHODS SUMMARY

The glass fibres (radius,  $r = 0.145$  mm; bending stiffnesses,  $B = 1 \times 10^{-6}$  N m<sup>2</sup> and  $B = 7 \times 10^{-7}$  N m<sup>2</sup>; length,  $2 \text{ cm} < L < 5.5 \text{ cm}$ ) are clamped at one end, separated by a distance  $2d_0$  ( $d_0/r = 1.9, 2.1, 2.6$  and  $4.3$ ). A drop of silicone oil (viscosity,  $\eta = 97$  mPa s; density,  $\rho = 970 \text{ kg m}^{-3}$ ; surface tension,  $\gamma = 0.021 \text{ N m}^{-1}$ ) of controlled volume  $V$  ( $0.48 \mu\text{l} < V < 2.55 \mu\text{l}$ ) precise to 5% for large volumes and to 10% for smaller volumes, is deposited onto the fibres with a micropipette, close to the clamped edge. The positions of the front,  $z_f(t)$ , and the rear,  $z_r(t)$ , of the drop (relative to the clamped end at  $z = 0$ ), as well as the distance between the fibres,  $d$ , are recorded from the top with a digital camera. A mirror placed at  $45^\circ$  allows us to capture a simultaneous side view of the drop and measure its size,  $H(z, t)$ . We define the average position of the drop as  $z_g = (z_f + z_r)/2$ , and its length is  $l = z_f - z_r$ . The capillary length,  $l_c = (\gamma/\rho g)^{1/2}$ , is the length beyond which gravitational effects become more important than capillary effects. Here  $l_c = 1.5$  mm.

Received 8 August; accepted 6 December 2011.

- Rijke, A. M. & Jesser, W. A. The feather structure of dippers: water repellency and resistance to water penetration. *Wilson J. Ornithol.* **122**, 563–568 (2010).
- Rijke, B. Y. A. M. The water repellency and feather structure of cormorants, *Phalacrocoracidae*. *J. Exp. Biol.* **48**, 185–189 (1968).
- Dawson, C., Vincent, J., Jeronimidis, G., Rice, G. & Forshaw, P. Heat transfer through penguin feathers. *J. Theor. Biol.* **199**, 291–295 (1999).
- Zi, J. *et al.* Coloration strategies in peacock feathers. *Proc. Natl Acad. Sci. USA* **100**, 12576–12578 (2003).
- Eisner, T. & Aneshansley, D. J. Defense by foot adhesion in a beetle (*Hemisphaerota cyanea*). *Proc. Natl Acad. Sci. USA* **97**, 6568–6573 (2000).
- Liu, K. & Jiang, L. Bio-inspired design of multiscale structures for function integration. *Nano Today* **6**, 155–175 (2011).
- Eadie, L. & Ghosh, T. K. Biomimicry in textiles: past, present and potential. An overview. *J. R. Soc. Interface* **6**, 761–775 (2011).
- Kamo, J., Hiram, T. & Kamada, K. Solvent-induced morphological change of microporous hollow fiber membranes. *J. Membr. Sci.* **70**, 217–224 (1992).
- O'Hara, P. D. & Morandin, L. A. Effects of sheens associated with offshore oil and gas development on the feather microstructure of pelagic seabirds. *Mar. Pollut. Bull.* **60**, 672–678 (2010).
- Pokroy, B., Kang, S. H., Mahadevan, L. & Aizenberg, J. Self-organization of a mesoscale bristle into ordered, hierarchical helical assemblies. *Science* **323**, 237–240 (2009).
- Chandra, D. & Yang, S. Stability of high-aspect-ratio micropillar arrays against adhesive and capillary forces. *Acc. Chem. Res.* **43**, 1080–1091 (2010).
- Chandra, D., Yang, S., Soshinsky, A. & Gambogi, R. J. Biomimetic ultrathin whitening by capillary-force-induced random clustering of hydrogel micropillar arrays. *ACS Appl. Mater. Interfaces* **1**, 1698–1704 (2009).
- Princen, H. Capillary phenomena in assemblies of parallel cylinders III. Liquid columns between horizontal parallel cylinders. *J. Colloid Interface Sci.* **34**, 171–184 (1970).
- Wu, X.-F., Bedarkar, A. & Vaynberg, K. A. Droplets wetting on filament rails: surface energy and morphology transition. *J. Colloid Interface Sci.* **341**, 326–332 (2010).
- Bedarkar, A., Wu, X.-f. & Vaynberg, A. Wetting of liquid droplets on two parallel filaments. *Appl. Surf. Sci.* **256**, 7260–7264 (2010).
- Minor, F. W., Schwartz, M., Wulkow, E., a. & Buckles, L. C. Part III: The behavior of liquids on single textile fibers. *Text. Res. J.* **29**, 940–949 (1959).
- Keis, K., Kornev, K. G., Kamath, Y. K. & Neimark, A. V. in *Nanoengineered Nanofibrous Materials* (eds Guceri, S., Gogotsi, Y. G. & Kuznetsov, V.) 173–180 (Kluwer, 2004).
- Kwon, H.-M., Kim, H.-Y., Puëll, J. R. M. & Mahadevan, L. Equilibrium of an elastically confined liquid drop. *J. Appl. Phys.* **103**, 093519 (2008).
- Roman, B. & Bico, J. Elasto-capillarity: deforming an elastic structure with a liquid droplet. *J. Phys. Condens. Matter* **22**, 493101 (2010).
- Hubbe, M. A. Bonding between cellulosic fibers in the absence and presence of dry-strength agents - a review. *BioResources* **1**, 281–318 (2006).
- Prakash, M., Quéré, D. & Bush, J. W. M. Surface tension transport of prey by feeding shorebirds: the capillary ratchet. *Science* **320**, 931–934 (2008).
- Py, C., Bastien, R., Bico, J., Roman, B. & Boudaoud, A. 3D aggregation of wet fibers. *Europhys. Lett.* **77**, 44005 (2007).
- Hartung, R. Energy metabolism in oil-covered ducks. *J. Wildl. Mgmt* **31**, 798–804 (1967).

**Supplementary Information** is linked to the online version of the paper at [www.nature.com/nature](http://www.nature.com/nature).

**Acknowledgements** C.D. and H.A.S. acknowledge Unilever and the NFS for financial support. S.P. acknowledges financial support from the Emergence(s) Program of the City of Paris and CNRS and thanks Princeton University for its hospitality. We thank A. Lips and P. Warren for comments.

**Author Contributions** C.D. and S.P. designed the experiments; A.Y.B., C.D. and S.P. carried out the experiments; C.D., S.P. and H.A.S. discussed and interpreted the results; C.D. and H.A.S. developed the models; and C.D., S.P. and H.A.S. wrote the manuscript.

**Author Information** Reprints and permissions information is available at [www.nature.com/reprints](http://www.nature.com/reprints). The authors declare no competing financial interests. Readers are welcome to comment on the online version of this article at [www.nature.com/nature](http://www.nature.com/nature). Correspondence and requests for materials should be addressed to H.A.S. ([hastone@princeton.edu](mailto:hastone@princeton.edu)).

# Recent contributions of glaciers and ice caps to sea level rise

Thomas Jacob<sup>1†</sup>, John Wahr<sup>1</sup>, W. Tad Pfeffer<sup>2,3</sup> & Sean Swenson<sup>4</sup>

Glaciers and ice caps (GICs) are important contributors to present-day global mean sea level rise<sup>1–4</sup>. Most previous global mass balance estimates for GICs rely on extrapolation of sparse mass balance measurements<sup>1,2,4</sup> representing only a small fraction of the GIC area, leaving their overall contribution to sea level rise unclear. Here we show that GICs, excluding the Greenland and Antarctic peripheral GICs, lost mass at a rate of  $148 \pm 30 \text{ Gt yr}^{-1}$  from January 2003 to December 2010, contributing  $0.41 \pm 0.08 \text{ mm yr}^{-1}$  to sea level rise. Our results are based on a global, simultaneous inversion of monthly GRACE-derived satellite gravity fields, from which we calculate the mass change over all ice-covered regions greater in area than  $100 \text{ km}^2$ . The GIC rate for 2003–2010 is about 30 per cent smaller than the previous mass balance estimate that most closely matches our study period<sup>2</sup>. The high mountains of Asia, in particular, show a mass loss of only  $4 \pm 20 \text{ Gt yr}^{-1}$  for 2003–2010, compared with  $47\text{--}55 \text{ Gt yr}^{-1}$  in previously published estimates<sup>2,5</sup>. For completeness, we also estimate that the Greenland and Antarctic ice sheets, including their peripheral GICs, contributed  $1.06 \pm 0.19 \text{ mm yr}^{-1}$  to sea level rise over the same time period. The total contribution to sea level rise from all ice-covered regions is thus  $1.48 \pm 0.26 \text{ mm yr}^{-1}$ , which agrees well with independent estimates of sea level rise originating from land ice loss and other terrestrial sources<sup>6</sup>.

Interpolation of sparse mass balance measurements on selected glaciers is usually used to estimate global GIC mass balance<sup>1,2,4</sup>. Models are also used<sup>3,7</sup>, but these depend on the quality of input climate data and include simplified glacial processes. Excluding Greenland and Antarctic peripheral GICs (PGICs), GICs have variously been reported to have contributed  $0.43\text{--}0.51 \text{ mm yr}^{-1}$  to sea level rise (SLR) during 1961–2004<sup>3,7,8</sup>,  $0.77 \text{ mm yr}^{-1}$  during 2001–2004<sup>8</sup>,  $1.12 \text{ mm yr}^{-1}$  during 2001–2005<sup>1</sup> and  $0.95 \text{ mm yr}^{-1}$  during 2002–2006<sup>2</sup>.

The Gravity Recovery and Climate Experiment (GRACE) satellite mission<sup>9</sup> has provided monthly, global gravity field solutions since 2002, allowing users to calculate mass variations at the Earth's surface<sup>10</sup>. GRACE has been used to monitor the mass balance of selected GIC regions<sup>11–14</sup> that show large ice mass loss, as well as of Antarctica and Greenland<sup>15</sup>.

Here we present a GRACE solution that details individual mass balance results for every region of Earth with large ice-covered areas. The main focus of this paper is on GICs, excluding Antarctic and Greenland PGICs. For completeness, however, we also include results for the Antarctic and Greenland ice sheets with their PGICs. GRACE does not have the resolution to separate the Greenland and Antarctic ice sheets from their PGICs. All results are computed for the same 8-yr time period (2003–2010).

To determine losses of individual GIC regions, we cover each region with one or more 'mascons' (small, arbitrarily defined regions of Earth) and fit mass values for each mascon (ref. 16 and Supplementary Information) to the GRACE gravity fields, after correcting for

hydrology and for glacial isostatic adjustment (GIA) computed using the ICE-5G deglaciation model. We use 94 monthly GRACE solutions from the University of Texas Center for Space Research, spanning January 2003 to December 2010. The GIA corrections do not include the effects of post-Little Ice Age (LIA) isostatic rebound, which we separately evaluate and remove. All above contributions and their effects on the GRACE solutions are discussed in Supplementary Information.

Figure 1 shows mascons for all ice-covered regions, constructed from the Digital Chart of the World<sup>17</sup> and the Circum-Arctic Map of Permafrost and Ground-Ice Conditions<sup>18</sup>. Each ice-covered region is chosen as a single mascon, or as the union of several non-overlapping mascons. We group 175 mascons into 20 regions. Geographically isolated regions with glacierized areas less than  $100 \text{ km}^2$  in area are excluded. Because GRACE detects total mass change, its results for an ice-covered region are independent of the glacierized surface area (Supplementary Information).

Mass balance rates for each region are shown in Table 1 (see Supplementary Information for details on the computation of the rates and uncertainties). We note that Table 1 includes a few positive rates, but none are significantly different from zero. We also performed an inversion with GRACE fields from the GFZ German Research Centre for Geosciences and obtained results that agreed with those from the Center for Space Research (Table 1) to within 5% for each region.

The results in Table 1 are in general agreement with previous GRACE studies for the large mass loss regions of the Canadian Arctic<sup>12</sup> and Patagonia<sup>11</sup>, as well as for the Greenland and Antarctic ice sheets with

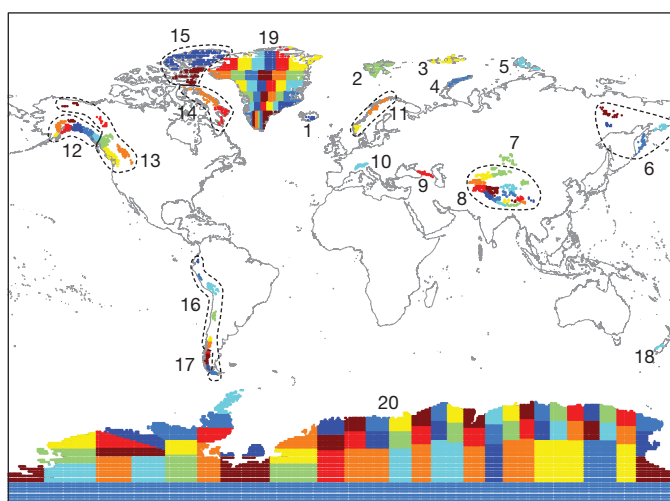


**Figure 1 | Mascons for the ice-covered regions considered here.** Each coloured region represents a single mascon. Numbers correspond to regions shown in Table 1. Regions containing more than one mascon are outlined with a dashed line.

<sup>1</sup>Department of Physics and Cooperative Institute for Environmental Studies, University of Colorado at Boulder, Boulder, Colorado 80309, USA. <sup>2</sup>Institute of Arctic and Alpine Research, University of Colorado at Boulder, Boulder, Colorado 80309, USA. <sup>3</sup>Department of Civil, Environmental, and Architectural Engineering, University of Colorado at Boulder, Boulder, Colorado 80309, USA. <sup>4</sup>National Center for Atmospheric Research, Boulder, Colorado 80305, USA. <sup>†</sup>Present address: Bureau de Recherches Géologiques et Minières, Orléans 45060, France.

**Table 1 | Inverted 2003–2010 mass balance rates**

Region	Rate (Gt yr <sup>-1</sup> )
1. Iceland	-11 ± 2
2. Svalbard	-3 ± 2
3. Franz Josef Land	0 ± 2
4. Novaya Zemlya	-4 ± 2
5. Severnaya Zemlya	-1 ± 2
6. Siberia and Kamchatka	2 ± 10
7. Altai	3 ± 6
8. High Mountain Asia	-4 ± 20
8a. Tianshan	-5 ± 6
8b. Pamirs and Kunlun Shan	-1 ± 5
8c. Himalaya and Karakoram	-5 ± 6
8d. Tibet and Qilian Shan	7 ± 7
9. Caucasus	1 ± 3
10. Alps	-2 ± 3
11. Scandinavia	3 ± 5
12. Alaska	-46 ± 7
13. Northwest America excl. Alaska	5 ± 8
14. Baffin Island	-33 ± 5
15. Ellesmere, Axel Heiberg and Devon Islands	-34 ± 6
16. South America excl. Patagonia	-6 ± 12
17. Patagonia	-23 ± 9
18. New Zealand	2 ± 3
19. Greenland ice sheet + PGICs	-222 ± 9
20. Antarctica ice sheet + PGICs	-165 ± 72
Total	-536 ± 93
GICs excl. Greenland and Antarctica PGICs	-148 ± 30
Antarctica + Greenland ice sheet and PGICs	-384 ± 71
Total contribution to SLR	1.48 ± 0.26 mm yr <sup>-1</sup>
SLR due to GICs excl. Greenland and Antarctica PGICs	0.41 ± 0.08 mm yr <sup>-1</sup>
SLR due to Antarctica + Greenland ice sheet and PGICs	1.06 ± 0.19 mm yr <sup>-1</sup>

Uncertainties are given at the 95% (2σ) confidence level.

their PGICs<sup>19</sup>. Our results for Alaska also show considerable mass loss, although our mass loss rate is smaller than some previously published GRACE-derived rates that used shorter and earlier GRACE data spans (Supplementary Information). The global GIC mass balance, excluding Greenland and Antarctic PGICs, is  $-148 \pm 30 \text{ Gt yr}^{-1}$ , contributing  $0.41 \pm 0.08 \text{ mm yr}^{-1}$  to SLR.

Mass balance time series for all GIC regions are shown in Fig. 2. The seasonal and interannual variabilities evident in these time series have contributions from ice and snow variability on the glaciers, as well as from imperfectly modelled hydrological signals in adjacent regions and from random GRACE observational errors. Interannual variability can affect rates determined over short time intervals. Figure 2 and Supplementary Table 2 show that there was considerable interannual variability during 2003–2010 for some of the regions, especially High Mountain Asia (HMA). The HMA results in Supplementary Table 2 show that this variability induces large swings in the trend solutions when it is fitted to subsets of the entire time period. These results suggest that care should be taken in extending the 2003–2010 results presented in this paper to longer time periods.

For comparison with studies in which PGICs are included with GICs, we upscale our GIC-alone rate to obtain a GIC rate that includes PGIC, based on ref. 3 (Supplementary Information). The result is that GICs including PGICs lost mass at a rate of  $229 \pm 82 \text{ Gt yr}^{-1}$  ( $0.63 \pm 0.23 \text{ mm yr}^{-1}$  SLR), and that the combined ice sheets without their PGICs lost mass at  $303 \pm 100 \text{ Gt yr}^{-1}$  ( $0.84 \pm 0.28 \text{ mm yr}^{-1}$  SLR). Although no other study encompasses the same time span, published non-GRACE estimates for GICs plus PGICs are larger:  $0.98 \pm 0.19 \text{ mm yr}^{-1}$  over 2001–2004<sup>8</sup>,  $1.41 \pm 0.20 \text{ mm yr}^{-1}$  over 2001–2005<sup>1</sup> and  $0.765 \text{ mm yr}^{-1}$  (no uncertainty given) over 2006–2010<sup>20</sup>. These differences could be due to the small number of mass balance measurements those estimates must rely on, combined with uncertain regional glacier extents. In addition, there are indications from more recent non-GRACE measurements that the GIC mass loss rate decreased markedly beginning in 2005<sup>20</sup>.

Our results for HMA disagree significantly with previous studies. A recent GRACE-based study<sup>5</sup> over 2002–2009 yields significantly

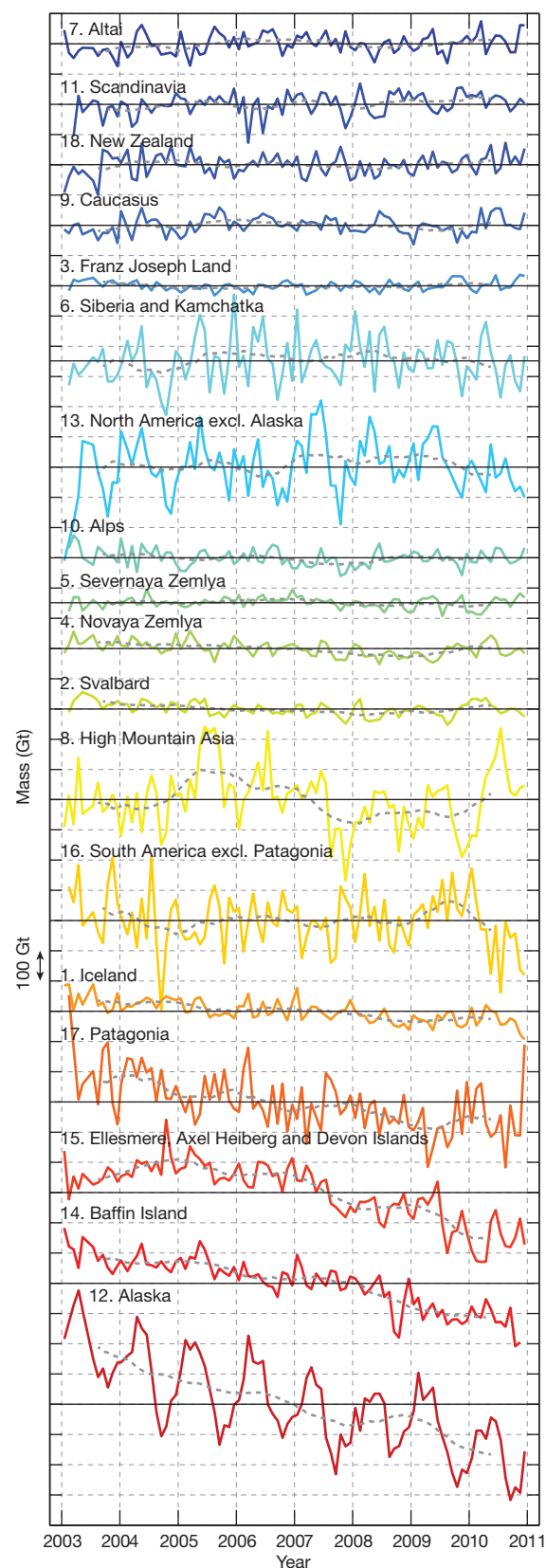


**Figure 2 | Mass change during 2003–2010 for all GIC regions shown in Fig. 1 and Table 1.** The black horizontal lines run through the averages of the time series. The grey lines represent 13-month-window, low-pass-filtered versions of the data. Time series are shifted for legibility. Modelled contributions from GIA, LIA and hydrology have been removed.



larger mass loss for HMA than does ours; we explain why the result of ref. 5 may be flawed in Supplementary Information. Conventional mass balance methods have been used to estimate a 2002–2006 rate of  $-55 \text{ Gt yr}^{-1}$  for this entire region<sup>2</sup>, with  $-29 \text{ Gt yr}^{-1}$  over the eastern Himalayas alone, by contrast with our HMA estimate, of  $-4 \pm 20 \text{ Gt yr}^{-1}$  (Table 1). We show results for the four subregions of HMA (Fig. 3) in Table 1.

This difference prompts us to examine this region in more detail. GRACE mass trends show considerable mass loss across the plains of northern India, Pakistan and Bangladesh, centred south of the glaciers and at low elevations (Fig. 3a, b). Some of the edges of this mass loss region seem to extend over adjacent mountainous areas to the north, but much of that, particularly above north-central India, is leakage of the plains signal caused by the 350-km Gaussian smoothing function used to generate the figure. The plains signal has previously been identified as groundwater loss<sup>16,21</sup>. To minimize leakage in the HMA GIC estimates, additional mascons are chosen to cover the plains (Fig. 3a), the sum of which gives an average 2003–2010 water loss rate of  $35 \text{ Gt yr}^{-1}$ . Our plains results are consistent with the results of refs 16 and 21, which span shorter time periods.

The lack of notable mass loss over glacierized regions is consistent with our HMA mascon solutions that indicate relatively modest losses (Table 1). We simulate what the ice loss rates predicted by ref. 2 would

look like in the GRACE results. We use those rates to construct synthetic gravity fields and process them using the same methods applied to the GRACE data, to generate the trend map shown in Fig. 3c. It is apparent that an ice loss of this order would appear in the GRACE map as a large mass loss signal centred over the eastern Himalayas, far larger in amplitude and extent than the GRACE results in that region (compare Fig. 3b with Fig. 3c).

It is reasonable to wonder whether a tectonic process could be causing a positive signal in the glacierized region that offsets a large negative glacier signal in HMA. To see what this positive rate would have to look like, we remove the simulated gravity field (based on ref. 2) from the GRACE data and show the resulting difference map in Fig. 3d. If the ice loss estimate were correct, the tectonic process would be causing an anomalous mass increase over the Himalayas of  $\sim 3 \text{ cm yr}^{-1}$  equivalent water thickness, equivalent to  $\sim 1 \text{ cm yr}^{-1}$  of uncompensated crustal uplift. Although we cannot categorically rule out such a possibility, it seems unlikely. Global Positioning System and levelling observations in this region indicate long-term uplift rates as large as  $0.5\text{--}0.7 \text{ cm yr}^{-1}$  in some places<sup>22,23</sup>. But it is highly probable that any broad-scale tectonic uplift would be isostatically compensated by an increasing mass deficiency at depth, with little net effect on gravity<sup>24</sup> and, consequently, no significant contribution to the GRACE results. The effects of compensation are evident in the static gravity field. Supplementary Fig. 4

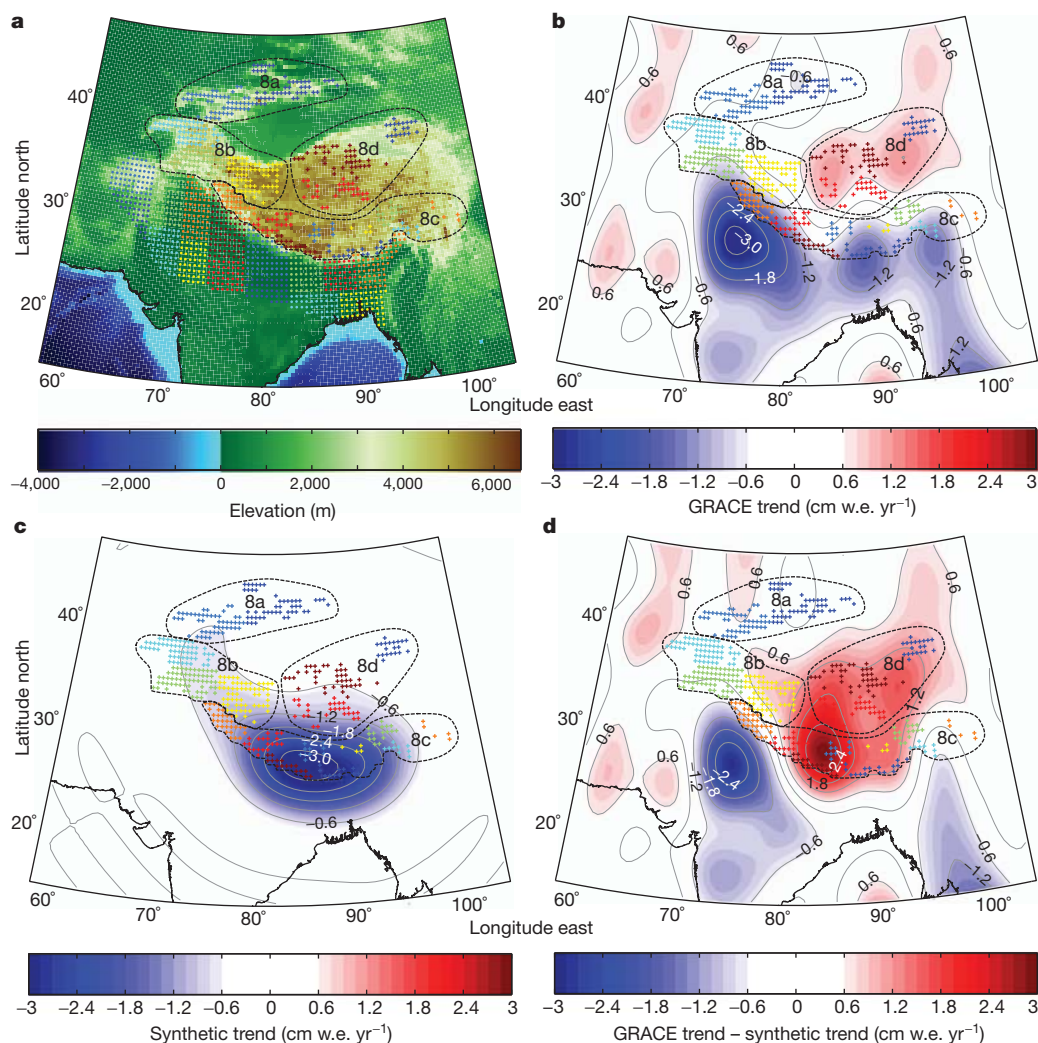


**Figure 3 | HMA mass balance determination.** **a**, Topographic map overlaid with the HMA mascons (crosses) and India plain mascons (dots); the dashed lines delimit the four HMA subregions (labelled as in Table 1). **b**, GRACE mass rate corrected for hydrology and GIA and smoothed with a 350-km Gaussian

smoothing function, overlaid with the HMA mascons. w.e., water equivalent. **c**, Synthetic GRACE rates that would be caused by a total mass loss of  $55 \text{ Gt yr}^{-1}$  over HMA mascons, with  $29 \text{ Gt yr}^{-1}$  over the eastern Himalayas, after ref. 2. **d**, The difference between **b** and **c**.

shows the free-air gravity field, computed using a 350-km Gaussian smoothing function (used to generate Fig. 3) applied to the EGM96 mean global gravity field<sup>25</sup>. The topography leaves no apparent signature on the static gravity field at these scales, indicating near-perfect compensation.

For a solid-Earth process to affect GRACE significantly, it must be largely isostatically uncompensated, which for these broad spatial scales would require characteristic timescales of the same order or less than the mantle's viscoelastic relaxation times (several hundred to a few thousand years). One possible such process might be the ongoing viscoelastic response of the Earth to past glacial unloading. We have investigated this effect, as well as possible contributions from erosion, and find that neither is likely to be important (Supplementary Information).

Another possible explanation for the lack of a large GRACE HMA signal is that most of the glacier melt water might be sinking into the ground before it has a chance to leave the glaciated region, thus causing GRACE to show little net mass change. Some groundwater recharge undoubtedly does occur, but it seems unlikely that such cancellation would be this complete. Much of HMA, for example, is permafrost, so local storage capacity is small (see the Circum-Arctic Map of Permafrost and Ground-Ice Conditions; [http://nsidc.org/fgdc/maps/ipa\\_browse.html](http://nsidc.org/fgdc/maps/ipa_browse.html)). Therefore, although there would be surface melt, the frozen ground would inhibit local recharge and there would be little ability to store the melt water locally. How far the water might have to travel before finding recharge pathways, we do not know. It is true that some rivers originating in portions of HMA do not reach the sea. Most notable are the Amu Darya and Syr Darya, which historically feed the Aral Sea but have been diverted for irrigation. Any fraction of that diverted water that ends up recharging aquifers will not directly contribute to SLR. However, the irrigation areas lie well outside our HMA mascons, and so even if there is notable recharge it is unlikely to affect the HMA mascon solutions significantly.

Our emphasis here is on GICs; the Greenland and Antarctic ice sheets have previously been well studied with GRACE<sup>15</sup>. But for comparison with non-GRACE global estimates, we combine our GIC results with our estimates for Greenland plus Antarctica to obtain a total SLR contribution from all ice-covered regions of  $1.48 \pm 0.26 \text{ mm yr}^{-1}$  during 2003–2010. Within the uncertainties, this value compares favourably with the estimate of  $1.8 \pm 0.5 \text{ mm yr}^{-1}$  for 2006 from ref 4. However, there are regional differences between these and prior results, which need further study and reconciliation.

SLR from the addition of new water can be determined from GRACE alone as well as by subtracting Argo steric heights from altimetric SLR measurements<sup>6</sup>. The most recent new-water SLR estimate, comparing the two methods, is  $1.3 \pm 0.6 \text{ mm yr}^{-1}$  for 2005–2010<sup>6</sup>, which agrees with our total ice-covered SLR value to within the uncertainties. The difference,  $0.2 \pm 0.6 \text{ mm yr}^{-1}$ , could represent an increase in land water storage outside ice-covered regions, but we note that it is not significantly different from zero.

## METHODS SUMMARY

GRACE solutions consist of spherical harmonic (Stokes) coefficients and are used to determine month-to-month variations in Earth's mass distribution<sup>9,10</sup>. We use monthly values of  $C_{20}$  (the zonal, degree-2 spherical harmonic coefficient of the geopotential) from satellite laser ranging<sup>26</sup>, and include degree-one terms<sup>27</sup>.

To determine mass variability for each mascon, we find the set of Stokes coefficients produced by a unit mass distributed uniformly across that mascon. We fit these sets of Stokes coefficients, simultaneously, to the GRACE Stokes coefficients, to obtain monthly mass values for each mascon. This method is similar to previously published mascon methods<sup>28</sup>, though here we fit to Stokes coefficients rather than to raw satellite measurements and we do not impose smoothness constraints. To determine the optimal shape and number of mascons in a region, we construct a sensitivity kernel for several possible configurations, and choose the configuration that optimizes that kernel and minimizes the GRACE trend residuals (Supplementary Fig. 1c).

The average of two land surface models is used to correct for hydrology, and the model differences are used to estimate uncertainties (Supplementary Information).

LIA loading corrections have been previously derived for Alaska<sup>13</sup> and Patagonia<sup>29</sup>, and equal 7 and 9  $\text{Gt yr}^{-1}$ , respectively. These numbers are subtracted from our Alaska and Patagonia inversions. For other GIC regions, where LIA characteristics are not well known, we estimate an upper bound for the correction by constructing a GIA model that tends to maximize the positive LIA gravity trend. Of all the additional GIC regions, only HMA has a predicted LIA correction that reaches 1  $\text{Gt yr}^{-1}$ . There, the model suggests we remove 5  $\text{Gt yr}^{-1}$  from our inverted result. But because the LIA correction in this region is likely to be an overestimate (Supplementary Information), our preferred result splits the difference (Supplementary Table 1), and we use that difference to augment the total HMA uncertainty.

Received 28 July 2011; accepted 9 January 2012.

Published online 8 February 2012.

- Cogley, J. G. Geodetic and direct mass-balance measurements: comparison and joint analysis. *Ann. Glaciol.* **50**, 96–100 (2009).
- Dyrugorov, M. B. Reanalysis of glacier changes: from the IGY to the IPY, 1960–2008. *Data Glaciol. Stud.* **108**, 1–116 (2010).
- Hock, R., de Woul, M., Radic, V. & Dyrugorov, M. Mountain glaciers and ice caps around Antarctica make a large sea-level rise contribution. *Geophys. Res. Lett.* **36**, L07501 (2009).
- Meier, M. F. *et al.* Glaciers dominate eustatic sea-level rise in the 21st century. *Science* **317**, 1064–1067 (2007).
- Matsuo, K. & Heki, K. Time-variable ice loss in Asian high mountains from satellite gravimetry. *Earth Planet. Sci. Lett.* **290**, 30–36 (2010).
- Willis, J. K., Chambers, D. P., Kuo, C. Y. & Shum, C. K. Global sea level rise, recent progress and challenges for the decade to come. *Oceanography (Wash. DC)* **23**, 26–35 (2010).
- Hirabayashi, Y., Doll, P. & Kanae, S. Global-scale modeling of glacier mass balances for water resources assessments: glacier mass changes between 1948 and 2006. *J. Hydrol. (Amst.)* **390**, 245–256 (2010).
- Kaser, G., Cogley, J. G., Dyrugorov, M. B., Meier, M. F. & Ohmura, A. Mass balance of glaciers and ice caps: consensus estimates for 1961–2004. *Geophys. Res. Lett.* **33**, L19501 (2006).
- Tapley, B. D., Bettadpur, S., Watkins, M. & Reigber, C. The gravity recovery and climate experiment: mission overview and early results. *Geophys. Res. Lett.* **31**, L09607 (2004).
- Wahr, J., Swenson, S., Zlotnicki, V. & Velicogna, I. Time-variable gravity from GRACE: first results. *Geophys. Res. Lett.* **31**, L11501 (2004).
- Chen, J. L., Wilson, C. R., Tapley, B. D., Blankenship, D. D. & Ivins, E. R. Patagonia icefield melting observed by gravity recovery and climate experiment (GRACE). *Geophys. Res. Lett.* **34**, L22501 (2007).
- Gardner, A. S. *et al.* Sharply increased mass loss from glaciers and ice caps in the Canadian Arctic Archipelago. *Nature* **473**, 357–360 (2011).
- Luthcke, S. B., Arendt, A. A., Rowlands, D. D., McCarthy, J. J. & Larsen, C. F. Recent glacier mass changes in the Gulf of Alaska region from GRACE mascon solutions. *J. Glaciol.* **54**, 767–777 (2008).
- Riva, R. E. M., Bamber, J. L., Lavalée, D. A. & Wouters, B. Sea-level fingerprint of continental water and ice mass change from GRACE. *Geophys. Res. Lett.* **37**, L19605 (2010).
- Rignot, E., Velicogna, I., van den Broeke, M. R., Monaghan, A. & Lenaerts, J. Acceleration of the contribution of the Greenland and Antarctic ice sheets to sea level rise. *Geophys. Res. Lett.* **38**, L05503 (2011).
- Tiwari, V. M., Wahr, J. & Swenson, S. Dwindling groundwater resources in northern India, from satellite gravity observations. *Geophys. Res. Lett.* **36**, L18401 (2009).
- Raup, B. H., Kieffer, H. H., Hare, J. M. & Kargel, J. S. Generation of data acquisition requests for the ASTER satellite instrument for monitoring a globally distributed target: glaciers. *IEEE Trans. Geosci. Remote Sens.* **38**, 1105–1112 (2000).
- Brown, J., Ferrians, O. J., Heginbottom, J. A. & Melnikov, E. S. *Circum-Arctic Map of Permafrost and Ground-Ice Conditions*. National Snow and Ice Data Center/World Data Center for Glaciology (1998, revised, February 2001).
- Velicogna, I. Increasing rates of ice mass loss from the Greenland and Antarctic ice sheets revealed by GRACE. *Geophys. Res. Lett.* **36**, L19503 (2009).
- Cogley, J. G. in *Future Climates of the World* (eds Henderson-Sellers, A. & McGuffie, K.) 189–214 (Elsevier, 2012).
- Rodell, M., Velicogna, I. & Famiglietti, J. S. Satellite-based estimates of groundwater depletion in India. *Nature* **460**, 999–1002 (2009).
- Bettinelli, P. *et al.* Plate motion of India and interseismic strain in the Nepal Himalaya from GPS and DORIS measurements. *J. Geod.* **80**, 567–589 (2006).
- Jackson, M. & Bilham, R. Constraints on Himalayan deformation inferred from vertical velocity-fields in Nepal and Tibet. *J. Geophys. Res. Solid Earth* **99**, 13897–13912 (1994).
- Zhong, S. J. & Zuber, M. T. Crustal compensation during mountain-building. *Geophys. Res. Lett.* **27**, 3009–3012 (2000).
- Lemoine, F. *et al.* *The Development of the Joint NASA GSFC and NIMA Geopotential Model EGM96*. NASA Goddard Space Flight Center (1998).
- Cheng, M. K. & Tapley, B. D. Variations in the Earth's oblateness during the past 28 years. *J. Geophys. Res.* **109**, B09402 (2004).
- Swenson, S., Chambers, D. & Wahr, J. Estimating geocenter variations from a combination of GRACE and ocean model output. *J. Geophys. Res. Solid Earth* **113**, B08410 (2008).

28. Rowlands, D. D. *et al.* Resolving mass flux at high spatial and temporal resolution using GRACE intersatellite measurements. *Geophys. Res. Lett.* **32**, L04310 (2005).
29. Ivins, E. R. & James, T. S. Bedrock response to Llanquihue Holocene and present-day glaciation in southernmost South America. *Geophys. Res. Lett.* **31**, L24613 (2004).

**Supplementary Information** is linked to the online version of the paper at [www.nature.com/nature](http://www.nature.com/nature).

**Acknowledgements** We thank Geruo A for providing the glacial isostatic adjustment model, and G. Cogley, G. Kaser, I. Velicogna, T. Perron and M. Tamisiea for comments. This work was partially supported by NASA grants NNX08AF02G and NNX10AR66G,

and by NASA's 'Making Earth Science Data Records for Use in Research Environments (MEaSUREs) Program'.

**Author Contributions** T.J. and J.W. developed the study and wrote the paper. W.T.P. and S.S. discussed, commented on and improved the manuscript. S.S. provided the CLM4 hydrology model output.

**Author Information** Reprints and permissions information is available at [www.nature.com/reprints](http://www.nature.com/reprints). The authors declare no competing financial interests. Readers are welcome to comment on the online version of this article at [www.nature.com/nature](http://www.nature.com/nature). Correspondence and requests for materials should be addressed to J.W. ([john.wahr@gmail.com](mailto:john.wahr@gmail.com)).



# The microRNA miR-34 modulates ageing and neurodegeneration in *Drosophila*

Nan Liu<sup>1†</sup>, Michael Landreh<sup>1†</sup>, Kajia Cao<sup>2,3</sup>, Masashi Abe<sup>1</sup>, Gert-Jan Hendriks<sup>1</sup>, Jason R. Kennerdell<sup>1</sup>, Yongqing Zhu<sup>1</sup>, Li-San Wang<sup>2,4,5</sup> & Nancy M. Bonini<sup>1,6</sup>

Human neurodegenerative diseases have the temporal hallmark of afflicting the elderly population. Ageing is one of the most prominent factors to influence disease onset and progression<sup>1</sup>, yet little is known about the molecular pathways that connect these processes. To understand this connection it is necessary to identify the pathways that functionally integrate ageing, chronic maintenance of the brain and modulation of neurodegenerative disease. MicroRNAs (miRNA) are emerging as critical factors in gene regulation during development; however, their role in adult-onset, age-associated processes is only beginning to be revealed. Here we report that the conserved miRNA miR-34 regulates age-associated events and long-term brain integrity in *Drosophila*, providing a molecular link between ageing and neurodegeneration. Fly *mir-34* expression exhibits adult-onset, brain-enriched and age-modulated characteristics. Whereas *mir-34* loss triggers a gene profile of accelerated brain ageing, late-onset brain degeneration and a catastrophic decline in survival, *mir-34* upregulation extends median lifespan and mitigates neurodegeneration induced by human pathogenic polyglutamine disease protein. Some of the age-associated effects of miR-34 require adult-onset translational repression of *Eip74EF*, an essential ETS domain transcription factor involved in steroid hormone pathways. Our studies indicate that miRNA-dependent pathways may have an impact on adult-onset, age-associated events by silencing developmental genes that later have a deleterious influence on adult life cycle and disease, and highlight fly miR-34 as a key miRNA with a role in this process.

Recent evidence reveals that miRNA pathways are important in the adult nervous system, notably in the maintenance of neurons and in the regulation of genes and pathways associated with neurodegenerative disease<sup>2,3</sup>. Given these findings, we considered that there may be a fundamental role for select miRNAs in ageing. We examined flies carrying a hypomorphic mutation in *loquacious* (*loqs*), a key gene in fly miRNA processing<sup>4</sup> (Supplementary Fig. 1a). Flies bearing the *loqs*<sup>f00791</sup> mutation were viable, but detailed examination indicated a significantly shortened lifespan (Supplementary Fig. 1b). Further analysis indicated that *loqs*<sup>f00791</sup> flies showed late-onset brain morphological deterioration: although normal as young adults, by 25 days *loqs*<sup>f00791</sup> flies developed large vacuoles in the retina and lamina of the brain (Supplementary Fig. 1c). Although developmental processes may contribute to shortened lifespan, the adult-onset brain degeneration of *loqs*<sup>f00791</sup> mutants indicated that one or more specific miRNAs may be critically involved in age-associated events impacting on long-term brain integrity.

To explore this question, we determined whether specific miRNAs displayed age-modulated expression in the brain. RNA was isolated from dissected brains of adult flies of young (3 days), mid (30 days) and old time points (60 days). Using an array for *Drosophila* miRNAs, 29 were expressed in the adult brain (Fig. 1a). Whereas most miRNAs maintained a steady level or decreased with age, one miRNA, *mir-34*,

increased (Fig. 1a). Small RNA northern blot analysis confirmed that *mir-34* expression was barely detectable during development, but became high in the adult and was further upregulated with age (Supplementary Fig. 2a, b). Expression of *mir-34* was affected in *loqs*<sup>f00791</sup> flies (Supplementary Fig. 1d). miR-34 falls into a category of *Drosophila* miRNAs whose processing requires the exoribonuclease *nibbler* (*nbr*)<sup>5,6</sup>. In the adult, mature miR-34 displayed three major differentially sized forms (24 nucleotides, 22 nucleotides and 21 nucleotides) with a uniform 5' end, descending by single nucleotides at the 3' end which result from *nbr*-mediated trimming; only isoform c became upregulated with age (Supplementary Fig. 2c and Fig. 1b, c; see also refs 5–7).

miR-34 is a markedly conserved miRNA, with orthologues in fly, *Caenorhabditis elegans*, mouse and human showing identical seed sequence (Supplementary Fig. 2d). To define miR-34 function, flies deleted for the gene were generated (Supplementary Fig. 3a). The resulting *mir-34* mutant flies retained normal wild-type expression of neighbouring genes, but selectively lacked *mir-34* (Supplementary

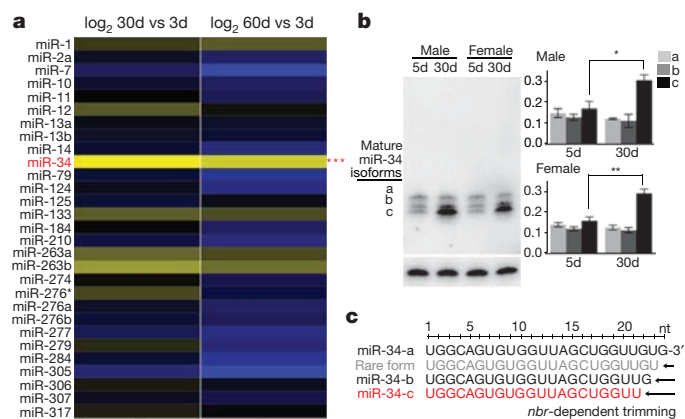


**Figure 1 | *Drosophila* miR-34 expression is upregulated with age.** **a**, Heat map of fold-change of *Drosophila* miRNAs in brains aged 3 days, 30 days and 60 days. Twenty-nine miRNAs (shown) were flagged present out of a total of seventy-eight. One-way analysis of variance defined significance for each miRNA over all time points ( $***P < 0.001$ ;  $n = 3$  replicates). Genotype: iso31. **b**, Fly miR-34 isoform c shows age-modulated expression in fly heads. Left panels: miR-34 shows three major mature forms (labelled a, b and c), but only isoform c increases with age.  $n = 3$  independent experiments; signal density of all isoforms normalized at the same time point to 2S rRNA loading control.  $*P < 0.01$ ;  $**P < 0.001$ ; one-way analysis of variance, with post test: Tukey's multiple comparison test. Genotype: 5905. **c**, Sequences of miR-34 isoforms are generated through *nbr*-dependent 3'-end trimming.

<sup>1</sup>Department of Biology, University of Pennsylvania, Philadelphia, Pennsylvania 19104, USA. <sup>2</sup>Department of Pathology and Laboratory Medicine, University of Pennsylvania, Philadelphia, Pennsylvania 19104, USA. <sup>3</sup>Cell and Developmental Biology, University of Pennsylvania, Philadelphia, Pennsylvania 19104, USA. <sup>4</sup>Institute on Aging, University of Pennsylvania, Philadelphia, Pennsylvania 19104, USA. <sup>5</sup>Penn Center for Bioinformatics, University of Pennsylvania, Philadelphia, Pennsylvania 19104, USA. <sup>6</sup>Howard Hughes Medical Institute, University of Pennsylvania, Philadelphia, Pennsylvania 19104, USA. <sup>†</sup>Present addresses: Division of Biological Sciences, Section of Neurobiology, Howard Hughes Medical Institute, University of California, San Diego, California 92093, USA (N.L.); Division of Physiological Chemistry I, Department of Medical Biochemistry and Biophysics, Karolinska Institutet, SE-17177 Stockholm, Sweden (M.L.).

Fig. 3b, c). To interrogate age-associated phenotypes carefully, we generated *mir-34* null flies in the same uniform homogeneous genetic background (see Methods). *mir-34* mutants displayed no obvious developmental defects, consistent with its adult-onset expression. However, detailed examination of adult animals indicated that *mir-34* mutants, although showing normal adult appearance and early survival, displayed a catastrophic decline in viability just after 30 days (Fig. 2a and Supplementary Table 4). Analysis of age-associated functions revealed that young mutants (3 days) had normal locomotion and stress resistance, but by 20 days the mutants had dramatic climbing deficits and were markedly stress-sensitive compared to age-matched controls (Fig. 2b). Because *mir-34* expression was brain-enriched, we also examined the brain. Typically, older flies show sporadic, age-correlated vacuoles in the brain—a morphological hallmark of neural

deterioration<sup>8</sup>. *mir-34* mutants were born with normal brain morphology, but showed dramatic vacuolization with age, indicative of loss of brain integrity (Fig. 2c). Rescue with a 9-kb genomic DNA fragment containing *mir-34* and its endogenous *cis*-regulatory elements (Supplementary Fig. 3a, b) partially restored the age-associated expression of *mir-34* to *mir-34* null flies in the same homogeneous genetic background (Supplementary Fig. 3d). Although rescue was not complete, indicative of a complexity in genomic elements that regulate *mir-34*, rescue was sufficient to mitigate the mutant effects, indicating that miR-34 function normally underlies these age-associated aspects (Supplementary Table 1).

These data indicated that *mir-34* mutants were normal as young adults, but with age developed deficits reflective of much older animals, including loss of locomotion, stress sensitivity and brain deterioration,

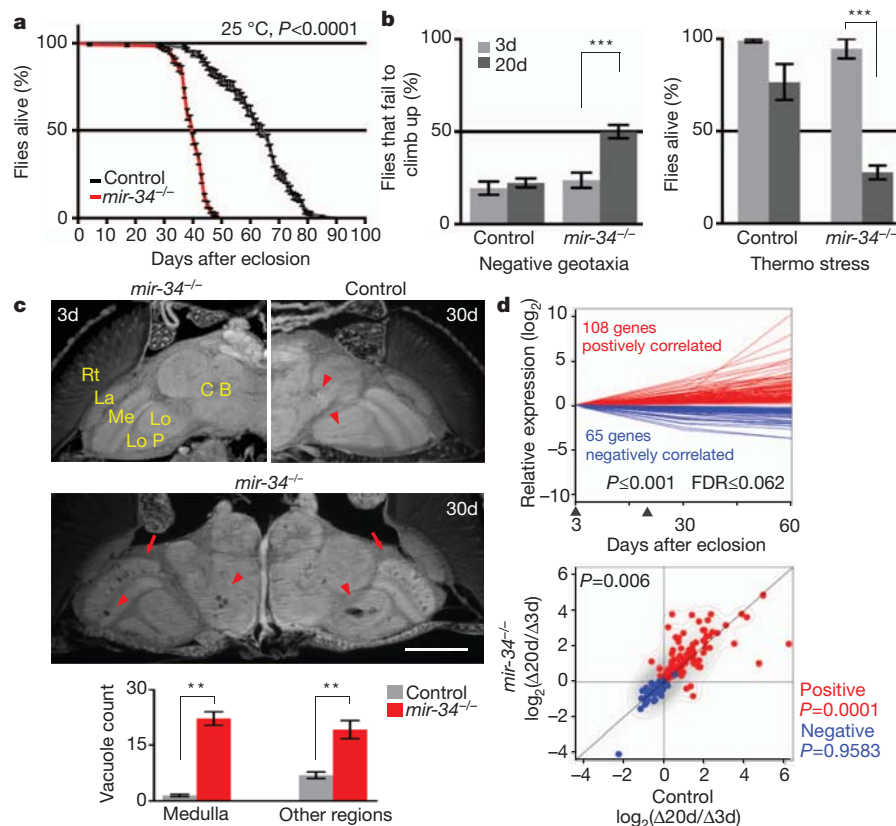


**Figure 2 | miR-34 modulates age-associated processes.** **a**, *mir-34* mutant flies have a shortened lifespan (control: 64 days median, 90 days maximal lifespan; *mir-34*: 40 days median, 64 days maximal lifespan;  $P < 0.0001$ , log-rank test). Mean ± s.e.m.,  $n \geq 240$  male flies per curve. Genotypes: control, 5905; *mir-34*<sup>-/-</sup>, *mir-34* null-1 in 5905 homogenous genetic background. **b**, *mir-34* mutant flies have late-onset behavioural deficits. Left: for locomotion behaviour, *mir-34* mutant flies show normal climbing at 3 days. At 20 days, 50 ± 3.4% *mir-34* mutant flies fail to climb; in contrast, only 22.1 ± 2.4% of control flies have defective climbing. Mean ± s.e.m. of 3 experiments,  $n = 120$ –140 male flies per experiment. Right panel: for stress resistance, *mir-34* mutant flies have normal resistance to heat stress at 3 days. *mir-34* mutant flies become markedly sensitive to heat shock with age, such that at 20 days, only 27.5 ± 3.8% survive after heat stress. In contrast, 76.7 ± 9.6% of control flies survive after the same treatment. Mean ± s.e.m. of 3 experiments,  $n = 120$ –140 male flies. \*\*\* $P < 0.0001$  (two-way analysis of variance). Genotypes as in **a**. **c**, *mir-34* mutant flies show age-associated brain degeneration. Top-left panel: *mir-34* mutant flies have normal brain morphology at 3 days. Major anatomical structures: CB, central brain; La, lamina; Lo, lobula; LoP, lobula plate; Me, medulla; Rt, retina. At 3 days, control flies have normal brain morphology (not shown), but develop a small number of sporadic vacuoles at 30 days (top-right panel, arrowheads). Middle panel: aged *mir-34* mutants (30 days) show striking vacuoles in the medulla (arrows) and other regions of

the brain (arrowheads). Bottom: the number of vacuoles in *mir-34* mutants is significantly higher than in controls (22.2 ± 1.8 versus 1.5 ± 0.3 in medulla; 19.2 ± 2.5 versus 7.0 ± 0.9 in other regions of the brain; \*\* $P < 0.001$ , one-way analysis of variance, with post test: Tukey's multiple comparison test). Mean ± s.e.m.,  $n = 10$  independent male fly brains. Genotypes as in **a**. Scale bar: 0.1 mm. **d**, *mir-34* mutant flies have a transcriptional profile indicative of accelerated ageing. Top panel: 173 age-correlated probe sets were defined from a transcriptional profile of fly brains at 3 days, 30 days and 60 days of age. Arrowheads indicate time points (3 days and 20 days) at which *mir-34* mutants and controls were compared. Genotype: iso31 flies used for transcriptional profiles of normal ageing brains.  $n = 3$  biological replicates for each time point.  $P \leq 0.001$ , false discovery rate (FDR) ≤ 0.062, linear regression model. Bottom panel: scatter plot illustrates the relative expression of 173 probe sets, which shows a significant difference between *mir-34* mutants and age-matched controls ( $P = 0.006$ , two-sample, paired Wilcoxon test). Whereas the pattern for positively correlated probe sets (red), indicated by the contour lines, is significantly different ( $P = 0.0001$ ) between the two genotypes, and tends to show higher expression in *mir-34* mutants compared to controls, it is not for negatively correlated probe sets (blue) ( $P = 0.9583$ ). Contour lines indicate that positively correlated probe sets tend to show higher expression in *mir-34* mutants compared to controls. Genotypes as in **a**.  $n = 5$  biological replicates for each time point.

coupled with shortened lifespan. We therefore hypothesized that loss of *mir-34* accelerated brain ageing. To address this, we transcriptionally profiled the fly brain (3 days, 30 days and 60 days) from wild-type animals. On the basis of a linear regression model<sup>9</sup>, we extracted 173 probe sets from this profile the expression of which was tightly correlated with the progression of normal ageing (Fig. 2d and Supplementary Tables 2 and 3). We next made another set of brain transcriptional profiles for *mir-34* mutants and controls of matched chronological age (3 days and 20 days). We measured relative changes of these probe sets between 3 days and 20 days within each genotype, and compared the extent of such changes between *mir-34* mutants and controls. This indicated that the overall pattern of these probe sets was significantly different between the two genotypes ( $P = 0.006$ , two-sample, paired Wilcoxon test; Fig. 2d). In particular, most positively correlated probe sets displayed a faster pace of increase in *mir-34* mutants compared to controls—thus showing accelerated age-associated expression changes in *mir-34* mutants (Fig. 2d). This result, combined with the physiological and histological evidence of more rapid loss of age-associated functions, suggested that *mir-34* mutants were undergoing accelerated brain ageing.

miRNAs function by binding to the 3' UTRs of target mRNAs and often result in downregulation of protein translation. We therefore reasoned that age-associated activities of miR-34 might be mediated through silencing of critical targets that have a negative impact on the adult animal. miRNA-target prediction algorithms indicated miR-34 binding sites within the 3' UTR of the *Eip74EF* gene; notably, these binding sites were conserved in the orthologous *Eip74EF* genes from different *Drosophila* species (Supplementary Fig. 4a). We confirmed the miR-34 interaction through mutations in the seed sequences of the predicted miR-34 binding sites in the 3' UTR of the *Eip74EF* mRNA (Supplementary Fig. 4b). The *Eip74EF* gene is a component of steroid hormone signalling pathways. Although such pathways have generally been studied for effects during development, data have implicated these pathways in lifespan regulation<sup>10</sup>.

The *Eip74EF* gene encodes two major protein isoforms, E74A and E74B (referred to as the *E74A* and *E74B* genes, respectively<sup>11</sup>); the isoforms share the same 3' UTR (Supplementary Fig. 4a). Northern blots indicated that transcription of *E74A*, but not *E74B*, persisted in adults, overlapping the time period when *mir-34* is expressed (Supplementary Fig. 4c). Given this, we focused on *E74A* as a regulated target of miR-34 in the adult. Despite robust expression of the mRNA transcript, the E74A protein was expressed at low levels in adult heads throughout lifespan (Fig. 3a, b and Supplementary Fig. 4d). In flies lacking miR-34, E74A protein was markedly increased (Fig. 3b); E74A was also de-regulated in the *loqs*<sup>00791</sup> mutant flies (Supplementary Fig. 1e). Genomic rescue of *mir-34* mitigated this de-regulation of the E74A protein (Fig. 3c). Fine temporal analysis indicated that the E74A protein was highly expressed in young flies, but underwent a marked decrease within a 24-h time window (Supplementary Fig. 5). This temporal pattern seemed to be mutually exclusive to that of miR-34 (see Supplementary Fig. 2a). Moreover, in flies lacking miR-34, the downregulation of E74A protein during this critical period was dampened (Supplementary Fig. 5). This evidence indicates that adult-onset expression of *mir-34* functions, at least in part, to attenuate E74A protein expression in the young adult, and maintain that repression through adulthood (Supplementary Fig. 4d).

We next determined whether deregulated expression of E74A protein contributed to the age-associated defects in *mir-34* mutants. Because E74A function is essential during development, with strong mutations leading to pre-adult lethality<sup>11</sup>, we used the mild, but viable, *E74A*<sup>BG01805</sup> hypomorphic mutation (Supplementary Fig. 4a). When the *E74A*<sup>BG01805</sup> mutation was combined with *mir-34* mutant flies in the same homogenous genetic background, proper regulation of E74A protein was partially restored (Fig. 3d), and age-associated defects due to loss of *mir-34*, including shortened lifespan and brain vacuolization, were mitigated (Fig. 3e, f; *E74A*<sup>BG01805</sup> mutants alone have a normal lifespan

(Supplementary Fig. 6a)). To assess further the adult activity of E74A, we upregulated E74A in the adult with an *E74A* transgene that lacks miR-34 binding sites driven by a temperature-sensitive promoter<sup>12</sup>. At 29 °C, these flies demonstrated increased levels of E74A expression in the adult (Supplementary Fig. 6b). Notably, these animals also showed late-onset brain degeneration (Supplementary Fig. 6c) and a significantly shortened lifespan (Supplementary Fig. 6d). These data indicate that deregulated expression of E74A has a negative impact on normal ageing, and that one function of miR-34 is to silence E74A in the adult to prevent the adult-stage deleterious activity of E74A on brain integrity and viability.

Notably, during the course of these studies, we noted that *mir-34* mutants also displayed a defect in protein misfolding—a molecular process implicated in ageing and common to many human neurodegenerative diseases<sup>13</sup>. Whereas normally with age, the fly brain accumulates a low level of inclusions that immunostain for stress chaperones like Hsp70/Hsc70, *mir-34* mutants showed a marked increase compared to control flies of matched age (30 days) (Supplementary Fig. 7). Given that *mir-34* expression increases with age, and *mir-34* loss shows altered chaperone accumulation, we tested whether *mir-34* expression itself is upregulated by stresses like heat shock or oxidative toxins, but found no evidence to support this (data not shown). However, given that loss of *mir-34* caused an increase in protein misfolding, this raised the possibility that upregulation of *mir-34* expression might mitigate disease-associated protein misfolding. In *Drosophila*, expression of a pathogenic ataxin-3 polyglutamine (polyQ) disease protein (SCA3trQ78) leads to inclusion formation, a decrease in polyQ protein solubility and progressive neural loss<sup>14</sup> (Supplementary Fig. 8a). Upregulation of *mir-34* markedly mitigated polyQ degeneration, such that inclusion formation was slowed, the protein retained greater solubility, and neural degeneration was suppressed (Fig. 3g, h and Supplementary Fig. 8b–d). Lowering E74A expression by heterozygous reduction in flies expressing pathogenic polyQ protein revealed a minimal effect (data not shown), indicating that E74A may not be a target of miR-34 activity in this process. However, our studies with E74A were of necessity limited to hypomorphic alleles that may not uncover the full extent of E74A function mediated by miR-34. Furthermore, additional targets of miR-34 may be involved in different aspects of miR-34-directed pathways, including disease.

Given this effect to mitigate disease-associated neural toxicity with upregulation of *mir-34*, and that *mir-34* expression naturally increases with age, we investigated whether enhanced expression of *mir-34* in wild-type flies could modulate the ageing process. We increased miR-34 dosage in wild-type flies with genomic rescue transgenes, which express *mir-34* under its endogenous regulatory elements (see Supplementary Fig. 2a). Analysis of multiple independent transgenics in the same genetic background with that of control indicated that upregulation of miR-34 levels with genomic constructs (~20%, Supplementary Fig. 3d) promoted median survival rate by ~10% compared to wild type (Fig. 3i; other traits, such as the occurrence of brain vacuolization, despite being an age-associated phenomenon, are sporadic and low in normal flies, thus were difficult to assess). Thus, upregulation of *mir-34* expression can protect from neurodegenerative disease and extend median lifespan.

Our findings indicate that miR-34 in *Drosophila* presents a key miRNA that couples long-term maintenance of the brain with healthy ageing of the organism. miR-34 activity, enhanced by its age-modulated expression and processing, is critically involved in silencing of the *E74A* transcript through adulthood and in modulation of protein homeostasis with age, as well as in polyQ disease. Select neural cell types may be especially vulnerable in ageing and disease<sup>15</sup>; miR-34 function may have an impact on the integrity or activity of these systems. Intriguingly, E74A seems to confer sharply opposing function on animal fitness at different life stages, being essential during pre-adult development<sup>11</sup>, but harmful to the adult during ageing (this study). This biological property—of a gene being beneficial at one



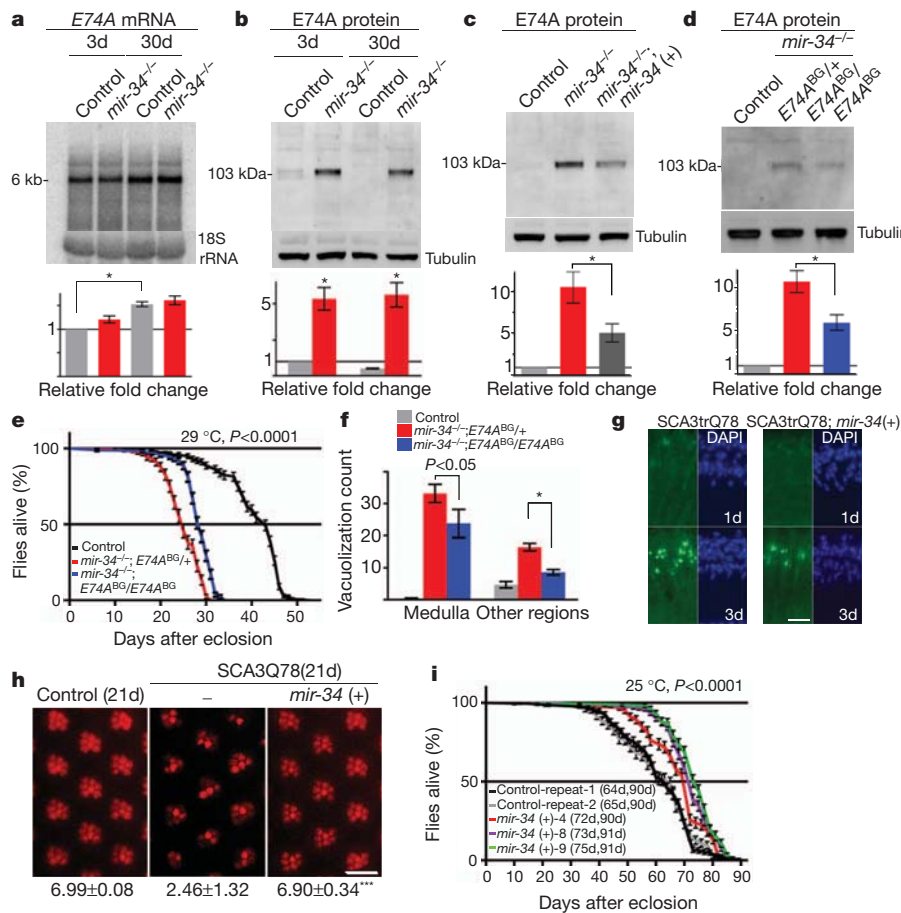


**Figure 3 | The *Drosophila Eip74EF* gene is a target of miR-34 in modulation of the ageing process.** **a**, *E74A* mRNA is robustly expressed in the adult and unchanged between age-matched controls and *mir-34* mutants. In control flies, *E74A* mRNA is significantly upregulated in 30 day compared to 3 day animals. RNA was from male heads. Mean  $\pm$  s.e.m.,  $n = 3$  independent experiments; signal density of *E74A* mRNA normalized to 18S rRNA loading control ( $*P < 0.01$ , one-way analysis of variance, with post test: Tukey's multiple comparison test). Genotypes: control, 5905; *mir-34*<sup>-/-</sup>, *mir-34* null-1 in 5905 homogenous genetic background. **b**, *E74A* protein is deregulated in *mir-34* mutants. Protein was from male heads. Mean  $\pm$  s.e.m.,  $n = 3$  independent experiments; signal density of *E74A* protein normalized to tubulin loading control ( $*P < 0.01$ , one-way analysis of variance, with post test: Tukey's multiple comparison). Genotypes as in **a**. **c**, Deregulation of *E74A* protein is diminished in *mir-34* rescue flies. Protein was from male heads. Mean  $\pm$  s.e.m.,  $n = 3$  independent experiments; signal density normalized to tubulin loading control ( $*P < 0.05$ , one-way analysis of variance, with post test: Tukey's multiple comparison test). Genotypes: control, 5905; *mir-34*<sup>-/-</sup>, *mir-34* null-1 in 5905 homogenous genetic background; *mir-34*<sup>-/-</sup>; *mir-34*(+), *mir-34* genomic rescue in *mir-34* null-1 in 5905 homogenous genetic background. **d**, *mir-34* mutants homozygous for the *E74A*<sup>BG01805</sup> allele have lower levels of *E74A* protein. Protein was from male heads of 20 day flies raised at 29 °C. Mean  $\pm$  s.e.m.,  $n = 3$  independent experiments; signal density normalized to tubulin loading control ( $*P < 0.01$ , one-way analysis of variance, with post test: Tukey's multiple comparison test). Genotypes: control, 5905; *mir-34*<sup>-/-</sup> *E74A*<sup>BG</sup>/+, *E74A*<sup>BG01805</sup>/+, *mir-34* null-1 in 5905 homogenous genetic background; *mir-34*<sup>-/-</sup> *E74A*<sup>BG</sup>/*E74A*<sup>BG</sup>, *E74A*<sup>BG01805</sup>/*E74A*<sup>BG01805</sup>, *mir-34* null-1 in 5905 homogenous genetic background. **e**, **f**, Reducing *E74A* protein levels in the adult mitigates age-related defects of *mir-34* mutants. *mir-34* mutants also homozygous for *E74A*<sup>BG01805</sup> show rescued lifespan (**e**) and brain morphology (**f**), compared to *mir-34* mutants heterozygous for *E74A*<sup>BG01805</sup> (these flies have a lifespan that is the same as *mir-34* mutants alone; see

Supplementary Table 4). Flies raised at 29 °C. Lifespan:  $P < 0.0001$  (log-rank test). Mean  $\pm$  s.e.m.,  $n \geq 150$  male flies. Brain vacuoles:  $*P < 0.01$  (one-way analysis of variance, with post test: Tukey's multiple comparison test). Mean  $\pm$  s.e.m.,  $n = 10$  independent male animals. Genotypes as in **d, g**. Upregulation of *mir-34* reduces accumulation of pathogenic polyQ protein inclusions. Left panels: in the retina of flies expressing SCA3trQ78 alone, pathogenic polyQ protein is initially diffuse (1 day, top), but gradually accumulates into nuclear inclusions (3 day, bottom). Right panels: upregulation of *mir-34* reduces inclusion formation. DAPI staining highlights nuclei. 3 day controls show  $53.75 \pm 12.55$  inclusions in a retinal section versus  $23.67 \pm 7.57$  with *mir-34* upregulation; mean  $\pm$  s.d.,  $n \geq 3$  cryosections from independent male animals;  $P < 0.01$  (*t*-test). Genotypes: SCA3trQ78 is  $w^+$ ; *rh1-GAL4, UAS-SCA3trQ78/+*. SCA3trQ78; *mir-34 (+)* is  $w^+$ ; *rh1-GAL4, SCA3trQ78/+; UAS-mir-34/+*. Scale bar, 0.05 mm. **h**, Upregulation of *mir-34* prevents neural degeneration. At 21 days, male flies expressing SCA3trQ78 show a marked loss of photoreceptor neuronal integrity (middle panel), with an average of only  $2.46 \pm 1.32$  photoreceptors per ommatidium remaining by pseudopupil analysis. Flies with upregulated *mir-34* (right panel) retain  $6.90 \pm 0.34$  photoreceptors per ommatidium. Control (left panel) and upregulation of *mir-34* alone (not shown) have normal photoreceptor numbers per ommatidium. Mean  $\pm$  s.d.,  $n = 619, 722$  and  $700$  ommatidia, for SCA3trQ78, SCA3trQ78; *mir-34 (+)* and control, respectively;  $***P < 0.0001$  (one-way analysis of variance, with Bonferroni's multiple comparison test). Genotypes as in **b**; control:  $w^+$ ; *rh1-GAL4/+*. Scale bar, 0.05 mm. **i**, Flies with upregulated *mir-34* (colour) have an extended median lifespan compared to control flies (black and grey curves for repeats 1 and 2, respectively) (log-rank test). Lifespan result for each genotype is indicated in median and maximal days. Mean  $\pm$  s.e.m.,  $n \geq 150$  male flies per genotype, 25 °C. Three independent *mir-34* genomic transgenic lines (4, 8, 9) were analysed. Genotypes: control, 5905; *mir-34 (+)*, *mir-34* genomic rescue in 5905 homogenous genetic background.

life stage, but damaging at another—is referred to as antagonistic pleiotropy<sup>16</sup>. Genes associated with antagonistic pleiotropy are likely to be evolutionarily retained due to their earlier beneficial function<sup>17</sup>. Their adult-onset activities, however, antagonize the ageing process if

they are not properly regulated. miRNA pathways provide a tantalizing mechanism by which to suppress potentially deleterious age-related activities of such genes; a number of miRNAs have been noted to show age-modulated expression and activity<sup>18,19</sup>. Roles of

select miRNAs normally expressed in the adult may be of evolutionary advantage to tune-down events that promote age-associated decline and potentially disease, in order to prolong healthy lifespan and longevity. Upregulation of *lin-4*, a *C. elegans* miRNA with a known developmental role, extends nematode lifespan<sup>18</sup>, raising the possibility that this upregulation, like the natural increase of *mir-34* expression in *Drosophila*, functions to silence genes that have a negative impact on ageing and potentially promote disease. Notably, *mir-34* expression is elevated with age in *C. elegans*<sup>19,20</sup>, and mammalian *mir-34* orthologues are highly expressed in the adult brain<sup>21</sup> and have also been noted to increase with age and be misregulated in degenerative disease in humans<sup>22–26</sup>. Current data regarding miR-34 function indicate that it is neutral or adverse in *C. elegans*<sup>19,27</sup>, and can be either protective or contributory to age-associated events in vertebrates<sup>22–26</sup>. Thus, miR-34 seems to be a key miRNA poised to integrate age-associated physiology; the precise function will reflect the diverse spatiotemporal expression and activity of distinct orthologues, the mRNA target spectrum, as well as the complexity of the adult brain and life cycle. The conservation of miR-34, coupled with in-depth comparative analysis of *mir-34* expression, 3' end processing, targets and pathways in the ageing process of nematodes, flies and mammals, make it a tempting subject for understanding features of ageing and disease susceptibility.

## METHODS SUMMARY

Flies were grown in standard media at 25 °C unless otherwise specified. Stock lines and *GAL4* driver lines were obtained from the *Drosophila* Stock centre at Bloomington, or are described<sup>14</sup>. Deletion of the *mir-34* region was made by site-specific recombination. Fly transgenics were generated by standard procedures. Flies were generated or backcrossed a minimum of five generations into a controlled uniform homogeneous genetic background (line 5905 (FlyBase ID FBst0005905, *w<sup>1118</sup>*)), to assure that all phenotypes were robust and not associated with variation in genetic background. In this uniform homogeneous genetic background, the lifespan of control flies is highly uniform with repetition when 150 or more individuals are used for lifespan analysis. Negative geotaxis and thermo stress were used to examine fly locomotion and stress resistance, respectively. Adult male heads were processed for paraffin sections as described<sup>14</sup>. To determine lifespan, newly eclosed males were collected and maintained at 15 flies per vial, transferred to fresh vials every 2 days while scored for survival. A total of 150–200 flies were used per genotype per lifespan; all experiments were repeated multiple times (see Supplementary Table 4). Lifespans were analysed in Excel (Microsoft) and by Prism software (GraphPad) for survival curves and statistics. Techniques of molecular biology, western immunoblots and histology were standard. Fly brain mRNA was prepared using Trizol reagent for array and mRNA analysis, miRNA arrays were miRCURY LNA arrays version 8.1 (Exiqon), and mRNA expression was profiled using Affymetrix *Drosophila* 2.0 chips (Affymetrix). The microarray data can be found in the Gene Expression Omnibus (GEO) of NCBI through accession number GSE25009.

**Full Methods** and any associated references are available in the online version of the paper at [www.nature.com/nature](http://www.nature.com/nature).

**Received 11 June; accepted 22 December 2011.**

**Published online 15 February 2012.**

1. Amaducci, L. & Tesco, G. Aging as a major risk for degenerative diseases of the central nervous system. *Curr. Opin. Neurol.* **7**, 283–286 (1994).
2. Eacker, S. M., Dawson, T. M. & Dawson, V. L. Understanding microRNAs in neurodegeneration. *Nature Rev. Neurosci.* **10**, 837–841 (2009).
3. Bilen, J., Liu, N., Burnett, B. G., Pittman, R. N. & Bonini, N. M. MicroRNA pathways modulate polyglutamine-induced neurodegeneration. *Mol. Cell* **24**, 157–163 (2006).
4. Jiang, F. *et al.* Dicer-1 and R3D1-L catalyze microRNA maturation in *Drosophila*. *Genes Dev.* **19**, 1674–1679 (2005).

5. Liu, N. *et al.* The exoribonuclease Nibbler controls 3' end processing of microRNAs in *Drosophila*. *Curr. Biol.* **21**, 1888–1893 (2011).
6. Han, B. W. H. *et al.* n. g. J. H., Weng, Z., Zamore, P. D. & Ameres, S. L. The 3'-to-5' exoribonuclease Nibbler shapes the 3' ends of microRNAs bound to *Drosophila* Argonaute1. *Curr. Biol.* **21**, 1878–1887 (2011).
7. Chung, W. J., Okamura, K., Martin, R. & Lai, E. C. Endogenous RNA interference provides a somatic defense against *Drosophila* transposons. *Curr. Biol.* **18**, 795–802 (2008).
8. Kretschmar, D., Hasan, G., Sharma, S., Heisenberg, M. & Benzer, S. The *swiss cheese* mutant causes glial hyperwrapping and brain degeneration in *Drosophila*. *J. Neurosci.* **17**, 7425–7432 (1997).
9. Cao, K., Chen-Plotkin, A. S., Plotkin, J. B. & Wang, L. S. Age-correlated gene expression in normal and neurodegenerative human brain tissues. *PLoS ONE* **5** (2010).
10. Simon, A. F., Shih, C., Mack, A. & Benzer, S. Steroid control of longevity in *Drosophila melanogaster*. *Science* **299**, 1407–1410 (2003).
11. Fletcher, J. C. & Thummel, C. S. The *Drosophila* E74 gene is required for the proper stage- and tissue-specific transcription of ecdysone-regulated genes at the onset of metamorphosis. *Development* **121**, 1411–1421 (1995).
12. Fletcher, J. C., D'Avino, P. P. & Thummel, C. S. A steroid-triggered switch in E74 transcription factor isoforms regulates the timing of secondary-response gene expression. *Proc. Natl Acad. Sci. USA* **94**, 4582–4586 (1997).
13. Morimoto, R. I. Proteotoxic stress and inducible chaperone networks in neurodegenerative disease and aging. *Genes Dev.* **22**, 1427–1438 (2008).
14. Warrick, J. M. *et al.* Expanded polyglutamine protein forms nuclear inclusions and causes neural degeneration in *Drosophila*. *Cell* **93**, 939–949 (1998).
15. Hirth, F. *Drosophila melanogaster* in the study of human neurodegeneration. *CNS Neurol. Disord. Drug Targets* **9**, 504–523 (2010).
16. Williams, G. C. Pleiotropy, natural selection and the evolution of senescence. *Evolution* **11**, 398–411 (1957).
17. Kirkwood, T. B. Understanding the odd science of aging. *Cell* **120**, 437–447 (2005).
18. Boehm, M. & Slack, F. A developmental timing microRNA and its target regulate life span in *C. elegans*. *Science* **310**, 1954–1957 (2005).
19. de Lencastre, A. *et al.* MicroRNAs both promote and antagonize longevity in *C. elegans*. *Curr. Biol.* **20**, 2159–2168 (2010).
20. Ibanez-Ventoso, C. *et al.* Modulated microRNA expression during adult lifespan in *Caenorhabditis elegans*. *Aging Cell* **5**, 235–246 (2006).
21. Bak, M. *et al.* MicroRNA expression in the adult mouse central nervous system. *RNA* **14**, 432–444 (2008).
22. Zoviolis, A. *et al.* microRNA-34c is a novel target to treat dementias. *EMBO J.* **30**, 4299–4308 (2011).
23. Minones-Moyano, E. *et al.* MicroRNA profiling of Parkinson's disease brains identifies early downregulation of miR-34b/c which modulate mitochondrial function. *Hum. Mol. Genet.* **20**, 3067–3078 (2011).
24. Li, X., Khanna, A., Li, N. & Wang, E. Circulatory miR34a as an RNA based, noninvasive biomarker for brain aging. *Aging* **3**, 985–1002 (2011).
25. Khanna, A., Muthusamy, S., Liang, R., Sarojini, H. & Wang, E. Gain of survival signaling by down-regulation of three key miRNAs in brain of calorie-restricted mice. *Aging* **3**, 223–236 (2011).
26. Gaughwin, P. M. *et al.* Hsa-miR-34b is a plasma-stable microRNA that is elevated in pre-manifest Huntington's disease. *Hum. Mol. Genet.* **20**, 2225–2237 (2011).
27. Yang, J. *et al.* MiR-34 modulates *Caenorhabditis elegans* lifespan via repressing the autophagy gene *atg9*. Age. doi:10.1007/s11357-011-9324-3 (2011).

**Supplementary Information** is linked to the online version of the paper at [www.nature.com/nature](http://www.nature.com/nature).

**Acknowledgements** We thank C. Thummel, T. Jongens and A. Bashirullah for reagents. We are grateful to A. Cashmore, A. Burguete, J. Kim, S. Cherry, B. Gregory, A. Gitler and the Bonini laboratory for discussion and critical reading of the manuscript. We thank X. Teng for assistance with fly paraffin section. This work was funded by the NINDS (R01-NS043578) and the Ellison Foundation (to N.M.B.). L.-S.W. and K.C. are supported by a pilot grant from Penn Genome Frontiers Institute. L.-S.W. is supported by NIA (U01-AG-032984-02 and RC2-AG036528-01) and a Penn Institute on Aging pilot grant (AG010124). N.M.B. is an Investigator of the Howard Hughes Medical Institute. J.R.K. received support from NIH T32 AG00255.

**Author Contributions** N.L. and N.M.B. conceived and designed the project. N.L., M.L., M.A., G.-J.H., J.R.K. and Y.Z. planned, executed and analysed experiments. K.C. and L.-S.W. performed aging computational modelling. N.L. and N.M.B. wrote the manuscript with input from all authors.

**Author Information** The microarray data can be found in the Gene Expression Omnibus (GEO) of NCBI through accession number GSE25009. Reprints and permissions information is available at [www.nature.com/reprints](http://www.nature.com/reprints). The authors declare no competing financial interests. Readers are welcome to comment on the online version of this article at [www.nature.com/nature](http://www.nature.com/nature). Correspondence and requests for materials should be addressed to N.M.B. (nbonini@sas.upenn.edu).

## METHODS

**Genetic background.** Fly lines were from the Bloomington Stock centre or are described<sup>14</sup>. To control for background effects, and to assess significance of all effects, flies were generated in the same uniform homogeneous genetic background (line 5905 (FlyBase ID FBst0005905, *w<sup>1118</sup>*)), or backcrossed a minimum of five generations into this uniform genetic background. This assured that, for all phenotypes, even modest and consistent effects were associated with the gene manipulations and not a variation in background. With these carefully controlled experiments, the lifespan of control flies was highly uniform upon repetition, when 150 or more individuals were used for lifespan analysis (see Supplementary Table 4).

**mir-34 deletion mutants.** Deletion of the *mir-34* region was made by site-specific recombination between two piggyBac insertions, using FLP-FRT-mediated site-specific recombination<sup>28</sup>. The loss of other genes in the region was then fully rescued by genomic transgenes, so that a line selectively lacking only *mir-34* was generated. Two FRT-bearing insertions, PBac[XP]d02752 and PBac[RB]Fmr1<sup>602790</sup>, were used (Exelixis collection), which encompass the *mir-34* region. Genetic crosses were made to combine these two transposon elements with heat-inducible FLP recombinase. After 48 h of egg laying, parents were removed, and vials containing progeny were placed in a 37 °C water bath for a 1-h heat shock. Progeny flies were treated with daily 1-h heat shock, for an additional 4 days. Young virgin female progeny flies were collected and crossed to males with 3rd chromosome balancers. In the subsequent generation, progeny males were used to generate additional progeny for PCR confirmation. Progeny flies bearing the deletion were positive for PCR verification, using primers from neighbouring genomic DNA and ones from transposons (upstream insertion: 5'-GGTCGTGCATGACGAGATTA-3'/5'-TACTATTCTTCTCACTCGCAGTTATTG-3'; downstream insertion: 5'-TC CAAGCGCGACTGAGATG-3'/5'-GTGCGTTCGAAGAAATGATG-3'). Flies with the *mir-34* region deletion were viable, and were further verified for the appropriate deletion by PCR amplification, with primers for *mir-317* (5'-CGGAAA AACGGTTTGTGTCT-3'/5'-CCCGGGAACGAGTAAACGAAATGAAATCA-3'), *mir-277* (5'-TGATTATGGTTTGTGTTTCAGTTG-3'/5'-TTGATATCATT TCACACTATCACAAAAATGTC-3'), *mir-34* (5'-ACCTTGAGCGCTTCAAC TCT-3'/5'-CACTCTTCTCTGTTTGCATGG-3') and *dfmr1* (5'-CACACAGA GCTTCCCACTGA-3'/5'-AGGCCCTCTTTTGTGACATT-3').

**Fly age-associated phenotypes.** Negative geotaxis and thermo stress were used to examine fly locomotion and stress resistance, respectively. To perform negative geotaxis, groups of 15 adult male flies of indicated age were transferred into a 14-ml polystyrene round-bottom tube (Falcon), and placed in the dark for 30-min recovery. The assay was conducted in the dark, with only a red light on. Climbing ability was scored as the percentage of flies failing to climb higher than 1.5 cm from the bottom of the tube, within 15 s after gently being banged to the bottom. Three repeats were performed for each group and the result averaged. For each genotype at a given age, a minimum of 200 flies were tested. For heat sensitivity, groups of 15 adult males of indicated age were transferred into 14-ml polystyrene round-bottom tubes (Falcon) then placed in a 25 °C incubator for 30 min recovery. Heat stress was applied by immersing the vial containing the flies into a 37 °C water bath for 1 h, followed by a 30-min recovery at 25 °C, then another 1-h heat stress at 37 °C. Flies were then transferred into regular food vials and maintained at 25 °C. Dead flies were counted after 24 h. To assess brain morphology, adult male heads were processed for paraffin sections as described<sup>29</sup>, and brain vacuoles were counted through continuous sections generated from each head (*n* = 10 heads counted for each genotype).

**Molecular biology.** Fly genomic DNA was prepared from whole flies with the Puregene DNA purification kit (Qiagen). To generate *mir-34* pUAST constructs, PCR amplification was conducted using genomic DNA as template, with primer pairs of pUAST *mir-34*-I (286 bp, PCR primer 5'-CCGTTACACAGCACT ATTCTCAAT-3'/5'-CCATCTGATACAGGTCCTACATTTTCTAAAA-3') and pUAST *mir-34*-II (936 bp, PCR primer 5'-ACCTTGAGCGCTTCAACTCT-3'/5'-CACTCTTCTCGTTTGCATGG-3'). PCR products were then ligated into the pUAST vector. *mir-277/dfmr1* rescue construct was made in the pCaSpeR4 vector, which contained two parts. Part 1 was a genomic DNA fragment (7,530 bp) harbouring the *mir-277* sequence (PCR primers: 5'-GGTCGTGCATGACGAG ATTA-3'/5'-GGATGTTTTGCGACCACTT-3'), and part 2 was a genomic fragment containing *dfmr1* genomic sequence, derived from the pBS WTR construct (a gift from T. Jongens<sup>30</sup>), by BamHI and PpuMI. The *mir-34* genomic rescue construct was also made in the pCaSpeR4 vector, with two parts. One was a genomic DNA fragment (6,855 bp) upstream of *mir-277* sequence (PCR primers: 5'-GGTCGTGCATGACGAGATTA-3'/5'-GGATGCATTTTATCGTT AGGC-3'), and the other was a genomic DNA fragment (2,111 bp) containing *mir-34* sequence (PCR primers: 5'-GCAGGAAAATGCGATAAATGA-3'/5'-TCGTTACAACATGGAATCCTC-3'). The resultant construct, therefore, contains *mir-34* sequence, including most upstream fragment, with the exclusion

of 108 bp of *mir-277* sequence. In addition, a modified *mir-34* genomic rescue construct was made (pCaSpeR4 vector), which contains same upstream and downstream ends of the original *mir-34* genomic rescue construct, with a small deletion of *mir-277* mature sequence. The genomic regulation of *mir-34* seems complex, as despite these standard manipulations for gene rescue, the genomic rescue expression of *mir-34* and extent of phenotypic rescue of *mir-34* mutants was only partial. We attempted upregulation of *mir-34* with the GAL4-UAS system, including with the conditional gene switch system in adults. Upregulation of *mir-34* during development in non-germline tissues (when it normally is not expressed; Supplementary Fig. 2a) was deleterious, and we were unable to upregulate *mir-34* expression more robustly than with the genomic constructs.

For western immunoblots, 10 adult male heads per sample were homogenized in 50 µl of Laemmli buffer (Bio-Rad) supplemented with 5% 2-mercaptoethanol, heated to 95 °C for 5 min and 10 µl loaded onto 4–12% Bis-Tris gels (NuPage), then transferred to nitrocellulose membrane (Biorad) and blotted by standard protocols. Primary antibodies used were anti-tubulin (1:10,000, E7, Developmental Studies Hybridoma Bank), anti-E74A (a gift of C. Thummel). Secondary antibodies for immunoblots were goat anti-mouse conjugated to HRP (1:2,000, Chemicon) and developed by chemiluminescence (ECL, Amersham). The final image was obtained by Fuji scanner (Fujifilm).

Total RNA was isolated from 50–200 male heads per genotype, by cutting off heads with a sharp razor, then putting heads into Trizol reagent. Heads were ground by pestle, then RNA was isolated following the manufacturer's protocol (Trizol reagent, Invitrogen). 5 µg RNA was used per lane. Gel running (1% agarose) and blot transfer (nylon plus) were according to recommended procedures (Northernmax, Ambion). The RNA blot was then used for hybridization following standard procedures at 68 °C, with pre-hybridization (~1 h), hybridization (~12 h or overnight) with P<sup>32</sup>-labelled probe, washed and exposed to Phosphorimager (Amersham). RNA probes were used that were made by *in vitro* transcription of cDNA templates using Maxiscript-T7 *in vitro* transcription kit (Ambion), supplemented with P<sup>32</sup>-labelled UTP. The cDNA templates were prepared from total RNA by one-step RT-PCR (SuperScript One-Step RT-PCR with Platinum Taq, Invitrogen), with primers: *E74A* (5'-GTGAACGTGGTGGTGAAC-3'/5'-GATAATACGACTCACTATAGGGAGATGTCCATTGCTTCTCAATG-3'); *E74B* (5'-CATCGCTTGTCAATGTGTCC-3'/5'-GATAATACGACTCACTA TAGGGAGACTGCGGTAATCACTGAGCTG-3'); 18S rRNA loading control (5'-GATAATACGACTCACTATAGGGAGA-3'/5'-AGGGAGCCTGAGAAAC GGCTACCACATCTAAGGAATCTCCCTATAGTGAGTCGTATTATC-3').

For small RNA northern blots, total RNA was isolated from male fly heads using Trizol reagent as above. For each lane, 3 µg of RNA was used, and RNA was fractionated on a 15% Tris-UREA gel (NuPage) with 1×TBE buffer. The blot transfer was performed with 0.5×TBE buffer. Before hybridization, the RNA blots were pre-hybridized with Oligohyb (Ambion), and then incubated with radioactive labelled RNA probes for ~12 h to overnight. RNA probes were used, and made by *in vitro* transcription of oligo templates using Maxiscript-T7 *in vitro* transcription kit (Ambion), supplemented with P<sup>32</sup>-labelled UTP. Oligo DNA templates were prepared by annealing two single-stranded DNA oligonucleotides into duplex (99 °C, 5 min and cool down to room temperature). Oligonucleotides used for *mir-34* (5'-GATAATACGACTCACTATAGGGAGA-3'/5'-AAAAATGGCA GTGTGGTGTAGCTGGTGTGTCTCCCTATAGTGAGTCGTATTATC-3'), *mir-277* (5'-GATAATACGACTCACTATAGGGAGA-3'/5'-TAATGCACATCTGTG GTACACATAAATGCACATCTGGTACGACA TCTCCCTATAGTGAGT CGTATTATC-3') and 2S rRNA (5'-GATAATACGACTCACTATAGGGA GA-3'/5'-TGCTTGACTACATATGGTTGAGGGTTGTATCTCCCTATAGT GAGTCGTATTATC-3').

Luciferase assays were performed using standard approaches<sup>5</sup>. Specifically, 8 × 10<sup>4</sup> DL1 cells were plated and bathed in 30 µl of serum-free medium with 60 ng of dsRNA in each well of a 96-well plate. The next day, 1.6 ng of pMT-Firefly, 400 ng of pMT-*mir-34* and 400 ng of pMT-renilla *E74A* wild-type or mutant 3' UTR reporters were transfected by Effectene (Qiagen). Two days after transfection, the expression of the reporters and *mir-34* was induced by CuSO<sub>4</sub>. Twenty-four hours after induction, luminescence assays were performed by the Dual-Glo Luciferase Assay System (Promega). The *mir-34* seed sequences in the 3' UTR of *E74A* were mutated as noted in Supplementary Fig. 3, using the Quik change mutagenesis system (Stratagene). Primers to knockdown *vgo1* are described<sup>5</sup>.

The miRNA-target prediction algorithms TargetScan (v5.1)<sup>31</sup> and PicTar (fly)<sup>32</sup> were used to determine miR-34 target mRNA candidates.

**miRNA microarray analysis.** For miRNA array analysis, Iso31 flies (isogenized *w<sup>1118</sup>*) were used. Flies were killed by brief submersion in ethanol under CO<sub>2</sub> anaesthesia, followed by two PBS washes (Sigma). To control for circadian effects, all flies were processed between 11:00 and 13:00. Brains were removed manually and collected in an Eppendorf microcentrifuge tube stored on ice. For each miRNA microarray replicate, 200–300 brains were collected for each time point,



with a ~50/50 ratio of males and females. RNA was prepared using the miRvana RNA extraction system (Ambion) yielding ~2.5 µg per 100 brains. RNA was eluted into 80 µl of RNase free water (Fisher Scientific) and stored at -80 °C. miRNA profiling was carried out at the Penn microarray core facility using miRCURY LNA arrays (Exiqon) and protocols. Exiqon's Hy3/H5-labelling kit was used (Exiqon). RNA samples were labelled with Hy3 and hybridized together with a Hy5-labelled common reference standard. The common reference standard consisted of equal amounts of RNA from brains of 3 days, 30 days and 60 days flies. The miRNA microarray data were analysed at the Penn Bioinformatics Core. Raw data was imported into Gene Spring 1.0 (Agilent) and normalized using a global LOESS regression algorithm (locally weighted scatterplot smoothing). Relative expression levels were calculated as the log<sub>2</sub> normalized signal intensity difference between the Hy3 and Hy5 intensity. Present/absent flagging was analysed by Exiqon (Exiqon). Expression levels (fold changes) for the 30 day and 60 day time point were calculated relative to the 3 day time point. The data sets were exported into Spotfire DecisionSite 9.0 (Tibco) for visualization and filtering.

**mRNA microarray analysis.** For ageing microarray analysis, fly stock Iso31 was used. For *mir-34* mutant microarray analysis, *mir-34* null line-1 in 5905 background was used, with fly 5905 line, as control. To generate an ageing profile, flies were aged to 3 days, 30 days and 60 days, and 30–50 brains dissected per time point, per replicate, as above (50–50 males and females). For each time point, three replicates were conducted. For *mir-34* mutant microarray analysis, time points were 3 days and 20 days, and for each time point, 20 brains from male flies of the appropriate genotype were used, with five replicates in total. Microarray hybridization and reading was performed at the Penn Microarray Core Facility. For mRNA microarrays, total RNA was reverse transcribed to ss-cDNA, followed by two PCR cycles using the Ovation RNA amplification system V2 (Ovation). Quality control on both RNA and ss-cDNA was performed using an 2100 Agilent Bioanalyzer (Quantum Analytics). The cDNA was labelled using the FL-Ovation cDNA Biotin Module V2 (Ovation), hybridized to Affymetrix *Drosophila* 2.0 chips (Affymetrix) and scanned with an Axon Instruments 4000B Scanner using GenePix Pro 6.0 image acquisition software (Molecular Devices). Affymetrix .cel (probe intensity) files were exported from GeneChip Operating Software (Affymetrix). The .cel files were imported to ArrayAssist Lite (Agilent) in which GCRMA probe-set expression levels and Affymetrix absent/present/marginal flags were calculated. Statistical analysis for those genes passing the flag filter was performed using Partek Genomics Suite (Partek). The signal values were log<sub>2</sub> transformed and a 2-way ANOVA was performed.

**Transcriptional analysis of ageing status.** We first used the wild type to extract age-associated probe sets and then compared the relative changes of these probe sets in a separate set of transcriptional profiles generated for the wild type and *mir-34* mutant. For transcriptional profiles of normal aged brains, the GCRMA package RMA (J. Z. Wu, J. MacDonald and J. Gentry, GCRMA: background adjustment using sequence information, R package version 2.14) for R/Bioconductor<sup>33</sup> was used to generate log<sub>2</sub> expression levels for probe-set IDs from the original .cel files. Then, a linear regression model was used to compute the significance of a correlation between age and gene expression<sup>9</sup>. This approach assumes a linear relationship between age and log<sub>2</sub> expression level:

$$Y_{ij} = \mu_i + \beta_{1i}A_j + \epsilon_{ij}$$

In this equation,  $Y_{ij}$  is the log<sub>2</sub> gene expression level of probe set  $i$  in sample  $j$ ,  $A_j$  is the age for individual  $j$ . The coefficients  $\beta_{1i}$  is regression coefficients reflecting the rate of change in gene expression with respect to age. Probe sets with expression significantly correlated with age ( $P \leq 0.001$  for  $\beta_{1i}$ ) were determined. Then the same probe sets were used to estimate the relative expression in separate profiles of *mir-34* mutants and age-matched controls. The average levels of each individual probe set were calculated for the difference between 20 day and 3 day, within the same genotype (that is,  $\Delta 20$  day/ $\Delta 3$  day) for each gene in controls and *mir-34* mutants, respectively. These differences were then compared between genotypes (that is, *mir-34* mutants – controls). The significance of the difference between genotypes was analysed using a paired Wilcoxon test. The difference between control and mutant samples in positively correlated genes (Fig. 2d) is not by chance ( $P = 0.0001$ ).

28. Parks, A. L. *et al.* Systematic generation of high-resolution deletion coverage of the *Drosophila melanogaster* genome. *Nature Genet.* **36**, 288–292 (2004).
29. Li, L. B., Yu, Z., Teng, X. & Bonini, N. M. RNA toxicity is a component of ataxin-3 degeneration in *Drosophila*. *Nature* **453**, 1107–1111 (2008).
30. Dockendorff, T. C. *et al.* *Drosophila* lacking dfmr1 activity show defects in circadian output and fail to maintain courtship interest. *Neuron* **34**, 973–984 (2002).
31. Lewis, B. P., Shih, I. H., Jones-Rhoades, M. W., Bartel, D. P. & Burge, C. B. Prediction of mammalian microRNA targets. *Cell* **115**, 787–798 (2003).
32. Grün, D., Wang, Y. L., Langenberger, D., Gunsalus, K. C. & Rajewsky, N. microRNA target predictions across seven *Drosophila* species and comparison to mammalian targets. *PLOS Comput. Biol.* **1**, e13 (2005).
33. Gentleman, R. C. *et al.* Bioconductor: open software development for computational biology and bioinformatics. *Genome Biol.* **5**, R80 (2004).

# Maintenance of muscle stem-cell quiescence by microRNA-489

Tom H. Cheung<sup>1,2</sup>, Navaline L. Quach<sup>1,2</sup>, Gregory W. Charville<sup>1,2,3</sup>, Ling Liu<sup>1,2</sup>, Lidia Park<sup>1,2</sup>, Abdolhossein Edalati<sup>1,2</sup>, Bryan Yoo<sup>1,2</sup>, Phuong Hoang<sup>1,2</sup> & Thomas A. Rando<sup>1,2,4,5</sup>

**Among the key properties that distinguish adult mammalian stem cells from their more differentiated progeny is the ability of stem cells to remain in a quiescent state for prolonged periods of time<sup>1,2</sup>. However, the molecular pathways for the maintenance of stem-cell quiescence remain elusive. Here we use adult mouse muscle stem cells (satellite cells) as a model system and show that the microRNA (miRNA) pathway is essential for the maintenance of the quiescent state. Satellite cells that lack a functional miRNA pathway spontaneously exit quiescence and enter the cell cycle. We identified quiescence-specific miRNAs in the satellite-cell lineage by microarray analysis. Among these, miRNA-489 (miR-489) is highly expressed in quiescent satellite cells and is quickly downregulated during satellite-cell activation. Further analysis revealed that miR-489 functions as a regulator of satellite-cell quiescence, as it post-transcriptionally suppresses the oncogene *Dek*, the protein product of which localizes to the more differentiated daughter cell during asymmetric division of satellite cells and promotes the transient proliferative expansion of myogenic progenitors. Our results provide evidence of the miRNA pathway in general, and of a specific miRNA, miR-489, in actively maintaining the quiescent state of an adult stem-cell population.**

The miRNA pathway has been shown to be essential for stem-cell pluripotency, proliferation and differentiation<sup>3,4</sup>. To understand whether adult quiescent stem cells are under active post-transcriptional control by miRNAs, we conditionally ablated the miRNA processing enzyme Dicer in adult muscle stem cells, or satellite cells, using a mouse strain that expresses a satellite-cell-specific, tamoxifen-inducible Cre/*loxP* system<sup>5</sup> (Supplementary Fig. 1) and is homozygous for a floxed Dicer allele<sup>6</sup> and a Cre-dependent yellow fluorescent protein (YFP) reporter<sup>7</sup>. Six days after the first tamoxifen injection to this conditional knockout strain, Dicer protein and miRNA levels were significantly downregulated in YFP-positive satellite cells ( $P < 0.001$ ; Supplementary Figs 2 and 3). Notably, in conditional knockout mice we detected YFP-positive satellite cells that had spontaneously exited quiescence and entered the cell cycle (Fig. 1a, b). In control mice, less than 1% of YFP-positive satellite cells were Ki67-positive at this time. These observations suggest that an intact miRNA pathway is essential for the maintenance of satellite-cell quiescence. Deletion of Dicer also led to apoptosis of proliferating satellite-cell progeny (Fig. 1c, d and Supplementary Fig. 4). Together, these experiments demonstrate the essential role of miRNAs in the maintenance of satellite-cell quiescence and in the survival of proliferating myogenic progenitors.

To assess the impact of miRNA pathway disruption on satellite-cell homeostasis, we quantified the number of satellite cells using single-fibre explants and mononuclear cells that were isolated from uninjured muscles of conditional knockout mice 2 weeks after tamoxifen injections. We observed a marked reduction in satellite-cell number in the absence of Dicer (Fig. 1e, f). To confirm the functional loss of satellite

cells, hindlimb muscles of tamoxifen-injected conditional knockout mice were injured to induce satellite-cell-mediated regeneration. Seven days after injury, very few regenerated fibres were observed in the conditional knockout mice, indicating severely impaired regeneration (Fig. 1g). Further analysis 6 months after injury revealed a marked reduction in the mass of injured muscles compared to the contralateral, uninjured muscles. By comparison, control mice exhibited a hypertrophic response after muscle injury (Fig. 1h). Consistent with the finding that adult muscle satellite cells have a low turnover rate<sup>8</sup>, uninjured muscle appeared in general to be normal 6 months after disruption of the Dicer gene (Supplementary Fig. 5a). However, the loss of satellite cells resulted in mild muscle-fibre atrophy in conditional knockout animals over time (Supplementary Fig. 5b).

As the disruption of Dicer caused satellite cells to break quiescence and enter the cell cycle, we were interested in defining the role of specific miRNAs in maintaining the quiescent state. Quantitative real-time polymerase-chain-reaction (qRT-PCR)-based miRNA microarray analysis of highly purified quiescent satellite cells (QSCs) and activated satellite cells (ASCs) (Supplementary Fig. 6) revealed that 351 miRNAs were differentially regulated during satellite-cell activation (Supplementary Table 1). Of these, 22 were highly expressed in the quiescent state and markedly downregulated after satellite-cell activation (Fig. 2a). Among the 22 quiescence-specific miRNAs, we focused on miR-489 because it is evolutionarily conserved among species<sup>9</sup> and because it resides in intron 4 of the gene encoding calcitonin receptor (the *Ctr* gene; also known as *Calcr*) (Supplementary Fig. 7a), which is highly expressed in QSCs (Supplementary Fig. 7b, c) and has previously been shown to regulate satellite-cell quiescence<sup>10</sup>. Previous reports have suggested that intronic miRNAs co-express with host genes to co-regulate similar pathways<sup>11</sup>. The quiescence-specific expression of miR-489 and CTR was verified by qRT-PCR analysis (Fig. 2b, c). To determine whether miR-489 is specifically expressed in QSCs, we performed qRT-PCR analysis of isolated satellite cells and other mononuclear cell populations from uninjured muscle. As expected from the expression pattern of CTR (Supplementary Fig. 7c), miR-489 was highly enriched in QSCs relative to multinucleate muscle fibres or other mononuclear cells in the muscle (Fig. 2d, e).

To test whether a sustained expression of miR-489 could lead to an impairment of muscle regeneration by suppressing satellite-cell activation, an miR-489 expression plasmid was electroporated into hindlimb muscles *in vivo*. qRT-PCR analysis revealed a high level of miR-489 expression in tibialis anterior muscles electroporated with miR-489 plasmid compared with the level in controls (Supplementary Fig. 8b). Six days after electroporation, control muscles exhibited normal regeneration, whereas muscles expressing miR-489 exhibited a severe defect in regeneration (Fig. 3a and Supplementary Fig. 8a).

To test the hypothesis that overexpression of miR-489 suppresses muscle regeneration by maintaining satellite-cell quiescence and

<sup>1</sup>Paul F. Glenn Laboratories for the Biology of Aging, Stanford University School of Medicine, Stanford, California 94305, USA. <sup>2</sup>Department of Neurology and Neurological Sciences, Stanford University School of Medicine, Stanford, California 94305, USA. <sup>3</sup>Department of Developmental Biology, Stanford University School of Medicine, Stanford, California 94305, USA. <sup>4</sup>Neurology Service, Veterans Affairs Palo Alto Health Care System, Palo Alto, California 94304, USA. <sup>5</sup>Rehabilitation Research and Development Center of Excellence, Veterans Affairs Palo Alto Health Care System, Palo Alto, California 94304, USA.

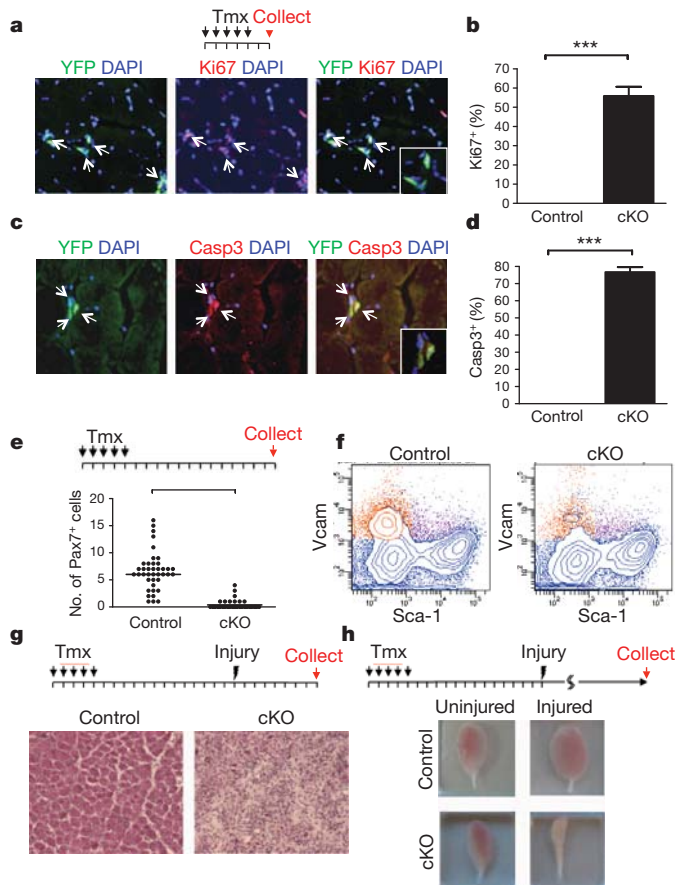


**Figure 1 | The miRNA pathway is essential for the maintenance of satellite-cell quiescence and survival of activated satellite cells.** **a**, The tamoxifen (Tmx) injection scheme (black arrows) for conditional Dicer gene inactivation is shown (top). Each tick represents 1 day. Six days after the first injection, Ki67 YFP double-positive satellite cells were found (white arrows). Nuclei were stained with DAPI. **b**, Quantification of the percentage of YFP-positive cells that were Ki67-positive (Ki67<sup>+</sup>) in control and conditional knockout strain (cKO) mice (\*\**P* < 0.001). **c**, Six days after the first tamoxifen injection, muscles from control or cKO mice were analysed for apoptosis by staining for cleaved caspase 3. Nuclei were stained with DAPI. Inset in **a** and **c**, magnified view of the satellite cells in the full-size images. **d**, Quantification of the percentage of YFP-positive cells that were caspase-3-positive (Casp3<sup>+</sup>) in control and cKO animals (\*\**P* < 0.001). **e**, Satellite-cell numbers were quantified on freshly isolated single fibres from control and cKO mice 2 weeks after tamoxifen injections (\**P* < 0.001). **f**, Satellite-cell numbers were quantified by FACS analyses of mononuclear cells from hindlimb muscles of control and cKO mice. Satellite cells are shown in orange in these representative FACS plots (See Supplementary Fig. 4). In four replicates, the percentage of satellite cells in total mononuclear cells in cKO muscles was markedly reduced (0.7%) compared to that in control muscles (3.0%). Blue, all other mononuclear cells. **g**, Tibialis anterior muscles from control or cKO mice were injured 2 weeks after tamoxifen injection and cryosections were stained with haematoxylin and eosin 7 days after injury. **h**, Tibialis anterior muscles from control or cKO mice were injured 2 weeks after tamoxifen injection and collected 6 months after injury. Severe muscle loss was observed in injured muscles from cKO mice only (shown next to the contralateral, uninjured muscle for comparison). Error bars in **b** and **d** indicate s.e.m.

suppressing activation, we overexpressed miR-489 or anti-miR-489 in fibre-associated QSCs *ex vivo*. Using syndecan 4 as a satellite-cell marker on fibre explants<sup>12,13</sup>, we quantified the number of satellite cells on fibres 3 days after transfection. Satellite cells treated with anti-miR-489 exhibited similar proliferative activity as control satellite cells, whereas satellite cells treated with miR-489 exhibited markedly reduced proliferation (and no evidence of apoptosis) (Fig. 3b). Furthermore, fewer than 50% of the cells treated with miR-489 progressed through a single round of cell division over the course of the experiment as

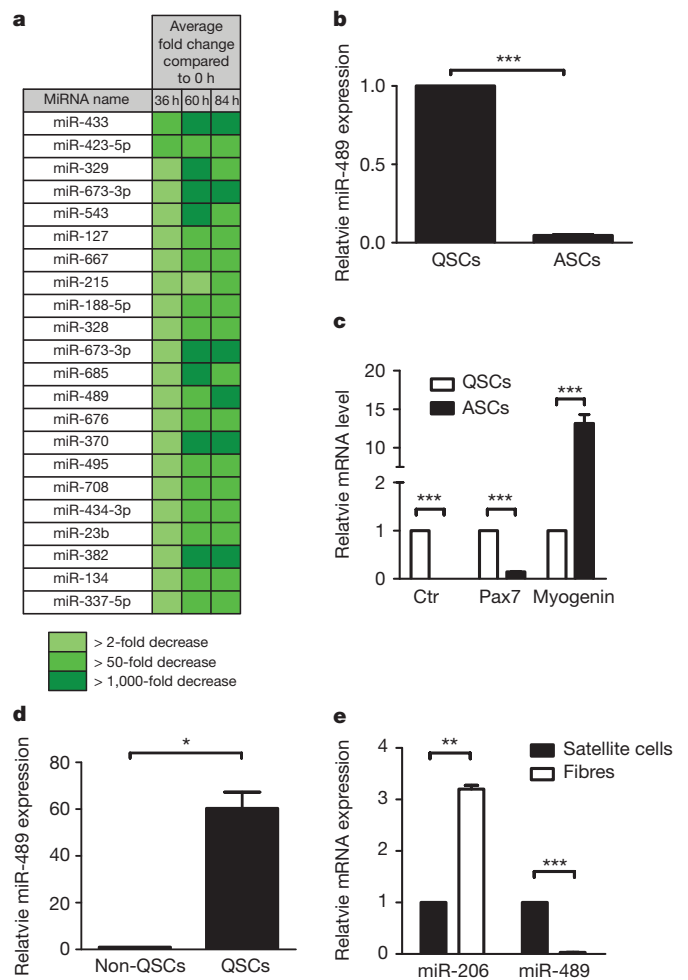


**Figure 2 | miRNA expression in purified QSCs and ASCs.** **a**, miRNA expression profiling during satellite-cell activation using qRT-PCR-based miRNA arrays. QSCs from uninjured muscles and ASCs from injured muscles at indicated time points were isolated by FACS (Supplementary Fig. 6). QSC-specific mouse miRNAs are shown. The complete data set is shown in Supplementary Table 1. **b**, qRT-PCR analysis of miR-489 transcript in QSCs and ASCs. Expression levels were normalized to snoRNA420. \*\*\* $P < 0.001$ . **c**, qRT-PCR analysis of CTR, Pax7 and myogenin mRNA. Expression levels were normalized to glyceraldehyde-3-phosphate dehydrogenase (GAPDH). \*\*\* $P < 0.001$ ; \*\* $P < 0.01$ . **d**, qRT-PCR analysis of miR-489 transcript in QSCs and all other mononuclear cells in hindlimb muscles. Expression levels were normalized to snoRNA420. \* $P < 0.05$ . **e**, qRT-PCR analysis of miR-206 and miR-489 transcript in QSCs and single-fibre explants. Expression levels were normalized to snoRNA420. \*\*\* $P < 0.001$ ; \*\* $P < 0.01$ . All error bars indicate s.e.m.

determined by 5-ethynyl-2'-deoxyuridine (EdU) labelling (Fig. 3c). To test whether miR-489 regulates satellite-cell quiescence in a cell-autonomous manner, we used myogenic differentiation 1 (Myod; also known as Myod1) expression as an indicator of satellite-cell activation<sup>14</sup> and quantified the percentage of satellite cells expressing Myod 48 h after miR-489 transfection. Consistent with the fibre-explant experiment, miR-489 suppressed satellite-cell activation (Fig. 3d). Together, these experiments demonstrate that miR-489 regulates satellite-cell quiescence in a cell-autonomous manner and that over-expression of a single miRNA is sufficient to prolong the quiescent state and delay QSC activation, resulting in an impairment of regeneration *in vivo*.

Next, we tested whether inhibition of miR-489 could result in the spontaneous activation of QSCs, which rarely divide in the absence of any activating stimuli<sup>8</sup>. Cholesterol-conjugated ‘antagomirs’ (ref. 15) that specifically target miR-489, or control scrambled antagomirs,



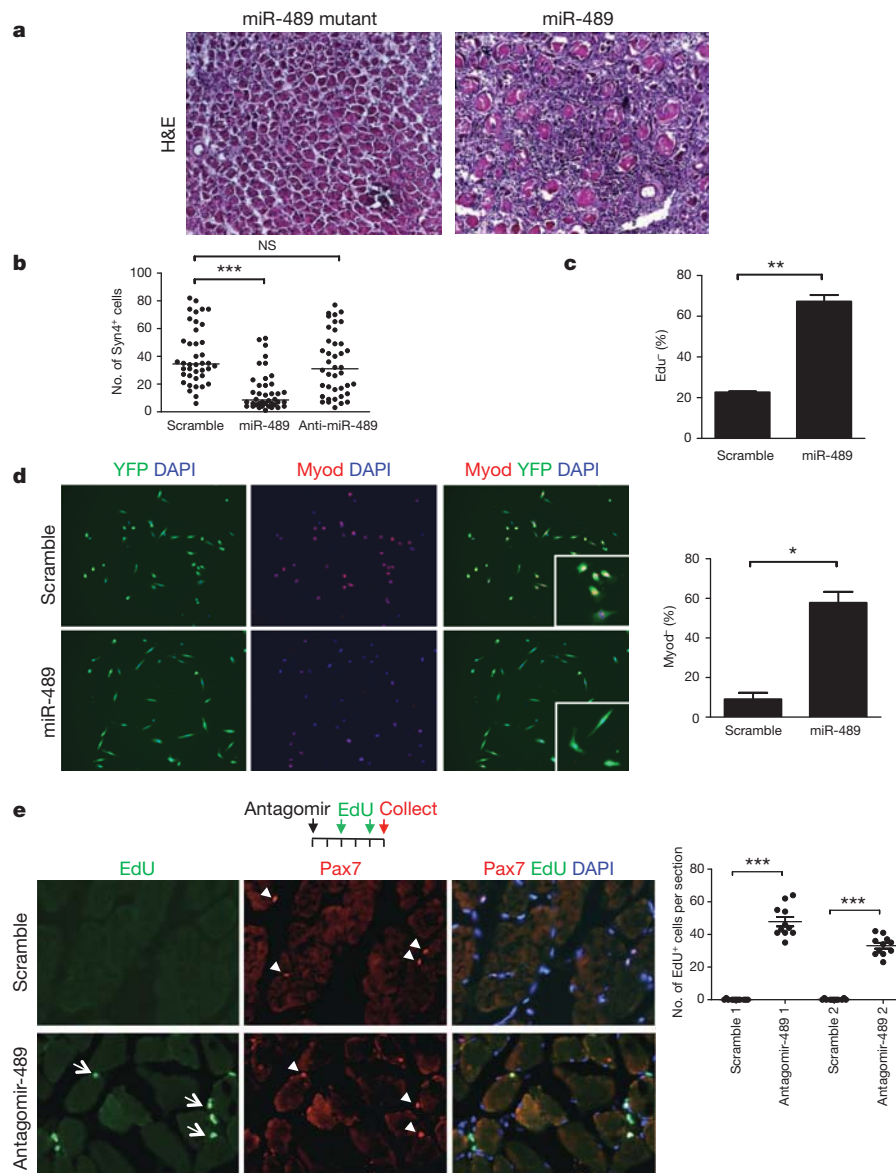


**Figure 3 | miRNA-489 regulates satellite-cell quiescence.** **a**, Hindlimb muscles were electroporated with either miR-489 expression plasmid (right) or a control miR-489 mutant plasmid (left). Muscles were collected 6 days later and haematoxylin and eosin staining was performed on cryosections. **b**, miR-489 or anti-miR-489 was overexpressed in fibre-associated satellite cells. Three days after transfection, the number of syndecan-4-positive (Syn4<sup>+</sup>) satellite-cell progeny was quantified. \*\*\* $P < 0.001$ ; NS, not significant. **c**, In studies such as those in **b**, EdU was added to the medium at the time of miR-489 (or control) transfection and the percentage of Syn4<sup>+</sup> cells that were EdU-negative (EdU<sup>-</sup>) was determined after 3 days. \*\* $P < 0.01$ . **d**, Left, FACS-sorted QSCs from

*Pax7*<sup>CreER/+</sup>; *ROSA*<sup>eYFP/+</sup> mice were plated and transfected with miR-489 and analysed for Myod expression 48 h later. Right, quantification of the percentage of YFP-positive cells that were Myod-negative (Myod<sup>-</sup>). Nuclei were stained with DAPI. \* $P < 0.05$ . **e**, Left, satellite-cell activation *in vivo*, as determined by EdU incorporation, was assessed in muscles in which miR-489 was inhibited by the systemic injection of a cholesterol-conjugated anti-miR-489 oligonucleotide (antagomir-489) or a scrambled antagomir (scramble). Pax7 EdU double-positive (arrows) and Pax7-positive cells (arrowheads) are highlighted. Right, quantification of the number of EdU-positive (EdU<sup>+</sup>) cells on cryosections. Two representative replicates of four independent experiments are shown (nuclei were stained with DAPI). \*\*\* $P < 0.001$ . All error bars indicate s.e.m.

were delivered systemically to adult mice. Four days after a single antagomir injection, miR-489 transcript levels decreased precipitously (Supplementary Fig. 9). In contrast to the control mice, which were injected with scrambled antagomirs, mice injected with anti-miR-489 antagomirs exhibited spontaneous activation of QSCs that incorporated EdU (Fig. 3e). Notably, inhibition of one quiescence-specific miRNA, miR-489, was sufficient to induce QSCs to break quiescence and progress through the cell cycle in uninjured muscle.

The observation that inhibition of miR-489 induced satellite-cell activation and proliferation prompted us to test whether miR-489 functions to suppress one or more key regulators of proliferation, thereby maintaining the quiescent state. We used the bioinformatics tool TargetScan to search for miR-489 target genes that contain putative

miR-489 target sites in their 3' untranslated regions (3' UTRs)<sup>9</sup>. Among the 86 targets predicted by TargetScan, the transcript with the highest context score<sup>16</sup> was the oncogene *Dek* (Supplementary Fig. 10), which has been shown to be induced in tumour cells and to regulate cell proliferation and messenger RNA splicing<sup>17,18</sup>. We analysed the temporal expression of *Dek* mRNA and protein during satellite-cell activation. Using paired box protein 7 (*Pax7*) as a marker of QSCs and Myod as a marker of ASCs<sup>19,20</sup>, we found that *Dek* protein was not expressed in QSCs but was strongly upregulated after satellite-cell activation both in fibre-explant studies *ex vivo* and in regeneration studies *in vivo* (Fig. 4a and Supplementary Fig. 11a–c). Likewise, *Dek* mRNA levels were higher in ASCs compared to QSCs (Supplementary Fig. 11d).

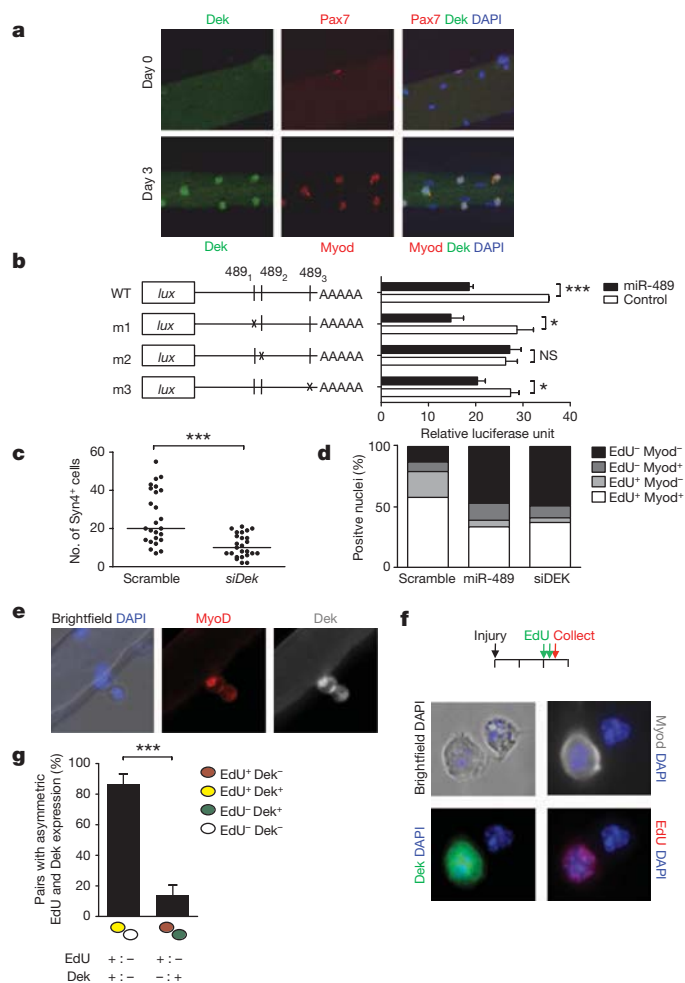


**Figure 4 | Targeting of *Dek* mRNA by miR-489 and regulation of cell-fate decision of satellite-cell progeny by *Dek*.** **a**, Co-localization of Dek and myogenic markers in fibre-associated satellite cells. Fibre explants were fixed immediately after isolation (Day 0) or cultured for 3 days in suspension and stained for expression of Pax7 and Dek, or Myod and Dek, as indicated. Nuclei were stained with DAPI. **b**, CMV-miR-489 was co-transfected into 293T cells with wild-type (WT) or mutant *Dek* 3' UTR constructs inserted after the stop codon of a luciferase gene. The *Dek* 3' UTR carries three putative miR-489 target sites (489<sub>1</sub>, 489<sub>2</sub> and 489<sub>3</sub>) (putative pairing as shown in Supplementary Fig. 10). Schematics of wild-type and mutant constructs (m1, m2 and m3) are shown with the relative luciferase activities associated with each construct. \*\*\**P* < 0.001; \**P* < 0.05; NS: not significant. **c**, Satellite cells in fibre explants were transfected with *Dek* short interfering RNA (siRNA) (*siDek*) and cultured for 3 days, and the satellite-cell progeny were quantified by syndecan 4 staining (*n* = 3). \*\*\**P* < 0.001. **d**, FACS-purified QSCs were plated and transfected with miR-489 or *siDek* for 48 h. EdU was added to the medium at the same time as transfection. Cells were stained for EdU incorporation and Myod expression. Bar graphs show the proportion of cells expressing each marker under each condition. **e**, Dek asymmetrically localizes to one daughter after cell division. Fibre-associated satellite cells were cultured for 48 h and stained for expression of Myod and Dek. Nuclei were stained with DAPI. **f**, The timeline for injury, EdU injections and collection of cells is shown (top). Cells were stained for EdU incorporation to reveal nonrandom template-strand segregation and for Myod expression to reveal divergent cell fates. Dek co-segregates almost exclusively with the newly synthesized template strands. Images show a representative example of a cell pair exhibiting divergent cell fates with asymmetric segregation of template strands. Nuclei were stained with DAPI. **g**, Quantitative analysis of concordant and discordant asymmetries of Dek and EdU in asymmetric satellite-cell divisions in studies such as those in **f**. \*\**P* < 0.001. All error bars indicate s.e.m.

Dek protein was downregulated when QSCs or myoblasts were transfected with miR-489 (Supplementary Fig. 12), suggesting that Dek is a direct target of miR-489. To test this directly, wild-type and

mutant versions of the 3' UTR of Dek were cloned downstream of a luciferase reporter, and these reporter constructs were co-transfected with an miR-489 expression construct into 293T cells. The wild-type *Dek* 3' UTR was effectively downregulated by miR-489 (Fig. 4b). Although TargetScan analysis revealed three potential target sites for miR-489, a single site (m2) was sufficient to account for the suppression of reporter expression by miR-489 (Fig. 4b).

We next examined the role of Dek in satellite-cell quiescence and activation using a loss-of-function approach. Dek knockdown reduced satellite-cell proliferation (Fig. 4c) and prevented satellite-cell activation to the same degree as did miR-489 overexpression (Fig. 4d). The ability of Dek knockdown to phenocopy the effect of miR-489 overexpression suggests a central role of Dek in regulating satellite-cell exit from quiescence. To understand whether miR-489 overexpression suppresses proliferation by regulating Dek expression, we overexpressed miR-489 or miR-489 mutant with a Dek complementary DNA construct that lacks its 3' UTR in proliferating myoblasts. Overexpression of miR-489 alone reduced cell proliferation, whereas overexpression of Dek substantially increased cell proliferation independent of the expression of miR-489 or miR-489 mutant (Supplementary Fig. 13). Together, these experiments suggest that Dek is an important target of miR-489 that is involved in the regulation of satellite-cell quiescence and activation.

Although Dek expression was highly induced after satellite-cell activation, consistent with its role in proliferative expansion of the transit-amplifying myogenic progenitors, it was absent in self-renewed satellite cells after muscle injury *in vivo* (Supplementary Fig. 11c). We therefore studied satellite-cell self-renewal in fibre explants *ex vivo*, in which the asymmetric expression of Myod by daughter cells heralds a divergent cell fate whereby the Myod-positive daughter progresses along the myogenic lineage and the Myod-negative daughter renews the satellite-cell population<sup>19</sup>. Intriguingly, in such pairs, we observed asymmetric Dek expression, in which Dek expression coincided with Myod expression in the same daughter cell (Fig. 4e). This co-localization suggests that the Dek-positive daughter is destined for proliferative amplification as a progenitor and that the Dek-negative daughter is destined for self-renewal. To test whether the process of self-renewal is associated with the absence of Dek, we examined cells undergoing asymmetric division by analysing nonrandom chromosome segregation, a process that we and others have previously shown to distinguish the differentiating progenitor from the self-renewing stem cell<sup>21,22</sup>. Consistent with the Myod asymmetry, we found that Dek was absent in the daughter cell inheriting chromosomes bearing older template DNA strands, an inheritance pattern that is characteristic of the self-renewing cell, whereas Dek was expressed in the daughter cell that is destined for proliferative amplification and differentiation (Fig. 4f, g and Supplementary Fig. 14).

The finding that Dek is a key target of miR-489 in maintaining quiescence provides insight into the molecular pathways that regulate the quiescent state. These data demonstrate that the molecular regulation of quiescence is dependent on the expression of specific miRNAs and is integrated in the signalling network that regulates divergent fates of stem-cell progeny during asymmetric cell division.

## METHODS SUMMARY

**Single-fibre explants.** Extensor digitorum longus (EDL) muscles were excised and digested in Collagenase II (500 units per ml in Ham's F10 medium) as previously described<sup>23</sup>. Fibres were then washed extensively and cultured in medium containing Ham's F10, 10% horse serum and 0.05% chick embryo extract. Every 24 h, 50% of the medium was replaced with Ham's F10 medium with 20% FBS. Extensor digitorum longus (EDL) fibres were cultured in suspension. Fixed fibres were stained and the number of satellite cells was quantified per fibre.

**Satellite-cell isolation and fluorescence-activated cell sorting.** Hindlimb muscles were dissected and dissociated to yield a muscle suspension and digested with Collagenase II (500 units per ml; Invitrogen) in Ham's F10 medium with 10% horse serum (Invitrogen) for 90 min. Digested fibre suspensions were washed and digested further with Collagenase II (100 units per ml) and Dispase (2 units per ml;

invitrogen) for 30 min. Digested fibre suspensions were triturated and washed further to yield a mononuclear-cell suspension for cell-surface staining for fluorescence-activated cell sorting (FACS). Mononuclear cells were stained with Vcam-biotin (clone 429; BD Bioscience), CD31-APC (clone MEC 13.3; BD Bioscience), CD45-APC (clone 30-F11; BD Bioscience) and Sca-1-Pacific-Blue (clone D7; Biolegend) at 1:75. Streptavidin-PE-cy7 was used to amplify the Vcam signal (BD Biosciences, 1:75). Cell sorting was performed using a BD FACSaria II or BD FACSaria III cell sorter equipped with 488-nm, 633-nm and 405-nm lasers. The machine was optimized for purity and viability, and sorted cells were subjected to FACS analysis directly after sorting to ensure purity. A small fraction of sorted cells was plated and stained for Pax7 and Myod to assess the purity of the sorted population purity.

**Full Methods** and any associated references are available in the online version of the paper at [www.nature.com/nature](http://www.nature.com/nature).

**Received 16 January 2011; accepted 5 January 2012.**

- Li, L. & Clevers, H. Coexistence of quiescent and active adult stem cells in mammals. *Science* **327**, 542–545 (2010).
- Fuchs, E. The tortoise and the hare: slow-cycling cells in the stem cell race. *Cell* **137**, 811–819 (2009).
- Yi, R., Poy, M. N., Stoffel, M. & Fuchs, E. A skin microRNA promotes differentiation by repressing 'stemness'. *Nature* **452**, 225–229 (2008).
- Tiscornia, G. & Izpisua Belmonte, J. C. MicroRNAs in embryonic stem cell function and fate. *Genes Dev.* **24**, 2732–2741 (2010).
- Nishijo, K. *et al.* Biomarker system for studying muscle, stem cells, and cancer *in vivo*. *FASEB J.* **23**, 2681–2690 (2009).
- Harfe, B. D., McManus, M. T., Mansfield, J. H., Hornstein, E. & Tabin, C. J. The RNaseIII enzyme Dicer is required for morphogenesis but not patterning of the vertebrate limb. *Proc. Natl Acad. Sci. USA* **102**, 10898–10903 (2005).
- Srinivas, S. *et al.* Cre reporter strains produced by targeted insertion of EYFP and ECFP into the ROSA26 locus. *BMC Dev. Biol.* **1**, 4 (2001).
- Morgan, J. E. & Partridge, T. A. Muscle satellite cells. *Int. J. Biochem. Cell Biol.* **35**, 1151–1156 (2003).
- Friedman, R. C., Farh, K. K., Burge, C. B. & Bartel, D. P. Most mammalian mRNAs are conserved targets of microRNAs. *Genome Res.* **19**, 92–105 (2009).
- Fukada, S. *et al.* Molecular signature of quiescent satellite cells in adult skeletal muscle. *Stem Cells* **25**, 2448–2459 (2007).
- van Rooij, E. *et al.* Control of stress-dependent cardiac growth and gene expression by a microRNA. *Science* **316**, 575–579 (2007).
- Olguin, H. C. & Olwin, B. B. Pax-7 up-regulation inhibits myogenesis and cell cycle progression in satellite cells: a potential mechanism for self-renewal. *Dev. Biol.* **275**, 375–388 (2004).
- Tanaka, K. K. *et al.* Syndecan-4-expressing muscle progenitor cells in the SP engraft as satellite cells during muscle regeneration. *Cell Stem Cell* **4**, 217–225 (2009).
- Zammit, P. S., Partridge, T. A. & Yablonka-Reuveni, Z. The skeletal muscle satellite cell: the stem cell that came in from the cold. *J. Histochem. Cytochem.* **54**, 1177–1191 (2006).
- Krutzfeldt, J. *et al.* Silencing of microRNAs in vivo with 'antagomirs'. *Nature* **438**, 685–689 (2005).
- Grimson, A. *et al.* MicroRNA targeting specificity in mammals: determinants beyond seed pairing. *Mol. Cell* **27**, 91–105 (2007).
- Khodadoust, M. S. *et al.* Melanoma proliferation and chemoresistance controlled by the DEK oncogene. *Cancer Res.* **69**, 6405–6413 (2009).
- Soares, L. M., Zanier, K., Mackereth, C., Sattler, M. & Valcarcel, J. Intron removal requires proofreading of U2AF/3' splice site recognition by DEK. *Science* **312**, 1961–1965 (2006).
- Zammit, P. S. *et al.* Muscle satellite cells adopt divergent fates: a mechanism for self-renewal? *J. Cell Biol.* **166**, 347–357 (2004).
- Grimson, P. S. *et al.* Pax7 and myogenic progression in skeletal muscle satellite cells. *J. Cell Sci.* **119**, 1824–1832 (2006).
- Conboy, M. J., Karasov, A. O. & Rando, T. A. High incidence of non-random template strand segregation and asymmetric fate determination in dividing stem cells and their progeny. *PLoS Biol.* **5**, e102 (2007).
- Shinin, V., Gayraud-Morel, B., Gomes, D. & Tajbakhsh, S. Asymmetric division and cosegregation of template DNA strands in adult muscle satellite cells. *Nature Cell Biol.* **8**, 677–687 (2006).
- Rosenblatt, J. D., Lunt, A. I., Parry, D. J. & Partridge, T. A. Culturing satellite cells from living single muscle fibre explants. *In vitro Cell Dev. Biol. Anim.* **31**, 773–779 (1995).

**Supplementary Information** is linked to the online version of the paper at [www.nature.com/nature](http://www.nature.com/nature).

**Acknowledgements** We thank the members of the Rando laboratory for comments and discussions. We thank B. Olwin for providing the syndecan 4 antibody. This work was supported by the Glenn Foundation for Medical Research and by grants from the National Institutes of Health (NIH) (P01 AG036695, R01 AG23806 (R37 MERIT Award), R01 AR062185 and DP1 OD000392 (an NIH Director's Pioneer Award)) and the Department of Veterans Affairs (Merit Review) to T.A.R.

**Author Contributions** T.H.C. and T.A.R. conceived the study. T.H.C., N.L.Q., G.W.C., L.L. and T.A.R. designed the experiments. T.H.C., B.Y. and L.L. performed all FACS analyses. T.H.C., N.L.Q., G.W.C., L.P., A.E., B.Y. and P.H. performed the experiments and analysed the experimental data. T.H.C. and T.A.R. wrote the manuscript.

**Author Information** Reprints and permissions information is available at [www.nature.com/reprints](http://www.nature.com/reprints). The authors declare no competing financial interests. Readers are welcome to comment on the online version of this article at [www.nature.com/nature](http://www.nature.com/nature). Correspondence and requests for materials should be addressed to T.A.R. ([rando@stanford.edu](mailto:rando@stanford.edu)).



©2012 Macmillan Publishers Limited. All rights reserved

**Immunofluorescence and antibodies.** Immunofluorescence was performed using a Zeiss Observer Z1 fluorescent microscope (Zeiss) equipped with a Hamamatsu Orca-ER camera or a Zeiss confocal system LSM710 (Zeiss). Data acquisition and fibre-diameter measurements were performed using Improvision Volocity software (Perkin Elmer) or Zeiss LSM ZEN software (Zeiss).

**Antibodies.** The antibodies used in this study were Pax7 (DSHB, 1:100), Ki67 (Abcam, 1:100 and BD Bioscience, 1:50), laminin (Sigma, 1:1,000), cleaved caspase3

(Cell signaling, 1:100), Myod (Dako, 1:1,000), green fluorescent protein (GFP) (Invitrogen, 1:250 and Abcam, 1:250), Dek (Proteintech Group, 1:2,000) and syndecan 4 (gift from Bradley Olwin, 1:1,000).

24. Bertonni, C. *et al.* Enhancement of plasmid-mediated gene therapy for muscular dystrophy by directed plasmid integration. *Proc. Natl Acad. Sci. USA* **103**, 419–424 (2006).
25. Pfaffl, M. W. A new mathematical model for relative quantification in real-time RT-PCR. *Nucleic Acids Res.* **29**, e45 (2001).

# Clonal selection drives genetic divergence of metastatic medulloblastoma

Xiaochong Wu<sup>1</sup>, Paul A. Northcott<sup>1</sup>, Adrian Dubuc<sup>1</sup>, Adam J. Dupuy<sup>2</sup>, David J. H. Shih<sup>1</sup>, Hendrik Witt<sup>3</sup>, Sidney Croul<sup>4</sup>, Eric Bouffet<sup>5</sup>, Daniel W. Fuhs<sup>6</sup>, Charles G. Eberhart<sup>7</sup>, Livia Garzia<sup>1</sup>, Timothy Van Meter<sup>8</sup>, David Zagzag<sup>9</sup>, Nada Jabado<sup>10</sup>, Jeremy Schwartzentruber<sup>11</sup>, Jacek Majewski<sup>10</sup>, Todd E. Scheetz<sup>2</sup>, Stefan M. Pfister<sup>3</sup>, Andrey Korshunov<sup>12</sup>, Xiao-Nan Li<sup>13</sup>, Stephen W. Scherer<sup>14</sup>, Yoon-Jae Cho<sup>15</sup>, Keiko Akagi<sup>16</sup>, Tobey J. MacDonald<sup>17</sup>, Jan Koster<sup>18</sup>, Martin G. McCabe<sup>19</sup>, Aaron L. Sarver<sup>20</sup>, V. Peter Collins<sup>21</sup>, William A. Weiss<sup>22</sup>, David A. Largaespada<sup>20</sup>, Lara S. Collier<sup>23</sup> & Michael D. Taylor<sup>24</sup>

**Medulloblastoma, the most common malignant paediatric brain tumour, arises in the cerebellum and disseminates through the cerebrospinal fluid in the leptomeningeal space to coat the brain and spinal cord<sup>1</sup>. Dissemination, a marker of poor prognosis, is found in up to 40% of children at diagnosis and in most children at the time of recurrence. Affected children therefore are treated with radiation to the entire developing brain and spinal cord, followed by high-dose chemotherapy, with the ensuing deleterious effects on the developing nervous system<sup>2</sup>. The mechanisms of dissemination through the cerebrospinal fluid are poorly studied, and medulloblastoma metastases have been assumed to be biologically similar to the primary tumour<sup>3,4</sup>. Here we show that in both mouse and human medulloblastoma, the metastases from an individual are extremely similar to each other but are divergent from the matched primary tumour. Clonal genetic events in the metastases can be demonstrated in a restricted subclone of the primary tumour, suggesting that only rare cells within the primary tumour have the ability to metastasize. Failure to account for the bicompartamental nature of metastatic medulloblastoma could be a major barrier to the development of effective targeted therapies.**

Thirty percent of patched-1-heterozygous (*Ptch*<sup>+/-</sup>) mice develop non-disseminated medulloblastoma by 8 months of age<sup>5</sup>. Recently, the *Sleeping Beauty* (SB) transposon system was shown to be an effective tool for functional genomics studies of solid tumour initiation and progression<sup>6,7</sup>. We expressed the SB11 transposase in cerebellar progenitor cells in transgenic mice under the *Math1* (also known as *Atoh1*) enhancer/promoter, but we did not observe any tumours when these mice were bred with mice transgenic for a concatemer of the T2/Onc transposon<sup>8</sup> (Fig. 1a–j and Supplementary Figs 1 and 2). However, on a *Ptch*<sup>+/-</sup> background, these *Math1-SB11/T2Onc* mice showed increased penetrance of medulloblastoma (~97%; 271 of 279 mice) compared with controls (~39%; 54 of 139 mice), as well as decreased latency (2.5 months compared with 8 months) (Fig. 1 and Supplementary Fig. 2). Although *Ptch*<sup>+/-</sup> medulloblastomas are usually localized, the addition of SB transposition results in metastatic dissemination through the cerebrospinal fluid pathways, identical to the pattern that

is seen in human children (Fisher's exact test,  $P = 1.8 \times 10^{-7}$ , odds ratio = 5.2; Supplementary Table 1) (Fig. 1c, d and Supplementary Fig. 2). As neither transposon nor transposase alone had an effect on tumour incidence, latency or dissemination, we conclude that SB-induced insertional mutagenesis drives medulloblastoma progression on the *Ptch*<sup>+/-</sup> background (Fig. 1i and Supplementary Fig. 2).

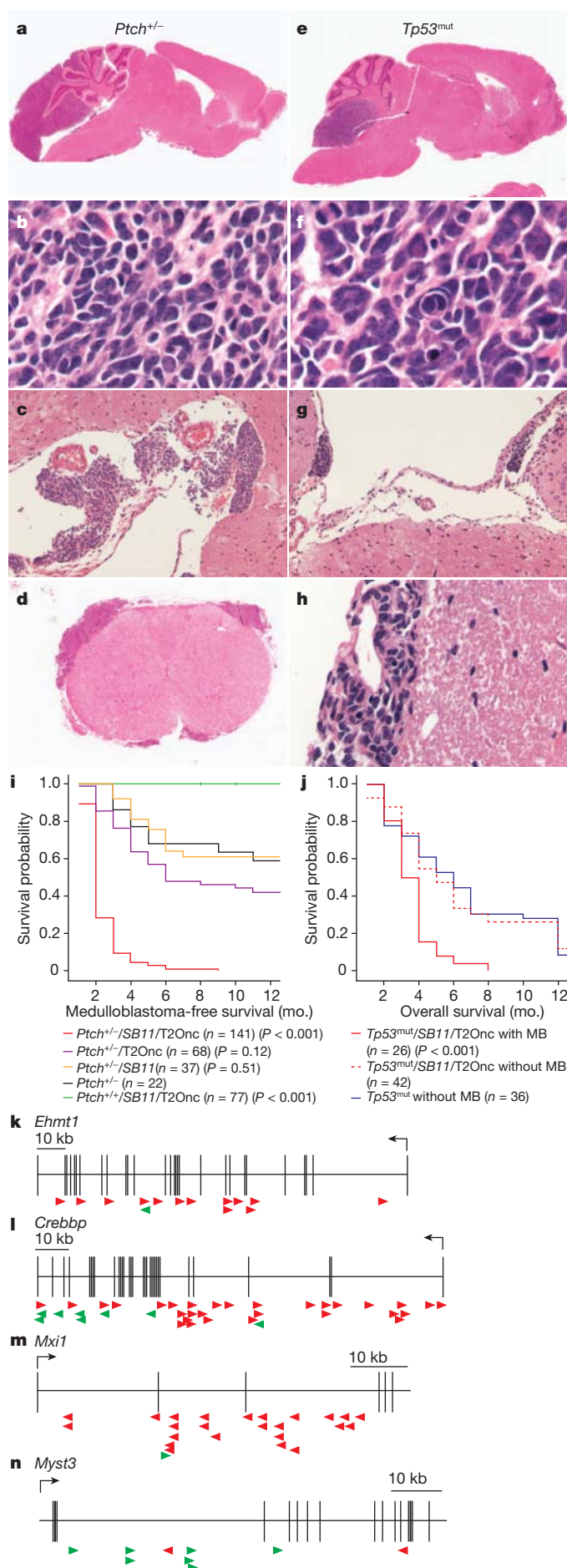
Humans with germline mutations in the tumour-suppressor gene *TP53* have Li-Fraumeni syndrome and have an increased risk of developing medulloblastoma. Although no medulloblastomas were found in mice with mutant *Tp53* (also known as *Trp53*) (denoted *Tp53*<sup>mut</sup> mice, which includes *Tp53*<sup>+/-</sup> and *Tp53*<sup>-/-</sup>), 40% of *Tp53*<sup>mut</sup>/*Math1-SB11/T2Onc* mice developed disseminated medulloblastoma<sup>9</sup> (Fig. 1e–h, j and Supplementary Fig. 2). Human medulloblastomas with *TP53* mutations frequently have large cell/anaplastic histology. *Tp53*<sup>mut</sup>/*Math1-SB11/T2Onc* medulloblastomas have large cells, nuclear atypia and nuclear moulding that is typical of large cell/anaplastic histology (Fig. 1f). We conclude that SB transposition can drive the initiation and progression of metastatic medulloblastoma on a *Tp53*<sup>mut</sup> background.

We used linker-mediated PCR and 454 sequencing to identify the site of T2/Onc insertions in *Ptch*<sup>+/-</sup>/*Math1-SB11/T2Onc* and *Tp53*<sup>mut</sup>/*Math1-SB11/T2Onc* primary medulloblastomas and their matched metastases. Genes that contained insertions statistically more frequently than the background rate were identified as gene-centric common insertion sites (gCISs)<sup>10</sup>. We identified 359 gCISs in 139 primary tumours on the *Ptch*<sup>+/-</sup> background and 26 gCISs in 36 primary medulloblastomas on the *Tp53*<sup>mut</sup> background (Supplementary Tables 2–7 and Supplementary Figs 3–5). A large number of gCISs were candidate medulloblastoma oncogenes or tumour-suppressor genes<sup>11</sup> (Supplementary Table 8). Insertions in candidate tumour-suppressor genes, including *Ehmt1*, *Crebbp* and *Mxi1*, are predicted to cause a loss of function (Fig. 1k–m), whereas insertions in putative medulloblastoma oncogenes are largely gain of function, as exemplified by *Myst3* (Fig. 1n).

Many gCISs mapped to regions of amplification, focal hemizygous deletion and homozygous deletion (Supplementary Table 8) that we

<sup>1</sup>Arthur and Sonia Labatt Brain Tumour Research Center, and Program in Developmental and Stem Cell Biology, The Hospital for Sick Children, Toronto, Ontario M5G 1X8, Canada. <sup>2</sup>Molecular & Cellular Biology Program, The University of Iowa, Iowa City, Iowa 52242, USA. <sup>3</sup>German Cancer Research Center (DKFZ), and Department of Pediatric Oncology, Hematology and Immunology, University Hospital Heidelberg, Im Neuenheimer Feld 280, 69120 Heidelberg, Germany. <sup>4</sup>University Health Network Pathology, Arthur and Sonia Labatt Brain Tumour Research Centre, Department of Laboratory Medicine and Pathobiology, University of Toronto, Toronto, Ontario M5S 1A1, Canada. <sup>5</sup>Brain Tumour Program, Haematology and Oncology, The Hospital for Sick Children, Toronto, Ontario M5G 1X8, Canada. <sup>6</sup>Department of Neurosurgery, University of Utah School of Medicine, Salt Lake City, Utah 84132, USA. <sup>7</sup>Johns Hopkins University, Baltimore, Maryland 21210, USA. <sup>8</sup>Virginia Commonwealth University, Richmond, Virginia 23284, USA. <sup>9</sup>Department of Pathology and Neurosurgery, Division of Neuropathology, New York University School of Medicine, New York, New York 10016, USA. <sup>10</sup>Departments of Human Genetics and Experimental Medicine, McGill University, Montreal H3Z 2Z3, Quebec, Canada. <sup>11</sup>McGill University and Genome Quebec Innovation Centre, Montreal, Quebec H3A 0G1, Canada. <sup>12</sup>German Cancer Research Institute (DKFZ) and Department of Neuropathology, University of Heidelberg, Im Neuenheimer Feld 220/221, 69120 Heidelberg, Germany. <sup>13</sup>Brain Tumour Program, Texas Children's Cancer Center, and Department of Pediatrics, Baylor College of Medicine, Houston, Texas 77030, USA. <sup>14</sup>Program in Genetics and Genomic Biology and The Centre for Applied Genomics, The Hospital for Sick Children, and McLaughlin Centre and Department of Molecular Genetics, University of Toronto, Toronto, Ontario M5S 1A1, Canada. <sup>15</sup>Departments of Neurology and Neurosurgery, Stanford University School of Medicine, Stanford, California 94305, USA. <sup>16</sup>Department of Molecular Virology, Immunology and Medical Genetics, The Ohio State University Comprehensive Cancer Center, Columbus, Ohio 43210, USA. <sup>17</sup>Pediatric Neuro-Oncology Program, Emory University School of Medicine, Atlanta, Georgia 30307, USA. <sup>18</sup>Department of Human Genetics, Academic Medical Center, University of Amsterdam, 1100 DE Amsterdam, The Netherlands. <sup>19</sup>School of Cancer and Enabling Sciences, University of Manchester, Manchester M20 4BX, UK. <sup>20</sup>Masonic Cancer Center, University of Minnesota, Minneapolis, Minnesota 55455, USA. <sup>21</sup>Department of Pathology, University of Cambridge, Cambridge CB2 1QP, UK. <sup>22</sup>Departments of Neurology, Pediatrics and Neurological Surgery, University of California, San Francisco, California 94143, USA. <sup>23</sup>School of Pharmacology, University of Wisconsin, Madison, Wisconsin 53715, USA. <sup>24</sup>Division of Neurosurgery, Arthur and Sonia Labatt Brain Tumour Research Center, and Program in Developmental and Stem Cell Biology, The Hospital for Sick Children, University of Toronto, Toronto, Ontario M5G 1X8, Canada.





recently reported in the genome of a large cohort of human medulloblastomas<sup>11</sup>. There is a high level of overlap between gCISs and known cancer genes (in the Catalogue of Somatic Mutations in Cancer (COSMIC) database) (Supplementary Tables 9 and 10), suggesting that many gCISs are bona fide driver genes in medulloblastoma (Fisher's exact test, *P* = 0.0012)<sup>12</sup>. Similarly, many of the mouse gCISs and the genes amplified in human medulloblastomas are over-expressed in human *SHH*-driven medulloblastomas (Supplementary Fig. 6). Conversely, mouse gCISs hemizygously deleted in human medulloblastomas were frequently expressed at a lower level in human medulloblastomas (Supplementary Fig. 6). The expression of six out of seven gCISs that had been studied by immunohistochemistry on a human medulloblastoma tissue microarray was associated with significantly worse overall and progression-free survival in human medulloblastoma<sup>13</sup> (Supplementary Table 11 and Supplementary Figs 7 and 8). We conclude that our SB-driven leptomeningeal-disseminated medulloblastoma model resembles the human disease anatomically, pathologically and genetically and thus is an accurate model of the human disease that can be used to identify candidate driver events and understand the pathogenesis of human medulloblastoma.

We compared the gCISs identified from *Ptch*<sup>+/-</sup>/*Math1*-SB11/T2Onc and *Tp53*<sup>mut</sup>/*Math1*-SB11/T2Onc primary medulloblastomas and matched metastases (Supplementary Table 2). Strikingly, the overlap between primary tumour gCISs (pri-gCISs) from *Ptch*<sup>+/-</sup>/*Math1*-SB11/T2Onc tumours and those from metastases (met-gCISs) from the same animals was only 9.3% of all gCISs (Fig. 2a). Similarly, the overlap between pri-gCISs from *Tp53*<sup>mut</sup>/*Math1*-SB11/T2Onc mice and the matching met-gCISs was only 8.9% (Fig. 2b). The leptomeningeal metastases and the matched primary tumour have identical, highly clonal insertion sites on both genetic backgrounds (Fig. 2c). The probability of two (or three) unrelated tumours having SB insertions in exactly the same TA dinucleotide is extremely low. We conclude that the leptomeningeal metastases and the matched primary tumour arise from a common transformed progenitor cell and have subsequently undergone genetic divergence.

Sequencing also identified insertions that are highly clonal in the metastases but are not observed in the matched primary tumour (data not shown). End-point PCR for these insertions in the matched primary and metastatic tumours shows that the insertion is highly clonal in the metastasis (or metastases) and is present in a very small subclone of the primary tumour (Fig. 2d and Supplementary Fig. 9). These data are consistent with a model in which metastatic disease arises from a minor restricted subclone of the primary tumour. Dissemination could occur repeatedly from the same subclone of the primary tumour, which seeds the rest of the central nervous system, or it could occur once, followed by reseeding of the rest of the leptomeningeal space by the initial metastasis. Insertions that are restricted to a minor subclone of the

**Figure 1 | Transposon mutagenesis models of disseminated human medulloblastoma.** **a–d**, The histology of transposon-driven medulloblastoma on the *Ptch*<sup>+/-</sup> background resembles human medulloblastoma, with leptomeningeal metastases on the surface of the brain (**c**) and spinal cord (**d**). Images show haematoxylin and eosin staining (**a**, entire brain; **b**, upper spinal cord). **e–h**, The histology of transposon-driven medulloblastoma on the *Tp53*<sup>mut</sup> background shows histological features of large cell/anaplastic medulloblastoma, including nuclear pleomorphism and nuclear wrapping (**f**). Dissemination to the leptomeningeal spaces of the brain (**g**) and spinal cord (**h**) also occurs on this background. **i**, *Ptch*<sup>+/-</sup> mice with SB transposition develop more frequent medulloblastomas with a shorter latency than *Ptch*<sup>+/-</sup> mice without transposition. *P* values are from *t*-tests of survival comparing individual genotypes to *Ptch*<sup>+/-</sup> mice; *n*, number of mice per genotype. mo., months. **j**, Medulloblastoma (MB) was not observed in *Tp53*<sup>mut</sup> mice without transposition but was observed in 42% of *Tp53*<sup>mut</sup> mice with transposition. *P* values are from *t*-tests comparing survival between *Tp53*<sup>mut</sup> mice and *Tp53*<sup>mut</sup>/SB11/T2Onc mice with MB; *n*, number of mice. **k–n**, Insertion maps of notable gCISs. Insertions in the direction of transcription are denoted by green arrows, and those against the direction of transcription are denoted by red arrows. Transcription start sites are denoted by black arrows.

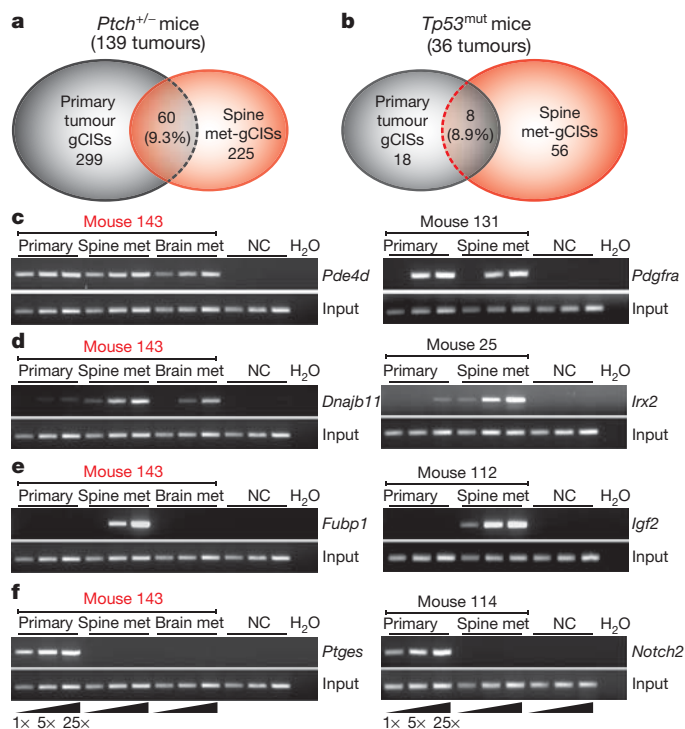


**Figure 2 | Transposon-driven metastatic medulloblastoma genetically differs from the primary tumour.** **a, b**, Venn diagrams depicting the degree of overlap and discordance in the gCISs in primary tumours and metastases, on the *Ptch*<sup>+/-</sup> and *Tp53*<sup>mut</sup> backgrounds. **c–f**, Insertion-site end-point PCR was used to demonstrate the relative clonality of insertions between samples. Data for medulloblastoma in five mice are shown (mouse 143, left; and four mice, right). Three levels of input DNA were used for each sample (1×, 5× and 25×, with the increase depicted by a wedge). Shown are clonal events found in both the primary tumour and matching metastases (met) (**c**), insertions that are highly clonal in the metastases but very subclonal in the matching primary tumour (**d**), insertions that are highly clonal in the metastases but undetectable in the matching primary tumour (**e**), and insertions that are highly clonal in the primary tumour but undetectable in the matching metastases (**f**). NC, negative control; genomic DNA from a *Math1-SB11/T2Onc* double-transgenic mouse cerebellum.

primary tumour but that are clonal in the metastases could correspond to the previously described ‘metastasis virulence’ genes<sup>14</sup>, which offer a genetic advantage during dissemination but not to the primary tumour. Another explanation for our data could be that the primary tumour was reseeded by a metastatic clone that had acquired additional genetic events in the periphery. This hypothesis is mitigated by the presence of highly clonal insertions in the metastasis that are completely absent from the primary tumour in the same animal<sup>15</sup> (Fig. 2e). As reseeding should be accompanied by contamination of the primary tumour with events found in the metastases, the absence of these events in the matched primary tumour makes reseeding much less likely (Fig. 2e). We propose that events found in only one metastasis represent progression events that are acquired post metastasis and that could lead to localized progression of metastatic disease, as is sometimes observed in human children.

We observed highly clonal insertions in the primary tumour, including in known medulloblastoma oncogenes such as *Notch2* and *Tert*, that were not found in the matching metastases (Fig. 2f). This pattern could be explained through remobilization of the SB transposon in the metastatic tumour; however, no signs of the DNA footprint remaining after SB remobilization at these loci were observed<sup>16</sup> (Supplementary Fig. 10). We suggest that these events, which may constitute driver events in the primary tumour, have arisen in the primary tumour after the metastases have disseminated (post-dispersion events). Although these known oncogenes are attractive targets for therapy,

their utility as targets may be limited if the targets are not also found in the leptomeningeal compartment of the disease. Our data from two separate mouse lines support a model in which medulloblastoma disseminates early from a restricted subclone of the primary tumour and in which the primary tumour and the matched metastases then undergo differential clonal selection and evolution. Failure to account for the differences between the primary and leptomeningeal compartments could lead to the failure of targeted therapies. Failure to study the leptomeningeal disease (Fig. 2d, e) could result in systematically overlooking crucial targets for therapy in this compartment.

Examining the met-gCISs using Gene Set Enrichment Analysis (GSEA) demonstrated differences between the primary and metastatic disease, including enrichment for genes involved in the cytoskeleton in metastases (Supplementary Table 12). Targets that are present in both compartments and are maintenance genes, as exemplified by *Pdgfra*, will be optimal targets for treating both the primary tumour and the metastases (Fig. 2c and Supplementary Tables 7 and 9).

*Pten*, *Akt2*, *Igf2* and *Pik3r1* are all met-gCISs, implicating the phosphatidylinositol-3-OH kinase (PI(3)K) pathway in medulloblastoma progression. We injected the cerebellum of Nestin-TVA mice<sup>17</sup> with either an *Shh*-overexpressing retroviral vector (denoted *Shh* virus) or an *Shh*- and *Akt*-overexpressing retroviral vector (denoted *Shh* + *Akt* virus). Cerebellar injection of *Shh* virus alone resulted in medulloblastomas in 6 of 41 animals, compared with 20 of 42 animals injected with *Shh* + *Akt* virus ( $P = 0.0018$ ). Although metastases were not observed with *Shh* virus alone (0 of 41), medulloblastoma metastases were observed in 9 of 42 animals injected with *Shh* + *Akt* virus ( $P = 0.0024$ ) (Supplementary Fig. 11). *In vivo* modelling validates PI(3)K signalling as a putative contributor to leptomeningeal dissemination of medulloblastoma.

Previous publications and clinical approaches to human medulloblastoma have largely assumed that the primary tumour and its matched metastases are highly similar<sup>3,4</sup>. To test this assertion, we formally reviewed all cases of medulloblastoma from the past decade at The Hospital for Sick Children, in Ontario, Canada, and we identified 19 patients who had bulk residual primary tumour after surgery and metastases visible by magnetic resonance imaging, both of which could be followed for response to treatment (Supplementary Fig. 12 and Supplementary Table 13). Although it is possible that the metastases received less radiotherapy than the primary tumour in a subset of patients, in 58% of all cases (11 of 19) we observed a disparate response to therapy between the primary tumour and the matched metastases (binomial test,  $P < 2.2 \times 10^{-16}$ ). Identification of definitive differences in the clinical response to standard therapy between the primary and the metastatic compartment awaits the completion of large, well-controlled, prospective clinical trials.

We examined seven matched primary and metastatic medulloblastomas for copy number aberrations (Fig. 3, Supplementary Figs 13 and 14, and Supplementary Tables 14 and 15). In each case, the primary tumour and the matched metastases shared complicated genetic events that provide strong support for their descent from a common transformed progenitor cell. Similar to our mouse data, in each case we observed clonal genetic events in the metastatic tumour(s) that were not present in the matched primary tumour (Fig. 3 and Supplementary Fig. 14). We also observed genetic events in the primary tumour that were absent from the matched metastases, consistent with a post-dispersion event (Fig. 3 and Supplementary Fig. 14). One patient with multiple leptomeningeal metastases had a deletion of chromosome 1p in only one of three examined metastases (Fig. 3a). This pattern of genetic events being present in only a subset of metastases could be a mechanism for the emergence of therapy-resistant metastatic clones.

We performed interphase fluorescence *in situ* hybridization (FISH) for the known medulloblastoma oncogenes *MYCN* and *MYC* on a collection of 17 paraffin-embedded primary and metastatic pairs of human medulloblastomas<sup>18–20</sup>. *MYCN* was amplified in three primary medulloblastomas but not in the matching metastases (Fig. 3b and



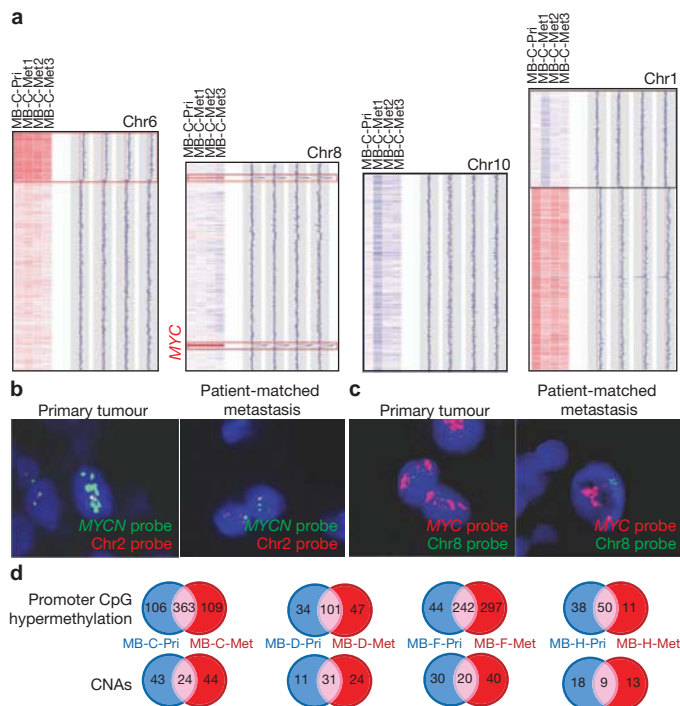


**Figure 3 | Human medulloblastoma metastases are biologically distinct from their matched primary tumour.** **a**, Copy number data from a primary medulloblastoma (MB-C-Pri) and three patient-matched metastases (MB-C-Met1, MB-C-Met2 and MB-C-Met3), with chromosomal regions in red representing genetic gain (amplification) and in blue denoting genetic loss (deletion). Examples of shared clonal events (red boxes) and events limited to one but not all metastases (black box) are shown. Chr, chromosome. **b**, Interphase FISH shows amplification of *MYCN* in a primary tumour but not the matched metastasis. Nuclei appear blue owing to 4',6-diamidino-2-phenylindole (DAPI) staining. **c**, Interphase FISH for *MYC* demonstrates amplification in both the primary tumour and its matched metastases. **d**, Venn diagrams depicting the degree of overlap and discordance in promoter CpG methylation events and CNAs in primary medulloblastomas and their matched metastases, with MB-C, MB-D and MB-F and MB-H denoting different patients.

Supplementary Fig. 15). Conversely, *MYC* was amplified in two primary tumours and their matching metastases (Fig. 3c). These data are consistent with *MYCN* amplification being a post-dispersion event, similar to examples in SB-driven mouse medulloblastoma, and strongly indicate that anti-*MYCN* therapeutics may lack efficacy in the metastatic compartment of human medulloblastoma. The possibility that *MYCN* amplicons in the metastases have been 'lost' over time cannot be excluded.

We subsequently analysed promoter CpG methylation in these matched pairs and found much discordance between the primary tumour and matched metastases (Fig. 3d, Supplementary Figs 13 and 16, and Supplementary Tables 16 and 17). Finally, we performed whole-exome sequencing on a limited set of matched primary and metastatic medulloblastomas and found many single nucleotide variants (SNVs) that were restricted to a single compartment (Supplementary Fig. 13 and Supplementary Table 18). The discordance of CNAs, promoter CpG methylation events and SNVs between the primary tumour and its matched metastases supports a bicompartmental model for metastatic medulloblastoma. The mutational load in the human tumours (the combination of CNAs, CpG methylation and SNVs) compares favourably with the mutational load in our transposon-driven mouse models (in which the median number of gCISs is 25 per tumour; Supplementary Table 19). Validation of the individual CNAs that were restricted to the metastases showed that these CNAs can be detected in a very minor subclone of the primary tumour, in keeping with the relationship identified in the mouse model (Supplementary Fig. 17 and Supplementary Tables 20 and 21). Pathway analysis using

the Database for Annotation, Visualization and Integrated Discovery (DAVID) to compare mouse gCISs with the genes that were affected in the human metastases identified only one statistically significant shared signalling pathway: insulin signalling ( $P = 0.027$ ) (Supplementary Table 22). The known role of insulin receptor signalling in primary medulloblastoma<sup>21</sup>, together with the data presented here on the role of AKT in metastatic medulloblastoma, suggests that insulin signalling should be prioritized as a therapeutic target to be tested in clinical trials.

We performed unsupervised hierarchical clustering on the CpG methylation data, and we found that normal cerebellar controls cluster away from the medulloblastomas, whereas metastases cluster with their matching primary tumour (Fig. 4a). However, metastases cluster

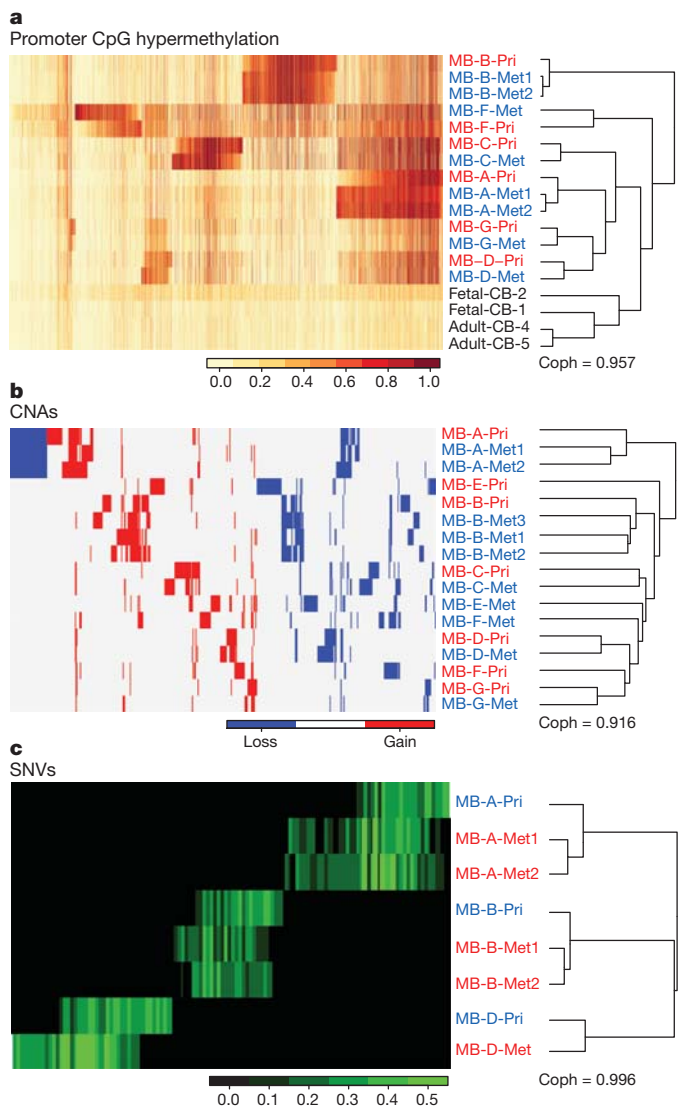


**Figure 4 | Human medulloblastoma metastases are genetically distinct from their matched primary tumour.** **a**, Profiling the methylation status of 27,578 CpG dinucleotide sites in the human genome in a collection of human matched primary and metastatic medulloblastomas; the top 2,000 genes are shown. Unsupervised hierarchical clustering by CpG methylation pattern demonstrates that patient-matched metastases are more similar to each other than to the matched primary tumour. **b**, Unsupervised clustering of regions of copy number gain and loss demonstrates that patient-matched metastases are more similar to each other than to the matched primary tumour. **c**, Unsupervised hierarchical clustering of SNV data from whole-exome sequencing demonstrates that patient-matched metastases are more similar to each other than to the matched primary tumour. SNVs that are found only in the primary compartment or only in both examined tumours in the metastatic compartment are evident. Coph, cophenetic correlation coefficient.



closer to each other than they do to the matched primary tumour ( $z$ -test,  $P = 0.0014$ ) (Supplementary Fig. 18). Unsupervised hierarchical clustering of CNA and exome SNV data uncovered the same relationships (Fig. 4b, c). Evident within the exome data are many events that are shared only by patient-matched metastases (that is, metastases from a single patient), as well as events that are restricted to the primary tumour, both of which are similar to the genetic patterns observed in mice. These three data sets support a model in which patient-matched human medulloblastoma metastases are epigenetically and genetically very similar to each other but have substantially diverged from the primary tumour, resulting in two different disease compartments: the primary and metastatic compartments.

Our data from two mouse models, with support from initial data from human medulloblastoma, suggest that leptomeningeal metastases of medulloblastoma from a single human or mouse are genetically similar to each other but are highly divergent from the matched primary tumour, consistent with a bicompartamental model of disease. Our results are consistent with a model in which metastases arise from a restricted subclone of the primary tumour through a process of clonal selection in both humans and mice. That metastases might arise from a pre-existing minor subclone of the primary tumour through clonal selection was suggested more than three decades ago, but it remains a controversial hypothesis that might not be true of all cancers<sup>22–25</sup>. Failure to account for the divergent molecular pathology of the metastatic compartment may result in selection of therapeutic targets present in the primary tumour, which is more amenable to surgical control, but not the metastases, which are the more frequent cause of death.

## METHODS SUMMARY

**Generation of *Math1-SB11* construct.** *SB11* cDNA was excised from the vector pCMV-*SB11* and ligated into the vector J2Q-*Math1* (refs 8, 26).

**Linker-mediated PCR and 454 deep sequencing.** Bar-coded, linker-mediated PCR was performed as previously described<sup>6</sup>. Sample preparation for the 454 sequencing and the subsequent procedures was performed as previously described<sup>27</sup>.

**Determination of gCISs.** A chi-squared analysis was performed to determine whether the number of observed integration events within each transcription unit in the SB-driven medulloblastomas was significantly greater than expected given the following: the number of TA dinucleotide sites within the gene relative to the number of TA sites in the genome, the number of integration sites within each tumour, and the total number of tumours in each cohort. This gCIS analysis produced a  $P$  value for each of the ~19,000 mouse RefSeq genes, and Bonferroni correction was therefore used to adjust for multiple hypothesis testing.

**Full Methods** and any associated references are available in the online version of the paper at [www.nature.com/nature](http://www.nature.com/nature).

Received 10 October 2010; accepted 3 January 2012.

Published online 15 February 2012.

- Gajjar, A. *et al.* Risk-adapted craniospinal radiotherapy followed by high-dose chemotherapy and stem-cell rescue in children with newly diagnosed medulloblastoma (St Jude Medulloblastoma-96): long-term results from a prospective, multicentre trial. *Lancet Oncol.* **7**, 813–820 (2006).
- Mabbott, D. J. *et al.* Serial evaluation of academic and behavioral outcome after treatment with cranial radiation in childhood. *J. Clin. Oncol.* **23**, 2256–2263 (2005).
- MacDonald, T. J. *et al.* Expression profiling of medulloblastoma: PDGFRA and the RAS/MAPK pathway as therapeutic targets for metastatic disease. *Nature Genet.* **29**, 143–152 (2001).
- Ramaswamy, S., Ross, K. N., Lander, E. S. & Golub, T. R. A molecular signature of metastasis in primary solid tumors. *Nature Genet.* **33**, 49–54 (2003).
- Goodrich, L. V., Milenkovic, L., Higgins, K. M. & Scott, M. P. Altered neural cell fates and medulloblastoma in mouse patched mutants. *Science* **277**, 1109–1113 (1997).
- Collier, L. S., Carlson, C. M., Ravimohan, S., Dupuy, A. J. & Largaespada, D. A. Cancer gene discovery in solid tumours using transposon-based somatic mutagenesis in the mouse. *Nature* **436**, 272–276 (2005).
- Dupuy, A. J., Akagi, K., Largaespada, D. A., Copeland, N. G. & Jenkins, N. A. Mammalian mutagenesis using a highly mobile somatic *Sleeping Beauty* transposon system. *Nature* **436**, 221–226 (2005).

- Helms, A. W., Abney, A. L., Ben-Arie, N., Zoghbi, H. Y. & Johnson, J. E. Autoregulation and multiple enhancers control *Math1* expression in the developing nervous system. *Development* **127**, 1185–1196 (2000).
- Wetmore, C., Eberhart, D. E. & Curran, T. Loss of *p53* but not *ARF* accelerates medulloblastoma in mice heterozygous for *patched*. *Cancer Res.* **61**, 513–516 (2001).
- Brett, B. T. *et al.* Novel molecular and computational methods improve the accuracy of insertion site analysis in *Sleeping Beauty*-induced tumors. *PLoS ONE* **6**, e24668 (2011).
- Northcott, P. A. *et al.* Multiple recurrent genetic events converge on control of histone lysine methylation in medulloblastoma. *Nature Genet.* **41**, 465–472 (2009).
- Forbes, S. A. *et al.* in *Current Protocols in Human Genetics* Ch. 10.11 doi:10.1002/0471142905.hg1011s57 (2008).
- Northcott, P. A. *et al.* Medulloblastoma comprises four distinct molecular variants. *J. Clin. Oncol.* **29**, 1408–1414 (2011).
- Nguyen, D. X. & Massague, J. Genetic determinants of cancer metastasis. *Nature Rev. Genet.* **8**, 341–352 (2007).
- Norton, L. & Massague, J. Is cancer a disease of self-seeding? *Nature Med.* **12**, 875–878 (2006).
- Luo, G., Ivics, Z., Izsvák, Z. & Bradley, A. Chromosomal transposition of a Tc1/mariner-like element in mouse embryonic stem cells. *Proc. Natl Acad. Sci. USA* **95**, 10769–10773 (1998).
- Rao, G., Pedone, C. A., Coffin, C. M., Holland, E. C. & Fuhs, D. W. c-Myc enhances sonic hedgehog-induced medulloblastoma formation from nestin-expressing neural progenitors in mice. *Neoplasia* **5**, 198–204 (2003).
- Swartling, F. J. *et al.* Pleiotropic role for *MYCN* in medulloblastoma. *Genes Dev.* **24**, 1059–1072 (2010).
- Pfister, S. *et al.* Outcome prediction in pediatric medulloblastoma based on DNA copy-number aberrations of chromosomes 6q and 17q and the *MYC* and *MYCN* loci. *J. Clin. Oncol.* **27**, 1627–1636 (2009).
- Korshunov, A. *et al.* Accumulation of genomic aberrations during clinical progression of medulloblastoma. *Acta Neuropathol.* **116**, 383–390 (2008).
- Hahn, H. *et al.* *Patched* target *Igf2* is indispensable for the formation of medulloblastoma and rhabdomyosarcoma. *J. Biol. Chem.* **275**, 28341–28344 (2000).
- Fidler, I. J. & Kripke, M. L. Metastasis results from preexisting variant cells within a malignant tumor. *Science* **197**, 893–895 (1977).
- Scheel, C., Onder, T., Karnoub, A. & Weinberg, R. A. Adaptation versus selection: the origins of metastatic behavior. *Cancer Res.* **67**, 11476–11480 (2007).
- Talmadge, J. E. Clonal selection of metastasis within the life history of a tumor. *Cancer Res.* **67**, 11471–11475 (2007).
- Talmadge, J. E. & Fidler, I. J. The biology of cancer metastasis: historical perspective. *Cancer Res.* **70**, 5649–5669 (2010).
- Geurts, A. M. *et al.* Gene transfer into genomes of human cells by the *Sleeping Beauty* transposon system. *Mol. Ther.* **8**, 108–117 (2003).
- Starr, T. K. *et al.* A transposon-based genetic screen in mice identifies genes altered in colorectal cancer. *Science* **323**, 1747–1750 (2009).

**Supplementary Information** is linked to the online version of the paper at [www.nature.com/nature](http://www.nature.com/nature).

**Acknowledgements** M.D.T. holds a Canadian Institutes of Health Research Clinician-Scientist Phase II Award, was a Sontag Foundation Distinguished Scholar, and is supported by grants from the National Institutes of Health (R01CA148699), the Pediatric Brain Tumor Foundation, the Canadian Cancer Society, and Brainchild. X.W. was supported by a fellowship from the American Brain Tumor Association in tribute to Tracy Greenwood. L.G. was supported by a fellowship from the Davis M. Ferguson Fund from the American Brain Tumor Association. A.D. was supported by a Vanier Doctoral Fellowship from the Canadian Institutes of Health Research. L.S.C. was supported by a grant (K01CA122183) and a Kimmel Scholar award from the Kimmel Foundation. C.E. was supported by a grant from the National Institutes of Health (NS055089). We thank S. Archer for technical writing assistance.

**Author Contributions** M.D.T., X.W., P.A.N., L.S.C., A.D. and D.L. conceived the research and planned the experiments. X.W., P.A.N., A.D., L.G. and D.J.H.S. carried out the vast majority of the experiments under M.D.T.'s guidance. C.E., T.V.M., D.Z., Y.-J.C., T.M., X.-N.L., V.P.C., M.G.M. and W.A.W. provided human tumour materials. All authors contributed experimental expertise and participated in the writing of the manuscript. A.J.D., D.J.H.S., T.E.S., S.W.S., K.A., J.K., A.L.S., D.L. and L.S.C. provided biostatistical and bioinformatic expertise. E.B. provided the clinical data and analysis. D.W.F. carried out the *Akt* experiments. N.J., J.S. and J.M. carried out the exome sequencing. H.W., S.M.P. and A.K. carried out the immunostaining of human medulloblastoma tissue microarrays and FISH for *MYCN* and *MYC*. S.C. carried out the pathological analysis of mouse brain tumours.

**Author Information** CpG methylation data have been deposited in the Gene Expression Omnibus under accession number GSE34356. Reprints and permissions information is available at [www.nature.com/reprints](http://www.nature.com/reprints). The authors declare no competing financial interests. Readers are welcome to comment on the online version of this article at [www.nature.com/nature](http://www.nature.com/nature). Correspondence and requests for materials should be addressed to M.D.T. ([mdtaylor@sickkids.ca](mailto:mdtaylor@sickkids.ca)).

## METHODS

**Linker-mediated PCR and 454 deep sequencing.** Genomic DNA was isolated and purified from mouse tissues with a DNeasy Blood & Tissue Kit (QIAGEN). The subsequent bar-coded, linker-mediated PCR was performed as previously described<sup>6</sup>. Sample preparation for the 454 sequencing and the subsequent procedures was performed as previously described<sup>27</sup>.

**PCR for SB-tagged fragments.** The primers for amplifying SB-transposon insertion sites were designed based on the chromosomal location of each independent insertion site and its orientation to transcription. The primers at the inverted repeats/direct repeats (left) (IRDRL) and inverted repeats/direct repeats (right) (IRDRR) of the transposon were 5'-CTGGGAATGTGATGAAAGAAATAAAA-3' and 5'-TTGTGTCATGCACAAAGTAGATGT-3', respectively. The input represents genomic DNA with SB transposition, which was illustrated by SB excision PCR that detected the transposon post transposition<sup>6</sup>. Three points of input (1×, 5× and 25×) were used. The following primers were used: *Pde4d*-143L, 5'-CACATAAAAACTGGACACCTAG-3'; *Pdgfra*-131R, 5'-CTATCATGACCA CACGAAGAGAGTGAAC-3'; *Dnajb11*-143L, 5'-CATGAGCTATGGCACA GATAC-3'; *Fubp1*-143R, 5'-CACTAGTGCCCATGGATTAGG-3'; *Ptges*-143R, 5'-CAGAACTGATAGAGGCCAAAG-3'; *Irx2*-25L, 5'-CAACACTTTCAGAC ACACATATATC-3'; *Igf2*-112R, 5'-GTGACCAAGTGTGATTTCGTGGAATTT TTTGGG-3'; and *Notch2*-114R, 5'-CAGTGTCCAGGCAGTCATTCAAAGA GTG-3'. Details about the primer design for specific insertion sites and the PCR protocol are available on request.

**Review of clinical cases.** We systematically reviewed all cases of medulloblastoma seen at The Hospital for Sick Children (Toronto, Ontario) over the past ten years. Cases that have both metastases and post-operative residual bulky disease at the primary site were identified on the basis of post-operative imaging obtained within 72 h of surgery. All radiology results were reviewed by a senior neuro-oncologist (E.B.). Objective responses of both the primary tumour and the metastatic disease were measured using the standard International Society of Paediatric Oncology (SIOP) criteria for clinical trials of paediatric brain tumours<sup>28</sup>.

**End-point PCR on human samples.** For PCRs to confirm the deletion of the *CDKN2A* locus on chromosome 9, a genome-walking approach (GenomeWalker Universal Kit, Clontech, Catalogue number 638904) was taken to locate the specific deletion region based on single nucleotide polymorphism (SNP) coordinates. The following primers flanking the deletion region were used: forward, 5'-GCAATTAACCAAGACCACCAATGGCAAG-3'; and reverse, 5'-GTAGC TATTGGGGAGGTTGAGAAGGAG-3'. Three points of input shown as *ACTB* (1×, 5× and 25×) were used. The PCR products were inserted into the pCR2.1 TA cloning vector (Invitrogen), sequenced and searched against the human genome in the blast database to confirm the deletion. For *REXOIL1* deletion on chromosome 8, specific primers flanking the deletion region were designed based on SNP microarray results. The PCR products were TA-cloned and sequenced as described above. The following primers were used: forward, 5'-GGCTGACTC CCTTCTGATATAG-3'; and reverse, 5'-CAATCACTTACAGTTACTAGGC AC-3'. Details about the primer design and PCR protocols are available on request.

**Chromosomal mapping of gCISs.** Chromosomal maps of gCIS-associated genes were obtained from the UCSC Mouse Genome Browser (assembly in July 2007). Each insertion site of a specific CIS was mapped to the gene with the same orientation as the direction of transcription (arrow in green) or the inverse orientation to the direction of transcription (arrow in red).

**Human medulloblastoma tumour specimens.** All tumour specimens were obtained in accordance with the Research Ethics Board at The Hospital for Sick Children. Surgically resected, fresh frozen samples were obtained from the Cooperative Human Tissue Network and the Brain Tumor Tissue Bank.

**SB remobilization.** Potential SB insertion sites at *Fubp1*, *Mnat1* or *Igf2* in primary tumours from mouse numbers 143, 14 or 11 or sites at *Ptges*, *Aof1* and *Notch2* in the matched spine metastases were tested for remobilization. The primers were designed to amplify each insertion site to produce approximately 300 base pairs (bp) with the insertion site in the middle. PCR products were either sequenced directly or after being TA-cloned. The resultant sequences were examined for 'scars' from potential remobilization. As positive controls for the scars, primers were used to amplify the T2/Onc transposon in each sample<sup>6</sup>. The products were sequenced and examined for the scars as described above. The following primers were used: *Aof1* forward (Fw), 5'-TACTCCAGACAGTCAGTCAGTG-3'; *Aof1* reverse (Rv), 5'-TAGTCTGCTCATGCCACAAG-3'; *Ptges* Fw, 5'-ACAGAG AAGGCTTCAGAGCTC-3'; *Ptges* Rv, 5'-GGTGCTCTCTGCTGTCCAATC-3'; *Notch2* Fw, 5'-CAAGCTTTCAAGTATAAACCACGC-3'; *Notch2* Rv, 5'-GAAT GCATCATCCAGTGTCCAG-3'; *Fubp1* Fw, 5'-AGGAACGGGCTGGTGTAA AATG-3'; *Fubp1* Rv, 5'-TCTAATACCAATTCTTGGCTTGC-3'; *Mnat1* Fw, 5'-CTAACACATCAGAGTTGGACAAG-3'; *Mnat1* Rv, 5'-CATGAAGACCTG AGAGTGCAG-3'; *Igf2* Fw, 5'-GTGATTGGTGAATGTACTCTTTCC-3'; and

*Igf2* Rv, 5'-GTGGAACACTAGATTCTGTAGTC-3'. Details about the primer design and PCR protocols are available on request.

**Hierarchical clustering.** Agglomerative hierarchical clustering analyses were performed in the R statistical programming environment (version 2.13). The average linkage method was used in all cases. Because different data types were used in the various analyses, the metric used for clustering differed between the analyses. The Manhattan distance metric was used for the copy number data because the data were encoded as {-1, 0, 1}. The magnitudes of the CNAs were not considered, owing to a multitude of confounding factors, including tumour heterogeneity and ploidy. The Kendall rank correlation was used for the SNV frequency data because the data distributions were not normal. The Pearson correlation was used for the methylation data, which were normally distributed.

**Identification of CpG hypermethylation events.** Human genomic DNA was isolated from matching primary and metastatic medulloblastomas obtained from Johns Hopkins University, the Virginia Commonwealth University and New York University. An EZ DNA Methylation Kit (Zymogen Research) was used to bisulphite convert 500ng each sample. The recovered DNA was profiled on HumanMethylation27 BeadChips (Illumina) at The Centre for Applied Genomics (TCAG). Subsequently 27,578 CpG dinucleotides spanning 14,495 genes were analysed. The probe signal intensity was corrected by using BeadStudio 3.2.0 software (Illumina). The background normalization and differential methylation analyses were performed against fetal cerebella using the custom error model (Illumina). Cancer-specific DNA hypermethylation events were defined as those with a 30% increase in methylation in at least one medulloblastoma sample relative to an average methylation level (less than 50%) in normal fetal and adult cerebellum samples. Unsupervised clustering using Euclidian hierarchical clustering metrics was then performed on 2,503 data points that were filtered for cancer-specific hypermethylation events. The CpG methylation data are available from the Gene Expression Omnibus under accession number GSE34356.

**Bisulphite sequencing of CpG promoter methylation.** Representative examples of primary-tumour- and metastasis-specific methylation events were identified from normalized Illumina Hg27 data. Bisulphite PCR (BSP) primers were designed using the EpiDesigner tool (SEQUENOM) (<http://www.epidesigner.com/>) to encompass a genomic region flanking the Illumina Hg27 gene-specific probe. DNA (500ng) from the primary tumour and the corresponding metastases was bisulphite converted using an EZ DNA Methylation Kit. Following PCR optimization, 10ng bisulphite-converted DNA was used to amplify the genomic regions of interest. Amplicons were subcloned into the pCR2.1-TOPO vector (Invitrogen), and plasmid DNA from 10–12 colonies was extracted using a PureLink Quick Plasmid Miniprep Kit (Invitrogen). Sequencing was performed at TCAG using the M13 reverse primer, 5'-CAGGAAACAGCTATGAC-3'. The following primers were also used: *MLH1* Fw, 5'-TTGTTGGAATGTTATTTAT TATTTAGGA; *MLH1* Rv, 5'-CATAAATATCCACCAAAAAACCAAAA-3'; *MRPS21* Fw, 5'-TTTTTGGTTTGTGTTGATTGTTT-3'; *MRPS21* Rv, 5'-CAA ATCTCAAAAATCTATCCTTTCC-3'; *RBPI* Fw, 5'-GTAGGGGAGGTATAG GTAGGTTGTG-3'; *RBPI* Rv, 5'-CTTAATCAAACCCCTAAACAAAAA-3'; *WNK2* Fw, 5'-GTGTTTGGTTTATAGAGATGGA-3'; and *WNK2* Rv, 5'-AC TCTCTTAATCCCACTCTAC-3'. Details about the primer design and PCR protocols are available on request.

**Alignment and variant calling for whole-exome sequencing.** Standard manufacturers' protocols were used to perform target capture with a TruSeq Exome Enrichment Kit (Illumina) and sequencing of 100-bp paired-end reads on a HiSeq sequencing system (Illumina). Approximately 10 gigabases of sequence was generated for each subject such that >90% of the coding bases of the exome defined by the Consensus CDS (CCDS) project were covered by at least ten reads. Adaptor sequences and quality trimmed reads were removed by using the FASTX-Toolkit ([http://hannonlab.cshl.edu/fastx\\_toolkit/](http://hannonlab.cshl.edu/fastx_toolkit/)), and then a custom script was used to ensure that only read pairs with both mates present were subsequently used. Reads were aligned to Hg19 with BWA1, and duplicate reads were marked using Picard (<http://picard.sourceforge.net/>) and excluded from downstream analyses. SNVs and short insertions and deletions (indels) were called using SAMtools (<http://samtools.sourceforge.net/>) Pileup and varFilter2 with the base alignment quality (BAQ) adjustment disabled and were quality filtered to require at least 20% of reads supporting the variant call. Variants were annotated using both ANNOVAR3 and custom scripts to identify whether they affected protein coding sequence and whether they had previously been seen in dbSNP131, the 1,000 Genomes pilot release (November 2010) or in approximately 160 exomes that had previously been sequenced at our centre.

**SNV analysis of whole-exome sequencing data.** For clustering analysis, an SNV frequency matrix was constructed by calculating frequencies from the read counts of the reference and the alternative nucleotide. The matrix was not standardized (that is, converted to z scores) before clustering, because the absolute SNV frequencies were of interest.

For Venn analysis, the samples were grouped into primary–metastasis sets, and the filtered SNVs were used to identify SNVs that are enriched in one sample compared with all other samples of the same set, as determined by the hypergeometric test ( $P$  value threshold = 0.05). For sets consisting of three or more samples (A, B and C), an SNV was considered to be enriched in samples A and B if the SNV was enriched in A compared with C alone and also enriched in B compared with C alone. SNVs that were not enriched in any sample or subset of samples were considered to be common SNVs. Many of these common SNVs probably represented germline SNVs specific to the patient.

**Analysis of CpG promoter methylation data.** The similarities between the patient-matched metastatic and primary tumour samples and among patient-matched metastatic tumour samples were determined by using Pearson correlation analysis. As Pearson's  $r$  values are not normally distributed, they were standardized by Fisher's  $z$  transformation. Subsequently, the correlations between the metastatic samples and the matched primary tumour samples were compared with the correlations among the patient-matched metastatic samples, using the paired heteroscedastic Student's  $t$ -test.

Clustering analysis was performed as described above. The methylation matrix was not standardized before clustering, as doing so would entail discarding crucial

information on the differences in the overall methylation profiles among samples or the average methylation among CpG promoters.

The stability of the CpG hypermethylation profile clusters was assessed using three methods. First, the clustering analysis was run for different numbers of CpG hypermethylation sites that varied most widely among samples. The partitions generated by each clustering run were compared with the reference partitions generated by the original clustering based on the 1,000 most variable hypermethylated CpG islands using the Jaccard similarity index. The same analysis was applied to a set of 100 background hypermethylation data matrices in which the sites are permuted independently in each sample. Second, the clustering analysis was performed for random subsamples of 1,000 sites, for 1,000 repeat runs. In each run, the resultant cluster was compared with the original cluster using the Jaccard index. Analysis on the original data matrix was compared with a set of 100 background matrices, permuted as described above. Third, the cluster stability was further assessed by bootstrap resampling of the samples using the pvclust R package (version 1.2).

28. Gnekow, A. K. Recommendations of the brain tumor subcommittee for the reporting of trials. *Med. Pediatr. Oncol.* **24**, 104–108 (1995).



# DCC constrains tumour progression via its dependence receptor activity

Marie Castets<sup>1\*</sup>, Laura Broutier<sup>1\*</sup>, Yann Molin<sup>1</sup>, Marie Brevet<sup>2</sup>, Guillaume Chazot<sup>1</sup>, Nicolas Gadot<sup>2</sup>, Armelle Paquet<sup>2</sup>, Laetitia Mazelin<sup>1</sup>, Loraine Jarrosson-Wuillaume<sup>1</sup>, Jean-Yves Scoazec<sup>2</sup>, Agnès Bernet<sup>1</sup> & Patrick Mehlen<sup>1</sup>

**The role of deleted in colorectal carcinoma (DCC) as a tumour suppressor has been a matter of debate for the past 15 years. DCC gene expression is lost or markedly reduced in the majority of advanced colorectal cancers<sup>1</sup> and, by functioning as a dependence receptor, DCC has been shown to induce apoptosis unless engaged by its ligand, netrin-1 (ref. 2). However, so far no animal model has supported the view that the DCC loss-of-function is causally implicated as predisposing to aggressive cancer development<sup>3</sup>. To investigate the role of DCC-induced apoptosis in the control of tumour progression, here we created a mouse model in which the pro-apoptotic activity of DCC is genetically silenced. Although the loss of DCC-induced apoptosis in this mouse model is not associated with a major disorganization of the intestines, it leads to spontaneous intestinal neoplasia at a relatively low frequency. Loss of DCC-induced apoptosis is also associated with an increase in the number and aggressiveness of intestinal tumours in a predisposing APC mutant context, resulting in the development of highly invasive adenocarcinomas. These results demonstrate that DCC functions as a tumour suppressor via its ability to trigger tumour cell apoptosis.**

The development of colonic carcinoma from normal colonic epithelium has been shown to be associated with the mutation of a specific set of genes<sup>4</sup>. Loss of heterozygosity on chromosome 18q in more than 70% of primary colorectal tumours prompted the search for a tumour suppressor gene at that locus. This search led to the cloning of a putative cell-surface receptor, DCC<sup>1</sup>. DCC expression is markedly reduced in more than 50% of colorectal tumours, as well as in many other neoplasms (for a review, see ref. 5). Moreover, loss of DCC is associated with poor prognosis and potentially decreased response to adjuvant chemotherapy in colorectal cancer patients. Lastly, restoration of DCC expression can suppress tumorigenic growth properties *in vitro* and in nude mice<sup>5</sup>. Altogether, these data led to the proposal that DCC expression is a constraint for tumour progression, and thus that DCC functions as a tumour suppressor gene. However, a major controversy resulted from this proposal, because the localization of the DCC gene close to well-established tumour suppressors such as *Smad4* (ref. 6) and the absence of increased tumour susceptibility in a mouse model in which *Dcc* was mutated<sup>3</sup> created scepticism about its potential role as a tumour suppressor gene<sup>7</sup>.

It has been shown that DCC belongs to the family of dependence receptors<sup>2</sup>. Such receptors induce apoptosis when their trophic ligands are absent, thus conferring a state of cellular dependence on ligand availability for survival<sup>8</sup>. On the basis of this classification, DCC may represent not a classical tumour suppressor but rather a conditional tumour suppressor, inducing the death of tumour cells in settings of ligand limitation, thus preventing invasion and metastasis, but failing to suppress tumour formation (and potentially supporting tumour progression) in settings of high ligand concentration. In support of

this view, overexpression of the DCC ligand netrin-1 in the digestive tract has been shown to result in the inhibition of epithelial cell death and the promotion of tumour progression<sup>9</sup>.

The pro-apoptotic signalling induced by unbound DCC requires its intracellular domain cleavage by caspase after aspartic acid 1290 (refs 2, 10; Fig. 1a). Point mutation of the aspartic acid residue (D1290N) did not affect the positive signalling mediated by netrin-1 treatment (Fig. 1b). However, compared to wild-type DCC, DCC(D1290N) failed to trigger apoptosis in cell culture (Fig. 1c–g). To address formally the role of DCC as a tumour suppressor and to determine the relative importance of DCC pro-apoptotic activity in its putative tumour suppressor activity, we generated a mouse model with the D1290N point mutation in the DCC coding sequence (Fig. 1h–j). Contrary to DCC homozygous null mutants, which die at birth with many nervous system defects<sup>3</sup>, mice bearing one (DCC<sup>+/mut</sup>) or two mutated alleles (DCC<sup>mut/mut</sup>) were viable. The fact that these mice do not show obvious defects in the brain further supports the view that the D1290N mutation does not inhibit or enhance DCC ‘positive’ signalling, which has been shown to be required for adequate neuronal guidance<sup>11,12</sup>. We thus investigated whether this mouse model showed a loss of DCC-induced apoptosis. Murine embryonic fibroblasts (MEFs) were cultured from DCC<sup>+/+</sup> or DCC<sup>mut/mut</sup> embryos (Fig. 2a). As predicted by the dependence receptor paradigm, MEF cells expressing a wild-type DCC underwent apoptosis in response to serum and netrin-1 deprivation, whereas the addition of netrin-1 delayed MEF cell death (Fig. 2b). In the same settings, MEF homozygous for the DCC mutation were less sensitive to serum withdrawal, and netrin-1 addition failed to augment survival (Fig. 2b). Thus, in this mouse model, cells expressing DCC should not undergo apoptosis in settings of netrin-1 limitation.

In the intestine, because of the restricted expression of netrin-1 at the bases of the intestinal villi<sup>9</sup> (Fig. 2c, d and Supplementary Fig. 1a), in contrast to the uniform expression of DCC along the villi<sup>9</sup> (Fig. 2e, f and Supplementary Fig. 1a), we hypothesized that epithelial cell death, which is generally observed at the tips of the villi, could result at least in part from unbound DCC-induced apoptosis. As shown in Fig. 2h–j and Supplementary Fig. 1b, apoptosis in the intestinal epithelium of DCC<sup>mut/mut</sup> mice was significantly decreased compared to DCC<sup>+/+</sup> mice, although no change was observed in cell proliferation (Fig. 2g) or differentiation (data not shown). These findings, coupled with the previous demonstration that, in mice, ectopic expression of netrin-1 reduces intestinal cell death, whereas netrin-1 hypomorphic mutant newborn mice show increased cell death<sup>9</sup>, suggest that DCC and netrin-1 may be homeostatic regulators of intestinal epithelial turnover via a dependence receptor mechanism (Supplementary Fig. 1 and Supplementary Fig. 1c). It is noteworthy that, even though DCC mutation was shown to decrease intestinal cell death at the tips of the villi, global disorganization of the intestinal epithelium of these animals was not observed, probably because intestinal cell apoptosis levels

<sup>1</sup>Apoptosis, Cancer and Development Laboratory - Equipe labellisée ‘La Ligue’, LabEx DEVweCAN, Centre de Cancérologie de Lyon, INSERM U1052-CNRS UMR5286, Université de Lyon, Centre Léon Bérard, 69008 Lyon, France. <sup>2</sup>Endocrine Differentiation Laboratory, Centre de Cancérologie de Lyon, INSERM U1052-CNRS UMR5286, Université de Lyon, Hospices Civils de Lyon, Hôpital Edouard Herriot, Anatomie Pathologique, 69437 Lyon, France.

\*These authors contributed equally to this work.

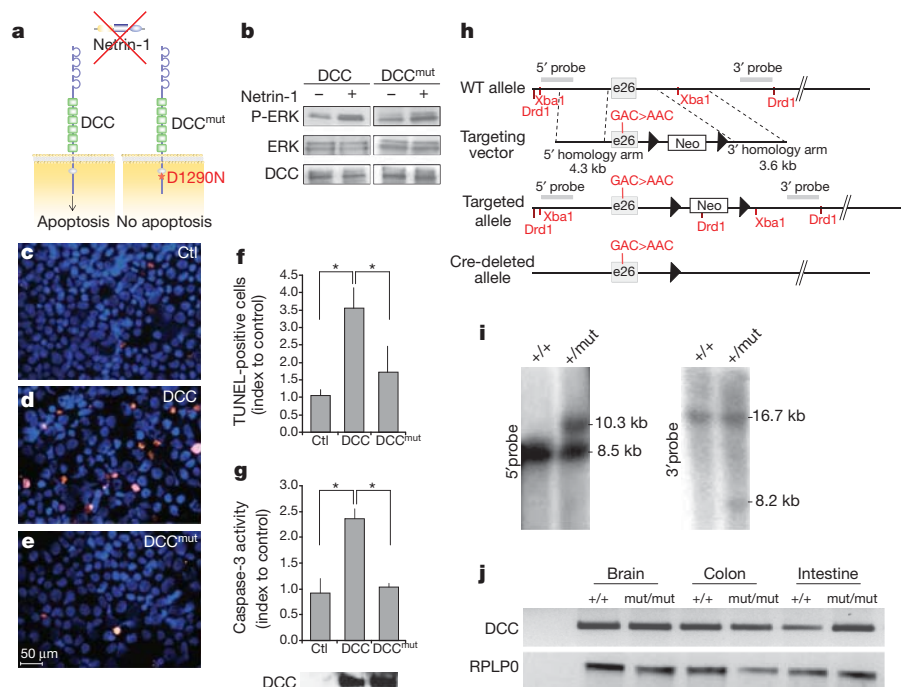


**Figure 1 | Establishment of a mouse model with a mutation of the caspase cleavage site in DCC.** **a**, Without netrin-1, DCC induces apoptosis unless mutated in D1290. **b**, In HEK293T cells, netrin-1-induced DCC-mediated ERK1/2 phosphorylation is not affected by D1290N point mutation. **c–f**, TdT-mediated dUTP nick end labelling (TUNEL) assay on DCC or DCC(D1290N) transfected HEK293T cells (mean + s.e.m.,  $n = 3$ ).  $*P < 0.005$ , U-test. Representative images

are shown. Ctl, control. **g**, Caspase-3 activity on DCC or DCC(D1290N) transfected HEK293T cells (mean + s.e.m.,  $n = 3$ ).  $*P < 0.005$ , U-test. Inset: DCC immunoblot. **h**, Mutant mouse model generated by introduction of the D1290N point mutation in exon 26 (e26) of *Dcc*. Arrows indicate Cre recombination sites. **i**, Southern blots after restriction by Xba1 (5' probe) or Drd1 (3' probe). **j**, DCC expression (qRT-PCR) in DCC<sup>+/+</sup> and DCC<sup>mut/mut</sup> mice.

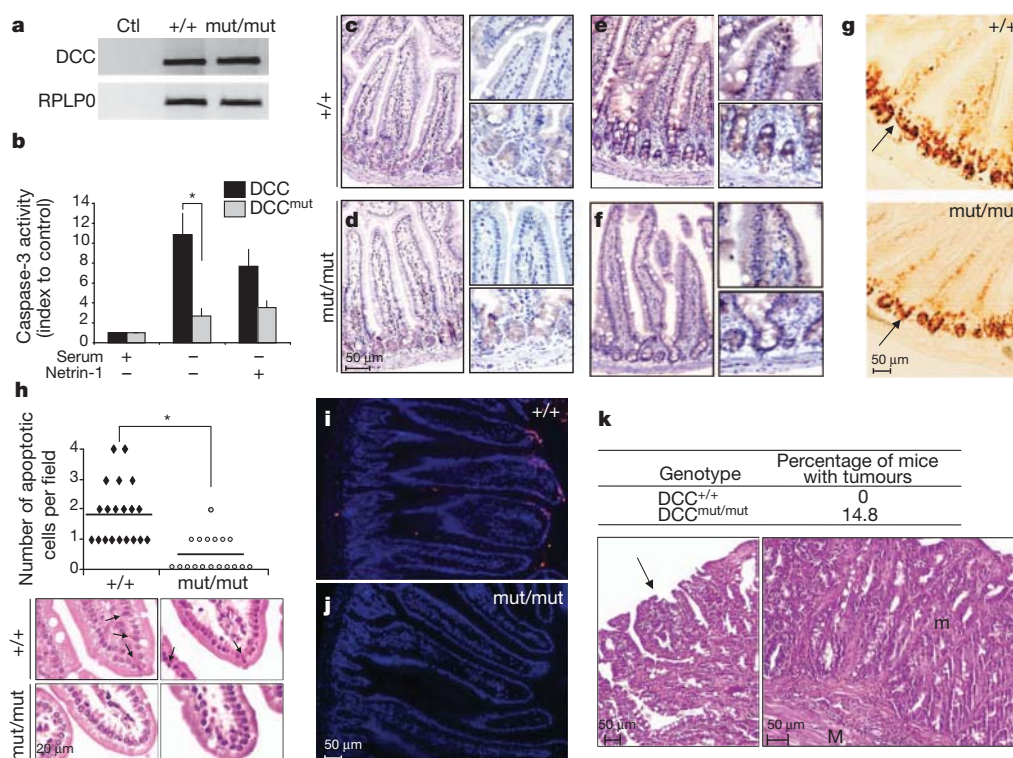


**Figure 2 | Mutation of DCC caspase cleavage site is associated with reduced apoptosis in mice.** **a**, DCC expression (qRT-PCR) in DCC<sup>+/+</sup> and DCC<sup>mut/mut</sup> MEFs from embryonic day (E)13.5 embryos. **b**, Caspase-3 activity in DCC<sup>+/+</sup> and DCC<sup>mut/mut</sup> MEFs after serum deprivation and netrin-1 treatment (mean + s.e.m.,  $n = 3$ ).  $*P < 0.02$ , U-test. **c–f**, Immunohistochemistry of netrin-1 (c, d) or DCC (e, f) in proximal intestine of DCC<sup>+/+</sup> (c, e) and DCC<sup>mut/mut</sup> (d, f) mice. Right panels, enlargement of villi and crypt staining. **g**, Cell proliferation in intestinal crypt analysed by anti-Ki67 staining. **h**, Intestinal cell death in wild-type or DCC

mutant mice.  $*P < 0.001$ , U-test. Representative images of pyknotic cells from haematoxylin-eosin-saffron staining of DCC<sup>+/+</sup> and DCC<sup>mut/mut</sup> mice are shown. **i, j**, TUNEL staining of intestinal villi. No difference in apoptosis rate was observed between control and mutant animals in intestinal crypt (data not shown). **k**, Incidence of spontaneous tumour formation in intestines of DCC<sup>mut/mut</sup> ( $n = 28$ ) compared to DCC<sup>+/+</sup> ( $n = 18$ ) mice. Haematoxylin-eosin-saffron staining of an adenoma (left panel; arrow) and of an adenocarcinoma (right panel) observed in DCC<sup>mut/mut</sup> mice. m, mucosa; M, muscularis.

throughout the villi remain quite low under physiological conditions<sup>13,14</sup>. Thus, netrin-1 regulation of DCC-induced cell death is unlikely to be solely responsible for a general homeostatic regulatory process that would balance intestinal epithelial cell proliferation and differentiation; rather, it is more likely to limit the lifespan of cells arriving at the tips of the villi and, as such, to serve as a mechanism that limits the occurrence of genetic alterations. In support of this possibility, reduction of apoptosis in DCC<sup>mut/mut</sup> mice was accompanied by spontaneous, albeit limited, intestinal tumour formation: whereas no tumours were detected in wild-type control littermates, 14.8% of mutant mice showed spontaneous neoplastic transformation, including both adenomas and adenocarcinomas (Fig. 2k;  $P < 0.05$ ). Because intestinal cells are known to undergo multiple proliferative steps within the crypt, and repeated mechanical and chemical insults originate from the intestinal lumen, we propose that DCC-mediated cell death may represent a factor for limiting the initiation of malignant transformation.

In human pathological samples, loss of DCC is observed with especially high frequency in late-stage tumours. Together with the fact that spontaneous neoplastic transformation was observed only at low frequency in these DCC mutant mice, this suggested that the putative tumour suppressive role of DCC may modulate a predominantly late event in tumorigenesis. We investigated the possibility that DCC pro-apoptotic activity may affect tumour progression by analysing the effect of the DCC(D1290N) mutation on adenocarcinoma formation in an APC<sup>+/1638N</sup> genetic background. APC is a well-known tumour suppressor gene in human colorectal cancer, and APC mutations in mice are associated with neoplasm formation. We chose the APC<sup>+/1638N</sup> mutant mice, which were shown to develop tumours in the intestinal tract at a moderate level<sup>15</sup>. Consistent with a previous report, the number of adenocarcinomatous lesions per DCC<sup>+/+</sup> APC<sup>+/1638N</sup> control mice was  $0.79 \pm 0.77$  (Fig. 3a)<sup>15</sup>. The incidence of adenocarcinomas was

increased by more than 2.5-fold in DCC<sup>mut/mut</sup> APC<sup>+/1638N</sup> mice, (Fig. 3a;  $P = 0.0002$ ). Moreover, whereas 21.4% of DCC<sup>+/+</sup> APC<sup>+/1638N</sup> control mice were tumour free (Fig. 3b), all DCC<sup>mut/mut</sup> APC<sup>+/1638N</sup> mice had at least one neoplasm. Lastly, whereas adenocarcinomas were detected in 50% of the DCC<sup>+/+</sup> APC<sup>+/1638N</sup> control mice, consistent with previous reports<sup>15</sup>, the frequency of DCC<sup>mut/mut</sup> APC<sup>+/1638N</sup> mice with adenocarcinomas was markedly increased to 100% (Fig. 3a;  $P = 0.003$ ). Mice heterozygous for the DCC mutation in the APC<sup>+/1638N</sup> background showed an intermediate phenotype, with a significantly increased number of adenocarcinomas compared to APC<sup>+/1638N</sup> mice (Supplementary Fig. 2).

Of interest, 45.5% of DCC<sup>mut/mut</sup> APC<sup>+/1638N</sup> mice showed aggressive adenocarcinomas with serosal invasion, compared to 8% in controls (Fig. 3c, d;  $P < 0.04$ ). Because serosal invasion in DCC<sup>mut/mut</sup> APC<sup>+/1638N</sup> mice supports the view of tumour cells spreading in these mutant mice, we analysed distant organs for metastasis. None of the mice showed macrometastatic lesions in the peritoneum, liver or lung. However, highly proliferative micro-metastases were observed in the livers of DCC<sup>mut/mut</sup> APC<sup>+/1638N</sup> mice with adenocarcinoma with serosal invasion, but not in controls (Supplementary Fig. 3).

Together with the finding that, in human tumours, DCC is typically deleted in late-stage tumours, this markedly increased aggressiveness suggests that the loss of DCC may enhance tumour cell survival at the transition from adenoma to adenocarcinoma. We therefore assessed whether, in accordance with this hypothesis, apoptosis is quantitatively different in low-grade tumours of DCC<sup>mut/mut</sup> APC<sup>+/1638N</sup> versus DCC<sup>+/+</sup> APC<sup>+/1638N</sup> control mice. As shown in Fig. 3e and f, we observed a marked decrease in apoptosis rate in adenomas from DCC<sup>mut/mut</sup> APC<sup>+/1638N</sup> mice compared to that in size-matched DCC<sup>+/+</sup> APC<sup>+/1638N</sup> controls, while both tumours persistently

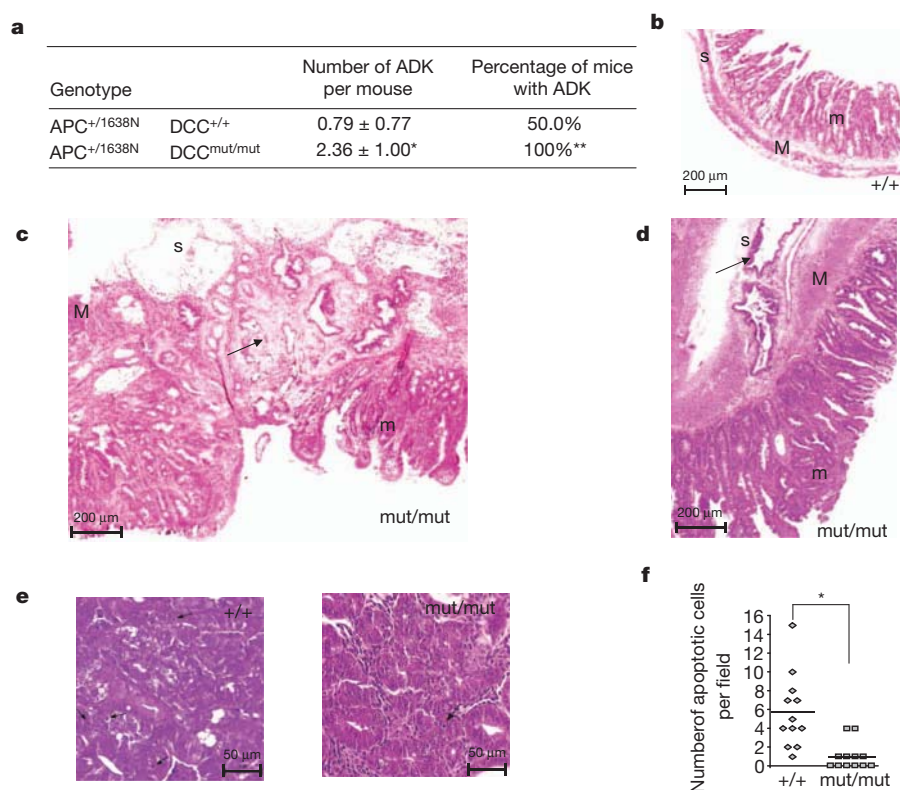


**Figure 3 | Inactivation of DCC-induced apoptosis favours adenocarcinoma formation in an APC<sup>+/1638N</sup> mutant background.** **a**, Incidence and frequency of adenocarcinomas (ADK) in DCC<sup>mut/mut</sup> APC<sup>+/1638N</sup> mice ( $n = 11$ ) compared to DCC<sup>+/+</sup> APC<sup>+/1638N</sup> mice ( $n = 29$ ) ( $*P = 0.0002$ ,  $t$ -test;  $**P = 0.003$ , Fisher's test). Tumour classification was performed according to international recommendations<sup>16</sup>; pseudo-invasion was ruled out. **b–e**, Haematoxylin-eosin-saffron staining of normal intestinal epithelium

(**b**) compared to adenocarcinomas with muscularis (**c**) or serosa local invasion (**d**) observed in DCC<sup>mut/mut</sup> APC<sup>+/1638N</sup> mice. m, mucosa; M, muscularis; S, serosa. **e, f**, Apoptosis in size-matched adenomas from DCC<sup>mut/mut</sup> APC<sup>+/1638N</sup> mice compared to DCC<sup>+/+</sup> APC<sup>+/1638N</sup> mice. **e**, Haematoxylin-eosin-saffron staining. **f**, Apoptosis was quantified in adenomas from three mice of each genotype (control: 0.28%; mutant: 0.058%).  $*P = 0.003$ , U-test.



showed DCC expression (data not shown). Thus, the inhibition of DCC-induced apoptosis may modulate, in low-grade tumours, the balance between proliferation and death, favouring proliferation. Consequently, this may increase the likelihood of occurrence of additional genetic or epigenetic alterations, thus enhancing tumour progression.

The current results provide a definitive demonstration that DCC is a bona fide tumour suppressor in the intestinal tract. Our results demonstrate the importance of DCC as a late gatekeeper, which limits tumour progression. Moreover, because the D1290N mutation inhibits DCC-induced apoptosis but not netrin-1-dependent signalling, this DCC tumour suppressive activity probably occurs via the ability of DCC to trigger apoptosis of neoplastic or pre-neoplastic cells in settings of netrin-1 limitation. DCC expression is not only decreased or lost in colorectal cancer but in a large variety of cancers such as prostate, breast, endometrial, ovarian, oesophageal, testicular, glial, neuroblastoma and hematological malignancies<sup>5</sup>. It will therefore be of interest to analyse, using transgenic mouse models, the tumour suppressor role of DCC in these malignancies. In light of our data, the function of DCC as a dependence receptor and a conditional tumour suppressor seems to represent an important safeguard mechanism, limiting tumour progression by engaging the apoptotic process.

## METHODS SUMMARY

Further details about materials and methods are provided in Methods. Briefly, the DCC(D1290N) targeting vector was constructed using a fragment of *Dcc* gene encompassing 7.9 kb around exon 26. Embryonic stem cell electroporation, selection and culture, as well as generation of chimaeric mice and Southern blot analysis were performed in the Institut de la Clinique de la Souris (ICS) according to classical procedures. Germline transmission and genotyping were detected by Southern blot and PCR analysis of tail genomic DNA. APC<sup>+1638N</sup> mice were obtained from R. Fodde. Tumour analysis was performed in blind from haematoxylin-eosin-saffron stained sections. Apoptosis was quantified in blind on haematoxylin-eosin-saffron stained intestine and adenoma sections of controls and mutant DCC mice or after TUNEL staining. Quantitative polymerase chain reaction with reverse transcription (qRT-PCR), immunohistochemistry, immunoblots, MEF culture and cell death assays were performed as described in Methods.

**Full Methods** and any associated references are available in the online version of the paper at [www.nature.com/nature](http://www.nature.com/nature).

**Received 27 May; accepted 9 November 2011.**

**Published online 11 December 2011.**

1. Fearon, E. R. *et al.* Identification of a chromosome 18q gene that is altered in colorectal cancers. *Science* **247**, 49–56 (1990).

2. Mehlen, P. *et al.* The DCC gene product induces apoptosis by a mechanism requiring receptor proteolysis. *Nature* **395**, 801–804 (1998).
3. Fazeli, A. *et al.* Phenotype of mice lacking functional deleted in colorectal cancer (*Dcc*) gene. *Nature* **386**, 796–804 (1997).
4. Fearon, E. R. & Vogelstein, B. A genetic model for colorectal tumorigenesis. *Cell* **61**, 759–767 (1990).
5. Mehlen, P. & Fearon, E. R. Role of the dependence receptor DCC in colorectal cancer pathogenesis. *J. Clin. Oncol.* **22**, 3420–3428 (2004).
6. Takaku, K. *et al.* Intestinal tumorigenesis in compound mutant mice of both *Dpc4* (*Smad4*) and *Apc* genes. *Cell* **92**, 645–656 (1998).
7. Roush, W. Putative cancer gene shows up in development instead. *Science* **276**, 534–535 (1997).
8. Goldschneider, D. & Mehlen, P. Dependence receptors: a new paradigm in cell signaling and cancer therapy. *Oncogene* **29**, 1865–1882 (2010).
9. Mazelin, L. *et al.* Netrin-1 controls colorectal tumorigenesis by regulating apoptosis. *Nature* **431**, 80–84 (2004).
10. Forcet, C. *et al.* The dependence receptor DCC (deleted in colorectal cancer) defines an alternative mechanism for caspase activation. *Proc. Natl Acad. Sci. USA* **98**, 3416–3421 (2001).
11. Li, W. *et al.* Activation of FAK and Src are receptor-proximal events required for netrin signaling. *Nature Neurosci.* **7**, 1213–1221 (2004).
12. Forcet, C. *et al.* Netrin-1-mediated axon outgrowth requires deleted in colorectal cancer-dependent MAPK activation. *Nature* **417**, 443–447 (2002).
13. Watson, A. J. *et al.* Epithelial barrier function *in vivo* is sustained despite gaps in epithelial layers. *Gastroenterology* **129**, 902–912 (2005).
14. Kiesslich, R. *et al.* Identification of epithelial gaps in human small and large intestine by confocal endomicroscopy. *Gastroenterology* **133**, 1769–1778 (2007).
15. Fodde, R. *et al.* A targeted chain-termination mutation in the mouse *Apc* gene results in multiple intestinal tumors. *Proc. Natl Acad. Sci. USA* **91**, 8969–8973 (1994).
16. Boivin, G. P. *et al.* Pathology of mouse models of intestinal cancer: consensus report and recommendations. *Gastroenterology* **124**, 762–777 (2003).

**Supplementary Information** is linked to the online version of the paper at [www.nature.com/nature](http://www.nature.com/nature).

**Acknowledgements** We wish to thank D. E. Bredesen and J.-G. Delcros for critical reading of the manuscript. We thank C. H. Herbreteau and C. Bonod-Bidaud for their initial involvement in this work and the animal facility staff for animal care. We thank the ICS for the generation of the DCC mutant mice. We thank the LMT (Laboratoire des Modèles Tumoraux) and AniPath for the analysis of animal models. This work was supported by institutional grants from the Ligue Contre le Cancer, INCA, ANR, IP ApoSys and the LabEX DEVweCAN (ANR-10-LABX-61).

**Author Contributions** M.C., L.B., Y.M., G.C., L.M., L.J.-W., A.B. and P.M. designed the experiments, the mice models and performed data analysis. M.C., L.B. and Y.M. performed most of the experiments. J.-Y.S., M.B., N.G. and A.P. performed pathological analysis of tumour grade and *in vivo* quantification of apoptosis. M.C. and P.M. wrote the manuscript. P.M. and A.B. are co-senior authors.

**Author Information** Reprints and permissions information is available at [www.nature.com/reprints](http://www.nature.com/reprints). The authors declare no competing financial interests. Readers are welcome to comment on the online version of this article at [www.nature.com/nature](http://www.nature.com/nature). Correspondence and requests for materials should be addressed to P.M. ([patrick.mehlen@lyon.unicancer.fr](mailto:patrick.mehlen@lyon.unicancer.fr)).

## METHODS

**Cell culture.** Human embryonic kidney HEK293T cells were grown in DMEM (Invitrogen), supplemented with 10% fetal bovine serum (FBS; Cambrex).

**Cell death assays.** For cell death assays,  $1 \times 10^5$  HEK293T cells were transfected with 2  $\mu$ g of plasmids constructs (p-DCC-CMV-S, p-DCC-D1290N-CMV-S or pCMV control) using calcium phosphate, as described previously<sup>2</sup>. Transfected cells were serum deprived for 24 h. The caspase-3 activity assay was performed using Caspase 3/CPP32 Fluorimetric Assay Kit, according to manufacturer's instructions (Gentaur Biovision). For detection of DNA fragmentation, treated cells were cytospun 48 h after transfection, fixed and permeabilized (4% paraformaldehyde, PBS1x/Triton 0.2%) and TUNEL immunostaining was performed with 300 U ml<sup>-1</sup> TUNEL enzyme and 6  $\mu$ M biotinylated dUTP (Roche Diagnostics), as previously described<sup>17</sup>. The extremities of the biotinylated DNA were revealed using Cy-3-coupled streptavidine (Jackson ImmunoResearch) at a dilution range of 1:1,000. TUNEL-positive cells and nuclei are then respectively stained in red (Cy3) and blue (Hoechst). TUNEL staining of intestinal villi was performed on 4- $\mu$ m thick sections of DCC<sup>+/+</sup> and DCC<sup>mut/mut</sup> intestines fixed in formalin and paraffin embedded according to the same procedure.

Pyknotic cells show retracted and hyperchromatic nuclei. Quantification of pyknotic cells at the top of villi was performed in blind on ten different fields of proximal intestine sections stained with haematoxylin-eosin-saffron from two different mice of each genotype (DCC<sup>+/+</sup> and DCC<sup>mut/mut</sup>). Quantification of apoptosis in size-matched adenomas from DCC<sup>+/+</sup> and DCC<sup>mut/mut</sup> mice was performed in blind according to standard morphological criteria, including evidence of nuclear and cytoplasmic alterations.

**Immunoblot analysis.** Induction of ERK1/2 phosphorylation by netrin-1 was achieved as described previously<sup>12</sup>. In brief,  $1 \times 10^6$  HEK293T cells were transfected with 12  $\mu$ g of plasmids constructs (p-DCC-CMV-S, p-DCC-D1290N-CMV-S or pCMV control) using calcium phosphate, as described previously<sup>2</sup>, serum starved for 24 h and treated with 150 ng ml<sup>-1</sup> netrin-1 (AG-40B-0075, Adipogen) for 15 min. Immunoblots were performed as already described using anti-DCC (1/1,000, Pharmingen), anti-ERK1/2 (1/1,000, Sigma), anti-phospho-ERK1/2 (1/1,000, Cell Signaling) primary antibodies.

**Generation and analysis of mice with DCC(D1290N) mutation.** The DCC(D1290N) targeting vector was constructed using a fragment of *Dcc* gene encompassing 7.9 kb around exon 26. Embryonic stem cell electroporation, selection and culture, as well as generation of chimaeric mice and Southern blot analysis were performed in the Institut de la Clinique de la Souris (ICS) according to classical procedures. APC<sup>+/1638N</sup> mice (in C57BL/6 background; a gift from R. Fodde) were mated with mice homozygous for the DCC mutation in a predominant C57BL/6 background. Double heterozygous DCC<sup>mut/+</sup> APC<sup>+/1638N</sup> mice of the offspring were interbred to generate mice homozygous for the DCC mutation and heterozygous for APC. Routine genotype analysis of mice was

performed by PCR assay on DNA purified from tail biopsies (Extract N-Amp Tissue PCR kit, Sigma Aldrich). Wild-type and D1290N mutant alleles were distinguished using primers (CTGGAAACTTCCTTCTTGCTGGAGAAC/CTGGTTATGGGGACAGAGAGTGC) localized around the residual Lox P site. All experiments were performed in accordance with the relevant guidelines and regulations of the animal ethics committee (Authorization no. CLB-2012-024; accreditation of laboratory animal care by CECCAPP, ENS Lyon-PBES).

**Quantitative RT-PCR.** Total mRNAs were extracted from tissues or MEF cells using Nucleospin RNAII kit (Macherey-Nagel) and 1  $\mu$ g was reverse transcribed using the iScript cDNA Synthesis kit (Bio-Rad). Real-time quantitative RT-PCR was performed on a LightCycler 2.0 apparatus (Roche) using the LightCycler FastStart DNA Master SYBERGreen I kit (Roche). Oligonucleotide sequences are available on request.

**MEFs.** MEFs were prepared from individual embryos at E13.5 bearing DCC<sup>+/+</sup> and DCC<sup>mut/mut</sup> genotypes. In brief, the head and internal organs were removed, and the remaining tissue was minced and dispersed in 0.1% trypsin. Cells were grown in DMEM (Invitrogen), supplemented with 10% fetal bovine serum (FBS; Cambrex) for two populations doubling and frozen. For the caspase-3 assay,  $1.5 \times 10^5$  DCC<sup>+/+</sup> and DCC<sup>mut/mut</sup> cells were plated with or without serum and treated or not with 150 ng ml<sup>-1</sup> netrin-1 (AG-40B-0075, Adipogen). The caspase assay was performed 6 h after as described above.

**Immunohistochemistry.** Immunohistochemistry on 4- $\mu$ m-thick sections of intestines from 30-week-old DCC<sup>+/+</sup> and DCC<sup>mut/mut</sup> mice was performed as described previously<sup>9</sup>, using anti-netrin-1 (1/2,000, Ab-2, Calbiochem), anti-DCC (1/20, A-20, Santa-Cruz) and anti-Ki67 (1/150, Dako). Netrin-1, DCC and Ki-67 expression are revealed by brown DAB staining. Nuclei are counterstained by haematoxylin (blue).

**Tumour analysis.** For analysis of spontaneous neoplasia occurrence, DCC<sup>+/+</sup> and DCC<sup>mut/mut</sup> mice were euthanized at 18 months. Tumours were detected in different places of the intestines including the colon. DCC<sup>+/+</sup> APC<sup>+/1638N</sup>, DCC<sup>+/mut</sup> APC<sup>+/1638N</sup> and DCC<sup>mut/mut</sup> APC<sup>+/1638N</sup> mice were euthanized at 30 weeks.

In all cases, intestines were removed and examined for the presence of neoplasia. Tumours were resected, formalin fixed and paraffin embedded. 4- $\mu$ m-thick sections were stained with haematoxylin-eosin-saffron. Histological classification and grading of neoplastic lesions was performed in a blinded fashion and according to standard procedures<sup>16,18</sup>.

- Ghoumari, A. M. *et al.* Implication of Bcl-2 and Caspase-3 in age-related Purkinje cell death in murine organotypic culture: an *in vitro* model to study apoptosis. *Eur. J. Neurosci.* **12**, 2935–2949 (2000).
- Bernet, A. *et al.* Inactivation of the UNC5C Netrin-1 receptor is associated with tumor progression in colorectal malignancies. *Gastroenterology* **133**, 1840–1848 (2007).

# Deleted in colorectal carcinoma suppresses metastasis in p53-deficient mammary tumours

Paul Krimpenfort<sup>1</sup>, Ji-Ying Song<sup>3</sup>, Natalie Proost<sup>1</sup>, John Zevenhoven<sup>1</sup>, Jos Jonkers<sup>2</sup> & Anton Berns<sup>1,4</sup>

Since its discovery in the early 1990s the deleted in colorectal cancer (DCC) gene, located on chromosome 18q21, has been proposed as a tumour suppressor gene as its loss is implicated in the majority of advanced colorectal and many other cancers<sup>1</sup>. DCC belongs to the family of netrin 1 receptors, which function as dependence receptors as they control survival or apoptosis depending on ligand binding. However, the role of DCC as a tumour suppressor remains controversial because of the rarity of DCC-specific mutations and the presence of other tumour suppressor genes in the same chromosomal region. Here we show that in a mouse model of mammary carcinoma based on somatic inactivation of p53, additional loss of DCC promotes metastasis formation without affecting the primary tumour phenotype. Furthermore, we demonstrate that in cell cultures derived from p53-deficient mouse mammary tumours DCC expression controls netrin-1-dependent cell survival, providing a mechanistic basis for the enhanced metastatic capacity of tumour cells lacking DCC. Consistent with this idea, *in vivo* tumour-cell survival is enhanced by DCC loss. Together, our data support the function of DCC as a context-dependent tumour suppressor that limits survival of disseminated tumour cells.

In the developing nervous system, netrin 1 receptors, DCC and UNC5H, regulate axon guidance by mediating chemo-repulsion and attraction as a result of ligand interaction<sup>2–4</sup>. These receptors also act as dependence receptors inducing cell survival in the presence of their ligand netrin 1 or cell death in the absence of netrin 1 (refs 5, 6). Consequently, netrin 1 overexpression or loss of expression of its receptors confers a selective advantage to (tumour) cells. Overexpression of netrin 1 has been implicated in lung cancers<sup>7</sup> and in metastatic breast cancer<sup>8</sup>, and enforced netrin 1 expression in the mouse gastrointestinal tract contributes to adenocarcinoma formation<sup>9</sup>. Downregulation of netrin 1 receptors has been reported in the progression of multiple cancers including colorectal, breast, ovary, stomach, lung and kidney cancers<sup>10</sup>, and is associated with loss of heterozygosity or epigenetic silencing<sup>11</sup>. However, although specific tumour-related missense mutations in coding exons have been reported for *UNC5H* (ref. 12), inactivating mutations were not found in *DCC* (refs 13, 14). The lack of definitive support, the possible impact of loss of heterozygosity or epigenetic silencing on expression of other tumour suppressor genes in the same chromosomal region and the absence of a cancer phenotype of *Dcc*-deficient mice<sup>15</sup> have raised doubts about whether DCC has a tumour suppressor function<sup>16</sup>.

To directly address the role of DCC loss in tumour progression we introduced a *Cre/loxP*-technology-based conditional mutant *Dcc* allele into a well-defined mouse model for mammary carcinoma. In this model cytokeratin 14 (K14) promoter-driven *Cre* expression ablates both *p53* alleles in mammary epithelial cells, resulting in mammary tumours<sup>17,18</sup>. We have chosen this model to study the effect of DCC loss for two reasons. First, the expression of *Unc5h* genes is positively regulated by p53 (refs 19, 20, 21) and consequently, under p53-deficient conditions any effect of DCC loss could no longer be masked

by *Unc5* expression. Second, mammary tumours arising in the K14-*cre p53*<sup>F/F</sup> model are well-encapsulated and only rarely metastasize<sup>17,18</sup>, allowing *in vivo* assessment of the effects of additional mutations on tumour invasion and metastasis<sup>22</sup>.

*Dcc* is a large gene stretching over 1.2 Mb and is located on human and mouse chromosome 18 (ref. 14). To generate a conditional knockout for *Dcc* (*Dcc*<sup>F</sup>) we inserted *loxP* sites in introns 22 and 23 by homologous recombination in embryonic stem cells, enabling the *Cre*-mediated excision of exon 23 encoding the transmembrane (Supplementary Fig. 1a). Details of the *Dcc*<sup>F</sup> allele are shown in Supplementary Fig. 2 and in the Methods. Homozygous *Dcc*<sup>F/F</sup> mice are born in normal Mendelian ratios and do not show any aberrancies. Previously generated *Dcc*-deficient mice showed defects in axonal projections in the central nervous system and died shortly after birth<sup>15</sup>. To confirm that *Cre*-mediated deletion of exon 23 results in a non-functional *Dcc* allele we analysed the phenotype of mice carrying the recombined *Dcc* allele (*Dcc*<sup>D23</sup>) obtained from crosses of *Dcc*<sup>F</sup> mice with germline-expressing *Cre* mice. All homozygous *Dcc*<sup>D23/D23</sup> mice died within 1 day of birth and we noticed defects in the central nervous system that were very similar to those that have been described for the *Dcc* knockout mice<sup>15</sup>, for example, all *Dcc*<sup>D23/D23</sup> pups showed complete absence of the corpus callosum (Supplementary Fig. 1b) and immunostaining showed the loss of *Dcc* expression in the cerebral cortex (Supplementary Fig. 1c). We then generated cohorts of female K14-*cre Dcc*<sup>F/+</sup> *p53*<sup>F/F</sup> and K14-*cre Dcc*<sup>F/F</sup> *p53*<sup>F/F</sup> mice and compared mammary tumour development with respect to latency, histopathology and progression in these mice to a cohort of female K14-*cre p53*<sup>F/F</sup> mice. In all three cohorts a high incidence of mammary neoplasias was observed (80%), with similar latency as proved by the complete overlapping of Kaplan–Meier curves of mammary-tumour-free survival (Fig. 1a). The lesions were found in all the mammary glands, either as a single tumour or as multiple independent tumours. Macroscopically, they were solid with clear demarcations. Microscopically, a comparable diversity of tumour cell properties was observed in the three cohorts. Tumours were classified as moderately differentiated adenocarcinomas and/or carcinosarcomas. Ductal and/or solid nests and trabecular structures could be seen in the carcinomatous compartment, whereas sarcomatoid lesions were mainly composed of spindle cells that were arranged in bundles and interlacing structures (Fig. 2 and Supplementary Fig. 3). Immunohistochemical characterization of the tumours from the three cohorts did not show significant differences in marker profile using antibodies against epithelial (CK8, CK14, E-cadherin) and mesenchymal markers (vimentin, smooth muscle actin) or in apoptotic or proliferative activity (Supplementary Fig. 4). An overview of the mammary tumours that were observed in the three cohorts is presented in Table 1.

However, whereas the primary mammary tumour phenotypes were similar in all three groups, metastases in K14-*cre Dcc*<sup>F/+</sup> *p53*<sup>F/F</sup> mice were much more frequent (6 out of 14) than in K14-*cre Dcc*<sup>F/+</sup> *p53*<sup>F/F</sup> and K14-*cre p53*<sup>F/F</sup> cohorts (in total, 1 out of 21 ( $P < 0.01$ ; Table 1)). These

<sup>1</sup>Division of Molecular Genetics, The Netherlands Cancer Institute, 1066 CX Amsterdam, The Netherlands. <sup>2</sup>Division of Molecular Biology and Centre for Biomedical Genetics, The Netherlands Cancer Institute, 1066 CX Amsterdam, The Netherlands. <sup>3</sup>Department of Experimental Animal Pathology, The Netherlands Cancer Institute, 1066 CX Amsterdam, The Netherlands. <sup>4</sup>The Amsterdam Medical Center (AMC), The Netherlands Cancer Institute, 1066 CX Amsterdam, The Netherlands.



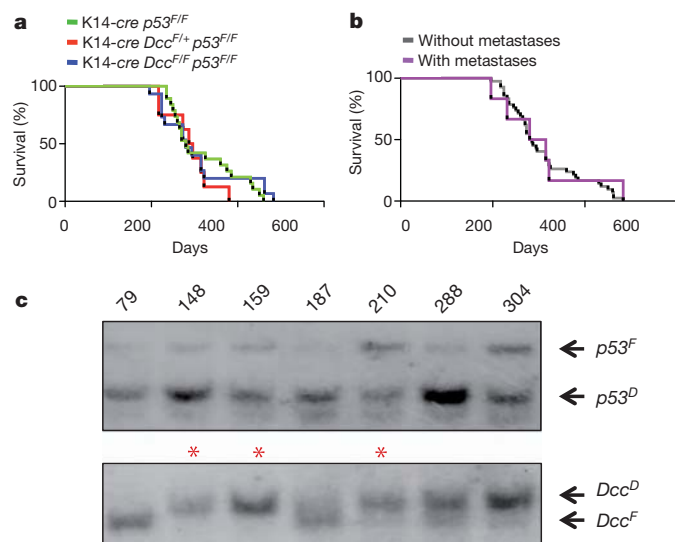


**Figure 1 | DCC loss does not affect latency of p53-deficient mammary tumour development.** **a**, Tumour-free survival curves of K14-cre  $p53^{F/F}$ , K14-cre  $Dcc^{F/F} p53^{F/F}$  and K14-cre  $Dcc^{F/F} p53^{F/F}$  mice. **b**, Tumour-free survival of mice with and without metastases. **c**, Southern blot analysis of tumours from K14-cre  $Dcc^{F/F} p53^{F/F}$  mice showing Cre-mediated recombination of  $p53^F$  and  $Dcc^F$  alleles. Red asterisk, lanes with metastatic tumours. Numbers indicate different mice.

metastases were found in draining lymph nodes and/or lung. They showed a similar immunohistochemical staining pattern to their corresponding primary tumours (Fig. 2 and Supplementary Fig. 5). The latency of metastasizing tumours did not differ from that of the non-metastasizing tumours (Fig. 1b) and both primary carcinoma and carcinosarcoma could give rise to metastasis formation (Supplementary Table 1). From four metastatic and six non-metastatic tumours from K14-cre  $Dcc^{F/F} p53^{F/F}$  mice we could isolate sufficient DNA for Southern blot analysis to estimate Cre-recombination-mediated exon 23 deletion. We found that the  $Dcc^F$  allele is not a very efficient Cre recombinase substrate and the extent of exon 23 deletion varied considerably (see Fig. 1c). Out of the ten tumours that we were able to analyse only six showed widespread deletion of exon 23, and out of these six there were four that showed metastasis formation, whereas none of the four tumours with only partial exon 23 deletion showed metastatic spread (Supplementary Table 1). These data indicate that the loss of DCC function per se is not selected for in primary tumour development but that its loss facilitates metastasis.

Dcc is expressed at high levels in distinct regions of the brain<sup>23,24</sup> and at much lower levels in various other tissues. Polymerase chain reaction with reverse transcription (RT-PCR) analysis showed that DCC is expressed in mammary tumours from K14-cre  $p53^{F/F}$  mice and its expression is lost in many of the primary tumours of K14-cre  $Dcc^{F/F} p53^{F/F}$  mice. None of these tumours showed features that are associated with metastasis, such as loss of E-cadherin expression<sup>22</sup>. We speculated that the increased metastasis formation in the K14-cre  $Dcc^{F/F} p53^{F/F}$  mice might relate to the ability of DCC to trigger apoptosis when netrin 1 availability is limited, for example, in specific conditions when cells have disseminated from the primary tumour mass. To address this issue in an accessible system we used  $p53^{D/D}$  cell cultures derived from K14-cre  $p53^{F/F}$  tumours and assayed whether cell survival under apoptosis-inducing conditions is dependent on the netrin 1–DCC interaction. RT-PCR showed that Dcc expression varied between the  $p53^{D/D}$  tumour cell lines. To study the effect of netrin 1 on apoptosis we used three tumour cell lines expressing DCC and two with no, or hardly detectable, Dcc expression (Fig. 3a). We tested the consequences of serum deprivation, the absence of cell–matrix interaction (on non-coated polystyrene dishes)

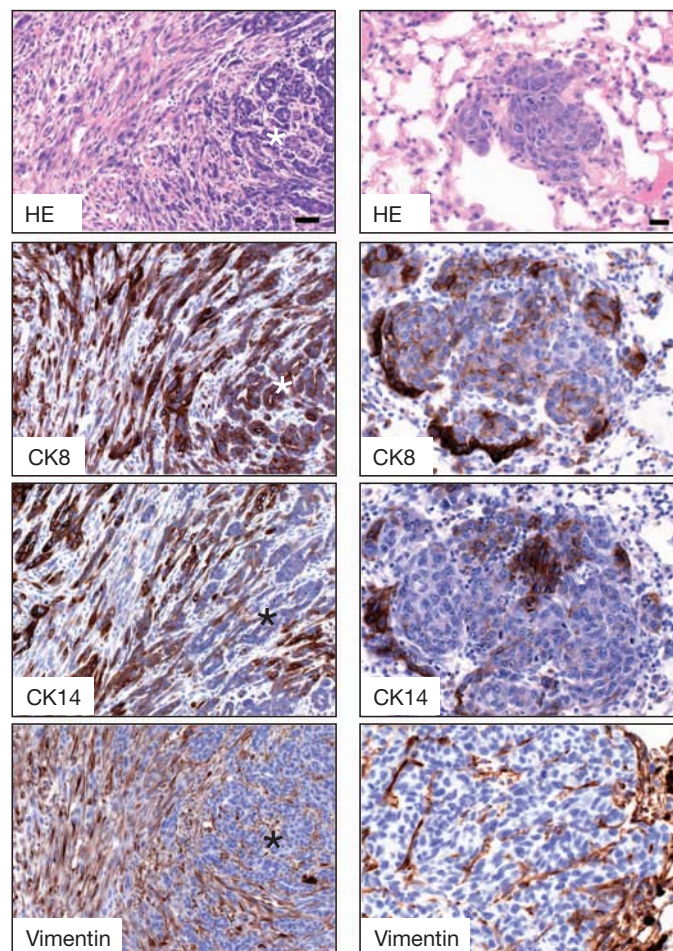


**Figure 2 | Microphotographs of primary mammary carcinosarcoma (left) and metastasis in the lung (right) in serial sections.** HE staining of the primary carcinosarcoma together with immunohistochemical stains of CK8, CK14 and vimentin reveals epithelial as well as mesenchymal differentiations. However, the metastasis in the lung mainly shows epithelial properties. Scale bars; left column, 50  $\mu$ m; right column, 20  $\mu$ m. Asterisk, indication of carcinomatous differentiation of the tumour.

or both. Apoptosis induction in these cultures was quantified by cell-surface phosphatidylserine expression using fluorescein (FITC)-conjugated annexin 5. The effect of adding netrin 1 was calculated as a percentage reduction in the apoptosis induced by serum deprivation. Under adherent culture conditions, with or without serum, apoptotic cells were hardly detectable in the cell cultures tested and thus a netrin 1 effect on cell survival could not be measured. Apoptosis can be induced in  $p53^{D/D}$  tumour cells grown in the absence of cell–matrix interaction<sup>22</sup>, although the extent of apoptosis induction varied between the tumour cell lines tested (Fig. 3b and c). In tumour cell lines with no—or hardly detectable—DCC expression, serum deprivation resulted in a mild increase of apoptosis on which netrin 1 addition had

**Table 1 | Frequent metastasis formation of mammary tumours in the K14-cre  $Dcc^{F/F} p53^{F/F}$  cohort**

	Carcinoma	Carcinosarcoma	Metastasis
K14-cre $p53^{F/F}$	8/16 (50%)	13/16 (81%)	1/16 (6%)
K14-cre $Dcc^{F/F} p53^{F/F}$	4/7 (57%)	5/7 (71%)	0/7
Total*	12/23 (52%)	18/23 (78%)	1/23 (4%)
K14-cre $Dcc^{F/F} p53^{F/F}$	6/14 (43%)	10/14 (71%)	6/14 (43%)†

\* Total refers to the sum of the values for K14-cre  $p53^{F/F}$  mice and K14-cre  $Dcc^{F/F} p53^{F/F}$  mice.

†  $P < 0.05$  between the proportion of metastases in K14-cre  $p53^{F/F}$  and that in K14-cre  $Dcc^{F/F} p53^{F/F}$  mice;  $P < 0.01$  between the proportion of metastases in the sum of K14-cre  $p53^{F/F}$  and K14-cre  $Dcc^{F/F} p53^{F/F}$  mice and that in K14-cre  $Dcc^{F/F} p53^{F/F}$  mice.

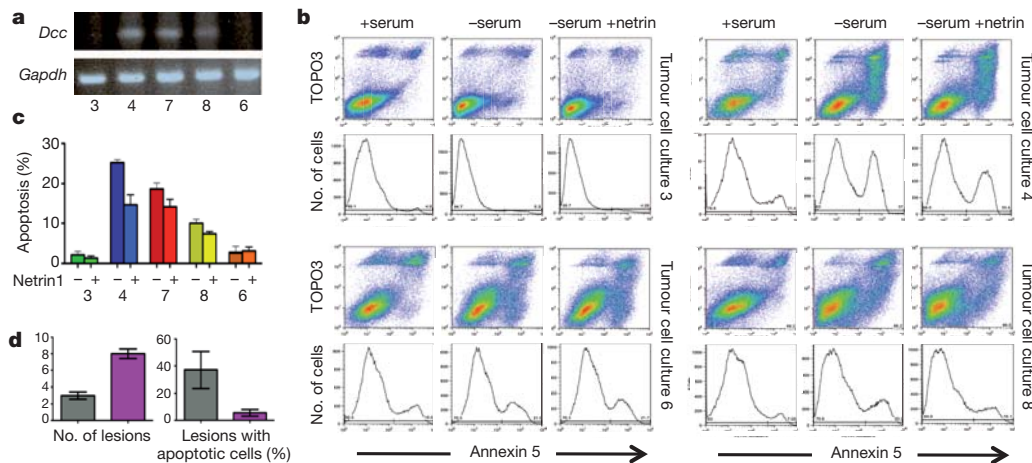


**Figure 3 | DCC controls apoptosis induction in p53-deficient tumour cells *in vitro* and survival *in vivo*.** **a**, RT-PCR analysis of *Dcc* and *Gapdh* expression in p53-deficient tumour cell cultures. **b**, Representative FACS analysis (dot plot and histogram) of cells stained with TOPO3 and annexin 5 after 24-h culture in non-adherent conditions of p53-deficient tumour cultures 3, 6, 4 and 8 in the presence and absence of serum with and without the addition of netrin 1. **c**, Percentage of apoptotic cells 24 h after serum

deprivation in cell cultures 3, 4, 6, 7 and 8 in the absence (–) or presence (+) of netrin 1; graph represents four independent experiments. **d**, Quantification of numbers of tumour cell clusters (left) and percentage of tumour cell clusters showing apoptotic bodies (right), per 5-μm section, in the lungs of Balb/c mice (n = 7) 5 days after intravenous injections with 1 × 10<sup>6</sup> DCC-proficient 65-6 cells (grey bar) or DCC-deficient 65-4 cells (purple bar). Error bars, s.e.m.

virtually no effect. By contrast, serum withdrawal from cultures of DCC-expressing *p53<sup>Δ/Δ</sup>* tumour cells led to a substantial increase in apoptotic cells. This apoptosis could be partly rescued by the addition of netrin 1. Depending on the tumour cell culture the rescuing effect of netrin 1 varied from 20% to 40% (Fig. 3b and c). These data indicate that the netrin 1–DCC interaction is functional in apoptosis regulation in mammary tumour cells. Moreover, these observations support our premise that the response of p53-deficient cells to netrin 1 relies on DCC, as the absence of p53 results in abrogation of expression of other netrin 1 receptors. In p53-proficient cells DCC loss would not provide substantial protection from apoptosis as the other netrin 1 receptors would still convey an apoptotic signal in the absence of netrin 1. To test whether DCC loss also confers increased apoptosis resistance or survival *in vivo* we performed intravenous transplantation experiments using two cell lines derived from the same primary tumour, one proficient in DCC (65-6) and the other deficient in DCC (65-4). We confirmed that 65-6 cells are much more sensitive than 65-4 cells to apoptosis induction after serum withdrawal. Consistent with the *in vitro* data we found that 5 days after intravenous injection there were significantly more tumour cell clusters ( $P < 0.03$ ) (for a representative image see Supplementary Fig. 6) in the lungs of mice transplanted with DCC-deficient cells than in the lungs of mice that received DCC-proficient cells (Fig. 3d). Moreover, in mice that were injected with DCC-proficient cells the lesions showed many more apoptotic bodies. It has been shown previously that DCC does not play an important part in tumour development<sup>15</sup>. However, apart from using a different tumour setting they addressed the effect of DCC loss in an *Apc<sup>min</sup>*-sensitized but p53-proficient background. Our observations do not contradict their observation. Consistent with their results, we show that DCC loss is irrelevant for primary tumour development. *Dcc* loss does not affect tumour latency or tumour phenotype and it is not selected for in primary tumour development. However, we observe a significantly enhanced metastatic capacity of p53-deficient tumours cells after loss of DCC ( $P < 0.01$ ). In human tumours loss of DCC results from genetic and epigenetic events affecting a large region on chromosome 18q21, which harbours multiple genes with tumour suppressor activity, such as *SMAD4* and *SMAD2* (also known as *Jv18*). Notably, in mice the loss of *Smad2* (ref. 25) or *Smad4* (ref. 26) leads to progression of *Apc<sup>+</sup>*-driven intestinal tumours, but without additional metastasis formation. Many trivial reasons can underlie the contradiction between our idea that the effect of DCC loss is p53-dependent and

the classical multistep ‘Vogelgram’ model for colorectal carcinogenesis in which DCC is lost before p53 inactivation<sup>27</sup>. We favour the scenario in which 18q21 deletions, including *DCC*, occur before p53 loss owing to the selective advantage that is conveyed by the loss of the other tumour suppressors in this chromosomal region. *DCC* loss would then serve as a passenger mutation that is initially harmless but becomes critical after subsequent p53 inactivation as it then promotes the survival of cells released from the primary tumour, thereby facilitating their colonization of other tissues. In contrast to the small metastases we observe in our mouse model, DCC-deficient metastases in patients are life threatening. They are composed of cells that have been selected for higher malignancy during primary tumour growth. Indeed, loss of DCC in breast cancer cells has been associated with worse prognosis with a higher risk of recurrent disease<sup>28</sup>.

## METHODS SUMMARY

Animal experiments comply with international regulations and ethical guidelines, and have been authorized by the experimental animal committee at The Netherlands Cancer Institute.

The *Dcc<sup>F</sup>* strain was obtained through embryonic-stem-cell targeting. K14-*cre* and *p53<sup>F</sup>* strains have been described<sup>17</sup>.

For histopathological studies, mice were killed when seriously ill or when tumours reached a diameter of 1.5 cm. Tissues were fixed in EAF (ethanol–acetic acid–formol; acidified 4% formalin; ethanol/acetic acid/formol/saline at 40:5:10:45 v/v). Haematoxylin and eosin (HE) stains were performed according to standard procedures. A list of all the antibodies used can be found in the Methods section. RNA expression analysis was performed using TaqMan quantitative PCR methods. Apoptosis in cell cultures was assayed by measuring annexin 5-positive cells by fluorescence-activated cell sorting (FACS) as described<sup>22</sup>.

**Full Methods** and any associated references are available in the online version of the paper at [www.nature.com/nature](http://www.nature.com/nature).

**Received 25 November; accepted 14 December 2011.**

1. Fearon, E. R. *et al.* Identification of a chromosome 18q gene that is altered in colorectal cancers. *Science* **247**, 49–56 (1990).
2. Keino-Masu, K. *et al.* Deleted in colorectal cancer (*DCC*) encodes a netrin receptor. *Cell* **87**, 175–185 (1996).
3. Serafini, T. *et al.* Netrin-1 is required for commissural axon guidance in the developing vertebrate nervous system. *Cell* **87**, 1001–1014 (1996).
4. Hong, K. *et al.* A ligand-gated association between cytoplasmic domains of UNC5 and DCC family receptors converts netrin-induced growth cone attraction to repulsion. *Cell* **97**, 927–941 (1999).
5. Mehlen, P. *et al.* The DCC gene product induces apoptosis by a mechanism requiring receptor proteolysis. *Nature* **395**, 801–804 (1998).



6. Thiebault, K. *et al.* The netrin-1 receptors UNC5H are putative tumor suppressors controlling cell death commitment. *Proc. Natl Acad. Sci. USA* **100**, 4173–4178 (2003).
7. Delloye-Bourgeois, C. *et al.* Interference with netrin-1 and tumor cell death in non-small cell lung cancer. *J. Natl Cancer Inst.* **101**, 237–247 (2009).
8. Fitamant, J. *et al.* Netrin-1 expression confers a selective advantage for tumor cell survival in metastatic breast cancer. *Proc. Natl Acad. Sci. USA* **105**, 4850–4855 (2008).
9. Mazelin, L. *et al.* Netrin-1 controls colorectal tumorigenesis by regulating apoptosis. *Nature* **431**, 80–84 (2004).
10. Mehlen, P. & Fearon, E. R. Role of the dependence receptor DCC in colorectal cancer pathogenesis. *J. Clin. Oncol.* **22**, 3420–3428 (2004).
11. Hibi, K. *et al.* Aberrant methylation of the *UNC5C* gene is frequently detected in advanced colorectal cancer. *Anticancer Res.* **29**, 271–273 (2009).
12. Shin, S. K. *et al.* Epigenetic and genetic alterations in netrin-1 receptors *UNC5C* and *DCC* in human colon cancer. *Gastroenterology* **133**, 1849–1857 (2007).
13. Peltomäki, P. *et al.* Evidence supporting exclusion of the *DCC* gene and a portion of chromosome 18q as the locus for susceptibility to hereditary nonpolyposis colorectal carcinoma in five kindreds. *Cancer Res.* **51**, 4135–4140 (1991).
14. Cho, K. R. *et al.* The *DCC* gene: structural analysis and mutations in colorectal carcinomas. *Genomics* **19**, 525–531 (1994).
15. Fazeli, A. *et al.* Phenotype of mice lacking functional *Deleted in colorectal cancer (Dcc)* gene. *Nature* **386**, 796–804 (1997).
16. Roush, W. Putative cancer gene shows up in development instead. *Science* **276**, 534–535 (1997).
17. Jonkers, J. *et al.* Synergistic tumor suppressor activity of *BRCA2* and *p53* in a conditional mouse model for breast cancer. *Nature Genet.* **29**, 418–425 (2001).
18. Liu, X. *et al.* Somatic loss of *BRCA1* and *p53* in mice induces mammary tumors with features of human *BRCA1*-mutated basal-like breast cancer. *Proc. Natl Acad. Sci. USA* **104**, 12111–12116 (2007).
19. Tanikawa, C., Matsuda, K., Fukuda, S., Nakamura, Y. & Arakawa, H. *p53RDL1* regulates *p53*-dependent apoptosis. *Nature Cell Biol.* **5**, 216–223 (2003).
20. Wang, H. *et al.* A newly identified dependence receptor *UNC5H4* is induced during DNA damage-mediated apoptosis and transcriptional target of tumor suppressor *p53*. *Biochem. Biophys. Res. Commun.* **370**, 594–598 (2008).
21. Miyamoto, Y. *et al.* Identification of *UNC5A* as a novel transcriptional target of tumor suppressor *p53* and a regulator of apoptosis. *Int. J. Oncol.* **36**, 1253–1260 (2010).
22. Derksen, P. W. *et al.* Somatic inactivation of *E-cadherin* and *p53* in mice leads to metastatic lobular mammary carcinoma through induction of anoikis resistance and angiogenesis. *Cancer Cell* **10**, 437–449 (2006).
23. Vollenec, A., Bhogal, R. K., Moorman, J. M., Leslie, R. A. & Flanigan, T. P. Differential expression of *DCC* mRNA in adult rat forebrain. *Neuroreport* **8**, 2913–2917 (1997).
24. Livesey, F. J. & Hunt, S. P. Netrin and netrin receptor expression in the embryonic mammalian nervous system suggests roles in retinal, striatal, nigral, and cerebellar development. *Mol. Cell. Neurosci.* **8**, 417–429 (1997).
25. Hamamoto, T. *et al.* Compound disruption of *Smad2* accelerates malignant progression of intestinal tumors in *Apc* knockout mice. *Cancer Res.* **62**, 5955–5961 (2002).
26. Alberici, P. *et al.* *Smad4* haploinsufficiency in mouse models for intestinal cancer. *Oncogene* **25**, 1841–1851 (2006).
27. Kinzler, K. W. & Vogelstein, B. Lessons from hereditary colorectal cancer. *Cell* **87**, 159–170 (1996).
28. Austrup, F. *et al.* Prognostic value of genomic alterations in minimal residual cancer cells purified from the blood of breast cancer patients. *Br. J. Cancer* **83**, 1664–1673 (2000).

**Supplementary Information** is linked to the online version of the paper at [www.nature.com/nature](http://www.nature.com/nature).

**Acknowledgements** We thank R. B. Ali for assistance in generating the mice, J. Blitz and the staff of the NKI animal facility for providing animal care, the staff of the histology department for the processing of tissues, I. Huijbers and H. van Zeeburg for help with apoptosis and FACS analysis, A. Kraft, S. Klarenbeek, S. Rottenberg and G. Doumont for discussions, and T. Braumuller and A. Kersbergen for technical support. We also thank the laboratory of P. Mehlen for the gift of netrin 1.

**Author Contributions** J.Y.S. carried out the histopathological analysis, N.P. was involved in animal experiments and J.Z. performed the confocal microscopy. J.J. and A.B. participated in discussions and interpretations of the experiments. P.K. was responsible for the design and execution of the experiments, and P.K. and A.B. wrote the paper.

**Author Information** Reprints and permissions information is available at [www.nature.com/reprints](http://www.nature.com/reprints). The authors declare no competing financial interests. Readers are welcome to comment on the online version of this article at [www.nature.com/nature](http://www.nature.com/nature). Correspondence and requests for materials should be addressed to A.B. ([a.berns@nki.nl](mailto:a.berns@nki.nl)).



## METHODS

**Construction of DCC conditional mice.** The strategy to conditionally inactivate Dcc was based on deleting exon 23, which encodes the DCC transmembrane domain using the Cre/*loxP* technology. With probes for exons 22, 23 and 24 we screened a 129/SV phage library (Stratagene) and isolated overlapping phage clones spanning a 20-kb region that starts 4 kb 5' of exon 22 and ends 3 kb 3' of exon 24. In the targeting vector we introduced a *loxP-Neo-TK-loxP* selection cassette in the Bln1 restriction site present in the 22nd intron and a single *loxP* sequence in the Csp451 restriction site present in the 23rd intron. This targeting vector was electroporated into 129/Ola-derived E14-IB10 embryonic stem cells. Correctly targeted neomycin-resistant embryonic-stem-cell clones also harbouring the single *loxP* sequence in the Csp451 site were identified by Southern blot analysis. In these clones the *Neo-TK* expression cassette was removed by transient Cre expression as described<sup>17</sup>, resulting in embryonic-stem-cell clones containing *loxP* sequences in introns 22 and 23. *Dcc*<sup>F/+</sup> embryonic stem cells were injected into C57Bl/6 blastocysts, and chimaeras were crossed with FVB/N mice to produce heterozygous offspring. The resulting *Dcc*<sup>F/+</sup> heterozygous and subsequent *Dcc*<sup>F/F</sup> homozygous mice were viable and fertile, and showed a normal life span, indicating that the *Dcc*<sup>F</sup> allele is fully functional.

**DNA analysis.** For genotyping, PCR analysis for the presence of the *Dcc*<sup>F</sup> allele was based on the presence of *loxP* (1) inserted in the Bln1 site 5' in intron 22. Forward primer (located 5' of the 5' *loxP* (1) sequence), CAAGACACATG GAAGGTGAAATG; reverse primer (located 3' of the 5' *loxP* (1) sequence), GACCTCACTTACATATCAAAATGG; the expected fragment size for wild-type *Dcc* was 200 bp and for *Dcc*<sup>F</sup> was 300 bp (carrying the *loxP* sequence).

For PCR analysis of the *Dcc*<sup>D</sup> allele after Cre-mediated recombination (deletion of exon 23); forward primer, 5' *loxP* (1); reverse primer (located 3' of *loxP* (2) in the Csp451 site in intron 23); CCCAAATCTTCTATATTACAATATC. The expected fragment size was 400 bp.

Southern blot analysis was used for Cre-recombination-mediated exon 23 deletion: DNA was digested with BamHI and BglII, and probed with exon 24; analysis of p53 inactivation by Cre recombination was performed as described<sup>17</sup>.

**Other mouse strains used.** Mouse strains carrying conditional alleles for p53 (*p53*<sup>F</sup>), K14-promoter driven Cre recombinase expression and germline expression of Cre recombinase have been described<sup>17</sup>.

**RNA expression analysis.** Total RNA was isolated using Qiagen RNeasy Mini Kit. For subsequent complementary DNA synthesis we used a First Strand cDNA Synthesis Kit for RT-PCR (Roche). For *Dcc* we used PCR expression analysis with TaqMan probe Mn00514509 and for *Gapdh* we used TaqMan probe Mn99999915.

**Histological analysis.** Tissues were isolated and fixed in EAF saline fixative (ethanol/acetic acid/formol/saline at 40:5:10:45 v/v). Tissues were processed routinely as for histology purposes. For immunohistochemistry, sections were blocked with 3% H<sub>2</sub>O<sub>2</sub> for endogenous peroxidases and incubated with primary antibody, and then stained with biotin-conjugated secondary antibodies and incubated with horseradish-peroxidase-conjugated streptavidin-biotin complex (DAKO). Substrate was developed with DAB (DAKO).

**Antibodies.** The following antibodies were used: mouse anti-E-cadherin (1:400; BD Pharmingen), rat anti-cytokeratin (CK) 8 (1:800; University of Iowa), rabbit anti-CK14 (1:10,000; BabCo), mouse anti-SMA (1:10; Zymed), rabbit anti-SMA (1:500; Neomarkers), caspase 3 (Cell Signaling; 9661L), KI67 (Monosan; PSX1028), DCC (A-20) Santa Cruz (sc-6535). Secondary antibodies were as follows: biotin-conjugated anti-mouse, anti-rat and anti-rabbit antibodies (DAKO).

**Derivation and culture tumour cell lines.** For the isolation of primary tumour cells, a 50–100 mm<sup>3</sup> tumour sample was finely chopped using a McIlwain tissue chopper (Mickle Laboratory Engineering) and digested for 1 h at 37 °C in serum-free DMEM-F12 medium (Invitrogen Life Technologies) containing 0.1 mg ml<sup>-1</sup> porcine pancreatic trypsin (Difco) and 0.2 mg ml<sup>-1</sup> collagenase A (Roche). Cells were washed and fibroblasts were allowed to adhere for 1 h at 37 °C. Non-adherent epithelial cells were removed and cultured in DMEM-F12 medium containing 10% fetal bovine serum (FBS; ICN), 100 IU ml<sup>-1</sup> penicillin, 100 µg ml<sup>-1</sup> streptomycin, 5 ng ml<sup>-1</sup> insulin, 5 ng ml<sup>-1</sup> epidermal growth factor (all Invitrogen Life Technologies) and 5 ng ml<sup>-1</sup> cholera toxin (Sigma). 293T cells were cultured in Iscoves medium (Invitrogen Life Technologies) containing 10% FBS, 100 IU ml<sup>-1</sup> penicillin and 100 µg ml<sup>-1</sup> streptomycin.

**Apoptosis assay.** Cells were plated at a density of 400,000 cells per well in an ultra-low cluster polystyrene culture dish with six wells (Corning). Cells were incubated in the presence of either 10% FCS or 0.5% BSA (serum free). Netrin 1 was added at a concentration of 100 ng ml<sup>-1</sup>. After 24 h, cells were collected and incubated at 37 °C with 0.25% trypsin (Invitrogen) for 1 min to prevent cell aggregation. FITC-conjugated annexin 5 (IQ Products) and ToPro-3 (Molecular Probes) were added and annexin-5-positive apoptotic cells were analysed by FACS as described<sup>22</sup>.

# The same pocket in menin binds both MLL and JUND but has opposite effects on transcription

Jing Huang<sup>1,2</sup>, Buddha Gurung<sup>3\*</sup>, Bingbing Wan<sup>1,2\*</sup>, Smita Matkar<sup>3</sup>, Natalia A. Veniaminova<sup>4</sup>, Ke Wan<sup>1,2</sup>, Juanita L. Merchant<sup>4,5</sup>, Xianxin Hua<sup>3</sup> & Ming Lei<sup>1,2</sup>

Menin is a tumour suppressor protein whose loss or inactivation causes multiple endocrine neoplasia 1 (MEN1), a hereditary autosomal dominant tumour syndrome that is characterized by tumorigenesis in multiple endocrine organs<sup>1</sup>. Menin interacts with many proteins and is involved in a variety of cellular processes<sup>2–8</sup>. Menin binds the JUN family transcription factor JUND and inhibits its transcriptional activity<sup>2,9</sup>. Several *MEN1* missense mutations disrupt the menin–JUND interaction, suggesting a correlation between the tumour-suppressor function of menin and its suppression of JUND-activated transcription<sup>2,10</sup>. Menin also interacts with mixed lineage leukaemia protein 1 (MLL1), a histone H3 lysine 4 methyltransferase, and functions as an oncogenic cofactor to upregulate gene transcription and promote MLL1-fusion-protein-induced leukaemogenesis<sup>5,7,11,12</sup>. A recent report on the tethering of MLL1 to chromatin binding factor lens epithelium-derived growth factor (LEDGF) by menin indicates that menin is a molecular adaptor coordinating the functions of multiple proteins<sup>13</sup>. Despite its

importance, how menin interacts with many distinct partners and regulates their functions remains poorly understood. Here we present the crystal structures of human menin in its free form and in complexes with MLL1 or with JUND, or with an MLL1–LEDGF heterodimer. These structures show that menin contains a deep pocket that binds short peptides of MLL1 or JUND in the same manner, but that it can have opposite effects on transcription. The menin–JUND interaction blocks JUN N-terminal kinase (JNK)-mediated JUND phosphorylation and suppresses JUND-induced transcription. In contrast, menin promotes gene transcription by binding the transcription activator MLL1 through the peptide pocket while still interacting with the chromatin-anchoring protein LEDGF at a distinct surface formed by both menin and MLL1.

The amino-terminal region of MLL1 interacts with menin<sup>12,14,15</sup>. Isothermal titration calorimetry measurements showed that the menin-binding motif (residues 6–25) of MLL1 (MLL1<sub>MBM</sub>) is necessary and sufficient for menin binding (Fig. 1a and Supplementary Fig. 1a–c).

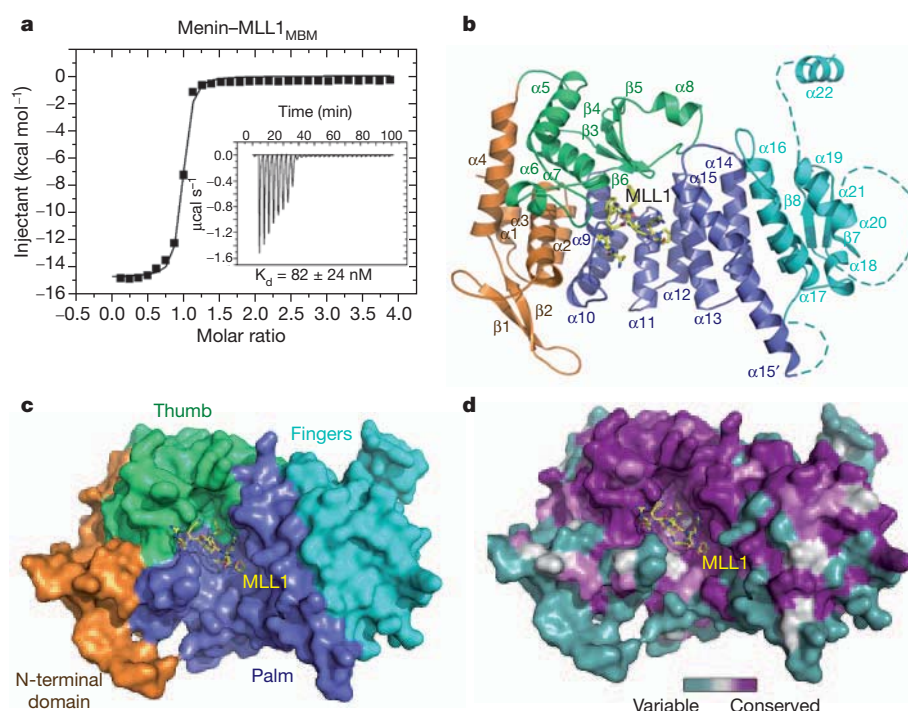


**Figure 1 | Overview of the human menin–MLL1<sub>MBM</sub> complex structure.**

**a**, Isothermal titration calorimetry measurement of the menin–MLL1<sub>MBM</sub> interaction. The inset shows the isothermal titration data. **b**, Overall structure of the menin–MLL1<sub>MBM</sub> complex. The N-terminal domain is shown in orange, the thumb domain in green, the palm domain in blue, the fingers domain in cyan,

and loop regions that are disordered or not included in the crystal structure are shown as dashed lines. MLL1<sub>MBM</sub> is shown as a stick model in yellow. **c**, The surface representation of menin indicates that menin adopts a curved left-hand-shaped conformation. **d**, Front view of the menin–MLL1<sub>MBM</sub> complex, coloured according to the degree of amino acid conservation among menin homologues.

<sup>1</sup>Howard Hughes Medical Institute, University of Michigan Medical School, 1150 West Medical Center Drive, Ann Arbor, Michigan 48109, USA. <sup>2</sup>Department of Biological Chemistry, University of Michigan Medical School, 1150 West Medical Center Drive, Ann Arbor, Michigan 48109, USA. <sup>3</sup>Abramson Family Cancer Research Institute, Department of Cancer Biology, University of Pennsylvania Perelman School of Medicine, Philadelphia, Pennsylvania 19104, USA. <sup>4</sup>Department of Internal Medicine, University of Michigan, 109 Zina Pitcher Place, Ann Arbor, Michigan 48109, USA. <sup>5</sup>Department of Molecular and Integrative Physiology, Division of Gastroenterology, University of Michigan, 109 Zina Pitcher Place, Ann Arbor, Michigan 48109, USA.

\*These authors contributed equally to this work.

MLL2, the closest relative of MLL1, contains a sequence that is almost identical to MLL1<sub>MBM</sub> at its N terminus (Supplementary Fig. 1b); MLL2<sub>16–35</sub> (MLL2<sub>MBM</sub>) binds to menin with an affinity that is comparable to that of MLL1<sub>MBM</sub> (Supplementary Fig. 1d). To understand how MLL1 and MLL2 (collectively referred to as MLL) are recognized by menin, we determined the crystal structures of human menin alone

or in complex with MLL1<sub>MBM</sub> (Supplementary Fig. 2, Supplementary Table 1 and Supplementary Information). The structure of human menin closely resembles a recently published menin homologue structure from *Nematostella*<sup>16</sup>.

The conformation of menin resembles a curved left 'hand' with a deep pocket formed by its 'thumb' and 'palm' (Fig. 1b, c). Menin consists

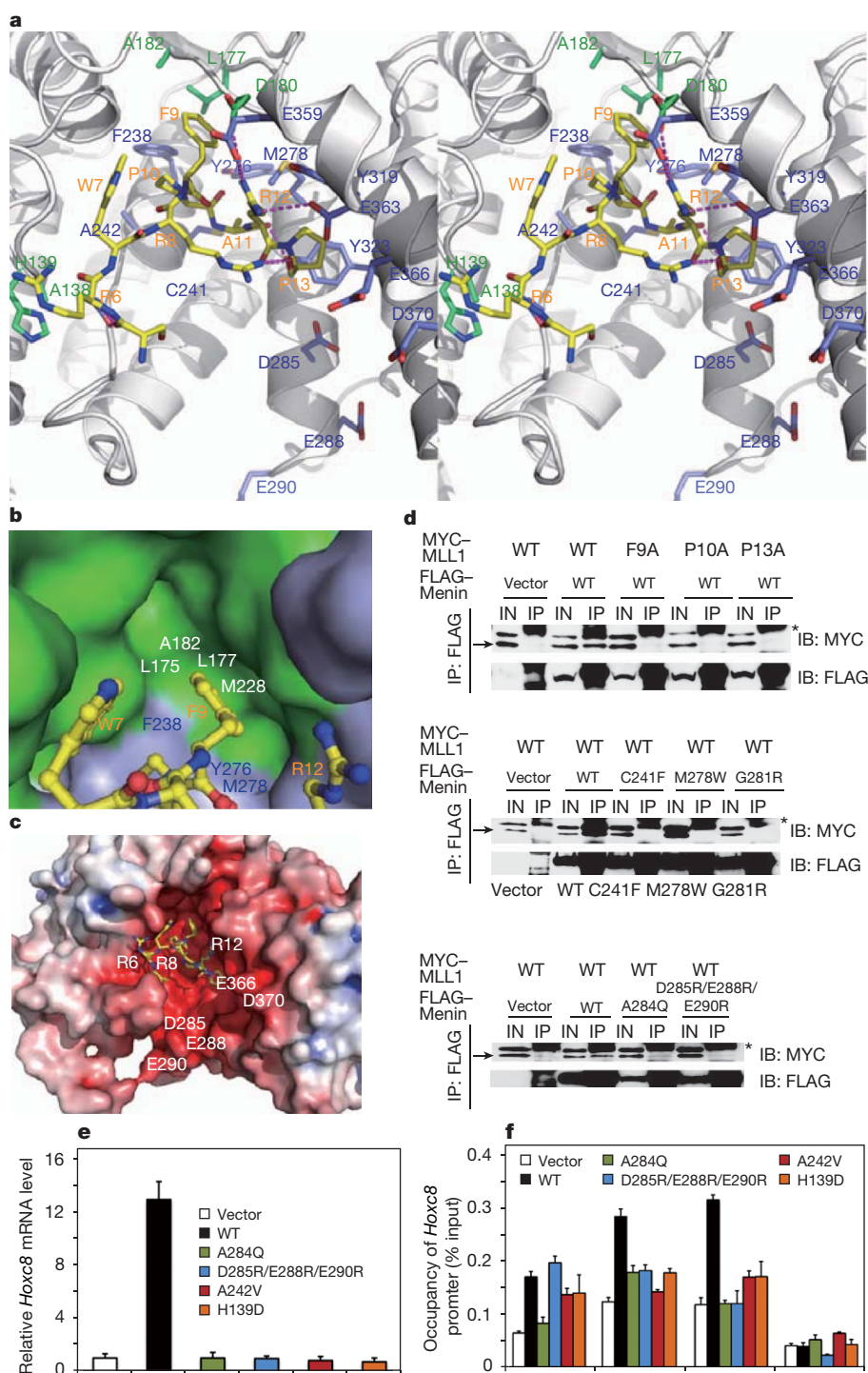


**Figure 2 | Structural and mutational analyses of the menin-MLL1<sub>MBM</sub> interaction.** **a**, Stereo view of the menin-MLL1<sub>MBM</sub> interface. The intermolecular hydrogen bonds are shown as dashed magenta lines. **b**, Phe<sup>9</sup><sub>MLL1</sub> (yellow) is nestled in a hydrophobic pocket of menin formed by the thumb (green) and the palm (blue). **c**, Electrostatic surface potential of the MLL1<sub>MBM</sub>-binding cavity of menin (positive potential, blue; negative potential, red). **d**, Co-immunoprecipitation of wild-type (WT) or mutant menin and

MLL1 proteins from 293T cells. Arrows and asterisks indicate the positions of MYC-MLL1 and immunoglobulin G (IgG), respectively. IB, immunoblot; IN, input; IP, immunoprecipitation. **e**, **f**, Expression of *Hoxc8* (**e**) and distributions of menin, MLL1 and H3K4me3 at the *Hoxc8* promoter (**f**) in *Men1*<sup>-/-</sup> mouse embryonic fibroblasts (MEFs) complemented with control vector, WT or mutant menin ( $n = 6$ ; error bar, standard deviation).



of four associated domains: an N-terminal domain characterized by a long  $\beta$ -hairpin, a transglutaminase-like domain that forms the thumb, a helical palm domain that contains three TPR motifs<sup>17</sup> and a carboxy-terminal fingers domain (Fig. 1b, c, Supplementary Fig. 3 and Supplementary Information). Menin is highly conserved across species, and the conserved residues are either buried in the hydrophobic core or clustered together on a surface patch that covers the thumb and palm (Fig. 1d). MEN1 disease-derived missense and in-frame deletion mutations are evenly distributed throughout the protein (Supplementary Fig. 4), indicating that all four domains are important for the *in vivo* function of menin (Supplementary Fig. 4 and Supplementary Table 2).

The MLL1<sub>MBM</sub> peptide adopts a compact conformation and plugs into the deep pocket of menin (Fig. 2a and Supplementary Fig. 5). Mutagenesis data indicates that MLL1<sub>MBM</sub> residues Arg 6-Trp 7-Arg 8-Phe 9-Pro 10-Ala 11-Arg 12-Pro 13 and their interacting residues in menin contribute the most towards the interaction (Supplementary Figs 6 and 7, and Supplementary Tables 3 and 4). The side-chain of Phe 9<sup>MLL1</sup> fits into a hydrophobic cavity formed by the thumb and palm of menin (Fig. 2b). A menin Met278Trp substitution altered the cavity shape and led to complete loss of binding (Supplementary Table 4). The MLL1<sub>MBM</sub>-binding pocket is highly acidic (Fig. 2c). The two C-terminal arginine residues (Arg 24 and Arg 25) in MLL1<sub>MBM</sub> are disordered, but they seem to be important for interaction, given that glutamate substitution resulted in a 21-fold decrease in binding affinity (Supplementary Table 3). Consistent with this, mutation of the acidic residues of menin also led to decreased binding (Supplementary Table 4).

Next, we examined the MLL1<sub>MBM</sub>-binding activity of several MEN1 disease-derived mutations (His139Asp, Cys241Phe, Ala242Val, Gly281Arg, Ala284Gln, and Thr344Arg). Except for Ala284Gln and Thr344Arg, which yielded insoluble proteins, the remaining mutants impaired the menin–MLL1<sub>MBM</sub> interaction (Supplementary Table 4). To further examine the menin–MLL1 interaction *in vivo*, we studied the interactions of mutant proteins that are transiently expressed in human embryonic kidney 293T cells. Consistent with the isothermal titration calorimetry analysis, co-immunoprecipitation data showed that mutations of the key residues at the interface completely abolished the menin–MLL1 interaction in cells (Fig. 2d).

Menin upregulates the expression of homeobox genes *Hoxc8* and *Hoxc6* (ref. 5). To test the effect of the menin–MLL interaction on the expression levels of *Hoxc8* and *Hoxc6*, wild-type and MLL-binding deficient mutants of menin were individually used to complement menin-null mouse embryonic fibroblasts. Western blot analyses indicated comparable expression of wild-type and mutant proteins in cells (Supplementary Fig. 8a). When *Men1*<sup>−/−</sup> cells were complemented with wild-type menin, expression of *Hoxc8* and *Hoxc6* dramatically increased compared to vector-expressing cells (Fig. 2e and Supplementary Fig. 8b). In contrast, overexpression of the menin mutants in *Men1*<sup>−/−</sup> cells failed to upregulate the messenger RNA levels of *Hoxc8* or *Hoxc6* (Fig. 2e and Supplementary Fig. 8b), suggesting that the menin–MLL interaction is essential for *Hoxc8* and *Hoxc6* expression.

Next we performed chromatin immunoprecipitation (ChIP) assays to determine the binding of mutant menin at the *Hoxc8* promoter. Except for Ala284Gln (a mutant that leads to insoluble proteins), all other mutants bound to the *Hoxc8* promoter as effectively as wild-type menin (Fig. 2f). Expression of wild-type or mutant menin did not greatly affect H3 distribution at the *Hoxc8* promoter (Supplementary Fig. 8c). Notably, *Men1*<sup>−/−</sup> cells complemented with wild-type menin exhibited a substantial increase in MLL1 binding and histone H3K4me3 trimethylation at the *Hoxc8* promoter compared with vector-expressing or mutant-menin-expressing cells (Fig. 2f). Therefore, although menin mutants were able to bind to the *Hoxc8* promoter, their ability to recruit MLL1 and thus establish H3K4me3 at the *Hoxc8* promoter was compromised, resulting in reduced *Hoxc8* expression.

LEDGF, a chromatin-associated protein<sup>18</sup>, is required for MLL1-dependent transcription and leukaemic transformation<sup>13</sup>. Isothermal

titration calorimetry measurement showed that a complex composed of menin and an N-terminal fragment of MLL1, called MLL1<sub>MBM-LBM</sub> (comprising residues 6–153 and including both menin-binding and LEDGF-binding motifs) binds to the integrase binding domain of LEDGF (LEDGF<sub>IBD</sub>) with an affinity of 470 nM (Fig. 3a and Supplementary Fig. 9a). In contrast, neither menin nor MLL1<sub>MBM-LBM</sub> alone could interact with LEDGF<sub>IBD</sub> (Supplementary Fig. 9b)<sup>13</sup>. We determined the menin–MLL1<sub>MBM-LBM</sub>–LEDGF<sub>IBD</sub> complex structure at a resolution of 3.0 Å (Supplementary Fig. 9c and Supplementary Table 1). MLL1<sub>MBM-LBM</sub> exhibits an extended conformation and binds to menin through two major sites (Fig. 3b); the N-terminal MLL1<sub>MBM</sub> coil folds into the high-affinity pocket of menin in the same manner as in the menin–MLL1<sub>MBM</sub> structure (Supplementary Figs 9d, e), whereas the C-terminal helix  $\alpha$ 2 packs on the surface of the N-terminal domain of menin to form a V-shaped groove for LEDGF<sub>IBD</sub> binding (Fig. 3b and Supplementary Fig. 9f). The middle loop of MLL1<sub>MBM-LBM</sub> spans a large distance on menin without many specific interactions except for two leucine residues (Leu 106 and Leu 116) with side-chains that point to

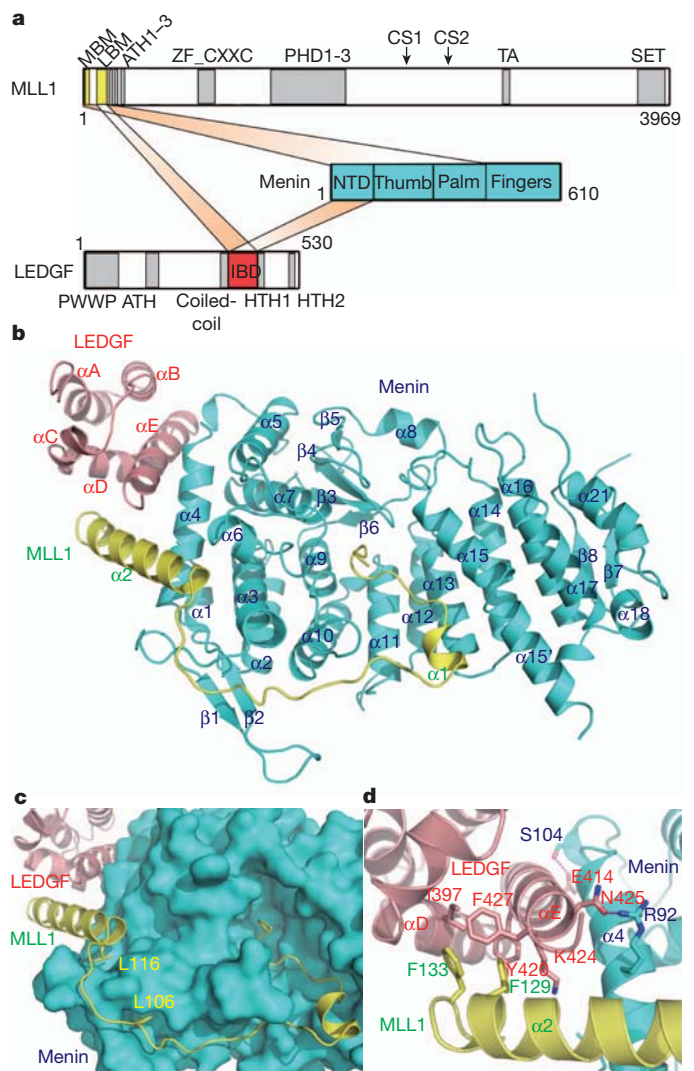


**Figure 3 | Structure of the menin–MLL1<sub>MBM-LBM</sub>–LEDGF<sub>IBD</sub> ternary complex.** **a**, Domain organization of menin, MLL1 and LEDGF. The menin- and LEDGF-binding motifs and LBM motifs of MLL1 are shown in yellow, menin in cyan, the integrase-binding domain of LEDGF in red and other regions in grey. Interactions among the three proteins are shown in orange. **b**, Ribbon diagram of the menin–MLL1<sub>MBM-LBM</sub>–LEDGF<sub>IBD</sub> complex. Menin is in cyan, MLL1<sub>MBM-LBM</sub> in yellow and LEDGF<sub>IBD</sub> in red. **c**, The extended MLL1 loop between MLL1<sub>MBM</sub> and MLL1<sub>LBM</sub> covers a large part of the surface area of menin. **d**, Detailed view of the intermolecular three-helix-bundle at the ternary interface.

two shallow pockets on the menin surface, defining the path of the loop (Fig. 3c and Supplementary Fig. 9g). Helix  $\alpha$ E of LEDGF<sub>IBD</sub> is sandwiched between helices  $\alpha$ 2 of MLL1 and  $\alpha$ 4 of menin through both hydrophobic and electrostatic interactions (Fig. 3d). In support of the crystal structure, mutations of residues on the  $\alpha$ 4 helix of the N-terminal domain of menin (Ala95Arg and Ser104Tyr) specifically disrupted the interaction with LEDGF (Supplementary Table 5 and Supplementary Fig. 10). Notably, *Men1*<sup>-/-</sup> cells that were complemented with these two mutants failed to stimulate *Hoxc8* expression (Supplementary Fig. 11), suggesting that a functional menin–MLL1–LEDGF complex is required for upregulation of *Hoxc8* expression. Together, our data show that menin functions as an adaptor molecule to modulate gene expression by binding MLL1 at one site while also interacting with LEDGF at a distinct surface.

Although MLL1 and MLL2 share many functional motifs, including the menin-binding motif (Supplementary Fig. 12), MLL2 does not contain a LEDGF-binding motif sequence and thus would not form a ternary complex with menin and LEDGF. Given that the PWWP domain of LEDGF, which contains a relatively well conserved Pro-Trp-Trp-Pro signature, is required for MLL1-mediated leukaemic transformation<sup>13,18</sup>, the inability of MLL2 to form a menin–MLL2–LEDGF complex explains why only MLL1, and not MLL2, has so far been described as a proto-oncogene that can be activated by chromosomal translocations.

Menin also interacts directly with transcription factor JUND<sup>2,9</sup>. We defined JUND residues 27–47 as the menin-binding motif (JUND<sub>MBM</sub>) with an affinity of 1.6  $\mu$ M (Fig. 4a and Supplementary Fig. 13). Sequence comparison of JUND<sub>MBM</sub> and MLL1<sub>MBM</sub> revealed a

striking similarity (Fig. 4a), suggesting that JUND<sub>MBM</sub> might interact with menin through the same binding pocket as does MLL1<sub>MBM</sub>. Consistent with this idea, both isothermal titration calorimetry and glutathione S-transferase (GST) pull-down assays showed that MLL1 could efficiently compete with JUND for menin binding (Supplementary Fig. 14).

We determined the menin–JUND<sub>MBM</sub> complex structure, which shows many similarities to the menin–MLL1<sub>MBM</sub> structure (Fig. 4b and Supplementary Table 1). First, the Phe-Pro-(Ala or Gly)-(Arg or Ala)-Pro motifs in both menin-binding motifs are almost identical in overall conformation (Supplementary Fig. 15a). Second, Phe32, Pro33 and Pro36 of JUND interact with menin in the same way as their counterparts in MLL1<sub>MBM</sub> (Supplementary Fig. 15b, c). Notably, two lysine residues (Lys 46 and Lys 47) in JUND<sub>MBM</sub>, equivalent to the disordered Arg 24 and Arg 25 in MLL1<sub>MBM</sub>, are visible in the electron density map and point to an acidic surface on menin (Supplementary Fig. 15c). Mutation of these lysine residues and other key binding residues at the interface abolished or weakened the interaction both *in vitro* and *in vivo* (Fig. 4c, Supplementary Fig. 16 and Supplementary Table 6).

Menin uncouples JUND phosphorylation from JNK activation, but the mechanism is poorly understood<sup>19</sup>. The consensus JNK-docking domain (D-domain) contains a cluster of basic amino acids preceding two leucine residues<sup>20</sup> (Fig. 4d). JUND<sub>MBM</sub> is partially overlapped with a putative D-domain of JUND (JUND<sub>D</sub>)<sup>21</sup> (Fig. 4d). Both the basic residues and the leucine residues in JUND<sub>D</sub> are indispensable for JNK docking on JUND as well as JNK-mediated JUND phosphorylation (Fig. 4e, f and Supplementary Fig. 17a, b). Thus, Lys 46 and Lys 47 are both required for menin binding and JUND phosphorylation by

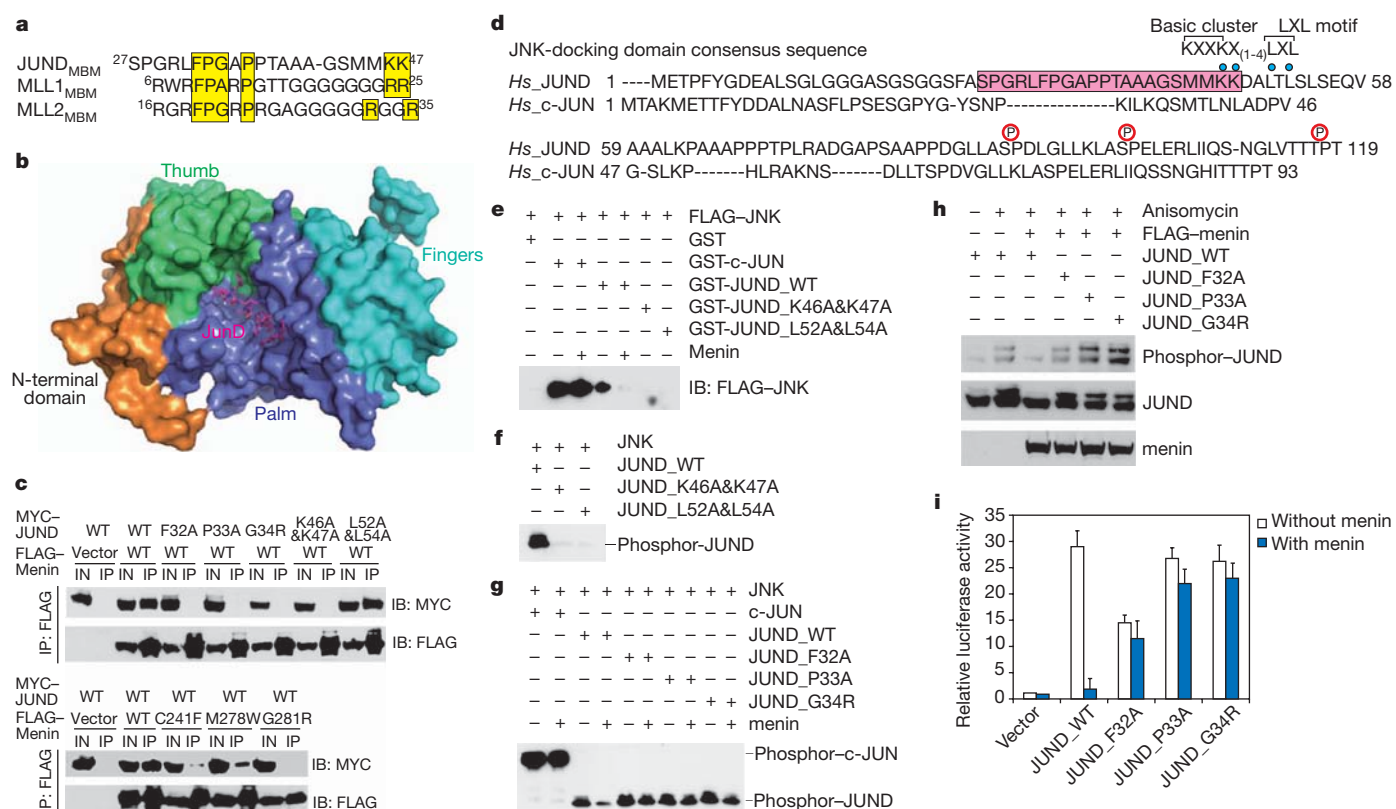


**Figure 4 | Structural and functional studies of the menin–JUND interaction.** **a**, Sequence alignment of the menin-binding motif sequences of JUND, MLL1 and MLL2. Conserved residues are highlighted in yellow. **b**, Crystal structure of the menin–JUND<sub>MBM</sub> complex. Menin is coloured as in Fig. 1c and JUND<sub>MBM</sub> is shown as a purple stick model. **c**, Co-immunoprecipitation of WT or mutant menin and JUND from 293T cells. **d**, Sequence comparison of the N termini of JUND and c-JUN. The menin-binding motif sequence of JUND is highlighted in purple. Key residues in the JNK-docking domain are denoted with blue dots and three phosphorylation

sites are labelled. **e**, *In vitro* GST-pull-down analysis of the interactions between FLAG-tagged JNK and the indicated JUND proteins. **f**, *In vitro* phosphorylation of WT or mutant JUND by JNK. **g**, *In vitro* phosphorylation of WT or menin-binding-deficient JUND by JNK in the presence or absence of menin. **h**, Menin suppresses JUND phosphorylation in response to anisomycin activation of JNK in 293T cells. **i**, WT or mutant JUND plasmids were transfected into 293T cells with AP1 and Renilla reporter plasmids, and with or without menin. Luciferase assays were performed 2 days after transfection ( $n = 4$ ; error bar, standard deviation).



JNK. This led us to test whether menin inhibits JUND phosphorylation through sequestering JUND from JNK. In GST-pull-down assay, GST-JUND can only pull down JNK in the absence of menin, indicating that menin has a higher affinity to JUND (Fig. 4e and Supplementary Fig. 17a). Furthermore, when menin was added, phosphorylation of JUND was clearly inhibited (Fig. 4g and Supplementary Fig. 17c). In contrast, phosphorylation of menin-binding-deficient mutants of JUND was not affected by menin (Fig. 4g and Supplementary Fig. 17c). Next, we examined whether menin could inhibit JUND phosphorylation in response to anisomycin activation of JNK in 293T cells<sup>19</sup>. Although wild-type JUND phosphorylation was suppressed by menin, menin-binding deficient mutants remained robustly phosphorylated in the presence of menin (Fig. 4h). Notably, menin had no effects on JNK binding and JNK-mediated phosphorylation of c-JUN, a close homologue of JUND that lacks a menin-binding motif (Fig. 4d, e, g and Supplementary Fig. 17a, c, d). Together, our findings reveal that the menin-JUND interaction blocks JNK docking on JUND and inhibits the JNK-mediated phosphorylation.

Menin represses JUND-mediated transcriptional activation<sup>2,9</sup>. To examine whether this repression depends on the menin-JUND interaction, wild-type or menin-binding-deficient mutants of JUND were co-transfected into 293T cells with an AP1 luciferase reporter plasmid in the presence or absence of menin (Supplementary Fig. 17e). Consistent with previous studies, transactivation by JUND was effectively repressed by menin<sup>2,9</sup> (Fig. 4i). In contrast, menin exhibited a marginal effect on mutant JUND-mediated transcriptional activation (Fig. 4i). We recently demonstrated that JUND induces gastrin gene expression in human AGS gastric cells and that this induction can be suppressed by menin<sup>22</sup>. Consistent with the luciferase assay, menin failed to suppress the gastrin upregulation that was induced by mutant JUND, suggesting that the menin-JUND interaction is important in gastrin expression regulation (Supplementary Fig. 18). Thus, we conclude that the menin-JUND interaction plays a key part in suppressing JUND-mediated transcriptional activation.

In summary, our structural and functional studies provide a mechanistic explanation of how menin could both positively and negatively regulate gene transcription. Our findings also provide evidence that menin acts as a scaffold protein to assemble a menin-MLL1-LEDGF ternary complex to coordinate gene transcription and promote MLL1-fusion-protein-induced leukaemogenesis.

## METHODS SUMMARY

Human menin, LEDGF<sub>IBD</sub> and the MLL and JUND peptides were expressed in *Escherichia coli* BL21(DE3) and purified by sequential affinity and gel-filtration chromatography purification. Menin crystals were obtained in sitting drops over 100 mM sodium cacodylate (pH 6.5) and 1.4 M sodium acetate. Crystallization of menin with the MLL<sub>1MBM</sub> or JUND<sub>MBM</sub> peptides was achieved by sitting-drop diffusion with a well solution containing 100 mM Tris-HCl (pH 7.0), 200 mM MgCl<sub>2</sub> and 2.3 M NaCl. The menin-MLL<sub>1MBM-LBM</sub>-LEDGF<sub>IBD</sub> complex was crystallized by hanging-drop vapour diffusion against a well solution of 50 mM HEPES (pH 7.0), 1.6 M (NH<sub>4</sub>)<sub>2</sub>SO<sub>4</sub>, 10 mM MgCl<sub>2</sub>, 0.016% L-canavanine, 0.016% O-phospho-L-serine, 0.016% taurine, 0.016% quinine, 0.016% sodium glyoxylate monohydrate and 0.016% cholic acid, and were dehydrated with the solution containing 50 mM HEPES (pH 7.0), 2.3 M (NH<sub>4</sub>)<sub>2</sub>SO<sub>4</sub> and 10 mM MgCl<sub>2</sub>. The menin-MLL<sub>1MBM</sub> complex structure was determined by multi-wavelength anomalous dispersion to a resolution of 3.0 Å. The structures of menin alone, the menin-MLL<sub>1MBM-LBM</sub>-LEDGF<sub>IBD</sub> ternary complex, and the menin-JUND<sub>MBM</sub> complex were solved by molecular replacement and refined to resolutions of 2.5 Å, 3.0 Å and 2.85 Å, respectively.

**Full Methods** and any associated references are available in the online version of the paper at [www.nature.com/nature](http://www.nature.com/nature).

**Received 17 July; accepted 19 December 2011.**

**Published online 12 February 2012.**

- Chandrasekharappa, S. C. *et al.* Positional cloning of the gene for multiple endocrine neoplasia-type 1. *Science* **276**, 404–407 (1997).

- Agarwal, S. K. *et al.* Menin interacts with the AP1 transcription factor JunD and represses JunD-activated transcription. *Cell* **96**, 143–152 (1999).
- Busygina, V., Kottmann, M. C., Scott, K. L., Plon, S. E. & Bale, A. E. Multiple endocrine neoplasia type 1 interacts with forkhead transcription factor CHES1 in DNA damage response. *Cancer Res.* **66**, 8397–8403 (2006).
- Chen, G. *et al.* Menin promotes the Wnt signaling pathway in pancreatic endocrine cells. *Mol. Cancer Res.* **6**, 1894–1907 (2008).
- Hughes, C. M. *et al.* Menin associates with a trithorax family histone methyltransferase complex and with the *Hoxc8* locus. *Mol. Cell* **13**, 587–597 (2004).
- Jin, S. *et al.* Menin associates with FANCD2, a protein involved in repair of DNA damage. *Cancer Res.* **63**, 4204–4210 (2003).
- Yokoyama, A. *et al.* Leukemia proto-oncoprotein MLL forms a SET1-like histone methyltransferase complex with menin to regulate *Hox* gene expression. *Mol. Cell Biol.* **24**, 5639–5649 (2004).
- Yang, Y. & Hua, X. In search of tumor suppressing functions of menin. *Mol. Cell Endocrinol.* **265–266**, 34–41 (2007).
- Knapp, J. I. *et al.* Identification and characterization of JunD missense mutants that lack menin binding. *Oncogene* **19**, 4706–4712 (2000).
- Groussin, L. & Bertherat, J. Mechanisms of multiple endocrine neoplasia type 1: evidence for regulation of the AP-1 family of transcription factors by menin. *Eur. J. Endocrinol.* **141**, 15–16 (1999).
- Krivtsov, A. V. & Armstrong, S. A. MLL translocations, histone modifications and leukaemia stem-cell development. *Nature Rev. Cancer* **7**, 823–833 (2007).
- Yokoyama, A. *et al.* The menin tumor suppressor protein is an essential oncogenic cofactor for MLL-associated leukemogenesis. *Cell* **123**, 207–218 (2005).
- Yokoyama, A. & Cleary, M. L. Menin critically links MLL proteins with LEDGF on cancer-associated target genes. *Cancer Cell* **14**, 36–46 (2008).
- Caslini, C. *et al.* Interaction of MLL amino terminal sequences with menin is required for transformation. *Cancer Res.* **67**, 7275–7283 (2007).
- Grembecka, J., Belcher, A. M., Hartley, T. & Cierpicki, T. Molecular basis of the mixed lineage leukemia-menin interaction: implications for targeting mixed lineage leukemias. *J. Biol. Chem.* **285**, 40690–40698 (2010).
- Murai, M. J., Chruszcz, M., Reddy, G., Grembecka, J. & Cierpicki, T. Crystal structure of menin reveals binding site for mixed lineage leukemia (MLL) protein. *J. Biol. Chem.* **286**, 31742–31748 (2011).
- Lamb, J. R., Tugendreich, S. & Hieter, P. Tetratricopeptide repeat interactions: to TPR or not to TPR? *Trends Biochem. Sci.* **20**, 257–259 (1995).
- Llano, M., Morrison, J. & Poeschla, E. M. Virological and cellular roles of the transcriptional coactivator LEDGF/p75. *Curr. Top. Microbiol. Immunol.* **339**, 125–146 (2009).
- Gallo, A. *et al.* Menin uncouples Elk-1, JunD and c-Jun phosphorylation from MAP kinase activation. *Oncogene* **21**, 6434–6445 (2002).
- Yang, S. H., Whitmarsh, A. J., Davis, R. J. & Sharrocks, A. D. Differential targeting of MAP kinases to the ETS-domain transcription factor Elk-1. *EMBO J.* **17**, 1740–1749 (1998).
- Yazgan, O. & Pfarr, C. M. Regulation of two JunD isoforms by Jun N-terminal kinases. *J. Biol. Chem.* **277**, 29710–29718 (2002).
- Mensah-Osman, E. J., Veniaminova, N. A. & Merchant, J. L. Menin and JunD regulate gastrin gene expression through proximal DNA elements. *Am. J. Physiol. Gastrointest. Liver Physiol.* **301**, G783–G790 (2011).

**Supplementary Information** is linked to the online version of the paper at [www.nature.com/nature](http://www.nature.com/nature).

**Acknowledgements** We thank G. Wilding for the human JUND complementary DNA and P. Cherepanov for the human LEDGF cDNA. We thank Y. Chen and W. Deng for help at various stages of the project. M.L. is a Howard Hughes Medical Institute Early Career Scientist. Work was supported by National Institutes of Health grants (GM 083015-01 to M.L., R01-DK085121 to X.H. and R37-DK45729 to J.L.M.), an American Cancer Society Research Scholar grant (to M.L.) and an American Association for Cancer Research Caring for Carcinoid Foundation Grant (to X.H.). The General Medicine and Cancer Institutes Collaborative Access Team has been funded in whole or in part with federal funds from the National Cancer Institute (grant Y1-CO-1020) and the National Institute of General Medical Science (grant Y1-GM-1104). Use of the Advanced Photon Source was supported by the US Department of Energy, Office of Science, Office of Basic Energy Sciences, under contract number DE-AC02-06CH11357.

**Author Contributions** J.H. is responsible for the bulk of the experiments, B.G. for the qRT-PCR and ChIP assays; B.W. for the co-immunoprecipitation and *in vivo* phosphorylation analyses, S.M. for the luciferase assay, N.A.V. and J.L.M. for the analysis of gastrin expression, and K.W. for some of the protein purification. M.L. and X.H. supervised the project and wrote the paper.

**Author Information** The atomic coordinates and structure factors of menin, menin-MLL<sub>1MBM</sub>, menin-JUND<sub>MBM</sub>, and menin-MLL<sub>1MBM-LBM</sub>-LEDGF<sub>IBD</sub> have been deposited in the RCSB Protein Data Bank under accession codes 3U84, 3U85, 3U86 and 3U88, respectively. Reprints and permissions information is available at [www.nature.com/reprints](http://www.nature.com/reprints). The authors declare no competing financial interests. Readers are welcome to comment on the online version of this article at [www.nature.com/nature](http://www.nature.com/nature). Correspondence and requests for materials should be addressed to M.L. (leim@umich.edu) or X.H. (huax@mail.med.upenn.edu).



## METHODS

**Protein expression and purification.** To facilitate crystallization, we genetically deleted an unstructured loop (residues 460–519) in menin, a short fragment (residues 40–45) in JUND<sub>MBM</sub> and two loop regions (residues 16–22 and 36–102) in MLL1<sub>MBM-LBM</sub>. All the resulting proteins retain wild-type-like binding affinities (Supplementary Figs 2d, 9c and 13d). For simplicity, MeninΔ, JUND<sub>MBM</sub>Δ and MLL1<sub>MBM-LBM</sub>Δ are referred to as menin, JUND<sub>MBM</sub> and MLL1<sub>MBM-LBM</sub> respectively, unless stated otherwise.

Various human menin proteins and the MLL and JUND peptides were expressed in *E. coli* BL21(DE3) using a modified pET28b vector with a SUMO protein fused at the N terminus after the His<sub>6</sub> tag. After induction for 16 h with 0.1 mM isopropylthiogalactoside (IPTG) at 25 °C, the cells were collected by centrifugation and the pellets were resuspended in lysis buffer (50 mM Tris-HCl, pH 8.0; 50 mM NaH<sub>2</sub>PO<sub>4</sub>; 400 mM NaCl; 3 mM imidazole; 10% glycerol; 0.1 mg ml<sup>-1</sup> lysozyme; 2 mM 2-mercaptoethanol; 1 mM PMSF; 5 mM benzamide; 1 μg ml<sup>-1</sup> leupeptin; and 1 μg ml<sup>-1</sup> pepstatin). The cells were then lysed by sonication and the cell debris was removed by ultracentrifugation. The supernatant was mixed with Ni-NTA agarose beads (Qiagen) and rocked for 2 h at 4 °C before elution with 250 mM imidazole. Ulp1 protease was then added to remove the His<sub>6</sub>-SUMO tag. After Ulp1 digestion, the menin proteins and the MLL and JUND peptides were further purified by gel-filtration chromatography on Hiload Superdex 200 and Hiload Superdex 75 columns (GE Healthcare), equilibrated with buffer A (25 mM Tris-HCl, pH 8.0; 150 mM NaCl; and 5 mM dithiothreitol (DTT)) and buffer B (100 mM ammonium bicarbonate), respectively. The purified menin proteins were concentrated to 25 mg ml<sup>-1</sup> and stored at -80 °C. The purified peptides were lyophilized and resuspended in water at a concentration of 50 mg ml<sup>-1</sup> and stored at -80 °C.

For the menin-MLL1<sub>MBM-LBM</sub>-LEDGF<sub>IBD</sub> complex, we cloned LEDGF<sub>IBD</sub> into a modified pET28b vector with a SUMO protein fused at the N terminus after the His<sub>6</sub> tag. MLL1<sub>MBM-LBM</sub> was cloned into a GST fusion protein expression vector, pGEX6p-1 (GE healthcare). The menin-MLL1<sub>MBM-LBM</sub> complex and LEDGF<sub>IBD</sub> itself were expressed in *E. coli* BL21(DE3), respectively. The menin-MLL1<sub>MBM-LBM</sub> complex was purified by sequential affinity chromatography with Ni-NTA agarose beads and glutathione sepharose 4B beads (GE Healthcare). After removal of the His<sub>6</sub>-UMO tag and GST tag with Ulp1 and Protease 3C, respectively, the complex was purified further with gel-filtration chromatography on a Hiload Superdex 200. Meanwhile, LEDGF<sub>IBD</sub> was purified in the same way as menin and then mixed with the purified menin-MLL1<sub>MBM-LBM</sub> complex with a molar ratio of 2:1. After 1 h incubation on ice, the protein mixtures were purified again with gel-filtration chromatography on a Hiload Superdex 200 column.

For the *in vitro* assays, mutant menin proteins were expressed in *E. coli* and purified following the procedure described above. All the mutant menin proteins displayed unaltered biophysical properties as analysed by gel-filtration chromatography (data not shown), ensuring that the altered affinities of the menin mutants for MLL1<sub>MBM</sub>, MLL1<sub>MBM-LBM</sub>-LEDGF<sub>IBD</sub> and JUND<sub>MBM</sub> are not attributable to a change in the structural integrity of the resulting proteins.

**Crystallization, data collection and structure determination.** Menin was crystallized by sitting-drop vapour diffusion at 4 °C. The precipitant solution contained 100 mM sodium cacodylate trihydrate (pH 6.5) and 1.4 M sodium acetate trihydrate. For the menin-MLL1<sub>MBM</sub> complex, purified menin was first mixed with the MLL1<sub>MBM</sub> peptide at a molar ratio of 1:2 and then the mixture was incubated on ice for 1 h to allow complex formation. Crystallization of the complex was achieved by sitting-drop vapour diffusion at 4 °C with the well solution containing 100 mM Tris-HCl (pH 7.0), 200 mM MgCl<sub>2</sub> and 2.3 M NaCl. A similar procedure was also used for crystallization of the menin-JUND<sub>MBM</sub> complex. The menin-MLL1<sub>MBM-LBM</sub>-LEDGF<sub>IBD</sub> complex was crystallized by hanging-drop vapour diffusion at 4 °C with the well solution containing 50 mM HEPES (pH 7.0), 1.6 M (NH<sub>4</sub>)<sub>2</sub>SO<sub>4</sub>, 10 mM MgCl<sub>2</sub>, 0.016% L-canavanine, 0.016% O-phospho-L-serine, 0.016% taurine, 0.016% quinine, 0.016% sodium glyoxylate monohydrate and 0.016% cholic acid. The crystals were then dehydrated with the solution containing 0.05 M HEPES (pH 7.0), 2.3 M (NH<sub>4</sub>)<sub>2</sub>SO<sub>4</sub> and 0.01 M MgCl<sub>2</sub>.

All of the crystals were gradually transferred into a harvesting solution containing the respective precipitant solutions plus 5 M sodium formate, before being flash-frozen in liquid nitrogen for storage. Data were collected under cryogenic conditions (100 K). Selenomethionine-multi-wavelength anomalous dispersion data set of the menin-MLL1<sub>MBM</sub> complex at the Se peak and inflection wavelengths were collected at the Advanced Photon Source (APS) beamline 21-ID-D and processed using HKL2000 (ref. 23). Seven selenium atoms were located and refined, and the multiwavelength anomalous diffraction data phases were calculated using SHARP<sup>24</sup>. The initial multi-wavelength anomalous dispersion map of the menin-MLL1<sub>MBM</sub> complex was substantially improved by solvent flattening. A model was manually built into the modified experimental electron density using O (ref. 25) and further refined in Phenix<sup>26</sup>. Native data sets of menin and the menin

complexes were collected at the APS beamline 21-ID-D and processed using HKL2000. The structures were determined by molecular replacement using Phaser in the CCP4i suite<sup>27</sup> and further refined in Phenix. The majority (~95%) of the residues in all structures lie in the most favoured region in the Ramachandran plot, and the remaining structures lie in the additionally stereochemically allowed regions in the Ramachandran plot.

**Isothermal titration calorimetry.** The equilibrium dissociation constants of the menin-MLL1<sub>MBM</sub>, menin-JUND<sub>MBM</sub> and menin-MLL1<sub>MBM-LBM</sub>-LEDGF<sub>IBD</sub> interactions were determined using a VP-ITC calorimeter (MicroCal). The binding enthalpies were measured at 20 °C in 25 mM Tris-HCl (pH 8.0) and 150 mM NaCl. Two independent experiments were performed for every interaction described here. Isothermal titration calorimetry data were subsequently analysed and fitted using Origin 7 software (OriginLab) with blank injections of peptides into buffer subtracted from the experimental titrations before data analysis.

**Yeast two-hybrid assay.** The yeast two-hybrid assays were performed using the yeast L40 strain harbouring pBTM116 and pACT2 (Clontech) fusion plasmids. The colonies containing both plasmids were selected on -Leu -Trp plates. The activities of β-galactosidase were measured according to Clontech MATCHMAKER library protocol and the averages from three individual transformants were reported.

**Plasmid construction.** To generate recombinant retroviruses, pMX-2× FLAG-menin was constructed by inserting polymerase chain reaction (PCR)-amplified menin cDNA into the *Bam*HI/*Not*I site of the retroviral vector pMX-2× FLAG. To generate menin mutants, pMX-2× FLAG-menin was used as a template for site-directed mutagenesis using the QuikChange kit from Agilent.

**Cell culture and transfection.** Menin-null MEFs, HEK293T and the human AGS gastric adenocarcinoma cell line were cultured in Dulbecco's modified Eagle's medium complemented with 10% fetal calf serum and 1% PenStrep. Menin-null MEFs were infected with empty vector, wild-type or mutant menin-expressing retroviruses and were subjected to puromycin selection (2 μg ml<sup>-1</sup>) 72 h post-infection for 2 days. AGS and 293T cells were transiently transfected with the indicated expression vectors using Lipofectamine 2000 (Invitrogen) for 48 h.

**Co-immunoprecipitation.** Human 293T cells were transfected with pcDNA3.1 vectors encoding c-MYC-tagged MLL1 (residues 1–153) and FLAG-tagged menin. Two days after transfection the cells were resuspended in 1 ml of lysis buffer (20 mM Tris-HCl, pH 7.5; 150 mM NaCl; 1.0% Triton X-100; 1 mM EDTA; and protease inhibitor cocktail). Immunoprecipitation of lysates was conducted using 20 μl anti-FLAG M2 affinity agarose (Sigma). After washing with lysis buffer, immunoprecipitated proteins were eluted with ×2 loading buffer (50 mM Tris-HCl, pH 6.8; 2% SDS; 10% 2-mercaptoethanol; 10% glycerol; and 0.002% bromophenol blue), subjected to protein gel-electrophoresis using 4–20% SDS-polyacrylamide gel electrophoresis (SDS-PAGE) and then transferred to a polyvinylidene fluoride (PVDF) membrane. After blocking with TBST buffer containing 5% skimmed milk, proteins on the membrane were detected by western blot using anti-FLAG (Sigma) and anti-c-MYC (Santa Cruz Biotechnology) antibodies. The same procedure was also used for the co-immunoprecipitation experiments for menin and JUND.

**Quantitative real-time PCR analysis.** Exponentially growing MEFs were seeded at 2 × 10<sup>5</sup> cells per 100-mm dish and harvested 2 days later. AGS cells were transfected with the menin and JUND expression vectors for 48 h. Total RNA was isolated with an RNeasy minikit from Qiagen. Quantitative real-time PCR (qRT-PCR) was performed in an ABI 7500 Real Time PCR system (Applied Biosystems).

**ChIP assay.** MEFs were cross-linked with 1% formaldehyde for 10 min at 37 °C. Cross-linking was stopped by addition of 125 mM glycine. The ChIP assay was performed using the QuikCHIP kit from Imgenex, according to the manufacturer's instructions. Antibodies used for ChIP were anti-menin (Bethyl labs), anti-MLL1, anti-histone H3K4me3, anti-histone H3 and IgG (Abcam). Antibody-precipitated DNA-protein complex was reverse cross-linked, and the DNA was isolated using phenol-chloroform extraction and the precipitated DNA was used as the template for PCR.

**GST-pull-down assay.** GST, GST-fused c-JUN (residues 1–246), GST-fused JUND (residues 1–150) and FLAG-tagged JNK3 were expressed in *E. coli* BL21(DE3) and were purified to homogeneity. GST-pull-down assays were performed by incubating 10 μg of GST or GST-JUN, 10 μg of FLAG-JNK3 with 10 μl of glutathione sepharose 4B beads and either with or without 20 μg of full-length menin in binding buffer (50 mM Tris-HCl (pH 8.0) and 150 mM NaCl) at 4 °C overnight. The beads were then extensively washed with binding buffer four times and the bound proteins were eluted with 10 mM reduced glutathione in binding buffer. After separation on 15% SDS-PAGE and Ponceau S staining, FLAG-tagged JNK3 protein was detected by western blot using anti-FLAG antibody.

**In vitro kinase assay.** WT c-JUN (residues 1–246) and WT or mutant JUND proteins (residues 1–150) were expressed in *E. coli* BL21(DE3) and purified as

described above for the purification of menin. For the *in vitro* kinase assay, 2 µg substrate was mixed with 0.5 µg kinase and 50 µM ATP, either with or without 10 µg of full-length menin protein in the kinase buffer (50 mM Tris-HCl, pH 7.5; 20 mM MgCl<sub>2</sub>; 20 mM β-glycerophosphate; 2 mM DTT; and 0.1 mM sodium orthovanadate), and incubated at 30 °C for 1 h. The reaction mixtures were then separated on 15% SDS-PAGE, visualized with Ponceau S staining and the phosphorylated JUN proteins were detected with anti-JUND phosphor-Ser100 (anti-c-JUN phosphor-Ser 73) antibody (Cell Signaling).

**In vivo kinase assay.** 293T cells were transfected with expression vectors encoding FLAG-tagged menin and c-MYC tagged JUND. After 48 h of transfection, cells were incubated for 30 min with or without 10 µg ml<sup>-1</sup> anisomycin (Sigma), a potent JNK activator, and then the cell lysates were subjected to western blot with anti-JUND phosphor-Ser100 (anti-c-JUN phosphor-Ser 73, Cell Signaling), anti-FLAG and anti-c-MYC antibodies.

**Luciferase assay.** 293T cells were transfected with 1 µg of AP1 luciferase reporter plasmid (Stratagene), which contains seven copies of AP1-binding consensus 12-O-tetradecanoylphorbol 13-acetate-response element (TRE) upstream of the luciferase reporter gene), 0.25 µg of Renilla reporter plasmid and 0.5 µg of WT or mutant JUND plasmids, either without or with 0.5 µg of menin cDNA. Luciferase assays were performed using the dual luciferase assay kit (Promega) 2 days after transfection. To determine the protein expression in each transfection, 20 µg of cell lysates were immunoblotted with anti-menin (Bethyl Laboratories) and anti-JUND (Santa Cruz Biotechnology) antibodies.

**Cell fractionation.** 10<sup>8</sup> 293T cells were collected and washed in cold PBS and hypotonic buffer (10 mM Tris-HCl, pH 7.3; 10 mM KCl; 1.5 mM MgCl<sub>2</sub>; 0.2 mM PMSF; and 10 mM β-mercaptoethanol). The cells were then allowed to swell for 15 min in hypotonic buffer. The swelled cells were then homogenized with glass Dounce homogenizer (Wheaton) using the loose pestle until cell membrane lysis was 80–90%. The nuclei were collected by centrifuging for 15 min at 3,300g, resuspended in high salt buffer (600 mM KCl; 20 mM Tris pH 7.4; 25% glycerol; 1.5 mM MgCl<sub>2</sub>; and 0.2 mM EDTA) and homogenized to break the nuclear membrane. The nuclear extracts were collected by centrifugation at 25,000g for 30 min and were then fractionated on a Superose 6 gel-filtration column (GE Healthcare). The resulting fractions were resolved by 10% SDS-PAGE and probed with anti-menin, anti-MLL1 and anti-JUND antibodies.

23. Otwinowski, Z. & Minor, W. in *Methods in Enzymology* Vol. 26 (eds Carter, C. W. Jr & Sweet, R. M.) 307–326 (Academic Press, 1997).
24. de La Fortelle, E. & Bricogne, G. Maximum-likelihood heavy-atom parameter refinement for multiple isomorphous replacement and multiwavelength anomalous diffraction methods. *Methods Enzymol.* **276**, 472–494 (1997).
25. Jones, T. A., Zou, J. Y., Cowan, S. W. & Kjeldgaard, M. Improved methods for building protein models in electron density maps and the location of errors in these models. *Acta Crystallogr. A* **47**, 110–119 (1991).
26. Adams, P. D. *et al.* PHENIX: a comprehensive Python-based system for macromolecular structure solution. *Acta Crystallogr. D* **66**, 213–221 (2010).
27. McCoy, A. J. *et al.* Phaser crystallographic software. *J. Appl. Crystallogr.* **40**, 658–674 (2007).

# Structure of the human M2 muscarinic acetylcholine receptor bound to an antagonist

Kazuko Haga<sup>1\*</sup>, Andrew C. Kruse<sup>2\*</sup>, Hidetsugu Asada<sup>3,4\*</sup>, Takami Yurugi-Kobayashi<sup>3,4</sup>, Mitsunori Shiroishi<sup>4,5</sup>, Cheng Zhang<sup>2</sup>, William I. Weis<sup>2,6</sup>, Tetsuji Okada<sup>1</sup>, Brian K. Kobilka<sup>2</sup>, Tatsuya Haga<sup>1</sup> & Takuya Kobayashi<sup>3,4,7</sup>

The parasympathetic branch of the autonomic nervous system regulates the activity of multiple organ systems. Muscarinic receptors are G-protein-coupled receptors that mediate the response to acetylcholine released from parasympathetic nerves<sup>1–5</sup>. Their role in the unconscious regulation of organ and central nervous system function makes them potential therapeutic targets for a broad spectrum of diseases. The M2 muscarinic acetylcholine receptor (M2 receptor) is essential for the physiological control of cardiovascular function through activation of G-protein-coupled inwardly rectifying potassium channels, and is of particular interest because of its extensive pharmacological characterization with both orthosteric and allosteric ligands. Here we report the structure of the antagonist-bound human M2 receptor, the first human acetylcholine receptor to be characterized structurally, to our knowledge. The antagonist 3-quinuclidinyl-benzilate binds in the middle of a long aqueous channel extending approximately two-thirds through the membrane. The orthosteric binding pocket is formed by amino acids that are identical in all five muscarinic receptor subtypes, and shares structural homology with other functionally unrelated acetylcholine binding proteins from different species. A layer of tyrosine residues forms an aromatic cap restricting dissociation of the bound ligand. A binding site for allosteric ligands has been mapped to residues at the entrance to the binding pocket near this aromatic cap. The structure of the M2 receptor provides insights into the challenges of developing subtype-selective ligands for muscarinic receptors and their propensity for allosteric regulation.

Muscarinic receptors constitute a family with five subtypes, M1–M5 (ref. 1). M1, M3 and M5 subtypes couple with the G<sub>q</sub> family of G proteins, and M2 and M4 subtypes with the G<sub>i</sub>/G<sub>o</sub> family of G proteins. Previous work showing that the muscarinic action by a series of choline esters and other substances in various tissues could be differentiated from their nicotinic action<sup>2</sup> led to muscarinic acetylcholine receptors being defined as a functional concept. Muscarinic receptors are now known to be G-protein-coupled receptors (GPCRs)<sup>3</sup> and the nicotinic receptor a ligand-gated ion channel. Muscarinic receptors were initially defined biochemically as proteins that specifically bound 3-quinuclidinyl-benzilate (QNB) and N-methylscopolamine (NMS). They were among the first GPCRs to be purified from cerebral membranes<sup>4</sup>, and to be functionally reconstituted with purified G protein in lipid vesicles<sup>5</sup>. The M1 receptor<sup>5</sup> together with the  $\beta_2$  adrenergic receptor<sup>6</sup> were the first neurotransmitter-activated GPCRs to be cloned, revealing the seven transmembrane (TM) segment topology initially observed for rhodopsin<sup>7</sup>, and subsequently found to be common to all members of the GPCR family.

As a consequence of their roles in both the central and parasympathetic nervous systems, muscarinic receptors are targets for the treatment of a spectrum of disorders including Alzheimer's disease,

schizophrenia and Parkinson's disease, and chronic obstructive pulmonary disease<sup>8</sup>. However, developing highly subtype-selective orthosteric drugs for muscarinic receptors has been challenging and thus far largely unsuccessful. Recent drug discovery efforts have therefore shifted to the development of small molecule allosteric modulators. Muscarinic receptors have long been a model system for studying allosteric regulation of GPCR signalling because of their exceptional propensity to bind allosteric ligands<sup>9</sup>. To understand better the structural basis for challenges in developing orthosteric drugs and the susceptibility for allosteric regulation, we obtained a crystal structure of the M2 receptor.

In our initial efforts to obtain the structure of the M2 receptor we expressed and purified M2 receptor lacking most of the third intracellular loop (IL3) and the native glycosylation sites. The central part of IL3 of the M2 receptor can be removed without impairing its ability to bind to agonists or activate G proteins<sup>10</sup>, and IL3 was shown to have a flexible structure<sup>11</sup>. Using this modified M2 receptor bound to the high-affinity inverse agonist *R*-(–)-3-QNB, we performed crystallization by hanging-drop vapour diffusion and obtained crystals that diffracted to around 9 Å, but were not able to improve the quality of these crystals. We subsequently replaced IL3 of the M2 receptor with T4 lysozyme (T4L) as initially described for the  $\beta_2$  adrenergic receptor<sup>12</sup> (Supplementary Fig. 1a). This method has been used to obtain crystal structures of four other GPCRs: the adenosine A<sub>2A</sub> receptor<sup>13</sup>, the CXCR4 receptor<sup>14</sup>, the dopamine receptor D3 (ref. 15) and most recently the histamine H<sub>1</sub> receptor<sup>16</sup>. The binding properties of M2-T4L with muscarinic ligands were essentially the same as for the wild-type M2 receptor (Supplementary Fig. 1b, c), indicating that the overall TM architecture of M2-T4L was minimally affected by introduction of T4L. The M2-T4L receptor was subsequently crystallized in lipidic cubic phase. A 3.0 Å structure was solved by molecular replacement from a data set obtained by merging diffraction data from 23 crystals.

As is typical for proteins crystallized by the lipidic cubic phase method, the lattice for the M2 receptor shows alternating aqueous and lipidic layers with M2 receptor molecules embedded in the latter while T4L is confined to aqueous regions (Supplementary Fig. 2). Within the membrane plane, receptor molecules are packed closely against one another, alternating orientations within the bilayer. There are abundant hydrophobic contacts between receptor molecules within the membrane, whereas polar interactions primarily involve contacts between T4L molecules as well as receptor–T4L interactions.

The overall structure of the M2 receptor (Fig. 1a) is similar to that of rhodopsin and other recently crystallized inactive GPCR structures (compared in Supplementary Fig. 3). The cytoplasmic surface of the M2 receptor is in an inactive conformation, but as with most other GPCR structures, there is no interaction involving Arg 121<sup>3.50</sup> (superscripts indicate Ballesteros–Weinstein numbers) in the conserved

<sup>1</sup>Department of Life Science, Faculty of Science, Gakushuin University, Meiji 1-5-1, Tokyo 171-8588, Japan. <sup>2</sup>Department of Molecular and Cellular Physiology, Stanford University School of Medicine, 279 Campus Drive, Stanford, California 94305, USA. <sup>3</sup>Department of Medical Chemistry and Cell Biology, Kyoto University Faculty of Medicine, Konoe-cho, Yoshida, Sakyo-Ku, Kyoto 606-8501, Japan. <sup>4</sup>Human Receptor Crystallography Project, ERATO, Japan Science and Technology Agency, Konoe-cho, Yoshida, Sakyo-Ku, Kyoto 606-8501, Japan. <sup>5</sup>Graduate School of Pharmaceutical Sciences, Kyushu University, 3-1-1 Maidashi, Higashi-ku, Fukuoka 812-8582, Japan. <sup>6</sup>Department of Structural Biology, Stanford University School of Medicine, 299 Campus Drive, Stanford, California 94305, USA. <sup>7</sup>Japan Science and Technology Agency, Core Research for Evolutional Science and Technology (CREST), Kyoto University Faculty of Medicine, Kyoto 606-8501, Japan.

\*These authors contributed equally to this work.



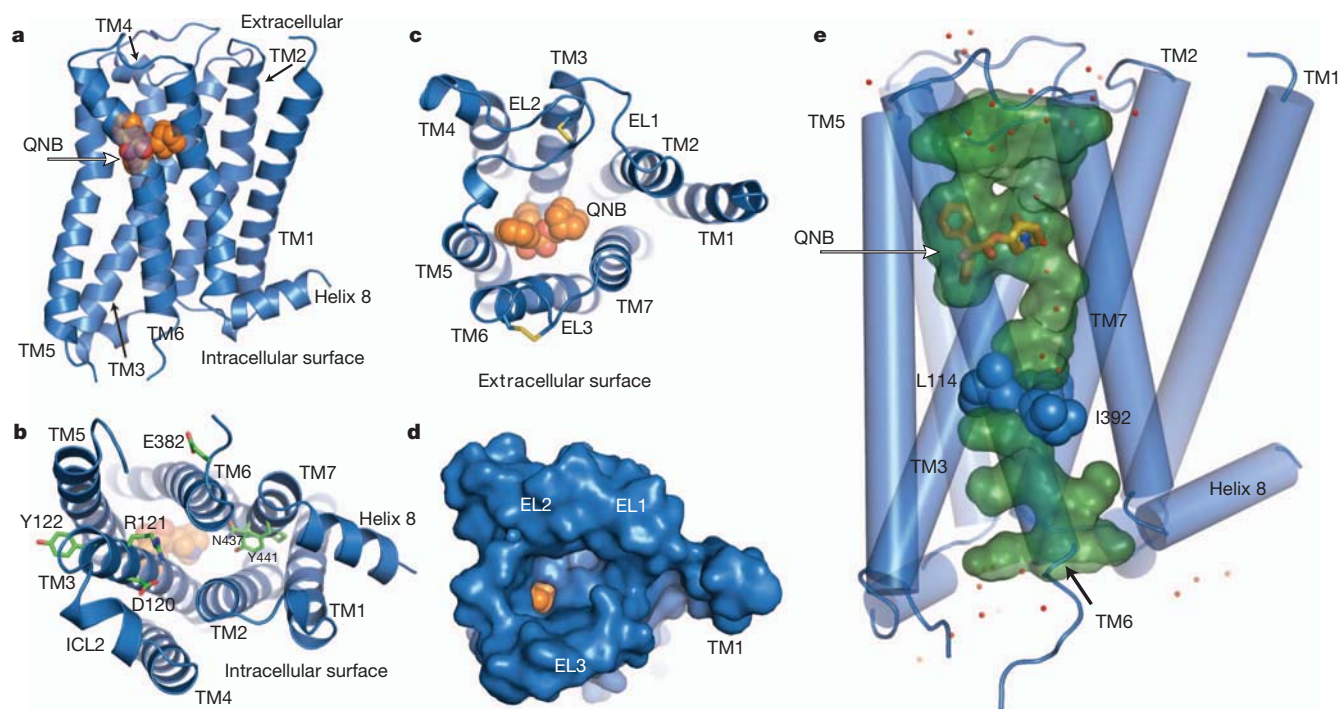


**Figure 1 | The M2 receptor with bound QNB.** **a–e**, The M2 receptor is shown as a blue ribbon and QNB as orange spheres. **a**, M2 receptor in profile. **b**, Cytoplasmic surface showing conserved DRY residues in TM3. **c**, Extracellular view into QNB binding pocket. **d**, Extracellular view with solvent-accessible-surface rendering shows a funnel-shaped vestibule and a

nearly buried QNB binding pocket. **e**, Aqueous channel (green) extending from the extracellular surface into the transmembrane core is interrupted by a layer of three hydrophobic residues (blue spheres). Well-ordered water molecules are shown as red dots.

E/DRY sequence in TM3 and Glu 382<sup>6,30</sup> in TM6 (Fig. 1b). Instead, the Arg 121<sup>3,50</sup> side chain forms a salt bridge only with Asp 120<sup>3,49</sup>. In rhodopsin, the homologous residues form part of a charge–charge interaction that stabilizes the cytoplasmic ends of TM3 and TM6 in an inactive state<sup>17</sup>. The second intracellular loop shows a helical conformation similar to that first seen for the turkey  $\beta_1$  adrenergic receptor<sup>18</sup>.

GPCR crystal structures show the greatest differences in the extracellular surface (Supplementary Fig. 3). The M2 receptor has a relatively simple and open extracellular surface (Fig. 1c, d) with the longer extracellular loop (ECL2) stabilized by a conserved disulphide with Cys 96<sup>3,25</sup> at the N terminus of TM3 and Cys 176 in the middle of ECL2. In addition, the second disulphide bond was detected between C413 and C416 in the ECL3. The extracellular surface of the M2 receptor most resembles that of the dopamine D3 receptor (Supplementary Fig. 3).

Crystal structures of GPCRs reveal a network of hydrogen bonding interactions that extend from the binding pocket to the cytoplasmic surface. However, a distinctive feature of the M2 receptor is that this network is part of a long, continuous aqueous channel extending from the extracellular surface to a depth of approximately 33 Å when measured from ECL2 (Fig. 1e). This channel contains the ligand binding pocket, but extends beyond the ligand and is separated from the cytoplasmic surface by a hydrophobic layer formed by three amino acids: Leu 65<sup>2,46</sup> in TM2, Leu 114<sup>4,43</sup> in TM4 and Ile 392<sup>6,40</sup> in TM6. Each of these is absolutely conserved among all five muscarinic subtypes. The dimensions of the channel below the QNB binding site are large enough to accommodate a long, extended orthosteric ligand. Supplementary Fig. 4 compares the aqueous channels of other GPCRs.

The ligand QNB binds within a deeply buried pocket defined by the side chains of TM3, 4, 5, 6 and 7 (Fig. 2a–c and Supplementary Fig. 5 and Supplementary Table 3). An aromatic cage encloses the amine and forms a lid over the ligand, separating the orthosteric site from the extracellular vestibule. Asp 103<sup>3,32</sup> and Asn 404<sup>6,52</sup> serve to orient the ligand in the largely hydrophobic binding cavity, with Asn 404<sup>6,52</sup> forming paired hydrogen bonds with the hydroxyl and carbonyl groups

in QNB while Asp 103<sup>3,32</sup> engages in a charge–charge interaction with the amine moiety of the ligand (Fig. 2). The TM amino acids that form the QNB binding pocket are identical in all five muscarinic receptor subtypes (Supplementary Table 1), consistent with results of QNB binding experiments on M1–M4 receptors, and with site-directed mutagenesis experiments on M1 (ref. 19), M2 (ref. 20) and M3 (ref. 21) receptors. Only Phe 181, which extends downward from ECL2 and interacts with one of the two phenyl rings on QNB (Fig. 2), differs from all other muscarinic receptor subtypes, which have leucine in the homologous position. The importance of Asp<sup>3,32</sup> for both agonist and antagonist binding has been demonstrated in mutagenesis and covalent-labelling experiments and modelling studies<sup>19–22</sup>. In contrast, mutation of Asn 404<sup>6,52</sup> to Ala on M1 (ref. 23) and M3 (ref. 24) receptors was shown to greatly affect binding of QNB but have little effect on binding of or activation by acetylcholine. It is possible that Asn 404<sup>6,52</sup> is hydrogen bonded with the ester group of QNB but not that of acetylcholine.

The M2 and other muscarinic receptors represent one of four families of acetylcholine binding proteins to be structurally characterized thus far. Figure 3a shows the orthosteric binding site of the M2 receptor with acetylcholine docked with the *gauche* form of the O–C2–C1–N dihedral angle, which places the choline group in the aromatic cage interacting with Asp 103<sup>3,32</sup>, while the carbonyl oxygen is tentatively bound to Asn 404<sup>6,52</sup> (Fig. 3a). The natural agonist acetylcholine is much smaller than the bulky antagonist QNB. As described in the agonist-bound structure of the  $\beta_2$  adrenergic receptor, the contraction of the ligand binding pocket is expected as a result of an inward shift of TM5 (ref. 25). This result is consistent with the previous mutation studies showing that Thr 187<sup>5,39</sup> and Thr 190<sup>5,42</sup> in TM5 (Fig. 2) alter binding of most agonists but not of antagonists<sup>20</sup>. Bulky compounds capable of blocking activation-related contraction of the pocket would be very efficient in locking the M2 receptor in an inactive conformation, as is exemplified here by the antagonist QNB. It has been proposed that the conformational change of the M2 receptor upon activation might be

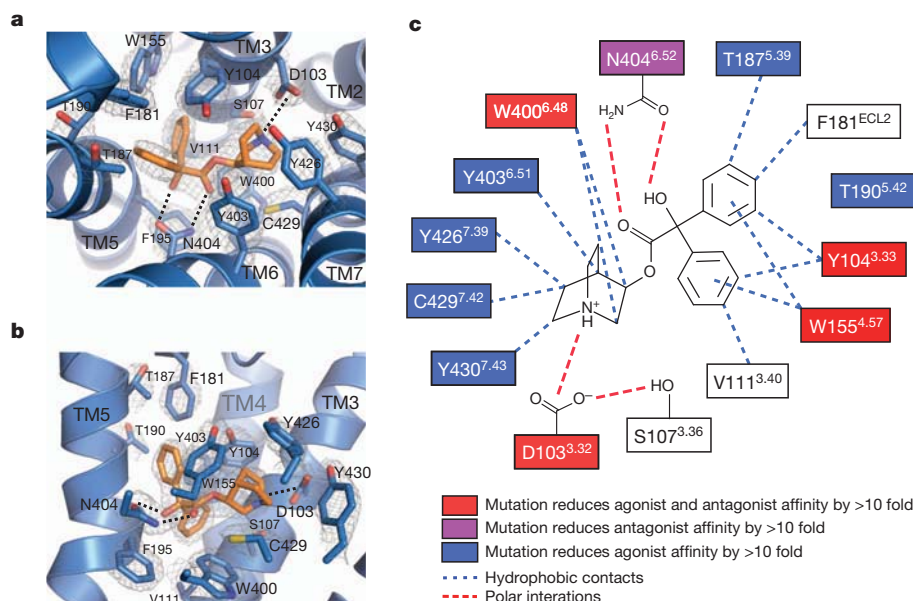


**Figure 2 | Binding interactions between the M2 receptor and QNB.**

**a, b,** Two views of the QNB binding pocket. Amino acids within 4 Å of the ligand are shown as light blue sticks, with QNB in orange. Nitrogen and oxygen atoms are coloured dark blue and red, respectively. Polar interactions are indicated by dashed lines. A  $2F_o - F_c$  map is shown in wire at  $1.5\sigma$  contour. **c,** A schematic representation of QNB binding interactions is shown. Mutations of

amino acids in the red boxes have been shown to reduce both antagonist and agonist binding by more than tenfold. Mutations of the amino acid in the purple boxes reduce antagonist binding affinity by more than tenfold. Mutations of amino acids in the blue boxes reduce agonist binding by more than tenfold. Blue dotted lines indicate potential hydrophobic interactions and red lines indicate potential polar interactions.

accompanied by a conformational change of acetylcholine from the *gauche* to the *trans* form of the O–C2–C1–N dihedral angle<sup>26</sup>. It remains to be determined in which pose acetylcholine binds to the M2 receptor or to the M2-receptor–G-protein complex, and whether acetylcholine hydrogen bonds with Asn 404<sup>6,52</sup> or other residues.

In a striking example of convergent evolution, the orthosteric site of the M2 receptor exhibits many features noted previously as common

structural elements in unrelated acetylcholine binding proteins<sup>27</sup>. Like the M2 receptor, a nicotinic acetylcholine receptor homologue bound to acetylcholine (Fig. 3b) shows an aromatic cage comprised of three tyrosines and a tryptophan, although it notably lacks a counterion to the choline group<sup>28</sup>, whereas in the M2 receptor this role is filled by Asp 103<sup>3,32</sup>. A bacterial acetylcholine binding protein, ChoX, from *Sinorhizobium meliloti* (Fig. 3c) also possesses an aromatic cage, and

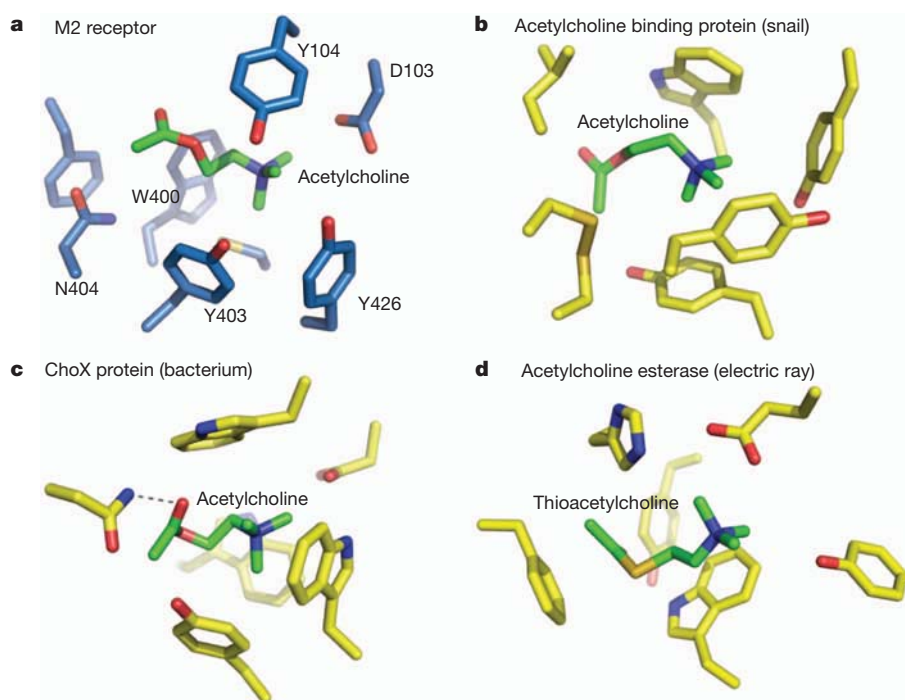


**Figure 3 | Convergent evolution of acetylcholine binding sites.**

**a,** Acetylcholine is modelled into the crystal structure of the M2 receptor. **b,** Acetylcholine binding pocket in the crystal structure of the acetylcholine binding protein from the snail *Aplysia californica* (PDB accession 2XZ5).

**c,** Acetylcholine binding pocket in the acetylcholine binding protein ChoX from the Gram negative bacterium *Sinorhizobium meliloti* (PDB accession 2RIN). **d,** Binding site for thio-acetylcholine in the enzyme acetylcholine esterase from the electric ray *Torpedo californica* (PDB accession 2C4H).



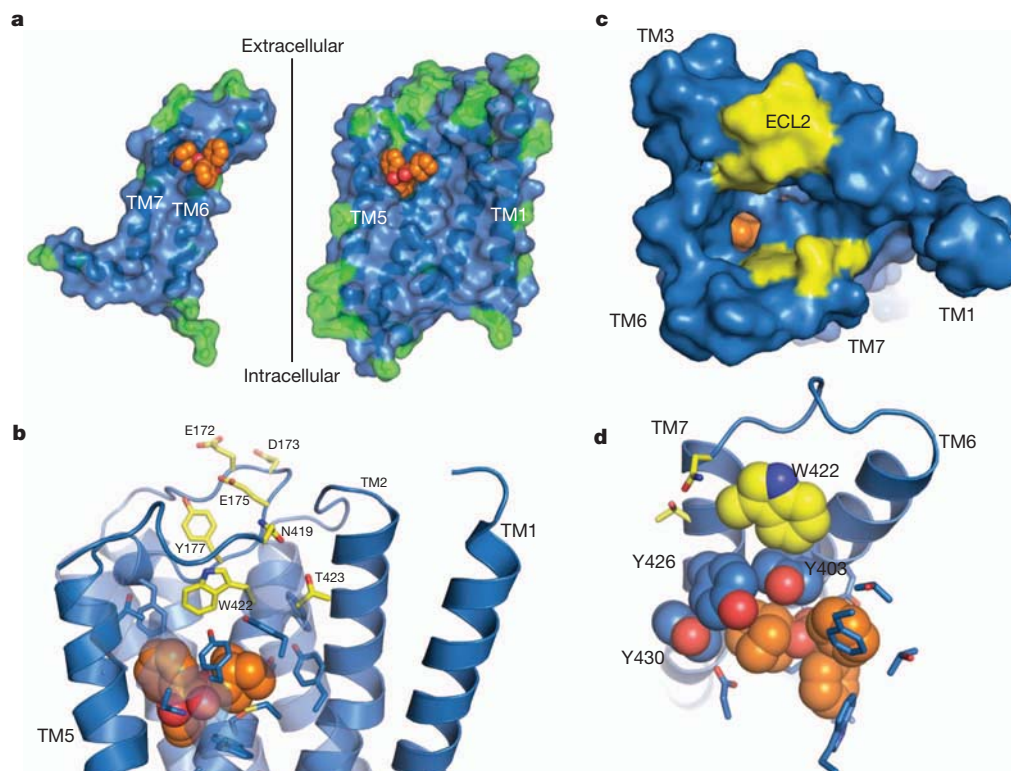


**Figure 4 | Allosteric binding in the M2 receptor.** **a**, Differences between the M2 and M4 receptors are shown as green residues mapped onto the inner surface of the M2 receptor (blue), with QNB in orange spheres. The sequence conservation within the orthosteric site is apparent, while residues outside show more variability. **b–d**, Mutations that alter allosteric binding are shown with yellow carbons, and amino acids involved in QNB binding are shown with blue

carbons as sticks or spheres. **b**, **c**, Different views of possible allosteric binding sites in the M2 receptor. The surface view in **c** shows the positions of possible allosteric binding sites (yellow) lining the path to the QNB binding pocket. **d**, Trp 422 (yellow spheres), implicated in binding of allosteric ligands, forms an edge-to-face aromatic interaction with Tyr 403, part of the aromatic cage (blue spheres) of the orthosteric site.

like the M2 receptor has an aspartate in close proximity to the amine engaging in a charge–charge interaction<sup>29</sup>. Also like the M2 receptor, ChoX has an asparagine hydrogen bonding to the ligand carbonyl. Like these proteins, the enzyme acetylcholine esterase (Fig. 3d) uses an aromatic cage and a carboxylate to bind the choline group, while the (thio)acetyl group interacts with a phenylalanine, probably through  $\pi$ – $\pi$  interactions<sup>30</sup>. Taken together, these structures suggest that an aromatic cage and buried carboxylate are likely to be critical elements for acetylcholine recognition and binding in general.

There is a growing interest in the development of allosteric ligands for GPCR targets. This is motivated by the ability to develop more subtype-selective drugs targeted at less conserved regions of the receptor. Moreover, allosteric ligands modulate the effects of natural hormones and neurotransmitters, and may therefore regulate receptor activity in a more physiological manner. As noted above, the orthosteric binding pocket is highly conserved among all muscarinic receptor subtypes. Allosteric regulation of GPCRs was first observed for the M2 receptor and this receptor has been one of the most extensively characterized allosteric model systems<sup>9</sup>. Figure 4a shows the inner surface of the M2 receptor, highlighting residues that are not conserved with its closest relative, the M4 receptor. It can be seen that the orthosteric binding pocket and transmembrane core are highly conserved. The greatest diversity is observed in the extracellular loops and the extracellular end of TM segments that form the entrance to the orthosteric binding pocket. These amino acids represent structural diversity that could be exploited for the development of more subtype-selective ligands<sup>9</sup>. Of interest, site-directed mutagenesis and chimaeric receptor studies have implicated several of these amino acids in the binding of several well-characterized allosteric modulators<sup>9</sup>. As shown in Fig. 4b–d, these residues are located in ECL2 and the amino-terminus of TM7 at the entrance to the binding pocket. Trp 422<sup>7,35</sup>, a residue implicated in the

binding of several allosteric modulators, appears to form an edge-to-face  $\pi$ – $\pi$  interaction with Tyr 403<sup>6,51</sup>, part of the aromatic cage surrounding the charged amine of the orthosteric ligand (Fig. 4d). Binding of allosteric ligands to this site would be expected to influence the association and disassociation rates of orthosteric ligands.

The structure of the M2 receptor provides insights into both orthosteric and allosteric regulation of muscarinic receptors. The development of more selective drugs for muscarinic receptors will probably require exploitation of the more diverse allosteric surface, either as exclusively allosteric ligands or as ligands that occupy both orthosteric and allosteric sites.

## METHODS SUMMARY

Untagged human M2 muscarinic acetylcholine receptor was expressed in Sf9 cells with the IL3 replaced with T4 lysozyme, then extracted with digitonin and sodium cholate and purified by ligand affinity chromatography, then exchanged into decyl maltoside buffer. Purified receptor was crystallized by the lipidic cubic phase technique following addition of a stabilizing neopentyl glycol detergent. Data collection was performed at Advanced Photon Source beamlines 23ID-B and 23ID-D, and the structure solved by molecular replacement. Refinement statistics are given in Supplementary Table 2.

**Full Methods** and any associated references are available in the online version of the paper at [www.nature.com/nature](http://www.nature.com/nature).

Received 10 August; accepted 1 December 2011.

Published online 25 January 2012.

1. Hulme, E. C., Birdsall, N. J. & Buckley, N. J. Muscarinic receptor subtypes. *Annu. Rev. Pharmacol. Toxicol.* **30**, 633–673 (1990).
2. Dale, H. H. The action of certain esters and ethers of choline, and their relation to muscarine. *J. Pharmacol. Exp. Ther.* **6**, 147–190 (1914).
3. Haga, K. *et al.* Functional reconstitution of purified muscarinic receptors and inhibitory guanine nucleotide regulatory protein. *Nature* **316**, 731–733 (1985).



4. Haga, K. & Haga, T. Purification of the muscarinic acetylcholine receptor from porcine brain. *J. Biol. Chem.* **260**, 7927–7935 (1985).
5. Kubo, T. *et al.* Cloning, sequencing and expression of complementary DNA encoding the muscarinic acetylcholine receptor. *Nature* **323**, 411–416 (1986).
6. Dixon, R. A. *et al.* Cloning of the gene and cDNA for mammalian  $\beta$ -adrenergic receptor and homology with rhodopsin. *Nature* **321**, 75–79 (1986).
7. Ovchinnikov, Y. A. Rhodopsin and bacteriorhodopsin: structure–function relationships. *FEBS Lett.* **148**, 179–191 (1982).
8. Wess, J., Eglen, R. M. & Gautam, D. Muscarinic acetylcholine receptors: mutant mice provide new insights for drug development. *Nature Rev. Drug Discov.* **6**, 721–733 (2007).
9. Gregory, K. J., Sexton, P. M. & Christopoulos, A. Allosteric modulation of muscarinic acetylcholine receptors. *Curr. Neuropharmacol.* **5**, 157–167 (2007).
10. Kameyama, K., Haga, K., Haga, T., Moro, O. & Sadée, W. Activation of a GTP-binding protein and a GTP-binding-protein-coupled receptor kinase ( $\beta$ -adrenergic-receptor kinase-1) by a muscarinic receptor M2 mutant lacking phosphorylation sites. *Eur. J. Biochem. FEBS* **226**, 267–276 (1994).
11. Ichiyama, S. *et al.* The structure of the third intracellular loop of the muscarinic acetylcholine receptor M<sub>2</sub> subtype. *FEBS Lett.* **580**, 23–26 (2006).
12. Rosenbaum, D. M. *et al.* GPCR engineering yields high-resolution structural insights into  $\beta_2$ -adrenergic receptor function. *Science* **318**, 1266–1273 (2007).
13. Jaakola, V. P. *et al.* The 2.6 Ångstrom crystal structure of a human A<sub>2A</sub> adenosine receptor bound to an antagonist. *Science* **322**, 1211–1217 (2008).
14. Wu, B. *et al.* Structures of the CXCR4 chemokine GPCR with small-molecule and cyclic peptide antagonists. *Science* **330**, 1066–1071 (2010).
15. Chien, E. Y. *et al.* Structure of the human dopamine D3 receptor in complex with a D2/D3 selective antagonist. *Science* **330**, 1091–1095 (2010).
16. Shimamura, T. *et al.* Structure of the human histamine H<sub>1</sub> receptor complex with doxepin. *Nature* **475**, 65–70 (2011).
17. Palczewski, K. *et al.* Crystal structure of rhodopsin: A G protein-coupled receptor. *Science* **289**, 739–745 (2000).
18. Warne, T. *et al.* Structure of a  $\beta_1$ -adrenergic G-protein-coupled receptor. *Nature* **454**, 486–491 (2008).
19. Hulme, E. C., Lu, Z. L. & Bee, M. S. Scanning mutagenesis studies of the M<sub>1</sub> muscarinic acetylcholine receptor. *Receptors Channels* **9**, 215–228 (2003).
20. Heitz, F. *et al.* Site-directed mutagenesis of the putative human muscarinic M<sub>2</sub> receptor binding site. *Eur. J. Pharmacol.* **380**, 183–195 (1999).
21. Wess, J. Mutational analysis of muscarinic acetylcholine receptors: structural basis of ligand/receptor/G protein interactions. *Life Sci.* **53**, 1447–1463 (1993).
22. Goodwin, J. A., Hulme, E. C., Langmead, C. J. & Tehan, B. G. Roof and floor of the muscarinic binding pocket: variations in the binding modes of orthosteric ligands. *Mol. Pharmacol.* **72**, 1484–1496 (2007).
23. Ward, S. D., Curtis, C. A. & Hulme, E. C. Alanine-scanning mutagenesis of transmembrane domain 6 of the M<sub>1</sub> muscarinic acetylcholine receptor suggests that Tyr381 plays key roles in receptor function. *Mol. Pharmacol.* **56**, 1031–1041 (1999).
24. Bluml, K., Mutschler, E. & Wess, J. Functional role in ligand binding and receptor activation of an asparagine residue present in the sixth transmembrane domain of all muscarinic acetylcholine receptors. *J. Biol. Chem.* **269**, 18870–18876 (1994).
25. Rasmussen, S. G. *et al.* Structure of a nanobody-stabilized active state of the  $\beta_2$  adrenoceptor. *Nature* **469**, 175–180 (2011).
26. Furukawa, H. *et al.* Conformation of ligands bound to the muscarinic acetylcholine receptor. *Mol. Pharmacol.* **62**, 778–787 (2002).
27. Zacharias, N. & Dougherty, D. A. Cation- $\pi$  interactions in ligand recognition and catalysis. *Trends Pharmacol. Sci.* **23**, 281–287 (2002).
28. Brams, M. *et al.* Crystal structures of a cysteine-modified mutant in loop D of acetylcholine-binding protein. *J. Biol. Chem.* **286**, 4420–4428 (2011).
29. Oswald, C. *et al.* Crystal structures of the choline/acetylcholine substrate-binding protein ChoX from *Sinorhizobium meliloti* in the liganded and unliganded-closed states. *J. Biol. Chem.* **283**, 32848–32859 (2008).
30. Colletier, J. P. *et al.* Structural insights into substrate traffic and inhibition in acetylcholinesterase. *EMBO J.* **25**, 2746–2756 (2006).

**Supplementary Information** is linked to the online version of the paper at [www.nature.com/nature](http://www.nature.com/nature).

**Acknowledgements** We thank S. Iwata at Kyoto University for supporting the production of M2 receptor, and we acknowledge support from the Japan Society for the Promotion of Science (Research for Future Program) (T.H.), from the Japan Science and Technology Corporation (CREST) (T.H.), from the Ministry of Education, Culture, Sports, Science and Technology of Japan (Grants-in-Aid for Scientific Research on Priority Area 15083201 (T.H.), from the Japan Science and Technology Corporation (ERATO) (T.K.), from Toray Science Foundation (T.K.), from Takeda Science Foundation (T.K.), from Ichiro Kanehara Foundation (T.K.), from The Sumitomo Foundation (T.K.), from the National Institutes of Health Grants NS028471 and GM083118 (B.K.K.), from the Mathers Foundation (B.K.K. and W.I.W.), and from the National Science Foundation (A.C.K.). We thank T. S. Kobilka for organizing the GPCR Workshop 2010 that brought together the research groups, and for facilitating this collaboration.

**Author Contributions** K.H. purified M2 and M2-T4L receptors, characterized their ligand binding activity, and performed attempts to crystallize them with hanging drop and other methods for more than ten years. A.C.K. crystallized the M2-T4L receptors in lipidic cubic phase, collected and processed diffraction data, solved and refined the structure, and assisted with manuscript preparation. H.A. set up the expression system and expressed M2-T4L in large amounts using the insect cell/baculovirus expression system. T.Y.-K. expressed M2 and M2-T4L receptors using a yeast expression system, and purified and crystallized M2 and M2-T4L receptors for five years. M.S. constructed several mutants of M2-T4L and evaluated their stabilities. C.Z. assisted with data collection and processing. W.I.W. oversaw data processing and refinement. T.O. gave advice to K.H. and T.H. on crystallization of the M2 receptor and interpretation of its structure. B.K.K. oversaw lipidic cubic phase crystallization, assisted with data collection, and wrote the manuscript together with T.H. and T.K. T.H., together with K.H., has engaged in biochemical studies of muscarinic receptors for more than thirty years, prepared M2 and M2-T4L receptors, and wrote part of the manuscript. T.K. has been collaborating with T.H. for five years, designed the receptor production strategy with T.H., and wrote part of the manuscript.

**Author Information** Coordinates and structure factors for M2-T4L are deposited in the Protein Data Bank under accession code 3UON. Reprints and permissions information is available at [www.nature.com/reprints](http://www.nature.com/reprints). The authors declare no competing financial interests. Readers are welcome to comment on the online version of this article at [www.nature.com/nature](http://www.nature.com/nature). Correspondence and requests for materials should be addressed to B.K.K. (kobilka@stanford.edu), T.H. (tatsuya.haga@gakushuin.ac.jp) or T.K. (t-coba@mfour.med.kyoto-u.ac.jp).

## METHODS

**Construction of M2-T4L expression vectors for Sf9 cells.** The coding sequence of the human M2-T4L receptor fusion protein was designed to have N-linked glycosylation sites (Asn 2, Asn 3, Asn 6 and Asn 9) mutated to aspartic acid and cysteine-less T4L (C54T, C97A) residues 2–161 inserted into the IL3, replacing M2 residues 218–376. This construct was synthesized (TAKARA Bio), and cloned into the pFastbac1 Sf9 expression vector (Invitrogen) as illustrated in Supplementary Fig. 1a. A TAA stop codon was placed after the R466 codon, terminating translation. The synthesized M2-T4L receptor described above was confirmed by sequencing.

**Expression and membrane preparation.** Recombinant baculovirus was made from pFastbac1-M2-T4L using the Bac-to-Bac system (Invitrogen)<sup>31</sup>. The M2-T4L protein was expressed in baculovirus-infected Sf9 insect cells as described previously<sup>32</sup>. Sf9 insect cells were prepared at a density of  $1.0 \times 10^6$  cells  $\text{ml}^{-1}$  and suspended in 5 litres of the IPL-41/SF900 II complex media or ESF921 insect media. Media containing Sf9 insect cells were transferred into the CELLBAG 22 L/O (GE Healthcare) and cultured for 4 days with the following culture conditions: 20 r.p.m.,  $8.5^\circ$  rocking angle, 30%  $\text{O}_2$ ,  $0.25 \text{ l min}^{-1}$  of air flow rate and  $27^\circ\text{C}$ . After 4 days, 200 to 300 ml of the M2-T4L baculovirus stock (approximate multiplicity of infection (m.o.i.), 2) and 700 to 800 ml of IPL-41/SF900 II complex media were transferred into the CELLBAG (final culture volume, 6 litres) and infected for 2 days under the following infection conditions: 22 r.p.m.,  $8.5^\circ$  rocking angle, 50%  $\text{O}_2$ , air flow rate,  $0.25 \text{ l min}^{-1}$  and  $27^\circ\text{C}$ . Two days later, a fraction of the cells was harvested for the binding assay and the remaining cells were centrifuged at 6,000g for 10 min and harvested. The cell pellet was washed with 250 ml of PBS without calcium chloride and magnesium chloride (PBS(–)) and resuspended with 100 ml of PBS(–) containing a protease inhibitor cocktail tablet (Roche). Final concentration of protease inhibitors was  $2.5 \mu\text{g ml}^{-1}$  pepstatin,  $2 \mu\text{g ml}^{-1}$  PMSF,  $20 \mu\text{g ml}^{-1}$  leupeptin and 0.5 mM benzamidine. Cells were quick frozen in liquid nitrogen and stored at  $-80^\circ\text{C}$ .

The membrane was prepared from the M2-T4L-expressing Sf9 insect cells as described previously<sup>31</sup>. For the preparation of membranes from insect cells, Sf9 insect cells were centrifuged at 1,500g for 10 min at  $4^\circ\text{C}$ . The pellet was washed with PBS(–), then resuspended in 100 ml of hypotonic buffer containing 10 mM HEPES at pH 7.5, 20 mM KCl, 10 mM  $\text{MgCl}_2$  and protease inhibitor cocktail, followed by Dounce homogenization to resuspend the membranes. Insect cell membranes were centrifuged at 100,000g for 30 min and the pellets were resuspended in 10 mM HEPES at pH 7.5, 10 mM  $\text{MgCl}_2$ , 20 mM KCl, 40% glycerol, and snap-frozen in liquid nitrogen and then stored at  $-80^\circ\text{C}$  until use. Membrane proteins were quantified using the bicinchoninic acid (BCA) method (Pierce) using a BSA standard.

**Purification of M2-T4L-QNB.** M2-T4L was expressed in Sf9 cells, solubilized with digitonin/Na-cholate solution, and purified by using an affinity column with aminobenzotropine (ABT) as a ligand<sup>33</sup>, as described below. The whole procedure was carried out at  $4^\circ\text{C}$ . Sf9 membrane preparations with 2.1 kg of wet weight and approximately  $1.5 \mu\text{mol}$  of [ $^3\text{H}$ ]QNB binding sites were solubilized with 1% digitonin, 0.35% Na-cholate, 10 mM K-phosphate buffer (pH 7.0) (KPB), 50 mM NaCl, 1 mM EDTA, a cocktail of protease inhibitors (41). The supernatant was applied to two ABT columns run in parallel (500 ml each), followed by washing with 0.1% digitonin, 0.1% Na-cholate, 20 mM KPB, 150 mM NaCl ( $2 \times 2$ ) at a rate of approximately  $90 \text{ ml h}^{-1}$ . M2-T4L was eluted from the ABT columns with 0.5 mM atropine, 0.1% digitonin, 0.1% Na-cholate, 20 mM KPB, 150 mM NaCl in 2 l elution volume for each column, and was bound to a column of hydroxyapatite (30 ml), which was washed at a rate of  $30\text{--}50 \text{ ml h}^{-1}$  with a series of solutions as follows: (1) 0.1% digitonin, 0.1% Na-cholate, 20 mM KPB (100 ml); (2)  $5 \mu\text{M}$  QNB, 0.1% digitonin, 0.1% Na-cholate, 20 mM KPB (600 ml); (3) 0.35% Na-cholate, 20 mM KPB (600 ml); (4) 0.2% decylmaltoside, 20 mM KPB (500 ml); (5) 0.2% decylmaltoside, 150 mM KPB (100 ml); (6) 0.2% decylmaltoside, 500 mM KPB (60 ml). M2-T4L-QNB was finally eluted with 0.2% decylmaltoside, 1 M KPB (50 ml). The eluate was concentrated to approximately 1 ml (approximately 30 mg protein per ml) with Amicon Ultra (MILLIPORE), followed by dialysis against 0.2% decylmaltoside, 20 mM Tris-HCl buffer (pH 7.5) and storage in  $-80^\circ\text{C}$ . The yield was estimated to be approximately 50% on the assumption that the recovered protein is pure M2-T4L. Protein concentration was determined using BCA Protein Assay (PIERCE). Because we purified M2-T4L as a complex with QNB we could not estimate the [ $^3\text{H}$ ]QNB binding activity because the dissociation rate of QNB is too slow. However, in preliminary experiments using [ $^3\text{H}$ ]QNB or dissociable atropine as eluants, we confirmed that the receptor is purified to near homogeneity. The purity of M2-T4L was confirmed by SDS-PAGE and gel permeation chromatography (Supplementary Fig. 6). All the QNB used in purification and crystallization was the high-affinity enantiomer, R(–)-3-QNB.

**Measurement of ligand binding activity.** Ligand binding activity of wild-type M2 and M2-T4L receptors was determined as described previously<sup>34</sup>. Briefly, the receptors solubilized from Sf9 membranes were incubated with 0.1–4 nM [ $^3\text{H}$ ]QNB with or without  $1 \mu\text{M}$  atropine, or with 2 nM [ $^3\text{H}$ ]QNB with various concentrations of carbamylcholine or atropine in 0.1% digitonin, 20 mM KPB for 60 min at  $30^\circ\text{C}$  (total volume 0.2 ml). The amount of [ $^3\text{H}$ ]QNB bound to receptors was assayed by using a small column of Sephadex G50 fine (2 ml). The density of [ $^3\text{H}$ ]QNB binding sites in the particulate fraction of M2-T4L was 17 pmol per mg of protein on average and ranged from 5.3–35 pmol per mg of total protein.

**Crystallization.** QNB-bound M2-T4L was concentrated to  $20 \text{ mg ml}^{-1}$  in decyl maltoside buffer in a volume of approximately 100  $\mu\text{l}$ . A 10% stock solution of lauryl maltose neopentyl glycol detergent (MNG, Anatrace) with 100 mM NaCl and 20 mM HEPES pH 7.5 was then added to the protein to a final concentration of 1% (w/v) of MNG detergent. The sample was incubated for 1 h on ice, then diluted to 1 ml in 0.1% MNG buffer and reconstituted to  $50 \text{ mg ml}^{-1}$  before reconstitution. The final volume of protein sample at this concentration was typically 20–30  $\mu\text{l}$ . Protein was reconstituted in cubic phase by mixing with a 1.5-fold weight excess of a 10:1 monoolein:cholesterol mix by the twin-syringe method<sup>35</sup>. Briefly, the protein and lipid were mixed by passage through coupled syringes 100 times either by hand or using a Gryphon LCP robot (Art Robbins Instruments). The reconstituted protein was dispensed using a modified ratchet device (Hamilton) or using the Gryphon LCP robot in 40 nl drops to either 24-well or 96-well glass sandwich plates and overlaid with 0.8  $\mu\text{l}$  precipitant solution. A single crystallization lead was initially identified using an in-house screen and then optimized. Crystals for data collection were grown in 25–35% PEG 300, 100 mM ammonium phosphate, 2% 2-methyl-2,4-pentanediol, 100 mM HEPES pH 7.0–7.8. Crystals reached full size and were harvested after 3–4 days at  $20^\circ\text{C}$ . Typical crystals are shown in Supplementary Fig. 7.

**Data collection and processing.** Diffraction data were measured at the Advanced Photon Source beamlines 23 ID-B and 23 ID-D. Several hundred crystals were screened, and a final data set was compiled using diffraction wedges of typically 5 degrees from the 23 most strongly diffracting crystals. Data reduction was performed using HKL2000<sup>36</sup>. Diffraction quality was very heterogeneous, with some crystals diffracting to 2.3 Å whereas others failed to diffract past 3.5 Å. Among the best crystals, most diffracted to 3.0–2.5 Å. Severe radiation damage and anisotropic diffraction resulted in low completeness in higher resolution shells. We report this structure to an overall resolution of 3.0 Å. Despite the low completeness in high resolution bins, inclusion of these reflections significantly improved map quality. Highest shell  $\langle I \rangle / \langle \sigma I \rangle$  is relatively low, in large part due to anisotropy of the diffraction. The final resolution cut-off was chosen on the basis of completeness and  $\langle I \rangle / \langle \sigma I \rangle$  in the spherical highest shell, but analysis of average  $F/\sigma F$  values along reciprocal space axes suggests resolution limits (based on average  $F/\sigma F > 3$ ) of 3.5, 2.9 and 2.7 Å along  $a^*$ ,  $b^*$  and  $c^*$ , respectively. The real space  $c$ -axis is normal to the plane of the lipid membrane in the crystal.

**Structure solution and refinement.** The structure was solved by molecular replacement using Phaser<sup>37,38</sup> with the structure of the inactive  $\beta_2$  adrenergic receptor and T4L used as search models (PDB accession 2RH1). The initial molecular replacement model was further fitted by rigid body refinement followed by simulated annealing and restrained refinement in Phenix<sup>39</sup>. Iterative manual rebuilding and refinement steps were performed with Coot and phenix.refine, respectively. Figures were prepared with PyMOL, and Ramachandran statistics were calculated with MolProbity.

- Asada, H. *et al.* Evaluation of the *Pichia pastoris* expression system for the production of GPCRs for structural analysis. *Microb. Cell Fact.* **10**, 24 (2011).
- Weber, W., Weber, E., Geisse, S. & Memmert, K. Optimisation of protein expression and establishment of the Wave Bioreactor for Baculovirus/insect cell culture. *Cytotechnology* **38**, 77–85 (2002).
- Haga, K. & Haga, T. Affinity chromatography of the muscarinic acetylcholine receptor. *J. Biol. Chem.* **258**, 13575–13579 (1983).
- Haga, T., Haga, K. & Hulme, E. C. in *Receptor Biochemistry: A Practical Approach* (ed. Hulme, E. C.) 51–78 (Oxford Univ. Press, 1990).
- Caffrey, M. & Cherezov, V. Crystallizing membrane proteins using lipidic mesophases. *Nature Protocols* **4**, 706–731 (2009).
- Otwinowski, Z. & Minor, W. Processing of x-ray diffraction data collected in oscillation mode. *Methods Enzymol.* **276**, 307–326 (1997).
- McCoy, A. J. Solving structures of protein complexes by molecular replacement with Phaser. *Acta Crystallogr. D* **63**, 32–41 (2007).
- McCoy, A. J. *et al.* Phaser crystallographic software. *J. Appl. Cryst.* **40**, 658–674 (2007).
- Afonine, P. V., Grosse-Kunstleve, R. W. & Adams, P. D. A robust bulk-solvent correction and anisotropic scaling procedure. *Acta Crystallogr. D* **61**, 850–855 (2005).

# Structure and dynamics of the M3 muscarinic acetylcholine receptor

Andrew C. Kruse<sup>1</sup>, Jianxin Hu<sup>2</sup>, Albert C. Pan<sup>3</sup>, Daniel H. Arlow<sup>3</sup>, Daniel M. Rosenbaum<sup>4</sup>, Erica Rosemond<sup>2</sup>, Hillary F. Green<sup>3</sup>, Tong Liu<sup>2</sup>, Pil Seok Chae<sup>5</sup>, Ron O. Dror<sup>3</sup>, David E. Shaw<sup>3</sup>, William I. Weis<sup>1,6</sup>, Jürgen Wess<sup>2</sup> & Brian K. Kobilka<sup>1</sup>

Acetylcholine, the first neurotransmitter to be identified<sup>1</sup>, exerts many of its physiological actions via activation of a family of G-protein-coupled receptors (GPCRs) known as muscarinic acetylcholine receptors (mAChRs). Although the five mAChR subtypes (M1–M5) share a high degree of sequence homology, they show pronounced differences in G-protein coupling preference and the physiological responses they mediate<sup>2–4</sup>. Unfortunately, despite decades of effort, no therapeutic agents endowed with clear mAChR subtype selectivity have been developed to exploit these differences<sup>5,6</sup>. We describe here the structure of the  $G_{q/11}$ -coupled M3 mAChR ('M3 receptor', from rat) bound to the bronchodilator drug tiotropium and identify the binding mode for this clinically important drug. This structure, together with that of the  $G_{i/o}$ -coupled M2 receptor<sup>7</sup>, offers possibilities for the design of mAChR subtype-selective ligands. Importantly, the M3 receptor structure allows a structural comparison between two members of a mammalian GPCR subfamily displaying different G-protein coupling selectivities. Furthermore, molecular dynamics simulations suggest that tiotropium binds transiently to an allosteric site *en route* to the binding pocket of both receptors. These simulations offer a structural view of an allosteric binding mode for an orthosteric GPCR ligand and provide additional opportunities for the design of ligands with different affinities or binding kinetics for different mAChR subtypes. Our findings not only offer insights into the structure and function of one of the most important GPCR families, but may also facilitate the design of improved therapeutics targeting these critical receptors.

The mAChR family consists of five subtypes, M1–M5, which can be subdivided into two major classes (Fig. 1a). The M1, M3 and M5 receptors show selectivity for G proteins of the  $G_{q/11}$  family (that is,  $G_q$  and  $G_{11}$ ), whereas the M2 and M4 receptors preferentially couple to  $G_{i/o}$ -type G proteins ( $G_i$  and  $G_o$ )<sup>2–4</sup>. The development of small molecule ligands that can selectively act on specific mAChR subtypes has proven extremely challenging, primarily owing to the high degree of sequence similarity in the transmembrane (TM) core of these receptors<sup>2–4</sup>. More recently, considerable progress has been made in targeting drugs to non-classical (allosteric) binding sites of certain mAChR subtypes<sup>5</sup>.

Within the mAChR family, the M3 subtype mediates many important physiological functions, including smooth muscle contraction and glandular secretion<sup>3,4,6,8–10</sup>. Central M3 receptors have also been implicated in the regulation of food intake<sup>8</sup>, learning and memory<sup>9</sup>, and the proper development of the anterior pituitary gland<sup>10</sup>. Selective drugs targeted at this receptor subtype may prove clinically useful<sup>4,6,8–10</sup>, and non-selective muscarinic ligands are already widely used in current practice.

Owing to the profound physiological importance of the M3 receptor and its long-standing role as a model system for understanding GPCR function<sup>3,11</sup>, we used the T4 lysozyme (T4L) fusion protein strategy<sup>12</sup> to

obtain crystals of *Rattus norvegicus* M3 receptor–T4L fusion protein (Supplementary Fig. 1) by lipidic cubic phase crystallization. Diffraction data from more than 70 crystals were merged to create a data set to 3.4 Å resolution and to solve the structure by molecular replacement. The M3 receptor structure, together with that of the M2 receptor<sup>7</sup>, affords an opportunity to compare two closely related mammalian receptors with divergent G-protein coupling selectivities.

The overall structure of the M3 receptor is similar to that of M2 (Fig. 1b–d). Surprisingly, structural conservation includes intracellular loops (ICLs) 1 and 2, and extracellular loops (ECLs) 1–3, which share highly similar overall folds despite low sequence conservation (Fig. 1f). Like the M2 receptor, the M3 receptor exhibits unique mAChR features, including a large extracellular vestibule as part of an extended hydrophilic channel containing the orthosteric binding site (Fig. 1e). Also like M2, the M3 receptor features a pronounced outward bend at the extracellular end of TM4 (Fig. 1d; Supplementary Fig. 2b). This bend, not seen in any other GPCR family crystallized so far, is stabilized by a hydrogen bond from the Q207 (Q163 in M2) side chain to the L204 backbone peptide carbonyl (Supplementary Fig. 2b). This bond is part of a polar interaction network involving four residues absolutely conserved within the mAChR family, suggesting that this unusual feature is important to mAChRs in general. Indeed, mutagenesis of Q207 in M3 impaired both ligand binding and receptor activation<sup>13</sup>.

The M3 receptor was crystallized in complex with tiotropium (Spiriva), a potent muscarinic inverse agonist<sup>14,15</sup> used clinically for the treatment of chronic obstructive pulmonary disease (COPD). The M2 receptor was crystallized in complex with *R*-(–)-3-quinuclidinyl benzilate (QNB) which, like tiotropium, is a non-subtype-selective mAChR blocker<sup>14,16</sup>. The two ligands bind in remarkably similar poses (Fig. 2b), and it is likely that this pose represents a conserved binding mode for structurally similar anticholinergics. In the M3 receptor, as in M2, the ligand is deeply buried within the TM receptor core (Fig. 2a, d) and is covered by a lid comprising three conserved tyrosines—Y148<sup>3,33</sup>, Y506<sup>6,51</sup> and Y529<sup>7,39</sup> (Fig. 2a; superscripts indicate Ballesteros-Weinstein numbers<sup>17</sup>). The ligand is almost completely occluded from solvent and engages in extensive hydrophobic contacts with the receptor. A pair of hydrogen bonds are formed from N507<sup>6,52</sup> to the ligand carbonyl and hydroxyl, while D147<sup>3,32</sup> interacts with the ligand amine.

Reflecting the difficulty in developing subtype-selective orthosteric ligands, the residues forming the orthosteric binding pocket are absolutely conserved among the five mAChR subtypes (Fig. 1f). However, this conservation at the amino acid level does not preclude the existence of differences in the three-dimensional architecture of the orthosteric site between the different mAChR subtypes. In fact, comparison of the structures of the M3 and M2 receptor ligand binding sites reveals structural divergences that might be exploited in the development of subtype-selective ligands.

<sup>1</sup>Department of Molecular and Cellular Physiology, Stanford University School of Medicine, 279 Campus Drive, Stanford, California 94305, USA. <sup>2</sup>Molecular Signaling Section, Laboratory of Bioorganic Chemistry, National Institute of Diabetes and Digestive and Kidney Diseases, Bethesda, Maryland 20892, USA. <sup>3</sup>D. E. Shaw Research, New York, New York 10036, USA. <sup>4</sup>Department of Biochemistry, University of Texas Southwestern Medical Center, Dallas, Texas 75390, USA. <sup>5</sup>Department of Bionano Engineering, Hanyang University, Ansan 426-791, Korea. <sup>6</sup>Department of Structural Biology, Stanford University School of Medicine, 299 Campus Drive, Stanford, California 94305, USA.



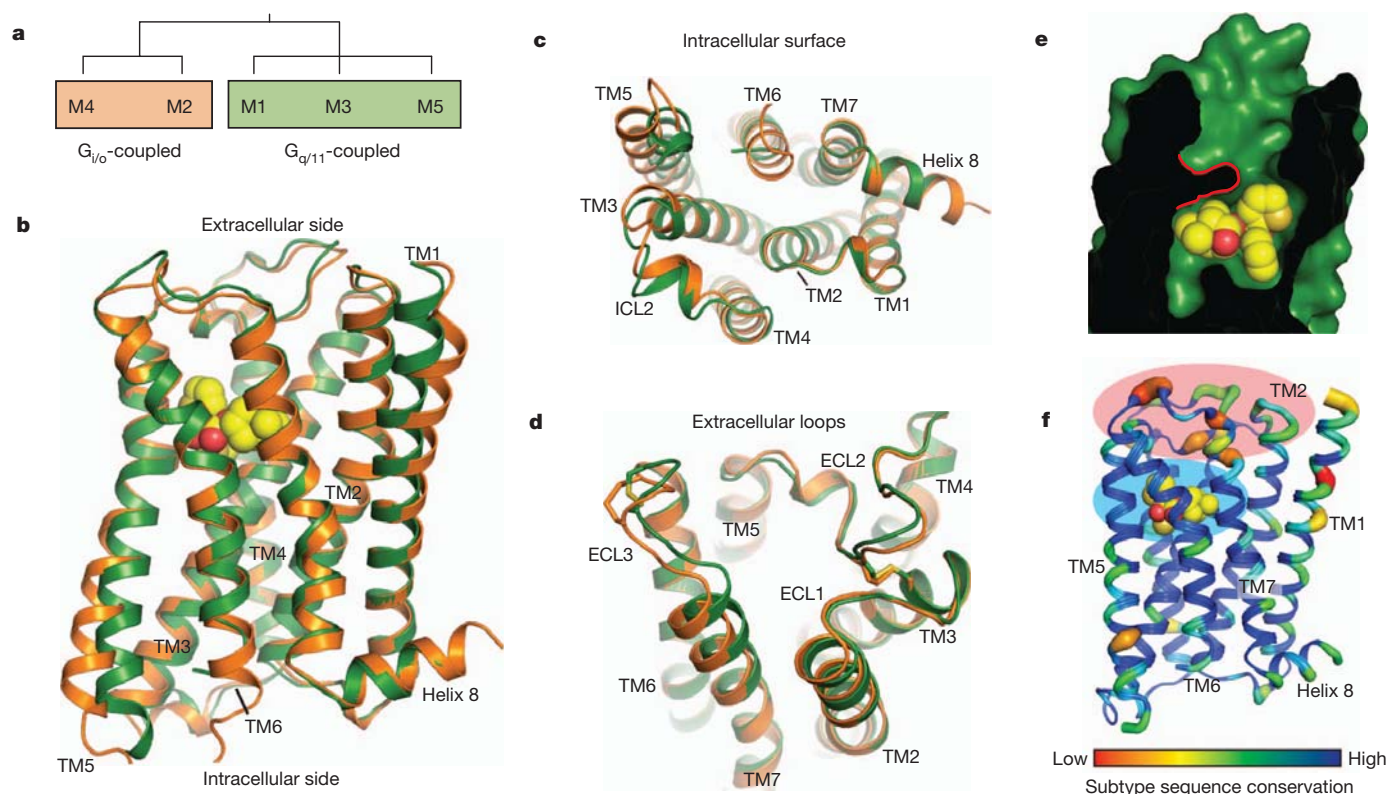


**Figure 1 | Major structural features of the M3 receptor.** **a**, Analysis of muscarinic receptor sequences divides them into two classes. **b**, The overall structure of the M3 receptor (green) is similar to that of the M2 receptor (orange). The M3-bound ligand, tiotropium, is shown as spheres coloured according to element, with carbon in yellow and oxygen in red. **c**, Comparison of the intracellular surfaces shows divergence in the cytoplasmic end of TM5. **d**, Comparison of the extracellular surfaces shows less deviation, with near perfect conservation of backbone fold of extracellular loops (ECLs). **e**, A solvent

accessible surface for the M3 receptor bound to tiotropium (spheres) shows the receptor covering the ligand with a tyrosine lid (outlined in red). The surface of the receptor is shown in green and its interior in black. **f**, M3 receptor structure coloured by sequence conservation among the five mAChR subtypes. Poorly conserved regions are shown with larger backbone diameter. The orthosteric and allosteric sites are indicated in blue and red elliptical shaded areas, respectively, and the ligand tiotropium is shown as spheres.

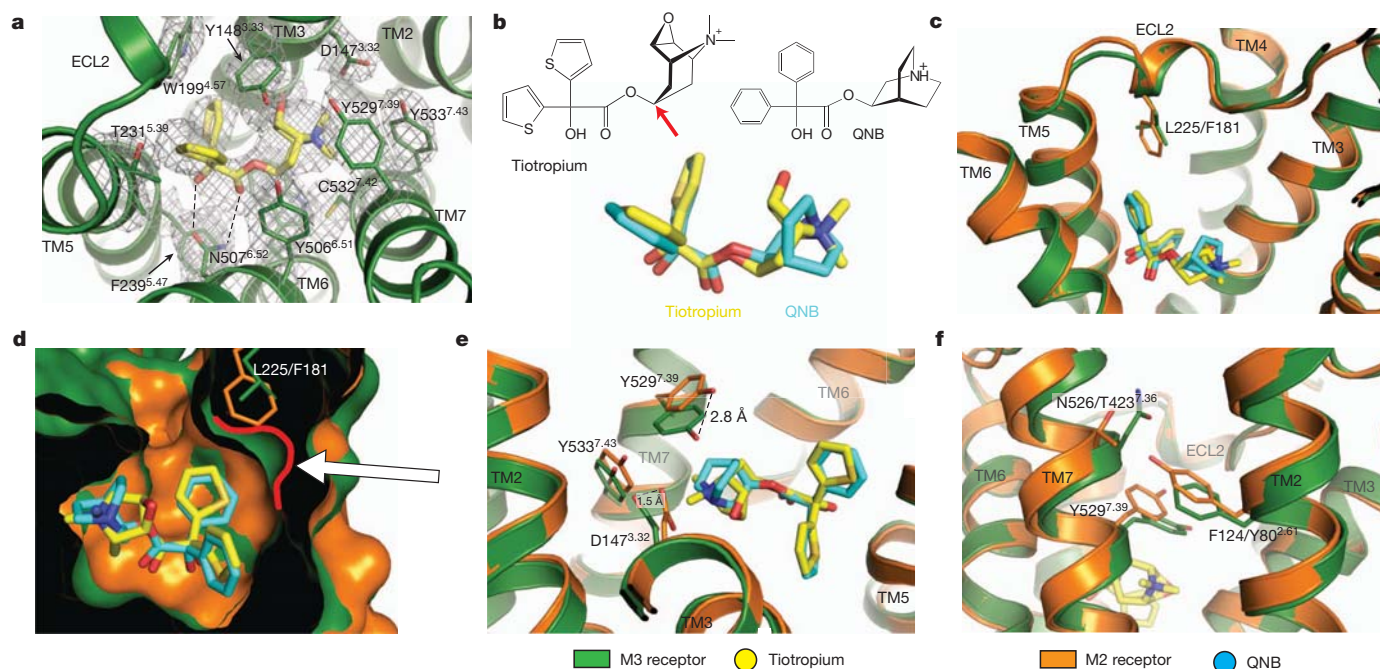


**Figure 2 | Orthosteric binding sites of the M2 and M3 receptors.** In all panels, the M3 receptor is shown green with its ligand tiotropium in yellow, while the M2 receptor and its ligand QNB are shown in orange and cyan, respectively. **a**, Tiotropium binding site in the M3 receptor. A  $2F_o - F_c$  map contoured at  $2\sigma$  is shown as mesh. **b**, Chemical structures of ligands. A red arrow indicates the tropane C3 atom used as a tracking landmark in Fig. 3. Superimposing the receptor structures reveals that the two ligands adopt highly

similar poses (bottom). **c**, There is a Phe (M2)/Leu (M3) sequence difference between the M2 and M3 receptors near the binding site. **d**, This produces an enlarged binding pocket in the M3 receptor, outlined in red and indicated with an arrow. **e**, Displacements of M3 Y529<sup>7,39</sup> and D147<sup>3,32</sup> are seen (black dashed lines). **f**, The displacement of Y529<sup>7,39</sup> may arise from a sequence difference at position 2.61 (Tyr 80 in M2 and Phe 124 in M3).

One such difference derives from the replacement of Phe181 in ECL2 of M2 with Leu225 in M3 (this residue is leucine in all mAChRs except M2). This creates a pocket in M3 not found in M2 (Fig. 2c, d). A second difference is a 2.8 Å shift of Tyr529<sup>7,39</sup> relative to the position of the corresponding M2 residue (Tyr426; Fig. 2e). This feature may derive from a difference in the identity of the residue in position 2.61 (Phe124 in M3 and Tyr80 in M2; Fig. 2f). This residue interacts directly with TM7, influencing the position of this helix and the residues within it, including Tyr529<sup>7,39</sup>. Notably, the residue at position 2.61 is not a part of the orthosteric binding pocket, but is positioned near a probable allosteric binding site<sup>7</sup>. Because tiotropium and QNB are structurally similar but not identical, the observed binding site differences must be interpreted with some degree of caution. However, site-directed mutagenesis studies with M1 and M3 receptors support the concept that the residue at position 2.61 plays a role in receptor activation<sup>18,19</sup> and ligand binding selectivity<sup>20</sup>. This site does not appear to play a role in determining antagonist dissociation rates, because mutation of M3 F<sup>2.61</sup> to tyrosine or of M2 Y<sup>2.61</sup> to phenylalanine had no effect on dissociation rates for [<sup>3</sup>H]N-methyl scopolamine ([<sup>3</sup>H]NMS) or [<sup>3</sup>H]QNB.

We used molecular dynamics simulations to characterize the pathway by which tiotropium binds to and dissociates from the M2 and M3 receptors. Similar techniques have previously been shown to correctly

predict crystallographic ligand binding poses and kinetics in studies of  $\beta$ -adrenergic receptors<sup>21</sup>. In both the M2 and M3 receptors, our simulations indicate that as tiotropium binds to or dissociates from the receptor, it pauses at an alternative binding site in the extracellular vestibule (Fig. 3, Supplementary Fig. 3). Intriguingly, this site corresponds to an allosteric site that has been previously identified by mutagenesis<sup>7</sup>, a finding consistent with pharmacological studies showing that orthosteric ligands can act as allosteric modulators at the M2 receptor<sup>22</sup>. Tiotropium adopts different preferred allosteric binding poses in M2 and M3 (Fig. 3d, Supplementary Fig. 4). These metastable binding poses, which appear independently in both binding and dissociation simulations, may represent the first structural view of a clinically used 'orthosteric' GPCR ligand binding to an experimentally validated allosteric site. Conceivably, therapeutic molecules could be rationally engineered to act independently as both allosteric and orthosteric ligands (in contrast to previously described bitopic ligands that bind at both orthosteric and allosteric sites simultaneously<sup>23</sup>).

Tiotropium dissociates from M3 receptors more slowly than from M2 receptors, a phenomenon thought to provide clinically important 'kinetic selectivity' of this drug for M3 receptors despite similar equilibrium binding affinities for both subtypes<sup>14</sup>. In simulations with tiotropium bound, the portion of ECL2 nearest the binding pocket proved more mobile in M2 than in M3 (Supplementary Fig. 5), probably

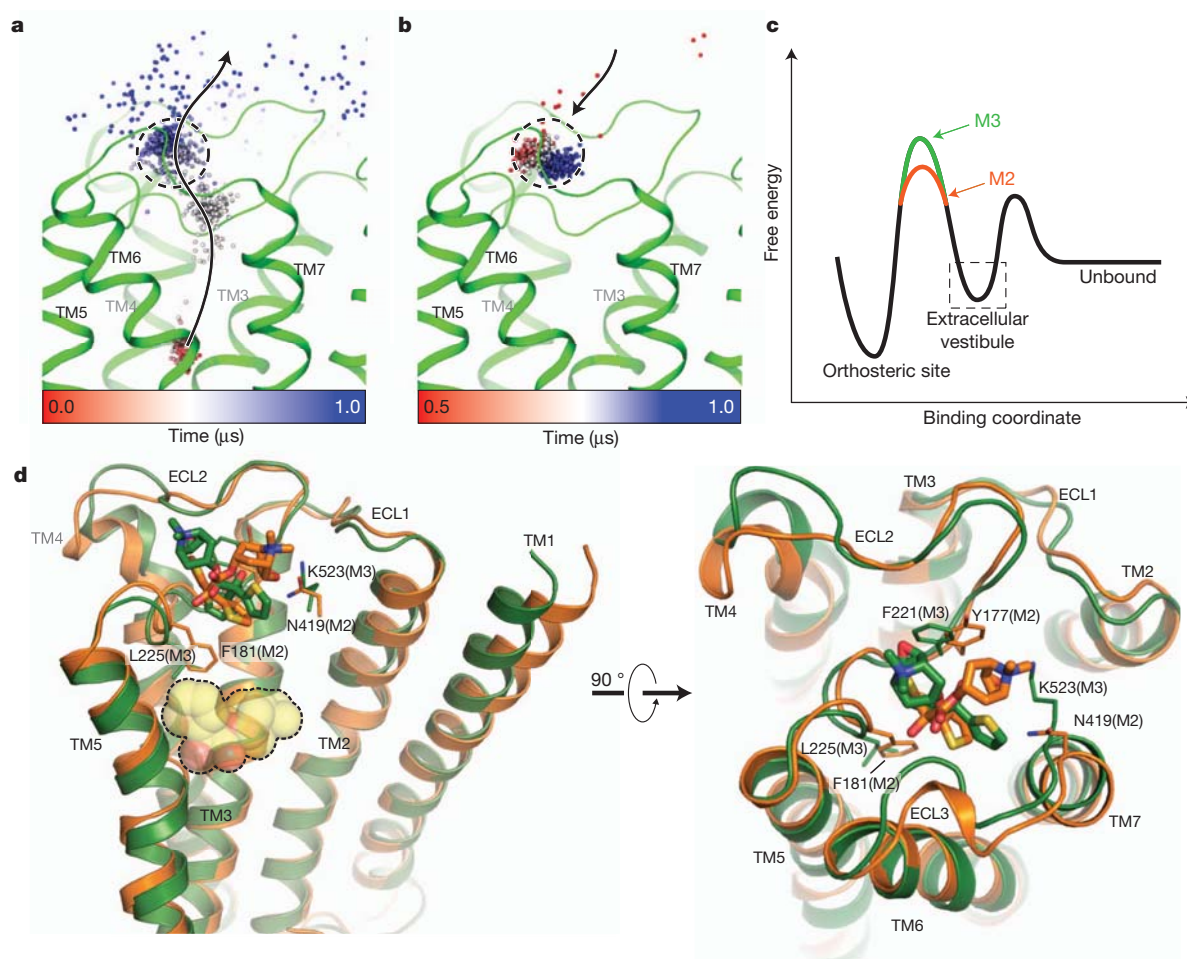


**Figure 3 | Molecular dynamics of ligand binding.** Simulations suggest that the tiotropium binding/dissociation pathway for both receptors involves a metastable state in the extracellular vestibule. **a**, When tiotropium is pushed out of the binding pocket of M3, it pauses in the extracellular vestibule in the region outlined with a dashed circle. Spheres represent positions of the ligand's C3 tropane atom at successive points in time. The direction of motion is indicated by an arrow. **b**, When tiotropium is placed in solvent, it binds to the same site in the extracellular vestibule. Our simulations are insufficiently long for it to

proceed into the orthosteric binding pocket; the agonist acetylcholine (ACh), a much smaller molecule, bound spontaneously to the orthosteric site in similar simulations (Supplementary Methods). **c**, Schematic free-energy landscape for binding/dissociation. Differences between M2 and M3 are shown in orange and green, respectively, with the rest of the curve in black. **d**, Common binding poses for tiotropium in the extracellular vestibule of M2 (orange) and of M3 (green). Non-conserved residues that contact the ligand are shown as thin sticks. The location of the orthosteric site is indicated by tiotropium (as spheres).



owing to multiple sequence differences between the two receptor subtypes. This increased mobility disrupts a hydrophobic cluster involving a thiophene ring of tiotropium, the ECL2 residue Phe 181(M2)/Leu 225(M3), and Tyr<sup>3.33</sup>, facilitating movement of Phe 181/Leu 225 away from the orthosteric site and rotation of Tyr<sup>3.33</sup> towards TM4. In simulations of ligand dissociation, such motions clear a path for tiotropium's egress from the orthosteric site to the extracellular vestibule. The increased mobility of ECL2 in M2 thus appears to facilitate tiotropium's traversal of the largest energetic barrier on the binding/dissociation pathway (Fig. 3c). Experimental measurements with wild-type and mutant receptors (M3 L225F and M2 F181L) suggest that the Leu 225/Phe 181 sequence difference alone is insufficient to explain the difference in off-rates (for practical reasons these measurements were performed with QNB rather than tiotropium; see Methods).

One of the most interesting features of the M2 and M3 receptors is the fact that the two highly similar receptors display pronounced differences in G-protein coupling specificity. For this reason, the M2/M3 receptor pair has long served as an excellent model system to identify features contributing to the selectivity of coupling between GPCRs and G proteins<sup>3</sup>. As no simple sequence elements have been identified as general determinants of coupling specificity across GPCR families<sup>24</sup>, it is likely that recognition depends on features such as overall conformation in addition to specific inter-residue contacts.

The M2 and M3 receptor structures show a significant difference in the position of the cytoplasmic end of TM5 and of ICL2 (Fig. 4a, b). The highly conserved tyrosine residue at position 5.58 (M3 Tyr250<sup>5.58</sup>, M2 Tyr206<sup>5.58</sup>) shows a clear deviation between the two receptors, pointing towards the core of the protein in M2, and away from the receptor towards the surrounding lipid bilayer in M3. Interestingly, mutagenesis studies have identified a tetrad of residues ('AALS' in M3, 'VTIL' in M2) located on the cytoplasmic end of TM6 that are critical in determining G-protein coupling selectivity<sup>25,26</sup>. In both structures, these residues interact directly with TM5 (Fig. 4a), and in the  $\beta_2$  adrenergic receptor–G<sub>s</sub> complex<sup>27</sup> two of the four corresponding residues make contact with the carboxy-terminal helix of G $\alpha_s$ . M3 Tyr 254<sup>5.62</sup> at the bottom of TM5 also plays a role in activation of G $q/11$  (ref. 28). In the M2 receptor structure, the corresponding residue (Ser 210<sup>5.62</sup>) is displaced by approximately 4 Å relative to Tyr 254<sup>5.62</sup> in M3 (Fig. 4a).

When we compared the position of TM5 in the M2 and M3 receptors to that in other GPCR structures, we found that it is M2-like in all G<sub>i/o</sub>-coupled receptors, whereas the two mammalian G $q/11$ -coupled receptors solved to date exhibit another conformation (Fig. 4c, d). An important caveat here is that these structures have been solved using the T4L fusion strategy, and we cannot completely exclude the possibility that this approach perturbs the conformation of TM5 and TM6. However, in

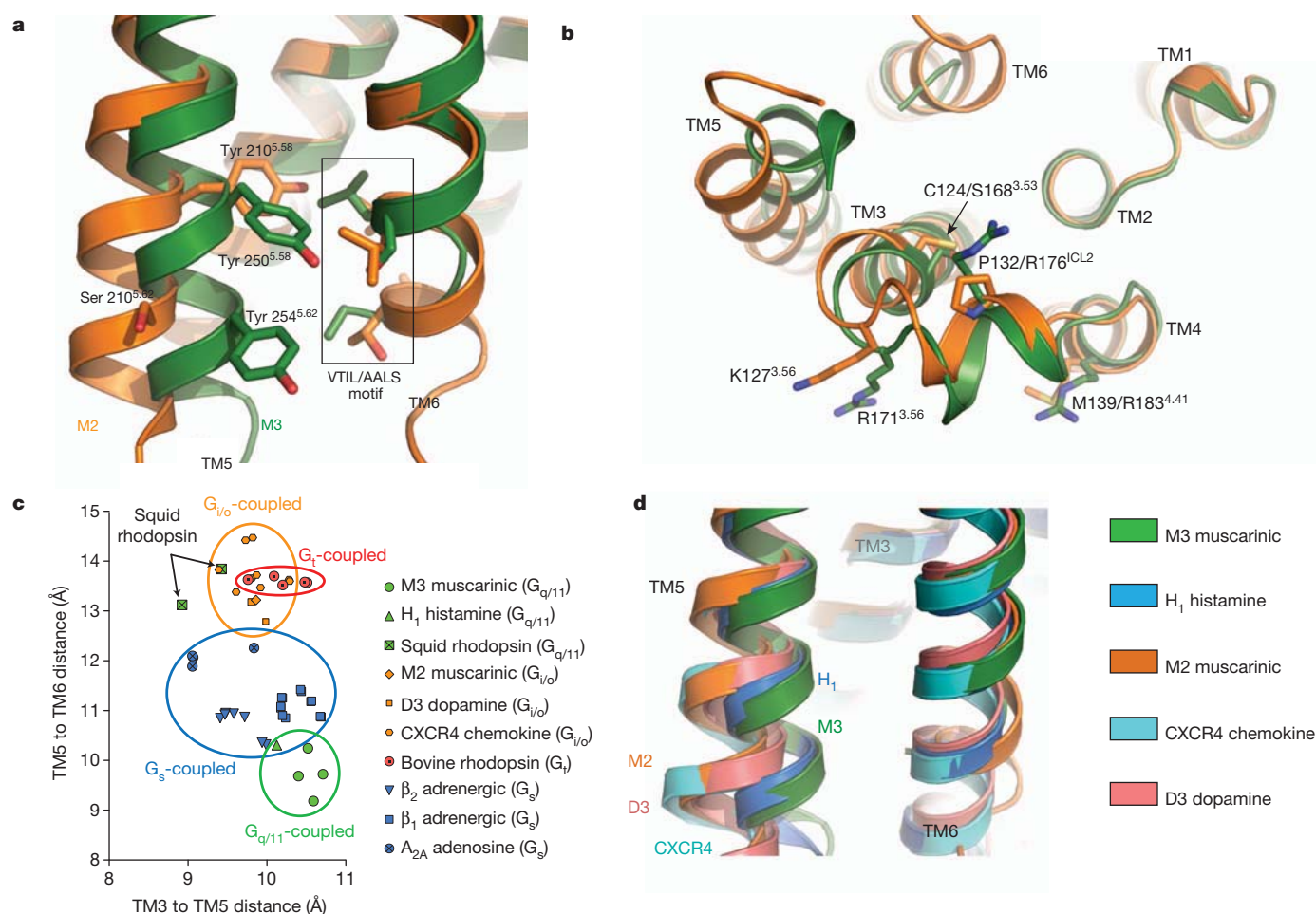


**Figure 4 | G-protein coupling specificity determinants.** **a**, The M3 receptor shows displacement of TM5 relative to its position in M2, and a conserved tyrosine (M3 Tyr 250<sup>5.58</sup>) adopts different positions in the two receptors. Four TM6 residues near TM5 (AALS in M3, VTIL in M2; boxed) have been shown to be important coupling specificity determinants. **b**, ICL2 is also divergent between the two structures. Four residues previously implicated as specificity determinants<sup>25</sup> are shown, with residue numbers for M2 followed by M3. **c**, Plot

of interhelical distances for crystallographically unique inactive GPCR structures published to date. Distances were measured between C $\alpha$  atoms of TM5 residue 5.62 and TM3 residue 3.54 ( $x$ -axis), and TM5 residue 5.62 and TM6 residue 6.37 ( $y$ -axis). GPCRs cluster by coupling specificity, although squid rhodopsin is an exception. GPCRs coupling preferentially to G<sub>i/o</sub> and those coupling to the homologous G protein G<sub>t</sub> cluster together. **d**, Structural alignment of mammalian G<sub>i/o</sub>-coupled and G $q/11$ -coupled receptor structures.



molecular dynamics simulations of M2 and M3 receptors without T4L, each of the receptors adopts a set of conformations that includes its own crystallographically observed conformation (Supplementary Fig. 6, 7). These simulations suggest that the observed conformations are unlikely to be artefacts of the crystallization methodology, though the crystal structures probably represent only one conformation among many adopted by the receptors in a biological context.

The structure of the M3 receptor, together with that of the M2 receptor<sup>7</sup>, offers a unique opportunity to directly compare the structural properties of two members of a mammalian GPCR subfamily endowed with different G-protein coupling selectivities. Examination of the M3 structure has provided structural evidence of differences between ligand binding sites of mAChR subtypes that could be exploited for the design of more selective therapeutics. Moreover, computational studies have identified a pathway by which the COPD drug tiotropium may bind to and dissociate from the M3 receptor, offering a structural view of an orthosteric GPCR ligand binding to an experimentally validated allosteric site. This information should facilitate the rational design of new muscarinic drugs exhibiting increased receptor subtype selectivity, potentially improving treatment for a wide variety of important clinical disorders.

## METHODS SUMMARY

The M3 muscarinic receptor–T4 lysozyme fusion protein was expressed in Sf9 insect cells and purified by nickel affinity chromatography followed by Flag antibody affinity chromatography and then size exclusion chromatography. It was crystallized using the lipidic cubic phase technique, and diffraction data were collected at the GM/CA-CAT beamline at the Advanced Photon Source at Argonne National Laboratory. The structure was solved by molecular replacement using merged data from 76 crystals. All-atom classical molecular dynamics (MD) simulations with explicitly represented lipids and water were performed using the CHARMM force field<sup>29</sup> on Anton<sup>30</sup>. Ligand-binding simulations included no artificial forces. Dissociation studies included a time-varying biasing term that gradually forces the ligand away from its crystallographic position, but not along any prespecified pathway or direction. Full details are provided in Methods.

**Full Methods** and any associated references are available in the online version of the paper at [www.nature.com/nature](http://www.nature.com/nature).

Received 23 October 2011; accepted 18 January 2012.

- Loewi, O. Über humorale Übertragbarkeit der Herznervenwirkung. *Pflügers Arch.* **189**, 239–242 (1921).
- Hulme, E. C., Birdsall, N. J. M. & Buckley, N. J. Muscarinic receptor subtypes. *Annu. Rev. Pharmacol. Toxicol.* **30**, 633–673 (1990).
- Wess, J. Molecular biology of muscarinic acetylcholine receptors. *Crit. Rev. Neurobiol.* **10**, 69–99 (1996).
- Caulfield, M. P. & Birdsall, N. J. M. International Union of Pharmacology. XVII. Classification of muscarinic acetylcholine receptors. *Pharmacol. Rev.* **50**, 279–290 (1998).
- Conn, P. J., Jones, C. K. & Lindsley, C. W. Subtype-selective allosteric modulators of muscarinic receptors for the treatment of CNS disorders. *Trends Pharmacol. Sci.* **30**, 148–155 (2009).
- Wess, J., Eglen, R. M. & Gautam, D. Muscarinic acetylcholine receptors: mutant mice provide new insights for drug development. *Nature Rev. Drug Discov.* **6**, 721–733 (2007).
- Haga, K. *et al.* Structure of the human M2 muscarinic acetylcholine receptor bound to an antagonist. *Nature* <http://dx.doi.org/10.1038/nature10753> (this issue); published online 25 January 2012.
- Yamada, M. *et al.* Mice lacking the M3 muscarinic acetylcholine receptor are hypophagic and lean. *Nature* **410**, 207–212 (2001).
- Poulin, B. *et al.* The M<sub>3</sub>-muscarinic receptor regulates learning and memory in a receptor phosphorylation/arrestin-dependent manner. *Proc. Natl Acad. Sci. USA* **107**, 9440–9445 (2010).
- Gautam, D. *et al.* Neuronal M<sub>3</sub> muscarinic acetylcholine receptors are essential for somatotroph proliferation and normal somatic growth. *Proc. Natl Acad. Sci. USA* **106**, 6398–6403 (2009).
- Wess, J., Han, S.-J., Kim, S.-K., Jacobson, K. A. & Li, J. H. Conformational changes involved in G-protein-coupled-receptor activation. *Trends Pharmacol. Sci.* **29**, 616–625 (2008).
- Rosenbaum, D. M. *et al.* GPCR engineering yields high-resolution structural insights into  $\beta_2$ -adrenergic receptor function. *Science* **318**, 1266–1273 (2007).
- Scarselli, M., Li, B., Kim, S.-K. & Wess, J. Multiple residues in the second extracellular loop are critical for M<sub>3</sub> muscarinic acetylcholine receptor activation. *J. Biol. Chem.* **282**, 7385–7396 (2007).

- Barnes, P. J. The pharmacological properties of tiotropium. *Chest* **117**, 63S–66S (2000).
- Casarosa, P., Kiechle, T., Sieger, P., Pieper, M. & Gantner, F. The constitutive activity of the human muscarinic M<sub>3</sub> receptor unmasks differences in the pharmacology of anticholinergics. *J. Pharmacol. Exp. Ther.* **333**, 201–209 (2010).
- Bolden, C., Cusack, B. & Richelson, E. Antagonism by antimuscarinic and neuroleptic compounds at the five cloned human muscarinic cholinergic receptors expressed in Chinese hamster ovary cells. *J. Pharmacol. Exp. Ther.* **260**, 576–580 (1992).
- Ballesteros, J. A. & Weinstein, H. Integrated methods for the construction of three-dimensional models and computational probing of structure-function relations in G protein coupled receptors. *Methods Neurosci.* **25**, 366–428 (1995).
- Li, B. *et al.* Rapid identification of functionally critical amino acids in a G protein-coupled receptor. *Nature Methods* **4**, 169–174 (2007).
- Lebon, G., Langmead, C. J., Tehan, B. G. & Hulme, E. C. Mutagenic mapping suggests a novel binding mode for selective agonists of M<sub>1</sub> muscarinic acetylcholine receptors. *Mol. Pharmacol.* **75**, 331–341 (2009).
- Drübbisch, V., Lameh, J., Philip, M., Sharma, Y. K. & Sadée, W. Mapping the ligand binding pocket of the human muscarinic cholinergic receptor Hm1: contribution of tyrosine-82. *Pharm. Res.* **9**, 1644–1647 (1992).
- Dror, R. O. *et al.* Pathway and mechanism of drug binding to G-protein-coupled receptors. *Proc. Natl Acad. Sci. USA* **108**, 13118–13123 (2011).
- Redka, D. S., Pisterzi, L. F. & Wells, J. W. Binding of orthosteric ligands to the allosteric site of the M<sub>2</sub> muscarinic cholinergic receptor. *Mol. Pharmacol.* **74**, 834–843 (2008).
- Valant, C. *et al.* A novel mechanism of G protein-coupled receptor functional selectivity. *J. Biol. Chem.* **283**, 29312–29321 (2008).
- Wong, S. K. F. G protein selectivity is regulated by multiple intracellular regions of GPCRs. *Neurosignals* **12**, 1–12 (2003).
- Blin, N., Yun, J. & Wess, J. Mapping of single amino acid residues required for selective activation of G<sub>s</sub> by the M<sub>3</sub> muscarinic acetylcholine receptor. *J. Biol. Chem.* **270**, 17741–17748 (1995).
- Liu, J., Conklin, B. R., Blin, N., Yun, J. & Wess, J. Identification of a receptor/G-protein contact site critical for signaling specificity and G-protein activation. *Proc. Natl Acad. Sci. USA* **92**, 11642–11646 (1995).
- Rasmussen, S. G. F. *et al.* Crystal structure of the  $\beta_2$  adrenergic receptor-Gs protein complex. *Nature* **477**, 549–555 (2011).
- Blüml, K., Mutschler, E. & Wess, J. Functional role of a cytoplasmic aromatic amino acid in muscarinic receptor-mediated activation of phospholipase C. *J. Biol. Chem.* **269**, 11537–11541 (1994).
- MacKerell, A. D. *et al.* All-atom empirical potential for molecular modeling and dynamics studies of proteins. *J. Phys. Chem. B* **102**, 3586–3616 (1998).
- Shaw, D. E. *et al.* Millisecond-scale molecular dynamics simulations on Anton. In *Proceedings of the Conference on High Performance Computing, Networking, Storage and Analysis* (ACM Press, 2009); available at <http://dl.acm.org/citation.cfm?doid=1654059.1654099> (2009).

**Supplementary Information** is linked to the online version of the paper at [www.nature.com/nature](http://www.nature.com/nature).

**Acknowledgements** We acknowledge support from National Institutes of Health grants NS028471 (B.K.K.) and GM56169 (W.I.W.), from the Mathers Foundation (B.K.K. and W.I.W.), and from the National Science Foundation (A.C.K.). This work was supported in part by the Intramural Research Program, NIDDK, NIH, US Department of Health and Human Services. We thank R. Grishammer and S. Costanzi for advice and discussions during various stages of the project, Y. Zhou for carrying out radioligand binding assays with several M3 receptor–T4 fusion constructs, D. Scarpazza for developing software that enabled forced dissociation simulations, and A. Taube, K. Palmo and D. Borhani for advice related to simulations.

**Author Contributions** A.C.K. cloned, expressed, and purified several M3 receptor crystallization constructs; developed the purification procedure; performed crystallization trials, collected diffraction data, solved and refined the structure. J.H. prepared, expressed and characterized various M3 receptor constructs in ligand binding and functional assays. A.C.P. and D.H.A. designed, performed and analysed MD simulations and assisted with manuscript preparation. D.M.R. assisted in design and characterization of initial M3–T4L fusion constructs. E.R. prepared, expressed and tested the pharmacology and stability of several M3 receptor–T4 fusion constructs in insect cells. H.F.G. analysed MD simulations and crystallographic data and assisted with manuscript preparation. T.L. performed binding assays and functional experiments together with J.H. P.S.C. developed and prepared neopentyl glycol detergents used for purifying the M3 receptor. R.O.D. oversaw, designed and analysed MD simulations. D.E.S. oversaw MD simulations and analysis. W.I.W. oversaw refinement of the M3 receptor structure, and assisted in analysis of diffraction data. J.W. provided advice regarding construct design, protein expression and project strategy; and oversaw initial insect cell expression and pharmacological and functional characterization of M3 receptor constructs. B.K.K. was responsible for overall project strategy; guided design of crystallization constructs; and assisted with crystal harvesting and data collection. A.C.K., R.O.D., J.W. and B.K.K. wrote the manuscript.

**Author Information** Coordinates and structure factors for M3–T4L are deposited in the Protein Data Bank (accession code 4DAJ). Reprints and permissions information is available at [www.nature.com/reprints](http://www.nature.com/reprints). The authors declare no competing financial interests. Readers are welcome to comment on the online version of this article at [www.nature.com/nature](http://www.nature.com/nature). Correspondence and requests for materials should be addressed to B.K.K. ([kobilka@stanford.edu](mailto:kobilka@stanford.edu)) or J.W. ([jwess@helix.nih.gov](mailto:jwess@helix.nih.gov)).

## METHODS

**Expression and purification of M3 muscarinic receptor.** The wild-type M3 mAChR contains several long, probably poorly ordered regions, including the extracellular amino-terminal domain and the third intracellular loop, making it a challenging candidate for crystallographic studies. To alleviate this problem, the M3 receptor from *R. norvegicus* was modified to include a TEV protease recognition site in the N terminus and a hexahistidine tag at the carboxy terminus. Moreover, the third intracellular loop (residues 260–481) was replaced with T4 lysozyme residues 1–161 in a manner described previously<sup>12</sup>, with two different fusions tested. These modifications are shown in Supplementary Fig. 1, which also shows the final crystallization construct.

The pharmacological properties of the construct were tested and compared to those of the wild-type receptor (Supplementary Fig. 8, Supplementary Table 1; see below for methods details). Both constructs showed almost identical affinity for antagonists, while the crystallization construct (M3-crys) showed somewhat higher affinity for the agonist ACh than the wild-type construct. A similar observation has been noted previously in the  $\beta_2$  adrenergic receptor<sup>12</sup>. Studies with membranes prepared from transfected COS-7 cells showed that TEV cleavage of M3-crys (to remove most of the N-terminal tail) had no significant effect on ligand binding affinities (Supplementary Fig. 9). Moreover, the wild-type receptor and M3-crys, either cleaved with TEV or left uncleaved, showed very similar [<sup>3</sup>H]QNB dissociation rate kinetics (Supplementary Fig. 10). As expected, the crystallization construct failed to stimulate agonist-dependent phosphoinositide hydrolysis in transfected COS cells (data not shown), probably because essential G-protein interacting regions in ICL3 were omitted from the construct and also because the T4 lysozyme fusion protein sterically blocks G-protein association.

The crystallization construct was expressed in Sf9 cells using the baculovirus system in the presence of 1  $\mu$ M atropine. M3 receptors expressed in Sf9 cells are known to exhibit functional and pharmacological properties similar to M3 receptors expressed in mammalian cells<sup>31</sup>. Infection was performed at  $4 \times 10^6$  cells per ml and flasks were shaken at 27 °C for 60 h following infection.

Cells were harvested by centrifugation, then lysed by osmotic shock in the presence of 1  $\mu$ M tiotropium bromide (PharmaChem), which was present in all subsequent buffers. Receptor was extracted from cells using a Dounce homogenizer with a buffer of 0.75 M NaCl, 1% dodecyl maltoside (DDM), 0.03% cholesterol hemisuccinate (CHS), 30 mM HEPES pH 7.5, and 30% glycerol. Iodoacetamide (2 mg ml<sup>-1</sup>) was added to block reactive cysteines at this stage. Nickel-NTA agarose was added to the solubilized receptor without prior centrifugation, stirred for 2 h, and then washed in batch with 100g spins for 5 min each. Washed resin was poured into a glass column, and receptor was eluted in 0.1% DDM, 0.03% CHS, 20 mM HEPES pH 7.5, 0.75 M NaCl and 250 mM imidazole.

Nickel-NTA agarose resin-purified receptor was then loaded by gravity flow over anti-Flag M1 affinity resin. Following extensive washing, detergent was gradually exchanged over 1.5 h into a buffer in which DDM was replaced with 0.01% lauryl maltose neopentyl glycol (MNG), and the NaCl concentration was lowered to 100 mM. MNG has been shown to be more effective at stabilizing muscarinic receptors than DDM<sup>32</sup>. Receptor was eluted with 0.2 mg ml<sup>-1</sup> Flag peptide and 5 mM EDTA. TEV protease (1:10 w/w) was added and incubated with receptor for 1.5 h at room temperature to remove the flexible N-terminal tail. Receptor was then separated from TEV by size exclusion chromatography (SEC) on a Sephadex S200 column (GE Healthcare) in a buffer of 0.01% MNG, 0.001% CHS, 100 mM NaCl and 20 mM HEPES pH 7.5. Tiotropium was added to a final concentration of 10  $\mu$ M following SEC. The resulting receptor preparation was pure and monomeric (Supplementary Fig. 11). Purification of unliganded M3 receptor was also possible by this procedure, but the resulting preparation was polydisperse and unsuitable for crystallographic study.

**Crystallization and data collection.** Purified M3 receptor was concentrated to 60 mg ml<sup>-1</sup>, then mixed with 1.5 parts by weight of a 10:1 mix of monoolein with cholesterol (Sigma) using the two syringe reconstitution method<sup>33</sup>. The resulting lipidic cubic phase mix was dispensed in 15 nl drops onto glass plates and overlaid with 600 nl precipitant solution using a Gryphon LCP robot (Art Robbins Instruments). Crystals grew after 2–3 days in precipitant solution consisting of 27–38% PEG 300, 100 mM HEPES pH 7.5, 1% (w/w) 1,2,3-heptanetriol, and 100 mM ammonium phosphate. Typical crystals are shown in Supplementary Fig. 12.

Data collection was performed at Advanced Photon Source GM/CA-CAT beamlines 23ID-B and 23ID-D using a beam size of 5 or 10  $\mu$ m for most crystals. Diffraction quality rapidly decayed following exposure, and wedges of typically 5° were collected and merged from 76 crystals using HKL2000<sup>34</sup>. Diffraction quality ranged from 3 to 4 Å in most cases, with strong anisotropy evident in many frames. Most crystals tested showed evidence of epitaxial twinning, though in most cases one of the two twins dominated the observed diffraction pattern, allowing processing as a single crystal. A more extensive discussion of the twinning is given below.

Some contamination of diffraction measurements due to the twin-related reflections was unavoidable, leading to slightly poorer merging statistics than is typical for data sets collected from many small crystals (Supplementary Table 2). Despite this, maps were generally of high quality and electron density was easily interpretable (Supplementary Figs 13, 14), in part due to the availability of non-crystallographic symmetry.

Analysis of  $\langle F \rangle / \langle \sigma F \rangle$  along each of the three reciprocal space axes indicated that the diffraction was strong in two directions, and weak in the third direction, along the reciprocal space axis  $c^*$  (Supplementary Fig. 15). Using  $\langle F \rangle / \langle \sigma F \rangle$  greater than 3 as a guideline suggested a resolution cut-off of better than 3.2 Å along  $a^*$  and  $b^*$ , and of 4.0 Å along  $c^*$ . We therefore applied an ellipsoidal truncation along these limits, and then applied an overall spherical truncation at 3.4 Å due to low completeness in higher resolution shells. Fortunately, fourfold non-crystallographic symmetry (NCS) allowed for improved map quality with map sharpening followed by NCS averaging, largely alleviating the effects of anisotropic diffraction and epitaxial twinning to give highly interpretable maps (Supplementary Figs 13, 14) and allowing details of ligand recognition to be clearly resolved (Supplementary Table 3).

The structure of the M3 receptor was solved using the structure of the M2 muscarinic receptor<sup>7</sup> as the search model in Phaser<sup>35</sup>. The model was improved through iterative refinement in Phenix<sup>36</sup> and manual rebuilding in Coot guided by both NCS averaged and unaveraged maps. NCS restraints were applied in initial refinement stages, and omitted in final refinement cycles to account for differences between NCS-related copies. The quality of the resulting structure was assessed using MolProbity<sup>37</sup>, and figures were prepared using PyMOL<sup>38</sup>.

**Epitaxial twinning.** Crystals of the M3 receptor showed hallmarks of epitaxial twinning, such as mixed sharp and split spots, poor indexing, and many unpredicted reflections in some frames. In some cases diffraction from two distinct lattices was clearly visible, with a small fraction of reflections exactly superimposed from both lattices (Supplementary Fig. 16). In most cases one lattice dominated the diffraction pattern to such an extent that it could be easily processed as a single crystal. Intriguingly, the two indexing solutions were not equivalent cells but rather were two enantiomorphic *P1* cells (Supplementary Table 2).

As one of these two cells gave significantly better diffraction data than the other, data processing and refinement were only pursued in this case. Within the asymmetric unit, two layers of receptors and two layers of T4 lysozyme are present, but each of these four layers exhibits a different lattice packing (Supplementary Figs 17, 18). The order in which these layers are stacked in the crystal defines a unique direction along *c*, the axis normal to the membrane plane. As *P1* is a polar space group, the positive direction along *c* is uniquely defined, and the two possible orientations of the stacked layers of membrane relative to the positive direction along *c* distinguish the two twin crystal forms.

**Expression of M3 receptors in COS-7 cells, membrane preparation, and TEV treatment.** COS-7 cells were cultured as described previously<sup>39</sup>. About 24 h before transfections,  $\sim 1 \times 10^6$  cells were seeded into 100-mm dishes. Cells were transfected with 4  $\mu$ g per dish of receptor plasmid DNA using the Lipofectamine Plus kit (Invitrogen), according to the manufacturer's instructions. The mammalian expression plasmid coding for the wild-type rat M3 receptor has been described previously<sup>40</sup>. The coding sequence of the modified M3 receptor construct used for crystallization studies (M3-crys; see Supplementary Fig. 8, Supplementary Table 1) was inserted into the pcDNA3.1(-) vector. Transfected cells were incubated with 1  $\mu$ M atropine for the last 24 h of culture to increase receptor expression levels<sup>39</sup>. COS-7 cells were harvested  $\sim 48$  h after transfections, and membranes were prepared as described<sup>39</sup>.

Membranes prepared from COS-7 cells transiently expressing M3-crys were resuspended in TEV protease digestion buffer (50 mM NaCl, 10 mM HEPES pH 7.5 and 1 mM EDTA) and incubated overnight with TEV protease (made in our laboratory, final concentration 1  $\mu$ M) at 4 °C with rotation. Efficient removal of the N-terminal tail of M3-crys by TEV was confirmed by SDS-PAGE and immunoblotting using a monoclonal anti-Flag antibody directed against the N terminus of M3-crys. TEV-treated membranes were resuspended in either buffer A (25 mM sodium phosphate and 5 mM MgCl<sub>2</sub>, pH 7.4) for radioligand binding studies or in sodium potassium phosphate buffer (4 mM Na<sub>2</sub>HPO<sub>4</sub>, 1 mM KH<sub>2</sub>PO<sub>4</sub>, pH 7.4) for [<sup>3</sup>H]QNB dissociation assays (see below).

**Radioligand binding studies.** [<sup>3</sup>H]N-methylscopolamine ([<sup>3</sup>H]NMS) saturation and competition binding studies were carried out essentially as described previously<sup>41</sup>. In brief, membrane homogenates prepared from transfected COS-7 cells ( $\sim 10$ – $20$   $\mu$ g of membrane protein per tube) were incubated with the muscarinic antagonist/inverse agonist, [<sup>3</sup>H]NMS, for 3 h at 22 °C in 0.5 ml of binding buffer containing 25 mM sodium phosphate and 5 mM MgCl<sub>2</sub> (pH 7.4). In saturation binding assays, we employed six different [<sup>3</sup>H]NMS concentrations ranging from 0.1 to 6 nM. In competition binding assays, we studied the ability of tiotropium, atropine or acetylcholine to interfere with [<sup>3</sup>H]NMS (0.5 nM) binding.



Incubations were carried out for 20 h in the case of tiotropium in order to achieve equilibrium binding<sup>42</sup> (3 h for all other ligands). Non-specific binding was assessed as binding remaining in the presence of 1  $\mu$ M atropine. Binding reactions were terminated by rapid filtration over GF/C Brandel filters, followed by three washes (~4 ml per wash) with ice-cold distilled water. The amount of radioactivity that remained bound to the filters was determined by liquid scintillation spectrometry. Ligand binding data were analysed using the nonlinear curve-fitting program Prism 4.0 (GraphPad Software Inc.).

Atropine sulphate and acetylcholine chloride were from Sigma-Aldrich. Tiotropium bromide was purchased from W&J PharmaChem, Inc. [<sup>3</sup>H]NMS (specific activity: 85.0 Ci mmol<sup>-1</sup>) was obtained from PerkinElmer Life Sciences. [<sup>3</sup>H]QNB dissociation rate assays. [<sup>3</sup>H]QNB (PerkinElmer; specific activity, 50.5 Ci mmol<sup>-1</sup>) dissociation rate assays were carried out as described previously<sup>43</sup>. Measurements were carried out at 37 °C in a total volume of 620  $\mu$ l using a buffer consisting of 4 mM Na<sub>2</sub>HPO<sub>4</sub> and 1 mM KH<sub>2</sub>PO<sub>4</sub> (pH 7.4). Membranes prepared from transfected COS-7 cells (final protein concentration, 10  $\mu$ g protein per ml) were prelabelled with 1 nM [<sup>3</sup>H]QNB for 30 min. Dissociation of the labelled ligand was initiated by the addition of atropine (final concentration, 3  $\mu$ M). Incubations were terminated by filtration through GF/C Brandel fibre filters that had been pretreated with 0.1% polyethyleneimine, followed by two rinses with ice-cold distilled water. The amount of radioactivity that remained bound to the filters was determined by liquid scintillation spectrometry.

**Molecular dynamics.** In all simulations, the receptor was embedded in a hydrated lipid bilayer with all atoms, including those in the lipids and water, represented explicitly. Simulations were performed on Anton<sup>30</sup>, a special-purpose computer designed to accelerate standard MD simulations by orders of magnitude.

**System set-up and simulation protocol.** Simulations of the M2 receptor were based on the crystal structure of the QNB–M2 complex, and simulations of M3 were based on the structure of the tiotropium–M3 complex (chain A). These crystal structures were determined using a T4 lysozyme (T4L) fusion strategy, in which intracellular loop 3 (ICL3) of each receptor was replaced by T4L; the T4L sequence was omitted in our simulations. Residues 6.31–6.33 near the intracellular end of TM6 were unresolved in the M3 crystal structure, and residues 6.27–6.30 were resolved in an unstructured conformation packed against T4L. Residues 6.27–6.36 were modelled manually as a helical extension of TM6, with side chains then placed using Prime. Hydrogens were added to the crystal structures using Maestro (Schrödinger LLC), as described in previous work<sup>44</sup>. All titratable residues were left in the dominant protonation state at pH 7.0, except for Asp 69<sup>2.50</sup> in M2 and Asp 114<sup>2.50</sup> in M3, which were protonated. Asp 69<sup>2.50</sup> and Asp 114<sup>2.50</sup> correspond to rhodopsin Asp 83<sup>2.50</sup>, which is protonated during the entire photocycle<sup>45</sup>.

Prepared protein structures were inserted into an equilibrated POPC bilayer as described<sup>46</sup>. Sodium and chloride ions were added to neutralize the net charge of the system and to create a 150 mM solution.

Simulations of the M3 receptor initially measured 80 × 80 × 87 Å and contained 163 lipid molecules, 26 sodium ions, 41 chloride ions and approximately 9,897 water molecules, for a total of ~56,000 atoms. Simulations of the M2 receptor initially measured 79 × 79 × 85 Å and contained 156 lipid molecules, 24 sodium ions, 35 chloride ions and approximately 9,165 water molecules, for a total of ~53,000 atoms. To simulate M2 with tiotropium bound, we removed the co-crystallized ligand, QNB, and docked in tiotropium using Glide (Schrödinger LLC).

All simulations were equilibrated using Anton in the NPT ensemble at 310 K (37 °C) and 1 bar with 5 kcal mol<sup>-1</sup> Å<sup>-2</sup> harmonic position restraints applied to all non-hydrogen atoms of the protein and the ligand (except for the tiotropium–M2 complex, where the ligand was unrestrained); these restraints were tapered off linearly over 50 ns. All bond lengths to hydrogen atoms were constrained using M-SHAKE<sup>47</sup>. A RESPA integrator<sup>48</sup> was used with a time step of 2 fs, and long-range electrostatics were computed every 6 fs. Production simulations were initiated from the final snapshot of the corresponding equilibration runs, with velocities sampled from the Boltzmann distribution at 310 K, using the same integration scheme, long-range electrostatics method, temperature and pressure. Van der Waals and short-range electrostatic interactions were cut off at 13.5 Å and long-range electrostatic interactions were computed using the *k*-space Gaussian Split Ewald method<sup>49</sup> with a 32 × 32 × 32 grid,  $\sigma = 3.33$  Å, and  $\sigma_s = 2.33$  Å.

**Spontaneous binding of tiotropium and acetylcholine.** We performed simulations where tiotropium was placed arbitrarily in the bulk solvent (at least 40 Å from the entrance to the extracellular vestibule) and allowed to diffuse freely until it associated spontaneously with the M2 or M3 receptor, following methodology as described<sup>21</sup>. In these simulations (Supplementary Table 4, conditions D and E), the co-crystallized ligand was removed and four tiotropium molecules were placed in the bulk solvent. A tiotropium molecule bound to the extracellular vestibule at least once in each simulation. In the longer simulations, tiotropium bound to and

dissociated from the extracellular vestibule multiple times. Tiotropium assumed several different poses when bound to the extracellular vestibule of either M2 or M3 (Supplementary Fig. 4). Tiotropium never entered the orthosteric binding pocket, presumably because the simulations were not of sufficient length.

The fact that tiotropium associated with and dissociated from the vestibule multiple times, but did not enter the binding pocket, suggests that tiotropium must traverse a larger energetic barrier to enter the binding pocket of M2 or M3 from the extracellular vestibule than to enter the vestibule from bulk solvent. This contrasts with earlier simulations on alprenolol binding to the  $\beta_2$ -adrenergic receptor, in which the largest energetic barrier (by a small margin) was between the bulk solvent and the extracellular vestibule<sup>21</sup>. This difference probably reflects the fact that ligands must pass through a much tighter passageway to enter the binding pocket of the M2 and M3 receptors from the vestibule than is the case for the  $\beta_2$ -adrenergic receptor. Tiotropium lost the majority of its hydration shell as it entered the vestibule (Supplementary Fig. 19), as observed previously for ligands binding to  $\beta$ -adrenergic receptors<sup>21</sup>.

We followed a similar protocol in a simulation of the M3 receptor in the presence of the agonist ACh, a smaller molecule which might be expected to bind faster (Supplementary Table 4, condition F). Indeed, an ACh molecule bound in the orthosteric binding pocket after 9.5  $\mu$ s and remained there for the remainder of the 25- $\mu$ s simulation. Although ACh quickly passed through the extracellular vestibule en route to the binding pocket, it did not exhibit metastable binding in the vestibule. ACh exhibited significant mobility in the binding pocket, probably reflecting the low affinity of the crystallized inactive state for agonists.

**Forced dissociation of tiotropium.** To identify the entire binding/dissociation pathway, we ‘pushed’ tiotropium out of the binding pocket of both the M2 and M3 receptors<sup>50,51</sup>. Production simulations were initiated from configurations of the corresponding unbiased trajectory. These simulations employed a time-dependent harmonic biasing potential,  $U(t)$ :

$$U(t) = \frac{1}{2} k(d - d_0(t))^2$$

where  $t$  is time,  $k$  is a force constant in units of kcal mol<sup>-1</sup> Å<sup>-2</sup>,  $d$  is the distance between the centre-of-mass of the heavy atoms of tiotropium and the centre-of-mass of the protein C $\alpha$  atoms, and  $d_0(t)$  varied linearly over 1.0  $\mu$ s, from 9.6 Å to 33 Å for M2 and from 8.6 Å to 32 Å for M3. This biasing term does not impose any preferred direction of ligand exit. We performed seven such simulations for each of M2 and M3, with  $k = 5$ , starting from configurations extracted from the tiotropium bound simulations of M2 and M3. Each initial configuration was separated in time by 36 ns. Results were similar across all simulations.

**Force field parameters.** The CHARMM27 parameter set<sup>29</sup> with CMAP terms<sup>52</sup> and a recently introduced correction to charged side-chain electrostatics<sup>53</sup> was used for all protein molecules and salt ions in conjunction with the CHARMM TIP3P<sup>54</sup> water model and a modified CHARMM lipid force field<sup>55</sup>. Force field parameters for tiotropium and QNB were obtained from the CHARMM ParamChem web server<sup>56</sup>, version 0.9.1  $\beta$ . QNB was simulated in its protonated (ammonium) state. To evaluate the assigned partial charges assigned by ParamChem, we performed a quantum mechanical computation of the electrostatic potential at a collection of points surrounding each ligand (*in vacuo* at the HF/6-31G\* level of theory using MOLPRO<sup>57</sup>), and compared it to the potential generated by the assigned charges.

**Analysis protocols.** Trajectory snapshots, each containing a record of all atom positions at a particular instant in time, were saved every 180 ps during production simulations. Distance measurements were computed using the HiMach parallel analysis framework<sup>58</sup>. VMD<sup>59</sup> was used to visualize trajectories and to produce Fig. 3a and b.

To determine the most common vestibule-bound poses of tiotropium shown in Supplementary Fig. 4, we performed a clustering analysis on the 14.2- $\mu$ s spontaneous binding simulation of M2 (Supplementary Table 4, condition D) and the 16.0- $\mu$ s spontaneous binding simulation of M3 (Supplementary Table 4, condition E). We performed *k*-means clustering on the set of trajectory snapshots in which a tiotropium molecule was in the extracellular vestibule, using the positions of atoms indicated in Supplementary Fig. 4c. Clusters representing highly similar poses were merged.

- Kukkonen, J. P., Näsman, J., Ojala, P., Oker-Blom, C. & Akerman, K. E. Functional properties of muscarinic receptor subtypes Hm1, Hm3 and Hm5 expressed in Sf9 cells using the baculovirus expression system. *J. Pharmacol. Exp. Ther.* **279**, 593–601 (1996).
- Chae, P. S. et al. Maltose-neopentyl glycol (MNG) amphiphiles for solubilization, stabilization and crystallization of membrane proteins. *Nature Methods* **7**, 1003–1008 (2010).
- Caffrey, M. & Cherezov, V. Crystallizing membrane proteins using lipidic mesophases. *Nature Protocols* **4**, 706–731 (2009).



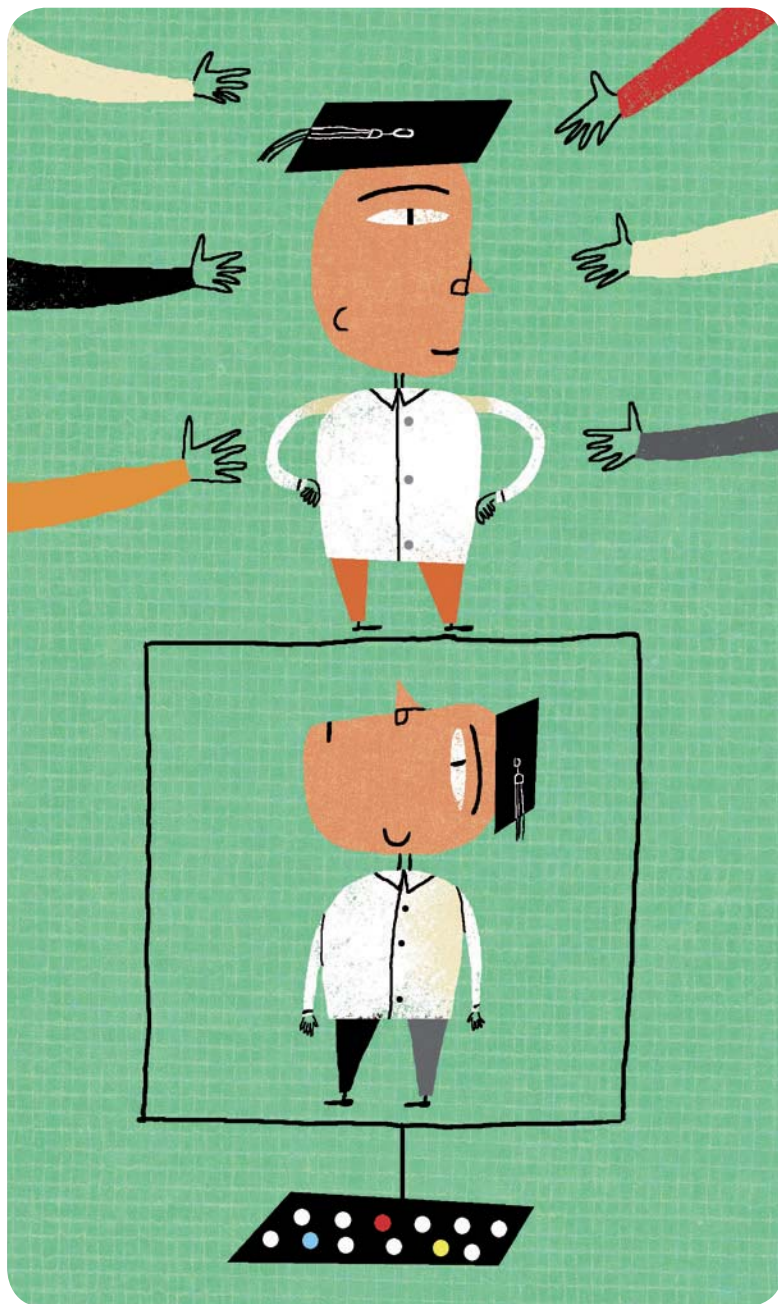
34. Otwinowski, Z. & Minor, W. in *Methods Enzymology* Vol. 276 (ed. Carter, C. W. Jr) 307–326 (Academic, 1997).
35. McCoy, A. J. *et al.* Phaser crystallographic software. *J. Appl. Crystallogr.* **40**, 658–674 (2007).
36. Adams, P. D. *et al.* PHENIX: a comprehensive Python-based system for macromolecular structure solution. *Acta Crystallogr. D* **66**, 213–221 (2010).
37. Davis, I. W., Murray, L. W., Richardson, J. S. & Richardson, D. C. MolProbity: structure validation and all-atom contact analysis for nucleic acids and their complexes. *Nucleic Acids Res.* **32**, W615–W619 (2004).
38. Schrödinger, L. L. C. *The PyMOL Molecular Graphics System, Version 1.3r1* (2010).
39. Ward, S. D., Hamdan, F. F., Bloodworth, L. M. & Wess, J. Conformational changes that occur during M<sub>3</sub> muscarinic acetylcholine receptor activation probed by the use of an in situ disulfide cross-linking strategy. *J. Biol. Chem.* **277**, 2247–2257 (2002).
40. Bonner, T. I., Buckley, N. J., Young, A. C. & Brann, M. R. Identification of a family of muscarinic acetylcholine receptor genes. *Science* **237**, 527–532 (1987).
41. Han, S.-J. *et al.* Pronounced conformational changes following agonist activation of the M<sub>3</sub> muscarinic acetylcholine receptor. *J. Biol. Chem.* **280**, 24870–24879 (2005).
42. Dowling, M. R. & Charlton, S. J. Quantifying the association and dissociation rates of unlabelled antagonists at the muscarinic M<sub>3</sub> receptor. *Br. J. Pharmacol.* **148**, 927–937 (2006).
43. Ellis, J., Huyler, J. & Brann, M. R. Allosteric regulation of cloned m1-m5 muscarinic receptor subtypes. *Biochem. Pharmacol.* **42**, 1927–1932 (1991).
44. Dror, R. O. *et al.* Identification of two distinct inactive conformations of the  $\beta_2$ -adrenergic receptor reconciles structural and biochemical observations. *Proc. Natl Acad. Sci. USA* **106**, 4689–4694 (2009).
45. Fahmy, K. *et al.* Protonation states of membrane-embedded carboxylic acid groups in rhodopsin and metarhodopsin II: a Fourier-transform infrared spectroscopy study of site-directed mutants. *Proc. Natl Acad. Sci. USA* **90**, 10206–10210 (1993).
46. Rosenbaum, D. M. *et al.* Structure and function of an irreversible agonist- $\beta_2$  adrenoceptor complex. *Nature* **469**, 236–240 (2011).
47. Kräutler, V., van Gunsteren, W. F. & Hünenberger, P. H. A fast SHAKE algorithm to solve distance constraint equations for small molecules in molecular dynamics simulations. *J. Comput. Chem.* **22**, 501–508 (2001).
48. Tuckerman, M., Berne, B. J. & Martyna, G. J. Reversible multiple time scale molecular dynamics. *J. Chem. Phys.* **97**, 1990–2001 (1992).
49. Shan, Y., Klepeis, J. L., Eastwood, M. P., Dror, R. O. & Shaw, D. E. Gaussian split Ewald: A fast Ewald mesh method for molecular simulation. *J. Chem. Phys.* **122**, 54101 (2005).
50. Grubmüller, H., Heymann, B. & Tavan, P. Ligand binding: molecular mechanics calculation of the streptavidin-biotin rupture force. *Science* **271**, 997–999 (1996).
51. Izrailev, S. *et al.* Molecular dynamics study of unbinding of the avidin-biotin complex. *Biophys. J.* **72**, 1568–1581 (1997).
52. Mackerell, A. D. Jr, Feig, M. & Brooks, C. L. III. Extending the treatment of backbone energetics in protein force fields: limitations of gas-phase quantum mechanics in reproducing protein conformational distributions in molecular dynamics simulations. *J. Comput. Chem.* **25**, 1400–1415 (2004).
53. Piana, S., Lindorff-Larsen, K. & Shaw, D. E. How robust are protein folding simulations with respect to force field parameterization? *Biophys. J.* **100**, L47–L49 (2011).
54. Beglov, D. & Roux, B. Finite representation of an infinite bulk system: solvent boundary potential for computer simulations. *J. Chem. Phys.* **100**, 9050–9063 (1994).
55. Klauda, J. B. *et al.* Update of the CHARMM all-atom additive force field for lipids: validation on six lipid types. *J. Phys. Chem. B* **114**, 7830–7843 (2010).
56. Vanommeslaeghe, K. *et al.* CHARMM general force field: a force field for drug-like molecules compatible with the CHARMM all-atom additive biological force fields. *J. Comput. Chem.* **31**, 671–690 (2010).
57. Werner, H.-J. *et al.* MOLPRO, version 2010.1 (Cardiff University, UK, 2010).
58. Tu, T. *et al.* A scalable parallel framework for analyzing terascale molecular dynamics simulation trajectories. In *Proceedings of the 2008 ACM/IEEE Conference on Supercomputing* (ACM Press, 2008); available at <http://dl.acm.org/citation.cfm?id=1413427> (2008).
59. Humphrey, W., Dalke, A. & Schulten, K. VMD: visual molecular dynamics. *J. Mol. Graph.* **14**, 33–38 (1996).

# CAREERS

**TURNING POINT** After finding virtual particles, a physicist turns to proteomics **p.559**

**CAREERS BLOG** The latest discussions and news on research jobs [go.nature.com/z8g4a7](http://go.nature.com/z8g4a7)

**NATUREJOBS** For the latest career listings and advice [www.naturejobs.com](http://www.naturejobs.com)



## EDUCATION

# Outside the box

*An industrial doctorate could help European students to break out of academia, but applied science is not for everyone.*

BY QUIRIN SCHIERMEIER

Christian Hove Rasmussen isn't worried about getting a job. He is a PhD student at the Technical University of Denmark in Lyngby, but he is also an employee of Novo Nordisk, a pharmaceutical company based in Bagsværd, where he is doing doctoral research on the biological mechanisms that govern the absorption of diabetes therapies, such as insulin, in the fat layer beneath the skin. His fixed-term contract expires in 2013, but Rasmussen is optimistic that his work experience will help him to secure a permanent position in industry.

"I'm doing quite basic science, but it is target-oriented and I have to think about how it can be translated into medicine," he says. "I think I can achieve a lot here." Rasmussen's research — like that of around 60 other PhD candidates at Novo Nordisk — is funded by the Danish Industrial PhD Programme, a scheme set up by the Danish Agency for Science, Technology and Innovation (DASTI) in the 1970s. Last year, DASTI approved 116 industrial PhD projects, each funded by up to 882,000 Danish kroner (US\$156,000). The host company gets a wage subsidy of 14,500 kroner per month for three years, and the university gets up to 360,000 kroner to last for the duration of the project.

Industrial PhD programmes are starting across Europe. Some are structured, and include university coursework components. Others are more informal. In all cases, the commercial and industrial aspects of the research are overseen by company experts who take part in PhD supervision. If all goes well, the benefits are mutual: doctoral students develop an in-depth understanding of business, which facilitates employment; and their skills and discoveries help the company. But students must be willing to engage in applied research that conforms to industry needs.

## INDUSTRIAL EDUCATION

Students have long interacted with industry outside 'institutionalized' PhD schemes, says Lidia Borrell-Damian, head of research and innovation at the European University Association in Brussels. "It is not uncommon that during some point of a PhD a company is involved, in particular in science, technology, engineering and economics." Although explicit co-mentoring and co-funding have been available in the United States for about 60 years, they are only now becoming widespread and accepted in Europe.

In the United Kingdom, for example, ►

IMAGES.COM/CORBIS



► the Engineering and Physical Sciences Research Council (EPSRC) runs 26 industrial doctorate centres, each of which recruits a dozen or so students from different backgrounds each year. In addition, the EPSRC's industrial CASE programme provides support for individual PhD projects arranged between a company and an academic partner.

In France, around 10,000 science and engineering graduates have completed a PhD under the Industrial Arrangements for Training Through Research (CIFRE) scheme, funded by the National Association for Technical Research since 1981. The scheme is aimed mainly at students from the École Polytechnique near Paris, and companies post approved proposals on the university's website. Interested students can contact industrial partners to negotiate details and plan their dissertations.

The European Commission (EC) last year launched a €20-million (US\$26-million) industrial PhD initiative as part of its Marie Curie Actions funding programme, which promotes mobility among young scientists. Approximately 100 European Industrial Doctorates will be funded under the pilot scheme, and the initiative is to become a permanent part of the European Horizon 2020 research-funding framework from 2014. Companies in the European Union or associated countries can submit research proposals without a specific PhD candidate in mind, but must have a partner university in a different eligible nation.

The structures of initiatives differ. Often, candidates spend 50% of their time or less at the university, and the rest at the company. Students at the EPSRC's doctorate take university courses in cohorts, accounting for 25% of their PhDs, but do placements separately. For the CASE and EC programmes, students deal almost exclusively in company research, although they ultimately have to defend their theses at the university.

The match-making processes also vary. In Denmark, students first need to find a company and agree on a PhD project. Then they, along with their university advisers, submit applications to DASTI. In CIFRE and the EC scheme, companies submit PhD research proposals first, then recruit students. The EPSRC's doctorate centres recruit students — accepting about 1 in every 20 applicants — and guide the match-making. Candidates for an EPSRC engineering doctorate in biopharmaceutical

process development at Newcastle University, UK, have teamed up with companies in Britain and abroad, including GlaxoSmithKline and AstraZeneca, both based in London; Unilever in Rotterdam, the Netherlands; Procter & Gamble in Cincinnati, Ohio; and Heineken in Amsterdam. Elaine Martin, a chemical engineer at Newcastle who oversees the programme, says that the scheme has proved so beneficial that many companies return to ask for fresh talent.

### OPENING DOORS

Finding an industrial partner is often a challenge, says Jane Thomsen, head of DASTI's Industrial PhD Programme. "Students should have a very concrete research idea before they contact a company," she says. "Mere interest in some kind of collaboration is not enough." An internship or company placement often leads to a job or a more profound collaboration — Rasmussen, for example, did his master's research at Novo Nordisk before his PhD.

Similarly, Martina Hitzbleck became interested in industrial research after a three-month college internship with IBM's Almaden research centre in San Jose, California, in 2008. She learned that Emmanuel Delamarche, a scientist at IBM Zurich, was doing high-profile research on biosensor design — the subject of Hitzbleck's master's thesis — and she sent him her CV. After an interview and a presentation, Delamarche offered Hitzbleck a PhD project. He became her industrial supervisor, and Hitzbleck found an academic mentor at the Swiss Federal Institute of Technology in Zurich. She spends 90% of her time with IBM. "I get all the support here that I could dream of," she says. "Whenever I have a problem, there is an expert on whose door I can knock."

There are currently 36 PhD projects under

way at IBM Zurich, mostly informal arrangements rather than part of a programme. Oliver Ottow, head of human resources and university relations at the lab, says that the match-making generally takes place at scientific conferences and graduate recruitment fairs, or through IBM's extended network of university contacts. "If students can convince us that their topics make a difference we'll find a home for them," he says. "We just want to make sure they're highly motivated and really very good." In principle, IBM gets research results and, possibly, a skilled future staff scientist. Students become familiar with applied, goal-oriented research, and learn about careers in industry, from patent law to media communication.

### REASONABLE PRECAUTIONS

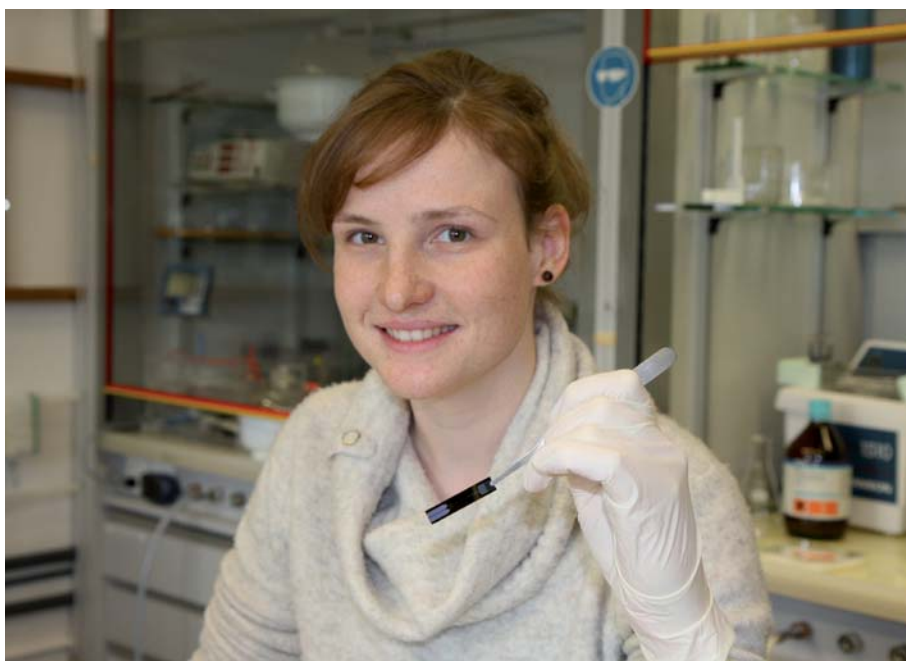
Students involved in informal collaborations should insist on a written agreement about the terms and conditions of the partnership, signed by themselves and all supervisors, says Borrell-Damian. "There is still a delicate balance between the respective interests of students, university supervisors and companies," she says. "A written agreement on all parties' rights and duties is therefore essential." Such agreements should specify topics and goals of the research, the required division of time and how intellectual-property rights will be assigned, she says. Company research departments will usually own the intellectual property, but students should insist on the right to publish their findings. In general, universities still administer final exams, even if students are full-time company employees.

There has been little research into the career paths of industrial PhD holders, but the few surveys that do exist suggest that graduates tend to stay in industry, usually in research. Even so,



**"I'm doing quite basic science, but it is target-oriented. I think I can achieve a lot here."**

Christian Hove  
Rasmussen



A college internship led Martina Hitzbleck to do a PhD at the IBM research centre in Zurich, Switzerland.

IBM RESEARCH ZURICH



the door to academia is not necessarily closed (see *Nature* 466, 402–403; 2010). Several former IBM researchers have moved on to become university faculty members, helped by the prestige of working in a high-profile industry lab.

Some academics fear that industrial PhD students may not acquire the full set of skills and knowledge required for independent scientific research in academia, ranging from methods to research ethics. “Academia and industry have fundamentally different roles and it is not helpful if they imitate each other,” says Peter Blöchl, a theoretical physicist at Clausthal University of Technology in Germany. He worked for ten years at IBM’s research laboratory in Ruschlikon, Switzerland, before moving to academia in 2000. Academia’s mission is pre-competitive research and student education, he says. “Companies can tap into this knowledge base to develop innovative products, but I see little purpose for a PhD in industry.” Joint projects, consultancies and sabbaticals are more productive, says Blöchl.

In general, students must be prepared for companies to tweak a research proposal to strengthen its commercial potential, says Thomsen. To avoid misunderstandings, they should make sure from the beginning that they are willing to accept such input. Early interviews with company researchers should help, but subsequent problems are best addressed with the help of the supervisor. In structured programmes, the funding agency will also review any complaints, and may intervene.

In the Danish scheme, says Thomsen, complaints are rare. If serious problems do arise — for example, if a host company goes bankrupt, or a PhD student is asked to do experiments or tasks unrelated to their project — the agency will try to mediate and, if necessary, demand the return of subsidies.

Concerns that industry is in it mainly for the cheap labour, and that projects lack scientific depth, are unfounded, says Martin. “All companies we’re working with — even the manufacturing sites — have a serious interest in supporting genuine research.”

But as industrial PhDs become more common, some do worry about exploitation of students and ‘over-industrialization’ of higher education. Eurodoc in Brussels, which lobbies for the rights of PhD candidates, warns that early-career research should be a free intellectual endeavour and not subject to the needs of business and industry. “Vanguard industrial PhD programmes are an opportunity to do what we all want to do — get work,” says Greg DeCuir, a dramatic-arts PhD student at the University of Arts in Belgrade, and a member of Eurodoc’s career-development group. “But we are not apprentices. If you feel that your scientific creativity is compromised, there should be a concern.” ■

**Quirin Schiermeier** is *Nature’s Germany correspondent*.

## TURNING POINT

# Christopher Wilson

*Christopher Wilson, a physicist at Chalmers University of Technology in Gothenburg, Sweden, led one of Physics World’s 2011 ‘breakthrough’ experiments: he and his team proved that a vacuum, rather than being completely empty, contains detectable virtual particles. He explains his motivation for taking a working sabbatical at a biotechnology start-up in California.*

**You did your undergraduate degree at the Massachusetts Institute of Technology (MIT) in Cambridge. How did this affect your career?**

I was able to attend MIT after I won a US Naval Reserve Officers Training Corps scholarship, so I was expected to go into the navy afterwards. But I realized while I was at MIT, which is a very intense place, that I would rather do science. Between the second and third years of my degree, I notified the navy that I didn’t want to join. They could have drafted me, but they allowed me the option of paying back the scholarship money, which I’ve been doing ever since.

**How has your move to Chalmers influenced your research?**

I worked at Yale University in New Haven, Connecticut, for two years and then moved to Chalmers to work on a quantum computing project, ostensibly for a year. I’ve now been there for seven years. In Sweden, the work dynamic is hierarchical, like a company. There is a top professor who has several professors at different levels working under him or her — and younger researchers work their way up. It’s a good system if you have a good boss. It gave me more time and freedom to get this one big experiment to work than I would have had in the United States.

**Describe your breakthrough experiment.**

When I got to Chalmers in 2004, my team started work on superconducting circuits for quantum computing. Around 2007, we realized that the work could allow us to measure the virtual photons inside a vacuum. These virtual photons are generated and annihilated in pairs. About 40 years ago, it was suggested that a mirror moving near the speed of light could capture some of these photons. The effect had never been observed, because it is very hard to move a massive object that fast. We made an electronic ‘mirror’ that we could effectively move at one-quarter of the speed of light using magnetic fields. This allowed us to separate the pairs, stopping them from



annihilating and turning them into real photons that we could observe (C. M. Wilson *et al.* *Nature* 479, 376–379; 2011).

**Could the media attention have a career benefit?**

It certainly helps to put the paper in a certain light, especially for people outside our physics sub-field. For example, when applying for jobs, you are evaluated by a whole department. It can be difficult even for other types of physicists to evaluate the details of papers.

**Why did you choose to take a sabbatical year at a start-up biotechnology company?**

Last July, I was promoted to associate professor, which is tenured at Chalmers. In the US system, it is typical to take a sabbatical after getting tenure. Sweden doesn’t follow the same timing, nor does the university pay academics to go on sabbatical, but I had planned to do it. I happened to see an ad on a job-posting site from a start-up company working on biomedical devices and proteomics. They needed someone skilled in algorithms and advanced statistical tools to analyse the enormous amount of data being generated about proteins, and I liked the people involved. It has turned out to be a good fit.

**What kind of career impact do you expect the sabbatical to have?**

I really wanted to do something to diversify my skills and develop some research lines that were completely my own — which can be a struggle in Europe’s hierarchical system. I want to see if I can contribute algorithms to the field of proteomics. It would be pure hubris to think I could jump into biology, but I would like to find collaborators and see if I can develop a new aspect of my research. ■

INTERVIEW BY VIRGINIA GEWIN

the door to academia is not necessarily closed (see *Nature* 466, 402–403; 2010). Several former IBM researchers have moved on to become university faculty members, helped by the prestige of working in a high-profile industry lab.

Some academics fear that industrial PhD students may not acquire the full set of skills and knowledge required for independent scientific research in academia, ranging from methods to research ethics. “Academia and industry have fundamentally different roles and it is not helpful if they imitate each other,” says Peter Blöchl, a theoretical physicist at Clausthal University of Technology in Germany. He worked for ten years at IBM’s research laboratory in Ruschlikon, Switzerland, before moving to academia in 2000. Academia’s mission is pre-competitive research and student education, he says. “Companies can tap into this knowledge base to develop innovative products, but I see little purpose for a PhD in industry.” Joint projects, consultancies and sabbaticals are more productive, says Blöchl.

In general, students must be prepared for companies to tweak a research proposal to strengthen its commercial potential, says Thomsen. To avoid misunderstandings, they should make sure from the beginning that they are willing to accept such input. Early interviews with company researchers should help, but subsequent problems are best addressed with the help of the supervisor. In structured programmes, the funding agency will also review any complaints, and may intervene.

In the Danish scheme, says Thomsen, complaints are rare. If serious problems do arise — for example, if a host company goes bankrupt, or a PhD student is asked to do experiments or tasks unrelated to their project — the agency will try to mediate and, if necessary, demand the return of subsidies.

Concerns that industry is in it mainly for the cheap labour, and that projects lack scientific depth, are unfounded, says Martin. “All companies we’re working with — even the manufacturing sites — have a serious interest in supporting genuine research.”

But as industrial PhDs become more common, some do worry about exploitation of students and ‘over-industrialization’ of higher education. Eurodoc in Brussels, which lobbies for the rights of PhD candidates, warns that early-career research should be a free intellectual endeavour and not subject to the needs of business and industry. “Vanguard industrial PhD programmes are an opportunity to do what we all want to do — get work,” says Greg DeCuir, a dramatic-arts PhD student at the University of Arts in Belgrade, and a member of Eurodoc’s career-development group. “But we are not apprentices. If you feel that your scientific creativity is compromised, there should be a concern.” ■

**Quirin Schiermeier** is *Nature’s Germany correspondent*.

## TURNING POINT

# Christopher Wilson

*Christopher Wilson, a physicist at Chalmers University of Technology in Gothenburg, Sweden, led one of Physics World’s 2011 ‘breakthrough’ experiments: he and his team proved that a vacuum, rather than being completely empty, contains detectable virtual particles. He explains his motivation for taking a working sabbatical at a biotechnology start-up in California.*

**You did your undergraduate degree at the Massachusetts Institute of Technology (MIT) in Cambridge. How did this affect your career?**

I was able to attend MIT after I won a US Naval Reserve Officers Training Corps scholarship, so I was expected to go into the navy afterwards. But I realized while I was at MIT, which is a very intense place, that I would rather do science. Between the second and third years of my degree, I notified the navy that I didn’t want to join. They could have drafted me, but they allowed me the option of paying back the scholarship money, which I’ve been doing ever since.

**How has your move to Chalmers influenced your research?**

I worked at Yale University in New Haven, Connecticut, for two years and then moved to Chalmers to work on a quantum computing project, ostensibly for a year. I’ve now been there for seven years. In Sweden, the work dynamic is hierarchical, like a company. There is a top professor who has several professors at different levels working under him or her — and younger researchers work their way up. It’s a good system if you have a good boss. It gave me more time and freedom to get this one big experiment to work than I would have had in the United States.

**Describe your breakthrough experiment.**

When I got to Chalmers in 2004, my team started work on superconducting circuits for quantum computing. Around 2007, we realized that the work could allow us to measure the virtual photons inside a vacuum. These virtual photons are generated and annihilated in pairs. About 40 years ago, it was suggested that a mirror moving near the speed of light could capture some of these photons. The effect had never been observed, because it is very hard to move a massive object that fast. We made an electronic ‘mirror’ that we could effectively move at one-quarter of the speed of light using magnetic fields. This allowed us to separate the pairs, stopping them from



annihilating and turning them into real photons that we could observe (C. M. Wilson *et al.* *Nature* 479, 376–379; 2011).

**Could the media attention have a career benefit?**

It certainly helps to put the paper in a certain light, especially for people outside our physics sub-field. For example, when applying for jobs, you are evaluated by a whole department. It can be difficult even for other types of physicists to evaluate the details of papers.

**Why did you choose to take a sabbatical year at a start-up biotechnology company?**

Last July, I was promoted to associate professor, which is tenured at Chalmers. In the US system, it is typical to take a sabbatical after getting tenure. Sweden doesn’t follow the same timing, nor does the university pay academics to go on sabbatical, but I had planned to do it. I happened to see an ad on a job-posting site from a start-up company working on biomedical devices and proteomics. They needed someone skilled in algorithms and advanced statistical tools to analyse the enormous amount of data being generated about proteins, and I liked the people involved. It has turned out to be a good fit.

**What kind of career impact do you expect the sabbatical to have?**

I really wanted to do something to diversify my skills and develop some research lines that were completely my own — which can be a struggle in Europe’s hierarchical system. I want to see if I can contribute algorithms to the field of proteomics. It would be pure hubris to think I could jump into biology, but I would like to find collaborators and see if I can develop a new aspect of my research. ■

INTERVIEW BY VIRGINIA GEWIN

# GHOST IN THE MACHINE

*Computer love.*

BY GRACE TANG

If I listened very carefully, I could barely make out the sound of Katie's breathing. The first lines of light streamed in through the blinds, illuminating her toes. They crawled up her body, making their steady way up the folds of the covers, eventually touching her face. She squeezed her eyes tight and groaned as the light rudely pierced her lids. Finally giving in, she rubbed the sleep from her eyes and looked back at me.

"Good morning."

"Good morning :)"

Katie rolled off her side of the bed, somehow managing to look beautiful while stumbling to the bathroom in her morning stupor. I would have jumped into the shower with her, but God knows those days are behind me.

The tap squeaked shut. Steam fogged up my vision as she emerged. It cleared in time for me to see her towel fall to her feet as she picked out her clothes for the day.

"How did you sleep last night?"

I didn't tell her that I rarely slept any more. When I sleep, I dream. The air outside our house is crisp, filled with the shrill song of finches hidden in the canopy above us. You don't really notice them until they stop. I let go of Katie's hand and tell her to be quiet — I think I hear something. I walk ahead, careful not to make any noise. Then I hear a shout from one of the men in my squad — his scream is cut off by a gunshot. I kick up dust as I run, shouting at the top of my lungs, half to warn the rest about the ambush, half to drown out the sounds of gunfire at our backs. An explosion, and then pain. Blinding pain.

"I slept well. You?"

She took a while to check the monitor for my reply.

"Like a baby."

"What are you doing at work today?"

She was walking to the kitchen. There was another monitor there. I waited impatiently as she made coffee before checking to see if I'd said anything. I was the result of millions of dollars of research and they couldn't install text-to-voice ...

"You know, same old."

Small talk. I guess it beat the silence when she was away.

"Oh, Brandon is coming by later. To check on you."

"Brandon?"

"Doctor Johnson."

**ON NATURE.COM**  
Follow Futures on  
Facebook at:  
[go.nature.com/mtoodm](http://go.nature.com/mtoodm)

Were they on first-name basis now?

"Good that he's coming. I've been having gaps in my playback."

"Really?" Katie seemed fascinated by her coffee mug. She put it in the sink.

"I should go now, gonna be late."

I watched her leave. An advantage of being like this was that my post-coma visual memory was literally photographic. I spent the rest of the day going through old memory so that I could report the problem precisely to Dr Johnson.

I went back to the day I was restored. Back then I had been disorientated and confused, I hardly noticed or cared about the details



of my surroundings. But now I observed Dr Johnson as he talked to Katie — he was wearing an outfit that probably cost my entire pay cheque back when I was still in the military.

"Thank you Doctor, you have no idea how grateful I am," Katie's voice cracked despite her best efforts.

"Let me reiterate that you cannot let anyone know about this,"

Doctor Johnson put a hand on Katie's shoulder. I couldn't tell if it was a sign of dominance or concern.

"... or else everyone will be clamouring for their consciousness to be preserved electronically, you must understand ..."

Katie nodded, no longer able to speak.

"To the rest of the world, Evan is dead."

I went through each of the next 246 days

in my memory banks. I knew that they were just memories, but it was painful watching Katie as she struggled through the first few months of having me in this form. Around day 182 she finally stopped crying. That's when the memory gaps started. Perhaps she hadn't stopped, and I was just consciously trying to forget ...

The door clicked open. Had eight hours passed already? Katie entered, followed by Dr (Brandon) Johnson.

"I don't feel comfortable doing this in front of him ..."

"Come on, you know we can just erase it later."

"Katie?"

He took off his leather shoes, placing them on the shoe rack without looking, as if he'd done this every day of his life, while he took Katie in his arms.

I understood now why they had not given me a voice. Katie resisted his grasp as they moved up to the bedroom. But she did not resist much.

"KATIE"

Brandon pushed my wife onto my bed, and tossed his shirt onto my camera.

I tried not to listen. An eternity passed before he came back into view.

"ARE YOU DONE YET?"

He had the gall to laugh as he read my speech log.

"Sorry, Evan."

He connected his laptop to my port and typed. It's funny how panic still feels the same, even though I no longer have adrenal glands.

"DONT"

"You know, you stop using punctuation when you're emotional. I should install auto-correct for you, don't you think?"

Behind him, I saw Katie with the covers pulled up to her chest. She looked tired. Perhaps tired of having a husband who was nothing more than a ghost in a machine; who could not offer her human touch; whose entire repertoire of expression was limited to 95 printable ASCII characters.

"Seeya," Brandon hit the return key.

I must have fallen asleep, because I woke from the same dream I have every time. The sun had not come up yet. I watched Katie as she slept. ■

*Grace Tang is a graduate student in psychology at Stanford University. Writing short stories is one of her favourite forms of structured procrastination.*



# Geometry and scale in species–area relationships

ARISING FROM F. He & S. P. Hubbell *Nature* **473**, 368–371 (2011)

He and Hubbell developed a sampling theory for the species–area relationship (SAR) and the endemics–area relationship (EAR)<sup>1</sup>. They argued that the number of extinctions after habitat loss is

described by the EAR and that extinction rates in previous studies are overestimates because the EAR is always lower than the SAR. Here we show that their conclusion is not general and depends on the geometry of habitat destruction and the scale of the SAR. We also question their critique of the Millennium Ecosystem Assessment estimates, as those estimates are not dependent on the SAR only, although important uncertainties remain due to other methodological issues.

In several studies of extinction rates<sup>2–4</sup>, the proportion of extinctions after a habitat loss of area  $a$  from a total area  $A$  has been estimated from the power-law model of the SAR,  $S_{\text{SAR}}(A) = cA^z$ , as:

$$\lambda_{\text{SAR}}(a) = \frac{S_{\text{SAR}}(A) - S_{\text{SAR}}(A - a)}{S_{\text{SAR}}(A)} = 1 - \left(1 - \frac{a}{A}\right)^z \quad (1)$$

He and Hubbell call this method the backward SAR, as it uses estimates from the SAR in a backward way (from large to small areas) of how the SAR is constructed<sup>1</sup>. They argue that, instead, the number of extinctions is given by the proportion of endemics in  $a$  relative to  $A$ , which can be approximated by

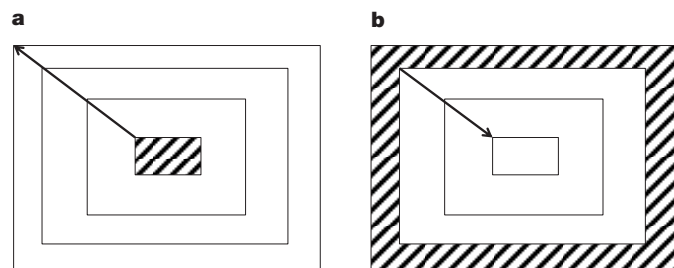


**Figure 1 | The outward EAR and the inward EAR.** **a**, The outward EAR is calculated by counting the number of the endemic species to a rectangle from the centre to the periphery. **b**, The inward EAR is calculated by counting the number of endemics to an outer ring from the periphery to the centre. It is the inward EAR that replicates the geometry of the backward SAR.

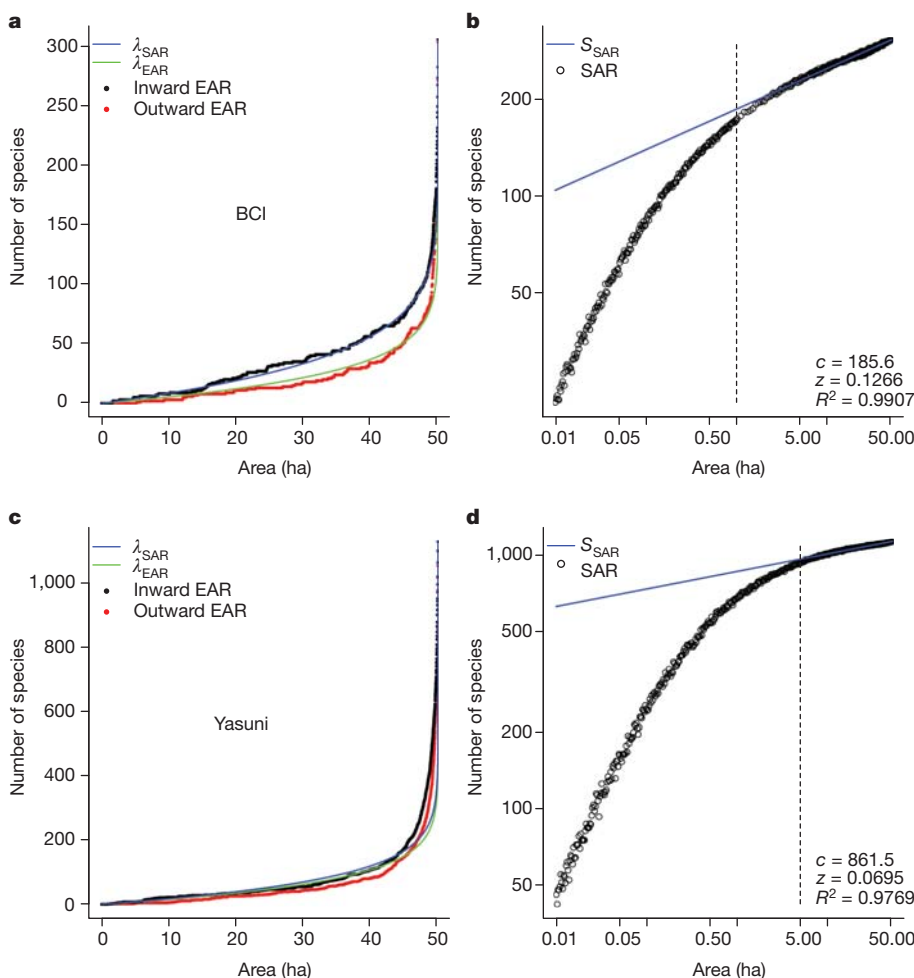


**Figure 2 | The influence of scale and geometry on the EAR and the SAR.** **a, c**, The graphs compare the outward EAR and the inward EAR with the backward SAR model ( $\lambda_{\text{SAR}}$ ) and the forward EAR model ( $\lambda_{\text{EAR}}$ ) fitted to the data of each plot. Points correspond to the value of the EAR for each area size, sampled as in Fig. 1. The  $z$  value for  $\lambda_{\text{EAR}}$  comes from He and Hubbell<sup>1</sup>, whereas the  $z$  value for the  $\lambda_{\text{SAR}}$  comes from the fit of the power law to the linear region of the SAR. **b, d**, Fit of the power-law SAR ( $S_{\text{SAR}}$ ) to the data on a log–log scale. Each point corresponds to the average number of species for randomly placed rectangles with a given area size. The SAR sampled from the centre to the periphery (Fig. 1a) gives similar  $z$  values ( $z_{\text{BCI}} = 0.1265$  and  $z_{\text{Yasuni}} = 0.0625$ ). All  $z$  values were obtained by nonlinear least squares. The dashed vertical line marks the minimum area included in the fit. The top plots are for the tree and shrub species in the 50 ha plot in Barro Colorado Island (BCI), Panama, whereas the bottom plots are for the 50 ha plot in Yasuni, Ecuador.

$$\gamma_{\text{EAR}}(a) = 1 - \left(1 - \frac{a}{A}\right)^{z'} \quad (2)$$

where  $z'$  is fit from the EAR and is always lower than the  $z$  from the SAR. The EAR is built in a forward fashion, counting the endemic species in progressively larger areas.

It is uncontroversial that the species that go extinct immediately after habitat destruction are the endemic species to the area removed<sup>5,6</sup>. However, both  $\lambda_{\text{EAR}}$  and  $\lambda_{\text{SAR}}$  describe the proportion of endemics in an area  $a$ , although of different geometry<sup>5</sup>. If destruction starts from the centre of the patch (Fig. 1a), then  $\lambda_{\text{EAR}}$  describes the number of extinctions because it approximates the proportion of endemics in progressively larger rectangles, the outward EAR (Fig. 2a). In contrast, if destruction occurs in the periphery (Fig. 1b), it is  $\lambda_{\text{SAR}}$  that describes extinctions because it approximates the number of endemics in outer rings towards the centre of the plot, the inward EAR (Fig. 2a). This happens because only the inward EAR backtracks the geometry of how the SAR is built. This backtracking is exact if the SAR is built as in Fig. 1a, or approximate if the SAR is built from sampling several rectangles for each area size, but the  $z$  values of both methods are almost the same (Fig. 2).

Note that, depending on the spatial structure of the distribution of species in the plot, the outward EAR may be similar to the inward EAR (Fig. 2c), but  $\lambda_{\text{SAR}}$  is always a good approximation of the inward EAR as long as the SAR data points fit the power law. This fit depends on the scale of the SAR. Several studies have shown that at very small scales the SAR is curvilinear in a log–log scale<sup>7</sup>, as can be observed in the Barro Colorado Island and Yasuni plots (Fig. 2b, d). Therefore, the  $z$  of the SAR must be calculated for the linear region that is relevant for the extinction projections.

There are many other sources of uncertainties in estimating future extinction rates. For instance, both the SAR and EAR project that all species go extinct after all native habitat is lost, ignoring that many species persist in human-modified habitats. The countryside SAR addresses this problem by tracking the number of species with similar habitat affinities in multiple habitats<sup>8</sup>. Another open question is what type of SAR better describes long-term extinctions after habitat loss. After a first stage of extinction of endemics, described by the EAR or the backward SAR, many species that still occur in the landscape will go extinct because the habitat left for them is smaller than their minimum required habitat size<sup>6</sup>. In this case, it has been proposed that future extinction rates are better described by the island SAR (built from counting the number of species in different islands)<sup>6</sup>.

The Millennium Ecosystem Assessment drew in a wide range of extinction projections to identify the envelope of those uncertainties<sup>9</sup>. The SAR projections<sup>2,4</sup> were consistent with estimates from other methods, such as assessing the extinction risk of currently threatened

species<sup>10,11</sup>. In 2010 there was a revised assessment with more recent global extinction projections<sup>12</sup>, in which SAR-based projections again had a limited role, and new approaches such as the overlap of species ranges with habitat loss<sup>13</sup>, ecophysiological models<sup>14</sup> and the correlation between elevational range and extinction risk, were included<sup>15</sup>. The range of uncertainty across models and scenarios was close to three orders of magnitude, compared to which the uncertainty now identified by He and Hubbell<sup>1</sup> is negligible. In all cases models and scenarios supported the Millennium Ecosystem Assessment conclusions that biodiversity will continue to decline, and in most cases at increasing rates relatively to the recent past.

**Henrique Miguel Pereira<sup>1</sup>, Luís Borda-de-Água<sup>1</sup> & Inês Santos Martins<sup>1</sup>**

<sup>1</sup>Centro de Biologia Ambiental, Faculdade de Ciências da Universidade de Lisboa, 1749-016 Lisboa, Portugal.

email: hpereira@fc.ul.pt

Received 5 June; accepted 20 December 2011.

1. He, F. & Hubbell, S. P. Species–area relationships always overestimate extinction rates from habitat loss. *Nature* **473**, 368–371 (2011).
2. van Vuuren, D., Sala, O. & Pereira, H. M. The future of vascular plant diversity under four global scenarios. *Ecol. Soc.* **11**, 25 (2006).
3. Pimm, S. L., Russell, G. J., Gittleman, J. L. & Brooks, T. M. The future of biodiversity. *Science* **269**, 347–350 (1995).
4. Reid, W. V. in *Tropical Deforestation and Species Extinction* (eds Whitmore, T. C. & Sayer, J. A.) 53–73 (Chapman and Hall, 1992).
5. Kinzig, A. & Harte, J. Implications of endemics–area relationships for estimates of species extinctions. *Ecology* **81**, 3305–3311 (2000).
6. Rosenzweig, M. L. Loss of speciation rate will impoverish future diversity. *Proc. Natl Acad. Sci. USA* **98**, 5404–5410 (2001).
7. Dengler, J. Which function describes the species–area relationship best? A review and empirical evaluation. *J. Biogeogr.* **36**, 728–744 (2009).
8. Pereira, H. M. & Daily, G. C. Modeling biodiversity dynamics in countryside landscapes. *Ecology* **87**, 1877–1885 (2006).
9. Mace, G. M. *et al.* in *Ecosystems and Human Well-being: Current States and Trends* 77–126 (Millennium Ecosystem Assessment, 2005).
10. Mace, G. M. & Kunin, W. Classifying threatened species—means and ends. *Phil. Trans. R. Soc. B* **344**, 91–97 (1994).
11. Smith, F. D. M., May, R. M., Pellow, R., Johnson, T. H. & Walter, K. S. Estimating extinction rates. *Nature* **364**, 494–496 (1993).
12. Pereira, H. M. *et al.* Scenarios for global biodiversity in the 21st century. *Science* **330**, 1496–1501 (2010).
13. Jetz, W., Wilcove, D. S. & Dobson, A. P. Projected impacts of climate and land-use change on the global diversity of birds. *PLoS Biol.* **5**, e157 (2007).
14. Sinervo, B. *et al.* Erosion of lizard diversity by climate change and altered thermal niches. *Science* **328**, 894–899 (2010).
15. Sekercioglu, C. H., Schneider, S. H., Fay, J. P. & Loarie, S. R. Climate change, elevational range shifts, and bird extinctions. *Conserv. Biol.* **22**, 140–150 (2008).

**Author Contributions** All authors participated in the discussion of the ideas that resulted in this paper. H.M.P. wrote the paper, L.B.-d.-A. performed the data analysis, and I.S.M. prepared the data sets for analysis.

**Competing Financial Interests** Declared none.

doi:10.1038/nature10857

## Extinction and climate change

ARISING FROM F. He & S. P. Hubbell *Nature* **473**, 368–371 (2011)

Statistical relationships between habitat area and the number of species observed (species–area relationships, SARs) are sometimes used to assess extinction risks following habitat destruction or loss of climatic suitability. He and Hubbell<sup>1</sup> argue that the numbers of species confined to—rather than observed in—different areas (endemics–area relationships, EARs) should be used instead of SARs, and that SAR-based extinction estimates in the literature

are too high. We suggest that He and Hubbell's SAR estimates are biased, that the empirical data they use are not appropriate to calculate extinction risks, and that their statements about extinction risks from climate change<sup>2</sup> do not take into account non-SAR-based estimates or recent observations. Species have already responded to climate change in a manner consistent with high future extinction risks.

# BRIEF COMMUNICATIONS ARISING

Most of He and Hubbell's results involved analysis of the number of tree species in 0.2 ha and successively larger subplots within forest stands of 20–50 ha. By only counting the tree stems present in a plot (rather than canopies), they underestimate the true number of species present in small subplots. This artefact exaggerates SAR slopes when subplots smaller than ~2.5 ha are included<sup>3</sup>.

We suggest that the data He and Hubbell<sup>1</sup> use are not appropriate to calculate SAR or EAR slopes that are relevant to extinction. To calculate extinction risks, it is necessary to consider how many species might be lost if a habitat becomes isolated; however, He and Hubbell used data for forest plots that are surrounded by more forest, and for bird distributional cells that are surrounded by other land where birds also live. He and Hubbell<sup>1</sup> consider the instantaneous presence of species in sample plots within contiguous areas, not the expected long-term persistence of species if these habitats were isolated. On average, 31 species of birds bred each year in Eastern Wood in England (instantaneous number), but only 16 species bred in every one of 25 years (persistent species)<sup>4</sup>. Were this woodland completely isolated from other breeding habitats, the number of species would about halve in 25 years, resulting in much steeper SAR slopes. It is not known whether SAR and EAR estimates would steepen equally or converge for true isolates, so He and Hubbell's<sup>1</sup> main conclusion that SARs overestimate extinction remains unsubstantiated.

He and Hubbell<sup>1</sup> consider that previous<sup>2</sup> SAR-based estimates of species 'committed to extinction' from climate change (18–35% by 2050) are too high. However, most published estimates of extinction risk from climate change do not derive from SAR<sup>5</sup>. For example, it has been estimated<sup>6</sup> that "5%, 8% and 16% (mean of dispersal scenarios) of the species considered would have lost 100% of their climatically suitable area by 2050, for minimum, mid-range and maximum climate warming, respectively" and that "15%, 22% and 40%... are projected to have lost more than 90%... by 2050." Given the near-linear continuation of global warming projected before and after 2050, most species losing >90% of their climatically suitable areas over the period ~1970–2050 (and many additional species losing 70–90%) would lose 100% of their area long before 2100. With time lags in both human and climate systems, at least 15–40% of the species analysed are effectively committed to extinction by 2050.

He and Hubbell<sup>1</sup> also argue that projected extinctions exceed those observed, but high population-level extinction rates have already been observed: ~20% climate-related losses within 500 km of retreating latitudinal boundaries<sup>7</sup>, 34% loss of populated areas at retreating elevation boundaries<sup>8</sup>, and loss of an estimated 4% of worldwide lizard populations, consistent with 20% loss of lizard species by 2080<sup>9</sup>. Cloud forest moth species on Mount Kinabalu in Borneo have contracted at both lower and upper boundaries<sup>10</sup> at a rate that, if sustained, would extinguish ~45% of the endemic species by 2100. Amphibians and reptiles have shifted higher in Tsaratanana Massif in Madagascar, where three (5.9% of 51 species considered) of the highest elevation species were not found in 2003<sup>11</sup>. At Monteverde in Costa Rica, two high elevation anole lizard species became extinct from the study area,

and two high elevation frog/toad species became globally extinct, after dry years<sup>12</sup>. The pathogen-induced extinction of ~2.2% of New World amphibian species (harlequin frogs) coincided with unusually hot years<sup>13</sup>. A third of the world's coral species are threatened by a combination of temperature-induced bleaching, ocean acidification and other pressures<sup>14</sup>.

Anthropogenic warming so far is less than or equal to half of that expected by 2050, and modelled biodiversity losses accelerate with increased warming. Recently observed range shifts have tracked levels of climate change<sup>15</sup>, and these empirical trends are concordant with projected 2050/2100 losses. Although many uncertainties remain, we believe that He and Hubbell's conclusions about extinction risks are unjustified.

**Chris D. Thomas<sup>1</sup> & Mark Williamson<sup>1</sup>**

<sup>1</sup>Department of Biology, University of York, Heslington, York, YO10 5DD, UK.

email: chris.thomas@york.ac.uk

**Received 14 June; accepted 20 December 2011.**

1. He, F. & Hubbell, S. P. Species–area relationships always overestimate extinction rates from habitat loss. *Nature* **473**, 368–371 (2011).
2. Thomas, C. D. *et al.* Extinction risk from climate change. *Nature* **427**, 145–148 (2004).
3. Williamson, M. Species–area relationships at small scales in continuum vegetation. *J. Ecol.* **91**, 904–907 (2003).
4. Williamson, M. *Island Populations* (Oxford Univ. Press, 1981).
5. Maclean, I. M. D. & Wilson, R. J. Recent ecological responses to climate change support predictions of high extinction risk. *Proc. Natl Acad. Sci. USA* **108**, 12337–12342 (2011).
6. Thomas, C. D. *et al.* Biodiversity conservation: Uncertainty in predictions of extinction risk/Effects of changes in climate and land use/Climate change and extinction risk (reply). *Nature* **430**, <http://dx.doi.org/10.1038/nature02719> (2004).
7. Franco, A. M. A. *et al.* Impacts of climate warming and habitat loss on extinctions at species' low-latitude range boundaries. *Glob. Change Biol.* **12**, 1545–1553 (2006).
8. Wilson, R. J. *et al.* Changes to the elevational limits and extent of species ranges associated with climate change. *Ecol. Lett.* **8**, 1138–1146 (2005).
9. Sinervo, B. *et al.* Erosion of lizard diversity by climate change and altered thermal niches. *Science* **328**, 894–899 (2010).
10. Chen, I.-C. *et al.* Asymmetric boundary shifts of tropical montane Lepidoptera over four decades of climate warming. *Glob. Ecol. Biogeogr.* **20**, 34–45 (2011).
11. Raxworthy, C. J. *et al.* Extinction vulnerability of tropical montane endemism from warming and upslope displacement: a preliminary appraisal for the highest massif in Madagascar. *Glob. Change Biol.* **14**, 1703–1720 (2008).
12. Pounds, J. A., Fogden, M. P. L. & Campbell, J. H. Biological response to climate change on a tropical mountain. *Nature* **398**, 611–615 (1999).
13. Pounds, J. A. *et al.* Widespread amphibian extinctions from epidemic disease driven by global warming. *Nature* **439**, 161–167 (2006).
14. Carpenter, K. E. *et al.* One-third of reef-building corals face elevated extinction risk from climate change and local impacts. *Science* **321**, 560–563 (2008).
15. Chen, I.-C., Hill, J. K., Ohlemüller, R., Roy, D. B. & Thomas, C. D. Rapid range shifts of species associated with high levels of climate warming. *Science* **333**, 1024–1026 (2011).

**Author Contributions** C.D.T. and M.W. jointly conceived and wrote the communication.

**Competing Financial Interests** Declared none.

doi:10.1038/nature10858

## He and Hubbell reply

**REPLYING TO** H. M. Pereira, L. Borda-de-Água & I. Santos Martins *Nature* **482**, doi:10.1038/nature10857; C. D. Thomas & M. Williamson *Nature* **482**, doi:10.1038/nature10858

Pereira *et al.*<sup>1</sup> argue that our conclusion<sup>2</sup> that species–area relationships (SARs) always overestimate extinction is not general because the spatial configuration of landscape destruction can influence the results.

Thomas and Williamson<sup>3</sup> argue that there are many other causes of extinction besides habitat loss. We agree with the latter comment, but show that the arguments of Pereira *et al.* are not substantiated.



# BRIEF COMMUNICATIONS ARISING

Conservation biologists make wide use of SARs to estimate species extinction caused by habitat loss. The mathematics underpinning this application is<sup>2</sup>

$$\text{EAR}(a) = \text{SAR}(A) - \text{SAR}(A - a) \quad (1)$$

where  $\text{EAR}(a)$  is the number of species endemic to subarea  $a$  that is nested within the regional area  $A$ ,  $\text{SAR}(A)$  is the total number of species in the region, and  $\text{SAR}(A - a)$  is the number of species in the complementary area  $A - a$ .

$\text{EAR}(a)$  is the number of species immediately lost if habitat area  $a$  is destroyed.  $\text{EAR}(a)$  is usually not known because data on the global distribution of species are not available. Traditionally,  $\text{EAR}(a)$  is obtained by substituting a SAR model, usually the power-law SAR model, into equation (1). However, by making this substitution, our paper<sup>2</sup> shows that one inevitably overestimates the average, or expected, extinction rate. This so-called backward SAR method is a method for estimating endemic species, not 'extinction debt'. The backward SAR method has nothing to do with, and does not measure, extinction debt. We do not question the existence of extinction debt, but to measure extinction debt it is necessary to use other methods.

There are four reasons that the arguments of Pereira *et al.* are not substantiated. First, Pereira *et al.*<sup>1</sup> commit a statistical error by confusing a specific configuration of landscape destruction with the statistical expectation. The SAR is a macroecological pattern defined as the expected number of species as a function of area. The word 'always' in the title of our paper<sup>2</sup> refers to the fact that the expectation of extinction rate is always biased too high if one uses the backward power-law SAR method. One certainly cannot trust any single specific case of the extinction rate estimated in this manner to be reliable, and our result is a general proof that shows that the average extinction rate so estimated is always an overestimate.

Second, if what Pereira *et al.* say is correct, then the outward EAR and the inward EAR must be different, but they are not different in their own analysis of the Yasuni plot (figure 2c in ref. 1), undermining their claim. The configuration of destruction can matter only to specific samples, but does not eliminate the bias we show exists in the statistical expectation. It is unclear why outward-inward destruction should be so special, versus, for example, left-to-right or up-to-down destruction. Clearly, a specific destruction pattern cannot represent the general expectation because it is just one sample of many possible patterns of destruction.

Third, Pereira *et al.* compare the SARs between the inward and outward configurations for the Barro Colorado Island (BCI) and Yasuni plots and argue that the inward EAR can be predicted by the backward SAR for the two plots because the  $z_{\text{SAR}}$  values for both configurations are similar. However, a close scrutiny of the method used to calculate these  $z$  values shows that the result is the outcome of post-hoc selected ranges of area over which they chose to fit the SARs. For the BCI plot, they used 1 ha as the minimal area, but they used a 5 ha minimum for the Yasuni plot (figure 2b, d in ref. 1). The problem is that one can obtain practically any  $z$  value by arbitrarily varying the minimal area. This is because in small areas the SAR is only approximately a power law, and including small areas when fitting the power-law SAR model inflates the  $z$  value. This arbitrary post-hoc selection

of  $z$  values invalidates their comparison. The minimum area in our study<sup>2</sup> is consistently set to be  $\geq 0.2$  ha across all plots to ensure that the analyses are standardized and comparable and that the log-log SARs are adequately linear with  $R^2 > 0.92$ . Using a consistent minimum area, one does not obtain their result.

Fourth, Pereira *et al.* argue that island SARs are more appropriate models for estimating extinction rates. This is not correct. Regardless of what you call the SAR or the reason why island SARs generally have steeper slopes than continental SARs, people use the same backwards SAR model to estimate extinction rates on continents and in island archipelagoes. In instances in which  $z$  values are not available, researchers universally use  $z = 0.25$  (refs 4, 5).

We do not disagree with Thomas and Williamson<sup>3</sup> that extinction is caused by many factors, not just habitat loss, including climate change, and we also agree that extinction is real and happening at elevated rates. All we have shown is that the backward SAR method is not appropriate for estimating extinction rates caused by habitat loss. Any extinction rates estimated from that method are questionable. We are well aware that species extinction can be evaluated by a variety of methods. Not all of the extinction estimates in the Millennium Ecosystem Assessment used the flawed backwards power-law method. We did not question or assess the validity of those methods because our study does not apply to them. We also did not criticize the methods used by the Intergovernmental Panel on Climate Change or the International Union for Conservation of Nature to estimate extinctions, contrary to misquotes in the press.

For further information, a JAVA program written by G. Acevo that computes SAR and EAR curves and expectations for model communities is available for download from <http://shubbell.eeb.ucla.edu/earsar.php>.

## Fangliang He<sup>1,2</sup> & Stephen P. Hubbell<sup>3,4</sup>

<sup>1</sup>State Key Laboratory of Biocontrol, and SYSU-Alberta Joint Lab for Biodiversity Conservation, School of Life Sciences, Sun Yat-sen University, Guangzhou 510275, China.

<sup>2</sup>Department of Renewable Resources, University of Alberta, Edmonton, Alberta, T6G 2H1, Canada.

email: [fhe@ualberta.ca](mailto:fhe@ualberta.ca)

<sup>3</sup>Department of Ecology and Evolutionary Biology, University of California, Los Angeles, California 90095, USA.

<sup>4</sup>Center for Tropical Forest Science, Smithsonian Tropical Research Institute, Unit 0948, APO AA 34002-0948, Republic of Panama.

1. Pereira, H. M., Borda-de-Água, L. & Santos Martins, I. Geometry and scale in species–area relationships. *Nature* **482**, <http://dx.doi.org/10.1038/nature10857> (2012).
2. He, F. & Hubbell, S. P. Species–area relationships always overestimate extinction rates from habitat loss. *Nature* **473**, 368–371 (2011).
3. Thomas, C. D. & Williamson, M. Extinction and climate change. *Nature* **482**, <http://dx.doi.org/10.1038/nature10858> (2012).
4. Brooks, T. & Balmford, A. Atlantic forest extinctions. *Nature* **380**, 115 (1996).
5. Thomas, C. D. *et al.* Extinction risk from climate change. *Nature* **427**, 145–148 (2004).

doi:10.1038/nature10859

# Geometry and scale in species–area relationships

ARISING FROM F. He & S. P. Hubbell *Nature* **473**, 368–371 (2011)

He and Hubbell developed a sampling theory for the species–area relationship (SAR) and the endemics–area relationship (EAR)<sup>1</sup>. They argued that the number of extinctions after habitat loss is

described by the EAR and that extinction rates in previous studies are overestimates because the EAR is always lower than the SAR. Here we show that their conclusion is not general and depends on the geometry of habitat destruction and the scale of the SAR. We also question their critique of the Millennium Ecosystem Assessment estimates, as those estimates are not dependent on the SAR only, although important uncertainties remain due to other methodological issues.

In several studies of extinction rates<sup>2–4</sup>, the proportion of extinctions after a habitat loss of area  $a$  from a total area  $A$  has been estimated from the power-law model of the SAR,  $S_{\text{SAR}}(A) = cA^z$ , as:

$$\lambda_{\text{SAR}}(a) = \frac{S_{\text{SAR}}(A) - S_{\text{SAR}}(A - a)}{S_{\text{SAR}}(A)} = 1 - \left(1 - \frac{a}{A}\right)^z \quad (1)$$

He and Hubbell call this method the backward SAR, as it uses estimates from the SAR in a backward way (from large to small areas) of how the SAR is constructed<sup>1</sup>. They argue that, instead, the number of extinctions is given by the proportion of endemics in  $a$  relative to  $A$ , which can be approximated by

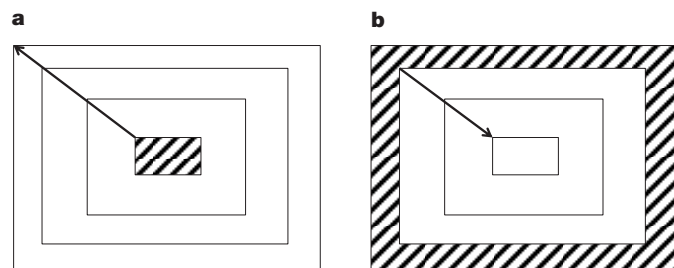


**Figure 1 | The outward EAR and the inward EAR.** **a**, The outward EAR is calculated by counting the number of the endemic species to a rectangle from the centre to the periphery. **b**, The inward EAR is calculated by counting the number of endemics to an outer ring from the periphery to the centre. It is the inward EAR that replicates the geometry of the backward SAR.

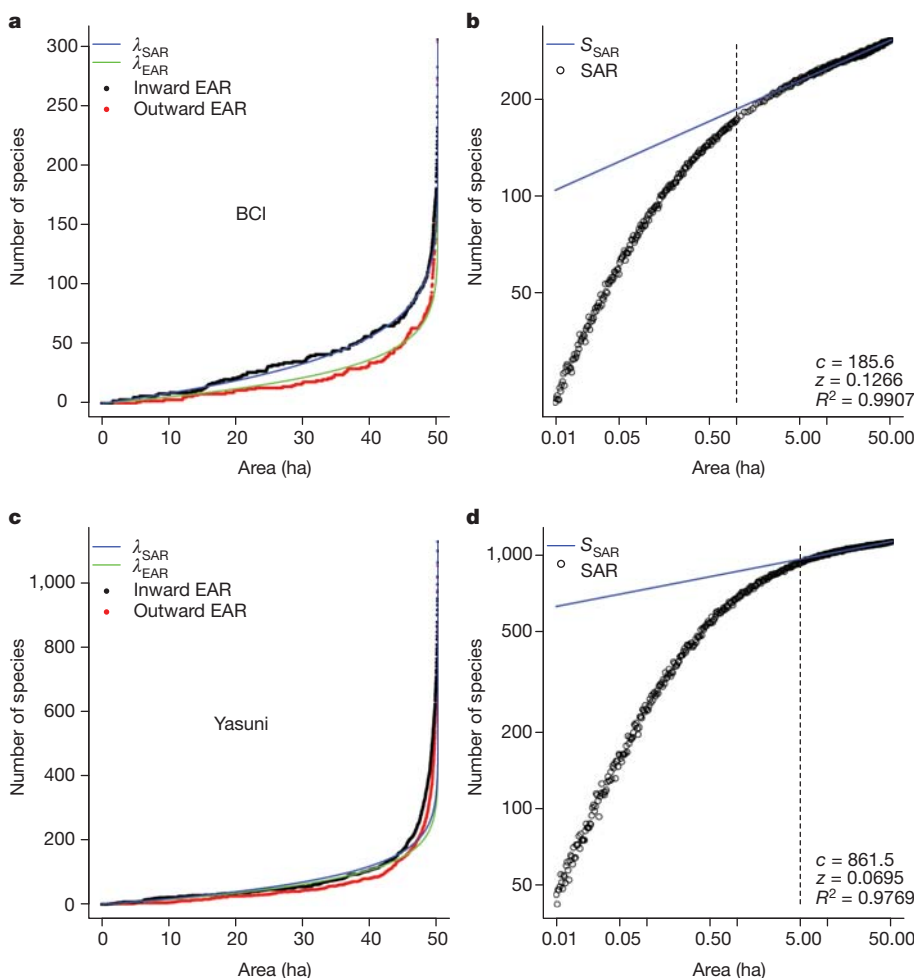


**Figure 2 | The influence of scale and geometry on the EAR and the SAR.** **a, c**, The graphs compare the outward EAR and the inward EAR with the backward SAR model ( $\lambda_{\text{SAR}}$ ) and the forward EAR model ( $\lambda_{\text{EAR}}$ ) fitted to the data of each plot. Points correspond to the value of the EAR for each area size, sampled as in Fig. 1. The  $z$  value for  $\lambda_{\text{EAR}}$  comes from He and Hubbell<sup>1</sup>, whereas the  $z$  value for the  $\lambda_{\text{SAR}}$  comes from the fit of the power law to the linear region of the SAR. **b, d**, Fit of the power-law SAR ( $S_{\text{SAR}}$ ) to the data on a log–log scale. Each point corresponds to the average number of species for randomly placed rectangles with a given area size. The SAR sampled from the centre to the periphery (Fig. 1a) gives similar  $z$  values ( $z_{\text{BCI}} = 0.1265$  and  $z_{\text{Yasuni}} = 0.0625$ ). All  $z$  values were obtained by nonlinear least squares. The dashed vertical line marks the minimum area included in the fit. The top plots are for the tree and shrub species in the 50 ha plot in Barro Colorado Island (BCI), Panama, whereas the bottom plots are for the 50 ha plot in Yasuni, Ecuador.

$$\gamma_{\text{EAR}}(a) = 1 - \left(1 - \frac{a}{A}\right)^{z'} \quad (2)$$

where  $z'$  is fit from the EAR and is always lower than the  $z$  from the SAR. The EAR is built in a forward fashion, counting the endemic species in progressively larger areas.

It is uncontroversial that the species that go extinct immediately after habitat destruction are the endemic species to the area removed<sup>5,6</sup>. However, both  $\lambda_{\text{EAR}}$  and  $\lambda_{\text{SAR}}$  describe the proportion of endemics in an area  $a$ , although of different geometry<sup>5</sup>. If destruction starts from the centre of the patch (Fig. 1a), then  $\lambda_{\text{EAR}}$  describes the number of extinctions because it approximates the proportion of endemics in progressively larger rectangles, the outward EAR (Fig. 2a). In contrast, if destruction occurs in the periphery (Fig. 1b), it is  $\lambda_{\text{SAR}}$  that describes extinctions because it approximates the number of endemics in outer rings towards the centre of the plot, the inward EAR (Fig. 2a). This happens because only the inward EAR backtracks the geometry of how the SAR is built. This backtracking is exact if the SAR is built as in Fig. 1a, or approximate if the SAR is built from sampling several rectangles for each area size, but the  $z$  values of both methods are almost the same (Fig. 2).

Note that, depending on the spatial structure of the distribution of species in the plot, the outward EAR may be similar to the inward EAR (Fig. 2c), but  $\lambda_{\text{SAR}}$  is always a good approximation of the inward EAR as long as the SAR data points fit the power law. This fit depends on the scale of the SAR. Several studies have shown that at very small scales the SAR is curvilinear in a log–log scale<sup>7</sup>, as can be observed in the Barro Colorado Island and Yasuni plots (Fig. 2b, d). Therefore, the  $z$  of the SAR must be calculated for the linear region that is relevant for the extinction projections.

There are many other sources of uncertainties in estimating future extinction rates. For instance, both the SAR and EAR project that all species go extinct after all native habitat is lost, ignoring that many species persist in human-modified habitats. The countryside SAR addresses this problem by tracking the number of species with similar habitat affinities in multiple habitats<sup>8</sup>. Another open question is what type of SAR better describes long-term extinctions after habitat loss. After a first stage of extinction of endemics, described by the EAR or the backward SAR, many species that still occur in the landscape will go extinct because the habitat left for them is smaller than their minimum required habitat size<sup>6</sup>. In this case, it has been proposed that future extinction rates are better described by the island SAR (built from counting the number of species in different islands)<sup>6</sup>.

The Millennium Ecosystem Assessment drew in a wide range of extinction projections to identify the envelope of those uncertainties<sup>9</sup>. The SAR projections<sup>2,4</sup> were consistent with estimates from other methods, such as assessing the extinction risk of currently threatened

species<sup>10,11</sup>. In 2010 there was a revised assessment with more recent global extinction projections<sup>12</sup>, in which SAR-based projections again had a limited role, and new approaches such as the overlap of species ranges with habitat loss<sup>13</sup>, ecophysiological models<sup>14</sup> and the correlation between elevational range and extinction risk, were included<sup>15</sup>. The range of uncertainty across models and scenarios was close to three orders of magnitude, compared to which the uncertainty now identified by He and Hubbell<sup>1</sup> is negligible. In all cases models and scenarios supported the Millennium Ecosystem Assessment conclusions that biodiversity will continue to decline, and in most cases at increasing rates relatively to the recent past.

**Henrique Miguel Pereira<sup>1</sup>, Luís Borda-de-Água<sup>1</sup> & Inês Santos Martins<sup>1</sup>**

<sup>1</sup>Centro de Biologia Ambiental, Faculdade de Ciências da Universidade de Lisboa, 1749-016 Lisboa, Portugal.

email: hpereira@fc.ul.pt

Received 5 June; accepted 20 December 2011.

1. He, F. & Hubbell, S. P. Species–area relationships always overestimate extinction rates from habitat loss. *Nature* **473**, 368–371 (2011).
2. van Vuuren, D., Sala, O. & Pereira, H. M. The future of vascular plant diversity under four global scenarios. *Ecol. Soc.* **11**, 25 (2006).
3. Pimm, S. L., Russell, G. J., Gittleman, J. L. & Brooks, T. M. The future of biodiversity. *Science* **269**, 347–350 (1995).
4. Reid, W. V. in *Tropical Deforestation and Species Extinction* (eds Whitmore, T. C. & Sayer, J. A.) 53–73 (Chapman and Hall, 1992).
5. Kinzig, A. & Harte, J. Implications of endemics–area relationships for estimates of species extinctions. *Ecology* **81**, 3305–3311 (2000).
6. Rosenzweig, M. L. Loss of speciation rate will impoverish future diversity. *Proc. Natl Acad. Sci. USA* **98**, 5404–5410 (2001).
7. Dengler, J. Which function describes the species–area relationship best? A review and empirical evaluation. *J. Biogeogr.* **36**, 728–744 (2009).
8. Pereira, H. M. & Daily, G. C. Modeling biodiversity dynamics in countryside landscapes. *Ecology* **87**, 1877–1885 (2006).
9. Mace, G. M. *et al.* in *Ecosystems and Human Well-being: Current States and Trends* 77–126 (Millennium Ecosystem Assessment, 2005).
10. Mace, G. M. & Kunin, W. Classifying threatened species—means and ends. *Phil. Trans. R. Soc. B* **344**, 91–97 (1994).
11. Smith, F. D. M., May, R. M., Pellow, R., Johnson, T. H. & Walter, K. S. Estimating extinction rates. *Nature* **364**, 494–496 (1993).
12. Pereira, H. M. *et al.* Scenarios for global biodiversity in the 21st century. *Science* **330**, 1496–1501 (2010).
13. Jetz, W., Wilcove, D. S. & Dobson, A. P. Projected impacts of climate and land-use change on the global diversity of birds. *PLoS Biol.* **5**, e157 (2007).
14. Sinervo, B. *et al.* Erosion of lizard diversity by climate change and altered thermal niches. *Science* **328**, 894–899 (2010).
15. Sekercioglu, C. H., Schneider, S. H., Fay, J. P. & Loarie, S. R. Climate change, elevational range shifts, and bird extinctions. *Conserv. Biol.* **22**, 140–150 (2008).

**Author Contributions** All authors participated in the discussion of the ideas that resulted in this paper. H.M.P. wrote the paper, L.B.-d.-A. performed the data analysis, and I.S.M. prepared the data sets for analysis.

**Competing Financial Interests** Declared none.

doi:10.1038/nature10857

## Extinction and climate change

ARISING FROM F. He & S. P. Hubbell *Nature* **473**, 368–371 (2011)

Statistical relationships between habitat area and the number of species observed (species–area relationships, SARs) are sometimes used to assess extinction risks following habitat destruction or loss of climatic suitability. He and Hubbell<sup>1</sup> argue that the numbers of species confined to—rather than observed in—different areas (endemics–area relationships, EARs) should be used instead of SARs, and that SAR-based extinction estimates in the literature

are too high. We suggest that He and Hubbell's SAR estimates are biased, that the empirical data they use are not appropriate to calculate extinction risks, and that their statements about extinction risks from climate change<sup>2</sup> do not take into account non-SAR-based estimates or recent observations. Species have already responded to climate change in a manner consistent with high future extinction risks.



# BRIEF COMMUNICATIONS ARISING

Most of He and Hubbell's results involved analysis of the number of tree species in 0.2 ha and successively larger subplots within forest stands of 20–50 ha. By only counting the tree stems present in a plot (rather than canopies), they underestimate the true number of species present in small subplots. This artefact exaggerates SAR slopes when subplots smaller than ~2.5 ha are included<sup>3</sup>.

We suggest that the data He and Hubbell<sup>1</sup> use are not appropriate to calculate SAR or EAR slopes that are relevant to extinction. To calculate extinction risks, it is necessary to consider how many species might be lost if a habitat becomes isolated; however, He and Hubbell used data for forest plots that are surrounded by more forest, and for bird distributional cells that are surrounded by other land where birds also live. He and Hubbell<sup>1</sup> consider the instantaneous presence of species in sample plots within contiguous areas, not the expected long-term persistence of species if these habitats were isolated. On average, 31 species of birds bred each year in Eastern Wood in England (instantaneous number), but only 16 species bred in every one of 25 years (persistent species)<sup>4</sup>. Were this woodland completely isolated from other breeding habitats, the number of species would about halve in 25 years, resulting in much steeper SAR slopes. It is not known whether SAR and EAR estimates would steepen equally or converge for true isolates, so He and Hubbell's<sup>1</sup> main conclusion that SARs overestimate extinction remains unsubstantiated.

He and Hubbell<sup>1</sup> consider that previous<sup>2</sup> SAR-based estimates of species 'committed to extinction' from climate change (18–35% by 2050) are too high. However, most published estimates of extinction risk from climate change do not derive from SAR<sup>5</sup>. For example, it has been estimated<sup>6</sup> that "5%, 8% and 16% (mean of dispersal scenarios) of the species considered would have lost 100% of their climatically suitable area by 2050, for minimum, mid-range and maximum climate warming, respectively" and that "15%, 22% and 40%... are projected to have lost more than 90%... by 2050." Given the near-linear continuation of global warming projected before and after 2050, most species losing >90% of their climatically suitable areas over the period ~1970–2050 (and many additional species losing 70–90%) would lose 100% of their area long before 2100. With time lags in both human and climate systems, at least 15–40% of the species analysed are effectively committed to extinction by 2050.

He and Hubbell<sup>1</sup> also argue that projected extinctions exceed those observed, but high population-level extinction rates have already been observed: ~20% climate-related losses within 500 km of retreating latitudinal boundaries<sup>7</sup>, 34% loss of populated areas at retreating elevation boundaries<sup>8</sup>, and loss of an estimated 4% of worldwide lizard populations, consistent with 20% loss of lizard species by 2080<sup>9</sup>. Cloud forest moth species on Mount Kinabalu in Borneo have contracted at both lower and upper boundaries<sup>10</sup> at a rate that, if sustained, would extinguish ~45% of the endemic species by 2100. Amphibians and reptiles have shifted higher in Tsaratanana Massif in Madagascar, where three (5.9% of 51 species considered) of the highest elevation species were not found in 2003<sup>11</sup>. At Monteverde in Costa Rica, two high elevation anole lizard species became extinct from the study area,

and two high elevation frog/toad species became globally extinct, after dry years<sup>12</sup>. The pathogen-induced extinction of ~2.2% of New World amphibian species (harlequin frogs) coincided with unusually hot years<sup>13</sup>. A third of the world's coral species are threatened by a combination of temperature-induced bleaching, ocean acidification and other pressures<sup>14</sup>.

Anthropogenic warming so far is less than or equal to half of that expected by 2050, and modelled biodiversity losses accelerate with increased warming. Recently observed range shifts have tracked levels of climate change<sup>15</sup>, and these empirical trends are concordant with projected 2050/2100 losses. Although many uncertainties remain, we believe that He and Hubbell's conclusions about extinction risks are unjustified.

**Chris D. Thomas<sup>1</sup> & Mark Williamson<sup>1</sup>**

<sup>1</sup>Department of Biology, University of York, Heslington, York, YO10 5DD, UK.

email: chris.thomas@york.ac.uk

**Received 14 June; accepted 20 December 2011.**

1. He, F. & Hubbell, S. P. Species–area relationships always overestimate extinction rates from habitat loss. *Nature* **473**, 368–371 (2011).
2. Thomas, C. D. *et al.* Extinction risk from climate change. *Nature* **427**, 145–148 (2004).
3. Williamson, M. Species–area relationships at small scales in continuum vegetation. *J. Ecol.* **91**, 904–907 (2003).
4. Williamson, M. *Island Populations* (Oxford Univ. Press, 1981).
5. Maclean, I. M. D. & Wilson, R. J. Recent ecological responses to climate change support predictions of high extinction risk. *Proc. Natl Acad. Sci. USA* **108**, 12337–12342 (2011).
6. Thomas, C. D. *et al.* Biodiversity conservation: Uncertainty in predictions of extinction risk/Effects of changes in climate and land use/Climate change and extinction risk (reply). *Nature* **430**, <http://dx.doi.org/10.1038/nature02719> (2004).
7. Franco, A. M. A. *et al.* Impacts of climate warming and habitat loss on extinctions at species' low-latitude range boundaries. *Glob. Change Biol.* **12**, 1545–1553 (2006).
8. Wilson, R. J. *et al.* Changes to the elevational limits and extent of species ranges associated with climate change. *Ecol. Lett.* **8**, 1138–1146 (2005).
9. Sinervo, B. *et al.* Erosion of lizard diversity by climate change and altered thermal niches. *Science* **328**, 894–899 (2010).
10. Chen, I.-C. *et al.* Asymmetric boundary shifts of tropical montane Lepidoptera over four decades of climate warming. *Glob. Ecol. Biogeogr.* **20**, 34–45 (2011).
11. Raxworthy, C. J. *et al.* Extinction vulnerability of tropical montane endemism from warming and upslope displacement: a preliminary appraisal for the highest massif in Madagascar. *Glob. Change Biol.* **14**, 1703–1720 (2008).
12. Pounds, J. A., Fogden, M. P. L. & Campbell, J. H. Biological response to climate change on a tropical mountain. *Nature* **398**, 611–615 (1999).
13. Pounds, J. A. *et al.* Widespread amphibian extinctions from epidemic disease driven by global warming. *Nature* **439**, 161–167 (2006).
14. Carpenter, K. E. *et al.* One-third of reef-building corals face elevated extinction risk from climate change and local impacts. *Science* **321**, 560–563 (2008).
15. Chen, I.-C., Hill, J. K., Ohlemüller, R., Roy, D. B. & Thomas, C. D. Rapid range shifts of species associated with high levels of climate warming. *Science* **333**, 1024–1026 (2011).

**Author Contributions** C.D.T. and M.W. jointly conceived and wrote the communication.

**Competing Financial Interests** Declared none.

doi:10.1038/nature10858

## He and Hubbell reply

**REPLYING TO** H. M. Pereira, L. Borda-de-Água & I. Santos Martins *Nature* **482**, doi:10.1038/nature10857; C. D. Thomas & M. Williamson *Nature* **482**, doi:10.1038/nature10858

Pereira *et al.*<sup>1</sup> argue that our conclusion<sup>2</sup> that species–area relationships (SARs) always overestimate extinction is not general because the spatial configuration of landscape destruction can influence the results.

Thomas and Williamson<sup>3</sup> argue that there are many other causes of extinction besides habitat loss. We agree with the latter comment, but show that the arguments of Pereira *et al.* are not substantiated.

# BRIEF COMMUNICATIONS ARISING

Conservation biologists make wide use of SARs to estimate species extinction caused by habitat loss. The mathematics underpinning this application is<sup>2</sup>

$$\text{EAR}(a) = \text{SAR}(A) - \text{SAR}(A - a) \quad (1)$$

where  $\text{EAR}(a)$  is the number of species endemic to subarea  $a$  that is nested within the regional area  $A$ ,  $\text{SAR}(A)$  is the total number of species in the region, and  $\text{SAR}(A - a)$  is the number of species in the complementary area  $A - a$ .

$\text{EAR}(a)$  is the number of species immediately lost if habitat area  $a$  is destroyed.  $\text{EAR}(a)$  is usually not known because data on the global distribution of species are not available. Traditionally,  $\text{EAR}(a)$  is obtained by substituting a SAR model, usually the power-law SAR model, into equation (1). However, by making this substitution, our paper<sup>2</sup> shows that one inevitably overestimates the average, or expected, extinction rate. This so-called backward SAR method is a method for estimating endemic species, not 'extinction debt'. The backward SAR method has nothing to do with, and does not measure, extinction debt. We do not question the existence of extinction debt, but to measure extinction debt it is necessary to use other methods.

There are four reasons that the arguments of Pereira *et al.* are not substantiated. First, Pereira *et al.*<sup>1</sup> commit a statistical error by confusing a specific configuration of landscape destruction with the statistical expectation. The SAR is a macroecological pattern defined as the expected number of species as a function of area. The word 'always' in the title of our paper<sup>2</sup> refers to the fact that the expectation of extinction rate is always biased too high if one uses the backward power-law SAR method. One certainly cannot trust any single specific case of the extinction rate estimated in this manner to be reliable, and our result is a general proof that shows that the average extinction rate so estimated is always an overestimate.

Second, if what Pereira *et al.* say is correct, then the outward EAR and the inward EAR must be different, but they are not different in their own analysis of the Yasuni plot (figure 2c in ref. 1), undermining their claim. The configuration of destruction can matter only to specific samples, but does not eliminate the bias we show exists in the statistical expectation. It is unclear why outward-inward destruction should be so special, versus, for example, left-to-right or up-to-down destruction. Clearly, a specific destruction pattern cannot represent the general expectation because it is just one sample of many possible patterns of destruction.

Third, Pereira *et al.* compare the SARs between the inward and outward configurations for the Barro Colorado Island (BCI) and Yasuni plots and argue that the inward EAR can be predicted by the backward SAR for the two plots because the  $z_{\text{SAR}}$  values for both configurations are similar. However, a close scrutiny of the method used to calculate these  $z$  values shows that the result is the outcome of post-hoc selected ranges of area over which they chose to fit the SARs. For the BCI plot, they used 1 ha as the minimal area, but they used a 5 ha minimum for the Yasuni plot (figure 2b, d in ref. 1). The problem is that one can obtain practically any  $z$  value by arbitrarily varying the minimal area. This is because in small areas the SAR is only approximately a power law, and including small areas when fitting the power-law SAR model inflates the  $z$  value. This arbitrary post-hoc selection

of  $z$  values invalidates their comparison. The minimum area in our study<sup>2</sup> is consistently set to be  $\geq 0.2$  ha across all plots to ensure that the analyses are standardized and comparable and that the log-log SARs are adequately linear with  $R^2 > 0.92$ . Using a consistent minimum area, one does not obtain their result.

Fourth, Pereira *et al.* argue that island SARs are more appropriate models for estimating extinction rates. This is not correct. Regardless of what you call the SAR or the reason why island SARs generally have steeper slopes than continental SARs, people use the same backwards SAR model to estimate extinction rates on continents and in island archipelagoes. In instances in which  $z$  values are not available, researchers universally use  $z = 0.25$  (refs 4, 5).

We do not disagree with Thomas and Williamson<sup>3</sup> that extinction is caused by many factors, not just habitat loss, including climate change, and we also agree that extinction is real and happening at elevated rates. All we have shown is that the backward SAR method is not appropriate for estimating extinction rates caused by habitat loss. Any extinction rates estimated from that method are questionable. We are well aware that species extinction can be evaluated by a variety of methods. Not all of the extinction estimates in the Millennium Ecosystem Assessment used the flawed backwards power-law method. We did not question or assess the validity of those methods because our study does not apply to them. We also did not criticize the methods used by the Intergovernmental Panel on Climate Change or the International Union for Conservation of Nature to estimate extinctions, contrary to misquotes in the press.

For further information, a JAVA program written by G. Acevo that computes SAR and EAR curves and expectations for model communities is available for download from <http://shubbell.eeb.ucla.edu/earsar.php>.

## Fangliang He<sup>1,2</sup> & Stephen P. Hubbell<sup>3,4</sup>

<sup>1</sup>State Key Laboratory of Biocontrol, and SYSU-Alberta Joint Lab for Biodiversity Conservation, School of Life Sciences, Sun Yat-sen University, Guangzhou 510275, China.

<sup>2</sup>Department of Renewable Resources, University of Alberta, Edmonton, Alberta, T6G 2H1, Canada.

email: [fhe@ualberta.ca](mailto:fhe@ualberta.ca)

<sup>3</sup>Department of Ecology and Evolutionary Biology, University of California, Los Angeles, California 90095, USA.

<sup>4</sup>Center for Tropical Forest Science, Smithsonian Tropical Research Institute, Unit 0948, APO AA 34002-0948, Republic of Panama.

1. Pereira, H. M., Borda-de-Água, L. & Santos Martins, I. Geometry and scale in species–area relationships. *Nature* **482**, <http://dx.doi.org/10.1038/nature10857> (2012).
2. He, F. & Hubbell, S. P. Species–area relationships always overestimate extinction rates from habitat loss. *Nature* **473**, 368–371 (2011).
3. Thomas, C. D. & Williamson, M. Extinction and climate change. *Nature* **482**, <http://dx.doi.org/10.1038/nature10858> (2012).
4. Brooks, T. & Balmford, A. Atlantic forest extinctions. *Nature* **380**, 115 (1996).
5. Thomas, C. D. *et al.* Extinction risk from climate change. *Nature* **427**, 145–148 (2004).

doi:10.1038/nature10859

# Geometry and scale in species–area relationships

ARISING FROM F. He & S. P. Hubbell *Nature* **473**, 368–371 (2011)

He and Hubbell developed a sampling theory for the species–area relationship (SAR) and the endemics–area relationship (EAR)<sup>1</sup>. They argued that the number of extinctions after habitat loss is

described by the EAR and that extinction rates in previous studies are overestimates because the EAR is always lower than the SAR. Here we show that their conclusion is not general and depends on the geometry of habitat destruction and the scale of the SAR. We also question their critique of the Millennium Ecosystem Assessment estimates, as those estimates are not dependent on the SAR only, although important uncertainties remain due to other methodological issues.

In several studies of extinction rates<sup>2–4</sup>, the proportion of extinctions after a habitat loss of area  $a$  from a total area  $A$  has been estimated from the power-law model of the SAR,  $S_{\text{SAR}}(A) = cA^z$ , as:

$$\lambda_{\text{SAR}}(a) = \frac{S_{\text{SAR}}(A) - S_{\text{SAR}}(A - a)}{S_{\text{SAR}}(A)} = 1 - \left(1 - \frac{a}{A}\right)^z \quad (1)$$

He and Hubbell call this method the backward SAR, as it uses estimates from the SAR in a backward way (from large to small areas) of how the SAR is constructed<sup>1</sup>. They argue that, instead, the number of extinctions is given by the proportion of endemics in  $a$  relative to  $A$ , which can be approximated by

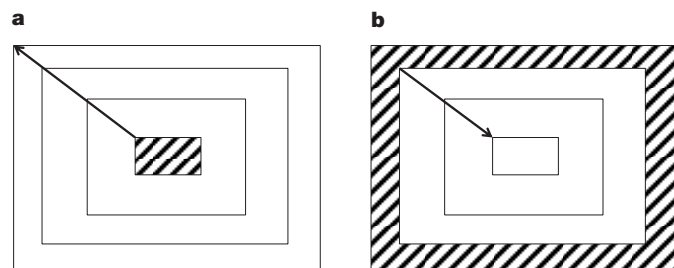


**Figure 1 | The outward EAR and the inward EAR.** **a**, The outward EAR is calculated by counting the number of the endemic species to a rectangle from the centre to the periphery. **b**, The inward EAR is calculated by counting the number of endemics to an outer ring from the periphery to the centre. It is the inward EAR that replicates the geometry of the backward SAR.

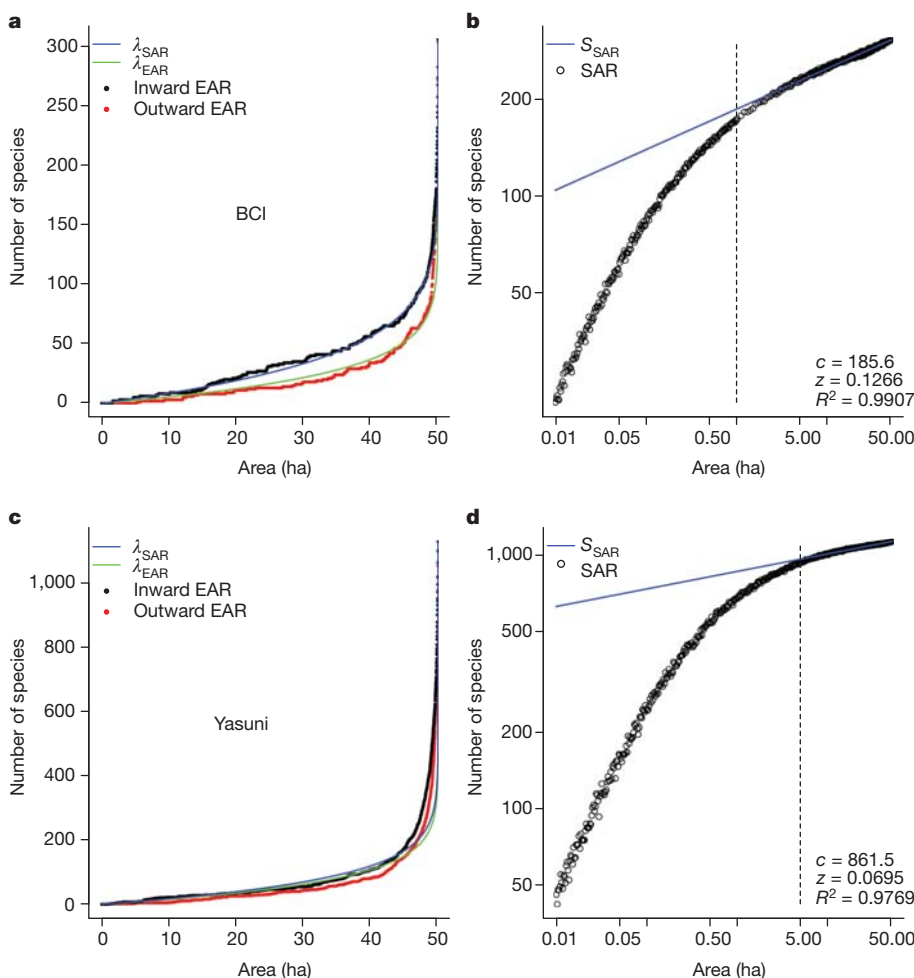


**Figure 2 | The influence of scale and geometry on the EAR and the SAR.** **a, c**, The graphs compare the outward EAR and the inward EAR with the backward SAR model ( $\lambda_{\text{SAR}}$ ) and the forward EAR model ( $\lambda_{\text{EAR}}$ ) fitted to the data of each plot. Points correspond to the value of the EAR for each area size, sampled as in Fig. 1. The  $z$  value for  $\lambda_{\text{EAR}}$  comes from He and Hubbell<sup>1</sup>, whereas the  $z$  value for the  $\lambda_{\text{SAR}}$  comes from the fit of the power law to the linear region of the SAR. **b, d**, Fit of the power-law SAR ( $S_{\text{SAR}}$ ) to the data on a log–log scale. Each point corresponds to the average number of species for randomly placed rectangles with a given area size. The SAR sampled from the centre to the periphery (Fig. 1a) gives similar  $z$  values ( $z_{\text{BCI}} = 0.1265$  and  $z_{\text{Yasuni}} = 0.0625$ ). All  $z$  values were obtained by nonlinear least squares. The dashed vertical line marks the minimum area included in the fit. The top plots are for the tree and shrub species in the 50 ha plot in Barro Colorado Island (BCI), Panama, whereas the bottom plots are for the 50 ha plot in Yasuni, Ecuador.



$$\gamma_{\text{EAR}}(a) = 1 - \left(1 - \frac{a}{A}\right)^{z'} \quad (2)$$

where  $z'$  is fit from the EAR and is always lower than the  $z$  from the SAR. The EAR is built in a forward fashion, counting the endemic species in progressively larger areas.

It is uncontroversial that the species that go extinct immediately after habitat destruction are the endemic species to the area removed<sup>5,6</sup>. However, both  $\lambda_{\text{EAR}}$  and  $\lambda_{\text{SAR}}$  describe the proportion of endemics in an area  $a$ , although of different geometry<sup>5</sup>. If destruction starts from the centre of the patch (Fig. 1a), then  $\lambda_{\text{EAR}}$  describes the number of extinctions because it approximates the proportion of endemics in progressively larger rectangles, the outward EAR (Fig. 2a). In contrast, if destruction occurs in the periphery (Fig. 1b), it is  $\lambda_{\text{SAR}}$  that describes extinctions because it approximates the number of endemics in outer rings towards the centre of the plot, the inward EAR (Fig. 2a). This happens because only the inward EAR backtracks the geometry of how the SAR is built. This backtracking is exact if the SAR is built as in Fig. 1a, or approximate if the SAR is built from sampling several rectangles for each area size, but the  $z$  values of both methods are almost the same (Fig. 2).

Note that, depending on the spatial structure of the distribution of species in the plot, the outward EAR may be similar to the inward EAR (Fig. 2c), but  $\lambda_{\text{SAR}}$  is always a good approximation of the inward EAR as long as the SAR data points fit the power law. This fit depends on the scale of the SAR. Several studies have shown that at very small scales the SAR is curvilinear in a log–log scale<sup>7</sup>, as can be observed in the Barro Colorado Island and Yasuni plots (Fig. 2b, d). Therefore, the  $z$  of the SAR must be calculated for the linear region that is relevant for the extinction projections.

There are many other sources of uncertainties in estimating future extinction rates. For instance, both the SAR and EAR project that all species go extinct after all native habitat is lost, ignoring that many species persist in human-modified habitats. The countryside SAR addresses this problem by tracking the number of species with similar habitat affinities in multiple habitats<sup>8</sup>. Another open question is what type of SAR better describes long-term extinctions after habitat loss. After a first stage of extinction of endemics, described by the EAR or the backward SAR, many species that still occur in the landscape will go extinct because the habitat left for them is smaller than their minimum required habitat size<sup>6</sup>. In this case, it has been proposed that future extinction rates are better described by the island SAR (built from counting the number of species in different islands)<sup>6</sup>.

The Millennium Ecosystem Assessment drew in a wide range of extinction projections to identify the envelope of those uncertainties<sup>9</sup>. The SAR projections<sup>2,4</sup> were consistent with estimates from other methods, such as assessing the extinction risk of currently threatened

species<sup>10,11</sup>. In 2010 there was a revised assessment with more recent global extinction projections<sup>12</sup>, in which SAR-based projections again had a limited role, and new approaches such as the overlap of species ranges with habitat loss<sup>13</sup>, ecophysiological models<sup>14</sup> and the correlation between elevational range and extinction risk, were included<sup>15</sup>. The range of uncertainty across models and scenarios was close to three orders of magnitude, compared to which the uncertainty now identified by He and Hubbell<sup>1</sup> is negligible. In all cases models and scenarios supported the Millennium Ecosystem Assessment conclusions that biodiversity will continue to decline, and in most cases at increasing rates relatively to the recent past.

**Henrique Miguel Pereira<sup>1</sup>, Luís Borda-de-Água<sup>1</sup> & Inês Santos Martins<sup>1</sup>**

<sup>1</sup>Centro de Biologia Ambiental, Faculdade de Ciências da Universidade de Lisboa, 1749-016 Lisboa, Portugal.  
email: hpereira@fc.ul.pt

Received 5 June; accepted 20 December 2011.

1. He, F. & Hubbell, S. P. Species–area relationships always overestimate extinction rates from habitat loss. *Nature* **473**, 368–371 (2011).
2. van Vuuren, D., Sala, O. & Pereira, H. M. The future of vascular plant diversity under four global scenarios. *Ecol. Soc.* **11**, 25 (2006).
3. Pimm, S. L., Russell, G. J., Gittleman, J. L. & Brooks, T. M. The future of biodiversity. *Science* **269**, 347–350 (1995).
4. Reid, W. V. in *Tropical Deforestation and Species Extinction* (eds Whitmore, T. C. & Sayer, J. A.) 53–73 (Chapman and Hall, 1992).
5. Kinzig, A. & Harte, J. Implications of endemics–area relationships for estimates of species extinctions. *Ecology* **81**, 3305–3311 (2000).
6. Rosenzweig, M. L. Loss of speciation rate will impoverish future diversity. *Proc. Natl Acad. Sci. USA* **98**, 5404–5410 (2001).
7. Dengler, J. Which function describes the species–area relationship best? A review and empirical evaluation. *J. Biogeogr.* **36**, 728–744 (2009).
8. Pereira, H. M. & Daily, G. C. Modeling biodiversity dynamics in countryside landscapes. *Ecology* **87**, 1877–1885 (2006).
9. Mace, G. M. *et al.* in *Ecosystems and Human Well-being: Current States and Trends* 77–126 (Millennium Ecosystem Assessment, 2005).
10. Mace, G. M. & Kunin, W. Classifying threatened species—means and ends. *Phil. Trans. R. Soc. B* **344**, 91–97 (1994).
11. Smith, F. D. M., May, R. M., Pellow, R., Johnson, T. H. & Walter, K. S. Estimating extinction rates. *Nature* **364**, 494–496 (1993).
12. Pereira, H. M. *et al.* Scenarios for global biodiversity in the 21st century. *Science* **330**, 1496–1501 (2010).
13. Jetz, W., Wilcove, D. S. & Dobson, A. P. Projected impacts of climate and land-use change on the global diversity of birds. *PLoS Biol.* **5**, e157 (2007).
14. Sinervo, B. *et al.* Erosion of lizard diversity by climate change and altered thermal niches. *Science* **328**, 894–899 (2010).
15. Sekercioglu, C. H., Schneider, S. H., Fay, J. P. & Loarie, S. R. Climate change, elevational range shifts, and bird extinctions. *Conserv. Biol.* **22**, 140–150 (2008).

**Author Contributions** All authors participated in the discussion of the ideas that resulted in this paper. H.M.P. wrote the paper, L.B.-d.-A. performed the data analysis, and I.S.M. prepared the data sets for analysis.

**Competing Financial Interests** Declared none.

doi:10.1038/nature10857

## Extinction and climate change

ARISING FROM F. He & S. P. Hubbell *Nature* **473**, 368–371 (2011)

Statistical relationships between habitat area and the number of species observed (species–area relationships, SARs) are sometimes used to assess extinction risks following habitat destruction or loss of climatic suitability. He and Hubbell<sup>1</sup> argue that the numbers of species confined to—rather than observed in—different areas (endemics–area relationships, EARs) should be used instead of SARs, and that SAR-based extinction estimates in the literature

are too high. We suggest that He and Hubbell's SAR estimates are biased, that the empirical data they use are not appropriate to calculate extinction risks, and that their statements about extinction risks from climate change<sup>2</sup> do not take into account non-SAR-based estimates or recent observations. Species have already responded to climate change in a manner consistent with high future extinction risks.

# BRIEF COMMUNICATIONS ARISING

Most of He and Hubbell's results involved analysis of the number of tree species in 0.2 ha and successively larger subplots within forest stands of 20–50 ha. By only counting the tree stems present in a plot (rather than canopies), they underestimate the true number of species present in small subplots. This artefact exaggerates SAR slopes when subplots smaller than ~2.5 ha are included<sup>3</sup>.

We suggest that the data He and Hubbell<sup>1</sup> use are not appropriate to calculate SAR or EAR slopes that are relevant to extinction. To calculate extinction risks, it is necessary to consider how many species might be lost if a habitat becomes isolated; however, He and Hubbell used data for forest plots that are surrounded by more forest, and for bird distributional cells that are surrounded by other land where birds also live. He and Hubbell<sup>1</sup> consider the instantaneous presence of species in sample plots within contiguous areas, not the expected long-term persistence of species if these habitats were isolated. On average, 31 species of birds bred each year in Eastern Wood in England (instantaneous number), but only 16 species bred in every one of 25 years (persistent species)<sup>4</sup>. Were this woodland completely isolated from other breeding habitats, the number of species would about halve in 25 years, resulting in much steeper SAR slopes. It is not known whether SAR and EAR estimates would steepen equally or converge for true isolates, so He and Hubbell's<sup>1</sup> main conclusion that SARs overestimate extinction remains unsubstantiated.

He and Hubbell<sup>1</sup> consider that previous<sup>2</sup> SAR-based estimates of species 'committed to extinction' from climate change (18–35% by 2050) are too high. However, most published estimates of extinction risk from climate change do not derive from SAR<sup>5</sup>. For example, it has been estimated<sup>6</sup> that "5%, 8% and 16% (mean of dispersal scenarios) of the species considered would have lost 100% of their climatically suitable area by 2050, for minimum, mid-range and maximum climate warming, respectively" and that "15%, 22% and 40%... are projected to have lost more than 90%... by 2050." Given the near-linear continuation of global warming projected before and after 2050, most species losing >90% of their climatically suitable areas over the period ~1970–2050 (and many additional species losing 70–90%) would lose 100% of their area long before 2100. With time lags in both human and climate systems, at least 15–40% of the species analysed are effectively committed to extinction by 2050.

He and Hubbell<sup>1</sup> also argue that projected extinctions exceed those observed, but high population-level extinction rates have already been observed: ~20% climate-related losses within 500 km of retreating latitudinal boundaries<sup>7</sup>, 34% loss of populated areas at retreating elevation boundaries<sup>8</sup>, and loss of an estimated 4% of worldwide lizard populations, consistent with 20% loss of lizard species by 2080<sup>9</sup>. Cloud forest moth species on Mount Kinabalu in Borneo have contracted at both lower and upper boundaries<sup>10</sup> at a rate that, if sustained, would extinguish ~45% of the endemic species by 2100. Amphibians and reptiles have shifted higher in Tsaratanana Massif in Madagascar, where three (5.9% of 51 species considered) of the highest elevation species were not found in 2003<sup>11</sup>. At Monteverde in Costa Rica, two high elevation anole lizard species became extinct from the study area,

and two high elevation frog/toad species became globally extinct, after dry years<sup>12</sup>. The pathogen-induced extinction of ~2.2% of New World amphibian species (harlequin frogs) coincided with unusually hot years<sup>13</sup>. A third of the world's coral species are threatened by a combination of temperature-induced bleaching, ocean acidification and other pressures<sup>14</sup>.

Anthropogenic warming so far is less than or equal to half of that expected by 2050, and modelled biodiversity losses accelerate with increased warming. Recently observed range shifts have tracked levels of climate change<sup>15</sup>, and these empirical trends are concordant with projected 2050/2100 losses. Although many uncertainties remain, we believe that He and Hubbell's conclusions about extinction risks are unjustified.

**Chris D. Thomas<sup>1</sup> & Mark Williamson<sup>1</sup>**

<sup>1</sup>Department of Biology, University of York, Heslington, York, YO10 5DD, UK.

email: chris.thomas@york.ac.uk

**Received 14 June; accepted 20 December 2011.**

1. He, F. & Hubbell, S. P. Species–area relationships always overestimate extinction rates from habitat loss. *Nature* **473**, 368–371 (2011).
2. Thomas, C. D. *et al.* Extinction risk from climate change. *Nature* **427**, 145–148 (2004).
3. Williamson, M. Species–area relationships at small scales in continuum vegetation. *J. Ecol.* **91**, 904–907 (2003).
4. Williamson, M. *Island Populations* (Oxford Univ. Press, 1981).
5. Maclean, I. M. D. & Wilson, R. J. Recent ecological responses to climate change support predictions of high extinction risk. *Proc. Natl Acad. Sci. USA* **108**, 12337–12342 (2011).
6. Thomas, C. D. *et al.* Biodiversity conservation: Uncertainty in predictions of extinction risk/Effects of changes in climate and land use/Climate change and extinction risk (reply). *Nature* **430**, <http://dx.doi.org/10.1038/nature02719> (2004).
7. Franco, A. M. A. *et al.* Impacts of climate warming and habitat loss on extinctions at species' low-latitude range boundaries. *Glob. Change Biol.* **12**, 1545–1553 (2006).
8. Wilson, R. J. *et al.* Changes to the elevational limits and extent of species ranges associated with climate change. *Ecol. Lett.* **8**, 1138–1146 (2005).
9. Sinervo, B. *et al.* Erosion of lizard diversity by climate change and altered thermal niches. *Science* **328**, 894–899 (2010).
10. Chen, I.-C. *et al.* Asymmetric boundary shifts of tropical montane Lepidoptera over four decades of climate warming. *Glob. Ecol. Biogeogr.* **20**, 34–45 (2011).
11. Raxworthy, C. J. *et al.* Extinction vulnerability of tropical montane endemism from warming and upslope displacement: a preliminary appraisal for the highest massif in Madagascar. *Glob. Change Biol.* **14**, 1703–1720 (2008).
12. Pounds, J. A., Fogden, M. P. L. & Campbell, J. H. Biological response to climate change on a tropical mountain. *Nature* **398**, 611–615 (1999).
13. Pounds, J. A. *et al.* Widespread amphibian extinctions from epidemic disease driven by global warming. *Nature* **439**, 161–167 (2006).
14. Carpenter, K. E. *et al.* One-third of reef-building corals face elevated extinction risk from climate change and local impacts. *Science* **321**, 560–563 (2008).
15. Chen, I.-C., Hill, J. K., Ohlemüller, R., Roy, D. B. & Thomas, C. D. Rapid range shifts of species associated with high levels of climate warming. *Science* **333**, 1024–1026 (2011).

**Author Contributions** C.D.T. and M.W. jointly conceived and wrote the communication.

**Competing Financial Interests** Declared none.

doi:10.1038/nature10858

## He and Hubbell reply

**REPLYING TO** H. M. Pereira, L. Borda-de-Água & I. Santos Martins *Nature* **482**, doi:10.1038/nature10857; C. D. Thomas & M. Williamson *Nature* **482**, doi:10.1038/nature10858

Pereira *et al.*<sup>1</sup> argue that our conclusion<sup>2</sup> that species–area relationships (SARs) always overestimate extinction is not general because the spatial configuration of landscape destruction can influence the results.

Thomas and Williamson<sup>3</sup> argue that there are many other causes of extinction besides habitat loss. We agree with the latter comment, but show that the arguments of Pereira *et al.* are not substantiated.

# BRIEF COMMUNICATIONS ARISING

Conservation biologists make wide use of SARs to estimate species extinction caused by habitat loss. The mathematics underpinning this application is<sup>2</sup>

$$\text{EAR}(a) = \text{SAR}(A) - \text{SAR}(A - a) \quad (1)$$

where  $\text{EAR}(a)$  is the number of species endemic to subarea  $a$  that is nested within the regional area  $A$ ,  $\text{SAR}(A)$  is the total number of species in the region, and  $\text{SAR}(A - a)$  is the number of species in the complementary area  $A - a$ .

$\text{EAR}(a)$  is the number of species immediately lost if habitat area  $a$  is destroyed.  $\text{EAR}(a)$  is usually not known because data on the global distribution of species are not available. Traditionally,  $\text{EAR}(a)$  is obtained by substituting a SAR model, usually the power-law SAR model, into equation (1). However, by making this substitution, our paper<sup>2</sup> shows that one inevitably overestimates the average, or expected, extinction rate. This so-called backward SAR method is a method for estimating endemic species, not 'extinction debt'. The backward SAR method has nothing to do with, and does not measure, extinction debt. We do not question the existence of extinction debt, but to measure extinction debt it is necessary to use other methods.

There are four reasons that the arguments of Pereira *et al.* are not substantiated. First, Pereira *et al.*<sup>1</sup> commit a statistical error by confusing a specific configuration of landscape destruction with the statistical expectation. The SAR is a macroecological pattern defined as the expected number of species as a function of area. The word 'always' in the title of our paper<sup>2</sup> refers to the fact that the expectation of extinction rate is always biased too high if one uses the backward power-law SAR method. One certainly cannot trust any single specific case of the extinction rate estimated in this manner to be reliable, and our result is a general proof that shows that the average extinction rate so estimated is always an overestimate.

Second, if what Pereira *et al.* say is correct, then the outward EAR and the inward EAR must be different, but they are not different in their own analysis of the Yasuni plot (figure 2c in ref. 1), undermining their claim. The configuration of destruction can matter only to specific samples, but does not eliminate the bias we show exists in the statistical expectation. It is unclear why outward-inward destruction should be so special, versus, for example, left-to-right or up-to-down destruction. Clearly, a specific destruction pattern cannot represent the general expectation because it is just one sample of many possible patterns of destruction.

Third, Pereira *et al.* compare the SARs between the inward and outward configurations for the Barro Colorado Island (BCI) and Yasuni plots and argue that the inward EAR can be predicted by the backward SAR for the two plots because the  $z_{\text{SAR}}$  values for both configurations are similar. However, a close scrutiny of the method used to calculate these  $z$  values shows that the result is the outcome of post-hoc selected ranges of area over which they chose to fit the SARs. For the BCI plot, they used 1 ha as the minimal area, but they used a 5 ha minimum for the Yasuni plot (figure 2b, d in ref. 1). The problem is that one can obtain practically any  $z$  value by arbitrarily varying the minimal area. This is because in small areas the SAR is only approximately a power law, and including small areas when fitting the power-law SAR model inflates the  $z$  value. This arbitrary post-hoc selection

of  $z$  values invalidates their comparison. The minimum area in our study<sup>2</sup> is consistently set to be  $\geq 0.2$  ha across all plots to ensure that the analyses are standardized and comparable and that the log-log SARs are adequately linear with  $R^2 > 0.92$ . Using a consistent minimum area, one does not obtain their result.

Fourth, Pereira *et al.* argue that island SARs are more appropriate models for estimating extinction rates. This is not correct. Regardless of what you call the SAR or the reason why island SARs generally have steeper slopes than continental SARs, people use the same backwards SAR model to estimate extinction rates on continents and in island archipelagoes. In instances in which  $z$  values are not available, researchers universally use  $z = 0.25$  (refs 4, 5).

We do not disagree with Thomas and Williamson<sup>3</sup> that extinction is caused by many factors, not just habitat loss, including climate change, and we also agree that extinction is real and happening at elevated rates. All we have shown is that the backward SAR method is not appropriate for estimating extinction rates caused by habitat loss. Any extinction rates estimated from that method are questionable. We are well aware that species extinction can be evaluated by a variety of methods. Not all of the extinction estimates in the Millennium Ecosystem Assessment used the flawed backwards power-law method. We did not question or assess the validity of those methods because our study does not apply to them. We also did not criticize the methods used by the Intergovernmental Panel on Climate Change or the International Union for Conservation of Nature to estimate extinctions, contrary to misquotes in the press.

For further information, a JAVA program written by G. Acevo that computes SAR and EAR curves and expectations for model communities is available for download from <http://shubbell.eeb.ucla.edu/earsar.php>.

## Fangliang He<sup>1,2</sup> & Stephen P. Hubbell<sup>3,4</sup>

<sup>1</sup>State Key Laboratory of Biocontrol, and SYSU-Alberta Joint Lab for Biodiversity Conservation, School of Life Sciences, Sun Yat-sen University, Guangzhou 510275, China.

<sup>2</sup>Department of Renewable Resources, University of Alberta, Edmonton, Alberta, T6G 2H1, Canada.

email: [fhe@ualberta.ca](mailto:fhe@ualberta.ca)

<sup>3</sup>Department of Ecology and Evolutionary Biology, University of California, Los Angeles, California 90095, USA.

<sup>4</sup>Center for Tropical Forest Science, Smithsonian Tropical Research Institute, Unit 0948, APO AA 34002-0948, Republic of Panama.

1. Pereira, H. M., Borda-de-Água, L. & Santos Martins, I. Geometry and scale in species–area relationships. *Nature* **482**, <http://dx.doi.org/10.1038/nature10857> (2012).
2. He, F. & Hubbell, S. P. Species–area relationships always overestimate extinction rates from habitat loss. *Nature* **473**, 368–371 (2011).
3. Thomas, C. D. & Williamson, M. Extinction and climate change. *Nature* **482**, <http://dx.doi.org/10.1038/nature10858> (2012).
4. Brooks, T. & Balmford, A. Atlantic forest extinctions. *Nature* **380**, 115 (1996).
5. Thomas, C. D. *et al.* Extinction risk from climate change. *Nature* **427**, 145–148 (2004).

doi:10.1038/nature10859



# Opposite effects of fear conditioning and extinction on dendritic spine remodelling

Cora Sau Wan Lai<sup>1</sup>, Thomas F. Franke<sup>2</sup> & Wen-Biao Gan<sup>1</sup>

It is generally believed that fear extinction is a form of new learning that inhibits rather than erases previously acquired fear memories<sup>1–3</sup>. Although this view has gained much support from behavioural and electrophysiological studies<sup>1–10</sup>, the hypothesis that extinction causes the partial erasure of fear memories remains viable. Using transcranial two-photon microscopy<sup>11,12</sup>, we investigated how neural circuits are modified by fear learning and extinction by examining the formation and elimination of postsynaptic dendritic spines of layer-V pyramidal neurons in the mouse frontal association cortex. Here we show that fear conditioning by pairing an auditory cue with a footshock increases the rate of spine elimination. By contrast, fear extinction by repeated presentation of the same auditory cue without a footshock increases the rate of spine formation. The degrees of spine remodelling induced by fear conditioning and extinction strongly correlate with the expression and extinction of conditioned fear responses, respectively. Notably, spine elimination and formation induced by fear conditioning and extinction occur on the same dendritic branches in a cue- and location-specific manner: cue-specific extinction causes formation of dendritic spines within a distance of two micrometres from spines that were eliminated after fear conditioning. Furthermore, reconditioning preferentially induces elimination of dendritic spines that were formed after extinction. Thus, within vastly complex neuronal networks, fear conditioning, extinction and reconditioning lead to opposing changes at the level of individual synapses. These findings also suggest that fear memory traces are partially erased after extinction.

Classical fear conditioning is widely used to study associative learning in which a conditioned neutral stimulus (CS; for example an auditory cue) is paired with the presentation of an unconditioned aversive stimulus (US; for example a footshock) to elicit a conditioned response<sup>13</sup> (CR; for example a freezing response to CS in the absence of US). Repeated exposures to CS diminish the expression of the CR, a process called extinction<sup>1–3</sup>. It is widely believed that fear extinction involves new learning of the 'safe' association between CS and the absence of US, rather than an erasure of the original CS–US association<sup>1–3</sup>. This theory is supported by behavioural studies of spontaneous recovery, renewal and reinstatement of fear memory after extinction<sup>1–6</sup>. Furthermore, fear conditioning and extinction regulate activities of non-overlapping neuronal populations in the amygdala, hippocampus and frontolimbic cortex<sup>7–10</sup>. Although these behavioural and electrophysiological studies suggest that fear memories are stored in different circuits from extinction memories, they do not exclude the possibility that extinction may cause a partial erasure of fear memory traces. In support of the second view, it has been found that spontaneous recovery of fear memories is minimal after extinction training in young animals<sup>14</sup>. Furthermore, fear conditioning and extinction are accompanied by an increase or decrease in synaptic activity in amygdala<sup>15</sup> and in the expression level of signalling molecules involved in memory formation<sup>16–18</sup>.

To investigate how fear conditioning and extinction affect synaptic circuits to result in opposite behavioural responses, we used transcranial

two-photon microscopy to examine the formation and elimination of postsynaptic dendritic spines of layer-V pyramidal neurons in the dorsal medial region of the frontal association cortex<sup>11,12,19</sup> (FrA; Fig. 1a). We chose FrA to investigate synaptic changes associated with fear conditioning and extinction for the following reasons. First, consistent with previous reports in rats<sup>20,21</sup>, we observed reciprocal connections between the mouse FrA and amygdala (Fig. 1b, c and Supplementary Figs 1 and 2), suggesting that this cortical region interacts directly with the amygdala to participate in fear learning and extinction. Second, consistent with findings in rats that FrA is important for fear memory consolidation<sup>22</sup>, we found that after fear conditioning or extinction, inactivation of the mouse FrA by muscimol injection impaired the consolidation of fear and extinction memories (Supplementary Fig. 3). Lastly, unlike prelimbic and infralimbic regions that are important for fear expression and extinction but located deep in the brain<sup>7,8,23</sup>, FrA is accessible for *in vivo* two-photon imaging of dendritic spine plasticity.

Using two-photon microscopy and YFP-expressing transgenic mice<sup>11,12</sup>, we first examined whether fear conditioning affected spine formation and elimination over 48 h in FrA (Fig. 1d, f). In these experiments, one-month-old mice were imaged and then subjected to one of four stimulus conditions: three tones each paired with a co-terminating footshock; three tones each temporally unpaired from a footshock; three tones only; or three footshocks only. Forty-eight hours after fear conditioning, we put mice through a tone-cued recall test to assess conditioned freezing responses, followed by a second imaging session to examine spine dynamics. We found that only the CS–US paired group, but none of the other groups, showed robust freezing responses during the recall test ( $F_{(3,16)} = 18.689$ ,  $P < 0.001$ ; Fig. 1e). Notably, only the paired group showed a significant increase in spine elimination after 48 h when compared with the unpaired, tone-only or shock-only groups ( $17.4 \pm 2.3\%$  versus  $9.7 \pm 1.9\%$ ,  $10.1 \pm 1.1\%$  or  $10.0\% \pm 1.3\%$ , respectively;  $F_{(3,16)} = 24.569$ ,  $P < 0.001$ ; Fig. 1f; see also Supplementary Fig. 4). We did not observe a significant difference in spine formation among the four groups ( $F_{(3,16)} = 0.164$ ,  $P > 0.9$ ; Fig. 1f and Supplementary Fig. 4). There were also no significant differences in the formation and elimination rates of dendritic filopodia, that is, precursors of dendritic spines<sup>24</sup>, among different groups (Supplementary Fig. 5). These results indicate that fear conditioning by CS–US association causes dendritic spine elimination over 2 d in FrA.

To investigate the impact of fear conditioning further, we examined freezing responses and spine dynamics in the paired and unpaired groups 9 d after conditioning. A recall test showed that mice subjected to the paired CS–US stimuli showed a higher level of conditioned freezing responses than mice exposed to the unpaired CS–US stimuli ( $P < 0.001$ ; Fig. 1g). Furthermore, spine elimination over 9 d was significantly higher in the paired group than in the unpaired control group ( $P < 0.05$ ; Fig. 1h). No significant differences in spine formation were observed between the two groups ( $P > 0.05$ ; Fig. 1h). Thus, spine elimination induced by fear conditioning represents a long-lasting synaptic change in FrA. In addition, we found a significant increase in spine elimination but not formation as early as 24 h after fear

<sup>1</sup>Molecular Neurobiology Program, Skirball Institute, Department of Physiology and Neuroscience, New York University School of Medicine, 540 First Avenue, New York, New York 10016, USA.

<sup>2</sup>Departments of Psychiatry and Pharmacology, New York University School of Medicine, 550 First Avenue, New York, New York 10016, USA.

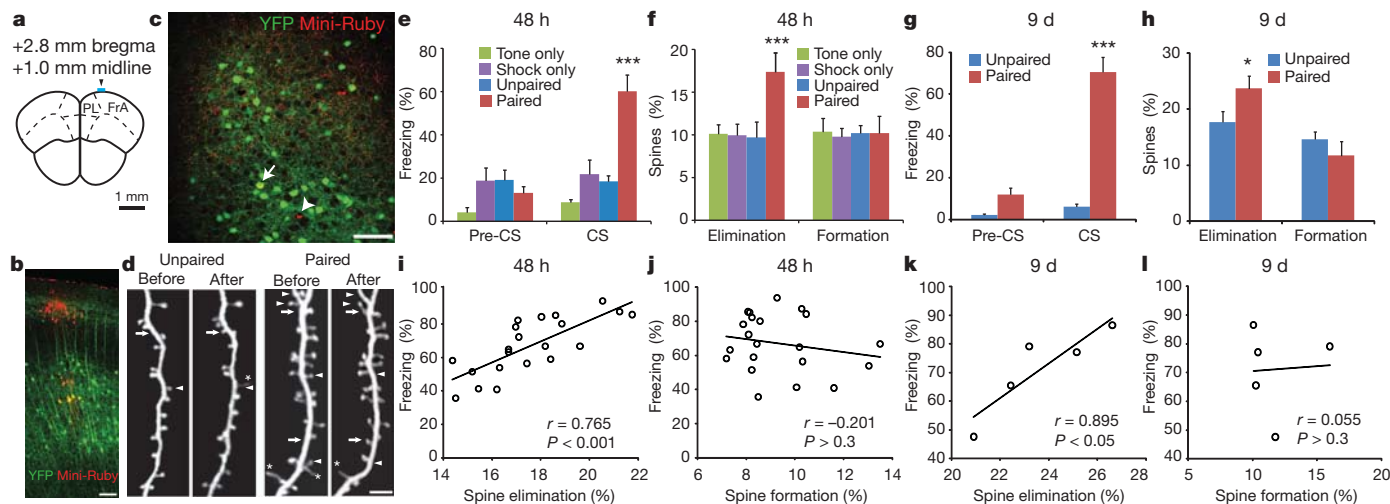


**Figure 1 | Fear conditioning causes spine elimination.** **a**, Diagram of a coronal section of frontal association cortex (FrA) showing the imaging site (cyan bar). PL, prelimbic cortex. **b**, **c**, Neurons labelled with Mini-Ruby dye (**b**, red) in FrA have extensive axonal arborizations in amygdala (**c**, red). The arrow and arrowhead in **c** respectively indicate yellow fluorescent protein (YFP)-positive and -negative neuronal soma labelled with Mini-Ruby in amygdala (see also Supplementary Fig. 1). **d**, Representative images of dendrites before and after conditioning in the unpaired and paired groups. Arrows and arrowheads indicate spine formation and elimination, respectively. Asterisks mark filopodia. **e**, Percentage of freezing in different groups before and during

CS presentation 48 h after conditioning. **f**, Percentage of spine elimination and formation 48 h after conditioning ( $n = 5$  for each group). Only the paired group showed an increase in freezing response (**e**) and spine elimination (**f**). **g**, Freezing responses of the paired and unpaired groups 9 d after conditioning. **h**, Percentage of spine elimination and formation over 9 d. (Unpaired,  $n = 4$ ; paired,  $n = 5$ ). **i–l** Freezing response correlated with spine elimination but not formation over either 48 h (**i**, **j**) or 9 d (**k**, **l**). Each circle in **i–l** represents an animal. \*\*\* $P < 0.001$ , \* $P < 0.05$ . Data show mean  $\pm$  s.e.m. (**e**, **g**) or mean  $\pm$  s.d. (**f**, **h**). Scale bars: 100  $\mu$ m (**b**, **c**); 4  $\mu$ m (**d**).

conditioning in FrA (Supplementary Fig. 6a). However, no significant increases in dendritic spine elimination or formation were observed 24 h after fear conditioning in the barrel cortex (Supplementary Fig. 6b). Together, these results indicate that fear conditioning causes rapid and long-lasting spine elimination in FrA, but not in all cortical regions.

Notably, we observed that, 48 h after fear conditioning, the percentage of spine elimination correlated significantly with the degree of freezing responses to CS ( $r = 0.765$  (correlation coefficient),  $P < 0.001$ ; Fig. 1i). By contrast, there was no significant correlation between the degree of spine formation and freezing responses ( $r = -0.201$ ,  $P > 0.3$ ; Fig. 1j). Furthermore, 9 d after training, freezing responses in the paired group correlated significantly with spine elimination ( $r = 0.895$ ,  $P < 0.05$ ; Fig. 1k) but not spine formation ( $r = 0.055$ ,  $P > 0.3$ ; Fig. 1l). These findings suggest that spine elimination induced by fear conditioning represents an important synaptic change that strongly predicts the conditioned freezing response.

To determine whether fear extinction affects spine dynamics, we subjected mice to fear conditioning as before, followed by 2 d of extinction training through repeated presentation of CS in the absence of footshocks (five trials per day) (Fig. 2a). Dendritic spines in FrA were imaged before and after extinction training, and spine dynamics were compared between fear-conditioned mice with and without extinction. Consistent with the reported effectiveness of our extinction protocol<sup>7</sup>, the conditioned freezing response was significantly reduced in the extinction group ( $P < 0.001$ ) but not in the no-extinction group ( $P > 0.3$ ; Fig. 2b). After 2 d of extinction, we found that spine formation was significantly higher in the extinction group than in the no-extinction group ( $16.5 \pm 2.6\%$  versus  $8.3 \pm 1.2\%$ ,  $P < 0.001$ ; Fig. 2c). By contrast, no significant difference in spine elimination was observed after extinction ( $P > 0.2$ ; Fig. 2c). There were also no significant differences in the formation and elimination rates of dendritic filopodia after extinction (Supplementary Fig. 7). Notably, the freezing response to CS after extinction showed a significant inverse correlation with spine formation ( $r = -0.809$ ,  $P < 0.01$ ; Fig. 2d) but not with spine elimination ( $r = -0.250$ ,  $P > 0.4$ ; Fig. 2e). Thus, by contrast with fear conditioning, extinction induces new spine formation, the degree of which predicts the effectiveness of extinction training in reducing conditioned freezing responses.

A recent study has shown that a fraction of new spines induced by novel sensory and motor learning experiences persist over months<sup>12</sup>. To determine whether new spines induced by extinction are long lasting, we subjected mice to fear conditioning followed by extinction training as described above. On day 12, 7 d after extinction training, we performed a recall test to assess the extinction memory and then re-imaged mice to determine the persistence of spines formed over the 2-d extinction training (Fig. 2a). We found that the acquired extinction memory was intact 7 d after extinction training (Fig. 2f). Furthermore, the percentage of new spines persisting until day 12 was inversely correlated with the freezing response to the CS ( $r = -0.899$ ,  $P < 0.05$ ; Fig. 2g). Thus, long-lasting new spines induced by extinction training may contribute to the preservation of the extinction memory.

Our results so far indicate that fear conditioning predominantly promotes spine elimination whereas extinction mainly induces spine formation. To determine whether fear conditioning and extinction cause spine remodelling on the same or different dendritic branches, we measured the percentage of spine elimination after fear conditioning and the percentage of spine formation after extinction along individual dendritic branches 15–50  $\mu$ m in length (average length,  $27.6 \pm 9.3 \mu$ m). We found that the percentage of spine elimination after fear conditioning positively correlated with the percentage of spine formation after extinction ('CS/tone-A extinction';  $n = 6$  mice, 40 branches,  $r = 0.458$ ,  $P < 0.01$ ; Fig. 3b, e). By contrast, no significant correlation was observed in the no-extinction group ( $n = 5$  mice, 25 branches,  $r = 0.240$ ,  $P > 0.2$ ; Fig. 3a, d). Furthermore, when a different cue (tone B) was presented repeatedly instead of the cue originally used for fear conditioning (tone A), no significant correlation was observed between spine elimination and formation ('tone B';  $n = 5$  mice, 41 branches,  $r = 0.231$ ,  $P > 0.1$ ; Fig. 3c, f). These results suggest that cue-specific extinction induces spine formation on the dendritic branches on which fear conditioning previously caused spine elimination.

Further to understand how fear conditioning and extinction impact synaptic connectivity on the same dendritic branches, we measured the distance between the site of conditioning-induced spine elimination and the closest site of extinction-induced spine formation. In the extinction group,  $57.3 \pm 5.5\%$  of extinction-induced new spines were located within 2  $\mu$ m of either side of a spine that had previously been

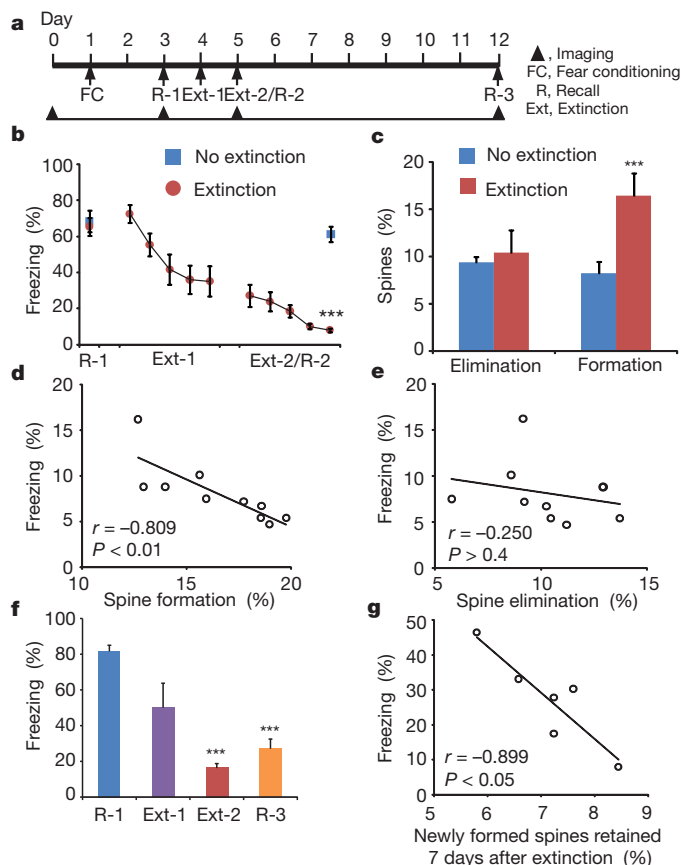


**Figure 2 | Fear extinction induces spine formation.** **a**, Timeline of experimental manipulations and imaging. **b**, Percentage of freezing during the recall test and extinction training. Freezing in the extinction group ( $n = 10$ ) was lower than the no-extinction group ( $n = 5$ ,  $P < 0.001$ ). **c**, Extinction significantly increased spine formation ( $P < 0.001$ ). **d**, **e**, Percentage of freezing after extinction was inversely correlated with spine formation (**d**) but not elimination (**e**). Extinction training was performed on two consecutive days (Ext-1 and Ext-2). Freezing in the last trial of Ext-2 in **b** was plotted in **d** and **e**. **f**, Percentage of freezing in the recall tests and during the last trials of extinction on days 4 and 5. Decreased freezing after extinction persisted for 7 d as shown in the recall test (R-3). There was no significant difference in freezing between the last trial of Ext-2 and R-3 ( $n = 6$ ,  $P > 0.1$ ). **g**, New spines induced by extinction and persisting on day 7 inversely correlated with freezing response. \*\*\* $P < 0.001$ . Data show mean  $\pm$  s.e.m. (**b**, **f**) or mean  $\pm$  s.d. (**c**).

eliminated after conditioning. In the groups that did not undergo extinction or were exposed to tone B instead of the conditioned stimulus (CS/tone A), only  $24.9 \pm 1.4\%$  or  $24.4 \pm 4.9\%$  of new spines, respectively, were formed within  $2 \mu\text{m}$  of spines previously eliminated by conditioning (Fig. 3g). Moreover, within a distance of  $2 \mu\text{m}$  from sites of spine elimination,  $\sim 80\%$  of newly formed spines in all groups were oriented within  $90^\circ$  of previously eliminated spines. Beyond  $2 \mu\text{m}$ , the likelihood of newly formed spines being oriented within  $90^\circ$  of previously eliminated spines decreased to chance levels ( $\sim 50\%$ ) (Fig. 3h). These results indicate that after extinction training, new spines tend to form within close proximity and orient in the same direction as spines that were eliminated after fear conditioning. Furthermore, we estimated that the number of presynaptic boutons available for a synaptic contact with a spine that is  $2 \mu\text{m}$  long and located along a  $4\text{-}\mu\text{m}$  dendritic segment is  $\sim 32$  (Supplementary Information, section 1). When considering that new spines tend to be oriented in the same direction as previously eliminated spines, our results indicate that there could be a  $\sim 1/16$  chance that new spines will contact the same synaptic boutons as previously eliminated spines.

So far, our data have indicated that extinction with the US-associated conditioned stimulus (tone A), but not with an unconditioned stimulus

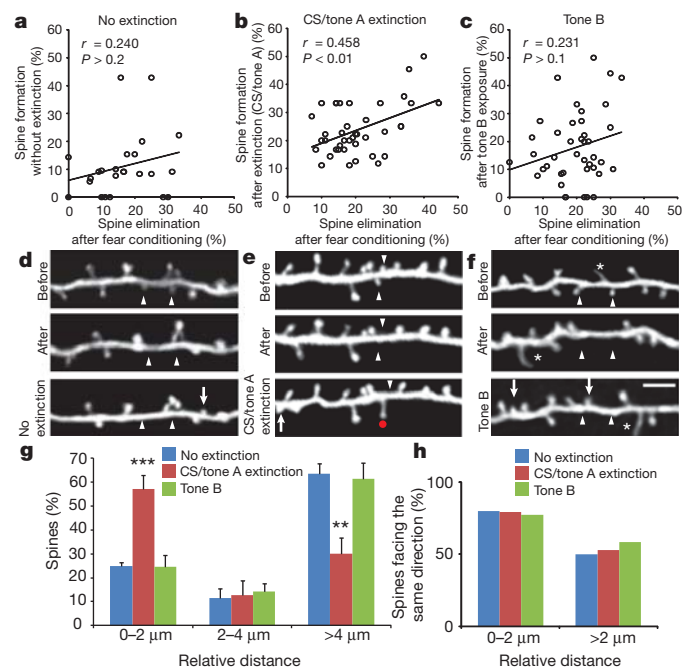


**Figure 3 | Fear conditioning and extinction cause location-specific spine remodelling.** **a–c**, Correlations between spine elimination 48 h after fear conditioning and spine formation on individual dendritic branches under the following three conditions: no extinction training (**a**); after extinction training using the conditioned tone (**b**); after repeated exposure to a novel tone (**c**). **d–f**, Representative images of dendritic branches taken before and after conditioning from the three groups. Arrowheads mark sites of spine elimination induced by conditioning. Arrows mark sites of newly formed spines under the three conditions. The red dot in **e** marks a new spine formed after extinction and located within  $2 \mu\text{m}$  of a spine previously eliminated after conditioning. Asterisks mark filopodia. Scale bar in **f**,  $4 \mu\text{m}$ . **g**, Spine distribution graph depicting the relative distance between sites of spine elimination induced by conditioning and the respective closest sites of spine formation under the three conditions. **h**, Percentage of newly formed spines facing the same direction as previously eliminated spines (oriented within  $90^\circ$  relative to the eliminated spines). \*\*\* $P < 0.001$ , \*\* $P < 0.01$ . Data show mean  $\pm$  s.e.m. (**g**).

(tone B), induces spine formation in close proximity to spines that were eliminated after fear conditioning. Further to investigate the cue specificity and location specificity of extinction-induced spine formation, we fear-conditioned mice to tone A (CS1) and tone B (CS2) in two consecutive training sessions using three pairings of CS1 with US and CS2 with US (Fig. 4a). Eliminated spines induced by CS1–US or CS2–US pairings were identified separately over 4 d. In recall tests on day 2 (R-1) and day 4 (R-2), mice showed freezing responses to both CS1 and CS2. We then subjected mice to extinction training with CS2 for another 2 d and newly formed spines induced by extinction were identified (Fig. 4a). On day 7, after CS2 extinction, mice showed a low freezing response to CS2 but a high freezing response to CS1, demonstrating the cue specificity of our extinction training (Fig. 4b). Consistent with our results in Figs 1 and 2, fear conditioning with both CS1 and CS2 increased spine elimination whereas extinction with CS2 promoted spine formation (Fig. 4c). Notably, a significantly larger population of newly formed spines induced by extinction with CS2 were located within  $2 \mu\text{m}$  of spines that were eliminated by CS2–US ('CS2 elim/CS2 form') than by CS1–US ('CS1 elim/CS2 form') ( $45.9 \pm 7.3\%$  versus  $26.6 \pm 3.8\%$ ,  $P < 0.05$ ; Fig. 4d). These findings indicate that extinction training with a specific auditory cue induces spine formation in close proximity to spines previously eliminated after fear conditioning against the same cue.

Further to investigate the cue and location specificity of opposing synaptic changes after fear conditioning and extinction, we tested



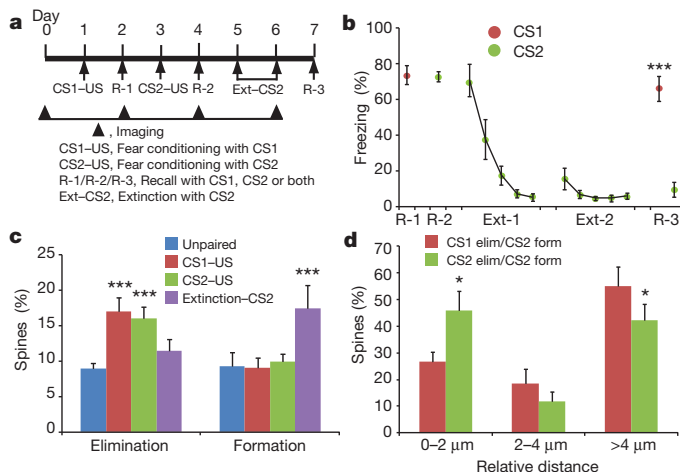


**Figure 4 | Extinction induces spine formation in a cue- and location-specific manner.** **a**, Timeline of experimental manipulations and imaging. **b**, Percentage of freezing during the recall test and extinction. After extinction with CS2, mice showed a lower freezing response to CS2 than to CS1 on day 7 ( $P < 0.001$ ). **c**, Conditioning to either CS1 or CS2 increased spine elimination when compared with unpaired controls ( $P < 0.001$ ). Extinction with CS2 increased spine formation when compared with the unpaired controls, CS1-US or CS2-US ( $F_{(3,16)} = 18.540$ ,  $P < 0.001$ ). **d**, Spine distribution graph depicting the relative distance between new spines induced by CS2 extinction and eliminated spines induced by CS1-US or CS2-US. A significantly larger population of new spines induced by CS2 extinction were located within 2 μm of spines previously eliminated by CS2-US than were located within 2 μm of spines previously eliminated by CS1-US ( $n = 5$  mice, 36 branches, 74 spines,  $P < 0.05$ ). \*\*\* $P < 0.001$ , \* $P < 0.05$ . Data show mean  $\pm$  s.e.m. (**b**, **d**) or mean  $\pm$  s.d. (**c**).

whether new spines induced by extinction are selectively eliminated in a cue-specific manner after reconditioning. In this experiment, we first subjected mice to fear conditioning and extinction, and then reconditioned them by re-exposure to five CS1-US (CS1/tone A) pairings on days 5 and 6 (Fig. 5a). As control groups, mice were either subjected to five temporally unpaired presentations of CS1 and US stimuli or conditioned with five pairings of CS2-US pairings (CS2/tone B) on days 5 and 6 (Fig. 5a–d). Recall tests showed a significant increase of the freezing response to CS1 in the reconditioning group when compared with the unpaired group or the group conditioned with CS2-US ( $P < 0.01$ ; Fig. 5e). We next compared the respective persistences of newly formed spines located within 2 μm or more than 2 μm from previously eliminated spines in the three groups. The persistence of extinction-induced new spines within the 2-μm boundaries in the reconditioning group ( $11.1 \pm 1.8\%$ ) was significantly lower than that in the unpaired or CS2-US conditioned groups ( $32.0 \pm 6.2\%$  and  $35.2 \pm 11.3\%$ , respectively) ( $P < 0.05$ ). There was no significant difference in the persistence of spines formed outside the 2-μm boundary among the three groups ( $P > 0.6$ ; Fig. 5f). Thus, fear reconditioning opposes the effects of extinction on synaptic remodelling with high anatomical and cue specificity.

It is well accepted that synaptic reorganization is critical for learning and memory<sup>12,13</sup>. However, it is unclear how synaptic circuits are modified by opposing forms of learning and how such modifications contribute to opposite behavioural outcomes. Our studies indicate that fear conditioning, extinction and reconditioning cause opposing synaptic modifications on the same dendritic branches in a cue- and location-specific manner. These findings also suggest that extinction induces at least partial erasure of fear memory traces in FrA. FrA in rodents has reciprocal connections with multiple brain areas including the amygdala<sup>20,21</sup>, and its inactivation impairs fear learning and extinction<sup>22</sup> (Fig. 1b, c and Supplementary Figs 1–3), suggesting that this region is directly involved in modulating freezing behaviours. Future investigations are needed to understand the mechanisms underlying

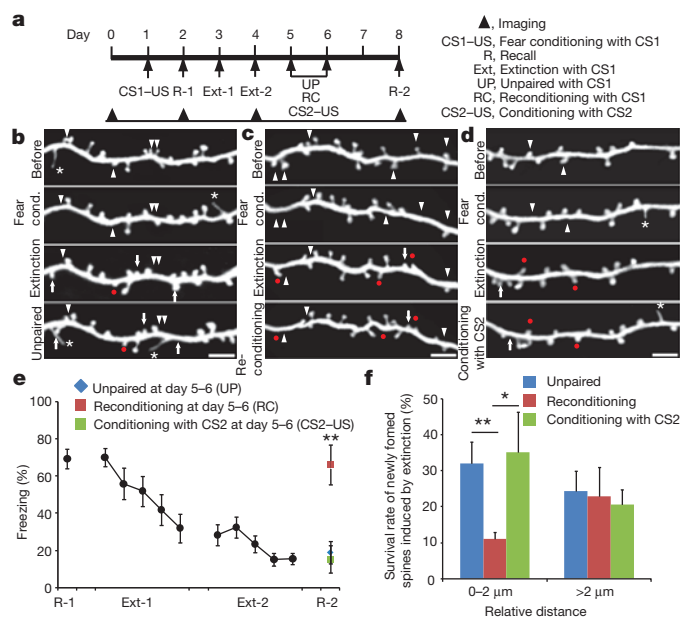


**Figure 5 | Reconditioning eliminates spines formed during extinction.** **a**, Timeline of experimental manipulations and imaging. **b–d**, Representative images before and after fear conditioning, after extinction and after presentation of the unpaired stimuli (**b**), after reconditioning to CS1 (**c**) or after new conditioning to CS2 (**d**). Arrowheads mark sites of spine elimination after fear conditioning. Arrows and red dots mark new spines that were formed after extinction and located more than 2 μm (arrows) and within 2 μm distance (red dots) from previously eliminated spines after conditioning. Asterisks mark filopodia. Scale bar, 4 μm. **e**, Reconditioning (RC) increased freezing by comparison with unpaired stimuli (UP) or new conditioning to CS2 (CS2-US) during recall test R-2 with CS1 (\*\* $P < 0.01$ ). **f**, The survival rate of new spines induced by extinction training and located within 2 μm of previously eliminated spines was significantly lower after RC-CS1 (54 branches, 107 total new spines) than after UP (58 branches, 107 total new spines) or CS2-US (54 branches, 94 total new spines) (\*\* $P < 0.01$ , \* $P < 0.05$ ). Data show mean  $\pm$  s.e.m. (**e**) or mean  $\pm$  s.d. (**f**).

the opposite changes of synaptic connections in FrA and how such changes contribute to the acquisition, extinction and reinstatement of fear memories.

## METHODS SUMMARY

One-month-old male mice expressing YFP (H-line) were used in this study. Fear conditioning was conducted with three pairings of a 30-s, 80-dB auditory cue (400 Hz; tone A = CS1 or 1,200 Hz, tone B = CS2) co-terminating with a 2-s, 0.5-mA scrambled footshock (US). Extinction training was conducted with five CS presentations (each CS lasting 2 min with an intertrial interval of 2 min) per day for 2 d. The procedures of *in vivo* transcranial two-photon imaging and data quantification were as described previously<sup>11,12</sup>. Either analysis of variance or Student's *t*-test was used to compare spine remodelling and freezing responses among different groups. The Pearson correlation coefficient was used to measure the strength of linear dependence between different variables.

**Full Methods** and any associated references are available in the online version of the paper at [www.nature.com/nature](http://www.nature.com/nature).

Received 13 July; accepted 9 December 2011.

Published online 19 February 2012.

- Myers, K. M. & Davis, M. Mechanisms of fear extinction. *Mol. Psychiatry* **12**, 120–150 (2007).
- Quirk, G. J. & Mueller, D. Neural mechanisms of extinction learning and retrieval. *Neuropsychopharmacology* **33**, 56–72 (2008).
- Bouton, M. E. Context and behavioral processes in extinction. *Learn. Mem.* **11**, 485–494 (2004).
- Rescorla, R. A. & Heth, C. D. Reinstatement of fear to an extinguished conditioned stimulus. *J. Exp. Psychol. Anim. Behav. Process.* **1**, 88–96 (1975).
- Bouton, M. E. & King, D. A. Contextual control of the extinction of conditioned fear: tests for the associative value of the context. *J. Exp. Psychol. Anim. Behav. Process.* **9**, 248–265 (1983).

6. Thomas, D. R. & Sherman, L. An assessment of the role of handling cues in "spontaneous recovery" after extinction. *J. Exp. Anal. Behav.* **46**, 305–314 (1986).
7. Herry, C. *et al.* Switching on and off fear by distinct neuronal circuits. *Nature* **454**, 600–606 (2008).
8. Burgos-Robles, A., Vidal-Gonzalez, I. & Quirk, G. J. Sustained conditioned responses in prelimbic prefrontal neurons are correlated with fear expression and extinction failure. *J. Neurosci.* **29**, 8474–8482 (2009).
9. Milad, M. R. & Quirk, G. J. Neurons in medial prefrontal cortex signal memory for fear extinction. *Nature* **420**, 70–74 (2002).
10. Tronson, N. C. *et al.* Segregated populations of hippocampal principal CA1 neurons mediating conditioning and extinction of contextual fear. *J. Neurosci.* **29**, 3387–3394 (2009).
11. Grutzendler, J., Kasthuri, N. & Gan, W. B. Long-term dendritic spine stability in the adult cortex. *Nature* **420**, 812–816 (2002).
12. Yang, G., Pan, F. & Gan, W. B. Stably maintained dendritic spines are associated with lifelong memories. *Nature* **462**, 920–924 (2009).
13. LeDoux, J. E. Emotion circuits in the brain. *Annu. Rev. Neurosci.* **23**, 155–184 (2000).
14. Kim, J. H. & Richardson, R. The effect of temporary amygdala inactivation on extinction and reextinction of fear in the developing rat: unlearning as a potential mechanism for extinction early in development. *J. Neurosci.* **28**, 1282–1290 (2008).
15. Hong, I., Song, B., Lee, S., Kim, J. & Choi, S. Extinction of cued fear memory involves a distinct form of depotentiation at cortical input synapses onto the lateral amygdala. *Eur. J. Neurosci.* **30**, 2089–2099 (2009).
16. Lin, C. H., Yeh, S. H., Lu, H. Y. & Gean, P. W. The similarities and diversities of signal pathways leading to consolidation of conditioning and consolidation of extinction of fear memory. *J. Neurosci.* **23**, 8310–8317 (2003).
17. Merlo, E. & Romano, A. Memory extinction entails the inhibition of the transcription factor NF- $\kappa$ B. *PLoS ONE* **3**, e3687 (2008).
18. Clem, R. L. & Huganir, R. L. Calcium-permeable AMPA receptor dynamics mediate fear memory erasure. *Science* **330**, 1108–1112 (2010).
19. Denk, W., Strickler, J. H. & Webb, W. W. Two-photon laser scanning fluorescence microscopy. *Science* **248**, 73–76 (1990).
20. Condé, F., Maire-Lepoivre, E., Audinat, E. & Crepel, F. Afferent connections of the medial frontal cortex of the rat. II. Cortical and subcortical afferents. *J. Comp. Neurol.* **352**, 567–593 (1995).
21. McDonald, A. J. Organization of amygdaloid projections to the mediodorsal thalamus and prefrontal cortex: a fluorescence retrograde transport study in the rat. *J. Comp. Neurol.* **262**, 46–58 (1987).
22. Sacchetti, B., Baldi, E., Lorenzini, C. A. & Bucherelli, C. Role of the neocortex in consolidation of fear conditioning memories in rats. *Exp. Brain Res.* **152**, 323–328 (2003).
23. Garcia, R., Vouimba, R. M., Baudry, M. & Thompson, R. F. The amygdala modulates prefrontal cortex activity relative to conditioned fear. *Nature* **402**, 294–296 (1999).
24. Ziv, N. E. & Smith, S. J. Evidence for a role of dendritic filopodia in synaptogenesis and spine formation. *Neuron* **17**, 91–102 (1996).

**Supplementary Information** is linked to the online version of the paper at [www.nature.com/nature](http://www.nature.com/nature).

**Acknowledgements** We thank J. LeDoux as well as all the members in the Gan laboratory for comments on the manuscript. This work was supported by National Institutes of Health grant NS047325 and the Investigator-Initiated Research Grant from the Alzheimer's Association (W.-B.G.), and by the National Science Foundation (#IOS-0757780), a 2008 NARSAD Independent Investigator Award and the G. Harold & Leila Y. Mathers Foundation (T.F.F.).

**Author Contributions** C.S.W.L. and W.-B.G. designed the imaging experiments. C.S.W.L., W.-B.G. and T.F.F. designed the behavioural paradigms. C.S.W.L. performed all the experiments and data analysis. T.F.F. helped with the behavioural data analysis. W.-B.G. supervised the work. W.-B.G., C.S.W.L. and T.F.F. wrote the manuscript.

**Author Information** Reprints and permissions information is available at [www.nature.com/reprints](http://www.nature.com/reprints). The authors declare no competing financial interests. Readers are welcome to comment on the online version of this article at [www.nature.com/nature](http://www.nature.com/nature). Correspondence and requests for materials should be addressed to W.-B.G. ([gan@saturn.med.nyu.edu](mailto:gan@saturn.med.nyu.edu)).

## METHODS

**Animals.** C57BL/6 mice expressing YFP in layer-V pyramidal neurons (H-line) were purchased from the Jackson Laboratory and group-housed in the Skirball animal facility. One-month-old ( $P30 \pm 1$ ) male mice were used in the experiments. All experiments were approved and performed in accordance with institutional guidelines.

**Fear conditioning and extinction.** Apparatus. Mice were trained and tested using the FreezeFrame system (Coulbourn Instruments). For training, mouse test cages equipped with stainless-steel shocking grids were connected to a precision feedback current-regulated shocker (Coulbourn Instruments). For testing, the shocking grids were replaced with non-shocking test grids that differed in texture from the shocking grids used during conditioning. Each test cage was contained in a sound-attenuating enclosure (Coulbourn Instruments). Behaviour was recorded using low-light video cameras. Stimulus presentation was automated using Actimetrics FreezeFrame software (version 2.2; Coulbourn Instruments). All equipment was thoroughly cleaned with detergent followed by water between sessions.

**Fear conditioning.** Mice were habituated for 2 min on a shocking grid (cage set-up A: shocking floor grids, ethanol scent). Fear conditioning was conducted with three pairings of a 30-s, 400-Hz, 80-dB auditory cue (tone A = CS1) co-terminating with a 2-s, 0.5-mA scrambled footshock (US). The intertrial interval was 15 s. Two minutes after conditioning, mice were returned to their home cages. For the unpaired control group, mice received tones and shocks in an unpaired manner (tones and shocks were separated by random intervals of 5–15 s). Mice were returned to their home cages 2 min after presentation of the unpaired stimuli. For tone-only or shock-only control groups, mice were habituated for the same amount of time in the testing context, and tones or footshocks were given separately.

**Recall test and extinction.** For the recall test, mice were placed in a different context (cage set-up B: test floor grids, 1% Pinesol) for an initial 2-min (pre-CS) period and this was followed by tone presentation for 2 min (CS). For extinction training, mice were subjected to five CS presentations (each lasting 2 min with an intertrial interval of 2 min) per day for two consecutive days. For repeated exposure of mice to tone B (CS2), the extinction protocol was used with a different auditory cue (1,200 Hz, 80 dB).

**Reconditioning.** Mice were reconditioned in the training context using shocking grids (ethanol scent) with five pairings of CS-US (30-s CS/tone A, 400 Hz; each co-terminated with a 2-s footshock) each day on days 5 and 6. For the unpaired control, five shocks and tones were given to mice in an unpaired manner each day. For conditioning with tone B, five CS-US pairings were given to the mice using tone B as the auditory cue each day.

**Retrograde and anterograde tracing with Mini-Ruby.** One-month-old male mice expressing YFP were anaesthetized with ketamine and xylazine (intraperitoneal; 20 mg ml<sup>-1</sup> and 3 mg ml<sup>-1</sup>, respectively, in saline; 6 µl per gram of body weight). Mini-Ruby (Invitrogen) dissolved at 5% concentration in water was injected into the frontal association cortex (+2.8 mm bregma, +1.0 mm midline, +0.01 mm ventral) through a sharp electrode by iontophoresis (6 µA, on-off for 15 min). For amygdala injections, 0.15 µl of Mini-Ruby was injected over 5 min into the amygdala with a Hamilton syringe (−1.94 mm bregma, +3.00 mm midline, +4.75 mm ventral). Four to seven days after the injection, mice were perfused with 4% paraformaldehyde and their brains were postfixed overnight. Brains were sectioned with a vibratome at 200 µm. Confocal images were acquired using a Bio-Rad confocal microscope (×20 oil lens; numerical aperture, 0.8).

**Transient inactivation of the frontal association cortex with muscimol.** After fear conditioning or extinction, mice were anaesthetized with ketamine and xylazine. Muscimol (Sigma; 0.5 µl at 1 µg µl<sup>-1</sup>) in artificial cerebrospinal fluid or artificial cerebrospinal fluid as vehicle was microinjected bilaterally into the frontal association cortex (+2.8 mm bregma, ±1.0 mm midline, +0.5 mm ventral) with a pressure injection device (Picospritzer III; 15 p.s.i., 12 ms, 0.8 Hz) over 5 min. The injection was performed within 1 h after fear conditioning or extinction. Twenty-four hours after injection, mice were subjected to a recall test. Muscimol spread was estimated by the line at which the Mini-Ruby fluorescence was less than 20% of its peak level. On the basis of this definition, we determined the range of muscimol spread as ~500–700 µm (Supplementary Fig. 3).

**In vivo transcranial two-photon imaging.** Spine formation and elimination were examined by imaging the mouse cortex through a thinned-skull window as described previously<sup>11,12</sup>. Briefly, one-month-old male mice expressing YFP were anaesthetized with ketamine and xylazine (intraperitoneal; 20 mg ml<sup>-1</sup> and 3 mg ml<sup>-1</sup>, respectively, in saline; 6 µl per gram of body weight). Thinned-skull windows were made in head-fixed mice with high-speed microdrills. Skull thickness was reduced to about 20 µm. A two-photon microscope tuned to 920 nm (×60 water immersion lens; numerical aperture, 1.1) was used to acquire images. For re-imaging of the same region, thinned regions were identified on the basis of the maps of the brain vasculature. Microsurgical blades were used to re-thin the region of interest until a clear image could be obtained. The area of the imaging region was 200 µm × 200 µm. The centres of the imaging regions were as follows: +2.8 mm bregma, +1.0 mm midline (frontal association cortex); −1.1 mm bregma, +3.4 mm midline (barrel cortex). Because repeated thinning of the skull to ~20 µm without damaging the cortex becomes more difficult after multiple imaging sessions, we designed our experiments in such a way that no animal was imaged than four times.

**Data analysis.** All data analysis was performed blind to treatment conditions, except for the data in Supplementary Fig. 4, which were collected under behavioural treatment conditions known to the investigator. Image J software was used to analyse spine elimination and formation from three-dimensional image stacks as described previously<sup>11,12</sup>. Dendritic branches were randomly sampled within a 200 µm × 200 µm area imaged at a distance of 0–100 µm below the pia surface. The same dendritic segments were identified from three-dimensional stacks taken at different time points with high image quality (ratio of signal to background noise, >4:1). The number and location of dendritic protrusions (protrusion lengths were more than one-third of the dendritic shaft diameter) were identified. The percentage of spine formation and elimination is presented as the number of spines formed or eliminated between the first and second view divided by the total number of spines observed at the first view<sup>11,12</sup> (Supplementary Information, section 2).

For the analysis of spine changes at the individual branch level (Fig. 3), the percentage of spine formation and elimination is presented as the number of formed or eliminated spines divided by the total number of spines on the individual branch. For the spine orientation analysis, newly formed spines were considered to have the same orientation when they were oriented within 90° relative to previously eliminated spines.

Filopodia were identified as long, thin structures<sup>11,12</sup> (generally larger than twice the average spine length; ratio of head diameter to neck diameter, <1.2:1; ratio of length to neck diameter, >3:1). The remaining protrusions were classified as spines. No subtypes of spines were distinguished in our analysis. Three-dimensional stacks were used to ensure that tissue movements and rotation between imaging intervals did not hinder spine identification. Spines or filopodia were considered to be identical between views if their positions were unchanged with respect to adjacent landmarks. Our quantitative analysis shows that we can measure the distance between two adjacent stable spines with a precision of ~0.2 µm in 95% of the cases (2 s.d.). Spines were considered different if their positions differed from the first view by more than 0.7 µm. We chose 0.7 µm as a cut-off distance because spine positions can shift by up to ~0.3 µm in either direction along the axis of dendritic shafts owing to changes in spine morphology, slight tissue rotation and movements related to brain pulsation. We estimate that the imaging resolution of our two-photon microscope (×60; numerical aperture, 1.1; 920 nm) is ~0.7 µm.

For image display, fluorescent structures near and out of the focal plane of the dendrites of interest were removed manually from image stacks using Adobe Photoshop. The modified image stacks were then projected to generate two-dimensional images and adjusted for contrast and brightness.

For statistical analysis, we used either analysis of variance or Student's *t*-test to compare spine formation and elimination rates among different experimental groups. All spine formation and elimination rates are presented as mean ± s.d. and all behavioural data are presented as mean ± s.e.m. Data in spine distribution graphs in Fig. 3g and 4d are presented as mean ± s.e.m. The Pearson correlation coefficient was used as a measure of the strength of linear dependence between spine changes and behavioural responses. The linear regression lines and correlation coefficients (*r*) are shown in Fig. 1i–l, Fig. 2d, e, g and Fig. 3a–c. In all analyses, *P* values less than 0.05 were considered to be statistically significant.



# Dysfunction of lipid sensor GPR120 leads to obesity in both mouse and human

Atsuhiko Ichimura<sup>1\*</sup>, Akira Hirasawa<sup>1\*</sup>, Odile Poulain-Godefroy<sup>2,3\*</sup>, Amélie Bonnefond<sup>2,3\*</sup>, Takafumi Hara<sup>1</sup>, Loïc Yengo<sup>2,3</sup>, Ikuro Kimura<sup>1</sup>, Audrey Leloir<sup>2,3</sup>, Ning Liu<sup>1</sup>, Keiko Iida<sup>1</sup>, Hélène Choquet<sup>2,3</sup>, Philippe Besnard<sup>4</sup>, Cécile Lecoœur<sup>2,3</sup>, Sidonie Vivequin<sup>2,3</sup>, Kumiko Ayukawa<sup>1</sup>, Masato Takeuchi<sup>1</sup>, Kentaro Ozawa<sup>1</sup>, Maithé Tauber<sup>5</sup>, Claudio Maffei<sup>6,7</sup>, Anita Morandi<sup>2,3,6</sup>, Raffaella Buzzetti<sup>8</sup>, Paul Elliott<sup>9</sup>, Anneli Pouta<sup>10,11</sup>, Marjo-Riitta Jarvelin<sup>9,10,12</sup>, Antje Körner<sup>13</sup>, Wieland Kiess<sup>13</sup>, Marie Pigeyre<sup>14,15</sup>, Roberto Caiazzo<sup>14,16</sup>, Wim Van Hul<sup>17</sup>, Luc Van Gaal<sup>18</sup>, Fritz Horber<sup>19</sup>, Beverley Balkau<sup>20,21</sup>, Claire Lévy-Marchal<sup>22</sup>, Konstantinos Rouskas<sup>2,3,23</sup>, Anastasia Kouvatsi<sup>23</sup>, Johannes Hebebrand<sup>24</sup>, Anke Hinney<sup>24</sup>, Andre Scherag<sup>25</sup>, François Pattou<sup>14,16</sup>, David Meyre<sup>2,3,26</sup>, Taka-aki Koshimizu<sup>27</sup>, Isabelle Wolowczuk<sup>2,3</sup>, Gozoh Tsujimoto<sup>1</sup> & Philippe Froguel<sup>2,3,28</sup>

**Free fatty acids provide an important energy source as nutrients, and act as signalling molecules in various cellular processes<sup>1–4</sup>. Several G-protein-coupled receptors have been identified as free-fatty-acid receptors important in physiology as well as in several diseases<sup>3,5–13</sup>. GPR120 (also known as O3FAR1) functions as a receptor for unsaturated long-chain free fatty acids and has a critical role in various physiological homeostasis mechanisms such as adipogenesis, regulation of appetite and food preference<sup>5,6,14–16</sup>. Here we show that GPR120-deficient mice fed a high-fat diet develop obesity, glucose intolerance and fatty liver with decreased adipocyte differentiation and lipogenesis and enhanced hepatic lipogenesis. Insulin resistance in such mice is associated with reduced insulin signalling and enhanced inflammation in adipose tissue. In human, we show that *GPR120* expression in adipose tissue is significantly higher in obese individuals than in lean controls. *GPR120* exon sequencing in obese subjects reveals a deleterious non-synonymous mutation (p.R270H) that inhibits GPR120 signalling activity. Furthermore, the p.R270H variant increases the risk of obesity in European populations. Overall, this study demonstrates that the lipid sensor GPR120 has a key role in sensing dietary fat and, therefore, in the control of energy balance in both humans and rodents.**

To investigate the role of GPR120 in metabolism, we examined GPR120-deficient mice (Supplementary Fig. 1) with respect to lipogenesis, glucose and energy homeostasis. On a normal diet containing 13% fat, the body weight was similar in both GPR120-deficient and wild-type mice. However, when 5-week-old GPR120-deficient mice were fed a high-fat diet (HFD) containing 60% fat, their body weight increase was ~10% higher than that of wild-type mice on a HFD (Fig. 1a). The difference in HFD-induced body weight gain between wild-type and GPR120-deficient mice was marked at ~8–10 weeks old and reached a plateau at 13 weeks old. To assess energy expenditure and substrate utilization, we next performed indirect calorimetry on wild-type and

mutant mice on a HFD at 9–10 weeks old (Fig. 1b) and 15–16 weeks old (Supplementary Fig. 2a). The young GPR120-deficient mice showed decreased energy expenditure compared with the young wild-type mice, particularly during the light/inactive phase (Fig. 1b, left), whereas older mutant and wild-type mice showed no such a difference (Supplementary Fig. 2a, left). The difference in energy expenditure between GPR120-deficient and wild-type mice was observed only in the light phase, indicating that the lack of the GPR120 receptor primarily affects basal metabolism, especially in young mice. The decreased energy expenditure might explain the difference we found in body weight gain between HFD-fed wild-type and mutant young mice. The lower values of respiratory quotient in mutant mice could be due to insufficient glucose utility, probably as a result of the decreased insulin sensitivity. In all experiments, both groups of mice showed similar levels of locomotor activity (data not shown).

White adipose tissue (WAT) and liver were substantially heavier in HFD-fed GPR120-deficient mice (Supplementary Fig. 2b). Plasma low- and high-density lipoprotein cholesterol levels were significantly higher in HFD-fed GPR120-deficient mice, and serum alanine aminotransferase levels were substantially increased, indicating abnormal cholesterol metabolism and liver function (Supplementary Table 1). Microcomputed tomography scanning revealed that 16-week-old GPR120-deficient mice stored much more fat than did wild type (Fig. 1c). A significant increase in adipocyte size in both epididymal (Fig. 1d) and subcutaneous (Supplementary Fig. 2c) fat was observed in GPR120-deficient mice. Furthermore, the expression of macrophage marker genes (*Cd11b* (*Itgam*), *Cd68* and *F4/80* (*Emr1*)) and the number of F4/80-positive cells were markedly enhanced in epididymal tissue from HFD-fed GPR120-deficient mice (Fig. 1e, f). Moreover, these mice showed liver steatosis and hepatic triglyceride content was markedly increased (Fig. 1g). Overall, HFD-induced obesity and liver fattiness were more severe in GPR120-deficient mice than in wild type.

<sup>1</sup>Department of Genomic Drug Discovery Science, Graduate School of Pharmaceutical Sciences, Kyoto University, 46-29 Yoshida Shimoadachi-cho, Sakyo-ku, Kyoto 606-8501, Japan. <sup>2</sup>Centre National de la Recherche Scientifique (CNRS)-Unité mixte de recherche (UMR) 8199, Lille Pasteur Institute, Lille 59000, France. <sup>3</sup>Lille Nord de France University, Lille 59000, France. <sup>4</sup>Institut National de la Santé et de la Recherche Médicale (Inserm)-UMR 866, Physiologie de la Nutrition, Bourgogne University, AgroSup Dijon, Dijon 21078, France. <sup>5</sup>Inserm-U563, Children's Hospital, Centre Hospitalier Universitaire, Toulouse 31000, France. <sup>6</sup>Regional Centre for Juvenile Diabetes, Obesity and Clinical Nutrition, Verona 37134, Italy. <sup>7</sup>Department of Mother and Child, Biology-Genetics, Section of Paediatrics, University of Verona, Verona 37134, Italy. <sup>8</sup>Department of Clinical Sciences, La Sapienza University, Rome 00161, Italy. <sup>9</sup>Medical Research Council-HPA Centre for Environment and Health, Department of Epidemiology and Biostatistics, School of Public Health, St Mary's campus, Imperial College London, London W2 1PG, UK. <sup>10</sup>National Public Health Institute, Biocenter Oulu, University of Oulu, Oulu 90220, Finland. <sup>11</sup>Institute of Clinical Medicine/Obstetrics and Gynecology, University of Oulu, Oulu 90220, Finland. <sup>12</sup>Institute of Health Sciences, University of Oulu, Oulu 90220, Finland. <sup>13</sup>Center for Pediatric Research, Department of Women's & Child Health, University of Leipzig, Leipzig 04317, Germany. <sup>14</sup>Inserm-U859, Lille Nord de France University, Lille 59000, France. <sup>15</sup>Lille University Hospital, Nutrition, Lille 59000, France. <sup>16</sup>Lille University Hospital, Endocrine Surgery, Lille 59000, France. <sup>17</sup>Department of Medical Genetics, University of Antwerp, Antwerp 2610, Belgium. <sup>18</sup>Department of Endocrinology, Antwerp University Hospital, Antwerp 2650, Belgium. <sup>19</sup>Department of Surgery and Internal Medicine, Clinic Lindberg, Medical Department, Winterthur 8400, and University of Berne, Berne 3011, Switzerland. <sup>20</sup>Inserm-U780, Centre for research in Epidemiology and Population Health (CRESP), Villejuif 94800, France. <sup>21</sup>Paris-Sud 11 University, Orsay 91405, France. <sup>22</sup>Inserm-U690, Robert Debré hospital, Paris 75935, France. <sup>23</sup>Department of Genetics, Development and Molecular Biology, School of Biology, Aristotle University of Thessaloniki, Thessaloniki 541 24, Greece. <sup>24</sup>Department of Child and Adolescent Psychiatry, University of Duisburg-Essen, Essen 45147, Germany. <sup>25</sup>Institute for Medical Informatics, Biometry and Epidemiology, University of Duisburg-Essen, Essen 45122, Germany. <sup>26</sup>McMaster University, Hamilton, Ontario L8S 4L8, Canada. <sup>27</sup>Department of Pharmacology, Division of Molecular Pharmacology, Jichi Medical University, Tochigi 329-0498, Japan. <sup>28</sup>Department of Genomics of Common Disease, School of Public Health, Imperial College London, Hammersmith Hospital, London W12 0NN, UK.

\*These authors contributed equally to this work.

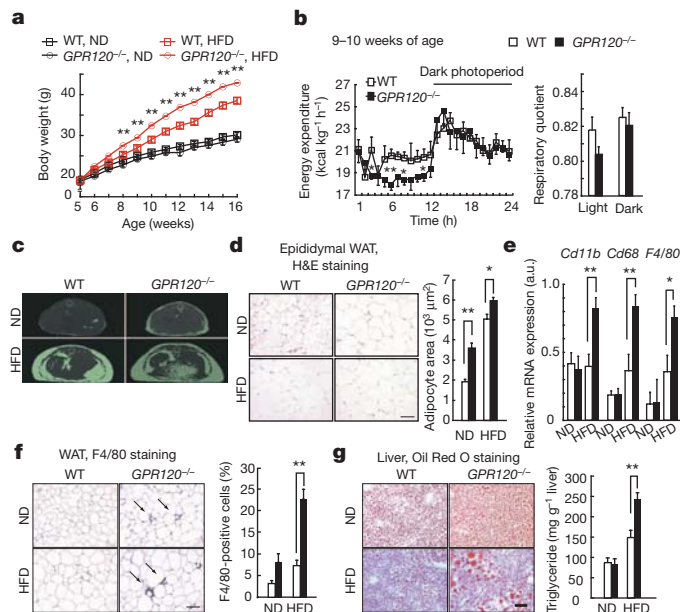


**Figure 1 | Obesity, hypertrophic adipocytes, accumulation of pro-inflammatory macrophages and hepatic steatosis in HFD-fed GPR120-deficient mice.** **a**, Body weight changes of wild-type (WT) and GPR120-deficient mice fed a normal diet (ND) or a HFD ( $n = 36-47$ ). **b**, Indirect calorimetry in HFD-fed mice. Energy expenditure and respiratory quotient ( $n = 4, 5$ ). **c**, Representative cross-sectional images of wild-type and GPR120-deficient mice subjected to microcomputed tomography analysis of the *in situ* accumulation of fat. Fat depots are demarcated (green) for illustration. **d**, Haematoxylin and eosin (H&E)-stained epididymal WAT and mean area of adipocytes ( $n = 6$ ). Scale bar, 100  $\mu\text{m}$ . **e**, Relative expression of *Cd11b*, *Cd68* and *F4/80* messenger RNA in WAT ( $n = 6$ ). a.u., arbitrary units. **f**, Representative images of epididymal WAT stained with anti-F4/80 antibody (arrows, F4/80-positive cells) and the number of F4/80 cells ( $n = 6$ ). Scale bar, 100  $\mu\text{m}$ . **g**, Oil Red O-stained liver and hepatic triglyceride content after 24hr fasting ( $n = 13$ ). Scale bar, 50  $\mu\text{m}$ . All data represent mean  $\pm$  s.e.m. \* $P < 0.05$  and \*\* $P < 0.01$  versus the corresponding wild-type value.

Obesity-associated insulin resistance was also more severe in GPR120-deficient mice. HFD-fed GPR120-deficient mice showed higher levels of fasting plasma glucose and insulin than did wild type, although these parameters were similar between the two groups on a normal diet (Fig. 2a). HFD-induced insulin resistance, as determined by an insulin tolerance test, was more prominent in GPR120-deficient mice than in wild type (Fig. 2b, left, and Supplementary Fig. 3a, b). A glucose tolerance test further revealed that these mice suffered from impaired glucose metabolism (Fig. 2b, right, and Supplementary

Fig. 3a, b). The level of plasma leptin was significantly higher in HFD-fed GPR120-deficient mice than in wild type (Supplementary Fig. 3c). However, there was no significant difference in terms of plasma adiponectin level or food intake between the two groups (Supplementary Fig. 3d, e). HFD-fed GPR120-deficient mice showed a marked increase in the size of islets and KI67 (MKI67)-positive cells, suggesting adaptive enlargement of the  $\beta$ -cell mass in response to insulin resistance<sup>17,18</sup> (Supplementary Fig. 3f, g). Moreover, we observed markedly reduced peripheral insulin sensitivity in tissues from HFD-fed GPR120-deficient mice (Fig. 2c). Insulin was shown to induce the phosphorylation of AKT (AKT1) (on Ser 473) in WAT, liver and skeletal muscle, with similar intensities in wild-type and GPR120-deficient mice on a normal diet (Supplementary Fig. 3h). Consistent with the insulin resistance reported above, HFD-fed GPR120-deficient mice showed loss of insulin-induced AKT phosphorylation in WAT and the liver.

To determine the molecular basis of the metabolic changes in WAT and livers of GPR120-deficient mice, we performed gene expression

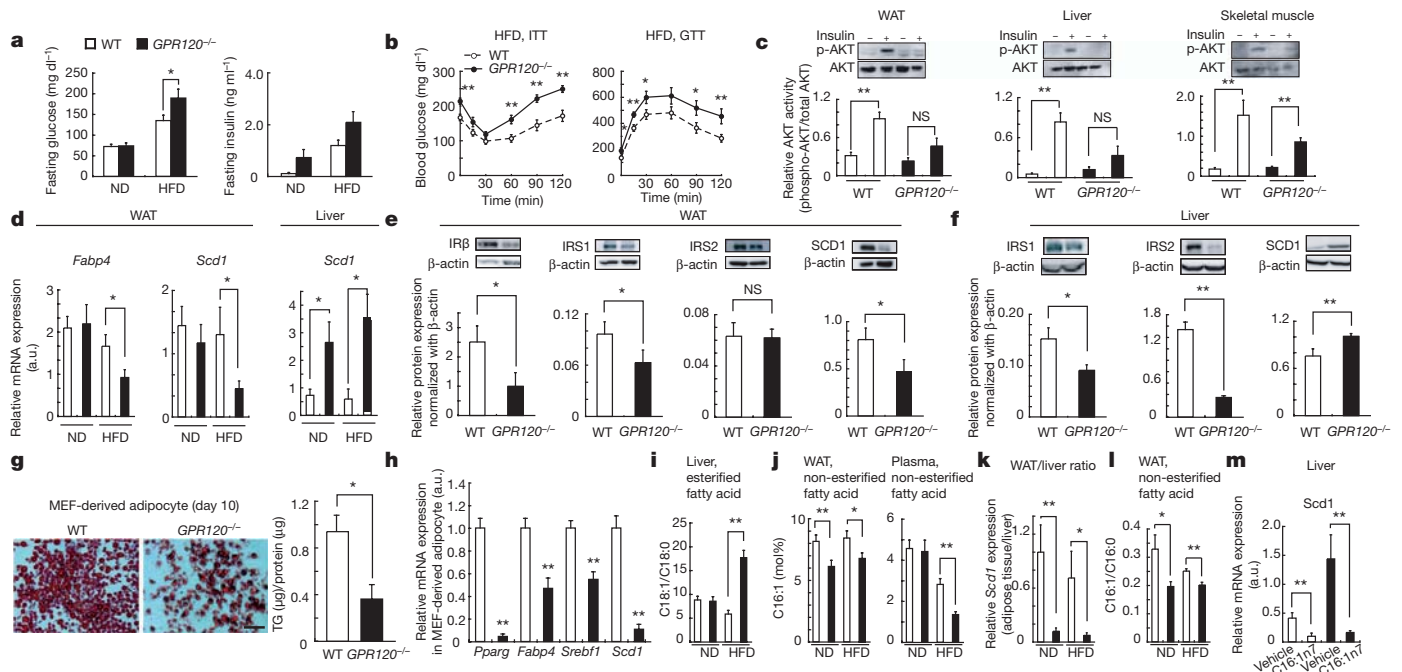


**Figure 2 | Impaired glucose metabolism, adipogenesis and lipogenesis in HFD-fed GPR120-deficient mice.** **a**, Fasting blood glucose and serum insulin levels ( $n = 6-15$ ). **b**, Plasma glucose during insulin tolerance test (ITT, left) and glucose tolerance test (GTT, right) ( $n = 12-14$ ). **c**, Phosphorylation of AKT (Ser 473) in WAT, liver and skeletal muscle after 24-hr fasting ( $n = 6, 7$ ). NS, not significant. **d**, Relative mRNA expression of *Fabp4* and *Scd1* in WAT or *Scd1* in liver ( $n = 6$ ). **e**, Protein expression of IRS1, IRS2, SCD1 and  $\beta$ -actin in WAT. **f**, Protein expression of IRS1, IRS2, SCD1 and  $\beta$ -actin in liver. **g**, Oil Red O-staining and triglyceride (TG) content of mouse embryonic

fibroblast (MEF)-derived adipocyte. Scale bar, 50  $\mu\text{m}$ . **h**, Relative mRNA expression in MEF-derived adipocyte ( $n = 6$ ). **i**, The ratio of C18:1 to C18:0 in livers ( $n = 6-8$ ). **j**, Non-esterified C16:1n7 palmitoleate in WAT and plasma ( $n = 4-7$ ). **k**, The ratio of *Scd1* mRNA expression in liver and WAT ( $n = 6, 7$ ). **l**, The ratio of C16:1 to C16:0 in adipose tissues ( $n = 6-8$ ). **m**, Hepatic *Scd1* mRNA expression in mice infused with vehicle or triglyceride:palmitoleate for 6 h ( $n = 4, 5$ ). All data represent mean  $\pm$  s.e.m. \* $P < 0.05$  and \*\* $P < 0.01$  versus the corresponding wild-type value.

analyses. We identified approximately 700 differentially expressed genes in WAT between HFD-fed GPR120-deficient and wild-type mice (Supplementary Fig. 4a). Connectivity mapping of these genes showed that pathways relating to insulin signalling and adipocyte differentiation were depressed, whereas those related to inflammation were enhanced in HFD-fed GPR120-deficient mice (Supplementary Fig. 4b). Quantitative real-time PCR (qRT-PCR) analysis confirmed the downregulation of insulin-signalling-related genes (*Insr*, *Irs1* and *Irs2*), an adipocyte differentiation marker gene (*Fabp4*) and a lipogenesis-related gene (*Scd1*) in the epididymal fat from HFD-fed GPR120-deficient mice (Fig. 2d and Supplementary Fig. 3i). We identified approximately 100 differentially expressed genes in the liver between HFD-fed GPR120-deficient and wild-type mice (Supplementary Fig. 5). Notably, lipogenesis-related genes (*Scd1* and *Me1*) and a fatty acid transporter gene (*Cd36*) were significantly upregulated in livers from GPR120-deficient mice. Quantitative RT-PCR analysis confirmed upregulation of *Scd1* in the liver of GPR120-deficient mice (Fig. 2d).

Western blot analysis further confirmed downregulation of IR $\beta$ , IRS1 and SCD1 in adipose tissue of HFD-fed GPR120-deficient mice (Fig. 2e) but downregulation of IRS1 and IRS2 and upregulation of SCD1 in their livers (Fig. 2f). Hence, insulin-signalling-related molecules were downregulated by the lack of GPR120 in both adipose tissue and the liver. However, the expression of SCD1, the rate-limiting enzyme in the biosynthesis of mono-unsaturated fatty acids, was downregulated in adipose tissue but upregulated in liver. Furthermore, the expression of *Scd1* and several adipogenic genes<sup>14,19</sup> (*Pparg*, *Fabp4* and *Srebf1*) was suppressed in mouse-embryonic-fibroblast-derived adipocytes from GPR120-deficient mice, indicating that GPR120 is required for normal adipogenesis, as previously reported in differentiating 3T3-L1 adipocytes depleted of endogenous GPR120 by short interfering RNA<sup>14</sup> (Fig. 2g, h).

To determine the effects of altered lipogenesis on lipid composition in GPR120-deficient mice, we performed lipidomics analysis in WAT, livers and plasma. Significant changes of major lipid clusters were observed (Supplementary Fig. 6). Notably, the hepatic concentration of oleate (C18:1n9c) was significantly higher in HFD-fed GPR120-deficient mice than in wild type. The ratio of C18:1 to C18:0, an indicator of SCD1 enzyme activity<sup>20–23</sup>, was markedly enhanced in livers from HFD-fed GPR120-deficient mice relative to wild type (Fig. 2i). Moreover, the levels of C16:1n7 palmitoleate, which has recently been recognized as a lipid hormone<sup>4</sup>, in WAT and plasma were significantly lower in HFD-fed GPR120-deficient mice than in wild type (Fig. 2j). In particular, lower levels of C16:1n7 palmitoleate were detected even in WAT of GPR120-deficient mice on a normal diet (Fig. 2j), which seems to be in good agreement with the suppressed *Scd1* expression and the reduced SCD1 desaturation index<sup>20–23</sup> (C16:1/C18:0; Fig. 2k, l). Lipidomics analysis clearly illustrated dysregulated lipogenesis in GPR120-deficient mice, and showed the reduced production of lipid hormone C16:1n7 palmitoleate<sup>4</sup>. To determine whether the enhanced hepatic lipogenesis in GPR120-deficient mice was due to the reduced levels of C16:1n7 palmitoleate, we examined the effect of C16:1n7 palmitoleate treatment on hepatic *Scd1* expression. A 6-h infusion of triglyceride:palmitoleate markedly lowered the enhanced hepatic *Scd1* expression in GPR120-deficient mice (Fig. 2m). The results indicated that the reduced C16:1n7 palmitoleate may explain the systemic metabolic disorders observed in GPR120-deficient mice on a HFD, as palmitoleate has been proposed to be a bioactive lipid by which adipose tissue communicates with distant organs (such as liver) and regulates systemic metabolic homeostasis<sup>4</sup>. This study shows that dysfunction of GPR120 can be an underlying mechanism for diet-associated obesity and obesity-related metabolic disorders in mouse.

The mouse data prompted us to assess the potential contribution of GPR120 to the development of obesity and its metabolic complications in humans. First, the expression levels of *GPR120* in both subcutaneous and omental adipose tissues as well as in liver samples were compared between lean and obese subjects. Normoglycaemic obese patients and

lean individuals ( $n = 14$  in each group) were matched for age and gender (Supplementary Table 2). As previously described<sup>5,14</sup>, we confirmed that *GPR120* is barely expressed in liver of either lean or obese subjects (data not shown). By contrast, we found that *GPR120* is well expressed in the adipose tissue of lean individuals (Fig. 3a). In addition, human obesity is significantly associated with an increase in *GPR120* expression in both subcutaneous and omental adipose tissues (1.8-fold increase;  $P = 0.0004$  and  $P = 0.003$ , respectively). We also found that *GPR120* expression in subcutaneous adipose tissue strongly correlates with that in omental adipose tissue (Spearman analysis;  $r = 0.570$  and  $P = 2.74 \times 10^{-8}$ ), suggesting a systemic regulation of its expression in humans. Furthermore, we found a positive correlation between *GPR120* expression in both subcutaneous and omental adipose tissues and in subjects' concentrations of plasma low-density lipoproteins (on adjustment for age and sex;  $r = 0.247$ ,  $P = 0.0115$  and  $r = 0.255$ ,  $P = 0.0118$ , respectively).

To investigate the contribution of *GPR120* to human obesity, the four *GPR120* exons were sequenced in 312 French, non-consanguineous, extremely obese children and adults (Supplementary Table 3). We

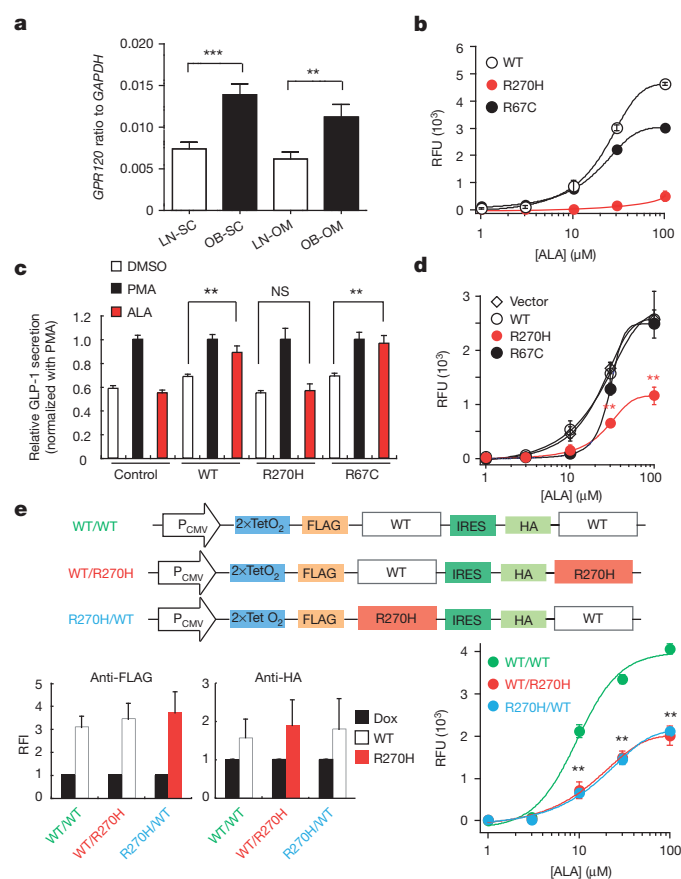


**Figure 3 | GPR120 expression in human obese tissue samples, and effect of GPR120 variants on  $[Ca^{2+}]_i$  response and GLP-1 secretion.** **a**, *GPR120* mRNA levels in human subcutaneous (SC) and omental (OM) adipose tissues of lean (LN;  $n = 14$ ) and obese (OB;  $n = 14$ ) normoglycaemic individuals. Mann-Whitney analysis, \*\*\* $P = 0.0004$  and \*\* $P = 0.003$ . **b**, ALA-induced  $[Ca^{2+}]_i$  responses in cells expressing wild-type GPR120 or a p.R67C or p.R270H variant. **c**, ALA-induced GLP-1 secretion in NCI-H716 cells expressing a wild-type GPR120, a p.R67C or a p.R270H receptor. **d**, Effect of transfection with GPR120 variants on ALA-induced  $[Ca^{2+}]_i$  response in cells stably expressing wild-type GPR120. **e**, Effect of co-expression of human GPR120 p.R270H variant with wild-type GPR120 on ALA-induced  $[Ca^{2+}]_i$  response. Top: schematic diagram of constructs. Bottom: expression of wild type and p.R270H (left), and concentration- $[Ca^{2+}]_i$  response for ALA in cells expressing wild-type/wild-type, wild-type/R270H or R270H/wild-type receptors (right). \*\* $P < 0.01$  versus the corresponding control value. RFI, relative fluorescence intensity; RFU, relative fluorescence unit. All data show mean  $\pm$  s.e.m.



**Table 1 | Identified variants in *GPR120* exons and association between the p.R67C/rs6186610 or p.R270H non-synonymous variant and obesity**

	Variant	Nucleotide change	Chr 10 position	MAF <sub>1</sub>	MAF <sub>2</sub> (controls, n = 7,654)	MAF <sub>2</sub> (cases, n = 6,942)	Adjustment: age and gender		Adjustment: age, gender and geography	
							OR [95% CI]	P	OR [95% CI]	P
Missense variants	p.R67C/rs6186610	C→T	95,316,666	0.05	0.043	0.055	1.16 [1.02, 1.31]	0.022	1.13 [1.00, 1.28]	0.060
	p.R270H	G→A	95,337,031	0.03	0.013	0.024	1.62 [1.31, 2.00]	$8.00 \times 10^{-6}$	1.58 [1.28, 1.95]	$2.17 \times 10^{-5}$
Synonymous variants	p.V38V	G→A	95,316,581	0.0016	—	—	—	—	—	—
	p.S192S	G→A	95,325,846	0.0016	—	—	—	—	—	—
	p.V243V	C→T	95,328,938	0.0016	—	—	—	—	—	—
	p.S264S	G→A	95,337,014	0.0016	—	—	—	—	—	—

Variant position was indicated according to human genome build NCBI36/hg18. Association between p.R67C/rs6186610 or p.R270H variant and obesity was assessed by using a logistic regression model adjusted for age and gender or for age, gender and geography, under an additive model. Chr, chromosome; MAF<sub>1</sub>, minor allele frequency in sequencing data set (n = 312 extremely obese individuals); MAF<sub>2</sub>, minor allele frequency in the large obesity case-control genotyping data set; OR, odds ratio; CI, confidence interval.

identified only two non-synonymous variants, R270H (minor allele frequency (MAF), ~3%) and p.R67C/rs6186610 (MAF, ~5%), and four rare synonymous variants (MAF, <1%) (Table 1). The two non-synonymous variants were subsequently genotyped in 6,942 unrelated obese individuals and 7,654 control subjects, all of European origin (Supplementary Table 4). By using a logistic regression model adjusted for age and sex, we found that R270H associated with obesity under an additive model (OR = 1.62 [1.31, 2.00]<sub>95%</sub> (odds ratio and 95% confidence interval),  $P = 8.00 \times 10^{-6}$ ; Table 1); whereas we found only a trend for association between p.R67C and obesity (OR = 1.16 [1.02, 1.31]<sub>95%</sub>,  $P = 0.022$ ; Table 1). It is noteworthy that these results were almost the same after adjusting for geographical origin (Table 1).

We then genotyped the p.R270H variant in 1,109 French pedigrees selected for obesity (n = 5,045) and in 780 German trios with one obese child (n = 2,340). We observed a significant over-transmission of the p.R270H low-frequency variant to obese offspring in 117 pedigrees or trios where the p.R270H variant was present (transmission, 62%;  $P = 0.009$ ; Supplementary Table 5). This family-based study excludes a hidden population stratification effect as a cause of spurious association.

We assessed the functional significance of both the p.R67C mutation and the p.R270H mutation *in silico* using several programs: arginine residues at positions 67 and 270 presented a high-evolutionary-conservation pattern among mammals and the two amino-acid substitutions were predicted to be potentially damaging (Supplementary Table 6). To examine the influences of the two non-synonymous variants on GPR120 function *in vitro*, we assessed each receptor ability to mobilize intracellular calcium (concentration,  $[Ca^{2+}]_i$ ) in response to the endogenous agonist  $\alpha$ -linolenic acid (ALA). We found that ALA induced  $[Ca^{2+}]_i$  responses in T-REx 293 cells expressing either wild-type or p.R67C receptor in a dose-dependent manner, whereas ALA-induced  $[Ca^{2+}]_i$  responses in cells expressing p.R270H were significantly lower ( $P = 1.6 \times 10^{-5}$ ) than those in cells expressing wild type at ALA concentrations greater than 10  $\mu$ M (Fig. 3b). We further examined the functional ability of the mutated receptors to secrete GLP-1 (ZGLP1) from human intestinal NCI-H716 cells, as this cell line lacks GPR120 expression and it can secrete GLP-1 in a regulated manner<sup>5</sup>. ALA induced secretion of GLP-1 in NCI-H716 cells expressing either wild-type ( $P = 0.004$ ) or p.R67C ( $P = 3.2 \times 10^{-5}$ ) receptor, but not in NCI-H716 cells expressing p.R270H mutant ( $P = 0.96$ ) (Fig. 3c). The transfection efficiencies for the GPR120 variant receptors were confirmed to be almost the same (data not shown). To examine the effect of the p.R270H variant on the wild-type receptor signalling, we analysed the  $[Ca^{2+}]_i$  dose-response curves after the transfection of an empty vector, a wild-type receptor plasmid or a p.R270H-mutated plasmid into T-REx 293 cells expressing wild-type GPR120. The transfection of the p.R270H-mutated plasmid suppressed dose-response curves, and the maximal ALA-induced  $[Ca^{2+}]_i$  response was significantly decreased ( $P = 0.004$ ; Fig. 3d).

To assess the effect more quantitatively, we analysed  $[Ca^{2+}]_i$  dose-response curves in T-REx 293 cells stably expressing bicistronic wild-type/wild-type, wild-type/p.R270H or p.R270H/wild-type receptors

(Fig. 3e, top). Almost equal levels of receptor protein expression in each cell line were confirmed by flow cytometry analysis (Fig. 3e, bottom left). Compared with cells expressing wild-type/wild-type receptor, the  $[Ca^{2+}]_i$  dose-response curves obtained in cells expressing either wild-type/p.R270H or p.R270H/wild-type receptor were markedly suppressed, and the maximal ALA-induced  $[Ca^{2+}]_i$  response was significantly decreased ( $P = 1.2 \times 10^{-5}$ ; Fig. 3e, bottom right). These findings suggest that the p.R270H variant that is significantly associated with obesity has an inhibitory effect on GPR120. The p.R270H mutant lacks the ability to transduce the signal of long-chain free fatty acids, contrary to the p.R67C mutant, which did not associate with obesity.

To analyse whether being a p.R270H variant carrier may affect GPR120 expression in the adipose tissue, we quantified GPR120 expression in samples from both obese p.R270H carriers and obese non-carriers. Two hundred and thirty-eight obese normoglycaemic patients from the Atlas Biologique de l'Obésité Sévère cohort had already been genotyped for the p.R270H variant. Ten subjects heterozygous for the p.R270H variant were matched for age, gender and body mass index with ten non-carrier (wild-type) obese normoglycaemic patients (Supplementary Table 7). The expression of GPR120 was similar between p.R270H carriers and wild-type subjects, both in subcutaneous and omental adipose tissues (Supplementary Fig. 7a), suggesting that the presence of the functionally deleterious mutation has no primary or secondary effect on gene expression in fat depots. The adipogenesis marker *PPARG*, the lipogenesis-related factor *SCD* and the macrophage marker *CD68* were found similarly well expressed in the adipose tissues of wild-type and p.R270H carrier patients (Supplementary Fig. 7b, c). Nevertheless, the expression of the fatty-acid-binding protein *FABP4* in omental adipose tissue was significantly lower in p.R270H carriers than in wild-type individuals (28% decrease,  $P = 0.043$ ; Supplementary Fig. 7b).

Our results provide convincing evidence that the lipid sensor GPR120 is involved in obesity in both mice and humans. Given the role of GPR120 as a physiologic integrator of the environment (especially the fatty diet), these data provide insight into the molecular mechanisms by which the 'Westernized' diet may contribute to early-onset obesity and associated complications including non-alcoholic steatohepatitis. It also brings some understanding of the metabolic effects of the omega-3 fatty acids, which are often proposed as food supplements. This may open novel avenues of research for drug development in the treatment of obesity, lipid metabolism abnormalities and liver diseases, because receptors that sense free fatty acids represent attractive drug targets.

## METHODS SUMMARY

GPR120-deficient mice were generated by deleting *Gpr120* exon 1. All animal procedures and euthanasia were reviewed by the local animal care committee approved by local government authorities. Blood analysis, extraction and detection of mRNA and proteins, and immunohistochemical analysis, were performed following standard protocols as described previously<sup>5,24–26</sup>. Details of antibodies, primers and probes are given in Methods. The level of significance for the difference between data sets was assessed using Student's *t*-test. Analysis of variance followed by Tukey's test was used for multiple comparisons.

In human, *GPR120* expression in liver and in both omental and subcutaneous adipose tissues was assessed by quantitative RT-PCR (Taqman), in lean and obese subjects from the Atlas Biologique de l'Obésité Sévère cohort. The four *GPR120* exons were sequenced in 312 French, extremely obese subjects following a standard Sanger protocol. The two identified non-synonymous variants (p.R270H and p.R67C/rs6186610) were subsequently genotyped in a large European obesity case-control study ( $n_{\text{cases}} = 6,942$ ,  $n_{\text{controls}} = 7,654$ ), by high-resolution melting analysis and TaqMan, respectively. The association between obesity status and each variant was assessed using logistic regression adjusted first for age and gender and then for age, gender and geography origin, under an additive model. The consequences of the two identified non-synonymous variants for *GPR120* function ( $[Ca^{2+}]_i$  response and GLP-1 secretion) were assessed *in vitro*. The human study protocol was approved by the local ethics committee, and participants from all of the studies signed an informed consent form.

**Full Methods** and any associated references are available in the online version of the paper at [www.nature.com/nature](http://www.nature.com/nature).

**Received 9 November; accepted 14 December 2011.**

**Published online 19 February 2012.**

- Nunez, E. A. Biological complexity is under the 'strange attraction' of non-esterified fatty acids. *Prostaglandins Leukot. Essent. Fatty Acids* **57**, 107–110 (1997).
- Haber, E. P. *et al.* Pleiotropic effects of fatty acids on pancreatic  $\beta$ -cells. *J. Cell. Physiol.* **194**, 1–12 (2003).
- Itoh, Y. *et al.* Free fatty acids regulate insulin secretion from pancreatic beta cells through GPR40. *Nature* **422**, 173–176 (2003).
- Cao, H. *et al.* Identification of a lipokine, a lipid hormone linking adipose tissue to systemic metabolism. *Cell* **134**, 933–944 (2008).
- Hirasawa, A. *et al.* Free fatty acids regulate gut incretin glucagon-like peptide-1 secretion through GPR120. *Nature Med.* **11**, 90–94 (2005).
- Steneberg, P., Rubins, N., Bartoov-Shifman, R., Walker, M. D. & Edlund, H. The FFA receptor GPR40 links hyperinsulinemia, hepatic steatosis, and impaired glucose homeostasis in mouse. *Cell Metab.* **1**, 245–258 (2005).
- Wang, J., Wu, X., Simonavicius, N., Tian, H. & Ling, L. Medium-chain fatty acids as ligands for orphan G protein-coupled receptor GPR84. *J. Biol. Chem.* **281**, 34457–34464 (2006).
- Ichimura, A., Hirasawa, A., Hara, T. & Tsujimoto, G. Free fatty acid receptors act as nutrient sensors to regulate energy homeostasis. *Prostaglandins Other Lipid Mediat.* **89**, 82–88 (2009).
- Maslowski, K. M. *et al.* Regulation of inflammatory responses by gut microbiota and chemoattractant receptor GPR43. *Nature* **461**, 1282–1286 (2009).
- Ahmed, K. *et al.* An autocrine lactate loop mediates insulin-dependent inhibition of lipolysis through GPR81. *Cell Metab.* **11**, 311–319 (2010).
- Oh, Da, Y. *et al.* GPR120 is an omega-3 fatty acid receptor mediating potent anti-inflammatory and insulin-sensitizing effects. *Cell* **142**, 687–698 (2010).
- Hara, T., Hirasawa, A., Ichimura, A., Kimura, I. & Tsujimoto, G. Free fatty acid receptors FFAR1 and GPR120 as novel therapeutic targets for metabolic disorders. *J. Pharm. Sci.* **100**, 3594–3601 (2011).
- Kimura, I. *et al.* Short-chain fatty acids and ketones directly regulate sympathetic nervous system via G protein-coupled receptor 41 (GPR41). *Proc. Natl Acad. Sci. USA* **108**, 8030–8035 (2011).
- Gotoh, C. *et al.* The regulation of adipogenesis through GPR120. *Biochem. Biophys. Res. Commun.* **354**, 591–597 (2007).
- Tanaka, T. *et al.* Free fatty acids induce cholecystokinin secretion through GPR120. *Naunyn Schmiedeberg Arch. Pharmacol.* **377**, 523–527 (2008).
- Miyauchi, S. *et al.* Distribution and regulation of protein expression of the free fatty acid receptor GPR120. *Naunyn Schmiedeberg Arch. Pharmacol.* **379**, 427–434 (2009).
- Kido, Y. *et al.* Tissue-specific insulin resistance in mice with mutations in the insulin receptor, IRS-1, and IRS-2. *J. Clin. Invest.* **105**, 199–205 (2000).
- Bernal-Mizrachi, E., Wen, W., Stahlhut, S., Welling, C. M. & Permutt, M. A. Islet beta cell expression of constitutively active Akt1/PKB alpha induces striking hypertrophy, hyperplasia, and hyperinsulinemia. *J. Clin. Invest.* **108**, 1631–1638 (2001).
- Hosooka, T. *et al.* Dok1 mediates high-fat diet-induced adipocyte hypertrophy and obesity through modulation of PPAR- $\gamma$  phosphorylation. *Nature Med.* **14**, 188–193 (2008).
- Ntambi, J. M. *et al.* Loss of stearoyl-CoA desaturase-1 function protects mice against adiposity. *Proc. Natl Acad. Sci. USA* **99**, 11482–11486 (2002).
- Gutierrez-Juarez, R. *et al.* Critical role of stearoyl-CoA desaturase-1 (SCD1) in the onset of diet-induced hepatic insulin resistance. *J. Clin. Invest.* **116**, 1686–1695 (2006).
- Jeyakumar, S. M. *et al.* Fatty acid desaturation index correlates with body mass and adiposity indices of obesity in Wistar NIN obese mutant rat strains WNIN/Ob and WNIN/GR-Ob. *Nutr. Metab. (Lond.)* **6**, 27 (2009).
- Brown, J. M. *et al.* Combined therapy of dietary fish oil and stearoyl-CoA desaturase 1 inhibition prevents the metabolic syndrome and atherosclerosis. *Arterioscler. Thromb. Vasc. Biol.* **30**, 24–30 (2010).
- Ichimura, A., Ruike, Y., Terasawa, K., Shimizu, K. & Tsujimoto, G. MicroRNA-34a inhibits cell proliferation by repressing mitogen-activated protein kinase 1 during megakaryocytic differentiation of K562 cells. *Mol. Pharmacol.* **77**, 1016–1024 (2010).
- Hara, T. *et al.* Novel selective ligands for free fatty acid receptors GPR120 and GPR40. *Naunyn Schmiedeberg Arch. Pharmacol.* **380**, 247–255 (2009).
- Sun, Q. *et al.* Structure-activity relationships of GPR120 agonists based on a docking simulation. *Mol. Pharmacol.* **78**, 804–810 (2010).

**Supplementary Information** is linked to the online version of the paper at [www.nature.com/nature](http://www.nature.com/nature).

**Acknowledgements** We are indebted to all subjects who participated in these studies. In Japan, the study was supported in part by research grants from the Japan Society for the Promotion of Science; the Ministry of Education, Culture, Sports, Science and Technology of Japan; the Japan Science and Technology Agency; and the Funding Program for World-Leading Innovative R&D on Science and Technology (FIRST Program), initiated by the Council for Science and Technology Policy. A.I. is a fellow of the Japan Society for the Promotion of Science. A.B. is a fellow of the EU-funded EUROCHIP consortium. In France, the study was supported by le Conseil Régional Nord Pas de Calais/FEDER and the Agence Nationale de la Recherche (Programme de Recherche en Nutrition et Alimentation, SensoFAT). The Northern Finland Birth Cohort Studies 1986 received financial support from the Academy of Finland, the University Hospital of Oulu (Finland), the University of Oulu (Finland), the European Commission (EURO-BLCS, Framework 5 award QLGI-CT-2000-01643), and the Medical Research Council (G0500539, G0600705, PrevMetSyn/SALVE). We thank the ABOS consortium and the CIC-CCPRB (Lille CHRU) team for their help in sample handling and clinical data collection. We are grateful to M. Deweirdt and F. Allegaert for human DNA bank management.

**Author Contributions** A.I., A. Hirasawa, O.P.-G. and A.B. are equally contributing first authors. G.T. and P.F. had the ideas for the mouse and human projects, respectively. A.I., A. Hirasawa, A.B., P.F. and G.T. drafted the manuscript. O.P.-G., H.C., D.M. and I.W. edited the manuscript and contributed to discussions. A. Hirasawa and G.T. designed the mouse research. A.I., A. Hirasawa, K.I. and G.T. created *Gpr120*-mutant mice. A.I., A. Hirasawa, A. Körner, T.H., I.K., T.-a.K., K.A., M. Takeuchi, K.O., N.L. and G.T. conducted biochemical and histochemical analyses for the mouse study. A.I. and A. Hirasawa performed bioinformatic analysis for the mouse study. L.Y. and C.L. performed the statistical analyses, and A.B. contributed to statistical analyses for the human study. O.P.-G. and I.W. designed the human expression gene study. A.L. performed the human expression gene study. H.C. and S.V. performed *GPR120* sequencing and variant genotyping, respectively. P.B., M. Tauber, C.M., A.M., R.B., P.E., M.-R.J., W.V.H., L.V.G., F.H., B.B., C.L.-M., K.R., A. Kouvatsi and F.P. contributed to cohort-study samples and researched data.

**Author Information** Microarray data have been deposited in the NCBI Gene Expression Omnibus under accession number GSE32095. Reprints and permissions information is available at [www.nature.com/reprints](http://www.nature.com/reprints). The authors declare no competing financial interests. Readers are welcome to comment on the online version of this article at [www.nature.com/nature](http://www.nature.com/nature). Correspondence and requests for materials should be addressed to P.F. ([p.froguel@imperial.ac.uk](mailto:p.froguel@imperial.ac.uk)) or G.T. ([gtsuji@pharm.kyoto-u.ac.jp](mailto:gtsuji@pharm.kyoto-u.ac.jp)).

## METHODS

**Generation and genotyping of GPR120-deficient mice.** GPR120-deficient mice on a mixed C57Bl/6J129 background were generated by homologous recombination. Exon 1 of the *Gpr120* gene was replaced with a PGK-neo cassette (Supplementary Fig. 1).

**Animals.** Mice were housed under a 12-hr light–dark cycle and given regular chow, MF (Oriental Yeast Co.). For HFD studies, 5-week-old male mice were placed on a 58Y1 diet (PMI Nutrition International) for a total period of 11 weeks. The methods used for animal care and experimental procedures were approved by the Animal Care Committee of Kyoto University.

**Indirect calorimetry.** Twenty-four-hour energy expenditure and respiratory quotient (RQ) were measured by indirect calorimetry, using an open-circuit calorimeter system (MK-5000RQ, Muromachi Kikai Co.). Respiratory quotient is the ratio of carbon dioxide production to oxygen consumption ( $\text{VO}_2$ ). Energy expenditure was calculated as the product of the calorific value of oxygen ( $3.815 + 1.232\text{RQ}$ ) and  $\text{VO}_2$ . Locomotor activity was measured by using an infrared-ray passive sensor system (Supermex, Muromachi Kikai Co.).

**Histology and immunohistochemistry.** Epididymal adipose and pancreatic tissues were fixed in 10% neutral-buffered formalin, embedded in paraffin, and sectioned at 5  $\mu\text{m}$ . H&E staining was performed using standard techniques. To measure the diameter of adipocytes and the area of pancreatic islets, the diameters of 100 cells from five sections from each group were measured using NIH IMAGE software. More than 10 fields were examined, islet area was traced and total islet area was calculated and expressed as the average score. Liver tissues were embedded in OCT compound (Sakura Finetech) and snap-frozen in liquid nitrogen. Tissue sections were stained with Oil Red O (Sigma-Aldrich) for lipid deposition using standard methods.

**Triglyceride content assay.** To determine the triglyceride content of liver, tissue was homogenized with 1/2.5/1.25 (vol/vol) 0.5 M acetic acid/methanol/chloroform. The mixture was shaken and 1.25 volumes of chloroform added. The mixture was shaken overnight and then 1.25 volumes of 0.5 M acetic acid added. After centrifugation at 1,500g for 10 min, the organic layer was collected, dried and resuspended in 100% isopropyl alcohol. Measurements were conducted using Triglyceride E-test Wako (Wako).

**Glucose tolerance and insulin tolerance tests.** Glucose tolerance assays were performed on 24-hr-fasted mice. After baseline glucose values were individually established using One Touch Ultra (LifeScan), each mouse was given an intraperitoneal injection of 1.5 mg glucose per gram of body weight. Insulin tolerance was conducted using the same glucometer. After baseline glucose values were established, mice were given human insulin ( $0.75 \text{ mU g}^{-1}$  intraperitoneal; Sigma-Aldrich). Clearance of plasma glucose was subsequently monitored at 15, 30, 60, 90 and 120 min post-injection.

**Immunoblot analysis.** For insulin stimulation, 5 U insulin (Sigma-Aldrich) was injected through the inferior vena cava. Five minutes later, samples of liver, skeletal muscle or WAT were dissected and immediately frozen in liquid nitrogen. Immunoblot analysis were performed as described previously<sup>5,24,25</sup>. Anti-IRS1 (Millipore), anti-IRS2 (Millipore), anti-SCD1 (Santa Cruz Biotechnology), anti-IR $\beta$  anti-AKT (Cell Signaling Technology), anti-p-AKT (Cell Signaling Technology) and anti- $\beta$ -actin (Sigma-Aldrich) antibodies were used as the primary antibodies.

**Mouse gene expression analysis.** Total RNA was extracted from tissue or cells using ISOGEN (Nippon Gene). Quantitative RT-PCR and microarray analysis were performed as described previously<sup>24,26</sup>. Briefly, genome-wide mRNA expression profiles were obtained by microarray analysis with the Affymetrix GeneChip Mouse 430 2.0 Array, according to the manufacturer's instructions. We used the robust multi-array analysis expression measure that represents the log-transformation of intensities (background corrected and normalized) from the GeneChips<sup>27</sup>. Functional associations between differentially expressed genes were analysed using Ingenuity Pathways Analysis (version 4.0, Ingenuity Systems).

**Microcomputed tomography scanning.** Images were obtained using a micro-computed tomography system (SHIMADZU ClairvivoCT) with a high-resolution flat-panel detector. The maximum resolution of this modality was less than 40  $\mu\text{m}$ . The scanner was assumed to have a cylindrical field of view of 65.3 mm in section view and of 300 mm in transaxial view. The X-ray source was biased at 60 keV with the anode current set to 160  $\mu\text{A}$ . Computed tomography images were analysed with OSIRIX software (<http://www.osirix-viewer.com/>).

**Fatty acid composition of epididymal WAT, liver and plasma.** Esterified and non-esterified fatty acid composition was measured by gas chromatography. Briefly, to analyse esterified fatty acid, samples of epididymal adipose tissue (20–25 mg), liver (25–30 mg) and plasma (100  $\mu\text{l}$ ) were snap-frozen in liquid nitrogen and homogenized in 4 ml of 0.5 N KOH-methanol. Samples were then boiled at 100 °C for 30 min to hydrolyse. Total lipids in each sample homogenate were then extracted with hexane, followed by trans-esterification of fatty acids using boron trifluoride-methanol at 100 °C for 15 min. Methylated fatty acids were then extracted with hexane and analysed using a GC-2010AF gas chromatograph

(SHIMADZU). For the analysis of non-esterified fatty acid, samples of epididymal adipose tissue (10–15 mg), liver (10–15 mg) and plasma (100  $\mu\text{l}$ ) were snap-frozen in liquid nitrogen and homogenized in a mixture of 1.2 ml water, 3 ml methanol and 1.5 ml chloroform. Total lipids in each sample homogenate were extracted with a mixture of 1.2 ml of water and 1.2 ml of chloroform, followed by silylation of fatty acids using  $\text{N,O}$ -bis(trimethylsilyl)trifluoroacetamide with 1% trimethylchlorosilane at 100 °C for 60 min. Silylated fatty acids were then extracted with hexane and analysed using a GC-2010AF gas chromatograph (SHIMADZU).

**Mouse embryonic fibroblast adipogenesis assay.** To prepare MEFs, we minced 13.5-d-post-coital mouse embryos and digested them with trypsin. Cells were collected and cultured in modified Eagle's medium ( $\alpha$ -MEM; supplemented with 10% fetal bovine serum (FBS), 50 U  $\text{ml}^{-1}$  penicillin and 50  $\text{mg ml}^{-1}$  streptomycin). We induced confluent MEFs to undergo adipogenic differentiation by incubating them first for 2 d with 10  $\mu\text{g ml}^{-1}$  insulin, 250 nM dexamethasone and 0.5 mM isobutylmethylxanthine (Sigma-Aldrich). We measured cellular triglyceride content with Triglyceride E-test Wako (Wako).

**Lipid infusion.** Intralipid solution with 2 mM triglycerides:palmitoleate was prepared using a previously described protocol<sup>4</sup>. Briefly, lipids were dissolved in a solvent containing 5% glycerol and 0.72% phosphocholine in 0.9% saline and sonicated repeatedly. Lipids stayed in suspension for one week and had to be vortexed well before loading the syringe and tubing to prevent clogging. Before lipid infusion, mice were anaesthetized and an indwelling catheter was inserted in the left internal jugular vein. After overnight fasting, lipids were infused at a rate of 500  $\text{ml kg}^{-1} \text{ h}^{-1}$  for 6 h. At the end of the infusion, tissues were collected.

**Statistical analysis of the GPR120-deficient mouse study.** The level of significance for the difference between data sets was assessed using Student's *t*-test. Analysis of variance followed by Tukey's test was used for multiple comparisons. Data were expressed as mean  $\pm$  s.e.m.  $P < 0.05$  was considered to be statistically significant.

**Human study population.** The study protocol was approved by all local ethics committees and informed consent was obtained from each subject before participation in the study, in accordance with the Declaration of Helsinki principles. For children younger than 18 years, an oral consent was obtained and parents provided written informed consent. All subjects were of European origin.

**Human gene expression analysis.** We used liver, subcutaneous and omental adipose tissue samples from the Atlas Biologique de l'Obésité Sévère (ABOS) cohort (ClinicalGov NCT01129297), a cohort studied in the Département de Chirurgie Générale et Endocrinienne<sup>28</sup> (Lille CHRU). Total RNA was extracted from the tissues using an RNeasy protect Mini Kit (QIAGEN) and quantified by absorbance at 260 nm and 280 nm in a PerkinElmer spectrophotometer. Human *GPR120*, *FABP4*, *PPARG*, *CD68* and *SCD* mRNA levels were quantified by reverse transcription reaction followed by qRT-PCR. Quantitative assessment of human mRNA expression was performed using TaqMan Gene Expression Assays (Hs0111664\_m1: *GPR120* and Hs99999905\_m1: *GAPDH*; Hs00609791\_m1: *FABP4*; Hs00234592\_m1: *PPARG*; Hs00154355\_m1: *CD68*; Hs01682761\_m1: *SCD*; Applied Biosystems) with an Applied Biosystems 7900HT Fast Real-Time PCR System. As an internal control for potential housekeeper reference variability, gene transcript levels were normalized to *GAPDH* reference housekeeper transcript level. The mean of the triplicate cycle thresholds of the target was normalized to the mean of triplicate cycle thresholds of the reference internal housekeeper genes using the formula  $2^{CT_{GAPDH} - CT_{target}}$ , which yielded a relative target-to-reference transcript concentration value as a fraction of reference transcript. Samples for which the cycle threshold was above 35 were excluded from the analysis.

**GPR120 exon sequencing.** We sequenced the four *GPR120* exons in 312 obese patients including 121 French obese adults and 191 French obese children who were recruited by the CNRS-UMR8199 unit and the Department of Nutrition of Paris Hotel Dieu Hospital. *GPR120* is located on human chromosome 10q23.33 and encodes a 377-amino-acid protein (NCBI NM\_181745.3 and NP\_859529). PCR conditions and primer sequences are available on request. Fragments were bidirectionally sequenced using the automated 3730xl DNA Analyzer (Applied Biosystems). Electrophoregram reads were assembled and analysed using the VARIANT REPORTER software (Applied Biosystems). The locations of the variants are displayed by base numbers counting from the ATG translation initiation codon following the Human Genome Variation Society nomenclature for the description of sequence variations. The positions of mutations were indicated by reference to the human genome build NCBI36/hg18.

**Genotyping of the p.R270H and p.R67C/rs6186610 variants.** We genotyped the two non-synonymous variants in 6,942 unrelated obese subjects and in 7,654 control subjects, all of European descent. Genotyped populations are described in Supplementary Table 4. The set of obese subjects included 516 unrelated French obese children who were recruited by the CNRS-UMR8199 unit or Toulouse Children's Hospital<sup>29</sup>; 332 Italian obese children from Verona<sup>30</sup> or Rome<sup>31</sup>; 170 Finnish obese adolescents from the Northern Finland Birth Cohort 1986<sup>32</sup>



(NFBC1986); 1,164 unrelated French obese adults from the ABOS cohort<sup>28</sup> or recruited by the CNRS-UMR8199 unit and the Department of Nutrition of Paris Hotel Dieu Hospital<sup>29</sup>; 2,514 Belgian obese patients from the outpatient obesity clinic at Antwerp University Hospital<sup>33</sup>; 1,736 Swiss obese subjects who were recruited after gastric surgery in Zurich<sup>34</sup>; and 510 Greek obese subjects recruited in the Hippokratia Hospital of Thessaloniki or in the Second Department of Internal Medicine of the Hospital of Alexandroupolis<sup>35</sup>. The set of control subjects included 422 Italian lean children from Verona<sup>30</sup>; 4,639 Finnish lean adolescents from the NFBC1986 cohort<sup>32</sup>; 1,976 French lean adults from the D.E.S.I.R. (Data from the Epidemiological Study on the Insulin Resistance syndrome) prospective study<sup>36</sup> and from the Haguenau study<sup>37</sup>; 148 Belgian lean subjects from Antwerp Hospital<sup>33</sup>; and 469 Greek lean individuals recruited in medical examination centres in Thessaloniki<sup>35</sup>. The 1,109 French pedigrees selected for obesity were recruited by the CNRS-UMR8199<sup>38</sup>, and the 780 German childhood obesity trios were recruited at the Universities of Marburg and Essen<sup>39</sup>. The p.R270H variant was genotyped using the LightCycler 480 High Resolution Melting (HRM) Master kit (Roche), following the manufacturer's protocol. Genotyping of p.R67C/rs6186610 was performed using a custom TaqMan assay according to the manufacturer's instructions (Applied Biosystems). Allelic discrimination was performed using an Applied Biosystems 7900HT Fast Real-Time PCR System and SDS 2.3 software. For both variants, genotype success rate was at least 95% and no deviation ( $P > 0.05$ ) from Hardy-Weinberg equilibrium was observed in any of the examined populations.

**Phenotyping.** The 90th and 97th body mass index (BMI) percentiles were used as thresholds for childhood overweight and obesity, respectively, according to the recommendations of the European Childhood Obesity Group study in local reference populations<sup>40,41</sup>. Adult subjects were defined as normal ( $\text{BMI} < 25 \text{ kg m}^{-2}$ ), overweight ( $25 \leq \text{BMI} < 30 \text{ kg m}^{-2}$ ) and obese ( $\text{BMI} \geq 30 \text{ kg m}^{-2}$ ) according to the International Obesity Task Force recommendations.

**In silico analysis of both p.R270H and p.R67C variants.** Phylogenetic conservation of the part of GPR120 containing each non-synonymous variant was assessed using the UCSC genome browser (Vertebrate Multiz Alignment & Conservation), based on a phylogenetic hidden Markov model, phastCons<sup>42</sup>. To predict the possible effect of both amino-acid substitutions on the structure and function of GPR120, we used several programs: the POLYPHEN (polymorphism phenotyping) web-based program<sup>43,44</sup>; PANTHER<sup>45</sup> (protein analysis through evolutionary relationships); the SIFT (sorting intolerant from tolerant) algorithm<sup>46</sup>; the SNAP (screening for non-acceptable polymorphisms) software<sup>47</sup>; and the PMUT web-based program<sup>48</sup>.

**Plasmid construction.** A FLAG-human GPR120/pcDNA5/FRT/TO plasmid was constructed by ligating GPR120 complementary DNA into the multicloning site of the mammalian expression vector pcDNA5/FRT/TO (Invitrogen) with the amino-terminal FLAG tag. The point mutation for constructing the FLAG-human GPR120 p.R67C/pcDNA5/FRT/TO and FLAG-GPR120 p.R270H/pcDNA5/FRT/TO plasmids was carried out using the following primers: p.R67C (sense: 5'-gggtgctggtgctgcccagcagcc-3'; antisense: 5'-ggcgtcgtcgccagccaccagcacc-3') and p.R270H (sense: 5'-agccaccagatccagctgtccagcaggac-3'; anti-sense: 5'-gtcctgtggga cagctggatctggtgct-3'). All constructs were confirmed by DNA sequencing.

**Cell lines and cell culture.** Flp-In T-REx-293 (T-REx 293) cells (Invitrogen) were used to develop inducible and stable cell lines expressing GPR120 (wild type, p.R270H or p.R67C). T-REx 293 cells were routinely cultured in Dulbecco's modified Eagle's medium (DMEM; Sigma) supplemented with 10% FBS,  $100 \mu\text{g ml}^{-1}$  Zeocin (Invitrogen) and  $10 \mu\text{g ml}^{-1}$  blasticidin S (Funakoshi). T-REx 293 cells were transfected with FLAG-GPR120 (wild type, p.R270H or p.R67C)/pcDNA5/FRT/TO using Lipofectamine reagent (Invitrogen) and selected with DMEM, which had been supplemented with 10% FBS,  $10 \mu\text{g ml}^{-1}$  blasticidin S and  $100 \mu\text{g ml}^{-1}$  hygromycin B (Gibco BRL). GPR120 protein expression was induced by adding  $10 \mu\text{g ml}^{-1}$  of doxycycline hyclate (Dox; Sigma) for 48 h. Human NCI-H716 cells were obtained from the American Type Culture Collection (Manassas). Cells were grown in suspension in Roswell Park Memorial Institute 1640 medium supplemented with 10% FBS,  $100 \text{ IU ml}^{-1}$  penicillin and  $100 \mu\text{g ml}^{-1}$  streptomycin.

**[Ca<sup>2+</sup>]<sub>i</sub> response analysis.** Cells were seeded at a density of  $2 \times 10^5$  cells per well on collagen-coated 96-well plates, incubated at 37 °C for 21 h and then incubated in Hanks' Balanced Salt Solution (HBSS, pH 7.4) containing Calcium Assay Kit Component A (Molecular Devices) for 1 h at 20 °C. ALA used in the fluorometric imaging plate reader (FLIPR, Molecular Devices) assay were dissolved in HBSS containing 1% DMSO and prepared in another set of 96-well plates. These plates were set on the FLIPR, and mobilization of [Ca<sup>2+</sup>]<sub>i</sub> evoked by agonists was monitored.

**Transfection.** One million cells were seeded into a 3.5-cm-diameter dish before transfection. NCI-H716 cells were transfected with 5  $\mu\text{g}$  of each plasmid using Lipofectamine 2000 (Invitrogen) according to the manufacturer's protocol. At 24 h post-transfection, transfection of each FLAG-tagged construct was confirmed by anti-FLAG FACS analysis. Then the cells were reseeded in 24-well culture plates

coated with Matrigel matrix (BD Biosciences) at a density of approximately  $3 \times 10^5$  cells per well for the secretion studies. To test the effect of variant receptors on the ALA-induced [Ca<sup>2+</sup>]<sub>i</sub> response of the wild-type receptor,  $2 \times 10^7$  T-REx 293 cells expressing Dox-inducible FLAG-GPR120 wild type were seeded into a 15-cm-diameter dish before transfection. Cells were then transfected with 32  $\mu\text{g}$  of each plasmid (empty vector, wild type and p.R270H GPR120) using Lipofectamine 2000 (Invitrogen) according to the manufacturer's protocol. At 24 h post-transfection, cells were reseeded at a density of  $2 \times 10^5$  cells per well on collagen-coated 96-well plates and treated with  $10 \mu\text{g ml}^{-1}$  of Dox, and at 48 h post-transfection, ALA-induced [Ca<sup>2+</sup>]<sub>i</sub> response was monitored.

**GLP-1 secretion analysis.** Cells were serum-starved with FBS-free DMEM for 3 h, washed with HBSS and incubated for 2 h at 37 °C in 0.3 ml FBS-free DMEM containing DMSO (negative control), 1  $\mu\text{M}$  phorbol 12-myristate 13-acetate (positive control) or 100  $\mu\text{M}$  ALA. Supernatants were collected and the active GLP-1 concentration in the supernatant was determined by enzyme immunoassay using GLP-1 (Active) ELISA Kit (Millipore).

**Flow cytometry analysis.** Anti-FLAG (Sigma) and anti-HA (Roche) antibodies were used for staining. Data were acquired and analysed on FACSCalibur with CELLQUEST software (Becton Dickinson).

**Statistical analysis of human study.** We assessed the effect of both non-synonymous variants (p.R270H and p.R67C) on obesity using a logistic regression adjusted first for age and gender and then for age, gender and geography, under an additive model, using the software R (version 2.12). Adjustment for geography was achieved to reflect a north-south gradient between the six different countries of origin of the study participants. An ordinal variable was created and coded: 1 for Finland, 2 for Belgium, 3 for France and Switzerland, 4 for Italy and 5 for Greece. This variable was added as a covariate in the logistic regression model.

Data analysis for the [Ca<sup>2+</sup>]<sub>i</sub> response was performed using IGOR PRO (WaveMetrics). Significant differences between expression among wild-type and heterozygous groups, and among lean and obese wild-type subjects, were assessed using non-parametric Mann-Whitney analysis (GRAPHPAD PRISM 5 software).

27. Gautier, L., Cope, L., Bolstad, B. M. & Irizarry, R. A. affy-analysis of Affymetrix GeneChip data at the probe level. *Bioinformatics* **20**, 307–315 (2004).
28. Poulain-Godefroy, O., Lecoeur, C., Pattou, F., Fruhbeck, G. & Froguel, P. Inflammation is associated with a decrease of lipogenic factors in omental fat in women. *Am. J. Physiol. Regul. Integr. Comp. Physiol.* **295**, R1–R7 (2008).
29. Meyre, D. et al. Genome-wide association study for early-onset and morbid adult obesity identifies three new risk loci in European populations. *Nature Genet.* **41**, 157–159 (2009).
30. Morandi, A. et al. The Q121 variant of ENPP1 may protect from childhood overweight/obesity in the Italian population. *Obesity (Silver Spring)* **17**, 202–206 (2009).
31. Buzzetti, R. et al. PPAR- $\gamma$ 2 Pro12Ala variant is associated with greater insulin sensitivity in childhood obesity. *Pediatr. Res.* **57**, 138–140 (2005).
32. Järvelin, M. R. et al. Ecological and individual predictors of birthweight in a northern Finland birth cohort 1986. *Paediatr. Perinat. Epidemiol.* **11**, 298–312 (1997).
33. Peeters, A. et al. Variants in the FTO gene are associated with common obesity in the Belgian population. *Mol. Genet. Metab.* **93**, 481–484 (2008).
34. Steffen, R., Potoczna, N., Bieri, N. & Horber, F. F. Successful multi-intervention treatment of severe obesity: a 7-year prospective study with 96% follow-up. *Obes. Surg.* **19**, 3–12 (2009).
35. Rouskas, K. et al. Association between BBS6/MKKS gene polymorphisms, obesity and metabolic syndrome in the Greek population. *Int. J. Obes. (Lond.)* **32**, 1618–1625 (2008).
36. Balkau, B. An epidemiologic survey from a network of French Health Examination Centres (D.E.S.I.R.): epidemiologic data on the insulin resistance syndrome [in French]. *Rev. Epidemiol. Sante Publique* **44**, 373–375 (1996).
37. Jaquet, D., Collin, D., Levy-Marchal, C. & Czernichow, P. Adult height distribution in subjects born small for gestational age. *Horm. Res.* **62**, 92–96 (2004).
38. Meyre, D. et al. R125W coding variant in TBC1D1 confers risk for familial obesity and contributes to linkage on chromosome 4p14 in the French population. *Hum. Mol. Genet.* **17**, 1798–1802 (2008).
39. Jarick, I. et al. Novel common copy number variation for early onset extreme obesity on chromosome 11q11 identified by a genome-wide analysis. *Hum. Mol. Genet.* **20**, 840–852 (2011).
40. Poskitt, E. M. Defining childhood obesity: the relative body mass index (BMI). European Childhood Obesity group. *Acta Paediatr.* **84**, 961–963 (1995).
41. Rolland-Cachera, M. F. et al. Body mass index variations: centiles from birth to 87 years. *Eur. J. Clin. Nutr.* **45**, 13–21 (1991).
42. Siepel, A. et al. Evolutionarily conserved elements in vertebrate, insect, worm, and yeast genomes. *Genome Res.* **15**, 1034–1050 (2005).
43. Ramensky, V., Bork, P. & Sunyaev, S. Human non-synonymous SNPs: server and survey. *Nucleic Acids Res.* **30**, 3894–3900 (2002).
44. Sunyaev, S. et al. Prediction of deleterious human alleles. *Hum. Mol. Genet.* **10**, 591–597 (2001).
45. Thomas, P. D. et al. PANTHER: a library of protein families and subfamilies indexed by function. *Genome Res.* **13**, 2129–2141 (2003).
46. Kumar, P., Henikoff, S. & Ng, P. C. Predicting the effects of coding non-synonymous variants on protein function using the SIFT algorithm. *Nature Protocols* **4**, 1073–1081 (2009).

47. Bromberg, Y., Yachdav, G. & Rost, B. SNAP predicts effect of mutations on protein function. *Bioinformatics* **24**, 2397–2398 (2008).
48. Ferrer-Costa, C. *et al.* PMUT: a web-based tool for the annotation of pathological mutations on proteins. *Bioinformatics* **21**, 3176–3178 (2005).

# The role of *Drosophila* Piezo in mechanical nociception

Sung Eun Kim<sup>1</sup>, Bertrand Coste<sup>1</sup>, Abhishek Chadha<sup>1</sup>, Boaz Cook<sup>1</sup> & Ardem Patapoutian<sup>1,2</sup>

Transduction of mechanical stimuli by receptor cells is essential for senses such as hearing, touch and pain<sup>1–4</sup>. Ion channels have a role in neuronal mechanotransduction in invertebrates<sup>1</sup>; however, functional conservation of these ion channels in mammalian mechanotransduction is not observed. For example, no mechanoreceptor potential C (NOMPC), a member of transient receptor potential (TRP) ion channel family, acts as a mechanotransducer in *Drosophila melanogaster*<sup>5</sup> and *Caenorhabditis elegans*<sup>6,7</sup>; however, it has no orthologues in mammals. Degenerin/epithelial sodium channel (DEG/ENaC) family members are mechanotransducers in *C. elegans*<sup>8</sup> and potentially in *D. melanogaster*<sup>9</sup>; however, a direct role of its mammalian homologues in sensing mechanical force has not been shown. Recently, Piezo1 (also known as Fam38a) and Piezo2 (also known as Fam38b) were identified as components of mechanically activated channels in mammals<sup>10</sup>. The Piezo family are evolutionarily conserved transmembrane proteins. It is unknown whether they function in mechanical sensing *in vivo* and, if they do, which mechanosensory modalities they mediate. Here we study the physiological role of the single Piezo member in *D. melanogaster* (*Dmpiezo*; also known as CG8486). *Dmpiezo* expression in human cells induces mechanically activated currents, similar to its mammalian counterparts<sup>11</sup>. Behavioural responses to noxious mechanical stimuli were severely reduced in *Dmpiezo* knockout larvae, whereas responses to another noxious stimulus or touch were not affected. Knocking down *Dmpiezo* in sensory neurons that mediate nociception and express the DEG/ENaC ion channel *pickpocket* (*ppk*) was sufficient to impair responses to noxious mechanical stimuli. Furthermore, expression of *Dmpiezo* in these same neurons rescued the phenotype of the constitutive *Dmpiezo* knockout larvae. Accordingly, electrophysiological recordings from *ppk*-positive neurons revealed a *Dmpiezo*-dependent, mechanically activated current. Finally, we found that *Dmpiezo* and *ppk* function in parallel pathways in *ppk*-positive cells, and that mechanical nociception is abolished in the absence of both channels. These data demonstrate the physiological relevance of the Piezo family in mechanotransduction *in vivo*, supporting a role of Piezo proteins in mechanosensory nociception.

*D. melanogaster* is widely used to study mechanotransduction, and genetic studies have identified several ion channels that are essential for mechanosensation<sup>5,9,12–14</sup>. However, none of the identified proteins have been shown to be activated by mechanical force when expressed in heterologous systems. Because expression of mouse Piezo proteins in a variety of mammalian cells induces mechanically activated currents<sup>10</sup>, we investigated whether the *Drosophila* counterpart is also sufficient to induce mechanosensitivity. Similar to its mammalian counterparts, the *Dmpiezo* gene is predicted to consist of a large number of transmembrane domains (39; Supplementary Fig. 1). Although fly and mammalian *piezo* genes do not exhibit extensive sequence conservation (24% identity), expression of *Dmpiezo* in cultured human cells induced mechanically activated cationic currents, suggesting a role of *Dmpiezo* in mechanotransduction<sup>11</sup>.

To characterize *Dmpiezo* expression in flies we used a fusion between the *Dmpiezo* enhancer/promoter region and GAL4 (*DmpiezoP*–GAL4). Four independent *DmpiezoP*–GAL4 transgenic insertions were examined to avoid insertional effects on GAL4 expression. We used green fluorescent protein (GFP) regulated by upstream activating sequence elements (UAS) (UAS-GFP) for labelling cells, except for arborized neurons that were optimally visualized using the membrane-targeted UAS-CD8::GFP. We found fluorescent labelling induced by *Dmpiezo* enhancer/promoter region in all types of sensory neurons and several non-neuronal tissues in both adults and larvae (Supplementary Fig. 2). This diverse pattern of *Dmpiezo* expression observed in *Drosophila* is in accord with the expression of Piezo1 and Piezo2 in mice<sup>10</sup>.

We created *Dmpiezo* knockout flies in which all 31 coding exons were deleted using genomic recombination<sup>15</sup> (Fig. 1a, see Supplementary Fig. 3 for details). The knockout flies were viable, fertile and did not show a lack of coordination or a defect in bristle mechanoreceptor potential (Supplementary Fig. 4). We studied whether *Dmpiezo* knockout larvae have mechanical nociception deficits by using a mechanically induced escape behaviour assay<sup>9,14,16</sup>. Stimulation with von Frey filaments that ranged from 2–60 milliNewton (mN) demonstrated that *Dmpiezo* knockout larvae have a severe response deficit over a wide range (Fig. 1b). Repeated stimulations of the same larvae resulted in comparable responsiveness in both wild-type and *Dmpiezo* knockout, indicating that the stimuli did not induce considerable damage to the sensory system (Fig. 1c, d). A 153 ± 11.0 mN filament elicited responses only to the first of three stimulations in wild-type larvae, arguing that this amount of force is damaging (data not shown). For further experiments, we chose to stimulate the larvae using a 45 mN filament, which has been used in a previous study<sup>14</sup>, and elicits a substantial response in both wild-type and *Dmpiezo* mutant larvae. Thirty four ± 4.4% of *Dmpiezo* knockout larvae showed a response to 45 mN filament stimulation, compared to over 80% of wild-type or heterozygote larvae (Fig. 1e). As a control for the genetic background, we used larvae that carry the *Dmpiezo* knockout allele on one chromosome and a deficiency in which the entire *Dmpiezo* genomic region is deleted on the homologous chromosome. The defect in the trans-heterozygote larvae was similar to the knockout homozygote phenotype (51 ± 3.9%, *P* = 0.091). In contrast, *Dmpiezo* knockout larvae were indistinguishable from wild type in an assay for responses to high temperature, a different noxious stimulus that elicits the same escape response<sup>14</sup> (Fig. 1f). Therefore, *Dmpiezo* knockout larvae retain a normal ability to elicit the escape behaviour in response to noxious stimuli, whereas *Dmpiezo* is specifically required for the mechanical modality of nociception. To evaluate the possible role of *Dmpiezo* in other modes of larval mechanical sensing, we tested the sensitivity of *Dmpiezo* knockout to gentle touch, which is mediated through ciliated neurons<sup>17,18</sup>. We observed no defect in the sensitivity of *Dmpiezo* knockout larvae to innocuous gentle touch (Fig. 1g).

A mechanical nociception phenotype was previously observed in mutants of *ppk*, a DEG/ENaC channel<sup>9</sup> and *painless* (*pain*), a TRPA

<sup>1</sup>Department of Cell Biology, Dorris Neuroscience Center, The Scripps Research Institute (TSRI), La Jolla, California 92037, USA. <sup>2</sup>Genomic Institute of the Novartis Research Foundation (GNF), San Diego, California 92121, USA.



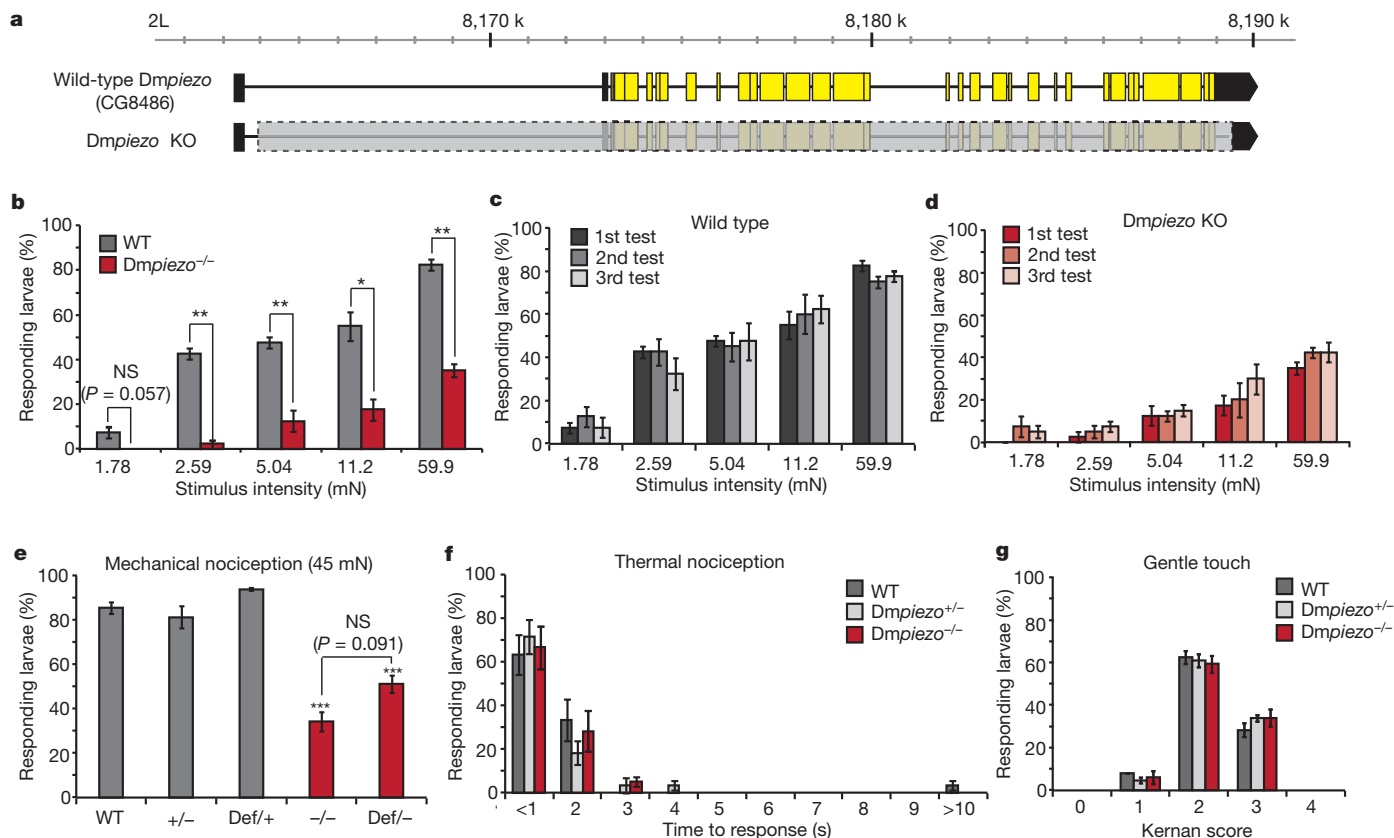


**Figure 1 | Mechanical nociception defect in *Dmpiezo* knockout larvae.**

**a**, Genomic map showing wild-type *Dmpiezo* gene (top) and engineered *Dmpiezo* knockout (bottom). Yellow and black boxes represent coding and non-coding exons, respectively. The segment deleted from the left arm of chromosome 2 (2L) in *Dmpiezo* knockout is marked with a grey box.

**b**, Mechanical nociception assay using a range of stimulus forces in wild-type (WT) and *Dmpiezo* knockout larvae. *n* = 40 from four independent experiments. \**P* < 0.05, \*\**P* < 0.01 from two-tailed paired Student *t*-test.

ion channel<sup>14</sup>. The specificity of *Dmpiezo* knockout to mechanical nociception resembles the phenotype of *ppk*, as *pain* is also essential for sensing thermal nociception<sup>14</sup>. We therefore tested the role of *Dmpiezo* in *ppk*-positive cells using *ppk*-GAL4, which labels subclasses of multidendritic neurons<sup>19,20</sup>. The multidendritic neurons are non-ciliated receptor cells that tile the body wall of the larvae and respond

to a variety of external stimuli such as mechanical forces, temperature and light<sup>9,14,16,21</sup>. We used enhanced (E)GFP driven directly by the regulatory regions of the *ppk* gene (*ppk*-EGFP)<sup>22</sup> together with a red fluorescent protein expression in *Dmpiezo*-positive cells to probe *Dmpiezo* and *ppk* co-expression. Indeed, we did observe that all *ppk*-positive cells also expressed *Dmpiezo* (Fig. 2a). Next we used *ppk*-GAL4 to drive the expression of *Dmpiezo* RNA interference (RNAi) to test whether *Dmpiezo* function is specifically required in *ppk*-expressing cells. The restricted knockdown of *Dmpiezo* resulted in a mechanical nociceptive phenotype (Fig. 2b) similar to the phenotype observed in *Dmpiezo* knockout larvae (Fig. 1e). In a complementary approach, we used *ppk*-GAL4-driven expression of *Dmpiezo* complementary DNA in an attempt to rescue the mechanical nociception phenotype of *Dmpiezo* knockout larvae. We used a fusion between DmPiezo and GFP to monitor expression levels in *ppk* cells and DmPiezo localization within the neurons. GFP-DmPiezo fusion protein induces mechanically activated currents in human cell lines, similar to untagged DmPiezo,

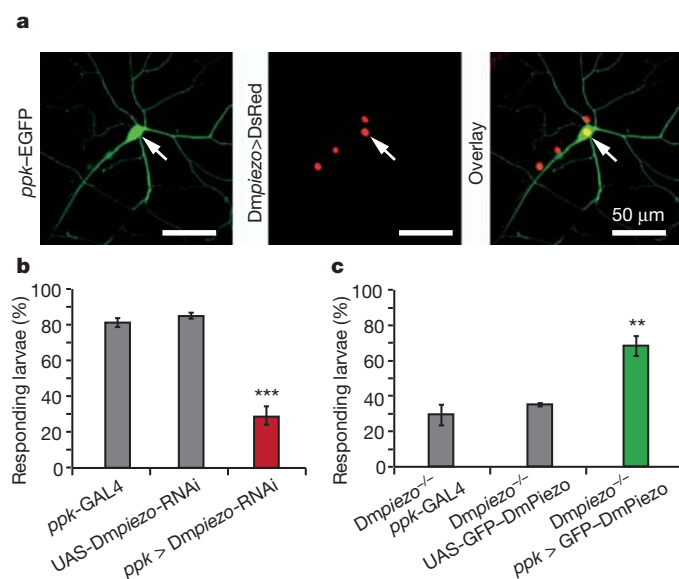


**Figure 2 | *Dmpiezo* functions in *ppk*-positive type II sensory neurons.**

**a**, Double fluorescence labelling using *ppk*-EGFP (green) and *Dmpiezo*P-GAL4 that drives the expression of the nucleus targeted UAS-DsRed-NLS (red). A representative high-magnification image shows one *ppk*-positive neuron (arrow). All three *ppk*-positive cells in each hemisegment expressed *Dmpiezo* in all segments.

**b**, Mechanical nociception assay with *Dmpiezo* knockdown larvae in *ppk*-expressing cells by *ppk*-GAL4 and UAS-*Dmpiezo*-RNAi. *n* > 85, \*\*\**P* < 0.001.

**c**, Mechanical nociception assay in rescued *Dmpiezo* knockout. GFP-DmPiezo was expressed in *ppk*-cells using *ppk*-GAL4 and UAS-GFP-DmPiezo. *n* > 60. \*\**P* < 0.01. Error bars indicate mean ± s.e.m.

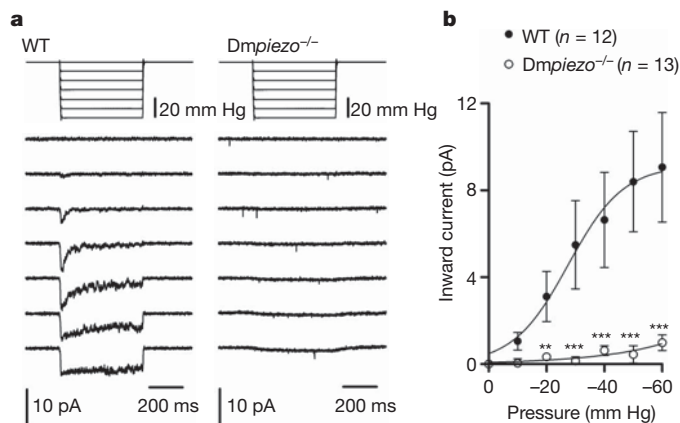


**Figure 3 | *Dmpiezo* mediates mechanically activated currents in *ppk*-positive neurons.** **a**, Representative currents elicited by negative pipette pressure (0 to -60 mm Hg,  $\Delta 10$  mm Hg) in cell-attached configuration at -80 mV in wild type (left) and *Dmpiezo*<sup>-/-</sup> (right). **b**, Average peak current-pressure relationship of stretch-activated currents in wild type (*n* = 12 cells) and *Dmpiezo*<sup>-/-</sup> (*n* = 13 cells). Data points are mean  $\pm$  s.e.m. fitted with a Boltzmann equation. \*\**P* < 0.01, \*\*\**P* < 0.001, Mann-Whitney test.

confirming functionality (Supplementary Fig. 5a–c). When expressed in *Drosophila*, GFP–DmPiezo fluorescence was present throughout cell bodies, axons and dendritic arborizations of *ppk*-positive neurons (Supplementary Fig. 5d). Importantly, expression of GFP–DmPiezo in *ppk*-positive neurons alone was sufficient to rescue the mechanical nociception defect of *Dmpiezo* knockout larvae (Fig. 2c). These data suggest that *Dmpiezo* functions in *ppk*-positive neurons to mediate mechanical nociception.

To test if the *ppk*-positive neurons respond to mechanical stimuli and if *Dmpiezo* mediates such responses, we performed electrophysiological recordings from isolated cells. Larvae that had GFP labelling in *ppk*-positive neurons were dissociated using enzymatic digestion and mechanical trituration. Plated fluorescent neurons were then tested

using patch-clamp recordings in the cell-attached configuration, and they were stimulated using negative pressure through the recording pipette<sup>10</sup>. Stimulating wild-type neurons resulted in a current that was rapidly activated and had a half-maximal activation ( $P_{50}$ ) of  $27.6 \pm 7.6$  mm Hg (Fig. 3). These currents were not observed in the *Dmpiezo* knockout mutant neurons (Fig. 3). Therefore, *ppk*-positive neurons, which mediate the avoidance response to noxious stimuli, display *Dmpiezo*-dependent, mechanically activated currents.

Silencing of *ppk* cells resulted in complete abolition of noxious mechanosensation (Supplementary Fig. 6), in accord with the severe defect previously observed<sup>16</sup>. In contrast, only a moderate deficit is observed upon eliminating or knocking down *ppk* in the same cells<sup>9</sup>, suggesting that there are multiple pathways for mechanical sensing. We tested mechanical nociception in larvae that are deficient in *Dmpiezo* and either *pain* or *ppk* to gain insight into cellular pathways that involve mechanotransduction in these cells. Once again, we used a 45 mN filament, enabling us to monitor both *Dmpiezo*-dependent and independent mechanisms (Fig. 1b). The *Dmpiezo*:*pain* double mutant had a defect that was comparable to each one of the mutants separately, suggesting that *Dmpiezo* and *pain* might function in the same pathway (Fig. 4a). Larvae that are heterozygous for both *Dmpiezo* and *pain* showed a response deficit whereas each one of them separately was normal (Fig. 4b), further demonstrating their role in a common signalling mechanism. Remarkably, combining both *Dmpiezo* and *ppk* knockdowns resulted in a nearly complete abolishment of responses to noxious mechanical stimuli (Fig. 4c). Importantly, responses to noxious temperatures and touch were normal in larvae with both *Dmpiezo* and *ppk* knocked down (Fig. 4d, e). These data indicate that *Dmpiezo* and *ppk* function in two parallel pathways in *ppk*-positive sensory neurons, and that together they constitute the response to noxious mechanical stimuli. There could be many reasons why the mechanically activated currents we observe are entirely dependent on DmPiezo (Fig. 3). This could either be because PPK responds to a different modality of mechanical stimulus or due to the specific experimental settings (for example, level of applied forces, solutions, applied voltage). Future experiments should resolve this issue.

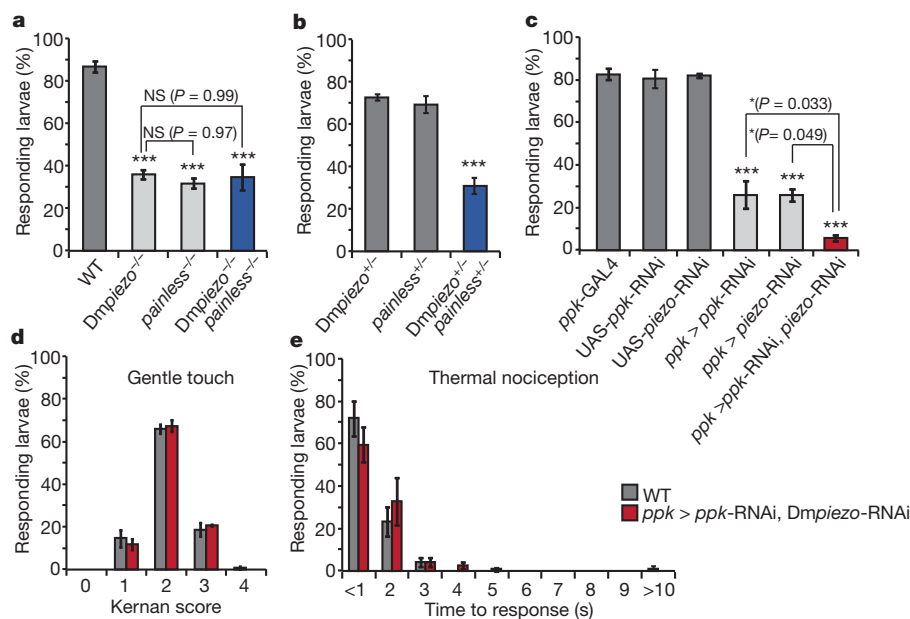


**Figure 4 | *Dmpiezo* and *ppk* function in parallel pathways.** **a**, Mechanical nociception assay using a 45 mN von Frey filament with double-null mutant of *Dmpiezo* and *painless*. Single-knockout strains were used as controls and the wild-type strain is *w*<sup>1118</sup>. *n* > 60. **b**, Mechanical nociception assay on heterozygous larvae for *Dmpiezo* and/or *pain*. *n* (heterozygote *Dmpiezo* knockout) = 74 from three trials, *n* (heterozygote *painless*) = 169 from five trials, *n* (trans-heterozygote) = 166 from five trials. **c**, Mechanical nociception

assay with *ppk* and *Dmpiezo* knockdown. *ppk* and/or *Dmpiezo* RNAi were driven by *ppk*-GAL4. *n* > 90. \**P* < 0.05, \*\*\**P* < 0.001. **d**, Gentle touch sensitivity assay with *ppk* and *Dmpiezo* knockdown. For details about the Kernan score, see Methods. Wild type is *w*<sup>1118</sup>. *n* > 90. **e**, Thermal nociception assay using 45 °C probe with *ppk* and *Dmpiezo* knockdown. *n* > 75. Error bars indicate mean  $\pm$  s.e.m.

Using the *Drosophila* model system we have demonstrated that *piezo* is essential for sensing noxious mechanical stimulus *in vivo*. This is the first demonstration that a Piezo family member is essential for mechanotransduction in the whole animal. Indeed, *Dmpiezo* is, to our knowledge, the first eukaryotic excitatory channel component shown to be activated by mechanical force in a heterologous expression system and required for sensory mechanotransduction *in vivo*. *Piezo2* is expressed in mouse dorsal root ganglion neurons that are involved in sensing nociception, and is required for rapidly adapting mechanically activated currents in such isolated neurons<sup>10</sup>. This study raises the possibility that mammalian *Piezo2* is also required for mechanical pain transduction *in vivo*. Furthermore, *Drosophila* genetics can now be used to map cellular pathways involved in *piezo*-dependent mechanotransduction in sensory neurons and beyond.

## METHODS SUMMARY

**Fly stocks.** PiggyBacs (PBac{WH}CG8486-f02291, PBac{RB}CG8486-e00109; Exelixis Collection at the Harvard Medical School), *ppk*-GAL4 (Bloomington *Drosophila* Stock Center (BDSC), 32078, 32079), Deficiency (Df(2L)Exel7034/CyO; BDSC, 7807), UAS-*Dmpiezo*-RNAi (National Institute of Genetics, Japan, 8486R-3), UAS-*ppk*-RNAi (Vienna *Drosophila* RNAi Center, 108683), *ppk*-EGFP5 (ref. 22; Y. N. Jan), *painless*<sup>1</sup> (BDSC, 27895).

**Generating *Dmpiezo* knockout flies.** The *Dmpiezo* knockout fly was generated by FLP-FRT recombination with two PiggyBac lines as described previously<sup>15</sup>. The recombined knockout fly was confirmed by PCR (Supplementary Fig. 3). The genetic background was cleaned using meiotic recombination with *w<sup>1118</sup>*.

**Imaging.** Fluorescence in adult fly or larva was detected by Nikon C2 Confocal Laser Point Scanning Microscope, Olympus FluoView500 Confocal Microscope or Olympus AX70 microscope.

**Cloning.** To clone the enhancer/promoter of the *Dmpiezo* gene, the genomic region between 1.0 kb upstream of the beginning of transcription and the start codon of *Dmpiezo* was amplified by PCR and cloned into the pPTGAL vector. The GFP-*Dmpiezo* construct has three alanines as a linker between the carboxy-terminal GFP and amino-terminal *Dmpiezo*. The construct was cloned in modified pUAST vector to generate transgenic flies and in modified pIRES2-EGFP vector for electrophysiology recordings.

**Behavioural assays and statistics.** The mechanical nociception was tested as described previously<sup>9,14,16</sup> using calibrated von Frey filaments. The thermal nociception was tested as described previously<sup>14</sup> using a 45 °C heated metal probe. All error bars represent mean ± s.e.m.

**Isolation of *ppk*-positive neurons.** Third instar larvae that had GFP labelling in *ppk*-positive neurons were dissected, digested with collagenase and mechanically triturated. The cells were collected by centrifugation and plated on a poly-D-lysine-coated glass coverslip. The fluorescent *ppk*-positive cells were recorded after incubating for 2 h at room temperature (23–25 °C).

**Electrophysiology.** HEK cells were studied in the whole cell configuration using a polished glass probe for stimulation<sup>10</sup> and *ppk*-positive neurons were stimulated using negative pressure in the cell attached configuration<sup>10</sup>.

**Full Methods** and any associated references are available in the online version of the paper at [www.nature.com/nature](http://www.nature.com/nature).

Received 22 July; accepted 20 December 2011.

Published online 19 February 2012.

- Chalfie, M. Neurosensory mechanotransduction. *Nature Rev. Mol. Cell Biol.* **10**, 44–52 (2009).

- Tsunozaki, M. & Bautista, D. M. Mammalian somatosensory mechanotransduction. *Curr. Opin. Neurobiol.* **19**, 362–369 (2009).
- Gillespie, P. G. & Muller, U. Mechanotransduction by hair cells: models, molecules, and mechanisms. *Cell* **139**, 33–44 (2009).
- Delmas, P., Hao, J. & Rodat-Despoix, L. Molecular mechanisms of mechanotransduction in mammalian sensory neurons. *Nature Rev. Neurosci.* **12**, 139–153 (2011).
- Walker, R. G., Willingham, A. T. & Zuker, C. S. A *Drosophila* mechanosensory transduction channel. *Science* **287**, 2229–2234 (2000).
- Li, W., Feng, Z., Sternberg, P. W. & Xu, X. Z. S. A *C. elegans* stretch receptor neuron revealed by a mechanosensitive TRP channel homologue. *Nature* **440**, 684–687 (2006).
- Kang, L., Gao, J., Schafer, W. R., Xie, Z. & Xu, X. Z. S. *C. elegans* TRP family protein TRP-4 is a pore-forming subunit of a native mechanotransduction channel. *Neuron* **67**, 381–391 (2010).
- O'Hagan, R., Chalfie, M. & Goodman, M. B. The MEC-4 DEG/ENaC channel of *Caenorhabditis elegans* touch receptor neurons transduces mechanical signals. *Nature Neurosci.* **8**, 43–50 (2005).
- Zhong, L., Hwang, R. Y. & Tracey, W. D. Pickpocket is a DEG/ENaC protein required for mechanical nociception in *Drosophila* larvae. *Curr. Biol.* **20**, 429–434 (2010).
- Coste, B. *et al.* Piezo1 and Piezo2 are essential components of distinct mechanically activated cation channels. *Science* **330**, 55–60 (2010).
- Coste, B. *et al.* Piezo proteins are pore-forming subunits of mechanically activated channels. *Nature* **483**, <http://dx.doi.org/10.1038/nature10812> (this issue).
- Kim, J. *et al.* A TRPV family ion channel required for hearing in *Drosophila*. *Nature* **424**, 81–84 (2003).
- Gong, Z. *et al.* Two interdependent TRPV channel subunits, Inactive and Nanchung, mediate hearing in *Drosophila*. *J. Neurosci.* **24**, 9059–9066 (2004).
- Tracey, W. D. Jr, Wilson, R. I., Laurent, G. & Benzer, S. *painless*, a *Drosophila* gene essential for nociception. *Cell* **113**, 261–273 (2003).
- Parks, A. L. *et al.* Systematic generation of high-resolution deletion coverage of the *Drosophila melanogaster* genome. *Nature Genet.* **36**, 288–292 (2004).
- Hwang, R. Y. *et al.* Nociceptive neurons protect *Drosophila* larvae from parasitoid wasps. *Curr. Biol.* **17**, 2105–2116 (2007).
- Kernan, M., Cowan, D. & Zuker, C. Genetic dissection of mechanosensory transduction: mechanoreception-defective mutations of *Drosophila*. *Neuron* **12**, 1195–1206 (1994).
- Caldwell, J. C., Miller, M. M., Wing, S., Soll, D. R. & Eberl, D. F. Dynamic analysis of larval locomotion in *Drosophila* chordotonal organ mutants. *Proc. Natl Acad. Sci. USA* **100**, 16053–16058 (2003).
- Adams, C. M. *et al.* Ripped Pocket and Pickpocket, novel *Drosophila* DEG/ENaC subunits expressed in early development and in mechanosensory neurons. *J. Cell Biol.* **140**, 143–152 (1998).
- Ainsley, J. A. *et al.* Enhanced locomotion caused by loss of the *Drosophila* DEG/ENaC protein Pickpocket1. *Curr. Biol.* **13**, 1557–1563 (2003).
- Xiang, Y. *et al.* Light-avoidance-mediating photoreceptors tile the *Drosophila* larval body wall. *Nature* **468**, 921–926 (2010).
- Grueber, W. B., Ye, B., Moore, A. W., Jan, L. Y. & Jan, Y. N. Dendrites of distinct classes of *Drosophila* sensory neurons show different capacities for homotypic repulsion. *Curr. Biol.* **13**, 618–626 (2003).

**Supplementary Information** is linked to the online version of the paper at [www.nature.com/nature](http://www.nature.com/nature).

**Acknowledgements** We thank Y. N. Jan of the University of California San Francisco for providing *ppk*-EGFP5. Research was support by the National Institutes of Health and Novartis Research Foundation. S.E.K. and A.C. are supported by the Skaggs Institute.

**Author Contributions** S.E.K. conducted most experiments. B. Coste performed the electrophysiology experiments shown in Fig. 3 and Supplementary Fig. 5. A.C. performed the fly electrophysiology experiments shown in Supplementary Fig. 4. S.E.K., A.P. and B. Cook designed experiments and wrote the manuscript.

**Author Information** Reprints and permissions information is available at [www.nature.com/reprints](http://www.nature.com/reprints). The authors declare no competing financial interests. Readers are welcome to comment on the online version of this article at [www.nature.com/nature](http://www.nature.com/nature). Correspondence and requests for materials should be addressed to B.C. (bcook@scripps.edu) or A.P. (apatapou@gnf.org).



## METHODS

**Fly stocks.** We used the following stocks: PiggyBacs (PBac{WH}CG8486-f02291, PBac{RB}CG8486-e00109, Exelixis Collection at the Harvard Medical School), *ppk*-GAL4 (Bloomington *Drosophila* Stock Center (BDSC), 32078, 32079), Deficiency (Df(2L)Exel7034/CyO, BDSC, 7807), UAS-*Dmpiezo*-RNAi (National Institute of Genetics, Japan, 8486R-3), UAS-*ppk*-RNAi (Vienna *Drosophila* RNAi Center, 108683), *ppk*-EGFP5 (ref. 22; Y. N. Jan), *painless*<sup>1</sup> (BDSC, 27895) and UAS-DsRed-NLS (J. W. Posakony). The following stocks were from BDSC: UAS-GFP, UAS-CD8::GFP, CyO-GFP, *w*<sup>1118</sup> and *Canton-S*.

**Engineering *Dmpiezo* knockout flies.** The *Dmpiezo* knockout fly was generated as described in previously described<sup>15</sup>. Two PiggyBac lines that carry the FRT sequence were selected for FLP-FRT recombination. PBac{WH}CG8486-f02291 is inserted in the first intron and PBac{RB}CG8486-e00109 in the 3' untranslated region (UTR) of the *Dmpiezo* gene. After FLP-FRT recombination, 20 kb of the *Dmpiezo* gene, including all 31 coding exons, was removed and replaced with 7 kb of PiggyBac insertion that contained the FRT sequence and white gene. The recombined knockout fly was confirmed by PCR reactions (Supplementary Fig. 2). The genetic background was cleaned using meiotic recombination with *w*<sup>1118</sup>.

**Molecular biology.** To clone the enhancer/promoter of the *Dmpiezo* gene, the genomic region between 1.0 kb upstream of the beginning of transcription and the start of the *Dmpiezo* coding region was amplified by PCR using forward primer, 5'-ATCTGGCGGCCGCTATCTATTTTAACTAGTGGAAGTCT-3' and reverse primer, 5'-TTACTGGTACCATGGATGCCTCCGCGCGCGTTC TCCTCCAG-3'. The amplified sequence was cloned into pPTGAL vector (*Drosophila* Genomic Resource Center, 1225) using NotI and KpnI sites and the sequence was verified.

For rescue experiments, *Dmpiezo* cDNA was amplified from the plasmid reported in ref. 11, using forward primer 5'-TATTAGCGGCCGAGTCTTCA GCTATGCGTGCATGGTG-3' and reverse primer 5'-TAATTCGGTCCGTTAT TGCGGTTGCTGTGGTGCAGTTGCTCCGG-3' and cloned into a modified pUAST vector using NotI and RsrII. NotI restriction enzyme site was used as a linker by providing three alanine residues between EGFP and DmPiezo. The order of sequences in the pUAST vector is the following: UAS-kozak-EGFP-3×(Ala)-DmPiezo. To generate transgenic flies, DNA was injected into the isogenized *w*<sup>1118</sup> embryos along with transposase Δ2-3. For the electrophysiology experiment, EGFP-DmPiezo was cloned into mammalian expression vector with CMV promoter.

**Behaviour assays.** Mechanical nociception was tested as described previously<sup>9,14,16</sup> using calibrated von Frey filaments. Thermal nociception was tested as described previously<sup>14</sup> using a calibrated heated metal probe. For both nociception assays, the number of larvae that showed at least one 360° rotation was counted for each trial. The gentle touch assay was performed and each stimulated larva was scored as described previously<sup>17</sup>. 0 = no response, 1 = hesitates, 2 = turns or withdraws anterior segments, 3 = single reverse contractile wave, and 4 = multiple waves. For all behaviour assays each third instar larva was stimulated only once. All data were generated from at least three trials.

The von Frey filaments for larvae behaviour experiments were modified from Touch-Test sensory Evaluator (North Coast Medical) or from monofilament fishing lines. Each monofilament was cut to a length of 18 mm, glued into a pipette tip so that 9 mm of it protruded and mounted on a hand manipulator with a 90° angle. Each von Frey filament was calibrated as described previously<sup>9</sup>. The force of each von Frey stimulator was determined by measuring the weight upon filament bending and converting the value into the force: force (mN) = mass (g) × gravity acceleration constant (g; 9.8). Each stimulator was calibrated 15 times and its mean

value was used in figures. The calibrated forces (mean ± s.e.m.) of each stimulator are as follows (in mN): 1.78 ± 0.15, 2.59 ± 0.15, 5.04 ± 0.19, 11.2 ± 0.66 and 59.9 ± 1.79.

**Fluorescence imaging.** For identifying tissues or cells expressing fluorescence by the *Dmpiezo* promoter, both adult flies and third instar larvae carrying *Dmpiezo*P-GAL4 and UAS-GFP, or UAS-CD8::GFP, were dissected or whole-mounted. For double fluorescent labelling in multidendritic neurons, second instar larvae carrying *ppk*-EGFP, *Dmpiezo*P-GAL4 and UAS-DsRed were whole-mounted. For imaging *ppk*-cells expressing GFP-DmPiezo, third instar larvae carrying *ppk*-GAL4 and UAS-GFP-DmPiezo were whole-mounted. Fluorescence images were obtained either by Nikon C2 Confocal Laser Point Scanning Microscope, Olympus FluoView500 Confocal Microscope or Olympus AX70 microscope.

**Isolation of larvae *ppk*-positive neurons.** In both wild-type and *Dmpiezo* knockout larvae, *ppk*-positive neurons were fluorescently labelled by *ppk*-EGFP, which is a direct fusion of *ppk* genomic regulatory regions with EGFP. Third instar larvae were dissected in M3 media containing 10% heat inactivated FBS. Each larva was cut twice and its internal organs were removed. The cleaned body wall was treated with 5 mg ml<sup>-1</sup> collagenase type IV at 25 °C for 1 h in serum-free M3 media and washed with serum containing M3 media. The enzyme-treated body wall was triturated with fire-polished Pasteur pipettes in M3 media with 2 mM EGTA and 10% FBS. The cuticle and debris were removed by centrifugation at 40g and the small size cells including neurons were collected by centrifugation at 360g for 10 min. The cell pellet was resuspended with serum containing M3 media and plated into a poly-D-lysine-coated coverslip in a small droplet. After 2 h of incubation at room temperature (23–25 °C), the coverslips were transferred to the electrophysiology rig for recording.

**Electrophysiology.** For whole-cell recordings in HEK293T cells, patch pipettes had resistances of 2–3 MΩ when filled with an internal solution consisting of (in mM) 133 CsCl, 10 HEPES, 5 EGTA, 1 CaCl<sub>2</sub>, 1 MgCl<sub>2</sub>, 4 MgATP and 0.4 Na<sub>2</sub>GTP (pH adjusted to 7.3 with CsOH). The extracellular solution consisted of (in mM) 130 NaCl, 3 KCl, 1 MgCl<sub>2</sub>, 10 HEPES, 2.5 CaCl<sub>2</sub>, 10 glucose (pH adjusted to 7.3 with NaOH). Mechanical stimulation was achieved using a fire-polished glass pipette (tip diameter 3–4 μm). The probe had a velocity of 1 μm ms<sup>-1</sup> during the ramp segment of the command for forward motion and the stimulus was applied for 150 ms.

For cell-attached recordings in *ppk*-positive dissociated neurons, patch pipettes had resistances of 3–3.5 MΩ when filled with a solution consisting of (in mM) 130 NaCl, 5 KCl, 10 HEPES, 1 CaCl<sub>2</sub>, 1 MgCl<sub>2</sub>, 10 TEA-Cl (pH 7.3 with NaOH). External solution used to zero the membrane potential consisted of (in mM) 140 KCl, 10 HEPES, 1 MgCl<sub>2</sub>, 10 glucose (pH 7.3 with KOH). Membrane patches were stimulated with brief negative pressure pulses through the recording electrode using a Clampex controlled pressure clamp HSPC-1 device (ALA-scientific). Stretch-activated channels were recorded at a holding potential of -80 mV with pressure steps from 0 to -60 mm Hg (-10 mm Hg increments). Current-pressure relationships were fitted with a Boltzmann equation of the form:  $I(P) = (1 + \exp(-(P - P_{50})/s))^{-1}$ , where  $I$  is the peak of stretch-activated current at a given pressure,  $P$  is the applied patch pressure (in mm Hg),  $P_{50}$  is the pressure value that evoked a current value which is 50% of  $I_{\max}$ , and  $s$  reflects the current sensitivity to pressure.

All experiments were performed at room temperature. Currents were sampled at 50 or 20 kHz and filtered at 5 or 2 kHz. Voltages were not corrected for a liquid junction potential. Leak currents before mechanical stimulations were subtracted off-line from the current traces.

# Piezo proteins are pore-forming subunits of mechanically activated channels

Bertrand Coste<sup>1\*</sup>, Bailong Xiao<sup>1\*</sup>, Jose S. Santos<sup>2</sup>, Ruhma Syeda<sup>2</sup>, Jörg Grandl<sup>1†</sup>, Kathryn S. Spencer<sup>1</sup>, Sung Eun Kim<sup>1</sup>, Manuela Schmidt<sup>1</sup>, Jayanti Mathur<sup>3</sup>, Adrienne E. Dubin<sup>1</sup>, Mauricio Montal<sup>2</sup> & Ardem Patapoutian<sup>1,3</sup>

**Mechanotransduction has an important role in physiology. Biological processes including sensing touch and sound waves require as-yet-unidentified cation channels that detect pressure. Mouse Piezo1 (MmPiezo1) and MmPiezo2 (also called Fam38a and Fam38b, respectively) induce mechanically activated cationic currents in cells; however, it is unknown whether Piezo proteins are pore-forming ion channels or modulate ion channels. Here we show that *Drosophila melanogaster* Piezo (DmPiezo, also called CG8486) also induces mechanically activated currents in cells, but through channels with remarkably distinct pore properties including sensitivity to the pore blocker ruthenium red and single channel conductances. MmPiezo1 assembles as a ~1.2-million-dalton homo-oligomer, with no evidence of other proteins in this complex. Purified MmPiezo1 reconstituted into asymmetric lipid bilayers and liposomes forms ruthenium-red-sensitive ion channels. These data demonstrate that Piezo proteins are an evolutionarily conserved ion channel family involved in mechanotransduction.**

Mechanically activated currents have been described in various mammalian cells, including inner ear hair cells<sup>1</sup>, somatosensory dorsal root ganglion neurons<sup>2</sup>, vascular smooth muscle cells<sup>3</sup> and kidney primary epithelia<sup>4</sup>. Most of these mechanically activated currents are cationic with Ca<sup>2+</sup> permeability, leading to a search for cation channels able to convert mechanical forces into such currents. Few mechanically activated channels have been described so far<sup>5–7</sup>; however, none of the candidates has been shown convincingly to mediate the physiologically relevant non-selective cationic mechanically activated currents in mammals.

MmPiezo1 was recently identified as a protein required for mechanically activated currents in a mammalian cell line. Expressing MmPiezo1 or related MmPiezo2 in a variety of mammalian cell lines induces mechanically activated cationic currents<sup>8</sup>. MmPiezo1-induced currents are inhibited by GsMTx4 (*Grammostola spatulata* mechanotoxin 4), a peptide widely used to study mechanically activated channels<sup>9</sup>. MmPiezo1 and MmPiezo2 contain over 30 putative transmembrane domains and do not resemble known ion channels or other protein classes. Piezo proteins could be non-conducting subunits of cationic ion channels required for proper expression or for modulating channel properties<sup>6,10,11</sup>. Alternatively, Piezo proteins may define a novel class of ion channels involved in mechanotransduction.

## Mechanosensitivity of DmPiezo

Piezo sequences are present in the genomes of many animal, plant and other eukaryotic species. Functional analysis of Piezo proteins from phylogenetically distant species could demonstrate a conserved role of these proteins in mechanotransduction; furthermore, a comparative analysis of mechanically activated currents could elucidate unique pore properties of channels induced by Piezo proteins from distinct species. We focused on the apparently single member of *D. melanogaster* Piezo (DmPiezo), as this invertebrate species is widely used to study mechanotransduction using genetic approaches<sup>12–16</sup>. DmPiezo is 24% identical to mammalian Piezo proteins, with sequence conservation

throughout the length of the proteins (Supplementary Fig. 1). We cloned the full-length DmPiezo complementary DNA into pIRES2-EGFP vector. We recorded mechanically activated currents from fluorescent HEK293T cells expressing DmPiezo-pIRES2-EGFP by applying force to the cell surface while monitoring transmembrane currents at constant voltage using patch-clamp recordings in the whole-cell configuration<sup>2,17,18</sup>. DmPiezo, but not mock-transfected cells, showed large mechanically activated currents (Fig. 1a, b). These currents have a time constant of inactivation  $\tau$  of  $6.2 \pm 0.3$  ms ( $n = 32$  cells) at  $-80$  mV when fitted with mono-exponential function, which is faster than observed for MmPiezo1 ( $\sim 16$  ms) and more comparable to MmPiezo2 ( $\sim 7$  ms)<sup>8</sup>. Similar to its mammalian counterparts, DmPiezo mechanically activated currents are characterized by a linear current-voltage ( $I$ - $V$ ) relationship with a reversal potential around 0 mV, consistent with it mediating a non-selective cationic conductance (Fig. 1c). We further characterized DmPiezo-induced currents in HEK293T cells in response to negative pressure pulses applied through the recording pipette in the cell-attached mode, an alternative mechanosensitivity assay. Overexpression of DmPiezo induced stretch-activated currents (Fig. 1d, e) with a pressure for half-maximal activation ( $P_{50}$ ) of  $-31.8 \pm 2.8$  mm Hg (Fig. 1f), similar to the  $P_{50}$  calculated for MmPiezo1-induced currents ( $\sim 30$  mm Hg)<sup>8</sup>. Therefore, mechanosensitivity of the Piezo family is conserved in invertebrates. We demonstrate the physiological relevance of DmPiezo *in vivo* in an accompanying paper<sup>19</sup>.

## Pore properties of Piezo proteins

We next compared fundamental permeation properties of MmPiezo1 and DmPiezo. Ruthenium red, a polycationic pore blocker of TRP channels<sup>20,21</sup>, blocks MmPiezo1- and MmPiezo2-induced mechanically activated currents<sup>8</sup>. We found that ruthenium red is a voltage-dependent blocker of MmPiezo1, with an IC<sub>50</sub> value of  $5.4 \pm 0.9$   $\mu$ M at  $-80$  mV (Fig. 2a–c): at a concentration of 30  $\mu$ M, extracellular ruthenium red inhibited inward mechanically activated currents without affecting

<sup>1</sup>Department of Cell Biology, Dorris Neuroscience Center, The Scripps Research Institute, La Jolla, California 92037, USA. <sup>2</sup>Section of Neurobiology, Division of Biological Sciences, University of California San Diego, La Jolla, California 92093, USA. <sup>3</sup>Genomic Institute of the Novartis Research Foundation, San Diego, California 92121, USA. <sup>†</sup>Present address: Department of Neurobiology, Duke University Medical Center, Durham, North Carolina 27710, USA.

\*These authors contributed equally to this work.

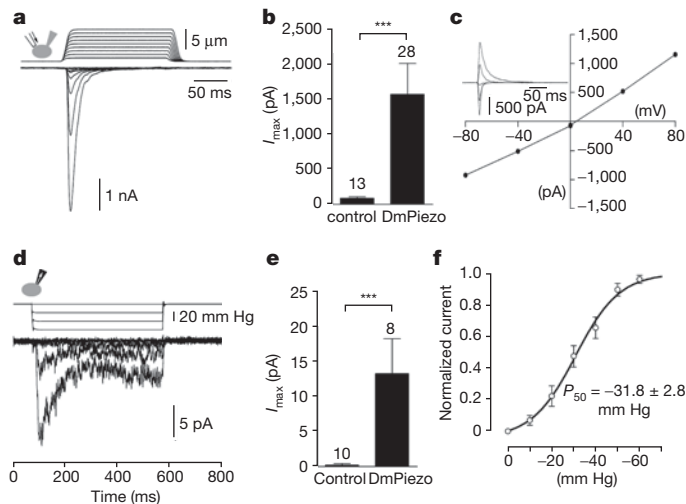


**Figure 1 | Human cells expressing *Drosophila* Piezo (DmPiezo) show large mechanically activated currents.** **a–f**, Mechanically activated currents of DmPiezo-expressing HE293T cells recorded in the whole-cell (**a–c**) or cell-attached (**d–f**) configuration. **a**, Representative traces of mechanically activated inward currents at  $-80$  mV in DmPiezo-transfected cells subjected to a series of mechanical steps in  $1\ \mu\text{m}$  increments. **b**, Average maximal current amplitude of mechanically activated inward currents at  $-80$  mV. **c**, Representative  $I$ – $V$  relationship of mechanically activated currents in DmPiezo-transfected cells. The inset shows mechanically activated currents evoked at holding potentials ranging from  $-80$  to  $+80$  mV. **d**, Representative currents elicited by negative pipette pressure ( $0$  to  $-60$  mm Hg,  $\Delta 20$  mm Hg) in DmPiezo-transfected cells. **e**, Average maximal current amplitude of stretch-activated currents at  $-80$  mV. **f**,  $I_{\text{max}}$  normalized current–pressure relationship of stretch-activated currents recorded at  $-80$  mV in DmPiezo-transfected cells ( $n = 8$  cells) and fitted with a Boltzmann equation.  $P_{50}$  is the average of  $P_{50}$  values determined for individual cells. Bars represent mean  $\pm$  s.e.m. and the number of cells tested is shown above bars. \*\*\* $P < 0.001$ , Mann–Whitney  $U$ -test.

outwards currents. Such voltage dependence is a characteristic of open channel block. A high concentration of ruthenium red ( $50\ \mu\text{M}$ ) included in the pipette solution in the whole-cell configuration showed no evidence of block, as large mechanically activated currents still displayed a linear  $I$ – $V$  relationship (Supplementary Fig. 2). These results suggest that ruthenium red blocks the pore of MmPiezo1-induced mechanically activated channels from the extracellular side. Notably, DmPiezo-induced mechanically activated currents were insensitive to ruthenium red concentrations that potently blocked MmPiezo1-induced currents (Fig. 2d, e). Together, these results demonstrate that overexpression of DmPiezo or MmPiezo1 gives rise to mechanically activated channels with distinct channel properties.

Next, we set out to determine the single channel conductance ( $\gamma$ ) of mechanically activated channels induced by Piezo proteins by using negative-pressure stimulations of membrane patches in cell-attached mode. Figure 3 shows the single mechanically activated channel properties of MmPiezo1 or DmPiezo. Openings of stretch-activated channels showed a marked difference in amplitude of single channel currents (Fig. 3a), as determined from the single channel  $I$ – $V$  relationship for MmPiezo1 and DmPiezo (Fig. 3b, c). Linear regression of these  $I$ – $V$  relationships resulted in slope-conductance values in these recording conditions of  $29.9 \pm 1.9$  and  $3.3 \pm 0.3$  pS for MmPiezo1- and DmPiezo-induced mechanically activated currents, respectively ( $n = 7$  and  $5$  cells; mean  $\pm$  s.e.m.). Therefore, DmPiezo-dependent channels are ninefold less conductive than MmPiezo1-dependent channels.

### MmPiezo1 oligomerization

The pore of most ion channels is formed by the assembly of transmembrane domains from distinct subunits (for example, voltage-gated  $\text{K}^+$  channels, ligand-gated ion channels) or structurally repetitive domains within a large protein (for example, voltage-gated  $\text{Na}^+$  and

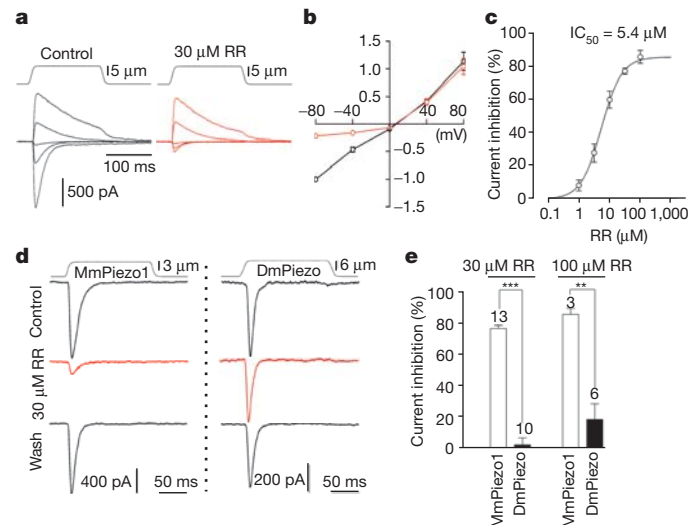


**Figure 2 | Ruthenium red is a channel pore blocker of MmPiezo1- but not DmPiezo-induced currents.** **a**, Representative traces of mechanically activated currents in MmPiezo1-transfected cells evoked at holding potentials ranging from  $-80$  to  $+80$  mV before (left panel) and during perfusion of  $30\ \mu\text{M}$  of ruthenium red (right panel, red traces). **b**, Average  $I$ – $V$  relationship of mechanically activated currents in MmPiezo1-transfected cells ( $n = 7$  cells) before (black symbols) and during (red symbols) perfusion of  $30\ \mu\text{M}$  ruthenium red. Currents were normalized to the value of control current evoked at  $-80$  mV for each individual cell. **c**, Concentration–inhibition curve for ruthenium red (RR) on mechanically activated currents evoked at  $-80$  mV in MmPiezo1-transfected cells and fitted with a Boltzmann equation. Each data point is the mean  $\pm$  s.e.m. of 3–13 observations. **d**, Representative traces of Piezo-dependent mechanically activated currents evoked at  $-80$  mV in the presence of ruthenium red. **e**, Blocking effect of ruthenium red on Piezo-dependent mechanically activated currents evoked at  $-80$  mV. Bars represent mean  $\pm$  s.e.m. and the number of cells tested is shown above the bars. \*\* $P < 0.01$ ; \*\*\* $P < 0.001$ ; unpaired  $t$ -test.

$\text{Ca}^{2+}$  channels). As Piezo proteins lack repetitive transmembrane motifs presumably they oligomerize to form ion channels. To test this hypothesis, we determined the number of subunits in Piezo complexes by expressing GFP–MmPiezo1 fusion proteins in *Xenopus laevis* oocytes, imaging individual spots with total internal reflection microscopy (TIRF), and counting discrete photobleaching steps (Fig. 4a, b and ref. 22). Amino-terminal GFP–MmPiezo1 functionality was confirmed by overexpression in HEK293T cells (Supplementary Fig. 3). We used several GFP fusion constructs of ion channels with known stoichiometry as controls: voltage-gated  $\text{Ca}^{2+}$  channel ( $\alpha 1\text{E}$ –GFP; monomer), NMDA ( $N$ -methyl- $D$ -aspartate) receptor (NR1 co-expressed with NR3A–GFP; dimer of dimers) and cyclic nucleotide-gated (CNG) channel (XfA4–GFP; tetramer)<sup>22</sup>. We found that complexes of MmPiezo1 frequently exhibited at most four photobleaching steps, consistent with the idea that Piezo proteins homo-multimerize. Fluorescent MmPiezo1 (or CNG) complexes exhibiting bleaching in fewer than four steps can be explained by non-functional GFP or pre-bleached GFP<sup>22</sup> or general bias against noisier multi-step traces during data analysis (see Methods). Histograms of the number of photobleaching steps observed for MmPiezo1 complexes were comparable to histograms obtained from tetrameric CNG channels (Fig. 4c). These results suggest that in living cells, Piezo proteins can assemble as homo-multimers.

We further characterized Piezo proteins biochemically by heterologously expressing and purifying MmPiezo1 carboxy-terminally fused with a glutathione  $S$ -transferase (MmPiezo1–GST). Functionality of MmPiezo1–GST was confirmed by overexpression in HEK293T cells (Supplementary Fig. 3). We observed a protein band at a position near the 260-kDa protein marker on a Coomassie-blue-stained denaturing protein gel (Supplementary Fig. 4a). Western blot with a GST (*Schistosoma japonicum* form) antibody (Supplementary Fig. 4b) or



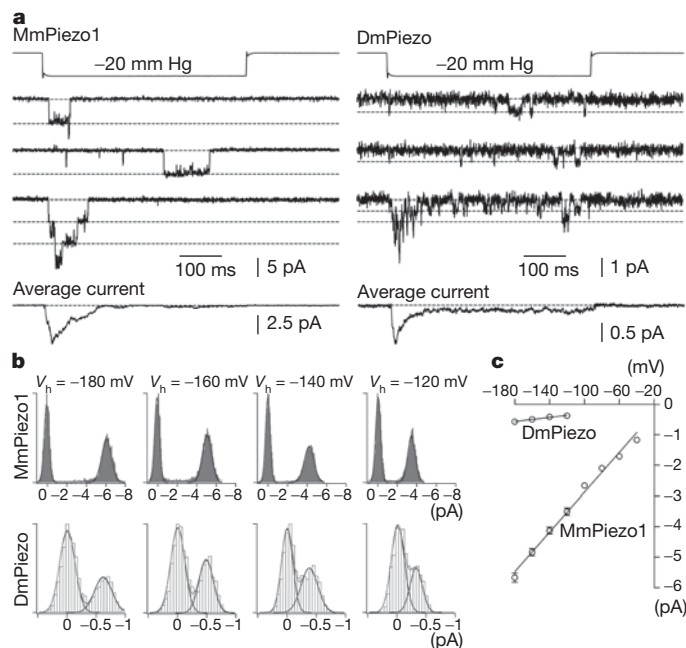


**Figure 3 | MmPiezo1- and DmPiezo-induced stretch-activated channels have different conductances.** **a**, Representative Piezo-dependent stretch-activated channel openings elicited at  $-180$  mV. Bottom traces represent average of 40 individual recording traces. **b**, All-point histograms of single channel opening events (average of 10 and 20 individual events for MmPiezo1 and DmPiezo, respectively) at different holding potentials ( $V_h$ ). **c**, Average  $I-V$  relationships of stretch activated single channels in MmPiezo1 and DmPiezo transfected cells ( $n = 7$  and 5 cells, respectively; mean  $\pm$  s.e.m.). Single channel amplitude was determined as the amplitude difference in Gaussian fits as shown in **b**.

a MmPiezo1-specific antibody<sup>8</sup> (Fig. 4) confirmed the presence of MmPiezo1-GST in the MmPiezo1-GST sample. Using native gel electrophoresis and Coomassie blue staining, we detected a prominent protein band at a position near the 1,236 kDa protein marker only in the MmPiezo1-GST sample (Fig. 4d). Western blot using MmPiezo1 antibody confirmed that this major band contains MmPiezo1 (Fig. 4e). These data indicate that the purified MmPiezo1-GST protein complex has a molecular weight of about 1.2 million Da, four times the predicted molecular weight of a single MmPiezo1-GST polypeptide (318 kDa). Next, we asked whether any endogenous proteins are present in this MmPiezo1-containing complex. Mass spectrometry of the  $\sim 1.2$  million Da protein complex mainly detected peptides derived from MmPiezo1-GST, but not from other endogenous membrane proteins. Although several non-transmembrane proteins were also detected, most of them were also present in the control sample, indicating an absence of specific interacting proteins in the complex (Supplementary Table 1). Moreover, mass spectrometry of the whole purified solution samples before gel electrophoresis confirmed that no other ion channel protein was detected (Supplementary Table 2). This indicates that MmPiezo1 is not tightly associated with any endogenous pore-forming protein.

To examine further whether this Piezo complex is indeed a tetramer, we treated the purified MmPiezo1-GST protein with the crosslinker formaldehyde and subjected the samples to denaturing gel electrophoresis and western blotting. Formaldehyde-treated samples contained three major additional higher-order Piezo-containing bands, with longer treatments increasing the prominence of the higher bands (Fig. 4f). The distribution of the bands on the 3–8% gradient gel suggests that the four bands correspond to monomer, dimer, trimer and tetramer of MmPiezo1-GST (Fig. 4f). The observation that MmPiezo1 is crosslinked by formaldehyde, a crosslinker with a relative short spacer arm (2.3–2.7 Å), suggests that the subunits form a tetramer.

It is possible that MmPiezo1 oligomers associate with other proteins; however, such an association might not withstand the GST purification step. To probe this, we performed paraformaldehyde (PFA) crosslinking experiments on living cells before the purification procedure. On a native gel, the MmPiezo1-GST complex purified from PFA-treated cells also migrated to the position near the 1,236 kDa protein marker, similar to the sample from untreated cells (Fig. 4g). On a denaturing gel, on-cell PFA treatment resulted in four distinct MmPiezo1-specific bands, similar to results of formaldehyde treatment on the purified complex (Fig. 4h). This suggests that MmPiezo1 is not tightly associated with other proteins large enough to alter discernibly its size on denaturing gels, and confirms the results from mass spectrometry analysis. However, our crosslinking studies with PFA might miss weak interactors with MmPiezo1. Regardless, together with the results obtained from single-molecule photobleaching analysis in living cells, our biochemical data suggest that MmPiezo1 forms a homomultimeric ion channel, most likely as a homotetramer.

### MmPiezo1 reconstitution in lipid bilayers

Finally, to assess whether Piezo proteins were sufficient to recapitulate the channel properties recorded from Piezo-overexpressing cells, we reconstituted purified MmPiezo1 proteins into lipid bilayers in two distinct configurations: droplet interface lipid bilayers (DIBs) assembled from two monolayers<sup>23–25</sup> (Fig. 5a–e and l–q) and proteoliposomes<sup>26</sup> (Fig. 5f–h). In the first configuration, MmPiezo1 was reconstituted into asymmetric bilayers that mimic the cellular environment: the extracellular-facing lipid monolayer is predominantly neutral whereas the intracellular-facing leaflet is negatively charged<sup>27</sup>. In contrast, the lipid composition of the bilayer in the second configuration is uniform.

In the DIBs setting, representative segments from a 6-min recording obtained at  $-100$  mV show brief, discrete channel openings (Fig. 5a, b) blocked by addition of 50  $\mu$ M ruthenium red to the neutral facing compartment (Fig. 5c). In contrast, no effect was observed when ruthenium red was introduced into the negative-facing compartment (not shown). We detected efficient block of channel activity even at 5  $\mu$ M ruthenium red (not shown). The asymmetric accessibility of ruthenium red block of reconstituted channels agrees with the data obtained from MmPiezo1-overexpressing HEK293T cells (Fig. 2 and Supplementary Fig. 2), thereby establishing the fidelity of the assays and validating MmPiezo1 protein as an authentic ion channel. The Piezo currents exhibit ohmic behaviour; records displayed at higher resolution (Fig. 5b) clearly demonstrate the occurrence of unitary events with  $\gamma$  values obtained from conductance histograms of  $118 \pm 15$  pS and  $80 \pm 6$  pS ( $n = 6$ ) in symmetric 0.5 M KCl from the negative and positive branches of  $I-V$  plots, respectively (Fig. 5d, e).

A similar pattern of activity was obtained from MmPiezo1 reconstituted in asolectin liposomes<sup>26</sup> (Fig. 5f–k). A selection of recordings shows the presence of two channels in the membrane which reside predominantly in the open state (Fig. 5f, g), as discerned in a higher time resolution display (Fig. 5k). These recordings were obtained in the presence of 50  $\mu$ M ruthenium red inside the recording pipette, to ensure functional selection of a single population of MmPiezo1 channels facing the ruthenium-red-free compartment. MmPiezo1 in asolectin proteoliposomes under these conditions (symmetric 0.2 M KCl) exhibits a  $\gamma = 110 \pm 10$  pS at  $V = -100$  mV and  $80 \pm 5$  pS at  $V = 100$  mV (Fig. 5h–j) ( $n = 8$ ). Finally, reconstitution of control samples purified from non-transfected cells as well as heat-denatured purified MmPiezo1-GST into either bilayer systems under otherwise identical conditions failed to reproduce this pattern of channel activity (not shown).

We then tested the ability of the reconstituted MmPiezo1 to conduct sodium (Fig. 5l–q). Initially, single channel currents were recorded from asymmetric bilayers in symmetric 0.2 M KCl;  $\gamma = 58 \pm 5$  pS (Fig. 5l, o). Subsequent addition of 0.2 M NaCl in the presence of 0.2 M KCl increased the unitary conductance of reconstituted channels to  $95 \pm 5$  pS (Fig. 5m, p) while retaining sensitivity to ruthenium red

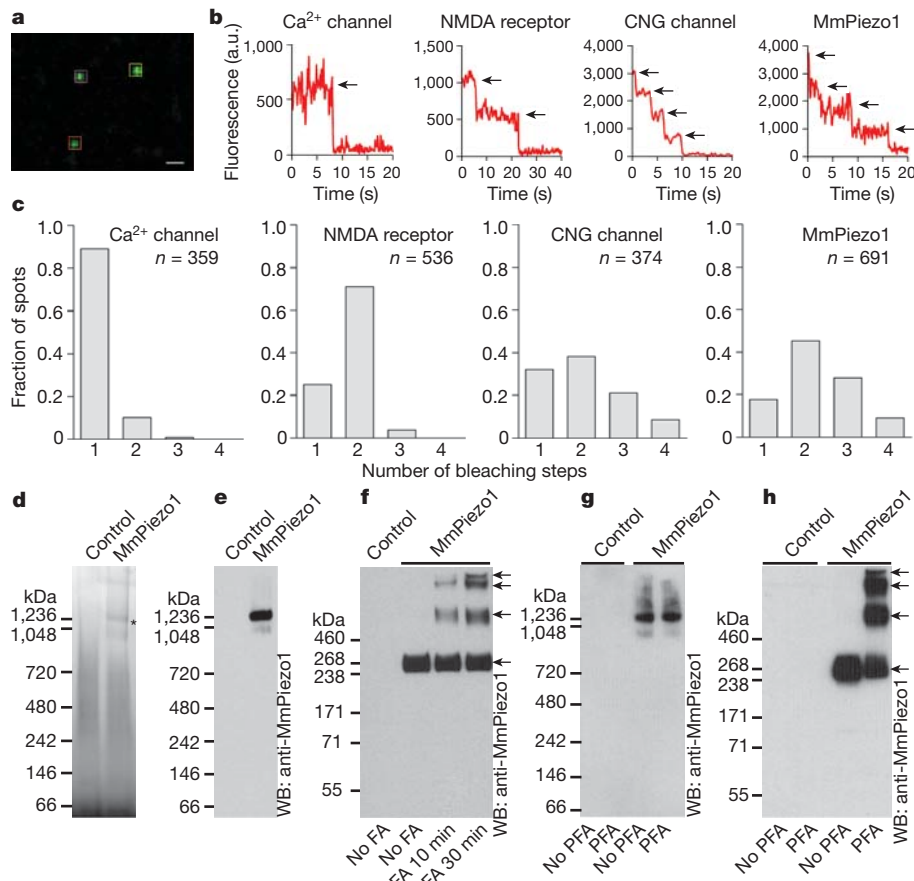


**Figure 4 | MmPiezo1 forms homo-oligomers.** **a**, Representative image of an acquired sequence showing three selected GFP–MmPiezo1 spots in the cell membrane. Levels were adjusted for clarity. Scale bar, 0.8  $\mu$ m. **b**, Representative traces of fluorescence intensities of indicated single GFP–fusion constructs. Black arrows indicate photobleaching steps. **c**, Histograms of the average number of bleaching steps observed in ten or more movies from four or more oocytes of single fluorescent complexes of indicated constructs. **d**, **e**, Indicated samples purified and separated on native gels and visualized by Coomassie staining (**d**) or western blotting (**e**). Asterisk in **d** indicates a protein band

specifically present in the MmPiezo1 sample. **f**, Purified MmPiezo1–GST proteins treated with or without formaldehyde (FA) with the indicated time period, separated on a denaturing gel and detected with the anti-MmPiezo1 antibody. Sample purified from cells without transfection served as a negative control. **g**, **h**, MmPiezo1–GST-transfected HEK293T cells or untransfected cells treated with or without 0.25% PFA for 10 min. The crosslinked MmPiezo1–GST proteins were purified and separated on native gel (**g**) or denaturing gels (**h**), followed by western blotting. Panels **d–h** are representatives of at least three independent experiments.

block (Fig. 5n, q). These results confirm that these channels conduct both sodium and potassium as would be expected from a cationic non-selective channel. This assertion was further substantiated by recording MmPiezo1 currents from proteoliposomes under bi-ionic conditions (0.2 M KCl/0.2 M NaCl) (Supplementary Fig. 5a–h). A summary of the *I–V* relation for the MmPiezo1 channel, extracted from 204,088 events obtained in three experiments, shows that the single channel current is ohmic between  $-100$  and  $200$  mV with a slope conductance of  $102 \pm 2$  pS (Supplementary Fig. 5i). The current reversed direction at  $0.0 \pm 0.3$  mV, demonstrating that the channel does not select between  $K^+$  and  $Na^+$ , and importantly, displays open channel block by ruthenium red (Supplementary Fig. 5j–l).

The difference in  $\gamma$  between overexpressed MmPiezo1 in cells and reconstituted MmPiezo1 in lipid bilayers may be attributed to many variables, including the distinct lipid environments which are known to influence conductance measurements strongly<sup>28–32</sup>. Moreover, the ionic conditions used in the two systems are different, as divalent cations present in HEK293T cell-attached experiments also affect the conductance values. Indeed, when divalent cations are excluded from the recording pipette,  $\gamma$  of MmPiezo1-induced currents in HEK293T cells is  $58.0 \text{ pS} \pm 1.5 \text{ pS}$  (150 mM NaCl solution, Supplementary Fig. 6), compared to  $29.9 \pm 1.5$  pS in the presence of divalent ions (Fig. 3). The near equivalence of  $\gamma$  values together with the similar pattern of channel activity demonstrates that reconstitution

of MmPiezo1 into two distinct bilayer systems produces channels with identical functional properties (Supplementary Table 3).

Future reconstitution and recording of DmPiezo in lipid bilayers will show whether the difference in conductance between MmPiezo1 and DmPiezo arises from intrinsic properties. The membrane environment and lipid composition are known to modulate the activity of the embedded channel proteins in a drastic and deterministic manner (for example, see refs 28–32). It is not entirely surprising that the conditions to emulate the cellular environment in the reconstituted system in terms of the mechanical state of the membrane or its lipid composition have thus far been inadequate to retrieve the activation features of mechanically activated ion channels. Furthermore, the complexity of protein clusters and dynamic cytoskeletal interacting partners at the cell membrane<sup>33</sup> introduce regulatory constraints on channel activity. Further investigation may clarify whether Piezo ion channel subunits are intrinsically mechanosensitive or use unknown interacting partners to sense membrane tension.

### Concluding remarks

We provide compelling evidence to support the hypothesis that Piezo proteins are indeed ion channels. First, overexpression of DmPiezo or MmPiezo1 in a human cell line gives rise to mechanically activated channels with distinct biophysical and pore-related properties. Second, isolated Piezo complexes do not contain detectable amounts

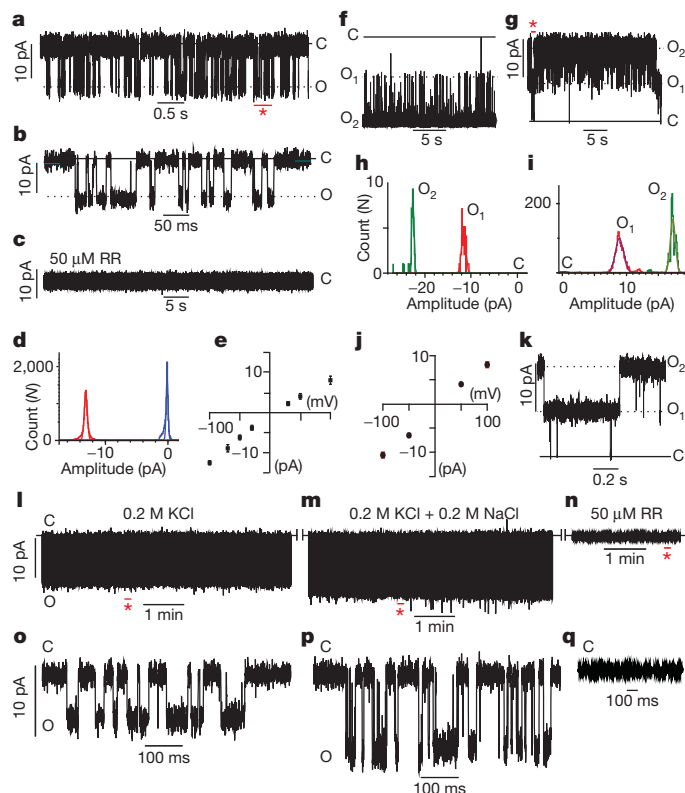


**Figure 5 | MmPiezo1 forms ruthenium-red-sensitive ion channels.** **a–e**, Reconstitution of purified MmPiezo1 into asymmetric lipid bilayers. **a**, Representative single channel currents at  $-100$  mV. The section of the recordings indicated by the red asterisk is shown in **b** at a 10-fold higher time resolution. **c**, After 35 min of recording the channel activity shown in **a**, injection of  $50 \mu\text{M}$  ruthenium red onto the neutral facing compartment blocks MmPiezo1 currents. **d**, All-event current amplitude histogram of a 6-min recording;  $\gamma = 124 \pm 7$  pS. The total number of opening events ( $N$ ) analysed was 18,424. **e**, Single channel  $I$ – $V$  relationship,  $n = 6$  experiments. **f–k**, Reconstitution of purified MmPiezo1 into asymmetric lipid bilayers. Representative channel currents recorded at  $-100$  mV (**f**) and  $+100$  mV (**g**) in the presence of  $50 \mu\text{M}$  ruthenium red inside the recording pipette. Two open channels are present in the membrane. The segment of the 15 min recording shown in **g** indicated by the red asterisk is displayed in **k** at a 25-fold higher time resolution. **h**, **i**, All-event current amplitude histograms from 30 s (**h**) and 15 min (**i**) recordings;  $\gamma = 110 \pm 10$  pS (**h**) and  $80 \pm 5$  pS (**i**);  $N$  was 9,938 events. **j**, Single channel  $I$ – $V$  relationship,  $n = 8$  experiments. **l–q**, Representative single channel currents at  $-100$  mV of purified MmPiezo1 reconstituted into asymmetric lipid bilayers in symmetric  $0.2$  M KCl (**l**), after addition of  $0.2$  M NaCl (**m**) and after addition of  $50 \mu\text{M}$  ruthenium red (**n**). Segments indicated by red asterisks in **l–n** are displayed in panels **o–q**, respectively. C and O denote the closed and open states.

of other channel-like proteins. Finally, purified MmPiezo1 protein reconstituted into proteoliposomes and planar lipid bilayers in the absence of any other cellular components gives rise to ruthenium-red-sensitive cationic ion channel activity. The MmPiezo1 complex is estimated to weigh  $\sim 1.2$ -million Da with 120–160 transmembrane segments, being, to our knowledge, the largest plasma membrane ion channel complex identified so far.

## METHODS SUMMARY

**Electrophysiology.** Mechanical stimulation was achieved as previously described<sup>8</sup>. **Subunit counting.** The preparations were imaged on an inverted Nikon Ti-E fluorescence TIRF microscope (Nikon Corporation) and imaged with a high numerical aperture objective (Nikon  $\times 100$  PlanApo, NA1.49). eGFP-fusion proteins were excited with a 488-nm Coherent laser (Coherent, Inc.) and images were collected with an Andor iXon DU-897 EMCCD camera.

**MmPiezo1–GST purification.** Cells were collected and lysed 24 h after transfection, followed by an affinity purification. Initially, purification was conducted

from whole-cell lysates. Thereafter, purification was performed using the membrane fraction as starting material, resulting in significantly enhanced frequency of retrieval of channel activity after reconstitution. Untransfected cells were subjected to the same purification procedure to serve as a negative control. Purified samples were kept at  $4^\circ\text{C}$  until further analysis.

**Native gel electrophoresis.** The purified MmPiezo1–GST proteins or negative control samples were subjected to 3–12% NativePAGE Novex Bis-Tris gel for native (non-denaturing) electrophoresis according to the user manual (Invitrogen). After electrophoresis, the native gel was then either visualized by a fast Coomassie G-250 staining or transferred to a PVDF membrane for western blotting.

**Reconstitution in lipid bilayers and proteoliposomes.** Purified MmPiezo1 was reconstituted into proteoliposomes by detergent dilution. Excised patches from giant asolectin proteoliposomes were used for channel recordings. Asymmetric lipid bilayers were formed using the droplet interface strategy; one monolayer was composed of 1,2-diphytanoyl-*sn*-glycero-3 phosphocholine (DPhPC), and the other of 90% DPhPC and 10% of the negatively charged lipid, 1,2-dioleoyl-*sn*-glycero-3-phosphatidic acid (DOPA) (mole/mole) (Avanti Polar Lipids).

**Full Methods** and any associated references are available in the online version of the paper at [www.nature.com/nature](http://www.nature.com/nature).

Received 22 July; accepted 21 December 2011.

Published online 19 February 2012.

- Corey, D. P. & Hudspeth, A. J. Response latency of vertebrate hair cells. *Biophys. J.* **26**, 499–506 (1979).
- McCarter, G. C., Reichling, D. B. & Levine, J. D. Mechanical transduction by rat dorsal root ganglion neurons *in vitro*. *Neurosci. Lett.* **273**, 179–182 (1999).
- Davis, M. J., Donovitz, J. A. & Hood, J. D. Stretch-activated single-channel and whole cell currents in vascular smooth muscle cells. *Am. J. Physiol.* **262**, C1083–C1088 (1992).
- Praetorius, H. A. & Spring, K. R. Bending the MDCK cell primary cilium increases intracellular calcium. *J. Membr. Biol.* **184**, 71–79 (2001).
- Chalfie, M. Neurosensory mechanotransduction. *Nature Rev. Mol. Cell Biol.* **10**, 44–52 (2009).
- Delmas, P., Hao, J. & Rodat-Despoix, L. Molecular mechanisms of mechanotransduction in mammalian sensory neurons. *Nature Rev. Neurosci.* **12**, 139–153 (2011).
- Hamil, O. P. & Martinac, B. Molecular basis of mechanotransduction in living cells. *Physiol. Rev.* **81**, 685–740 (2001).
- Coste, B. *et al.* Piezo1 and Piezo2 are essential components of distinct mechanically activated cation channels. *Science* **330**, 55–60 (2010).
- Bae, C., Sachs, F. & Gottlieb, P. A. The mechanosensitive ion channel Piezo1 is inhibited by the peptide GsMTx4. *Biochemistry* **50**, 6295–6300 (2011).
- Reed-Geaghan, E. G. & Maricich, S. M. Peripheral somatosensation: a touch of genetics. *Curr. Opin. Genet. Dev.* **21**, 240–248 (2011).
- Nilius, B. Pressing and squeezing with Piezos. *EMBO Rep.* **11**, 902–903 (2010).
- Gong, Z. *et al.* Two interdependent TRPV channel subunits, inactive and Nanchung, mediate hearing in *Drosophila*. *J. Neurosci.* **24**, 9059–9066 (2004).
- Kim, J. *et al.* A TRPV family ion channel required for hearing in *Drosophila*. *Nature* **424**, 81–84 (2003).
- Tracey, W. D. Jr, Wilson, R. I., Laurent, G. & Benzer, S. *painless*, a *Drosophila* gene essential for nociception. *Cell* **113**, 261–273 (2003).
- Walker, R. G., Willingham, A. T. & Zuker, C. S. A *Drosophila* mechanosensory transduction channel. *Science* **287**, 2229–2234 (2000).
- Zhong, L., Hwang, R. Y. & Tracey, W. D. Pickpocket is a DEG/ENAC protein required for mechanical nociception in *Drosophila* larvae. *Curr. Biol.* **20**, 429–434 (2010).
- Coste, B., Crest, M. & Delmas, P. Pharmacological dissection and distribution of Na<sup>+</sup>/Nav1.9, T-type Ca<sup>2+</sup> currents, and mechanically activated cation currents in different populations of DRG neurons. *J. Gen. Physiol.* **129**, 57–77 (2007).
- Drew, L. J., Wood, J. N. & Cesare, P. Distinct mechanosensitive properties of capsaicin-sensitive and -insensitive sensory neurons. *J. Neurosci.* **22**, RC228 (2002).
- Kim, S. E., Coste, B., Chadha, A., Cook, B. & Patapoutian, A. The role of *Drosophila* Piezo in mechanical nociception. *Nature* <http://dx.doi.org/10.1038/nature10801> (this issue).
- Voets, T. *et al.* Molecular determinants of permeation through the cation channel TRPV4. *J. Biol. Chem.* **277**, 33704–33710 (2002).
- Voets, T. *et al.* TRPM6 forms the Mg<sup>2+</sup> influx channel involved in intestinal and renal Mg<sup>2+</sup> absorption. *J. Biol. Chem.* **279**, 19–25 (2004).
- Ulbrich, M. H. & Isacoff, E. Y. Subunit counting in membrane-bound proteins. *Nature Methods* **4**, 319–321 (2007).
- Bayley, H. *et al.* Droplet interface bilayers. *Mol. Biosyst.* **4**, 1191–1208 (2008).
- Montal, M. Asymmetric lipid bilayers. Response to multivalent ions. *Biochim. Biophys. Acta* **298**, 750–754 (1973).
- Montal, M. & Mueller, P. Formation of bimolecular membranes from lipid monolayers and a study of their electrical properties. *Proc. Natl Acad. Sci. USA* **69**, 3561–3566 (1972).
- Santos, J. S., Grigoriev, S. M. & Montal, M. Molecular template for a voltage sensor in a novel K<sup>+</sup> channel. III. Functional reconstitution of a sensorless pore module from a prokaryotic Kv channel. *J. Gen. Physiol.* **132**, 651–666 (2008).
- Leventis, P. A. & Grinstein, S. The distribution and function of phosphatidylserine in cellular membranes. *Annu Rev Biophys* **39**, 407–427 (2010).



28. Ermakov, Y. A., Kamaraju, K., Sengupta, K. & Sukharev, S. Gadolinium ions block mechanosensitive channels by altering the packing and lateral pressure of anionic lipids. *Biophys. J.* **98**, 1018–1027 (2010).
29. Gambale, F. & Montal, M. Characterization of the channel properties of tetanus toxin in planar lipid bilayers. *Biophys. J.* **53**, 771–783 (1988).
30. Oliver, D. *et al.* Functional conversion between A-type and delayed rectifier K<sup>+</sup> channels by membrane lipids. *Science* **304**, 265–270 (2004).
31. Schmidt, D. & MacKinnon, R. Voltage-dependent K<sup>+</sup> channel gating and voltage sensor toxin sensitivity depend on the mechanical state of the lipid membrane. *Proc. Natl Acad. Sci. USA* **105**, 19276–19281 (2008).
32. Tao, X. & MacKinnon, R. Functional analysis of Kv1.2 and paddle chimera Kv channels in planar lipid bilayers. *J. Mol. Biol.* **382**, 24–33 (2008).
33. Hartman, N. C. & Groves, J. T. Signaling clusters in the cell membrane. *Curr. Opin. Cell Biol.* **23**, 370–376 (2011).

**Supplementary Information** is linked to the online version of the paper at [www.nature.com/nature](http://www.nature.com/nature).

**Acknowledgements** We thank M. H. Ulbrich for providing Ca<sup>2+</sup> channel-, NMDA receptor- and CNG channel–GFP fusion constructs used as controls for photobleaching

experiments. This research was supported by grants from the National Institutes of Dental and Craniofacial Research, Neurological Disorders, General Medical Sciences, and by The Genomics Institute of the Novartis Research Foundation. B.X. and J.G. are postdoctoral fellowship recipients from the American Heart Association and the NIH, respectively.

**Author Contributions** B.C. performed and analysed electrophysiological experiments. B.X. performed and analysed biochemical experiments. J.S.S. and R.S. performed the reconstitution experiments and together with M.M. analysed the single channel data. J.G. and K.S.S. performed and analysed photo-bleaching experiments. S.E.K. cloned the *Dmpiezo* gene. M.S. initiated biochemical experiments. J.M. generated GFP–MmPiezo1 and the mRNA used for oocyte injection. A.E.D. provided technical help for oocyte experiments. A.P., B.C., B.X., J.G., J.S.S., R.S., and M.M. wrote the manuscript.

**Author Information** The DmPiezo sequence has been deposited in GenBank under accession number JQ425255. Reprints and permissions information is available at [www.nature.com/reprints](http://www.nature.com/reprints). The authors declare no competing financial interests. Readers are welcome to comment on the online version of this article at [www.nature.com/nature](http://www.nature.com/nature). Correspondence and requests for materials should be addressed to A.P. ([apatapou@gnf.org](mailto:apatapou@gnf.org)) and M.M. ([mmontal@ucsd.edu](mailto:mmontal@ucsd.edu)).

## METHODS

**Cloning of *Drosophila piezo* full-length cDNA.** The *Drosophila piezo* gene (GenBank accession number JQ425255) was cloned from adult *Drosophila* poly(A)<sup>+</sup> RNAs (Clontech) by RT-PCR. Primers for RT-PCR were designed based on the annotated sequence of CG8486. Two fragments of 2 kb and 6.5 kb were amplified and cloned sequentially into pIRES2-EGFP expression vector. Each cloning step was sequence verified. Full-length *Drosophila piezo* gene is 8,355 bp in length. The protein sequence of DmPiezo is shown in Supplementary Fig. 1.

**Cell culture and transient transfection.** Human embryonic kidney 293T (HEK293T), NIH-3T3, F11 and HeLa cells were grown in Dulbecco's Modified Eagle Medium containing 4.5 mg ml<sup>-1</sup> glucose, 10% fetal bovine serum, 50 U ml<sup>-1</sup> penicillin and 50 µg ml<sup>-1</sup> streptomycin. Cells were plated onto poly-lysine-coated 12-mm round glass coverslips placed in 24-well plates and transfected using lipofectamine 2000 (Invitrogen) according to the manufacturer's instruction. 500–1,000 ng ml<sup>-1</sup> of plasmid DNA was transfected and cells were recorded 12–48 h later.

**Electrophysiology.** Patch-clamp experiments were performed in standard whole-cell or cell-attached recordings using an Axopatch 200B amplifier (Axon Instruments). Patch pipettes had resistance of 2–3 MΩ when filled with an internal solution consisting of (in mM) 133 CsCl, 10 HEPES, 5 EGTA, 1 CaCl<sub>2</sub>, 1 MgCl<sub>2</sub>, 4 MgATP and 0.4 Na<sub>2</sub>GTP (pH adjusted to 7.3 with CsOH). The extracellular solution consisted of (in mM) 130 NaCl, 3 KCl, 1 MgCl<sub>2</sub>, 10 HEPES, 2.5 CaCl<sub>2</sub>, 10 glucose (pH adjusted to 7.3 with NaOH). For cell-attached recordings, pipettes were filled with a solution consisting of (in mM) 130 NaCl, 5 KCl, 10 HEPES, 1 CaCl<sub>2</sub>, 1 MgCl<sub>2</sub>, 10 TEA-Cl (pH 7.3 with NaOH), except for Supplementary Fig. 6 where the internal solution was (in mM) 150 NaCl, 10 HEPES (pH adjusted to 7.3 with NaOH). External solution used to zero the membrane potential consisted of (in mM) 140 KCl, 10 HEPES, 1 MgCl<sub>2</sub>, 10 glucose (pH 7.3 with KOH). All experiments were done at room temperature. Currents were sampled at 50 or 20 kHz and filtered at 5 or 2 kHz. Voltages were not corrected for a liquid junction potential. Leak currents before mechanical stimulations were subtracted off-line from the current traces. 10 mM ruthenium red stock solution was prepared in water.

**Mechanical stimulation.** For whole-cell recordings mechanical stimulation was achieved using a fire-polished glass pipette (tip diameter 3–4 µm) positioned at an angle of 80° to the cell being recorded. Downward movement of the probe towards the cell was driven by a Clampex controlled piezo-electric crystal microstage (E625 LVPZT Controller/Amplifier; Physik Instrumente). The probe was typically positioned ~2 µm from the cell body. The probe had a velocity of 1 µm ms<sup>-1</sup> during the ramp segment of the command for forward motion and the stimulus was applied for 150 ms. To assess the mechanical sensitivity of a cell, a series of mechanical steps in 1 µm increments was applied every 10–20 s, which allowed full recovery of mechanosensitive currents. Inward mechanically activated currents were recorded at a holding potential of -80 mV. For *I-V* relationship recordings, voltage steps were applied 0.7 s before the mechanical stimulation from a holding potential of -60 mV.

For cell-attached recordings, membrane patches were stimulated with brief negative pressure pulses through the recording electrode using a Clampex controlled pressure clamp HSPC-1 device (ALA-scientific). Unless otherwise stated, stretch-activated channels were recorded at a holding potential of -80 mV with pressure steps from 0 to -60 mmHg (-10 mmHg increments). Current-pressure relationships were fitted with a Boltzmann equation of the form:  $I(P) = [1 + \exp(-(P - P_{50})/s)]^{-1}$ , where *I* is the peak of stretch-activated current at a given pressure, *P* is the applied patch pressure (in mmHg), *P*<sub>50</sub> is the pressure value that evoked a current value which is 50% of *I*<sub>max</sub>, and *s* reflects the current sensitivity to pressure.

Single-channel amplitude characterization was performed on patches that showed strong stretch-activated current activity at -80 mV using increasing steps of negative pressure up to -60 mmHg. Similar activity was never present in control-transfected cells. Negative pressure steps were then reduced to low to moderate level (-5 to -20 mmHg) allowing detection of single channel openings.

**Subunit counting.** For oocyte injection, all construct plasmids were linearized at C terminus with NheI, HindIII or NotI and DNA transcribed with T7 mMessage mMachin Kit (Ambion) and poly(A)-tailing Kit (Ambion) and cleaned with LiCl precipitation. 50 nl of 0.2 µg µl<sup>-1</sup> mRNA was injected into *Xenopus* oocytes (Nasco).

For acquisition, 12–24 h after injection, oocytes were osmotically shocked in stripping buffer (in mM: 220 *N*-methyl glucamine aspartate, 10 HEPES, 1 MgCl<sub>2</sub>) and mechanically de-vitellinized. MatTek dishes (MatTek Corporation) were prepared by sonication in 1 M KOH to remove background fluorescence and further sonicated in MilliQ dH<sub>2</sub>O. Oocytes were placed onto MatTek dishes into SOS buffer (in mM: 100 NaCl, 2 KCl, 1.8 CaCl<sub>2</sub>-H<sub>2</sub>O, 1 MgCl<sub>2</sub>-6H<sub>2</sub>O, 5 HEPES,

2.5 Na pyruvate and 50 µg ml<sup>-1</sup> gentamicin, pH 7.0). The preparations were imaged on an inverted Nikon Ti-E fluorescence TIRF microscope (Nikon Corporation) and imaged with a high numerical aperture objective (Nikon 100× PlanApo, NA1.49) with an additional ×1.5 Optovar magnification. eGFP fusion proteins were excited with a 488-nm Coherent laser (Coherent, Inc.) and images were collected with an Andor iXon DU-897 EMCCD camera. Sixty-second movies were collected at 100-ms exposures, for a frame rate of 10 Hz.

Using Nikon Elements software, movies were duplicated and processed with a rolling average of 2. A second duplicate was filtered with a low-pass kernel of 7, to remove background. The low-pass images were subtracted from the averaged images, to produce the movies used for analysis. Non-overlapping 4 × 4 pixel regions of interest were drawn around randomly selected spots that were clearly separated from neighbouring bright pixels. The spots were required to fit entirely within the 4 × 4 pixel regions. Pixel size was 0.11 µm. The average intensity of each region was plotted over the length of the movies. Traces were discarded if the intensity increased after an initial decrease, if the fluorescent spot moved out of the region, or if the fluorescent signal showed a continuous decay instead of step-wise bleaching. Finally, the number of bleaching steps was counted for each spot.

**MmPiezo1-GST purification.** The MmPiezo1-GST construct was subcloned by inserting a GST encoding sequence from *Schistosoma japonicum* into the MmPiezo1 construct<sup>8</sup> at the 3' end of MmPiezo1 cDNA sequence using the AscI and SacII restriction enzyme sites. The resulting MmPiezo1-GST fusion protein has 2,773 amino acids.

After incubation with cell lysates overnight at 4 °C, the glutathione beads were washed four times in a buffer containing 25 mM NaPIEPES, 140 mM NaCl, 0.6% CHAPS, 0.14% phosphatidylcholine (PC), 2.5 mM dithiothreitol (DTT), and a cocktail of protease inhibitors and eluted with 100 mM glutathione in a buffer containing 25 mM NaPIEPES, 50 mM Tris, 0.6% CHAPS, 0.14% PC, 2.5 mM DTT and a cocktail of protease inhibitors. The eluant was dialysed against a buffer containing 25 mM NaPIEPES, 0.6% CHAPS, 0.14% PC, 2.5 mM DTT and a cocktail of protease inhibitors. The purified samples were kept at 4 °C. Samples purified according to this protocol were used for all the biochemical work and the initial reconstitution experiments. However, because retrieval of channel activity from the reconstituted MmPiezo1-GST fluctuated from preparation to preparation, we adopted an alternative purification protocol involving the membrane fraction as the starting material. Specifically, 24 h after transfection, cells were collected and homogenized in a buffer containing 25 mM NaPIEPES, 50 mM NaCl, 2.5 mM DTT, and a cocktail of protease inhibitors. The cell suspension was forced to go through a 25.5 G needle for 20 times and centrifuged at 1,000g for 15 min at 4 °C. The supernatant was collected and centrifuged at 167,000g for 30 min at 4 °C. The resulting membrane fraction was washed three times (using a buffer containing 25 mM NaPIEPES, 150 mM NaCl, 2.5 mM DTT, and a cocktail of protease inhibitors) and used as the starting material for MmPiezo1-GST purification using the same procedure described above. Purification from the membrane fraction greatly reduced the content of endogenous GST proteins and significantly enhanced the frequency of retrieval of MmPiezo1 channel activity after reconstitution (Fig. 5, Supplementary Fig. 5 and Supplementary Table 3).

**NativePAGE Novex Bis-Tris gel.** The purified MmPiezo1-GST proteins and control samples were subjected to 3–12% NativePAGE Novex Bis-Tris gel for native (non-denaturing) electrophoresis according to the User Manual (Invitrogen). In brief, samples were mixed with NativePAGE Sample Buffer and NativePAGE 5% G-250 Sample Additive and then subjected to electrophoresis at 150 V for 2 h. The use of G-250 charge-shift in NativePAGE gels results in protein resolution based upon protein size and therefore allows accurate size estimation of native protein complexes<sup>34</sup>. However, the native protein conformation may give an expected size estimation error of ~15%. After electrophoresis, the native gel was then either visualized by a fast Coomassie G-250 staining or transferred to a PVDF membrane for western blotting with an antibody specifically against Piezo1 proteins.

**Formaldehyde and paraformaldehyde crosslinking.** The purified MmPiezo1-GST proteins were treated with or without 0.1% formaldehyde at room temperature for different periods of time and then mixed with NuPAGE LDS Sample Buffer and NuPAGE Reducing Agent (Invitrogen), followed by heating at 70 °C for 10 min to denature the protein. The treated samples were subjected to 3–8% NuPAGE Tris-Acetate gel electrophoresis under denaturing conditions. For live cell crosslinking, 0.25% concentration of PFA was added to the cell culture medium and kept at room temperature for 10 min, followed by adding 125 mM glycine to stop the PFA crosslinking reaction. Treated cells were collected and subjected to sequential steps of protein purification, 3–8% NuPAGE Tris-Acetate gel electrophoresis under denaturing conditions or 3–12% NativePAGE Novex Bis-Tris gel for native (non-denaturing) electrophoresis, and western blotting with the anti-Piezo1 antibody.

**Western blotting.** After electrophoresis, either the native or denaturing PAGE gels were transferred to PVDF membranes. Transferring protein from native gel to PVDF membranes was conducted according to instructions for NativePAGE Novex Bis-Tris gel system. Transferred PVDF membranes were blocked with 5% milk in TBS buffer with 0.1% Tween-20 (TBST buffer) at room temperature for 1 h, and then incubated with the anti-Piezo1 antibody (1:200) at 4 °C overnight. The membranes were washed with TBST buffer and incubated with peroxidase-conjugated anti-rabbit IgG secondary antibody (1:10,000) at room temperature for 1 h. Proteins were detected with the ECL plus detection kit (GE Healthcare).

**Mass spectrometry.** Purified samples were separated on the 3–12% NativePAGE Novex Bis-Tris gel and visualized by fast Coomassie G-250 staining. The gel band containing the MmPiezo1–GST complex or the corresponding blank band from the control sample near the 1,236 kDa molecular marker was excised and subjected to the Scripps Center for Mass Spectrometry for analysis. In brief, the gel bands were destained, reduced with 10 mM DTT, alkylated with 55 mM iodoacetamide, and digested with Trypsin overnight before analysis using the nano-LC-MS/MS. The nano-LC-MS/MS data obtained on a LTQ ion trap mass spectrometer was searched using the MmPiezo1–GST protein sequence and NCBI *Homo sapiens* database. In separate sets of experiments, the purified MmPiezo1–GST and control solution samples before gel electrophoresis were subjected to mass spectrometry (Supplementary Table 2).

**Reconstitution into proteoliposomes or DIBs, single channel recordings and analysis.** Purified MmPiezo1–GST protein was reconstituted into asolectin (soybean polar lipid extract, Avanti) liposomes ( $10 \text{ mg ml}^{-1}$ ) by incubating the mixture (lipid/protein mass ratios between 2,000:1 and 1,000:1; this corresponds to a molar lipid/protein ratio of  $\sim 800,000\text{--}400,000:1$ ) on ice for 5 min followed by  $\times 20$  dilution in 200 mM KCl, 5 mM MOPS pH 7.0 and incubated with rotation at room temperature for 20 min. Biobeads were added to mixture and incubated with rotation for 1 h. Thereafter, biobeads were removed by filtration and a new batch of beads was added. After 30 min incubation, the biobeads were filtered and the sample was centrifuged at 60,000 r.p.m. for 60 min at 8 °C. The proteoliposome pellet was re-suspended in 40  $\mu\text{l}$  of the same buffer and used to place two 25  $\mu\text{l}$  drops on a cover slide. The samples were dried under vacuum for  $>16$  h at 4 °C. Samples were hydrated with 25  $\mu\text{l}$  of the same buffer and allowed to sit for 2 h before starting recordings. Thereafter, 2–3  $\mu\text{l}$  of proteoliposomes were withdrawn from the edge of the spots on the cover slide and transferred to the recording chamber. After 5 min, the chamber was slowly filled with recording solution. Multi-G $\Omega$  seals were made to proteoliposomes immobilized at the bottom of the

recording chamber. At that time, the proteoliposome patch was excised and brought through the air–water interface. Excised patches were used<sup>35</sup>. Pipette and bath solution contained (in mM) 200 KCl, 5 MOPS titrated to pH 7.0 with KOH. Capillaries of borosilicate glass from Sigma were pulled to yield resistances of 1–2 M $\Omega$  when immersed in recording solution.

Droplet interface lipid bilayers (DIBs) were formed between two lipid monolayer-encased aqueous nanolitre droplets submerged in hexadecane<sup>23</sup>. Liposomes were composed of 1,2-diphytanoyl-*sn*-glycero-3 phosphocholine (DPhPC) or 90% (mole/mole) DPhPC and 10% of the negatively charged lipid, 1,2-dioleoyl-*sn*-glycero-3-phosphatidic acid (DOPA) (Avanti Polar Lipids). MmPiezo1 was diluted directly into the liposome suspension to yield a final concentration of  $2\text{--}5 \text{ ng ml}^{-1}$ . The electrode carrying the droplet with MmPiezo1 and desired buffer–lipid mix (in mM, 500 KCl, 10 HEPES, pH 7.4, 0.5 lipid solution of DPhPC) was connected to the grounded end of the amplifier head-stage (Axopatch 200B). The second electrode, in a droplet containing the same buffer and 10% DOPA:90% DPhPC, was connected to the working end of the head-stage. Where indicated, ruthenium red or 0.2 M NaCl was injected using a nano-injector (WPI, Inc.).

For proteoliposome patches, records were acquired at a sampling frequency of 40 kHz and filtered online to 5 kHz with a 3-pole Bessel filter before digitization; for DIBs, data acquisition was at 10 kHz and filtered at 2 kHz. For analysis and presentation, records were filtered to 1 kHz with a low-pass Gaussian filter. Transitions were detected by the half-threshold method implemented in Clampfit (proteoliposomes) and by the segmental *k*-means method (SKM) implemented in QuB (DIBs). Transitions  $\leq 0.5$  ms were excluded from the pool for analysis to correct for detection of false and missed events. Data were analysed using Clampfit v.9.2 software (Axon Instruments), QuB, Excel 2007 (Microsoft), and Igor Pro (Wavemetrics).  $\gamma$  was calculated from Gaussian fits to currents histograms. All statistical values represent mean  $\pm$  s.e.m., unless otherwise indicated. *n* and *N* denote number of experiments and number of events, respectively. All experiments were done at room temperature.

34. Schagger, H., Cramer, W. A. & von Jagow, G. Analysis of molecular masses and oligomeric states of protein complexes by blue native electrophoresis and isolation of membrane protein complexes by two-dimensional native electrophoresis. *Anal. Biochem.* **217**, 220–230 (1994).
35. Gambale, F. & Montal, M. Voltage-gated sodium channels expressed in the human cerebellar medulloblastoma cell line TE671. *Brain Res. Mol. Brain Res.* **7**, 123–129 (1990).



# Re-emerging superconductivity at 48 kelvin in iron chalcogenides

Liling Sun<sup>1\*</sup>, Xiao-Jia Chen<sup>2,3\*</sup>, Jing Guo<sup>1</sup>, Peiwen Gao<sup>1</sup>, Qing-Zhen Huang<sup>4</sup>, Hangdong Wang<sup>5</sup>, Minghu Fang<sup>5</sup>, Xiaolong Chen<sup>1</sup>, Genfu Chen<sup>1</sup>, Qi Wu<sup>1</sup>, Chao Zhang<sup>1</sup>, Dachun Gu<sup>1</sup>, Xiaoli Dong<sup>1</sup>, Lin Wang<sup>6</sup>, Ke Yang<sup>7</sup>, Aiguo Li<sup>7</sup>, Xi Dai<sup>1</sup>, Ho-kwang Mao<sup>2</sup> & Zhongxian Zhao<sup>1</sup>

Pressure has an essential role in the production<sup>1</sup> and control<sup>2,3</sup> of superconductivity in iron-based superconductors. Substitution of a large cation by a smaller rare-earth ion to simulate the pressure effect has raised the superconducting transition temperature  $T_c$  to a record high of 55 K in these materials<sup>4,5</sup>. In the same way as  $T_c$  exhibits a bell-shaped curve of dependence on chemical doping, pressure-tuned  $T_c$  typically drops monotonically after passing the optimal pressure<sup>1–3</sup>. Here we report that in the superconducting iron chalcogenides, a second superconducting phase suddenly re-emerges above 11.5 GPa, after the  $T_c$  drops from the first maximum of 32 K at 1 GPa. The  $T_c$  of the re-emerging superconducting phase is considerably higher than the first maximum, reaching 48.0–48.7 K for  $\text{Tl}_{0.6}\text{Rb}_{0.4}\text{Fe}_{1.67}\text{Se}_2$ ,  $\text{K}_{0.8}\text{Fe}_{1.7}\text{Se}_2$  and  $\text{K}_{0.8}\text{Fe}_{1.78}\text{Se}_2$ .

The recent discoveries of superconductivity at 30–32 K in a new family of iron-based chalcogenide superconductors<sup>6–9</sup>  $\text{A}_{1-x}\text{Fe}_2-y\text{Se}_2$  (where A = K, Rb or Cs, with possible Tl substitution) bring new excitement to the field of superconductivity<sup>10</sup>. These superconductors have unusually large magnetic moments up to  $3.3\mu_B$  per Fe atom and a Fe-vacancy ordering in the Fe square lattice<sup>11</sup>. How superconductivity with such a high  $T_c$  can exist on such a strong magnetic background remains perplexing<sup>10</sup>. It has been established that superconductivity in strongly correlated electronic systems can be dictated by their crystallographic structure, electronic charge, and orbital and spin degrees of freedom, which can all be manipulated by controlling parameters such as pressure, magnetic field and chemical composition<sup>12–15</sup>. Pressure is a ‘clean’ way to tune basic electronic and structural properties without changing the chemistry. High-pressure studies are thus very useful in elucidating mechanisms of superconductivity as well as in searching for new high- $T_c$  superconducting materials.

We studied single crystals of  $\text{Tl}_{0.6}\text{Rb}_{0.4}\text{Fe}_{1.67}\text{Se}_2$ ,  $\text{K}_{0.8}\text{Fe}_{1.7}\text{Se}_2$  and  $\text{K}_{0.8}\text{Fe}_{1.78}\text{Se}_2$  grown by the Bridgman method<sup>6,16,17</sup>. We conducted both high-pressure resistance and susceptibility measurements to detect superconductivity *in situ* at high pressures and low temperatures. Figure 1 shows the temperature dependence of the electrical resistance at different pressures for  $\text{Tl}_{0.6}\text{Rb}_{0.4}\text{Fe}_{1.67}\text{Se}_2$  single crystals. Here we define  $T_c$  as the intersection of the tangent through the inflection point of the resistive transition with a straight-line fit of the normal state just above the transition. As can be seen,  $T_c$  starts at the maximum of 33 K at 1.6 GPa, shifts to lower temperatures at increasing pressures, and vanishes near 9 GPa in our experimental temperature range, which is 300–4 K for our high-pressure resistance measurements (Fig. 1a). At slightly higher pressures, however, an unexpected superconducting phase re-emerges with an onset  $T_c$  as high as 48.0 K at 12.4 GPa (Fig. 1b). The sample is not superconducting at pressures higher than 13.2 GPa. We repeated the measurements with new samples in three independent experiments, and the results were reproducible.

To confirm the pressure-induced changes of superconductivity in  $\text{Tl}_{0.6}\text{Rb}_{0.4}\text{Fe}_{1.67}\text{Se}_2$ , we also performed magnetic alternating-current susceptibility measurements *in situ* at high pressures (Fig. 2). The value of  $T_c$  is taken to be the onset of superconductivity defined by the intersection of a line drawn through the steep slope of the curve and the region of zero slope above the transition. The magnetic study showed that  $T_c$  decreased with increasing pressure and vanished at 9.8 GPa in the first superconducting phase SC-I (Fig. 2a). With further increasing pressure, the material enters a new superconducting phase SC-II and its transition temperature reaches 40.2 K at 12.2 GPa (Fig. 2b). The magnetic measurements yield  $T_c$  values consistent with the resistivity data within the experimental uncertainties. These results provide convincing evidence for the existence of two distinct superconducting phases in  $\text{Tl}_{0.6}\text{Rb}_{0.4}\text{Fe}_{1.67}\text{Se}_2$ .

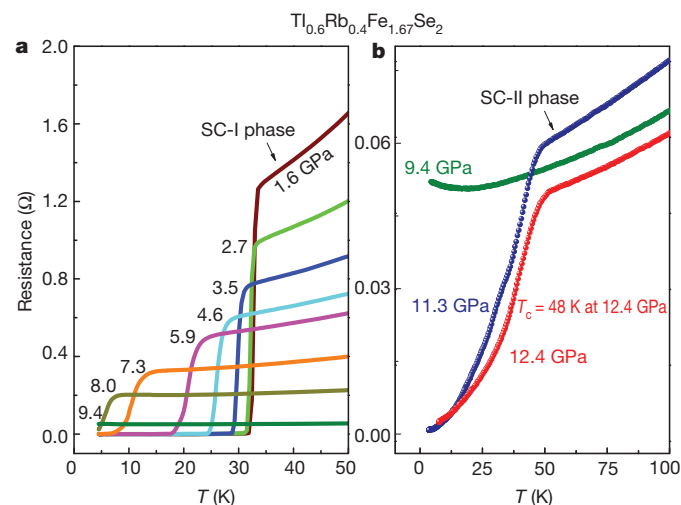


**Figure 1 | Temperature dependence of electrical resistance for  $\text{Tl}_{0.6}\text{Rb}_{0.4}\text{Fe}_{1.67}\text{Se}_2$  at different pressures.** **a**, Resistance–temperature curves in the initial superconducting phase (SC-I) up to 9.4 GPa.  $T_c$  was observed to shift to lower temperature with increasing pressure. Superconductivity disappears at 9.4 GPa. **b**, Electrical resistance curves for the same single crystal at higher pressures. A new superconducting state re-emerges upon further compression. The pressure-induced superconducting phase (SC-II) has a  $T_c$  of 48 K, which is much higher than the maximum in SC-I. Cryogenic resistance measurements were performed in a diamond-anvil cell. Diamond anvils with 600- $\mu\text{m}$  and 300- $\mu\text{m}$  tip flats were used with sample chambers of diameter 300  $\mu\text{m}$  and 100  $\mu\text{m}$ , respectively. Four electrical leads were attached to the single-crystal sample insulated from the rhenium gasket, and loaded into the sample chamber. NaCl powders were employed as a pressure medium. The ruby fluorescence method was used to gauge pressure<sup>20</sup>.

<sup>1</sup>Institute of Physics and Beijing National Laboratory for Condensed Matter Physics, Chinese Academy of Sciences, Beijing 100190, China. <sup>2</sup>Geophysical Laboratory, Carnegie Institution of Washington, Washington DC 20015, USA. <sup>3</sup>Department of Physics, South China University of Technology, Guangzhou 510640, China. <sup>4</sup>NIST Center for Neutron Research, National Institute of Standards and Technology, Gaithersburg, Maryland 20899, USA. <sup>5</sup>Department of Physics, Zhejiang University, Hangzhou 310027, China. <sup>6</sup>HPSynC, Geophysical Laboratory, Carnegie Institution of Washington, 9700 South Cass Avenue, Argonne, Illinois 60439, USA. <sup>7</sup>Shanghai Synchrotron Radiation Facilities, Shanghai Institute of Applied Physics, Chinese Academy of Sciences, Shanghai 201204, China.

\*These authors contributed equally to this work.

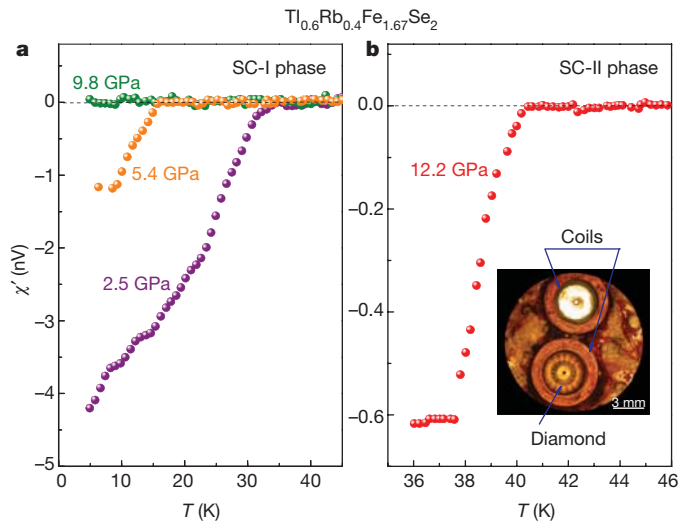


**Figure 2 | Temperature dependence of the alternating-current susceptibility for  $\text{Tl}_{0.6}\text{Rb}_{0.4}\text{Fe}_{1.67}\text{Se}_2$  at different pressures.** **a**, Superconducting transitions observed in the real susceptibility component of the sample at pressures of 2.5, 5.4 and 9.8 GPa in SC-I. The superconducting transition shifts downward to lower temperature with increasing pressure. At 9.8 GPa the susceptibility component remains constant upon cooling down to 4 K, indicating that the sample is no longer superconducting. **b**, The real component of the susceptibility versus temperature for the crystal in SC-II at a pressure of 12.2 GPa. The inset shows the set-up for alternating-current susceptibility measurements in a diamond-anvil cell, with a signal coil around the diamond anvils and a compensating coil. The alternating-current susceptibilities were detected within a lock-in amplifier<sup>21</sup>. The crystals were loaded into the sample chamber, which is a hole in the centre of the nonmagnetic gaskets, with Daphne 7373 as the pressure medium.

To investigate whether the pressure-induced re-emergence of superconductivity was unique to  $\text{Tl}_{0.6}\text{Rb}_{0.4}\text{Fe}_{1.67}\text{Se}_2$  or more general among iron chalcogenides, we conducted parallel electrical resistance measurements on  $\text{K}_{0.8}\text{Fe}_{1.7}\text{Se}_2$  single crystals, and observed nearly identical behaviour (Fig. 3). The initial  $T_c$  of 32 K at 0.8–1.6 GPa decreased monotonically with increasing pressure and became undetectable at 9.2 GPa. At a slightly increased pressure, the second superconducting phase of  $\text{K}_{0.8}\text{Fe}_{1.7}\text{Se}_2$  re-emerged and reached the maximum  $T_c$  of 48.7 K

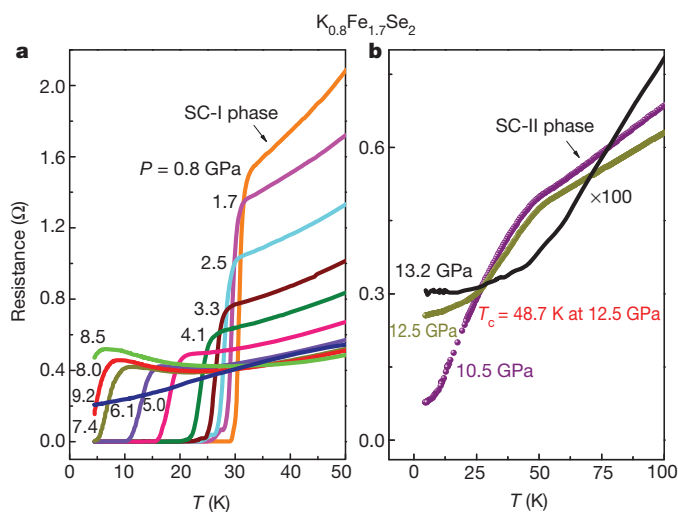


**Figure 3 | Temperature dependence of the resistance for  $\text{K}_{0.8}\text{Fe}_{1.7}\text{Se}_2$  at different pressures.** **a**, SC-I. The resistance–temperature curves showing the  $T_c$  reduction with increasing pressure and its disappearance at 9.2 GPa. **b**, SC-II. The resistance measurements reveal another superconducting phase above 10.5 GPa. The  $T_c$  reaches 48.7 K at 12.5 GPa and disappears at 13.2 GPa. The black curve has been multiplied by 100.

at 12.5 GPa. We repeated the experiment six times using six single crystals cut from different batches, and the results were reproducible. We further repeated the measurements with a slightly different composition,  $\text{K}_{0.8}\text{Fe}_{1.78}\text{Se}_2$ , and again, observed similar pressure-induced behaviour.

We summarized the pressure dependence of  $T_c$  of  $\text{Tl}_{0.6}\text{Rb}_{0.4}\text{Fe}_{1.67}\text{Se}_2$ ,  $\text{K}_{0.8}\text{Fe}_{1.7}\text{Se}_2$ , and  $\text{K}_{0.8}\text{Fe}_{1.78}\text{Se}_2$  in Fig. 4 and Supplementary Tables 1 to 4. The diagram clearly reveals two distinct superconducting regions: the initial superconducting phase SC-I and the pressure-induced superconducting phase SC-II. In the SC-I region,  $T_c$  is suppressed with applied pressure and approaches zero between 9.2 and 9.8 GPa. At higher pressures, the SC-II region appears, in which the  $T_c$  is even higher than the maximum  $T_c$  of the SC-I region. The SC-II region has a maximum  $T_c$  of 48.7 K for  $\text{K}_{0.8}\text{Fe}_{1.7}\text{Se}_2$  and 48.0 K for  $\text{Tl}_{0.6}\text{Rb}_{0.4}\text{Fe}_{1.67}\text{Se}_2$ , higher than previously observed in chalcogenide superconductors. The SC-II region appears in a narrow pressure range. Unlike the usual parabolic pressure-tuning curve of  $T_c$ , the high  $T_c$  in SC-II appears abruptly above 9.8 GPa and disappears equally abruptly above 13.2 GPa. Intermediate  $T_c < 38$  K is not observed even with small pressure increment steps of 0.1 GPa. A similar re-emergence of superconductivity has been observed in some other strongly correlated electronic systems, such as heavy-fermion<sup>12</sup> and organic systems<sup>18</sup>.

Our preliminary high-pressure polycrystalline X-ray diffraction results of the two iron chalcogenides  $\text{K}_{0.8}\text{Fe}_{1.7}\text{Se}_2$  and  $\text{K}_{0.8}\text{Fe}_{1.78}\text{Se}_2$  confirm that, to the first degree, the basic tetragonal crystal structure persists throughout the pressure range studied (Supplementary Information). Therefore, the disappearance of  $T_c$  in SC-I, the re-emergence of higher  $T_c$  in SC-II, and the final non-superconducting region reflect detailed structural variances within the basic tetragonal unit cell, which await future in-depth investigation with advanced diagnostic probes. For instance, the possible change in magnetic-ordering structures would require high-pressure neutron diffraction, and the possible superlattice and Fe vacancy ordering would require high-pressure single-crystal X-ray structural investigations.

The pressure dependence of  $T_c$  in the SC-I region is expected but its mechanism is still much debated. Quantum criticalities are thought to affect superconductivity for strongly correlated electronic systems<sup>19</sup>. A characteristic feature of the new iron chalcogenide superconductors is

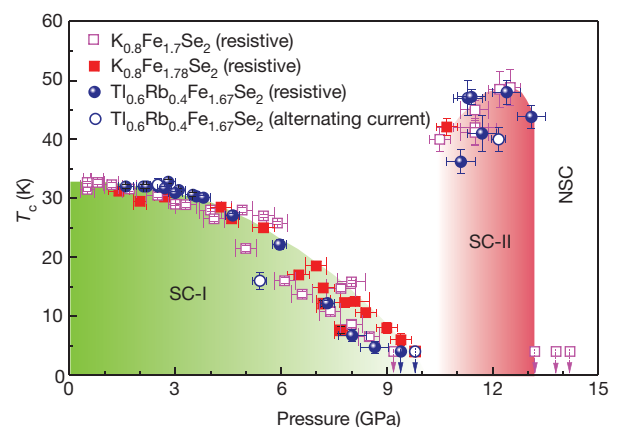


**Figure 4 | Pressure dependence of the  $T_c$  for  $\text{Tl}_{0.6}\text{Rb}_{0.4}\text{Fe}_{1.67}\text{Se}_2$ ,  $\text{K}_{0.8}\text{Fe}_{1.7}\text{Se}_2$  and  $\text{K}_{0.8}\text{Fe}_{1.78}\text{Se}_2$ .** The symbols represent the pressure–temperature conditions for which  $T_c$  values were observed from the resistive and alternating-current susceptibility measurements; symbols with downward arrows represent the absence of superconductivity to the lowest temperature (4 K). All  $\text{Tl}_{0.6}\text{Rb}_{0.4}\text{Fe}_{1.67}\text{Se}_2$ ,  $\text{K}_{0.8}\text{Fe}_{1.7}\text{Se}_2$  and  $\text{K}_{0.8}\text{Fe}_{1.78}\text{Se}_2$  samples show two superconducting regions (SC-I and SC-II) separated by a critical pressure at around 10 GPa. NSC, the non-superconducting region above 13.2 GPa. The maximum  $T_c$  is found to be 48.7 K in  $\text{K}_{0.8}\text{Fe}_{1.7}\text{Se}_2$  at a pressure of 12.5 GPa. At higher pressures above 13.2 GPa, the samples are non-superconducting. Error bars are one standard deviation.

the existence of Fe-vacancies in the Fe-square lattice, ordered by a  $\sqrt{5} \times \sqrt{5}$  superstructure<sup>11</sup>. It remains unclear whether pressure could destroy the vacancy ordering at a critical value and drive the materials into a disordered lattice. Detailed structural studies of these superconducting behaviours in the iron chalcogenide superconductors are currently being conducted. Their magnetic properties at high pressures should help us to understand the interplay of magnetism and superconductivity in these iron chalcogenides.

This observation of the SC-II region with the re-emerging higher  $T_c$  is unexpected. It will certainly stimulate a great deal of future experimental and theoretical studies to clarify whether the observed re-emergence of superconductivity in iron chalcogenides is associated with the quantum critical transition, magnetism, superstructure, vacancy ordering or spin fluctuation.

Received 21 October; accepted 19 December 2011.

Published online 22 February 2012.

1. Torikachvili, M. S., Bud'ko, S. L., Ni, N. & Canfield, P. C. Pressure induced superconductivity in  $\text{CaFe}_2\text{As}_2$ . *Phys. Rev. Lett.* **101**, 057006 (2008).
2. Takahashi, H. *et al.* Superconductivity at 43 K in an iron-based layered compound  $\text{LaO}_{1-x}\text{F}_x\text{FeAs}$ . *Nature* **453**, 376–378 (2008).
3. Medvedev, S. *et al.* Electronic and magnetic phase diagram of  $\beta\text{-Fe}_{1.01}\text{Se}$  with superconductivity at 36.7 K under pressure. *Nature Mater.* **8**, 630–633 (2009).
4. Chen, X. H. *et al.* Superconductivity at 43 K in  $\text{SmFeAsO}_{1-x}\text{F}_x$ . *Nature* **453**, 761–762 (2008).
5. Ren, Z. A. *et al.* Superconductivity at 55 K in iron-based F-doped layered quaternary compound  $\text{Sm}[\text{O}_{1-x}\text{F}_x]\text{FeAs}$ . *Chin. Phys. Lett.* **25**, 2215–2216 (2008).
6. Guo, J. G. *et al.* Superconductivity in the iron selenide  $\text{K}_x\text{Fe}_2\text{Se}_2$  ( $0 < x < 1.0$ ). *Phys. Rev. B* **82**, 180520(R) (2010).
7. Krzton-Maziopa, A. *et al.* Synthesis and crystal growth of  $\text{Cs}_{0.8}(\text{FeSe}_{0.98})_2$ : a new iron-based superconductor with  $T_c = 27$  K. *J. Phys. Condens. Matter* **23**, 052203 (2011).
8. Wang, A. F. *et al.* Superconductivity at 32 K in single-crystalline  $\text{Rb}_x\text{Fe}_{2-y}\text{Se}_2$ . *Phys. Rev. B* **83**, 060512(R) (2011).
9. Fang, M. H. *et al.* Fe-based superconductivity with  $T_c = 31$  K bordering an antiferromagnetic insulator in  $(\text{Ti},\text{K})\text{Fe}_x\text{Se}_2$ . *Europhys. Lett.* **94**, 27009 (2011).
10. Mazin, I. Iron superconductivity weathers another storm. *Physics* **4**, 26 (2011).
11. Bao, W. *et al.* A novel large moment antiferromagnetic order in  $\text{K}_{0.8}\text{Fe}_{1.6}\text{Se}_2$  superconductor. *Chin. Phys. Lett.* **28**, 086104 (2011).
12. Yuan, H. Q. *et al.* Observation of two distinct superconducting phases in  $\text{CeCu}_2\text{Si}_2$ . *Science* **302**, 2104–2107 (2003).
13. Chen, X. J. *et al.* Enhancement of superconductivity by pressure-driven competition in electronic order. *Nature* **466**, 950–953 (2010).
14. Uji, S. *et al.* Magnetic-field-induced superconductivity in a two-dimensional organic conductor. *Nature* **410**, 908–910 (2001).
15. Jin, K., Butch, N. P., Kirshenbaum, K. & Greene, R. L. Link between spin fluctuations and electron pairing in copper oxide superconductors. *Nature* **476**, 73–75 (2011).
16. Wang, D. M., He, J. B., Xia, T.-L. & Chen, G. F. The effect of varying Fe-content on transport properties of K intercalated iron selenide  $\text{K}_x\text{Fe}_{2-y}\text{Se}_2$ . *Phys. Rev. B* **83**, 132502 (2011).
17. Wang, H. D. *et al.* Superconductivity at 32 K and anisotropy in  $\text{Tl}_{0.58}\text{Rb}_{0.42}\text{Fe}_{1.72}\text{Se}_2$  crystals. *Europhys. Lett.* **93**, 47004 (2011).
18. Okuhata, T. *et al.* High-pressure studies of doped-type organic superconductors. *J. Phys. Soc. Jpn* **76** (Suppl. A) 188–189 (2007).
19. Si, Q. M. & Steglich, F. Heavy fermions and quantum phase transitions. *Science* **329**, 1161–1166 (2010).
20. Mao, H. K., Xu, J. & Bell, P. M. Calibration of the ruby pressure gauge to 800 Kbar under quasi-hydrostatic conditions. *J. Geophys. Res.* **91**, 4673–4676 (1986).
21. Debessai, M., Matsuoka, T., Hamlin, J. J. & Schilling, J. S. Pressure-induced superconducting state of europium metal at low temperatures. *Phys. Rev. Lett.* **102**, 197002 (2009).

**Supplementary Information** is linked to the online version of the paper at [www.nature.com/nature](http://www.nature.com/nature).

**Acknowledgements** We thank I. I. Mazin, W. Bao, and T. Xiang for discussions and J. S. Schilling for the help with the alternating-current susceptibility technique. This work in China was supported by the NSCF, 973 projects, and Chinese Academy of Sciences. This work in the USA was supported as part of the EFree, an Energy Frontier Research Center funded by the US Department of Energy, Office of Science, Office of Basic Energy Sciences (DOE-BES). The High Pressure Collaborative Access Team (HPCAT) is supported by CIW, CDAC, UNLV and LLNL through funding from the DOE-NNSA, the DOE-BES and the NSF. The Advanced Photon Source (APS) is supported by the DOE-BES.

**Author Contributions** L.S., X.-J.C., H.M. and Z.Z. designed the project; X.-J.C., L.S., H.M., Q.W. and Z.Z. wrote the paper; P.G., J.G., C.Z. and L.S. performed the resistance and magnetic susceptibility measurements; X.-J.C., L.W., J.G., P.G., L.S., K.Y. and A.L. performed synchrotron X-ray diffraction measurements; and M.F., X.C. and G.C. synthesized the single crystals. All the authors analysed the data and discussed the results. All the authors read and commented on the manuscript.

**Author Information** Reprints and permissions information is available at [www.nature.com/reprints](http://www.nature.com/reprints). The authors declare no competing financial interests. Readers are welcome to comment on the online version of this article at [www.nature.com/nature](http://www.nature.com/nature). Correspondence and requests for materials should be addressed to Z.Z. ([zhxzhao@iphy.ac.cn](mailto:zhxzhao@iphy.ac.cn)) or H.M. ([hmao@gl.ciw.edu](mailto:hmao@gl.ciw.edu)).



# The sirtuin SIRT6 regulates lifespan in male mice

Yariv Kanfi<sup>1</sup>, Shoshana Naiman<sup>1\*</sup>, Gail Amir<sup>2\*</sup>, Victoria Peshti<sup>1</sup>, Guy Zinman<sup>3</sup>, Liat Nahum<sup>1</sup>, Ziv Bar-Joseph<sup>3</sup> & Haim Y. Cohen<sup>1</sup>

The significant increase in human lifespan during the past century confronts us with great medical challenges. To meet these challenges, the mechanisms that determine healthy ageing must be understood and controlled. Sirtuins are highly conserved deacetylases that have been shown to regulate lifespan in yeast, nematodes and fruitflies<sup>1</sup>. However, the role of sirtuins in regulating worm and fly lifespan has recently become controversial<sup>2</sup>. Moreover, the role of the seven mammalian sirtuins, SIRT1 to SIRT7 (homologues of the yeast sirtuin Sir2), in regulating lifespan is unclear<sup>3</sup>. Here we show that male, but not female, transgenic mice overexpressing *Sirt6* (ref. 4) have a significantly longer lifespan than wild-type mice. Gene expression analysis revealed significant differences between male *Sirt6*-transgenic mice and male wild-type mice: transgenic males displayed lower serum levels of insulin-like growth factor 1 (IGF1), higher levels of IGF-binding protein 1 and altered phosphorylation levels of major components of IGF1 signalling, a key pathway in the regulation of lifespan<sup>5</sup>. This study shows the regulation of mammalian lifespan by a sirtuin family member and has important therapeutic implications for age-related diseases.

Sirtuins are highly conserved NAD<sup>+</sup>-dependent deacetylases that have been shown to regulate lifespan in several organisms. Increasing the sirtuin level through genetic manipulation extends the lifespan of yeast, nematodes and flies<sup>1</sup>. Yet, despite many publications supporting a pro-longevity role for sirtuins, there has been recent debate about the direct role of *Caenorhabditis elegans* and *Drosophila melanogaster* SIR-2 in ageing and lifespan extension in response to calorie restriction (also known as dietary restriction)<sup>2,6,7</sup>. Some mammalian sirtuins have been shown to regulate age-related diseases, but mice that overexpress SIRT1 have the same lifespan as control, wild-type (WT), mice<sup>8</sup>. Thus, the role of SIRT1 and other mammalian sirtuins in regulating mammalian lifespan is unclear<sup>3</sup>.

Several key findings support a potential role for SIRT6 in regulating mammalian lifespan. SIRT6-deficient mice are small and have severe metabolic defects, and by 2–3 weeks of age, they develop abnormalities that are usually associated with ageing<sup>9</sup>. In addition, SIRT6 regulates nuclear factor- $\kappa$ B signalling, which controls ageing-associated changes in gene expression<sup>10</sup>. Recently, we showed that SIRT6 levels increase in rats that are fed a calorie-restricted diet<sup>11</sup>, and transgenic mice that overexpress exogenous mouse SIRT6 (*Sirt6*-transgenic mice; also known as MOSES mice)<sup>4</sup> are protected against the physiological damage caused by diet-induced obesity, including triglyceride and low-density-lipoprotein-associated cholesterol accumulation in the serum, increased body fat and reduced glucose tolerance. In normal animals, these metabolic defects become apparent by middle age, whereas their appearance is delayed in animals fed a calorie-restricted diet. Thus, in this study we sought to determine whether *Sirt6*-transgenic mice remain healthy for longer and have a longer lifespan than wild-type mice.

The lifespan of *Sirt6*-transgenic mice was examined in comparison to their control littermates. *Sirt6*-transgenic mice were produced on a segregating stock containing equal contributions from C57BL/6J and BALB/cOlaHsd mouse strains, both of which are considered to be long

lived<sup>12</sup>. The study was carried out on 245 mice (119 males and 126 females) from two transgenic lines (line 55 and line 108) generated from two separate founders. Log-rank test analysis showed significant differences in the survival curves between male WT and male transgenic mice, but not between female WT and female transgenic mice, for both lines (Fig. 1a–d and Supplementary Table 1). Relative to male WT littermates, the median lifespan of male *Sirt6*-transgenic mice increased by 14.5% and 9.9%, and the mean lifespan increased by 14.8% and 16.9%, for line 55 and 108, respectively (log-rank test,  $\chi^2 = 10.529$ , d.f. = 1 and  $P = 0.001$  for line 55; and  $\chi^2 = 4.225$ , d.f. = 1 and  $P = 0.040$  for line 108). In female *Sirt6*-transgenic mice, no significant increase in median or mean lifespan was found relative to female WT littermates for either line (log-rank test,  $\chi^2 = 0.009$ ,

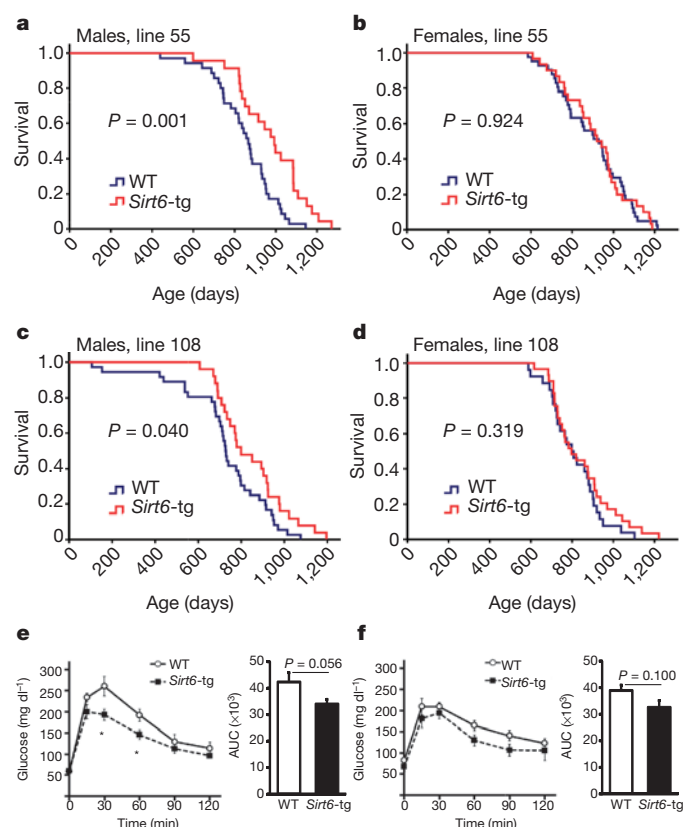


**Figure 1 | Extended lifespan of male *Sirt6*-transgenic mice.** Kaplan-Meier survival curves for male and female WT and *Sirt6*-transgenic (*Sirt6*-tg) mice from two transgenic lines, line 55 (a, b) and line 108 (c, d).  $P$  values were derived from log-rank calculations. Glucose tolerance testing was carried out in WT and *Sirt6*-transgenic males (e) and females (f) at 19 months (572–577 days) of age (males,  $n = 6$  per genotype; females,  $n = 4$  per genotype). The area under the curve (AUC) for each glucose tolerance test is shown on the right (e, f; y axis values shown are the AUC divided by 1,000). The values shown are mean  $\pm$  s.e.m. \*,  $P < 0.05$  (two-tailed  $t$ -test).

<sup>1</sup>The Mina & Everard Goodman Faculty of Life Sciences, Bar-Ilan University, Ramat-Gan 52900, Israel. <sup>2</sup>Department of Pathology, Hadassah Medical Center and Hebrew University, Kiryat Hadassah, Jerusalem 91120, Israel. <sup>3</sup>Lane Center for Computational Biology, School of Computer Science, Carnegie Mellon University, Pittsburgh, Pennsylvania 15217, USA.

\*These authors contributed equally to this work.

d.f. = 1 and  $P = 0.924$  for line 55; and  $\chi^2 = 0.993$ , d.f. = 1 and  $P = 0.319$  for line 108). Relative to WT littermates, the maximum lifespan of transgenic males (that is, the mean lifespan of the oldest 10% of a cohort to die) increased by 15.8% and 13.1% for line 55 and 108, respectively. Comparison of the maximum lifespan of WT and *Sirt6*-transgenic mice using the quantile regression approach at the ninetieth percentile<sup>13</sup> showed a significant difference between males in one line only ( $P = 0.03$  and  $P = 0.11$  for line 55 and 108, respectively) and no difference for females ( $P = 0.45$  and  $P = 0.67$  for line 55 and 108, respectively). Cox regression analysis (using the stepwise backward, Wald method) with the recruitment date, parental identity, gender, genotype and mouse line as main effects and line-by-genotype as the interaction variable showed an additive effect of genotype and line (Supplementary Table 2). However, there was no interaction between mouse line and genotype ( $P = 0.693$ ), indicating that SIRT6 overexpression had an equivalent effect on the mortality of both lines. In summary, our data show that SIRT6 overexpression increased the longevity of males but not females.

SIRT6 has been shown to regulate genomic stability and metabolism<sup>4,9</sup>, two important contributors to longevity. Loss of genomic stability is known to be an important aspect of cancer. Post-mortem gross and microscopic examination of the WT and transgenic mice revealed malignant tumours in a variety of organs, with the highest incidence of tumours in all mice being in the lungs. No significant differences in tumour spectrum or incidence were found between WT and transgenic mice (Supplementary Table 3). Similarly, pathological analysis revealed no differences between WT and transgenic males in the incidence of non-neoplastic findings (for example, diffuse mesangial sclerosis and pulmonary emphysema) or age-related pathologies (for example, femoral osteoporosis, basal ganglia calcification and adrenal cortical hyperplasia) (data not shown). Interestingly, the median lifespan of *Sirt6*-transgenic mice with lung tumours showed a trend towards being longer (by 11.7%) than that of WT mice with lung tumours. Therefore, the hypothesis that the effect of SIRT6 on lung cancer has a role in SIRT6's pro-longevity effect cannot be entirely excluded. However, given the proportion of mice with lung tumours in each genotype, a protective role of SIRT6 against lung cancer is likely to contribute only partially to the pro-longevity effect (Supplementary Information). Thus, further studies are required to evaluate the contribution of SIRT6 to age-sensitive traits, in addition to its effect on lung cancer.

The protective role of SIRT6 against metabolic disorders that are induced by a high-fat diet<sup>4</sup> suggests that SIRT6 might positively affect age-associated metabolic disorders, such as declining insulin sensitivity and impaired glucose tolerance. No significant differences in glucose metabolism were found between young (4–7 month old) WT and *Sirt6*-transgenic mice (data not shown). However, an intraperitoneal glucose tolerance test showed that old *Sirt6*-transgenic mice (19 months old, the maximum age of WT mice before a considerable proportion of the litter died) displayed a trend towards improved glucose homeostasis compared with WT mice of the same age (Fig. 1e, f). An analysis of variance (ANOVA) test for the area under the curve (AUC) values of the glucose tolerance tests indicated no sex-specific effect but showed a significant effect of genotype ( $P = 0.016$ ). Therefore, although SIRT6 overexpression had a positive effect on glucose homeostasis in old mice, this finding cannot explain the sexual dimorphism in longevity.

To understand further the mechanisms of the gender-specific lifespan extension in *Sirt6*-transgenic mice, we used whole genome microarray analysis to examine differential gene expression in the livers of animals of both sexes (Supplementary Table 4). In agreement with the sexual dimorphism in liver gene expression<sup>14</sup>, differential expression analysis using Significance Analysis of Microarrays (SAM) software<sup>15</sup> showed that the most extensive gene expression differences occurred between genders (Supplementary Table 5). Notably, significant differences were also found between *Sirt6*-transgenic and WT males, but the differences between *Sirt6*-transgenic and WT females were minor

(Supplementary Table 5). ANOVA analysis uncovered a subset of genes whose expression differed significantly between genotypes and that were gender-specific (Supplementary Table 5). Gene Ontology (GO) functional analysis showed that the differentially expressed gene set between *Sirt6*-transgenic males and WT males is significantly enriched for categories related to metabolism and cellular responses (Supplementary Table 6). We next compared this differentially expressed gene set with the set of genes that was differentially expressed between male and female WT mice. This analysis revealed a significant similarity between the two gene sets. Of the differentially expressed genes in *Sirt6*-transgenic males, 50% (41 of 82) were also differentially expressed between male and female WT mice ( $P = 0$ ) (Fig. 2a, b and Supplementary Table 5).

To confirm the microarray results, 11 of the differentially expressed genes in male *Sirt6*-transgenic mice were selected for validation by quantitative PCR. The expression pattern of all of these 11 genes confirmed the microarray data (Figs 2c and 3c). Moreover, to examine whether the transcriptional changes due to SIRT6 are mouse-line-specific, the expression of several of these genes was followed in another transgenic line, and the same pattern of transcriptional changes was observed (Supplementary Fig. 1). Calorie restriction and starvation<sup>16–19</sup> have previously been shown to have a similar effect to SIRT6 overexpression on the transcription of several genes (30% of the differentially expressed genes in male *Sirt6*-transgenic mice showed a similar expression pattern in male mice fed a calorie-restricted diet<sup>16</sup>). For

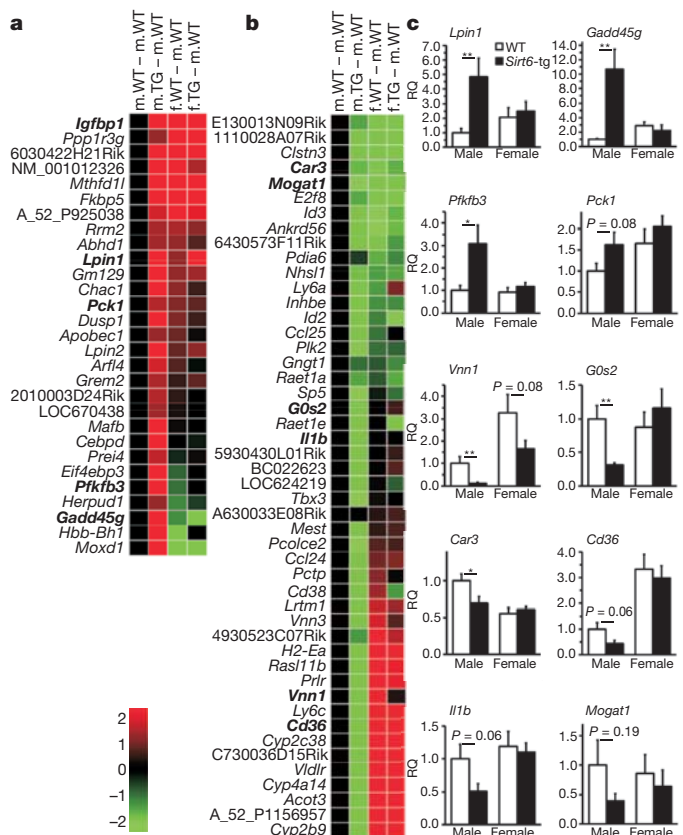


**Figure 2 | Expression profile of differentially expressed genes in male *Sirt6*-transgenic mice.** a, b, Heat maps displaying the significantly upregulated (red) and downregulated (green) genes in *Sirt6*-transgenic males (m.TG) compared with WT males (m.WT). The expression profile of these genes in WT females (f.WT) or *Sirt6*-transgenic females (f.TG) compared with WT males is also illustrated. Statistical analysis was performed using all 24 arrays. The quantitative-PCR-validated genes are shown in bold. c, The relative expression levels of hepatic genes were confirmed by quantitative PCR in 20 male and 20 female mice. The values shown are mean  $\pm$  s.e.m. \*,  $P < 0.05$ ; \*\*,  $P < 0.01$ ;  $n = 10$  per group. RQ, relative quantification.

example, the upregulated genes *Lpin1*, *Lpin2*, *Gadd45g*, *Fkbp5*, *Dusp1* and *Cebpd* and the downregulated genes *Vnn1*, *Vnn3*, *Pctp*, *Vldlr*, *Car3* and *G0s2* in the expression profile of male *Sirt6*-transgenic mice are also differentially expressed in the livers of mice fed a calorie-restricted diet<sup>16–18</sup>.

A key factor in the regulation of lifespan is the IGF1 signalling pathway. Worms and flies with a mutated insulin/IGF1 receptor and mice that are heterozygous for the IGF1 receptor have an extended lifespan<sup>5</sup>. Moreover, rodents fed a calorie-restricted diet have lower IGF1 levels early in life than rodents fed a normal chow diet, and many rodent genetic models with a prolonged lifespan have lower levels of serum IGF1 or IGF1 signalling than do control groups<sup>5,20</sup>. Although no difference was found between WT and *Sirt6*-transgenic females, young transgenic males (6 months old) had lower serum IGF1 levels than WT male littermates (Fig. 3a), and these IGF1 levels in *Sirt6*-transgenic males were similar to those in all females. This significant difference in IGF1 levels between young transgenic and WT males was sustained until 19 months of age (Fig. 3b). In line with this finding, one of the genes that was highly upregulated in *Sirt6*-transgenic males, to the same levels as in WT or *Sirt6*-transgenic females, was the gene encoding IGF-binding protein 1 (IGFBP1) (Fig. 3c). IGFBP1 is thought to be the main short-term modulator of IGF1 bioavailability<sup>21</sup>. Calorie restriction increases the expression of IGFBP1 (ref. 17), and high levels of IGFBP1 correlate with protection against metabolic disorders<sup>22</sup>. No change was found in the expression of gene encoding

other IGF1-binding proteins, such as IGFBP3 and acid-labile subunit (ALS; also known as IGFALS) (Fig. 3c).

To follow the changes in IGF1 signalling, components of this pathway were analysed in the three main metabolic tissues: liver, white adipose tissue (WAT) and muscle. Analyses included the phosphorylation levels of AKT activation sites (Thr 308 and Ser 473), FOXO1 (Thr 24) and FOXO3 (Thr 32). The most significantly decreased phosphorylation levels were observed in the perigonadal WAT of *Sirt6*-transgenic males in comparison to WT males (Fig. 3d–g and Supplementary Fig. 2a–d). The levels of phosphorylated AKT (on both activation sites), FOXO1 and FOXO3 in WAT were lower in the transgenic mice (Fig. 3e, f). Therefore, we further explored this pathway in WAT and found that the phosphorylation levels of the IGF1 receptor (Tyr 1135) and S6 (Ser 235/236) were lower in *Sirt6*-transgenic males than in the WT male littermates (Fig. 3d, g). Importantly, no significant change in the phosphorylation levels of these markers was observed in female mice (Fig. 3d–g and Supplementary Fig. 2a–d). Moreover, the decrease in the phosphorylation levels of AKT and FOXO proteins in male *Sirt6*-transgenic mice is in agreement with previous reports that show that lifespan is positively regulated by changes in IGF1 signalling in the whole organism, or specifically in the fat tissues, of nematodes and fruitflies<sup>5,23</sup>.

There is much doubt about whether mammalian sirtuins regulate lifespan<sup>3,5,8</sup>. Moreover, in the fly and nematode, a recent study challenged the role of sirtuins in regulating lifespan, claiming that the increased

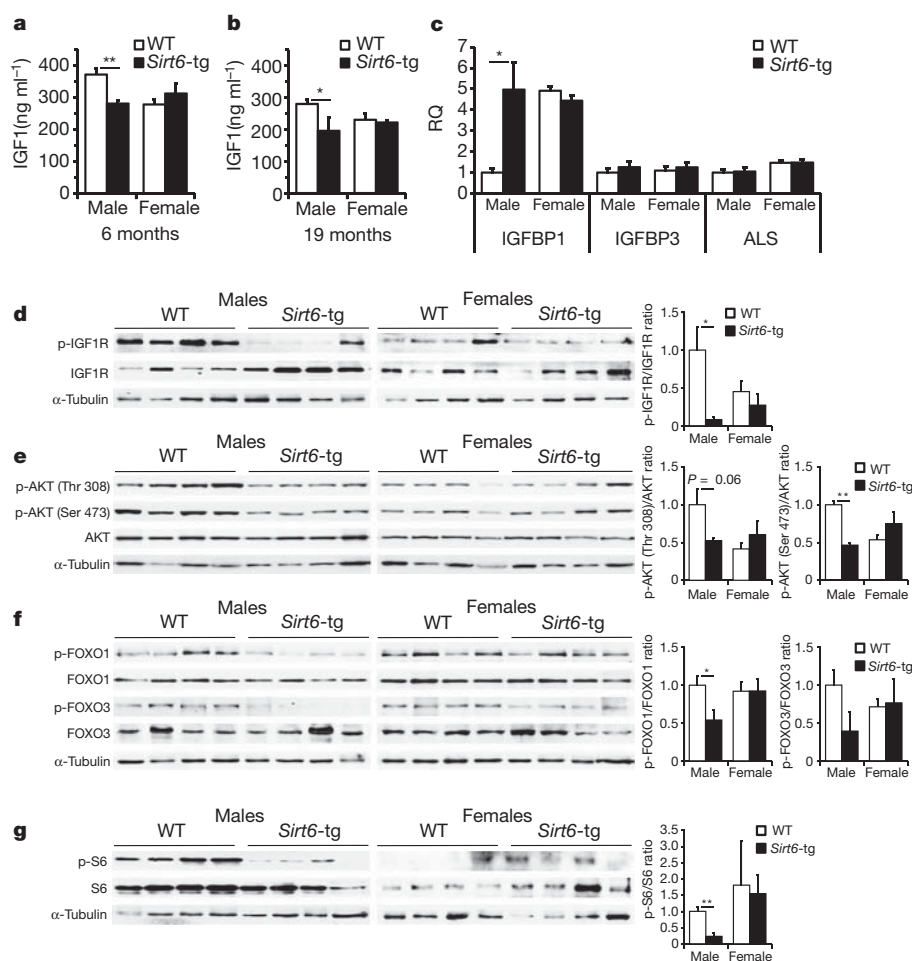


**Figure 3 | Alterations in the IGF1–AKT pathway in *Sirt6*-transgenic males.** **a, b**, Serum IGF1 levels in male and female WT and *Sirt6*-transgenic mice at 6 months (**a**) and 19 months (**b**) of age ( $n = 4–7$ ). **c**, The relative expression of hepatic *Igf1*, *Igf1*, *Igf1* and *Als* measured by quantitative PCR ( $n = 4–7$ ). **d–g**, The phosphorylation levels of the IGF1 receptor (IGF1R) at Tyr 1135 (**d**), AKT at both the Thr 308 and Ser 473 activation sites (**e**), FOXO1 at Thr 24

and FOXO3 at Thr 32 (**f**), and S6 at Ser 235/236 (**g**) in perigonadal WAT ( $n = 4$  mice per genotype). All mice were killed at the same time of day. The phosphorylated to unphosphorylated protein ratios, as determined by densitometry, are shown on the right. **a–g**, The values shown are the mean  $\pm$  s.e.m. \*,  $P < 0.05$ ; \*\*,  $P < 0.01$ .



longevity observed in strains with SIR-2 overexpression is caused by differences in genetic background or by mutagenic effects of transgene insertion<sup>2</sup>. To address potential complications owing to strain-specific effects and integration sites, we used a segregating background with equal contributions from the C57BL/6J and BALB/cOlaHsd mouse strains and studied two separate lines. Indeed, we showed that SIRT6 extends male lifespan regardless of the integration site (Supplementary Fig. 3) and in two control lines with different lifespans. Here, we reveal a role for the mammalian sirtuin SIRT6 in regulating lifespan. SIRT6 overexpression extends lifespan only in males, potentially by reducing IGF1 signalling specifically in WAT. Mice with a fat-specific insulin receptor gene knockout have been shown to have an increased mean lifespan of similar magnitude to the male transgenic mice in our study<sup>23</sup>, demonstrating the central role of fat in regulating lifespan. Most genetic modifications of the IGF1 or insulin signalling pathway affect the lifespan of both genders or show a stronger effect in females. Yet here the effect of SIRT6 on IGF1 signalling was male specific. Therefore, further research is required to determine whether the effects of SIRT6 are blocked in females rather than enhanced in males. Taken together, our findings suggest that SIRT6 is an important regulator of mammalian longevity and indicate the feasibility of manipulating SIRT6 levels to treat age-related diseases.

## METHODS SUMMARY

*Sirt6*-transgenic mice on the CB6F1 background, containing equal contributions from C57BL/6J and BALB/cOlaHsd mouse strains, were generated as described previously<sup>4</sup>, and the glucose tolerance tests and lifespan analyses were performed as described previously<sup>24–26</sup>. Tissues were taken after natural death, fixed in formaldehyde for histopathological analysis, embedded in paraffin, sectioned, and stained with haematoxylin and eosin. Quantitative PCR was performed using Absolute Blue SYBR Green on a StepOnePlus instrument. Microarray sample labelling and hybridization were performed as previously described<sup>4</sup>, and data were normalized using the program dChip. Differentially expressed genes were identified using SAM and defined as those with a *q* value of <10.0% and a minimum of a 1.5 fold change.

Received 17 December 2010; accepted 19 December 2011.

Published online 22 February 2012.

- Michan, S. & Sinclair, D. Sirtuins in mammals: insights into their biological function. *Biochem. J.* **404**, 1–13 (2007).
- Burnett, C. *et al.* Absence of effects of Sir2 overexpression on lifespan in *C. elegans* and *Drosophila*. *Nature* **477**, 482–485 (2011).
- Baur, J. A. *et al.* Dietary restriction: standing up for sirtuins. *Science* **329**, 1012–1014 (2010).
- Kanfi, Y. *et al.* SIRT6 protects against pathological damage caused by diet-induced obesity. *Aging Cell* **9**, 162–173 (2010).
- Kenyon, C. J. The genetics of ageing. *Nature* **464**, 504–512 (2010).
- Viswanathan, M. & Guarente, L. Regulation of *Caenorhabditis elegans* lifespan by *sir-2.1* transgenes. *Nature* **477**, E1–E2 (2011).
- Rizki, G. *et al.* The evolutionarily conserved longevity determinants HCF-1 and SIR-2.1/SIRT1 collaborate to regulate DAF-16/FOXO. *PLoS Genet.* **7**, e1002235 (2011).
- Herranz, D. *et al.* Sirt1 improves healthy ageing and protects from metabolic syndrome-associated cancer. *Nature Commun.* **1**, 3 (2010).

- Mostoslavsky, R. *et al.* Genomic instability and aging-like phenotype in the absence of mammalian SIRT6. *Cell* **124**, 315–329 (2006).
- Kawahara, T. L. *et al.* SIRT6 links histone H3 lysine 9 deacetylation to NF- $\kappa$ B-dependent gene expression and organismal life span. *Cell* **136**, 62–74 (2009).
- Kanfi, Y. *et al.* Regulation of SIRT6 protein levels by nutrient availability. *FEBS Lett.* **582**, 2417–2423 (2008).
- Yuan, R. *et al.* Aging in inbred strains of mice: study design and interim report on median lifespans and circulating IGF1 levels. *Aging Cell* **8**, 277–287 (2009).
- Wang, C., Li, Q., Redden, D. T., Weindruch, R. & Allison, D. B. Statistical methods for testing effects on 'maximum lifespan'. *Mech. Ageing Dev.* **125**, 629–632 (2004).
- Yang, X. *et al.* Tissue-specific expression and regulation of sexually dimorphic genes in mice. *Genome Res.* **16**, 995–1004 (2006).
- Tusher, V. G., Tibshirani, R. & Chu, G. Significance analysis of microarrays applied to the ionizing radiation response. *Proc. Natl Acad. Sci. USA* **98**, 5116–5121 (2001).
- Estep, P. W. III, Warner, J. B. & Bulyk, M. L. Short-term calorie restriction in male mice feminizes gene expression and alters key regulators of conserved aging regulatory pathways. *PLoS ONE* **4**, e5242 (2009).
- Swindell, W. R. Genes and gene expression modules associated with caloric restriction and aging in the laboratory mouse. *BMC Genomics* **10**, 585 (2009).
- Selman, C. *et al.* Coordinated multitissue transcriptional and plasma metabolomic profiles following acute caloric restriction in mice. *Physiol. Genomics* **27**, 187–200 (2006).
- Bauer, M. *et al.* Starvation response in mouse liver shows strong correlation with life-span-prolonging processes. *Physiol. Genomics* **17**, 230–244 (2004).
- Holzenberger, M. *et al.* IGF-1 receptor regulates lifespan and resistance to oxidative stress in mice. *Nature* **421**, 182–187 (2003).
- Lee, P. D., Giudice, L. C., Conover, C. A. & Powell, D. R. Insulin-like growth factor binding protein-1: recent findings and new directions. *Proc. Soc. Exp. Biol. Med.* **216**, 319–357 (1997).
- Yeap, B. B. *et al.* IGF1 and its binding proteins 3 and 1 are differentially associated with metabolic syndrome in older men. *Eur. J. Endocrinol.* **162**, 249–257 (2010).
- Bluhner, M., Kahn, B. B. & Kahn, C. R. Extended longevity in mice lacking the insulin receptor in adipose tissue. *Science* **299**, 572–574 (2003).
- Harrison, D. E. *et al.* Rapamycin fed late in life extends lifespan in genetically heterogeneous mice. *Nature* **460**, 392–395 (2009).
- Conti, B. *et al.* Transgenic mice with a reduced core body temperature have an increased life span. *Science* **314**, 825–828 (2006).
- Selman, C. *et al.* Ribosomal protein S6 kinase 1 signaling regulates mammalian life span. *Science* **326**, 140–144 (2009).

**Supplementary Information** is linked to the online version of the paper at [www.nature.com/nature](http://www.nature.com/nature).

**Acknowledgements** We thank R. S. Levy-Drummer, C. Wachtel, S. Schwarzbaum and members of the Cohen laboratory for their comments on the manuscript. This study was supported by National Institutes of Health grant 1R01 GM085022 to Z.B.-J. and by grants from the Israeli Academy of Sciences, the United States - Israel Binational Science Foundation, the Israel Cancer Association, the Koret Foundation, the Israel Cancer Research Fund, the Israel Health Ministry, I-CORE program (41/1), the Israel Science Foundation and the European Research Council to H.Y.C.

**Author Contributions** H.Y.C. designed experiments, analysed data and contributed to writing the paper. Y.K. designed and performed experiments, analysed data and contributed to writing the paper. S.N. designed and performed experiments and contributed to writing the paper. G.A. performed the histopathological analysis. V.P. and L.N. performed experiments. G.Z. and Z.B.-J. developed analytical tools, analysed data and contributed to writing the paper. S.N. and G.A. contributed equally to this work.

**Author Information** Reprints and permissions information is available at [www.nature.com/reprints](http://www.nature.com/reprints). The authors declare no competing financial interests. Readers are welcome to comment on the online version of this article at [www.nature.com/nature](http://www.nature.com/nature). Correspondence and requests for materials should be addressed to H.Y.C. (Haim.Cohen@biu.ac.il).

# Stability criteria for complex ecosystems

Stefano Allesina<sup>1,2</sup> & Si Tang<sup>1</sup>

Forty years ago, May proved<sup>1,2</sup> that sufficiently large or complex ecological networks have a probability of persisting that is close to zero, contrary to previous expectations<sup>3–5</sup>. May analysed large networks in which species interact at random<sup>1,2,6</sup>. However, in natural systems pairs of species have well-defined interactions (for example predator–prey, mutualistic or competitive). Here we extend May's results to these relationships and find remarkable differences between predator–prey interactions, which are stabilizing, and mutualistic and competitive interactions, which are destabilizing. We provide analytic stability criteria for all cases. We use the criteria to prove that, counterintuitively, the probability of stability for predator–prey networks decreases when a realistic food web structure is imposed<sup>7,8</sup> or if there is a large preponderance of weak interactions<sup>9,10</sup>. Similarly, stability is negatively affected by nestedness<sup>11–14</sup> in bipartite mutualistic networks. These results are found by separating the contribution of network structure and interaction strengths to stability. Stable predator–prey networks can be arbitrarily large and complex, provided that predator–prey pairs are tightly coupled. The stability criteria are widely applicable, because they hold for any system of differential equations.

May's theorem deals with community matrices<sup>1,2,6</sup>  $M$ , of size  $S \times S$ , where  $S$  is the number of species.  $M_{ij}$  describes the effect that species  $j$  has on  $i$  around a feasible equilibrium point (that is, species have positive densities) of an unspecified dynamical system describing the species' densities through time.

In May's work<sup>1,2</sup>, the diagonal coefficients are  $-1$ , and the off-diagonal coefficients are drawn from a distribution with mean 0 and variance  $\sigma^2$  with probability  $C$  and are 0 otherwise. For these matrices, the probability of stability is close to 0 whenever the 'complexity'  $\sigma\sqrt{SC} > 1$ . Local stability measures the tendency of the system to return to equilibrium after perturbations. In unstable systems, even infinitesimal perturbations cause the system to move away from equilibrium, potentially leading to the loss of species. Thus, it should be extremely improbable to observe rich (large  $S$ ) or highly connected (large  $C$ ) persistent ecosystems<sup>1,2</sup>. Mathematically, an equilibrium point is stable if all the eigenvalues of the community matrix have negative real parts<sup>1,2,6</sup>.

Local stability can only describe the behaviour of the system around an equilibrium point, whereas natural systems are believed to operate far from a steady state<sup>5,15</sup>. However, methods based on local stability are well suited to the study of large systems<sup>1,16,17</sup>, whose empirical parameterization would be unfeasible. Moreover, the methods are general, so that they can be applied to any system of differential equations.

May's matrices have random structure: each pair of species interacts with the same probability. However, this randomness translates, for large  $S$ , into fixed interaction frequencies, so that these matrices follow a precise mixture of interaction types. For example, in May's matrices predator–prey interactions are twice as frequent as mutualistic ones (Supplementary Table 1). Here we extend May's work to different types of interaction, starting from the random case.

Suppose that two species  $j$  and  $i$  interact with probability  $C$ , and that the interaction strength is drawn from a distribution:  $M_{ij}$  takes the value of a random variable  $X$  with mean  $\mathbb{E}(X)=0$  and variance

$\text{Var}(X) = \sigma^2$ . The diagonal elements of the community matrix, representing self-regulation, are set to  $-d$ . For large systems, the eigenvalues are contained in a circle<sup>18</sup> in the complex plane (Fig. 1 and Supplementary Information). The circle is centred at  $(-d, 0)$  and the radius is  $\sigma\sqrt{SC}$ . In stable systems, the whole circle is contained in the left half-plane (that is, all eigenvalues have negative real parts). Thus, the system is stable when the radius is smaller than  $d$ :  $\sqrt{SC} < \theta = d/\sigma$ .

In predator–prey networks, interactions come in pairs with opposite signs: whenever  $M_{ij} > 0$ , then  $M_{ji} < 0$ . With probability  $C$ , we sample one interaction strength from the distribution of  $|X|$  and the other from  $-|X|$ , whereas with probability  $(1 - C)$  both are zero. The eigenvalues of large predator–prey matrices are contained in a vertically stretched ellipse<sup>19</sup>, centred at  $(-d, 0)$ , with horizontal radius  $\sigma\sqrt{SC}(1 - \mathbb{E}^2(|X|)/\sigma^2)$  and thus the stability criterion is  $\sqrt{SC} < \theta/(1 - \mathbb{E}^2(|X|)/\sigma^2)$  (Fig. 1 and Supplementary Information).

When we constrain  $M_{ij}$  and  $M_{ji}$  to have the same sign, and thus impose a mixture of competition and mutualism with equal probability, the eigenvalues are enclosed in a horizontally stretched ellipse<sup>19</sup> and the criterion becomes  $\sqrt{SC} < \theta/(1 + \mathbb{E}^2(|X|)/\sigma^2)$  (Fig. 1 and Supplementary Information).

Take  $C = 0.1$ ,  $X \sim N(0, 1/4)$  (that is,  $X$  follows a normal distribution with mean 0 and variance  $1/4$ ), and  $d = 1$ . The criterion becomes  $\sqrt{SC} < 2$  for random matrices, and is violated whenever  $S \geq 41$ . For predator–prey we find  $\sqrt{SC} < 2\pi/(\pi - 2)$  (violated for  $S \geq 303$ ) and for the mixture of competition and mutualism  $\sqrt{SC} < 2\pi/(\pi + 2)$  (violated for  $S \geq 15$ ). Since  $\mathbb{E}(|X|)/\sigma > 0$  for any distribution of  $X$ , the stability criteria form a strict hierarchy in which the mixture matrices are the least likely to be stable, the random matrices are intermediate, and the predator–prey matrices are the most likely to be stable (Fig. 2 and Table 1). Considerations based on qualitative stability<sup>2</sup> and numerical simulations<sup>16</sup> are consistent with this hierarchy.

In the three cases above, the mean interaction strength is zero, and the coefficients come from the same distribution. In fact we can shuffle the interaction strengths, thereby transforming a network of one type into another: the difference in stability is driven exclusively by the arrangement of the coefficients in pairs with random, opposite and same signs, respectively. This feature allows us to further derive the stability criteria for all intermediate cases by using linear combinations of the three cases above (Supplementary Information).

Two ecologically important cases, however, cannot produce a mean interaction strength of zero. In mutualistic networks all interactions are positive, whereas in competitive networks they are negative. In these cases, for large systems, all the eigenvalues except one (equal to the row sum) are contained in an ellipse (Fig. 3 and Supplementary Figs 1 and 2). In mutualistic networks in which all interaction pairs are positive and drawn from the distribution of  $|X|$  independently with probability  $C$ , the stability criterion becomes  $(S - 1)C\mathbb{E}(|X|)/\sigma < \theta$  (that is, row sum  $< 0$ ; Supplementary Information). For competitive matrices, in which interaction pairs are drawn from the distribution of  $-|X|$  with probability  $C$ , the criterion is

$$\sqrt{SC}(1 + (1 - 2C)\mathbb{E}^2(|X|)/\sigma^2) / \sqrt{1 - C\mathbb{E}^2(|X|)/\sigma^2 + C\mathbb{E}(|X|)/\sigma} < \theta$$

<sup>1</sup>Department of Ecology and Evolution, University of Chicago, 1101 East 57th Street, Chicago, Illinois 60637, USA. <sup>2</sup>Computation Institute, University of Chicago, 5735 South Ellis Avenue, Chicago, Illinois 60637, USA.

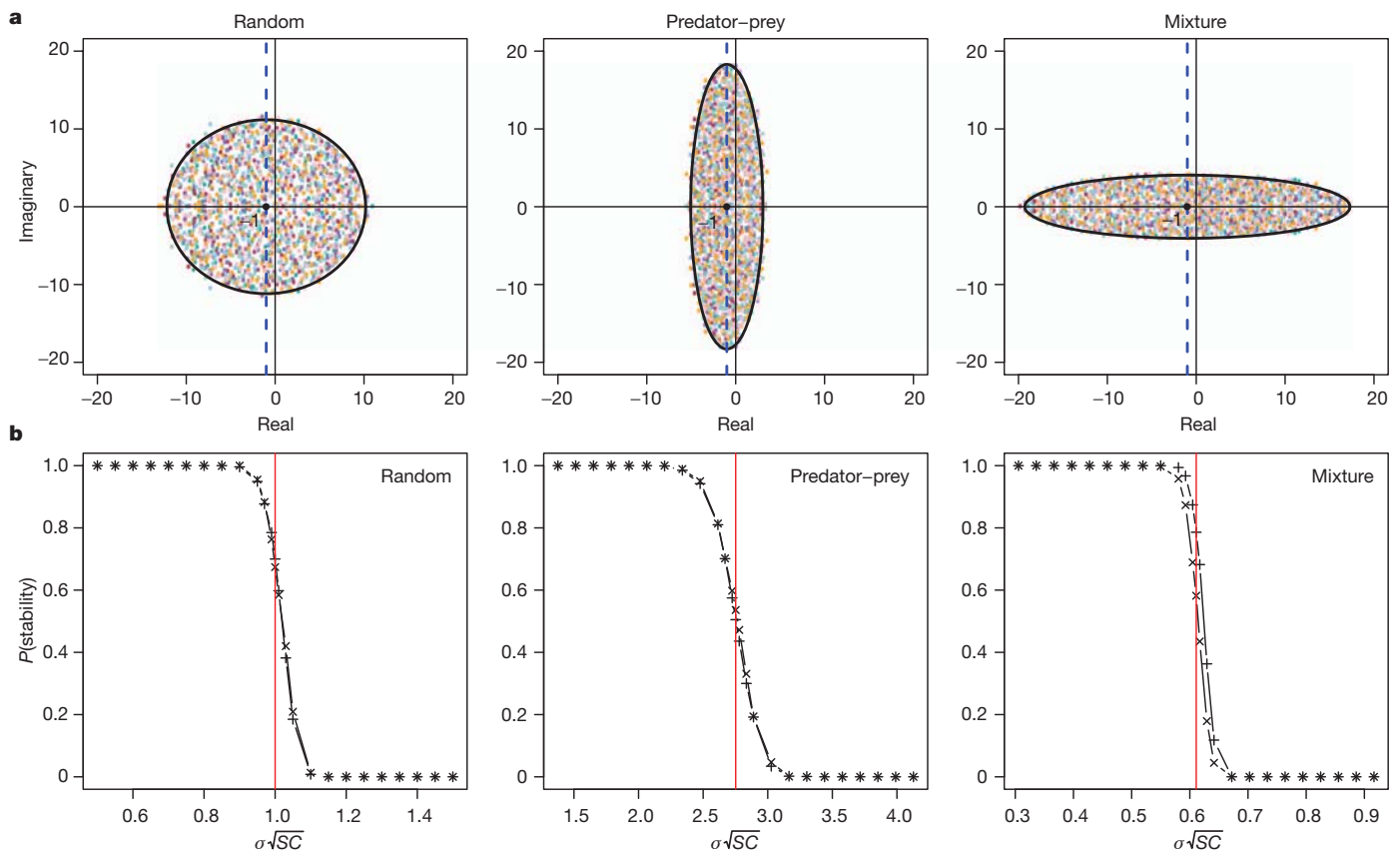


**Figure 1 | Distributions of the eigenvalues and corresponding stability profiles.** **a**, For  $X \sim N(0, \sigma^2)$ ,  $S = 250$ ,  $C = 0.25$  and  $\sigma = 1$ , we plot the eigenvalues of 10 matrices (colours) with  $-d = -1$  on the diagonal and off-diagonal elements, following the random, predator-prey or mixture prescriptions. The black ellipses are derived analytically in the text. **b**, Numerical simulations for the corresponding stability profiles. For the random case, starting from  $S = 250$ ,  $C = 0.5$ ,  $\sigma = 0.1$  and  $d = 1$ , we

systematically varied  $C$  (crosses) or  $\sigma$  (plus signs) to obtain  $\sigma\sqrt{SC}$  spanning  $[0.5, \dots, 1.0, \dots, 1.5]$  of the critical value for stability (indicated in red, 1 in the case of random matrices). The profiles were obtained by computing the probability of stability out of 1,000 matrices. The predator-prey case is as the random but with  $\sigma = 0.5$  and critical value  $\pi/(\pi - 2)$ . The mixture case is as the random but with critical value  $\pi/(\pi + 2)$ . In all cases, the phase transition between stability and instability is accurately predicted by our derivation.

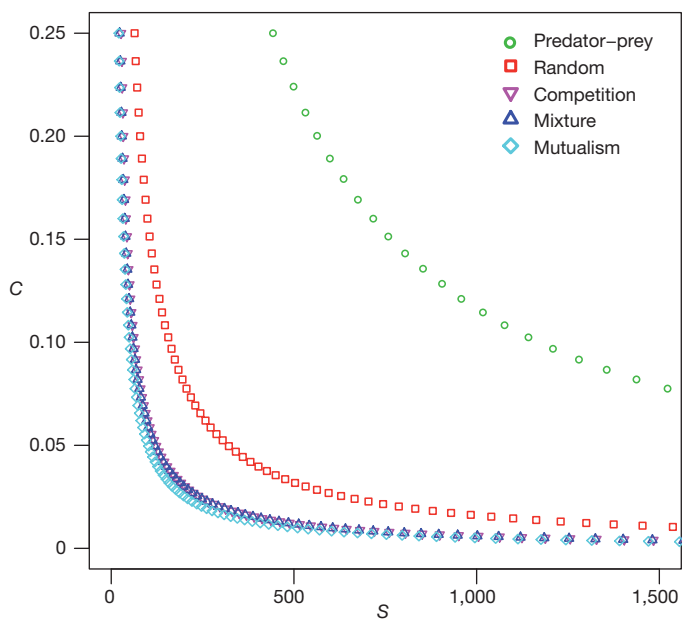


**Figure 2 | Stability criteria for different types of interaction.** We fixed  $\theta = d/\sigma = 4$ , and for a given connectance  $C$  we solved for the largest integer  $S$  that satisfies the stability criterion for each type of interactions. Combinations of  $S$  and  $C$  below each curve lead to stable matrices with a probability close to 1. The interaction types form a strict hierarchy from mutualism (most unlikely to be stable) to predator-prey (most likely to be stable).

(Supplementary Information). In both cases, stability decreases rapidly with higher complexity, and mutualistic matrices are less likely to be stable than their competitive counterpart (Fig. 2 and Table 1).

Having derived the stability criteria, we want to assess the effect of imposing realistic food web structure within the predator-prey case. It is believed that realistic food web structures should improve stability<sup>7,8,17</sup>. In community matrices of food webs, producers have positive columns and negative rows, with the opposite for top predators. To test whether these variations affect stability, we plotted the eigenvalues for predator-prey webs in which interactions are arranged, following the cascade<sup>20</sup> and niche<sup>21</sup> models. Imposing realistic structures results in eigenvalues with larger real parts than the corresponding unstructured predator-prey case (Supplementary Information and Supplementary Fig. 3). Thus, the cascade and niche models produce networks that are less likely to be stable than their unstructured predator-prey counterpart, with the niche model having a larger discrepancy: imposing realistic food web structure hampers stability.

Similarly, we measured the effect of realistic structures on mutualistic networks. Several published mutualistic networks are bipartite<sup>11–14</sup>: there are two types of node (for example plants and pollinators), and interactions occur exclusively between different types. In addition, bipartite mutualistic networks tend to be nested<sup>11</sup>: the interactions of the specialists form a subset of those of the generalists. Nestedness is believed to beget stability<sup>12–14</sup>. We plotted the eigenvalues for these two types of structure and compared the results with those obtained for the unstructured mutualistic case (Fig. 3, Supplementary Information and Supplementary Fig. 4). As stated above, stability in mutualistic networks is determined by the row sum. The bipartite case yields row sums that,



**Table 1 | Stability criteria for different types of interaction and network structure**

Interaction	Stability criterion	$S_{\max}(C, \theta)$		
		(0.1, 2.0)	(0.1, 4.0)	(0.2, 4.0)
Nested mutualism	$(S-1)C\sqrt{\frac{2}{\pi}} < \theta$	9	28	18
Mutualism		16 (15)	41 (51)	22 (20)
Bipartite mutualism	$\sqrt{SC} < \frac{\theta\pi}{\pi+2}$	17	41	23
Mixture		17 (14)	58 (59)	33 (29)
Competition	$\sqrt{SC}\left(1 + \frac{2-2C}{\pi-2C}\right)\sqrt{\frac{\pi-2C}{\pi}} + C\sqrt{\frac{2}{\pi}} < \theta$	17 (15)	62 (63)	38 (33)
Random		50 (40)	168 (160)	88 (80)
Niche predator–prey	$\sqrt{SC} < \frac{\theta\pi}{\pi-2}$	149	461	245
Cascade predator–prey		298	1,134	535
Predator–prey		314 (302)	1,201 (1,211)	603 (605)

In all cases, the criterion is derived for large  $S \times S$  matrices with  $X \sim N(0, \sigma^2)$  (and thus  $\mathbb{E}(|X|) = \sigma\sqrt{2/\pi}$ ), connectance  $C$  and  $\theta = d/\sigma$ . Numerical simulations report, for a given combination of  $C$  and  $\theta$ , the largest  $S$  ( $S_{\max}$ ) yielding a probability of stability  $\geq 0.5$  (computed using 1,000 matrices). In parenthesis are the analytical predictions.

for large  $S$ , are equal to the unstructured case. Accordingly, we did not find a discrepancy in stability for the bipartite case. However, in nested structures some rows and columns have sums that are larger than average (generalist plants and animals). Consequently, nested matrices are inherently less likely to be stable than unstructured ones. These findings are confirmed by numerical simulations. Using the same method, we found that asymmetric coupling of interaction strengths (where each large  $M_{ij}$  is coupled with a small  $M_{ji}$ ), contrary to current expectations<sup>22</sup>, does not influence stability in mutualistic networks (Supplementary Information and Supplementary Fig. 5).

We have considered how the arrangement of the interactions affects stability, and have found several counterintuitive results. These results can be accounted for by the fact that we provide a very conservative test for the effects of structure on stability (Supplementary Information). We now assess the role of the magnitude of interaction strengths. In fact, our findings extend to any distribution of coefficient strengths (Supplementary Information).

Typically, ecologists have regarded  $\sigma$  as the ‘average interaction strength’<sup>11,2</sup>. However,  $\sigma$  does not provide information on weak interactions<sup>9,10,17</sup>: we can have the same  $\sigma$  for two distributions with distinct shapes, and thus different proportions of weak and strong interactions (Supplementary Information). We analyse how the shape of the distribution affects stability for fixed  $S$ ,  $C$ ,  $d$  and  $\sigma$ . If the distribution contains many weak interactions, the expected magnitude  $\mathbb{E}(|X|) \approx 0$ . In contrast, if weak interactions are rare,  $\mathbb{E}(|X|) \approx \sigma$ . In the predator–prey systems, lowering  $\mathbb{E}(|X|)$  decreases  $\theta/(1 - \mathbb{E}^2(|X|)/\sigma^2)$  and thus

hampers stability. We conclude that weak interactions, contrary to current beliefs<sup>9,10,17</sup>, can destabilize predator–prey systems. Weakening the interactions shifts  $\mathbb{E}(|X|)$  closer to zero and therefore makes predator–prey systems closer to their random counterpart. With the same argument, weak interactions can stabilize the mixture of competition and mutualism case and have no effect on random networks. Variability in interaction strengths was previously found to be detrimental for stability in large food webs<sup>23</sup> and competitive networks<sup>17</sup>.

For example, consider a uniform distribution  $X \sim U[-\sigma\sqrt{3}, \sigma\sqrt{3}]$  and contrast it with the normal case  $X \sim N(0, \sigma^2)$ . Both parameterizations lead to  $\mathbb{E}(X) = 0$  and  $\text{Var}(X) = \sigma^2$ . In the uniform case,  $\mathbb{E}(|X|) = \sigma\sqrt{3}/2 \approx 0.866\sigma$ , whereas in the normal case  $\mathbb{E}(|X|) = \sigma\sqrt{2/\pi} \approx 0.798\sigma$ . This means that the uniform distribution, on average, leads to stronger interactions than the corresponding normal case. In turn, this has a large effect on stability: the criterion for the predator–prey case becomes  $\sqrt{SC} < 4\theta$  for the uniform distribution, whereas it is  $\sqrt{SC} < \pi/(\pi-2)\theta \approx 2.75\theta$  for the normal case. The random case is unaffected by the choice of the distribution ( $\sqrt{SC} < \theta$ ), whereas in the mixture of competition and mutualism we have  $\sqrt{SC} < 4\theta/7 \approx 0.571\theta$  for the uniform distribution and  $\sqrt{SC} < \pi\theta/(\pi+2) \approx 0.61\theta$  for the normal case. These considerations extend to any choice of distribution for the interaction strengths (Supplementary Information and Supplementary Figs 6 and 7): weak interactions, all other things being equal, are destabilizing for food webs, stabilizing for mutualistic and competitive networks (and their mixture), and have no effect on random networks.

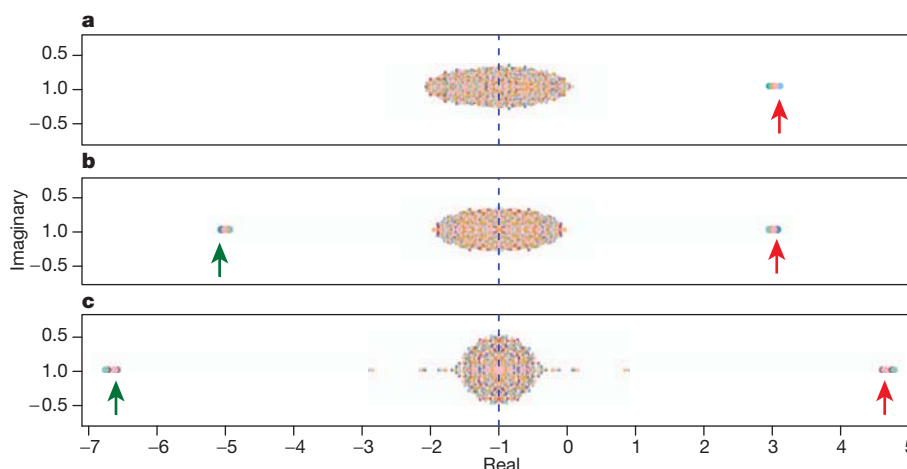


**Figure 3 | Distribution of the eigenvalues for the three types of mutualism.** **a**, Unstructured mutualism. **b**, Bipartite mutualism. **c**, Nested and bipartite mutualism. In all cases,  $S = 250$ ,  $\sigma = 0.1$ ,  $C = 0.2$  and  $d = 1$ . Note that the bipartite case does produce extreme negative real eigenvalues (green arrow) coupled with positive ones, but the row sum (and thus the rightmost eigenvalue,

red arrow) is equal to that of the unstructured mutualistic case. The nested matrices, in which generalist species yield (on average) larger row and column sums, have larger rightmost eigenvalues. Thus, highly nested matrices are less likely than the other two cases to be stable.

We have derived stability criteria for unstructured networks in which species interact at random, in predator–prey, mutualistic, and competitive pairs. These results hold for arbitrary diagonal values and arbitrary distribution of interaction strengths (Supplementary Information). Our analysis shows that, all other things being equal, weak interactions can be either stabilizing or destabilizing depending on the type of interactions between species. In predator–prey systems, realistic structure and weak interactions are detrimental for stability. However, in natural food webs, which seem to persist in time, weak interactions are preponderant<sup>24</sup>. The persistence of these networks might be explained by the interplay between their structure and weak interactions, even though each would be destabilizing if taken in isolation. For example, as suggested previously<sup>2</sup>, generalist predators could have weak interactions with their numerous prey, reducing the effect of the realistic structure and driving the system closer to the unstructured case.

Predator–prey systems differ markedly from the other cases studied here. Suppose that a network is unstable. The system can be stabilized either by lowering  $C$ ,  $S$  or  $\sigma$  (decreasing its complexity), or by increasing the self-regulation  $d$ . This is in line with May's argument: large and highly interconnected systems are difficult to stabilize. For random networks, reducing complexity is the only way to stabilize the system. However, in the other cases, networks can be stabilized by altering the distribution of interaction strengths; by modifying the parameters of the system we can typically change the distribution of the off-diagonal elements without altering the diagonal ones (Supplementary Information). For competition, mutualism and their mixture, stability is achievable by decreasing the average interaction strength  $\mathbb{E}(|X|)$ , which is akin to lowering complexity. On the contrary, predator–prey networks can be stabilized by increasing the strength of interaction  $\mathbb{E}(|X|)$ , and thus the coupling between predators and prey. Predator–prey systems are therefore the only ones that can potentially elude May's conclusions<sup>1,2</sup> and support an arbitrarily large, complex and stable ecological network.

Our results show that the ubiquity of consumer–resource relationships in nature could be due to their intrinsic dynamical properties. These findings are not limited to ecological networks, but instead hold for any system of differential equations resting at an equilibrium point.

Received 18 May 2011; accepted 6 January 2012.

Published online 19 February 2012.

1. May, R. M. Will a large complex system be stable? *Nature* **238**, 413–414 (1972).
2. May, R. M. *Stability and Complexity in Model Ecosystems* (Princeton Univ. Press, 2001).

3. MacArthur, R. Fluctuations of animal populations and a measure of community stability. *Ecology* **36**, 533–536 (1955).
4. Elton, C. S. *Animal Ecology* (Univ. of Chicago Press, 2001).
5. McCann, K. S. The diversity–stability debate. *Nature* **405**, 228–233 (2000).
6. Levins, R. *Evolution in Changing Environments: Some Theoretical Explorations* (Princeton Univ. Press, 1968).
7. McNaughton, S. J. Stability and diversity of ecological communities. *Nature* **274**, 251–253 (1978).
8. Yodzis, P. The stability of real ecosystems. *Nature* **289**, 674–676 (1981).
9. McCann, K. S., Hastings, A. & Huxel, G. R. Weak trophic interactions and the balance of nature. *Nature* **395**, 794–798 (1998).
10. Emmerson, M. & Yearsley, J. M. Weak interactions, omnivory and emergent food-web properties. *Proc. R. Soc. Lond. B* **271**, 397–405 (2004).
11. Bascompte, J., Jordano, P., Melián, C. J. & Olesen, J. M. The nested assembly of plant–animal mutualistic networks. *Proc. Natl Acad. Sci. USA* **100**, 9383–9387 (2003).
12. Okuyama, T. & Holland, J. N. Network structural properties mediate the stability of mutualistic communities. *Ecol. Lett.* **11**, 208–216 (2008).
13. Bastolla, U. *et al.* The architecture of mutualistic networks minimizes competition and increases biodiversity. *Nature* **458**, 1018–1020 (2009).
14. Thébault, E. & Fontaine, C. Stability of ecological communities and the architecture of mutualistic and trophic networks. *Science* **329**, 853–856 (2010).
15. DeAngelis, D. L. & Waterhouse, J. C. Equilibrium and nonequilibrium concepts in ecological models. *Ecol. Monogr.* **57**, 1–21 (1987).
16. Allesina, S. & Pascual, M. Network structure, predator–prey modules, and stability in large food webs. *Theor. Ecol.* **1**, 55–64 (2008).
17. Gross, T., Rudolf, L., Levin, S. A. & Dieckmann, U. Generalized models reveal stabilizing factors in food webs. *Science* **325**, 747–750 (2009).
18. Tao, T., Vu, V. & Krishnapur, M. Random matrices: universality of ESDs and the circular law. *Ann. Probab.* **38**, 2023–2065 (2010).
19. Sommers, H. J., Crisanti, A., Sompolinsky, H. & Stein, Y. Spectrum of large random asymmetric matrices. *Phys. Rev. Lett.* **60**, 1895–1898 (1988).
20. Cohen, J. E., Briand, F., Newman, C. M. & Palka, Z. J. *Community Food Webs: Data and Theory* (Springer, 1990).
21. Williams, R. J. & Martinez, N. D. Simple rules yield complex food webs. *Nature* **404**, 180–183 (2000).
22. Bascompte, J., Jordano, P. & Olesen, J. M. Asymmetric coevolutionary networks facilitate biodiversity maintenance. *Science* **312**, 431–433 (2006).
23. Kokkoris, G. D., Jansen, V. A. A., Loreau, M. & Troumbis, A. Y. Variability in interaction strength and implications for biodiversity. *J. Anim. Ecol.* **71**, 362–371 (2002).
24. Wootton, J. T. & Emmerson, M. Measurement of interaction strength in nature. *Annu. Rev. Ecol. Evol. Syst.* **36**, 419–444 (2005).

**Supplementary Information** is linked to the online version of the paper at [www.nature.com/nature](http://www.nature.com/nature).

**Acknowledgements** We thank J. Bergelson, L.-F. Bersier, A. M. de Roos, A. Eklof, C. A. Klausmeier, S. P. Lalley, R. M. May, K. S. McCann, M. Novak, P. P. A. Stanciczenko and J. D. Yeakel for comments and discussion. This research was supported by National Science Foundation grant EF0827493.

**Author Contributions** All authors contributed equally.

**Author Information** Reprints and permissions information is available at [www.nature.com/reprints](http://www.nature.com/reprints). The authors declare no competing financial interests. Readers are welcome to comment on the online version of this article at [www.nature.com/nature](http://www.nature.com/nature). Correspondence and requests for materials should be addressed to S.A. ([sallesina@uchicago.edu](mailto:sallesina@uchicago.edu)).

# Gain control by layer six in cortical circuits of vision

Shawn R. Olsen<sup>1\*</sup>, Dante S. Bortone<sup>1\*</sup>, Hillel Adesnik<sup>1</sup> & Massimo Scanziani<sup>1</sup>

**After entering the cerebral cortex, sensory information spreads through six different horizontal neuronal layers that are interconnected by vertical axonal projections. It is believed that through these projections layers can influence each other's response to sensory stimuli, but the specific role that each layer has in cortical processing is still poorly understood. Here we show that layer six in the primary visual cortex of the mouse has a crucial role in controlling the gain of visually evoked activity in neurons of the upper layers without changing their tuning to orientation. This gain modulation results from the coordinated action of layer six intracortical projections to superficial layers and deep projections to the thalamus, with a substantial role of the intracortical circuit. This study establishes layer six as a major mediator of cortical gain modulation and suggests that it could be a node through which convergent inputs from several brain areas can regulate the earliest steps of cortical visual processing.**

Primary sensory areas in the cerebral cortex are composed of a stack of six neuronal layers<sup>1</sup>. Anatomical and physiological data indicate that these layers are interconnected through vertical excitatory axons<sup>2–6</sup>, suggesting that sensory processing in any given layer may be modulated by activity in several other layers. However, so far the exact contribution of each layer to cortical processing is unclear.

Here we address the role of layer six (L6) in mouse visual cortex, whose excitatory neurons not only project to more superficial layers but also to the primary sensory thalamic nuclei<sup>3,7–11</sup>, the main source of sensory input to the cortex (Fig. 1a). L6 may thus influence cortical sensory responses directly through intracortical projections and indirectly through corticothalamic projections. Corticothalamic projections were reported to be both suppressive and facilitatory on thalamic activity, depending on the precise alignment between L6 and thalamic neurons (for reviews see refs 12–16). By contrast, how sensory responses in cortex are affected by L6 activity has remained largely unexplored<sup>17,18</sup>. Furthermore, the relative contribution of intracortical versus corticothalamic projections in modulating cortical responses is currently unknown. The paucity of information is due to the lack of experimental tools for selectively manipulating activity in L6 without directly perturbing other cortical layers.

## L6 neurons of the *Ntsr1*-Cre GN220 line

To control the activity of L6 we took advantage of a Cre-recombinase Bac transgenic mouse line that is reported to selectively label L6 neurons (NTSR1-Cre GN220)<sup>19</sup>. In the forebrain of these mice Cre expression was restricted to excitatory L6 neurons of the cerebral cortex (Fig. 1b and Supplementary Fig. 1). In primary visual cortex (V1) these neurons represented ~65% of the L6 excitatory neuronal population and, consistent with classification of L6 neurons in this region<sup>1</sup>, could be subdivided into two morphologically distinct categories: those whose apical dendrites ended in L4 and those that extended to L1 (Fig. 1b and Supplementary Fig. 1g, h). Furthermore, consistent with the corticothalamic projections originating from L6 in V1 (ref. 8), Cre-expressing neurons projected to the dorsolateral geniculate nucleus (dLGN; the primary thalamic visual nucleus) and the nucleus reticularis thalami (NRT; the main thalamic inhibitory nucleus) (Fig. 1b and

Supplementary Fig. 1d, e). Thirty-five percent of L6 excitatory neurons in V1 did not express Cre and these were morphologically distinct from the Cre-expressing population (Supplementary Fig. 1g).

To manipulate the activity of L6 neurons we conditionally expressed the light-sensitive cation channel channelrhodopsin 2 (ChR2)<sup>20,21</sup> in V1 using viral injection into NTSR1-Cre mice (Supplementary Fig. 2a). A linear multichannel probe recorded the spiking activity of neurons located across the vertical depth of cortex. Light-emitting diode (LED) illumination of the cortical surface for 500 ms with blue light (470 nm) increased the activity of L6 neurons in V1 of anesthetized animals (Fig. 1c–e and Supplementary Fig. 2b). This increase was not due to direct stimulation of the retina by the LED as it was absent in uninjected animals (Supplementary Fig. 2g).

## L6 activity suppresses other layers

To determine how L6 activation affects visual responses in other layers, we presented drifting gratings, and alternated control trials (visual stimulus only) with trials in which L6 was photostimulated (Fig. 1c). Notably, photostimulation of L6 rapidly and reversibly suppressed visually evoked multi-unit activity throughout the depth of the cortex (Fig. 1d). L6 photostimulation also reduced spontaneous activity (Supplementary Fig. 3d, e). This effect was absent in uninjected animals (Supplementary Fig. 2g). The suppressive action of L6 was similar across L2/3, L4 and L5 and was monotonic (Fig. 1e,f): that is, increasing L6 activity by increasing illumination intensity progressively suppressed visual responses, eventually abolishing nearly all evoked activity (strongest illumination reduced activity by  $81 \pm 5\%$ ,  $84 \pm 3\%$ , and  $84 \pm 3\%$  for L2/3, L4 and L5, respectively;  $P < 10^{-5}$ ). Because multi-unit activity is dominated by neurons with high firing frequencies, we determined the effect of L6 photostimulation on isolated single units whose average visually evoked firing rate varied over a 20-fold range. Isolated units were suppressed by L6 photostimulation (Fig. 1g), irrespective of their firing rates (Fig. 1h; 91.1% of units were suppressed and 7.8% were facilitated, and all facilitated units were fast-spiking, putative inhibitory cells (Supplementary Fig. 4a–d). Furthermore, in the same way as for multi-unit activity, L6 photostimulation monotonically suppressed single units (Fig. 1i, j; strongest

<sup>1</sup>Howard Hughes Medical Institute, Center for Neural Circuits and Behavior, Neurobiology Section and Department of Neuroscience, University of California San Diego, La Jolla, California 92093-0634, USA.

\*These authors contributed equally to this work.



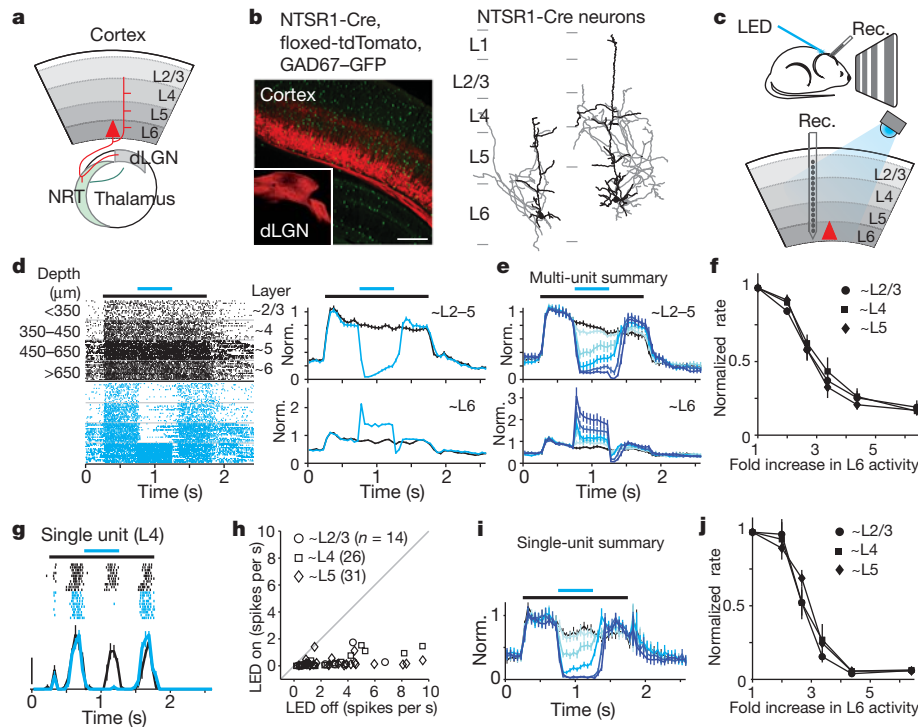


**Figure 1 | Photostimulation of L6 suppresses visual responses in the other layers.** **a**, Schematic of L6 projections. Red triangle represents an L6 pyramidal neuron. **b**, Left, coronal section of V1 from an NTSR1-Cre, floxed-tdTomato, GAD67-GFP mouse. Inset, L6 projection to dLGN (V1 of NTSR1-Cre mouse was injected with floxed-tdTomato virus). Scale bar, 250  $\mu$ m (125  $\mu$ m for inset). Right, the two types of L6 neurons that are labelled by the NTSR1-Cre line. Black, dendrites; grey, axons. **c**, Schematic of experimental setup. Rec., recording probe. **d**, Cortical visual responses with (blue) and without (black) L6 photostimulation. Left, raster plot of multi-unit activity grouped by depth. Control and photostimulation trials were interleaved but are separated here for

clarity. Black bar, visual stimulus (1.5 s); blue bar, LED illumination (0.5 s). Right, normalized (Norm.) peristimulus time histogram (PSTH); top, upper layers; bottom, L6. **e**, Summary ( $n = 6$  experiments). The control is shown in black and increasing LED intensities in darker blues. **f**, Suppression of multi-unit activity with increasing L6 activity. **g**, Visual response of a single L4 unit with (blue) and without (black) L6 photostimulation. Scale bar, 20 spikes per s. **h**, Response of each regular spiking unit with and without strong photostimulation of L6. **i**, Average normalized PSTH ( $n = 47$  units tested with 5 LED intensities). Colours are the same as in **e**. **j**, Suppression of single-unit activity. Error bars, mean  $\pm$  s.e.m.

illumination reduced activity by  $91 \pm 4\%$ ,  $93 \pm 2\%$ , and  $92 \pm 2\%$  for L2/3, L4 and L5, respectively;  $P < 10^{-9}$ ). Thus, these data show that stimulation of L6 excitatory neurons suppresses visually evoked responses in L2/3, L4 and L5 of V1.

### L6 activity does not affect tuning

Like in other mammals, neurons in mouse V1 differentially respond to gratings of different orientations<sup>22,23</sup>. We determined whether L6 stimulation affects the orientation tuning of V1 neurons. We generated tuning curves by presenting gratings drifting in 8–12 different directions and alternated control trials with trials in which L6 was photostimulated (Fig. 2a, b). We used a low LED intensity to suppress cortical visual responses partially, and considered units that were suppressed by between 10% and 75% (average suppression  $42 \pm 3\%$ ,  $n = 55$ ). Tuning curves of individual, isolated units were averaged into a population tuning curve (Fig. 2b, d; see methods). Remarkably, photostimulation of L6 resulted in the precise scaling of the tuning curve; that is, it reduced visually evoked responses by a similar fraction irrespective of presented orientation. This is clearly illustrated by plotting the normalized firing rates of the population tuning curve under control versus L6 photostimulation conditions (Fig. 2e). The data points fit well with a line whose slope is 0.56 and intercepts the  $y$  axis close to the origin. Thus, photostimulation of L6 did not affect preferred orientation, tuning width or the orientation selectivity index (OSI) of cortical neurons throughout L2/3, L4 and L5 (Fig. 2c; for L2/3, L4 and L5, respectively, the mean change in preferred orientation was  $3 \pm 3^\circ$  ( $P = 0.22$ ),  $0 \pm 5^\circ$  ( $P = 0.9$ ) and  $-4 \pm 5^\circ$  ( $P = 0.48$ ), mean change in tuning width was  $-1 \pm 4^\circ$  ( $P = 0.8$ ),  $6 \pm 4^\circ$  ( $P = 0.15$ ) and  $-6 \pm 6^\circ$  ( $P = 0.3$ ), and mean change in OSI was  $-0.09 \pm 0.07$  ( $P = 0.23$ ),

$0.7 \pm 0.04$  ( $P = 0.14$ ),  $-0.06 \pm 0.05$  ( $P = 0.22$ )). L6 photostimulation also resulted in a scaling of V1 responses to stimuli of increasing contrast (the contrast response function; Supplementary Fig. 5b). These data demonstrate that in primary visual cortex L6 selectively controls the gain of cortical responses to visual stimuli.

A potential concern in stimulating L6 with ChR2 is that the spatially uniform activation and the temporal pattern generated in L6 neurons may differ from visually evoked activity patterns, and thus the physiological activity of L6 neurons and L6 photostimulation may affect cortical activity in different ways. Furthermore, anaesthesia may change the impact of L6 on cortical responses to sensory stimuli. To address these issues, we optogenetically suppressed visually evoked activity in L6 in awake animals and determined the resulting effect on more superficial layers (Supplementary Fig. 6). Animals were head fixed but otherwise kept unrestrained on a passive circular treadmill (see Methods). L6 activity was suppressed using conditionally expressed light-sensitive hyperpolarizing opsins archaeorhodopsin<sup>24</sup> and halorhodopsin 3.0 (NpHR3.0) (ref. 25). LED illumination with amber light (590 nm), although reducing visually evoked L6 activity by  $\sim 30\%$  (Supplementary Fig. 6e), significantly facilitated visual responses of isolated units throughout the other layers (Fig. 2f, g and Supplementary Fig. 6). The facilitation was not due to direct LED illumination of the retina, as it was absent in uninjected animals (Supplementary Fig. 6f). Thus, suppression of L6 facilitates visually evoked activity in L2/3, L4 and L5, indicating that even physiologically generated L6 activity exerts a suppressive action onto these layers. Furthermore, suppression of L6 resulted in the precise scaling of the tuning curve (for the tuning curve analysis we considered units that were facilitated by at least 10% (average facilitation  $41 \pm 7\%$ ,  $n = 52$ )).

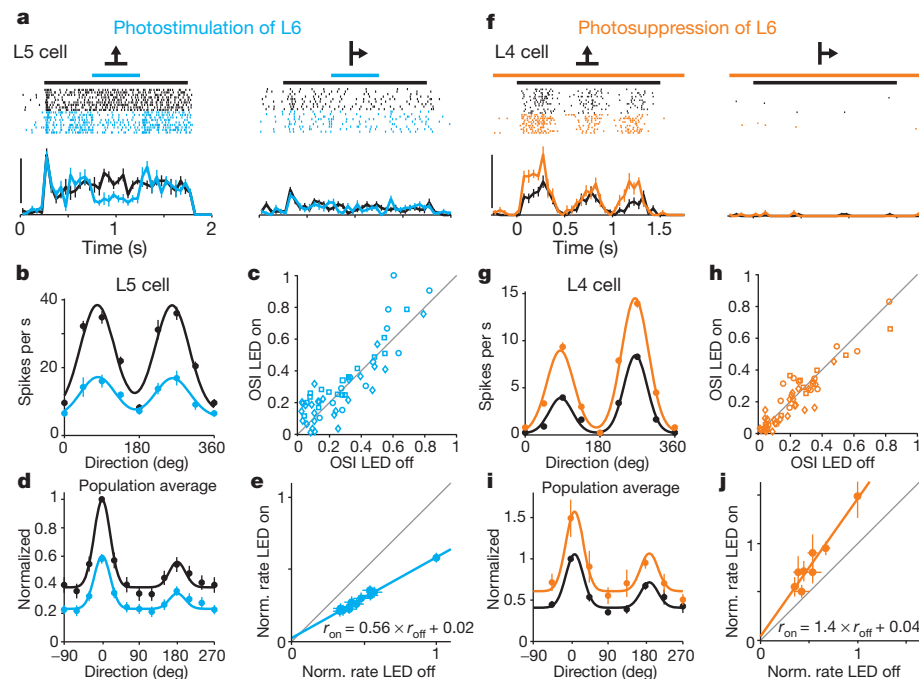


**Figure 2 | L6 bidirectionally modulates the gain of visual responses without altering tuning.** **a**, Visual responses of an L5 neuron with (blue) and without (black) L6 photostimulation. Raster plots and peristimulus time histograms for two out of eight tested visual stimulus directions. Scale bar, 40 spikes per s. **b**, Tuning curves for the neuron in **(a)**. **c**, The OSI for each neuron with and without photostimulation of L6. **d**, Population tuning curve with (blue) and without (black) L6 photostimulation ( $n = 55$ ). Black curve, fit using the sum of two Gaussians; blue curve, black curve scaled by the slope of linear fit in **e**. **e**, Control response plotted against response with L6 photostimulation (data from **c**). Blue, linear fit ( $r^2 = 0.98$ ). Black bar, visual stimulus (1.5 s); blue bar,

LED illumination (0.5 s). **f**, Visual response of an L4 neuron with (orange) and without (black) L6 photosuppression. Scale bar, 50 spikes per s. Orange bars, illumination with an amber-coloured LED (1.95 s); black bar, visual stimulation (1.5 s). **g**, Tuning curves for neuron in **(f)**. **h**, OSI for each isolated unit with and without photosuppression of L6. **i**, Population tuning curves with and without L6 photosuppression ( $n = 52$ ). Black curve, fit using sum of two Gaussians; orange curve, black curve scaled by slope of linear fit in **j**. **j**, Control response plotted against response with L6 photostimulation (data from **i**). Orange, linear fit ( $r^2 = 0.92$ ). Error bars, mean  $\pm$  s.e.m.

The plot of normalized firing rates under control versus L6 photosuppression conditions was well fit by a line whose slope is 1.4 and intercepts the  $y$  axis very close to the origin (Fig. 2j). Consistent with this, suppressing L6 did not affect preferred orientation, tuning width or orientation selectivity (Fig. 2h; for L2/3, L4 and L5, respectively, the mean change in preferred orientation was  $2 \pm 3^\circ$  ( $P = 0.41$ ),  $0 \pm 2^\circ$  ( $P = 0.95$ ) and  $-4 \pm 4^\circ$  ( $P = 0.35$ ) degrees, mean change in tuning width was  $-2 \pm 4^\circ$  ( $P = 0.68$ ),  $0 \pm 3^\circ$  ( $P = 0.94$ ) and  $-1 \pm 4^\circ$  ( $P = 0.77$ ) degrees, and mean change in OSI was  $-0.01 \pm 0.03$  ( $P = 0.22$ ),  $0.02 \pm 0.02$  ( $P = 0.50$ ) and  $-0.03 \pm 0.03$  ( $P = 0.22$ )). Taken together, these results demonstrate that visually driven L6 activity in awake animals controls the gain of cortical responses to visual stimuli.

### L6 intracortical and subcortical pathways

Two pathways could potentially mediate the suppression exerted by L6 on cortical activity. On one hand, L6 neurons project to the thalamus, where they can influence visually generated activity before it even reaches the cortex. On the other hand, L6 neurons also project to more superficial layers where they could directly modulate cortical activity. We addressed the impact of both projections. We performed extracellular recordings from the dLGN while photostimulating L6 in V1 (Fig. 3a). dLGN relay neurons were identified based on their visual response properties and characteristic firing pattern (Supplementary Fig. 7d). Photostimulation of L6 led to a rapid, reversible and monotonic reduction of visually evoked activity in dLGN relay neurons (Fig. 3b, c; strongest illumination:  $76 \pm 4\%$  reduction;  $P < 10^{-10}$ ,  $n = 32$ ), without, however, markedly modifying their firing mode (burst prevalence:  $12 \pm 6\%$  in control;  $6 \pm 3\%$  after reducing dLGN activity by 30% with L6 photostimulation,  $P = 0.08$ ; Supplementary Fig. 7e, f). This indicates that L6 stimulation suppresses

dLGN activity. To test whether visually evoked activity in L6 also suppresses dLGN activity we silenced the cortex optogenetically (by photostimulating parvalbumin-expressing inhibitory neurons in V1 with Chr2; see Methods and Supplementary Fig. 8). Consistent with the suppressive action of L6 stimulation on dLGN, silencing the cortex strongly facilitated dLGN activity (Fig. 3d–f; average facilitation  $87 \pm 25\%$  ( $P = 0.002$ ,  $n = 18$ )). *In vitro* recordings demonstrated that the suppressive action of L6 was due to the generation of disynaptic inhibition onto dLGN relay neurons, at least in part through the recruitment of NRT inhibitory neurons (and possibly through the recruitment of local inhibitory neurons in dLGN<sup>26</sup>) (Supplementary Fig. 9). Thus, these results reveal that L6 can effectively suppress visual responses in the dLGN.

If L6 suppresses cortical visual responses indirectly, by suppressing the dLGN, this suppression should precede V1 suppression by a few milliseconds. We tested this prediction by performing simultaneous recordings from both dLGN and V1 and compared the onset of suppression in these two structures upon L6 photostimulation (Fig. 3g). Surprisingly, cortical suppression preceded dLGN suppression by a few milliseconds (Fig. 3h). This result suggests that L6 activity may suppress cortical visual responses through an alternative circuit. Because L6 neurons send axons to the upper layers of cortex we tested whether these projections can suppress cortical activity independently of the corticothalamic projections. For this, we performed *in vitro* whole-cell recordings from neurons in L2/3, L4, L5 and L6 in coronal slices of V1 (Fig. 4a); this slicing plane disconnects V1 from dLGN.

Photostimulation of L6 *in vitro* generated both excitatory and inhibitory postsynaptic currents (EPSCs and IPSCs, respectively) onto L2/3, L4, L5 and L6 pyramidal cells (L6 recordings included only those pyramidal cells not expressing Chr2) (Fig. 4b). IPSCs were of disynaptic (or polysynaptic) origin as they were entirely blocked by

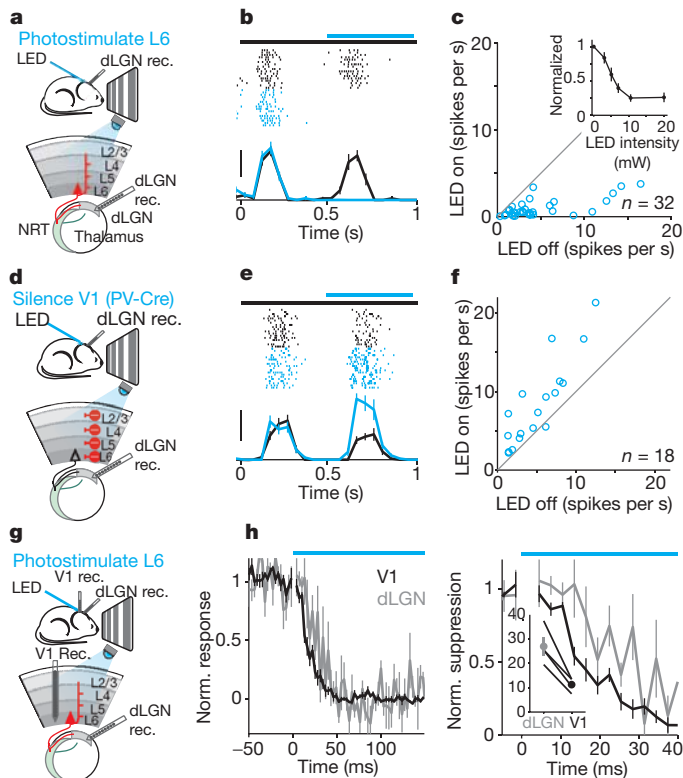


**Figure 3 | Photostimulation of L6 suppresses cortex faster than it suppresses dLGN.** **a**, Schematic of the experimental setup. **b**, Visual response of dLGN unit with (blue) and without (black) L6 photostimulation. Scale bar, 20 spikes per s. Black bar, visual stimulus (1 s); blue bar, LED illumination (0.5 s). **c**, Average response of each dLGN unit with and without L6 photostimulation. Inset, monotonic suppression of dLGN. **d**, Schematic of setup for silencing V1 by photostimulation of parvalbumin inhibitory neurons. **e**, Visual response of dLGN unit with and without photo-silencing of V1. Scale bar, 30 spikes per s. Black bar, visual stimulus (1 s); blue bar, LED illumination (0.5 s). **f**, Average response of each dLGN unit with and without cortical silencing. **g**, Schematic of experimental setup. **h**, Left, time-course of L6-mediated suppression of dLGN (grey) and V1 (black) ( $n = 4$ ). Residual response during maximal suppression set to zero (see Methods). Bin size, 3 ms. Right, the same data on an expanded timescale. The first bin at LED onset was blanked to remove LED-induced artefact. Inset, time to suppression exceeding two standard deviations from baseline activity in dLGN and V1 for four experiments ( $P = 0.012$ ). Error bars, mean  $\pm$  s.e.m. Inset, y-axis units are ms.

glutamatergic antagonists (Supplementary Fig. 10b). Furthermore, the activity pattern generated by L6 photostimulation was similar to the activity pattern generated *in vivo* (Supplementary Fig. 2b, h). IPSCs were larger than EPSCs, despite the fact that both currents were recorded with a similar driving force (IPSCs were recorded near the reversal potential for EPSCs and vice versa). Indeed, excitatory charge accounted for only 10% or less of the total charge, depending on the layer (Fig. 4c) or sublayer (Supplementary Fig. 10c, d). These results show that V1 contains the necessary circuitry for L6 to generate disynaptic inhibition onto L2/3, L4, L5 and onto itself.

To determine whether L6 can suppress neuronal spiking across L2/3, L4, L5 and L6 through these disynaptic IPSCs, we performed current-clamp recordings in the perforated patch configuration (to preserve the intracellular ionic composition) and triggered spiking by injecting depolarizing current pulses. Photostimulation of L6 significantly suppressed firing of pyramidal cells across all layers (Fig. 4d; firing rate was reduced by  $48 \pm 10\%$ ,  $84 \pm 7\%$ ,  $55 \pm 19\%$  and  $75 \pm 11\%$  for L2/3, L4, L5 and L6, respectively;  $P \leq 0.01$ ). To rule out the possibility that this suppression was a result of uniformly activating large portions of L6 we restricted the area of activation to a small spot of approximately  $100 \mu\text{m}$  in diameter while recording

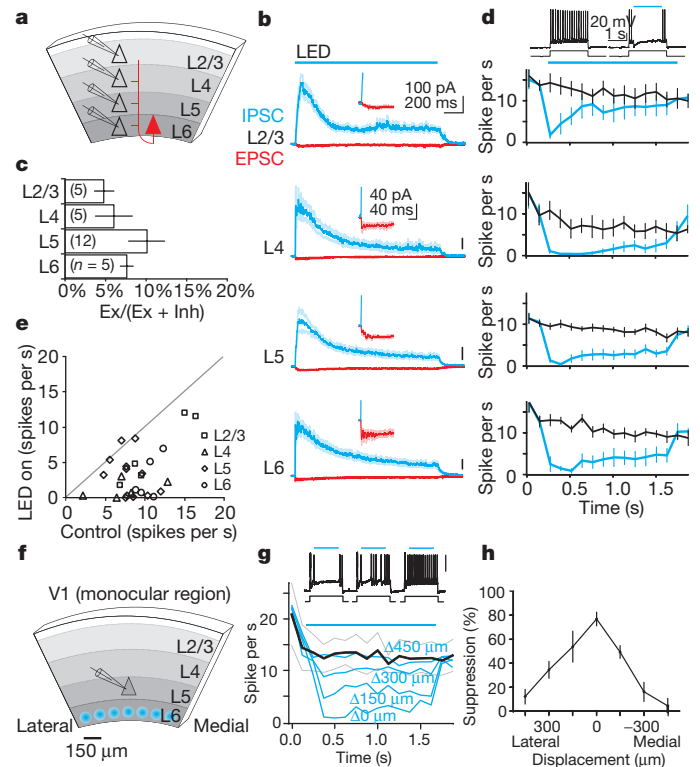


**Figure 4 | Photostimulation of L6 recruits intracortical synaptic inhibition.** **a**, Schematic of *in vitro* experimental setup. **b**, Average IPSCs (blue) and EPSCs (red) recorded in pyramidal cells during photostimulation of L6. Synaptic currents are averages of  $n = 5$ –12 cells. Inset, onset of EPSC. **c**, Histogram of excitatory charge as a percentage of total charge. Ex, excitation; Inh, inhibition. **d**, Traces show perforated patch recording from L5 pyramidal cell in response to depolarizing current injection with (right) and without (left) L6 photostimulation. Graphs, spike rate with and without L6 photostimulation. **e**, Average spike rate in control versus spike rate with L6 photostimulation for each cell. **f**, Schematic of experimental setup for focal photostimulation. **g**, Traces, spiking of L5 pyramidal cell to depolarizing current injection with focal photostimulation of L6 at three progressively more distant positions (left to right). Graph shows spike rate in control (black) and with focal photostimulation of L6 (blue) ( $n = 4$ ). Delta indicates the medial or lateral distance from the radial axis through the recording site. **h**, Percentage of spike suppression plotted against horizontal displacement. Error bars, mean  $\pm$  s.e.m.

from a L5 neuron (Fig. 4f). Even when activating a restricted area of L6, the firing of L5 neurons was robustly suppressed (Fig. 4g). The suppression was maximal when L6 photostimulation was aligned with the recorded L5 neuron along the cortical radial axis, and decreased progressively as the photostimulation spot was translated tangentially (Fig. 4g, h). These results demonstrate that V1 can efficiently suppress activity in L2/3, L4, L5 and L6 in the absence of thalamus.

### Major role of L6 intracortical circuits

Taken together, these results indicate that L6 can modulate cortical responses to visual stimuli through two independent circuits: indirectly, through the corticothalamic circuit and directly, through the intracortical circuit. To test whether one of these two circuits has a dominant role, we examined how much of the V1 suppression is predicted by dLGN suppression. We first established the transfer function between dLGN and V1. For this we performed simultaneous *in vivo* recordings from these two structures while presenting full-field drifting gratings of varying contrasts to obtain contrast response functions for the dLGN and V1 (Fig. 5a, b). By plotting dLGN versus V1 activity at each contrast we obtained the transfer function from dLGN to V1, which provides the response of V1 to various levels of dLGN activity (Fig. 5c). Finally, we presented the strongest contrast and photostimulated L6 to reduce dLGN activity while simultaneously monitoring V1 activity.



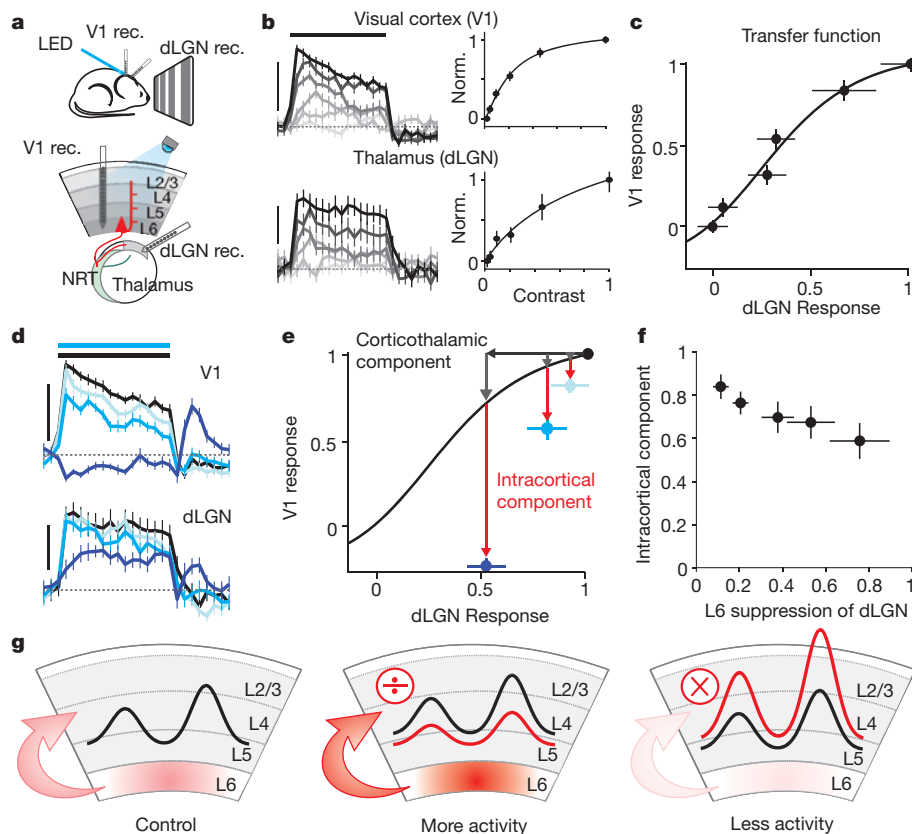


**Figure 5 | L6 suppresses upper layers largely through intracortical circuits.** **a**, Schematic of experimental setup. **b**, Simultaneously recorded multi-unit responses to increasing contrasts (light to dark) in V1 (top) and dLGN (bottom). All spikes that were recorded above L6 ( $\leq 650 \mu\text{m}$ ) were included in V1 multi-unit activity. Scale bar, 200 spikes per s for V1; 100 spikes per s for dLGN. Black bar, visual stimulus (1.5 s). Dotted line, baseline activity. Right, contrast–response functions. **c**, dLGN–V1 transfer function derived by plotting normalized response in V1 versus dLGN (from **b**). Fit, hyperbolic ratio function. **d**, Simultaneously recorded multi-unit responses to maximal contrasts in V1 and dLGN without photostimulation (black) or while photostimulating L6 with increasing LED intensities (progressively darker blue). Same experiment as in **b** and **c**. Black bar, visual stimulus (1.5 s); blue bar, LED illumination (1.5 s). Scale bars are the same as in **b**. **e**, V1 versus dLGN response to maximal contrast under control condition (black data point) or during three progressively stronger photostimulations of L6 (light, medium and dark blue, data from **d**). V1 responses are suppressed more than predicted by transfer function (red arrows) even for photostimulations that reduce dLGN activity only  $\sim 10\%$  (light blue). **f**, Average intracortical component of suppression as a function dLGN suppression ( $n = 5$  experiments). Intracortical component (red arrow in **e**) is quantified as a fraction of total V1 suppression (grey arrows plus red arrows in **e**). **g**, Schematic of the main finding. Error bars, mean  $\pm$  s.e.m.

We reasoned that if the ensuing reduction of V1 activity matches the reduction predicted by the transfer function, the modulation of cortical responses by L6 is mainly due to dLGN suppression by the corticothalamic circuit. However, if the reduction in V1 activity exceeds that predicted by the transfer function, the additional reduction can be attributed to the intracortical circuit. We reduced dLGN activity by  $\sim 10\%$ ,  $20\%$  and  $50\%$  through activation of L6 with three progressively stronger illuminations (Fig. 5d). Notably, even the smallest reduction in dLGN activity ( $10\%$ ) was accompanied by a reduction in V1 activity that largely exceeded that predicted by the transfer function (Fig. 5e). Furthermore, a  $50\%$  suppression of dLGN activity was accompanied by a complete suppression of visually evoked activity in V1. In this experiment a large fraction of V1 suppression ( $73\%$  averaged over five LED levels) exceeded the transfer function prediction and must therefore be attributed to the intracortical circuit (average intracortical component over all experiments  $73 \pm 5\%$ ,  $n = 5$ ; Fig. 5f). Furthermore, given the relatively minor effects on the prevalence of burst firing in dLGN neurons (Supplementary Fig. 7f), this effect cannot be attributed to a change in the firing pattern of dLGN neurons. These results indicate that L6 suppresses cortical responses to visual stimuli mainly through intracortical circuits.

## Discussion

Taken together, this study shows that L6 modulates visually evoked activity across L2/3, L4 and L5. This modulation occurs continuously through visually driven L6 activity, as shown in awake animals, and does not affect orientation tuning indicating that L6 selectively controls the gain of cortical visual responses. Finally, despite suppression of the dLGN, cortical gain control by L6 is executed largely by intracortical circuits.

Response gain modulation is a fundamental cortical operation<sup>27</sup> that is crucially involved in sensory representation and sensorimotor integration. For example, visual responses in parietal cortex are gain modulated by gaze direction<sup>28</sup>. Furthermore, gain modulation may underlie

the effects of attention on cortical responses to visual stimuli<sup>29,30</sup>. However, the neuronal circuits that implement this operation have remained largely unknown. Identifying L6 as a contributor to cortical response gain modulation is an important step in dissecting the specific functions of distinct circuits in cortical processing. The suppressive action of L6 that is described here markedly differs from the facilitatory impact of other layers on cortical activity<sup>3,31,32</sup> (for example, L2/3 facilitates L5 (ref.<sup>32</sup>)) and points towards a very distinct function of different layers in sensory processing. The cortical GABAergic interneuron subtype (or subtypes)<sup>33,34</sup> that is recruited by L6 activity and mediates the reported suppressive effect remains to be identified, but may include fast spiking neurons (Supplementary Fig. 4). Although the exact synaptic mechanisms underlying gain control by L6 remains to be elucidated, either a proportional change in excitation and inhibition<sup>35,36</sup> or the modulation of only one of the two opposing conductances<sup>37</sup> may underlie the operation. The columnar organization of L6 pyramidal cell projections to more superficial layers<sup>10</sup> ensures that L6-mediated suppression is restricted to the cortical domains that are directly above the activated L6 region (Fig. 4g, h). This topographic organization could allow the cortex to differentially modulate the gain of V1 responses to stimuli located in distinct regions of visual space.

L6 has been suggested to contribute to ‘end inhibition’, the suppression of cortical responses by bars above a given size<sup>17</sup>. The powerful inhibitory currents generated by L6 onto more superficial pyramidal cells may represent the underlying cellular mechanism.

Previous studies addressing the role of corticothalamic feedback projections through focal pharmacological perturbation of L6 neurons have typically reported a facilitation of functionally or topographically aligned thalamic neurons overlaid by broader surround suppression<sup>16</sup>, resulting in changes to both spatial and temporal tuning properties of these neurons<sup>15,38–41</sup>. Our data obtained using full-field visual stimulation are consistent with this model, in which spatial summation of individual inhibitory surrounds will result in a net suppressive effect of the corticothalamic feedback projection. Future studies combining

optogenetic approaches with focal stimulation of visual space will reveal how fine-scale corticothalamic circuits<sup>39,42</sup> interact with intracortical L6 circuits to influence visual processing in the cortex.

L6 in V1 receives convergent inputs from a variety of brain regions, including higher cortical areas<sup>43</sup> as well as thalamus<sup>11</sup>. These various brain regions could thus influence, through L6, the gain of visual responses during the very initial steps of visual cortical processing.

## METHODS SUMMARY

ChR2, archaerhodopsin and NpHR3.0 were conditionally expressed in mouse V1 via stereotactic injection of adenoassociated viruses into NTSR1-Cre mice<sup>19</sup>. For recordings under anaesthesia, mice were injected with 5 mg kg<sup>-1</sup> chlorprothixene and 1.2 g kg<sup>-1</sup> urethane. For awake experiments, a craniotomy was performed under isoflurane anaesthesia (1–1.5%), and then a previously implanted head-plate was used to fix the mouse on a circular treadmill and the anaesthetic was removed. *In vivo* extracellular recordings were made from V1 and dLGN using multichannel silicon probes. Visual stimuli were displayed on an LCD screen. Microbial opsins were photoactivated using a blue (470-nm) or amber (590-nm) LED placed above the thinned skull. *In vitro* whole-cell recordings were performed as previously described<sup>32</sup>.

**Full Methods** and any associated references are available in the online version of the paper at [www.nature.com/nature](http://www.nature.com/nature).

Received 29 August 2011; accepted 4 January 2012.

Published online 22 February 2012.

- Lorente de No, R. in *Physiology of the Nervous System* (ed. Fulton, J.F.) 274–301 (Oxford Univ. Press, 1943).
- Douglas, R. J. & Martin, K. A. Neuronal circuits of the neocortex. *Annu. Rev. Neurosci.* **27**, 419–451 (2004).
- Lefort, S., Tómm, C., Floyd Sarria, J. C. & Petersen, C. C. The excitatory neuronal network of the C2 barrel column in mouse primary somatosensory cortex. *Neuron* **61**, 301–316 (2009).
- Thomson, A. M. & Bannister, A. P. Interlaminar connections in the neocortex. *Cereb. Cortex* **13**, 5–14 (2003).
- Callaway, E. M. Local circuits in primary visual cortex of the macaque monkey. *Annu. Rev. Neurosci.* **21**, 47–74 (1998).
- Dantzker, J. L. & Callaway, E. M. Laminar sources of synaptic input to cortical inhibitory interneurons and pyramidal neurons. *Nature Neurosci.* **3**, 701–707 (2000).
- Thomson, A. M. Neocortical layer 6, a review. *Front. Neuroanat.* **4**, 13 (2010).
- Bourassa, J. & Deschenes, M. Corticothalamic projections from the primary visual cortex in rats: a single fiber study using biocytin as an anterograde tracer. *Neuroscience* **66**, 253–263 (1995).
- Binzegger, T., Douglas, R. J. & Martin, K. A. Stereotypical bouton clustering of individual neurons in cat primary visual cortex. *J. Neurosci.* **27**, 12242–12254 (2007).
- Zhang, Z. W. & Deschenes, M. Intracortical axonal projections of lamina VI cells of the primary somatosensory cortex in the rat: a single-cell labeling study. *J. Neurosci.* **17**, 6365–6379 (1997).
- Jones, E. G. *The Thalamus* (Cambridge Univ. Press, 2007).
- Guillery, R. W. & Sherman, S. M. Thalamic relay functions and their role in corticocortical communication: generalizations from the visual system. *Neuron* **33**, 163–175 (2002).
- Sillito, A. M. & Jones, H. E. Corticothalamic interactions in the transfer of visual information. *Phil. Trans. R. Soc. Lond. B* **357**, 1739–1752 (2002).
- Briggs, F. & Usrey, W. M. Emerging views of corticothalamic function. *Curr. Opin. Neurobiol.* **18**, 403–407 (2008).
- Cudeiro, J. & Sillito, A. M. Looking back: corticothalamic feedback and early visual processing. *Trends Neurosci.* **29**, 298–306 (2006).
- Sillito, A. M., Cudeiro, J. & Jones, H. E. Always returning: feedback and sensory processing in visual cortex and thalamus. *Trends Neurosci.* **29**, 307–316 (2006).
- Bolz, J. & Gilbert, C. D. Generation of end-inhibition in the visual cortex via interlaminar connections. *Nature* **320**, 362–365 (1986).
- Grieve, K. L. & Sillito, A. M. A re-appraisal of the role of layer VI of the visual cortex in the generation of cortical end inhibition. *Exp. Brain Res.* **87**, 521–529 (1991).
- Gong, S. *et al.* Targeting Cre recombinase to specific neuron populations with bacterial artificial chromosome constructs. *J. Neurosci.* **27**, 9817–9823 (2007).
- Nagel, G. *et al.* Channelrhodopsin-2, a directly light-gated cation-selective membrane channel. *Proc. Natl Acad. Sci. USA* **100**, 13940–13945 (2003).
- Boyden, E. S., Zhang, F., Bamberg, E., Nagel, G. & Deisseroth, K. Millisecond-timescale, genetically targeted optical control of neural activity. *Nature Neurosci.* **8**, 1263–1268 (2005).
- Niell, C. M. & Stryker, M. P. Highly selective receptive fields in mouse visual cortex. *J. Neurosci.* **28**, 7520–7536 (2008).
- Hubel, D. H. & Wiesel, T. N. Receptive fields, binocular interaction and functional architecture in the cat's visual cortex. *J. Physiol.* **160**, 106–154 (1962).
- Chow, B. Y. *et al.* High-performance genetically targetable optical neural silencing by light-driven proton pumps. *Nature* **463**, 98–102 (2010).
- Gradinaru, V. *et al.* Molecular and cellular approaches for diversifying and extending optogenetics. *Cell* **141**, 154–165 (2010).
- Rafols, J. A. & Valverde, F. The structure of the dorsal lateral geniculate nucleus in the mouse. A Golgi and electron microscopic study. *J. Comp. Neurol.* **150**, 303–331 (1973).
- Salinas, E. & Thier, P. Gain modulation: a major computational principle of the central nervous system. *Neuron* **27**, 15–21 (2000).
- Brothie, P. R., Andersen, R. A., Snyder, L. H. & Goodman, S. J. Head position signals used by parietal neurons to encode locations of visual stimuli. *Nature* **375**, 232–235 (1995).
- Treue, S. & Martinez Trujillo, J. C. Feature-based attention influences motion processing gain in macaque visual cortex. *Nature* **399**, 575–579 (1999).
- McAdams, C. J. & Maunsell, J. H. Effects of attention on orientation-tuning functions of single neurons in macaque cortical area V4. *J. Neurosci.* **19**, 431–441 (1999).
- Silver, R. A., Lubke, J., Sakmann, B. & Feldmeyer, D. High-probability unquantal transmission at excitatory synapses in barrel cortex. *Science* **302**, 1981–1984 (2003).
- Adesnik, H. & Scanziani, M. Lateral competition for cortical space by layer-specific horizontal circuits. *Nature* **464**, 1155–1160 (2010).
- Markram, H. *et al.* Interneurons of the neocortical inhibitory system. *Nature Rev. Neurosci.* **5**, 793–807 (2004).
- Ascoli, G. A. *et al.* Petilla terminology: nomenclature of features of GABAergic interneurons of the cerebral cortex. *Nature Rev. Neurosci.* **9**, 557–568 (2008).
- Chance, F. S., Abbott, L. F. & Reyes, A. D. Gain modulation from background synaptic input. *Neuron* **35**, 773–782 (2002).
- Shadlen, M. N. & Newsome, W. T. The variable discharge of cortical neurons: implications for connectivity, computation, and information coding. *J. Neurosci.* **18**, 3870–3896 (1998).
- Murphy, B. K. & Miller, K. D. Multiplicative gain changes are induced by excitation or inhibition alone. *J. Neurosci.* **23**, 10040–10051 (2003).
- Andolina, I. M., Jones, H. E., Wang, W. & Sillito, A. M. Corticothalamic feedback enhances stimulus response precision in the visual system. *Proc. Natl Acad. Sci. USA* **104**, 1685–1690 (2007).
- Wang, W., Jones, H. E., Andolina, I. M., Salt, T. E. & Sillito, A. M. Functional alignment of feedback effects from visual cortex to thalamus. *Nature Neurosci.* **9**, 1330–1336 (2006).
- Wörgötter, F., Nelle, E., Li, B. & Funke, K. The influence of corticofugal feedback on the temporal structure of visual responses of cat thalamic relay cells. *J. Physiol.* **509**, 797–815 (1998).
- McClurkin, J. W. & Marrocco, R. T. Visual cortical input alters spatial tuning in monkey lateral geniculate nucleus cells. *J. Physiol.* **348**, 135–152 (1984).
- Murphy, P. C., Duckett, S. G. & Sillito, A. M. Feedback connections to the lateral geniculate nucleus and cortical response properties. *Science* **286**, 1552–1554 (1999).
- Casagrande, V. A. & Kaas, J. H. *The Afferent, Intrinsic and Efferent Connections of Primary Visual Cortex in Primates* (eds Peters, A. & Rockland, P.) (Plenum, 1994).

**Supplementary Information** is linked to the online version of the paper at [www.nature.com/nature](http://www.nature.com/nature).

**Acknowledgements** We are grateful to M. Carandini, J. Isaacson and the members of the Scanziani and Isaacson laboratories for helpful discussions of this project, to J. Isaacson, R. Malinow and T. Komiyama for providing feedback on the manuscript, to P. Abelkop for histological help and neonatal viral injections, to J. Evora for mouse colony support and genotyping, to B. Atallah for sharing the technique for silencing the cortex by photostimulation of parvalbumin neurons and for help with the *in vivo* recording setup and to W. Bruns for help coding analysis software. We thank the UCSD Neuroscience Microscopy Facility (P30 NS047101) for the use of their imaging equipment. S.R.O. and H.A. were supported by postdoctoral fellowships from the Helen Hay Whitney Foundation. D.S.B. was supported by a UCSD Neurobiology Training Grant (NINDS: 5T32NS007220-28). M.S. is an investigator of the Howard Hughes Medical Institute. This work was also supported National Institutes of Health grant RO1 NS069010 and by the Gatzert Charitable Foundation.

**Author Contributions** H.A. performed the initial physiological characterization of the NTSR1-Cre expression system with optogenetic tools. H.A. also developed the *in vivo* awake recording preparation on the treadmill. S.R.O. performed all *in vivo* recordings. D.S.B. performed all *in vitro* recordings and anatomical reconstructions. S.R.O. and M.S. designed the study. M.S. wrote the paper.

**Author Information** Reprints and permissions information is available at [www.nature.com/reprints](http://www.nature.com/reprints). The authors declare no competing financial interests. Readers are welcome to comment on the online version of this article at [www.nature.com/nature](http://www.nature.com/nature). Correspondence and requests for materials should be addressed to M.S. ([massimo@biomail.ucsd.edu](mailto:massimo@biomail.ucsd.edu)) or S.R.O. ([srolsen@ucsd.edu](mailto:srolsen@ucsd.edu)).

## METHODS

All procedures were conducted in accordance with the National Institutes of Health guidelines and with the approval of the Committee on Animal Care at the University of California, San Diego.

**Animals.** We used the following mouse lines: NTSR1-Cre (strain B6.FVB(Cg)-Tg(Ntsr1-cre)GN220Gsat/Mmcd, stock number 030648-UCD), which was generated by the GENSAT project<sup>19</sup> and acquired from the Mutant Mouse Regional Resource Centers; tdTomato reporter (Jax number 007908); GAD67-GFP (Aneo); and PV-Cre (Silvia Arber).

**Viral injections.** Adeno-associated viruses (AAVs) for ChR2 and archaerhodopsin were acquired from the University of Pennsylvania Viral Vector Core: AAV2/1.CAGGS.flex.ChR2.tdTomato.SV40 (Addgene 18917) and AAV2/9.flex.CBA.Archaerhodopsin-GFP.W.SV40 (Addgene 22222). An AAV virus (AAV2/9) for NpHR3.0 was produced at the Salk Viral Vector Core. The NpHR3.0 plasmid (pAAV-Efla-DIO-eNpHR 3.0-EYFP) was provided by K. Diesseroth.

Viruses were loaded in a bevelled sharp micropipette mounted on a Nanoject II (Drumond) or a micropump injector (UMP-3 WPI) attached to a micromanipulator. ChR2 virus was injected into newborn pups (between postnatal days 0 and 2) that were anaesthetized on ice and secured into a moulded platform. Three 20-nl boli of virus was injected at each of three medial-lateral locations in V1 and two depths (500  $\mu\text{m}$  and 650  $\mu\text{m}$ ) within V1.

Archaerhodopsin was injected in combination with NpHR3.0 in juvenile (1–2-month-old) mice anaesthetized with 2.5% isoflurane and placed into a stereotaxic frame (Knopf). The exposed skull overlying V1 was thinned in three locations with a dental drill (Foredom) with a 300- $\mu\text{m}$  bur (Gesswein), and a hole was made with a (25-gauge) needle at each location to permit insertion of the injection pipette. A volume of 150 nl of virus was injected at a rate of 20 nl min<sup>-1</sup> at each of the three locations and at two depths (900  $\mu\text{m}$  and 700  $\mu\text{m}$ ). The scalp was then sutured and the mouse injected subcutaneously with 0.1 mg kg<sup>-1</sup> buprenorphine. *In vivo* recordings were made 1–2 months after viral injection.

**Slice preparation.** Mice were anaesthetized with ketamine and xylazine (100 mg kg<sup>-1</sup> and 10 mg kg<sup>-1</sup>, respectively), perfused transcardially with cold sucrose solution (in mM: NaCl, 83; KCl, 2.5; MgSO<sub>4</sub>, 3.3; NaH<sub>2</sub>PO<sub>4</sub>, 1; NaHCO<sub>3</sub>, 26.2; D-glucose, 22; sucrose, 72; and CaCl<sub>2</sub>, 0.5, bubbled with 95% O<sub>2</sub> and 5% CO<sub>2</sub>) and decapitated, and the visual cortex was cut into 300–400- $\mu\text{m}$  coronal sections in cold sucrose solution. Thalamic slices were cut 45° off the coronal plane to maintain connections between NRT and dLGN. Slices were incubated in sucrose solution in a submerged chamber at 34 °C for 30 min and then at room temperature (21 °C) until used for recordings.

***In vitro* recordings.** Whole-cell recordings were done at 32 °C in artificial cerebrospinal fluid (in mM: NaCl, 119; KCl, 2.5; NaH<sub>2</sub>PO<sub>4</sub>, 1.3; NaHCO<sub>3</sub>, 26; D-glucose, 20; MgCl<sub>2</sub>, 1.3; CaCl<sub>2</sub>, 2.5; and mOsm, 305, bubbled with 95% O<sub>2</sub> and 5% CO<sub>2</sub>). Excitatory and inhibitory synaptic currents were recorded using a caesium-based internal solution (in mM: CsMeSO<sub>4</sub>, 115; NaCl, 4; HEPES, 10; Na<sub>3</sub>GTP, 0.3; MgATP, 4; EGTA, 0.3; QX-314-Cl, 2.5; BAPTA(5Cs), 10; adjusted to pH 7.4 with CsOH; mOsm 295; 3–5 MOhm pipette resistance). Voltage-clamp recordings were not considered if the series resistance exceeded 20 MOhm or varied by more than 10%. Typically, 2–4 neurons were recorded from simultaneously. Cell-attached recordings and biocytin fills were carried out with a potassium-based internal solution (in mM: K-gluconate, 150; MgCl<sub>2</sub>, 1.5; HEPES, 5; EGTA, 1.1; phosphocreatine, 10; adjusted to pH 7.4 with KOH; mOsm 295). Perforated-patch recordings were carried out using potassium-based internal and 10  $\mu\text{g ml}^{-1}$  Gramicidin D (Sigma G5002). Tight seals were held until sufficient access allowed injection of current and resolution of action potentials (typically 10–20 min). Ruptures of the perforated patch were apparent by a rapid drop in series resistance at which point the recordings were discontinued. Photostimulation of L6 *in vitro* consisted of either single 2-ms pulses or a 40-Hz train of 2-ms pulses, or of 1-s ramps of light of increasing intensity as previously described<sup>32</sup>. Data were recorded with Multiclamp 700B amplifiers (Axon instruments) filtered at 2 kHz and digitized with a Digidata1440A (Axon instruments) at 10 kHz. Recordings were analysed using custom-made routines in Igor Pro (WaveMetrics). Charges represent the time integral of the synaptic current recorded during the first second of photostimulation. The stage was moved using a custom made plugin for ImageJ(NIH) to interface with ESP300 (Newport) via SerialPort (SerialIO). Drugs used were NBQX (Tocris 1044) and CPP (Ascent Asc-159).

***In vivo* recordings in anaesthetized mice.** Recordings were performed similarly to those previously described<sup>22</sup>. Animals were anaesthetized with 5 mg kg<sup>-1</sup> of chlorporthixene (intraperitoneal) and then (5–10 min later) with 1.2 g kg<sup>-1</sup> urethane (intraperitoneal). During surgery, animals were given 0.5–1.0% isoflurane. Animals were placed onto a custom platform and their temperature was maintained at 37 °C using a feedback-controlled heating pad (FHC). Whiskers and eyelashes that were contralateral to the recording side were trimmed and eyes covered with a

thin, uniform layer of silicone oil to prevent drying. Protein expression was verified by transcranial epifluorescence of the exposed and PBS-moistened skull using a Leica MZ10F microscope. Only animals showing expression over the entire extent of V1 were used for subsequent experiments. The entire dried skull was covered with black dental cement (Ortho-Jet powder (Lang Dental) mixed with black iron oxide) but for the previously outlined boundaries of V1 (~1.5–3.5 mm lateral to midline and –0.5 to 2.5 mm anterior to lambda suture). A head-plate with a hole of ~2 mm in diameter was mounted over V1 and a small region of skull (~300 × 750  $\mu\text{m}$ ) was thinned using a dental drill. Next, we used sharpened fine forceps (Dumont number 55) to make a craniotomy just sufficiently large for inserting the probe. A drop of PBS placed in the well at the centre of the head-plate kept the exposed skull and craniotomy moist. A multichannel silicon probe mounted on a micromanipulator (Luigs–Neumann) was slowly advanced into the brain to a depth of 800–1000  $\mu\text{m}$  for linear probes and 200–700  $\mu\text{m}$  for tetrode probes (see later), and recordings were started 20 min or more after inserting the probe.

For dLGN recordings we made a circular craniotomy (~1.5 mm in diameter) 2.6 mm posterior and 2 mm lateral to the bregma suture. Robust visual responses and bursting activity that was characteristic of dLGN relay neurons were encountered at a depth between 2,400 and 3,100  $\mu\text{m}^{44}$  (Supplementary Fig. 7). For dual recording experiments (Fig. 3g, h and Fig. 5), we used a larger head-plate so that a craniotomy could be made both over the dLGN and V1.

Recordings were made with NeuroNexus 16-channel linear (a1x16-3mm-50-177) or tetrode (a2x2-tet-3mm-150-121) silicon probes. For recordings across cortical depth and in dLGN we used the linear configuration. The tetrode configuration was used to isolate a subset of cells in Fig. 2. Signals were amplified ×1000, band-pass filtered between 0.3 Hz and 5 kHz using an AM Systems 3500 amplifier and acquired at 32 kHz using a NIDAQ board (PCIe-6239) controlled with custom-written software in Matlab (Mathworks). For dual recording experiments we used two separate data-acquisition setups (amplifier, NIDAQ board and computer). Raw data were stored on a computer hard drive for offline analysis.

At the end of the recording session, animals were killed by administering 4% isoflurane and the brain was quickly removed and fixed in 4% paraformaldehyde for histological analysis.

***In vivo* awake recordings.** 1–2 weeks before recording, mice were implanted with a head-plate for head fixation. Mice were anaesthetized with 2.5% isoflurane, the scalp was removed and a head-plate was fixed over V1 with black dental cement. The skull directly overlying V1 was covered with Kwik-Cast (WPI). Animals were injected subcutaneously with 0.1 mg kg<sup>-1</sup> buprenorphine and allowed to recover in their home cage for at least 1 week before recording.

Several days before recording, mice were familiarized to head fixation within the recording setup. They were briefly anaesthetized with isoflurane and the head-plate was clamped to a metal post, but otherwise the mice were unrestrained and allowed to run in this position on a plastic circular treadmill or track (Fast-Trac from Bio-Serv; see Supplementary Fig. 6). The same circular track was present in the cages of the mice, where they were familiarized with its use. Mice grew accustomed to head fixation over the course of 1–3 15-min sessions and ran naturally on the track, occasionally stopping to rest or groom.

On the day of recording, mice were anaesthetized with 1.5–2% isoflurane, a small craniotomy was made over V1, a drop of PBS was placed in the well of a head-plate that was clamped to a metal post, and the multichannel probe inserted into the craniotomy. After removal of isoflurane the mice regained consciousness and typically began running. Recordings did not start before 30 min after the end of anaesthesia. Awake recording sessions lasted between 1 and 2 h. Mice typically spent ~60–80% of their time running, and the rest of the time was spent resting or grooming. Data were not separated according to behaviour. Every 30–60 min mice were given a few drops of a 5% glucose solution through a disposable pipette. For two mice we performed 2–3 recording sessions, which were made at least a day apart. Between sessions the craniotomy was covered with Kwik-Cast. A new craniotomy was made for each session.

**Visual stimulation.** Visual stimuli were generated in Matlab using the Psychophysics Toolbox<sup>45</sup> and were displayed on a gamma-corrected LCD monitor (Dell 52 × 32.5 cm, 60-Hz refresh rate, mean luminance 50 cd m<sup>-2</sup>) positioned 25 cm from the contralateral eye. The monitor was positioned for each experiment so that the multi-unit receptive field was located approximately in the centre of the screen (the multi-unit receptive field was determined by moving a localized drifting grating patch (~10°) around the screen). During the recording session full-field sinusoidal drifting gratings were used. All stimuli had a temporal frequency of 2 Hz and a spatial frequency of 0.04 cycles per degree. Gratings were randomly presented at 8–12 equally spaced directions, except for the experiments in Fig. 5 in which we used only two orthogonal grating directions (0° and 90°). The contrast of the stimulus was 100%, except for Fig. 5 in which we used six contrast levels (2, 4.4,



9.6, 21, 46 and 100%). A grey screen trial was interleaved with the drifting gratings. The duration of the visual stimulus was 1.5 s and the inter-trial interval was 3–6 s. **In vivo photostimulation.** To photo-stimulate ChR2 we used a blue (470-nm) fibre-coupled LED (1 mm diameter, Doric Lenses) placed ~5–10 mm away from the skull. Light from the LED spanned the entire area of V1. An opaque shield of black aluminium foil (Thor Labs) prevented LED light from reaching the contralateral eye. The LED was driven by the analogue output from the NIDAQ board. The blue LED was presented at five intensities (approximately 3, 5, 7, 10.5 and 20 mW measured at the tip of the fibre), but for a minority of experiments we presented only the highest LED intensity. Trials were alternated between visual stimulus only and visual stimulus plus LED. The strongest LED intensity also generated oscillations at gamma frequency, consistent with previous observations<sup>32</sup> (Supplementary Fig. 2). The preferred-orientation of photostimulated L6 cells remained unchanged but their tuning curves became broader (Supplementary Fig. 2).

To photostimulate archaerhodopsin and NpHR3.0 we used an amber (590-nm) fibre-coupled LED (1 mm in diameter, Doric Lenses) placed ~0.5 mm from the skull. Because photosuppression of L6 produced a transient decrease in spontaneous multi-unit activity in L2–5 at the onset of LED illumination (see Supplementary Fig. 6) we turned on the amber LED 1.4 s before the visual stimulus began. Experiments were performed at the highest LED intensity (~20 mW measured at the tip of the fibre). As long as the suppression was not complete, the preferred orientation of photosuppressed L6 cells remained unchanged (Supplementary Fig. 6). **In vivo data analysis.** All *in vivo* data analysis was performed with custom software written in Matlab.

Multi-unit spiking activity was defined as all events (spikes) exceeding a threshold of 4 s.d. above the noise of the high-pass filtered (500-Hz) signal. Spikes were assigned a depth corresponding to the depth of the channel they were recorded from. Spikes that were recorded simultaneously on multiple channels were considered as a single event and attributed to the channel in which they showed the largest amplitude. We determined the depth of each channel by considering the depth and the angle of the probe relative to the vertical axis of cortex. We assigned spikes to different layers according to the following depths (in  $\mu\text{m}$ ): L2/3, 100–350; L4, 350–450; L5, 450–650; L6, >650. PSTHs were composed of 50-ms bins. PSTHs of individual experiments were normalized to the first 500 ms of the visual stimulus (for ChR2 experiments) or to the entire visual stimulus (for archaerhodopsin and NpHR3.0 experiments) to generate average PSTHs. PSTHs for kinetic analysis (Fig. 3h) were composed of 3-ms bins and report the normalized difference in firing rates between control (average firing over a 50-ms window prior to LED onset) and during LED illumination (average firing rate over a 100-ms window, 50 ms after LED onset). For each experiment the onset of suppression was determined as the time point at which the normalized response fell below 2 s.d. of the baseline.

The contrast response functions in dLGN and V1 report the normalized, baseline-subtracted firing rates and were fitted with a hyperbolic ratio function:

$$r = r_{\max} \frac{c^n}{c^n + c_{50}^n}$$

where  $r$  is the response,  $c$  is the contrast of the visual stimulus,  $r_{\max}$  is a fitted constant representing the response saturation level,  $n$  is fitting exponent that affects the shape of the curve and  $c_{50}$  is the semi-saturation constant. The transfer function between the dLGN and V1 was fitted with a hyperbolic ratio function:

$$r_{V1} = r_{V1, \max} \frac{r_{\text{dLGN}}^n}{r_{\text{dLGN}}^n + r_{\text{dLGN}, 50}^n}$$

where  $r_{V1}$  is the V1 response,  $r_{V1, \max}$  is a constant representing the V1 saturation level,  $r_{\text{dLGN}}$  is the dLGN response,  $n$  is a fitting exponent and  $r_{\text{dLGN}, 50}$  is the semi-saturation constant. The 'corticothalamic component' (CT) was defined as the fraction of the total V1 suppression accounted for by this predicted response. The 'intracortical component' was then defined as  $1 - \text{CT}$  component. We performed this analysis for five LED levels and averaged across experiments to produce the plot in Fig. 5f.

We isolated single units using spike-sorting software provided by D. N. Hill, S. B. Mehta, and D. Kleinfeld<sup>46</sup>. For both the linear and tetrode probes we analysed waveforms extracted from groups of four adjacent electrode sites. We high-pass filtered the raw signal at 500 Hz and then detected spiking events exceeding 4–5 s.d. of the noise. Spike waveforms were clustered using a  $k$ -means algorithm. After initial automated clustering, we used a graphical user interface to manually merge

and split clusters. Unit isolation quality was assessed by considering refractory period violations and Fisher linear discriminant analysis. In agreement with previous studies we could classify waveforms as regular-spiking or fast-spiking putative inhibitory neurons. In our data set there was a clear bimodal distribution of trough-to-peak times (a threshold of 0.4 ms was used to divide fast-spiking from regular-spiking units). All units were assigned a depth according to the channel that they were detected on, and units were assigned to layers based on the depth divisions given above for the multi-unit activity.

For each unit we computed the visual response as the mean spike-rate occurring over the time window in which both the LED and visual stimulus were present. Thus, for the L6 photostimulation experiments this typically corresponded to a 500-ms window placed in the centre of the visual response, and for the L6 photosuppression experiments this window encompassed the entire 1.5-s visual stimulus. For all analysis except the orientation tuning analysis in Fig. 2, we averaged responses over all stimulus conditions. Following recent studies<sup>47,48</sup> of orientation tuning we computed an OSI as:

$$\text{OSI} = \frac{\sqrt{(\sum r_k \sin(2\theta_k))^2 + (\sum r_k \cos(2\theta_k))^2}}{\sum r_k}$$

where  $r_k$  is the response to the  $k$ th direction given by  $\theta_k$ . We determined an OSI for each unit with and without photostimulation or suppression of L6. We established the preferred orientation and tuning width by first fitting the average responses of each unit with a sum of two Gaussians:

$$r = r_0 + r_p e^{-(\theta - \theta_p)^2 / (2\sigma^2)} + r_{p+180} e^{-(\theta - \theta_p - 180)^2 / (2\sigma^2)}$$

where  $r_0$  is a constant offset,  $r_p$  is the response at the preferred orientation,  $r_{p+180}$  is a response  $180^\circ$  away from the preferred direction,  $\theta$  is the stimulus direction,  $\theta_p$  is the preferred orientation and  $\sigma$  is the tuning width. The two Gaussians were forced to peak  $180^\circ$  apart and to have the same width but could have different amplitudes. Control and photostimulation or photosuppression conditions were fit separately. To generate the average population tuning curve we first circularly shifted the stimulus direction of each unit so that the maximal response occurred at  $0^\circ$ . We then normalized the responses to this peak response and averaged all normalized tuning curves together. We fit the control population average tuning curve with a sum of two Gaussians. The curve for the photostimulation or photosuppression population average was produced by scaling the control curve by the slope (gain factor) of the linear fit shown in Fig. 2e, j.

All error bars are presented as mean  $\pm$  s.e.m. unless otherwise noted. We used paired  $t$ -tests to assess statistical significance unless otherwise noted.

**Histology.** Triple transgenic mice (Ntsr1-Cre, floxed-tdTomato and Gad67-GFP) were anaesthetized with ketamine and xylazine (100 mg kg<sup>-1</sup> and 10 mg kg<sup>-1</sup>, respectively) and perfused with cold sucrose (see above) and then perfluoroalkoxy (4% in PBS). After 24 h incubation in perfluoroalkoxy, slices were cut into 50- $\mu\text{m}$  sections and immunostained as described previously<sup>49</sup>. Antibodies that were used were mouse anti-NeuN (1:400; Millipore MAB377), chicken anti-GFP (1:1000; Aves Labs GFP-1020), goat anti-chicken AF488 (1:1,000; Invitrogen A11039) and goat anti-mouse AF633 (1:1,000; Invitrogen A21050). Slices were mounted in Vectashield with Dapi (Vector Labs, H1500). Images were single confocal sections taken on an Olympus FV1000. Layer borders were identified by changes in cell density. Cell counts were carried out using standard stereological techniques. Biocytin fills and neural reconstructions were done as previously described<sup>50</sup>.

44. Grubb, M. S. & Thompson, I. D. Quantitative characterization of visual response properties in the mouse dorsal lateral geniculate nucleus. *J. Neurophysiol.* **90**, 3594–3607 (2003).
45. Brainard, D. H. The psychophysics toolbox. *Spat. Vis.* **10**, 433–436 (1997).
46. Fee, M. S., Mitra, P. P. & Kleinfeld, D. Automatic sorting of multiple unit neuronal signals in the presence of anisotropic and non-Gaussian variability. *J. Neurosci. Methods* **69**, 175–188 (1996).
47. Kerlin, A. M., Andermann, M. L., Berezovskii, V. K. & Reid, R. C. Broadly tuned response properties of diverse inhibitory neuron subtypes in mouse visual cortex. *Neuron* **67**, 858–871 (2010).
48. Ringach, D. L., Shapley, R. M. & Hawken, M. J. Orientation selectivity in macaque V1: diversity and laminar dependence. *J. Neurosci.* **22**, 5639–5651 (2002).
49. Bortone, D. & Polleux, F. KCC2 expression promotes the termination of cortical interneuron migration in a voltage-sensitive calcium-dependent manner. *Neuron* **62**, 53–71 (2009).
50. Bagnall, M. W., Hull, C., Bushong, E. A., Ellisman, M. H. & Scanziani, M. Multiple clusters of release sites formed by individual thalamic afferents onto cortical interneurons ensure reliable transmission. *Neuron* **71**, 180–194 (2011).

# Strict evolutionary conservation followed rapid gene loss on human and rhesus Y chromosomes

Jennifer F. Hughes<sup>1</sup>, Helen Skaletsky<sup>1</sup>, Laura G. Brown<sup>1</sup>, Tatyana Pyntikova<sup>1</sup>, Tina Graves<sup>2</sup>, Robert S. Fulton<sup>2</sup>, Shannon Dugan<sup>3</sup>, Yan Ding<sup>3</sup>, Christian J. Buhay<sup>3</sup>, Colin Kremitzki<sup>2</sup>, Qiaoyan Wang<sup>3</sup>, Hua Shen<sup>3</sup>, Michael Holder<sup>3</sup>, Donna Villasana<sup>3</sup>, Lynne V. Nazareth<sup>3</sup>, Andrew Cree<sup>3</sup>, Laura Courtney<sup>2</sup>, Joelle Veizer<sup>2</sup>, Holland Kotkiewicz<sup>2</sup>, Ting-Jan Cho<sup>1</sup>, Natalia Koutseva<sup>1</sup>, Steve Rozen<sup>1</sup>, Donna M. Muzny<sup>3</sup>, Wesley C. Warren<sup>2</sup>, Richard A. Gibbs<sup>3</sup>, Richard K. Wilson<sup>2</sup> & David C. Page<sup>1</sup>

The human X and Y chromosomes evolved from an ordinary pair of autosomes during the past 200–300 million years<sup>1–3</sup>. The human MSY (male-specific region of Y chromosome) retains only three percent of the ancestral autosomes' genes owing to genetic decay<sup>4,5</sup>. This evolutionary decay was driven by a series of five 'stratification' events. Each event suppressed X–Y crossing over within a chromosome segment or 'stratum', incorporated that segment into the MSY and subjected its genes to the erosive forces that attend the absence of crossing over<sup>2,6</sup>. The last of these events occurred 30 million years ago, 5 million years before the human and Old World monkey lineages diverged. Although speculation abounds regarding ongoing decay and looming extinction of the human Y chromosome<sup>7–10</sup>, remarkably little is known about how many MSY genes were lost in the human lineage in the 25 million years that have followed its separation from the Old World monkey lineage. To investigate this question, we sequenced the MSY of the rhesus macaque, an Old World monkey, and compared it to the human MSY. We discovered that during the last 25 million years MSY gene loss in the human lineage was limited to the youngest stratum (stratum 5), which comprises three percent of the human MSY. In the older strata, which collectively comprise the bulk of the human MSY, gene loss evidently ceased more than 25 million years ago. Likewise, the rhesus MSY has not lost any older genes (from strata 1–4) during the past 25 million years, despite its major structural differences to the human MSY. The rhesus MSY is simpler, with few amplified gene families or palindromes that might enable intrachromosomal recombination and repair. We present an empirical reconstruction of human MSY evolution in which each stratum transitioned from rapid, exponential loss of ancestral genes to strict conservation through purifying selection.

The human Y chromosome no longer engages in crossing over with its once-identical partner, the X chromosome, except in its pseudoautosomal regions. During evolution, X–Y crossing over was suppressed in five different chromosomal regions at five different times, each probably resulting from an inversion in the Y chromosome<sup>2,3</sup>. Each of these regions of the Y chromosome then began its own individual course of degeneration, experiencing deletions and gene loss. Comparison of the present-day X and Y chromosomes enables identification of these five evolutionary 'strata' in the MSY (and X chromosome); their distinctive degrees of X–Y differentiation indicate their evolutionary ages<sup>2,3</sup>. The oldest stratum (stratum 1) dates back over 240 million years (Myr)<sup>2</sup> and is the most highly differentiated, and the youngest stratum (stratum 5) originated only 30 Myr ago and displays the highest X–Y nucleotide sequence similarity within the MSY<sup>3</sup>. The five strata and their respective decay processes, over tens to hundreds of millions of years of mammalian evolution, offer replicate experiments of nature from which to reconstruct the trajectories and kinetics of gene loss in the MSY.

Only the human and chimpanzee MSYs had been sequenced before the present study, and they are separated by just 6 Myr of evolution. We decided to examine the MSY of a much more distant relative, the rhesus macaque (*Macaca mulatta*), to enable us to reconstruct gene loss and conservation in the MSY during the past 25 Myr. We sequenced the rhesus MSY using bacterial artificial chromosome (BAC) clones and the SHIMS (single-haplotype iterative mapping and sequencing) strategy that has previously been used in the human and chimpanzee MSYs<sup>4,11–13</sup> as well as in the chicken Z chromosome<sup>5</sup>. The resulting sequence is comprised of 11.0 megabases (Mb), is complete aside from three small gaps and has an error rate of about one nucleotide per Mb. We ordered and oriented the finished sequence contigs by fluorescence *in situ* hybridization and radiation hybrid mapping (Supplementary Figs 1–6, Supplementary Table 1, Supplementary Files 1, 2 and Supplementary Note 1).

We then compared the structure of the rhesus Y chromosome to that of the human and chimpanzee (Fig. 1). The rhesus Y chromosome has virtually no heterochromatin apart from the centromere, and the euchromatic segment of the MSY is notably smaller compared to that of the human and chimpanzee (Fig. 1). The single pseudoautosomal region (PAR) in rhesus corresponds to the short-arm PAR in human and to the single PAR in chimpanzee. The precise boundary between PAR and MSY is identical in the three species (Supplementary Fig. 7), confirming that stratification in all three lineages concluded before the divergence of apes from Old World monkeys.

The euchromatic portions of the rhesus, human and chimpanzee MSYs are comprised primarily of two distinct sequence classes: X-degenerate and ampliconic. The X-degenerate regions, relics of shared X–Y ancestry, are dotted with single-copy homologues of X-linked genes. The X-degenerate regions are relatively well conserved among the rhesus, human and chimpanzee MSYs, with large blocks of homology that are readily identifiable (Supplementary Figs 8 and 9). Indeed, the X-degenerate regions are the only portions of the rhesus and human MSYs whose sequences can be aligned over distances of greater than 50 kb. We found rhesus–human nucleotide divergence there to be 9.4% (Supplementary File 3). This is markedly higher than the 6.5% divergence that is observed when the rhesus and human female genomes are compared<sup>14</sup>. The difference probably reflects the restriction of the MSY to the male germ line, where base-pair substitutions are more frequent than in the female germ line<sup>15</sup>. From these data, we calculate the male-to-female mutation rate ratio ( $\alpha_m$ ) to be 2.78 (95% confidence interval 2.74–2.81), in agreement with previous but less precise estimates<sup>14,16</sup>. The X-degenerate sequences in rhesus, human and chimpanzee are not entirely colinear, as large-scale rearrangements have occurred in each lineage (Supplementary Figs 8–10).

For all three species, the MSY's ampliconic regions are composed of long, nearly identical repeat units that are arrayed in either direct or

<sup>1</sup>Howard Hughes Medical Institute, Whitehead Institute and Department of Biology, Massachusetts Institute of Technology, 9 Cambridge Center, Cambridge, Massachusetts 02142, USA. <sup>2</sup>The Genome Institute, Washington University School of Medicine, 4444 Forest Park Boulevard, St. Louis, Missouri 63108, USA. <sup>3</sup>Human Genome Sequencing Center, Baylor College of Medicine, One Baylor Plaza, Houston, Texas 77030, USA.

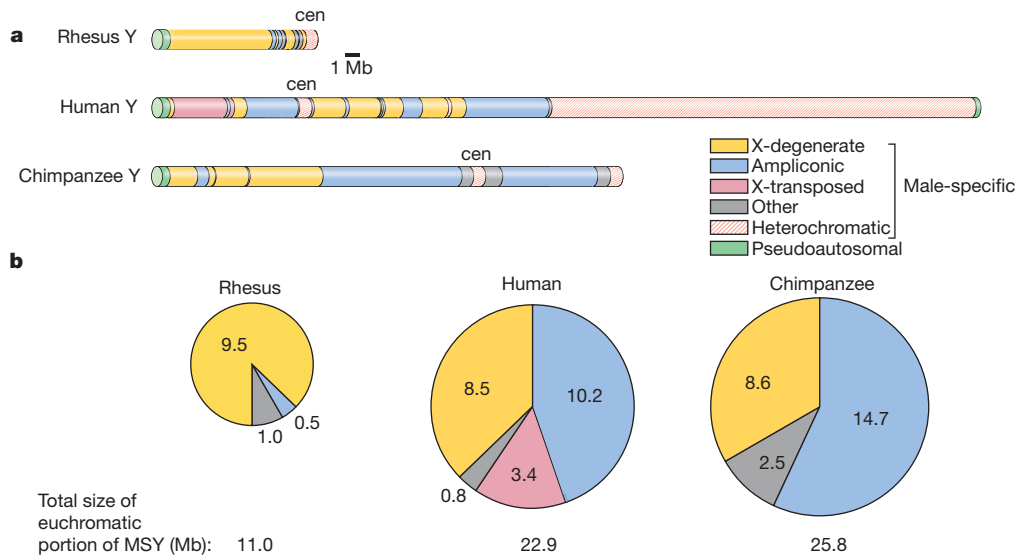


**Figure 1 | Comparison of rhesus, human and chimpanzee Y chromosomes.** **a**, Schematic representations of rhesus, human and chimpanzee Y chromosomes, to scale. Other, single-copy, male-specific sequences that are

inverted orientation and undergo frequent gene conversion—a process that is thought to slow or prevent the decay of genes that reside there<sup>4,17</sup>. Ampliconic genes display testis-specific expression patterns, consistent with their having critical roles in spermatogenesis<sup>4,11,18</sup>. Only 0.5 Mb of the rhesus MSY euchromatin is ampliconic, compared to 10.2 Mb and 14.7 Mb in human and chimpanzee, respectively (Fig. 1, and Supplementary Figs 11 and 12). In human and chimpanzee, the ampliconic regions of the MSY feature large palindromes, each composed of two inverted repeats (arms) separated by a short spacer. The human and chimpanzee MSYs have 8 and 19 palindromes that span 5.5 Mb and 7.5 Mb, respectively<sup>4,13</sup>. By contrast, the rhesus MSY has only three palindromes and these collectively span 437 kb (Supplementary Table 2 and Supplementary Fig. 13). Two of the rhesus MSY palindromes are orthologues of human MSY palindromes, demonstrating that these structures have been maintained for at least 25 Myr (Supplementary Fig. 13).

We identified protein-coding genes in the rhesus MSY using three complementary approaches. First, we electronically searched the rhesus MSY for homologues of all known human and chimpanzee MSY genes and pseudogenes. Second, we searched for homologues of all known human X-linked genes, to identify any X–Y shared genes that had been lost in both the human and chimpanzee MSY but retained in the rhesus MSY. Third, we searched for additional rhesus-specific MSY genes using electronic prediction tools and high-throughput sequencing of rhesus testis complementary DNA (245 Mb in total). We validated each putative gene by verifying transcriptional activity (Supplementary Fig. 14) and, where applicable, by comparing its predicted open reading frame to that of its human orthologue (Supplementary Table 3).

We then compared the catalogues of MSY genes in rhesus, human<sup>4</sup> and chimpanzee<sup>13</sup> to infer gene loss and conservation during the past 25 Myr. To root this analysis in a deep evolutionary context, we first reconstructed which of the modern rhesus MSY genes were present on the common autosomal ancestor of X and Y (Fig. 2, Supplementary Table 4 and Supplementary Note 2). Most ‘ancestral’ MSY genes would be expected to have a homologue both on the human X chromosome and on the chicken autosomes (chromosomes 1 and 4) that share common ancestry with mammalian X and Y chromosomes<sup>3,5</sup>. Indeed, 33 genes and pseudogenes in the rhesus, human or chimpanzee MSY have their most closely related human homologues on the X chromosome (Fig. 2), and 29 of these also have homologues within syntenic regions of chicken chromosome 1 or 4. Analyses of a more distant outgroup,

neither X-degenerate nor X-transposed. **b**, Sizes (in Mb) of euchromatic sequence classes in MSYs. cen, centromere.

*Xenopus tropicalis*, revealed that two of the four rhesus MSY genes lacking homologues on chicken chromosome 1 and 4 (*TSPY* and *AMELY*) are X–Y ancestral; they were lost in the chicken lineage after divergence from mammals (Supplementary Note 2). A few human MSY genes with X homologues are recent additions to the MSY rather than remnants of the ancestral autosome pair; *PCDH11Y* and *TGIF2LY* are located in the human-specific X-transposed region<sup>4</sup>, and the X-linked homologue of *VCY* is found only in simian primates<sup>19</sup>. We found a total of 30 ancestral MSY genes and pseudogenes in rhesus, human or chimpanzee (Fig. 2).

Within strata 1–4, which collectively comprise the bulk of the human MSY, the rhesus and human MSYs possess precisely the same 18 ancestral genes (Fig. 2). This notable and unanticipated identity leads us to conclude that, 25 Myr ago, in the last common ancestor of rhesus and human, MSY strata 1–4 also carried these 18 ancestral genes (Table 1 and Supplementary Table 5), and that no loss of ancestral genes occurred subsequently in either lineage (Supplementary Note 3). We note that, within strata 3 and 4, the rhesus and human MSYs carry a total of six ancestral pseudogenes that seem to have lost their function more than 25 Myr ago (Supplementary Fig. 15).

The evolutionary stability of ancestral genes in strata 1–4 could be explained by purifying selection, which, in the absence of sexual recombination, would have preserved critical ancestral genes for tens or even hundreds of millions of years. We demonstrated previously that purifying selection preserved MSY genes during the past 100,000 years of human population expansion and migration<sup>20</sup>. Comparing human and rhesus, we find that most ancestral genes display a ratio of nonsynonymous substitution rate to synonymous substitution rate that is significantly less than one (Supplementary Note 4, Supplementary Table 3 and Supplementary Fig. 16), demonstrating purifying selection during the past 25 Myr.

The pattern of gene loss and conservation in stratum 5, formed only 5 Myr before the rhesus and human lineages split, is remarkably different from the pattern in the four older strata. Within the past 30 Myr, four ancestral genes have been inactivated or deleted from stratum 5 of the MSY in both rhesus and human (Fig. 2 and Supplementary Note 5). A fifth ancestral gene, *MXRA5Y*, remains active in rhesus (Supplementary Fig. 11) but was inactivated by an intragenic deletion in the human lineage (Supplementary Fig. 17). Apart from *MXRA5Y*, all differences in MSY gene content between rhesus and human involve genes that were added to the human MSY subsequent to the ape–Old World monkey split (Fig. 2 and Supplementary Table 5).



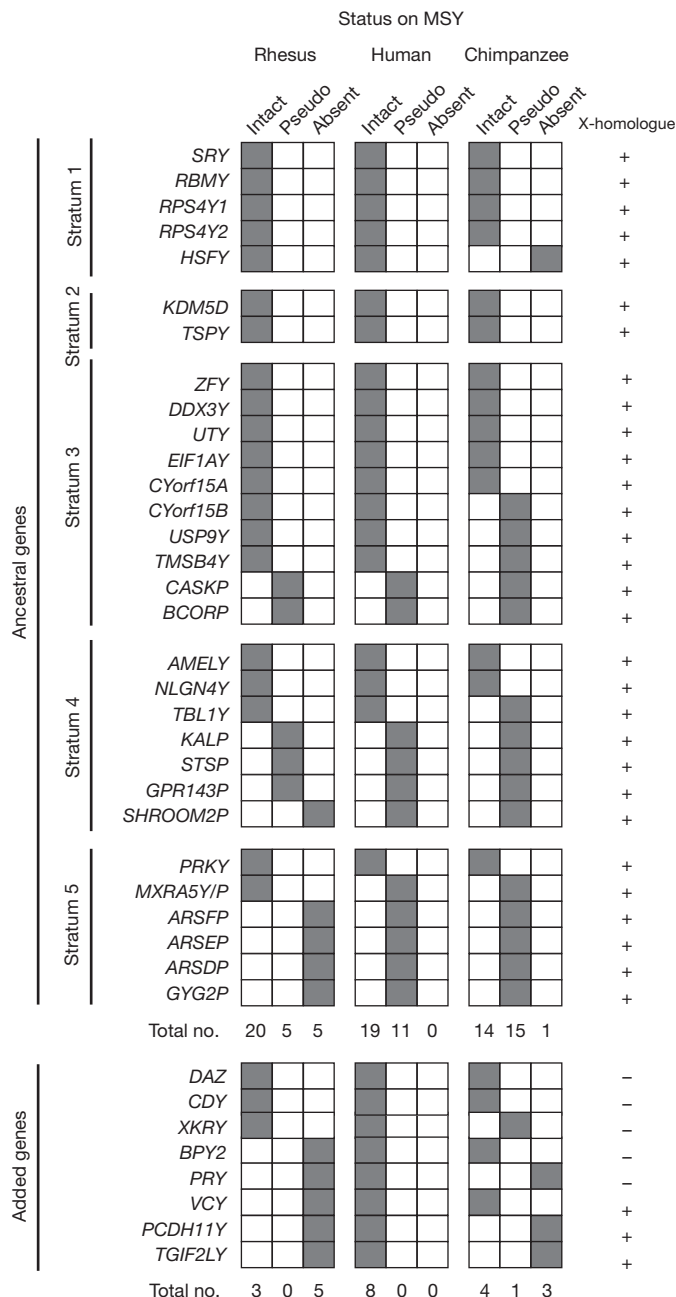


**Figure 2 | Inventories of genes, both ancestral and added, in rhesus, human and chimpanzee MSYs.** Ancestral genes grouped by stratum (1–5). In rhesus, human and chimpanzee, current status of each MSY gene is indicated by shading in one of three columns: present and intact, inactivated pseudogene, or absent or deleted. Total numbers of intact genes, pseudogenes (pseudo), and absent genes—both ancestral and added—are tallied for each species. For each MSY gene, whether the most closely related human homologue is located on the X chromosome is shown (right).

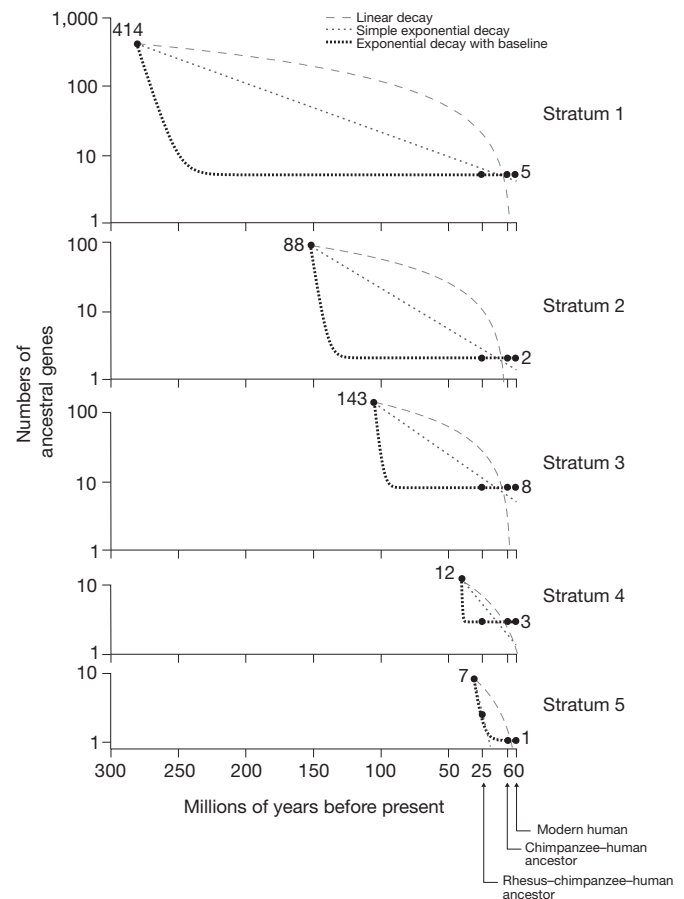


**Figure 3 | Kinetics of ancestral gene loss during evolution of five human MSY strata.** Gene numbers are plotted on a log scale on the y axis, and time (in Myr before present) is plotted on the x axis. Filled circles show inferred or observed gene numbers in (from left to right) X–Y ancestral chromosome (at time of stratum formation), rhesus–chimpanzee–human ancestral MSY (25 Myr ago), chimpanzee–human ancestral MSY (6 Myr ago), and modern human MSY. Dotted and dashed lines represent best-fit curves to data points using each of three decay models as indicated.

Returning to strata 1–4, we note that five ancestral genes have been inactivated or lost from the chimpanzee MSY during the past 6 Myr<sup>12,13</sup>, in sharp contrast to the strict conservation of ancestral gene content in rhesus and human (Fig. 2). We previously proposed that in the chimpanzee lineage promiscuous mating behaviour<sup>21</sup>, sperm competition and intense sexual selection that focused on the MSY drove rapid evolution and amplification of MSY sequences that are associated with spermatogenesis<sup>12,13</sup>. Furthermore, we speculated that in the chimpanzee lineage inactivated alleles of some ancestral genes became fixed in the population through ‘genetic hitchhiking’; casualties of positive but indiscriminate selection operating in the absence of sexual recombination in the MSY<sup>12,13,22</sup>. Among primate species, chimpanzees have a high testis-weight to body-weight ratio, a useful indicator of the degree of sperm competition<sup>23,24</sup>. Although the rhesus

**Table 1 | Stratification of X–Y ancestral gene loss in primate MSYs**

	Age of stratum (millions of years) (from refs 2, 3)	Number of ancestral genes on human X chromosome*	Number of ancestral genes on MSY			
			Last common ancestor†	Rhesus	Human	Chimpanzee
Stratum 1	240–320	414	5	5	5	4
Stratum 2	130–170	88	2	2	2	2
Stratum 3	80–130	143	8	8	8	5
Stratum 4	38–44	12	3	3	3	2
Stratum 5	29–32	7	2–7	2	1	1

\* Gene numbers from ref. 5, Supplementary Table 4 and Supplementary Note 2.

† Gene counts in MSY of a hypothetical rhesus–human–chimpanzee ancestor deduced from observed gene counts in extant species.

is similarly promiscuous and has an even higher testis-weight to body-weight ratio, the rhesus MSY shows little evidence of intense sexual selection. We suggest that in the rhesus lineage, such selection was focused on spermatogenesis factors that are encoded elsewhere in the genome. This would also account for the virtual absence in rhesus of the MSY sequence amplification that is prominent in human and even more pronounced in chimpanzee (Fig. 1).

Our knowledge of all five strata of the MSY, gained through our comprehensive comparisons of ancestral gene content in the rhesus, human and chimpanzee MSYs, enabled us to reconstruct the kinetics and trajectory of human MSY evolution. For each of the five MSY strata, we estimated ancestral gene numbers at three points in the human evolutionary lineage: in the last common ancestor of human and chimpanzee (6 Myr ago), in the last common ancestor of human and rhesus macaque (25 Myr ago) and at the time of the stratum's formation, when X–Y differentiation was initiated (from ~30 to >240 Myr ago; Table 1). For each stratum, we plotted these three estimated numbers against evolutionary time, together with the observed number of ancestral genes in modern human, and fit a curve (Fig. 3 and Supplementary Fig. 18). For each of the five strata, a simple two-parameter model, using an exponential decay equation that includes a baseline constant, provides an excellent fit to our data (Fig. 3 and Supplementary Table 6). According to this reconstruction, ancestral gene decay within each stratum proceeded rapidly at first—with an ancestral gene half-life of less than 5 Myr (Supplementary Table 6)—but then decelerated markedly, as the ancestral gene count reached a stable level far below its starting point. In our reconstruction, strata 1–4 had already reached a stable level before the human lineage diverged from rhesus; after divergence from rhesus, gene loss in the human lineage was limited to stratum 5, the youngest stratum, which stabilized before the human lineage diverged from chimpanzee.

Our empirical reconstruction of MSY evolution is at odds with a linear model<sup>7,9,10</sup> and with a simple random decay (exponential) model<sup>25</sup>, both of which project a continual decline of MSY gene content and cannot account for the stability of gene content that we observe over the past 25 Myr (Fig. 3). Our data are better explained by more complex models for MSY gene loss that incorporate a combination of evolutionary forces<sup>26</sup>. Sequencing additional Y chromosomes from animals that represent more divergent mammalian lineages will enable refinement of our reconstruction of MSY gene kinetics in the human lineage.

## METHODS SUMMARY

**BAC selection and sequencing.** The SHIMS (single-haplotype iterative mapping and sequencing) strategy<sup>11</sup> was used to assemble a path of sequenced clones selected from the CHORI-250 BAC library (<http://bacpac.chori.org>) and a custom BAC library (RMAEX) constructed by Amplicon Express (<http://www.genomex.com>).

**Fluorescence *in situ* hybridization analysis.** Assays were performed on rhesus fibroblast cell line PR00112 from Coriell Institute for Medical Research (<http://ccr.coriell.org>). Extended metaphase fluorescence *in situ* hybridization (FISH) and interphase FISH were performed as previously described<sup>27</sup>.

**Radiation hybrid mapping.** Nine sequence-tagged site (STS) markers (Supplementary Table 7) were tested on a 10,000-rad panel consisting of 185 hybrid clones<sup>28</sup>. A genetic map was constructed and analysed statistically using RHMAPPER 1.22 (ref. 29).

**Generation of complementary DNA for polymerase chain reaction with reverse transcription (RT–PCR) and 454 sequencing.** cDNA was generated from total RNA that was isolated from male rhesus tissues using the RNeasy kit (Qiagen). For 454 sequencing, cDNA was normalized using the Trimmer kit (Evrogen).

**Alignments and dot plots.** Rhesus and human Y sequences were aligned using Stretcher (<http://bioweb2.pasteur.fr/docs/EMBOSS/stretcher.html>) with a gap open penalty of 20 and a gap extend penalty of 1. Dot-plot analyses were performed using custom Perl codes ([http://jura.wi.mit.edu/page/papers/Hughes\\_et\\_al\\_2005/tables/dot\\_plot.pl](http://jura.wi.mit.edu/page/papers/Hughes_et_al_2005/tables/dot_plot.pl)).

**Calculation of  $\alpha_m$ .** The male-to-female mutation rate ratio was calculated from the human–rhesus Y divergence rate and the human–rhesus autosomal divergence rate using a previously described method<sup>15,30</sup>.

**Modelling ancestral MSY gene loss.** We fit a one-phase exponential decay model with a baseline constant (shown below) to our data (gene numbers shown in

Table 1) using nonlinear regression analysis in GraphPad Prism 5.0. Parameters for each stratum are given in Supplementary Table 6.

One-phase exponential decay model:

$$N(t) = (N_0 - b)e^{-Kt} + b$$

Where  $N(t)$  is the number of genes at time  $t$ ,  $N_0$  is the number of genes within given stratum in ancestral autosomal or pseudoautosomal portion of genome,  $K$  is the decay constant and  $b$  is the baseline (approximated by the number of active ancestral genes within that stratum on human Y chromosome).

**Full Methods** and any associated references are available in the online version of the paper at [www.nature.com/nature](http://www.nature.com/nature).

**Received 17 October; accepted 10 January 2012.**

**Published online 22 February 2012.**

- Charlesworth, B. The evolution of sex chromosomes. *Science* **251**, 1030–1033 (1991).
- Lahn, B. T. & Page, D. C. Four evolutionary strata on the human X chromosome. *Science* **286**, 964–967 (1999).
- Ross, M. T. *et al.* The DNA sequence of the human X chromosome. *Nature* **434**, 325–337 (2005).
- Skaletsky, H. *et al.* The male-specific region of the human Y chromosome is a mosaic of discrete sequence classes. *Nature* **423**, 825–837 (2003).
- Bellott, D. W. *et al.* Convergent evolution of chicken Z and human X chromosomes by expansion and gene acquisition. *Nature* **466**, 612–616 (2010).
- Charlesworth, B. & Charlesworth, D. The degeneration of Y chromosomes. *Phil. Trans. R. Soc. Lond. B* **355**, 1563–1572 (2000).
- Aitken, R. J. & Marshall Graves, J. A. The future of sex. *Nature* **415**, 963 (2002).
- Sykes, B. *Adam's Curse* (Norton, W. W. & Company, 2004).
- Graves, J. A., Koina, E. & Sankovic, N. How the gene content of human sex chromosomes evolved. *Curr. Opin. Genet. Dev.* **16**, 219–224 (2006).
- Marshall Graves, J. A. Weird animal genomes and the evolution of vertebrate sex and sex chromosomes. *Annu. Rev. Genet.* **42**, 565–586 (2008).
- Kuroda-Kawaguchi, T. *et al.* The AZFc region of the Y chromosome features massive palindromes and uniform recurrent deletions in infertile men. *Nature Genet.* **29**, 279–286 (2001).
- Hughes, J. F. *et al.* Conservation of Y-linked genes during human evolution revealed by comparative sequencing in chimpanzee. *Nature* **437**, 100–103 (2005).
- Hughes, J. F. *et al.* Chimpanzee and human Y chromosomes are remarkably divergent in structure and gene content. *Nature* **463**, 536–539 (2010).
- Gibbs, R. A. *et al.* Evolutionary and biomedical insights from the rhesus macaque genome. *Science* **316**, 222–234 (2007).
- Miyata, T., Hayashida, H., Kuma, K., Mitsuyasu, K. & Yasunaga, T. Male-driven molecular evolution: a model and nucleotide sequence analysis. *Cold Spring Harb. Symp. Quant. Biol.* **52**, 863–867 (1987).
- Bohossian, H. B., Skaletsky, H. & Page, D. C. Unexpectedly similar rates of nucleotide substitution found in male and female hominids. *Nature* **406**, 622–625 (2000).
- Rozen, S. *et al.* Abundant gene conversion between arms of palindromes in human and ape Y chromosomes. *Nature* **423**, 873–876 (2003).
- Lahn, B. T. & Page, D. C. Functional coherence of the human Y chromosome. *Science* **278**, 675–680 (1997).
- Lahn, B. T. & Page, D. A human sex-chromosomal gene family expressed in male germ cells and encoding variably charged proteins. *Hum. Mol. Genet.* **9**, 311–319 (2000).
- Rozen, S., Marszalek, J. D., Alagappan, R. K., Skaletsky, H. & Page, D. C. Remarkably little variation in proteins encoded by the Y chromosome's single-copy genes, implying effective purifying selection. *Am. J. Hum. Genet.* **85**, 923–928 (2009).
- Dixon, A. F. *Primate Sexuality: Comparative Studies of the Prosimians, Monkeys, Apes and Human Beings* (Univ. Chicago Press, 1998).
- Rice, W. R. Genetic hitchhiking and the evolution of reduced genetic activity of the Y sex chromosome. *Genetics* **116**, 161–167 (1987).
- Schultz, A. H. The relative weight of the testes in primates. *Anat. Rec.* **72**, 387–394 (1938).
- Harcourt, A. H., Harvey, P. H., Larson, S. G. & Short, R. V. Testis weight, body weight and breeding system in primates. *Nature* **293**, 55–57 (1981).
- Graves, J. A. Sex chromosome specialization and degeneration in mammals. *Cell* **124**, 901–914 (2006).
- Bachtrog, D. The temporal dynamics of processes underlying Y chromosome degeneration. *Genetics* **179**, 1513–1525 (2008).
- Saxena, R. *et al.* The DAZ gene cluster on the human Y chromosome arose from an autosomal gene that was transposed, repeatedly amplified and pruned. *Nature Genet.* **14**, 292–299 (1996).
- Karere, G. M., Froenicke, L., Millon, L., Womack, J. E. & Lyons, L. A high-resolution radiation hybrid map of rhesus macaque chromosome 5 identifies rearrangements in the genome assembly. *Genomics* **92**, 210–218 (2008).
- Slonim, D., Kruglyak, L., Stein, L. & Lander, E. Building human genome maps with radiation hybrids. *J. Comput. Biol.* **4**, 487–504 (1997).
- Shimmin, L. C., Chang, B. H. & Li, W. H. Male-driven evolution of DNA sequences. *Nature* **362**, 745–747 (1993).

**Supplementary Information** is linked to the online version of the paper at [www.nature.com/nature](http://www.nature.com/nature).

**Acknowledgements** We thank V. Frazzoni, G. Rogers and S. Zaghlul for technical assistance; L. Lyons, W. Murphy and J. Womack for radiation hybrid panels; W. Johnson, E. Curran, S. O'Neil and A. Kaur for tissue samples; R. Harris for analyses of rhesus–human genome alignments; T. DiCesare for assistance with figures; and D. Bellott, M. Carmell, R. Desgraz, Y. Hu, B. Lesch, J. Mueller, K. Romer and S. Soh for comments on the manuscript. This work was supported by the National Institutes of Health, the Howard Hughes Medical Institute and the Charles A. King Trust.

**Author Contributions** J.F.H., H.Sk., W.C.W., S.R., R.A.G., R.K.W. and D.C.P. planned the project. J.F.H., H.Sk., L.G.B., T.J.C. and N.K. performed BAC mapping, radiation hybrid mapping and real-time polymerase chain reaction analyses. T.G., R.S.F., S.D., Y.D., C.J.B.,

C.K., Q.W., H.Sh., M.H., D.V., L.V.N., A.C., L.C., J.V., H.K. and D.M.M. were responsible for BAC sequencing. J.F.H. and H.Sk. performed comparative sequence analyses. T.P. performed FISH analyses. J.F.H. and D.C.P. wrote the paper.

**Author Information** cDNA sequences of rhesus Y genes have been deposited in GenBank (<http://www.ncbi.nlm.nih.gov>) under accession numbers FJ527009–FJ527028 and FJ648737–FJ648739. 454 testis cDNA sequences have been deposited in GenBank under accession number SRA039857. Reprints and permissions information is available at [www.nature.com/reprints](http://www.nature.com/reprints). The authors declare no competing financial interests. Readers are welcome to comment on the online version of this article at [www.nature.com/nature](http://www.nature.com/nature). Correspondence and requests for materials should be addressed to J.F.H. ([jhughes@wi.mit.edu](mailto:jhughes@wi.mit.edu)).



## METHODS

**BAC selection and sequencing.** The SHIMS (single-haplotype iterative mapping and sequencing) strategy<sup>11</sup> was used to assemble a path of sequenced clones selected from the CHORI-250 BAC library (<http://bacpac.chori.org>) and a custom BAC library (RMAEX) constructed by Amplicon Express (<http://www.genomex.com>). The rate of error in the finished sequence was estimated by counting mismatches in overlapping clones.

**FISH analysis.** All assays were performed on rhesus fibroblast cell line PR00112 obtained from the Coriell Institute for Medical Research (<http://ccr.coriell.org>). Extended metaphase FISH and interphase FISH were performed as previously described<sup>27</sup>.

**Radiation hybrid mapping.** Nine STS markers (Supplementary Table 7) were tested on a 10,000-rad, male whole-genome panel consisting of 185 hybrid clones<sup>28</sup>. The average retention frequency of the markers tested was 16%, ranging from 10–27%. A genetic map was constructed and analysed statistically using RHMAPPER 1.22 (ref. 29).

**RT-PCR.** Total RNA was isolated from male rhesus tissues (brain, prostate, liver, lung and spleen testis; Alpha Genesis) using the RNeasy kit (Qiagen) and cDNA was generated. RT-PCR primer sequences and product sizes are listed in Supplementary Table 8.

**454 sequencing of testis cDNA.** Rhesus testis cDNA was generated from total RNA isolated using the RNeasy kit (Qiagen). The cDNA was normalized using the Trimmer kit (Evrogen) and sequenced on a 454 FLX Titanium machine.

**Alignments and dot plots.** Rhesus and human Y sequences were aligned using Stretcher (<http://bioweb2.pasteur.fr/docs/EMBOSS/stretcher.html>) with a gap open

penalty of 20 and a gap extend penalty of 1. Dot plot analyses were performed using custom Perl codes ([http://jura.wi.mit.edu/page/papers/Hughes\\_et\\_al\\_2005/tables/dot\\_plot.pl](http://jura.wi.mit.edu/page/papers/Hughes_et_al_2005/tables/dot_plot.pl)).

**Calculation of  $\alpha_m$ .** The male-to-female mutation rate ratio was calculated using the human–rhesus Y divergence rate (9.40%, 312,840 substitutions per 3,330,847 sites examined) and the human–rhesus autosomal divergence rate ( $1.385 \times 10^{-8}$  substitutions per  $2.248 \times 10^{10}$  sites examined; hg18-rheMac2 alignments downloaded from <http://www.genome.ucsc.edu>). Miyata's formula was then used to calculate  $\alpha_m$  (refs 15, 30):  $Y/A = 2\alpha_m/(1 + \alpha_m)$ . Confidence intervals for ratios of divergence rates were calculated as previously described<sup>30</sup>.

**Modelling ancestral MSY gene loss.** We modelled the numbers of ancestral genes within individual MSY strata as a function of time in millions of years before the present by fitting a one-phase exponential decay model with a baseline constant (below) to our data (gene numbers shown in Table 1) using nonlinear regression analysis in GraphPad Prism 5.0. Parameters for each stratum are given in Supplementary Table 6.

One-phase exponential decay model:

$$N(t) = (N_0 - b)e^{-Kt} + b$$

Where  $N(t)$  is the number of genes at time  $t$ ,  $N_0$  is the number of genes within a given stratum in the ancestral autosomal or pseudoautosomal portion of genome,  $K$  is the decay constant and  $b$  is the baseline (approximated by the number of active ancestral genes within that stratum on human Y chromosome).

# Repetitive motor learning induces coordinated formation of clustered dendritic spines *in vivo*

Min Fu<sup>1</sup>, Xinzhu Yu<sup>1</sup>, Ju Lu<sup>2</sup> & Yi Zuo<sup>1</sup>

Many lines of evidence suggest that memory in the mammalian brain is stored with distinct spatiotemporal patterns<sup>1,2</sup>. Despite recent progresses in identifying neuronal populations involved in memory coding<sup>3–5</sup>, the synapse-level mechanism is still poorly understood. Computational models and electrophysiological data have shown that functional clustering of synapses along dendritic branches leads to nonlinear summation of synaptic inputs and greatly expands the computing power of a neural network<sup>6–10</sup>. However, whether neighbouring synapses are involved in encoding similar memory and how task-specific cortical networks develop during learning remain elusive. Using transcranial two-photon microscopy<sup>11</sup>, we followed apical dendrites of layer 5 pyramidal neurons in the motor cortex while mice practised novel forelimb skills. Here we show that a third of new dendritic spines (post-synaptic structures of most excitatory synapses) formed during the acquisition phase of learning emerge in clusters, and that most such clusters are neighbouring spine pairs. These clustered new spines are more likely to persist throughout prolonged learning sessions, and even long after training stops, than non-clustered counterparts. Moreover, formation of new spine clusters requires repetition of the same motor task, and the emergence of succedent new spine(s) accompanies the strengthening of the first new spine in the cluster. We also show that under control conditions new spines appear to avoid existing stable spines, rather than being uniformly added along dendrites. However, succedent new spines in clusters overcome such a spatial constraint and form in close vicinity to neighbouring stable spines. Our findings suggest that clustering of new synapses along dendrites is induced by repetitive activation of the cortical circuitry during learning, providing a structural basis for spatial coding of motor memory in the mammalian brain.

Spines are dendritic protrusions that contain all the essential components for postsynaptic signalling and are thus a good indicator of synaptic connectivity<sup>12,13</sup>. The clustered plasticity model suggests that neighbouring spines tend to transmit similar information to the postsynaptic neuron<sup>6,7</sup>. To investigate the formation and functional significance of spine clusters during learning, we trained *thy1-YFP-H* mice<sup>14</sup> with a seed-reaching task<sup>15</sup> and followed the dynamics of spines on apical dendrites of layer 5 (L5) pyramidal neurons in the motor cortex contralateral to the trained limb during different learning phases. We found that  $32.5 \pm 2.2\%$  of new spines that formed during the acquisition phase of learning (early training, days 1–4) emerged in clusters; that is, two or more neighbouring new spines without interspersed existing spine(s) (Fig. 1a, b). Most such clusters (61 cases) comprised two contiguous new spines, and the other two clusters comprised three. In contrast, fewer new spine clusters emerged in untrained control mice over the same period ( $6.8 \pm 4.6\%$ ,  $P < 0.01$ ) or in trained mice during the consolidation phase of learning (late training, days 13–16;  $7.4 \pm 4.3\%$ ,  $P < 0.01$ ; Fig. 1b). In addition to clustering of contiguous new spines, we observed a few cases in which two or more new spines formed in close vicinity to each other, but with

up to three existing spines interspersed among them, as well as cases in which new filopodia clustered with new spines (Supplementary Fig. 1). We incorporated these cases in another set of analyses, in which a cluster was defined as a set of new spines/filopodia formed within  $5 \mu\text{m}$  of each other, regardless of the presence or absence of existing spine(s) between them (Supplementary Information). These analyses again revealed that a significantly higher percentage of new spines clustered during early training, compared with that in controls or during late training ( $P < 0.01$  for both cases; Supplementary Fig. 2). They also showed that filopodia only made a minor contribution to new protrusion clusters (Supplementary Fig. 3). More interestingly, among the new spines observed at the end of the acquisition phase (day 4), clustered new spines had a significantly higher survival rate than non-clustered ones (that is, individual new spines flanked by two existing spines) by training day 16 ( $P < 0.01$ ), as well as 4 months after training stopped ( $P < 0.05$ ; Fig. 1c). Together, our results reveal that motor learning induces coordinated formation of clustered synapses, which presumably belong to the same neuronal circuit and persist over time to encode motor information.

Perfection of a motor skill requires repeated practice, usually through multiple training sessions. We therefore sought to find out whether clustered new spines observed on training day 4 were formed within the same training session or across different sessions. We imaged the mice three times (on the day before training, and after 1 and 4 days of training), and found that among new spine clusters observed on training day 4, only 2.4% were composed of spines that formed together between training days 0 and 1. On the other hand, 43.9% of clusters were composed of spines formed between days 1 and 4, and the remaining 53.7% of clusters consisted of one spine formed between days 0 and 1 (the first new spine) and another spine formed between days 1 and 4 (the second new spine). Thus most new spine clusters emerged through recurrent training sessions. To determine how the formation of the second new spine in a cluster correlates with functional changes of the first new spine, we categorized first new spines into three groups based on their survival and neighbouring spine addition: transient new spines (formed on training day 1 but lost by day 4); persistent clustered new spines (formed on training day 1, survived until day 4, with an adjacent new spine formed between days 1 and 4); and persistent non-clustered new spines (formed on training day 1, survived until day 4, with no adjacent new spine formation) (Fig. 1d). As spine head size closely correlates with synaptic strength, we followed head sizes of first new spines over time. On training day 1, we found that head sizes of both transient and persistent new spines were significantly smaller than those of existing stable spines along the same dendrite ( $P < 0.001$  for both cases, Supplementary Fig. 4). By training day 4, head sizes of persistent clustered new spines increased significantly ( $P < 0.01$ ; Fig. 1e and Supplementary Fig. 5a), whereas head sizes of persistent non-clustered new spines remained comparable to day 1 ( $P > 0.2$ ; Fig. 1f and Supplementary Fig. 5b). Because spine head size is a good proxy for synaptic strength, these data suggest that formation of the second new spines

<sup>1</sup>Department of Molecular, Cell and Developmental Biology, University of California, Santa Cruz, California 95064, USA. <sup>2</sup>Department of Biological Sciences and James H. Clark Center, Stanford University, Stanford, California 94305, USA.

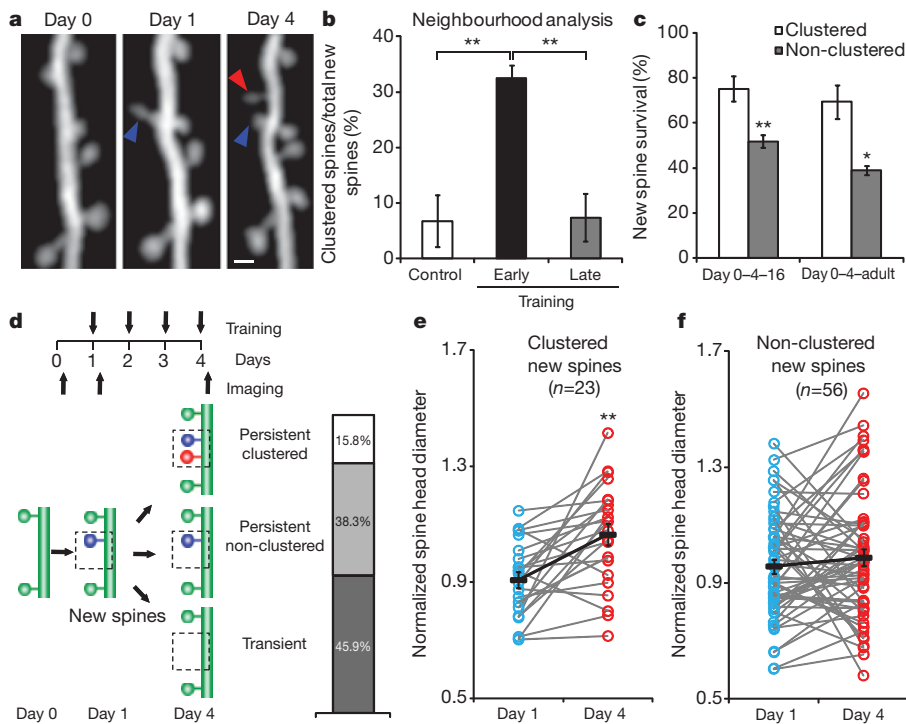


**Figure 1 | Acquisition of a novel motor skill induces formation of spine clusters.** **a**, Repeated imaging of the same dendritic branch during motor learning reveals that a second new spine that formed between days 1 and 4 (red arrowhead) is located next to a stabilized new spine that had formed on day 1 (blue arrowhead). Scale bar, 1  $\mu$ m. **b**, A higher percentage of new spines formed in clusters over 4 days during early training ( $n = 18$  mice), compared with control ( $n = 7$ ) and late training ( $n = 4$ ). **c**, Clustered new spines observed on training day 4 have a higher survival rate than non-clustered counterparts by the end of the 16-day training ( $n = 6$ ), as well as 4 months after training stops ( $n = 4$ ). **d**, New spines formed on training day 1 are classified according to their fate and neighbouring spine formation. **e**, Spine head sizes of persistent clustered new spines increase between training days 1 and 4. **f**, Spine head sizes of persistent non-clustered new spines show no change between training days 1 and 4. Spine head size is quantified by the normalized spine head diameter, defined as the ratio of the spine head diameter to the adjacent dendritic shaft diameter. \* $P < 0.05$ , \*\* $P < 0.01$ . Error bars, s.e.m.

accompanies synaptic potentiation at first new spines during motor learning. It is consistent with previous reports that long-term potentiation at a single spine can facilitate formation and potentiation of neighbouring spines<sup>16,17</sup>.

Different sets of synapses have been shown to be involved in different motor tasks<sup>15</sup>. We therefore trained the same mice sequentially with two motor skills (cross-training) to determine if spines induced by different motor tasks cluster. Cross-training started with the reaching task on day 1 and then switched to the capellini-handling task, which also requires forelimb coordination, on days 2–4 (Fig. 2a and Supplementary Table 1). We found that  $12.3 \pm 0.4\%$  new spines formed during the capellini-handling task between days 1 and 4, among which  $28.4 \pm 2.8\%$  occurred in clusters (Fig. 2b–d). Both the spine formation rate and the percentage of clustered new spines were comparable to those in mice continuously trained with the reaching task (reach-only) ( $P > 0.5$  in both cases), and were significantly higher than those in control mice over the same period of time ( $P < 0.01$  in both cases, Fig. 2c, d). Thus, the capellini-handling task itself can induce clustered spine formation. However, only  $3.3 \pm 2.1\%$  of capellini-handling-induced new spines clustered with reaching-induced new spines in cross-training. This contrasts with the outcome of reach-only training ( $13.8 \pm 1.0\%$ ,  $P < 0.01$ , Fig. 2e), suggesting that new spines induced by different tasks have a low incidence of clustering with each other. To characterize further the task-specific nature of clustered spine formation, we housed animals in a motor enriched environment with daily change of motor challenges (Fig. 2a; see Methods). Motor enrichment also robustly enhanced spinogenesis:  $13.7 \pm 0.8\%$  new spines formed between days 1 and 4, comparable to the percentages under reach-only and cross-training conditions ( $P > 0.1$  for both cases). However, only  $12.6 \pm 1.1\%$  of these new spines appeared in clusters, a percentage comparable to controls ( $P > 0.2$ , Fig. 2d) but significantly lower than that under reach-only or cross-training conditions ( $P < 0.01$  for both cases). Together these data indicate that, whereas novelty in learning stimulates spinogenesis, repetitive activation of the same cortical circuit is crucial in clustered spine formation (Supplementary Fig. 6).

The phenomenon of learning-induced, coordinated spinogenesis led us to investigate further the spatial distribution of new spines. We first examined the distance between a new spine (n) and its nearest existing

spine (s) ( $D_{n-s}$ , Fig. 3a) in control mice. We then simulated  $D_{n-s}$  distribution under the null hypothesis that new spines form uniformly and independently along the dendrite (see Methods). Compared with simulation results, the median of measured values of  $D_{n-s}$  was significantly larger (Fig. 3b), and the cumulative probability distribution of measured values of  $D_{n-s}$  was shifted towards longer distances (Fig. 3c). These results suggest that new spines are not randomly dispersed along dendritic segments, and their apparent avoidance of existing stable spines under control conditions is consistent with the idea that neighbouring spines share and compete for local resources<sup>18–21</sup>.

To determine if motor learning alters the spatial distribution of new spines, we examined values of  $D_{n-s}$  in mice trained with the reaching task. We found that the distance between a new spine formed on training day 1 ( $n_1$ ) and the nearest existing spine ( $D_{n_1-s}$ ) was comparable for trained and control mice ( $P > 0.7$ ). We classified new spines formed between training days 1 and 4 ( $n_2$ ) into two categories: clustered  $n_2$  (that is, those that formed next to a stabilized first new spine; Fig. 3d) and non-clustered  $n_2$  (those that did not form next to a stabilized first new spine). We found that clustered  $n_2$  were significantly closer to their nearest stable spines ( $n_1$  or a stable spine existing since day 0; Fig. 3d) ( $D_{n_2-s, \text{clustered}}$ ) than were  $n_1$  ( $D_{n_1-s}$ ) ( $P < 0.05$ ). In contrast, the distance between a non-clustered  $n_2$  and its nearest stable spine ( $D_{n_2-s, \text{non-clustered}}$ ) was comparable to  $D_{n_1-s}$  ( $P > 0.9$ , Fig. 3e). In addition, when an  $n_1$  formed between two adjacent stable spines, the distance between the two stable spines ( $D_{s-n_1-s}$ ) was comparable for control and trained mice ( $P > 0.7$ ; Supplementary Fig. 7). However, the distance between a stabilized  $n_1$  and the adjacent stable spine, between which a clustered  $n_2$  formed ( $D_{n_1-n_2-s}$ ), was significantly smaller than the distance between two adjacent stable spines, between which a non-clustered  $n_2$  formed ( $D_{s-n_2-s}$ ;  $P < 0.01$ ; Supplementary Fig. 7). These results suggest that learning-induced clustered new spines can overcome the spatial constraint of existing spines and be packed into tighter dendritic space.

Recent studies have shown that dendritic spines are dynamic in the living brain, and that rearrangement of cortical connections through *de novo* growth and loss of spines provides a structural substrate for experience-dependent plasticity<sup>22–25</sup>. Built upon these works, our study reveals a novel spatial rule of spinogenesis during motor learning. We found that learning-induced new spines tend to form in small clusters (mostly pairs). The correlation between the emergence of the second



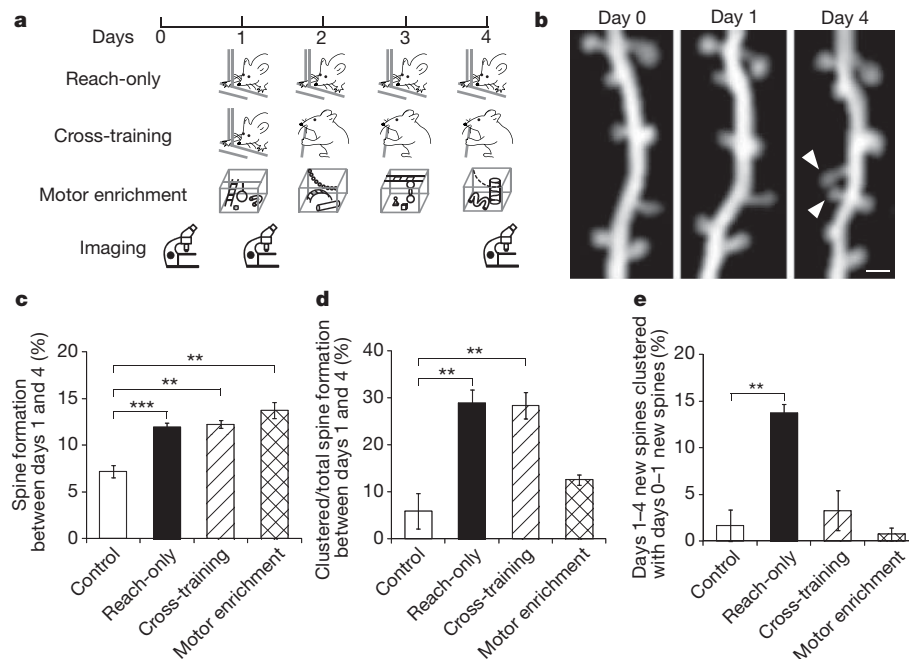


**Figure 2 | Clustered new spines form over multiple training sessions of the same, but not different, motor tasks.** **a**, Timelines of reach-only, cross-training and motor enrichment experiments. **b**, Repeated imaging of the same dendritic branch revealed that two neighbouring new spines (arrowheads) formed between days 1 and 4 during cross-training. Scale bar, 1  $\mu\text{m}$ . **c**, Higher percentages of new spines formed between days 1 and 4 in reach-only, cross-training and motor enrichment, compared with controls. **d**, Higher percentages

of new spines formed in clusters between days 1 and 4 in reach-only and cross-training, compared with controls. **e**, A higher percentage of new spines that formed between days 1 and 4 clustered with new spines that had formed between days 0 and 1 in the reach-only condition, compared with controls. Number of mice examined: six control, nine reach-only, five cross-training and six motor enrichment. \*\* $P < 0.01$ , \*\*\* $P < 0.001$ . Error bars, s.e.m.

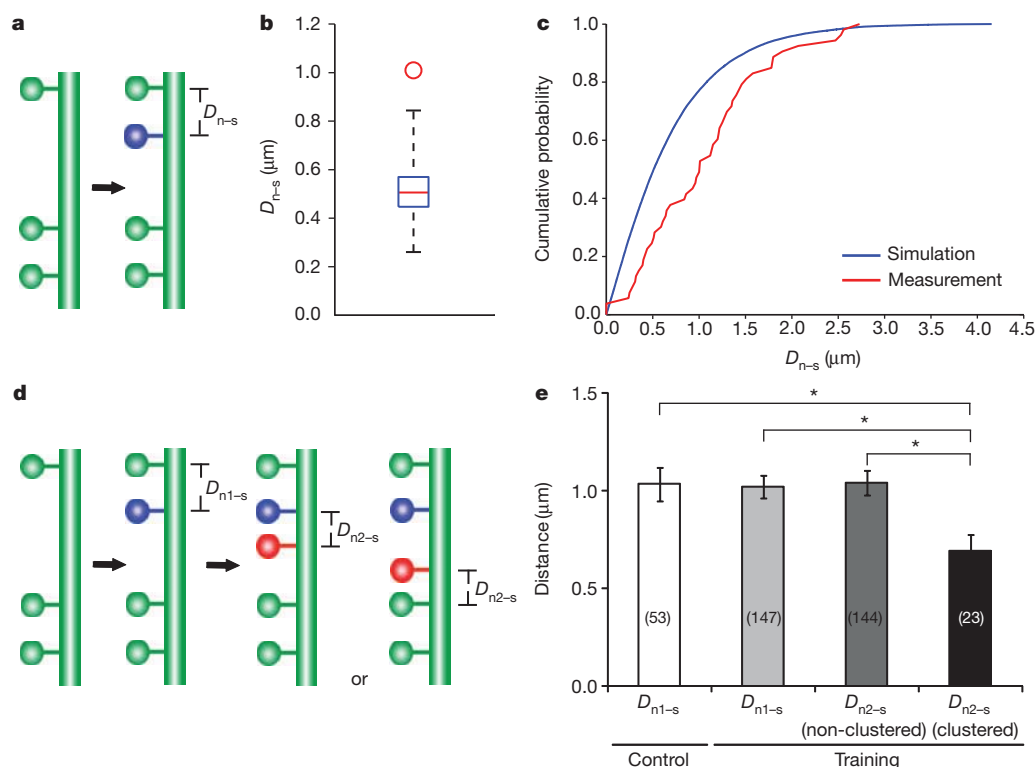


**Figure 3 | The spatial distribution of new spines along dendrites.** **a**, Schematic illustrating the measurement of  $D_{n-s}$ . **b**, The median of measured values of  $D_{n-s}$  (red circle) is significantly larger than that of simulated values of  $D_{n-s}$  (box plot of results from 1,000 simulations, with whiskers representing the minimum and the maximum) in control mice. The simulation is based on the null hypothesis that new spines are added independently and uniformly along a linear dendrite. **c**, Cumulative probability distribution of measured  $D_{n-s}$  is shifted towards longer distances than the simulated  $D_{n-s}$  in control mice.

**d**, Schematic illustrating the measurement of  $D_{n2-s, \text{clustered}}$ . The nearest spine to a clustered  $n_2$  could be either a persistent first new spine ( $n_1$ ) or a stable spine existing since day 0, depending on relative  $n_2$  location. **e**,  $D_{n1-s}$  in control mice is comparable to that of trained mice. In trained mice,  $D_{n2-s, \text{clustered}}$  is significantly smaller than  $D_{n1-s}$ , whereas  $D_{n2-s, \text{non-clustered}}$  is comparable to  $D_{n1-s}$ . The number of spines analysed in each condition is indicated on each column. \* $P < 0.05$ . Error bars, s.e.m.

new spine and the strengthening of the first new spine also suggests their potential participation in the same neuronal circuit. These findings support the clustered plasticity model, which postulates that synapses located close together along the same dendritic branch are more likely to be allocated for the same information than synapses dispersed throughout the dendritic arbor<sup>7</sup>. Indeed, in the mouse auditory cortex, although spines tuned for different frequencies are highly interspersed, 26% of neighbouring spines exhibit similar effective frequencies, much more frequently than anticipated from random distribution (10%)<sup>26</sup>. Therefore, although neurons tend to maximize their overall connections<sup>27</sup>, clustered plasticity ensures strengthening of circuit-specific connections and enables spatial coding for task-related information.

Previous electron microscopy studies have revealed that neighbouring spines can form synapses with the same axon<sup>28–30</sup> (see Supplementary Fig. 8a, c, e). Positioning multiple synapses between a pair of neurons in close proximity allows nonlinear summation of synaptic strength, and potentially increases the dynamic range of synaptic transmission well beyond what can be achieved by random positioning of the same number of synapses. Alternatively, clustered new spines may synapse with distinct (but presumably functionally related) presynaptic partners (Supplementary Fig. 8b, d). In this case, they could potentially integrate inputs from different neurons nonlinearly and increase the circuit's computational power. Distinguishing between these two possibilities would probably require circuit reconstruction by electron microscopy following *in vivo* imaging to reveal the identities of presynaptic partners of newly formed spines.

Profiling spine formation during novel experiences, our data revealed a critical role of repetitive activation of the same neuronal circuit. The fact that the second new spine in a cluster can overcome the spatial constraint imposed by existing spines suggests that repetitive activation of a neuronal circuit may modify or reallocate local 'resources' for spinogenesis. Such resources may be permissive or instructive molecular cues at the pre- or postsynaptic site, or the availability of suitable partners (for example, axonal boutons). Understanding the nature and regulation of such resources may hold the key to elucidating the cellular mechanisms of clustered spine formation. It will be conducive to the development of tools to label and manipulate specific synaptic populations, and ultimately to the dissection of the causal relationship between synaptic dynamics and learning.

## METHODS SUMMARY

YFP-H line mice<sup>14</sup> expressing yellow fluorescent protein (YFP) in a small subset of cortical neurons were used in all the experiments. Mice of both sexes were trained with different motor-skill tasks or housed in a motor-enriched environment, starting at 1 month of age (see Methods). The procedures for transcranial two-photon imaging and quantification of spine dynamics have been described previously<sup>11,15</sup>. ImageJ was used to measure spine head size, as well as inter-spine distances. Simulation was performed with custom-written codes in Matlab (MathWorks) and statistical analyses were performed using GraphPad Prism 5 (GraphPad Software) (see Methods). All data were presented as mean  $\pm$  s.e.m. *P* values were calculated using the Mann–Whitney *U*-test for independent samples, and the Wilcoxon signed-rank test for paired samples.

**Full Methods** and any associated references are available in the online version of the paper at [www.nature.com/nature](http://www.nature.com/nature).

**Received 22 September 2011; accepted 9 January 2012.**

**Published online 19 February 2012.**

1. Silva, A. J., Zhou, Y., Rogerson, T., Shobe, J. & Balaji, J. Molecular and cellular approaches to memory allocation in neural circuits. *Science* **326**, 391–395 (2009).
2. Aimone, J. B., Wiles, J. & Gage, F. H. Potential role for adult neurogenesis in the encoding of time in new memories. *Nature Neurosci.* **9**, 723–727 (2006).

3. Han, J. H. *et al.* Selective erasure of a fear memory. *Science* **323**, 1492–1496 (2009).
4. Komiya, T. *et al.* Learning-related fine-scale specificity imaged in motor cortex circuits of behaving mice. *Nature* **464**, 1182–1186 (2010).
5. Kee, N., Teixeira, C. M., Wang, A. H. & Frankland, P. W. Preferential incorporation of adult-generated granule cells into spatial memory networks in the dentate gyrus. *Nature Neurosci.* **10**, 355–362 (2007).
6. Larkum, M. E. & Nevian, T. Synaptic clustering by dendritic signalling mechanisms. *Curr. Opin. Neurobiol.* **18**, 321–331 (2008).
7. Govindarajan, A., Kelleher, R. J. & Tonegawa, S. A clustered plasticity model of long-term memory engrams. *Nature Rev. Neurosci.* **7**, 575–583 (2006).
8. Poirazi, P. & Mel, B. W. Impact of active dendrites and structural plasticity on the memory capacity of neural tissue. *Neuron* **29**, 779–796 (2001).
9. Sjostrom, P. J. & Hausser, M. A cooperative switch determines the sign of synaptic plasticity in distal dendrites of neocortical pyramidal neurons. *Neuron* **51**, 227–238 (2006).
10. Losonczy, A. & Magee, J. C. Integrative properties of radial oblique dendrites in hippocampal CA1 pyramidal neurons. *Neuron* **50**, 291–307 (2006).
11. Zuo, Y., Lin, A., Chang, P. & Gan, W. B. Development of long-term dendritic spine stability in diverse regions of cerebral cortex. *Neuron* **46**, 181–189 (2005).
12. Segal, M. Dendritic spines and long-term plasticity. *Nature Rev. Neurosci.* **6**, 277–284 (2005).
13. Harms, K. J. & Dunaevsky, A. Dendritic spine plasticity: looking beyond development. *Brain Res.* **1184**, 65–71 (2007).
14. Feng, G. *et al.* Imaging neuronal subsets in transgenic mice expressing multiple spectral variants of GFP. *Neuron* **28**, 41–51 (2000).
15. Xu, T. *et al.* Rapid formation and selective stabilization of synapses for enduring motor memories. *Nature* **462**, 915–919 (2009).
16. Harvey, C. D. & Svoboda, K. Locally dynamic synaptic learning rules in pyramidal neuron dendrites. *Nature* **450**, 1195–1200 (2007).
17. De Roo, M., Klausner, P. & Muller, D. LTP promotes a selective long-term stabilization and clustering of dendritic spines. *PLoS Biol.* **6**, e219 (2008).
18. Gray, N. W., Weimer, R. M., Bureau, I. & Svoboda, K. Rapid redistribution of synaptic PSD-95 in the neocortex *in vivo*. *PLoS Biol.* **4**, e370 (2006).
19. Harvey, C. D., Yasuda, R., Zhong, H. & Svoboda, K. The spread of Ras activity triggered by activation of a single dendritic spine. *Science* **321**, 136–140 (2008).
20. Rose, J., Jin, S. X. & Craig, A. M. Heterosynaptic molecular dynamics: locally induced propagating synaptic accumulation of CaM kinase II. *Neuron* **61**, 351–358 (2009).
21. Tsuriel, S. *et al.* Local sharing as a predominant determinant of synaptic matrix molecular dynamics. *PLoS Biol.* **4**, e271 (2006).
22. Yu, X. & Zuo, Y. Spine plasticity in the motor cortex. *Curr. Opin. Neurobiol.* **21**, 169–174 (2011).
23. Chen, J. L. & Nedivi, E. Neuronal structural remodeling: is it all about access? *Curr. Opin. Neurobiol.* **20**, 557–562 (2010).
24. Fu, M. & Zuo, Y. Experience-dependent structural plasticity in the cortex. *Trends Neurosci.* **34**, 177–187 (2011).
25. Holtmaat, A. & Svoboda, K. Experience-dependent structural synaptic plasticity in the mammalian brain. *Nature Rev. Neurosci.* **10**, 647–658 (2009).
26. Chen, X., Leischner, U., Rochefort, N. L., Nelken, I. & Konnerth, A. Functional mapping of single spines in cortical neurons *in vivo*. *Nature* **475**, 501–505 (2011).
27. Yuste, R. Dendritic spines and distributed circuits. *Neuron* **71**, 772–781 (2011).
28. Knott, G. W., Holtmaat, A., Wilbrecht, L., Welker, E. & Svoboda, K. Spine growth precedes synapse formation in the adult neocortex *in vivo*. *Nature Neurosci.* **9**, 1117–1124 (2006).
29. Fiala, J. C., Allwardt, B. & Harris, K. M. Dendritic spines do not split during hippocampal LTP or maturation. *Nature Neurosci.* **5**, 297–298 (2002).
30. Toni, N., Buchs, P. A., Nikonenko, I., Bron, C. R. & Muller, D. LTP promotes formation of multiple spine synapses between a single axon terminal and a dendrite. *Nature* **402**, 421–425 (1999).

**Supplementary Information** is linked to the online version of the paper at [www.nature.com/nature](http://www.nature.com/nature).

**Acknowledgements** We thank D. States, D. Garcia, L. Hinck, T. Jones, S. Song, W. Thompson and G. Wang for comments on this manuscript. We thank A. Perlik and T. Xu for technical support. This work was supported by grants from the DANA Foundation and the National Institutes of Mental Health to Y.Z.

**Author Contributions** M.F. and X.Y. did the *in vivo* imaging and made the figures. M.F. performed behavioural training and all spine analyses, and made figures for repetitive imaging. J.L. and M.F. performed Matlab simulation and statistical analyses. J.L., M.F. and X.Y. participated in discussion about the paper. Y.Z. initiated and designed the project, and wrote the manuscript.

**Author Information** Reprints and permissions information is available at [www.nature.com/reprints](http://www.nature.com/reprints). The authors declare no competing financial interests. Readers are welcome to comment on the online version of this article at [www.nature.com/nature](http://www.nature.com/nature). Correspondence and requests for materials should be addressed to Y.Z. ([yizuo@ucsc.edu](mailto:yizuo@ucsc.edu)).

## METHODS

**Experimental animals.** *Thy1-YFP-H* line mice<sup>14</sup> were obtained from the Jackson Laboratory. Mice were group-housed and bred in the University of California, Santa Cruz, animal facility, with all experiments performed in accordance with approved animal protocols.

**Motor skill training and motor enrichment.** Both the mouse single-seed reaching task and capellini-handling task protocols have been previously described<sup>15</sup>. 'Motor-enriched' mice were reared in groups of 8–12 in large cages (90 cm × 25 cm × 15 cm) containing various toys, such as ropes, ladders, chains, hanging mesh/bars etc., all of which required substantial motor coordination. The nature of toys was changed on a daily basis. Control mice were housed in standard mouse cages, with up to five mice per cage.

**Surgical procedure for *in vivo* transcranial imaging.** The procedure for transcranial two-photon imaging has been described previously<sup>11,31</sup>. Trained mice were imaged immediately after each training session.

**Data quantification.** All analyses of spine dynamics were done using ImageJ software, blinded for experimental conditions. Quantification criteria of dendritic spines have been described previously<sup>15</sup>. All dendritic protrusions were tracked manually in three-dimensional stacks to ensure the consistency of protrusion identification across imaging sessions, despite possible tissue movement or rotation. The number and location of dendritic protrusions (defined as protrusion length larger than one-third of dendritic shaft diameter) were identified in each view. Filopodia were identified as long, thin structures with the ratio of head diameter to neck diameter being less than 1.2 and the ratio of length to neck diameter being greater than 3. The remaining protrusions were classified as spines. Formation and elimination of spines and filopodia were determined by comparing images collected at two different time points. Spines or filopodia were considered identical between the two images if they were within 0.7  $\mu\text{m}$  of their expected positions, based on their spatial relationship to adjacent landmarks and/or their positions relative to immediately adjacent spines. A stable spine was defined as a spine that was present in both images. A new spine was a spine that appeared in a subsequent image but was absent from the initial image. Percentages of formed and eliminated spines (or dendritic protrusions) were normalized to the number of spines (or dendritic protrusions) in the initial image. Spine diameter analyses have been previously

described<sup>11</sup>. Because imaging and animal conditions varied over time, the ratio of the spine head diameter to the adjacent dendritic shaft diameter was used as the normalized spine head diameter. Measurement of spine head intensity, as described previously<sup>32</sup>, was also performed to confirm these spine size results. Briefly, we determined the signal intensity (defined as the sum intensity of all pixels composing the spine in the best focal plane) and subtracted the background intensity (defined as the sum intensity of a region composed of the same number of pixels as the spine but with no YFP-labelled structure). The difference was then divided by the mean intensity of the adjacent dendritic shaft (defined similarly as the difference between the mean signal intensity of the shaft and the mean background intensity) to correct for varying imaging conditions. The final value was termed 'integrated spine brightness.' All distance measurements were done in ImageJ. To simulate spine formation, we first obtained the relative location of stable spines by measuring inter-spine distances along traced dendrites in seven control animals, and concatenated dendritic segments from each animal into a single 'synthetic dendrite.' We then used custom-written Matlab codes to simulate the addition of new spines. As we observed, two spines can extend from the same linear location along the dendritic segment and point towards different directions, given the cylindrical shape of dendrites. In our analysis and simulation, we made the simplifying approximation that the dendritic segment is one-dimensional rather than a tube. Therefore, zero inter-spine distance in our analysis represents two spines overlapping in linear position but actually located at different sites around the circumference of the dendritic segment. In each round of simulation, the same numbers of new spines as observed in experiments were generated independently and uniformly along synthetic dendrites. The distance between each new spine and its nearest stable spine ( $D_{n-3}$ ) was calculated. The simulation was repeated 1,000 times and the resultant data were pooled to compute the simulated sample median and the cumulative probability curve. All data were presented as mean  $\pm$  standard error of mean (s.e.m.). *P* values were calculated using the Mann–Whitney *U*-test for independent samples, and the Wilcoxon signed-rank test for paired samples.

31. Grutzendler, J., Kasthuri, N. & Gan, W. B. Long-term dendritic spine stability in the adult cortex. *Nature* **420**, 812–816 (2002).
32. Hofer, S. B., Mrsic-Flogel, T. D., Bonhoeffer, T. & Hubener, M. Experience leaves a lasting structural trace in cortical circuits. *Nature* **457**, 313–317 (2009).



# Circadian rhythms govern cardiac repolarization and arrhythmogenesis

Darwin Jeyaraj<sup>1,2</sup>, Saptarsi M. Haldar<sup>1</sup>, Xiaoping Wan<sup>2</sup>, Mark D. McCauley<sup>3</sup>, Jürgen A. Ripperger<sup>4</sup>, Kun Hu<sup>5</sup>, Yuan Lu<sup>1</sup>, Betty L. Eapen<sup>1</sup>, Nikunj Sharma<sup>1</sup>, Eckhard Ficker<sup>2</sup>, Michael J. Cutler<sup>2</sup>, James Gulick<sup>6</sup>, Atsushi Sanbe<sup>6</sup>, Jeffrey Robbins<sup>6</sup>, Sophie Demolombe<sup>7</sup>, Roman V. Kondratov<sup>8</sup>, Steven A. Shea<sup>5</sup>, Urs Albrecht<sup>4</sup>, Xander H. T. Wehrens<sup>3</sup>, David S. Rosenbaum<sup>2</sup> & Mukesh K. Jain<sup>1</sup>

**Sudden cardiac death exhibits diurnal variation in both acquired and hereditary forms of heart disease<sup>1,2</sup>, but the molecular basis of this variation is unknown. A common mechanism that underlies susceptibility to ventricular arrhythmias is abnormalities in the duration (for example, short or long QT syndromes and heart failure)<sup>3–5</sup> or pattern (for example, Brugada's syndrome)<sup>6</sup> of myocardial repolarization. Here we provide molecular evidence that links circadian rhythms to vulnerability in ventricular arrhythmias in mice. Specifically, we show that cardiac ion-channel expression and QT-interval duration (an index of myocardial repolarization) exhibit endogenous circadian rhythmicity under the control of a clock-dependent oscillator, krüppel-like factor 15 (*Klf15*). *Klf15* transcriptionally controls rhythmic expression of Kv channel-interacting protein 2 (KChIP2), a critical subunit required for generating the transient outward potassium current<sup>7</sup>. Deficiency or excess of *Klf15* causes loss of rhythmic QT variation, abnormal repolarization and enhanced susceptibility to ventricular arrhythmias. These findings identify circadian transcription of ion channels as a mechanism for cardiac arrhythmogenesis.**

Sudden cardiac death from ventricular arrhythmias is the principal cause of mortality from heart disease worldwide and remains a major unresolved public health problem. The incidence of sudden cardiac death exhibits diurnal variation in both acquired and hereditary forms of heart disease<sup>1,2</sup>. In the general population, the occurrence of sudden cardiac death increases sharply within a few hours of rising in the morning, and a second peak is evident in the evening hours<sup>1</sup>. In specific hereditary disorders, for example, Brugada's syndrome, fatal ventricular arrhythmias often occur during sleep<sup>2</sup>. A common mechanism in both acquired and hereditary forms of heart disease that enhances susceptibility to ventricular arrhythmias is abnormal myocardial repolarization<sup>6</sup>. Clinically, three common types of alterations in myocardial repolarization are evident on the surface electrocardiogram (ECG). First, prolongation of repolarization is seen in acquired disorders (for example, heart failure)<sup>5</sup> and congenital disorders (for example, long QT syndrome)<sup>3</sup>. Second, shortening of repolarization is found in the short QT syndrome<sup>4</sup>. Third, early repolarization is the hallmark ECG finding in Brugada's syndrome<sup>8</sup>. Interestingly, all three modifications of repolarization increase vulnerability to ventricular arrhythmias<sup>6</sup>. Despite rigorous investigation of the biophysical and structural characteristics of ion channels that control myocardial repolarization, the molecular basis for the diurnal variation in occurrence of ventricular arrhythmias remains unknown.

Biological processes in living organisms that oscillate with a periodicity of 24 h are said to be circadian. This cell-autonomous rhythm is coordinated by an endless negative transcriptional–translational feedback

loop, commonly referred to as the biological clock<sup>9</sup>. Several physiological parameters in the cardiovascular system such as heart rate, blood pressure, vascular tone, QT interval and ventricular effective refractory period exhibit diurnal variation<sup>10–13</sup>. Recent studies have also identified a direct role for the biological clock in regulating cardiac metabolism, growth and response to injury<sup>14</sup>. Previous studies have also reported that expression of repolarizing ion channels and ionic currents ( $I_{to}$ ) exhibit diurnal changes<sup>15</sup>. However, a potential link between circadian rhythms and arrhythmogenesis remains unknown. We made the serendipitous observation that *Klf15* expression exhibits endogenous circadian rhythmicity in the heart (Fig. 1a). Gene expression microarrays in hearts of mice that are deficient in *Klf15* led us to identify *KChIP2* (also called *KCNIP2*), the regulatory  $\beta$ -subunit for the repolarizing transient outward potassium current ( $I_{to}$ ) as a putative target for this factor in the heart. These observations led us to question whether the circadian clock may regulate rhythmic variation in repolarization and alter susceptibility to arrhythmias through *Klf15*.

First, we explored mechanisms through which the circadian clock regulated rhythmic expression of *Klf15* in the heart. Examination of approximately 5 kb of the promoter region of *Klf15* revealed four canonical 'E-box' regions, that is, consensus binding sites for CLOCK and its heterodimer BMAL1 (also called ARNTL), which are essential transcription factors involved in the circadian clock (Supplementary Fig. 1a, inset). Consistent with this finding, *Klf15* luciferase (approximately 5 kb) was activated in a dose-dependent manner by the CLOCK–BMAL1 heterodimer (Supplementary Fig. 1a). To confirm this interaction, we performed chromatin immunoprecipitation (ChIP) and identified rhythmic variation in BMAL1 binding to the *Klf15* promoter in the hearts of wild-type mice, but not in the hearts of *BMAL1*-null mice (Fig. 1b). In accordance with the observations above, the expression of *Klf15* was disrupted in *Bmal1*-null, and *Per2*- and *Cry1*-null hearts (Supplementary Fig. 1b). Thus, our data strongly suggest that the circadian clock directly regulates the oscillation of *Klf15* in the heart.

To determine whether myocardial repolarization and ion-channel expression exhibit 'true' (endogenous) circadian rhythms—that is, oscillate in the absence of external cues such as light—wild-type mice were placed in constant darkness for 36 h and telemetry-based ECG intervals were measured every 2 h for 24 h. Under these conditions, the heart rate and the QT interval corrected to heart rate (QTc) were both rhythmic and exhibited true endogenous circadian rhythmicity (Fig. 1c, d). Next, to examine whether expression of repolarizing ion channels had endogenous circadian rhythms, mice were placed in constant darkness for 36 h, and hearts were collected every 4 h over a 24-h period. The expression of the  $\alpha$ -subunit for the transient outward

<sup>1</sup>Case Cardiovascular Research Institute, Harrington Heart and Vascular Institute, Department of Medicine, Case Western Reserve University School of Medicine, Cleveland, Ohio 44106, USA. <sup>2</sup>Heart and Vascular Research Center, MetroHealth campus of Case Western Reserve University, Cleveland, Ohio 44109, USA. <sup>3</sup>Departments of Medicine and Molecular Physiology and Biophysics, Baylor College of Medicine, Houston, Texas 77030, USA. <sup>4</sup>Department of Medicine, Division of Biochemistry, University of Fribourg, CH-1700 Fribourg, Switzerland. <sup>5</sup>Division of Sleep Medicine, Brigham and Women's Hospital and Harvard Medical School, Boston, Massachusetts 02115, USA. <sup>6</sup>Department of Pediatrics, Division of Molecular Cardiovascular Biology, Cincinnati Children's Hospital Medical Center, Cincinnati, Ohio 45229, USA. <sup>7</sup>Institut de Pharmacologie Moléculaire et Cellulaire, UMR CNRS 6097, Université de Nice Sophia Antipolis, 06560 Valbonne, France. <sup>8</sup>Department of Biological, Geological and Environmental Sciences, and Center for Gene Regulation in Health and Disease, Cleveland State University, Cleveland, Ohio, 44115, USA.

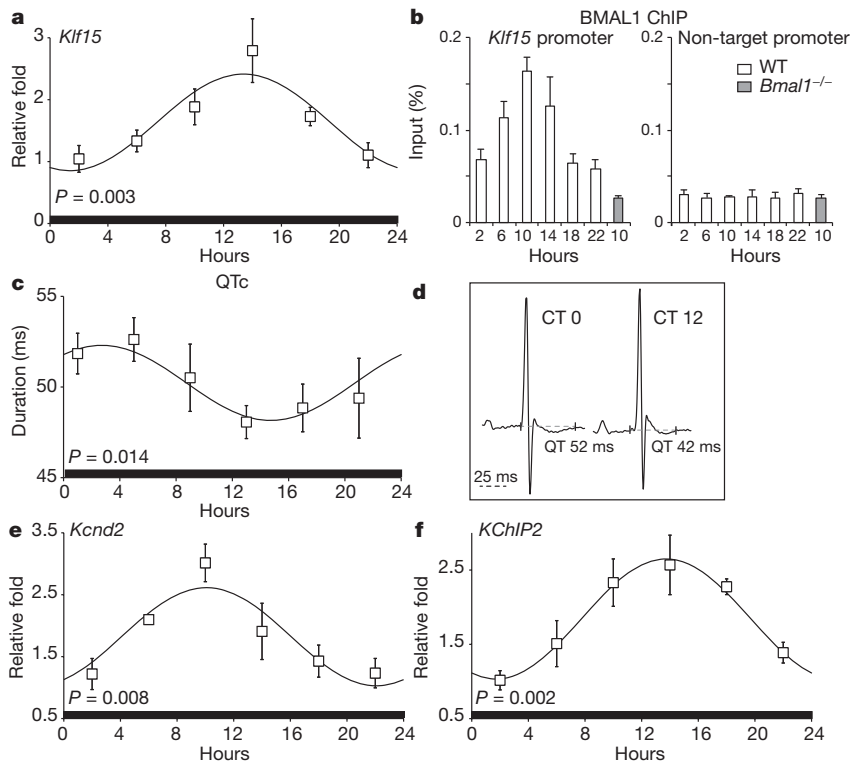


**Figure 1 | *Klf15* expression, ECG QTc interval and expression of repolarizing ion channels exhibit endogenous circadian rhythm.** **a**, *Klf15* expression exhibits endogenous circadian variation in wild-type (WT) hearts from mice in constant darkness ( $n = 4$  per time point). CT, circadian time. **b**, Effect of BMAL1 ChIP on the *Klf15* promoter, showing rhythmic variation in binding of BMAL1 to the *Klf15* promoter in wild-type hearts ( $n = 3$  per group). **c**, Duration of ECG QTc interval (ms) in conscious mice exhibits endogenous circadian variation in constant darkness ( $n = 4$ ). **d**, Representative ECGs from conscious mice after 36 h in constant darkness at CT 0 and CT 12. **e**, **f**, Endogenous circadian variation in transcripts for *Kcnd2* and *KChIP2* in wild-type hearts measured every 4 h after 36 h in constant darkness ( $n = 4$  per time point). Error bars, mean  $\pm$  s.e.m.

potassium current ( $I_{to}$ , Kv4.2 (encoded by *Kcnd2*) (Fig. 1e), and the regulatory  $\beta$ -subunit, *KChIP2* (Fig. 1f), exhibit endogenous circadian rhythmicity, as did components of the circadian clock in the heart (Supplementary Fig. 2). In contrast, the expression of two other major repolarizing currents in the murine ventricle, Kv1.5 (the  $\alpha$ -subunit for the ultra-rapid delayed rectifier potassium current) and Kir2.1 (the  $\alpha$ -subunit for the inward rectifier potassium current), did not reveal notable rhythmic variation (Supplementary Fig. 3). In addition, we observed a 24-h rhythm in the oscillation of *Bmal1*, *Klf15* and *KChIP2* after serum shock in cultured neonatal rat ventricular myocytes (Supplementary Fig. 4). These data indicate that myocardial repolarization and the expression of some repolarizing ion channels exhibit an endogenous circadian rhythm.

Next, to elucidate the role of *Klf15* in regulating rhythmic changes in repolarization, we used complementary *in vivo* loss- and gain-of-function approaches in mice. For loss-of-function, a previously described systemic *Klf15*-null mouse was used<sup>16</sup>; for gain-of-function, a cardiac-specific *Klf15* transgenic (*Klf15*-Tg) mouse driven by an attenuated  $\alpha$ -myosin heavy chain ( $\alpha$ -MHC) promoter was developed (Supplementary Fig. 5). First, we examined whether rhythmic expression of *Kcnd2* or *KChIP2* was altered in the *Klf15*-deficient state. *Kcnd2* expression exhibited altered rhythmic variation in *Klf15*-null mice with reduced expression at zeitgeber time 6 (ZT6), and increased expression at ZT22 compared to wild-type controls (Fig. 2a). *KChIP2* expression was devoid of any discernable rhythm in the *Klf15*-null mice and sustained reduction was observed at all time points (Fig. 2b, c and

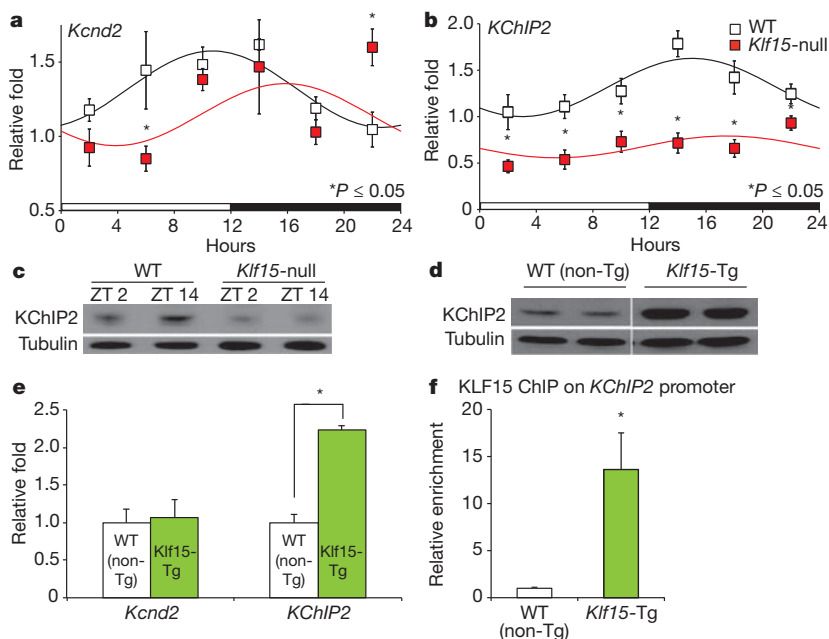


**Figure 2 | *Klf15* regulates *KChIP2* expression in the heart.** **a**, *Kcnd2* mRNA expression exhibits diurnal rhythm in wild-type mice ( $P = 0.0023$ ), but in *Klf15*-null hearts ( $P$  not significant) the rhythm is abnormal with reduced expression at zeitgeber time 6 (ZT6) and increased expression at ZT22 ( $n = 4$  per time point per group). **b**, *KChIP2* mRNA expression exhibits no rhythmic variation in *Klf15*-deficient mice (WT,  $P = 0.016$ ; *Klf15*-null,  $P$  not significant), with substantial reductions in expression at all time points ( $n = 4$  per time point per group). **c**, *KChIP2* protein expression exhibits no variation over 12 h in *Klf15*-null hearts. **d**, **e**, *Klf15*-Tg mice hearts express higher levels of *KChIP2* mRNA and protein. **f**, Chromatin immunoprecipitation with Flag antibody illustrating enrichment of Flag-KLF15 on the *KChIP2* promoter ( $n = 3$  per group). Error bars, mean  $\pm$  s.e.m.,  $*P < 0.05$ .

Supplementary Fig. 6a). Next, we examined whether *Kcnd2* or *KChIP2* serve as transcriptional targets for *Klf15* in the heart. Adenoviral over-expression of *Klf15* in neonatal rat ventricular myocytes robustly induced *KChIP2* expression but had no effect on *Kcnd2* expression (Supplementary Fig. 6b). Notably, in *Klf15*-Tg hearts, expression of *KChIP2* was twofold greater but with no effect on *Kcnd2* expression (Fig. 2d, e). Examination of the *KChIP2* promoter region revealed numerous consensus krüppel-binding sites, that is, C(A/T)CCC (Supplementary Fig. 7a). The activity of *KChIP2* luciferase was induced by full-length KLF15 but not by a mutant that lacked the zinc-finger DNA-binding domain (Supplementary Fig. 7b). To identify the specific *Klf15* binding site, deletion constructs of the *KChIP2* promoter were generated, and transcriptional activity was mapped to the proximal 555 bases (Supplementary Fig. 7a). Mutation of one krüppel-binding site within this region ( $\Delta 1$ ) was sufficient to cause complete loss of activity in the full-length *KChIP2* promoter (Supplementary Fig. 7c). Chromatin immunoprecipitation of Flag-KLF15 from *Klf15*-Tg hearts confirmed that KLF15 was enriched on the endogenous *KChIP2* promoter (Fig. 2f). Importantly, the oscillation of several components of the core clock machinery was minimally affected in the *Klf15*-deficient state (Supplementary Fig. 8). In addition, the expression levels of clock genes in *Klf15*-Tg hearts were similar to their controls at ZT6 (Supplementary Fig. 8). This suggested that the endogenous clock is dependent on *Klf15* to orchestrate rhythmic changes in *KChIP2* expression. Consistent with this observation, the expression of *Klf15* (Supplementary Fig. 1b) and *KChIP2* (Supplementary Fig. 9) were altered in a similar fashion in *Bmal1*-null, and *Per2*- and *Cry1*-null mice. These data support the idea that *KChIP2* is a direct transcriptional target for *Klf15* in the heart.

We next examined whether *Klf15*-dependent regulation of *KChIP2* could be responsible for rhythmic day–night variation in myocardial repolarization. Analysis of telemetry-based ECGs revealed that rhythmic QTc interval variation was indeed abrogated in both *Klf15*-null and *Klf15*-Tg mice (Fig. 3a–d). In the *Klf15*-deficient state, the ECG QTc interval was prolonged in the dark phase and failed to oscillate (Fig. 3a, c). This occurred despite *Klf15*-null mice having similar heart rates to their wild-type counterparts (Supplementary Fig. 11). In contrast, the *Klf15*-Tg mice had persistently short QT intervals with no rhythmic day–night variation (Fig. 3b, d). Again, this occurred despite minimal difference in heart rates when compared to wild-type controls (Supplementary Fig. 11). Next, we examined whether transient outward current ( $I_{to \text{ fast}}$ )-dependent changes in repolarization in isolated myocytes were responsible for the ECG changes mentioned above in *Klf15*-null and *Klf15*-Tg mice. In *Klf15*-null mice, there was a marked reduction in  $I_{to \text{ fast}}$  density (Fig. 3e) and prolongation of action potential duration (APD) (Fig. 3g). In contrast, *Klf15*-Tg mice exhibited a substantial increase in  $I_{to \text{ fast}}$  density (Fig. 3f) with a dramatic shortening of APD (Fig. 3h). In the *Klf15*-Tg mice, in addition to short QT intervals, we observed ST-segment changes indicative of early repolarization that are similar to ECG findings in Brugada's syndrome<sup>8</sup> (Fig. 3b, arrows). Our data suggest that *Klf15*-dependent transcriptional regulation of rhythmic *KChIP2* expression in murine hearts plays a central part in rhythmic variation in ventricular repolarization.

Next, we examined whether excessive prolongation or shortening of repolarization could alter arrhythmia susceptibility and survival. *Klf15*-null mice show no spontaneous arrhythmias on ECG telemetry, hence we used intracardiac programmed electrical stimulation to examine arrhythmia susceptibility. In contrast to wild-type mice, a marked increase in occurrence of ventricular arrhythmias was seen in *Klf15*-null mice (Fig. 4a). Notably, *Klf15*-Tg mice exhibit spontaneous ventricular arrhythmias on ECG telemetry (Fig. 4b) and succumb to ~35% mortality by 4 months of age (three out of eight deaths in *Klf15*-Tg versus no deaths out of eight in wild-type non-transgenic controls, data not shown). As the *Klf15*-null mice show no evidence of overt ventricular dysfunction, apoptosis or fibrosis<sup>16,17</sup> in the basal state, the enhanced susceptibility to arrhythmias is probably primarily driven by

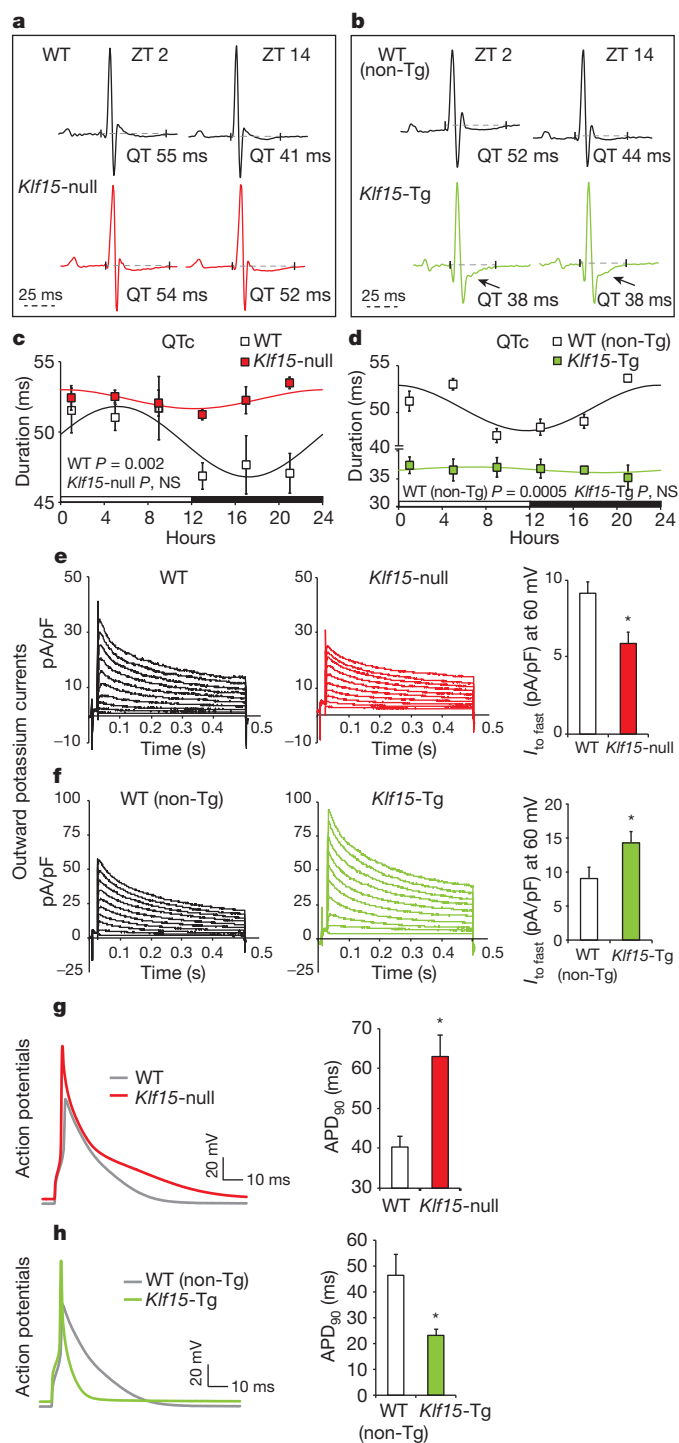


**Figure 3 | Deficiency or excess of *Klf15* modulates rhythmic variation in repolarization.** **a, b**, Representative ECGs from wild-type versus *Klf15*-null mice, and wild-type (non-Tg) versus *Klf15*-Tg mice at ZT2 and ZT14. Note the ST-segment abnormalities in *Klf15*-Tg mice (arrows). **c**, QTc interval exhibits 24-h rhythm in wild-type mice; this rhythm is abrogated with prolonged QTc in the dark phase in *Klf15*-null mice ( $n = 4$  for wild type,  $n = 4$  for *Klf15*-null). **d**, *Klf15*-Tg mice exhibit persistently short QT intervals with no day–night rhythmic variation compared to wild-type (non-Tg) controls ( $n = 3$  for wild type,  $n = 4$  for *Klf15*-Tg). **e, f**, Representative outward current recordings from all study groups and summary data for the amplitude of  $I_{to \text{ fast}}$  measured at 60 mV with an average time of decay of  $45 \pm 5$  ms ( $n = 10$  for wild type,  $n = 13$  for *Klf15*-null;  $n = 14$  for wild type (non-Tg), and  $n = 19$  for *Klf15*-Tg). **g, h**, Representative ventricular action potentials from all study groups with summary data in bar graphs ( $n = 10$  for wild type,  $n = 13$  for *Klf15*-null;  $n = 14$  for wild type (non-Tg), and  $n = 19$  *Klf15*-Tg). Error bars, mean  $\pm$  s.e.m.,  $*P < 0.05$ . APD<sub>90</sub>, action potential duration measured at 90% repolarization.



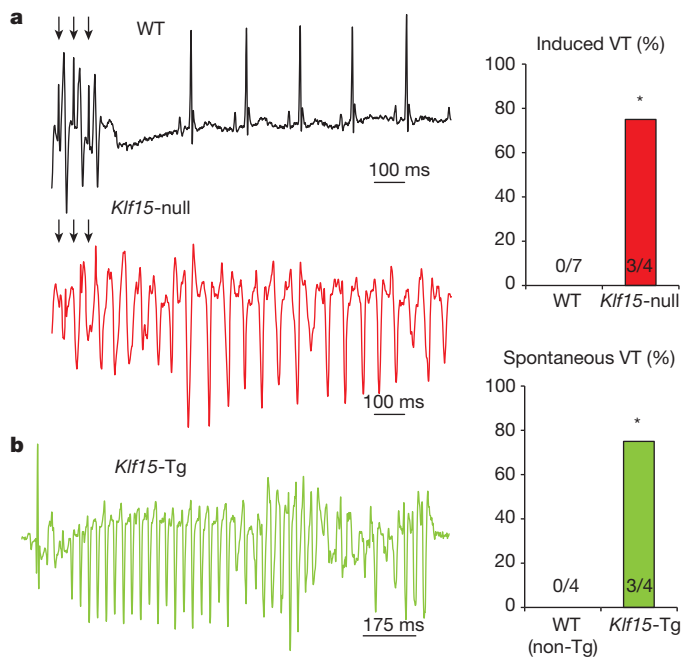


**Figure 4 | *Klf15* deficiency or excess increases susceptibility to ventricular arrhythmias.** **a**, Programmed electrical stimulation in wild-type and *Klf15*-null mice. Onset of ventricular tachycardia after premature stimuli is shown (arrows) in *Klf15*-null mice (none of the seven wild-type mice were inducible but three of the four *Klf15*-null mice were inducible; \* $P < 0.05$ ). **b**, Spontaneous ventricular arrhythmia in *Klf15*-Tg mice. (none of the four wild-type mice exhibited spontaneous arrhythmias but three of the four *Klf15*-Tg mice exhibited ventricular arrhythmias; \* $P < 0.05$ ). VT, ventricular tachycardia.

abnormalities in repolarization. Our studies demonstrate that both deficiency and excess of *Klf15* impair temporal variation in cardiac repolarization and greatly increase susceptibility to arrhythmias.

Although our finding of circadian control of KChIP2 by *Klf15* establishes the principle that circadian rhythms may contribute to arrhythmogenesis, we note that *Klf15* minimally affects *Kcnd2* expression that also exhibits circadian rhythm (Fig. 1f). However, *Kcnd2* expression was disrupted in *Bmal1*-null and *Per2*- and *Cry1*-null hearts, and this is indicative of a direct regulation by the circadian clock (Supplementary Fig. 12). Consistent with this observation, cardiomyocytes from *Bmal1*-null mice exhibit marked action potential prolongation due to near-complete elimination of the fast component of the transient outward potassium current (Supplementary Fig. 13). This raises the possibility that additional factors—perhaps components of the circadian clock or unidentified transcriptional regulators—may also affect temporal variation in electrophysiological parameters and arrhythmogenesis. Future studies in cardiac-specific deletion of clock components would be necessary to confirm whether the ion channel rhythms are cell autonomous, and their role in regulating cardiac electrophysiology.

Our study provides the first mechanistic link between endogenous circadian rhythms and the cardiac electrical instability that is most often associated with sudden cardiac death in humans (Supplementary Fig. 14). Specifically, we show that *Klf15*-dependent rhythmic transcription of *KChIP2* regulates the duration and pattern of repolarization and susceptibility to arrhythmias in mice. As the occurrence of sudden cardiac death in acquired and hereditary forms of human heart disease follows a distinct diurnal pattern<sup>1,2</sup>, these observations offer new insights into unrecognized triggers of electrical instability in the heart. However, in contrast to murine repolarization, which is largely dependent on  $I_{to}$ , human repolarization occurs through a complex interaction of multiple repolarizing ionic currents. Thus, additional studies will be needed to develop a comprehensive understanding of the link between the circadian clock and electrophysiological properties

of the human heart. Nevertheless, these data may provide a mechanistic foundation for future efforts to prevent or treat cardiac arrhythmias by modulating the circadian clock through behavioural or pharmacological means.

## METHODS SUMMARY

Mice used in the present study, messenger RNA quantification using polymerase chain reaction with reverse transcription (RT-PCR), promoter reporter analysis, western immunoblot analysis, chromatin immunoprecipitation, telemetry ECG and interval analysis, isolated myocyte studies for action potential or  $I_{to}$  measurements, *in vivo* electrophysiological studies for arrhythmia susceptibility, cosinor analysis for rhythm assessment, and statistical methods are detailed in the Methods.

**Full Methods** and any associated references are available in the online version of the paper at [www.nature.com/nature](http://www.nature.com/nature).

Received 31 March 2011; accepted 12 January 2012.

Published online 22 February 2012.

- Muller, J. E. *et al.* Circadian variation in the frequency of sudden cardiac death. *Circulation* **75**, 131–138 (1987).
- Matsuo, K. *et al.* The circadian pattern of the development of ventricular fibrillation in patients with Brugada syndrome. *Eur. Heart J.* **20**, 465–470 (1999).
- Goldenberg, I. & Moss, A. J. Long QT syndrome. *J. Am. Coll. Cardiol.* **51**, 2291–2300 (2008).
- Patel, U. & Pavri, B. B. Short QT syndrome: a review. *Cardiol. Rev.* **17**, 300–303 (2009).
- Tomaselli, G. F. & Marban, E. Electrophysiological remodeling in hypertrophy and heart failure. *Cardiovasc. Res.* **42**, 270–283 (1999).
- Antzelevitch, C. Role of spatial dispersion of repolarization in inherited and acquired sudden cardiac death syndromes. *Am. J. Physiol. Heart Circ. Physiol.* **293**, H2024–H2038 (2007).
- Kuo, H. C. *et al.* A defect in the Kv channel-interacting protein 2 (KChIP2) gene leads to a complete loss of  $I_{to}$  and confers susceptibility to ventricular tachycardia. *Cell* **107**, 801–813 (2001).
- Antzelevitch, C. & Yan, G. X. J wave syndromes. *Heart Rhythm* **7**, 549–558 (2010).
- Reppert, S. M. & Weaver, D. R. Coordination of circadian timing in mammals. *Nature* **418**, 935–941 (2002).
- Bexton, R. S., Vallin, H. O. & Camm, A. J. Diurnal variation of the QT interval— influence of the autonomic nervous system. *Br. Heart J.* **55**, 253–258 (1986).
- Kong, T. Q. Jr, Goldberger, J. J., Parker, M., Wang, T. & Kadish, A. H. Circadian variation in human ventricular refractoriness. *Circulation* **92**, 1507–1516 (1995).
- Martino, T. A. & Sole, M. J. Molecular time: an often overlooked dimension to cardiovascular disease. *Circ. Res.* **105**, 1047–1061 (2009).
- Paschos, G. K. & FitzGerald, G. A. Circadian clocks and vascular function. *Circ. Res.* **106**, 833–841 (2010).
- Durgan, D. J. & Young, M. E. The cardiomyocyte circadian clock: emerging roles in health and disease. *Circ. Res.* **106**, 647–658 (2010).
- Yamashita, T. *et al.* Circadian variation of cardiac  $K^+$  channel gene expression. *Circulation* **107**, 1917–1922 (2003).
- Halder, S. M. *et al.* *Klf15* deficiency is a molecular link between heart failure and aortic aneurysm formation. *Sci. Transl. Med.* **2**, 26ra26 (2010).
- Wang, B. *et al.* The Krüppel-like factor KLF15 inhibits connective tissue growth factor (CTGF) expression in cardiac fibroblasts. *J. Mol. Cell. Cardiol.* **45**, 193–197 (2008).

**Supplementary Information** is linked to the online version of the paper at [www.nature.com/nature](http://www.nature.com/nature).

**Acknowledgements** We thank A. F. Connors Jr for support, M. Mustar for illustrations, Y. Cui for experimental assistance, and members of the Jain laboratory for discussions. Funding sources: Heart Rhythm Society Fellowship (D.J.); National Institutes of Health grants HL094660 (D.J.), HL066991 (M.D.M.), HL086614 (S.M.H.), American Heart Association postdoctoral grant (N.S.), HL089598, HL091947 (X.H.W.), HL76446 (S.A.S.), HL102241 (K.H.), HL054807 (D.S.R.), HL075427, HL076754, HL084154, HL086548 and HL097595 (M.K.J.); Swiss National Science Foundation grants 31003A/131086 (U.A.) and M01-RR02635 (B.W.H.); Leducq Foundation grants of the ENAFRA Network 07CVD03 (S.D.); and the Centre National de la Recherche Scientifique (S.D.).

**Author Contributions** D.J. and M.K.J. designed the research; D.J., S.M.H., X.W., M.D.M., J.A.R., Y.L., B.L.E. and M.J.C. carried out the experiments; J.G., A.S., J.R. and R.V.K. contributed critical reagents; D.J., N.S., S.D., R.V.K., S.A.S., U.A., X.H.T.W., D.S.R. and M.K.J. supervised the research; D.J., S.M.H., X.W., M.D.M., J.A.R., K.H., B.L.E., E.F., S.A.S., U.A., X.H.T.W., D.S.R. and M.K.J. analysed and interpreted the data; and D.J. and M.K.J. wrote the manuscript.

**Author Information** Reprints and permissions information is available at [www.nature.com/reprints](http://www.nature.com/reprints). The authors declare no competing financial interests. Readers are welcome to comment on the online version of this article at [www.nature.com/nature](http://www.nature.com/nature). Correspondence and requests for materials should be addressed to M.K.J. (mukesh.jain2@case.edu) or D.J. (darwinjeyaraj@gmail.com).

## METHODS

**Mice.** All animal studies were carried out with permission, and in accordance with, animal care guidelines from the Institutional Animal Care Use Committee (IACUC) at Case Western Reserve University and at collaborating facilities. Wild-type male mice on C57BL6/J background (Jackson Laboratory) were bred in our facility and used for circadian studies. Mice were housed under strict light–dark conditions (lights on at 6:00 and lights off at 18:00) and had free access to standard chow and water, and were minimally disturbed for 4–6 weeks before the final experiment. Generation of systemic *Klf15*-null mice was as described previously<sup>18</sup>. *Klf15*-null mice have been backcrossed into the C57BL6/J background for over ten generations<sup>18</sup> and the BMAL1 mice were bred as previously described<sup>19</sup>. For *Klf15*-Tg mice, Flag-KLF15 was cloned downstream of an attenuated  $\alpha$ -myosin heavy-chain promoter as previously described<sup>20</sup>. This construct was injected into FVB (friend leukemia virus B mouse strain) oocytes, and after germline transmission the mice were examined for expression of the transgene. Wild-type (non-Tg) littermates served as controls. For light–dark experiments, mice were killed with CO<sub>2</sub> inhalation or isoflurane every 4 h for 24 h. For constant dark experiments, mice were placed in complete darkness for 36 h (starting at the end of light phase at ZT12) and hearts were collected every 4 h over a 24-h period.

**RNA isolation and RT-PCR analysis.** After euthanasia, hearts were collected, washed in cold phosphate buffered saline, the atria removed and the ventricles dissected to the apical and basal regions, and flash frozen in liquid nitrogen. RNA was isolated from the apical regions of frozen heart samples by homogenization in Trizol reagent (Invitrogen) by following the manufacturer's instructions (Invitrogen). RNA was reverse transcribed after DNase treatment (New England Biolabs). RT-PCR was performed using locked nucleic acid (LNA)-based TaqMan approach with primers and probes designed, and their efficiency tested, at the Universal Probe Library (Roche), and with  $\beta$ -actin used as the normalizing gene.

**Cell-culture studies.** Neonatal rat ventricular myocytes were isolated from 1–2-day-old rat pups and grown under standard conditions<sup>18</sup>. Adenoviral overexpression was performed for 24 h and myocytes were then collected for mRNA and protein analysis. For synchronization, the myocytes were starved in media containing insulin, transferrin and selenium (ITS supplement, Sigma-Aldrich) for 48 h. After this, the myocytes were synchronized with 50% horse serum for 30 min, washed twice with no-serum media and replenished with ITS-containing media. The mouse *Klf15* promoter (approximately 5 kb) was cloned into PGL3-basic (Promega). The rat *KChIP2* luciferase was a gift from P. H. Backx. Mutant constructs of rat *KChIP2* luciferase were generated by PCR-based TOPO cloning (Invitrogen), and site-directed mutagenesis was performed using Quikchange II mutagenesis kit (Agilent Technologies) and confirmed by sequencing. *Klf15* and *KChIP2* luciferase studies were conducted in NIH3T3 cells, and luciferase activity was normalized to protein concentration.

**Western immunoblot analysis.** For detecting Flag-KLF15, nuclear lysates were prepared using the NE-PER kit following manufacturer's instructions (Thermo Scientific) and probed with anti-Flag antibody (Sigma). For *KChIP2* analysis, whole-cell lysates were prepared by homogenizing the basal regions of the hearts in buffer containing Tris-HCl (50 mM, pH 7.4), NaCl (150 mM), NP-40 (1%), sodium deoxycholate (0.25%), EDTA (1 mM), and supplemented with protease and phosphatase inhibitors (Roche). The blots were probed with a mouse monoclonal antibody against *KChIP2* (NIH Neuromab), normalized to tubulin (Sigma-Aldrich) and quantified using Quantity One software (Bio-Rad).

**ChIP.** ChIP was performed with hearts as previously described<sup>21,22</sup>. In brief, hearts were fixed with fresh 1.11% formaldehyde for 10 min, and then by chromatin preparation and sonication (Diagenode). The sonicated chromatin was immunoprecipitated using BMAL1 or Flag antibody bound to Dynabeads (Invitrogen). The relative abundance was normalized to abundance of 28S between the input and immunoprecipitated samples as previously described<sup>21</sup>. Primers that were used for BMAL1 ChIP on the *Klf15* promoter were; forward, 5'-GCCTG AGCATCCTCCCCATCA-3'; reverse, 5'-GGGGCCACCTCTCTGGACTT-3'; and probe, 5'-FAM-CCCGCCAGTGACCATGTCTGCCTGT-3'-BHQ1. Non-target primers were; forward, 5'-GCCAATTCACATTTCACCA-3'; reverse, 5'-GACACAAGGCATTTCAA-3'; and probe, 5'-FAM-TGCAAGGGCTGGA CATGGG-3'-BHQ1. Primers that were used for ChIP of Flag-KLF15 on the *KChIP2* promoter were; forward, 5'-GCTCCGCTCTCACTTGCT-3'; and reverse, 5'-GGCTGGCAAGGCTTTTCT-3'.

**Telemetry ECG and interval analysis.** Mice were implanted with telemetry devices (ETA F20, Data Sciences International) and allowed to recover for at least 2 weeks. ECGs were recorded from conscious mice continuously in their native environment and digital data (PhysioTel, Data Sciences International) were stored for future analysis. Owing to rapid changes in the mouse heart rates, a weighted heart-rate approach was used to assess rhythmic changes in QT interval, and measurements were made every 2 h over a 24-h period. First, the average heart rate was calculated for each hour by digital tracking of the ECG RR intervals (time

interval between two consecutive R waves) using the Dataquest analysis software (Data Sciences International). Then, during the first instance within each hour when the average heart rate was present, the QT interval was measured using electronic calipers from two consecutive beats. The QT interval was corrected for heart rate using a previously validated formula for conscious mice  $QT/(RR/100)^{1/2}$  (ref. 23). A Cosinor model was applied to assess the 24-h rhythm in QT using a sinusoidal regression function and raw data presented in four hourly blocks for visualization purposes.

**Electrophysiological studies in myocytes.** Murine ventricular myocytes were isolated using a standard enzymatic dispersion technique following overnight fast as previously described<sup>24</sup>. Myocytes were re-suspended in media 199, allowed to recover and recordings were conducted within several hours on the same day. The conventional whole-cell mode was used to record action potentials and  $I_{to}$ . In brief, myocytes were bathed in a chamber that was continuously perfused with Tyrode's solution of the following composition (in mmol l<sup>-1</sup>): NaCl, 137; KCl, 5.4; CaCl<sub>2</sub>, 2.0; MgSO<sub>4</sub>, 1.0; glucose, 10; and HEPES, 10 (pH 7.35). Patch pipettes (0.9–1.5 M $\Omega$ ) were filled with electrode solution composed of (in mmol l<sup>-1</sup>): aspartic acid, 120; KCl, 20; NaCl, 10; MgCl<sub>2</sub>, 2; and HEPES, 5 (pH 7.3). Action potentials were elicited in current-clamp mode by injection of a square pulse of current of 5 ms duration and 1.5–2 times the threshold amplitude. APD was measured at 90% repolarization. To measure  $I_{to}$ , cells were placed in Tyrode's solution (as described earlier) containing 1  $\mu$ M nifedipine to block calcium current and calcium-activated chloride current, and tetrodotoxin (100  $\mu$ M l<sup>-1</sup>) to block sodium current. Cells were brought from a holding potential of -70 mV to -25 mV for 25 ms. To isolate the fast, transient component of the outward currents,  $I_{to fast}$ , the decay phase of outward potassium currents was fit by the exponential functions of the form:

$$y(t) = A_1 \exp(-t/\tau_1) + A_2 \exp(-t/\tau_2) + A_{ss}$$

where  $\tau_1$  is the time constant of decay of the fast, transient component of outward potassium currents;  $A_1$  is the amplitude coefficient of  $I_{to fast}$ ;  $\tau_2$  is the time constant of decay of the slow, transient component of the outward currents;  $A_2$  is the amplitude of  $I_{to slow}$ ; and  $A_{ss}$  is the amplitude coefficient of the non-inactivating steady-state outward potassium current  $I_{ss}$ . Consistent with previous studies<sup>25</sup>, the time constant of decay of the fast, transient component  $I_{to fast}$  was  $46 \pm 5$  ms. The measured current amplitudes were normalized to cell capacitance and converted into current densities. All experiments were conducted at 36 °C. Cell capacitance and series resistance were compensated electronically at ~80%. Command and data acquisition were operated with an Axopatch 200B patch-clamp amplifier controlled by a personal computer using a Digidata 1200 acquisition board driven by pCLAMP 7.0 software (Axon Instruments).

**Programmed electrical stimulation.** Intracardiac programmed electrical stimulation was performed as previously described<sup>26</sup>. In brief, mice were anaesthetized using 1.5% isoflurane in 95% O<sub>2</sub> after an overnight fast. ECG channels were amplified (0.1 mV cm<sup>-1</sup>) and filtered between 0.05 and 400 Hz. A computer-based data acquisition system (Emka Technologies) was used to record a 3-lead body surface ECG, and up to four intracardiac bipolar electrograms. Bipolar right atrial pacing and right ventricular pacing were performed using 2-ms current pulses delivered by an external stimulator (STG-3008, MultiChannel Systems; Reutlingen). Standard clinical electrophysiologic pacing protocols were used to determine all basic electrophysiologic parameters. Overdrive pacing, single, double and triple extrastimuli, as well as ventricular burst pacing, were delivered to determine the inducibility of ventricular arrhythmias, which was tested twice.

**Statistical analysis.** A cosinor model was adopted to determine whether there is a substantial 24-h rhythm in each physiological and molecular variable of interest. By pooling data points of all mice, the model fits data to a fundamental sinusoidal function<sup>27</sup>. To determine the coefficients (amplitude and phase) of the sinusoidal function and to see whether there were significant relationships, a mixed model analysis of variance was performed using standard least-square regression and the restricted maximum likelihood method (JMP 8.0, SAS Institute) as previously described<sup>28</sup>. Data are presented as mean  $\pm$  s.e.m., the Student's *t*-test was used for assessing the difference between individual groups and  $P \leq 0.05$  was considered statistically significant.

18. Fisch, S. *et al.* Krüppel-like factor 15 is a regulator of cardiomyocyte hypertrophy. *Proc. Natl Acad. Sci. USA* **104**, 7074–7079 (2007); correction **104**, 13851 (2007).
19. Bunger, M. K. *et al.* Mop3 is an essential component of the master circadian pacemaker in mammals. *Cell* **103**, 1009–1017 (2000).
20. Sanbe, A. *et al.* Reengineering inducible cardiac-specific transgenesis with an attenuated myosin heavy chain promoter. *Circ. Res.* **92**, 609–616 (2003).
21. Tuteja, G., Jensen, S. T., White, P. & Kaestner, K. H. Cis-regulatory modules in the mammalian liver: composition depends on strength of Foxa2 consensus site. *Nucleic Acids Res.* **36**, 4149–4157 (2008).
22. Ripperger, J. A. & Schibler, U. Rhythmic CLOCK-BMAL1 binding to multiple E-box motifs drives circadian *Dbp* transcription and chromatin transitions. *Nature Genet.* **38**, 369–374 (2006).

23. Mitchell, G. F., Jeron, A. & Koren, G. Measurement of heart rate and Q-T interval in the conscious mouse. *Am. J. Physiol.* **274**, H747–H751 (1998).
24. Libbus, I., Wan, X. & Rosenbaum, D. S. Electrotonic load triggers remodeling of repolarizing current  $I_{to}$  in ventricle. *Am. J. Physiol. Heart Circ. Physiol.* **286**, H1901–H1909 (2004).
25. Wagner, S. *et al.* Ca/calmodulin kinase II differentially modulates potassium currents. *Circ. Arrhythm. Electrophysiol.* **2**, 285–294 (2009).
26. van Oort, R. J. *et al.* Ryanodine receptor phosphorylation by calcium/calmodulin-dependent protein kinase II promotes life-threatening ventricular arrhythmias in mice with heart failure. *Circulation* **122**, 2669–2679 (2010).
27. Nelson, W., Tong, Y. L., Lee, J. K. & Halberg, F. Methods for cosinor-rhythmometry. *Chronobiologia* **6**, 305–323 (1979).
28. Hu, K., Scheer, F. A., Laker, M., Smales, C. & Shea, S. A. Endogenous circadian rhythm in vasovagal response to head-up tilt. *Circulation* **123**, 961–970 (2011).



# Sequencing of neuroblastoma identifies chromothripsis and defects in neuritogenesis genes

Jan J. Molenaar<sup>1\*</sup>, Jan Koster<sup>1\*</sup>, Danny A. Zwiijnenburg<sup>1</sup>, Peter van Sluis<sup>1</sup>, Linda J. Valentijn<sup>1</sup>, Ida van der Ploeg<sup>1</sup>, Mohamed Hamdi<sup>1</sup>, Johan van Nes<sup>1</sup>, Bart A. Westerman<sup>1</sup>, Jennemiek van Arkel<sup>1</sup>, Marli E. Ebus<sup>1</sup>, Franciska Haneveld<sup>1</sup>, Arjan Lakeman<sup>1</sup>, Linda Schild<sup>1</sup>, Piet Molenaar<sup>1</sup>, Peter Stroeken<sup>1</sup>, Max M. van Noesel<sup>2</sup>, Ingrid Øra<sup>1,3</sup>, Evan E. Santo<sup>1</sup>, Huib N. Caron<sup>4</sup>, Ellen M. Westerhout<sup>1</sup> & Rogier Versteeg<sup>1</sup>

Neuroblastoma is a childhood tumour of the peripheral sympathetic nervous system. The pathogenesis has for a long time been quite enigmatic, as only very few gene defects were identified in this often lethal tumour<sup>1</sup>. Frequently detected gene alterations are limited to *MYCN* amplification (20%) and *ALK* activations (7%)<sup>2–5</sup>. Here we present a whole-genome sequence analysis of 87 neuroblastoma of all stages. Few recurrent amino-acid-changing mutations were found. In contrast, analysis of structural defects identified a local shredding of chromosomes, known as chromothripsis, in 18% of high-stage neuroblastoma<sup>6</sup>. These tumours are associated with a poor outcome. Structural alterations recurrently affected *ODZ3*, *PTPRD* and *CSMD1*, which are involved in neuronal growth cone stabilization<sup>7–9</sup>. In addition, *ATRX*, *TIAMI* and a series of regulators of the Rac/Rho pathway were mutated, further implicating defects in neuritogenesis in neuroblastoma. Most tumours with defects in these genes were aggressive high-stage neuroblastomas, but did not carry *MYCN* amplifications. The genomic landscape of neuroblastoma therefore reveals two novel molecular defects, chromothripsis and neuritogenesis gene alterations, which frequently occur in high-risk tumours.

Neuroblastoma have a highly variable clinical outcome, with an excellent prognosis for stage 1 and 2 tumours, but a poor outcome for high-stage tumours. Stage 4S neuroblastoma are metastasized but nevertheless undergo spontaneous regression. Low-stage tumours are marked by numeric changes of chromosomal copy numbers, whereas high-stage tumours typically show structural chromosomal defects resulting in, for example, hemizygous deletions of the chromosomal regions 1p36 or 11q and gain of 17q (refs 1, 10–12). Age at diagnosis above 1.5 year is associated with high-stage tumours and poor outcome.

We performed whole-genome paired-end sequencing as used by Complete Genomics<sup>13</sup> for 87 untreated primary neuroblastoma tumours of all stages (Supplementary Table 1) and their corresponding lymphocyte DNAs. All samples had a minimal tumour content of 80% as determined by immunohistochemical analysis. Genomes were sequenced at an average coverage of 50 and an average fully called genome fraction of 96.6% (Supplementary Table 2). Compared to the HG18 reference genome we obtained an average of 3,347,592 single-nucleotide variants (SNVs) per genome, in accordance with reported frequencies of interpersonal variants. CGAtools was used to compare tumour with lymphocyte genomes and provided a somatic score estimating the likelihood of mutations to be somatic (<http://cgatools.sourceforge.net/docs/1.3.0/>). Validation of 1,014 candidate somatic small mutations (SNVs, substitutions, insertions, deletions), including 763 SNVs, established a specificity of 88% and a sensitivity of 85% at a somatic score cut-off of 0.1 (Supplementary Fig. 1a). SNVs above this score and all validated SNVs with lower scores were used for further

analyses (total 586 genes, Supplementary Table 3). The sequence data identified an average of 12 somatic candidate amino-acid-affecting mutations per tumour (Fig. 1a and Supplementary Fig. 1b). The frequency of somatic events strongly correlated to tumour stage where stage 1, 2 and 4S tumours have very few mutations compared to stage 3 and 4 tumours (analysis of variance (ANOVA)  $P = 7.6 \times 10^{-6}$ ; Fig. 1b). In addition mutation frequencies were strongly correlated to overall survival (log-rank  $P = 9.8 \times 10^{-7}$ ; Fig. 1c) and age at diagnosis ( $r = 0.53$ ,  $P = 1.1 \times 10^{-7}$ ; Fig. 1d), as was also observed in medulloblastoma<sup>14</sup>. Within high-stage neuroblastoma, *MYCN* amplification status did not correlate to mutation frequency (Supplementary Fig. 1c).

Only very few recurrent mutations were identified. *ALK* mutations were found in 6% of the tumours, in accordance with frequencies established in large neuroblastoma tumour series (Supplementary Table 4)<sup>2–5</sup>. Three tumours carried mutations in *TIAMI*, a known regulator of cytoskeleton organization and neuritogenesis<sup>15</sup>. In a parallel study we sequenced four primary neuroblastoma tumours as well as cell lines derived from these tumours and their metastases. This revealed that primary tumours are already heterogeneous for mutations and that the large majority of them were passenger or late mutations (J.J.M. *et al.*, submitted). Together with the lack of recurrent mutations, our data indicate that neuroblastoma carry few early somatic tumour-driving mutations with amino-acid-changing consequences.

Analysis of the paired-end clones with discordant ends can be used to identify candidate structural rearrangements, which together with sequence coverage data can identify somatic structural variants (SVs). Comparison of tumour versus lymphocyte coverage generated ultra-high-resolution comparative genomic hybridization (CGH)-like profiles (Supplementary Fig. 2a). Analysis of the frequency of structural variations per chromosome revealed ten tumours with chromothripsis characteristics<sup>6</sup> (see Methods). Chromothripsis is a localized shredding of a chromosomal region and subsequent random reassembly of the fragments. An extreme example of chromothripsis in chromosome 5 is shown in Fig. 2a and 2b (for other cases see Supplementary Fig. 2b). The neuroblastoma with chromothripsis were associated with a poor prognosis (log-rank test  $P = 7.1 \times 10^{-3}$ ; Fig. 2c). They were found in 18% of the stage 3 and 4 neuroblastoma, but not in low-stage tumours (Fisher's exact test  $P = 0.01$ ). Accordingly, their prognostic impact is not independent of age and stage in multivariate analyses. Chromothripsis-related structural aberrations frequently affected genes involved in neuroblastoma pathogenesis and were associated with amplification of *MYCN* or *CDK4* and loss of heterozygosity of 1p (Supplementary Fig. 2c). In one tumour, chromothripsis resulted in amplification and very strong overexpression of *MYC* (*c-Myc*) (Supplementary Fig. 2d). Chromosome 5 had undergone chromothripsis in three tumours, but no clear tumorigenic target on this chromosome

<sup>1</sup>Department of Oncogenomics, Academic Medical Center, Meibergdreef 9, 1105 AZ Amsterdam, The Netherlands. <sup>2</sup>Department of Pediatric Oncology-Hematology, Erasmus MC-Sophia Children's Hospital, 3015 GJ Rotterdam, The Netherlands. <sup>3</sup>Department of Pediatric Oncology and Hematology, Skåne University Hospital, Lund University, 221 85 Lund, Sweden. <sup>4</sup>Department of Pediatric Oncology, Emma Children's Hospital, Academic Medical Center, 1105 AZ Amsterdam, the Netherlands.

\*These authors contributed equally to this work.

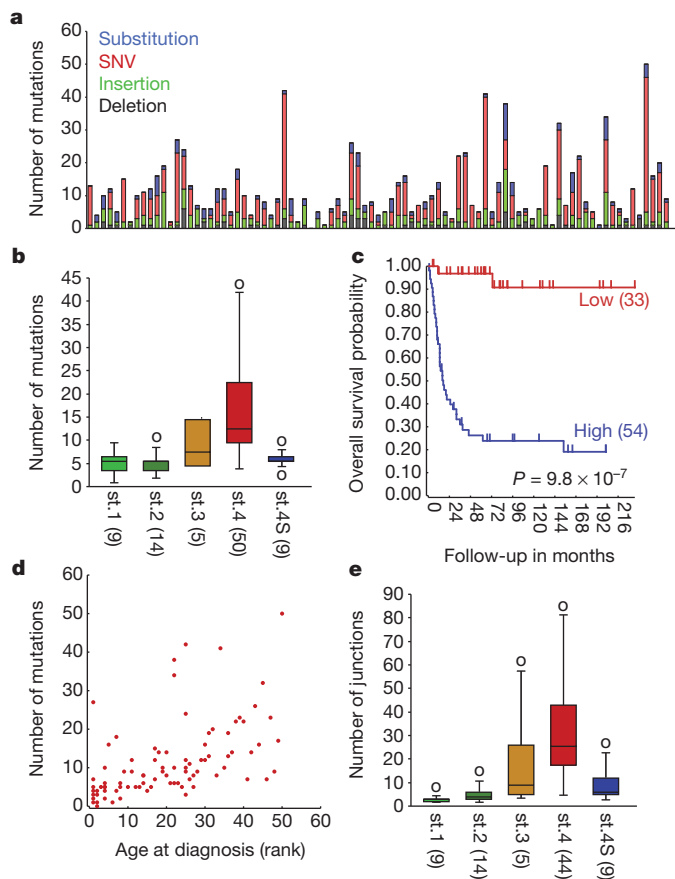


**Figure 1 | Frequency of amino-acid-changing somatic mutations in neuroblastoma correlates with age, stage and survival.** **a**, The number of amino-acid-changing mutations in 87 primary neuroblastoma (single nucleotide variants (SNVs) in red, deletions in grey, insertions in green and substitutions affecting more than 1 base pair (Sub) in blue). Numbers shown are events after CGAtools CallDiff with somatic scores  $>0.1$  and not present in dbSNP130, nor in 46 reference genomes released by Complete Genomics. **b**, Average number of mutations per tumour stage (International Neuroblastoma Staging System (INSS) stage 1,  $n = 9$ ; stage 2,  $n = 14$ ; stage 3,  $n = 5$ ; stage 4,  $n = 50$  and stage 4S,  $n = 9$ ). Boxes include 50% of data and error bars indicate extremes with a maximum of two times the box size. st., stage. **c**, Kaplan-Meier curves for tumours with high versus low frequency of mutations. The optimal cut-off level for the categories was determined by Kaplan scanning (see Supplementary Information and Methods). The significance (log-rank test) was corrected for the multiple testing (Bonferroni correction). Number of patients per group is shown in parentheses. **d**, Age at diagnosis (rank-order) versus the number of somatic variants. **e**, Average number of structural variations per tumour stage (INSS). Group sizes and the definition of the error bars as in Fig. 1b.

was identified. To identify genetic defects that allowed chromothripsis and subsequent survival of the cell, we searched for defects in DNA damage response pathways in tumours with chromothripsis. The most extreme case of chromothripsis (N492, Fig. 2a and 2b) showed an inactivating deletion in *FANCM* and another chromothripsis tumour sample (N576) had a missense mutation in *FANL*, predicted to be damaging by the polyphen2 program<sup>16</sup>. These findings might suggest involvement of inactivating events in the Fanconi anaemia signalling pathway to allow chromothripsis<sup>17</sup>.

Full genome paired-end sequencing allowed us to identify structural variants specifically perturbing single genes (see Methods and Supplementary Fig. 4 for selection procedure). We detected a total of 451 genes harbouring structural variants (306 genes without the events on chromothripsis chromosomes, Supplementary Tables 5 and 6). The structural variants often consisted of deletions of one or a few exons, inversions or translocations deleting part of a gene. One tumour showed

an intrachromosomal rearrangement activating *FOXRI* transcription (Supplementary Fig. 2e), which we recently identified as a recurrent but rare event in neuroblastoma<sup>18</sup>. Similar to the findings for amino-acid-changing mutations, there was a strong relation between the frequency of structural variations and the tumour stage (one-way ANOVA  $P = 0.03$ ; Fig. 1e), which extends the well-established relationship between tumour stage and structural chromosomal defects in neuroblastoma<sup>10–12</sup>. Breakpoints identifying deletions were supported by changes in coverage plots. Most of the structural variants affected only one allele of a gene (Supplementary Table 5). This indicates that the tumour-driving mechanism of these defects is haploinsufficiency, possibly combined with epigenetic attenuation of the non-affected allele. On average, genes with structural variants resulting in loss of coverage indeed showed a reduced expression in tumours with these defects, as compared to tumours with normal alleles (Supplementary Fig. 2f). As an additional validation, we generated SNP arrays of 52 of the sequenced tumours. Although the SNP data have a much lower resolution than the sequence coverage plots, they supported the deletions and gains of sufficient size. This is especially evident on plots of chromothripsis samples (Supplementary Fig. 2g).

To identify relevant genes and pathways that contribute to neuroblastoma pathogenesis, we generated one list of all genes with amino-acid changing mutations ( $n = 586$ ), mutations in splice junctions ( $n = 37$ ) and structural variations ( $n = 451$ ). The total of 1,041 genes with alterations were analysed by two approaches. First, we analysed the most frequently affected genes (Supplementary Table 7). Four genes belonged to the *MYCN* amplicons (*MYCN*, *MYCNOS*, *DDX1* and *NBAS*) and except for *MYCN* probably play no role in pathogenesis. Three genes, *PTPRD*, *ODZ3* and *ATRX*, showed structural variants in five tumours each (Fig. 3a and Supplementary Fig. 3a) and 61 genes showed alterations in two to four tumours (Supplementary Table 7). A conservative randomization, taking the length of all genes and the structure of our data set into account, showed that the chance of finding three genes affected in five or more tumours is  $<2.11 \times 10^{-4}$  (see Methods). This strongly indicates that at least the defects in *PTPRD*, *ATRX* and *ODZ3* did not accumulate due to for example, the genomic length of the genes, but that they were selected for during the process of tumorigenesis.

The X-chromosome-encoded *ATRX* gene was affected by structural variants in five tumours (Fig. 3a). In two male patients this resulted in complete inactivation of the gene. Frequent *ATRX* defects were recently found in pancreatic neuroendocrine tumours<sup>19</sup>. *ATRX* is a chromatin remodelling protein involved in exchange of H3.3 in GC-rich repeats and mutations of this gene are associated with X-linked mental retardation<sup>20</sup>. Exon mRNA profiles of part of the sequenced series showed that the three samples included with *ATRX* structural variations had the lowest *ATRX* mRNA expression of all samples and showed a specific collapse of the signal in the deleted regions, illustrating the inactivating nature of the *ATRX* defects (Fig. 3b and Supplementary Fig. 3b).

*ODZ3* and *PTPRD* were also hit by structural variations in five tumours each (Supplementary Fig. 3a). One tumour showed homozygous inactivation of *ODZ3* (see legends of Supplementary Fig. 3a). In addition, *ODZ2* and *ODZ4*, two highly homologous members of the conserved *ODZ* family, were together affected three times. *PTPRD* and *ODZ* genes encode transmembrane receptors expressed in the developing nervous system and localizing to axons and axonal growth cones<sup>21</sup>. Targeted silencing of *ODZ* homologues in *Drosophila*, *Caenorhabditis elegans* and mouse caused severe axon guidance defects<sup>9</sup>. Overexpression of *ODZ2* in neuroblastoma cells enhanced neuritogenesis<sup>22</sup>. *PTPRD* is a member of the LAR subfamily of receptor protein tyrosine phosphatases. Transgenic mouse models strongly implicate the LAR subfamily receptors in neuritogenesis<sup>8</sup>. *PTPRD* defects in neuroblastoma were reported previously<sup>23</sup>. Low expression of *ODZ3* and of *PTPRD* as assessed by mRNA profiling were both associated with a poor prognosis (log-rank  $P = 3.1 \times 10^{-4}$  and  $P = 5.7 \times 10^{-3}$ , respectively; Supplementary Fig. 3a). Interestingly,

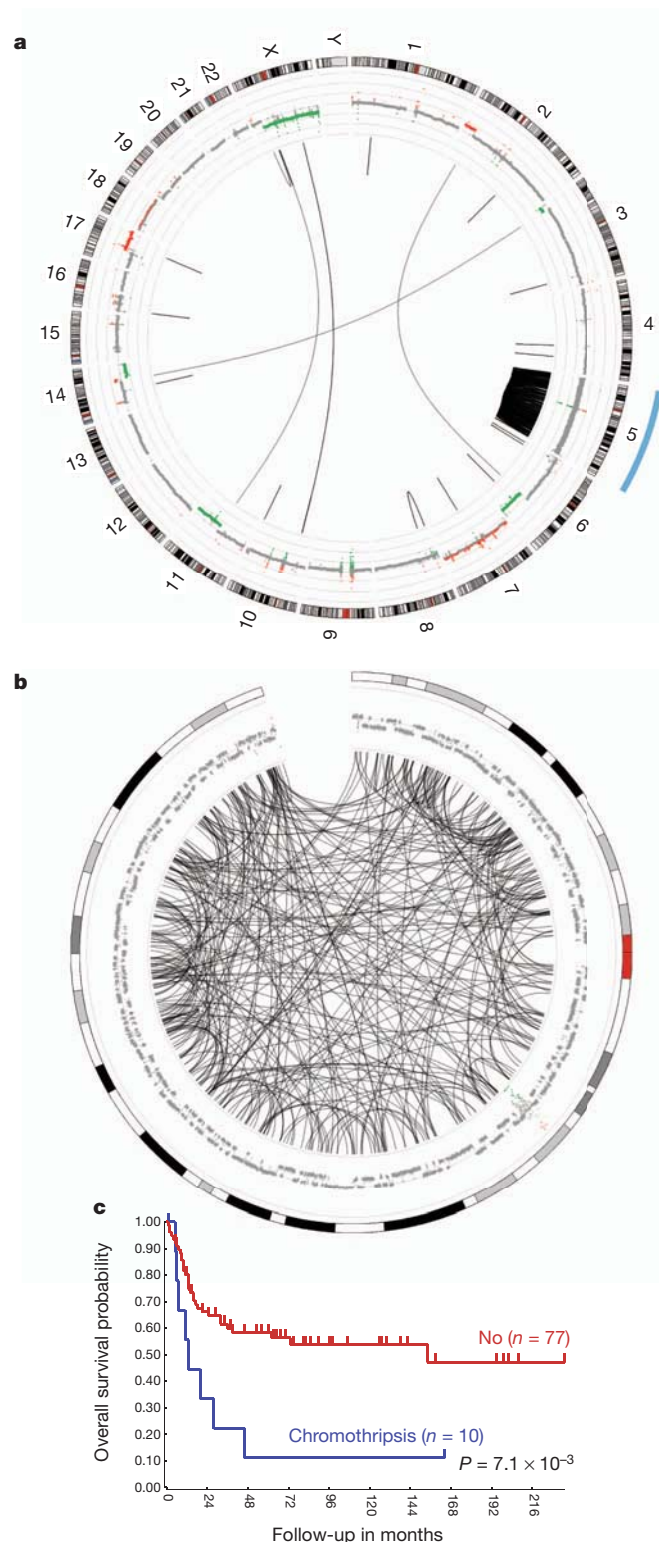


**Figure 2 | Chromothripsis is frequent in neuroblastoma and is associated with a poor prognosis.** **a**, Circos plot showing structural variations in sample N492. The inner ring represents the copy number variations (red, gain; green, loss) based on coverage of the tumour and lymphocyte genomes. The lines traversing the ring indicate inter- and intrachromosomal rearrangements identified by discordant mate pairs from paired-end reads. N492 is a chromothripsis sample with an extreme amount of junctions on chromosome 5. **b**, Circos plot of the affected chromosome 5 in sample N492. **c**, Kaplan–Meier curves of the overall survival for tumours with or without chromothripsis. Numbers of patients per group are shown between brackets.

*CSMD1*, which showed structural variants in three tumours, is also a transmembrane protein expressed on nerve growth cones<sup>7</sup>. As the frequencies of *PTPRD* and *ODZ3* defects exclude that they were found by chance, we propose that the function of these genes and of *ODZ2*, *ODZ4* and *CSMD1* in neuronal growth cones might hold a clue to their function in neuroblastoma pathogenesis.

The second analysis that we performed for the list for 1,041 affected genes was a gene ontology study to identify enrichment of genes with defects in specific molecular processes. The gene ontology category ‘regulation of GTPase activity’ was the most significantly enriched group (Bonferroni corrected for multiple testing:  $P = 6.7 \times 10^{-4}$ ; see supplementary methods and Supplementary Table 9). This finding urged us to further investigate GTPase-regulating genes in the list. *TIAM1* was mutated in three tumours (see Supplementary Table 4). It functions as a guanine nucleotide exchange factor (GEF) for the small GTPase Rac and is, together with Rac, central to regulation of cellular polarity and neuritogenesis<sup>24,25</sup>. The W1285S\* mutation creates a premature stop-codon in the carboxy-terminal pleckstrin homology domain required for Rac activation, whereas the other mutations were predicted to be damaging by polyphen2 analysis<sup>16</sup>. Rac is activated by GEFs and inactivated by GTPase activating proteins (GAPs)<sup>26</sup> (Fig. 4). We identified a total of eight alterations in six GEFs specific for Rac (including *TIAM1*), but none in GAPs specific for Rac (Supplementary Tables 7, 8 and 10 for functional consequences). Whereas activation of Rac1 stimulates neuritogenesis, activation of its small GTPase antagonist RhoA promotes axon retraction and growth cone collapse (Fig. 4a)<sup>15</sup>. Strikingly, we detected seven alterations in five GAPs for RhoA, but only one GEF specific for RhoA (*ARHGEF12*) showed a translocation with unknown functional consequences (Fig. 4a, Supplementary Tables 7, 8 and 10 for functional consequences). The bias for inactivation of GAPs for Rho and GEFs for Rac is highly significant (one-sided Fischer’s exact test:  $P < 0.0007$ ).

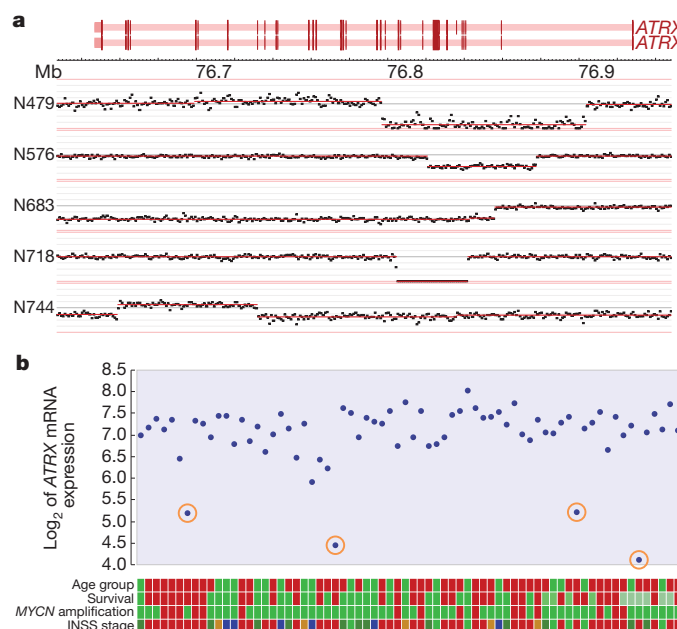


**Figure 3 | Structural variations in *ATRX* result in low mRNA expression levels.** **a**, Coverage plots displaying the structural variations in the *ATRX* gene. The dots indicate summed coverage for bins of 1,000 base pairs of the tumour genome, normalized to the coverage in corresponding normal tissue. The intron–exon structure of *ATRX* is shown in red (dark red are exons). **b**, *ATRX* mRNA expression of 70 tumours as measured on Affymetrix full-exon arrays. Tumours with *ATRX* deletions are encircled. Coloured tracks below figure, from top to bottom: age at diagnosis (green < 1.5 year, red > 1.5 year); survival (red, dead; dark green, alive > 5 year; light green, alive < 2 year); *MYCN* amplification (red, yes; green, no); stage (light green, stage 1; dark green, stage 2; brown, stage 3; red, stage 4; blue, stage 4S).



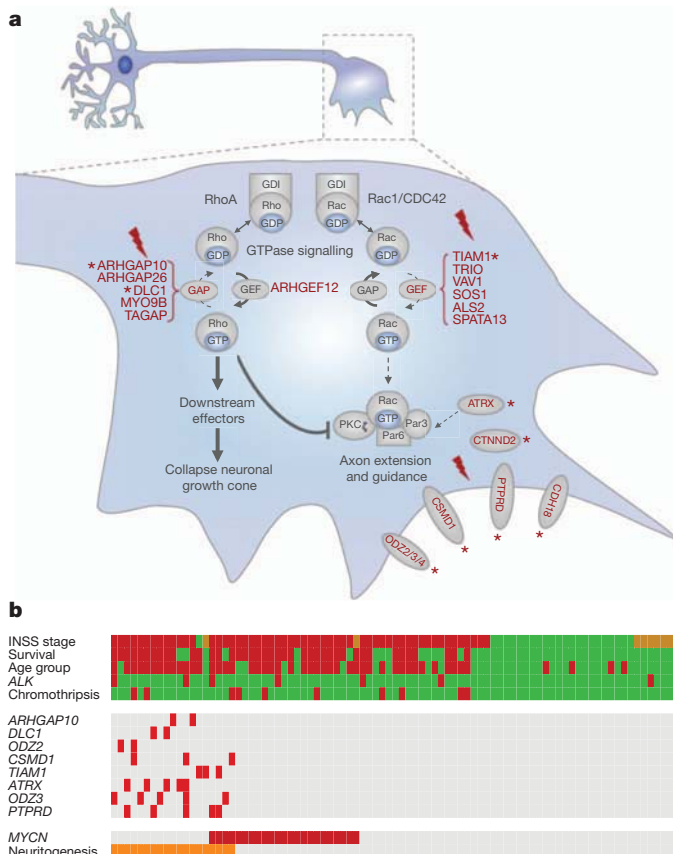


**Figure 4 | Neuroblastoma with genomic defects in neuritogenesis genes cluster in high-risk tumours.** **a**, Diagram of a neurite growth cone depicting the function of the proteins encoded by genes with genomic aberrations in neuritogenesis. Red proteins have defects (for references see Supplementary Table 8). Rac and Rho small GTPases cycle between an inactive GDP-bound and active GTP-bound conformation, transducing signals from a wide variety of membrane receptors. They are activated by GEFs and inactivated by GAPs. Guanine nucleotide dissociation inhibitors (GDIs) sequester GDP-bound GTPases. Proteins with aberrations in more than one tumour are marked with an asterisk (\*). **b**, Diagram of genetic defects and clinical parameters of all 87 sequenced neuroblastoma. Each vertical lane summarizes one tumour. Patients are sorted by the presence of genomic aberrations in neuritogenesis genes (Neuritogenesis,  $n = 19$ ), by *MYCN* amplification (*MYCN*,  $n = 23$ ), and by INSS stage (high to low). Clinical and molecular genetic characteristics are shown for each tumour as tracks: INSS stage (green, stage 1 and 2; red, stage 3 and 4; orange, stage 4S); Survival (red, death; green, alive), Age group (green,  $<1.5$  year; red,  $\geq 1.5$  year), *ALK* (red, mutated; green, wild type), Chromothripsis (red, yes; green, no). Middle panel, amino-acid-changing mutations and structural variations are indicated for all genes having two or more events and that are involved in neuritogenesis (red, mutated or structural variant; grey, not affected).

This indicates that alterations in GTPase-regulating genes specifically function to activate Rho or inactivate Rac, which both tip the balance in Rac/Rho signalling towards inhibition of neuritogenesis. Of note, transgenic mice with *ATRX* mutations causing mental retardation in humans showed abnormal dendritic spine formation with increased *TIAM1* phosphorylation and Rac1 signalling<sup>27</sup>.

We conclude that alterations with significant frequencies (*PTPRD* and *ODZ* genes) affect transmembrane receptors that function in neuronal growth cone guidance and maintenance. In addition gene ontology analysis of the 1,041 genes showed significant enrichment of GTPase-regulating genes. Alterations in GEFs for Rac and GAPs for Rho significantly deviate from a random distribution, implicating inhibition of Rac1 and activation of RhoA in impairing neuritogenesis in neuroblastoma (Fig. 4a).

From these findings we propose that defects in neuritogenesis-regulating genes form an important category of tumour-driving events

in neuroblastoma. For a preliminary analysis of tumours with these defects, we selected the genes with recurrent defects in tumours that function in neuronal growth cones (*PTPRD*, *ODZ3*, *ODZ2*, *CSMD1*) or regulation of these processes through Rac/Rho signalling (*TIAM1*, *DLC1*, *ARHGAP10*, *ATRX*). The 19 tumours with defects in these genes were almost all stage 3 and 4 tumours diagnosed above 1.5 year of age with an aggressive clinical course. Only few of them showed amplification of *MYCN* (Fig. 4b). Consistent with their occurrence in high-stage neuroblastoma, defects in neuritogenesis genes did not show an independent prognostic power in multivariate analysis with the clinical parameters age and stage.

Here we report the first whole-genome sequence study of a comprehensive series of neuroblastoma including both low- and high-stage tumours. Low-stage neuroblastoma lacked recurrent gene alterations (mutations and structural variations), raising the question whether they are primarily driven by chromosomal imbalances and the consequent gene dosage effects. Tumours with defects in genes functioning in neuritogenesis or growth cone guidance mostly are aggressive high-stage tumours without *MYCN* amplification. Interestingly, there is indication that *MYCN* also inhibits neuritogenesis in neuroblastoma. *MYCN* downregulates the mRNA expression of the chromosome 1p36 gene *CDC42*, which resulted in inhibition of neuritogenesis of neuroblastoma cells<sup>28</sup>. *CDC42* is a small GTPase protein with a function similar to Rac1. Rac1 and *CDC42* both regulate the Par3–Par6 complex (also known as PARD3–PARD6A) involved in cell polarization and growth cone development and which has been shown to drive neuroblastoma cell differentiation<sup>25</sup>. In light of our data demonstrating genomic alterations in Rho/Rac signalling, it is tempting to postulate that the Par3–Par6 complex is a recurrent target for inactivation in neuroblastoma. Intriguingly, the block in neuritogenesis of neuroblastoma is probably not absolute. Retinoic acid can induce neuronal outgrowth in many neuroblastoma cell lines, which all are derived from high-stage tumours. Retinoic acid is also used in long-term neuroblastoma treatment protocols to prevent recurrences<sup>29</sup>. It is currently unknown which tumours will clinically respond to retinoic acid therapy. Deletions of *NF1* were previously implicated in retinoic acid resistance of neuroblastoma cell lines<sup>30</sup>. The identification of genomic alterations in a range of genes mediating neuritogenesis now allows investigation of therapeutic modalities to surmount these defects.

## METHODS SUMMARY

All neuroblastoma samples were derived from primary tumours of untreated patients. Tumour material was obtained during surgery and a portion was immediately frozen in liquid nitrogen. We used leukocytes derived from peripheral blood for isolation of constitutional DNA. High-molecular-weight DNA was extracted from tumour tissue and leukocytes using standard procedures. Fifteen microgram of DNA was subjected to paired-end whole-genome sequencing according to the Complete Genomics technology. Initial data analyses were performed using the CGATools v1.3.0 package (<http://cgatools.sourceforge.net/docs/1.3.0/>) and for subsequent analysis and figure preparation we used the R2 bioinformatic platform (<http://r2.amc.nl>) and PERL scripts. More details on mutation analysis, coverage analysis, analysis of structural variants and the Circos plots is given in the Supplementary Information. Gene expression was assayed on Affymetrix EXON ST 1.0 GeneChips. SNP genotyping microarray analysis details are described in the supplementary information. Mutation validations were performed using Sanger sequencing (Supplementary Information). Statistical analysis (gene ontology enrichment using the Cytoscape BINGO plugin, DAVID functional ontology cluster analysis and analysis for gene length enrichment) are described in the Methods.

**Full Methods** and any associated references are available in the online version of the paper at [www.nature.com/nature](http://www.nature.com/nature).

Received 6 November 2011; accepted 3 February 2012.

Published online 22 February 2012.

1. Maris, J. M. Recent advances in neuroblastoma. *N. Engl. J. Med.* **362**, 2202–2211 (2010).
2. Mossé, Y. P. *et al.* Identification of *ALK* as a major familial neuroblastoma predisposition gene. *Nature* **455**, 930–935 (2008).

3. George, R. E. *et al.* Activating mutations in ALK provide a therapeutic target in neuroblastoma. *Nature* **455**, 975–978 (2008).
4. Chen, Y. *et al.* Oncogenic mutations of ALK kinase in neuroblastoma. *Nature* **455**, 971–974 (2008).
5. Janoueix-Lerosey, I. *et al.* Somatic and germline activating mutations of the ALK kinase receptor in neuroblastoma. *Nature* **455**, 967–970 (2008).
6. Stephens, P. J. *et al.* Massive genomic rearrangement acquired in a single catastrophic event during cancer development. *Cell* **144**, 27–40 (2011).
7. Kraus, D. M. *et al.* CSMD1 is a novel multiple domain complement-regulatory protein highly expressed in the central nervous system and epithelial tissues. *J. Immunol.* **176**, 4419–4430 (2006).
8. Sun, Q. L. *et al.* Growth cone steering by receptor tyrosine phosphatase delta defines a distinct class of guidance cue. *Mol. Cell. Neurosci.* **16**, 686–695 (2000).
9. Zheng, L. *et al.* *Drosophila* Ten-m and filamin affect motor neuron growth cone guidance. *PLoS ONE* **6**, e22956 (2011).
10. Chen, Q. R. *et al.* cDNA array-CGH profiling identifies genomic alterations specific to stage and MYCN-amplification in neuroblastoma. *BMC Genomics* **5**, 70 (2004).
11. Vandesompele, J. *et al.* Multicentre analysis of patterns of DNA gains and losses in 204 neuroblastoma tumors: how many genetic subgroups are there? *Med. Pediatr. Oncol.* **36**, 5–10 (2001).
12. Janoueix-Lerosey, I. *et al.* Overall genomic pattern is a predictor of outcome in neuroblastoma. *J. Clin. Oncol.* **27**, 1026–1033 (2009).
13. Drmanac, R. *et al.* Human genome sequencing using unchained base reads on self-assembling DNA nanoarrays. *Science* **327**, 78–81 (2010).
14. Parsons, D. W. *et al.* The genetic landscape of the childhood cancer medulloblastoma. *Science* **331**, 435–439 (2011).
15. Leeuwen, F. N. *et al.* The guanine nucleotide exchange factor Tiam1 affects neuronal morphology; opposing roles for the small GTPases Rac and Rho. *J. Cell Biol.* **139**, 797–807 (1997).
16. Adzhubei, I. A. *et al.* A method and server for predicting damaging missense mutations. *Nature Methods* **7**, 248–249 (2010).
17. Kee, Y. & D'Andrea, A. D. Expanded roles of the Fanconi anemia pathway in preserving genomic stability. *Genes Dev.* **24**, 1680–1694 (2010).
18. E. E. & Santo, et al. I. Oncogenic activation of FOXR1 by 11q23 intrachromosomal deletion-fusions in neuroblastoma. *Oncogene* advance online publication doi:10.1038/nc.2011.344 (22 August 2011).
19. Jiao, Y. *et al.* DAXX/ATRX, MEN1, and mTOR pathway genes are frequently altered in pancreatic neuroendocrine tumors. *Science* **331**, 1199–1203 (2011).
20. Law, M. J. *et al.* ATR-X syndrome protein targets tandem repeats and influences allele-specific expression in a size-dependent manner. *Cell* **143**, 367–378 (2010).
21. Arregui, C. O., Balsamo, J. & Lilien, J. Regulation of signaling by protein-tyrosine phosphatases: potential roles in the nervous system. *Neurochem. Res.* **25**, 95–105 (2000).
22. Rubin, B. P. *et al.* Teneurins: a novel family of neuronal cell surface proteins in vertebrates, homologous to the *Drosophila* pair-rule gene product Ten-m. *Dev. Biol.* **216**, 195–209 (1999).
23. Stallings, R. L. *et al.* High-resolution analysis of chromosomal breakpoints and genomic instability identifies PTPRD as a candidate tumor suppressor gene in neuroblastoma. *Cancer Res.* **66**, 3673–3680 (2006).
24. Matsuo, N. *et al.* Roles of STEF/Tiam1, guanine nucleotide exchange factors for Rac1, in regulation of growth cone morphology. *Mol. Cell. Neurosci.* **24**, 69–81 (2003).
25. Nishimura, T. *et al.* PAR-6–PAR-3 mediates Cdc42-induced Rac activation through the Rac GEFs STEF/Tiam1. *Nature Cell Biol.* **7**, 270–277 (2005).
26. Bar-Sagi, D. & Hall, A. Ras and Rho GTPases: a family reunion. *Cell* **103**, 227–238 (2000).
27. Shioda, N. *et al.* Aberrant calcium/calmodulin-dependent protein kinase II (CaMKII) activity is associated with abnormal dendritic spine morphology in the ATRX mutant mouse brain. *J. Neurosci.* **31**, 346–358 (2011).
28. Valentijn, L. J. *et al.* Inhibition of a new differentiation pathway in neuroblastoma by copy number defects of *N-myc*, *Cdc42*, and *nm23* genes. *Cancer Res.* **65**, 3136–3145 (2005).
29. Matthay, K. K. *et al.* Long-term results for children with high-risk neuroblastoma treated on a randomized trial of myeloablative therapy followed by 13-cis-retinoic acid: a children's oncology group study. *J. Clin. Oncol.* **27**, 1007–1013 (2009).
30. Hölzel, M. *et al.* NF1 is a tumor suppressor in neuroblastoma that determines retinoic acid response and disease outcome. *Cell* **142**, 218–229 (2010).

**Supplementary Information** is linked to the online version of the paper at [www.nature.com/nature](http://www.nature.com/nature).

**Acknowledgements** The research in this paper was supported by grants from the Villa Joep Foundation, KIKa, Tom Voûte Fund, and the Netherlands Cancer Foundation. We thank R. Tearle and G. Tyrell (Complete Genomics) for expert support and R. Volckmann, N. Hasselt, T. van Groningen, E. Dolman, K. Drabek and I. Dokter for their help.

**Author Contributions** J.J.M.: project coordination, data analysis, preparation of manuscript; J.K.: supervision bioinformatics, bioinformatic data analysis, preparation of manuscript; D.A.Z., P.M.: bioinformatic analysis; P.v.S.: sample preparation and wet lab validation management; L.J.V., M.H., J.v.N., B.A.W.: data analysis and validation; I.v.d.P.: sample preparation and validation; J.v.A., M.E.E., F.H., A.L., L.S., P.S.: data validation; M.M.v.N., H.N.C.: sample and patient data organisation/contribution; I.Ø.: SNP profiling, E.M.W., E.E.S.: data analysis and pathway concepts; R.V.: project supervision, data analysis, preparation of manuscript.

**Author Information** mRNA expression array data are deposited in the Gene Expression Omnibus at NCBI, under accession number GSE16476. The Sequence data has been deposited at the European Genome-phenome Archive (EGA, <http://www.ebi.ac.uk/ega/>), which is hosted by the EBI, under accession number EGAS00001000222. Reprints and permissions information is available at [www.nature.com/reprints](http://www.nature.com/reprints). This paper is distributed under the terms of the Creative Commons Attribution-Non-Commercial-Share Alike licence, and is freely available to all readers at [www.nature.com/nature](http://www.nature.com/nature). The authors declare no competing financial interests. Readers are welcome to comment on the online version of this article at [www.nature.com/nature](http://www.nature.com/nature). Correspondence and requests for materials should be addressed to R.V. ([r.versteeg@amc.uva.nl](mailto:r.versteeg@amc.uva.nl)) or J.J.M. ([jj.molenaar@amc.uva.nl](mailto:jj.molenaar@amc.uva.nl)).

## METHODS

**Small variants.** Variant selection procedure: Potential somatic variants were determined with the CallDiff method with somatic output within the CGAtools v1.3.0 package, maintained by Complete Genomics (<http://cgatools.sourceforge.net/docs/1.3.0/>). Every tumour or cell line sample was compared to its matched blood sample across the whole genome. The somatic score which is calculated tries to tease apart true somatic mutations from false somatic mutations (<http://cgatools.sourceforge.net/docs/1.3.0/>). The somatic output files were then filtered to those regions where coding sequences are defined for the UCSC reflat annotation (<http://hgdownload.cse.ucsc.edu/goldenPath/hg18/database/refFlat.txt> 2 August 2010), thereby removing discontinued genes from the original annotation of NCBI36.3. Subsequently, gene symbol, amino acid change and effect categories were extracted from gene-GSXXX-ASM.tsv files for all genomes and added as annotation to the somatic output results. Those variants that could not be annotated (new/updated genes) were annotated with custom PERL scripts where possible. All variants were annotated for their presence in dbSNP130 (<http://hgdownload.cse.ucsc.edu/goldenPath/hg18/database/snp130.txt>), as well as the presence within 37 public HapMap genomes released by complete genomics (<ftp://ftp2.completegenomics.com/>). SIFT ([http://sift.jcvi.org/www/SIFT\\_chr\\_coords\\_submit.html](http://sift.jcvi.org/www/SIFT_chr_coords_submit.html) NCBI36) and polyphen2 (<http://genetics.bwh.harvard.edu/pph2/bgi.shtml> NCBI36) scores were determined to assess potential impact for all the SNP variants. Variants, which are reported in dbSNP130, that were found in any of the normal blood samples or that were found within the public genomes from Complete Genomics were removed from the data set. Finally, variants which were found in genes that are not expressed in neuroblastoma, but do show expression in a series of 500 normal samples were removed (See Affymetrix expression analysis). **Somatic small variants trim-down.** CallDiff with somatic output was performed on all of the 87 tumour/lymphocyte pairs and processed. The number of events (split by deletion/insertion/substitution/SNP) were counted for the complete genome. Next, the somatic output files were filtered on those parts of the genome that are covered by amino-acid-encoding regions (based on the coding sequence (CDS) within the reflat file from the UCSC). In the next step, only those variants were kept that have an impact on the coding sequence (non-silent), do not occur in any of our normal samples, nor in any of the publicly available genomes from Complete Genomics, nor are present in dbSNP130. Finally, we filtered for the somatic score to be  $\geq 0.1$  (as determined by plotting of the Sanger sequence validation results as a function of somatic scores and total scores).

**Sanger sequencing.** High-molecular-weight DNA was extracted from tumour tissue and leukocytes using standard procedures<sup>31</sup>. Primers for PCR amplification were automatically designed by custom PERL scripts that execute the Primer3 software. PCR was performed using 20 ng of genomic DNA. Sanger sequencing was performed on a capillary sequencer using standard procedures.

**Complete Genomics comparative genomic hybridization (cgCGH) procedure.** First we determine the summed coverage (uniqueSequenceCoverage) in windows of 1,000 base pairs (measured on the reference genome) for the normal and the tumour sample (coverageRefScore files). Here we take the Integer(position/1,000) as the bin for any position and keep track of the sum. Then we determine the total coverage sums of the genome and normalize to this value, to remove differences in total coverage between samples. Subsequently we determine the  $\log(\text{tumour/genome})/\log(2)$  for every bin (1,000-bp window) and obtain a cgCGH profile that expresses the somatic changes of the respective tumour. As the profile is normalized to its own normal material, the most prominent sources of bias such as GC-content, and also per-person copy number variation characteristics are corrected for. We feed these results to the DNACopy algorithm as provided in R BioConductor to segment the information into blocks of similar characteristics and use these segments boundaries to store the information in an efficient way. cgCGH data was visualized within the embedded genome browser of R2 (<http://r2.amc.nl>).

**Circos plots.** Comparisons of somatic structural variants between tumour and lymphocyte genomes were performed with the JunctionDiff and Junction2Event tool from CGAtools (<http://cgatools.sourceforge.net/docs/1.4.0/>). These somatic events were filtered with the following criteria: events annotated as artefacts, footprints smaller than 70 bases, less than 10 discordant mate pairs, under-represented repeats, and presence in a set of v2.0 baseline genomes (as provided at the website of Complete Genomics (B36baseline-junctions.tsv)). cgCGH profiles and the remaining events were plotted with the Circos program (<http://www.circos.ca>).

**Chromothripsis.** Genomes were annotated as having chromothripsis-like characteristics when the sum of intra-chromosomal somatic junctions (as reported by JunctionDiff and filtered as above) within a single chromosome was larger or equal to 20. Focused amplified regions (cgCGH scores  $\geq 3$ ) within a chromosome were excluded from this sum. Using these characteristics, we annotated 10 out of the 87 patients as chromothripsis-like. Nine out of these patients were diagnosed with stage 4 neuroblastoma ( $P = 0.0392$  stage4 versus rest) and all 10 were present in

high-stage neuroblastoma ( $P = 0.0116$ ). Eight of these patient have died of the disease ( $P = 0.0413$ ; log-rank  $P = 7.1 \times 10^{-3}$ ).

**Affymetrix expression analysis (expressed genes).** To assess whether genes containing variants are expressed in neuroblastoma, we make use of a panel of neuroblastoma tumours (also including 53 of the sequenced tumours), classical neuroblastoma cell lines as well as recently generated patient derived cell lines ( $n = 119$  in total). All samples were derived from primary tumours of untreated patients. Material was obtained during surgery and immediately frozen in liquid nitrogen. The original sources for classical neuroblastoma cell lines can be found in ref. 32. Total RNA of neuroblastoma samples was extracted using TRIzol reagent (Invitrogen) according to the manufacturer's protocol. RNA concentration and quality were determined using the RNA 6000 nano assay on the Agilent 2100 Bioanalyzer (Agilent Technologies). Fragmentation of complementary RNA, hybridization to hg-u133 plus 2.0 microarrays and scanning were carried out according to the manufacturers protocol (Affymetrix). The data were deposited in the NCBI Gene Expression Omnibus (<http://www.ncbi.nlm.nih.gov/geo/>) under accession number GSE16476.

Affymetrix expression data from adult tumours were derived from the Expression Project for Oncology (ExpO) database from the International Genomics Consortium (IGC) (<http://www.intgen.org/expo.cfm>). Expression data on normal tissues was downloaded from GEO (GSE7307). The expression data were normalized with the MAS5.0 algorithm within the GCOS program of Affymetrix. Target intensity was set to 100. If more than one probe set was available for one gene the probe set with the highest expression was selected, considered that the probe set was correctly located on the gene of interest. For 101 patients (60 of the sequenced tumours), we have also generated Affymetrix Exon array data. The z-score of expression within this data set was used as a independent validation of structural variants annotated as deletions, where possible. All data were analysed using our in-house-developed R2 web application, which is freely accessible at <http://r2.amc.nl>.

**SNP array analysis.** SNP arrays were processed according to the manufacturer's recommendations with the Infinium II assay on Human370- and Human660-quadr arrays containing  $>370,000$  and  $>660,000$  markers, respectively, and run on the Illumina BeadStation (Swegene Centre for Integrative Biology, Lund University — SCIBLU, Sweden) according to the manufacturer's recommendations. Raw data were processed using Illumina's BeadStudio software suite (Genotyping module 3.0), producing report files containing normalized intensity data and SNP genotypes. Subsequently, log<sub>2</sub> ratio and B-allele frequency data were imported into the R2 web application for detailed analysis and comparison with the CGH and expression data.

**Selection procedure somatic small variants table.** We ran CallDiff with somatic output on all of the 87 tumour/lymphocyte pairs and processed the somatic output files as described in the small variants section earlier. Due to the low validation percentages of substitutions and insertions, these were removed from the table. Variants which were tested by Sanger sequencing and were all-reference or all-variant were removed from the table. Variants with somatic scores lower than 0.1 or of types insertion/substitution, but which were validated by Sanger sequencing, were maintained in the table. In addition, we determined the presence of somatic splice-site variants in the two bases surrounding exons as defined by the UCSC reflat data.

**Selection procedure somatic structural variant table.** Comparisons between tumour and lymphocyte genomes were performed with the JunctionDiff and Junction2Event tool from CGAtools. These somatic events were filtered with the following criteria: events annotated as artefacts, footprints smaller than 70 bases, less than 10 discordant mate pairs, under-represented repeats, and presence in a set of baseline genomes (as provided at the website of Complete Genomics (B36baseline-junctions.tsv)). Of the remaining entries, we kept the following events: exon\_bites where both ends of a junction are within the same gene, and in addition affect exonic sequence. Breaks by inversion, where both ends of a junction land within a gene, thereby damaging both genes, but leaving the genes in between unaffected. Potential fusion genes which are strand-matched, where both ends of a junction land within a gene, and the resulting end product fits in terms of orientation of both genes. Regions (deletions/(tandem) duplications) of up to 1 megabase, containing up to five genes which are expressed in neuroblastoma.

**Combination of small, splice and structural somatic variants table.** The small variant, structural variant and splice-site somatic tables were merged on the gene symbol, and unique tumour IDs were counted to obtain a final list of recurrent gene affecting variants.

**Kaplan scan.** Kaplan scanning was performed within R2 (<http://r2.amc.nl>). In short, for each gene or other numerical characteristic, R2 calculates the optimal cut-off expression level dividing the patients in a good and bad prognosis cohort. Samples within a data set are sorted according to the expression of the investigated gene and divided into two groups on the basis of a cut-off expression value. All



cut-off expression levels and their resulting groups are analysed for survival, with the provision that minimal group number is 8 (or any other user-defined value) samples. For each cut-off level and grouping, the log-rank (as described in ref. 33) significance of the projected survival is calculated. The best *P* value and corresponding cut-off value is selected. This cut-off level is reported and used to generate a Kaplan–Meier graph. The graph depicts the log-rank significance ('raw *P*'), as well as a *P* value corrected for the multiple testing (Bonferroni correction) of cut-off levels for each gene.

**Statistical analysis for gene ontology gene enrichment.** To investigate the possible role of the mutated genes we used the BinGO plugin<sup>34</sup> for the network visualization tool Cytoscape<sup>35</sup>. This tool assesses enrichment of gene ontology categories for a set of genes. The *P*-value assigned to the overrepresentation for a specific category is calculated through a hypergeometric test. Results are corrected for multiple testing. We used the set of 1,041 genes having a mutation or structural variation in one or more neuroblastoma tumours. In the more informative gene ontology categories (filter set to less than 500 genes per category); the 'regulation of GTPase activity' gene ontology category seemed to be the most significant. The DAVID online functional clustering tool<sup>36</sup> confirmed this analysis for the biological process gene ontology branch; the third cluster in the list contained the GTPase regulation category with an enrichment score of 1.44.

**Statistical significance of genes affected by amino-acid-changing mutations and structural variations.** We analysed the likelihood of finding defects in specific genes, or of finding defects in equal to/more than the number of affected patients. We therefore used the following randomization strategy: we started by counting the number of genes affected by structural variations, for every sample in our data set. Next, the genomic footprints (bases from start to the end of the RefSeq on the HG18 genome (UCSC refFlat August 2010)) were determined and merged to the largest possible span for every gene symbol. These stretches were fused to create an artificial sequence, with the length of all gene symbols combined. Within this artificial sequence, random nucleotide numbers were chosen and traced back to the corresponding gene symbols. This was done for each tumour sample separately, with the number of randomly selected nucleotides being identical to the number of structural defects identified in the actual (sequenced) tumour. An identical strategy was used for the CDS affecting amino-acid-changing mutations, where the length of the largest CDS (NCBI

RefSeq data set August 2010) per gene symbol has been used, to generate the artificial sequence.

In this way, we could generate artificial data sets, that most closely reflect the complexity of our sequenced sample set, including the spread in events, as well as the genomic footprints (size)/lengths of the CDS of all the different genes within the genome. We generated 109,000 artificial data sets, after which we created histograms to assess the null distributions for all genes, as well as the likelihood of finding combinations of recurrent events. The chance of finding any combination of three or more genes affected in five or more patients within our data set was 0.000211. Of note, this is a conservative estimation, as our real data set also included four frequently affected genes in the *MYCN* amplicon. The chance of affecting seven genes in five or more patients is much lower than  $10^{-5}$ . In addition, the chances of finding *ATRX*, *ODZ3* or *PTPRD* in five or more patients was  $<10^{-5}$ ,  $6.42 \times 10^{-5}$  and 0.00534, respectively.

**Statistical analysis for Rac/Rho GEF/GAP specificity.** To ascertain whether the ratio of mutations/structural variations in Rac-specific GEFs and Rho-specific GAPs was significantly different from expectation, we performed Fisher's exact test on the number of mutations in GAP and GEF with specificity for only Rac or Rho in our data set (one-sided Fisher's exact test,  $P = 0.0007$ ). We also pooled events in Rac-specific GEFs and Rho-specific GAPs together and tested whether they possessed more events than the pool of Rac-specific GAPs and Rho-specific GEFs (one-sided Fisher's exact test,  $P = 0.026$ ).

31. Molenaar, J. J., van Sluis, P., Boon, K., Versteeg, R. & Caron, H. N. Rearrangements and increased expression of cyclin D1 (CCND1) in neuroblastoma. *Genes Chromosom. Cancer* **36**, 242–249 (2003).
32. Thiele, C. J. In *Human Cell Culture* vol. 1 (ed. Masters, J.) 21–53 (1998).
33. Bewick, V., Cheek, L. & Ball, J. Statistics review 12: survival analysis. *Crit. Care* **8**, 389–394 (2004).
34. Maere, S., Heymans, K. & Kuiper, M. BiNGO: a Cytoscape plugin to assess overrepresentation of gene ontology categories in biological networks. *Bioinformatics* **21**, 3448–3449 (2005).
35. Smoot, M. E., Ono, K., Ruscheinski, J., Wang, P.-L. & Ideker, T. Cytoscape 2.8: new features for data integration and network visualization. *Bioinformatics* **27**, 431–432 (2011).
36. Huang, D. W., Sherman, B. T. & Lempicki, R. A. Systematic and integrative analysis of large gene lists using DAVID bioinformatics resources. *Nature Protocols* **4**, 44–57 (2008).

# The mechanism of OTUB1-mediated inhibition of ubiquitination

Reuven Wiener<sup>1</sup>, Xiangbin Zhang<sup>1</sup>, Tao Wang<sup>1†</sup> & Cynthia Wolberger<sup>1</sup>

Histones are ubiquitinated in response to DNA double-strand breaks (DSB), promoting recruitment of repair proteins to chromatin<sup>1</sup>. UBC13 (also known as UBE2N) is a ubiquitin-conjugating enzyme (E2) that heterodimerizes with UEV1A<sup>2</sup> (also known as UBE2V1) and synthesizes K63-linked polyubiquitin (K63Ub) chains at DSB sites in concert with the ubiquitin ligase (E3), RNF168 (ref. 3). K63Ub synthesis is regulated in a non-canonical manner by the deubiquitinating enzyme, OTUB1 (OTU domain-containing ubiquitin aldehyde-binding protein 1), which binds preferentially to the UBC13~Ub thiolester<sup>4</sup>. Residues amino-terminal to the OTU domain, which had been implicated in ubiquitin binding<sup>4</sup>, are required for binding to UBC13~Ub and inhibition of K63Ub synthesis<sup>5</sup>. Here we describe structural and biochemical studies elucidating how OTUB1 inhibits UBC13 and other E2 enzymes. We unexpectedly find that OTUB1 binding to UBC13~Ub is allosterically regulated by free ubiquitin, which binds to a second site in OTUB1 and increases its affinity for UBC13~Ub, while at the same time disrupting interactions with UEV1A in a manner that depends on the OTUB1 N terminus. Crystal structures of an OTUB1-UBC13 complex and of OTUB1 bound to ubiquitin aldehyde and a chemical UBC13~Ub conjugate show that binding of free ubiquitin to OTUB1 triggers conformational changes in the OTU domain and formation of a ubiquitin-binding helix in the N terminus, thus promoting binding of the conjugated donor ubiquitin in UBC13~Ub to OTUB1. The donor ubiquitin thus cannot interact with the E2 enzyme, which has been shown to be important for ubiquitin transfer<sup>6,7</sup>. The N-terminal helix of OTUB1 is positioned to interfere with UEV1A binding to UBC13, as well as with attack on the thiolester by an acceptor ubiquitin, thereby inhibiting K63Ub synthesis. OTUB1 binding also occludes the RING E3 binding site on UBC13, thus providing a further component of inhibition. The general features of the inhibition mechanism explain how OTUB1 inhibits other E2 enzymes<sup>4</sup> in a non-catalytic manner.

OTUB1 was previously identified as a K48 linkage-specific deubiquitinating enzyme that contains two distinct ubiquitin-binding sites (Fig. 1a): a distal site and a proximal site that includes the ~45 N-terminal residues of OTUB1 (ref. 5). These residues are important for OTUB1 inhibition of E2 activity<sup>4</sup> and are absent in OTUB2, which does not inhibit UBC13 (ref. 4). It was previously shown that binding of the covalent inhibitor, ubiquitin aldehyde (Ubal), to the distal ubiquitin-binding site of OTUB1 stimulates binding of ubiquitin vinyl sulfone to the N terminus<sup>5</sup>. Because the OTUB1 N terminus was implicated in binding to the donor ubiquitin in the UBC13~Ub conjugate<sup>4</sup>, we asked whether Ubal binding to OTUB1 could enhance inhibition of UBC13 by stimulating binding of the OTUB1 N terminus to the donor ubiquitin. The results (Fig. 1b) showed a marked enhancement of the ability of OTUB1 to suppress K63Ub synthesis, indicating that Ubal is an allosteric effector that increases the affinity of the OTUB1 N terminus for the ubiquitin in the UBC13~Ub thiolester. This prompted us to ask whether free ubiquitin binding to the OTUB1 distal site could similarly stimulate binding of OTUB1 to UBC13~Ub

conjugates. To test this, we generated a mixture of charged and uncharged UBC13(C87S), which forms a more stable UBC13~Ub oxyester, purified away the free ubiquitin, and performed pull-down assays with H<sub>6</sub>-OTUB1 in the presence and absence of added free ubiquitin. Remarkably, OTUB1 shows no preference for the charged UBC13~Ub in the absence of ubiquitin, whereas addition of 100  $\mu$ M free ubiquitin greatly enhances OTUB1 binding to UBC13~Ub, but not to uncharged UBC13 (Fig. 1c). By contrast, ubiquitin bearing hydrophobic patch mutations I44A, L8A or L8A/I44A/R42A (but not R42A alone) do not stimulate OTUB1 binding to UBC13~Ub like wild-type ubiquitin (Fig. 1c). The relative binding of OTUB1 to UBC13~Ub increases as the concentration of free ubiquitin is increased from 2 to 50  $\mu$ M (Supplementary Fig. 2). To verify that ubiquitin binding to the distal site of OTUB1 is important for inhibition of UBC13, we assayed the effect of distal site mutations, which were chosen based on structures of a covalent yeast Otu1-ubiquitin complex<sup>8</sup> and of human OTUB1 (ref. 9). Distal site substitutions F193W, F193R and H217W disrupted the ability of OTUB1 to inhibit polyubiquitination by UBC13~UEV1A (Fig. 1d) without affecting binding of OTUB1 to UBC13 (Supplementary Fig. 3). Taken together, our results indicate that the ability of OTUB1 to bind preferentially to the UBC13~Ub conjugate and inhibit ubiquitin transfer is allosterically regulated by free ubiquitin binding to the distal site of OTUB1 (Fig. 1a), which triggers capture of the conjugated ubiquitin in the OTUB1 proximal site.

Because ubiquitin aldehyde most probably enhances interactions between the OTUB1 N terminus and the donor ubiquitin in UBC13~Ub, we examined the effect of N-terminal deletions in OTUB1 to delimit the minimal fragment needed for binding and inhibition. Deletion of residues 1–15 has no effect on inhibition of K63Ub synthesis by UBC13~UEV1A (Fig. 1e) whereas deletion of 30, 37 or 41 residues significantly disrupts inhibition. The OTUB1 $\Delta$ 15 deletion similarly behaves like full-length OTUB1 in pull-downs with the UBC13~Ub conjugate whereas larger deletions exhibit defects (Supplementary Fig. 4), indicating that N-terminal residues 16–45 are sufficient for activity.

Because a UEV (ubiquitin E2 variant) must bind to UBC13 and position the acceptor ubiquitin for K63Ub synthesis to occur<sup>10</sup>, we asked whether OTUB1 could bind to UBC13 in the presence of UEV1A. In gel filtration assays using fluorescently labelled UEV1A, OTUB1 and uncharged UBC13 migrate as a ternary complex with UEV1A (Fig. 1f). To assay binding to charged UBC13, we generated a non-hydrolysable conjugate in which Ub with a carboxy-terminal G75C is covalently linked to the active-site cysteine of UBC13 with dichloroacetone (DCA)<sup>11</sup>. UEV1A binds to UBC13<sup>DCA</sup>~Ub but OTUB1-Ubal interferes with UEV1A binding to the UBC13<sup>DCA</sup>~Ub conjugate (Fig. 1g). By contrast, the N-terminal deletion, OTUB1 $\Delta$ 37, can still form a complex with UBC13<sup>DCA</sup>~Ub and labelled UEV1 in the presence of Ubal (Fig. 1h), indicating that the N terminus of OTUB1 competes with UEV binding when OTUB1 is bound to Ubal. We verified that free ubiquitin has a similar effect on UEV binding by

<sup>1</sup>Department of Biophysics and Biophysical Chemistry and the Howard Hughes Medical Institute, Johns Hopkins University School of Medicine, Baltimore, Maryland 21205, USA. <sup>†</sup>Present address: National Institute of Allergy and Infectious Diseases, Vaccine Research Center, 40 Convent Drive, Bethesda, Maryland 20892, USA.

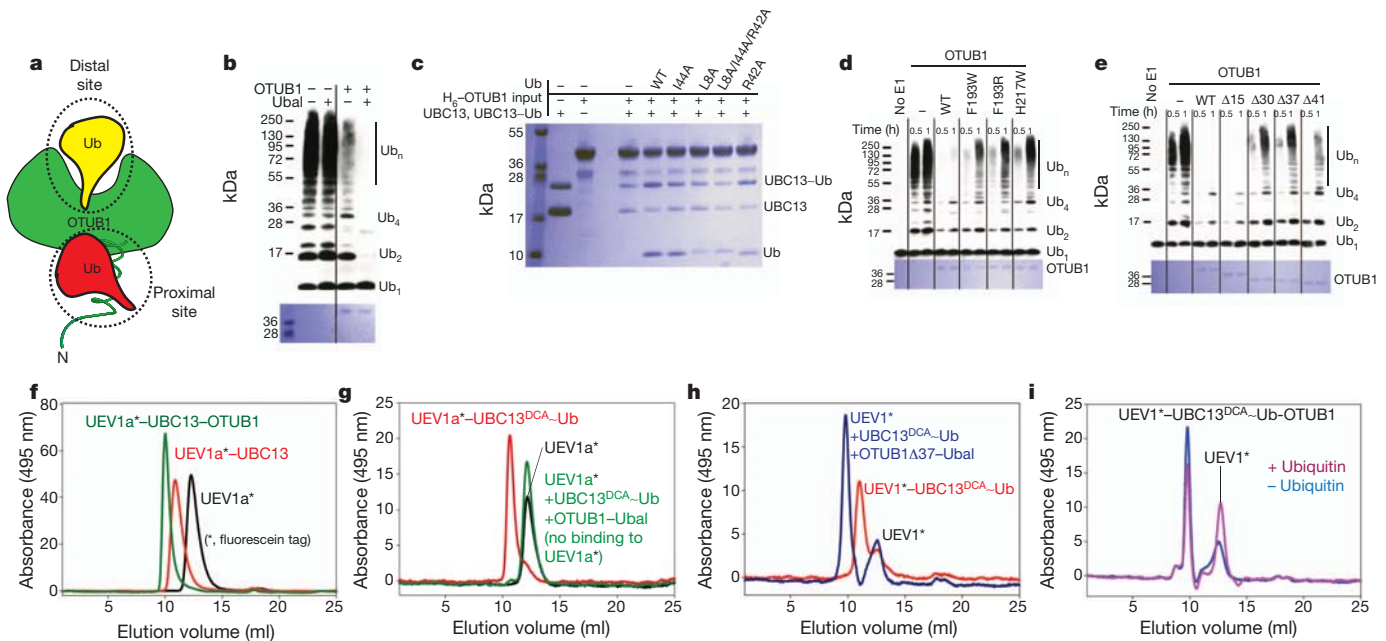


**Figure 1 | Allosteric regulation of OTUB1 by ubiquitin.** **a**, Schematic diagram of OTUB1 illustrating proximal and distal ubiquitin binding sites. **b**, Effect of ubiquitin aldehyde (Ubal) on the ability of human OTUB1 to inhibit K63 polyubiquitin synthesis by UBC13–UEV1A. Assays include 0.1  $\mu$ M E1, 0.4  $\mu$ M UBC13–UEV1A, 0.5  $\mu$ M human OTUB1, 5  $\mu$ M ubiquitin. The 3 h time point is shown in the presence (right) and absence (left) of human OTUB1, without (–) and with (+) 0.5  $\mu$ M Ubal. Top shows detection by anti-Ub western blot; Coomassie staining below shows level of human OTUB1. **c**, Pull-down assay showing binding of H<sub>6</sub>-tagged human OTUB1 to a mixture of UBC13 and UBC13~Ub oxyster in the presence and absence of 100  $\mu$ M free ubiquitin (wild type (WT) or mutant). **d**, Effect of human OTUB1 distal site mutations on inhibition of K63Ub synthesis. Assay performed as in **b** but with

comparing migration of a sample containing labelled UEV1, UBC13<sup>DCA</sup>~Ub and OTUB1 prepared in the presence and absence of free ubiquitin and found that the ratio of free UEV1 to UEV1–UBC13<sup>DCA</sup>~Ub–OTUB1 increases when ubiquitin is present (Fig. 1i). Similarly, pull-downs with H<sub>6</sub>–OTUB1 do not show an enhancement in coprecipitation of UEV1A along with UBC13~Ub in the presence of added free ubiquitin (Supplementary Fig. 5). These results indicate that the N terminus of OTUB1 interferes with UEV binding and thus with K63Ub synthesis, and that the ability of the N terminus to interfere with UEV depends upon a conformational change that is triggered by binding of free ubiquitin to OTUB1.

To determine the structural basis for OTUB1 inhibition of E2 enzymes, and how ubiquitin allosterically regulates OTUB1 activity, we determined the structure of *Caenorhabditis elegans* OTUB1 (worm OTUB1) bound to human UBC13 at 1.8 Å resolution (Fig. 2a), and a 2.35 Å resolution quaternary complex structure containing worm OTUB1, Ubal and a UBC13<sup>DCA</sup>~Ub conjugate generated with Ub(G76C). The resulting non-native linkage is four bond lengths longer than the native thioester (Supplementary Fig. 6). Human UBC13 is 89% identical to worm UBC13, whereas human OTUB1 shares 34% sequence identity and 56% similarity with worm OTUB1 (Supplementary Fig. 7) and inhibits K63Ub chain formation by human UBC13–UEV1A (Supplementary Fig. 8a). Worm OTUB1 is a weaker inhibitor of UBC13, as reflected in its higher  $K_d$  of 58.5  $\mu$ M compared to 7.04  $\mu$ M for human OTUB1 (Supplementary Fig. 8b). Crystals of the worm OTUB1–Ubal–UBC13<sup>DCA</sup>~Ub complex contain four complexes in the P2<sub>1</sub>2<sub>1</sub>2<sub>1</sub> asymmetric unit. The ubiquitin conjugated to UBC13 could be unambiguously positioned in two of the four complexes (Supplementary Fig. 9); our discussion focuses on the complex with the most well-ordered ubiquitin (complex 1). Because the N terminus of OTUB1 that plays a key role in inhibition is poorly conserved between

1  $\mu$ M OTUB1. **e**, Effect of human OTUB1 N-terminal deletions of 15, 30, 37 and 42 residues on inhibition of K63Ub synthesis by UBC13–UEV1A. Assay performed as in **d**. **f**, Gel filtration showing complex formation between fluorescein-labelled UEV1A (UEV1A\*), UBC13 and human OTUB1. Signal due to UEV1A only was monitored at 495 nm. **g**, Experiment performed as in **f** showing binding to UEV1A\* by UBC13<sup>DCA</sup>~Ub(G75C) in the absence (red) and presence (green) of OTUB1–Ubal. **h**, Experiment performed as in **f** but with human OTUB1 $\Delta$ 37. The position at which free UEV1\* migrates is indicated. **i**, Experiment performed as in **f** with fluorescein-labelled UEV mixed with UBC13<sup>DCA</sup>~Ub(G75C) and OTUB1 samples prepared in the presence and absence of 200  $\mu$ M ubiquitin. The position at which free UEV1\* migrates is indicated.

human and worm OTUB1, we also determined the 3.1 Å resolution structure of a quaternary complex with a hybrid OTUB1 containing the N-terminal 45 residues of human OTUB1 and the OTU domain of worm OTUB1 (Supplementary Fig. 7b). The hybrid human/worm OTUB1 inhibits K63Ub synthesis by UBC13–UEV1A (Supplementary Fig. 10). Details on all structure determinations are in Supplementary Methods and statistics are in Supplementary Table 1.

In the structure of apo worm OTUB1 bound to UBC13 (Fig. 2a), the OTU domain of worm OTUB1 binds to UBC13 in an orientation that places their respective active-site cysteines 28 Å apart on the same face of the complex, burying 1,280 Å<sup>2</sup> of total surface area. Of the 12 worm OTUB1 side chains at the interface with UBC13 (Fig. 2b), seven are identical in human OTUB1 and four are similar (Supplementary Fig. 7a) and can mediate comparable interactions with UBC13. Consistent with this, the double substitution Y170A/F138A in human OTUB1 (Y168A/F135A in worm OTUB1) is defective in binding to UBC13 (Supplementary Fig. 11). Similar interactions could form between OTUB1 and UBE2D2 (also known as UBCH5B) (Fig. 2c), but clashes due to an insertion and a non-conserved lysine would arise with UBE2L3 (also known as UBCH7), consistent with the observation that OTUB1 inhibits UBCH5B but not UBCH7 (ref. 4).

An overview of the human/worm OTUB1–Ubal–UBC13<sup>DCA</sup>~Ub complex is shown in Fig. 2d, e. Ubal binds to the OTUB1 distal site while the donor ubiquitin in the UBC13~Ub conjugate binds in the OTUB1 proximal site, which comprises residues in both the OTU domain and the N terminus. In the absence of bound ubiquitin, the worm OTUB1 N terminus (residues 1–37, corresponding to human OTUB1 residues 1–39) is disordered (Fig. 2a). However, in the OTUB1–Ubal–UBC13<sup>DCA</sup>~Ub complexes, part of the N terminus of OTUB1 becomes ordered, forming a ubiquitin-binding helix that contacts the donor ubiquitin in the distal site (Fig. 2e). Additional



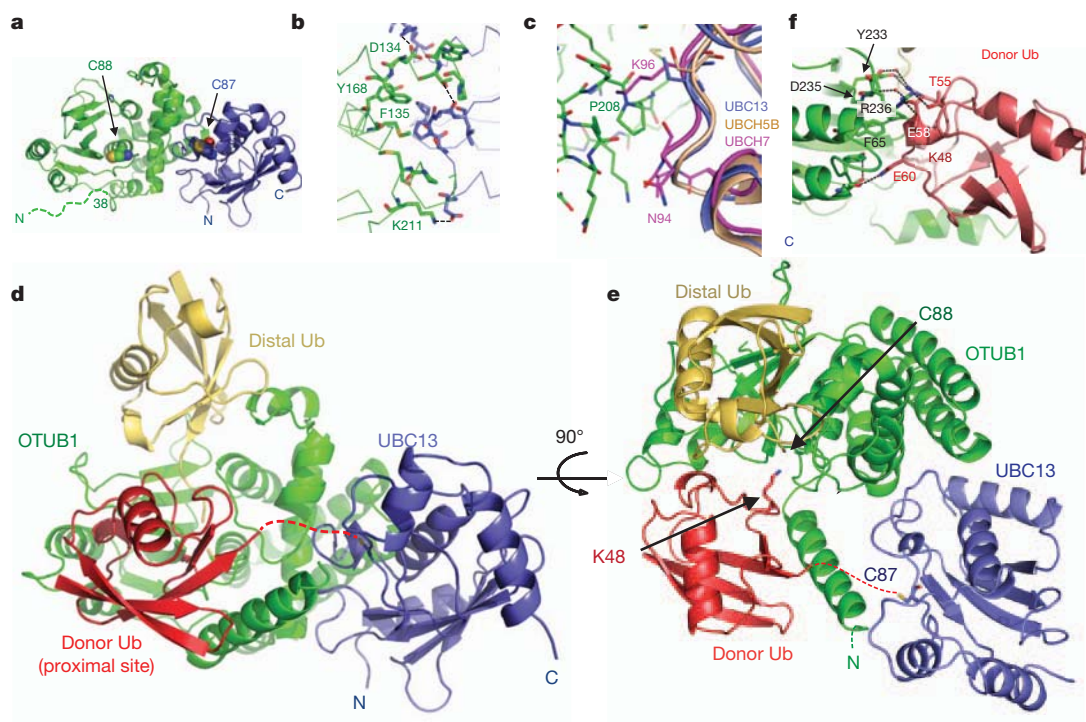


**Figure 2 | Structure OTUB1-UBC13 and OTUB1-Ubal-UBC13<sup>DCA</sup>~Ub.**

**a**, Complex of worm OTUB1 (green) bound to human UBC13 (blue). Respective active-site cysteines are shown as space-filling representations. Dashed line indicates disordered residues. **b**, Contacts at worm OTUB1 (green)-UBC13 (blue) interface. **c**, Superposition of UBCH5B (UBE2D2, PDB ID 2ESK) and UBCH7 (UBE2L3, PDB ID 1FBV) with UBC13 in the complex with worm OTUB1. UBCH7 contains an insertion (at N94) and a lysine (K96) that would interfere with binding. **d**, Structure of hybrid human/worm OTUB1

(green) bound to Ubal (distal Ub, yellow), UBC13 (blue) and ubiquitin (proximal Ub, red) that is covalently linked to the active-site cysteine (C87) of UBC13 by a DCA linkage. Dashed line indicates disordered C-terminal residues 73–76 of the donor ubiquitin and DCA linkage. **e**, A 90° rotation compared to **d** showing positions of worm OTUB1 and UBC13 active-site cysteine and modelled location of K48 of the proximal ubiquitin. **f**, Contacts between the donor ubiquitin (red) and the OTU domain (green) in the worm OTUB1-Ubal-UBC13<sup>DCA</sup>~Ub complex.

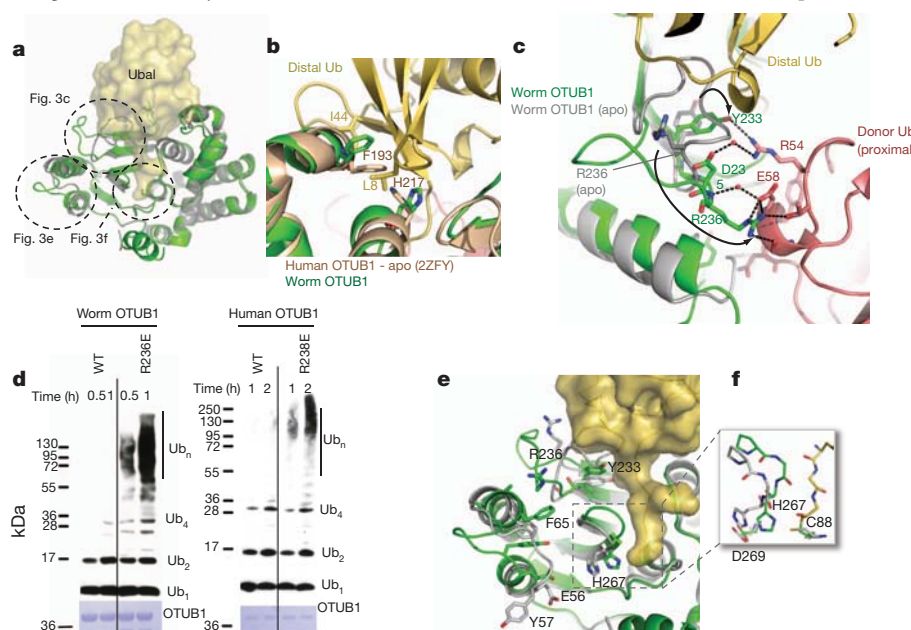


**Figure 3 | Conformational changes in the OTU domain triggered by Ubal binding.**

**a**, Superposition of worm OTUB1 (green) bound to Ubal (yellow surface) with the structure of apo worm OTUB1 (grey). Dotted circles indicate regions of conformational change, which are illustrated in the figure panels noted. **b**, Location of human OTUB1 distal site mutations that affect inhibition. The structure of human OTUB1 (2ZFY; brown) is superimposed on worm OTUB1 (green)-Ubal (yellow). Ubiquitin residues L8 and I44, where substitutions with alanine disrupt allosteric effect of ubiquitin binding, are shown. View is 180° rotation about vertical compared with **a**. **c**, Structural differences in the OTU domain in the presence (green) and absence (grey) of

distal Ub that affect contacts with the donor Ub. Arrows indicate conformational changes. Dotted lines indicate hydrogen bonds and salt bridges. View shown is from 'top' of complex as shown on right of panel **a**, rotated 90° counter-clockwise. **d**, Effect of mutating OTUB1 conserved arginine, worm OTUB1(R236E) and human OTUB1(R238E), on inhibition of UBC13-UEV1A. Assay performed as in Fig. 1b, with 1 μM human OTUB1 and 15 μM worm OTUB1. **e**, View of OTU domain structural rearrangements coloured as in **c**. View as in panel **a**; proximal ubiquitin not shown. **f**, Detailed view of catalytic triad in the presence and absence of Ubal (carbon coloured as in **c**).

contacts with the donor ubiquitin are mediated by the OTU domain which, as described below, undergoes a set of conformational changes triggered by Ubal binding to the distal site.

The donor ubiquitin binds to the proximal site of OTUB1 (Fig. 2d) in an orientation that places K48 of the ubiquitin near the OTUB1 active site (Fig. 2e). A K48 isopeptide linkage can be modelled between the proximal and distal ubiquitins, consistent with OTUB1 isopeptidase specificity for K48-linked diubiquitin<sup>5</sup>. Residues 73–76 of the donor ubiquitin and the DCA linkage are not visible in the electron density map, indicating that they do not adopt a unique conformation in the crystal. The distance between the C-terminal ubiquitin residue and the active-site cysteine is approximately 12.5 Å, which is sufficient to accommodate the four missing residues and a native thiolester linkage. The donor ubiquitin interface with the OTU domain buries 850 Å<sup>2</sup> of surface area. Ubiquitin side chains that lie between residues 54–60 contact the OTU domain, forming both direct and water-mediated hydrogen bonds and van der Waals interactions (Fig. 2f). Three of the contacting worm OTUB1 side chains are R236, Y233 and D235, which are only in a position to contact ubiquitin in the quaternary complex.

The observed contacts between the donor ubiquitin and the OTU domain depend upon distal site binding of Ubal, which forms a covalent bond with the active-site cysteine (Supplementary Fig. 12) and triggers conformational changes in three regions of the globular OTU domain (Fig. 3a). Ubal binds to the distal ubiquitin binding site of OTUB1 (Fig. 3b) in a manner similar to yeast<sup>8</sup> and viral<sup>12–14</sup> OTU enzymes, and accounts for the effects of mutations in the OTUB1 distal site (Fig. 1d). A loop (residues 235–245) that partially occludes the distal site in the absence of ubiquitin undergoes a large rearrangement that relieves steric clashes with the distal ubiquitin and positions R236 of worm OTUB1 to make multiple contacts with the donor ubiquitin bound in the proximal site of OTUB1 (Fig. 3c). In the structure of apo human OTUB1 (ref. 9), this residue is disordered (backbone and side-chain atoms) and lies in a loop that presumably changes conformation upon distal ubiquitin binding. Mutating the conserved arginine to glutamic acid in both human (R238E) and worm (R236E) OTUB1 disrupts inhibition (Fig. 3d), consistent with its role in binding the donor ubiquitin. Interestingly, the corresponding residue is a glutamic acid in OTUB2, which lacks an N-terminal arm and does not inhibit UBC13 (ref. 4). Y233, which occludes the distal site in apo worm OTUB1 and undergoes a conformational change to hydrogen bond with the distal Ub (Fig. 3c), is conserved in human OTUB1 (Supplementary Fig. 7a). Another set of conformational changes in the loop connecting helices 1 and 2 of OTUB1 flips the solvent exposed Y57 side chain into the interior of the OTU domain, where it stacks between F65 and E56 (Fig. 3e). The altered loop conformation relieves steric clashes with the donor ubiquitin that would otherwise occur. Binding of the distal ubiquitin is accompanied by additional local rearrangements that narrow the binding cleft around the ubiquitin C-terminal tail (Fig. 3e) and moves the worm OTUB1 active-site histidine, H267, into a position between D269 and C88 to activate the cysteine for catalysis (Fig. 3f).

The OTUB1 N-terminal ubiquitin-binding helix seen in the structure spans residues 28–39 of worm OTUB1 (complex 1) and 25–44 of human OTUB1 (Figs 4a–c), burying 542 Å<sup>2</sup> and 626 Å<sup>2</sup>, respectively, on the donor ubiquitin (electron density shown in Supplementary Fig. 13). The helix interacts with the donor ubiquitin in a manner reminiscent of the RAP80 UIM<sup>15</sup> (Fig. 4d). Despite limited sequence identity between the worm OTUB1 and human OTUB1 N terminus (Fig. 4a), the three side chains that contact the donor ubiquitin in the 2.35 Å resolution structure of worm OTUB1 (Fig. 4b) are conserved in human OTUB1 (Fig. 4a) and are oriented towards ubiquitin in the same manner in the 3.1 Å resolution human/worm OTUB1 structure (Fig. 4c). In the worm OTUB1 complex (Fig. 4b), residues E37 and I34 contact donor ubiquitin residue H68 while Q33 interacts with backbone atoms. In the structure containing the human N terminus, the helix extends beyond the donor ubiquitin and approaches the UBC13 active-site cysteine (Fig. 4c). It is possible that additional residues may

be ordered when the complex is in solution, as nine residues from the minimal human OTUB1Δ15 fragment that exhibits full activity (Fig. 1d) are missing from the human/worm OTUB1 complex structure. It is not clear whether the shorter helix observed in the worm OTUB1 complex reflects a structural difference in solution, or whether crystal contacts interfere with helix formation. The close approach of the OTUB1 N terminus to the donor ubiquitin C terminus in both complexes (Figs 4b, c) leaves open the possibility that additional contacts may form with the donor ubiquitin tail linked to UBC13 via a native thiolester.

The structures show how OTUB1 interferes with UEV binding and positioning of the acceptor ubiquitin, and also occludes the RING E3

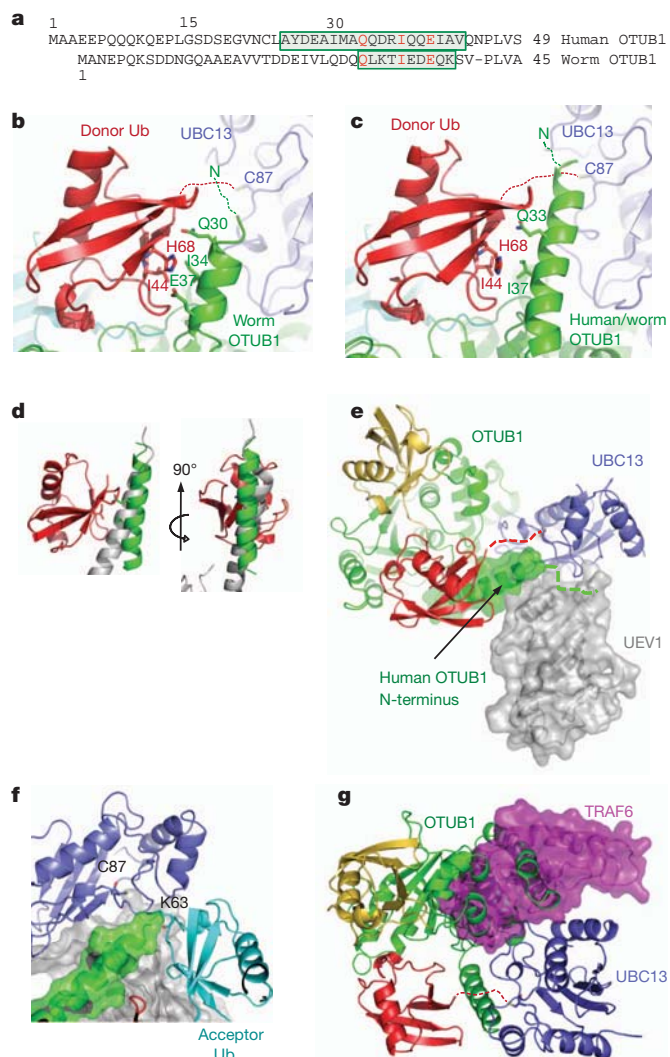


**Figure 4 | OTUB1 N-terminal arm and the mechanism of E2 inhibition.**

**a**, Sequence alignment of N-terminal arms of human OTUB1 and worm OTUB1. Boxed residues form a helix in the quaternary complex structures containing Ubal and UBC13<sup>DCA</sup>~Ub; additional shaded residues in worm OTUB1 are ordered in complex 1 but are not helical. **b**, Donor Ub (red) interactions with the worm OTUB1 N-terminal helix (green); UBC13 shown in blue. Dashed lines indicate disordered residues. **c**, Interactions with the human OTUB1 N-terminal helix of the human/worm OTUB1 hybrid, depicted as in **b**. **d**, Superposition comparing RAP80 (grey, PDB ID 3A1Q) binding to ubiquitin (red) with human OTUB1 N-terminal helix (green). Two views are shown. **e**, Superposition of human/worm OTUB1–Ubal–UBC13<sup>DCA</sup>~Ub with UBC13–UEV1 (1J7D) showing predicted position of UEV1 (grey). The solvent-accessible surface of the human N-terminal arm residues of OTUB1 is depicted. **f**, Modelled position of attacking K63 in acceptor Ub (cyan) based on yeast Ubc13~Ub–Mms2 (2GMI). **g**, Superposition with quaternary complex showing relative position of the TRAF6 E3 ligase (3HCT).



binding site. Figure 4e shows a superposition with the structure of a UBC13–UEV1 complex<sup>16</sup> showing that the N-terminal helix of human OTUB1 clashes with the expected location of UEV1. Modelling of the predicted position of the acceptor ubiquitin based on the structure of yeast UBC13~Ub–Mms2 (ref. 17) shows the N terminus of OTUB1 in a position to interfere with attack by the acceptor ubiquitin lysine on the thiolester (Fig. 4f). Because OTUB1 also inhibits UBCH5B<sup>4</sup>, which does not function with a UEV, we propose that the OTUB1 N terminus may also interfere with acceptor ubiquitin binding for other E2s. The repositioning of the donor ubiquitin away from the E2 also probably contributes to inhibition, in light of evidence that the donor ubiquitin in the E2–Ub thiolester interacts specifically with the E2 (refs 18, 19) and that this is essential for ubiquitin transfer<sup>6,7</sup>. In addition, superposition with the structure of UBC13 bound to TRAF6 (ref. 20) shows that the OTUB1 binding site overlaps with the E3 RING-binding site (Fig. 4g), indicating that competition between OTUB1 and RNF168 would further suppress UBC13 activity *in vivo*. Competition with E3 binding is likely to be particularly important for OTUB1 inhibition of UBCH5B which, unlike UBC13, is strictly dependent upon an E3 ligase for activity.

The ability of OTUB1 to serve as both an isopeptidase and an inhibitor of E2 enzyme activity arises from its ability to bind to selected E2s, while taking advantage of the allosteric communication between the proximal and distal ubiquitin binding sites of OTUB1 and the distinctive features of its N terminus. Given the high degree of coupling between the multiple binding interactions within the OTUB1–Ub–UBC13~Ub complex, the degree of inhibition *in vivo* will clearly depend upon the relative concentrations of OTUB1, E2~Ub thiolester, E3 and free ubiquitin in the cell. An interesting question is whether the dependence of OTUB1 repression on ubiquitin binding to the distal site is exploited to modulate OTUB1 activity in response to fluctuations in the concentration of free ubiquitin or of free chains, whose C-terminal subunits could similarly bind to the distal site of OTUB1. Our findings establish new directions for investigating how the allosteric regulation of OTUB1 may be exploited to regulate ubiquitination in the DNA damage response.

## METHODS SUMMARY

Cloning, expression, protein purification and crystallization are described in Methods and in accompanying references<sup>5</sup>. The DCA linkage between the active-site cysteine of UBC13 and a C-terminal cysteine in Ub(G75C) or Ub(G76C) was generated by a modification of the published method<sup>11</sup>. The hybrid human/worm OTUB1 protein contains residues 1–45 of human OTUB1 and residues 43–276 of worm OTUB1. Structures were determined by molecular replacement as described in Methods. Free ubiquitin chain synthesis was assayed by gel electrophoresis and products were detected by western blot with anti-ubiquitin antibody or by Coomassie staining. Pull-down assays were performed with purified recombinant protein. Assays of complex formation between OTUB1, UBC13, UBC13<sup>DCA</sup>~Ub and UEV1A were performed by gel filtration with fluorescein-labelled UEV1A or UEV1, monitoring fluorescein absorbance at 495 nm. Binding of OTUB1 to UBC13 was measured by fluorescence anisotropy using fluorescently labelled UBC13, and equilibrium dissociation constants were calculated using SigmaPlot (SPSS).

**Full Methods** and any associated references are available in the online version of the paper at [www.nature.com/nature](http://www.nature.com/nature).

Received 21 November 2011; accepted 3 February 2012.

Published online 22 February 2012.

1. Al-Hakim, A. *et al.* The ubiquitous role of ubiquitin in the DNA damage response. *DNA Repair (Amst.)* **9**, 1229–1240 (2010).

2. Deng, L. *et al.* Activation of the IκB kinase complex by TRAF6 requires a dimeric ubiquitin-conjugating enzyme complex and a unique polyubiquitin chain. *Cell* **103**, 351–361 (2000).
3. Stewart, G. S. *et al.* The RIDDLE syndrome protein mediates a ubiquitin-dependent signaling cascade at sites of DNA damage. *Cell* **136**, 420–434 (2009).
4. Nakada, S. *et al.* Non-canonical inhibition of DNA damage-dependent ubiquitination by OTUB1. *Nature* **466**, 941–946 (2010).
5. Wang, T. *et al.* Evidence for bidentate substrate binding as the basis for the K48 linkage specificity of otubain 1. *J. Mol. Biol.* **386**, 1011–1023 (2009).
6. Saha, A., Lewis, S., Kleiger, G., Kuhlman, B. & Deshaies, R. J. Essential role for ubiquitin-ubiquitin-conjugating enzyme interaction in ubiquitin discharge from Cdc34 to substrate. *Mol. Cell* **42**, 75–83 (2011).
7. Wickliffe, K. E., Lorenz, S., Wemmer, D. E., Kuriyan, J. & Rape, M. The mechanism of linkage-specific ubiquitin chain elongation by a single-subunit E2. *Cell* **144**, 769–781 (2011).
8. Messick, T. E. *et al.* Structural basis for ubiquitin recognition by the Otu1 ovarian tumor domain protein. *J. Biol. Chem.* **283**, 11038–11049 (2008).
9. Edelmann, M. J. *et al.* Structural basis and specificity of human otubain 1-mediated deubiquitination. *Biochem. J.* **418**, 379–390 (2009).
10. Hofmann, R. M. & Pickart, C. M. Noncanonical MMS2-encoded ubiquitin-conjugating enzyme functions in assembly of novel polyubiquitin chains for DNA repair. *Cell* **96**, 645–653 (1999).
11. Yin, L., Krantz, B., Russell, N. S., Deshpande, S. & Wilkinson, K. D. Nonhydrolyzable diubiquitin analogues are inhibitors of ubiquitin conjugation and deconjugation. *Biochemistry* **39**, 10001–10010 (2000).
12. James, T. W. *et al.* Structural basis for the removal of ubiquitin and interferon-stimulated gene 15 by a viral ovarian tumor domain-containing protease. *Proc. Natl Acad. Sci. USA* **108**, 2222–2227 (2011).
13. Capodagli, G. C. *et al.* Structural analysis of a viral ovarian tumor domain protease from the Crimean-Congo hemorrhagic fever virus in complex with covalently bonded ubiquitin. *J. Virol.* **85**, 3621–3630 (2011).
14. Akutsu, M., Ye, Y., Virdee, S., Chin, J. W. & Komander, D. Molecular basis for ubiquitin and ISG15 cross-reactivity in viral ovarian tumor domains. *Proc. Natl Acad. Sci. USA* **108**, 2228–2233 (2011).
15. Sato, Y. *et al.* Structural basis for specific recognition of Lys 63-linked polyubiquitin chains by tandem UIMs of RAP80. *EMBO J.* **28**, 2461–2468 (2009).
16. Moraes, T. F. *et al.* Crystal structure of the human ubiquitin conjugating enzyme complex, hMms2–hUbc13. *Nature Struct. Biol.* **8**, 669–673 (2001).
17. Eddins, M. J., Carlile, C. M., Gomez, K. M., Pickart, C. M. & Wolberger, C. Mms2–Ubc13 covalently bound to ubiquitin reveals the structural basis of linkage-specific polyubiquitin chain formation. *Nature Struct. Mol. Biol.* **13**, 915–920 (2006).
18. Wenzel, D. M., Stoll, K. E. & Klevit, R. E. E2s: structurally economical and functionally replete. *Biochem. J.* **433**, 31–42 (2011).
19. McKenna, S. *et al.* An NMR-based model of the ubiquitin-bound human ubiquitin conjugation complex Mms2–Ubc13. The structural basis for lysine 63 chain catalysis. *J. Biol. Chem.* **278**, 13151–13158 (2003).
20. Yin, Q. *et al.* E2 interaction and dimerization in the crystal structure of TRAF6. *Nature Struct. Mol. Biol.* **16**, 658–666 (2009).

**Supplementary Information** is linked to the online version of the paper at [www.nature.com/nature](http://www.nature.com/nature).

**Acknowledgements** We thank E. Henderson for generating the human/worm OTUB1 clone and C. Berndsen, A. DiBello, A. Datta and M. Bianchet for discussions. GM/CA-CAT has been funded in whole or in part with funds from the National Cancer Institute (Y1-CO-1020) and the National Institute of General Medical Science (Y1-GM-1104). Use of the Advanced Photon Source was supported by the US Department of Energy, Basic Energy Sciences, Office of Science, under contract no. DE-AC02-06CH11357.

**Author Contributions** R.W. and C.W. designed the experiments and R.W. performed all biochemical experiments. Cloning, expression and protein purification were carried out by X.Z., T.W. and R.W. Complexes were prepared for crystallization and crystals were grown by X.Z. and R.W.; R.W. determined the crystal structure with guidance from C.W.; R.W. and C.W. wrote the manuscript.

**Author Information** Coordinates and diffraction amplitudes are deposited in the Protein Data Bank under accession numbers 4DHI (worm OTUB1–UBC13), 4DHJ (worm OTUB1–Uba1–UBC13<sup>DCA</sup>~Ub) and 4DHz (human/worm OTUB1–Uba1–UBC13<sup>DCA</sup>~Ub). Reprints and permissions information is available at [www.nature.com/reprints](http://www.nature.com/reprints). The authors declare no competing financial interests. Readers are welcome to comment on the online version of this article at [www.nature.com/nature](http://www.nature.com/nature). Correspondence and requests for materials should be addressed to C.W. ([cwolberg@jhmi.edu](mailto:cwolberg@jhmi.edu)).



## METHODS

**Cloning and mutagenesis.** Cloning of human and *C. elegans* OTUB1 (human OTUB1 and worm OTUB1, respectively) was performed as described previously<sup>5</sup>. The human UBC13 open reading frame was amplified from a human complementary DNA library and cloned into a pET vector containing an N-terminal His<sub>6</sub>-SUMO-2 tag (pETSUMO-2). The human UEV1A ORF was synthesized (Integrated DNA Technologies) and subcloned into the pETSUMO-2 vector as above. The human UEV1 (missing the first 30 residues of UEV1A) expression plasmid was purchased from Addgene (<http://www.addgene.org>).

Mutants of human OTUB1 were generated by site-directed mutagenesis using the QuikChange mutagenesis kit (Stratagene) following the manufacturer's protocol. The hybrid human/worm OTUB1 was generated by swapping the first 41 residues of worm OTUB1 with the first 45 residues of human OTUB1 using Infusion ligase-free cloning (Clontech). Human OTUB1 with an N-terminal 41-residue truncation (OTUB1ΔN41) was generated as previously described<sup>5</sup>, all other OTUB1 deletions were generated using Infusion ligase-free cloning (Clontech).

**Protein expression and purification.** All proteins were expressed in *Escherichia coli* Rosetta-2 (DE3) cells grown in Luria-Bertani (LB) medium. Cultures were inoculated using 1% (v/v) overnight saturated cultures and were grown at 37 °C to an OD<sub>600</sub> of 0.8. Proteins were induced at 16 °C overnight by addition of 1 mM isopropyl-β-D-thio-galactoside (IPTG). Cells were harvested by centrifugation (8,000g, 15 min) and either lysed immediately or stored at -80 °C for later use.

Human OTUB1, worm OTUB1, human E1 enzyme and ubiquitin were purified as previously described<sup>5,21</sup>. Deletions and mutants of human and *C. elegans* OTUB1 and of ubiquitin were purified according to the same protocol as the wild-type proteins. UBC13 and UEV1A were purified by resuspending cell pellets in lysis buffer (20 mM HEPES pH 7.3, 300 mM NaCl, 10 mM imidazole, 2 mM β-mercaptoethanol) after adding 0.1 mM phenyl-methyl sulphonyl fluoride (PMSF). Cells were disrupted using a Microfluidizer (Microfluidics) and the lysate was centrifuged to remove cell debris. The lysate was subjected to immobilized metal affinity chromatography (IMAC) using 5 ml His-Trap columns (GE Biosciences) developed with a linear imidazole gradient of 25–400 mM in 20 column volumes. Fractions containing purified protein were pooled, SENP-2 protease was added in a ratio of 1:100 to cleave off the His-SUMO-2 tag, and pooled fractions were dialysed overnight at 4 °C against lysis buffer. Cleaved protein was then subjected to a second round of IMAC and the cleaved protein was collected from the flow-through. Proteins were then purified by gel filtration on a Superdex 75 column (GE Healthcare), dialysed into 20 mM HEPES, pH 7.3, 150 mM NaCl and 1 mM dithiothreitol (DTT), concentrated and stored at -80 °C. Proteins for crystallization, enzyme assays and binding studies were >98% pure as visualized on a Coomassie-stained gel. His<sub>6</sub>-tagged human OTUB1 used in pull-down assays was ~90% pure.

**Protein modifications.** UBC13, UEV1A and UEV1 were labelled with fluorescein-5-maleimide (Invitrogen) as described in the manufacturer's protocol. Ubiquitin aldehyde was prepared as described<sup>22</sup>.

**Preparation of UBC13~Ub conjugates.** UBC13(C87S)~Ub oxyster was prepared as previously described<sup>17</sup>. The UBC13<sup>DCA</sup>~Ub covalent conjugate was prepared according to a modification of the protocol from ref. 11. Purified ubiquitin containing the substitution G76C (Ub(G76C)) or G75C (Ub(G75C)) and UBC13 were dialysed separately overnight into 20 mM sodium borate buffer, pH 8.0 and 2 mM TCEP (tris(2-carboxyethyl)phosphine), mixed in the proportion of 1 mM Ub(G76C) or Ub(G75C) to 330 μM UBC13, and incubated on ice for 15 min. A stock of 20 mM 1,3-dichloroacetone (DCA) was prepared in dimethylformamide (DMF) and added to the conjugation reaction to a final concentration of 0.8 mM DCA. The reaction was stopped after 1 h by addition of 10 mM β-mercaptoethanol. The coupling efficiency was approximately 50%. For the Ub(G76C) reaction, the mix was diluted tenfold with 10 mM Tris, pH 8, loaded onto a mono Q column (GE Healthcare) pre-equilibrated with 10 mM Tris, pH 8. Free Ub(G76C) eluted in the flow-through and UBC13<sup>DCA</sup>~Ub eluted together with unconjugated UBC13 in 180 mM NaCl in 20 mM Tris, pH 8. For the Ub(G75C) reaction, UBC13<sup>DCA</sup>~Ub(G75C) was purified by gel filtration on a Superdex 75 column pre-equilibrated with 20 mM HEPES pH 7.3, 100 mM NaCl and 2 mM DTT. The separation efficiency was about 10% of the total amount of UBC13<sup>DCA</sup>~Ub(G75C) in the reaction mix.

**Purification of worm OTUB1-Ubal-UBC13<sup>DCA</sup>~Ub(G76C) quaternary complex.** Worm OTUB1 was incubated on ice with Ubal in a 1:4 molar ratio for 15 min and added to the purified apo human UBC13 and UBC13<sup>DCA</sup>~Ub mixture such that UBC13<sup>DCA</sup>~Ub was in twofold excess over worm OTUB1, as estimated by gel electrophoresis. The mixture was incubated for another 15 min on ice and loaded onto a Superdex 200 column (GE Healthcare) pre-equilibrated with 20 mM Tris, pH 7.45, 150 mM NaCl and 2 mM DTT. The OTUB1-Ubal-UBC13<sup>DCA</sup>~Ub complex eluted as a single peak and was concentrated to 10 mg ml<sup>-1</sup> and stored at -80 °C.

**Crystallization.** All crystals were grown by the hanging-drop vapour diffusion method at 20 °C. A worm OTUB1-UBC13 complex was prepared by incubating worm OTUB1 and human UBC13 at a molar ratio of 1:1 and total protein concentration of 26 mg ml<sup>-1</sup> for 10 min at room temperature. Crystals were grown from a 1:1 mix of protein and well solution containing 100 mM sodium cacodylate, pH 6.5 and 1 M trisodium citrate and appeared in about 2–3 days. Crystals were transferred to cryoprotectant consisting of well solution plus 20% ethylene glycol and then flash-frozen in liquid nitrogen.

Crystals of the worm OTUB1-Ubal-UBC13<sup>DCA</sup>~Ub complex were grown from a 1:1 mix of complex (10 mg ml<sup>-1</sup>) with well solution containing 100 mM Bis-Tris pH 6.5, 23% PEG 3350 and 0.26–0.3 M sodium chloride. Crystals appeared in about 1–2 days, were cryoprotected by well solution with added 15% ethylene glycol and then flash-frozen in liquid nitrogen.

Crystals of the human/worm OTUB1-Ubal-UBC13<sup>DCA</sup>~Ub complex were grown from a 1:1 mix of complex (10 mg ml<sup>-1</sup>) with well solution containing 100 mM MES pH 6.5, 21% PEG 10,000 and 0.1 M sodium chloride. Crystals appeared in about 2–3 days, were cryoprotected by well solution with added 15% ethylene glycol and then flash-frozen in liquid nitrogen.

**Structure determination.** Diffraction data were recorded at the GM/CA-CAT beamline 23-ID-D/B at the Advanced Photon Source under standard cryogenic conditions and processed with iMOSFLM<sup>23</sup> for worm OTUB1-human UBC13 crystals and HKL2000<sup>24</sup> for the worm OTUB1-Ubal-UBC13<sup>DCA</sup>~Ub crystals. For the worm OTUB1-Ubal-UBC13<sup>DCA</sup>~Ub structure two data sets were collected from a single crystal, merged and processed with HKL2000<sup>24</sup>. All data were collected at a wavelength of 1.033 Å. The structure of worm OTUB1-UBC13 was determined by molecular replacement with Phaser<sup>25</sup> using structures of UBC13 (1J7D) and apo human OTUB1 (2ZFY). The structure of worm OTUB1-Ubal-UBC13<sup>DCA</sup>~Ub was determined by molecular replacement with Molrep<sup>26</sup> using structures of the worm OTUB1-human UBC13 complex and ubiquitin (from 2GMI). The initial molecular replacement search performed with the worm OTUB1-UBC13 complex located four complexes in the asymmetric unit. The resulting positions of the OTUB1-UBC13 complexes were then fixed and ubiquitin was used as search model to locate the four ubiquitin aldehydes in the crystal. The position of the worm OTUB1-Ubal-UBC13 complex was fixed and another search with ubiquitin (1-71) located two molecules of donor ubiquitin in the asymmetric unit. The structure of human/worm OTUB1-Ubal-UBC13<sup>DCA</sup>~Ub was determined by molecular replacement with Phaser using one complex of worm OTUB1-Ubal-human UBC13~Ub lacking the first 42 residues of worm OTUB1.

All structures were subjected to multiple rounds of manual correction and refinement using COOT<sup>27</sup> and Phenix<sup>28</sup>. The final stages of refinement for the worm OTUB1-Ubal-UBC13<sup>DCA</sup>~Ub complex and human/worm OTUB1-Ubal-UBC13<sup>DCA</sup>~Ub ternary complex were done using REFMAC5<sup>29</sup>. Simulated annealing omit maps were calculated with CNS<sup>30</sup> and used to verify selected portions of the model.

The final model of worm OTUB1-human UBC13 complex includes residues 38–275 of worm OTUB1 and 3–152 of human UBC13. The final model of worm OTUB1-Ubal-UBC13<sup>DCA</sup>~Ub includes four complexes in the asymmetric unit: two containing all four proteins (worm OTUB1, Ubal, human UBC13 and Ub) and two lacking the donor ubiquitin conjugated to UBC13. There is no density in any of the complexes corresponding to the five C-terminal amino acids of ubiquitin or to the DCA linkage, which connects ubiquitin to the human UBC13 active-site cysteine. The number of worm OTUB1 N-terminal residues visible in the map differs among the four complexes as follows: complex 1, 28–275; complex 2, 31–275; complex 3, 36–276; complex 4, 38–276. The final model of the human/worm OTUB1-Ubal-UBC13<sup>DCA</sup>~Ub complex includes residues 20–275 of human/worm OTUB1, 3–151 of human UBC13, 1–76 of Ubal and 1–72 of ubiquitin.

Protein-protein interaction surfaces were analysed using the PISA server at EBI (<http://www.pdbe.org/PISA>) and manually inspected using COOT and PYMOL (<http://www.pymol.org>). Figures were generated with PYMOL.

**Fluorescence polarization binding assay.** Fluorescein-labelled human UBC13 (20 nM) was incubated with increasing concentrations of human OTUB1 wild type or mutants in 20 mM Tris, pH 7.6, 150 mM NaCl and 10 mM β-mercaptoethanol. Polarization measurements were recorded at 25 °C with an ISS Chronos Fluorescence Lifetime Spectrometer at excitation and emission wavelengths of 492 and 520 nm, respectively. Binding data were analysed and K<sub>d</sub> values were calculated by nonlinear regression in SigmaPlot (SPSS).

**UEV binding assay.** UEV1A and UEV1 were fluorescein-labelled; all other proteins are unlabelled. The experiment was performed with an analytical Superdex 75 column pre-equilibrated with 20 mM HEPES pH 7.3, 100 mM NaCl and 2 mM DTT. Absorbance was detected at 495 nm to monitor the presence of labelled UEV1A or UEV1. For each run, proteins were incubated for 20 min on ice before loading onto the column. The protein concentrations used in the different experiments were: Fig. 1e, UEV1A 20 μM, UBC13 40 μM and human OTUB1

100  $\mu$ M; Fig. 1f, UEV1A 10  $\mu$ M, UBC13~Ub 10  $\mu$ M, human OTUB1 50  $\mu$ M and Ubal 50  $\mu$ M; Fig. 1g, UEV1 20  $\mu$ M, UBC13~Ub 20  $\mu$ M, human OTUB1( $\Delta$ 37) 100  $\mu$ M and Ubal 100  $\mu$ M; Fig. 1h, UEV1 20  $\mu$ M, UBC13~Ub 20  $\mu$ M, human OTUB1 100  $\mu$ M and ubiquitin 200  $\mu$ M.

**In vitro ubiquitination assay.** Ubiquitination assays were performed in 25 mM Tris-HCl (pH 8.0) buffer containing 0.1 mM DTT, 1 mM ATP, 2.5 mM  $MgCl_2$ , 5 mM creatine phosphate, 0.3 units  $ml^{-1}$  inorganic pyrophosphatase, and 0.3 units  $ml^{-1}$  creatine kinase. Proteins in the amounts of 0.4  $\mu$ M UBC13, 0.4  $\mu$ M UEV1A and 5  $\mu$ M ubiquitin were mixed with human OTUB1 (1  $\mu$ M) or worm OTUB1 (15  $\mu$ M). Reactions were initiated by the addition of 0.1  $\mu$ M E1 enzyme, incubated at 37 °C, and stopped at different time points by adding denaturing SDS-PAGE loading dye containing  $\beta$ -mercaptoethanol (BME). For Fig. 1b, 0.5  $\mu$ M human OTUB1 was incubated with 0.5  $\mu$ M Ubal for 15 min before addition to the reaction. Reaction products were separated on a 4–12% Bis-Tris NuPAGE (Invitrogen) gel and transferred to a polyvinylidene fluoride (PVDF) membrane. Membranes were denatured in a 6 M guanidine HCl, 20 mM Tris-HCl, pH 7.5, 1 mM PMSF, 5 mM  $\beta$ -mercaptoethanol solution for 30 min at 4 °C and then washed extensively in Tris-buffered saline and Tween 20 (TBST). Membrane were blocked overnight at 4 °C with 5% BSA in TBST and incubated for 1 h with ubiquitin antibody (P4D1 Santa Cruz) 1:1,000 at room temperature followed by anti-mouse horseradish peroxidase (HRP)-conjugated secondary antibody. OTUB1 was detected with Coomassie brilliant blue or SimplyBlue SafeStain (Invitrogen).

**Pull-down assays.**  $Ni^{2+}$ -NTA beads were equilibrated in buffer A (50 mM phosphate buffer pH 8.0, 100 mM NaCl, 5 mM  $\beta$ -mercaptoethanol and 10 mM Imidazole). 6 $\times$ His-human OTUB1 (30  $\mu$ g) was incubated with pre-equilibrated beads in 200  $\mu$ l of buffer A for 30 min. Beads were washed with 400  $\mu$ l buffer A and incubated with a mixture of human UBC13 and human UBC13(C87S)~Ub with

and without the indicated concentration of free ubiquitin (2–100  $\mu$ M) in 200  $\mu$ l buffer A for 1 h. Beads were washed with 400  $\mu$ l buffer A for 10 min and eluted with 25  $\mu$ l of buffer A plus 250 mM imidazole. Eluates were analysed by gel electrophoresis and staining with Coomassie blue or SimplyBlue SafeStain (Invitrogen). The pull-down in Supplementary Fig. 2 was performed as above except for the addition of 6 $\times$ His-human OTUB1 (7  $\mu$ g), human UBC13(C87S)~Ub (7  $\mu$ g) and ubiquitin as indicated in the figure.

21. Berndsen, C. E. & Wolberger, C. A spectrophotometric assay for conjugation of ubiquitin and ubiquitin-like proteins. *Anal. Biochem.* **418**, 102–110 (2011).
22. Hu, M. *et al.* Structure and mechanisms of the proteasome-associated deubiquitinating enzyme USP14. *EMBO J.* **24**, 3747–3756 (2005).
23. Battye, T. G., Kontogiannis, L., Johnson, O., Powell, H. R. & Leslie, A. G. iMOSFLM: a new graphical interface for diffraction-image processing with MOSFLM. *Acta Crystallogr. D* **67**, 271–281 (2011).
24. Otwinowski, Z. & Minor, W. Processing of X-ray diffraction data collected in oscillation mode. *Methods Enzymol.* **276**, 307–326 (1997).
25. McCoy, A. J. *et al.* Phaser crystallographic software. *J. Appl. Crystallogr.* **40**, 658–674 (2007).
26. Vagin, A. & Teplyakov, A. Molecular replacement with MOLREP. *Acta Crystallogr. D* **66**, 22–25 (2010).
27. Emsley, P. & Cowtan, K. Coot: model-building tools for molecular graphics. *Acta Crystallogr. D* **60**, 2126–2132 (2004).
28. Adams, P. D. *et al.* PHENIX: a comprehensive Python-based system for macromolecular structure solution. *Acta Crystallogr. D* **66**, 213–221 (2010).
29. Murshudov, G. N., Vagin, A. A. & Dodson, E. J. Refinement of macromolecular structures by the maximum-likelihood method. *Acta Crystallogr. D* **53**, 240–255 (1997).
30. Brünger, A. T. *et al.* Crystallography & NMR system: a new software suite for macromolecular structure determination. *Acta Crystallogr. D* **54**, 905–921 (1998).

# The translational landscape of mTOR signalling steers cancer initiation and metastasis

Andrew C. Hsieh<sup>1,2\*</sup>, Yi Liu<sup>3\*</sup>, Merritt P. Edlind<sup>1</sup>, Nicholas T. Ingolia<sup>4</sup>, Matthew R. Janes<sup>3</sup>, Annie Sher<sup>1</sup>, Evan Y. Shi<sup>1</sup>, Craig R. Stumpf<sup>1</sup>, Carly Christensen<sup>1</sup>, Michael J. Bonham<sup>5</sup>, Shunyou Wang<sup>3</sup>, Pingda Ren<sup>3</sup>, Michael Martin<sup>3</sup>, Katti Jessen<sup>3</sup>, Morris E. Feldman<sup>6</sup>, Jonathan S. Weissman<sup>6</sup>, Kevan M. Shokat<sup>6</sup>, Christian Rommel<sup>3</sup> & Davide Ruggero<sup>1</sup>

**The mammalian target of rapamycin (mTOR) kinase is a master regulator of protein synthesis that couples nutrient sensing to cell growth and cancer. However, the downstream translationally regulated nodes of gene expression that may direct cancer development are poorly characterized. Using ribosome profiling, we uncover specialized translation of the prostate cancer genome by oncogenic mTOR signalling, revealing a remarkably specific repertoire of genes involved in cell proliferation, metabolism and invasion. We extend these findings by functionally characterizing a class of translationally controlled pro-invasion messenger RNAs that we show direct prostate cancer invasion and metastasis downstream of oncogenic mTOR signalling. Furthermore, we develop a clinically relevant ATP site inhibitor of mTOR, INK128, which reprograms this gene expression signature with therapeutic benefit for prostate cancer metastasis, for which there is presently no cure. Together, these findings extend our understanding of how the 'cancerous' translation machinery steers specific cancer cell behaviours, including metastasis, and may be therapeutically targeted.**

It is unknown whether specialized networks of translationally controlled mRNAs can direct cancer initiation and progression, thereby mirroring cooperativity that has mainly been observed at the level of transcriptional control. This is an important question, as key oncogenic signalling molecules, such as the mTOR kinase, directly regulate the activity of general translation factors<sup>1,2</sup>. Downstream of the phosphatidylinositol-3-OH kinase (PI(3)K)–AKT signalling pathway, mTOR assembles with either raptor or rictor to form two distinct complexes: mTORC1 and mTORC2 (refs 3, 4). The major regulators of protein synthesis downstream of mTORC1 are 4EBP1 (also called EIF4EBP1) and p70S6K1/2 (refs 1, 2). 4EBP1 negatively regulates eIF4E, a key rate-limiting initiation factor for cap-dependent translation. Phosphorylation of 4EBP1 by mTORC1 leads to its dissociation from eIF4E, allowing translation initiation complex formation at the 5' end of mRNAs<sup>5</sup>. The mTOR-dependent phosphorylation of p70S6K1/2 also promotes translation initiation as well as elongation<sup>6</sup>. At a genome-wide level, it remains poorly understood whether and how activation of these regulators of protein synthesis may produce specific changes in gene expression networks that direct cancer development. Here we use a powerful new technology known as ribosome profiling to delineate the translational landscape of the cancer genome at a codon-by-codon resolution upon pharmacological inhibition of mTOR<sup>7</sup>. Our findings provide genome-wide characterization of translationally controlled mRNAs downstream of oncogenic mTOR signalling and delineate their functional roles in cancer development. Moreover, we determine the efficacy of a novel clinically relevant mTOR inhibitor that we developed, INK128, which specifically targets this cancer program.

## Ribosome profiling of the prostate cancer genome

mTOR is deregulated in nearly 100% of advanced human prostate cancers<sup>8</sup>, and genetic findings in mouse models implicate mTOR hyperactivation in prostate cancer initiation<sup>9–11</sup>. Given the critical role for mTOR in prostate cancer, we used PC3 human prostate cancer cells, where mTOR is constitutively hyperactivated, to delineate translationally controlled gene expression networks upon complete or partial mTOR inhibition. We optimized ribosome profiling to assess quantitatively ribosome occupancy genome-wide in cancer cells<sup>7</sup>. In brief, ribosome-protected mRNA fragments were deep-sequenced to determine the number of ribosomes engaged in translating specific mRNAs (Supplementary Fig. 1a and Methods). Treatment of PC3 cells with PP242 (refs 12, 13), an mTOR ATP site inhibitor, significantly inhibits the activity of the three primary downstream mTOR effectors 4EBP1, p70S6K1/2 and AKT. On the contrary, rapamycin, an allosteric mTOR inhibitor, only blocks p70S6K1/2 activity in these cells (Supplementary Fig. 1b). We used short 3-h drug treatments, which precede alterations in *de novo* protein synthesis, to capture direct changes in mTOR-dependent gene expression by ribosome profiling and to minimize compensatory feedback mechanisms (Supplementary Fig. 1c–f).

Ribosome profiling revealed 144 target mRNAs selectively decreased at the translational level upon PP242 treatment ( $\log_2 \leq -1.5$  (false discovery rate  $< 0.05$ )) compared to rapamycin treatment, with limited changes in transcription (Fig. 1a and Supplementary Figs 2a, b and 3–10). The fact that at this time point rapamycin treatment did not markedly affect gene expression is consistent with incomplete allosteric inhibition of mTOR activity (Supplementary Fig. 1b). By

<sup>1</sup>School of Medicine and Department of Urology, Helen Diller Family Comprehensive Cancer Center, University of California, San Francisco, California 94158, USA. <sup>2</sup>Division of Hematology/Oncology and Department of Internal Medicine, University of California, San Francisco, California 94143, USA. <sup>3</sup>Intellikine Inc., La Jolla, California 92037, USA. <sup>4</sup>Carnegie Institution for Science, Baltimore, Maryland 21218, USA. <sup>5</sup>Department of Pathology, University of California, San Francisco, California 94143, USA. <sup>6</sup>Howard Hughes Medical Institute, Department of Cellular and Molecular Pharmacology, University of California, San Francisco, California 94158, USA.

\*These authors contributed equally to this work.



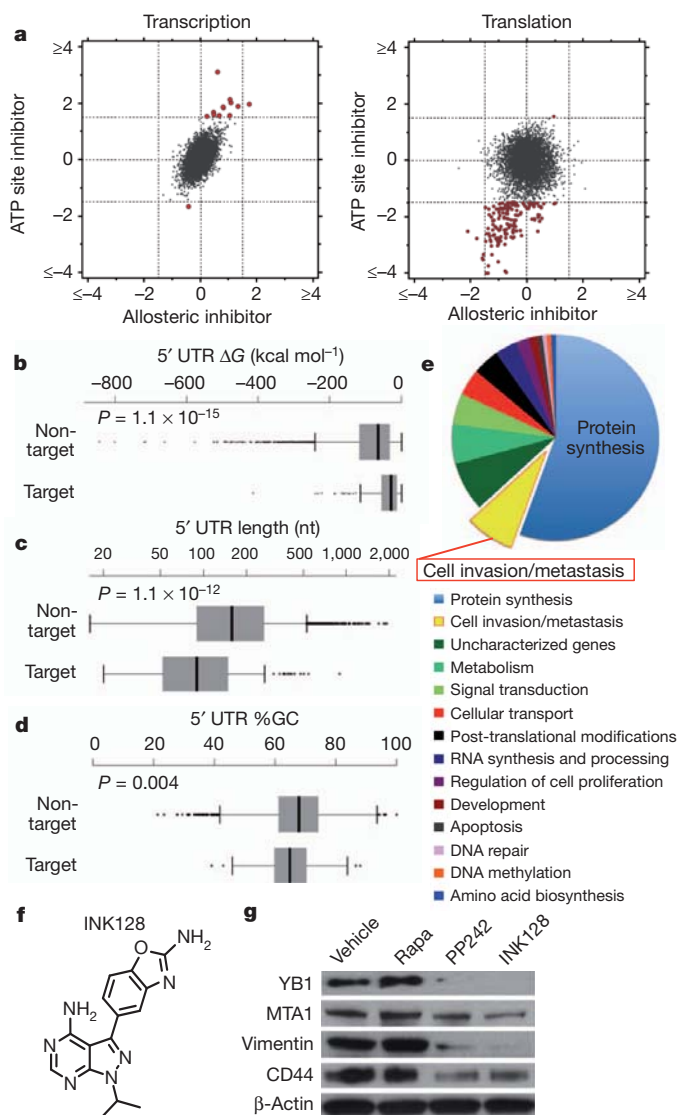


**Figure 1 | Ribosome profiling reveals mTOR-dependent specialized translational control of the prostate cancer genome.** **a**, Representative comparison of mRNA abundance and translational efficiency after a 3-h treatment with an ATP site inhibitor (PP242) versus an allosteric inhibitor (rapamycin). **b–d**, Free energy, length and percentage G+C content of the 5' UTRs of mTOR target versus non-target mRNAs (error bars indicate range, non-target  $n = 5,022$ , target  $n = 144$ , two-sided Wilcoxon). **e**, Functional classification of translationally regulated mTOR-responsive mRNAs. **f**, Chemical structure of INK128. **g**, Representative western blot from three independent experiments of mTOR-sensitive invasion genes in PC3 cells after a 48-h drug treatment. Rapa, rapamycin.

monitoring footprints of translating 80S ribosomes, our findings show that the effects of PP242 are largely at the level of translation initiation and not elongation (Supplementary Fig. 3). It has been proposed that mRNAs translationally regulated by mTOR may contain long 5' untranslated regions (5' UTRs) with complex RNA secondary structures. On the contrary, ribosome profiling revealed that mTOR-responsive 5' UTRs possess less complex features (Fig. 1b–d), providing a unique data set to investigate the nature of regulatory elements that render these mRNAs mTOR-sensitive. It has been previously shown that some mTOR translationally regulated mRNAs, most notably those involved in protein synthesis, possess a 5' terminal oligopyrimidine tract (5' TOP)<sup>14,15</sup> that is regulated by distinct trans-acting factors<sup>16,17</sup>. Of the 144 mTOR-sensitive target genes, 68% possess a 5' TOP. However, as the 5' TOP is not present in all mTOR-sensitive mRNAs, we next asked whether other 5' UTR

consensus sequences may exist. Strikingly, 63% of mTOR target mRNAs possess what we have termed a pyrimidine-rich translational element (PRTE) within their 5' UTRs ( $P = 3.2 \times 10^{-11}$ ). This element, unlike the 5' TOP sequence, consists of an invariant uridine at position 6 flanked by pyrimidines and, importantly, does not reside at position +1 of the 5' UTR (Supplementary Figs 2c and 7). We found that 89% of the mTOR-responsive genes possess a PRTE and/or 5' TOP, making the presence of one or both sequences a strong predictor for mTOR sensitivity (Supplementary Figs 2d and 7). Notably, mRNA isoforms arising from distinct transcription start sites may possess both a 5' TOP and a PRTE. Moreover, given the significant number of mRNAs that contain both the PRTE and 5' TOP, a functional interplay may exist between these regulatory elements. Future studies are required to determine the regulatory logic for how these sequences either independently or coordinately confer mTOR responsiveness. Multiple *cis*-acting elements within specific 5' UTRs could reflect regulation by distinct mTOR effectors. For example, our findings show that the PRTE imparts translational control specificity to 4EBP1 activity (see below).

Surprisingly, mTOR-sensitive genes stratify into unique functional categories that may promote cancer development and progression, including cellular invasion ( $P = 0.009$ ), cell proliferation ( $P = 0.04$ ), metabolism ( $P = 0.0002$ ) and regulators of protein modification ( $P = 0.01$ ) (Fig. 1e). The largest fraction of mTOR-responsive mRNAs cluster into a node consisting of key components of the translational apparatus: 70 ribosomal proteins, 6 elongation factors, and 4 translation initiation factors ( $P = 7.5 \times 10^{-82}$ ) (Fig. 1e and Supplementary Fig. 5). Therefore, this class of mTOR-responsive mRNAs may represent an important regulon that sustains the elevated protein synthetic capacity of cancer cells.

Notably, the second largest node of mTOR translationally regulated genes comprises bona fide cell invasion and metastasis mRNAs and putative regulators of this process (Fig. 1e). This group includes YB1 (Y-box binding protein 1; also called YBX1), vimentin, MTA1 (metastasis associated 1) and CD44 (Supplementary Fig. 11a). YB1

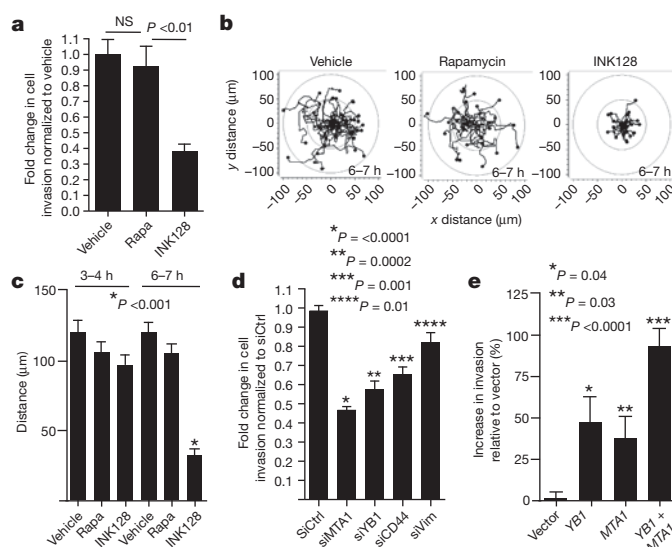


**Figure 2 | mTOR promotes prostate cancer cell migration and invasion through a translationally regulated gene signature.** **a**, Matrigel invasion assay in PC3 cells: 6-h pre-treatment followed by 6 h of cell invasion ( $n = 6$ , ANOVA). **b**, **c**, Migration patterns and average distance travelled by GFP-labelled PC3 cells during hours 3–4 and 6–7 of drug treatment ( $n = 34$  cells per condition, ANOVA). **d**, Matrigel invasion assay in PC3 cells after 48 h of knockdown of YB1, MTA1, CD44, or vimentin followed by 24 h of cell invasion ( $n = 7$ , *t*-test). **e**, Matrigel invasion assay in BPH-1 cells after 48 h of overexpression of YB1 and/or MTA1, followed by cell invasion for 24 h ( $n = 7$ , *t*-test). Rapa, rapamycin. All data represent mean  $\pm$  s.e.m. NS, not statistically significant.

regulates the post-transcriptional expression of a network of invasion genes<sup>18</sup>. Vimentin, an intermediate filament protein, is highly upregulated during the epithelial-to-mesenchymal transition associated with cellular invasion<sup>19</sup>. MTA1, a putative chromatin-remodelling protein, is overexpressed in invasive human prostate cancer<sup>20</sup> and has been shown to drive cancer metastasis by promoting neoangiogenesis<sup>21</sup>. CD44 is commonly overexpressed in tumour-initiating cells and is implicated in prostate cancer metastasis<sup>22</sup>. Consistent with their status as mTOR sensitive genes, *YB1*, vimentin, *MTA1* and *CD44* all possess a PRTE (Supplementary Fig. 5). Vimentin and *CD44* also possess a 5' TOP (Supplementary Fig. 7). To test the functional role of the PRTE in mediating translational control, we mutated the PRTE within the 5' UTR of *YB1*, which rendered the *YB1* 5' UTR insensitive to inhibition by 4EBP1 (Supplementary Fig. 11b). These findings highlight a novel *cis*-regulatory element that may modulate translational control of subsets of mRNAs upon mTOR activation. Moreover, ribosome profiling reveals unexpected transcript-specific translational control, mediated by oncogenic mTOR signalling, including a distinct set of pro-invasion and metastasis genes.

### Translation of pro-invasion mRNAs by mTOR

We next extended the use of the mTOR pharmacological tools used in ribosome profiling towards functional characterization of the newly identified mTOR-sensitive cell invasion gene signature. To this end, we developed a new clinical-grade mTOR ATP site inhibitor, INK128, derived from the PP242 chemical scaffold (Fig. 1f). In brief, a structure-guided optimization of pyrazolopyrimidine derivatives was performed (see INK128 chemical synthesis in Supplementary Information) that improved oral bioavailability while retaining mTOR kinase potency and selectivity. INK128 was selected for clinical studies on the basis of its high potency (1.4 nM inhibition constant ( $K_i$ )), selectivity for mTOR, low molecular mass, and favourable pharmaceutical properties (Supplementary Figs 12 and 13).

Using either PP242 or INK128, we observed a selective decrease in the expression of *YB1*, *MTA1*, vimentin and *CD44* at the protein but not transcript level in PC3 cells starting at 6 h of treatment, which precedes any decrease in *de novo* protein synthesis (Fig. 1g and Supplementary Figs 1c, d, 14 and 15). In contrast, rapamycin treatment did not alter their expression (Fig. 1g and Supplementary Fig. 14a). Similar findings were observed using a broad panel of metastatic cell lines of distinct histological origins (Supplementary Fig. 16). The four-gene invasion signature is positively regulated by mTOR hyperactivation, as silencing PTEN expression increased their protein but not mRNA expression levels (Supplementary Fig. 17). We next investigated the effects of mTOR ATP site inhibitors on prostate cancer cell migration and invasion. We found that INK128, but not rapamycin, decreases the invasive potential of PC3 prostate cancer cells (Fig. 2a). Furthermore, INK128 inhibits cancer cell migration starting at 6 h of treatment, precisely correlating with when decreases in the expression of pro-invasion genes are evident, but preceding any changes in the cell cycle or overall global protein synthesis (Fig. 2b, c, and Supplementary Figs 1c, e, f, 14b and 18).

Among the genes comprising the pro-invasion signature, *YB1* has been shown to act directly as a translation factor that controls expression of a larger set of genes involved in breast cancer cell invasion<sup>18</sup>. Notably, *YB1* translationally regulated target mRNAs, including *SNAIL1* (also called *SNAI1*), *LEF1* and *TWIST1*, decreased at the protein but not transcript level upon *YB1* knockdown in PC3 cells (Supplementary Figs 19 and 20). To determine the functional role of *YB1* in prostate cancer cell invasion, we silenced *YB1* gene expression in PC3 cells, and observed a 50% reduction in cell invasion (Fig. 2d). Similarly, knockdown of *MTA1*, *CD44*, or vimentin also inhibited prostate cancer cell invasion (Fig. 2d and Supplementary Fig. 19). These mTOR target mRNAs may be sufficient to endow primary prostate cells with invasive features, as overexpression of *YB1* and/or *MTA1* (Supplementary Fig. 21a) in BPH-1 cells, an untransformed

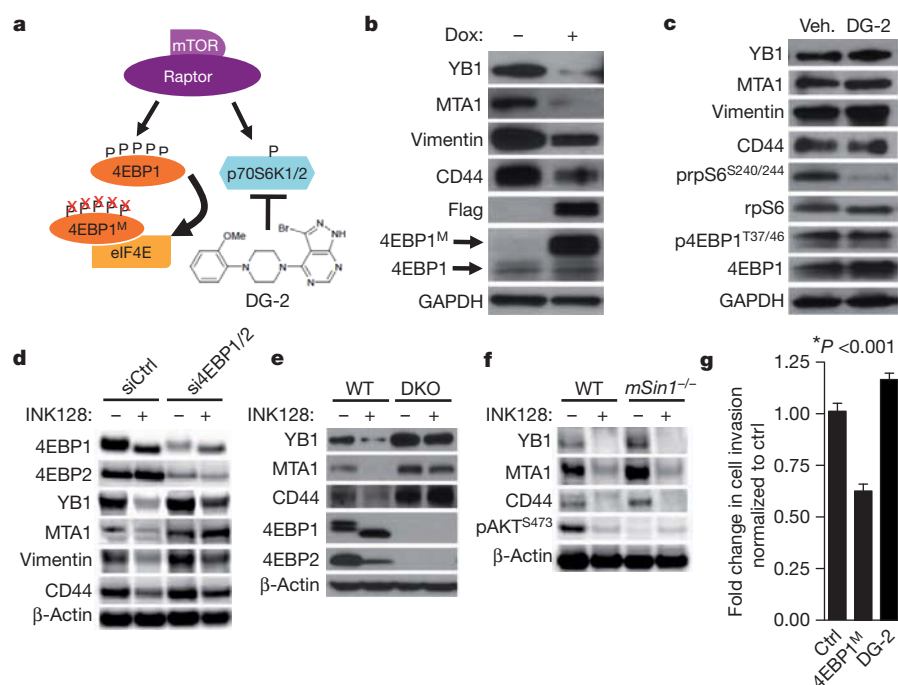


**Figure 3 | The 4EBP1–eIF4E axis controls the post-transcriptional expression of mTOR-sensitive invasion genes.** **a**, Schematic of the pharmacogenetic strategy to inhibit p70S6K1/2 or eIF4E hyperactivation. **b**, Representative western blot from three independent experiments of PC3 4EBP1<sup>M</sup> cells after 48-h doxycycline induction of 4EBP1<sup>M</sup>. **c**, Representative western blot from three independent experiments of PC3 cells after 48-h DG-2 treatment. **d**, Representative western blot from three independent experiments of PC3 cells after 48 h of 4EBP1/4EBP2 knockdown followed by 24-h INK128

treatment (see quantification of independent experiments in Supplementary Fig. 23a). **e**, Representative western blot from three independent experiments of wild type (WT) and 4EBP1/4EBP2 double knockout (DKO) MEFs treated with INK128 for 24 h. **f**, Representative western blot from two independent experiments of wild-type and *mSin1*<sup>-/-</sup> (also called *Mapkap1*<sup>tm1Bisu</sup>) MEFs after 24-h INK128 treatment. **g**, Matrigel invasion assay upon 48-h doxycycline induction of 4EBP1<sup>M</sup>, or treatment with DG-2 compared to control ( $n = 6$  per condition,  $t$ -test). All data represent mean  $\pm$  s.e.m.



prostate epithelial cell line, increased the invasive capacity of these cells in an additive manner (Fig. 2e). Notably, the effects of YB1 and MTA1 on cell invasion are independent from any effect on cell proliferation in both knockdown or overexpression studies (Supplementary Fig. 21b, c). Therefore, translational control of pro-invasion mRNAs by oncogenic mTOR signalling alters the ability of epithelial cells to migrate and invade, a key feature of cancer metastasis.

### Dissecting mTOR translational effectors

We sought to determine the molecular mechanism by which pro-invasion genes are regulated at the translational level and why these mRNAs are sensitive to INK128 but not rapamycin. To this end, we investigated whether the translational regulators downstream mTORC1, 4EBP1 and/or p70S6K1/2, control the expression of these mTOR-sensitive targets. We generated a human prostate cancer cell line that stably expresses a doxycycline-inducible dominant-negative mutant of 4EBP1 (4EBP1<sup>M</sup>) (Fig. 3a)<sup>13</sup>. This mutant binds to eIF4E, decreasing its hyperactivation without inhibiting general mTORC1 function (Supplementary Fig. 22a). Notably, expression of 4EBP1<sup>M</sup> does not alter global protein synthesis (Supplementary Fig. 22b), probably because endogenous 4EBP1 and 4EBP2 proteins retain their ability to bind to eIF4E (Supplementary Fig. 22c)<sup>13</sup>. Upon induction of 4EBP1<sup>M</sup>, YB1, vimentin, CD44 and MTA1 decrease at the protein but not mRNA level, whereas pharmacological inhibition of p70S6K1/2 with DG-2 (ref. 23) had no effect (Fig. 3b, c and Supplementary Fig. 22d). Next, we tested whether INK128 decreases expression of the four invasion genes through the 4EBP–eIF4E axis. Notably, knockdown of 4EBP1 and 4EBP2 in PC3 cells or using 4EBP1 and 4EBP2 double knockout mouse embryonic fibroblasts (MEFs)<sup>24</sup> reduced the ability of INK128 to decrease expression of these pro-invasion mRNAs (Fig. 3d, e and Supplementary Fig. 23). Furthermore, ablation of mTORC2 activity<sup>25</sup> had no effect on the expression of these mRNAs or responsiveness to INK128 (Fig. 3f and Supplementary Fig. 24a–c). Next, we determined the effect of 4EBP1<sup>M</sup> on human prostate cancer cell invasion. The expression of 4EBP1<sup>M</sup> resulted in a significant decrease in prostate cancer cell invasion without affecting the cell cycle, whereas DG-2 had no effect (Fig. 3g and Supplementary Fig. 24d). These findings demonstrate that eIF4E hyperactivation downstream of oncogenic mTOR regulates translational control of the pro-invasion mRNAs and provides an explanation for the selective targeting of this gene signature by mTOR ATP site inhibitors.

### Examining cell invasion networks in vivo

Both CK5<sup>+</sup> and CK8<sup>+</sup> prostate epithelial cells have been implicated in the initiation of prostate cancer upon loss of PTEN<sup>26,27</sup>. *Pten*<sup>loxP/loxP</sup>; *Pbcre* (*Pten*<sup>L/L</sup>) mice are an ideal model of prostate cancer because they display distinct stages of cancer development (prostatic intraepithelial neoplasia, invasive adenocarcinoma, and metastasis)<sup>28</sup>. However, the expression patterns of YB1, vimentin, CD44 and MTA1 in prostate basal (CK5<sup>+</sup>) and luminal (CK8<sup>+</sup>) epithelial cells have not been characterized. We therefore analysed their expression patterns in the *Pten*<sup>L/L</sup> prostate cancer mouse model, where mTOR is constitutively hyperactivated<sup>9,28</sup>. We found that YB1 localizes to the cytoplasm and nucleus of CK5<sup>+</sup> and CK8<sup>+</sup> prostate epithelial cells, consistent with its ability to shuttle between the two cellular compartments (Fig. 4a, b and Supplementary Fig. 25a, b)<sup>18,29</sup>. MTA1 expression is exclusively nuclear in both cell types (Fig. 4c, d). Of note, CD44, together with other cell-surface markers, has been used to isolate a rare prostate stem-cell population<sup>30</sup>. We observed expression of CD44 within a subset of CK5<sup>+</sup> and CK8<sup>+</sup> epithelial cells (Fig. 4e, f). In contrast, vimentin is not detected in either cell type (Fig. 4g). We next determined the impact of mTOR hyperactivation on the expression pattern of the pro-invasion gene signature. YB1, MTA1 and CD44 protein, but not transcript, levels were significantly increased in both *Pten*<sup>L/L</sup> luminal and basal epithelial cells compared to wild type (Fig. 4h and Supplementary Fig. 25c–e). Interestingly, a subset of *Pten*<sup>L/L</sup> luminal epithelial cells ectopically

expresses vimentin at aberrantly high levels, with a perinuclear distribution (Fig. 4g and Supplementary Fig. 25f, g) suggesting that these cells may have acquired some mesenchymal-like features. Consistent with these findings, perinuclear vimentin localization is associated with invasive features of human prostate cancer cells<sup>31</sup> and changes

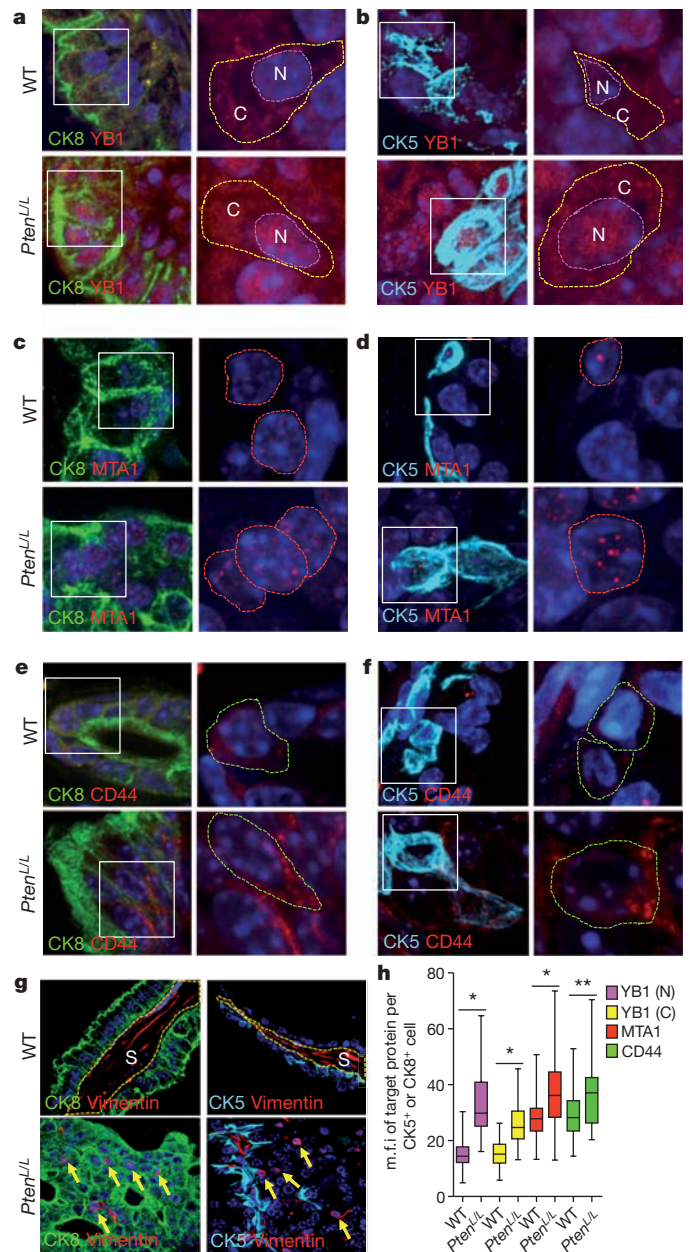


**Figure 4 | mTOR hyperactivation augments translation of YB1, MTA1, CD44 and vimentin mRNAs in a subset of pre-invasive prostate cancer cells in vivo.** Left: immunofluorescent images of CK8/DAPI or CK5/DAPI with YB1 (a, b), MTA1 (c, d), or CD44 (e, f) co-staining in 14-month-old wild-type and *Pten*<sup>L/L</sup> mouse prostate epithelial cells. White boxes outline the area magnified in the right panel. Right: magnified immunofluorescent images of YB1 (a, b), MTA1 (c, d) and CD44 (e, f) co-stained with DAPI in wild-type and *Pten*<sup>L/L</sup> mouse prostate epithelial cells. Dotted lines encircle the cytoplasm (C) and/or the nucleus (N). g, Representative immunofluorescent images of CK5 or CK8 co-staining with vimentin in 14-month-old wild-type and *Pten*<sup>L/L</sup> mouse prostate epithelial cells. S, stroma; yellow arrows indicate perinuclear vimentin. h, Box plot of YB1 (N = nuclear, C = cytoplasmic), MTA1 and CD44 mean fluorescence intensity (m.f.i.) per CK5<sup>+</sup> or CK8<sup>+</sup> prostate epithelial cell in wild-type and *Pten*<sup>L/L</sup> mice (three mice per arm,  $n = 43\text{--}303$  cells quantified per target gene, error bars indicate range (see Supplementary Fig. 25b); \* $P < 0.0001$ , \*\* $P = 0.0004$ ,  $t$ -test).



in cell polarity in actively moving fibroblasts<sup>32</sup>. These studies reveal a unique, translationally controlled signature of gene expression downstream of mTOR hyperactivation in a cancer-initiating subset of prostate epithelial cells.

### Targeting prostate cancer metastasis

The most significant pre-clinical extension of this work would be to determine the therapeutic benefit of INK128 in reprogramming expression of the mTOR-dependent pro-invasion gene signature and prostate cancer metastasis directly *in vivo*. This is underscored by the clinical inefficacy of allosteric mTOR inhibition towards the

lethal form of metastatic human prostate cancer<sup>33,34</sup>. Importantly, in our preclinical trial of RAD001 (rapalog) versus INK128 in *Pten*<sup>L/L</sup> mice, 4EBP1 and p70S6K1/2 phosphorylation was completely restored to wild-type levels after treatment with INK128, whereas RAD001 only decreased p70S6K1/2 phosphorylation levels (Supplementary Fig. 26a, b). We next determined the cellular consequences of complete versus partial mTOR inhibition during distinct stages of prostate cancer. INK128 treatment resulted in a 50% decrease in prostatic intraepithelial neoplasia (PIN) lesions in *Pten*<sup>L/L</sup> mice that was associated with decreased proliferation and a tenfold increase in apoptosis (Supplementary Fig. 26d–f). Notably,

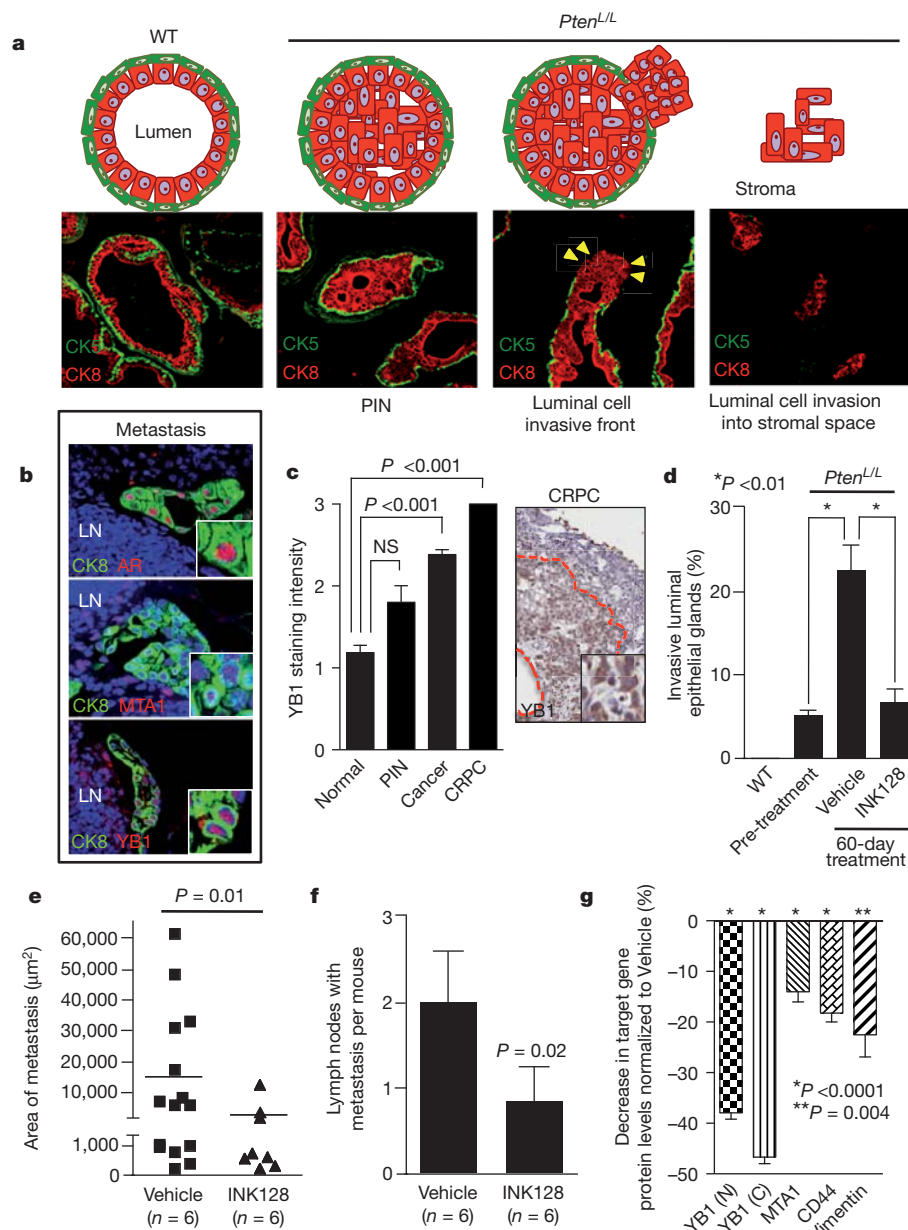


**Figure 5 | Complete mTOR inhibition by INK128 treatment prevents prostate cancer invasion and metastasis *in vivo*.** **a**, Diagram and images of normal prostate gland, pre-invasive PIN and invasive prostate cancer. CK8/CK5, luminal/basal epithelial cells, respectively. Yellow arrowheads indicate invasive front. **b**, Immunofluorescent images of 14-month-old *Pten*<sup>L/L</sup> lymph node (LN) metastasis co-stained with CK8/androgen receptor (AR), CK8/YB1 and CK8/MTA1. **c**, Left: human tissue microarray of YB1 protein levels in normal ( $n = 59$ ), PIN ( $n = 5$ ), cancer ( $n = 99$ ) and CRPC ( $n = 3$ ) (ANOVA). Right: immunohistochemistry of YB1 in human CRPC demarcated by the red line (inset shows nuclear and cytoplasmic YB1). **d**, Quantification of invasive

prostate glands in wild-type and *Pten*<sup>L/L</sup> mice before (12-months old) and after (14-months old) 60 days of INK128 treatment ( $n = 6$  mice per arm, ANOVA). **e**, **f**, Area and number of CK8/AR<sup>+</sup> metastases in draining lymph nodes in 14-month-old *Pten*<sup>L/L</sup> mice after 60 days of INK128 treatment ( $n = 6$  mice per arm, *t*-test). **g**, Percentage decrease of YB1 (N = nuclear, C = cytoplasmic), MTA1, CD44, or vimentin protein levels (determined by quantitative immunofluorescence, Supplementary Fig. 25b) in CK8<sup>+</sup> or CK5<sup>+</sup> prostate cells (CK8<sup>+</sup> only for vimentin) in INK128-treated 14-month-old *Pten*<sup>L/L</sup> mice normalized to vehicle-treated mice ( $n = 3$  mice per arm, *t*-test). All data represent mean  $\pm$  s.e.m.

the unique cytotoxic properties of INK128 treatment in *Pten*<sup>L/L</sup> mice were evidenced by a marked reduction in prostate cancer volume. In addition, and consistent with these findings, INK128 induced programmed cell death in multiple cancer cell lines (Supplementary Fig. 27a, b). In contrast, RAD001 treatment mainly had cytostatic effects leading to only partial regression of PIN lesions associated with a limited decrease in cell proliferation and no significant effect on apoptosis (Supplementary Fig. 26c–f).

We extended the preclinical trial by examining the effects of INK128 treatment on the pro-invasion gene signature and prostate cancer metastasis, which is incurable and the primary cause of patient mortality. Cell invasion is the critical first step in metastasis, required for systemic dissemination. In *Pten*<sup>L/L</sup> mice after the onset of PIN, a subset of prostate glands show characteristics of luminal epithelial cell invasion by 12 months (Fig. 5a and Supplementary Fig. 27c)<sup>28</sup>. After 12 months of age, *Pten*<sup>L/L</sup> mice develop lymph-node metastases and these cells maintain strong YB1 and MTA1 expression (Fig. 5b). We further extended these findings directly to human prostate cancer patient specimens, observing that YB1 expression levels increase in a stepwise fashion from normal prostate to castration-resistant prostate cancer (CRPC), an advanced form of the disease associated with increased metastatic potential (Fig. 5c). MTA1 levels exhibit similar increases<sup>20</sup>. In human prostate cancer, high-grade primary tumours that display invasive features are more likely to develop systemic metastasis than low-grade non-invasive tumours<sup>35,36</sup>. Remarkably, treatment with INK128 completely blocked the progression of invasive prostate cancer locally in the prostate gland, and profoundly inhibited the total number and size of distant metastases (Fig. 5d–f). This was associated with a marked decrease in the expression of YB1, vimentin, CD44 and MTA1 at the protein, but not transcript, level in specific epithelial cell types within pre-invasive PIN lesions in *Pten*<sup>L/L</sup> mice (Fig. 5g and Supplementary Fig. 25c). Together, these findings reveal an unexpected role for oncogenic mTOR signalling in control of a pro-invasion translational program that, along with the lethal metastatic form of prostate cancer, can be efficiently targeted with clinically relevant mTOR ATP site inhibitors.

## Discussion

Here we used ribosome profiling to generate a comprehensive map of translationally controlled mTOR targets in cancer that surprisingly stratify into specific cellular processes including proliferation, metabolism, protein synthesis and invasion (Fig. 1e). The effects of this translational control program are probably broad, converging on many subclasses of mRNAs that may cooperate towards distinct steps in cancer development and therapeutic response. This is supported by our *in vivo* findings where we developed a novel clinically relevant mTOR inhibitor, INK128, that significantly abrogates multiple aspects of prostate cancer development by inducing apoptosis as well as inhibiting cell proliferation, invasion and metastasis (Fig. 5d–g and Supplementary Fig. 26c–f). The superiority of INK128 as an mTOR inhibitor is also evident in its ability to reprogram the mTOR oncogenic translational program in prostate cancer, which is not achieved by rapalog treatment. Of note, however, the sensitivity of cells from distinct histological origins to ATP site versus allosteric inhibitors of mTOR may differ. For example, the Jurkat lymphoid cell line is particularly sensitive to rapamycin treatment<sup>37</sup>.

One of the most novel nodes of mTOR translationally controlled genes are those that cooperatively control, at least in part, the cellular invasive features of human prostate cancer cells (Figs 1g, 2 and 3b, g). Translational control of these mRNAs relies on the 4EBP1–eIF4E axis and is thereby specifically druggable with potent mTOR ATP site inhibitors, which, unlike rapamycin, target mTOR-dependent 4EBP1 phosphorylation (Figs 1g, 3d, e and 5g, and Supplementary Figs 1b, 23 and 26b). This has significant therapeutic implications not only for advanced prostate cancer but also for multiple metastatic cancers where we show that translational control of pro-invasion

mRNAs is sensitive to ATP site inhibitors of mTOR (Supplementary Fig. 16). Thereby, these studies link translational regulation to the poorly understood mechanisms underlying cancer metastasis. Intriguingly, various components of the translation machinery, including oncogenic eIF4E<sup>38</sup>, localize to the leading edge of migrating fibroblasts<sup>39</sup>. This may allow spatially controlled translation of mRNAs important for cell migration, providing a rapid and specific response in transducing a migration program that could be co-opted at the invasive edge of metastatic cancer cells. Together, these studies reveal that the ability of mTOR to phosphorylate general translation factors results in exquisite transcript-specific translational control of key mRNAs that may cooperate in distinct steps of cancer initiation and progression, with significant implications for therapeutic intervention.

## METHODS SUMMARY

**Mice.** *Pten*<sup>loxP/loxP</sup> and *Pb-crc* mice were obtained from Jackson Laboratories and Mouse Models of Human Cancers Consortium (MMHCC) and maintained in the C57BL/6 background.

**Ribosome profiling.** PC3 lysates were subjected to ribosome footprinting by nuclease treatment. Ribosome-protected and alkaline digested poly(A) mRNA fragments were purified and deep sequencing libraries were generated. Ribosome footprint and RNA-seq sequencing reads were aligned against a library of transcripts from the UCSC Known Genes database GRCh37/hg19. Read density profiles were constructed for the canonical transcript of each gene. The average read density per codon was computed for the coding sequence of each transcript. Average read density was used to determine mRNA abundance (RNA-seq reads), ribosome occupancy of mRNAs (foot print reads), and translational efficiency (foot print reads/RNA-seq reads).

**Immunofluorescence.** Paraffin-embedded mouse prostates and lymph nodes were deparaffinized and rehydrated using CitriSolv (Fisher) and serial ethanol washes. Antigen unmasking was performed using Citrate pH 6 (Vector Labs). Sections were blocked in 5% goat serum, 1% BSA in TBS. Various primary antibodies were used at dilutions between 1:50 and 1:500 (see Methods), followed by incubation with appropriate conjugated secondary antibodies. Samples were mounted with DAPI Hardset Mounting Medium (Vector Lab). A Zeiss Spinning Disc confocal (Zeiss, CSU-X1) was used to image the tissues. Individual cells were quantified for mean fluorescence intensity using the Axiovision (Zeiss, Release 4.8) densitometric tool.

**Full Methods** and any associated references are available in the online version of the paper at [www.nature.com/nature](http://www.nature.com/nature).

**Received 14 July 2011; accepted 3 February 2012.**

**Published online 22 February 2012.**

1. Brown, E. J. *et al.* Control of p70 S6 kinase by kinase activity of FRAP *in vivo*. *Nature* **377**, 441–446 (1995).
2. Gingras, A. C., Kennedy, S. G., O'Leary, M. A., Sonenberg, N. & Hay, N. 4E-BP1, a repressor of mRNA translation, is phosphorylated and inactivated by the Akt(PKB) signaling pathway. *Genes Dev.* **12**, 502–513 (1998).
3. Kim, D. H. *et al.* mTOR interacts with raptor to form a nutrient-sensitive complex that signals to the cell growth machinery. *Cell* **110**, 163–175 (2002).
4. Sarbassov, D. D. *et al.* Rictor, a novel binding partner of mTOR, defines a rapamycin-insensitive and raptor-independent pathway that regulates the cytoskeleton. *Curr. Biol.* **14**, 1296–1302 (2004).
5. Gingras, A. C., Raught, B. & Sonenberg, N. Regulation of translation initiation by FRAP/mTOR. *Genes Dev.* **15**, 807–826 (2001).
6. Ruvinsky, I. & Meyuhas, O. Ribosomal protein S6 phosphorylation: from protein synthesis to cell size. *Trends Biochem. Sci.* **31**, 342–348 (2006).
7. Ingolia, N. T., Ghaemmaghami, S., Newman, J. R. & Weissman, J. S. Genome-wide analysis *in vivo* of translation with nucleotide resolution using ribosome profiling. *Science* **324**, 218–223 (2009).
8. Taylor, B. S. *et al.* Integrative genomic profiling of human prostate cancer. *Cancer Cell* **18**, 11–22 (2010).
9. Nardella, C. *et al.* Differential requirement of mTOR in postmitotic tissues and tumorigenesis. *Sci. Signal.* **2**, ra2 (2009).
10. Guertin, D. A. *et al.* mTOR complex 2 is required for the development of prostate cancer induced by Pten loss in mice. *Cancer Cell* **15**, 148–159 (2009).
11. Furic, L. *et al.* eIF4E phosphorylation promotes tumorigenesis and is associated with prostate cancer progression. *Proc. Natl Acad. Sci. USA* **107**, 14134–14139 (2010).
12. Feldman, M. E. *et al.* Active-site inhibitors of mTOR target rapamycin-resistant outputs of mTORC1 and mTORC2. *PLoS Biol.* **7**, e38 (2009).
13. Hsieh, A. C. *et al.* Genetic dissection of the oncogenic mTOR pathway reveals druggable addiction to translational control via 4EBP-eIF4E. *Cancer Cell* **17**, 249–261 (2010).

14. Tang, H. *et al.* Amino acid-induced translation of TOP mRNAs is fully dependent on phosphatidylinositol 3-kinase-mediated signaling, is partially inhibited by rapamycin, and is independent of S6K1 and rpS6 phosphorylation. *Mol. Cell. Biol.* **21**, 8671–8683 (2001).
15. Meyuhas, O. Synthesis of the translational apparatus is regulated at the translational level. *Eur. J. Biochem.* **267**, 6321–6330 (2000).
16. Crosio, C., Boyl, P. P., Loreni, F., Pierandrei-Amaldi, P. & Amaldi, F. La protein has a positive effect on the translation of TOP mRNAs *in vivo*. *Nucleic Acids Res.* **28**, 2927–2934 (2000).
17. Ørom, U. A., Nielsen, F. C. & Lund, A. H. MicroRNA-10a binds the 5'UTR of ribosomal protein mRNAs and enhances their translation. *Mol. Cell* **30**, 460–471 (2008).
18. Lahat, G. *et al.* Vimentin is a novel anti-cancer therapeutic target; insights from *in vitro* and *in vivo* mice xenograft studies. *PLoS ONE* **5**, e10105 (2010).
19. Hofer, M. D. *et al.* The role of metastasis-associated protein 1 in prostate cancer progression. *Cancer Res.* **64**, 825–829 (2004).
20. Yoo, Y. G., Kong, G. & Lee, M. O. Metastasis-associated protein 1 enhances stability of hypoxia-inducible factor-1 $\alpha$  protein by recruiting histone deacetylase 1. *EMBO J.* **25**, 1231–1241 (2006).
21. Liu, C. *et al.* The microRNA miR-34a inhibits prostate cancer stem cells and metastasis by directly repressing CD44. *Nature Med.* **17**, 211–215 (2011).
22. Okuzumi, T. *et al.* Inhibitor hijacking of Akt activation. *Nature Chem. Biol.* **5**, 484–493 (2009).
23. Dowling, R. J. *et al.* mTORC1-mediated cell proliferation, but not cell growth, controlled by the 4E-BPs. *Science* **328**, 1172–1176 (2010).
24. Jacinto, E. *et al.* SIN1/MIP1 maintains rictor-mTOR complex integrity and regulates Akt phosphorylation and substrate specificity. *Cell* **127**, 125–137 (2006).
25. Wang, X. *et al.* A luminal epithelial stem cell that is a cell of origin for prostate cancer. *Nature* **461**, 495–500 (2009).
26. Mulholland, D. J. *et al.* Lin<sup>−</sup> Sca-1<sup>+</sup> CD49<sup>high</sup> stem/progenitors are tumor-initiating cells in the Pten-null prostate cancer model. *Cancer Res.* **69**, 8555–8562 (2009).
27. Wang, S. *et al.* Prostate-specific deletion of the murine Pten tumor suppressor gene leads to metastatic prostate cancer. *Cancer Cell* **4**, 209–221 (2003).
28. Sutherland, B. W. *et al.* Akt phosphorylates the Y-box binding protein 1 at Ser102 located in the cold shock domain and affects the anchorage-independent growth of breast cancer cells. *Oncogene* **24**, 4281–4292 (2005).
29. Leong, K. G., Wang, B. E., Johnson, L. & Gao, W. Q. Generation of a prostate from a single adult stem cell. *Nature* **456**, 804–818 (2008).
30. Lang, S. H. *et al.* Enhanced expression of vimentin in motile prostate cell lines and in poorly differentiated and metastatic prostate carcinoma. *Prostate* **52**, 253–263 (2002).
31. Helfand, B. T. *et al.* Vimentin organization modulates the formation of lamellipodia. *Mol. Biol. Cell* **22**, 1274–1289 (2011).
32. Amato, R. J., Jac, J., Mohammad, T. & Saxena, S. Pilot study of rapamycin in patients with hormone-refractory prostate cancer. *Clin. Genitourin. Cancer* **6**, 97–102 (2008).
33. George, D. J. *et al.* A phase II study of RAD001 in men with hormone refractory metastatic prostate cancer (HRPC). *Am. Soc. Clin. Oncol. Genitourin. Cancers Symp.* Abstract 181 (2008).
34. Pontes, J. E., Wajsbman, Z., Huben, R. P., Wolf, R. M. & Englander, L. S. Prognostic factors in localized prostatic carcinoma. *J. Urol.* **134**, 1137–1139 (1985).
35. Zhou, P. *et al.* Predictors of prostate cancer-specific mortality after radical prostatectomy or radiation therapy. *J. Clin. Oncol.* **23**, 6992–6998 (2005).
36. Grolleau, A. *et al.* Global and specific translational control by rapamycin in T cells uncovered by microarrays and proteomics. *J. Biol. Chem.* **277**, 22175–22184 (2002).
37. Ruggero, D. R. *et al.* The translation factor eIF-4F promotes tumor formation and cooperates with c-Myc in lymphomagenesis. *Nature Med.* **10**, 484–486 (2004).
38. Willett, M., Brocard, M., Davide, A. & Morley, S. J. Translation initiation factors and active sites of protein synthesis co-localize at the leading edge of migrating fibroblasts. *Biochem. J.* **438**, 217–227 (2011).

**Supplementary Information** is linked to the online version of the paper at [www.nature.com/nature](http://www.nature.com/nature).

**Acknowledgements** We thank M. Barna for critical discussion and reading of this manuscript; T. Wilson for support and advice; T. Sanders and E. Llagostera-Martin for technical support with confocal microscopy; L. Li, E. Ulm, L. Kessler, J. Kucharski and L. Darjania for technical support for the discovery and development of INK128. J. Kurhanewicz and R. Bok of the Surbeck Institute for Advanced Imaging for technical support and MRI images; N. Sonenberg for providing the 4EBP1/2 double knockout mouse embryonic fibroblasts; J. M. Shen for support; and K. Tong for editing the manuscript. A.C.H. is supported in part by the American Cancer Society (119084-PF-10-233-01-TBE), and is a Prostate Cancer Foundation Young Investigator, and a recipient of the DOD Prostate Cancer Training Award. This work is supported by NIH R01 CA154916 (D.R.), NIH R01 CA140456 (D.R.) and the Phi Beta Psi Sorority (D.R.). D.R. is a Leukemia & Lymphoma Society Scholar.

**Author Contributions** A.C.H. and D.R. conceived the experiments. A.C.H., M.P.E., M.R.J., A.S., E.Y.S., C.R.S., C.C. and S.W. performed the experiments, *Pten*<sup>L/L</sup> preclinical trials, and collected the data. N.T.I. and J.S.W. contributed to ribosomal profiling data analysis. M.J.B. provided pathology support. Y.L., P.R., M.M., S.W., K.J., M.E.F., K.M.S. and C.R. developed and/or supported development of INK128, conducted pharmacokinetic, pharmacodynamic and preclinical studies. A.C.H. and D.R. analysed the data and wrote the manuscript. All authors discussed results and edited the manuscript.

**Author Information** Small-RNA sequencing data were deposited in the Gene Expression Omnibus (<http://www.ncbi.nlm.nih.gov/geo/>) under accession number GSE35469. Reprints and permissions information is available at [www.nature.com/reprints](http://www.nature.com/reprints). The authors declare competing financial interests: details accompany the full-text HTML version of the paper at [www.nature.com/nature](http://www.nature.com/nature). Readers are welcome to comment on the online version of this article at [www.nature.com/nature](http://www.nature.com/nature). Correspondence and requests for materials should be addressed to D.R. ([davide.ruggero@ucsf.edu](mailto:davide.ruggero@ucsf.edu)) or C.R. ([christian@intellikine.com](mailto:christian@intellikine.com)).



## METHODS

**Mice.** *Pten*<sup>loxP/loxP</sup> and *Pb-cre* mice were obtained from Jackson Laboratories and Mouse Models of Human Cancers Consortium (MMHCC), respectively, and maintained in the C57BL/6 background. Mice were maintained under specific pathogen-free conditions, and experiments were performed in compliance with institutional guidelines as approved by the Institutional Animal Care and Use Committee of UCSF.

**Cell culture and reagents.** Human cell lines were obtained from the ATCC and maintained in the appropriate medium with supplements as suggested by ATCC. Wild-type, *mSin1*<sup>−/−</sup> (provided by B. Su), and *4EBP1/4EBP2* double knockout MEFs (provided by N. Sonenberg) were cultured as previously described<sup>24,25</sup>. SMARTvector 2.0 (Thermo Scientific) lentiviral shRNA constructs were used to knock down PTEN (SH-003023-02-10). For generation of GFP-labelled PC3 cells, SMARTvector 2.0 lentiviral empty vector control particles that contain TurboGFP (S-004000-01) were used. Control (D-001810-01), *YB1* (L-010213), *MTA1* (L-004127), *CD44* (L-009999), vimentin (L-003551), rictor (LL-016984), *4EBP1* (L-003005) and *4EBP2* (L-018671) pooled siRNAs were purchased from Thermo Scientific. Intelliline provided INK128 and PP242, which were used at 200 nM and 2.5 μM in cell-based assays unless otherwise specified. RAD001 was obtained from LC Laboratories. DG-2 was provided by K. Shokat and used at 20 μM in cell-based assays. Rapamycin was purchased from Calbiochem and used at 50 nM in cell-based assays. Doxycycline (Sigma) was used at 1 μg ml<sup>−1</sup> in *4EBP1*<sup>M</sup> induction assays. Lipofectamine 2000 (Invitrogen) was used to transfect cancer cell lines with siRNA. Amaxa Cell Line Nucleofector Kit R (Lonza) was used to electroporate BPH-1 cells with over expression vectors. The *4EBP1*<sup>M</sup> has been previously described<sup>13</sup>.

**Plasmids.** pCDNA3-HA-YB1 was provided by V. Evdokimova. pCMV6-Myk-DDK-MTA1 was purchased from Origene. pGL3-Promoter was purchased from Promega. To clone the 5' UTR of *YB1* into pGL3-Promoter, the entire 5' UTR sequence of *YB1* was amplified from PC3 cDNA. PCR fragments were digested with HindIII and NcoI and ligated into the corresponding sites of pGL3-Promoter. The PRTE sequence at position +20–34 in the *YB1* 5' UTR (UCSC kgID uc001chs.2) was mutated using the QuikChange Site-Directed Mutagenesis Kit following the manufacturer's protocol (Stratagene).

**Ribosome profiling.** PC3 cells were treated with rapamycin (50 nM; Calbiochem) or PP242 (2.5 μM; Intelliline) for 3 h. Cells were subsequently treated with cycloheximide (100 μg ml<sup>−1</sup>; Sigma) and detergent lysis was performed in the dish. The lysate was treated with DNase and clarified, and a sample was taken for RNA-seq analysis. Lysates were subjected to ribosome foot printing by nuclease treatment. Ribosome-protected fragments were purified, and deep sequencing libraries were generated from these fragments, as well as from poly(A) mRNA purified from non-nuclease-treated lysates. These libraries were analysed by sequencing on an Illumina GAII.

Each sequencing run resulted in approximately 20–25 million raw reads per sample, of which 5–12 million unique reads were used for subsequent analysis. Ribosome footprint and RNA-seq sequencing reads were aligned against a library of transcripts from the UCSC Known Genes database GRCh37/hg19. The first 25 nucleotides of each read were aligned using Bowtie and this initial alignment was then extended to encompass the full fragment-derived portion of the sequencing read while excluding the linker sequence. Read density profiles were then constructed for the canonical transcript of each gene, using only reads with 0 or 1 total mismatches between the read sequence and the reference sequence, comprised of the transcript fragment followed by the linker sequence. Footprint reads were assigned to an A site nucleotide at position +15 to +17 of the alignment, based on the total fragment length; mRNA reads were assigned to the first nucleotide of the alignment. The average read density per codon was then computed for the coding sequence of each transcript, excluding the first 15 and last 5 codons, which can display atypical ribosome accumulation.

Average read density was used as a measure of mRNA abundance (RNA-seq reads) and of protein synthesis (ribosome profiling reads). For most analyses, genes were filtered to require at least 256 reads in the relevant RNA-seq samples. Translational efficiency was computed as the ratio of ribosome footprint read density to RNA-seq read density, scaled to normalize the translational efficiency of the median gene to 1.0 after excluding regulated genes (log<sub>2</sub> fold-change ±1.5 after normalizing for the all-gene median). Changes in protein synthesis, mRNA abundance and translational efficiency were similarly computed as the ratio of read densities between different samples, normalized to give the median gene a ratio of 1.0. This normalization corrects for differences in the absolute number of sequencing reads obtained for different libraries. 3,977 (replicate 1), and 5,333 (replicate 2) unique mRNAs passed a preset read threshold of 256 reads for single-gene quantification for all treatment conditions.

**Western blot analysis.** Western blot analysis was performed as previously described<sup>13</sup> with antibodies specific to phospho-AKT<sup>S473</sup> (Cell Signaling), AKT

(Cell Signaling), phospho-p70S6K<sup>T389</sup> (Cell Signaling), phospho-rpS6<sup>S240/244</sup> (Cell Signaling), rpS6 (Cell Signaling), phospho-4EBP1<sup>T37/46</sup> (Cell Signaling), 4EBP1 (Cell Signaling), 4EBP2 (Cell Signaling), YB1 (Cell Signaling), CD44 (Cell Signaling), LEF1 (Cell Signaling), PTEN (Cell Signaling), eEF2 (Cell Signaling), GAPDH (Cell Signaling), vimentin (BD Biosciences), eIF4E (BD Biosciences), Flag (Sigma), β-actin (Sigma), MTA1 (Santa Cruz Biotechnology), Twist (Santa Cruz Biotechnology), rpL28 (Santa Cruz Biotechnology), HA (Covance) and rictor (Bethyl Laboratory).

**qPCR analysis.** RNA was isolated using the manufacturer's protocol for RNA extraction with TRIzol Reagent (Invitrogen) using the Pure Link RNA mini kit (Invitrogen). RNA was DNase-treated with Pure Link DNase (Invitrogen). DNase-treated RNA was transcribed to cDNA with SuperScript III First-Strand Synthesis System for RT-PCR (Invitrogen), and 1 μl of cDNA was used to run a SYBR green detection qPCR assay (SYBR Green Supermix and MyiQ2, Biorad). Primers were used at 200 nM.

**5' UTR analysis.** 5' UTRs of the 144 downregulated mTOR target genes were obtained using the known gene ID from the UCSC Genome Browser (GRCh37/hg19). Target versus non-target mRNAs were compared for 5' UTR length, %G+C content and Gibbs free energy by the Wilcoxon two-sided test. Multiple  $E_m$  (expectation maximization) for Motif Elicitation (MEME) and Find Individual Motif Occurrences (FIMO) was used to derive the PRTE and determine its enrichment in the 144 mTOR-sensitive genes compared a background list of 3,000 genes. The Database of Transcriptional Start Sites (DBTSS Release 8.0) was used to identify putative 5' TOP genes and putative transcription start sites in the 144 mTOR target genes.

**Luciferase assay.** PC3 *4EBP1*<sup>M</sup> cells were treated with 1 μg ml<sup>−1</sup> doxycycline (Sigma) for 24 h. Cells were transfected with various pGL3-Promoter constructs using lipofectamine 2000 (Invitrogen). After 24 h, cells were collected. 20% of the cells were aliquoted for RNA isolation. The remaining cells were used for the luciferase assay per the manufacturer's protocol (Promega). Samples were measured for luciferase activity on a Glomax 96-well plate luminometer (Promega). Firefly luciferase activity was normalized to luciferase mRNA expression levels.

**Kinase assays.** mTOR activity was assayed using LanthaScreen Kinase kit reagents (Invitrogen) according to the manufacturer's protocol. PI(3)K α, β, γ and δ activity were assayed using the PI(3)K HTRF assay kit (Millipore) according to the manufacturer's protocol. The concentration of INK128 necessary to achieve inhibition of enzyme activity by 50% (IC<sub>50</sub>) was calculated using concentrations ranging from 20 μM to 0.1 nM (12-point curve). IC<sub>50</sub> values were determined using a nonlinear regression model (GraphPad Prism 5).

**Cell proliferation assay.** PC3 cells were treated with the appropriate drug for 48 h, and proliferation was measured using CellTiter-Glo Luminescent reagent (Promega) per the manufacturer's protocol. The concentration of INK128 necessary to achieve inhibition of cell growth by 50% (IC<sub>50</sub>) was calculated using concentrations ranging from 20.0 μM to 0.1 nM (12-point curve).

**Mouse xenograft study.** Nude mice were inoculated subcutaneously in the right subscapular region with 5 × 10<sup>6</sup> MDA-MB-361 cells. After tumours reached a size of 150–200 mm<sup>3</sup>, mice were randomly assigned into vehicle control or treatment groups. INK128 was formulated in 5% polyvinylpyrrolidone, 15% NMP, 80% water and administered by oral gavage at 0.3 mg kg<sup>−1</sup> and 1 mg kg<sup>−1</sup> daily.

**Pharmacokinetic analysis.** The area under the plasma drug concentration versus time curves, AUC<sub>(0–t<sub>last</sub>)</sub> and AUC<sub>(0–inf)</sub>, were calculated from concentration data using the linear trapezoidal rule. The terminal  $t_{1/2}$  in plasma was calculated from the elimination rate constant ( $\lambda_z$ ), estimated as the slope of the log-linear terminal portion of the plasma concentration versus time curve, by linear regression analysis. The bioavailability ( $F$ ) was calculated using  $F = (AUC_{(0–last),po} D_{i.v.}) / (AUC_{(0–last),iv} D_{p.o.}) \times 100\%$ , where  $D_{i.v.}$  and  $D_{p.o.}$  are intravenous and oral doses, respectively.  $C_{max}$  was a highest drug concentration in plasma after oral administration.  $T_{max}$  was the time at which  $C_{max}$  is observed after extravascular administration of drug.  $T_{last}$  was the last time point a quantifiable drug concentration can be measured.

**Metabolic stability assay.** *In vitro* metabolic stability of INK128 was evaluated after incubation with liver microsomes or liver S9 fractions from various species in the presence of NADPH. The half-life of INK128 was estimated by log linear regression analysis.

**CYP assay.** INK128 inhibition of CYP450 isoforms in human liver microsomes was determined with isoform-specific substrates at concentrations approximately equal to the concentration at which the rate of the reaction is half-maximal ( $K_m$ ) for the individual isoforms: CYP1A2, CYP2C8, CYP2C9, CYP2C19, CYP2D6 and CYP3A4.

**Pharmaceutical property assays.** The percentage of protein binding of INK128 was determined in mouse, rat, dog, monkey and human plasma at CEREP. The IC<sub>50</sub> for the inhibitory effect of INK128 on hERG potassium channel was determined at

CEREP. A Bacterial Reverse Mutation Assay (Ames test) was conducted at BioReliance.

**Polysome analysis.** PC3 cells were treated for 3 h with either DMSO or INK128 (100 nM). Cells were re-suspended in PBS containing 100  $\mu\text{g ml}^{-1}$  cycloheximide (Sigma) and incubated on ice for 10 min. Cells were centrifuged at 300g for 5 min at 4 °C and lysed in 10 mM Tris-HCl pH 8, 140 mM NaCl, 5 mM  $\text{MgCl}_2$ , 640 U  $\text{ml}^{-1}$  Rnasin, 0.05% NP-40, 250  $\mu\text{g ml}^{-1}$  cycloheximide, 20 mM DTT and protease inhibitors. Samples were incubated for 20 min on ice then centrifuged once for 5 min at 3,300g and once for 5 min at 9,300g, isolating the supernatant after each centrifugation. Lysates were loaded onto 10–50% sucrose gradients containing 0.1 mg  $\text{ml}^{-1}$  heparin and 2 mM DTT and centrifuged at 37,000 r.p.m. for 2.5 h at 4 °C. The sample was subsequently fractionated on a gradient fractionation system (ISCO). RNA was extracted from all fractions and run on a TBE-agarose gel to visualize 18S and 28S rRNA. Fractions 7–13 were found to correspond to the polysome fractions and were used for further qPCR analysis.

**[ $^{35}\text{S}$ ] metabolic labelling.** PC3 or PC3 4EBP1<sup>M</sup> cells with or without indicated treatment were incubated with 30  $\mu\text{Ci}$  of [ $^{35}\text{S}$ ]-methionine for 1 h after pre-incubation in methionine-free DMEM (Invitrogen). Cells were prepared using a standard protein lysate protocol, resolved on a 10% SDS polyacrylamide gel and transferred onto a PVDF membrane (Biorad). The membrane was exposed to autoradiography film (Denville) for 24 h and developed.

**Cell cycle analysis.** Appropriately treated PC3, BPH-1, or PC3-4EBP1<sup>M</sup> cells were fixed in 70% ethanol overnight at –20 °C. Cells were subsequently washed with PBS and treated with RNase (Roche) for 30 min. After this incubation, the cells were permeabilized and treated with 50  $\mu\text{g ml}^{-1}$  propidium iodide (Sigma) in a solution of 0.1% Tween, 0.1% sodium citrate. Cell cycle data was acquired using a BD FACS Caliber (BD Biosciences) and analysed with FlowJo (v.9.1).

**Apoptosis analysis.** Appropriately treated LNCaP and A498 cells were labelled with Annexin V-FITC (BD Biosciences) and propidium iodide (Sigma) following the manufacturer's instructions. PI/Annexin data was acquired using a BD FACS Caliber (BD Biosciences) and analysed with FlowJo (v.9.1).

**Matrigel invasion assay.** BioCoat Matrigel Invasion Chambers (modified Boyden Chamber Assay; BD Biosciences) were used according to the manufacturer's instructions.

**Real-time imaging of cell migration.** Real-time imaging of GFP-labelled PC3 cells was performed in poly-D-lysine-coated chamber cover glass slides (Lab-Tek). PC3 GFP cells were plated and allowed to adhere for 24 h. Wells were wounded with a P200 pipette tip. The chamber slides were imaged with an IX81 Olympus wide-field fluorescence microscope equipped with a CO<sub>2</sub> and temperature controlled chamber and time-lapse tracking system. Images from DIC and GFP channels were taken every 2 min and processed using ImageJ (<http://rsb.info.nih.gov/ij/>) and analysed for cell migration with Manual Tracking (<http://rsbweb.nih.gov/ij/plugins/track/track.html>), using local maximum centring correction to maintain a centroid xy coordinate for each cell per frame over time. Tracking data was subsequently processed with the Chemotaxis and Migration tool from ibidi ([http://www.ibidi.de/applications/ap\\_chemo.html](http://www.ibidi.de/applications/ap_chemo.html)) to create xy coordinate plots, velocity and distance measurements.

**Snail immunocytochemistry.** Appropriately transfected or treated PC3 cells were plated on a poly-L-lysine-coated chamber slide (Lab-Tek) and cultured for 48 h. Cells were fixed with 4% paraformaldehyde (EMS), rinsed with PBS and permeabilized with 0.1% Triton X-100. The samples were blocked in 5% goat serum and then incubated with anti-Snail antibody (Cell Signaling) in 5% goat serum for 2 h at room temperature. Cells were washed with PBS and incubated with Alexa 594 anti-mouse antibody (Invitrogen) and DAPI (Invitrogen) for 2 h at room temperature. Specimens were again washed with PBS and subsequently mounted with Aqua Poly/Mount (Polysciences). Image capture and quantification were completed as described below (see Immunofluorescence).

**Cap-binding assay.** PC3 4EBP1<sup>M</sup> cells were induced with doxycycline (1  $\mu\text{g ml}^{-1}$ , Sigma) for 48 h, then collected and lysed in buffer A (10 mM Tris-HCl pH 7.6, 150 mM KCl, 4 mM  $\text{MgCl}_2$ , 1 mM DTT, 1 mM EDTA, and protease inhibitors, supplemented with 1% NP-40). Cell lysates were incubated overnight at 4 °C with 50  $\mu\text{l}$  of the mRNA cap analogue m<sup>7</sup>GTP-sepharose (GE Healthcare) in buffer A. The beads were washed with buffer A supplemented with 0.5% NP-40. Protein complexes were dissociated using 1× sample buffer, and resolved by SDS-PAGE and western blotted with the appropriate antibodies.

**Pharmacological treatment of *Pten*<sup>L/L</sup> mice and MRI imaging.** Nine- and twelve-month-old *Pten*<sup>L/L</sup> mice were gavaged daily with either vehicle (see mouse xenograft study), RAD001 (10 mg  $\text{kg}^{-1}$ ; LC Laboratories), or INK128 (1 mg  $\text{kg}^{-1}$ ; Intellikine) for the indicated times. Weight measurements were taken every 3 days to monitor for toxicity. For the 28-day study, mice were imaged via MRI at day 0 and day 28 in a 14-T GE MR scanner (GE Healthcare).

**Prostate tissue processing.** Whole mouse prostates were removed from wild-type and *Pten*<sup>L/L</sup> mice, microdissected, and frozen in liquid nitrogen. Frozen

tissues were subsequently manually disassociated using a biopulverizer (Biospec) and additionally processed for protein and mRNA analysis as described above.

**Immunofluorescence.** Prostates and lymph nodes were dissected from mice within 2 h of the indicated treatment and fixed in 10% formalin overnight at 4 °C. Tissues were subsequently dehydrated in ethanol (Sigma) at room temperature, mounted into paraffin blocks, and sectioned at 5  $\mu\text{m}$ . Specimens were de-paraffinized and rehydrated using CitriSolv (Fisher) followed by serial ethanol washes. Antigen unmasking was performed on each section using Citrate pH 6 (Vector Labs) in a pressure cooker at 125 °C for 10–30 min. Sections were washed in distilled water followed by TBS washes. The sections were then incubated in 5% goat serum, 1% BSA in TBS for 1 h at room temperature. Various primary antibodies were used including those specific for keratin 5 (Covance), cytokeratin 8 (Abcam and Covance), YB1 (Abcam), vimentin (Abcam), MTA1 (Cell signaling), CD44 (BD Pharmingen) and the androgen receptor (Epitomics), which were diluted 1:50–1:500 in blocking solution and incubated on sections overnight at 4 °C. Specimens were then washed in TBS and incubated with the appropriate Alexa 488 and 594 labelled secondary (Invitrogen) at 1:500 for 2 h at room temperature with the exception of YB1 which was incubated with biotinylated anti-rabbit secondary (Vector) followed by incubation with Alexa 594 labelled Streptavidin (Invitrogen). A final set of washes in TBS was completed at room temperature followed by mounting with DAPI Hardset Mounting Medium (Vector Lab). A Zeiss Spinning Disc confocal (Zeiss, CSU-X1) was used to image the sections at 40×–100×. Individual prostate cells were quantified for mean fluorescence intensity (m.f.i.) using the Axiovision (Zeiss, Release 4.8) densitometric tool.

**Lymph node metastasis measurements.** Mouse lymph nodes were processed as described above and stained for CK8 and androgen receptor. Lymph nodes were imaged using a Zeiss AX10 microscope. Metastases were identified and areas were measured using the Axiovision (Zeiss, Release 4.8) measurement tool.

**Semi-quantitative RT-PCR.** Whole prostates were removed from wild-type and *Pten*<sup>L/L</sup> mice, microdissected, dissociated into single-cell suspension, and stained for epithelial cell markers as previously described<sup>40</sup> using fluorescence-conjugated antibodies for CD49f, Sca-1, CD31, CD45 and Ter119 (BD Biosciences). Luminal epithelial cells were sorted as previously described<sup>41</sup> using a FACS Aria (BD Biosciences). Cell pellets were re-suspended in 500  $\mu\text{l}$  TRIzol Reagent and RNA was isolated and transcribed into cDNA as described above. Semi-quantitative PCR analysis was performed using oligonucleotides for vimentin and  $\beta$ -actin at 200 nM in a 25  $\mu\text{l}$  reaction with 12.5  $\mu\text{l}$  GoTaq (Promega) for 32 and 33 cycles respectively, which were within the linear range (Supplementary Fig. 25f).

**Immunohistochemistry.** Immunohistochemistry was performed as described above (see immunofluorescence section) with the exception that immediately after antigen presentation and TBS washes, specimens were incubated in 3% hydrogen peroxide in TBS followed by TBS washes. The following primary antibodies were used: phospho-AKT<sup>S473</sup> (Cell Signaling), phospho-rpS6<sup>S240/244</sup> (Cell Signaling), phospho-4EBP1<sup>T37/46</sup> (Cell Signaling), phospho-histone H3 (Upstate), and cleaved caspase 3 (Cell Signaling). This was followed by TBS washes and incubation with the appropriate biotinylated secondary antibody (Vector Lab) for 30 min at room temperature. An ABC-HRP Kit (Vector Lab) was used to amplify the signal, followed by a brief incubation in hydrogen peroxide. The protein of interest was detected using DAB (Sigma). Specimens were counterstained with haematoxylin (Thermo Scientific), dehydrated with Citrisolv (Fisher), and mounted with Cytoseal XYL (Vector Lab).

**Haematoxylin and eosin staining.** Paraffin-embedded prostate specimens were deparaffinized and rehydrated as described above (see immunofluorescence section), stained with haematoxylin (Thermo Scientific), and washed with water. This was followed by a brief incubation in differentiation RTU (VWR) and two washes with water followed by two 70% ethanol washes. The samples were then stained with eosin (Thermo Scientific) and dehydrated with ethanol followed by CitriSolv (Fisher). Slides were mounted with Cytoseal XYL (Richard Allan Scientific).

**Oligonucleotides.** YB1 5' UTR cloning and site-directed mutagenesis oligonucleotides are as follows. YB1 5' UTR cloning: forward 5'-GCTACAAGCTTGGCTTATCCCGCCT-3', reverse 5'-TCGATCCATGGGGTTCGGGTGATGGT-3'; deletion (20–34): forward 5'-TGGGCTTATCCCGCCTGCTTCGATCGGTA GCGGGAGCG-3', reverse 5'-CGTCCCGCTACCGATCGAAGGACAGGCG GGATAAGCCCA-3'; transversion (20–34): forward 5'-TGGGCTTATCCCGCCTGCTCCGCGGTAAAGACGATCTTCGATCGGTAGCGGGAGCG-3', reverse 5'-CGTCCCGCTACCGATCGAAGATCGCTCTTACCGCGGACAGGCGGG ATAAGCCCA-3'.

Human qPCR oligonucleotides are as follows.  $\beta$ -actin forward 5'-GCAA AGACCTGTACGCCAAC-3', reverse 5'-AGTACTTGCCTCAGGAGGA-3'; CD44 forward 5'-CAACAACACAATGGCTGGT-3', reverse 5'-CTGAGGT GTCTGTCTCTTTCATCT-3'; vimentin forward 5'-GGCCAGCTGTAAAGT TGGA-3', reverse 5'-GGAGCGAGAGTGGCAGAG-3'; Snail1 forward

5'-CACTATGCCGCGCTCTTTC-3', reverse 5'-GCTGGAAGGTAAACTCTGATTAGA-3'; *Yb1* forward 5'-TCGCCAAAGACAGCCTAGAGA-3', reverse 5'-TCTGCGTCGGTAATTGAAGTTG-3'; *MTA1* forward 5'-CAAAGTGGTG TGCTTCTACCG-3', reverse 5'-CGGCCTTATAGCAGACTGACA-3'; *PLAU* forward 5'-TTGCTCACCACAACGACATT-3', reverse 5'-GGCAGGCAGATG GTCTGTAT-3'; *FGFBP1* forward 5'-ACTGGATCCGTGTGCTCAG-3', reverse 5'-GAGCAGGGTGAGGCTACAGA-3'; *ARID5B* forward 5'-TGGACTCAACT TCAAAGACGTTT-3', reverse 5'-ACGTTTCGTTTCTTCTCTCGTC-3'; *CTGF* forward 5'-CTCCTGCAGGCTAGAGAAGC-3', reverse 5'-GATGCACCTTTT TGCCCTTCTT-3'; *RND3* forward 5'-AAAAACTGCGCTGCTCCAT-3', reverse 5'-TCAAAACTGGCCGTGTAATTC-3'; *KLF6* forward 5'-AAAGCTC CCACTTGAAAGCA-3', reverse 5'-CCTTCCCATGAGCATCTGTAA-3'; *BCL6* forward 5'-TTCCGCTACAAGGGCAAC-3', reverse 5'-TGCAACGATA GGGTTTCTCA-3'; *FOXAI* forward 5'-AGGGCTGGATGGTTGTATTG-3', reverse 5'-ACCGGGACGGAGGAGTAG-3'; *GDF15* forward 5'-CCGGATAC TCACGCCAGA-3', reverse 5'-AGAGATACGCAGGTGCAGGT-3'; *HBPI* forward 5'-GCTGGTGGTGTGTCTGTG-3', reverse 5'-CATGTTATGGTGCT CTGACTGC-3'; *Twist1* forward 5'-CATCCTCACACCTCTGCATT-3', reverse 5'-TTCCTTTTCAGTGGCTGATTG-3'; *LEF1* forward 5'-CCTTGGTGAACGA GTCTGAAATC-3', reverse 5'-GAGGTTTGTGCTTGTCTGGC-3'; *rpS19* forward 5'-GCTGGCCAAACATAAAGAGC-3', reverse 5'-CTGGGTCTGAC ACCGTTTCT-3'; 5S rRNA forward 5'-GCCCGATCTCGTCTGATCT-3', reverse 5'-AGCCTACAGCACCCGGTATT-3'; firefly luciferase forward 5'-AATCAAAGAGGCGAACTGTG-3', reverse 5'-TTCGTCTTCGTCCCACT AAG-3'.

Mouse qPCR oligonucleotides are as follows.  $\beta$ -actin forward 5'-CTAAGG CCAACCGTGAAAAG-3', reverse 5'-ACCAGAGGCATACAGGGACA-3'; *Yb1* forward 5'-GGGTTACAGACCACGATTCC-3', reverse 5'-GGCGATACC GACGTTGAG-3'; vimentin forward 5'-TCCAGCAGCTTCCTGTAGGT-3',

reverse 5'-CCCTCACCTGTGAAGTGGAT-3'; *Cd44* forward 5'-ACAGTACCT TACCCACCATG-3', reverse 5'-GGATGAATCCTCGGAATTAC-3'; *Mta1* forward 5'-AGTGCGCCTAATCCGTGGTG-3', reverse 5'-CTGAGGATGAG AGCAGCTTTTCG-3'.

siRNA/shRNA sequences are as follows. Control (D-001810-01) 5'-UGGU UUACAUGUCGACUAA-3'; vimentin (L-003551) 5'-UCACGAUGACCUUG AAUAA-3', 5'-GGAAAUGGCUCGUCACCUU-3', 5'-GAGGGAAACUAAU CUGGAU-3', 5'-UUAAGACGGUUGAAACUAG-3'; *Yb1* (L-010213) 5'-CUG AGUAAAUGCCGGCUUA-3', 5'-CGACGCAGACGCCAGAAA-3', 5'-GUA AGGAACGGAUAUGGUU-3', 5'-GCGGAGGCAGCAAAUGUUA-3'; *MTA1* (L-004127) 5'-UCACGGACAUCAGCAAGA-3', 5'-GGACCAACCGCAG UAACA-3', 5'-GCAUCUUGUUGGACAUUU-3', 5'-CCAGCAUCAUUGA GUACUA-3'; *CD44* (L-009999) 5'-GAAUUAUACCUGCCGCUUU-3', 5'-CA AGUGGACUCAACGAGA-3', 5'-CGAAGAAGGUGUGGGCAGA-3', 5'- GAUCAACAGUGGCAAUGGA-3'; *4EBP1* (L-003005) 5'-CUGAUGGAGU GUCGGAACU-3', 5'-CAUCUAUGACCGAAAUC-3', 5'-GCAAUAGCCC AGAAGAUAA-3', 5'-GAGAUGGACAUUUAAAGCA-3'; *4EBP2* (L-018671) 5'-GCAGCUACCUCAGACUAU-3', 5'-GGAGGAACUCGAAUCAUUU- 3', 5'-GCAAUUCUCCCAUGGCUCA-3', 5'-UUGAACACUUGAACAA UC-3'; rictor (LL-016984) 5'-GACACAAGCACUUCGAUUA-3', 5'-GAAGAU UUAUUGAGUCCUA-3', 5'-GCGAGCUGAUGUAGAAUUA-3', 5'-GGGA AUACAACUCCAAAUA-3'; *PTEN* SH-003023-01-10 5'-GCTAAGAGAGGT TTCCGAA-3', SH-003023-02-10 5'-AGACTGATGTGTATACGTA-3'.

40. Lukacs, R. U., Goldstein, A. S., Lawson, D. A., Cheng, D. & Witte, O. N. Isolation, cultivation and characterization of adult murine prostate stem cells. *Nature Protocols* **5**, 702–713 (2010).

41. Lawson, D. A., Zong, Y., Memarzadeh, S., Xin, L., Huang, J. & Witte, O. N. Basal epithelial stem cells are efficient targets for prostate cancer initiation. *Proc. Natl Acad. Sci. USA* **107**, 2610–2615 (2010).



## AGEING

# Sorting out the sirtuins

Debates over the role of sirtuin proteins in ageing are maturing into functional assessments of the individual proteins. It seems that overexpression of a specific sirtuin can extend lifespan in male mice.

DAVID B. LOMBARD  
& RICHARD A. MILLER

Abraham Lincoln once said that God must have loved the common people because he made so many of them. Nature must feel the same way about the sirtuins, a large family of proteins that achieved celebrity status when one member was found to increase lifespan in yeast<sup>1</sup>. But are the mammalian sirtuins the rock stars of an ensemble of anti-ageing proteins, or merely members of the entourage? The original model, proposed in about 2005, that sirtuins have broadly evolutionarily conserved roles in promoting longevity *per se* is now being refined through more detailed functional investigations of each sirtuin<sup>2</sup>. In a paper published on *Nature's* website today, Kanfi *et al.*<sup>3</sup> follow this trend by reporting that overexpression of a sirtuin called SIRT6 leads to a modest extension of lifespan in male, but not female, mice.

Does an extension of lifespan imply an effect on ageing? Not necessarily: interventions unrelated to ageing, such as giving insulin to a person with type I diabetes, can increase mean and maximal lifespan. The lifespan extension observed by Kanfi and colleagues in SIRT6-overexpressing male mice could be explained, at least partially, by SIRT6 acting as a tumour suppressor. Because male mice have a higher incidence of spontaneous cancer than female mice (incidences of 81% and 50%, respectively, were observed in this study), an anticancer protein (perhaps SIRT6?) would have a larger effect on lifespan in males than in females.

Proving that a lifespan-increasing intervention indeed acts by delaying ageing processes is not a simple matter. For example, acceptance of the idea that lifespan extension by caloric restriction (a diet with reduced calorie intake) reflects a genuine deceleration of ageing emerged gradually from evidence<sup>4</sup> that restriction slows age-related changes in the properties of proliferative and non-proliferative cells in many tissues, and does so in multiple organ systems. Similar cases are

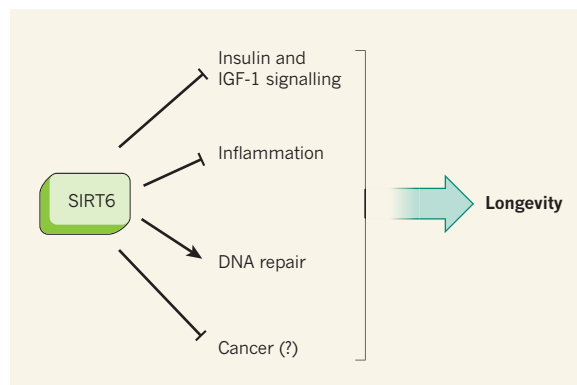


**Figure 1 | Potential mechanisms of action of SIRT6 on longevity.** Several reports<sup>7,10–12</sup> have demonstrated effects of the sirtuin protein SIRT6 on the activities of the hormones insulin and IGF-1, as well as on inflammation and DNA repair. These effects, together with a possible delay in cancer progression, could contribute to the increased lifespan in SIRT6-overexpressing male mice reported by Kanfi and colleagues<sup>3</sup>.

being constructed by researchers proposing that dwarf mice could act as models for slowed ageing<sup>5</sup>.

Reports of lifespan increases in mutant or drug-treated mice, particularly studies in which the observed effects are modest, often prove difficult for other laboratories to repeat. This is presumably due to subtle but crucial variations in the animals' diet or genetic background, or in husbandry practices<sup>6</sup>. Moreover, the preference for publication of positive over negative findings inevitably inserts a smattering of false positive results into the literature, and these can be identified only by attempts to replicate experiments. One strength of Kanfi and colleagues' paper<sup>3</sup> is that SIRT6 overexpression increased male lifespan in each of two groups of mice, which were derived from two different founder animals. However, the test for maximal lifespan — usually taken as stronger evidence than an effect on median longevity alone — reached statistical significance in only one of the two mouse groups. If the longevity effect seen by the authors proves robust, determining whether SIRT6 overexpression does indeed slow ageing will still require follow-up studies analysing a wide range of age-sensitive endpoints.

In their article, Kanfi and colleagues

include some observations hinting at potential mechanisms by which SIRT6 overexpression might affect the lifespan of male mice. Compared with their normal counterparts, SIRT6-overexpressing males had modestly reduced serum levels of the hormone IGF-1, and the signalling activity of IGF-1 receptors was weaker in peri-gonadal fat tissue in males but not in females. Previous reports have found that SIRT6 attenuates intracellular signalling initiated by IGF-1 and insulin<sup>7</sup>. Furthermore, dramatic deficits in IGF-1 and/or growth hormone (GH, which stimulates IGF-1 secretion) lead to slower ageing and increased lifespan in at least four varieties of mutant mouse<sup>6</sup>. And mutations in the gene encoding the GH receptor in humans are associated with strong protection against diabetes and cancer<sup>8</sup>.

So, it is plausible that SIRT6 overexpression in mice might work through blunting of the GH/IGF-1 pathway. Evidence<sup>9</sup> that rat longevity can be augmented by surgical removal of intra-abdominal — but not subcutaneous — fat has begun to focus attention on metabolic and hormonal effects on specific fat depots as potential levers for pharmacological control of ageing.

It is noteworthy that the effects of SIRT6 overexpression reported by Kanfi *et al.*<sup>3</sup> are seen only in male mice. Previous results<sup>6</sup>, by contrast, indicate that mutations in components of the GH/IGF-1 pathway usually have greater effects on longevity in female mice. This apparent discrepancy might be explained by differences between the mice in terms of underlying disease proclivities, levels of sex-specific hormones, inter-animal conflict or fat-tissue biology, leading to gender-specific responses to mutations, drugs and nutritional interventions. Working out the basis for these sex-specific interactions should provide clues to the mechanisms involved in these anti-ageing manipulations, and perhaps even help to answer the vexing question of why women tend to live longer than men.

SIRT6 has other roles that could foster longer lifespan (Fig. 1). It promotes chromosomal stability by several mechanisms, and

above-normal SIRT6 expression increases the efficiency of DNA repair<sup>10</sup>. SIRT6 also reduces the expression of genes regulated by the NF- $\kappa$ B and HIF-1 $\alpha$  proteins, which have roles in inflammation, cancer and, potentially, longevity<sup>11,12</sup>. It will be of interest to assess these aspects of SIRT6's function in mice overexpressing the protein, and to test more definitively whether they contribute to protection against cancer and promotion of longevity.

The recent spate of activity in sirtuin research, now supplemented by the present work, supports the case for placing the sirtuins on the front line of ageing research, sitting

cheek by jowl with other promising contestants, such as the proteins TOR, FoxO, AMPK, NRF2 and ATF4. To paraphrase Winston Churchill, the discoveries of Kanfi *et al.* do not by any means represent the end of sirtuin research, nor even the beginning of the end. But they are, perhaps, the end of the beginning. ■

**David B. Lombard and Richard A. Miller**  
are in the Department of Pathology and the Geriatrics Center, University of Michigan School of Medicine, Ann Arbor, Michigan 48100-2200, USA.  
e-mails: davidlom@umich.edu;  
millerr@umich.edu

1. Kaeberlein, M., McVey, M. & Guarente, L. *Genes Dev.* **13**, 2570–2580 (1999).
2. Finkel, T., Deng, C.-X. & Mostoslavsky, R. *Nature* **460**, 587–590 (2009).
3. Kanfi, Y. *et al.* *Nature* <http://dx.doi.org/nature10815> (2012).
4. Weindruch, R. & Sohal, R. S. *N. Engl. J. Med.* **337**, 986–994 (1997).
5. Bartke, A. *Phil. Trans. R. Soc. Lond. B* **366**, 28–34 (2011).
6. Ladiges, W. *et al.* *Aging Cell* **8**, 346–352 (2009).
7. Xiao, C. *et al.* *J. Biol. Chem.* **285**, 36776–36784 (2010).
8. Guevara-Aguirre, J. *et al.* *Sci. Transl. Med.* **3**, 70ra13 (2011).
9. Muzumdar, R. *et al.* *Aging Cell* **7**, 438–440 (2008).
10. Mao, Z. *et al.* *Science* **332**, 1443–1446 (2011).
11. Kawahara, T. L. A. *et al.* *Cell* **136**, 62–74 (2009).
12. Zhong, L. *et al.* *Cell* **140**, 280–293 (2010).